Advances in Experimental Medicine and Biology 1293

Hiromu Yawo
Hideki Kandori
Amane Koizumi
Ryoichiro Kageyama *Editors*

# Optogenetics

## Light-Sensing Proteins and Their Applications in Neuroscience and Beyond

*Second Edition*

Springer

# Advances in Experimental Medicine and Biology

Volume 1293

*Advances in Experimental Medicine and Biology* provides a platform for scientific contributions in the main disciplines of the biomedicine and the life sciences. This series publishes thematic volumes on contemporary research in the areas of microbiology, immunology, neurosciences, biochemistry, biomedical engineering, genetics, physiology, and cancer research. Covering emerging topics and techniques in basic and clinical science, it brings together clinicians and researchers from various fields.

*Advances in Experimental Medicine and Biology* has been publishing exceptional works in the field for over 40 years, and is indexed in SCOPUS, Medline (PubMed), Journal Citation Reports/Science Edition, Science Citation Index Expanded (SciSearch, Web of Science), EMBASE, BIOSIS, Reaxys, EMBiology, the Chemical Abstracts Service (CAS), and Pathway Studio.

2019 Impact Factor: 2.450 5 Year Impact Factor: 2.324

More information about this series at http://www.springer.com/series/5584

Hiromu Yawo • Hideki Kandori
Amane Koizumi • Ryoichiro Kageyama
Editors

# Optogenetics

## Light-Sensing Proteins and Their Applications in Neuroscience and Beyond

Second Edition

Springer

*Editors*
Hiromu Yawo
The Institute for Solid State Physics
The University of Tokyo
Kashiwa, Japan

Hideki Kandori
OptoBioTechnology Research Center
Nagoya Institute of Technology
Nagoya, Japan

Amane Koizumi
National Institutes of Natural Sciences
Tokyo, Japan

Ryoichiro Kageyama
Institute for Frontier Life
and Medical Sciences
Kyoto University
Kyoto, Japan

ISSN 0065-2598 ISSN 2214-8019 (electronic)
Advances in Experimental Medicine and Biology
ISBN 978-981-15-8762-7 ISBN 978-981-15-8763-4 (eBook)
https://doi.org/10.1007/978-981-15-8763-4



This Springer imprint is published by the registered company Springer Nature Singapore Pte Ltd.
The registered company address is: 152 Beach Road, #21-01/04 Gateway East, Singapore 189721, Singapore

# Preface

Optogenetics is a fast-growing field involving the invention and use of molecules that are genetically expressed in cells, and then either reporting on the cellular physiology in optical form, or enabling the control of specific pathways in cells actuated by light. Optogenetics has several advantages over conventional stimulation/recording methods: higher spatiotemporal resolution, parallel stimulations/recordings at multiple sites, less invasiveness and greater convenience. Light-sensing proteins of various living organisms are now available for exogenous expression in neurons and other target cells both in vivo and in vitro. Cellular functions such as the membrane potential and the gene expression can thus be manipulated or probed by light. In 2010, optogenetics was chosen as the Method of the Year (MOTY) across all fields of science and engineering by the interdisciplinary research journal *Nature Methods*.

The twenty-first century should become "the era of life sciences." Various biological sciences are now growing with new techniques such as gene editing techniques and regenerative medicine. On the other hand, "the era of light" is just beginning. People have begun to learn how to manipulate light just as our ancestors learned to handle fire over 500 thousand years ago. A revolution of science and technology is now under way in optogenetics, integrating biological systems, such as brain, and the optical systems, such as optoelectronics devices, using light as the link. Since optogenetics is borderless, it has interactions with a variety of fields. It will grow together with the progress of basic technologies and soon make important contributions to human life and society.

Since the publication of the first edition of our book, *Optogenetics: Light-sensing proteins and their applications*, rapid progress has been made in various directions, including physical, chemical, and biological topics of light-sensing proteins, their application in biological systems, particularly in neuroscience and medicine, and the optical sciences. What used to be only a dream has already been realized. Indeed, the number of related publications increased to over 3400 (360 reviews) in these 5 years, whereas it was 1328 before December 2014 (188 reviews) (Web of Science). This makes it difficult for people, particularly for young students, or even for the experts to learn the principles as well as the current progress of this multidisciplinary science. We thus include the state-of-the-art topics in each discipline as well as the basic knowledge in the second edition, which consists of six parts: "I. Light-

Sensitive Channels and Transporters," "II. Light-Sensitive Signaling Molecules," "III. Optogenetics in Biological Systems," "IV. Optogenetics in Neuroscience," "V. Medical Optogenetics," and "VI. Opto-electro-nano Technologies for Optogenetics."

In Part I, Hideki Kandori provides an overview of the molecular mechanisms of ion transport by rhodopsins, which are most frequently used as light-sensitive actuator molecules (Chap. 1). Ken-ichi Wakabayashi and his colleagues provide the biological background by which channelrhodopsins regulate the algal behavior (Chap. 2). Hideaki E. Kato discusses the molecular dynamics involved in ion transport (Chap. 3). Takashi Kikukawa reviews the variation and functional mechanisms of $Cl^-$ pumps (Chap. 4). Hisao Tsukamoto and Yuji Furukawa present topics concerned with ion channel modulation via light-dependent G-protein activation (Chap. 5). Next, Keiichi Inoue gives us an extensive review and perspectives on the ion-pumping functions by various rhodopsins (Chap. 6).

The light-dependent manipulation of intracellular signaling mechanisms is another target of optogenetics. In Part II, Mineo Iseki and Sam-Yong Park provide an overview of recent progress in photoactivated adenylyl cyclases as well as their pioneering work in this area (Chap. 7). Akihisa Terakita and his colleagues give an overview of animal rhodopsins as tools to regulate G-protein-coupled signaling cascades by light (Chap. 8). Satoshi P. Tsunoda and his colleagues address topics on the rhodopsins with enzymatic activities and discuss their potential applications (Chap. 9). Keiji Fushimi and Rei Narikawa review the molecular mechanisms and applications of the linear tetrapyrrole-binding photoreceptors, such as phytochromes and cyanobacteriochromes (Chap. 10), whereas Tatsuya Iwata and Shinji Masuda summarize the current understanding of the photoactivation mechanisms of flavoprotein photoreceptors and discuss their applications (Chap. 11).

How are these optogenetic tools applied in living organisms? Several examples are included in Part III. Thomas Knöpfel and his colleagues provide an outline of the genetically encoded voltage indicators (GEVIs) with their development and imaging technologies (Chap. 12). Kazuhiro Aoki and his colleagues address topics on the visualization and manipulation of intracellular signaling (Chap. 13), Akihiro Isomura on optogenetic systems that enable the investigation of the dynamic control of gene expression patterns in mammalian cells (Chap. 14), and Mizuki Endo and Takeaki Ozawa on recent advances in the optogenetic tools that modulate the function of a receptor protein involved in chemical transduction or mechano-transduction (Chap. 15). On the other hand, Takeharu Nagai and his colleagues discuss another approach to inactivate the signaling molecules by light (Chap. 16). Ken Berglund and his colleagues review new methods for activating optogenetic tools using bioluminescence (Chap. 17). Hideji Murakoshi introduces 2-photon fluorescence lifetime imaging microscopy (2pFLIM) and its applications. Optogenetics has been applied and will continue to be applied in various animal models: mice, rats, flies (Chap. 19 by Hiroshi Kohsaka and Akinao Nose), nematodes (Chap. 20 by Yuki Tsukada and

Ikue Mori), zebrafish (Chap. 21 by Wataru Shoji), and nonhuman primates (Chap. 22 by Ken-ichi Inoue and his colleagues). Non-neural cells, such as muscle cells, stem cells (Chap. 23 by Hiromu Yawo and his colleagues), and cardiac cells (Chap. 24 by Callum M. Zgierski-Johnston and Franziska Schneider-Warme) are also targets for optogenetics.

Optogenetics has contributed to a revolution in neuroscience by enabling investigations of the network activity underlying a neural function. In Part IV, Tomomi Tsunematsu reviews optogenetics analyses on how neural activities regulate an animal's behavior such as sleep/wakefulness (Chap. 25). Srikanta Chowdhury and Akihiro Yamanaka address topics on the near-infrared light optogenetics for free-moving animals (Chap. 26). Nao Chuhma covers the functional connectomics to map the network dynamics (Chap. 27). Takashi Kitamura and his colleagues summarize conceptual advancements in the neurobiology of learning and memory made by technological improvements in optogenetics (Chap. 28). Optogenetics is also useful for investigating how a neural rhythm such as the respiratory rhythm is regulated (Chap. 29 by Hiroshi Onimaru and Keiko Ikeda) and how a visceral function such as the cardiac rhythm is neurally regulated (Chap. 30 by Toya Okonogi and Takuya Sasaki). Optogenetics is a powerful tool for investigating the neural dynamics underlying neural functions, particularly when combined with other neurophysiological methods such as an endoscope imaging system (Chap. 31 by Makoto Osanai and his colleagues), opto-electrical silicon probes (Chap. 32 by Tetsu Tanaka and his colleagues), behavioral virtual reality systems (Chap. 33 by Norihiro Katayama and his colleagues), and mathematical analyses of oscillatory neural activities (Chap. 34 by Hajime Mushiake and his colleagues).

Optogenetics has potential of medical applications (Part V), as described by Toshihiro Kushibiki (Chap. 35). Toru Takumi and his colleagues review optogenetics studies on neural dysfunctions such as autism spectrum disorders (Chap. 36). Currently, an optogenetic retinal prosthesis for the loss of vision is approaching clinical application (Chap. 37 by Hiroshi Tomita and Eriko Sugano; Chap. 38 by Qi Lu and Zhuo-Hua Pan). Shin-ichiro Osawa and Teiji Tominaga present topics concerning optogenetics for epilepsy research.

Part VI includes a discussion on how to overcome such difficulties as delivering light deeply with spatiotemporal patterning. Massimo De Vittorio and Ferruccio Pisanello provide an overview of various methods using optical fibers (Chap. 40). Takashi Tokuda and his colleagues address topics on the neural interface with patterned inputs/outputs (Chap. 41). Makoto Sekino introduces soft and wide-area light sources and their potential applications (Chap. 42). Weijian Yang and Rafael Yuste present the principles and applications of holographic microscopy, which enables all-optical interrogation of neural activity in 3D (Chap. 43). Finally, Xiaogang Liu and his colleagues interpret upconversion optogenetics from fundamental physics and fabrication chemistry to neurophysiological applications (Chap. 44).

This book should be a treasure for many readers, from beginners to experts. In every chapter, you will find new ideas, concepts, and methods. As with the first edition, this second edition should be a milestone indicating the development, expansion, and future direction of this wonderful science, optogenetics.

Kashiwa, Japan — Hiromu Yawo
Nagoya, Japan — Hideki Kandori
Tokyo, Japan — Amane Koizumi
Kyoto, Japan — Ryoichiro Kageyama

# Contents

# Part I

# Light-Sensitive Channels and Transporters

# History and Perspectives of Ion-Transporting Rhodopsins

1

Hideki Kandori

**Abstract**

The first light-sensing proteins used in optogenetics were rhodopsins. The word "rhodopsin" originates from the Greek words "rhodo" and "opsis," indicating rose and sight, respectively. Although the classical meaning of rhodopsin is the red-colored pigment in our eyes, the modern meaning of rhodopsin encompasses photoactive proteins containing a retinal chromophore in animals and microbes. Animal and microbial rhodopsins possess 11-*cis* and all-*trans* retinal, respectively, to capture light in seven transmembrane α-helices, and photoisomerizations into all-*trans* and 13-*cis* forms, respectively, initiate each function. We are able to find ion-transporting proteins in microbial rhodopsins, such as light-gated channels and light-driven pumps, which are the main tools in optogenetics. In this chapter, historical aspects and molecular properties of rhodopsins are introduced. In the first part, "what is rhodopsin?", general introduction of rhodopsin is presented. Then, molecular mechanism of bacteriorodopsin, a light-driven proton pump and the best-studied microbial rhodopsin, is described. In the section of channelrhodopsin, the light-gated ion channel, molecular properties, and several variants are introduced. As the history has proven, understanding the molecular mechanism of microbial rhodopsins is a prerequisite for useful functional design of optogenetics tools in future.

**Keywords**

Animal rhodopsin · Microbial rhodopsin · Retinal · Photoisomerization · Pump · Channel · Photocycle · Proton transfer · Hydrogen bond · Structural change

## Abbreviations

| | |
|---|---|
| ACR | Anion channel rhodopsin |
| Arch | Archaerhodopsin 3 |
| ASR | Anabaena sensory rhodopsin |
| BR | Bacteriorhodopsin |
| ChR | Channelrhodopsin |
| CP | Cytoplasmic |
| EC | Extracellular |
| GPCR | G-protein-coupled receptors |
| GtCCR4 | Cation channel rhodopsin from *Guillardia theta* |
| HeR | Heliorhodopsin |
| HR | Halorhodopsin |
| PoXeR | Rhodopsin from *Parvularcula oceani* |
| Rh-GC | Light-activated guanylyl cyclase rhodopsin |

H. Kandori (✉)
Department of Life Science and Applied Chemistry & OptoBioTechnology Research Center, Nagoya Institute of Technology, Nagoya, Japan
e-mail: kandori@nitech.ac.jp



H. Yawo et al. (eds.), *Optogenetics*, Advances in Experimental Medicine and Biology 1293,
https://doi.org/10.1007/978-981-15-8763-4_1

| | |
|---|---|
| Rh-PDE | Light-activated phosphodiesterase rhodopsin |
| RSB | Retinal Schiff base |
| SRI | Sensory rhodopsin I |
| SRII | Sensory rhodopsin II |

## 1.1 What Is Rhodopsin?

The word "rhodopsin" originates from the Greek words "rhodo" and "opsis," which indicate rose and sight, respectively. Thus, the classical meaning of rhodopsin is the red-colored pigment in the retinal rods of eyes. The chromophore molecule that absorbs light is retinal, which is the origin of red color. Retinal, the aldehyde of vitamin A, is derived from β-carotene and is bound to the protein in the shape of 11-*cis* forms (Fig. 1.1) (Shichida and Matsuyama 2009; Hofmann et al. 2009; Palczewski 2012; Koyanagi and Terakita 2014; Ernst et al. 2014). Then, similar colored retinal-binding proteins were found in microbes, largely expanding the definition of the word rhodopsin (Lanyi 2004; Grote et al. 2014; Brown 2014; Ernst et al. 2014; Inoue et al. 2015; Govorunova et al. 2017). In case of microbial rhodopsins, all-*trans* retinal is bound to the protein (Fig. 1.1). The modern meaning of rhodopsin encompasses photoactive proteins containing a retinal chromophore in animals and microbes (Ernst et al. 2014). Rhodopsins are now found in all domains of life and are classified into two groups. While lower organisms utilize the family of microbial rhodopsins for various functions including light-driven ion pump and light-gated ion channel, animals use the photosensory functions of a different family of rhodopsins (animal rhodopsin), a specialized subset of G-protein-coupled receptors (GPCRs). Microbial and animal rhodopsins share a common architecture of seven transmembrane α-helices (TM1–7) with the N- and C-terminus facing outwards from and inside of the cell, respectively, but have almost no sequence homology and differ largely in their functions (Fig. 1.2a) (Ernst et al. 2014). Retinal is attached by a Schiff base linkage to the ε-amino group of a lysine side chain in the middle of the seventh helix, and this retinal Schiff base (RSB) is protonated ($RSBH^+$) in most cases (Fig. 1.1).

In this chapter, I introduce ion-transporting rhodopsins as they were first used in optogenetics. In living cells, the lipid bilayer effectively repels electrically charged ions that the cell must transport in order to live. Transport of ions is carried out by ion-transporting proteins, which are classified into two types (Fig. 1.2b) (Kandori et al. 2018). In ion channels, ion transport is bidirectional and dissipates energy, leading to a decrease in the ion's electrochemical potential (free energy). The second type, ion pumps, gains free energy of the system by ion transport, for which energy input is a prerequisite. This is the ion pump. Ion pathways are necessary for both channels and pumps, and each pathway is fully connected between both sides of the membrane when the channel is open. The process by which a channel is opened and closed is referred to as "gating" in this field of study, and channels need at least one gate (Fig. 1.2b) (Hille 1984). A lot of ions are transported upon opening of the gate. For pumps, in contrast, ion pathways cannot be fully connected at one time between both sides of the membrane because the formed ion gradient will easily collapse. This is an important aspect when distinguishing pumps from channels. In other words, pumps require at least two gates, whose regulated opening requires energy input (Fig. 1.2b). To explain complex mechanism of ion pumps, alternating access model and Panama Canal model are used, where transported ion (s) are bound in the resting state (Tanford 1983; Kandori et al. 2018). Only the bound ion(s) are transported during the activation cycle, and consequently, much less ions can be transported in pumps than in channels.

Microbial rhodopsins were first found in the Archaea (*Halobacterium salinarum*) (Oesterhelt and Stoeckenius 1971) and were therefore initially termed archaeal rhodopsins. *H. salinarum* contains bacteriorhodopsin (BR) (Oesterhelt and Stoeckenius 1971) and halorhodopsin (HR) (Matsuno-Yagi and Mukohata 1977) that act as a light-driven outward proton pump or an inward $Cl^-$ ion pump, respectively. BR and HR contribute to the formation of

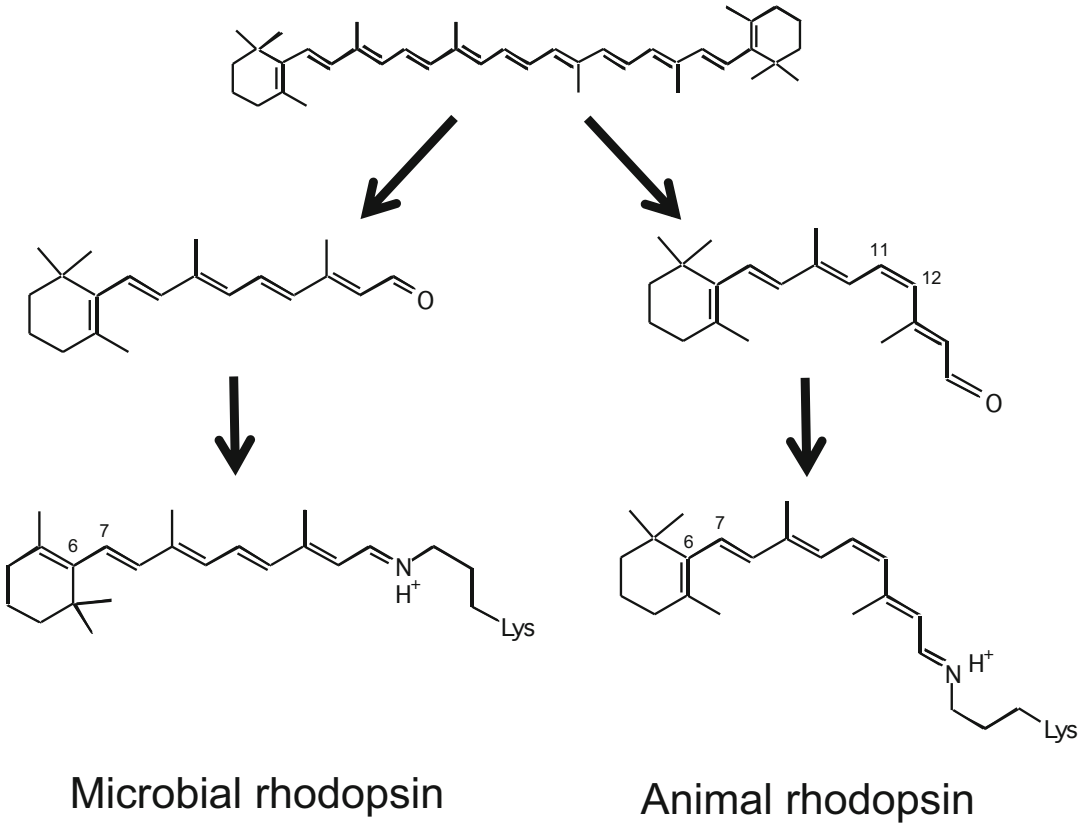


**Fig. 1.1** Chromophore molecules of microbial (left) and animal (right) rhodopsins. β-Carotene (top) is the source of the chromophore, and all-*trans* and 11-*cis* retinal are bound to protein to form microbial and animal rhodopsins, respectively

a membrane potential and thus function in light-energy conversion. The two other *H. salinarum* rhodopsins are sensory rhodopsins I and II (SRI and SRII) (Spudich and Bogomolni 1984; Jung et al. 2003), which act as positive and negative phototaxis sensors, respectively. For the first 30 years since the early 1970s, microbial rhodopsins were epitomized by haloarchaeal proteins, the first-discovered and best-studied light-driven proton pump BR and its close relatives (HR, SRI, and SRII). However, over the past 15 years, thousands of related photoactive proteins with similar or different functions were identified in *Archaea*, *Eubacteria*, and *Eukaryota* (Brown 2014; Govorunova et al. 2017). Since the original discovery of BR in *H. salinarum*, similar rhodopsins have been found in *Eubacteria* and lower *Eukaryota*, and they are now called microbial rhodopsins. Channelrhodopsins (ChRs), another group of microbial rhodopsins, were discovered in green algae where they function as light-gated cation channels within the algal eye to depolarize the plasma membrane upon light absorption (Fig. 1.2) (Nagel et al. 2002, 2003). Thus, ChRs naturally function as signaling photoreceptors as well. Discovery of ChR led to the emergence of a new field, optogenetics (Miesenbock 2011), in which light-gated ion channels and light-driven ion pumps are used to depolarize and hyperpolarize selected cells of neuronal networks. This new method is highly expected to understand the circuitry of the brain (Deisseroth 2011; Diester et al. 2011).

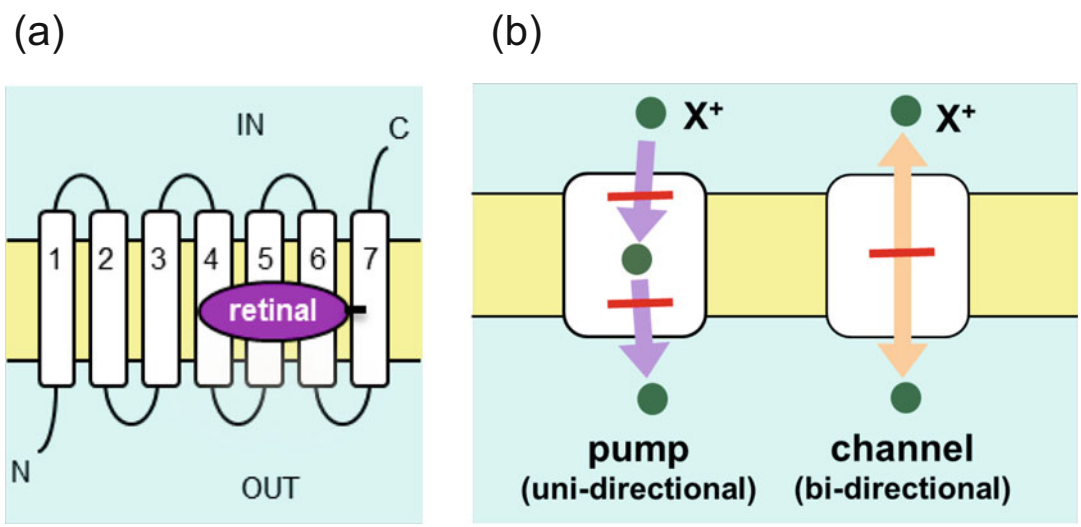


**Fig. 1.2** (**a**) Architecture of rhodopsins. In the rhodopsin field, by convention the cytoplasmic and extracellular sides are drawn at the upper and lower sides of figure, respectively, which is opposite to the conventional drawing of membrane proteins such as G-protein-coupled receptors and transporters. (**b**) Ion transports of ion pump and channel are unidirectional and bidirectional, respectively

It should be noted that microbial rhodopsins are used in optogenetics in which animal brain functions are studied by incorporating microbial rhodopsins, but not animal rhodopsins, into the animal brain. There are three reasons for this. One is the isomeric structure of the chromophore. An 11-*cis* retinal (Fig. 1.1), the chromophore molecule of animal rhodopsins, is not generally abundant in animal cells. In contrast, endogenous all-*trans* retinal, the chromophore molecule of microbial rhodopsins, is sufficient for optogenetics in animal cells. The second reason is "bleaching." Upon light absorption, animal and microbial rhodopsins exhibit retinal isomerization from the 11-*cis* to all-*trans*, and all-*trans* to 13-*cis* forms, respectively (Fig. 1.3). While the isomerization reaction initiates each function, the end of the photoreaction differs between animal and microbial rhodopsins. The isomerized all-*trans* retinal is released in our visual pigments and does not return to the 11-*cis* form, and is thus called "photobleaching" (Fig. 1.3) (Ernst et al. 2014). This is not a problem in human visual cells because enzymatically isomerized 11-*cis* retinal is newly supplied, but this is not the case in other animal cells. In contrast, the 13-*cis* form is thermally isomerized into the all-*trans* form, and the spontaneous return is termed the "photocycle" in microbial rhodopsins (Fig. 1.3). The third reason is that ion-transporting properties of light-gated ion channels and light-driven ion pumps enable the direct manipulation of membrane potentials of selected cells in neuronal networks without additional elements. Due to the existence of naturally abundant all-*trans* retinal and its photocycle feature, ion-transporting microbial rhodopsins have become a tool in optogenetics.

## 1.2 Bacteriorhodopsin, the First Ion Transport by Light

BR from *H. salinarum*, the first-discovered microbial rhodopsin in 1971 (Oesterhelt and Stoeckenius 1971), is the first membrane protein whose structure was found to be composed of seven helices by electron microscopy (Henderson and Unwin 1975), and was also the first membrane protein to have its amino acid sequence determined (Khorana et al. 1979). As the best-studied microbial rhodopsin, it serves as a paradigm of a light-driven retinal-binding ion pump

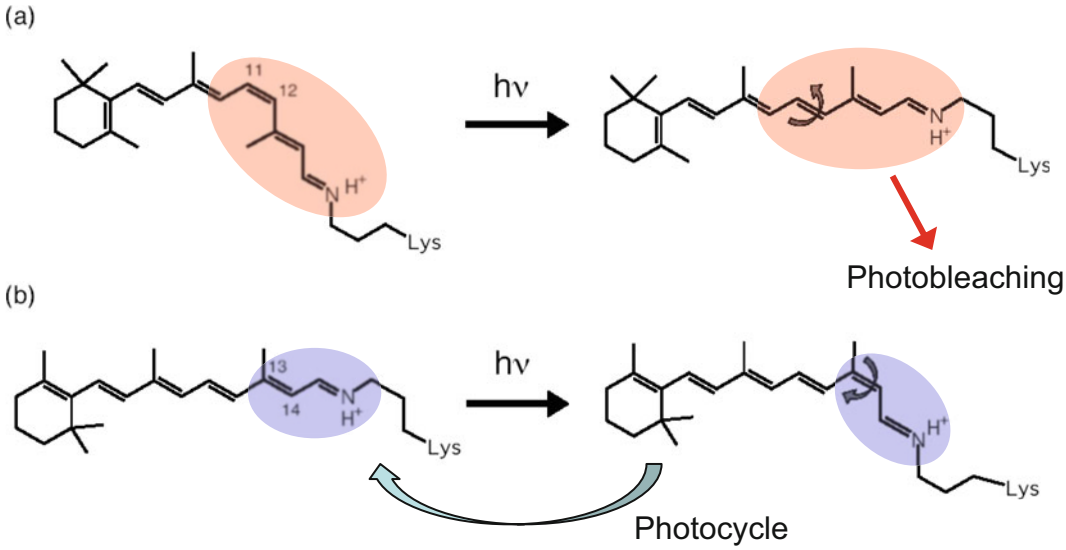


**Fig. 1.3** Photoreactions in animal (**a**) and microbial (**b**) rhodopsins. Photoisomerizations from the 11-*cis* to the all-*trans* form and from the all-*trans* to the 13-*cis* form are the primary reactions in animal and microbial rhodopsins, respectively

and aids in studies of novel rhodopsins (Lanyi 2004; Ernst et al. 2014). Archaerhodopsin 3 (Arch), a homologous proton-pump protein, is the best used in optogenetics as a neural silencer (Chow et al. 2010), sharing 58% amino acid identity with BR. Similar molecular mechanisms were assumed for the light-dependent ion transport function between Arch and BR.

Figure 1.4 illustrates the overall structure of BR, highlighting the conserved aromatic amino acids with an important function. The retinal-binding pocket is the most conserved common element of the structure. Strongly conserved Trp86 and Trp182 constitute an important part of the chromophore binding site by sandwiching all-*trans*-retinal vertically (Fig. 1.4). The presence of these bulky groups possibly determines the isomerization pathway from the all-*trans* to the 13-*cis* form (Gozem et al. 2017). Moreover, the interaction of photoisomerized retinal with Trp182 may serve as the mechanical transducer for passing the energy stored in retinal deformation into the functionally important changes of the helical tilts necessary for function (Weidlich et al. 1996). Another important position occupied by aromatic amino acids in the retinal-binding pocket is that of Tyr185 in BR (Fig. 1.4), which participates in hydrogen-bonding stabilization of the Schiff base counterion for many rhodopsins. This is replaced by a Phe in ChRs, suggesting that the lack of a hydrogen-bonding interaction at this position is important for channel function.

In addition to the aromatic sidechain rings, electrostatic and hydrogen-bonding interactions in the proximal part of retinal are crucial in defining the functionality of microbial rhodopsins (Lanyi 2004; Ernst et al. 2014). The sidechain of BR Lys216 (or its homologs in other microbial rhodopsins) forms a covalent bond with the retinal molecule through the Schiff base (Fig. 1.1). Since the Schiff base is usually protonated, Lys216 and super-conserved Arg82 of helix C in BR provide two positive charges within the protein (Fig. 1.5), which requires two negative charges for electrostatic stabilization. This dictates the most common configuration of the Schiff base counterions made by two carboxylic acids (Asp85 and Asp212 in BR), which are perfectly conserved for proton-pumping microbial rhodopsins (Fig. 1.5) (Ernst et al. 2014; Kandori 2015).

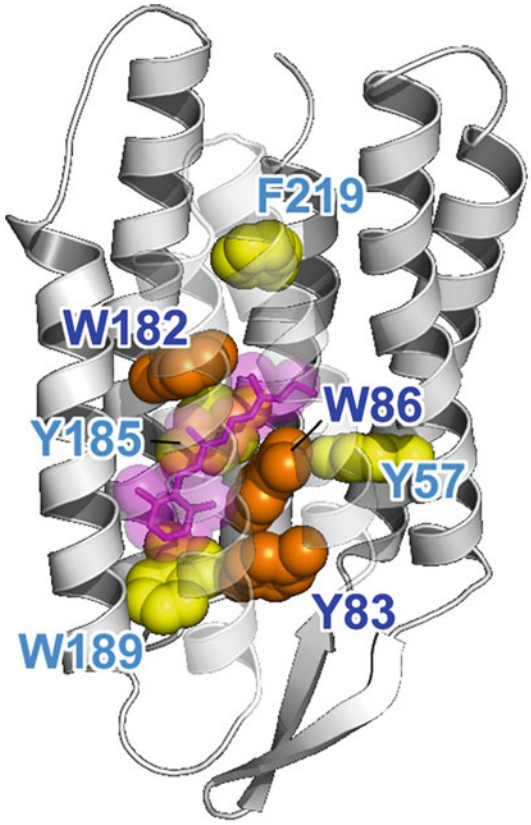


**Fig. 1.4** Structure of bacteriorhodopsin (BR) with conserved aromatic residues (PDB: 1QM8). Tyr83, Trp86, and Trp182 are strongly conserved among microbial rhodopsins (orange). Aromatic residues are strongly conserved at the Tyr185, Trp189, and Phe219 positions (yellow). In BR, Trp86, Trp182, Tyr185, and Trp189 constitute the chromophore binding pocket for all-*trans* retinal (red)

The proton pathway across the membrane from the cytoplasmic to the extracellular side in BR is shown in Fig. 1.6, together with protonatable groups and the order of respective proton transfers (Kandori 2015; Gerwert et al. 2014). A summary of the photocycle is shown in Fig. 1.7, which illustrates key intermediate states for most microbial rhodopsins. Although the photocycle of BR contains six intermediates, namely J, K, L, M, N, and O states that are named alphabetically, only three states (K, M, and N) are shown in Fig. 1.7 to show the mechanism clearly. After light absorption, photoisomerization occurs from the all-*trans*- to 13-*cis*-form in $10^{-13}$ s (Ernst et al. 2014; Gozem et al. 2017). The ultrafast retinal isomerization yields the formation of red-shifted J and K intermediates in which J is the precursor of the K state. As the protein cavity, which accommodates retinal, cannot change its shape promptly, the K intermediate contains twisted 13-*cis* retinal and an altered hydrogen-bonding network in the Schiff base region, which yield higher free energy in K than in the original state. This leads to subsequent protein structural changes that accompany relaxation.

In the case of BR, relaxation of the K intermediate leads to the formation of the blue-shifted L intermediate. For proton-pumping (and some of the photosensory) rhodopsins, the L intermediate serves as the precursor of the proton transfer reaction from the Schiff base to its primary carboxylic proton acceptor, by which the M intermediate is formed. This is a key step in proton transport. Since the M intermediate has a deprotonated 13-*cis* chromophore, it exhibits a characteristically strong blue-shifted absorption ($\lambda_{max}$ at 360–410 nm), and is well isolated from other intermediates. In BR, the proton acceptor ($X^-$ in Fig. 1.7) is Asp85 so that the primary proton transfer takes place from the Schiff base to Asp85. In the case of chloride pump HR, the Schiff base does not deprotonate during the photocycle because Asp85 in BR is replaced by Thr. In HR, $X^-$ in Fig. 1.7 is a chloride ion, which is directly translocated upon decay of the L intermediate.

If the Schiff base of M is reprotonated from Asp85 in BR, no proton transport occurs. In reality, the Schiff base is reprotonated from Asp96 in the cytoplasmic region (Fig. 1.6), by which the N intermediate is formed. The molecular mechanism of unidirectional transport of protons in BR has attracted the attention of many researchers, and it is believed that the primary proton transfer from the Schiff base to Asp85 and the subsequent proton transfer from Asp96 to the Schiff base determine the unidirectionality from the cytoplasmic to the extracellular region. The crystal structure of BR exhibits an asymmetric pattern of hydration, while seven internal water molecules are found in the extracellular half, only two are observed in the cytoplasmic

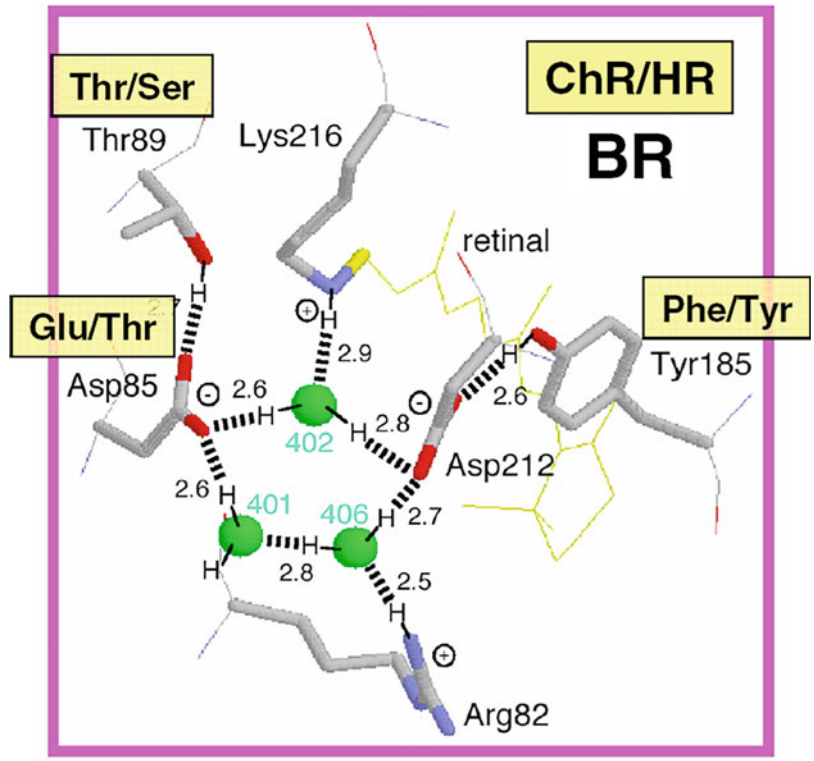


**Fig. 1.5** Structure of the Schiff base region in bacteriorhodopsin (BR). This is the side view of the Protein Data Bank structure 1C3W, which has a resolution of 1.55 Å (Luecke et al. 1999). The membrane normal is approximately in the vertical direction of this figure. Hydrogen atoms and hydrogen bonds (dashed lines) are supposed from the structure, while the numbers indicate hydrogen-bonding distances in Å. Arg, Asp, and Lys at positions 82, 212, and 216, respectively, are fully conserved in ChR and HR, while Asp85, Thr89, and Tyr185 in BR are replaced in ChR and HR, as shown in the figure

half (Fig. 1.6). Such asymmetry makes sense in view of BR's function, as the water molecules build a hydrogen-bonding network on the extracellular side for fast proton release while the cytoplasmic side is likely inaccessible in the dark and allows proton uptake only after the light-induced accessibility switch (Ernst et al. 2014). Such asymmetric access (EC open and CP closed) is not only the case for the unphotolyzed state but also the case for the K and M intermediates, as shown in Fig. 1.7.

To make proton conduction in the cytoplasmic region possible (CP open), an additional conformational change allowing the entrance of water into the vicinity of Asp96 should take place. Such a conformational alteration is realized mainly by changes in helical tilts (especially of the cytoplasmic half of helix F), and the N intermediate is often characterized by the largest changes in the protein backbone conformation, most notably, outward tilts of the cytoplasmic end of helix F. Such helical motions are functionally significant both for ion transport and interactions with transducers of sensory rhodopsins. The photocycle usually ends with another red-shifted intermediate, known as the O intermediate, serving as a last step in resetting the original unphotolyzed conformation.

In the chloride-pumping HR, the negatively charged Asp85 in BR is replaced by Thr (Fig. 1.5), and the lack of a negative charge is compensated by the binding of $Cl^-$ near the Schiff base region. Consequently, $Cl^-$ stabilizes the protonated Schiff base as the counterion ($X^-$ in Fig. 1.7). During the photocycle of HR, protonation of the Schiff base is maintained and $Cl^-$ is translocated, unlike $H^+$-pumping BR (Kandori 2015). This is also the case in eubacterial light-driven $Cl^-$ pumps. Resemblance of light-driven $H^+$ and $Cl^-$ pumps has been demonstrated by functional conversion by mutation. In 1995, BR was successfully converted into a $Cl^-$ pump by replacement of a single amino acid (Asp85 to Thr) (Sasaki et al. 1995). In contrast, HR was

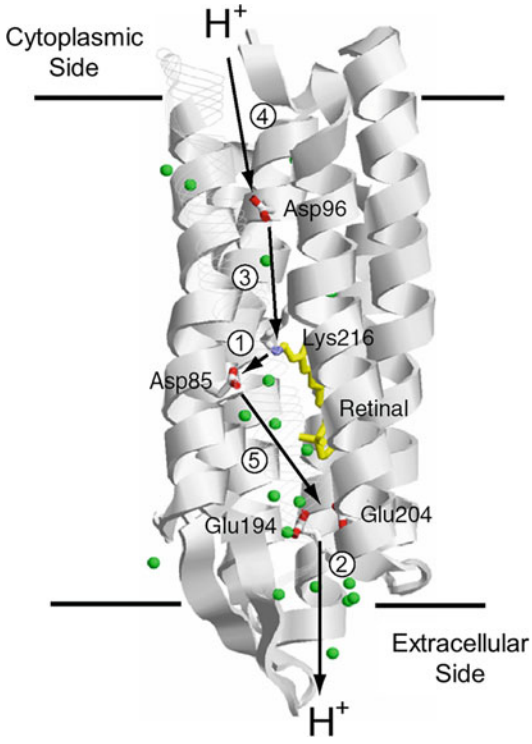


**Fig. 1.6** Proton transport pathway in bacteriorhodopsin (BR). Arrows indicate each proton transfer, and the numbers indicate a temporal order; (1) Schiff base to Asp85, (2) proton release, (3) Asp96 to Schiff base, (4) uptake, and (5) Asp85 to the proton release group

not converted into a $H^+$ pump by mutation, where protein-bound water molecules play crucial role (Muroda et al. 2012). In case of eubacterial pumps, $Cl^-$ pump was converted into $H^+$ pump (Hasemi et al. 2016; Inoue et al. 2016a), but $H^+$ pump could not be converted into $Cl^-$ pump (Inoue et al. 2016a). Asymmetric functional conversion was observed for both archaeal and eubacterial light-driven pumps, whereas the direction of successful conversion was opposite between them.

## 1.3 Channelrhodopsin, the Light-Gated Ion Channel by Light

The molecular mechanism of the light-driven proton pump in BR is well established although the detailed directionality remains uncertain. In pumps, the transport pathways between the two sides of the membrane cannot be fully connected because the gradient formed by active transport will collapse. This view is clearly explained in the case of BR. This is an important aspect when distinguishing pumps from channels. The former needs energy input, which ensures the unidirectionality of transport across the membrane. The protein architecture of BR in Figs. 1.4 and 1.6 effectively explains the unidirectional transport in which the extracellular side contains many water molecules while the cytoplasmic side has no pathway (EC open and CP closed in Fig. 1.7). Therefore, an alternative pump-specific conformation must work, in which the protein releases a proton first on one side, and takes up a proton from the other side (EC closed and CP open in Fig. 1.7). In contrast, a channel needs a fully connected ion pathway for passive transport of ions upon opening (EC and CP open). From the structure of BR (Figs. 1.4 and 1.6), the channel function is most likely impossible for microbial rhodopsins.

In 2002–2003, three groups independently identified novel DNA sequences that encode microbial-type rhodopsins in *Chlamydomonas* (Nagel et al. 2002; Sineshchekov et al. 2002; Suzuki et al. 2003). Furthermore, a light-gated ion channel function was proved for two proteins, channelrhodopsin-1 (ChR1) and channelrhodopsin-2 (ChR2), in *Xenopus* oocytes using two electrode voltage clamp measurements (Nagel et al. 2002, 2003). ChR2 was also shown to be expressed and used to depolarize mammalian cells in response to light (Boyden et al. 2005; Ishizuka et al. 2006). Then, several groups began to work with ChRs, primarily with a truncated version of ChR2 that expressed better than the full-length protein and much better than ChR1 (Ernst et al. 2014; Deisseroth 2011). This was the dawn of optogenetics. Surprisingly, the mammalian brain contains sufficient retinoid levels to allow wild-type ChR2 to function without the addition of exogenous retinoid cofactors.

ChR is a light-gated ion channel, implying that the channel is closed in the dark, and opens upon light absorption. Initially, researchers suspected that the channel pathway lay inside the seven

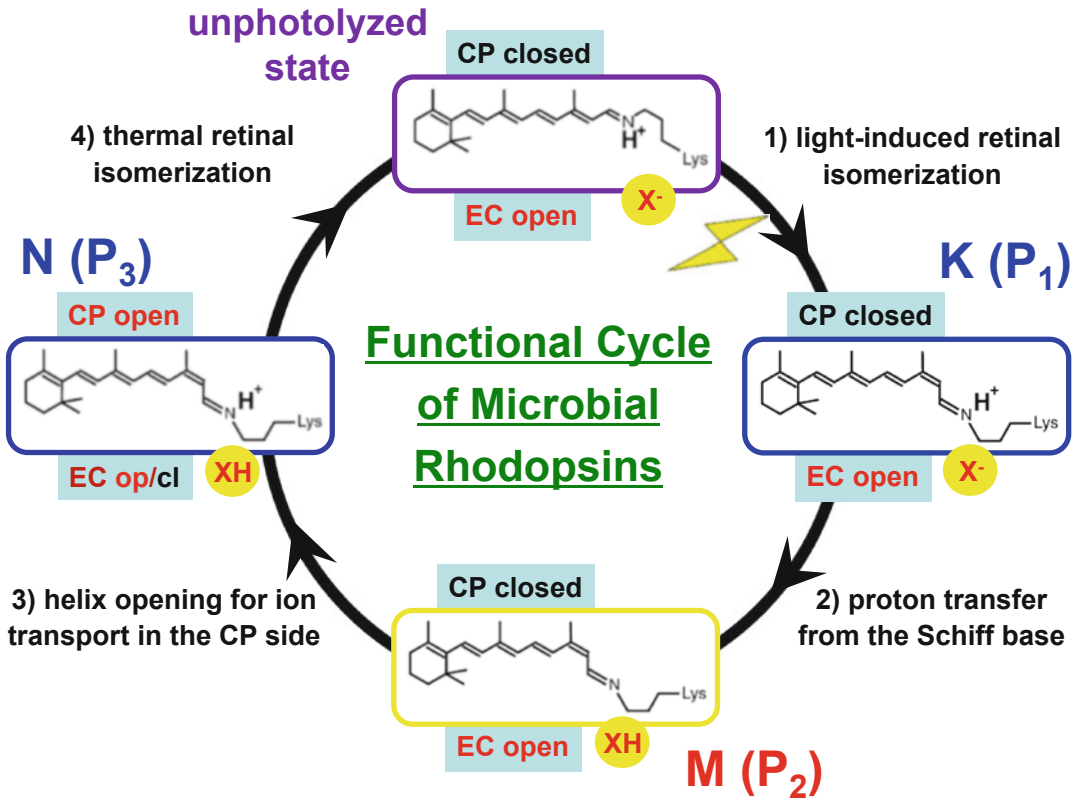


**Fig. 1.7** Typical photocycle of microbial rhodopsins showing isomeric and protonation state of retinal. Names of the photocycle intermediates are for BR, while those in parenthesis are for ChR. $X^-$ represents the Schiff base counterion, and Asp85 in BR also acts as the proton acceptor from the Schiff base. $X^-$ is Glu123 in ChR2, whereas the proton acceptor of the Schiff base is not well established. In the chloride pump HR, $X^-$ is a chloride ion so that the M intermediate is not formed because the Schiff base is not deprotonated. Instead, the chloride ion is transported upwards (in this figure) in HR. CP and EC indicate cytoplasmic and extracellular domains, respectively. In the unphotolyzed state of microbial rhodopsins, the EC side is open through a hydrogen-bonding network, but the CP side is closed. While this is persistent in the K (P1) and M (P2) states, the CP side is open in the N (P3) state. When the EC side is closed (black), the CP side is open, as is the case for an ion pump, as occurs in the N intermediate of BR. When the EC side is open (red), the CP side is open, as is the case for an ion channel, as occurs for the P3 intermediate of ChR

transmembrane helices as well as the proton pathway in BR (Fig. 1.6). Instead, it is more likely that ChR forms a dimer and that the intra-dimer cavity constitutes the ion conduction pathway. However, mutation studies of ChR suggested that the ion conduction pathway lay inside the seven transmembrane helices (Ernst et al. 2014). In addition, X-ray crystallography of a chimeric protein of ChR1 and ChR2 showed the presence of the channel cavity at the extracellular domain, strongly suggesting that the ion conduction pathway lay inside the seven transmembrane helices (Kato et al. 2012). It is now believed that a monomer is the functional unit of ChR. The crystal structure of ChR showed that the protein architecture is common to all microbial rhodopsins (Kato et al. 2012; Volkov et al. 2017), but that some structural modification must be linked to their unique function. For instance, in all microbial rhodopsins, the hydrogen-bonding acceptor of the Schiff base is a water molecule (Fig. 1.5), whereas crystal structure and FTIR spectroscopy

revealed the direct interaction of the Schiff base with the counterion (Glu at the position of Asp85 in BR; Fig. 1.5) (Kato et al. 2012; Ito et al. 2014).

Like BR, the ChR photocycle has been studied by various methods, and it is now established that ChR has a photocycle similar to other microbial rhodopsins (Ernst et al. 2014; Lórenz-Fonfría and Heberle 2014; Schneider et al. 2015). After the absorption of light, photoisomerization occurs from the all-*trans*- to the 13-*cis*-form very rapidly, and forms the red-shifted K-like intermediate (P1 in Fig. 1.7). As the protein cavity, which accommodates retinal, cannot respond promptly, the P1 intermediate contains twisted 13-*cis* retinal and an altered hydrogen-bonding network in the Schiff base region, which possesses higher free energy than in the original state. This yields subsequent protein structural changes that accompany relaxation as well as the case in BR. Then, the proton is transferred from the Schiff base, forming the M-like P2 intermediate. The P2 intermediate has a deprotonated 13-*cis* chromophore whose absorption is strongly blue-shifted ($\lambda_{max}$ at 380 nm). The N-like P3 intermediate is formed by reprotonation of the Schiff base, and it is believed to be the ion-conducting state. It is reasonable to assume that the N-like state exhibits the largest conformational changes in microbial rhodopsins. When the CP side is open, the EC side must also be open in ChR so that a transient ion conduction pathway is created. Therefore, in Fig. 1.7, pumps and channels show the N-like intermediate in CP open/EC closed and CP open/EC open conformations, respectively.

The channel property of ChR is important for optogenetic applications. In particular, absorption color, ion selectivity, and open/close dynamics should be taken into account. Thus far, various mutants have been shown to improve the properties of ChR. How then were these variants designed before structural determination? Knowledge of BR has contributed significantly to the design of mutants. For instance, two important Asp in BR, Asp85 and Asp96, correspond to Glu123 and His134 in ChR2, respectively, to which mutations were attempted. In the case of E123T/A, channel closure is faster than that of the wild type, allowing for a 10-times higher repetition rate (200 Hz) than the wild type in optogenetics (Fig. 1.8) (Gunaydin et al. 2010). The E123T/A mutant also shows red-shifted absorption, caused by neutralization of the Schiff base counterion (Glu123; $X^-$ in Fig. 1.7) (Ernst et al. 2014). In the case of H134R, channel closure is slower than that of the wild type, improving conductivity and changing ion selectivity (Nagel et al. 2005). Asp96 and His134 in BR and ChR2, respectively, are located at important positions of the cytoplasmic domain (Figs. 1.6 and 1.8), presumably influencing ion transport. In BR, Thr90, Asp115, and Met118 (Cys128, Asp156, and Thr159 in ChR2, respectively) are located near the retinal chromophore (Fig. 1.8). D156A/C128S exhibits an extremely slow photocycle, leading to a permanently open channel that can be photoconverted to the original state by orange light (Berndt et al. 2011). Since ion conductance was increased for T159C, it was used under weak light conditions (Berndt et al. 2009). These examples show how specific variants of ChR2 have been applied in optogenetics (Zhang et al. 2011).

Despite the creation of useful ChR2 variants, there are still many requirements for channel function. Limited conductance of ChR2 needs to be improved. However, unlike other channel proteins, ion pathway is not straight as ions are conducted inside seven transmembrane helices in ChR2. This is the substantial limitation of low conductance of ChR2, and creation of wider pores through molecular engineering may be a challenge. Ion selectivity of ChR2 is much higher for $H^+$ than for $Na^+$ (the permeability ratio, $P_H/P_{Na}$, is about $10^6$) (Nagel et al. 2003), indicating that ChR2 should be recognized as a light-gated $H^+$ channel rather than an $Na^+$ channel, and if pH differs between inside and outside of cells, ChR2 acts as a proton channel. ChR2 has some permeability of $Ca^{2+}$. No conduction or increased conduction of $Ca^{2+}$ is highly demanded, and $Ca^{2+}$-permeable channelrhodopsin CatCh (L132C ChR2) was reported, though it does not remarkably increase $Ca^{2+}$ permeability (Kleinlogel et al. 2011). Absorbing color is another problem of ChR2, which absorbs blue light maximally (470–480 nm). Blue light is harmful to organisms

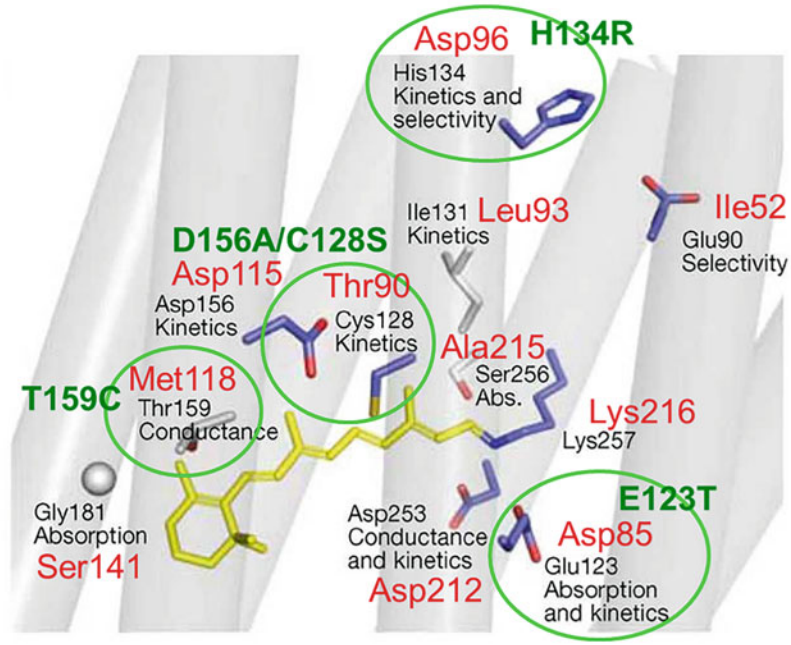


**Fig. 1.8** Key amino acids for ChR2 channel activity based on the BR structure, which is modified from Hegemann and Möglich (2011). Red and black characters correspond to the residue numbers in BR and ChR2, respectively, and stick drawings represent the residues in ChR2. The residues conserved or different in ChR1 and ChR2 from *Chlamydomonas reinhardtii* and *Volvox carteri* are colored blue or gray, respectively. Mutations of these residues substantially influence absorption, conductance, kinetics, and ion selectivity, as indicated for each residue. In particular, four mutations, E123T, H134R, D156A/C128S, and T159C, described in the text, are highlighted by green circles

and also penetrates them less than red light. Therefore, red-absorbing ChRs have been reported such as ReaChR and Chrimson (Zhang et al. 2008; Lin et al. 2013; Klapoetke et al. 2014).

While ChR2 was used for neural excitation by depolarizing cells, neural silencing tools were highly demanded from the beginning. Light-driven ion pumps such as a light-driven $H^+$-pump BR and a light-driven $Cl^-$-pump HR were the candidates as they can hyperpolarize cells by light. However, at that time, I was skeptical about the practical usage of these pumps because of efficiency. In light-driven pumps, a single ion is translocated by a single photocycle (Figs. 1.4 and 1.5), while multiple ions can be transported when light-gated ion channel is activated by a single photocycle. Nevertheless, a light-driven $Cl^-$ pump HR was successfully used for neural silencing by hyperpolarizing cells (Zhang et al. 2007). Optogenetics was actually established by neural excitation and silencing, using ChR2 and HR, respectively, in 2007. Then, various light-driven $H^+$ pumps were tested as a tool of neural silencing, among which Arch has been best used (Chow et al. 2010).

## 1.4 Novel Ion-Transporting Rhodopsins as Optogenetics Tools

A light-gated channel was discovered in 2002, and optogenetics began in 2005 by using ChR2 as a neural excitation tool. Optogenetic was fully established a few years later by using light-driven $H^+$ and $Cl^-$ pumps as neural silencing tools, which were discovered in 1970s. During this decade, new microbial rhodopsins have been

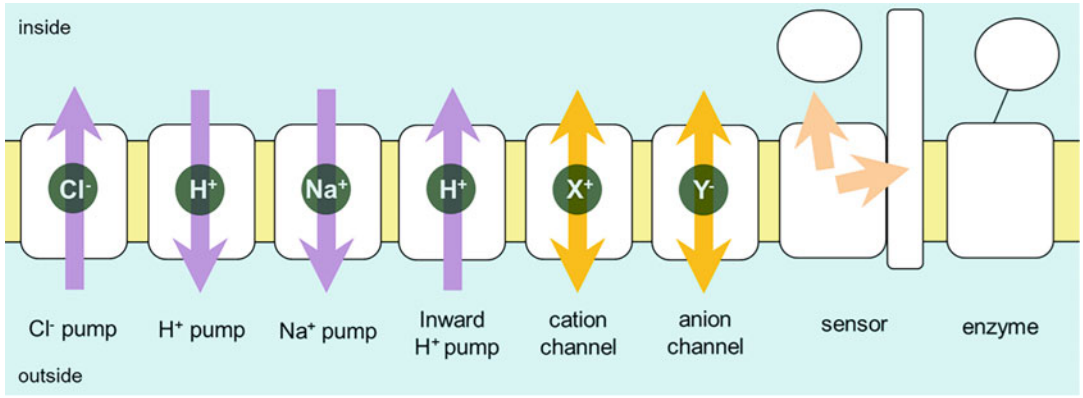


**Fig. 1.9** Function of rhodopsins; light-driven $Cl^-$ pump, light-driven $H^+$ pump, light-driven $Na^+$ pump, light-driven inward $H^+$ pump, light-gated cation channel, light-gated anion channel, light sensor with transmembrane transducer and soluble transducer, and light-activated enzyme. Purple or orange arrows indicate unidirectional or bidirectional transport of ions in pumps or channels, respectively. On the other hand, pale orange arrows show the signal transduction from rhodopsins to either soluble or transmembrane transducer proteins

discovered and actively applied to optogenetics. They are summarized in Figs. 1.9 and 1.10, and briefly introduced below.

Existence of $Na^+$-pumping rhodopsin was a surprise in the field. In active transporter, substrate is bound to the resting state, and the transporting mechanism is described by alternating access model or Panama Canal model (Kandori et al. 2018). In rhodopsins, positively charged protonated Schiff base is a key element for the usage of light, and light-driven $H^+$ and $Cl^-$ pumps bind the substrates $H^+$ and $Cl^-$, respectively, in this region (Figs. 1.5 and 1.7). In contrast, we believed $Na^+$-binding unlikely because of electrostatic repulsion with the protonated Schiff base. However, nature created light-driven $Na^+$ pump rhodopsin (Fig. 1.9) (Inoue et al. 2013). Interestingly, this protein does not need $Na^+$ to be bound to the resting state, indicating that light-driven $Na^+$ pumps are a unique active transporter. Unidirectional transport of $Na^+$ is controlled by passive diffusion of $Na^+$ from the cytoplasmic side. Ion selectivity filter is located at the intracellular surface, whose modification led to the creation of light-driven pumps of $K^+$, $Rb^+$, and $Cs^+$ (Kato et al. 2015; Konno et al. 2016). Light-driven $Na^+$ pumps are also used as neural silencing tools in optogenetics (Fig. 1.10) (Tsunoda et al. 2017; Grimm et al. 2018).

Existence of light-driven inward $H^+$ pump was another surprise because inward $H^+$ transport competes with ATP synthase function. In 2009, we successfully created inward $H^+$ transport using a mutant of a photochromic sensor, Anabaena sensory rhodopsin (D217E ASR) (Kawanabe et al. 2009). While this was an example of engineering success, we reported that nature also created an inward $H^+$ pump in 2016 (Fig. 1.9) (Inoue et al. 2016b). A rhodopsin from *Parvularcula oceani* (PoXeR) is in the same family of ASR, and the mechanistic analyses revealed that small differences in interactions at the active center determine the direction of primary $H^+$ transfer between outward and inward $H^+$ pumps, even though the retinal chromophore structure and primary photoisomerization are identical (Inoue et al. 2016b; Shevchenko et al. 2017). In view of optogenetics, inward $H^+$ pump functions for depolarizing cells (Fig. 1.10), but cation channels are more superior as pump transports one proton per one photon. On the other hand, inward $H^+$ pump is more beneficial for intracellular organelle optogenetics. While intracellular organelle can be acidified by light-driven $H^+$ pump, alkalization tool of intracellular organelle

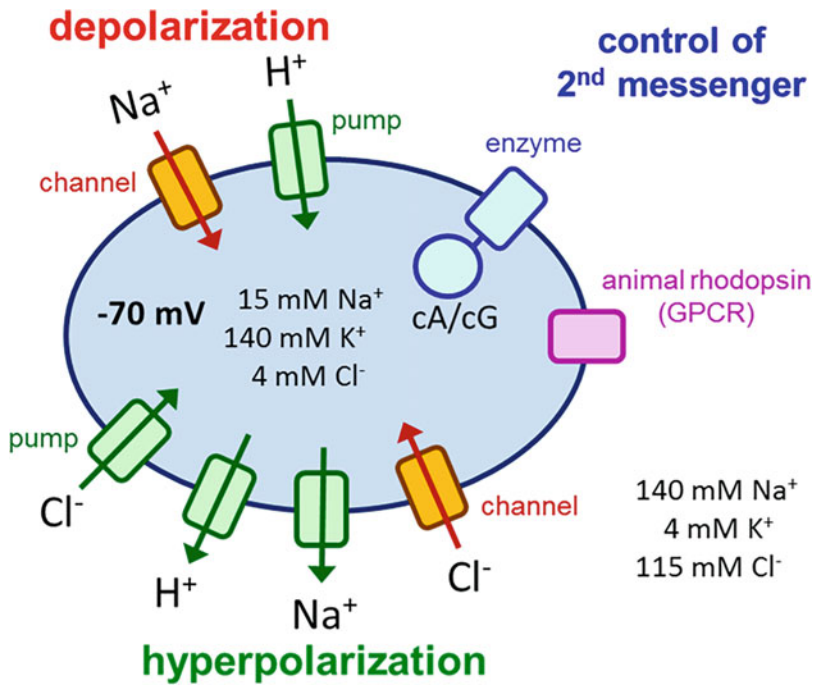


**Fig. 1.10** Role of photoreceptive proteins in optogenetics. Channels and pumps perform passive and active transports of ions, respectively. At the beginning of optogenetics, light-gated cation channel (ChR2) depolarizes neural cells by influx of $Na^+$, leading to generation of action potential (neural excitation), while light-driven $Cl^-$ pump (HR) hyperpolarizes neural cells by influx of $Cl^-$, leading to inhibition of action potential (neural silencing). More optogenetics tools are now at hand. Light-driven inward $H^+$ pumps depolarize cells, while light-driven (outward) $H^+$ and $Na^+$ pumps and light-gated anion channels hyperpolarize cells. Recently discovered enzyme rhodopsins, one family of microbial rhodopsins, are used to control concentrations of cAMP and cGMP. In addition, animal rhodopsins are also used for optogenetics

has been demanded. In fact, D217E ASR was used to alkalize AMPA-type glutamate receptor endocytosis in the study of long-term depression of AMPA-type glutamate receptor (AMPA receptor)-mediated synaptic transmission for learning and memory (Kakegawa et al. 2018).

Cellular inside is negatively charged (−70 mV), but $Cl^-$ ions are uptaken upon opening of anion channel because concentration of $Cl^-$ is much higher in extracellular side than in cytoplasm (Fig. 1.10). In general, channels are more efficient tool than pumps because of multiple ion permeation. Thus, light-gated anion channels have been strongly required in optogenetics, and in fact, they were engineered from cation channels (Wietek et al. 2014; Berndt et al. 2014). On the other hand, natural anion channel rhodopsin (ACR) was discovered from a cryptophyte *Guillardia theta* in 2015 (Fig. 1.9) (Govorunova et al. 2015). Conduction of ACR is more than cation channel rhodopsins, and natural ACR is considered better neural silencing tools than light-driven ion pumps. Structures of ACR and engineered anion-channel rhodopsin were determined (Kim et al. 2018; Kato et al. 2018), and knowledge of structure and mechanism of ACR will be used for the improvement of tools, and contributes to neural silencing (Wiegert et al. 2017), as was the case for ChR2.

*Guillardia theta* possesses more than 40 genes of rhodopsins, and light-gated cation channels from *Guillardia theta* are also noted. A light-driven $H^+$ pump BR contains a DTD motif at positions 85, 89, and 96, which is unique to archaeal $H^+$ pumps. Recently, two groups independently reported that the DTD rhodopsins from

*Guillardia theta* are light-gated cation channel, not pump (Govorunova et al. 2016; Yamauchi et al. 2017). One of these proteins, GtCCR4, permeates little protons and $Ca^{2+}$ (Shigemura et al. 2019), which is a remarkable contrast to those of ChR2. If influx of $Ca^{2+}$ is problematic in optogenetic experiments, GtCCR4 is a suitable tool. A recently reported new cation channel, named ChRmine (Marshel et al. 2019), is in the same family of the DTD cation channels.

## 1.5 Conclusion and Perspectives

The original meaning of rhodopsin is the red-colored pigment for vision, but similar colored retinal proteins were found in microbes. Consequently the definition of the word rhodopsin is largely expanded, and the modern meaning of rhodopsin encompasses photoactive proteins containing a retinal chromophore in animals and microbes. While the meaning of rhodopsin has been altered in history, it is also the case on the word "optogenetics." Optogenetics is originally the combination of "optics" and "genetics," which describes optical control of neural activity by use of ion-transporting microbial rhodopsins such as channelrhodopsin and light-driven $Cl^-$ pump (Fig. 1.10). This allows rapid temporal response, which was required in the brain function researches. On the other hand, extensive studies largely expanded the definition of the word optogenetics.

Function of no ion-transporting rhodopsins was recognized as light sensor, such as SRI and SRII, which activate membrane-bound transducer proteins. In case of a photochromic sensor ASR, its transducer is a soluble protein. Animal rhodopsins are G-protein-coupled receptors, whose transducers are also soluble (heterotrimeric G-protein) that are anchored to the membrane. As various signaling processes in mammalian cells are regulated by GPCR, animal rhodopsins are potential candidate in optogenetics, where photobleaching property has to be improved. In this sense, bistable pigments of animal rhodopsin, such as melanopsin (Ye et al. 2011) and opn3 (Koyanagi et al. 2013), are useful, and microbial rhodopsin can be used as a template for light activation of G-protein (Sasaki et al. 2014). To control intracellular second messengers, enzyme rhodopsins should be noted, which are composed of a membrane-embedded rhodopsin domain and a C-terminal cytoplasmic enzyme domain that are activated when light is absorbed by the all-*trans*-retinal chromophore (Fig. 1.9). A fungal light-activated guanylyl cyclase (Rh-GC) and light-activated phosphodiesterase (Rh-PDE) from a unicellular and colonial single flagellate eukaryote were reported in 2014 and 2017, respectively (Avelar et al. 2014; Yoshida et al. 2017). Rh-GC increases centration of cGMP by light, while Rh-PDE decreases the concentrations of cGMP and cAMP by light. As cAMP and cGMP are known to be the second messengers in intracellular signaling, they are new optogenetic tools to control concentration of the second messengers (Fig. 1.10). I introduced various rhodopsins in this chapter, and heliorhodopsin (HeR) should be finally noted. It has been believed that microbial rhodopsin (also called type-1 rhodopsin) and animal rhodopsin (also called type-2 rhodopsin) are the only rhodopsins. Nevertheless, a previously unrecognized diverse family, heliorhodopsins (HeRs), was recently discovered through the use of functional metagenomics (Pushkarev et al. 2018). HeRs have inverted membrane topology compared to other retinal proteins (Shihoya et al. 2019), have no ion-transport activity, and their slow photocycle suggests a light-sensor function. Therefore, HeRs will be a new optogenetics tool in future.

**Acknowledgments** This work was supported by Japanese Ministry of Education, Culture, Sports and Technology Grants 18H03986, 19H04959, and JST CREST Grant JPMJCR1753.

## References

Avelar GM, Schumacher RI, Zaini PA, Leonard G, Richards TA, Gomes SL (2014) A rhodopsin-guanylyl cyclase gene fusion functions in visual perception in a fungus. Curr Biol 24:1234–1240

Berndt A, Yizhar O, Gunaydin LA, Hegemann P, Deisseroth K (2009) Bistable neural state switches. Nat Neurosci 12:229–234

Berndt A, Schoenenberger P, Mattis J, Tye KM, Deisseroth K, Hegemann P, Oertner TG (2011) High-efficiency channelrhodopsins for fast neuronal stimulation at low light levels. Proc Natl Acad Sci U S A 108:7595–7600

Berndt A, Lee SY, Ramakrishnan C, Deisseroth K (2014) Structure-guided transformation of channelrhodopsin into a light-activated chloride channel. Science 344:420–424

Boyden ES, Zhang F, Bamberg E, Nagel G, Deisseroth K (2005) Millisecond-timescale, genetically targeted optical control of neural activity. Nat Neurosci 8:1263–1268

Brown LS (2014) Eubacterial rhodopsins - Unique photosensors and diverse ion pumps. Biochim Biophys Acta 1837:553–561

Chow BY, Han X, Dobry AS, Qian X, Chuong AS, Li M, Henninger MA, Belfort GM, Lin Y, Monahan PE, Boyden ES (2010) High-performance genetically targetable optical neural silencing by light-driven proton pumps. Nature 463:98–102

Deisseroth K (2011) Optogenetics. Nat Methods 8:26–29

Diester I, Kaufman MT, Mogri M, Pashaie R, Goo W, Yizhar O, Ramakrishnan C, Deisseroth K, Shenoy KV (2011) An optogenetic toolbox designed for primates. Nat Neurosci 14:387–397

Ernst OP, Lodowski DT, Elstner M, Hegemann P, Brown LS, Kandori H (2014) Microbial and animal rhodopsins: structures, functions, and molecular mechanisms. Chem Rev 114:126–163

Gerwert K, Freier E, Wolf S (2014) The role of protein-bound water molecules in microbial rhodopsins. Biochim Biophys Acta 1837:606–613

Govorunova EG, Sineshchekov OA, Janz R, Liu X, Spudich JL (2015) Neuroscience. Natural light-gated anion channels: a family of microbial rhodopsins for advanced optogenetics. Science 349:647–650

Govorunova EG, Sineshchekov OA, Spudich JL (2016) Structurally distinct cation channelrhodopsins from cryptophyte algae. Biophys J 110:2302–2304

Govorunova EG, Sineshchekov OA, Li H, Spudich JL (2017) Microbial rhodopsins: diversity, mechanisms, and optogenetic applications. Annu Rev Biochem 86:845–872

Gozem S, Luk HL, Schapiro I, Olivucci M (2017) Theory and simulation of the ultrafast double-bond isomerization of biological chromophores. Chem Rev 117:13502–13565

Grimm C, Silapetere A, Vogt A, Bernal Sierra YA, Hegemann P (2018) Electrical properties, substrate specificity and optogenetic potential of the engineered light-driven sodium pump eKR2. Sci Rep 8:9316

Grote M, Engelhard M, Hegemann P (2014) Of ion pumps, sensors and channels - perspectives on microbial rhodopsins between science and history. Biochim Biophys Acta 1837:533–545

Gunaydin LA, Yizhar O, Berndt A, Sohal VS, Deisseroth K, Hegemann P (2010) Ultrafast optogenetic control. Nat Neurosci 13:387–392

Hasemi T, Kikukawa T, Kamo N, Demura M (2016) Characterization of a cyanobacterial chloride-pumping rhodopsin and its conversion into a proton pump. J Biol Chem 291:355–362

Hegemann P, Möglich A (2011) Channelrhodopsin engineering and exploration of new optogenetic tools. Nat Methods 8:39–42

Henderson R, Unwin PN (1975) Three-dimensional model of purple membrane obtained by electron microscopy. Nature 257:28–32

Hille B (1984) Ion channels and excitable membranes. Oxford University Press, Oxford

Hofmann KP, Scheerer P, Hildebrand PW, Choe HW, Park JH, Heck M, Ernst OP (2009) A G protein-coupled receptor at work: the rhodopsin model. Trends Biochem Sci 34:540–552

Inoue K, Ono H, Abe-Yoshizumi R, Yoshizawa S, Ito H, Kogure K, Kandori H (2013) A light-driven sodium ion pump in marine bacteria. Nat Commun 4:1678

Inoue K, Kato Y, Kandori H (2015) Light-driven ion-translocating rhodopsins in marine bacteria. Trends Microbiol 23:91–98

Inoue K, Nomura Y, Kandori H (2016a) Asymmetric functional conversion of eubacterial light-driven ion pumps. J Biol Chem 291(19):9883–9893

Inoue K, Ito S, Kato Y, Nomura Y, Shibata M, Uchihashi T, Tsunoda SP, Kandori H (2016b) A natural light-driven inward proton pump. Nat Commun 7:13415

Ishizuka T, Kakuda M, Araki R, Yawo H (2006) Kinetic evaluation of photosensitivity in genetically engineered neurons expressing green algae light-gated channels. Neurosci Res 54:85–94

Ito S, Kato HE, Taniguchi R, Iwata T, Nureki O, Kandori H (2014) Water-containing hydrogen-bonding network in the active center of channelrhodopsin. J Am Chem Soc 136:3475–3482

Jung KH, Trivedi VD, Spudich JL (2003) Demonstration of a sensory rhodopsin in eubacteria. Mol Microbiol 47:1513–1522

Kakegawa W, Katoh A, Narumi S, Miura E, Motohashi J, Takahashi A, Kohda K, Fukazawa Y, Yuzaki M, Matsuda S (2018) Optogenetic control of synaptic AMPA receptor endocytosis reveals roles of LTD in motor learning. Neuron 99:985–998

Kandori H (2015) Ion-pumping microbial rhodopsins. Front Mol Sci 2:52

Kandori H, Inoue K, Tsunoda SP (2018) Light-driven sodium-pumping rhodopsin: a new concept of active transport. Chem Rev 118:10646–10658

Kato HE, Zhang F, Yizhar O, Ramakrishnan C, Nishizawa T, Hirata K, Ito J, Aita Y, Tsukazaki T, Hayashi S, Hegemann P, Maturana AD, Ishitani R, Deisseroth K, Nureki O (2012) Crystal structure of the channelrhodopsin light-gated cation channel. Nature 482:369–374

Kato HE, Inoue K, Abe-Yoshizumi R, Kato Y, Ono H, Konno M, Hososhima S, Ishizuka T, Hoque MR, Kunitomo H, Ito J, Yoshizawa S, Yamashita K,

Takemoto M, Nishizawa T, Taniguchi R, Kogure K, Maturana AD, Iino Y, Yawo H, Ishitani R, Kandori H, Nureki O (2015) Structural basis for $Na^+$ transport mechanism by a light-driven $Na^+$ pump. Nature 521:48–53

Kato HE, Kim YS, Paggi JM, Evans KE, Allen WE, Richardson C, Inoue K, Ito S, Ramakrishnan C, Fenno LE, Yamashita K, Hilger D, Lee SY, Berndt A, Shen K, Kandori H, Dror RO, Kobilka BK, Deisseroth K (2018) Structural mechanisms of selectivity and gating in anion channelrhodopsins. Nature 561:349–354

Kawanabe A, Furutani Y, Jung KH, Kandori H (2009) Engineering an inward proton transport from a bacterial sensor rhodopsin. J Am Chem Soc 131:16439–16444

Khorana HG, Gerber GE, Herlihy WC, Gray CP, Anderegg RJ, Nihei K, Biemann K (1979) Amino acid sequence of bacteriorhodopsin. Proc Natl Acad Sci U S A 76:5046–5050

Kim YS, Kato HE, Yamashita K, Ito S, Inoue K, Ramakrishnan C, Fenno LE, Evans KE, Paggi JM, Dror RO, Kandori H, Kobilka BK, Deisseroth K (2018) Crystal structure of the natural anion-conducting channelrhodopsin GtACR1. Nature 561:343–348

Klapoetke NC, Murata Y, Kim SS, Pulver SR, Birdsey-Benson A, Cho YK, Morimoto TK, Chuong AS, Carpenter EJ, Tian Z, Wang J, Xie Y, Yan Z, Zhang Y, Chow BY, Surek B, Melkonian M, Jayaraman V, Constantine-Paton M, Wong GK, Boyden ES (2014) Indepeendent optical excitation of distinct neural populations. Nat Methods 11:338–346

Kleinlogel S, Feldbauer K, Dempski RE, Fotis H, Wood PG, Bamann C, Bamberg E (2011) Ultra light-sensitive and fast neuronal activation with the $Ca^{2+}$-permiable channelrhodopsin CatCh. Nat Neurosci 14:513–518

Konno M, Kato Y, Kato HE, Inoue K, Nureki O, Kandori H (2016) Mutant of a light-driven sodium ion pump can transport cesium ions. J Phys Chem Lett 7:51–55

Koyanagi M, Terakita A (2014) Diversity of animal opsin-based pigments and their optogenetic potential. Biochim Biophys Acta 1837:710–716

Koyanagi M, Takada E, Nagata T, Tsukamoto H, Terakita A (2013) Homologs of vertebrate Opn3 potentially serve as a light sensor in nonphotoreceptive tissue. Proc Natl Acad Sci U S A 110:4998–5003

Lanyi JK (2004) Bacteriorhodopsin. Annu Rev Physiol 66:665–688

Lin JY, Knutsen PM, Muller A, Kleinfeld D, Tsien RY (2013) ReaChR: a red-shifted variant of channelrhodopsin enables deep transcranial optogenetic excitation. Nat Neurosci 16:1499–1508

Lórenz-Fonfría VA, Heberle J (2014) Channelrhodopsin unchained: structure and mechanism of a light-gated cation channel. Biochim Biophys Acta 1837:626–642

Luecke H, Schobert B, Richter HT, Cartailler JP, Lanyi JK (1999) Structure of bacteriorhodopsin at 1.55 Å resolution. J Mol Biol 291:899–911

Marshel JH, Kim YS, Machado TA, Quirin S, Benson B, Kadmon J, Raja C, Chibukhchyan A, Ramakrishnan C, Inoue M, Shane JC, McKnight DJ, Yoshizawa S, Kato HE, Ganguli S, Deisseroth K (2019) Cortical layer-specific critical dynamics triggering perception. Science 365:6453

Matsuno-Yagi A, Mukohata Y (1977) Two possible roles of bacteriorhodopsin; a comparative study of strains of *Halobacterium halobium* differing in pigmentation. Biochem Biophys Res Commun 78:237–243

Miesenbock G (2011) Optogenetic control of cells and circuits. Annu Rev Cell Dev Biol 27:731–758

Muroda K, Nakashima K, Shibata M, Demura M, Kandori H (2012) Protein-bound water as the determinant of asymmetric functional conversion between light-driven proton and chloride pumps. Biochemistry 51:4677–4684

Nagel G, Ollig D, Fuhrmann M, Kateriya S, Musti AM, Bamberg E, Hegemann P (2002) Channelrhodopsin-1: a light-gated proton channel in green algae. Science 296:2395–2398

Nagel G, Szellas T, Huhn W, Kateriya S, Adeishvili N, Berthold P, Ollig D, Hegemann P, Bamberg E (2003) Channelrhodopsin-2, a directly light-gated cation-selective membrane channel. Proc Natl Acad Sci U S A 100:13940–13945

Nagel G, Brauner M, Liewald JF, Adeishvili N, Bamberg E, Gottschalk A (2005) Light activation of channelrhodopsin-2 in excitable cells of *Caenorhabditis elegans* triggers rapid behavioral responses. Curr Biol 15:2279–2284

Oesterhelt D, Stoeckenius W (1971) Rhodopsin-like protein from the purple membrane of *Halobacterium halobium*. Nat New Biol 233:149–152

Palczewski K (2012) Chemistry and biology of vision. J Biol Chem 287:1612–1619

Pushkarev A, Inoue K, Larom S, Flores-Uribe J, Singh M, Konno M, Tomida S, Ito S, Nakamura R, Tsunoda SP, Philosof A, Sharon I, Yutin N, Koonin EV, Kandori H, Béjà O (2018) A distinct abundant group of microbial rhodopsins discovered using functional metagenomics. Nature 558:595–599

Sasaki J, Brown LS, Chon YS, Kandori H, Maeda A, Needleman R, Lanyi J (1995) Conversion of bacteriorhodopsin into a chloride ion pump. Science 269:73–75

Sasaki K, Yamashita T, Yoshida K, Inoue K, Shichida Y, Kandori H (2014) Chimeric proton-pumping rhodopsins containing the cytoplasmic loop of bovine rhodopsin. PLoS One 9:e91323

Schneider F, Grimm C, Hegemann P (2015) Biophysics of Channelrhodopsin. Annu Rev Biophys 44:167–186

Shevchenko V, Mager T, Kovalev K, Polovinkin V, Alekseev A, Juettner J, Chizhov I, Bamann C, Vavourakis C, Ghai R, Gushchin I, Borshchevskiy V, Rogachev A, Melnikov I, Popov A, Balandin T, Rodriguez-Valera F, Manstein DJ, Bueldt G, Bamberg E, Gordeliy V (2017) Inward $H^+$ pump

xenorhodopsin: mechanism and alternative optogenetic approach. Sci Adv 3:e1603187

Shichida Y, Matsuyama T (2009) Evolution of opsins and phototransduction. Philos Trans R Soc Lond Ser B Biol Sci 364:2881–2895

Shigemura S, Hososhima S, Kandori H, Tsunoda SP (2019) Ion channel properties of a cation channelrhodopsin, Gt_CCR4. Appl Sci 9:3440

Shihoya W, Inoue K, Singh M, Konno M, Hososhima S, Yamashita K, Ikeda K, Higuchi A, Izume T, Okazaki S, Hashimoto M, Mizutori R, Tomida S, Yamauchi Y, Abe-Yoshizumi R, Katayama K, Tsunoda SP, Shibata M, Furutani Y, Pushkarev A, Béjà O, Uchihashi T, Kandori H, Nureki O (2019) Crystal structure of heliorhodopsin. Nature 572:132–136

Sineshchekov OA, Jung KH, Spudich JL (2002) Two rhodopsins mediate phototaxis to low- and high-intensity light in *Chlamydomonas reinhardtii*. Proc Natl Acad Sci U S A 99:8689–8694

Spudich JL, Bogomolni RA (1984) Mechanism of colour discrimination by a bacterial sensory rhodopsin. Nature 312:509–513

Suzuki T, Yamasaki K, Fujita S, Oda K, Iseki M, Yoshida K, Watanabe M, Daiyasu H, Toh H, Asamizu E, Tabata S, Miura K, Fukuzawa H, Nakamura S, Takahashi T (2003) Archaeal-type rhodopsins in *Chlamydomonas*: model structure and intracellular localization. Biochem Biophys Res Commun 301:711–717

Tanford C (1983) Mechanism of free energy coupling in active transport. Annu Rev Biochem 52:379–409

Tsunoda SP, Prigge M, Abe-Yoshizumi R, Inoue K, Kozaki Y, Ishizuka T, Yawo H, Yizhar O, Kandori H (2017) Functional characterization of sodium-pumping rhodopsins with different pumping properties. PLoS One 12:e0179232

Volkov O, Kovalev K, Polovinkin V, Borshchevskiy V, Bamann C, Astashkin R, Marin E, Popov A, Balandin T, Willbold D, Büldt G, Bamberg E, Gordeliy V (2017) Structural insights into ion conduction by channelrhodopsin 2. Science 358:6366

Weidlich O, Schalt B, Friedman N, Sheves M, Lanyi JK, Brown LS, Siebert F (1996) Steric interaction between the 9-methyl group of the retinal and tryptophan 182 controls 13-cis to all-trans reisomerization and proton uptake in the bacteriorhodopsin photocycle. Biochemistry 35:10807–10814

Wiegert JS, Mahn M, Prigge M, Printz Y, Yizhar O (2017) Silencing neurons: tools, applications, and experimental constraints. Neuron 95:504–529

Wietek J, Wiegert JS, Adeishvili N, Schneider F, Watanabe H, Tsunoda SP, Vogt A, Elstner M, Oertner TG, Hegemann P (2014) Conversion of channelrhodopsin into a light-gated chloride channel. Science 344:409–412

Yamauchi Y, Konno M, Ito S, Tsunoda SP, Inoue K, Kandori H (2017) Molecular properties of a DTD channelrhodopsin from Guillardia theta. Biophys Physicobiol 14:57–66

Ye H, Daoud-El Baba M, Peng RW, Fussenegger M (2011) A synthetic optogenetic transcription device enhances blood-glucose homeostasis in mice. Science 332:1565–1568

Yoshida K, Tsunoda SP, Brown LS, Kandori H (2017) A unique choanoflagellate enzyme rhodopsin exhibits light-dependent cyclic nucleotide phosphodiesterase activity. J Biol Chem 292:7531–7541

Zhang F, Wang LP, Brauner M, Liewald JF, Kay K, Watzke N, Wood PG, Bamberg E, Nagel G, Gottschalk A, Deisseroth K (2007) Multimodal fast optical interrogation of neural circuitry. Nature 446:633–639

Zhang F, Prigge M, Beyrière F, Tsunoda SP, Mattis J, Yizhar O, Hegemann P, Deisseroth K (2008) Red-shifted optogenetic excitation: a tool for fast neural control derived from Volvox carteri. Nat Neurosci 11:631–633

Zhang F, Vierock J, Yizhar O, Fenno LE, Tsunoda S, Kianianmomeni A, Prigge M, Berndt A, Cushman J, Polle J, Magnuson J, Hegemann P, Deisseroth K (2011) The microbial opsin family of optogenetic tools. Cell 147:1446–1457

# 2 Channelrhodopsin-Dependent Photo-Behavioral Responses in the Unicellular Green Alga *Chlamydomonas reinhardtii*

Ken-ichi Wakabayashi, Atsuko Isu, and Noriko Ueki

**Abstract**

Channelrhodopsins (ChRs) are the light-gated ion channels that have opened the research field of optogenetics. They were originally identified in the green alga *Chlamydomonas reinhardtii*, a biciliated unicellular alga that inhabits in freshwater, swims with the cilia, and undergoes photosynthesis. It has various advantages as an experimental organism and is used in a wide range of research fields including photosynthesis, cilia, and sexual reproduction. ChRs function as the primary photoreceptor for the cell's photo-behavioral responses, seen as changes in the manner of swimming after photoreception. In this chapter, we will introduce *C. reinhardtii* as an experimental organism and explain our current understanding of how the cell senses light and shows photo-behavioral responses.

**Keywords**

Channelrhodopsin · *Chlamydomonas* · Cilia · Eyespot · Photoresponse · Phototaxis

## Abbreviation

| | |
|---|---|
| CGL | Carotenoid granule layers |
| ChR | Channelrhodopsin |
| Cop | Chlamyopsin |
| EST | Expressed sequence tag |
| IFT | Intraflagellar transport |
| PRC | Photoreceptor current |
| PSY | Phytoene synthase |

## 2.1 *Chlamydomonas reinhardtii* as an Experimental Organism

*Chlamydomonas reinhardtii* is a freshwater unicellular green alga having two cilia (also called flagella), one cup-shaped chloroplast, and a photoreceptive organelle called the eyespot (Fig. 2.1). Swimming with the two cilia, *C. reinhardtii* cells show photo-behavioral responses (hereinafter referred to as photoresponses) upon photoreception by the eyespot, to inhabit in a suitable environment for photosynthesis (Hegemann and Berthold 2009). *C. reinhardtii* is an excellent model organism in various research fields of biology including those of cilia, sensory transduction, sexual

K. Wakabayashi (✉)
Laboratory for Chemistry and Life Science, Institute of Innovative Research, Tokyo Institute of Technology, Yokohama, Japan

School of Life Science and Technology, Tokyo Institute of Technology, Yokohama, Japan
e-mail: wakaba@res.titech.ac.jp

A. Isu
Laboratory for Chemistry and Life Science, Institute of Innovative Research, Tokyo Institute of Technology, Yokohama, Japan

N. Ueki
Science Research Center, Hosei University, Tokyo, Japan



H. Yawo et al. (eds.), *Optogenetics*, Advances in Experimental Medicine and Biology 1293,
https://doi.org/10.1007/978-981-15-8763-4_2

reproduction, and photosynthesis (Harris 2009a). Nowadays, *C. reinhardtii* is also used in the study of biofuel productions because it produces hydrogen and lipids as byproducts of photosynthesis (Melis et al. 2000; Kong et al. 2019; Scranton et al. 2015).

*C. reinhardtii* has several advantageous characteristics as an experimental organism. First, it is haploid and easy to obtain mutants (Harris 2009b). Forward genetic studies using this organism have promoted wide areas of research. Various mutants are available from *Chlamydomonas* Resource Center (https://www.chlamycollection.org/) at University of Minnesota, USA. The Center also provides various useful tools such as expression plasmids.

Second, it possesses two mating types and undergoes sexual reproduction under starvation conditions (Harris 2009b). Thanks to this feature, classical genetic analysis called tetrad analysis can be applied to dissect the genetic relationship between various mutants (Gross et al. 1988; Ranum et al. 1988). When a new mutant is obtained, detailed genetic analyses of tetrads obtained from the cross of that mutant with reference mutants will locate the mutation on the genetic map, and eventually identify the mutated gene with the aid of the genome database (Gallaher et al. 2015; Merchant et al. 2007).

Third, genome editing is now available. For a long time, a demerit of using *C. reinhardtii* had been its low efficiency of homologous recombination. Knockout experiments on genes of interest were mostly unsuccessful, and only a few cases were reported (Sodeinde and Kindle 1993; Gumpel et al. 1994; Nelson and Lefebvre 1995). Even after the advent of CRISPR/Cas9-based technology, genome editing in *C. reinhardtii* met a great difficulty in the beginning (Jinek et al. 2012; Cong et al. 2013; Jiang et al. 2014). This was due to a highly toxic nature of Cas9 protein expressed in this organism. This problem was circumvented by introducing target RNA and Cas9 protein by electroporation rather than by gene expression (Greiner et al. 2017). Presence of Cas9 protein in the cell only for a short time enables both genome editing and cell survival.

Lastly, several valuable databases are available. The whole genome sequence was published in 2007 and made available at Phytozome (https://phytozome.jgi.doe.gov/pz/portal.html) (Merchant et al. 2007). An EST (expressed sequence tags) database (http://est.kazusa.or.jp/en/plant/chlamy/EST/) is available at Kazusa DNA Institute, Japan (Asamizu et al. 2000, 1999).

The identification of ChRs provides a good example to show the power of the experimental system of *C. reinhardtii*. The EST database, released in 2000, was particularly important for identification of ChRs. Before the identification of ChRs, several studies suggested that the photoreceptor for the photoresponses in *C. reinhardtii* is a rhodopsin-like protein. This idea was based on the finding that action spectra of phototaxis and photoshock response peaked at ~500 nm, which is similar to vertebrate rhodopsin (Foster and Smyth 1980). Also, introduction of retinal analog to the carotenoid-deficient, non-phototactic mutant, *fn68*, restored phototaxis of the mutant (Foster et al. 1984). In fact, the EST database revealed the presence of proteins that contained rhodopsin-like sequences. Immediately after the release of the EST database, three research groups independently identified the nucleotide sequences of the rhodopsins and called them by different names (Nagel et al. 2002, 2003; Sineshchekov et al. 2002; Suzuki et al. 2003). Afterwards the names were unified as channelrhodopsins.

## 2.2 The Eyespot and Photoreception in *C. reinhardtii*

### 2.2.1 The Eyespot

The eyespot (the eyespot apparatus or the stigma) is a primary photoreceptive organelle for photoresponses (Hartshorne 1953; Dieckmann 2003). It is located near the cell equator, appearing as an orange or red spot under the microscope (Fig. 2.1). The eyespot is composed of two components: carotenoid-rich granule

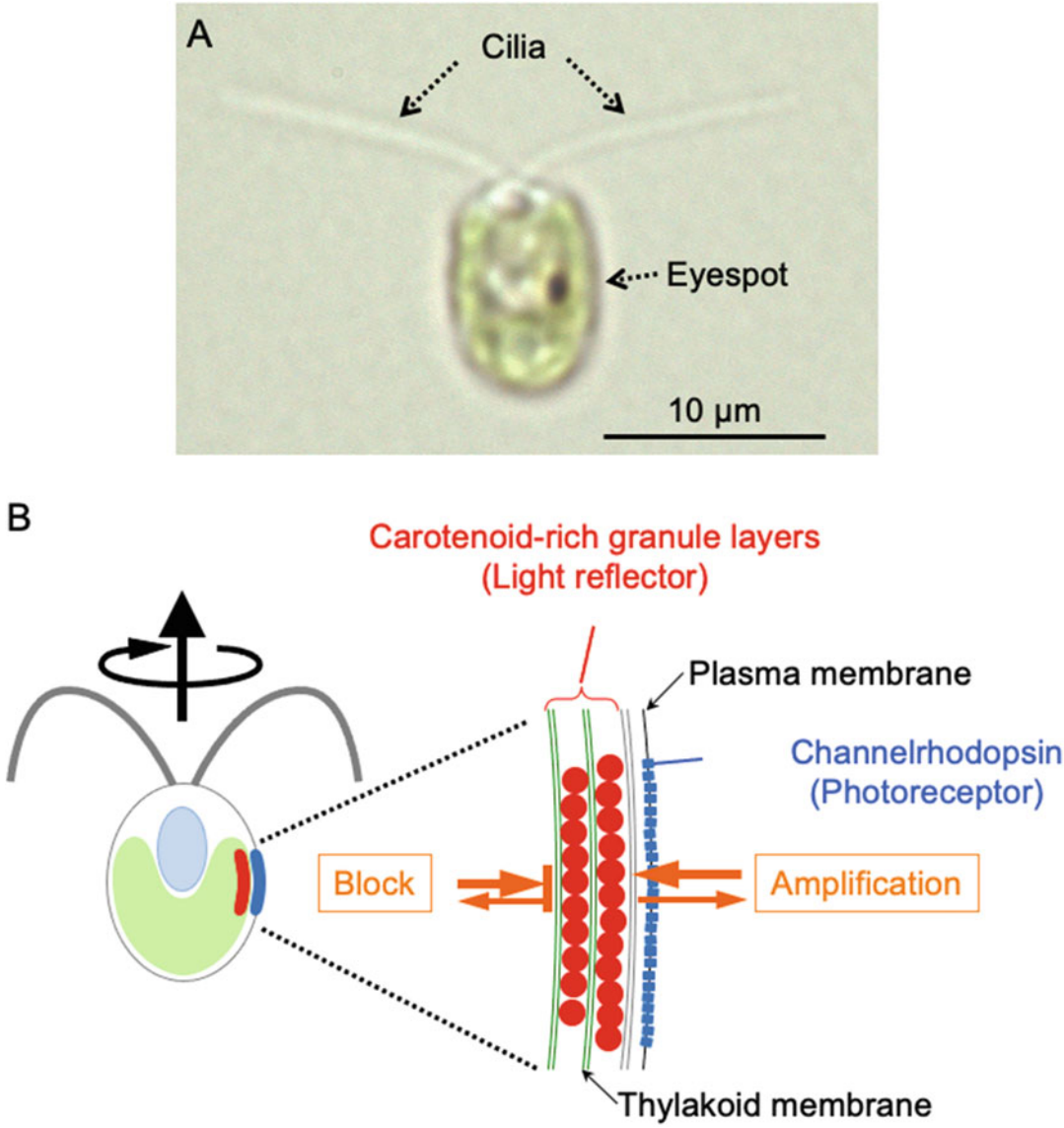


**Fig. 2.1** (**a**) *Chlamydomonas reinhardtii*. The eyespot is a red spot near the cell equator. (**b**) Schematic models of the cell and the eyespot. The cell has a cup-shaped chloroplast that surrounds the nucleus. It swims forward (i.e., with the cilia front) by beating the cilia like human's breast stroke. It swims with bodily rotation, and the rotation is counterclockwise when viewed toward the swimming direction. The eyespot consists of carotenoid granule layers (red) and photoreceptor proteins, channelrhodopsins (blue). The carotenoid layers reflect the light beam (orange arrows) and amplifies the light signal coming from the outside of the cell to ChRs while blocking the light from the inside of the cell. Adapted from Ueki et al. (2016) with modifications

layers (CGL) within the chloroplast and the light receptor molecule ChRs within the plasma membrane. The color of the eyespot is derived from the carotenoids in CGL. The eyespot in a narrow definition denotes the CGL part. In that definition, the combination of CGL and ChRs is called the eyespot apparatus (In this chapter, "the eyespot" means the whole structure of the CGL and ChRs.)

Major carotenoids in the CGL are β-carotene (~60%) and lutein (~30%) (Eichenberger et al. 1986; Niyogi et al. 1997). Phytoene synthase (PSY) is the key enzyme in the biosynthesis

pathway of carotenoids that catalyze geranylgeranyl-diphosphate to 15-*cis*-phytoene (Gregonis and Rilling 1974). Several PSY-deficient mutants have been isolated (McCarthy et al. 2004). The null mutants (*lts1–30* and *lts1–201* through *210*) have transparent cell bodies and are called the white mutants. A PSY mutant with one amino acid substitution at the catalytic domain, *lts1–211*, retains carotenoids to some extent and has a normal green cell; however, the eyespot is colorless (Ueki et al. 2016). This suggests that the synthesized carotenoids are predominantly used in chloroplast for protection of photosystems, and only the rest of the carotenoids are used for the eyespot.

ChR1 and ChR2 are light-gated channel proteins (Nagel et al. 2002, 2003, 2005; Zhang et al. 2006). These ChRs conduct cations into cells upon isomerization of retinal from all-*trans* to 13-*cis*-retinal and subsequent structural changes. These are nonspecific cation channels that conduct $H^+$, $Na^+$, $K^+$, and $Ca^{2+}$. RNAi-based knockdown experiments showed that ChR1 is the main photoreceptor for photoresponses (Berthold et al. 2008).

*C. reinhardtii* has been known to possess totally eight opsin-like proteins including ChR1/2, collectively called chlamyopsin (Cop). Cop1 and Cop2 are encoded by the same gene and produced by its alternative splicing (Fuhrmann et al. 2003). They were initially found as proteins similar to invertebrate opsins, but knockdown experiment showed that they do not serve as photoreceptor for photoresponses (Fuhrmann et al. 2001). Recently, the study on their homolog in *Volvox carteri* (Vop1) revealed that Vop1 is actually a basal body protein; Cop1/2 was then renamed as Babo1 (von der Heyde and Hallmann 2020). Cop3 and Cop4 are former names of ChR1 and ChR2, respectively. Cop5–Cop8 commonly possess rhodopsin domain, as well as histidine kinase domain and response regulator domain (Awasthi et al. 2016; Kateriya et al. 2004). Among these, Cop8 is a multidomain protein that also possesses potassium channel-, cNMP-, and cyclase domains, and is suggested to be transported to the eyespot and cilia via the IFT system (see below) together with ChR1 (Awasthi et al. 2016). However, functions of Cop5–Cop8 are still to be clarified.

The relative position of ChRs and the CGL makes the eyespot a highly directional photoreceptor (Fig. 2.1b). The key feature is that CGL functions as a quarter-wave stack that reflects light (Foster and Smyth 1980; Morel-Laurens and Feinleib 1983). When light is illuminated from the outside of the cell (i.e., from the ChR side), the light is reflected by the CGL and the light signal detected by ChRs is amplified. When the light is illuminated from the inside of the cell (i.e., from the CGL-side), it cannot reach the ChRs because of the reflection.

The position of the eyespot is determined by the microtubule bundles called the microtubular rootlet (hereinafter referred to as rootlet) (Fig. 2.2). There are four rootlets projecting from the ciliary basal body region (containing two basal bodies). From each basal body, a bundle of four microtubules and another bundle of two microtubules grow at the right angle (when viewed from the top) and run right beneath the plasma membrane (Fig. 2.2) (Goodenough and Weiss 1978). The basal body is replicated in a semi-conservative manner, such that one probasal body is grown from each basal body and they align diagonally with respect to each other (Dutcher 2003; Geimer and Melkonian 2004). During mitosis, the combination of a basal body and a probasal body is distributed into a single daughter cell and matures as the pair of new basal bodies, and then new probasal bodies are nucleated from them. The two basal bodies in the daughter cell, although looking similar, are distinct; one is a mature basal body in the mother cell (mother basal body), and the other (daughter basal body) is the one newly matured from the probasal body. The eyespot is located at the distal portion of four-microtubule rootlet generated from the daughter basal body termed D4 (Fig. 2.2) (Holmes and Dutcher 1989; Kreimer 2009).

Several eyespot mutants have been isolated, which gave insights into the molecular

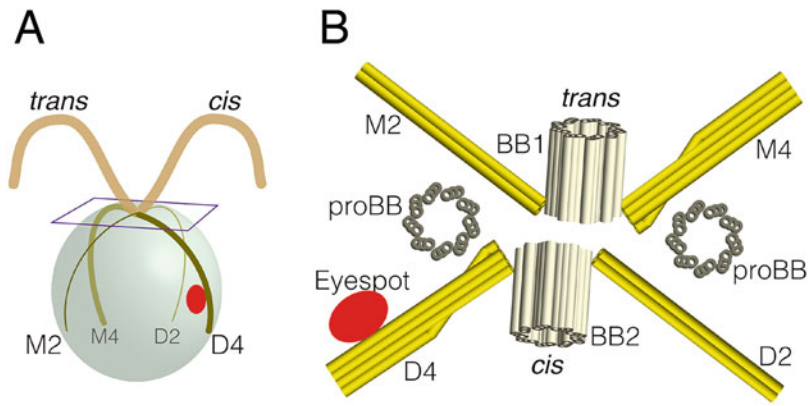


**Fig. 2.2** (**a**) Schematic model of the cell showing the position of the eyespot. The cilium closest to the eyespot is generated from the daughter basal body and called *cis*-cilium. The cilium, the farthest one, is generated from the mother basal body and called *trans*-cilium. Four rootlets project from the ciliary basal body region. From each basal body, a four-microtubule rootlet and a two-microtubule rootlet grow; a pair growing from the mother basal body is called M4 and M2, and a pair growing from the daughter basal body is called D4 and D2, respectively. The eyespot is localized to the D4 rootlet. (**b**) Schematic model of the basal body region (a purple rectangle in **a.**) viewed from the anterior end of the cell. The basal body (BB) has a cylindrical structure composed of nine microtubule triplets. BB1 is the mother basal body that generates the *trans*-cilium, and BB2 is the daughter basal body that generates the *cis*-cilium. There are two immature basal bodies (proBBs) between the basal bodies. Drawn based on Holmes and Dutcher (1989)

mechanism underlying the determination of the eyespot position. The mutants *mlt1* and *mlts2* have multiple eyespots at wrong positions (Mittelmeier et al. 2015; Boyd et al. 2011a). Mlt1p is a large (>300 kDa) low-complexity protein (>50% are Ala, Gly, Ser, or Pro) without any domains localizing to the D4 rootlet (Mittelmeier et al. 2015). Mlt2p is also a low-complexity protein of ~96 kDa with seven leucine-rich repeats (Mittelmeier et al. 2015). Mlt1p is unstable in the *mlt2*-null mutant, suggesting a functional interaction between the two proteins. Also, eyespot-less mutants, *eye1*~*eye3*, have been isolated (Lamb et al. 1999; Smyth et al. 1975). Eye2p is a thioredoxin-like protein that localizes to the chloroplast envelope (Boyd et al. 2011b, a). Eye3p is a Ser/Thr kinase that localizes to the CGL (Boyd et al. 2011a, b). These proteins may function together in determining the eyespot construction at the correct position. Mutants with small eyespots, *min1* and *min2*, have also been isolated (Boyd et al. 2011a). The products of the corresponding genes may contribute to eyespot stabilization. However, further analysis is necessary to understand the whole mechanisms of the eyespot construction.

ChRs are suggested to be transported by the intraflagellar transport (IFT) system along the rootlet microtubules (Awasthi et al. 2016). IFT is an essential system for generation of cilia (Kozminski et al. 1995; Cole 2003). Ciliary components are transported attaching to the IFT particle, a large protein complex with ~20 subunits. During ciliary elongation, kinesin-II transports the IFT particles together with the ciliary components to the tip of cilium, and the ciliary components are released either at the tip or at the middle portion of the cilium (called the anterograde IFT). During ciliary resorption, cytoplasmic dynein transports the IFT particles together with dissociated ciliary components (called the retrograde IFT) (Pazour et al. 1999; Kozminski et al. 1995). Interestingly, under light conditions, some fraction of ChR1 is suggested to be transported also to ciliary membrane by IFT, and it disappears in the dark (Awasthi et al. 2016). Currently the function of ChR1 (and another opsin called Cop8) in the cilia is unknown.

### 2.2.2 Photoreception in Swimming *C. reinhardtii* Cells

A *C. reinhardtii* cell swims with self-rotation (Figs. 2.1b and 2.3), caused by the skew of the beating planes of the two cilia. This rotation is another key to understanding the directional photoreception of *C. reinhardtii*. If the light is illuminated from the side of the swimming path, the eyespot senses the light intensity fluctuation due to the bodily rotation (Kamiya and Witman 1984; Isogai et al. 2000). Because the light induces cation influx through ChRs, the light fluctuation is converted to the fluctuation of intracellular cation concentrations (Matsuda et al. 1998; Sineshchekov et al. 1992, 1994). Cells correctly detect the direction of the light source from the intracellular cation concentration, which is maximum when the eyespot faces the light source.

Interestingly, the sensitivity of ChRs is optimized for the self-rotation frequency of *C. reinhardtii* cells, 1–5 Hz, the average being ~2 Hz (Yoshimura and Kamiya 2001; Choudhary et al. 2019). The photoreceptor current (PRC) (ion influx into the cell through ChRs) elicited by repetitive light stimuli was found to sensitively respond to stimuli of 1–5 Hz, but not to those under 1 Hz or over 5 Hz (Yoshimura and Kamiya 2001). Thus, light fluctuations caused by sources other than the bodily rotation, such as the back-and-forth vibration of the cell during the forward swimming (typically 50–60 Hz), do not disturb the detection of the light source direction (Wakabayashi and King 2006; Kamiya and Hasegawa 1987).

The light reflection by the CGL is indispensable for the accurate detection of light direction. The *lts-211* mutant has a colorless eyespot as mentioned above. The cells show phototaxis, but the sign (or direction) is opposite to the wild type; when the wild-type cells show positive phototaxis (swimming toward the light source), the *lts1–211* cells show negative phototaxis (swimming against the light source), and vice versa (Ueki et al. 2016). This is caused by the cellular lensing effect, i.e., the cell functions as a convex lens (Fig. 2.3). Without the CGL, the signal of light coming through the cell body to ChRs is due to the lens effect of the cell body, greater than that of the light coming directly onto ChRs from the outside of the cell. This leads to the cell's "misunderstanding" of the light direction. Thus, the wild-type cells and the *lts1–211* cells swim in opposite directions. Other so-called eyeless mutants, *eye1~eye3*, with defects in carotenoid accumulation to the eyespot also show the opposite-sign phototaxis (Ueki et al. 2016).

## 2.3 Photoresponses in *C. reinhardtii*

*C. reinhardtii* cells show three types of photoresponses by changing manners of ciliary beating after light illumination: phototaxis, photoshock response, and photokinesis (Hegemann and Berthold 2009). Phototaxis, or phototactic response, is the cellular behavior in which cells swim toward or away from the light source (positive or negative phototaxis, respectively). Photoshock response, or photophobic response, is a response to sudden changes in the light intensity in which cells swim backward or stop swimming for a short period (typically <1 s). Photokinesis is a response in which cells swim faster when illuminated than in the dark (Pazour et al. 1995). Especially the former two responses are important for cells to inhabit under optimal light conditions; cells need to harvest the light energy, but at the same time they to escape from too strong light to avoid the high-light stress (Demmig-Adams and Adams 1992). These two responses are suggested to be ChR-dependent and are explained in detail in the following (Berthold et al. 2008).

### 2.3.1 Phototaxis

The phototaxis pathway in *C. reinhardtii* is suggested to consist of roughly three steps: (1) photoreception at ChRs; (2) increase in intraciliary $[Ca^{2+}]$; and (3) change of the beating

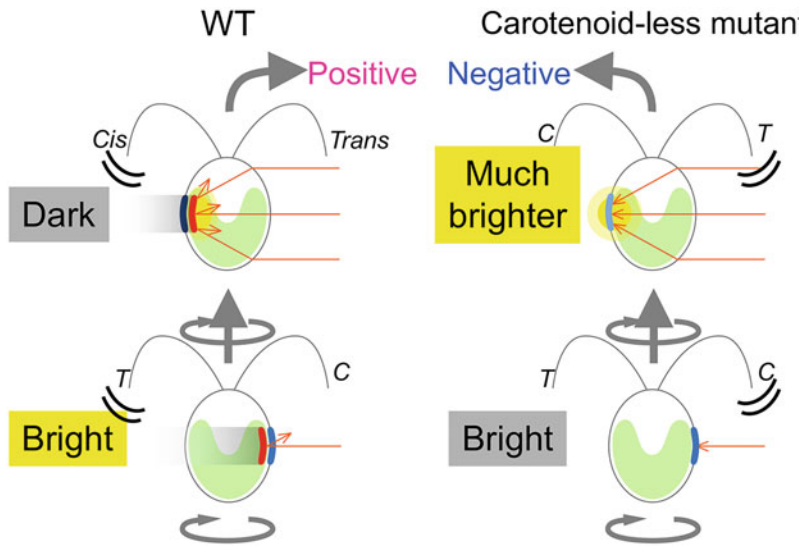


**Fig. 2.3** Schematic models showing the effect of light illumination in the wild type (WT, left) and the carotenoid-less mutant (right). Carotenoid granule layers (red) reflect and amplify the light signal (orange arrows) onto the photoreceptors (blue) when the eyespot faces the light source. These layers shield the photoreceptors from the light condensed by the lens effect of the cell when the eyespot faces the side opposite the light source in WT. In the carotenoid-less mutant, the photoreceptors receive stronger light stimulation when facing away from the light source, i.e., in an opposite manner to that of WT. In contrast, under the same light conditions, the carotenoidless mutant cells show negative phototaxis by beating the *cis*-cilium stronger than the *trans*-cilium when the eyespot faces the light source and vice versa. Adapted from Ueki et al. (2016) with modifications

balance between two cilia (Fig. 2.4a). Step (1) is obviously the step that initiates phototaxis. The ChRs-deficient mutant does not show phototaxis at all (Fig. 2.4b). Step (2) has been suggested by several previous studies, but no direct evidence has been shown to date (Kamiya and Witman 1984; Stavis and Hirschberg 1973). Step (3) directly regulates the phototactic turning. The cilium closest to the eyespot (i.e., the cilium generated from "new" basal body) is called the *cis*-cilium, and the other one (generated from the "old" basal body) is called the *trans*-cilium (see Section 2-i) and Fig. 2.2). If the *trans*-cilium beats stronger than the *cis*-cilium immediately after the photoreception, the cell will turn to the light source and show positive phototaxis; conversely, if the *cis*-cilium beats stronger than the other, the cell will show negative phototaxis (Fig. 2.4a). To accomplish this model, the properties of the two cilia must be somewhat different, but currently no structural or biochemical difference has been found.

There are two known differences between the two cilia. First, the beating frequencies are different. The *trans*-cilium tends to beat at 30–40% higher frequency than the *cis*-cilium in vitro (Kamiya and Hasegawa 1987). Though live *C. reinhardtii* cells swim like human's breast stroke, two cilia do not always beat synchronously, and the synchrony is often interrupted by the acceleration of the *trans*-cilium, but not the *cis*-cilium (Rüffer and Nultsch 1987). Second, the two cilia are different in their $Ca^{2+}$-sensitivity. Phototaxis in *C. reinhardtii* has been shown to be $Ca^{2+}$-mediated because cells do not show phototaxis in solutions containing the $Ca^{2+}$ chelator EGTA (Stavis and Hirschberg 1973). To test the difference in $Ca^{2+}$ sensitivity between the two cilia, following experiments were carried out. After detergent-extracted cell models (i.e., dead cells) are supplied with ATP, the motility of cell models is reactivated, as the ciliary inner structure (axoneme) is undamaged after extraction. When the motility is reactivated in a series of $Ca^{2+}$

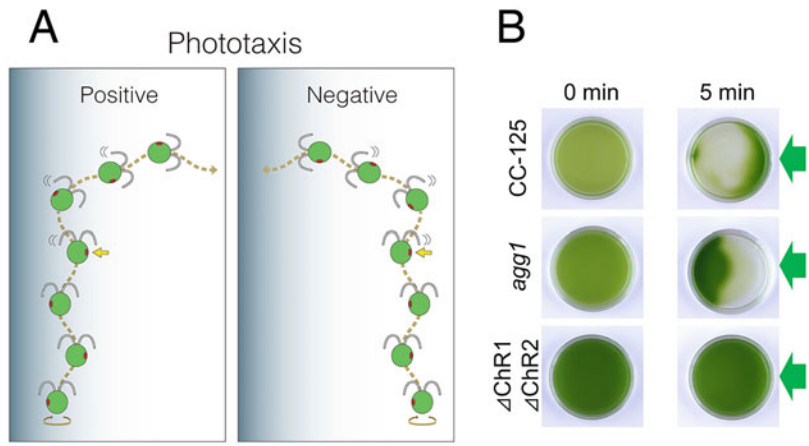


**Fig. 2.4** (**a**) Models for phototaxis. The light is illuminated from the right side. (Left) A cell showing positive phototaxis. When the cell perceived light during the forward swimming with bodily rotations (yellow arrow), it turns to the light source side by beating the *trans*-cilium stronger than *cis*-cilium when the eyespot faces the light source, or by beating the *cis*-cilium stronger than the *trans*-cilium when the eyespot faces the side opposite to the light source. This model is consistent with the results in Isogai et al. (2000). (Right) A cell showing negative phototaxis. Two cilia respond in an opposite manner; it turns to the side opposite to the light source side by beating the *cis*-cilium stronger than *trans*-cilium when the eyespot faces the light source, or by beating the *trans*-cilium stronger than the *cis*-cilium when the eyespot faces the side opposite to the light source. This model is consistent with the results in Rüffer and Nultsch (1991). (**b**) Dish phototaxis assay. Cell suspension is put in a 3.5-cm dish and pictured before (left) and 5 min after (right) the onset of green light illumination from the right. The strain at the top is CC-125, a wild-type strain that shows positive phototaxis. The strain in the middle is *agg1* (CC-124), which shows strong negative phototaxis. The strain at the bottom is ⊿ChR1⊿ChR2 (CC-5499), in which ChR1 and ChR2 are disrupted by genome editing with CRISPR/Cas9. This strain does not show phototaxis. CC-5499 was made by Ms. Olga Baidukova in the Peter Hegemann's Lab in Humboldt University of Berlin and purchased from the *Chlamydomonas* Resource Center (https://www.chlamycollection.org/)

buffers, the cell models tend to swim in circular paths. At $Ca^{2+}$ concentrations $>10^{-7}$ M, the cell models swim in circular paths with the eyespot inside because the *trans*-cilium beat stronger than the *cis*-cilium; conversely, in low-$Ca^{2+}$ buffers ($<10^{-8}$ M), the cell models swim with the eyespot outside because the *cis*-cilium beat stronger than the *trans*-cilium; at $\sim10^{-8}$ M, the two cilia beat nearly equally strongly and the cells tended to swim straight (Fig. 2.5) (Kamiya and Witman 1984; Okita et al. 2005).

This difference suggests a manner of $Ca^{2+}$ regulation in phototaxis. The intracellular $Ca^{2+}$ concentration is presumably $\sim10^{-8}$ M at the basal state. When it increases/decreases from the basal state, one cilium is activated and beats stronger than the other. When the eyespot faces the light source, the photoreception by ChRs possibly leads to $[Ca^{2+}]_i$ elevation either directly or indirectly. The *trans*-cilium then becomes dominant and the cell turns to the light source. After the cell rotates 180°, ChRs are shielded from the stimulus light by the CGL, $[Ca^{2+}]_i$ decreases, and the *cis*-cilium becomes dominant. In this way, the cell shows positive phototaxis.

This model explains well the mechanism of positive phototaxis, but not that of negative phototaxis (Isogai et al. 2000). There are several negatively phototactic strains, and in the strain known as *agg1*, the *cis*-cilium beats stronger than the *trans*-cilium (Iomini et al. 2006; Rüffer and Nultsch 1991). This indicates that the properties of the two cilia are reversed between positively phototactic strain and negatively phototactic strain. However, no difference has been found between the positively phototactic cells and the *agg1* cells with respect to the in vitro $Ca^{2+}$-sensitivities of the two cilia (Wakabayashi et al.

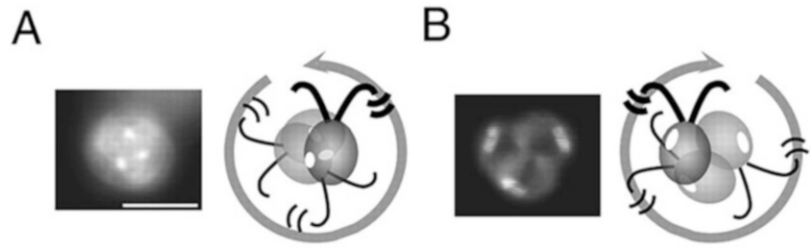


**Fig. 2.5** $Ca^{2+}$-dependent dominance switching between the *cis*- and *trans*-axonemes. (**a**, **b**) Superimposed images of rotating cell models reactivated with ATP. Cells tended to rotate with the eyespot pointing inward in a solution containing $10^{-6}$ M $Ca^{2+}$ (**a**) and outwards in $Ca^{2+}$-free solution (**b**), suggesting that the *trans*- and the *cis*-cilium is dominantly beating, respectively. Bar: 10μm. Adapted from Okita et al. (2005)

2011). Moreover, the Agg1p amino acid sequence suggests that it is a mitochondrial protein (Ide et al. 2016). To date, how the difference between the two cilia is established and how the strong-beating cilium is switched in positively phototactic and negatively phototactic strains are totally unknown.

### 2.3.2 Photoshock Response

Photoshock response occurs when cells are illuminated by sudden strong light. Upon photoshock, cells swim backward (i.e., to the cell body direction) for a short period (Fig. 2.6). During the backward swimming, ciliary waveform changes from asymmetrical type to symmetrical type in a $Ca^{2+}$-dependent manner. In vitro experiments wherein the motility of demembranated cilia was reactivated by addition of ATP in the absence of $Ca^{2+}$, the demembranated cilia beat with an asymmetrical waveform, similar to the one observed in live swimming cells (Fig. 2.7) (Hyams and Borisy 1978; Bessen et al. 1980; Wakabayashi et al. 1997). The waveform converts to the symmetrical waveform when the $Ca^{2+}$ concentration was raised to $10^{-4}$ M.

In addition to the ciliary waveform, the angle between the two cilia also changes depending on the $Ca^{2+}$ concentration; it is 80–120° at $<10^{-7}$ M $Ca^{2+}$, but decreases to 60°–100° at $>10^{-6}$ M $Ca^{2+}$ (Hayashi et al. 1998). This change may be caused by the contraction of the centrin-containing fiber (called the distal striated fiber) that connects the two basal bodies (Salisbury et al. 1988; Wright et al. 1985). This response may facilitate the backward swimming of *C. reinhardtii* cells caused by the waveform conversion for photoshock response.

As written above, the photoshock response is $Ca^{2+}$-regulated, and the $Ca^{2+}$ channel responsible for this response was identified from a mutant with defects in the photoshock response. The mutant *ppr2* (*photophobic response 2*) isolated as a mutant unable to display the photoshock response was found to lack functional CAV2, a subunit of a voltage-dependent $Ca^{2+}$ channel (Matsuda et al. 1998; Fujiu et al. 2009). In wild-type *C. reinhardtii*, membrane depolarization caused by photoreception by ChRs opens the voltage-dependent $Ca^{2+}$ channel. The ChRs-deficient mutant naturally does not show any photoshock response (Fig. 2.6b). It is interesting to note that the CAV2 localizes to the ciliary tips (Fujiu et al. 2009). This localization may be important to avoid deciliation upon photoshock because the $Ca^{2+}$ concentration required for waveform conversion ($10^{-4}$ M) is sufficiently high to induce deciliation if attained in the ciliary basal portion (Sanders and Salisbury 1989).

## 2.4 Conclusions and Open Questions

In this chapter, we outlined how *C. reinhardtii* cells perceive light at the eyespot, how they detect the light direction, and how they change their behavior in response to the light stimulus. Recent

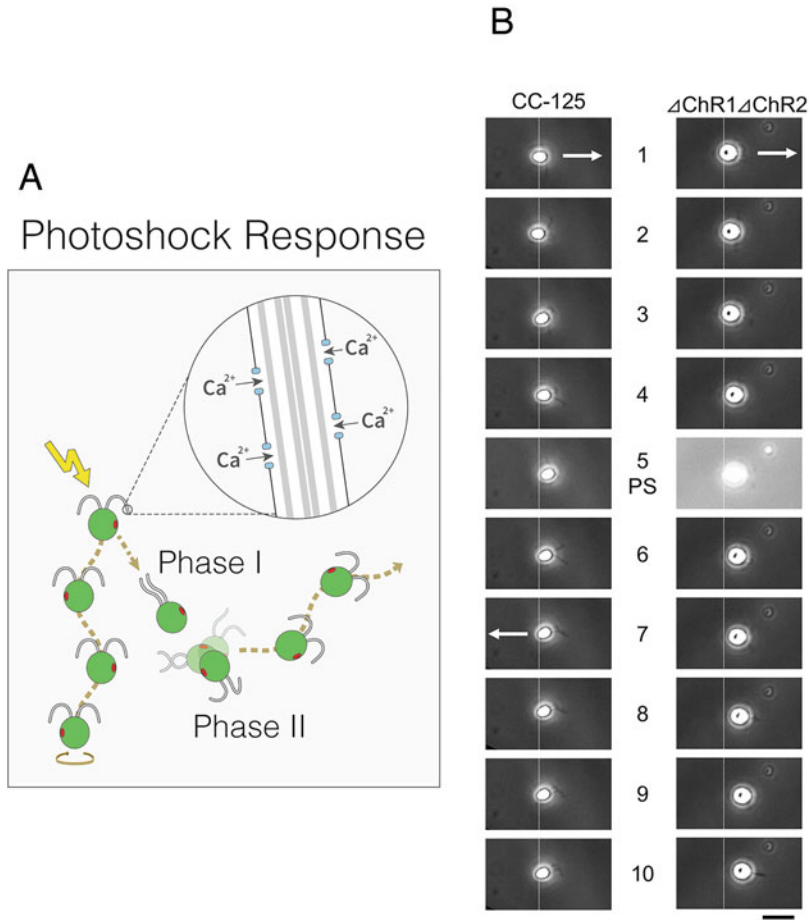


**Fig. 2.6** (**a**) Model for photoshock response. Upon reception of strong light (yellow arrow), a voltage-dependent $Ca^{2+}$-channel localized at the ciliary tip portion opens. After subsequent $Ca^{2+}$ influx to the cilia, a cell shows waveform conversion from an asymmetrical type to a symmetrical type and swims backward (Phase I). After a short period of time (typically <1 s), the cell rotates to randomize the swimming direction (Phase II), and, subsequently, the cell resumes forward swimming. Adapted from Wakabayashi and King (2006) with modifications. (**b**) Sequential high-speed images of *C. reinhardtii* cells swimming observed under a phase-contrast microscope. The left panels show CC-125, a wild-type strain, and the right panels show ⊿ChR1⊿ChR2 (CC-5499). Time interval, 12.5 ms. Photoshock (PS) is applied at panel 5. The CC-125 cell stops beating the cilia in panel 6 and starts backward swimming from panel 7. In contrast, ⊿ChR1⊿ChR2 cell does not respond to the photoshock. White arrows show the swimming direction. Dotted lines are the reference for the position of the cell, set at the posterior end of the cell in panel 5. Bar: 20μm. CC-5499 was made by Ms. Olga Baidukova in the Peter Hegemann's Lab in Humboldt University of Berlin and purchased from the *Chlamydomonas* Resource Center (https://www.chlamycollection.org/)

studies have established that *C. reinhardtii* cells have a smart system to detect the accurate light source direction, made possible by the combined functions of directional photodetection at the eyespot and the self-rotational swimming. However, several important questions are still open. How does the $Ca^{2+}$ influx for phototaxis occur? Unlike in the photoshock response, the voltage-dependent $Ca^{2+}$ channel for phototaxis has not been identified. How are the carotenoids packed into the granules? How do those granules align? What is the physiological significance of ChR1 in cilia? These questions should be answered by further analysis. In addition, functional analysis

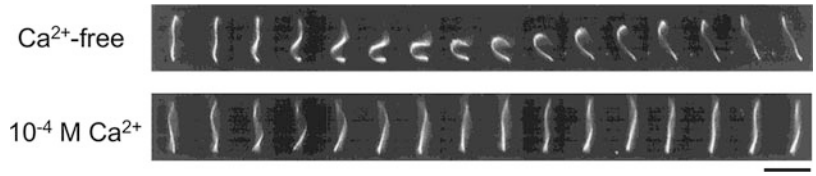


**Fig. 2.7** $Ca^{2+}$-dependent waveform conversion in wild-type ciliary axonemes. Axonemes were reactivated with 20μM ATP. In a $Ca^{2+}$-free solution (top), the axoneme beats in an asymmetrical waveform. In a solution containing $10^{-4}$ M $Ca^{2+}$ (bottom), the axoneme beats in a symmetrical waveform. Time interval, 1/60 s. The axonemes shown were attached to the glass surface by the proximal end (the end nearer to the bottom of the page). Bar: 10μm. Adapted from Wakabayashi et al. (1997) with modifications

of Cop5–Cop8 may contribute to optogenetics in the future.

**Acknowledgments** We would like to thank Dr. Ritsu Kamiya (Univ. Tokyo, Chuo Univ.) for critical reading of this manuscript, and Dr. Masafumi Hirono (Hosei Univ.) and Mr. Satoaki So (Tokyo Tech) for discussion. CC-5499 was made by Ms. Olga Baidukova in the Peter Hegemann's Laboratory in Humboldt University of Berlin, and purchased from *Chlamydomonas* Resource Center. This work was supported by Japan Society for the Promotion of Science KAKENHI Grants 19H03242 to KW, 19K23758 to NU, by Ohsumi Frontier Science Foundation to KW, by Dynamic Alliance for Open Innovation Bridging Human, Environment and Materials to KW, and by the Assistant Staffing Program by the Gender Equality Promotion Section, Office of Public Engagement, Tokyo Institute of Technology to AI and KW.

## References

Asamizu E, Nakamura Y, Sato S, Fukuzawa H, Tabata S (1999) A large scale structural analysis of cDNAs in a unicellular green alga, *Chlamydomonas reinhardtii*. I. Generation of 3433 non-redundant expressed sequence tags. DNA Res 6:369–373

Asamizu E et al (2000) Generation of expressed sequence tags from low-$CO_2$ and high-$CO_2$ adapted cells of *Chlamydomonas reinhardtii*. DNA Res 7:305–307

Awasthi M, Ranjan P, Sharma K, Veetil SK, Kateriya S (2016) The trafficking of bacterial type rhodopsins into the *Chlamydomonas* eyespot and flagella is IFT mediated. Sci Rep 6:34646

Berthold P, Tsunoda SP, Ernst OP, Mages W, Gradmann D, Hegemann P (2008) Channelrhodopsin-1 initiates phototaxis and photophobic responses in *Chlamydomonas* by immediate light-induced depolarization. Plant Cell 20:1665–1677

Bessen M, Fay RB, Witman GB (1980) Calcium control of waveform in isolated flagellar axonemes of *Chlamydomonas*. J Cell Biol 86:446–455

Boyd JS, Lamb MR, Dieckmann CL (2011a) Miniature- and multiple-eyespot loci in *Chlamydomonas reinhardtii* define new modulators of eyespot photoreception and assembly. G3 (Bethesda) 1:489–498

Boyd JS, Mittelmeier TM, Lamb MR, Dieckmann CL (2011b) Thioredoxin-family protein EYE2 and Ser/Thr kinase EYE3 play interdependent roles in eyespot assembly. Mol Biol Cell 22:1421–1429

Choudhary SK, Baskaran A, Sharma P (2019) Reentrant efficiency of Phototaxis in *Chlamydomonas reinhardtii* cells. Biophys J 117:1508–1513

Cole DG (2003) The intraflagellar transport machinery of *Chlamydomonas reinhardtii*. Traffic 4:435–442

Cong L et al (2013) Multiplex genome engineering using CRISPR/Cas systems. Science 339:819–823

Demmig-Adams B, Adams WW 3rd (1992) Photoprotection and other responses of plants to high light stress. Ann Rev Plant Physiol Plant Mol Biol 43:599–626

Dieckmann CL (2003) Eyespot placement and assembly in the green alga Chlamydomonas. Bioessays 25:410–416

Dutcher SK (2003) Elucidation of basal body and centriole functions in *Chlamydomonas reinhardtii*. Traffic 4:443–451

Eichenberger W, Boschetti A, Michel HP (1986) Lipid and pigment composition of a chlorophyll beta-deficient mutant of Chlamydomonas reinhardii. Physiol Plant 66:589–594

Foster KW, Smyth RD (1980) Light antennas in phototactic algae. Microbiol Rev 44:572–630

Foster KW, Saranak J, Patel N, Zarilli G, Okabe M, Kline T, Nakanishi K (1984) A rhodopsin is the functional photoreceptor for phototaxis in the unicellular eukaryote *Chlamydomonas*. Nature 311:756–759

Fuhrmann M, Stahlberg A, Govorunova E, Rank S, Hegemann P (2001) The abundant retinal protein of the *Chlamydomonas* eye is not the photoreceptor for phototaxis and photophobic responses. J Cell Sci 114:3857–3863

Fuhrmann MDW, Kateriya S, Hegemann P (2003) Rhodopsinrelated proteins, cop1, cop2 and chop1, in Chlamydomonas reinhardtii. In: Batschauer A (ed) Photoreceptors and light signaling. Royal Society of Chemistry, Cambridge

Fujiu K, Nakayama Y, Yanagisawa A, Sokabe M, Yoshimura K (2009) *Chlamydomonas CAV2* encodes a voltage- dependent calcium channel required for the flagellar waveform conversion. Curr Biol 19:133–139

Gallaher SD, Fitz-Gibbon ST, Glaesener AG, Pellegrini M, Merchant SS (2015) Chlamydomonas genome resource for laboratory strains reveals a mosaic of sequence variation, identifies true strain histories, and enables strain-specific studies. Plant Cell 27:2335–2352

Geimer S, Melkonian M (2004) The ultrastructure of the *Chlamydomonas reinhardtii* basal apparatus: identification of an early marker of radial asymmetry inherent in the basal body. J Cell Sci 117:2663–2674

Goodenough UW, Weiss RL (1978) Interrelationships between microtubules, a striated fiber, and the gametic mating structure of *Chlamydomonas reinhardi*. J Cell Biol 76:430–438

Gregonis DE, Rilling HC (1974) The stereochemistry of *trans*-phytoene synthesis. Some observations on lycopersene as a carotene precursor and a mechanism for the synthesis of *cis*- and *trans*-phytoene. Biochemistry 13:1538–1542

Greiner A, Kelterborn S, Evers H, Kreimer G, Sizova I, Hegemann P (2017) Targeting of photoreceptor genes in *Chlamydomonas reinhardtii* via zinc-finger nucleases and CRISPR/Cas9. Plant Cell 29:2498–2518

Gross CH, Ranum LPW, Lefebvre PA (1988) Extensive restriction fragment length polymorphisms in a new isolate of *Chlamydomonas reinhardtii*. Curr Genet 13:503–508

Gumpel NJ, Rochaix JD, Purton S (1994) Studies on homologous recombination in the green alga *Chlamydomonas reinhardtii*. Curr Genet 26:438–442

Harris EH (2009a) *Chlamydomonas* in the laboratory. In: Harris EH (ed) The *Chlamydomonas* sourcebook, vol 1, 2nd edn. Academic Press, London, pp 241–302

Harris EH (2009b) The sexual cycle. In: Harris EH (ed) The *Chlamydomonas* sourcebook, vol 1, 2nd edn. Academic Press, London, pp 119–157

Hartshorne JN (1953) The function of the eyespot in *Chlamydomonas*. New Phytol 52:292–297

Hayashi M, Yagi T, Yoshimura K, Kamiya R (1998) Real-time observation of $Ca^{2+}$−induced basal body reorientation in *Chlamydomonas*. Cell Motil Cytoskeleton 41:49–56

Hegemann P, Berthold P (2009) Sensory photoreceptors and light control of flagellar activity. In: Witman GB (ed) The *Chlamydomonas* sourcebook, vol 3, 2nd edn. Academic Press, San Diego, CA, pp 395–429

Holmes JA, Dutcher SK (1989) Cellular asymmetry in *Chlamydomonas reinhardtii*. J Cell Sci 94:273–285

Hyams JS, Borisy GG (1978) Isolated flagellar apparatus of *Chlamydomonas*: characterization of forward swimming and alteration of waveform and reversal of motion by calcium ions *in vitro*. J Cell Sci 33:235–253

Ide T, Mochiji S, Ueki N, Yamaguchi K, Shigenobu S, Hirono M, Wakabayashi K (2016) Identification of the *agg1* mutation responsible for negative phototaxis in a "wild-type" strain of *Chlamydomonas reinhardtii*. Biochem Biophys Rep 7:379–385

Iomini C, Li L, Mo W, Dutcher SK, Piperno G (2006) Two flagellar genes, *AGG2* and *AGG3*, mediate orientation to light in *Chlamydomonas*. Curr Biol 16:1147–1153

Isogai N, Kamiya R, Yoshimura K (2000) Dominance between the two flagella during phototactic turning in *Chlamydomonas*. Zool Sci 17:1261–1266

Jiang W, Brueggeman AJ, Horken KM, Plucinak TM, Weeks DP (2014) Successful transient expression of Cas9 and single guide RNA genes in *Chlamydomonas reinhardtii*. Eukaryot Cell 13:1465–1469

Jinek M, Chylinski K, Fonfara I, Hauer M, Doudna JA, Charpentier E (2012) A programmable dual-RNA-guided DNA endonuclease in adaptive bacterial immunity. Science 337:816–821

Kamiya R, Hasegawa E (1987) Intrinsic difference in beat frequency between the two flagella of Chlamydomonas reinhardtii. Exptl Cell Res 173, 299–304

Kamiya R, Witman GB (1984) Submicromolar levels of calcium control the balance of beating between the two flagella in demembranated models of *Chlamydomonas*. J Cell Biol 98:97–107

Kateriya S, Nagel G, Bamberg E, Hegemann P (2004) "Vision" in single-celled algae. News Physiol Sci 19:133–137

Kong F, Yamaoka Y, Ohama T, Lee Y, Li-Beisson Y (2019) Molecular genetic tools and emerging synthetic biology strategies to increase cellular oil content in *Chlamydomonas reinhardtii*. Plant Cell Physiol 60:1184–1196

Kozminski KG, Beech PL, Rosenbaum JL (1995) The *Chlamydomonas* kinesin-like protein FLA10 is involved in motility associated with the flagellar membrane. J Cell Biol 131:1517–1527

Kreimer G (2009) The green algal eyespot apparatus: a primordial visual system and more? Curr Genet 55:19–43

Lamb MR, Dutcher SK, Worley CK, Dieckmann CL (1999) Eyespot-assembly mutants in *Chlamydomonas reinhardtii*. Genetics 153:721–729

Matsuda A, Yoshimura K, Sineshchekov OA, Hirono M, Kamiya R (1998) Isolation and characterization of novel *Chlamydomonas* mutants that display phototaxis but not photophobic response. Cell Motil Cytoskeleton 41:353–362

McCarthy SS, Kobayashi MC, Niyogi KK (2004) White mutants of *Chlamydomonas reinhardtii* are defective in phytoene synthase. Genetics 168:1249–1257

Melis A, Zhang L, Forestier M, Ghirardi ML, Seibert M (2000) Sustained photobiological hydrogen gas production upon reversible inactivation of oxygen evolution in the green alga *Chlamydomonas reinhardtii*. Plant Physiol 122:127–136

Merchant SS et al (2007) The *Chlamydomonas* genome reveals the evolution of key animal and plant functions. Science 318:245–250

Mittelmeier TM, Thompson MD, Lamb MR, Lin H, Dieckmann CL (2015) MLT1 links cytoskeletal

asymmetry to organelle placement in Chlamydomonas. Cytoskeleton (Hoboken) 72:113–123
Morel-Laurens NML, Feinleib MEH (1983) Photomovement in an "eyeless" mutant of Chlamydomonas. Photochem Photobiol 37:189–194
Nagel G, Ollig D, Fuhrmann M, Kateriya S, Musti AM, Bamberg E, Hegemann P (2002) Channelrhodopsin-1: a light-gated proton channel in green algae. Science 296:2395–2398
Nagel G et al (2003) Channelrhodopsin-2, a directly light-gated cation-selective membrane channel. Proc Natl Acad Sci U S A 100:13940–13945
Nagel G, Szellas T, Kateriya S, Adeishvili N, Hegemann P, Bamberg E (2005) Channelrhodopsins: directly light-gated cation channels. Biochem Soc Trans 33:863–866
Nelson JA, Lefebvre PA (1995) Targeted disruption of the *NIT8* gene in *Chlamydomonas reinhardtii*. Mol Cell Biol 15:5762–5769
Niyogi KK, Bjorkman O, Grossman AR (1997) The roles of specific xanthophylls in photoprotection. Proc Natl Acad Sci U S A 94:14162–14167
Okita N, Isogai N, Hirono M, Kamiya R, Yoshimura K (2005) Phototactic activity in *Chlamydomonas* 'non-phototactic' mutants deficient in $Ca^{2+}$-dependent control of flagellar dominance or in inner-arm dynein. J Cell Sci 118:529–537
Pazour GJ, Sineschekov OA, Witman GB (1995) Mutational analysis of the phototransduction pathway of *Chlamydomonas reinhardtii*. J Cell Biol 131:427–440
Pazour GJ, Dickert BL, Witman GB (1999) The DHC1b (DHC2) isoform of cytoplasmic dynein is required for flagellar assembly. J Cell Biol 144:473–481
Ranum LP, Thompson MD, Schloss JA, Lefebvre PA, Silflow CD (1988) Mapping flagellar genes in Chlamydomonas using restriction fragment length polymorphisms. Genetics 120:109–122
Rüffer U, Nultsch W (1987) Comparison of the beating of cis- and trans-flagella of *Chlamydomonas* cells held on micropipettes. Cell Motil 7:87–93
Rüffer U, Nultsch W (1991) Flagellar photoresponses of *Chlamydomonas* cells held on micropipettes: II. Change in flagellar beat pattern. Cell Motil Cytoskeleton 18:269–278
Salisbury JL, Baron AT, Sanders MA (1988) The centrin-based cytoskeleton of *Chlamydomonas reinhardtii*: distribution in interphase and mitotic cells. J Cell Biol 107:635–641
Sanders MA, Salisbury JL (1989) Centrin-mediated microtubule severing during flagellar excision in *Chlamydomonas reinhardtii*. J Cell Biol 108:1751–1760
Scranton MA, Ostrand JT, Fields FJ, Mayfield SP (2015) *Chlamydomonas* as a model for biofuels and bio-products production. Plant J 82:523–531
Sineshchekov OA, Govorunova EG, Der A, Keszthelyi L, Nultsch W (1992) Photoelectric responses in phototactic flagellated algae measured in cell-suspension. J Photoch Photobio B Biol 13:119–134
Sineshchekov OA, Govorunova EG, Der A, Keszthelyi L, Nultsch W (1994) Photoinduced electric currents in carotenoid-deficient *Chlamydomonas* mutants reconstituted with retinal and its analogs. Biophys J 66:2073–2084
Sineshchekov OA, Jung K-H, Spudich JL (2002) Two rhodopsins mediate phototaxis to low- and high-intensity light in *Chlamydomonas reinhardtii*. Proc Natl Acad Sci U S A 99:8689–8694
Smyth RD, Martinek GW, Ebersold WT (1975) Linkage of six genes in *Chlamydomonas reinhardtii* and the construction of linkage test strains. J Bacteriol 124:1615–1617
Sodeinde OA, Kindle KL (1993) Homologous recombination in the nuclear genome of *Chlamydomonas reinhardtii*. Proc Natl Acad Sci U S A 90:9199–9203
Stavis RL, Hirschberg R (1973) Phototaxis in *Chlamydomonas reinhardtii*. J Cell Biol 59:367–377
Suzuki T et al (2003) Archaeal-type rhodopsins in *Chlamydomonas*: model structure and intracellular localization. Biochem Biophys Res Commun 301:711–717
Ueki N et al (2016) Eyespot-dependent determination of the phototactic sign in *Chlamydomonas reinhardtii*. Proc Natl Acad Sci U S A 113:5299–5304
von der Heyde EL, Hallmann A (2020) Babo1, formerly Vop1 and Cop1/2, is no eyespot photoreceptor but a basal body protein illuminating cell division in *Volvox carteri*. Plant J 102:276–298
Wakabayashi K, King SM (2006) Modulation of *Chlamydomonas reinhardtii* flagellar motility by redox poise. J Cell Biol 173:743–754
Wakabayashi K, Yagi T, Kamiya R (1997) $Ca^{2+}$–dependent waveform conversion in the flagellar axoneme of *Chlamydomonas* mutants lacking the central-pair/radial spoke system. Cell Motil Cytoskeleton 38:22–28
Wakabayashi K, Misawa Y, Mochiji S, Kamiya R (2011) Reduction-oxidation poise regulates the sign of phototaxis in *Chlamydomonas reinhardtii*. Proc Natl Acad Sci U S A 108:11280–11284
Wright RL, Salisbury J, Jarvik JW (1985) A nucleus-basal body connector in *Chlamydomonas reinhardtii* that may function in basal body localization or segregation. J Cell Biol 101:1903–1912
Yoshimura K, Kamiya R (2001) The sensitivity of *Chlamydomonas* photoreceptor is optimized for the frequency of cell body rotation. Plant Cell Physiol 42:665–672
Zhang F, Wang LP, Boyden ES, Deisseroth K (2006) Channelrhodopsin-2 and optical control of excitable cells. Nat Methods 3:785–792

# Structure–Function Relationship of Channelrhodopsins

3

Hideaki E. Kato

**Abstract**

Ion-translocating rhodopsins, especially channelrhodopsins (ChRs), have attracted broad attention as a powerful tool to modulate the membrane potential of cells with light (optogenetics). Because of recent biophysical, spectroscopic, and computational studies, including the structural determination of cation and anion ChRs, our understanding of the molecular mechanism underlying light-gated ion conduction has been greatly advanced. In this chapter, I first describe the background of rhodopsin family proteins including ChR, and how the optogenetics technology has been established from the discovery of first ChR in 2002. I later introduce the recent findings of the structure–function relationship of ChR by comparing the crystal structures of cation and anion ChRs. I further discuss the future goal in the fields of ChR research and optogenetic tool development.

**Keywords**

Channelrhodopsin · Optogenetics · Structural biology · Structure-guided engineering · Structure-guided mining

## Abbreviations

| | |
|---|---|
| 7TM | Seven transmembrane |
| ACR | Anion-conducting channelrhodopsin |
| ATR | All-trans-retinal |
| CCR | Cation-conducting channelrhodopsin |
| *Cr*ChR2 (or ChR2) | Cation channelrhodopsin-2 from *Chlamydomonas reinhardtii* |
| dACR | Designed anion-conducting channelrhodopsin |
| GPCR | G protein-coupled receptor |
| HR | Halorhodopsins |
| HsBR | Bacteriorhodopsin from *Halobacterium salinarum* |
| MD simulation | Molecular dynamics simulation |
| nACR | Natural anion-conducting channelrhodopsin |
| *Np*HR | Halorhodopsin from *Natronomonas pharaonis* |
| TR-SFX | Time-resolved serial femtosecond crystallography |
| TR-SMX | Time-resolved serial millisecond crystallography |

## 3.1 Classification of Rhodopsin

Light is one of the most useful resources for energy and information, and most animals capture

H. E. Kato (✉)
Komaba Institute for Science, The University of Tokyo, Tokyo, Japan
e-mail: hekato@bio.c.u-tokyo.ac.jp



H. Yawo et al. (eds.), *Optogenetics*, Advances in Experimental Medicine and Biology 1293,
https://doi.org/10.1007/978-981-15-8763-4_3

light using rhodopsin family proteins. Based on their primary sequences, rhodopsin family proteins are largely classified into two groups: microbial (type I) and animal (type II) (Ernst et al. 2014). They are both characterized by seven transmembrane (7TM) helices that bind a chromophore retinal, but their functions are very different. Animal rhodopsins primarily work as G-protein-coupled receptors (GPCRs). In most animal rhodopsins, the *11-cis* form of retinal is covalently bound to opsin via a Schiff base and light illumination triggers the isomerization of *11-cis* retinal to *all-trans*-retinal (ATR). Activated rhodopsin with ATR activates downstream signaling proteins such as heterotrimeric G proteins and arrestin, and these proteins transduce signals to various intracellular effectors (Fig. 3.1).

On the other hand, the functions of microbial rhodopsins are very divergent. Unlike animal rhodopsins, most microbial rhodopsins possess ATR in the dark state, and ATR is isomerized to *13-cis* retinal upon light absorption. Retinal isomerization causes a conformational change in protein moiety, allowing to perform distinct functions depends on the sequence of opsin. For example, bacteriorhodopsin from *Halobacterium salinarum* (*Hs*BR) transports proton from intracellular to extracellular side, and cation channelrhodopsin-2 from *Chlamydomonas reinhardtii* (*Cr*ChR2 or ChR2) conducts monovalent and divalent cations down the electrochemical gradient. So far, four functionally different ion pump-type rhodopsins (i.e., outward $H^+$ pump, inward $H^+$ pump, inward $Cl^-$ pump, and outward $Na^+$ pump), two ion channel-type rhodopsins (i.e., non-selective cation channel and non-selective anion channel), and four signaling/enzyme rhodopsins (i.e., histidine kinase, guanylyl cyclase, phosphodiesterase, and sensor) have been discovered from nature (Bogomolni and Spudich 1982; Govorunova et al. 2015; Inoue et al. 2013, 2016; Luck et al. 2012; Matsuno-Yagi and Mukohata 1977; Nagel et al. 2002; Oesterhelt and Stoeckenius 1971; Scheib et al. 2015; Yoshida et al. 2017) (Fig. 3.1). These rhodopsins have been extensively studied from the biophysical, structural, spectroscopic, and computational perspectives, and they have also attracted much attention as powerful research tools to control activities of cells, especially neurons, within living tissue in a light-dependent manner. This technology termed optogenetics has enabled us to analyze the causal relationship between electrical activity in specific neural circuits and behavioral states, the generation of intracellular second messenger (e.g., cyclic nucleotide or $Ca^{2+}$) and physiological response, and so on (Deisseroth 2015; Rost et al. 2017).

In this chapter, I will focus on ion channel-type rhodopsins, the most widely used type of optogenetics tools. I will review the discovery and engineering of cation and anion channelrhodopsin variants, the structure–function relationship of these light-gated ion channels, and briefly discuss the future goals of structural and engineering work of opsin-based optogenetics tools.

## 3.2 Discovery and Engineering of Cation and Anion Channelrhodopsins

In 1990–1991, Lajos Keszthelyi's and Peter Hegemann's groups found that the fast electrical current was involved in the rhodopsin-mediated phototactic responses in green algae (Harz and Hegemann 1991; Sineshchekov et al. 1990). Since the currents occurred only within 500 μs after light illumination, it was suggested that the photoreceptor and the ion channel formed a protein complex or were the same protein. In 2002–2003, Hegemann's, John Spudich's, and Tetsuo Takahashi's groups isolated new microbial rhodopsins from the algae (Nagel et al. 2002; Sineshchekov et al. 2002; Suzuki et al. 2003). They discovered that two archaeal-type new rhodopsins were expressed in an organelle called eyespot, and these rhodopsins were named channelrhodopsin-1 and -2 (ChR1 and ChR2) (Nagel et al. 2002), *Chlamydomonas* sensory rhodopsins A and B (CsrA and CsrB) (Sineshchekov et al. 2002), or Archaeal-type *chlamydomonas* opsins-1 and -2 (Acop-1 and Acop-2)(Suzuki et al. 2003). Hegemann's group heterologously expressed ChR1 and ChR2 in

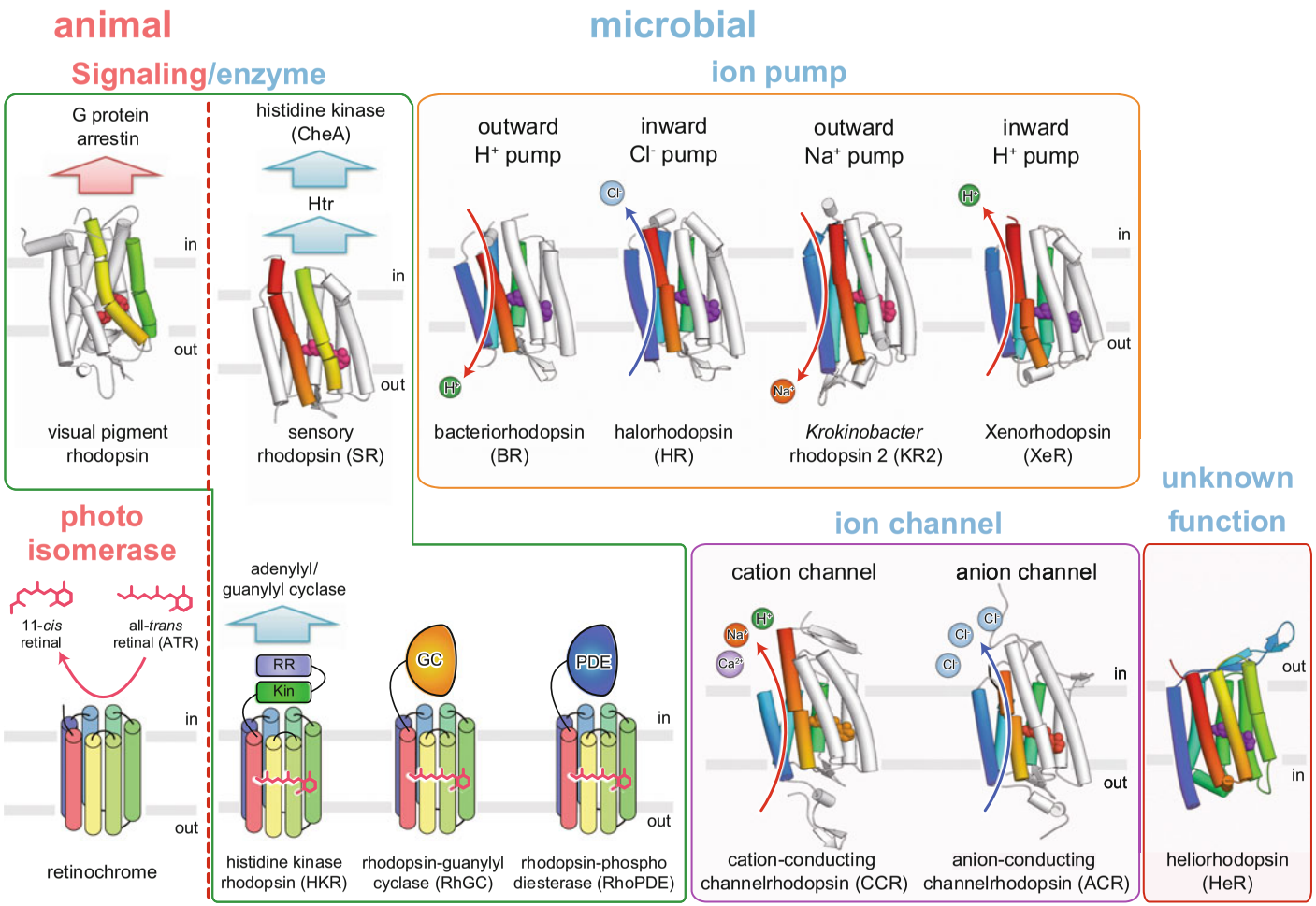


**Fig. 3.1** Classification of rhodopsin family proteins

*Xenopus* oocytes and/or mammalian cells, and identified them as light-gated cation channels using electrophysiological methods (Nagel et al. 2002, 2003). His group also demonstrated that these two proteins permeate various monovalent and divalent cations, including $H^+$, $Na^+$, $K^+$, and $Ca^{2+}$(Berthold et al. 2008; Nagel et al. 2002, 2003). (When ChR1 was first characterized in 2002, it was thought that ChR1 could only permeate $H^+$. However, Hegemann's group re-analyzed the functional properties of ChR1 and reported in 2008 that ChR1 permeated $Na^+$, $K^+$, and $Ca^{2+}$, like ChR2 (Berthold et al. 2008).) 2–3 years later, five groups in the USA, Japan, and Germany (i.e., Karl Deisseroth's, Hiromu Yawo's, Stefan Herlitze's, Alexander Gottschalk's, Hua Pan's, groups) independently succeeded in activating neurons using ChR2 (Bi et al. 2006; Boyden et al. 2005; Ishizuka et al. 2006; Li et al. 2005; Nagel et al. 2005). Notably, Gottschalk's group was the first lab using ChR2 to control the behavior (swimming behavior) in freely moving animal (*C. elegans*) (Nagel et al. 2005), and Deisseroth's group was the first to control the behavior (the sleep–wake behavior) in freely moving mammal (mouse) (Adamantidis et al. 2007). Since these studies, cation-conducting channelrhodopsins (CCRs) have begun to be used widely in the fields of neuroscience (Deisseroth 2011), and many different CCRs have been discovered or engineered with faster or slower kinetics (Bamann et al. 2010; Berndt et al. 2009; Dawydow et al. 2014; Gunaydin et al. 2010; Klapoetke et al. 2014; Kleinlogel et al. 2011; Lin et al. 2009; Mager et al. 2018; Yizhar et al. 2011), shifted absorption/action spectra (Govorunova et al. 2013, 2016; Hochbaum et al. 2014; Hou et al. 2012; Kato et al. 2015; Klapoetke et al. 2014; Lin et al. 2013; Marshel et al. 2019; Oda et al. 2018; Prigge et al. 2012; Rajasethupathy et al. 2015; Szundi et al. 2015; Zhang et al. 2008), altered ion selectivity (Cho et al. 2019; Duan et al. 2019; Kleinlogel et al. 2011; Scholz et al. 2017; Zabelskii et al. 2020), and increased light sensitivity and photocurrent amplitude (Berndt et al. 2011; Cho et al. 2019; Duan et al. 2019; Hochbaum et al. 2014; Lin et al. 2009; Marshel et al. 2019; Nagel et al. 2005; Wang et al. 2009; Yamauchi et al. 2017).

CCRs have enabled us to analyze the sufficiency of particular neural activity patterns for specific behaviors and cognitive processes, but they have not allowed us to study its necessity. To solve the problem, Deisseroth's and Boyden's groups explored $Cl^-$ pump rhodopsins, halorhodopsins (HRs), and found that HR from *Natronomonas pharaonis* (*Np*HR) is suitable to optically inhibit neural activity (Han and Boyden 2007; Zhang et al. 2007). Boyden's group later discovered that an outward $H^+$ pump rhodopsin from *Halorubrum sodomense* (archaerhodopsin-3 or Arch), and another $Cl^-$ pump rhodopsin from *Halobacterium salinarum* strain Shark with K200R and W214F mutations (Jaws) can mediate powerful silencing of neural activity (Chow et al. 2010; Chuong et al. 2014). However, pump-type rhodopsins can transport only a single ion per absorbed photon. Thus, successful silencing generally requires high protein expression levels and high light intensities that are potentially toxic to the cell. In 2014, Deisseroth's and Hegemann's groups overcame this issue by engineering anion-conducting channelrhodopsins (ACRs). Based on high-resolution structural information of C1C2, a chimeric CCR between *Cr*ChR1 and *Cr*ChR2 (Kato et al. 2012), Deisseroth's and Hegemann's groups introduced 9 and 2 mutations along the cation-conducting pathway of C1C2 and *Cr*ChR2, respectively, and converted their functions from cation to anion channel (Berndt et al. 2014; Wietek et al. 2014). Original variants, iC1C2 (C1C2 with T98S/E129S/E140S/V156K/E162S/H173R/V281K/T285N/N297Q) and ChloC (*Cr*ChR2 with E90R/T159C), still have residual $H^+$ conductance, but they continued optimization and successfully developed iC++ (C1C2 with T98S/E122N/E129Q/E140S/V156R/E162S/V281R/T285N/N297Q/E312S) and iChloC (*Cr*ChR2 with E83Q/E90R/E101S/D156N/T159C) with higher $Cl^-$ selectivity and conductivity (Berndt et al. 2016; Wietek et al. 2015). Around the same time, naturally occurring ACRs were isolated from *Guillardia theta* (*Gt*ACR1 and *Gt*ACR2) by Spudich group (Govorunova et al. 2015). These designed and

natural ACRs (dACRs and nACRs) show enhanced performance and solved major drawbacks of pumps: ACRs can translocate $10^4$–$10^5$ ions per second and can exhibit $10^2$–$10^4$-fold higher light sensitivity than inhibitory pump-type rhodopsins. Moreover, recent genome mining and structure-guided engineering approaches have found novel dACRs and nACRs with diverse properties, and the toolkit of inhibitory opsins has been greatly expanded (Govorunova et al. 2017, 2018, 2020; Oppermann et al. 2019; Wietek et al. 2017). Widely used natural and engineered ChR variants are summarized in Tables 3.1 and 3.2.

## 3.3 Overall Structure

First ChR was discovered in 2002, but the high-resolution structural information was not available until 2012. ChR has canonical 7TM domain, which is shared by all rhodopsins, and crystal structures of BR and HR were reported in 1996 and 2000, respectively (Kolbe et al. 2000; Pebay-Peyroula et al. 1997). However, it was not easy to build the reliable homology model of ChR because TMs 1 and 2 have very low similarity to those of pump-type rhodopsins. Early studies predicted that glutamates in TM2 form the part of the ion-conducting pathway and point to the outside of the TM bundle, suggesting that the ion-conducting pathway is formed between the trimer interface (Hegemann 2008; Suzuki et al. 2003). The 6-Å projection map of the two-dimensional crystal of *Cr*ChR2 revealed its dimeric architecture but led to the prediction that the ion-conducting pathway would be positioned between two monomers (Muller et al. 2011). There was no consensus regarding the position of the channel pore. In 2012, Nureki's group solved the 2.3-Å crystal structure of C1C2 (TMs 1–5 are derived from *Chlamydomonas reinhardtii* ChR1 and TMs 6–7 are from *Chlamydomonas reinhardtii* ChR2), and the structure confirmed its dimeric oligomerization state (Kato et al. 2012) (Fig. 3.2). Interfacial interactions occur in the extracellular domain, extracellular loop 1, TM3, and TM4 of each molecule. Notably, three cysteine residues in the extracellular domain form three disulfide bonds between protomers, suggesting that C1C2 dimer is physiological rather than a crystallization artifact. Moreover, glutamates in TM2 do not reside in the dimer interface but form a pore with TMs 1, 2, 3, and 7 within a monomer. The pore is accessible only from the extracellular side of the membrane, and the intracellular side is occluded by several hydrogen bonds. However, the electronegative surface of the pore strongly suggests that it works as a part of the cation-conducting pathway. This finding is further supported by electrophysiological and computational studies (Gaiko and Dempski 2013; Kuhne et al. 2015; Li et al. 2014; Richards and Dempski 2012; Takemoto et al. 2015; Watanabe et al. 2013). So far, crystal structures of four CCR variants (i.e., C1C2, *Cr*ChR2, C1Chrimson, and OLPVR1) and two ACR variants (i.e., *Gt*ACR1 and iC++) were reported, and they all share same oligomerization states and similar ion-conducting pathways: dimeric architecture and the pore within the monomer near the Schiff base (Kato et al. 2012, 2018; Kim et al. 2018; Oda et al. 2018; Volkov et al. 2017; Zabelskii et al. 2020).

## 3.4 Ion-Conducting Pathway

All available crystal structures of ChRs represent the closed state, so the ion-conducting pore is occluded by several constriction sites preventing ion leaks in dark conditions. The position and shape of ChRs' ion-conducting pathway are roughly conserved, and it is mainly formed by TMs 1, 2, 3, and 7. However, the detail shape and volume of the pore are significantly different between ChRs. In this review, we will see the pore by dividing it into the extracellular cavity, the central constriction site, and the intracellular cavity (Fig. 3.3).

### 3.4.1 Extracellular Cavity

As shown in Figs. 3.3 and 3.4, the extracellular cavity is generally larger than the intracellular

**Table 3.1** Widely used naturally occurring ChR variants

| Name | Source | Channel function | Characteristics | Appendix | Year | References |
|---|---|---|---|---|---|---|
| CrChR1 | Chlamydomonas reinhardtii | *Cation* | – | First ChR characterized in 2002 | 2002 | Nagel et al. (2002) |
| *CrChR2* | Chlamydomonas reinhardtii | *Cation* | – | Most classical excitatory optogenetics tool | 2003 | Nagel et al. (2003) |
| *VChR1* | Volvox carteri | *Cation* | Blue shifted absorption spectrum | | 2008 | Zhang et al. (2008) |
| PsChR (PsChR2, PsuCCR) | Platymonas subcordiformis | *Cation* | Blue shifted absorption spectrum | | 2013, 2015, 2016 | Govorunova et al. (2013), Szundi et al. (2015), Govorunova et al. (2016) |
| CaChR1 (CaCCR1) | Chlamydomonas augustae | *Cation* | Red shifted, frequently used for spectroscopic studies | | 2012 | Hou et al. (2012) |
| *sdChR* | Scherffelia dubia | *Cation* | Blue-shifted, high light sensitivity | | 2014 | Klapoetke et al. (2014) |
| *Chrimson (CnChR1)* | Chlamydomonas noctigama | *Cation* | Red shifted absorption spectrum, proton selective | | 2014 | Klapoetke et al. (2014) |
| CsChR | Chloromonas subdivisa | *Cation* | | Used for CsChrimson | 2014 | Klapoetke et al. (2014) |
| *CoChR* | Chloromonas oogama | *Cation* | Blue-shifted action spectrum, high conductance | | 2014 | Klapoetke et al. (2014) |
| *Chronos (ShChR)* | Stigeoclonium helveticum | *Cation* | One of the fastest kinetics | | 2014 | Klapoetke et al. (2014) |
| TsChR | Tetraselmis striata | *Cation* | Blue shifted absorption spectrum | | 2014 | Klapoetke et al. (2014) |
| GtCCR4 | Guillardia theta | *Cation* | High light sensitivity, rapid desensitization | "Bacteriorhodopsin-like" CCR (BCCR) | 2017 | Yamauchi et al. (2017) |
| *ChRmine (RlCCR1)* | Tiarina fusus (Rhodomonas lens) | *Cation* | Red-shifted action spectrum, high conductance, high light sensitivity | "Bacteriorhodopsin-like" CCR (BCCR) | 2019 | Marshel et al. (2019) |
| RaCCR1 | Rhodomonas abbreviata | *Cation* | Very rapid desensitization, UV-absorbing intermediate | "Bacteriorhodopsin-like" CCR (BCCR) | 2019 | Duan et al. (2019) |

(continued)

**Table 3.1** (continued)

| Name | Source | Channel function | Characteristics | Appendix | Year | References |
|---|---|---|---|---|---|---|
| RsCCR1 | Rhodomonas salina | *Cation* | Very rapid desensitization, UV-absorbing intermediate | "Bacteriorhodopsin-like" CCR (BCCR) | 2019 | Duan et al. (2019) |
| OLPVR1 | Organic Lake phycodnavirus | *catIon* | | Viral CCR | 2020 | Zabelskii et al. (2020) |
| VirChR1 | | *Cation* | No Ca2+ permeability | Viral CCR | 2020 | Zabelskii et al. (2020) |
| *GtACR1* | Guillardia theta (CCMP2712) | *Anion* | | First ACR discovered from nature | 2015 | Govorunova et al. (2015) |
| *GtACR2* | Guillardia theta (CCMP2712) | *Anion* | Blue shifted absorption spectrum | First ACR discovered from nature | 2015 | Govorunova et al. (2015) |
| ZipACR (PsuACR_973) | Proteomonas sulcata (CCMP704) | *Anion* | Fast kinetics | Cryptophyte ACRs, possible proton leak | 2017 | Govorunova et al. (2017) |
| RlACR_477 | | *Anion* | Blue shifted absorption spectrum | Cryptophyte ACRs | 2017 | Govorunova et al. (2017) |
| C1ACR_023 | | *Anion* | Blue shifted absorption spectrum | Cryptophyte ACRs | 2017 | Govorunova et al. (2017) |
| RapACR (RsACR_665) | Rhodomonas salina | *Anion* | Very fast kinetics | | 2018 | Govorunova et al. (2018) |
| MerMAID1 | | *Anion* | Rapid desensitization | MerMAIDs | 2019 | Oppermann et al. (2019) |
| MerMAID6 | | *Anion* | Rapid desensitization | MerMAIDs | 2019 | Oppermann et al. (2019) |
| A1ACR1 | Aurantiochytrium sp. KH105 | *Anion* | Red shifted absorption spectrum | RubyACRs | 2020 | Govorunova et al. (2020) |
| HfACR1 | Hondaea fermentalgiana FCC1311 | *Anion* | Red shifted absorption spectrum | RubyACRs | 2020 | Govorunova et al. (2020) |

cavity and the shape is more divergent. In CCR crystal structures, the apparent exit of the pore is positioned between ECL1 and ECL3. The volume of the pore is small in the order of *Cr*ChR2, C1Chrimson, and C1C2, and C1C2's extracellular cavity connects the extracellular bulk solvent and the central constriction site. Two glutamates on TM2 (E136 and E140 in C1C2; E97 and E101 in *Cr*ChR2; E139 and E143 in C1Chrimson), which are conserved in most CCRs, are involved in several aspects of CCRs' properties: conductance, ion selectivity, kinetic, and/or action spectrum (Sugiyama et al. 2009; Vierock et al. 2017) (Fig. 3.4). In contrast, while there is a cavity between ECL1 and ECL3, the main extracellular pore in ACRs is connected to the bulk solvent via the exit located between TM1 and TM2. Unlike CCRs, there is no conserved positively charged residue on TM2 of ACRs. Instead, iC++ has three arginine residues (R156, R159, and R281) along the extracellular pore, and R281 is known to be especially involved in anion conduction. *Gt*ACR1 has K33 and R94 (N92 and R159 in iC++) along the pore, and

**Table 3.2** Widely used engineered ChR variants

| Name | Engineering method | Template | Channel function | Mutations | Characteristics | Appendix | Year | References |
|---|---|---|---|---|---|---|---|---|
| ChR2 H134R | Point mutations | CrChR2 | *Cation* | H134R | Relatively large photocurrent | | 2005 | Nagel et al. (2005) |
| *SFO* | Point mutations | CrChR2 | *Cation* | C128A, C128T, or C128S | Slow kinetics | | 2009 | Berndt et al. (2009) |
| | Point mutations | CrChR2 | *Cation* | D156A | Slow kinetics | | 2010 | Bamann et al. (2010) |
| *SSFO* | Point mutations | CrChR2 | *Cation* | C128S/D156A | Extremely slow tau off, high light sensitivity | | 2011 | Yizhar et al. (2011) |
| ChR2-XXL | Point mutations | CrChR2 | *Cation* | D156C | High expression, long kinetics | | 2014 | Dawydow et al. (2014) |
| ChR2-XXM | Point mutations | CrChR2 | *Cation* | D156H | Enhanced Na+ and Ca2+ conductance | | 2017 | Scholz et al. (2017) |
| PsChR D139H | Point mutations | PsChR (Platymonas subcordiformis) | *cation* | D139H | Larger photocurrent, enhanced Na+ and Ca2+ conductance | | 2019 | Duan et al. (2019) |
| ChRFR | Chimera | TM1-2 from CrChR1 and TM3-7 from CrChR2 | *Cation* | - | | | 2009 | Sugiyama et al. (2009) |
| *ChRWR, ChEF, C1C2* | Chimera | TM1-5 from CrChR1 and TM6-7 from CrChR2 | *Cation* | - | Large photocurrent, small desensitization | Three opsins are almost identical | 2009, 2009, 2012 | Lin et al. (2009), Sugiyama et al. (2009), Kato et al. (2012) |
| *ChIEF* | Point mutations | ChEF | *Cation* | I170V | Fast kinetics | | 2009 | Lin et al. (2009) |
| *CatCh* | Point mutations | CrChR2 | *Cation* | L132C | Higher Ca2+ permeability | | 2011 | Kleinlogel et al. (2011) |
| *ChETA* | Point mutations | CrChR2 | *Cation* | E123T | Fast kinetics | | 2010 | Gunaydin et al. (2010) |
| ET/TC | Point mutations | CrChR2 | *Cation* | E123T/T159C | Fast photocurrents with large amplitudes | | 2011 | Berndt et al. (2011) |
| *C1V1* | Chimera | TM1-3 from CrChR1 and TM3-7 from VChR1 | *Cation* | - | Red-shifted | | 2012 | Prigge et al. (2012) |
| C1V1-ET (C1V1T) | Point mutations | C1V1 | *Cation* | E162T | | E123T in CrChR2 | 2012 | Prigge et al. (2012) |

| | | | | | | | | |
|---|---|---|---|---|---|---|---|---|
| C1V1-ET-ET (C1V1TT) | Point mutations | C1V1 | *Cation* | E122T/E162T | | E83T/E123T in CrChR2 | 2012 | Prigge et al. (2012) |
| *ReaChR* | Chimera | N-terminus from CrChR1, TM1-5 and 7 from VChR1, TM6 from VChR2 | *Cation* | L171I | Red shifted absorption spectrum | L171 is I170 in ChEF | 2013 | Lin et al. (2013) |
| *bReaChES* | Chimera | N-terminus from CrChR2 and CrChR1, TM1-5 and 7 from VChR1, TM6 from VChR2 | *CATION* | E123S/L132I | Red-shifted, improved trafficking and kinetics | L132 is I171 in ReaChR | 2015 | Rajasethupathy et al. (2015) |
| ChrimsonR | Point mutations | Chrimson | *cation* | K176R | Faster off kinetics | H134R in CrChR2 | 2014 | Klapoetke et al. (2014) |
| CsChrimson | Chimera | N-terminus from CsChR, TM1-7 from Chrimson | *Cation* | | | | 2014 | Klapoetke et al. (2014) |
| *CheRiff* | Point mutations | sdChR | *Cation* | E154A | Blue-shifted, high light sensitivity, and rapid kinetics | Optopatch actuator | 2014 | Hochbaum et al. (2014) |
| C1C2GA | Point mutations | C1C2 | *Cation* | T198G/G202A | Blue shifted absorption spectrum | T159G/G163A in CrChR2 | 2015 | Kato et al. (2015) |
| C1Chrimson | Chimera | N-terminus from CrChR1, TM1-7 from Chrimson | *Cation* | | | | 2018 | Oda et al. (2018) |
| ChrimsonSA | Point mutations | Chrimson | *Cation* | S169A | Red shifted absorption spectrum | | 2018 | Oda et al. (2018) |
| vf-Chrimson | Point mutations | Chrimson | *Cation* | K176R/Y261F/S267M | Faster off kinetics | | 2018 | Mager et al. (2018) |
| ChromeQ | Point mutations | CrChR2 | *Cation* | A71S/E90A/H114G/R115S | Improve photocurrent, reduced calcium and proton conductance | | 2019 | Cho et al. (2019) |
| iC1C2 | Point mutations | C1C2 | *Anon* | T98S/E129S/E140S/V156K/E162S/H173R/V281K/T285N/N297Q | Some proton leak | First engineered Cl- conducing channelrhodopsin | 2014 | Berndt et al. (2014) |
| ChloC | Point mutations | CrChR2 | *Anon* | E90R/T159C | Some proton leak | First engineered Cl- conducing channelrhodopsin | 2014 | Wietek et al. (2014) |
| iC++ | Point mutations | iC1C2 | *Anon* | T98S/E122N/E129Q/E140S/V156R/E162S/ | Almost no proton leak current | | 2015 | Berndt et al. (2016) |

(continued)

**Table 3.2** (continued)

| Name | Engineering method | Template | Channel function | Mutations | Characteristics | Appendix | Year | References |
|---|---|---|---|---|---|---|---|---|
| | | | | V281R/T285N/N297Q/E312S | | | | |
| iChloC | Point mutations | ChloC | *Anon* | E83Q/E90R/E101S/D156N/T159C | Almost no proton leak current | | 2015 | Wietek et al. (2015) |
| SwiChR | Point mutations | iC1C2 | *Anon* | C167A or C167T | Longer kinetics | | 2014 | Berndt et al. (2014) |
| SwiChR++ | Point mutations | iC++ | *Anon* | C167A | Longer kinetics | | 2015 | Berndt et al. (2016) |
| Phobos | Point mutations | iC++ | *Anon* | T198G/G202A | Blue shifted action spectrum | | 2017 | Wietek et al. (2017) |
| Aurora | Point mutations | bReaChES | *Anon* | T98S/E122N/E129Q/E140S/V156R/E162S/V281R/T285N/N297Q/E312S in iC1C2 | | | 2017 | Wietek et al. (2017) |
| FLASH | Point mutations | GtACR1 | *Anon* | R83Q/N239Q | Faster kinetics with large photocurrent | | 2018 | Kato et al. (2018) |

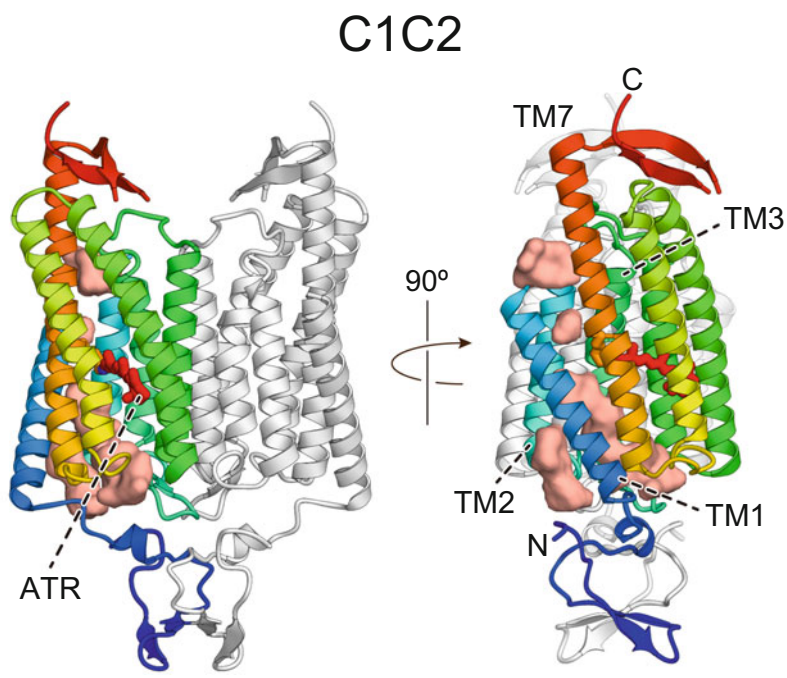


**Fig. 3.2** Overall architecture of ChR

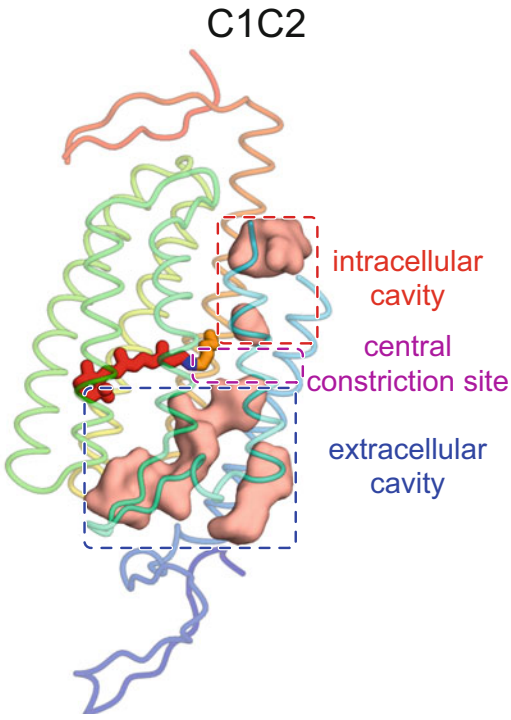


**Fig. 3.3** The architecture of ChR's ion-conducting pathway

R94 is involved in the kinetics of the channel (Kato et al. 2018) (Fig. 3.4). Notably, the extracellular exits of CCRs and ACRs are significantly different in crystal structures, but several computational studies show that two cavities are connected during the simulation (Kato et al. 2018; Takemoto et al. 2015), suggesting that the current small extracellular exits between ECL1 and ECL3 and between TM1 and TM2 would be connected and become the larger single cavity in the open state.

### 3.4.2 Central Constriction Site

The intracellular and extracellular cavities are divided by the central constriction site near the retinal Schiff base (Fig. 3.4). Although the position and architecture of the central constriction site are similar between ChRs, the exact amino acids forming the constriction are not the same: in C1C2, S102, E129, and N297 form the gate by hydrogen bonds, whereas in *Cr*ChR2, the glutamate (E90) and asparagine (N258) are conserved, but these two residues no longer interact and E90 forms the constriction via the water-mediated

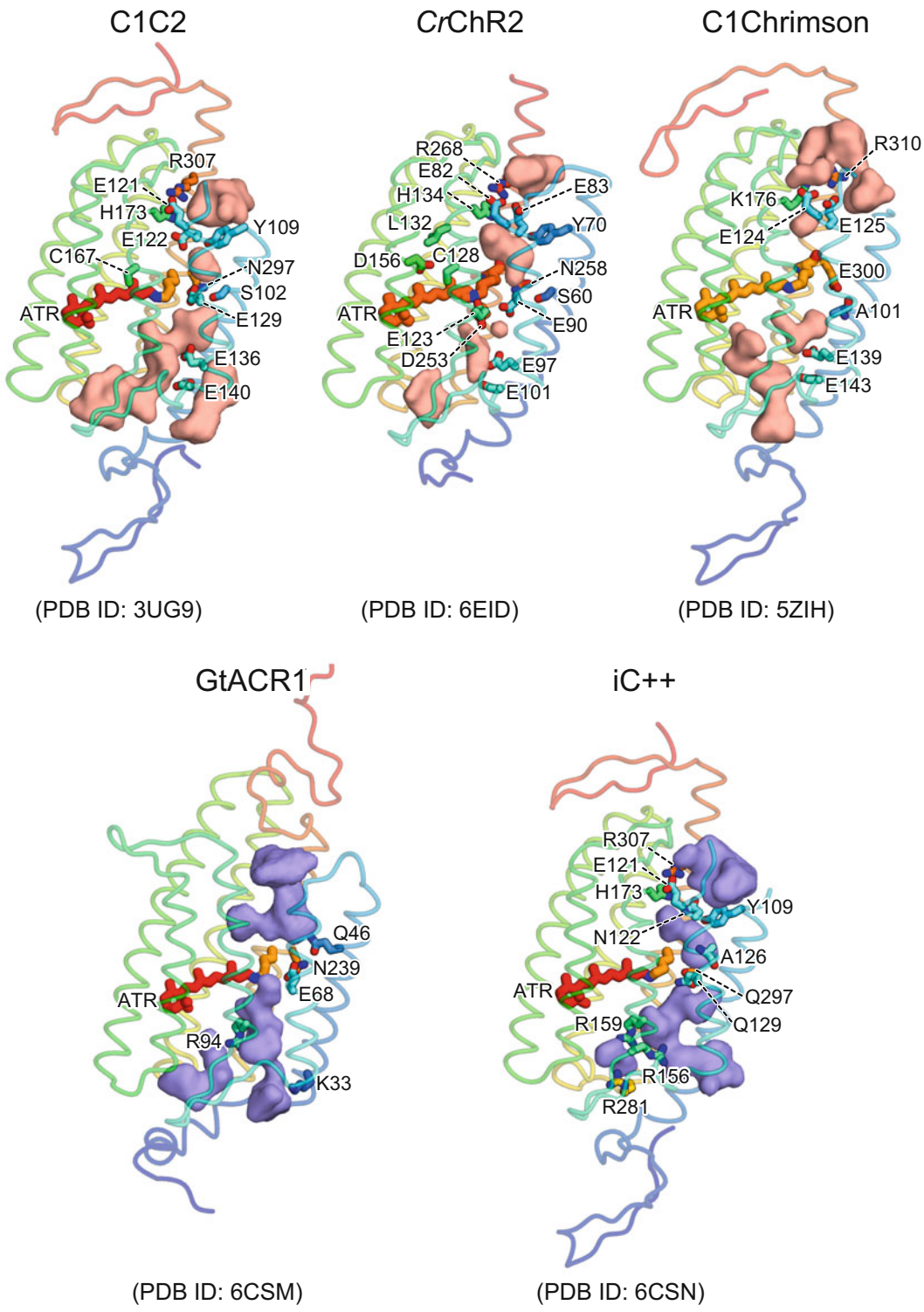


**Fig. 3.4** Ion-conducting pathways of cation and anion ChRs

hydrogen bonds with E123 and D253. In *Gt*ACR1, the corresponding residues of E129 and N297 (E68 and N239) form hydrogen bonds, but Q46 instead of S102 strengthens the constriction site formed by E68 and N239. In C1Chrimson, the asparagine is replaced by glutamate (E300), and E300 forms a hydrogen bond with the backbone carbonyl of A101, which is not involved in the gate formation in C1C2, *Gt*ACR1, or *Cr*ChR2. The constriction site of iC++ would be more flexible: Q129 and Q297 (E129 and N297 in C1C2) form a hydrogen bond in the crystal structure, but computational analysis reveals that the interaction is not very strong and N297 often flips and forms new interaction with A126 (Kato et al. 2018). The mutations to these residues dramatically change the properties of the channel: for example, E90R or E90K mutation to *Cr*ChR2 converts its function from cation channel to anion channel, and N239Q mutation to *Gt*ACR1 accelerates the closing kinetics of the channel by ~30 times. These results, together with other computational analyses, suggest that the hydrogen bonding network in the central constriction site will be significantly rearranged upon the channel opening, and the ion goes through the central constriction site. E90 in *Cr*ChR2 is assumed to change its protonation state during the photocycle, and previous studies suggest that the deprotonation of E90 is important for channel gating (Kuhne et al. 2015; Sugiyama et al. 2009; Vierock et al. 2017), but more recent spectroscopic studies of *Cr*ChR2 and C1C2 doubt the relationship between the deprotonation of E90 (E129 in C1C2) and channel opening (Inaguma et al. 2015; Lorenz-Fonfria et al. 2013), and the exact mechanism of channel gating remains elusive. Interestingly, the recent QM/MM simulation study proposed an alternative ion-conducting pathway and channel gating mechanism; the 13-methyl group of isomerized retinal pushes TM3 and water (and possibly cation) goes through the extra space created between the retinal polyene chain and TM6 (Cheng et al. 2018). This model would partly explain why the mutation to C128 in *Cr*ChR2 and C167 in C1C2 dramatically extends the lifetime of the open state (Berndt et al. 2009; Yizhar et al. 2011), and L132C mutant of *Cr*ChR2 shows different ion selectivity (i.e., higher selectivity against $Ca^{2+}$) (Kleinlogel et al. 2011). Further study, especially the structural analysis of open-state ChRs, will be needed to reveal how the substrate ion is transferred from extracellular to intracellular side.

### 3.4.3 Intracellular Cavity

The intracellular cavity is characterized by TM1, 2, and 7, and except for *Gt*ACR1, the cavity is further separated into two small cavities by the intracellular constriction site (Fig. 3.4). In the C1C2 and iC++ structures, the intracellular constriction site was formed by Y109 and two hydrogen bonds between E121-R307 and E122-H173 (E121-R307 and N122-H173 in iC++). In *Cr*ChR2, E83 (E122 in C1C2) is flipped and interacts with R307, so the constriction site is formed by the hydrogen bonds between E82, R268, and E83 (E121, R307, and E122 in C1C2, respectively). In the C1Chrimson structure, the histidine is substituted with lysine (K176), and only the hydrogen bond between E125 and R310 (E122 and R307 in C1C2) is observed. This interaction, together with the side chains of E124 and K176, forms the intracellular constriction site. While E124 and K176 do not interact with any surrounding residues in the crystal structure, there would be water-mediated hydrogen bond interactions that fix the position of their side chains. Notably, the H134R mutant of *Cr*ChR2 enhances the photocurrent amplitude (Nagel et al. 2005), whereas the corresponding mutation of C1C2 does not change the conductance but affects the ion selectivity (Berndt et al. 2014). It would reflect the difference in the interaction in which the histidine is involved between *Cr*ChR2 and C1C2.

## 3.5 Future Perspective

### 3.5.1 Revealing the Dynamics

So far, several crystal structures of cation and anion channelrhodopsins have been reported,

but all these structures are crystallized in the dark condition and represent the closed, dark state. No high-resolution structural information of any ChRs is available, but several spectroscopic, structural, and computational studies suggest that the large conformational change has occurred during the photocycle. A two-dimensional electron crystallography of *Cr*ChR2 C128T mutant reveals the displacement of TM2, 6, and 7 (Muller et al. 2015), and electron paramagnetic resonance studies for *Cr*ChR2 show outward movements of the cytoplasmic sides of TM2 and 6 (Krause et al. 2013; Sattig et al. 2013). Several MD simulation studies also report the conformational change of TM2, 6, and/or 7 (Ardevol and Hummer 2018; Cheng et al. 2018; Kuhne et al. 2015; Takemoto et al. 2015), so it is assumed that these three helices have key roles for the channel opening and ion conduction. To understand the photocycle in more detail, further structural studies, including the determination of high-resolution structures in the intermediate states, as well as further electrophysiological, spectroscopic, and computational studies are clearly needed. Determining intermediate structures is very challenging, but time-resolved serial femtosecond crystallography (TR-SFX) and millisecond crystallography (TR-SMX) techniques would be promising approaches. Several intermediate structures of HsBR and KR2 have been solved, and the details of their photocycle have been recently revealed using these approaches (Kovalev et al. 2020; Nango et al. 2016; Nogly et al. 2018; Skopintsev et al. 2020; Weinert et al. 2019). One possible problem these techniques have would be crystal packing; the protein molecules are densely packed in the crystal so that the large conformational change occurred to the protein becomes significantly inhibited (Hirai et al. 2009; Wickstrand et al. 2015). The conformational change of ChR is reported to be larger than that of *Hs*BR (Radu et al. 2009; Ritter et al. 2008), TR-SFX, and -SMX would not be the best method to trap intermediate states, especially the open state, of ChR. However, as demonstrated by the recent studies of *Hs*BR and *Cr*ChR2, the careful screening of crystal packing may overcome the issue (Muller et al. 2015; Weinert et al. 2019). Otherwise, we may need to develop a new technique that does not need a crystal to solve the structure.

### 3.5.2 Exploring the New Channelrhodopsin Variants

As shown in Tables 3.1 and 3.2, several ChR variants have been engineered or discovered since 2002, when the first ChR, *Cr*ChR2, was isolated from *Chlamydomonas reinhardtii* (Nagel et al. 2002). The $\lambda_{max}$ of the absorption spectrum of CCR variants is ranging from ~435 (*Ps*ChR and *Ts*ChR) (Govorunova et al. 2013, 2016; Klapoetke et al. 2014; Szundi et al. 2015) to 607 nm (ChrimsonSA) (Oda et al. 2018), and the off kinetics of the channel ($\tau_{off}$) is from ~3 ms (Chronos and vf-Chrimson) (Klapoetke et al. 2014; Mager et al. 2018) to ~29 min (*Cr*ChR2 SSFO)(Yizhar et al. 2011). CCRs with unique properties such as high light sensitivity (ChRmine, $EPD_{50}$ = 0.03 mW/mm$^2$) or rapid desensitization (*Rs*CCR1) are also discovered from nature (Marshel et al. 2019; Sineshchekov et al. 2020). ACRs have a shorter history than CCRs, but recent studies reported the ACR variants with very short (*Rl*ACR_477 and *C1*ACR_023, 445 nm) and long (*A1*ACR1 and *Hf*ACR1, 610 nm) $\lambda_{max}$ of the absorption spectrum (Govorunova et al. 2017, 2020), short $\tau_{off}$ (FLASH and ZipACR) (Govorunova et al. 2017; Kato et al. 2018), high light sensitivity (RapACR) (Govorunova et al. 2018), or rapid desensitization (MerMAIDs) (Oppermann et al. 2019).

One missing ACR-based optogenetics tool would be the one with very long $\tau_{off}$. So far, *Gt*ACR1 SFO mutant such as *Gt*ACR1 C102A has one of the longest $\tau_{off}$ (~20 s) (Kim et al. 2018; Sineshchekov et al. 2015), but it is still 50–100 times shorter than that of CCR SSFO mutant. The early attempt to make the *Gt*ACR1 SSFO mutant by introducing mutation to the corresponding residue of D156 in *Cr*ChR2 failed (Kim et al. 2018; Sineshchekov et al. 2015), probably because D156 is substituted with S130 in *Gt*ACR1, and the hydrogen bonding network is different between *Cr*ChR2 and *Gt*ACR1. Once

the molecular mechanism of how SFO and SSFO mutations significantly extend the lifetime of the open state of CCRs is revealed, we would be able to engineer the ACR variant with much longer $\tau_{off}$. Another interesting and probably more useful ChR variant would be a $K^+$-selective CCR. While ACRs are powerful inhibitory optogenetic tools and they can effectively inhibit somatic spiking, it is reported that the ACR activation at synaptic boutons does not inhibit but enhance the neurotransmitter release, probably because the intra-axonal chloride concentration is high (Mahn et al. 2016; Wiegert et al. 2017). $K^+$-selective CCR will solve the problem and allow us to perform the inhibitory optogenetic experiment with unprecedented high spatial resolution. It is still controversial whether the ChRs can possess the high cation selectivity, but a recent study shows that a single point mutation introduced to KR2 converts the function from a light-driven $Na^+$ pump to a light-gated $K^+$ channel (Vogt et al. 2019). Although this mutant can work only under the strong alkaline condition and cannot be used as an inhibitory optogenetic tool in vivo, it demonstrated that the microbial rhodopsin architecture can possess a cation channel function with strict ion selectivity. Further engineering and mining of new ChR variants will continuously expand our toolkit of optogenetics and the research frontier of neuroscience.

**Acknowledgments** This work was supported by JST PRESTO (JPMJPR1782), UTEC-Utokyo FSI Research Grant Program, Yamada Science Foundation, and The Nakajima Foundation.

## References

Adamantidis AR, Zhang F, Aravanis AM, Deisseroth K, de Lecea L (2007) Neural substrates of awakening probed with optogenetic control of hypocretin neurons. Nature 450:420–424

Ardevol A, Hummer G (2018) Retinal isomerization and water-pore formation in channelrhodopsin-2. Proc Natl Acad Sci U S A 115:3557–3562

Bamann C, Gueta R, Kleinlogel S, Nagel G, Bamberg E (2010) Structural guidance of the photocycle of channelrhodopsin-2 by an interhelical hydrogen bond. Biochemistry (Mosc) 49:267–278

Berndt A, Yizhar O, Gunaydin LA, Hegemann P, Deisseroth K (2009) Bi-stable neural state switches. Nat Neurosci 12:229–234

Berndt A, Schoenenberger P, Mattis J, Tye KM, Deisseroth K, Hegemann P, Oertner TG (2011) High-efficiency channelrhodopsins for fast neuronal stimulation at low light levels. Proc Natl Acad Sci U S A 108:7595–7600

Berndt A, Lee SY, Ramakrishnan C, Deisseroth K (2014) Structure-guided transformation of channelrhodopsin into a light-activated chloride channel. Science 344:420–424

Berndt A, Lee SY, Wietek J, Ramakrishnan C, Steinberg EE, Rashid AJ, Kim H, Park S, Santoro A, Frankland PW et al (2016) Structural foundations of optogenetics: determinants of channelrhodopsin ion selectivity. Proc Natl Acad Sci U S A 113:822–829

Berthold P, Tsunoda SP, Ernst OP, Mages W, Gradmann D, Hegemann P (2008) Channelrhodopsin-1 initiates phototaxis and photophobic responses in chlamydomonas by immediate light-induced depolarization. Plant Cell 20:1665–1677

Bi A, Cui J, Ma YP, Olshevskaya E, Pu M, Dizhoor AM, Pan ZH (2006) Ectopic expression of a microbial-type rhodopsin restores visual responses in mice with photoreceptor degeneration. Neuron 50:23–33

Bogomolni RA, Spudich JL (1982) Identification of a third rhodopsin-like pigment in phototactic Halobacterium halobium. Proc Natl Acad Sci U S A 79:6250–6254

Boyden ES, Zhang F, Bamberg E, Nagel G, Deisseroth K (2005) Millisecond-timescale, genetically targeted optical control of neural activity. Nat Neurosci 8:1263–1268

Cheng C, Kamiya M, Takemoto M, Ishitani R, Nureki O, Yoshida N, Hayashi S (2018) An atomistic model of a precursor state of light-induced channel opening of Channelrhodopsin. Biophys J 115:1281–1291

Cho YK, Park D, Yang A, Chen F, Chuong AS, Klapoetke NC, Boyden ES (2019) Multidimensional screening yields channelrhodopsin variants having improved photocurrent and order-of-magnitude reductions in calcium and proton currents. J Biol Chem 294:3806–3821

Chow BY, Han X, Dobry AS, Qian X, Chuong AS, Li M, Henninger MA, Belfort GM, Lin Y, Monahan PE et al (2010) High-performance genetically targetable optical neural silencing by light-driven proton pumps. Nature 463:98–102

Chuong AS, Miri ML, Busskamp V, Matthews GA, Acker LC, Sorensen AT, Young A, Klapoetke NC, Henninger MA, Kodandaramaiah SB et al (2014) Non-invasive optical inhibition with a red-shifted microbial rhodopsin. Nat Neurosci 17:1123–1129

Dawydow A, Gueta R, Ljaschenko D, Ullrich S, Hermann M, Ehmann N, Gao S, Fiala A, Langenhan T, Nagel G et al (2014) Channelrhodopsin-2-XXL, a powerful optogenetic tool for low-light applications. Proc Natl Acad Sci U S A 111:13972–13977

Deisseroth K (2011) Optogenetics. Nat Methods 8:26–29
Deisseroth K (2015) Optogenetics: 10 years of microbial opsins in neuroscience. Nat Neurosci 18:1213–1225
Duan X, Nagel G, Gao S (2019) Mutated channelrhodopsins with increased sodium and calcium permeability. Appl Sci 9:664
Ernst OP, Lodowski DT, Elstner M, Hegemann P, Brown LS, Kandori H (2014) Microbial and animal rhodopsins: structures, functions, and molecular mechanisms. Chem Rev 114:126–163
Gaiko O, Dempski RE (2013) Transmembrane domain three contributes to the ion conductance pathway of channelrhodopsin-2. Biophys J 104:1230–1237
Govorunova EG, Sineshchekov OA, Li H, Janz R, Spudich JL (2013) Characterization of a highly efficient blue-shifted channelrhodopsin from the marine alga Platymonas subcordiformis. J Biol Chem 288:29911–29922
Govorunova EG, Sineshchekov OA, Janz R, Liu X, Spudich JL (2015) Neuroscience. Natural light-gated anion channels: a family of microbial rhodopsins for advanced optogenetics. Science 349:647–650
Govorunova EG, Sineshchekov OA, Spudich JL (2016) Structurally distinct cation Channelrhodopsins from Cryptophyte algae. Biophys J 110:2302–2304
Govorunova EG, Sineshchekov OA, Rodarte EM, Janz R, Morelle O, Melkonian M, Wong GK, Spudich JL (2017) The expanding family of natural anion Channelrhodopsins reveals large variations in kinetics, conductance, and spectral sensitivity. Sci Rep 7:43358
Govorunova EG, Sineshchekov OA, Hemmati R, Janz R, Morelle O, Melkonian M, Wong GK, Spudich JL (2018) Extending the time domain of neuronal silencing with Cryptophyte anion Channelrhodopsins. eNeuro 5:ENEURO.0174
Govorunova EG, Sineshchekov OA, Li H, Wang Y, Brown LS, Spudich JL (2020) RubyACRs, nonalgal anion channelrhodopsins with highly red-shifted absorption. Proc Natl Acad Sci U S A 117:22833–22840
Gunaydin LA, Yizhar O, Berndt A, Sohal VS, Deisseroth K, Hegemann P (2010) Ultrafast optogenetic control. Nat Neurosci 13:387–392
Han X, Boyden ES (2007) Multiple-color optical activation, silencing, and desynchronization of neural activity, with single-spike temporal resolution. PLoS One 2: e299
Harz H, Hegemann P (1991) Rhodopsin-regulated calcium currents in Chlamydomonas. Nature 351:489–491
Hegemann P (2008) Algal sensory photoreceptors. Annu Rev Plant Biol 59:167–189
Hirai T, Subramaniam S, Lanyi JK (2009) Structural snapshots of conformational changes in a seven-helix membrane protein: lessons from bacteriorhodopsin. Curr Opin Struct Biol 19:433–439
Hochbaum DR, Zhao Y, Farhi SL, Klapoetke N, Werley CA, Kapoor V, Zou P, Kralj JM, Maclaurin D, Smedemark-Margulies N et al (2014) All-optical electrophysiology in mammalian neurons using engineered microbial rhodopsins. Nat Methods 11:825–833
Hou SY, Govorunova EG, Ntefidou M, Lane CE, Spudich EN, Sineshchekov OA, Spudich JL (2012) Diversity of Chlamydomonas channelrhodopsins. Photochem Photobiol 88:119–128
Inaguma A, Tsukamoto H, Kato HE, Kimura T, Ishizuka T, Oishi S, Yawo H, Nureki O, Furutani Y (2015) Chimeras of channelrhodopsin-1 and -2 from Chlamydomonas reinhardtii exhibit distinctive light-induced structural changes from channelrhodopsin-2. J Biol Chem 290:11623–11634
Inoue K, Ono H, Abe-Yoshizumi R, Yoshizawa S, Ito H, Kogure K, Kandori H (2013) A light-driven sodium ion pump in marine bacteria. Nat Commun 4:1678
Inoue K, Ito S, Kato Y, Nomura Y, Shibata M, Uchihashi T, Tsunoda SP, Kandori H (2016) A natural light-driven inward proton pump. Nat Commun 7:13415
Ishizuka T, Kakuda M, Araki R, Yawo H (2006) Kinetic evaluation of photosensitivity in genetically engineered neurons expressing green algae light-gated channels. Neurosci Res 54:85–94
Kato HE, Zhang F, Yizhar O, Ramakrishnan C, Nishizawa T, Hirata K, Ito J, Aita Y, Tsukazaki T, Hayashi S et al (2012) Crystal structure of the channelrhodopsin light-gated cation channel. Nature 482:369–374
Kato HE, Kamiya M, Sugo S, Ito J, Taniguchi R, Orito A, Hirata K, Inutsuka A, Yamanaka A, Maturana AD et al (2015) Atomistic design of microbial opsin-based blue-shifted optogenetics tools. Nat Commun 6:7177
Kato HE, Kim YS, Paggi JM, Evans KE, Allen WE, Richardson C, Inoue K, Ito S, Ramakrishnan C, Fenno LE et al (2018) Structural mechanisms of selectivity and gating in anion channelrhodopsins. Nature 561:349–354
Kim YS, Kato HE, Yamashita K, Ito S, Inoue K, Ramakrishnan C, Fenno LE, Evans KE, Paggi JM, Dror RO et al (2018) Crystal structure of the natural anion-conducting channelrhodopsin GtACR1. Nature 561:343–348
Klapoetke NC, Murata Y, Kim SS, Pulver SR, Birdsey-Benson A, Cho YK, Morimoto TK, Chuong AS, Carpenter EJ, Tian Z et al (2014) Independent optical excitation of distinct neural populations. Nat Methods 11:338–346
Kleinlogel S, Feldbauer K, Dempski RE, Fotis H, Wood PG, Bamann C, Bamberg E (2011) Ultra light-sensitive and fast neuronal activation with the Ca(2)+-permeable channelrhodopsin CatCh. Nat Neurosci 14:513–518
Kolbe M, Besir H, Essen LO, Oesterhelt D (2000) Structure of the light-driven chloride pump halorhodopsin at 1.8 A resolution. Science 288:1390–1396
Kovalev K, Astashkin R, Gushchin I, Orekhov P, Volkov D, Zinovev E, Marin E, Rulev M, Alekseev A, Royant A et al (2020) Molecular mechanism of light-driven sodium pumping. Nat Commun 11:2137

Krause N, Engelhard C, Heberle J, Schlesinger R, Bittl R (2013) Structural differences between the closed and open states of channelrhodopsin-2 as observed by EPR spectroscopy. FEBS Lett 587:3309–3313

Kuhne J, Eisenhauer K, Ritter E, Hegemann P, Gerwert K, Bartl F (2015) Early formation of the ion-conducting pore in channelrhodopsin-2. Angew Chem Int Ed Engl 54:4953–4957

Li X, Gutierrez DV, Hanson MG, Han J, Mark MD, Chiel H, Hegemann P, Landmesser LT, Herlitze S (2005) Fast noninvasive activation and inhibition of neural and network activity by vertebrate rhodopsin and green algae channelrhodopsin. Proc Natl Acad Sci U S A 102:17816–17821

Li H, Govorunova EG, Sineshchekov OA, Spudich JL (2014) Role of a helix B lysine residue in the photoactive site in channelrhodopsins. Biophys J 106:1607–1617

Lin JY, Lin MZ, Steinbach P, Tsien RY (2009) Characterization of engineered channelrhodopsin variants with improved properties and kinetics. Biophys J 96:1803–1814

Lin JY, Knutsen PM, Muller A, Kleinfeld D, Tsien RY (2013) ReaChR: a red-shifted variant of channelrhodopsin enables deep transcranial optogenetic excitation. Nat Neurosci 16:1499–1508

Lorenz-Fonfria VA, Resler T, Krause N, Nack M, Gossing M, Fischer von Mollard G, Bamann C, Bamberg E, Schlesinger R, Heberle J (2013) Transient protonation changes in channelrhodopsin-2 and their relevance to channel gating. Proc Natl Acad Sci U S A 110:E1273–E1281

Luck M, Mathes T, Bruun S, Fudim R, Hagedorn R, Tran Nguyen TM, Kateriya S, Kennis JT, Hildebrandt P, Hegemann P (2012) A photochromic histidine kinase rhodopsin (HKR1) that is bimodally switched by ultraviolet and blue light. J Biol Chem 287:40083–40090

Mager T, Lopez de la Morena D, Senn V, Schlotte J, D Errico A, Feldbauer K, Wrobel C, Jung S, Bodensiek K, Rankovic V et al (2018) High frequency neural spiking and auditory signaling by ultrafast red-shifted optogenetics. Nat Commun 9:1750

Mahn M, Prigge M, Ron S, Levy R, Yizhar O (2016) Biophysical constraints of optogenetic inhibition at presynaptic terminals. Nat Neurosci 19:554–556

Marshel JH, Kim YS, Machado TA, Quirin S, Benson B, Kadmon J, Raja C, Chibukhchyan A, Ramakrishnan C, Inoue M et al (2019) Cortical layer-specific critical dynamics triggering perception. Science 365:eaaw5202

Matsuno-Yagi A, Mukohata Y (1977) Two possible roles of bacteriorhodopsin; a comparative study of strains of Halobacterium halobium differing in pigmentation. Biochem Biophys Res Commun 78:237–243

Muller M, Bamann C, Bamberg E, Kuhlbrandt W (2011) Projection structure of channelrhodopsin-2 at 6 A resolution by electron crystallography. J Mol Biol 414:86–95

Muller M, Bamann C, Bamberg E, Kuhlbrandt W (2015) Light-induced helix movements in channelrhodopsin-2. J Mol Biol 427:341–349

Nagel G, Ollig D, Fuhrmann M, Kateriya S, Musti AM, Bamberg E, Hegemann P (2002) Channelrhodopsin-1: a light-gated proton channel in green algae. Science 296:2395–2398

Nagel G, Szellas T, Huhn W, Kateriya S, Adeishvili N, Berthold P, Ollig D, Hegemann P, Bamberg E (2003) Channelrhodopsin-2, a directly light-gated cation-selective membrane channel. Proc Natl Acad Sci U S A 100:13940–13945

Nagel G, Brauner M, Liewald JF, Adeishvili N, Bamberg E, Gottschalk A (2005) Light activation of channelrhodopsin-2 in excitable cells of Caenorhabditis elegans triggers rapid behavioral responses. Curr Biol 15:2279–2284

Nango E, Royant A, Kubo M, Nakane T, Wickstrand C, Kimura T, Tanaka T, Tono K, Song C, Tanaka R et al (2016) A three-dimensional movie of structural changes in bacteriorhodopsin. Science 354:1552–1557

Nogly P, Weinert T, James D, Carbajo S, Ozerov D, Furrer A, Gashi D, Borin V, Skopintsev P, Jaeger K et al (2018) Retinal isomerization in bacteriorhodopsin captured by a femtosecond x-ray laser. Science:361

Oda K, Vierock J, Oishi S, Rodriguez-Rozada S, Taniguchi R, Yamashita K, Wiegert JS, Nishizawa T, Hegemann P, Nureki O (2018) Crystal structure of the red light-activated channelrhodopsin Chrimson. Nat Commun 9:3949

Oesterhelt D, Stoeckenius W (1971) Rhodopsin-like protein from the purple membrane of Halobacterium halobium. Nat New Biol 233:149–152

Oppermann J, Fischer P, Silapetere A, Liepe B, Rodriguez-Rozada S, Flores-Uribe J, Peter E, Keidel A, Vierock J, Kaufmann J et al (2019) MerMAIDs: a family of metagenomically discovered marine anion-conducting and intensely desensitizing channelrhodopsins. Nat Commun 10:3315

Pebay-Peyroula E, Rummel G, Rosenbusch JP, Landau EM (1997) X-ray structure of bacteriorhodopsin at 2.5 angstroms from microcrystals grown in lipidic cubic phases. Science 277:1676–1681

Prigge M, Schneider F, Tsunoda SP, Shilyansky C, Wietek J, Deisseroth K, Hegemann P (2012) Color-tuned channelrhodopsins for multiwavelength optogenetics. J Biol Chem 287:31804–31812

Radu I, Bamann C, Nack M, Nagel G, Bamberg E, Heberle J (2009) Conformational changes of channelrhodopsin-2. J Am Chem Soc 131:7313–7319

Rajasethupathy P, Sankaran S, Marshel JH, Kim CK, Ferenczi E, Lee SY, Berndt A, Ramakrishnan C, Jaffe A, Lo M et al (2015) Projections from neocortex mediate top-down control of memory retrieval. Nature 526:653–659

Richards R, Dempski RE (2012) Re-introduction of transmembrane serine residues reduce the minimum pore diameter of channelrhodopsin-2. PLoS One 7:e50018

Ritter E, Stehfest K, Berndt A, Hegemann P, Bartl FJ (2008) Monitoring light-induced structural changes of Channelrhodopsin-2 by UV-visible and Fourier transform infrared spectroscopy. J Biol Chem 283:35033–35041

Rost BR, Schneider-Warme F, Schmitz D, Hegemann P (2017) Optogenetic tools for subcellular applications in neuroscience. Neuron 96:572–603

Sattig T, Rickert C, Bamberg E, Steinhoff HJ, Bamann C (2013) Light-induced movement of the transmembrane helix B in channelrhodopsin-2. Angew Chem Int Ed Engl 52:9705–9708

Scheib U, Stehfest K, Gee CE, Korschen HG, Fudim R, Oertner TG, Hegemann P (2015) The rhodopsin-guanylyl cyclase of the aquatic fungus Blastocladiella emersonii enables fast optical control of cGMP signaling. Sci Sign 8:rs8

Scholz N, Guan C, Nieberler M, Grotemeyer A, Maiellaro I, Gao S, Beck S, Pawlak M, Sauer M, Asan E et al (2017) Mechano-dependent signaling by Latrophilin/CIRL quenches cAMP in proprioceptive neurons. elife 6:28360

Sineshchekov OA, Litvin FF, Keszthelyi L (1990) Two components of photoreceptor potential in phototaxis of the flagellated green alga Haematococcus pluvialis. Biophys J 57:33–39

Sineshchekov OA, Jung KH, Spudich JL (2002) Two rhodopsins mediate phototaxis to low- and high-intensity light in Chlamydomonas reinhardtii. Proc Natl Acad Sci U S A 99:8689–8694

Sineshchekov OA, Govorunova EG, Li H, Spudich JL (2015) Gating mechanisms of a natural anion channelrhodopsin. Proc Natl Acad Sci U S A 112:14236–14241

Sineshchekov OA, Govorunova EG, Li H, Wang Y, Melkonian M, Wong GK, Brown LS, Spudich JL (2020) Conductance mechanisms of rapidly desensitizing cation Channelrhodopsins from Cryptophyte algae. mBio 11:e00657–20

Skopintsev P, Ehrenberg D, Weinert T, James D, Kar RK, Johnson PJM, Ozerov D, Furrer A, Martiel I, Dworkowski F et al (2020) Femtosecond-to-millisecond structural changes in a light-driven sodium pump. Nature. Epub ahead of print

Sugiyama Y, Wang H, Hikima T, Sato M, Kuroda J, Takahashi T, Ishizuka T, Yawo H (2009) Photocurrent attenuation by a single polar-to-nonpolar point mutation of channelrhodopsin-2. Photochem Photobiol Sci 8:328–336

Suzuki T, Yamasaki K, Fujita S, Oda K, Iseki M, Yoshida K, Watanabe M, Daiyasu H, Toh H, Asamizu E et al (2003) Archaeal-type rhodopsins in Chlamydomonas: model structure and intracellular localization. Biochem Biophys Res Commun 301:711–717

Szundi I, Bogomolni R, Kliger DS (2015) Platymonas subcordiformis Channelrhodopsin-2 (PsChR2) function: II. Relationship of the photochemical reaction cycle to channel currents. J Biol Chem 290:16585–16594

Takemoto M, Kato HE, Koyama M, Ito J, Kamiya M, Hayashi S, Maturana AD, Deisseroth K, Ishitani R, Nureki O (2015) Molecular dynamics of Channelrhodopsin at the early stages of channel opening. PLoS One 10:e0131094

Vierock J, Grimm C, Nitzan N, Hegemann P (2017) Molecular determinants of proton selectivity and gating in the red-light activated channelrhodopsin Chrimson. Sci Rep 7:9928

Vogt A, Silapetere A, Grimm C, Heiser F, Ancina Moller M, Hegemann P (2019) Engineered passive potassium conductance in the KR2 sodium pump. Biophys J 116:1941–1951

Volkov O, Kovalev K, Polovinkin V, Borshchevskiy V, Bamann C, Astashkin R, Marin E, Popov A, Balandin T, Willbold D et al (2017) Structural insights into ion conduction by channelrhodopsin 2. Science 358:eaan8862

Wang H, Sugiyama Y, Hikima T, Sugano E, Tomita H, Takahashi T, Ishizuka T, Yawo H (2009) Molecular determinants differentiating photocurrent properties of two channelrhodopsins from chlamydomonas. J Biol Chem 284:5685–5696

Watanabe HC, Welke K, Sindhikara DJ, Hegemann P, Elstner M (2013) Towards an understanding of channelrhodopsin function: simulations lead to novel insights of the channel mechanism. J Mol Biol 425:1795–1814

Weinert T, Skopintsev P, James D, Dworkowski F, Panepucci E, Kekilli D, Furrer A, Brunle S, Mous S, Ozerov D et al (2019) Proton uptake mechanism in bacteriorhodopsin captured by serial synchrotron crystallography. Science 365:61–65

Wickstrand C, Dods R, Royant A, Neutze R (2015) Bacteriorhodopsin: would the real structural intermediates please stand up? Biochim Biophys Acta 1850:536–553

Wiegert JS, Mahn M, Prigge M, Printz Y, Yizhar O (2017) Silencing neurons: tools, applications, and experimental constraints. Neuron 95:504–529

Wietek J, Wiegert JS, Adeishvili N, Schneider F, Watanabe H, Tsunoda SP, Vogt A, Elstner M, Oertner TG, Hegemann P (2014) Conversion of channelrhodopsin into a light-gated chloride channel. Science 344:409–412

Wietek J, Beltramo R, Scanziani M, Hegemann P, Oertner TG, Wiegert JS (2015) An improved chloride-conducting channelrhodopsin for light-induced inhibition of neuronal activity in vivo. Sci Rep 5:14807

Wietek J, Rodriguez-Rozada S, Tutas J, Tenedini F, Grimm C, Oertner TG, Soba P, Hegemann P, Wiegert JS (2017) Anion-conducting channelrhodopsins with tuned spectra and modified kinetics engineered for optogenetic manipulation of behavior. Sci Rep 7:14957

Yamauchi Y, Konno M, Ito S, Tsunoda SP, Inoue K, Kandori H (2017) Molecular properties of a DTD channelrhodopsin from Guillardia theta. Biophys Physicobiol 14:57–66

Yizhar O, Fenno LE, Prigge M, Schneider F, Davidson TJ, O'Shea DJ, Sohal VS, Goshen I, Finkelstein J, Paz JT et al (2011) Neocortical excitation/inhibition balance in information processing and social dysfunction. Nature 477:171–178

Yoshida K, Tsunoda SP, Brown LS, Kandori H (2017) A unique choanoflagellate enzyme rhodopsin exhibits light-dependent cyclic nucleotide phosphodiesterase activity. J Biol Chem 292:7531–7541

Zabelskii D, Alekseev A, Kovalev K, Oliviera AS, Balandin T, Soloviov D, Bratanov D, Volkov L, Vaganova S, Astashkin R et al (2020) Viral channelrhodopsins: calcium-dependent $Na^+/K^+$ selective light-gated channels. bioRxiv. https://doi.org/10.1101/2020.02.14.949966

Zhang F, Wang LP, Brauner M, Liewald JF, Kay K, Watzke N, Wood PG, Bamberg E, Nagel G, Gottschalk A et al (2007) Multimodal fast optical interrogation of neural circuitry. Nature 446:633–639

Zhang F, Prigge M, Beyriere F, Tsunoda SP, Mattis J, Yizhar O, Hegemann P, Deisseroth K (2008) Red-shifted optogenetic excitation: a tool for fast neural control derived from Volvox carteri. Nat Neurosci 11:631–633

# Functional Mechanism of $Cl^-$-Pump Rhodopsin and Its Conversion into $H^+$ Pump

4

Takashi Kikukawa

**Abstract**

$Cl^-$-pump rhodopsin is the second discovered microbial rhodopsin. Although its physiological role has not been fully clarified, its functional mechanism has been studied as a model for anion transporters. After the success of neural activation by channel rhodopsin, the first $Cl^-$-pump halorhodopsin (HR) had become widely used as a neural silencer. The emergence of artificial and natural anion channel rhodopsins lowered the importance of HRs. However, the longer absorption maxima of approximately 585–600 nm for HRs are still advantageous for applications in mammalian brains and collaborations with neural activators possessing shorter absorption maxima. In this chapter, the variation and functional mechanisms of $Cl^-$ pumps are summarized. After the discovery of HR, $Cl^-$-pump rhodopsins were confined to only extremely halophilic haloarchaea. However, after 2014, two $Cl^-$-pump groups were newly discovered in marine and terrestrial bacteria. These $Cl^-$ pumps are phylogenetically distinct from HRs and have unique characteristics. In particular, the most recently identified $Cl^-$ pump has close similarity with the $H^+$ pump bacteriorhodopsin and was converted into the $H^+$ pump by a single amino acid replacement.

**Keywords**

Halorhodopsin · Bacteriorhodopsin · Photocycle · Ion pump · Chloride pump · Membrane protein · Microbial rhodopsin

## Abbreviations

| | |
|---|---|
| BR | Bacteriorhodopsin |
| Brub | Bacterioruberin |
| CP | Cytoplasmic |
| DDM | *n*-dodecyl-β-D-maltoside |
| EC | Extracellular |
| FR | $Cl^-$ pump from *Fulvimarina pelagi* |
| HR | Halorhodopsin |
| HsHR | HR from *Halobacterium salinarum* |
| Htr | Halobacterial transducer |
| MrHR | $Cl^-$ pump from *Mastigocladopsis repens* |
| NaR | $Na^+$-pump rhodopsin |
| NM-R3 | $Cl^-$ pump from *Nonlabens marinus* S1-08$^T$ |
| NpHR | HR from *Natronomonas pharaonis* |
| PRC | $H^+$-release complex |
| PSB | Protonated Schiff base |

T. Kikukawa (✉)
Faculty of Advanced Life Science, Hokkaido University, Sapporo, Japan

Global Station for Soft Matter, Global Institution for Collaborative Research and Education, Hokkaido University, Sapporo, Japan
e-mail: kikukawa@sci.hokudai.ac.jp



H. Yawo et al. (eds.), *Optogenetics*, Advances in Experimental Medicine and Biology 1293,
https://doi.org/10.1007/978-981-15-8763-4_4

SyHR $Cl^-$ pump from *Synechocystis* sp. PCC 7509

## 4.1 $Cl^-$-Pump Rhodopsins in Nature

### 4.1.1 The First $Cl^-$ Pump Halorhodopsin

The first $Cl^-$ pump was discovered from an extremely halophilic haloarchaeon, *Halobacterium salinarum* (Matsuno-Yagi and Mukohata 1977). This finding was achieved by a careful observation of a naturally occurring mutant strain. The archaeon *H. salinarum* expresses a large amount of bacteriorhodopsin (BR), which is the first discovered microbial rhodopsin. BR acts as an outward $H^+$ pump. Thus, illumination induces a decrease in the pH in the cell suspension. In 1977, Matsuno-Yagi and Mukohata isolated an altered colored strain and observed an opposite pH change, i.e., a light-induced increase in pH, which indicated the presence of another ion-pump rhodopsin and was detectable due to lower expression level of BR (Matsuno-Yagi and Mukohata 1977). Later, this rhodopsin was named "halorhodopsin (HR)" (Matsuno-Yagi and Mukohata 1980; Mukohata and Kaji 1981) and was found to pump $Cl^-$ inwardly (Schobert and Lanyi 1982). The observed increase in pH was the result of passive $H^+$ influx in response to the inner negative membrane potential created by the HR activity. HR can also pump larger halide ions, $Br^-$ and $I^-$, and polyatomic monovalent anions, $NO_3^-$ and $SCN^-$ (Hazemoto et al. 1984; Bamberg et al. 1984; Duschl et al. 1990; Seki et al. 2007). In addition to HR from *H. salinarum* (HsHR), its homolog from *Natronomonas pharaonis* (NpHR) has been functionally analyzed.

### 4.1.2 The Second and Third $Cl^-$-Pump Groups

Microbial rhodopsins used be considered to be present only in the haloarchaea. However, after 1999, their relatives began to be identified in various microorganisms due to the development of genome analysis technology (Bieszke et al. 1999). Currently, microbial rhodopsins are known to be ubiquitous in the microbial world and have divergent functions, such as being light-driven ion pumps, light sensors, light-gated ion channels, and light-switchable enzymes (Fig. 4.1) (see for reviews; Ernst et al. 2014; Inoue et al. 2014a; Kandori 2015; Govorunova et al. 2017). Similar to HR, all archaeal rhodopsins were discovered through careful observations of the cell itself. In contrast, other rhodopsins were discovered through the identification of their genes and were functionally characterized after their heterologous expression. The second and third $Cl^-$-pump groups were also discovered through gene analyses (Yoshizawa et al. 2014; Hasemi et al. 2016).

The second $Cl^-$-pump group was discovered from the genomes of marine flavobacteria and alphaproteobacteria (Yoshizawa et al. 2014). They are large eubacterial categories inhabiting the ocean. Thus, these $Cl^-$ pumps might be abundant in marine environments. The second group is designated here as NTQ rhodopsins according to their "motif" residues, whose details will be described in Table 4.1. Thus far, two members have been functionally characterized. One is a rhodopsin from *Nonlabens marinus* S1-08$^T$ (NM-R3) (Yoshizawa et al. 2014; Hosaka et al. 2016; Tsukamoto et al. 2017), and the other is a rhodopsin from *Fulvimarina pelagi* (FR) (Inoue et al. 2014b). Similar to HR, these NTQ rhodopsins pump not only $Cl^-$ but also other halide ions and polyatomic monovalent anions. However, they are phylogenetically distant from the HR group and close to $Na^+$-pump rhodopsins (NaR), which have an NDQ motif (Fig. 4.1). Thus, NTQ rhodopsins seem to have independently evolved from HR.

The third $Cl^-$-pump group was discovered from the genomes of cyanobacteria (Hasemi et al. 2016). Most of them were isolated from terrestrial environments. The first characterized member from this group is a rhodopsin from *Mastigocladopsis repens*. It was named MrHR because the "TSD" motif of this group is close to the "TSA" of HR. According to this motif, the

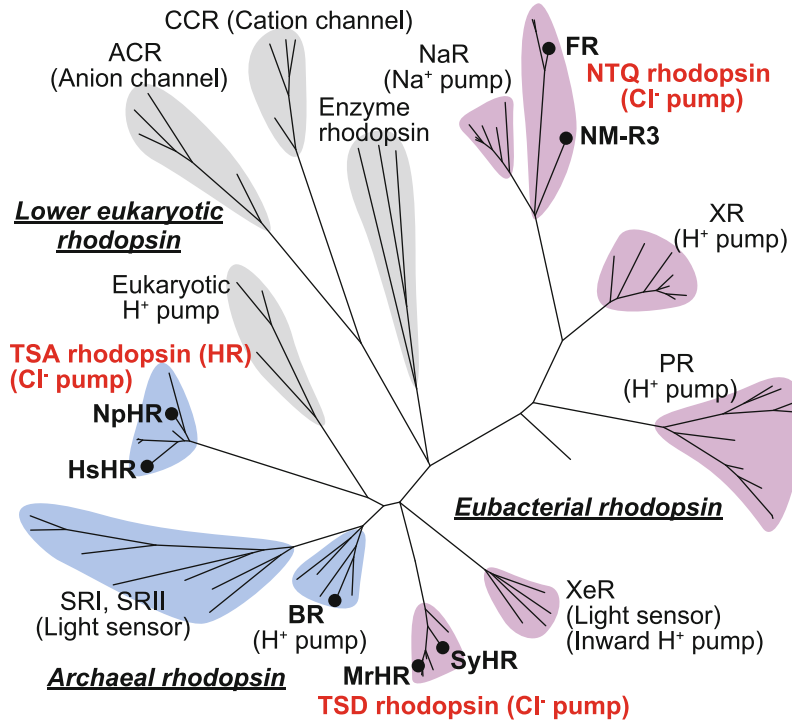


**Fig. 4.1** Phylogenetic relationships of microbial rhodopsins. *CCR* cation channel rhodopsin, *ACR* anion channel rhodopsin, *SRI* sensory rhodopsin I, *SRII* sensory rhodopsin II, *XeR* xenorhodopsin, *PR* proteorhodopsin, *XR* xanthorhodopsin

third group is designated here as TSD rhodopsins. The cluster of this group is phylogenetically close to HR (Fig. 4.1). MrHR pumps only smaller halide ions, $Cl^-$ and $Br^-$. Thus, this group appears to have a restricted ion-selective filter. It was subsequently shown that a homolog, named SyHR, from *Synechocystis* sp. PCC 7509 can additionally pump $SO_4^{2-}$, even though it cannot pump $I^-$ and $NO_3^-$, making SyHR similar to MrHR (Niho et al. 2017). Thus, SyHR might pump $SO_4^{2-}$ in a different mode from that for the smaller halide ions.

### 4.1.3 Presumed Physiological Roles of $Cl^-$ Pumps

The physiological significance of these $Cl^-$ pumps remains under debate. One possibility is a contribution to ATP production. The $Cl^-$ pumps

**Table 4.1** Comparison of the characteristic residues among the ion pumps. The motifs are indicated in parentheses and the residues are listed in bold

| | | | | | | | | | | | | |
|---|---|---|---|---|---|---|---|---|---|---|---|---|
| No. in BR | | 82 | **85** | **89** | 93 | **96** | 175 | 178 | 194 | 204 | 212 | 216 |
| No. in NpHR | | 123 | **126** | **130** | 134 | **137** | 215 | 218 | 234 | 244 | 252 | 256 |
| No. in NM-R3 | | 95 | **98** | **102** | 106 | **109** | 194 | 197 | 213 | 223 | 231 | 235 |
| No. in MrHR | | 71 | **74** | **78** | 82 | **85** | 163 | 166 | 182 | 192 | 200 | 204 |
| $H^+$ pump | BR (DTD) | R | **D** | **T** | L | **D** | R | T | E | E | D | K |
| $Na^+$ pump | KR2 (NDQ) | R | **N** | **D** | L | **Q** | W | F | L | R | D | K |
| $Cl^-$ pump | NpHR (TSA) | R | **T** | **S** | I | **A** | K | T | E | T | D | K |
| | NM-R3 (NTQ) | R | **N** | **T** | L | **Q** | F | M | F | R | D | K |
| | MrHR (TSD) | R | **T** | **S** | L | **D** | V | H | E | E | D | K |

*KR2* $Na^+$-pump rhodopsin from *Krokinobacter eikastus*

create a negative membrane potential, which strengthens the electrochemical gradient of $H^+$ and thus contributes to driving the $H^+$-ATP synthetase. However, the destination of transported $Cl^-$ is still unknown. For sustainable contributions to ATP production, there should be a pathway to expel $Cl^-$. Otherwise, the accumulated $Cl^-$ hinders further transport by $Cl^-$-pump rhodopsins. For TSD rhodopsins, their contributions to ATP production might be especially small. Their host strains contain a photosynthetic apparatus, which should be a main player in ATP production under illumination. Another proposed role of $Cl^-$ pumps is to maintain the cellular osmotic balance (Oesterhelt 1995). The host strains of HRs and NTQ rhodopsins inhabit marine and hypersaline environments. Thus, these cells are probably exposed to a large osmotic pressure during the volume increase of the growing cells. To maintain the osmotic balance, the internal salt concentration should increase. Due to the interior negative membrane potential, cations could be passively transported inside. However, anions need an active transport system, such as $Cl^-$-pump rhodopsins. A similar scenario might be applicable for TSD rhodopsins (Hasemi et al. 2016). Most of their host strains inhabit terrestrial and nonaqueous environments, where those cells are occasionally exposed to drought stress conditions. Under such desiccated conditions, the internal salt concentration should increase to preserve the intracellular water content. Thus, TSD rhodopsins might contribute to elevating the salt concentration and helping cells survive in nonaqueous environments.

## 4.2 "Motif" Residues and Anion-Binding Sites

### 4.2.1 "Motif" Residues of $Cl^-$-Pump Rhodopsins

All microbial rhodopsins have common structural folds composed of seven transmembrane helices and the chromophore retinal, which binds to a conserved Lys residue on helix G (the seventh helix) via a protonated Schiff base (PSB). In the upper panels of Fig. 4.2, the tertiary structures of BR, NpHR (HR), and NM-R3 (NTQ rhodopsin) are shown with characteristic residues, which are summarized in Table 4.1. The "motif" residues are underlined in Fig. 4.2 and in bold in Table 4.1. The expanded views of the respective Schiff base regions are shown in the lower panels of Fig. 4.2. The tertiary structure of MrHR has not been solved. Thus, its corresponding residues are indicated in parentheses in the NpHR structure.

After the discovery of NaR, "motif" residues began to be utilized for the classification of microbial rhodopsins (Inoue et al. 2013). The significances of the respective residues are different for each rhodopsin. For BR, the motif is "DTD," which corresponds to Asp85, Thr89, and Asp96. Of these, the two Asp residues are especially important for the $H^+$-pump function. Asp85 is a counter ion of the PSB and acts as a $H^+$ acceptor from the PSB after illumination. This primary $H^+$ transfer is essential to drive all subsequent $H^+$-transfer reactions. Asp96 acts as a $H^+$ donor for the deprotonated Schiff base and then accepts another $H^+$ from the cytoplasmic (CP) medium. The removal of Asp96 substantially slows the $H^+$ transfer in the CP channel and thus significantly weakens the $H^+$-pump efficiency. For all $Cl^-$ pumps, the Asp85 of BR is replaced by neutral residues, which are Thr126 for NpHR (TSA), Thr74 for MrHR (TSD), and Asn98 for NM-R3 (NTQ). Consequently, $Cl^-$ ions can bind near their respective PSBs as their counter ions. These $Cl^-$ ions are considered to be transported upon illumination. In Fig. 4.2e, f, the precise positions of $Cl^-$ ions are shown with spheres (labeled "$Cl^-$"). As shown, the first two motif residues (Thr126 and Ser130 for NpHR; Asn98 and Thr102 for NM-R3) directly interact with $Cl^-$ ions and form binding sites. These direct interactions are probably conserved in MrHR, which was experimentally suggested. Reflecting the direct interactions, these two residues in the motif are considered important for both of $Cl^-$ binding in the dark states and $Cl^-$ translocation after illumination. In fact, mutations of these

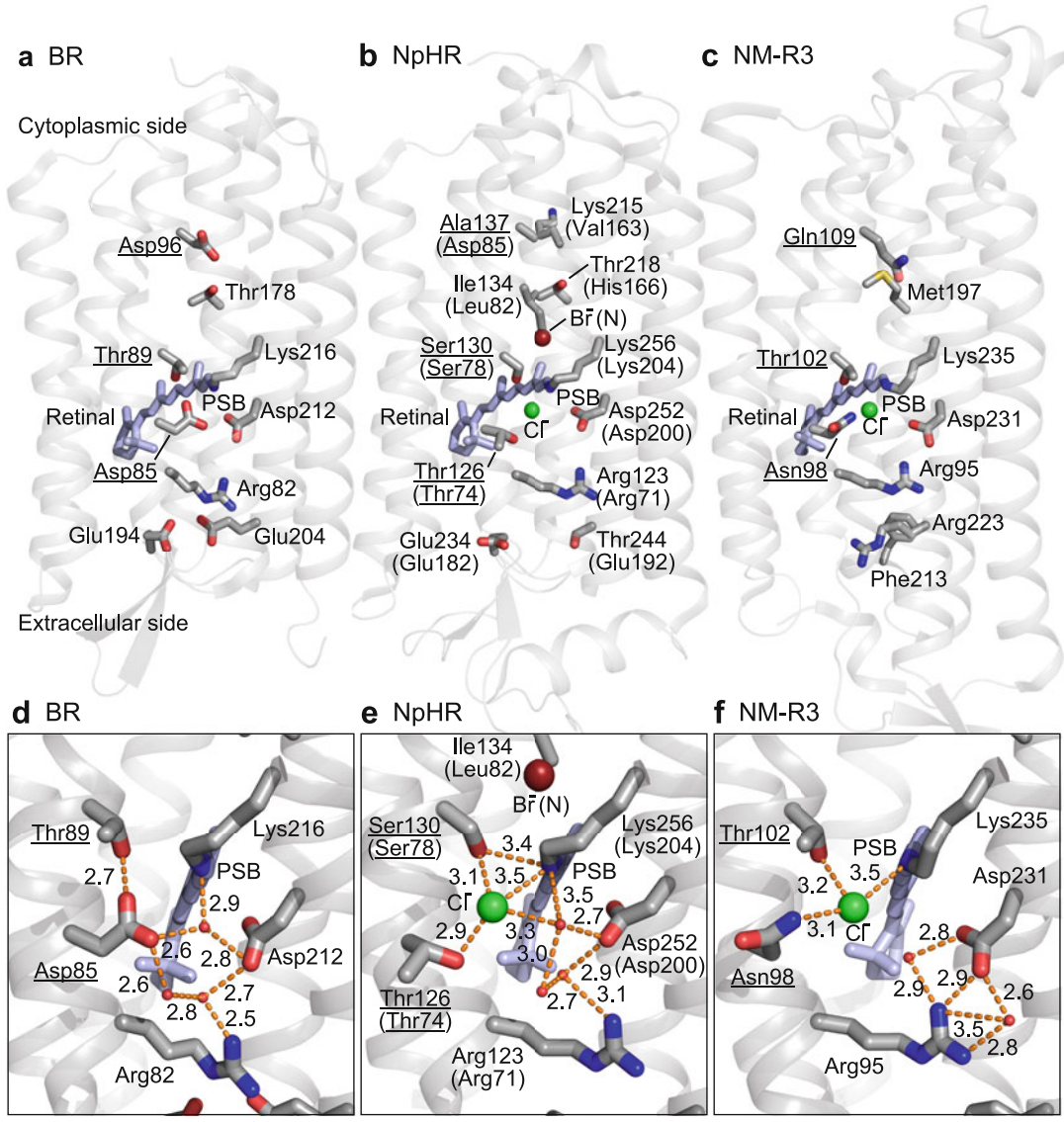


**Fig. 4.2** Tertiary structures of BR (**a**), NpHR (**b**), and NM-R3 (**c**). The motif residues are underlined, and their respective Schiff base regions are expanded in the corresponding lower panels. The structure of MrHR is not available. Thus, its corresponding residues are shown in parentheses in the NpHR structure, where two residues, Ile134 (Leu82) and Lys215 (Val163), are additionally shown. These residues are referred in the text. After illumination, NpHR and NM-R3 transport $Cl^-$ ions (spheres labeled "$Cl^-$"), which are initially bound near the PSB. The sphere labeled "$Br^-$ (N)" in the NpHR structure indicates the position of the halide ion ($Br^-$) at the N intermediate. In panels **d–f**, water molecules are shown as small spheres, and polar contacts within 3.5 Å are shown with dashed lines, whose distances are also indicated in Å. The Protein Data Bank codes are 1C3W for BR, 3A7K and 4QRY for NpHR, and 5G28 for NM-R3

residues weaken the $Cl^-$-pump activities for all three pumps (Hosaka et al. 2016; Rüdiger and Oesterhelt 1997; Kim et al. 2016; Hasemi et al. 2019; and our unpublished results). For NpHR and MrHR, these mutations were also proven to weaken the $Cl^-$-binding affinity (Hasemi et al.

2019; Sato et al. 2003, 2005). In contrast, the third residue of this motif (Ala137 for NpHR; Asp85 for MrHR; and Gln109 for NM-R3) seems not to have important roles for all three pumps. Of these, the Asp85 for MrHR is unique because this acidic residue is also conserved in BR (Asp96) as mentioned above. FTIR measurement suggested the light-induced deprotonation of Asp85 (Harris et al. 2017). However, mutating this residue did not affect either the $Cl^-$-pump activity or the $Cl^-$-binding affinity in the dark state (Hasemi et al. 2019).

### 4.2.2 Environments Around the PSB and the $Cl^-$-Binding Site

The $Cl^-$ bindings induce the absorption spectral shifts of retinal chromophores. From their $Cl^-$-concentration dependencies, the dissociation constants of $Cl^-$ can be determined. These values are similar between NpHR (1–5 mM) (Sato et al. 2003, 2005; Scharf and Engelhard 1994; Váró et al. 1995a; Kikukawa et al. 2015) and MrHR (2 mM) (Hasemi et al. 2016, 2019), but are especially large for NM-R3 (24 mM) (Tsukamoto et al. 2017). These values might reflect the characteristic differences in the hydrogen bonding network around the $Cl^-$ ions (Fig. 4.2e, f). For NpHR and probably for MrHR, their $Cl^-$ ions are surrounded by an extensive hydrogen bonding network, which includes the PSB, two motif residues (Thr and Ser), one Asp residue (Asp252 for NpHR, Asp200 for MrHR), one Arg residue (Arg123 for NpHR, Arg71 for MrHR), and three water molecules. NM-R3 also conserves the Asp and Arg residues (Asp231 and Arg95) (Fig. 4.2f). However, these two residues do not connect to the network around $Cl^-$, unlike the residues in NpHR (Fig. 4.2e). For HRs (NpHR and HsHR) and MrHR, the importance of these Arg and Asp residues was experimentally proven (Seki et al. 2007; Rüdiger and Oesterhelt 1997; Hasemi et al. 2019; Sato et al. 2005; Kubo et al. 2009). The positive charges at the Arg positions are commonly important for $Cl^-$ binding. Especially for HRs, $Cl^-$ binding completely disappeared due to the mutations to neutral residues (Rüdiger and Oesterhelt 1997; Sato et al. 2005; Kubo et al. 2009). For Asp residues (Asp252 for NpHR, Asp200 for MrHR), characteristic differences were observed between NpHR and MrHR (Hasemi et al. 2019), probably reflecting that the Asp residue is deprotonated in NpHR but protonated in MrHR. Due to different protonation states, the replacement by Asn weakens the $Cl^-$ binding in NpHR but does not affect that in MrHR. Nevertheless, this mutation completely removes the $Cl^-$-pump activities in both proteins (Hasemi et al. 2019; Chen et al. 2016). The protonation states of the Asp residues will be discussed in the following.

In Fig. 4.2d–f, polar contacts within 3.5 Å are shown with dashed lines. For NpHR (Fig. 4.2e), the PSB contacts Ser130, $Cl^-$, and a water molecule. The interaction with $Cl^-$ was reported to be weak, and the water molecule was assigned as a main hydrogen bonding partner of the PSB (Shibata et al. 2005). On the other hand, the PSB of NM-R3 interacts only with $Cl^-$. Thus, this interaction should be strong. These characteristic differences were consistent with the observations of halide ion-induced spectral shifts. In $CHCl_3$, the PSB directly binds with halide ions. The resulting $\lambda_{max}$ largely depends on the size of the ions (Blatz et al. 1972). A similar tendency was observed for NM-R3 and FR (Inoue et al. 2014b; Tsukamoto et al. 2017). For NpHR and HsHR, their $\lambda_{max}$ values show a little halide ion dependence, indicating an indirect interaction between the PSB and halide ions (Scharf and Engelhard 1994; Walter and Braiman 1994). This slight dependence was also observed for MrHR (Hasemi et al. 2016). Thus, the local environments in MrHR and probably in SyHR (another TSD rhodopsin) seem to be similar to those in NpHR and HsHR. These different interactions between the $Cl^-$ and PSB might be the reason for different photoreactions. The first half of the photoreaction is especially similar between HRs and TSD rhodopsins. Their photoreactions commonly include largely blue-shifted L intermediates (50–60 nm) (Hasemi et al. 2016, 2019; Niho et al. 2017; Váró et al. 1995a, c). For NTQ rhodopsins, similar intermediates also appear, but their blueshift

widths are very faint (~10 nm) (Tsukamoto et al. 2017; Inoue et al. 2014b).

As mentioned above, several data indicate a similar environment around the PSB between NpHR and MrHR. However, characteristic differences other than the protonation state of the Asp residue (Asp252 for NpHR, Asp200 for MrHR) also exist. For NpHR, Arg123 and Ser130 are essential for $Cl^-$-pump functions (Sato et al. 2003; Sato et al. 2005; and our unpublished results). For MrHR, their mutations are not fatal as their replacement mutants still show $Cl^-$-pump activity (Hasemi et al. 2019). Moreover, NpHR does not become a $H^+$ pump with the T126D mutation (Váró et al. 1996; Muroda et al. 2012). However, with the corresponding mutation, MrHR begins to pump $H^+$ outwardly (Hasemi et al. 2016). These differences will be described in the following.

## 4.3 Photoreaction Cycles

### 4.3.1 Photocycle Schemes of NpHR, NM-R3, and MrHR

Most microbial rhodopsins dominantly contain retinal in the all-*trans*/15-*anti* configuration. Upon illumination, retinal isomerizes to a 13-*cis*/15-*anti* configuration. This isomerization elevates the protein to the excited state, which is thermally relaxed to the original state via various photointermediates. During this cyclic reaction called "photocycle," microbial rhodopsin performs various functions. For NpHR and HsHR, their photocycles have been analyzed using various techniques. Especially for NpHR, the tertiary structures of each intermediate have also been reported (Kouyama et al. 2015). For NTQ and TSD rhodopsins, their levels of analyses are not comparable to that of NpHR, but outlines of their photocycles have been examined by time-resolved spectroscopies (Tsukamoto et al. 2017; Inoue et al. 2014b; Hasemi et al. 2019; Niho et al. 2017; Harris et al. 2017). Here, the photocycles of NpHR, MrHR, and NM-R3 will be mainly discussed. Their homologs (e.g., HsHR, SyHR, and FR) were also analyzed and revealed that they underwent photoreactions that were similar to their counterparts.

Figure 4.3 shows the photocycle schemes of three $Cl^-$ pumps based on our analyses of flash-induced visible absorption changes (Tsukamoto et al. 2017; Hasemi et al. 2019; Kikukawa et al. 2015; Hasegawa et al. 2007; Shibasaki et al. 2013). Here, we adopted a sequential irreversible model (Chizhov et al. 1996): P0 → P1 → P2 → ···· → Pn → P0, where P0 corresponds to the original dark state. The other Pi ($i = 1$–$n$) states represent the photolyzed states, which are defined to appear sequentially with no back reactions. The "photolyzed states" mean kinetically distinguishable states, which might include several photointermediates if a quasi-equilibrium exists between them. The inner circles in Fig. 4.3 indicate suitable irreversible schemes, where the lifetimes of the respective Pi states are also shown. The "true" photocycle schemes are shown in the outer circles, where the $\lambda_{max}$ values of the dark states and the photointermediates are denoted in their subscripts. In these circles, some intermediates are connected by double-headed arrows, indicating that these intermediates form quasi-equilibrium states due to the back reactions. Respective intermediates were named after those of BR by mainly referring to the absorption $\lambda_{max}$ values. The $Cl^-$-translocation steps should be closely related to the isomerization and reisomerization processes of the retinal. These retinal configurations at each intermediate are determined in detail for NpHR and partially for MrHR, but not for NM-R3. In the following subsections, the details of the NpHR photocycle will be discussed, and then the features of the NM-R3 and MrHR photocycles will be introduced.

### 4.3.2 $Cl^-$-Releasing Step in the NpHR Photocycle

The NpHR photocycle in Fig. 4.3 is essentially the same as that proposed by Lanyi and coworkers (Váró et al. 1995a, b; Ludmann et al. 2000). They detected the accelerations of N ← O

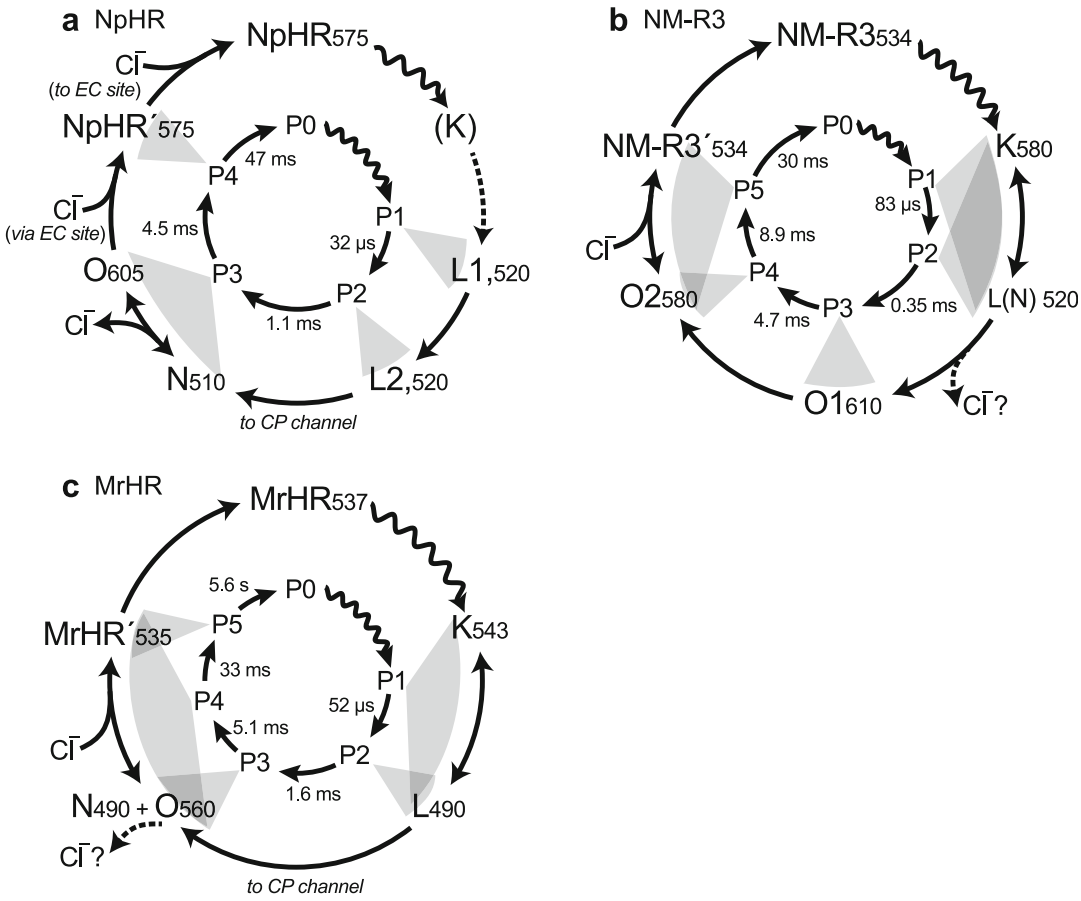


**Fig. 4.3** Photocycles of three $Cl^-$ pumps. (**a**) NpHR, (**b**) NM-R3, and (**c**) MrHR. These models were based on our analysis results according to the sequential irreversible model (Tsukamoto et al. 2017; Hasemi et al. 2019; Kikukawa et al. 2015; Hasegawa et al. 2007; Shibasaki et al. 2013). For details, see the text. The inner circles indicate suitable irreversible schemes. The "true" photocycle schemes are shown in the outer circles. The gray circular sectors indicate the "true" intermediates involved in the respective Pi states. The $Cl^-$ release and recapture timings are also indicated, although $Cl^-$ releases for NM-R3 and MrHR lack convincing data. The "to CP channel" represents the timing of the $Cl^-$ movement over the Schiff base region. For NpHR, the $Cl^-$-binding site on the EC surface (EC site) is suggested to contribute to the $Cl^-$-recapture processes (Shibasaki et al. 2013). They are indicated by two arrows during O→NpHR′ and NpHR′ → NpHR. Their details are described in the text. For NpHR, K was not detected by our apparatus; thus, the photocycle after L formation was analyzed. For MrHR, N and O appear simultaneously; thus, they are shown as "N + O." All samples included 1 M $Cl^-$. NpHR was embedded in the native cell membrane fragment (Kikukawa et al. 2015), and the other two pumps were in the detergent-solubilized state (Tsukamoto et al. 2017; Hasemi et al. 2019)

and O → NpHR′ transitions by elevating the $Cl^-$ concentration and thus concluded that $Cl^-$ is released and captured during the formation and decay of O. This view was supported by various results, including the transient electrogenicities (Ludmann et al. 2000), $Cl^-$-diffusion signals (Inoue et al. 2009), and similarities between the O and $Cl^-$-free unphotolyzed state (Sato et al. 2002; Guijarro et al. 2006). In our analysis, the blueshifted N and the redshifted O appear almost simultaneously to form a quasi-equilibrium state (Fig. 4.3a) (Kikukawa et al. 2015; Hasegawa et al. 2007; Shibasaki et al. 2013). As the $Cl^-$ concentration increases, the equilibrium shifts toward N,

indicating that O is a $Cl^-$-free state. From the $Cl^-$-concentration dependence of the equilibrium, the dissociation constant of $Cl^-$ was determined. This value was approximately 1 M in the solubilized state with *n*-dodecyl-β-D-maltoside (DDM) (Hasegawa et al. 2007; Shibasaki et al. 2013) and 4 M in the native *N. pharaonis* membrane (Kikukawa et al. 2015). The dissociation constant in the dark state is 1–5 mM in the solubilized state and 6 mM in the native membrane (Sato et al. 2003, 2005; Scharf and Engelhard 1994; Váró et al. 1995a; Kikukawa et al. 2015). Thus, NpHR causes at least a 200-fold increase in the dissociation constant to release $Cl^-$ into the CP medium. As mentioned above, N and O appear simultaneously. Thus, in our analysis, the order of appearance for N and O could not be determined. However, this problem was solved by using the claret membrane, which is a cell membrane fragment containing NpHR and carotenoid bacterioruberin (Brub) (Kikukawa et al. 2015). Carotenoid alters its absorption spectrum in response to the electrostatic environment. Indeed, Brub altered its spectrum when unphotolyzed NpHR was bound to $Cl^-$. During the photocycle, the opposite spectral change of Brub appeared. This spectral change was associated with the accumulations of O and NpHR′ but not was associated with N. This result indicates that O forms from N and decays to NpHR′. A larger spectral change of Brub associated with O supports $Cl^-$ release during the transition from N to O. NpHR′ already binds another $Cl^-$ but probably remains a protein conformational change for $Cl^-$ release, which sustains the spectral change of Brub.

### 4.3.3 $Cl^-$ Movement Over the Schiff Base Region in the NpHR Photocycle

In all $Cl^-$ pumps, $Cl^-$ commonly binds at the vicinity of a Schiff base $NH^+$, which is oriented toward the extracellular (EC) side. By the all-*trans*/15-*anti* to 13-*cis*/15-*anti* isomerization of retinal during K formation, the $NH^+$ is turned toward the CP side. This $NH^+$ motion is probably the origin to drive the $Cl^-$ movement to the CP channel. When and how does this $Cl^-$ movement occur? For NpHR, large electrogenicities were observed during the L2 → N and N → O transitions (Ludmann et al. 2000; Muneyuki et al. 1999). N → O is the $Cl^-$ release process. Thus, the preceding L2 → N was assigned to the $Cl^-$ movement to the CP channel. The same conclusion was also drawn by using the NpHR mutant, which can bind with the halobacterial transducer (Htr) (Hasegawa et al. 2007). In native cells, Htr makes a complex with sensory rhodopsin (SR) and inhibits the outward movement of the CP half channel in SR. Upon complex formation with Htr, NpHR loses the $Cl^-$-pump activity, and its photocycle lacks N–O equilibrium. The $Cl^-$ movement probably requires a CP opening. Thus, both the $Cl^-$ movement and CP opening appear to occur during the L2 → N transition. This $Cl^-$ movement might be triggered by the change in the hydration environment. As mentioned above, the Schiff base interacts with the water molecule in the dark state (Fig. 4.2e). FTIR measurements revealed that this interaction also exists at L1, even though the $NH^+$ direction is already turned to the CP side (Shibata et al. 2005). Thus, the $NH^+$ might remove the water molecule from the original position. The resultant hydrophobic environment around $Cl^-$ is suggested to trigger the $Cl^-$ movement to the CP side.

### 4.3.4 Detailed Discussion of the NpHR Photocycle with Reference to the Intermediate Structures

For NpHR, structures of many intermediates were solved in a low-temperature crystallographic study (Kouyama et al. 2015). These structures were assigned to those from L1 to O based on the analyses of the absorption spectra, retinal configurations, and predicted $Cl^-$ positions at each intermediate. Thus, the assignments seem not so conclusive, but the structures are highly suggestive. In the structural analyses, $Br^-$ was used instead of $Cl^-$ to clearly determine the ion position. The L1, L2, and N structures commonly

contain 13-*cis*/15-*anti* retinal and one $Br^-$ inside the protein, but the $Br^-$ gradually moves toward the CP side (Kouyama et al. 2015). At L1, $Br^-$ remains near the original position. At L2, it moves to the site between Ser130 and the Schiff base (Fig. 4.2e). This is consistent with the importance of Ser130, whose mutations substantially distorted the photocycle (Sato et al. 2003). Indeed, regardless of the replacement of Ser130 by Thr, the $Cl^-$-pump activity completely disappeared (our unpublished result). Upon the formation of N, $Br^-$ moves over the Schiff base region and binds to the site between the Schiff base and the Ile134 side chain (sphere labeled "$Br^-$ (N)" in Fig. 4.2b and e), where $Br^-$ directly interacts with the $NH^+$ of the Schiff base and the OH of Ser130 (Kouyama et al. 2015). Thus, this position is still close to that at L2. This small displacement does not seem to match the relatively large electrogenicity observed at the L2 → N transition described above (Ludmann et al. 2000; Muneyuki et al. 1999). Concomitant with this $Br^-$ movement, the original binding site shrinks due to an inward movement of the EC half of helix C (Kouyama et al. 2015). This shrinkage might assist $Br^-$ movement. In the CP half channel, N formation also involves a large conformational change, i.e., CP interhelical space is opened due to the kink at Lys215 on helix F (Fig. 4.2b), creating a long water channel that seems to connect the $Br^-$ and CP membrane surface (Kouyama et al. 2015). Thus, $Br^-$ might be released along this channel during the N decay. Thr218 is one of a few hydrophilic residues in the hydrophobic CP channel (Fig. 4.2b), and its mutation greatly altered the dissociation constant for the $Cl^-$ release (Shibasaki et al. 2013). This mutation effect might reflect the participation of Thr218 in the water channel, where the OH of Thr218 makes hydrogen bonds with two water molecules and thus seems to adjust their positions (Kouyama et al. 2015). As mentioned above, N formation was inhibited by the association with Htr (Hasegawa et al. 2007). This observation might relate to the large conformational change at N; the bound Htr might restrict the conformational change, and thus N cannot be formed. After N, $Br^-$ is released, and then O forms. In the O structure, $Br^-$ is absent, and retinal takes an all-*trans*/15-*anti* conformation (Kouyama et al. 2015). Simultaneously, the CP half channel is closed, and the water channel also disappears. This relaxed structure does not seem to agree with previous observations (Shibasaki et al. 2013). When the hydrostatic pressure is increased, the N–O equilibrium shifts toward N, indicating that O has a larger volume than N. The difference in partial molar volumes is approximately 24 mL/mol. The hydration involves an increase in the volume. Thus, "true" O seems to still be hydrated and/or cause large conformation changes in different regions. The structure of another intermediate named N′ was also determined (Kouyama et al. 2015). This intermediate contains 13-*cis*/15-*syn* retinal and lacks $Br^-$, but maintains the large conformational change at N. The presence of N′ and the subsequent photocycle analysis resulted in a proposal of a complex model (Kouyama et al. 2018), where O′ containing 13-*cis*/15-*syn* retinal is supposed to be a precursor of O and to make a $Cl^-$-dependent equilibrium with its precursors N and N′ (N↔N′↔O′). O′ might maintain a large conformational change and thus have a larger volume than N and N′. However, O′ is currently supposed to have a similar structure to O (Kouyama et al. 2018).

As shown in Fig. 4.3, for NpHR, the last intermediate is NpHR′, which forms from O and has almost the same spectrum as the original state. Judging from the spectrum, NpHR′ already binds to $Cl^-$ near the original position. However, its decay is slow, indicating significant difference from the original state. This slow decay might reflect the two-step $Cl^-$ uptake. The O → NpHR′ transition showed complex $Cl^-$-concentration dependence, which could be explained by the presence of the $Cl^-$-binding site around the EC surface (Shibasaki et al. 2013). This $Cl^-$ at the EC site might first move to the Schiff base region during O → NpHR′, and then, the EC site captures another $Cl^-$ during NpHR′ → NpHR. This capture might involve a substantial conformational change and thus require a long decay time. This kind of $Cl^-$-binding site was suggested by the X-ray crystal structure (Kanada et al. 2011)

and the $Cl^-$-concentration dependence of the PSB stability (Mevorat-Kaplan et al. 2006). In a recent model (Kouyama et al. 2018), the 13-*cis* configuration was proposed for NpHR′, where two branching pathways were supposed for the decay of O′ described above; at a lower $Cl^-$ concentration, O′ becomes a "true" O, which has all-*trans*/15-*anti* retinal and then returns to the original state by capturing another $Cl^-$. At a high $Cl^-$ concertation, O′ captures $Cl^-$ without isomerization and then becomes NpHR′. Thus, in this model, NpHR′ still contains 13-*cis*/15-*syn* retinal, whose $NH^+$ of the Schiff base should face toward the EC side. The captured $Cl^-$ might stabilize this configuration of retinal and then slow down the recovery to the original state with all-*trans*/15-*anti* retinal.

### 4.3.5 Photocycles of NM-R3 and MrHR

As shown in Fig. 4.3, the overall photocycles of NM-R3 and MrHR are similar to that of NpHR. However, the $Cl^-$-translocation steps have not been clarified in detail. For NpHR, O was a key intermediate to consider in the $Cl^-$-translocation steps because this intermediate shows clear $Cl^-$-concentration dependence in its formation and decay and thus was relatively easily assigned to the $Cl^-$-releasing state. Similar to NpHR, both NM-R3 and MrHR exhibited redshifted intermediates named O that appear in the latter halves of their photocycles (Hasemi et al. 2016, 2019; Tsukamoto et al. 2017). However, their $Cl^-$-releasing states have not been clearly determined. For NM-R3, two redshifted intermediates appear sequentially and are named O1 and O2 (Tsukamoto et al. 2017). The latter O2 and the subsequent NM-R3′ form a transient equilibrium, which shifts toward NM-R3′ at high $Cl^-$ concentrations. Thus, the O2 → NM-R3′ transition was assigned to the $Cl^-$ recapture process (Fig. 4.3b). NM-R3′ has almost the same spectrum as that of the dark state, indicating that NM-R3′ surely contains $Cl^-$ near the original position. On the other hand, there is no conclusive evidence to define the $Cl^-$-release process.

For MrHR, its intermediate O exhibits a transient equilibrium with a blueshifted intermediate, which was named N, similar to NpHR (Hasemi et al. 2016, 2019). This equilibrium shows only a slight $Cl^-$-concentration dependence, which makes it difficult to discuss the $Cl^-$-releasing state (Fig. 4.3c). The equilibrium between N and O is shown as "N + O" in Fig. 4.3c, reflecting their simultaneous formation and decay. Although their appearance order has not been determined, their formation is probably associated with the $Cl^-$ movement over the Schiff base region. This consideration is based on the analyses for $I^-$-bound MrHR. By the addition of $I^-$, MrHR shows a $\lambda_{max}$ shift, reflecting $I^-$ binding to the vicinity of the PSB (Hasemi et al. 2016). However, this $I^-$-bound MrHR does not show pump activity. Thus, $I^-$ is probably not transported to the CP channel in the photolyzed MrHR. The $I^-$-bound MrHR undergoes a photocycle lacking the intermediate after L, indicating that the L → N + O transition is associated with $Cl^-$ movement (Hasemi et al. 2019).

As similar to NpHR′ and NM-R3′, the last intermediate MrHR′ has almost the same spectrum as that of the dark state. Thus, $Cl^-$ is located near the original position in MrHR′. However, it was suggested for MrHR′ that its retinal is still in a 13-*cis* configuration and that substantial conformational changes remain in the protein moiety (Harris et al. 2017). The extremely slow decay of MrHR′ (~6 s) might reflect its significantly distorted conformation (Fig. 4.3c).

## 4.4 MrHR: A Novel $Cl^-$ Pump with Close Similarity to the $H^+$ Pump

### 4.4.1 Conversion of MrHR into the $H^+$ Pump by a Single Amino Acid Replacement

In 1995, BR was converted into a $Cl^-$ pump by a single amino acid mutation, where the $H^+$-acceptor residue, Asp85, was replaced with a Thr, the corresponding residue in HR (Fig 4.2d, e,

Table 4.1) (Sasaki et al. 1995). Thus, this "D to T" mutation replaced the first motif residue in "DTD" of BR to the "TSA" motif of HR. After this success, the reverse conversion from "HR to BR" was attempted (Váró et al. 1996; Muroda et al. 2012; Havelka et al. 1995). However, this conversion failed even though ten residues of NpHR were replaced. In 2016, this reverse mutation was first achieved in MrHR by a single amino acid replacement (Hasemi et al. 2016).

MrHR conserves characteristic residues for the BR-type $H^+$ pump (Fig. 4.2a, b, Table 4.1). The representative is the third motif residue, which is Asp96 in BR (DTD) and Asp85 in MrHR (TSD). In addition, Glu194 and Glu204 of BR are also conserved as Glu182 and Glu192 in MrHR. As described above, Asp96 of BR acts as a $H^+$ donor residue for the Schiff base and is thus essential for $H^+$-pump function. On the other hand, two Glu residues of BR act as a $H^+$-release complex (PRC) to the EC medium and contribute to a strong $H^+$-pump activity. Thus, MrHR seems to be a $Cl^-$ pump just after the differentiation from the BR-type $H^+$ pump. This consideration was proven by the conversion of MrHR into a $H^+$ pump by replacing Thr74, a first motif residue (TSD), into the corresponding Asp residue in BR (DTD). Thus, this "T to D" mutation is a simple introduction of the Asp85 of BR, a $H^+$ acceptor residue from the PSB. The resultant T74D MrHR begins to pump $H^+$ outwardly (Hasemi et al. 2016). Moreover, this mutant underwent a completely different photocycle from that of wild-type MrHR (Fig. 4.4a, b). Specifically, the M intermediate was observed at approximately 390 nm (Fig. 4.4b), indicating that the introduced Asp residue indeed acts as a $H^+$ acceptor from the PSB. This $H^+$ transfer occurs at a very fast rate, which is comparable with those of natural $H^+$ pumps. For unphotolyzed BR, the corresponding Asp85 has a low pKa of approximately 2.6, and this value is the lowest pH to accept $H^+$ after illumination (Balashov et al. 1993). The corresponding pKa for T74D MrHR is approximately 2 (our unpublished result), suggesting that the embedded Asp residue is surrounded by an environment similar to that of BR. Upon M formation, BR releases $H^+$ to the medium from the PRC. This fast $H^+$ release also occurs in the T74D MrHR, suggesting the presence of active PRC, although its pH range ($5.5 < pH < 7$; our unpublished result) is narrower than that of BR ($5 < pH < 10$) (Tamogami et al. 2009). After the M decay, two intermediates appear sequentially and correspond

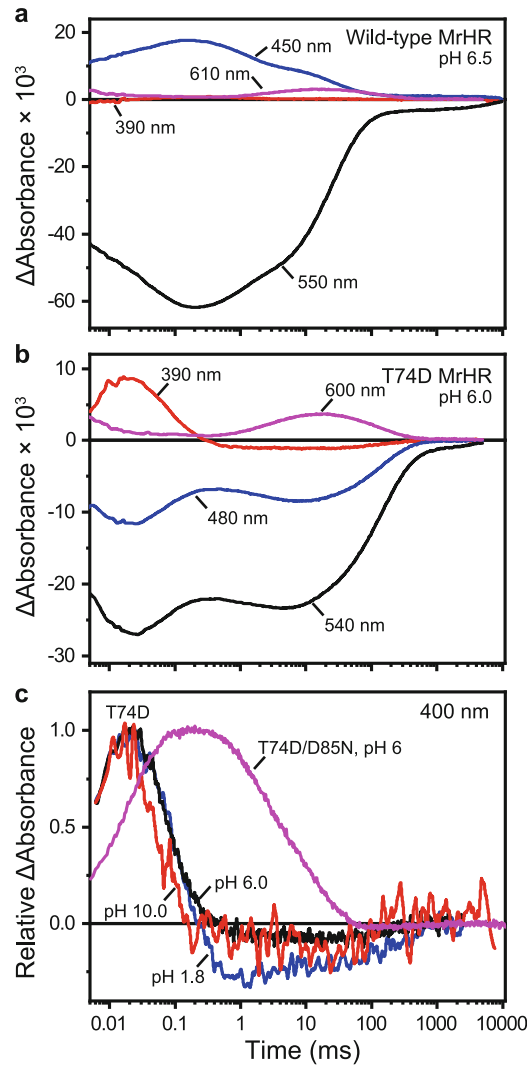


**Fig. 4.4** Flash-induced absorbance changes of MrHR and the mutants. The purified proteins were activated by 7-ns green laser pulses, and transient absorbance changes at typical wavelengths were recorded (Hasemi et al. 2016). All samples were suspended in 0.1 M NaCl and 0.05% DDM at 25 °C. The pH values are indicated in the panels

to N (480 nm) and O (600 nm) in natural $H^+$ pumps (Fig. 4.4b). The M → N transition reflects $H^+$ movement from the donor to the Schiff base, and the subsequent N → O transition reflects $H^+$ uptake from the CP medium by the donor. Both transitions in T74D occur at a fast rate, which is comparable with those of natural $H^+$ pumps. For BR, the M decay becomes slow above pH 8; at such high pH levels, M is in equilibrium with N, and they decay together due to the slow $H^+$ uptake from the medium. For the T74D MrHR, the M decay rate does not slow even at pH 10 (Fig. 4.4c). Thus, the conserved Asp85 in MrHR functions as a donor residue over a very wide pH range. Indeed, its replacement by Asn (T74D/D85N) significantly slowed the M decay (Fig. 4.4c). As shown in Fig. 4.4b, M, N, and O of T74D MrHR appear sequentially without a quasi-equilibrium. This reflects the strict "accessibility switch" of the donor, which communicates with the Schiff base during the M–N transition; then, the accessibility switches to the CP medium to facilitate the N–O transition. In a $H^+$ pump, this switch contributes to the one-way (irreversible) $H^+$ transport (for reviews, see Balashov 2000; Lanyi 2004). These facts suggest that MrHR maintains not only the essential residues but also the structural factors for an effective $H^+$ pump.

### 4.4.2 Lacking the Optimizations for Matured $Cl^-$ Pumps

In wild-type MrHR, the Asp85 residue is not essential for the $Cl^-$-pump function, which was confirmed by an alanine replacement mutant (Hasemi et al. 2019). However, in the T74D MrHR, both the introduced Asp74 and the conserved Asp85 function as an excellent $H^+$ acceptor and donor, respectively. In addition, the conserved PRC also functions in T74D MrHR although its active pH range is narrow. These facts suggest that MrHR evolved from a BR-type $H^+$ pump, but the residues and structure have not been optimized into a mature $Cl^-$ pump. This lack of optimization might relate to the substantially slow lifetime of MrHR′ (~6 s) (Figs. 4.3c and 4.4a), which is a rate-limiting process of the photocycle (Hasemi et al. 2019). Ion-pump rhodopsins generally undergo faster photocycles (<100 ms) and then generate larger electrochemical gradients of ions. For NpHR, the corresponding NpHR′ was suggested to be photoactive, and thus, its decay can be bypassed under constant illumination (Feroz et al. 2018). For MrHR, the structure of MrHR′ still remains largely distorted as mentioned above (Harris et al. 2017). Thus, its decay might define the turnover rate of the $Cl^-$-transport cycle. To accelerate the MrHR′ decay, some kind of optimization might be necessary. Another kind of optimization might have also occurred in the vicinity of the Asp200 residue of MrHR. This residue is superconserved and assumed to be deprotonated in most microbial rhodopsins. In contrast, Asp200 of MrHR is probably protonated in the dark state (Hasemi et al. 2019). Reflecting this protonation, its D200N mutation affected neither the $Cl^-$-binding affinity nor the absorption spectrum, unlike the corresponding D252N NpHR. However, D200N MrHR completely lacks $Cl^-$-pump functions, similar to D252N NpHR (Hasemi et al. 2019; Chen et al. 2016). Thus, $Cl^-$ pumps commonly utilize the negative charge at this position to drive the $Cl^-$ movement to the CP side. For other $Cl^-$ pumps, this negative charge is already present in the dark state. However, Asp200 of MrHR needs to deprotonate during the photocycle to create the negative charge. Indeed, a $H^+$ release was detected for photolyzed MrHR during the L decay (Hasemi et al. 2019). The absence of a negative charge in the dark state might contribute to strong $Cl^-$ binding. However, deprotonation during the photocycle might have a negative effect on $Cl^-$ translocation. Judging from the position of Asp200, the $H^+$ is probably released into the EC medium. The resultant dipole moment might hamper the opposite movement of $Cl^-$ into the CP channel and then weaken the $Cl^-$ pump activity. Thus, other $Cl^-$ pumps might be optimized so that they can bind $Cl^-$ with a high

affinity and then transport it, even though the Asp residues are always deprotonated.

### 4.4.3 One-Way Functional Conversion Between BR and HR

For HR, the introduction of the $H^+$-acceptor residue never induced M formation (Váró et al. 1996; Muroda et al. 2012; Havelka et al. 1995). On the other hand, BR easily became a $Cl^-$ pump by the D85T mutation (Sasaki et al. 1995). Thus, a distinct difference between HR and BR seems to exist. One hypothesis might be the difference in the residue arrangement. As mentioned above, $Cl^-$ in NpHR interacts with the PSB via a water molecule. On the other hand, for D85S BR, which was proven to pump $Cl^-$ and $Br^-$, the halide ion ($Br^-$) directly binds to the PSB (Facciotti et al. 2003). Thus, halide ions in D85S BR are near the PSB compared to that of HR. This difference originates from the difference in the Cα positions of the first motif residues (Asp85 for BR and Thr126 for NpHR); the distances between the PSB and Cα positions are 6.6 Å for BR (PDB ID: 1C3W) but 8.2 Å for NpHR (PDB ID: 3A7K). Due to this longer distance, M formation in the HR mutants seems to be prohibited even though the acceptor residue is introduced. This consideration might be consistent with the protonation state of Asp200 in MrHR. For D85T BR, the corresponding Asp212 has an elevated pKa of ~6.9 (Tittor et al. 1997), probably due to the closed position of the bound $Cl^-$. Thus, the Cα positions of the first motif residues might be almost the same between BR and MrHR. Consequently, MrHR might contain a protonated Asp200 in the dark state (Hasemi et al. 2019) and easily become a $H^+$ pump by the simple introduction of a $H^+$ acceptor residue (Hasemi et al. 2016). However, this consideration cannot apply for NTQ rhodopsins. After the successful conversion of MrHR, an NTQ-rhodopsin FR was also converted into a $H^+$ pump by a simple motif mutation (Inoue et al. 2016), where the "NTQ" motif was converted into the "DTD" motif of BR. Thus, M formation was archived by a simple introduction of the $H^+$ acceptor residue as in MrHR. Nevertheless, the Cα of the first motif residue is located far from the PSB. This distance is approximately 8.1 Å (PDB ID: 5G28), which is close to 8.2 Å for NpHR. Thus, no M formation for HR mutants is still an open question.

## 4.5 Concluding Remarks

$Cl^-$-pump rhodopsin had been confined to only haloarchaea even after many rhodopsins had begun to be discovered from various microorganisms. After a long delay, two $Cl^-$-pump groups were discovered (Yoshizawa et al. 2014; Hasemi et al. 2016). Currently, $Cl^-$ pumps are recognized to widely exist in the microbial world. Their wide presence suggests their physiological significance, which should be clarified in future investigations.

Regarding the $Cl^-$-pump mechanism, many aspects have been clarified, especially for NpHR. Now, we can imagine the $Cl^-$-transport processes based on intermediate structures (Kouyama et al. 2015). Moreover, novel $Cl^-$ pumps have unique features. MrHR only pumps smaller halide ions, $Cl^-$ and $Br^-$, despite a motif similar to that of HR (Hasemi et al. 2016). On the other hand, SyHR additionally pumps $SO_4^{2-}$, even though it cannot pump $I^-$ and $NO_3^-$ (Niho et al. 2017), which is similar to MrHR. The amino acid identity between MrHR and SyHR is 68%, indicating that only small differences in the residues probably confer the $SO_4^{2-}$ pump ability of SyHR. The understanding of these differences is an attractive issue, which might enable us to make a rhodopsin able to pump large anions that are physiologically important. This development might induce a new trend in optogenetics. Moreover, experimental results suggested that MrHR evolved from a BR-type $H^+$ pump, but it is not as fully developed as HR. Thus, comparative studies of three rhodopsins, MrHR, HR, and BR, might provide insights into how sophisticated $Cl^-$ pumps evolved from $H^+$ pumps. The other $Cl^-$ pump group, NTQ rhodopsins, is also unique. This group is phylogenetically distant from HR and MrHR and obviously close to $Na^+$-pump rhodopsins (Fig. 4.1). Thus, nature developed

completely different mechanisms to pump $Cl^-$ using almost the same framework. The detailed analyses of novel $Cl^-$ pumps, in particular the $Cl^-$-transport pathways, structures of intermediates, and elementary processes during the intermediate transitions, will be necessary to understand the minimum requirements for the light-driven anion pump functions.

**Acknowledgments** The author thanks the collaborators and the financial supports from JSPS KAKENHI (17K07326, 26440042, 23510251, 19614001) and the Global Station for Soft Matter, a project of the Global Institution for Collaborative Research and Education at Hokkaido University.

## References

Balashov SP (2000) Protonation reactions and their coupling in bacteriorhodopsin. Biochim Biophys Acta 1460(1):75–94

Balashov SP, Govindjee R, Kono M, Imasheva E, Lukashev E, Ebrey TG, Crouch RK, Menick DR, Feng Y (1993) Effect of the arginine-82 to alanine mutation in bacteriorhodopsin on dark adaptation, proton release, and the photochemical cycle. Biochemistry 32(39):10331–10343

Bamberg E, Hegemann P, Oesteriielt D (1984) Reconstitution of the light-driven electrogenic ion pump halorhodopsin in black lipid membranes. Biochim Biophys Acta 773(1):53–60

Bieszke JA, Braun EL, Bean LE, Kang S, Natvig DO, Borkovich KA (1999) The *nop-1* gene of *Neurospora crassa* encodes a seven transmembrane helix retinal-binding protein homologous to archaeal rhodopsins. Proc Natl Acad Sci U S A 96(14):8034

Blatz PE, Mohler JH, Navangul HV (1972) Anion-induced wavelength regulation of absorption maxima of Schiff bases of retinal. Biochemistry 11(5):848–855. https://doi.org/10.1021/bi00755a026

Chen XR, Huang YC, Yi HP, Yang CS (2016) A unique light-driven proton transportation signal in Halorhodopsin from *Natronomonas pharaonis*. Biophys J 111(12):2600–2607. https://doi.org/10.1016/j.bpj.2016.11.003

Chizhov I, Chernavskii DS, Engelhard M, Mueller KH, Zubov BV, Hess B (1996) Spectrally silent transitions in the bacteriorhodopsin photocycle. Biophys J 71 (5):2329–2345

Duschl A, Lanyi JK, Zimányi L (1990) Properties and photochemistry of a halorhodopsin from the haloalkalophile, *Natronobacterium pharaonis*. J Biol Chem 265(3):1261–1267

Ernst OP, Lodowski DT, Elstner M, Hegemann P, Brown LS, Kandori H (2014) Microbial and animal rhodopsins: structures, functions, and molecular mechanisms. Chem Rev 114(1):126–163. https://doi.org/10.1021/cr4003769

Facciotti MT, Cheung VS, Nguyen D, Rouhani S, Glaeser RM (2003) Crystal structure of the bromide-bound D85S mutant of bacteriorhodopsin: principles of ion pumping. Biophys J 85(1):451–458. https://doi.org/10.1016/s0006-3495(03)74490-7

Feroz H, Ferlez B, Lefoulon C, Ren T, Baker CS, Gajewski JP, Lugar DJ, Gaudana SB, Butler PJ, Huhn J, Lamping M, Parak WJ, Hibberd JM, Kerfeld CA, Smirnoff N, Blatt MR, Golbeck JH, Kumar M (2018) Light-driven chloride transport kinetics of Halorhodopsin. Biophys J 115(2):353–360. https://doi.org/10.1016/j.bpj.2018.06.009

Govorunova EG, Sineshchekov OA, Li H, Spudich JL (2017) Microbial rhodopsins: diversity, mechanisms, and optogenetic applications. Annu Rev Biochem 86:845–872. https://doi.org/10.1146/annurev-biochem-101910-144233

Guijarro J, Engelhard M, Siebert F (2006) Anion uptake in halorhodopsin from *Natromonas pharaonis* studied by FTIR spectroscopy: consequences for the anion transport mechanism. Biochemistry 45(38):11578–11588

Harris A, Saita M, Resler T, Hughes-Visentin A, Maia R, Pranga-Sellnau F, Bondar AN, Heberle J, Brown LS (2017) Molecular details of the unique mechanism of chloride transport by a cyanobacterial rhodopsin. Phys Chem Chem Phys 20:3184–3199. https://doi.org/10.1039/c7cp06068h

Hasegawa C, Kikukawa T, Miyauchi S, Seki A, Sudo Y, Kubo M, Demura M, Kamo N (2007) Interaction of the halobacterial transducer to a halorhodopsin mutant engineered so as to bind the transducer: $Cl^-$ circulation within the extracellular channel. Photochem Photobiol 83(2):293–302. https://doi.org/10.1562/2006-06-09-RA-916

Hasemi T, Kikukawa T, Kamo N, Demura M (2016) Characterization of a cyanobacterial chloride-pumping rhodopsin and its conversion into a proton pump. J Biol Chem 291(1):355–362. https://doi.org/10.1074/jbc.M115.688614

Hasemi T, Kikukawa T, Watanabe Y, Aizawa T, Miyauchi S, Kamo N, Demura M (2019) Photochemical study of a cyanobacterial chloride-ion pumping rhodopsin. Biochim Biophys Acta Bioenerg 1860 (2):136–146. https://doi.org/10.1016/j.bbabio.2018.12.001

Havelka WA, Henderson R, Oesterhelt D (1995) Three-dimensional structure of halorhodopsin at 7 Å resolution. J Mol Biol 247(4):726–738

Hazemoto N, Kamo N, Kobatake Y, Tsuda M, Terayama Y (1984) Effect of salt on photocycle and ion-pumping of halorhodopsin and third rhodopsinlike pigment of *Halobacterium halobium*. Biophys J 45 (6):1073–1077. https://doi.org/10.1016/s0006-3495(84)84254-x

Hosaka T, Yoshizawa S, Nakajima Y, Ohsawa N, Hato M, DeLong EF, Kogure K, Yokoyama S, Kimura-

Someya T, Iwasaki W, Shirouzu M (2016) Structural mechanism for light-driven transport by a new type of chloride ion pump, *Nonlabens marinus* Rhodopsin-3. J Biol Chem 291(34):17488–17495. https://doi.org/10.1074/jbc.M116.728220

Inoue K, Kubo M, Demura M, Kamo N, Terazima M (2009) Reaction dynamics of halorhodopsin studied by time-resolved diffusion. Biophys J 96 (9):3724–3734

Inoue K, Ono H, Abe-Yoshizumi R, Yoshizawa S, Ito H, Kogure K, Kandori H (2013) A light-driven sodium ion pump in marine bacteria. Nat Commun 4:1678. https://doi.org/10.1038/ncomms2689

Inoue K, Kato Y, Kandori H (2014a) Light-driven ion-translocating rhodopsins in marine bacteria. Trends Microbiol 23:91–98. https://doi.org/10.1016/j.tim.2014.10.009

Inoue K, Koua FH, Kato Y, Abe-Yoshizumi R, Kandori H (2014b) Spectroscopic study of a light-driven chloride ion pump from marine bacteria. J Phys Chem B 118 (38):11190–11199. https://doi.org/10.1021/jp507219q

Inoue K, Nomura Y, Kandori H (2016) Asymmetric functional conversion of eubacterial light-driven ion pumps. J Biol Chem 291(19):9883–9893. https://doi.org/10.1074/jbc.M116.716498

Kanada S, Takeguchi Y, Murakami M, Ihara K, Kouyama T (2011) Crystal structures of an O-like blue form and an anion-free yellow form of *pharaonis* halorhodopsin. J Mol Biol 413(1):162–176

Kandori H (2015) Ion-pumping microbial rhodopsins. Front Mol Biosci 2:52. https://doi.org/10.3389/fmolb.2015.00052

Kikukawa T, Kusakabe C, Kokubo A, Tsukamoto T, Kamiya M, Aizawa T, Ihara K, Kamo N, Demura M (2015) Probing the $Cl^-$-pumping photocycle of *pharaonis* halorhodopsin: examinations with bacterioruberin, an intrinsic dye, and membrane potential-induced modulation of the photocycle. Biochim Biophys Acta Bioenerg 1847(8):748–758. https://doi.org/10.1016/j.bbabio.2015.05.002

Kim K, Kwon SK, Jun SH, Cha JS, Kim H, Lee W, Kim JF, Cho HS (2016) Crystal structure and functional characterization of a light-driven chloride pump having an NTQ motif. Nat Commun 7:12677. https://doi.org/10.1038/ncomms12677

Kouyama T, Kawaguchi H, Nakanishi T, Kubo H, Murakami M (2015) Crystal structures of the L1, L2, N, and O states of *pharaonis* halorhodopsin. Biophys J 108(11):2680–2690. https://doi.org/10.1016/j.bpj.2015.04.027

Kouyama T, Ihara K, Maki K, Chan SK (2018) Three-step isomerization of the retinal chromophore during the anion pumping cycle of Halorhodopsin. Biochemistry 57(41):6013–6026. https://doi.org/10.1021/acs.biochem.8b00631

Kubo M, Kikukawa T, Miyauchi S, Seki A, Kamiya M, Aizawa T, Kawano K, Kamo N, Demura M (2009) Role of Arg123 in light-driven anion pump mechanisms of *pharaonis* halorhodopsin. Photochem Photobiol 85(2):547–555

Lanyi JK (2004) Bacteriorhodopsin. Annu Rev Physiol 66:665–688

Ludmann K, Ibron G, Lanyi JK, Váró G (2000) Charge motions during the photocycle of *pharaonis* halorhodopsin. Biophys J 78(2):959–966

Matsuno-Yagi A, Mukohata Y (1977) Two possible roles of bacteriorhodopsin; a comparative study of strains of *Halobacterium halobium* differing in pigmentation. Biochem Biophys Res Commun 78(1):237–243

Matsuno-Yagi A, Mukohata Y (1980) ATP synthesis linked to light-dependent proton uptake in a red mutant strain of *Halobacterium* lacking bacteriorhodopsin. Arch Biochem Biophys 199(1):297–303

Mevorat-Kaplan K, Brumfeld V, Engelhard M, Sheves M (2006) The protonated Schiff base of halorhodopsin from *Natronobacterium pharaonis* is hydrolyzed at elevated temperatures. Photochem Photobiol 82 (6):1414–1421

Mukohata Y, Kaji Y (1981) Light-induced membrane-potential increase, ATP synthesis, and proton uptake in *Halobacterium halobium* $R_1$mR catalyzed by halorhodopsin: effects of *N, N′*-dicyclohexylcarbodiimide, triphenyltin chloride, and 3, 5-di-*tert*-butyl-4-hydroxybenzylidenemalononitrile (SF6847). Arch Biochem Biophys 206(1):72–76

Muneyuki E, Shibazaki C, Ohtani H, Okuno D, Asaumi M, Mogi T (1999) Time-resolved measurements of photovoltage generation by bacteriorhodopsin and halorhodopsin adsorbed on a thin polymer film. J Biochem 125(2):270–276

Muroda K, Nakashima K, Shibata M, Demura M, Kandori H (2012) Protein-bound water as the determinant of asymmetric functional conversion between light-driven proton and chloride pumps. Biochemistry 51:4677–4684

Niho A, Yoshizawa S, Tsukamoto T, Kurihara M, Tahara S, Nakajima Y, Mizuno M, Kuramochi H, Tahara T, Mizutani Y, Sudo Y (2017) Demonstration of a light-driven $SO_4^{2-}$ transporter and its spectroscopic characteristics. J Am Chem Soc 139:4376–4389. https://doi.org/10.1021/jacs.6b12139

Oesterhelt D (1995) Structure and function of halorhodopsin. Isr J Chem 35(3–4):475–494

Rüdiger M, Oesterhelt D (1997) Specific arginine and threonine residues control anion binding and transport in the light-driven chloride pump halorhodopsin. EMBO J 16(13):3813–3821

Sasaki J, Brown LS, Chon YS, Kandori H, Maeda A, Needleman R, Lanyi JK (1995) Conversion of bacteriorhodopsin into a chloride ion pump. Science 269 (5220):73–75. https://doi.org/10.1126/science.7604281

Sato M, Kanamori T, Kamo N, Demura M, Nitta K (2002) Stopped-flow analysis on anion binding to blue-form halorhodopsin from *Natronobacterium pharaonis*: comparison with the anion-uptake process during the photocycle. Biochemistry 41(7):2452–2458

Sato M, Kikukawa T, Araiso T, Okita H, Shimono K, Kamo N, Demura M, Nitta K (2003) Roles of Ser130 and Thr126 in chloride binding and photocycle of *pharaonis* halorhodopsin. J Biochem 134(1):151–158

Sato M, Kubo M, Aizawa T, Kamo N, Kikukawa T, Nitta K, Demura M (2005) Role of putative anion-binding sites in cytoplasmic and extracellular channels of *Natronomonas pharaonis* halorhodopsin. Biochemistry 44(12):4775–4784

Scharf B, Engelhard M (1994) Blue halorhodopsin from *Natronobacterium pharaonis*: wavelength regulation by anions. Biochemistry 33(21):6387–6393

Schobert B, Lanyi JK (1982) Halorhodopsin is a light-driven chloride pump. J Biol Chem 257 (17):10306–10313

Seki A, Miyauchi S, Hayashi S, Kikukawa T, Kubo M, Demura M, Ganapathy V, Kamo N (2007) Heterologous expression of *pharaonis* halorhodopsin in *Xenopus laevis* oocytes and electrophysiological characterization of its light-driven $Cl^-$ pump activity. Biophys J 92(7):2559–2569. https://doi.org/10.1529/biophysj.106.093153

Shibasaki K, Shigemura H, Kikukawa T, Kamiya M, Aizawa T, Kawano K, Kamo N, Demura M (2013) Role of Thr218 in the light-driven anion pump halorhodopsin from *Natronomonas pharaonis*. Biochemistry 52(51):9257–9268. https://doi.org/10.1021/bi401295e

Shibata M, Muneda N, Sasaki T, Shimono K, Kamo N, Demura M, Kandori H (2005) Hydrogen-bonding alterations of the protonated Schiff base and water molecule in the chloride pump of *Natronobacterium pharaonis*. Biochemistry 44(37):12279–12286. https://doi.org/10.1021/bi050726d

Tamogami J, Kikukawa T, Miyauchi S, Muneyuki E, Kamo N (2009) A tin oxide transparent electrode provides the means for rapid time-resolved pH measurements: application to photoinduced proton transfer of bacteriorhodopsin and proteorhodopsin. Photochem Photobiol 85(2):578–589. https://doi.org/10.1111/j.1751-1097.2008.00520.x

Tittor J, Haupts U, Haupts C, Oesterhelt D, Becker A, Bamberg E (1997) Chloride and proton transport in bacteriorhodopsin mutant D85T: different modes of ion translocation in a retinal protein. J Mol Biol 271 (3):405–416. https://doi.org/10.1006/jmbi.1997.1204

Tsukamoto T, Yoshizawa S, Kikukawa T, Demura M, Sudo Y (2017) Implications for the light-driven chloride ion transport mechanism of *Nonlabens marinus* rhodopsin 3 by its photochemical characteristics. J Phys Chem B 121(9):2027–2038. https://doi.org/10.1021/acs.jpcb.6b11101

Váró G, Brown LS, Sasaki J, Kandori H, Maeda A, Needleman R, Lanyi JK (1995a) Light-driven chloride ion transport by halorhodopsin from *Natronobacterium pharaonis*. I. The photochemical cycle. Biochemistry 34(44):14490–14499

Váró G, Needleman R, Lanyi JK (1995b) Light-driven chloride ion transport by halorhodopsin from *Natronobacterium pharaonis*. II. Chloride release and uptake, protein conformation change, and thermodynamics. Biochemistry 34(44):14500–14507

Váró G, Zimányi L, Fan X, Sun L, Needleman R, Lanyi JK (1995c) Photocycle of halorhodopsin from *Halobacterium salinarium*. Biophys J 68 (5):2062–2072

Váró G, Brown LS, Needleman R, Lanyi JK (1996) Proton transport by halorhodopsin. Biochemistry 35 (21):6604–6611. https://doi.org/10.1021/bi9601159

Walter TJ, Braiman MS (1994) Anion-protein interactions during halorhodopsin pumping: halide binding at the protonated Schiff base. Biochemistry 33 (7):1724–1733. https://doi.org/10.1021/bi00173a015

Yoshizawa S, Kumagai Y, Kim H, Ogura Y, Hayashi T, Iwasaki W, DeLong EF, Kogure K (2014) Functional characterization of flavobacteria rhodopsins reveals a unique class of light-driven chloride pump in bacteria. Proc Natl Acad Sci U S A 111(18):6732–6737. https://doi.org/10.1073/pnas.1403051111

# Optogenetic Modulation of Ion Channels by Photoreceptive Proteins

5

Hisao Tsukamoto and Yuji Furutani

**Abstract**

In these 15 years, researches to control cellular responses by light have flourished dramatically to establish "optogenetics" as a research field. In particular, light-dependent excitation/inhibition of neural cells using channelrhodopsins or other microbial rhodopsins is the most powerful and the most widely used optogenetic technique. New channelrhodopsin-based optogenetic tools having favorable characteristics have been identified from a wide variety of organisms or created through mutagenesis. Despite the great efforts, some neuronal activities are still hard to be manipulated by the channelrhodopsin-based tools, indicating that complementary approaches are needed to make optogenetics more comprehensive. One of the feasible and complementary approaches is optical control of ion channels using photoreceptive proteins other than channelrhodopsins. In particular, animal opsins can modulate various ion channels via light-dependent G protein activation. In this chapter, we summarize how such alternative optogenetic tools work and they will be improved.

**Keywords**

G protein-coupled receptor · Ion channel · Membrane protein · Opsin · Optogenetics · Rhodopsin

## Abbreviations

| | |
|---|---|
| $Ca_v$ | Voltage-sensitive $Ca^{2+}$ channel |
| ChR | Channelrhodopsin |
| GIRK | G protein-gated inwardly rectifying $K^+$ channel |
| GPCR | G protein-coupled receptor |
| PAC | Photo-activated adenylyl cyclase |

## 5.1 Introduction

Since channelrhodopsins (ChRs) were identified as light-gated cation channels in 2002–2003 (Nagel et al. 2002, 2003) and photo-induced

H. Tsukamoto (✉)
Department of Life and Coordination-Complex Molecular Science, Institute for Molecular Science, Okazaki, Japan

Japan Science and Technology Agency (JST), Precursory Research for Embryonic Science and Technology (PRESTO), Kawaguchi, Japan

Department of Biology, Kobe University, Kobe, Japan
e-mail: tsukamoh@people.kobe-u.ac.jp

Y. Furutani
Department of Life and Coordination-Complex Molecular Science, Institute for Molecular Science, Okazaki, Japan

Department of Life Science and Applied Chemistry, Nagoya Institute of Technology, Nagoya, Japan
e-mail: furutani.yuji@nitech.ac.jp



H. Yawo et al. (eds.), *Optogenetics*, Advances in Experimental Medicine and Biology 1293,
https://doi.org/10.1007/978-981-15-8763-4_5

excitation of neural cells through ChR2 was achieved in 2005 (Boyden et al. 2005), optogenetics has dramatically progressed day by day. Many factors contribute to the rapid progress, and one major factor is finding and making of variants of ChRs as well as other microbial rhodopsins having different molecular characteristics such as absorption spectrum, ion selectivity, on/off kinetics, and so on (Yizhar et al. 2011). By using the ChR-based optogenetic tools, researchers can manipulate a wide variety of cellular activities by light. However, some neuronal activities are still hard to be regulated by ChRs, and thus complementary techniques are needed. Actually, many optogenetic tools using other photoreceptive proteins have provided alternative techniques (Paoletti et al. 2019; Wiegert et al. 2017; Yizhar et al. 2011). In this chapter, we introduce these alternative optogenetic tools and discuss their advantages as well as disadvantages. In particular, our main focus is ion channel modulation by animal opsins to regulate activities of neurons and other tissues.

## 5.2 Channelrhodopsins: Great Functionalities and Limitations to be Overcome

Because molecular characteristics and usefulness of ChRs are thoroughly reviewed in other chapters, we here briefly discuss neuronal activities that ChRs can or cannot modulate. ChR2 and other cation-selective ChRs are basically non-selective cation channels and preferably conduct small cations (Nagel et al. 2002, 2003). In particular, proton ($H^+$) permeability is the highest in some cation-selective ChRs due to its small size and the conduction through hydrogen-bonding networks, but under physiological condition (at neutral pH; $[H^+] \approx 10^{-7}$ M, and at $[Na^+]_{out} \approx 10^{-1}$ M), the ChRs dominantly conduct $Na^+$ leading to depolarization of the target cells. Also, the high proton permeability in ChR2 was utilized to manipulate intracellular acidification in glial cells (Beppu et al. 2014). On the other hand, $Ca^{2+}$ permeability in ChRs is relatively low (but detectable), and optical control of Ca signalings by ChRs would be difficult. Despite of this difficulty, in some cases, $Ca^{2+}$ inflow was successfully regulated in a light-dependent manner using ChR2 or its derivatives (Asano et al. 2018; Figueiredo et al. 2014; Perea et al. 2014). Of course, efforts to improve ion selectivity of ChRs are in progress (Cho et al. 2019).

Regarding anion-conducting inhibitory ChRs such as GtACR (Govorunova et al. 2015) and iChloC (Wietek et al. 2015), light-induced opening of the channels leads to hyperpolarization by $Cl^-$ inflow or "shunt" effect caused by increase of $Cl^-$ conductance (Wiegert et al. 2017). The inhibitory effect of the anion-conducting ChRs is much more effective than $H^+$ or $Cl^-$ pumping microbial rhodopsins due to higher ion conductance. On the other hand, in some cells such as premature neurons (Kaila et al. 2014), olfactory sensory neurons (Kaneko et al. 2004), and rod bipolar cells (Satoh et al. 2001), intracellular $Cl^-$ concentration is substantially high (typically more than 20–25 mM), and the anion channel opening induces depolarization (excitation) by $Cl^-$ outflow (Arosio and Ratto 2014). Furthermore, in axons, light activation of anion-conducting ChRs stimulates (not suppresses) presynaptic activities probably due to locally high $Cl^-$ concentration (Mahn et al. 2016; Wiegert et al. 2017). Unlike the case of $Cl^-$, intracellular $K^+$ concentration is universally so high that $K^+$ channel opening should suppress neural activities in any cells via hyperpolarization. Thus, extensive "gene mining" or rational design in order to find/make ChRs selectively conducting $K^+$ is challenged all over the world. Notably, a mutant of $Na^+$ pumping rhodopsin (KR2) acts as light-activated $K^+$-selective channel, but unfortunately, the mutant works only at non-physiological alkaline pH (~10) (Vogt et al. 2019). Additional mutations would be required for making the KR2 mutant functional at neutral pH.

Taken together, a wide variety of ChRs can excite or inhibit neural cells efficiently, but they are not very good at manipulating $K^+$ or $Ca^{2+}$ currents. Modulation of resident $K^+$ or $Ca^{2+}$ selective channels is an alternative way to manipulate $K^+$- or $Ca^{2+}$-dependent cellular activities. In comparison with ChRs, modulation of ion channels

by an animal opsin or another photoreceptive protein is a less direct way to control cellular excitability, and thus the light-induced cellular responses need to be carefully interpreted. On the other hand, careful studies using such indirect tools would make optogenetics more comprehensive. We thus introduce optogenetic tools based on animal opsins or other photoreceptive proteins, and discuss how they can regulate $K^+$-, $Ca^{2+}$-, or other channels. In Table 5.1, we summarize (potential) optogenetic tools mentioned in this chapter.

## 5.3 Animal Opsins as Modulator of Ion Channels via Trimeric G Proteins

Animal opsin is light-sensitive G protein-coupled receptor (GPCR), and trimeric G proteins can modulate various ion channels including $K^+$/$Ca^{2+}$ channels directly or indirectly. Thus, animal opsins would be good alternative tools to regulate excitable cells by light, especially by a light-dependent modulation of $K^+$ or $Ca^{2+}$ current through trimeric G proteins. In this section, we introduce how the opsins work and discuss their abilities and potentials to modulate ion channels.

### 5.3.1 Binding Ability and Photo-Convertibility of Chromophore in "Vertebrate-Type" and "Invertebrate-Type" Opsins

Success of ChR-based optogenetics proved that the chromophore molecule retinal, the aldehyde form of vitamin A (Fig. 5.1), is present in mammalian neurons (Deisseroth 2011). ChRs act as fine optogenetic tools in various cells without addition of the retinal, and animal opsins also use retinal as chromophore. So, it is a natural idea to utilize animal opsin as an alternative optogenetic tool, but there are some concerns.

Animal opsin uses different retinal isomers from ChR (and other microbial rhodopsin). In ChRs, all-*trans* to 13-*cis* photoisomerization of the retinal (Fig. 5.1) leads channel opening (Hegemann et al. 1991; Lawson et al. 1991). In animal opsins, G protein activation is triggered by 11-*cis* to all-*trans* isomerization (Figs. 5.1 and 5.2) (Shichida and Imai 1998; Terakita 2005; Wald 1968). In retina, a specific enzymatic system named "visual cycle" works to provide 11-*cis*-retinal from normal (all-*trans*) retinoids (Wang and Kefalov 2011; Yau and Hardie 2009), but other tissues lack the system. When "Opto-XR" (see Sect. 5.3.3) was reported to function in the mammalian brain (Airan et al. 2009), researchers of animal opsin were surprised by the fact that exogenous *cis*-retinal is not necessary. This is because the "Opto-XR" is a derivative of vertebrate visual pigment, and the visual pigment can directly bind 11- (or 9-) *cis*-retinal only (Fig. 5.2a) (Jager et al. 1996; Tsukamoto and Terakita 2010). One possibility is that 9-*cis*-retinal (Fig. 5.1) is present in the brain, because tiny amounts of the visual pigment binds to 9-*cis*-retinal in retina of mice lacking an essential enzyme (RPE65) producing 11-*cis*-retinal (Fan et al. 2003, 2005). Current general consensus is substantial amounts of *cis*-retinal endogenously exists at least in the mammalian brain (Deisseroth 2011; Wiegert et al. 2017), but it may not be the case in some other tissues.

On the other hand, invertebrate opsins possess different molecular properties from vertebrate visual pigments (Hubbard and St George 1958; Terakita 2005, 2010; Tsukamoto and Terakita 2010; Yau and Hardie 2009). Regarding direct binding of retinal isomers, some (maybe not all) of invertebrate opsins can bind exogenous all-*trans*-retinal (Koutalos et al. 1989; Tsukamoto et al. 2017, 2005), and all-*trans*-retinal-bound (active) and 11-*cis*-retinal-bound (inactive) forms are interconvertible by light absorption (Fig. 5.2b). The opsins with these properties in invertebrates (and vertebrates) are called as "bistable" opsins (Koyanagi et al. 2004; Tsukamoto and Terakita 2010). As a typical example of invertebrate (bistable) opsin, we show the data of cOpsin1 from marine ragworm *Platynereis dumerilii* (Fig. 5.2c, d, e). The opsin shows bidirectional photoreactions upon illumination with different colors of light (Fig. 5.2c)

**Table 5.1** Molecular properties of photoreceptive proteins to modulate $K^+$ or $Ca^{2+}$ channels

| Photoreceptive protein | G protein(s) | Effector channel | Activation | $\tau_{ON}$ | Deactivation | $\tau_{OFF}$ | Tested cell | References |
|---|---|---|---|---|---|---|---|---|
| *Animal opsin* | | | | | | | | |
| Vertebrate rhodopsin | $G_{i/o}$ | GIRK | Green | s | Light off | s | HEK293 | Li et al. (2005) |
| | | | | | | | | Masseck et al. (2014) |
| | $G_{i/o}$ | $Ca_v2$ | Green | s | Light off | s | HEK293 | Li et al. (2005) |
| Vertebrate SWS-opsin | $G_{i/o}$ | GIRK | Blue | s | Light off | s | HEK293 | Masseck et al. (2014) |
| Vertebrate LWS-opsin | $G_{i/o}$ | GIRK | Orange | s | Light off | s | HEK293 | Masseck et al. (2014) |
| *Platynereis* cOpsin1 | $G_{i/o}$ | GIRK | UV | s | Yellow | s | *Xenopus* oocyte | Tsukamoto et al. (2017) |
| Lamprey parapinopsin | $G_{i/o}$ | GIRK | UV | <s | Blue | s | HEK293 | Eickelbeck et al. (2020) |
| Vertebrate rhodopsin | Independent | Kir6.2 | White | s | Light off | >min | *Xenopus* oocyte | Caro et al. (2012) |
| Jellyfish opsin | $G_s$ | $Ca_v1$ | Blue | s | Light off | min | Cardiomyocyte | Makowka et al. (2019) |
| Human/mouse melanopsin | $G_q$, $G_{i/o}$, ($G_s$?) | GIRK | Blue | <s | Green | s | HEK293 | Spoida et al. (2016) |
| | | HCN2 | Blue | s | Light off | s | Retinal ganglion cell | Jiang et al. (2018) |
| *Flavin-based photoreceptive protein* | | | | | | | | |
| LOV2 (in BLINK1) | Independent | Kcv | Blue | s | Light off | min | *Xenopus* oocyte | Cosentino et al. (2015) |
| LOV2 (in OptoRGK) | Independent | $Ca_v1$ | Blue | s | Light off | min | HEK293 | Ma et al. (2018) |
| PAC | Independent | SthK | Blue | s | Light off | min | *Xenopus* oocyte | Beck et al. (2018) |
| | | | Blue | s | Light off | min | HEK293 | Bernal Sierra et al. (2018) |

Note that experimental conditions such as light intensities are quite different between studies

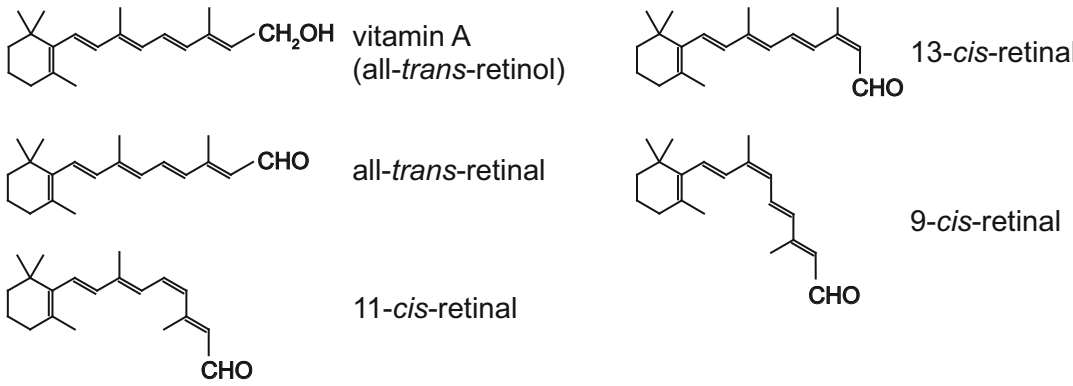


**Fig. 5.1** Chemical structures of the retinal isomers. When the retinal isomers bind to opsins, the Schiff base linkage is formed between the aldehyde group and a specific lysine residue in the opsin

and possesses direct binding ability for not only 11-*cis*- but also all-*trans*- retinal isomers (Fig. 5.2d). Furthermore, the bidirectional photoisomerization of retinal between 11-*cis* and all-*trans* isomers accompanies with reversible structural changes, which was demonstrated by light-induced difference FTIR spectroscopy for *Platynereis* cOpsin1 (Fig. 5.2e) and jumping spider Rh1 (Ehrenberg et al. 2019). The light-induced reversible changes in the protein conformation were successfully monitored by the amide I modes (1665, 1650, 1642, and 1631 $cm^{-1}$ in Fig. 5.2e, and also see (Ehrenberg et al. 2019)). The properties of invertebrate opsins as the ON–OFF photo-switch for G protein activation (Fig. 5.2b) were also confirmed by various techniques (Ashida et al. 2004; Emanuel and Do 2015; Kawano-Yamashita et al. 2015; Spoida et al. 2016; Stavenga and Schwemer 1984; Tsukamoto et al. 2017, 2005). Therefore, these invertebrate opsins can function where ChRs can work with endogenous all-*trans*-retinal. Interestingly, in vertebrates, some opsins function in various cells other than visual photoreceptor cells, and these "non-visual" opsins show similar retinal binding ability and bidirectional photoreactions to invertebrate opsins rather than to vertebrate visual pigments (Matsuyama et al. 2012; Panda et al. 2005; Yamashita et al. 2010). For clarity, we hereafter describe invertebrate opsin and vertebrate non-visual opsin having bistable properties as "invertebrate-type" opsin, and use "vertebrate-type" opsin only for vertebrate visual pigments (rod and cone pigments) (see Fig. 5.2a, b).

### 5.3.2 Ion Channel Modulation via $G_{i/o}$-Coupled Animal Opsins

In rod and cone photoreceptor cells, "vertebrate-type" opsins are coupled with transducin (Kefalov 2012; Yau and Hardie 2009), eye-specific $G_{i/o}$-type trimeric G protein, and they can activate $G_{i/o}$ when reconstituted (Kanaho et al. 1984; Terakita et al. 2002). Classically, invertebrates were thought to possess only $G_q$-coupled opsins, but $G_{i/o}$-coupled "invertebrate-type" opsins have been identified (Arendt et al. 2004; Koyanagi et al. 2013). As optogenetic tools, these $G_{i/o}$-coupled opsins would regulate cellular activities via $G_{i/o}$ activation, whereas arrestin signalings could also be driven by them (Spangler and Bruchas 2017).

The most major response upon $G_{i/o}$ activation is inhibition of adenylyl cyclase by $G_{i/o}\alpha$ (Taussig et al. 1994). In fact, intracellular cAMP concentrations can be suppressed by light activation of "vertebrate-type" opsins (Koyanagi et al. 2013). Furthermore, "invertebrate-type" opsins

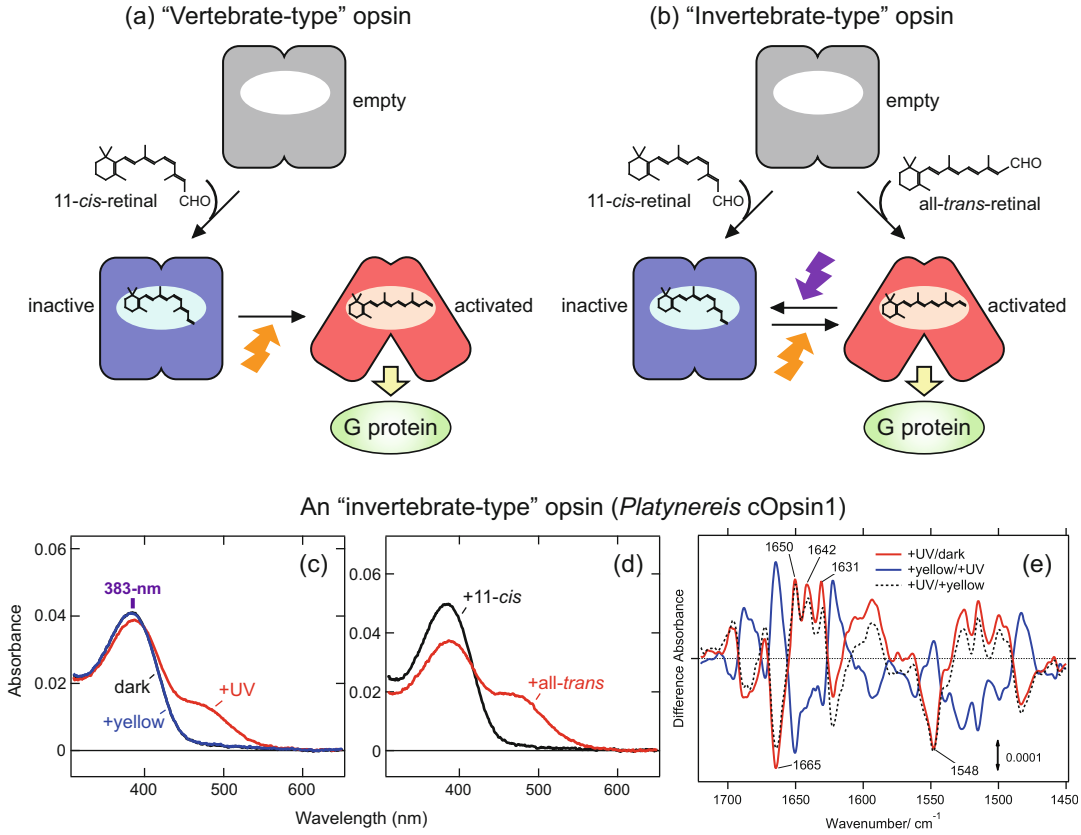


**Fig. 5.2** Binding ability for the retinal isomers and photoactivation scheme of animal opsins. (**a**) Retinal binding and activation scheme of “vertebrate-type” opsins. As mentioned in the main text, “vertebrate-type” opsins selectively bind 11- (or 9-) *cis*-retinal, and the photoactivation is irreversible. (**b**) Retinal binding and activation scheme of “invertebrate-type” (bistable) opsins. Unlike “vertebrate-type” opsins, “invertebrate-type” opsins can bind all-*trans*-retinal directly, and the photoactivation is reversible. A typical example of “invertebrate-type” opsin (cOpsin1 from marine ragworm *Platynereis dumerilii* (Tsukamoto et al. 2017)). (**c**) Absorption spectra of the “invertebrate-type” opsin. The opsin is a UV-sensitive opsin (*black line*), and UV irradiation converts it to the activated form (*red line*). The photoreaction is reversed by irradiation of yellow light (*blue line*). (**d**) Absorption spectra of the “invertebrate-type” opsin directly bound to 11-*cis*-retinal (*black line*) or all-*trans*-retinal (*red line*), indicating that the opsin can bind both 11-*cis*- and all-*trans*-retinals directly. (**e**) Light-induced difference FTIR spectra of the “invertebrate-type” opsin. The spectrum plotted with a solid line is calculated by subtracting the spectrum recorded in dark from that recorded after UV irradiation (+*UV/dark*). The spectrum plotted with a gray line is calculated by subtracting the spectrum recorded after UV irradiation from that recorded after successive yellow-light irradiation (+*yellow/+UV*), which shows a mirror image of the first one. The reversible photoreaction is also confirmed by the spectrum collected in the second round of the UV irradiation (+*UV/+yellow*), which is almost identical to the first one. The bands which can be assigned to amide I (1665, 1650, 1642, and 1632 $cm^{-1}$) and amide II (1548 $cm^{-1}$) modes of protein are tagged

can decrease and increase (reverse) the cAMP levels by stimulation of different colors of lights via interconvertible photoreaction between inactive and active forms (Figs. 5.2 and 5.3) (Kawano-Yamashita et al. 2015; Koyanagi et al. 2013). However, since basal intracellular cAMP levels are usually low (nM order) (Binkowski et al. 2011; Violin et al. 2008), further decrease in cAMP concentrations by light might little affect activities of target cells.

Rather, a $K^+$ channel, GIRK (or Kir3), is a more promising target of optogenetics as well as

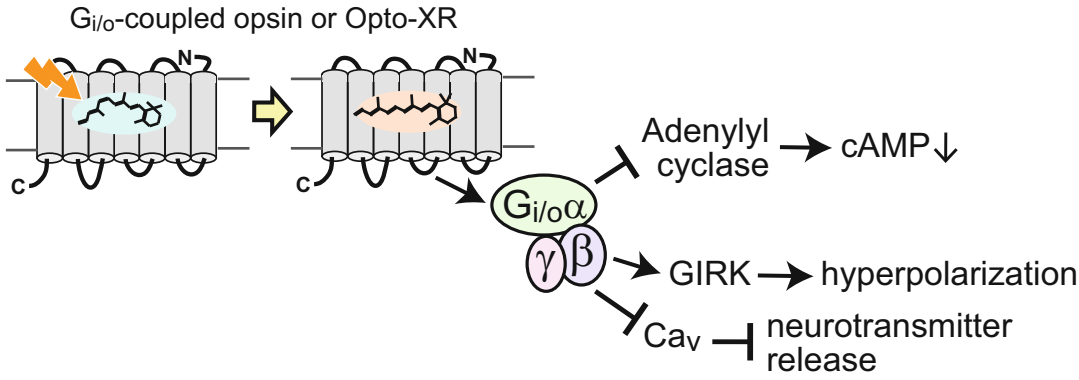


**Fig. 5.3** Typical signaling pathways driven by $G_{i/o}$-coupled opsins and Opto-XRs. The signaling pathways shown in Figs. 5.3, 5.4, and 5.6 would be oppositely modulated in a light-dependent manner when "OFF-type" opsin-based tools are used (see Sect. 5.3.6)

chemogenetics using $G_{i/o}$-coupled receptors (Roth 2016; Wiegert et al. 2017). GIRK is mainly localized in the postsynaptic membrane of various neurons and activated by βγ subunit of $G_{i/o}$ (Luscher and Slesinger 2010; Nagi and Pineyro 2014). Thus, light activation of $G_{i/o}$-coupled opsins expressed in a neuron would cause increase in $K^+$ outflow, leading to suppression of neuronal excitation (Fig. 5.3). In this way, $G_{i/o}$-coupled opsins act as inhibitory optogenetics tools. GIRK activation by GPCR is independent from effector enzymes and diffusible second messengers, and the activation is spatially localized "membrane delimited" process (Nagi and Pineyro 2014; Soejima and Noma 1984). Therefore, animal opsin-induced GIRK activation would be fast and applicable for optical control of subcellular compartments.

"Vertebrate-type" opsins have already been experimentally proved to work well as inhibitory tools in mammalian neurons (Gutierrez et al. 2011; Li et al. 2005). Among "vertebrate-type" opsins, cone pigments possess much faster off kinetics than rod pigments due to rapid inactivation via spontaneous release of all-*trans*-retinal and/or arrestin binding (Kefalov 2012; Shichida and Imai 1998). Also, cone pigments in various vertebrates show a wide variety of absorption spectra (Yokoyama 2008), indicating that researchers find some tools which can be activated by a specific color on demand. Masseck et al. showed that a rod pigment (rhodopsin) can modulate GIRK current with slow off kinetics, and two (SWS and LWS) cone pigments induce rapidly attenuated GIRK responses with different colors of light (Masseck et al. 2014). The cone pigments-induced GIRK current suppressed action potential firing in serotonergic neurons of mice (Masseck et al. 2014). In addition, these photo-responses can be repeated many times, indicating sufficient supply of *cis*-retinal.

"Invertebrate-type" opsins also can regulate GIRK activity. A UV-sensitive "invertebrate-type" opsin from marine ragworm can increase GIRK current by UV light, and the UV-induced $K^+$ current is canceled by visible light in *Xenopus* oocytes (Tsukamoto et al. 2017). Another UV-sensitive bistable opsin, lamprey parapinopsin (Koyanagi et al. 2004), can also induce ON–OFF cycle of GIRK current by UV and visible light in HEK293 cells (Eickelbeck et al. 2020). They have not been tested in neural cells but would be nice tools that can be turn on and off by different color stimulations.

Interestingly, one study showed that a $K^+$ channel can be directly activated by an animal opsin itself. Caro et al. reported that a fusion protein of bovine rhodopsin (rod pigment) followed by a $K^+$ channel Kir6.2 produces significant $K^+$ current in the dark, and light illumination

decreases the current, indicating that the rhodopsin activation suppresses the $K^+$ channel activity (Caro et al. 2012). Intriguingly, deletion of the G protein interaction site in the rhodopsin moiety has almost no effect on the light-dependent suppression of the channel activity, indicating that the channel regulation is independent form G proteins. This study concluded that in the fusion protein, light-induced conformational changes in rhodopsin directly induce closure in the Kir6.2 moiety. It is not clear if such a direct coupling of opsin and channel activities can occur in other combinations. Currently many crystal or cryo-EM structures of ion channels and GPCRs are available (Cheng 2018; Weis and Kobilka 2018), and activation processes of channels and opsins are also extensively studied using various biophysical techniques. These structural information with molecular docking simulations could find or predict another ion channel that can be directly regulated by some opsin.

In addition to GIRK, neuronal voltage-sensitive $Ca^{2+}$ channels (P/Q- and N- types, $Ca_v2$) are also modulated by $G_{i/o}$ (Catterall 2000; Dolphin 2003). The $Ca_v$ channels are localized in axon terminal, and negatively regulated by βγ subunit of $G_{i/o}$ leading to suppression of neurotransmitter release. As mentioned in Sect. 5.2, anion-conducting ChRs could not act as inhibitory tools in axon, but $G_{i/o}$-coupled opsins could function as effective axonal inhibitory tools (Fig. 5.3). Actually, a "vertebrate-type" opsin can suppress presynaptic neurotransmitter release in hippocampal neurons upon photo-stimulation (Li et al. 2005). Activation and inactivation of "invertebrate-type" opsins by different colors of light could be used as an "OFF–ON" switch for $Ca_v2$ channels in presynaptic regions.

### 5.3.3 Ion Channel Modulation via $G_s$-Coupled Opsins and Opto-XRs

Since vertebrate visual pigments are $G_{i/o}$-coupled, other G protein subtypes including $G_s$ cannot be modulated by intact them. However, $G_s$-coupled opsins have been identified from Cnidarians such as jellyfish (Koyanagi et al. 2008; Kozmik et al. 2008; Suga et al. 2008). In mammalian cultured cells expressing a jellyfish opsin, and photo-stimulation induces elevation of intracellular cAMP concentrations via adenylyl cyclase activation by $G_s\alpha$ (Bailes et al. 2017) (Fig. 5.4). Alternatively, chimeric receptors named "Opto-XRs" of vertebrate visual pigments and other GPCRs have overcome this limitation (Airan et al. 2009; Spangler and Bruchas 2017; Tichy et al. 2019). In this section, we describe architecture and functionality of Opto-XRs and how $G_s$-coupled opsins and Opto-XRs can modulate ion channels.

Even before the optogenetics era, it had been reported that G protein coupling specificity of animal opsins as well as other GPCRs can be changed by replacement of cytoplasmic regions that interact with G proteins (Kim et al. 2005; Liu et al. 1995; Terakita et al. 2002; Yamashita et al. 2000). "Opto-XRs" utilize this insight. In an Opto-XR, an animal opsin (typically vertebrate visual pigment) is an "acceptor," and an "XR" (target GPCR) is a "donor" providing

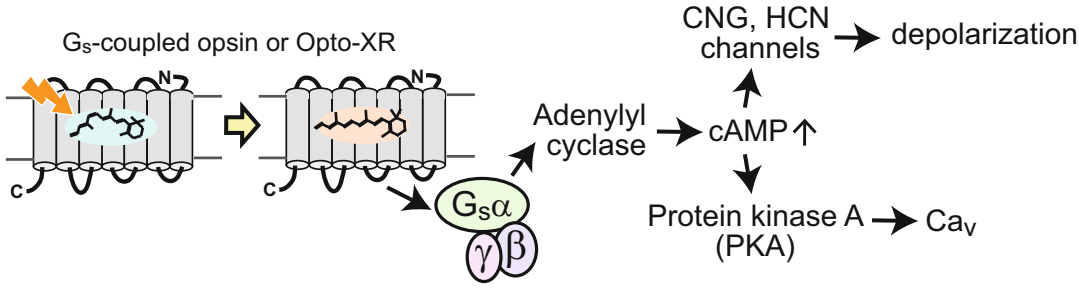


**Fig. 5.4** Typical signaling pathways driven by $G_s$-coupled opsins and Opto-XRs

cytoplasmic loops and C-terminus. In the constructed "Opto-XR," extracellular and transmembrane regions are from the "acceptor" opsin and G protein interaction sites are from the "donor" GPCR (Fig. 5.5) (Airan et al. 2009, Spangler and Bruchas 2017, Tichy et al. 2019). The Opto-XR can activate G proteins (and arrestins) that are coupled to the "donor" receptor in a light-dependent manner. The most widely used tool based on this approach is the Opto-$\beta_2$AR, in which cytoplasmic regions of $G_s$-coupled $\beta_2$-adrenergic receptor are introduced into $G_{i/o}$-coupled bovine (or other vertebrate) rhodopsin (rod opsin) (Airan et al. 2009; Siuda et al. 2015b). The Opto-$\beta_2$AR can drive $G_s$-dependent pathways, and successfully modulated activity of neural cells and animal behaviors by light stimulation (Airan et al. 2009, Siuda et al. 2015b), although it is less clear how the tool regulates neuronal activities.

Even $G_{i/o}$-coupled receptors are used as "donor" for Opto-XR (Siuda et al. 2015a). This is probably because replacement of $G_{i/o}$ interaction sites would improve fine-tuning of G protein coupling specificity (e.g., $G_i$ vs $G_o$, $G_{i1}$ vs $G_{i2}$), interactions with arrestins, and trafficking in target cells. However, conformational changes upon activation are somewhat different between GPCRs coupled to different G protein subtypes (Kang et al. 2018; Kato et al. 2019; Koehl et al. 2018; Rasmussen et al. 2011). Furthermore, there are some differences in the conformational changes even among $G_{i/o}$-coupled "vertebrate-type" and "invertebrate-type" opsins (Tsukamoto et al. 2009). Taken together, signaling characteristics of Opto-XRs may be somewhat different from those of the "donor" receptors (XRs), although basic properties in G protein activation can be successfully transferred into the "acceptor" opsins.

Regarding ion channel modulation by $G_s$-coupled opsins and Opto-XRs, CNG and HCN channels can be positively regulated by binding of cyclic nucleotides produced by adenylyl cyclase activated by $G_s\alpha$. Since CNG and HCN channels are non (or less) selective cation channels, opening of these channels by $G_s$-coupled opsins and Opto-XRs would cause depolarization of the target cells in a light-dependent manner (Fig. 5.4).

Another attractive target of the $G_s$-coupled opsin-based optogenetic tools is cardiac voltage-sensitive $Ca^{2+}$ channel (L-type, $Ca_v1$). In cardiomyocytes, adrenergic signals activate β-adrenergic receptors leading to increase of beating rate via potentiation of cardiac $Ca_v$ channels

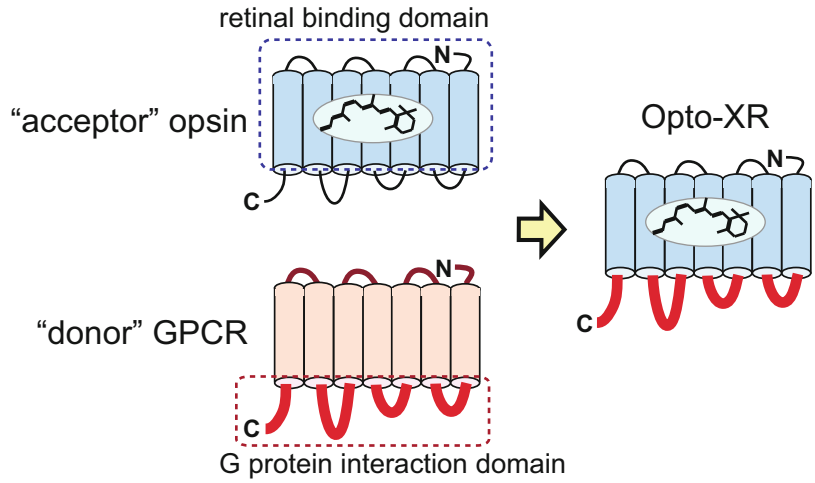


**Fig. 5.5** Molecular architecture of chimeric Opto-XRs. In Opto-XRs, animal opsin is an "acceptor" to provide extracellular and transmembrane domains (*blue*) for retinal binding and photoreception. Target GPCR is a "donor" to provide intracellular domain (*red*) to interact with and activate specific G proteins. See the main text in more detail

(Catterall 2000; Hagiwara et al. 1988). The signaling pathway between the receptor activation and the $Ca_v$ potentiation is activation of adenylyl cyclase by $G_s\alpha$ leading to elevation of cAMP levels which in turn stimulates the protein kinase A to phosphorylate the $Ca_v$ channels (Fig. 5.4). Thus, the $G_s$-coupled optogenetic tools are expected to regulate heartbeat in a light-dependent manner. Recently, a $G_s$-coupled jellyfish opsin was introduced into cardiomyocytes, and photo-stimulation successfully increased intracellular cAMP levels and contradiction rate in isolated cardiomyocytes (Makowka et al. 2019). Furthermore, activation of the jellyfish opsin can increase beating rate of explanted heart at the level comparable to stimulation of an adrenergic agonist (Makowka et al. 2019). This study beautifully proved usefulness of the $G_s$-coupled opsin as a powerful optogenetic tool.

### 5.3.4 Ion Channel Modulation via $G_q$-Coupled Opsins

"Opto-XR" approach can be applied to $G_q$-coupled receptors: introduction of cytoplasmic regions of $G_q$-coupled GPCRs enables "acceptor" opsin to interact with $G_q$ (Airan et al. 2009; Morri et al. 2018). It is known that opsins in eyes of invertebrates such as mollusks and insects are $G_q$-coupled (Koyanagi and Terakita 2008; Terakita 2005). Furthermore, even many vertebrates including mammals possess $G_q$-coupled opsins named as melanopsin (or Opn4), which functions in some of retinal ganglion cells to regulate circadian rhythms and pupil constriction (Do and Yau 2010; Do 2019). Mammalian melanopsins can be activated by blue light and inactivated by green light (Emanuel and Do 2015; Matsuyama et al. 2012; Spoida et al. 2016), and in the classification of this chapter, mammalian melanopsin is regarded as "invertebrate-type" opsin.

As optogenetic tools, $G_q$-coupled Opto-XRs and opsins are notable because $G_q$ activation leads to opening of $Ca^{2+}$ channels. The major pathway in this process is that $G_q\alpha$ activates phospholipase C (PLC) to produce signaling molecules (typically, $IP_3$ and diacylglycerol) that activate several $Ca^{2+}$ channels, such as $IP_3$ receptor and TRP channels (Fig. 5.6). Actually, Opto-$\alpha_1$AR, in which $G_q$-coupled $\alpha_{1a}$-aderenergic receptor is a "donor," has already been proved to activate some neurons in a light-dependent manner (Airan et al. 2009), and mammalian melanopsins also have been used as optogenetic tools to drive $G_q$-dependent signaling pathways.

Natively $G_q$-coupled mouse and human melanopsins produce sustained and transient $Ca^{2+}$ current by blue light stimulation, respectively (Spoida et al. 2016), probably because like vertebrate cone pigments (Kefalov et al. 2005), human melanopsin releases the retinal more frequently (Tsukamoto et al. 2015). Mammalian melanopsins have been proved to optically control activities of various types of cells (Beiert et al. 2014; Mederos et al. 2019; Tsunematsu et al. 2013; Ye et al. 2011), but their G protein coupling promiscuousness should be considered. Mammalian (mouse and human) melanopsins are reported to activate not only $G_q$ but also other G protein subtypes. In mammalian cultured cells expressing mammalian melanopsins, light stimulation induces GIRK activation and Gβγ translocation, indicating that the melanopsins can

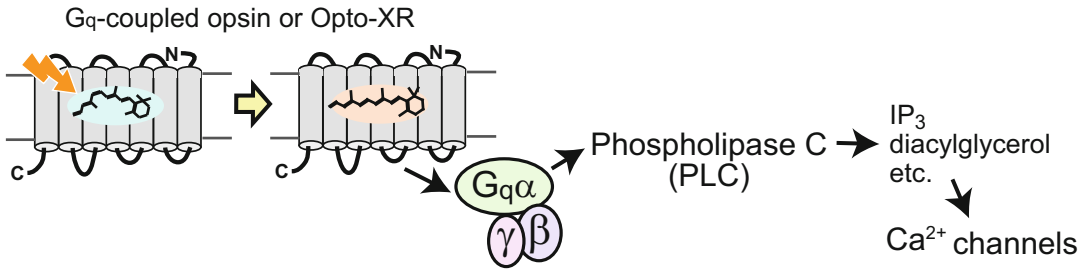


**Fig. 5.6** Typical signaling pathways driven by $G_q$-coupled opsins and Opto-XRs

activate $G_{i/o}$-type G protein (Kankanamge et al. 2018; Spoida et al. 2016). Furthermore, a recent study showed that in some population (M2- and M4-types) of melanopsin-expressing retinal ganglion cells, some cyclic nucleotide (probably cAMP) concentration is increased by melanopsin activation leading to opening of HCN channel (Jiang et al. 2018). Although it is unclear which G protein subtypes are responsible for the melanopsin-dependent elevation of cyclic nucleotide levels, one possibility is that melanopsin can activate $G_s$. If so, mammalian melanopsin possesses a coupling ability with $G_q$, $G_{i/o}$, and $G_s$ (Figs. 5.3, 5.4, and 5.6). Anyway, if researchers use mammalian melanopsin in optogenetics, they should consider multiple signaling pathways that the melanopsin can drive. In other words, for selective activation of $G_q$-dependent pathway, other $G_q$-coupled opsins or Opto-XRs are better to be used.

### 5.3.5 Opto-XRs Coupled with $G_{12}$

$G_{12}$-coupled opsins are not identified yet, but like $G_s$- or $G_q$- coupled receptors, some Opto-XRs can drive $G_{12}$-dependent pathways in a light-dependent manner (Morri et al. 2018). Typically, $G_{12}$ activates Rho followed by intracellular MAPK cascades, and some ion channels could be regulated indirectly.

### 5.3.6 "OFF-Type" Animal Opsins

Animal opsins activate by 11-*cis* to all-*trans* isomerization of the chromophore retinal (Terakita 2005; Wald 1968), and they selectively or preferentially bind 11-*cis*-retinal (Jager et al. 1996; Tsukamoto et al. 2005) (Fig. 5.2). However, an atypical opsin named peropsin possesses higher affinity for all-*trans*-retinal, and upon illumination, the retinal is isomerized to 11-*cis* form (Koyanagi et al. 2002). It is unclear if native peropsin is coupled to G proteins, but peropsin can be a "acceptor" of Opto-XR (Nagata et al. 2018). Interestingly, the peropsin-based Opto-XRs are inactivated by light stimulation, leading to decrease in G protein activity (Nagata et al. 2018). In addition, Opn5L1, a vertebrate non-visual opsin, also prefers to bind all-*trans*-retinal, and light absorption causes decrease in $G_i$ activity via all-*trans* to 11-*cis* isomerization followed by formation of an additional covalent bond between the retinal and the extracellular region (Sato et al. 2018).

Taken together, peropsin- or Opn5L1-based Opto-XRs can be used as an "OFF" photo-switch for G protein signalings and G protein-mediated ion channel modulation (Figs. 5.3, 5.4 and 5.6). Again, the ability to directly bind all-*trans*-retinal is advantageous for applying to optogenetics (see Sect. 5.3.1).

## 5.4 Optogenetic Tools Modulating $K^+/Ca^{2+}$ Channels Using Other Photoreceptive Proteins

In Sect. 5.3, we summarized animal opsins as optogenetic tools to modulate ion channels, in particular $K^+$ or $Ca^{2+}$ channels. As already discussed, one advantage of animal opsins as well as ChRs is that the chromophore molecule exists endogenously in native tissues. However, there are other photoreceptive proteins that do not need addition of chromophore molecules to function in cells. For example, the blue light-sensitive LOV domain is derived from a plant photoreceptor protein phototropin (Christie et al. 1999; Tokutomi et al. 2008), and its chromophore flavin mononucleotide (FMN) is abundant in animal tissues. Hereafter, we briefly introduce several flavin-based optogenetic tools to modulate $K^+$ or $Ca^{2+}$ channels.

To our knowledge, BLINK1 is the first light-gated $K^+$ channel, in which the LOV2-Jα photo-switch is fused with a viral $K^+$ channel Kcv (Cosentino et al. 2015). When BLINK1 is illuminated with blue light, conformational changes occur in the LOV2-Jα photo-switch, the changes induce opening of the Kcv moiety. BLINK1 works well in HEK293T cell lines and can regulate behaviors of zebrafish larvae in a

blue-light-dependent manner. On the other hand, the tool is not useful in mammalian neurons very much (Wiegert et al. 2017).

OptoRGK is a LOV domain-based optogenetic tool regulating voltage-sensitive $Ca^{2+}$ channels ($Ca_v$) (Ma et al. 2018). OptoRGK consists of two components: one component is a membrane-tethered LOV2 domain-containing ssrA protein and another component is a soluble ssrB protein fused with Rem, a negative modulator of $Ca_v$ channels. When the LOV2 domain is irradiated with blue light, conformational changes enable ssrA protein dimerizes with ssrB, leading to translocation of Rem to the plasma membrane and suppression of the $Ca_v$ channels. The study proved that upon light stimulation, OptoRGK can suppress cardiac $Ca_v$ channel-dependent responses in cell lines (Ma et al. 2018). When OptoRGK is used in neurons, some additional modification may be needed to localize the tools in presynaptic areas where $Ca_v$ channels function.

Photo-activated adenylyl cyclase (PAC) can be used as a modulator of a bacterial cAMP-gated $K^+$ channel, SthK (Brams et al. 2014). PAC utilizes flavin adenine dinucleotide (FAD) as a chromophore, and FAD is also abundant in animal cells. Recent studies showed that fusion constructs of PAC with SthK function well as light-sensitive $K^+$ channels (Beck et al. 2018; Bernal Sierra et al. 2018).

In this chapter, we focus on optogenetic tools that do not need supplement of cofactors to target cells, but there are many useful tools that utilize photo-activatable (in many cases, an azobenzene moiety is introduced) exogenous ligand. In particular, a bacterial $K^+$-selective glutamate receptor mutant can be modulated by a covalently bound photo-activatable agonist (Janovjak et al. 2010), and small compounds named as LOGO and VLOGO can act as photo-sensitive activators to GIRK channels (Barber et al. 2016; Trads et al. 2016). Such techniques are very useful for light-dependent modulation of $K^+/Ca^{2+}$ channel in tissues where these photo-activatable ligands are successfully delivered. For further discussion, please read many excellent reviews (Berlin and Isacoff 2017; Kienzler and Isacoff 2017; Paoletti et al. 2019).

## 5.5 Conclusion

In this chapter, we introduced several optogenetic tools based on photoreceptive proteins other than ChRs, and discussed their functionalities and usefulness. Currently most of optogenetic studies utilize ChRs, and making use of other photoreceptive molecules such as animal opsins, flavin-based photoreceptive proteins, and organic chemicals will further expand usefulness of optogenetics.

**Acknowledgments** We cordially thank to Hiroe Motomura and Kayo Inaba for sample preparation of *Platynereis* cOpsin1. This work is partly supported by grants from the Japanese Ministry of Education, Culture, Sports, Science, and Technology to H. T. (25840122 and 17K15109) and Y. F. (26708002), JST CREST to Y. F. (Grant Number JPMJCR17N5), and JST PRESTO to H. T. (JPMJPR1787).

## References

Airan RD, Thompson KR, Fenno LE, Bernstein H, Deisseroth K (2009) Temporally precise in vivo control of intracellular signalling. Nature 458 (7241):1025–1029

Arendt D, Tessmar-Raible K, Snyman H, Dorresteijn AW, Wittbrodt J (2004) Ciliary photoreceptors with a vertebrate-type opsin in an invertebrate brain. Science 306(5697):869–871

Arosio D, Ratto GM (2014) Twenty years of fluorescence imaging of intracellular chloride. Front Cell Neurosci 8:258

Asano T, Igarashi H, Ishizuka T, Yawo H (2018) Organelle optogenetics: direct manipulation of intracellular Ca(2+) dynamics by light. Front Neurosci 12:561

Ashida A, Matsumoto K, Ebrey TG, Tsuda M (2004) A purified agonist-activated G-protein coupled receptor: truncated octopus acid Metarhodopsin. Zool Sci 21 (3):245–250

Bailes HJ, Milosavljevic N, Zhuang LY, Gerrard EJ, Nishiguchi T, Ozawa T, Lucas RJ (2017) Optogenetic interrogation reveals separable G-protein-dependent and -independent signalling linking G-protein-coupled receptors to the circadian oscillator. BMC Biol 15 (1):40

Barber DM, Schonberger M, Burgstaller J, Levitz J, Weaver CD, Isacoff EY, Baier H, Trauner D (2016)

Optical control of neuronal activity using a light-operated GIRK channel opener (LOGO). Chem Sci 7 (3):2347–2352

Beck S, Yu-Strzelczyk J, Pauls D, Constantin OM, Gee CE, Ehmann N, Kittel RJ, Nagel G, Gao S (2018) Synthetic light-activated ion channels for optogenetic activation and inhibition. Front Neurosci 12:643

Beiert T, Bruegmann T, Sasse P (2014) Optogenetic activation of Gq signalling modulates pacemaker activity of cardiomyocytes. Cardiovasc Res 102(3):507–516

Beppu K, Sasaki T, Tanaka KF, Yamanaka A, Fukazawa Y, Shigemoto R, Matsui K (2014) Optogenetic countering of glial acidosis suppresses glial glutamate release and ischemic brain damage. Neuron 81(2):314–320

Berlin S, Isacoff EY (2017) Synapses in the spotlight with synthetic optogenetics. EMBO Rep 18(5):677–692

Bernal Sierra YA, Rost BR, Pofahl M, Fernandes AM, Kopton RA, Moser S, Holtkamp D, Masala N, Beed P, Tukker JJ, Oldani S, Bonigk W, Kohl P, Baier H, Schneider-Warme F, Hegemann P, Beck H, Seifert R, Schmitz D (2018) Potassium channel-based optogenetic silencing. Nat Commun 9(1):4611

Binkowski BF, Butler BL, Stecha PF, Eggers CT, Otto P, Zimmerman K, Vidugiris G, Wood MG, Encell LP, Fan F, Wood KV (2011) A luminescent biosensor with increased dynamic range for intracellular cAMP. ACS Chem Biol 6(11):1193–1197

Boyden ES, Zhang F, Bamberg E, Nagel G, Deisseroth K (2005) Millisecond-timescale, genetically targeted optical control of neural activity. Nat Neurosci 8 (9):1263–1268

Brams M, Kusch J, Spurny R, Benndorf K, Ulens C (2014) Family of prokaryote cyclic nucleotide-modulated ion channels. Proc Natl Acad Sci U S A 111 (21):7855–7860

Caro LN, Moreau CJ, Estrada-Mondragon A, Ernst OP, Vivaudou M (2012) Engineering of an artificial light-modulated potassium channel. PLoS One 7(8):e43766

Catterall WA (2000) Structure and regulation of voltage-gated $Ca^{2+}$ channels. Annu Rev Cell Dev Biol 16:521–555

Cheng Y (2018) Membrane protein structural biology in the era of single particle cryo-EM. Curr Opin Struct Biol 52:58–63

Cho YK, Park D, Yang A, Chen F, Chuong AS, Klapoetke NC, Boyden ES (2019) Multidimensional screening yields channelrhodopsin variants having improved photocurrent and order-of-magnitude reductions in calcium and proton currents. J Biol Chem 294 (11):3806–3821

Christie JM, Salomon M, Nozue K, Wada M, Briggs WR (1999) LOV (light, oxygen, or voltage) domains of the blue-light photoreceptor phototropin (nph1): binding sites for the chromophore flavin mononucleotide. Proc Natl Acad Sci U S A 96(15):8779–8783

Cosentino C, Alberio L, Gazzarrini S, Aquila M, Romano E, Cermenati S, Zuccolini P, Petersen J, Beltrame M, Van Etten JL, Christie JM, Thiel G, Moroni A (2015) Optogenetics. Engineering of a light-gated potassium channel. Science 348 (6235):707–710

Deisseroth K (2011) Optogenetics. Nat Methods 8 (1):26–29

Do MTH (2019) Melanopsin and the intrinsically photosensitive retinal ganglion cells: biophysics to behavior. Neuron 104(2):205–226

Do MT, Yau KW (2010) Intrinsically photosensitive retinal ganglion cells. Physiol Rev 90(4):1547–1581

Dolphin AC (2003) G protein modulation of voltage-gated calcium channels. Pharmacol Rev 55(4):607–627

Ehrenberg D, Varma N, Deupi X, Koyanagi M, Terakita A, Schertler GFX, Heberle J, Lesca E (2019) The two-photon reversible reaction of the bistable jumping spider Rhodopsin-1. Biophys J 116 (7):1248–1258

Eickelbeck D, Rudack T, Tennigkeit SA, Surdin T, Karapinar R, Schwitalla JC, Mucher B, Shulmann M, Scherlo M, Althoff P, Mark MD, Gerwert K, Herlitze S (2020) Lamprey parapinopsin ("UVLamP"): a bistable UV-sensitive optogenetic switch for ultrafast control of GPCR pathways. Chembiochem 21(5):612–617

Emanuel AJ, Do MT (2015) Melanopsin tristability for sustained and broadband phototransduction. Neuron 85(5):1043–1055

Fan J, Rohrer B, Moiseyev G, Ma JX, Crouch RK (2003) Isorhodopsin rather than rhodopsin mediates rod function in RPE65 knock-out mice. Proc Natl Acad Sci U S A 100(23):13662–13667

Fan J, Woodruff ML, Cilluffo MC, Crouch RK, Fain GL (2005) Opsin activation of transduction in the rods of dark-reared Rpe65 knockout mice. J Physiol 568 (Pt 1):83–95

Figueiredo M, Lane S, Stout RF Jr, Liu B, Parpura V, Teschemacher AG, Kasparov S (2014) Comparative analysis of optogenetic actuators in cultured astrocytes. Cell Calcium 56(3):208–214

Govorunova EG, Sineshchekov OA, Janz R, Liu X, Spudich JL (2015) Neuroscience. Natural light-gated anion channels: a family of microbial rhodopsins for advanced optogenetics. Science 349(6248):647–650

Gutierrez DV, Mark MD, Masseck O, Maejima T, Kuckelsberg D, Hyde RA, Krause M, Kruse W, Herlitze S (2011) Optogenetic control of motor coordination by Gi/o protein-coupled vertebrate rhodopsin in cerebellar Purkinje cells. J Biol Chem 286 (29):25848–25858

Hagiwara N, Irisawa H, Kameyama M (1988) Contribution of two types of calcium currents to the pacemaker potentials of rabbit sino-atrial node cells. J Physiol 395:233–253

Hegemann P, Gartner W, Uhl R (1991) All-trans retinal constitutes the functional chromophore in Chlamydomonas rhodopsin. Biophys J 60 (6):1477–1489

Hubbard R, St George RC (1958) The rhodopsin system of the squid. J Gen Physiol 41(3):501–528

Jager S, Palczewski K, Hofmann KP (1996) Opsin/all-trans-retinal complex activates transducin by different mechanisms than photolyzed rhodopsin. Biochemistry 35(9):2901–2908

Janovjak H, Szobota S, Wyart C, Trauner D, Isacoff EY (2010) A light-gated, potassium-selective glutamate receptor for the optical inhibition of neuronal firing. Nat Neurosci 13(8):1027–1032

Jiang Z, Yue WWS, Chen L, Sheng Y, Yau KW (2018) Cyclic-nucleotide- and HCN-channel-mediated phototransduction in intrinsically photosensitive retinal ganglion cells. Cell 175(3):652–64.e12

Kaila K, Price TJ, Payne JA, Puskarjov M, Voipio J (2014) Cation-chloride cotransporters in neuronal development, plasticity and disease. Nat Rev Neurosci 15 (10):637–654

Kanaho Y, Tsai SC, Adamik R, Hewlett EL, Moss J, Vaughan M (1984) Rhodopsin-enhanced GTPase activity of the inhibitory GTP-binding protein of adenylate cyclase. J Biol Chem 259(12):7378–7381

Kaneko H, Putzier I, Frings S, Kaupp UB, Gensch T (2004) Chloride accumulation in mammalian olfactory sensory neurons. J Neurosci 24(36):7931–7938

Kang Y, Kuybeda O, de Waal PW, Mukherjee S, Van Eps N, Dutka P, Zhou XE, Bartesaghi A, Erramilli S, Morizumi T, Gu X, Yin Y, Liu P, Jiang Y, Meng X, Zhao G, Melcher K, Ernst OP, Kossiakoff AA, Subramaniam S, Xu HE (2018) Cryo-EM structure of human rhodopsin bound to an inhibitory G protein. Nature 558(7711):553–558

Kankanamge D, Ratnayake K, Samaradivakara S, Karunarathne A (2018) Melanopsin (Opn4) utilizes Galphai and Gbetagamma as major signal transducers. J Cell Sci 131(11):jcs212910

Kato HE, Zhang Y, Hu H, Suomivuori CM, Kadji FMN, Aoki J, Krishna Kumar K, Fonseca R, Hilger D, Huang W, Latorraca NR, Inoue A, Dror RO, Kobilka BK, Skiniotis G (2019) Conformational transitions of a neurotensin receptor 1-Gi1 complex. Nature 572 (7767):80–85

Kawano-Yamashita E, Koyanagi M, Wada S, Tsukamoto H, Nagata T, Terakita A (2015) Activation of transducin by bistable pigment parapinopsin in the pineal organ of lower vertebrates. PLoS One 10(10): e0141280

Kefalov VJ (2012) Rod and cone visual pigments and phototransduction through pharmacological, genetic, and physiological approaches. J Biol Chem 287 (3):1635–1641

Kefalov VJ, Estevez ME, Kono M, Goletz PW, Crouch RK, Cornwall MC, Yau KW (2005) Breaking the covalent bond—a pigment property that contributes to desensitization in cones. Neuron 46(6):879–890

Kienzler MA, Isacoff EY (2017) Precise modulation of neuronal activity with synthetic photoswitchable ligands. Curr Opin Neurobiol 45:202–209

Kim JM, Hwa J, Garriga P, Reeves PJ, RajBhandary UL, Khorana HG (2005) Light-driven activation of beta 2-adrenergic receptor signaling by a chimeric rhodopsin containing the beta 2-adrenergic receptor cytoplasmic loops. Biochemistry 44(7):2284–2292

Koehl A, Hu H, Maeda S, Zhang Y, Qu Q, Paggi JM, Latorraca NR, Hilger D, Dawson R, Matile H, Schertler GFX, Granier S, Weis WI, Dror RO, Manglik A, Skiniotis G, Kobilka BK (2018) Structure of the micro-opioid receptor-Gi protein complex. Nature 558(7711):547–552

Koutalos Y, Ebrey TG, Tsuda M, Odashima K, Lien T, Park MH, Shimizu N, Derguini F, Nakanishi K, Gilson HR et al (1989) Regeneration of bovine and octopus opsins in situ with natural and artificial retinals. Biochemistry 28(6):2732–2739

Koyanagi M, Terakita A (2008) Gq-coupled rhodopsin subfamily composed of invertebrate visual pigment and melanopsin. Photochem Photobiol 84 (4):1024–1030

Koyanagi M, Terakita A, Kubokawa K, Shichida Y (2002) Amphioxus homologs of Go-coupled rhodopsin and peropsin having 11-cis- and all-trans-retinals as their chromophores. FEBS Lett 531(3):525–528

Koyanagi M, Kawano E, Kinugawa Y, Oishi T, Shichida Y, Tamotsu S, Terakita A (2004) Bistable UV pigment in the lamprey pineal. Proc Natl Acad Sci U S A 101(17):6687–6691

Koyanagi M, Takano K, Tsukamoto H, Ohtsu K, Tokunaga F, Terakita A (2008) Jellyfish vision starts with cAMP signaling mediated by opsin-G(s) cascade. Proc Natl Acad Sci U S A 105(40):15576–15580

Koyanagi M, Takada E, Nagata T, Tsukamoto H, Terakita A (2013) Homologs of vertebrate Opn3 potentially serve as a light sensor in nonphotoreceptive tissue. Proc Natl Acad Sci U S A 110(13):4998–5003

Kozmik Z, Ruzickova J, Jonasova K, Matsumoto Y, Vopalensky P, Kozmikova I, Strnad H, Kawamura S, Piatigorsky J, Paces V, Vlcek C (2008) Assembly of the cnidarian camera-type eye from vertebrate-like components. Proc Natl Acad Sci U S A 105 (26):8989–8993

Lawson MA, Zacks DN, Derguini F, Nakanishi K, Spudich JL (1991) Retinal analog restoration of photophobic responses in a blind Chlamydomonas reinhardtii mutant. Evidence for an archaebacterial like chromophore in a eukaryotic rhodopsin. Biophys J 60(6):1490–1498

Li X, Gutierrez DV, Hanson MG, Han J, Mark MD, Chiel H, Hegemann P, Landmesser LT, Herlitze S (2005) Fast noninvasive activation and inhibition of neural and network activity by vertebrate rhodopsin and green algae channelrhodopsin. Proc Natl Acad Sci U S A 102(49):17816–17821

Liu J, Conklin BR, Blin N, Yun J, Wess J (1995) Identification of a receptor/G-protein contact site critical for signaling specificity and G-protein activation. Proc Natl Acad Sci U S A 92(25):11642–11646

Luscher C, Slesinger PA (2010) Emerging roles for G protein-gated inwardly rectifying potassium (GIRK) channels in health and disease. Nat Rev Neurosci 11 (5):301–315

Ma G, Liu J, Ke Y, Liu X, Li M, Wang F, Han G, Huang Y, Wang Y, Zhou Y (2018) Optogenetic control of voltage-gated calcium channels. Angew Chem Int Ed Engl 57(24):7019–7022

Mahn M, Prigge M, Ron S, Levy R, Yizhar O (2016) Biophysical constraints of optogenetic inhibition at presynaptic terminals. Nat Neurosci 19(4):554–556

Makowka P, Bruegmann T, Dusend V, Malan D, Beiert T, Hesse M, Fleischmann BK, Sasse P (2019) Optogenetic stimulation of Gs-signaling in the heart with high spatio-temporal precision. Nat Commun 10 (1):1281

Masseck OA, Spoida K, Dalkara D, Maejima T, Rubelowski JM, Wallhorn L, Deneris ES, Herlitze S (2014) Vertebrate cone opsins enable sustained and highly sensitive rapid control of Gi/o signaling in anxiety circuitry. Neuron 81(6):1263–1273

Matsuyama T, Yamashita T, Imamoto Y, Shichida Y (2012) Photochemical properties of mammalian melanopsin. Biochemistry 51(27):5454–5462

Mederos S, Hernandez-Vivanco A, Ramirez-Franco J, Martin-Fernandez M, Navarrete M, Yang A, Boyden ES, Perea G (2019) Melanopsin for precise optogenetic activation of astrocyte-neuron networks. Glia 67 (5):915–934

Morri M, Sanchez-Romero I, Tichy AM, Kainrath S, Gerrard EJ, Hirschfeld PP, Schwarz J, Janovjak H (2018) Optical functionalization of human class A orphan G-protein-coupled receptors. Nat Commun 9 (1):1950

Nagata T, Koyanagi M, Lucas R, Terakita A (2018) An all-trans-retinal-binding opsin peropsin as a potential dark-active and light-inactivated G protein-coupled receptor. Sci Rep 8(1):3535

Nagel G, Ollig D, Fuhrmann M, Kateriya S, Musti AM, Bamberg E, Hegemann P (2002) Channelrhodopsin-1: a light-gated proton channel in green algae. Science 296(5577):2395–2398

Nagel G, Szellas T, Huhn W, Kateriya S, Adeishvili N, Berthold P, Ollig D, Hegemann P, Bamberg E (2003) Channelrhodopsin-2, a directly light-gated cation-selective membrane channel. Proc Natl Acad Sci U S A 100(24):13940–13945

Nagi K, Pineyro G (2014) Kir3 channel signaling complexes: focus on opioid receptor signaling. Front Cell Neurosci 8:186

Panda S, Nayak SK, Campo B, Walker JR, Hogenesch JB, Jegla T (2005) Illumination of the melanopsin signaling pathway. Science 307(5709):600–604

Paoletti P, Ellis-Davies GCR, Mourot A (2019) Optical control of neuronal ion channels and receptors. Nat Rev Neurosci 20(9):514–532

Perea G, Yang A, Boyden ES, Sur M (2014) Optogenetic astrocyte activation modulates response selectivity of visual cortex neurons in vivo. Nat Commun 5:3262

Rasmussen SG, DeVree BT, Zou Y, Kruse AC, Chung KY, Kobilka TS, Thian FS, Chae PS, Pardon E, Calinski D, Mathiesen JM, Shah ST, Lyons JA, Caffrey M, Gellman SH, Steyaert J, Skiniotis G, Weis WI, Sunahara RK, Kobilka BK (2011) Crystal structure of the beta2 adrenergic receptor-Gs protein complex. Nature 477(7366):549–555

Roth BL (2016) DREADDs for neuroscientists. Neuron 89 (4):683–694

Sato K, Yamashita T, Ohuchi H, Takeuchi A, Gotoh H, Ono K, Mizuno M, Mizutani Y, Tomonari S, Sakai K, Imamoto Y, Wada A, Shichida Y (2018) Opn5L1 is a retinal receptor that behaves as a reverse and self-regenerating photoreceptor. Nat Commun 9(1):1255

Satoh H, Kaneda M, Kaneko A (2001) Intracellular chloride concentration is higher in rod bipolar cells than in cone bipolar cells of the mouse retina. Neurosci Lett 310(2–3):161–164

Shichida Y, Imai H (1998) Visual pigment: G-protein-coupled receptor for light signals. Cell Mol Life Sci 54(12):1299–1315

Siuda ER, Copits BA, Schmidt MJ, Baird MA, Al-Hasani R, Planer WJ, Funderburk SC, McCall JG, Gereau RW, Bruchas MR (2015a) Spatiotemporal control of opioid signaling and behavior. Neuron 86 (4):923–935

Siuda ER, McCall JG, Al-Hasani R, Shin G, Il Park S, Schmidt MJ, Anderson SL, Planer WJ, Rogers JA, Bruchas MR (2015b) Optodynamic simulation of beta-adrenergic receptor signalling. Nat Commun 6:8480

Soejima M, Noma A (1984) Mode of regulation of the ACh-sensitive K-channel by the muscarinic receptor in rabbit atrial cells. Pflugers Arch 400(4):424–431

Spangler SM, Bruchas MR (2017) Optogenetic approaches for dissecting neuromodulation and GPCR signaling in neural circuits. Curr Opin Pharmacol 32:56–70

Spoida K, Eickelbeck D, Karapinar R, Eckhardt T, Mark MD, Jancke D, Ehinger BV, Konig P, Dalkara D, Herlitze S, Masseck OA (2016) Melanopsin variants as intrinsic optogenetic on and off switches for transient versus sustained activation of G protein pathways. Curr Biol 26(9):1206–1212

Stavenga DG, Schwemer J (1984) Visual pigments of invertebrates. In: Ali MA (ed) Photoreception and vision in invertebrates. Plenum Press, NewYork, pp 11–61

Suga H, Schmid V, Gehring WJ (2008) Evolution and functional diversity of jellyfish opsins. Curr Biol 18 (1):51–55

Taussig R, Tang WJ, Hepler JR, Gilman AG (1994) Distinct patterns of bidirectional regulation of mammalian adenylyl cyclases. J Biol Chem 269(8):6093–6100

Terakita A (2005) The opsins. Genome Biol 6(3):213

Terakita A (2010) Diversity and evolution of animal rhodopsins and phototransduction cascade. In: Collignon LN, Normand CB (eds) Photobiology: principles, applications and effects. Nova Science Publishers, Inc., Hauppauge, NY, pp 179–193

Terakita A, Yamashita T, Nimbari N, Kojima D, Shichida Y (2002) Functional interaction between bovine

rhodopsin and G protein transducin. J Biol Chem 277 (1):40–46
Tichy AM, Gerrard EJ, Sexton PM, Janovjak H (2019) Light-activated chimeric GPCRs: limitations and opportunities. Curr Opin Struct Biol 57:196–203
Tokutomi S, Matsuoka D, Zikihara K (2008) Molecular structure and regulation of phototropin kinase by blue light. Biochim Biophys Acta 1784(1):133–142
Trads JB, Burgstaller J, Laprell L, Konrad DB, de la Osa de la Rosa L, Weaver CD, Baier H, Trauner D, Barber DM (2016) Optical control of GIRK channels using visible light. Org Biomol Chem 15(1):76–81
Tsukamoto H, Terakita A (2010) Diversity and functional properties of bistable pigments. Photochem Photobiol Sci 9(11):1435–1443
Tsukamoto H, Terakita A, Shichida Y (2005) A rhodopsin exhibiting binding ability to agonist all-trans-retinal. Proc Natl Acad Sci U S A 102(18):6303–6308
Tsukamoto H, Farrens DL, Koyanagi M, Terakita A (2009) The magnitude of the light-induced conformational change in different rhodopsins correlates with their ability to activate G proteins. J Biol Chem 284 (31):20676–20683
Tsukamoto H, Kubo Y, Farrens DL, Koyanagi M, Terakita A, Furutani Y (2015) Retinal attachment instability is diversified among mammalian Melanopsins. J Biol Chem 290(45):27176–27187
Tsukamoto H, Chen IS, Kubo Y, Furutani Y (2017) A ciliary opsin in the brain of a marine annelid zooplankton is ultraviolet-sensitive, and the sensitivity is tuned by a single amino acid residue. J Biol Chem 292 (31):12971–12980
Tsunematsu T, Tanaka KF, Yamanaka A, Koizumi A (2013) Ectopic expression of melanopsin in orexin/hypocretin neurons enables control of wakefulness of mice in vivo by blue light. Neurosci Res 75(1):23–28
Violin JD, DiPilato LM, Yildirim N, Elston TC, Zhang J, Lefkowitz RJ (2008) beta2-adrenergic receptor signaling and desensitization elucidated by quantitative modeling of real time cAMP dynamics. J Biol Chem 283(5):2949–2961
Vogt A, Silapetere A, Grimm C, Heiser F, Ancina Moller M, Hegemann P (2019) Engineered passive potassium conductance in the KR2 sodium pump. Biophys J 116(10):1941–1951
Wald G (1968) The molecular basis of visual excitation. Nature 219(156):800–807
Wang JS, Kefalov VJ (2011) The cone-specific visual cycle. Prog Retin Eye Res 30(2):115–128
Weis WI, Kobilka BK (2018) The molecular basis of G protein-coupled receptor activation. Annu Rev Biochem 87:897–919
Wiegert JS, Mahn M, Prigge M, Printz Y, Yizhar O (2017) Silencing neurons: tools, applications, and experimental constraints. Neuron 95(3):504–529
Wietek J, Beltramo R, Scanziani M, Hegemann P, Oertner TG, Wiegert JS (2015) An improved chloride-conducting channelrhodopsin for light-induced inhibition of neuronal activity in vivo. Sci Rep 5:14807
Yamashita T, Terakita A, Shichida Y (2000) Distinct roles of the second and third cytoplasmic loops of bovine rhodopsin in G protein activation. J Biol Chem 275 (44):34272–34279
Yamashita T, Ohuchi H, Tomonari S, Ikeda K, Sakai K, Shichida Y (2010) Opn5 is a UV-sensitive bistable pigment that couples with Gi subtype of G protein. Proc Natl Acad Sci U S A 107(51):22084–22089
Yau KW, Hardie RC (2009) Phototransduction motifs and variations. Cell 139(2):246–264
Ye H, Daoud-El Baba M, Peng RW, Fussenegger M (2011) A synthetic optogenetic transcription device enhances blood-glucose homeostasis in mice. Science 332(6037):1565–1568
Yizhar O, Fenno LE, Davidson TJ, Mogri M, Deisseroth K (2011) Optogenetics in neural systems. Neuron 71 (1):9–34
Yokoyama S (2008) Evolution of dim-light and color vision pigments. Annu Rev Genomics Hum Genet 9:259–282

# Diversity, Mechanism, and Optogenetic Application of Light-Driven Ion Pump Rhodopsins

6

Keiichi Inoue

**Abstract**

Ion-transporting microbial rhodopsins are widely used as major molecular tools in optogenetics. They are categorized into light-gated ion channels and light-driven ion pumps. While the former passively transport various types of cations and anions in a light-dependent manner, light-driven ion pumps actively transport specific ions, such as $H^+$, $Na^+$, $Cl^-$, against electrophysiological potential by using light energy. Since the ion transport by these pumps induces hyperpolarization of membrane potential and inhibit neural firing, light-driven ion-pumping rhodopsins are mostly applied as inhibitory optogenetics tools. Recent progress in genome and metagenome sequencing identified more than several thousands of ion-pumping rhodopsins from a wide variety of microbes, and functional characterization studies has been revealing many new types of light-driven ion pumps one after another. Since light-gated channels were reviewed in other chapters in this book, here the rapid progress in functional characterization, molecular mechanism study, and optogenetic application of ion-pumping rhodopsins were reviewed.

**Keywords**

Light-driven ion pump · Microbial rhodopsin · Proton pump · Chloride pump · Sodium pump · Retinal

## Abbreviations

| | |
|---|---|
| AntR | Inward $H^+$ pumping Antarctic rhodopsin |
| AR | *Acetabularia* rhodopsin |
| Arch or AR3 | Archaerhodopsin-3 |
| ASR | *Anabaena* sensory rhodopsin |
| $ASR_T$ | *Anabaena* sensory rhodopsin transducer |
| ATR-FTIR | Attenuated total reflection-Fourier transform infrared |
| BacHR | Bacterial halorhodopsin |
| BR | Bacteriorhodopsin |
| ChR | Channelrhodopsin |
| ClR | Bacterial $Cl^-$ pump rhodopsin |
| CP | Cytoplasmic |
| cryoEM | Cryo-electron microscopy |
| CsR | *Coccomyxa subellipsoidea* rhodopsin |
| DNP | Dynamic nuclear-polarization |
| *Ds*NaR | *Dokdonia* sp. PRO95 $Na^+$ pump rhodopsin |

K. Inoue (✉)
The Institute for Solid State Physics, The University of Tokyo, Chiba, Japan

PRESTO, Japan Science and Technology Agency, Saitama, Japan
e-mail: inoue@issp.u-tokyo.ac.jp



H. Yawo et al. (eds.), *Optogenetics*, Advances in Experimental Medicine and Biology 1293,
https://doi.org/10.1007/978-981-15-8763-4_6

| | |
|---|---|
| EPR | Paramagnetic electron resonance |
| ER | Endoplasmic reticulum |
| ESR | *Exiguobacterium sibiricum* rhodopsin |
| *Fd*NaR | *Flagellimonas* sp_DIK $Na^+$ pump rhodopsin |
| FR | *Fulvimarina pelagi* rhodopsin |
| FTIR | Fourier transform infrared |
| *Gl*NaR | *Gillisia limnaea* $Na^+$ pump rhodopsin |
| GPCR | G-protein coupled receptor |
| GR | *Gloeobacter* rhodopsin |
| HKR | Histidine kinase rhodopsin |
| HR | Halorhodopsin |
| HS-AFM | High-speed atomic force microscopy |
| *Hs*HR | *Halobacterium salinarum* halorhodopsin |
| IAA | Indole-3-acetic acid |
| *Ia*NaR | *Indibacter alkaliphilus* $Na^+$ pump rhodopsin |
| IC | Internal cavity |
| KR2 or *De*NaR | *Krokinobacter eikastus* rhodopsin 2 |
| LR | *Leptosphaeria* rhodopsin |
| *Mr*HR | *Mastigocladopsis repens* halorhodopsin |
| NaR | $Na^+$ pump rhodopsin |
| NMR | Nuclear magnetic resonance |
| NM-R3 or *Nm*ClR | *Nonlabens marinus* bacterial $Cl^-$ pump rhodopsin |
| NR | *Neurospora* rhodopsin |
| *Ns*XeR | *Nanosalina* xenorhodopsin |
| *Ny*NaR | *Nonlabens* sp. YIK_SED-11 $Na^+$ pump rhodopsin |
| OLPVRII | Organic Lake Phycodnavirus rhodopsin II |
| ORP | Opsin-related proteins |
| *Pa*R | DTG rhodopsins from *Pantoea ananatis* |
| PhaeoRD | *Phaeosphaeria* rhodopsin |
| *p*HR or *Np*HR | *Natronomonas pharaonis* halorhodopsin |
| *Po*ClR | *Parvularcula oceani* bacterial $Cl^-$ pump rhodopsin |
| *Po*XeR | *Parvularcula oceani* xenorhodopsin |
| PR | Proteorhodopsin |
| PRG | Proton release group |
| *Psp*R | DTG rhodopsins from *Pseudomonas putida* |
| *Pv*R | DTG rhodopsins from *Pantoea vagans* |
| QM/MM | Quantum mechanics/molecular mechanics |
| RhGC | Rhodopsin guanylyl cyclase |
| Rh-PDE | Rhodopsin phosphodiesterase |
| *Rm*XeR | *Rubricoccus marinus* xenorhodopsin |
| RSB | Retinal Schiff base |
| RxR | *Rubrobacter xylanophilus* rhodopsin |
| SFX | Serial femtosecond crystallography |
| *Sy*HR | *Synechocystis* sp. PCC 7509 halorhodopsin |
| SzR | Schizorhodopsin |
| TM | Transmembrane |
| TR | Thermophilic rhodopsin |
| TR-SFX | Time-resolved serial femtosecond crystallography |
| XeR | Xenorhodopsin |
| XFEL | X-ray free electron laser. |

## 6.1 Introduction

Rhodopsins (also called retinylidene proteins) are a large family of photoreceptive heptahelical transmembrane proteins having a retinylidene chromophore binding to a conserved lysine in the seventh transmembrane helix via a Schiff base linkage (Ernst et al. 2014). Evolutionary independent two types of rhodopsins are known so far: microbial rhodopsins found in diverse microorganisms and animal rhodopsins mainly found in animal retina and nerve system (they are also called type 1 and type 2 rhodopsins, respectively) (Spudich and Jung 2005). While most animal rhodopsins are involved in the visual and non-visual signal transduction as members of G-protein-coupled receptors (GPCRs) family, the functions of microbial rhodopsins are more diverse: light-driven ion pumps, light-gated ion

channels, phototactic receptors, light-dependent regulation of gene expression, light-dependent enzymes, and so on (Ernst et al. 2014). With a few exceptions, all microbial rhodopsins use all-*trans* retinal as the chromophore, which isomerizes to 13-*cis* form upon light illumination (Fig. 6.1a) (Braiman and Mathies 1980; Pettei et al. 1977). The altered interaction between isomerized retinal and protein moiety (called opsin) triggers subsequent larger structural changes leading to biological activity (Nango et al. 2016). The photo-activated microbial rhodopsin recovers to the initial state with thermal isomerization of the retinal from 13-*cis* to all-*trans* forms. This cyclic reaction is called "photocycle" which enables multi-time photoactivation of the protein. In contrast, in the case of vertebrate rhodopsins which are most well-studied animal rhodopsins, 11-*cis*-to-all-*trans* photo-isomerization of retinal triggers formation of the activated state (Meta-II), and the isomerized retinal is eventually dissociated from protein moiety (opsin) (Ernst et al. 2014; Shichida and Yoshizawa 2004).

The first-identified microbial rhodopsin, bacteriorhodopsin (BR), was found in halophilic archaeon, *Halobacterium salinarum* (formerly referred as *H. halobium*) in 1971 (Oesterhelt and Stoeckenius 1971). BR forms two-dimensional lattice patches called "purple membrane" in the plasma membrane of *H. salinarum*, and it works as a light-driven outward proton ($H^+$) pump which actively transports $H^+$ from the cytoplasm to extracellular side of the cell during the photocycle (Oesterhelt and Stoeckenius 1973). After the discovery of BR, several homologous rhodopsins including light-driven inward $Cl^-$ pump, halorhodopsin (HR), and phototactic sensors, sensory rhodopsins I (positive and negative phototactic dual color sensor for orange and UV light, respectively) and II (also called phoborhodopsin, pR, negative phototactic sensor for blue light) were reported from 1970s to 1990s (Bogomolni and Spudich 1982; Matsuno-Yagi and Mukohata 1977; Mukohata et al. 1991, 1988; Schobert and Lanyi 1982; Takahashi et al. 1985; Spudich et al. 1986; Tomioka et al. 1986). Then, the speed of identification of rhodopsins has been highly accelerated due to the development of new sequencing technology such as next-generation sequencers and worldwide metagenomic surveys from 2000 (Béjà et al. 2000, 2001; de la Torre et al. 2003; Man et al. 2003; Stingl et al. 2007a, b; Venter et al. 2004; Yoshizawa et al. 2012). Whereas there are various enzymatic rhodopsins in which microbial rhodopsins are fused with enzymatic domains such as histidine kinase (histidine kinase rhodopsin, HKR) (Luck et al. 2012), guanylyl cyclase (rhodopsin–guanylyl cyclase, RhGC) (Scheib et al. 2015), and cyclic nucleotide phosphodiesterase (Rh-PDE) (Yoshida et al. 2017); the most abundant types of new rhodopsins are new groups of light-driven pumps and light-gated channels (Figs. 6.1 and 6.2). In contrast to BR and HR families which are mostly present in archaea, various types of proton ($H^+$), chloride ($Cl^-$), and sodium ($Na^+$) pump rhodopsins were discovered in the bacterial world (Béjà and Lanyi 2014; Inoue et al. 2014a). The light-gated channelrhodopsins (ChRs) were exclusively discovered in eukaryotic algae and protists, and they passively transport various ions according to the membrane potential of the cells and chemical gradient of the ions through cation-specific or anion-specific channels (Deisseroth and Hegemann 2017; Govorunova and Koppel 2016; Schneider et al. 2015). Recently, one of viral rhodopsin which is a large family of microbial rhodopsins from giant viruses, Organic Lake Phycodnavirus rhodopsin II, OLPVRII, was suggested to be a light-gated channel based on its structural features, but the ion-channeling function has not been experimentally confirmed yet (Bratanov et al. 2019). Also, horizontal gene tranfer between green algae and giant viruses was recently revealed (Rozenberg et al. 2020).

Both microbial and animal rhodopsins have been used as optogenetic tools so far to regulate membrane potential, the levels of cAMP/cGMP, G-protein activity, and so on as reviewed in other chapters. Especially, the large variety of ion-transporting microbial rhodopsins provided us not only a good model system to study the diversity of the ion-transporting mechanism of membrane proteins which was evolved in a wide range of species in nature but also a novel methodology to optically control neuronal activity

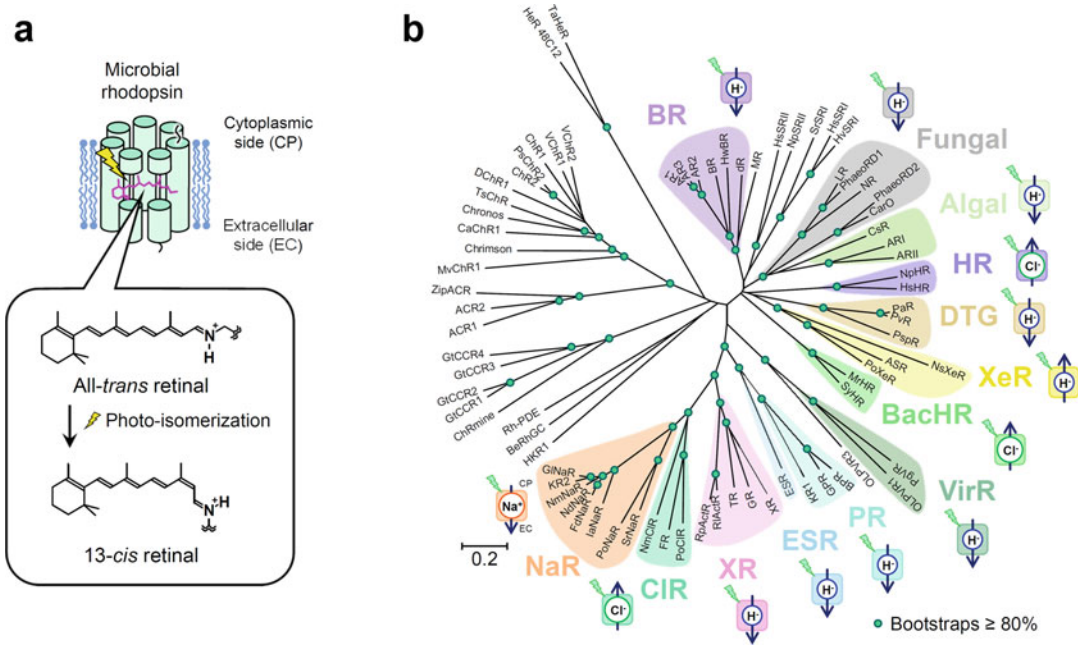


**Fig. 6.1** Structure and diversity of microbial rhodopsins. (**a**) The schematic structure of microbial rhodopsin and photo-isomerization of retinal chromophore. (**b**) The phylogenetic tree of representative microbial rhodopsins. The evolutionary history was inferred using the Neighbor-Joining method (Saitou and Nei 1987). The optimal tree with the sum of branch length = 32.12749828 is shown. The tree is drawn to scale, with branch lengths in the same units as those of the evolutionary distances used to infer the phylogenetic tree. The evolutionary distances were computed using the Poisson correction method (Zuckerkandl and Pauling 1965) and are in the units of the number of amino acid substitutions per site. The analysis involved 75 amino acid sequences. All ambiguous positions were removed for each sequence pair. There were a total of 452 positions in the final dataset. Evolutionary analyses were conducted in MEGA6 (Tamura et al. 2011). The transporting-ion species and the direction of transport of each ion-pumping rhodopsins are indicated by the schematic diagram

in vivo by heterologously expressing them in animal neurons (Boyden et al. 2005; Chow et al. 2010; Deisseroth 2015). Since ChRs are extensively reviewed in other chapters, here the various families of recently identified light-driven pumps, their molecular mechanisms which are involved in the transport of various ionic species in different directions, and their optogenetic applications are reviewed.

## 6.2 Outward Proton Pumps

### 6.2.1 Bacteriorhodopsins

Bacteriorhodopsin is the best-studied microbial rhodopsin so far by biochemical, molecular scientific, structural, spectroscopic, and computational approaches. Since there are many review articles on the subject (Balashov 2000; Birge 1981; Chou 1993; Dencher et al. 2000; Ernst et al. 2014; Haupts et al. 1999; Heberle 2000; Kalaidzidis et al. 2001; Kandori 2000, 2004; Khorana 1988; Kouyama et al. 1988; Lanyi 1992, 1993, 1998, 2004; Lanyi and Schobert 2004; Luecke 2000; Maeda et al. 1997; Neutze et al. 2002; Wickstrand et al. 2015), here we do not discuss a large number of studies for BR in detail, but summarize key elements of its $H^+$ transport process as a standard model which is useful to understand the transport mechanism of other new ion-transporting rhodopsins.

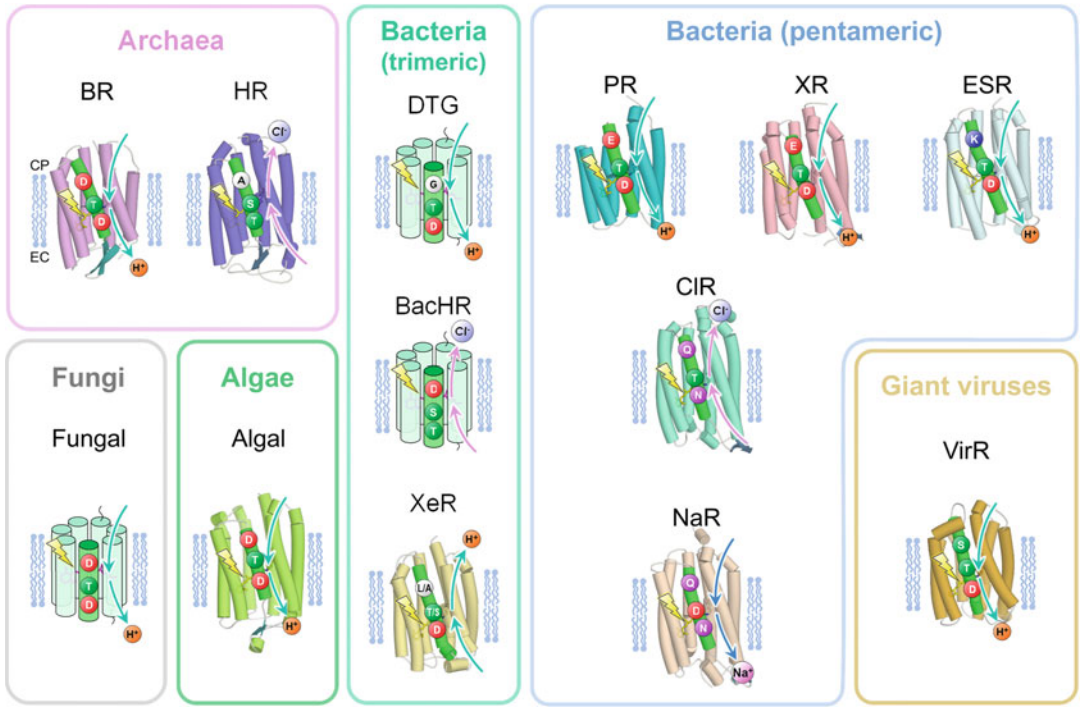


**Fig. 6.2** The structures and motifs of ion-transporting rhodopsins. The helix C of ion-pumping rhodopsins including three-character motifs is colored in true green. The reported crystal structure was used to make cylndrical model for BR (PDB ID: 1IW6 (Matsui et al. 2002)), HR (PDB ID: 3A7K (Kouyama et al. 2010)), algal rhodopsin (PDB ID: 5AWZ (Furuse et al. 2015)), xenorhodopsin (XeR) (PDB ID: 6EYU (Shevchenko et al. 2017b)), proteorhodopsin (PR) (PDB ID: 4JQ6 (Ran et al. 2013)), xanthorhodopsin (XR) (PDB ID: 3DDL (Luecke et al. 2008)), *Exiguobacterium sibiricum* rhodopsin (ESR) (PDB ID: 4HYJ (Gushchin et al. 2013)), bacterial $Cl^-$ pump rhodopsin (ClR) (PDB ID: 5B2N (Hosaka et al. 2016)), $Na^+$ pump rhodopsin (NaR) (PDB ID:3X3C (Kato et al. 2015a)), viral rhodopsin (VirR) (PDB ID: 6JO0 (Needham et al. 2019)). The ion pumps from bacterial origins are classified into two groups according to the oligomeric structures: trimeric (the clade including DTG, bacterial halorhodopsin (BacHR), and XeR close to archaeal (BR, HR), fungal, and algal branches in Fig. 6.1) and pentameric (the clade including PR, XR, ESR, ClR, and NaR in Fig. 6.1) ones

#### 6.2.1.1 The Dynamics of the Photocycle of BR

By a number of spectroscopic, structural, and mutational studies, the residues crucial for the $H^+$ pump function and $H^+$ transport pathway in BR are thought to be almost completely revealed (Fig. 6.3) (Brown et al. 1995; Butt et al. 1989; Dioumaev et al. 1999; Garczarek and Gerwert 2006; Garczarek et al. 2004; Gerwert et al. 1989; Holz et al. 1989; Kandori et al. 1997; Lórenz-Fonfría and Kandori 2009; Maeda et al. 1992; Mogi et al. 1988; Otto et al. 1989; Thorgeirsson et al. 1991; Zscherp et al. 2001).

BR shows dark and light adaptation, that is, while it has all-*trans* and 13-*cis* retinal in the dark with about 50:50 ratio, the former exclusively accumulates when the protein is placed under light. The functional photocycle is initiated by the excitation of all-*trans* form, and it comprises J, K, KL, L, $M_1$, $M_2$, N, N′, and O intermediates (Chizhov et al. 1996; Lanyi 2004; Lórenz-Fonfría and Kandori 2009; Mathies et al. 1988; Shichida et al. 1983; Váró and Lanyi 1991). Whereas many internal water molecules were observed around hydrophilic residues on the extracellular side of BR, a small number of water molecule is present in the cytoplasmic half

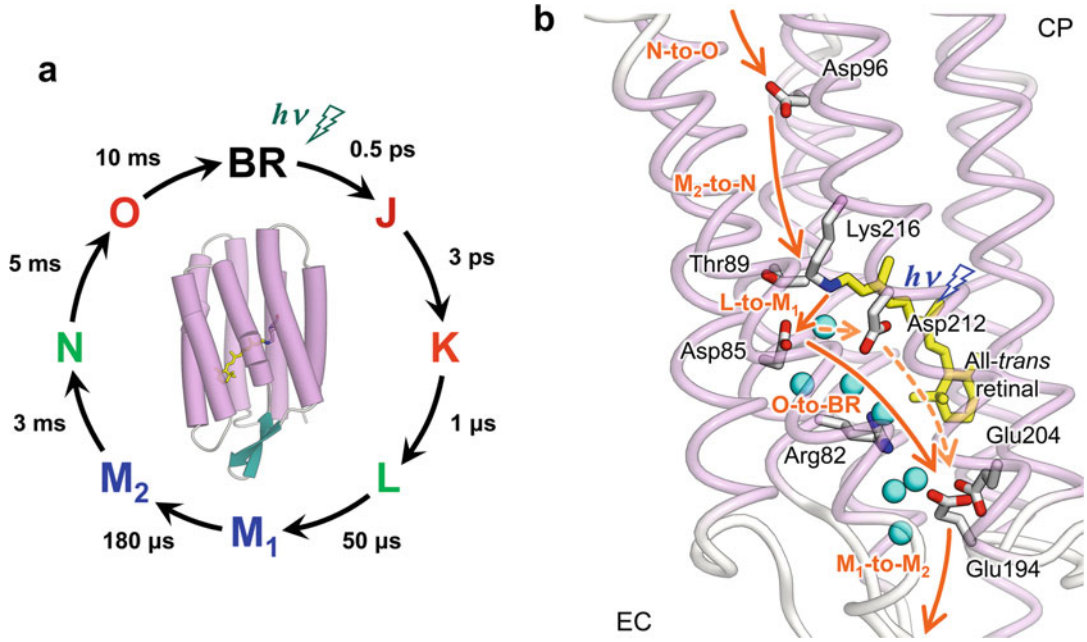


**Fig. 6.3** (**a**) The photocycle of BR. The lifetimes of each intermediates are according to previously reported values in Refs. (Chizhov et al. 1996; Ernst et al. 2014; Lórenz-Fonfría and Kandori 2009; Mathies et al. 1988). (**b**) The $H^+$ transport pathway in BR (PDB ID: 1IW6 (Matsui et al. 2002)). The $H^+$ transfer between retinal Schiff base (RSB) and acidic carboxylic residues is indicated by solid orange arrows. The $H^+$ transfer from Asp85 to proton release group (PRG) (Glu194, 204 and water molecules) via Asp212 was also suggested (dashed orange arrows) (Dioumaev et al. 1999; Zscherp et al. 2001)

of protein in the X-ray crystallographic structure of BR in the dark state (Fig. 6.3) (Luecke et al. 1999; Matsui et al. 2002; Pebay-Peyroula et al. 1997). This suggests that BR is mainly outward-opened in the dark. The retinal isomerization induces structural change in protein moiety making the pKa of retinal Schiff base (RSB) lower than that of Asp85 and an $H^+$ transfer occurs on L-to-$M_1$ (Butt et al. 1989; Nango et al. 2016; Thorgeirsson et al. 1991). Then, further vectorial $H^+$ transfers occur on $M_1$-to-$M_2$ (from proton release group (PRG) to extracellular solvent), $M_2$-to-N (from Asp96 to RSB), N-to-O (Asp96 receives an $H^+$ from the cytoplasmic milieu), and O-to-BR (from Asp85 to PRG) (Ernst et al. 2014; Garczarek and Gerwert 2006; Haupts et al. 1999; Lanyi 2004). Many structural studies suggested that the structure of BR switches from outward-opened to inward-opened state in the $M_1$-to-$M_2$ transition (Sass et al. 2000, 1997; Subramaniam and Henderson 2000). Importantly, cryogenic electron and X-ray crystallography, time-resolved serial synchrotron crystallography, time-resolved paramagnetic electron resonance (EPR) spectroscopy, and high-speed atomic force microscopy (HS-AFM) suggested the tilting of cytoplasmic part of the helix F, and concomitant rearrangement of the helix G occurs in the inward-opened state to take up an $H^+$ from the cytoplasmic milieu (Chen and Lanyi 2009; Radzwill et al. 2001; Sass et al. 2000; Shibata et al. 2010; Subramaniam et al. 1999; Weinert et al. 2019). Fourier transform infrared (FTIR) spectroscopy of PRG mutant observed that Asp212 receives an $H^+$ from Asp85 on the O′ state which appears after the O (Dioumaev et al. 1999; Zscherp et al. 2001), suggesting $H^+$ transfers occur in the order of Asp85→Asp212→PRG at the last stage of the photocycle (Fig. 6.3, dashed arrows).

Since photo-intermediates similar to those of BR (K, L, M, N, and O) are observed in the

photocycle of most of other microbial rhodopsins including new families focused on in this review, the comparison of their occurrences, lifetimes, and so on will be insightful to understand the difference and similarity of the photocycles between different rhodopsins. Also, the alternative access model involving the switching between outward-opened and inward-opened states suggested for the vectorial $H^+$ transport of BR is considered to also play critical role in the ion transport by other pumps.

#### 6.2.1.2 Optogenetic Applications

Many $H^+$ pumping rhodopsins homologous to BR were identified in divergent archaea (Kamo et al. 2006; Mukohata et al. 1991; Tateno et al. 1994). Especially, archaerhodopsin-3 (abbreviated as Arch or AR3) from *Halorubrum sodomense* shows the highest photo-current in mammalian neurons (Chow et al. 2010), and homologous protein from *Halorubrum* strain TP009 (ArchT) also shows similar large photo-current (Han et al. 2011). They were used as hyperpolarizing inhibitory optogenetic tool in many researches (Eshel et al. 2015; Jennings et al. 2013; Ramirez et al. 2015). Meanwhile Arch emits fluorescence whose intensity linearly depends on membrane potential (Kralj et al. 2011). By this attribute, Arch can be used as genetically encoded voltage indicator (GEVI) to image the action firing in brain tissue in real time. Although the fluorescence of original Arch was relatively weak, directed molecular evolution engineering developed more intense, rapidly responding, well membrane localized, and highly photo-stable variants like QuasAr series (Hochbaum et al. 2014), and Archon series (Piatkevich et al. 2018). These highly bright GEVIs enable simultaneous excitation by ChRs and live monitoring of membrane potential change called all-optical electrophysiology (Piatkevich et al. 2018).

### 6.2.2 Proteorhodopsins and Xanthorhodopsins

#### 6.2.2.1 Proteorhodopsins

For more than 25 years after the discovery of BR, no $H^+$ pump rhodopsin was found outside the archeal species. However, a microbial rhodopsin-like gene was identified in the genomic fragment derived from an uncultivated marine γ-proteobacterium belonging to SAR86 group, abundant and uncultivated marine bacterial lineage, in 2000 (Béjà et al. 2000). This rhodopsin showed outward $H^+$ pump function when it was heterologously expressed in *E. coli* cells in the presence of exogenous retinal, and it was named "proteorhodopsin (PR)" on the basis of the name of the natural host species (Béjà et al. 2000). After the first discovery of PR, many homologous proteins have been identified in several thousands of bacteria in aquatic environment such as oceans, lakes, and rivers (de la Torre et al. 2003; Koh et al. 2010; Pushkarev and Béjà 2016; Rusch et al. 2007; Sabehi et al. 2007; Venter et al. 2004; Yoshizawa et al. 2012), and more than 50% of bacteria in the surface water is demonstrated to have PR (Finkel et al. 2013). They are currently the most abundant group of microbial rhodopsins.

The sequence alignments and comparison of three-dimensional structures between PR and BR suggest homologous transmembrane architecture and many conserved residues such as BR's Tyr57, Arg82, Tyr83, Asp85, Trp86, Thr89, Pro91, Met118, Gly122, Trp182, Tyr185, Pro186, Trp189, and Asp212 at identical positions (Béjà et al. 2000; Ernst et al. 2014). The one of most prominent differences between BR and PR is found on the cytoplasmic side in which a glutamic acid is present in the PR family at the position of BR's Asp96. That is, whereas BR has Asp85-Thr89-Asp96 (DTD) motif in the helix C, PR has a "DTE" motif at the homologous position (Fig. 6.2). Whereas many PRs including the first discovered one from uncultured γ-proteobacterium show their absorption in green-light region (~520–525 nm), other members of PR group showing more blue-shifted absorption at around 490 nm were reported (Man

et al. 2003). On the basis of their absorption wavelengths, the former and the latter are referred to as green- and blue-absorbing proteorhodopsin (GPR and BPR), respectively. The color determining residue between GPR and BPR was identified in the position of BR's Leu93 in the helix C, whereas GPR also has a leucine (GPR's Leu105, based on the amino acid numbering of the first PR of uncultured γ-proteobacterium), and it is replaced by Gln in BPR. The interconverting mutation between GPR Leu105 and BPR Gln105 makes not only their absorption wavelengths but also photoreaction cycles identical to those of their counterparts (Man et al. 2003).

The first three-dimensional structure of PR obtained by solution nuclear magnetic resonance (NMR) spectroscopy revealed lack of extracellular anti-parallel β-sheet between helices B and C observed in BR and many other microbial rhodopsins (Reckel et al. 2011). Then, the X-ray crystallographic structure was solved for BPR derived from the Mediterranean Sea at 12-m depth (*Med12*BPR) and the mutants of another BPR derived from the Pacific Ocean near Hawaii islands at 75-m depth (*HOT75*BPR D97N and D97N/Q105L) (Ran et al. 2013). Interestingly, whereas *Med12*BPR showed hexameric oligomerization, *HOT75*BPR mutants formed pentamers. This suggests that the oligomeric structure of PR group is quite different from the trimeric ones observed in archeal groups such as BR and HR (Kolbe et al. 2000; Kouyama et al. 2010; Luecke et al. 1999; Pebay-Peyroula et al. 1997; Sato et al. 1999). Interestingly, atomic-force-microscopy (AFM) imaging of GPR showed coexisting pentamers and hexamers in lipid bilayer (Klyszejko et al. 2008; Shibata et al. 2018). Hence, both of pentameric and hexameric structures observed in the crystals are presumably biologically relevant. The dynamic nuclear-polarization (DNP)-enhanced solid-state NMR suggested inter-protomer salt bridge between Asp52 and Arg51′ ("′" indicates a residue in neighboring protomer) on the CP side of the helix A. The disruption of the salt bridge by mutations (GPR R51A or D52N) leads to the formation of hexamer (Maciejko et al. 2015). While three water molecules interacting with the RSB and counterions were observed in the crystal structure of BR (Luecke et al. 1999; Matsui et al. 2002), no water molecule was present in the RSB region in the structure of BPR (Ran et al. 2013). However, low-temperature FTIR spectroscopy observed the several water molecules including that forming a strong hydrogen bond, which would be important for the $H^+$ function, in the RSB region in the dark state of GPR (Furutani et al. 2006a; Ikeda et al. 2007). At physiological pH (8.0–8.5) to pH 9.5, the $H^+$ uptake from the cytoplasmic milieu precedes the $H^+$ release to the extracellular bulk solvent which is opposed to the order in BR photocycle, presumably related to the absence of PRG in PR (Dioumaev et al. 2002; Krebs et al. 2002; Tamogami et al. 2009). The FTIR spectroscopy revealed protonation of Asp97 and deprotonation of Glu108 during the photocycle indicating the former and the latter work as $H^+$ acceptor and $H^+$ donor as expected from the analogy to BR (Dioumaev et al. 2002; Friedrich et al. 2002).

The pKa of counter ion in GPR (Asp97) is 7.5 which is higher than that of BR's Asp85 (pKa = ~2.5) (Hempelmann et al. 2011). This higher pKa of Asp97 is lowered by the mutation of His75 in the helix B which is highly conserved in PR subgroup (Bergo et al. 2009; Inoue et al. 2016b). Solid-state NMR study revealed a hydrogen-bonding interaction between Asp97 and His75 (Hempelmann et al. 2011). His75 also interacts with Trp34 in the neighboring protomer which results in the formation cross-protomer Asp-His-Trp triad revealed by DNP-enhanced solid-state NMR (Maciejko et al. 2019). Hence, His75 contributes to both of the control of counterion pKa and stabilizing GPR oligomer.

#### 6.2.2.2 Xanthorhodopsins

Another outward $H^+$ pump rhodopsin with the DTE motif was identified in an extremely halophilic bacterium, *Salinibacter ruber*, and it was named "xanthorhodopsin (XR)" (Balashov et al. 2005). The genus *Salinibacter* has many genes which show higher homology to those in the archeal family *Halobacteriaceae* suggesting

lateral gene transfer occurred between these species (Oren 2013; Sharma et al. 2006), and one archeal HR-like and two archeal SRI-like genes are present in the genome of *S. ruber* in addition to XR (Kitajima-Ihara et al. 2008). The cell-membrane vesicles prepared from *S. ruber* show acidification of the external medium indicating light-driven outward $H^+$ pump function. The action spectrum of the $H^+$ transport was unexpectedly complicated, and it consists of two sharp peaks at 521 and 486 nm and a shoulder at 560 nm. This unusual action spectra of $H^+$ transport by rhodopsin was identical to that of the absorption spectrum of XR in suspended *S. ruber* membrane which also showed intense and sharp peaks at 519 and 487 nm (Balashov et al. 2006). After the bleaching of XR with hydroxylamine, the sharp peaks were broadened and the spectrum became identical to that of salinixanthin, which is the carotenoid predominantly present in *S. ruber* membrane (Oren 2013), in the bulk. Hence, the results indicate that not only XR binds salinixanthin as the second chromophore but also this is the first example of using energy transfer from an antennae carotenoid (salinixanthin) to retinal to drive the isomerization of the latter, which is followed by the outward $H^+$ transport. By comparing the contributions in the action spectrum originated from retinal and salinixanthin and those in the absorption spectrum of purified XR, the efficiency of energy transfer from salinixanthin to retinal is estimated to be ca. 40%, and it was more precisely determined to be 45 ± 5% by fluorescence spectroscopy (Balashov et al. 2008), increasing the optical cross section of light-driven $H^+$ pump by a factor of about 2. The higher efficiency of the energy transfer implied strong interaction between salinixanthin and retinal, and fluorescence excitation anisotropy spectrum estimated the angle between their dipole moments to be 56 ± 3° (Balashov et al. 2008). These were indeed revealed to be consistent with the X-ray crystallographic structure of XR (Luecke et al. 2008). In the structure, β-ionone ring is located near the 4-keto ring of salinixanthin through a small hole opened on the protein surface between the helices E and F

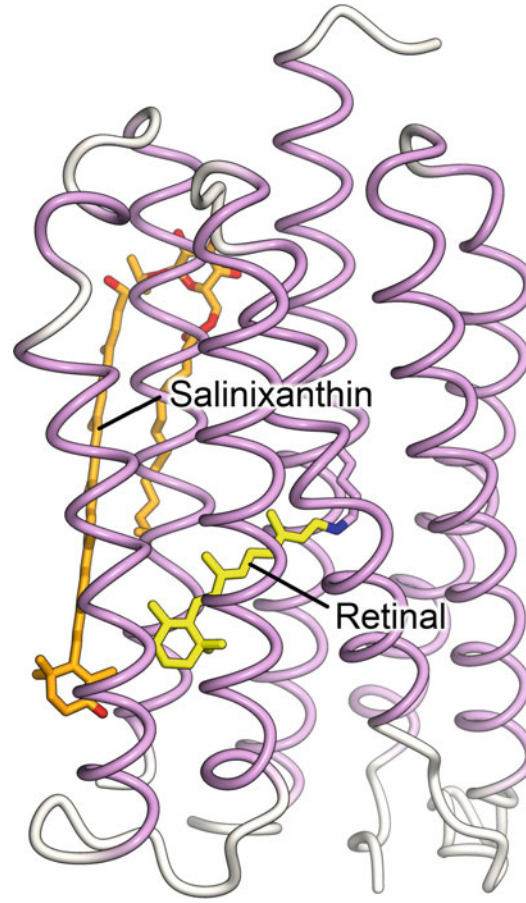


**Fig. 6.4** The three-dimensional configuration between retinal and salinixanthin in the crystallographic structure of XR (PDB ID: 1DDL (Luecke et al. 2008))

(Fig. 6.4), and the angle between their π-conjugated systems is 68°. If we compare the residues around the hole, BR's Trp138 is replaced with a glycine in XR (XR's Gly156) and the hole is opened by the difference in the size of their side chains. The short distance between salinixanthin and retinal enables fast energy transfer ($\tau$ = 165–192 fs) (Polívka et al. 2009; Zhu et al. 2010) to achieve the higher energy transfer efficiency. The computational study by the *ab initio* quantum mechanical/molecular mechanical (QM/MM) method and the transition-density-fragment interaction (TDFI) method also suggested that the binding site of salinixanthin is maximally tuned up in natural XR to achieve the

highest energy transfer (Fujimoto and Hayashi 2009).

Although XR has the DTE-motif, it belongs to a subgroup different from that of PR (Fig. 6.1). Because XR's Gly156 which is considered to be important for the salinixanthin binding is conserved in this subgroup, other members are also expected to bind an antennae carotenoid. Indeed, *Gloeobacter* rhodopsin (GR), which is a member of the same subgroup as XR from a cyanobacterium *Gloeobacter violaceus*, heterologously expressed in *E. coli*, showed binding of exogenous salinixanthin and the energy transfer from the salinixanthin to retinal (Imasheva et al. 2009). Furthermore, the mutation of GR's Gly178 (homologous to XR's Gly156) to a tryptophan eliminated the salinixanthin binding indicating the carotenoid binding ability is achieved in this group with the crucial glycine residue. Although salinixanthin is not present in *Gloeobacter violaceus*, the species has other carotenoids such as echinenone, β-carotene, and oscillol. Especially, echinenone has a 4-keto group as salinixanthin, and it also binds to GR and shows energy transfer to the retinal (Balashov et al. 2010). In contrast, β-carotene without 4-keto group does not bind to GR. This implies the 4-keto group plays a crucial role of binding to GR, and it is further evidenced by the fact that an analogue of salinixanthin, salinixanthol in which 4-keto group is replaced with hydroxyl, does not bind and show an energy transfer (Balashov et al. 2010). Later, XR was also shown not to bind salinixanthol (Imasheva et al. 2011). Recently, the X-ray crystallographic structure of GR was reported (Morizumi et al. 2019); it will provide further structural insights on its carotenoid binding.

Drs. Sudo, Tsukamoto et al. (2013) identified the first microbial rhodopsin (TR) from thermophilic bacterium (*Thermus thermophilus* JL-18) (Tsukamoto et al. 2013). TR, which belongs to XR group, was recently shown to be able to bind exogenous salinixanthin (Misra et al. 2019). TR shows extremely high thermal stability compared to other microbial rhodopsins, and >85% of TR protein does not denature against incubation at 75 °C for 210 min in DDM (Tsukamoto et al. 2013). The difference in the denaturation rate between TR and GR indicates that the former is more than two orders of magnitude stable than the latter, despite the high amino acid identity (42.7%) between them. The structural origin of this thermal stability has been suggested on the basis of crystallographic structure of TR (Tsukamoto et al. 2016). The overall structure of TR was quite similar to that of XR (RMSD = 1.11 Å), and the putative carotenoid binding site was observed. The optogenetic application of TR was also suggested by the optical control of neuronal system in *Caenorhabditis elegans*, and it was shown to be able to more rapidly control the locomotion behavior than AR3 (Tsukamoto et al. 2016). Recently, a new rhodopsin (RxR) distinct from the group of XR and TR was identified from a thermophilic eubacterium *Rubrobacter xylanophilus* DSM 9941T, and it showed 16 times higher thermal stability than that of TR (Kanehara et al. 2017).

### 6.2.3 Exiguobacterium Rhodopsins

A new type of proton pump rhodopsin (*Exiguobacterium sibiricum* rhodopsin, ESR) from a psychrotrophic gram-positive bacterium, *Exiguobacterium sibiricum* which was isolated from permafrost sample frozen for three million years, was reported in 2010 (Petrovskaya et al. 2010). In contrast to other $H^+$ pumps having an acidic amino acid residue (Asp or Glu) at the position of BR's Asp96, ESR has a lysine at the same position. In addition to *E. sibiricum*, *Exiguobacterium* AT1b, marine uncultured MG-II *Euryarchaeota* and other bacteria also have rhodopsins with DTK motif. ESR is phylogenetically close to PR, and it also has a histidine, His57, which is conserved in the helix B in PR and XR families. In X-ray crystallographic structure, this histidine directly interacts with the RSB counterion (ESR's Asp85, the distance between His57 and Asp85 is 2.6–2.7 Å, Fig. 6.5a) (Gushchin et al. 2013), suggesting His57 affects the pKa of Asp85. The visible absorption of ESR WT shows complicated pH dependence, in which a redshift of the absorption

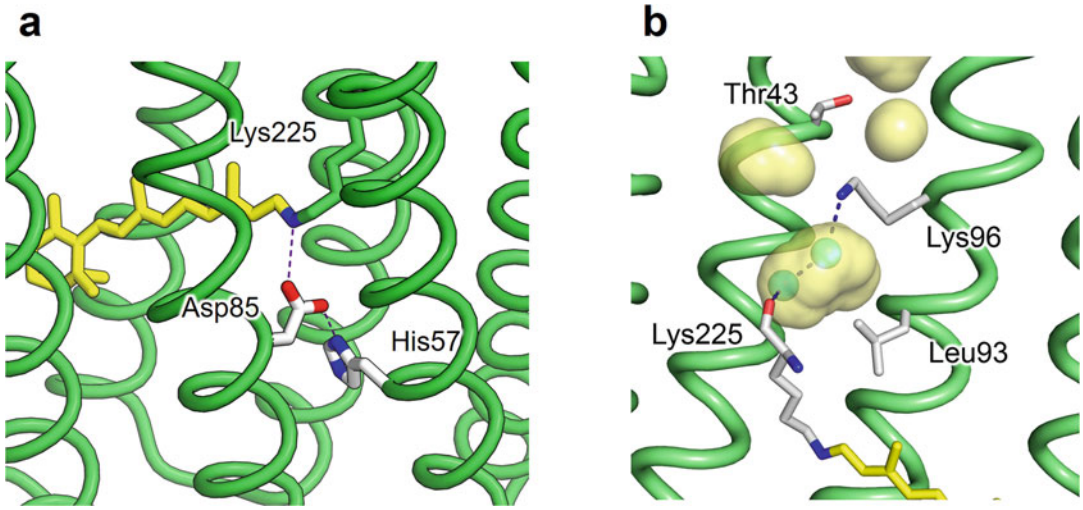


**Fig. 6.5** (**a**) The hydrogen-bonding network between His57, Asp85 (counterion), and RSB in ESR (PDB ID: 4HYJ). (**b**) Internal cavities (pale yellow) and hydrogen-bonding network in X-ray crystallographic structure around Lys96 on the cytoplasmic side of ESR (PDB ID: 4HYJ)

occurs upon titration from alkaline to acidic pH with three pKa values at 2.3, 6.0, and 9.1 (Balashov et al. 2012). In contrast, ESR H57M shows a single pKa at 6.3 (Balashov et al. 2012). While the counterion Asp85 in the WT shows partial protonation even at very acidic pH (~2), it is almost fully protonated upon the titration of pKa 6.3 in the H57M mutant. Therefore, His57 is considered to play a role to stabilize the deprotonated state of the counterion over a wide pH range so that the protein is kept to be functional. Indeed, a robust $H^+$ transport was observed at pH 4.5–8.5 for the ESR WT in *E. coli* cells and proteoliposomes (Balashov et al. 2012). The decrease in pKa of counterion by the His-Aps interaction is opposed to GPR in which His75 is considered to "elevate" pKa of counterion, Asp97 (Hempelmann et al. 2011). The opposing effect of the histidines to counterion pKa would represent the structural difference between these two pumps, and further study is required to understand it.

The photocycle of ESR revealed by the laser flash photolysis and FTIR spectroscopy is shown as follows: ESR $\xrightarrow{h\nu}$ pre-K$\rightarrow$K$_E\rightarrow$K$_L \rightleftharpoons$ L$_{\sim 530} \rightleftharpoons$ M$_{400} \rightleftharpoons$ N$_{580} \rightleftharpoons$ N$_{605} \rightleftharpoons$ N$_{537}$ (O)$\rightarrow$ESR where subscript numbers represent absorption wavelength of each intermediate and the presence of two different K-like states are suggested by the low-temperature FTIR spectroscopy following primary pre-K intermediate (Dioumaev et al. 2013). After the M state, a red-shifted intermediate was observed. Although the red-shifted absorption is reminiscent of the O state in the BR photocycle, the 13-*cis* retinal configuration revealed by the FTIR spectroscopy suggested that it should be identical to the N state of BR (Dioumaev et al. 2013). Unexpectedly, despite the robust $H^+$ pump ability over wide pH range (pH 4.5–8.5), the accumulation of M becomes negligible at pH $<$ 7.6 and 4.8 in DDM and proteoliposomes, respectively. The $H^+$ transport without significant M-accumulation looks quite unusual. One possible explanation is that the M-accumulation is suppressed by a kinetic reason in which the rate of the M-rise becomes much slower than that of the M-decay. Indeed, it was indicated by the FTIR spectroscopy observing $H^+$ transfer to the counterion Asp85 on the N state (Dioumaev et al. 2013) as well as the analysis of the photocycle of ESR K96A mutant, which showed very slow M-accumulation at 12 ms at pH 7.6 (Balashov et al. 2012). The timing of the $H^+$ uptake and release in ESR was

investigated by pH-indicating dyes, and the former precedes the latter (Balashov et al. 2013, 2012; Petrovskaya et al. 2010). While the $H^+$ release occurs at the last stage of the photocycle, that is the N-decay, the rate of $H^+$ uptake is very close to the M-decay. Although this makes difficult to reveal whether $H^+$ uptake or RSB reprotonation is faster, the photocycle in $D_2O$ showed the former is significantly faster than the latter (Balashov et al. 2013). On the basis of these spectroscopic results, the order of $H^+$ transfer events in the ESR photocycle is determined as (1) the deprotonation of RSB (L→M), (2) $H^+$ uptake from the bulk to the cytoplasmic donor, (3) reprotonation of RSB from the donor (M→N), and (4) proton release to EC side. While the amplitude of M-accumulation of ESR WT sigmoidally depends on the external pH which is well reproduced by a Henderson-Hasselbalch equation with a pKa of 8.8, the pKa shifted to 6.3 for ESR H57M with the acceleration of the rate of M-accumulation (Balashov et al. 2012). The pKa of the latter coincides with that of the titration of full-protonation of Asp85 in the H57M mutant in the dark. In contrast, Asp85 in the wild type is deprotonated over wide pH range (pH 2–10.5). The photo-isomerization of retinal would disrupt the interaction between Asp85 and His57 leading to the increase of pKa of Asp85 and the $H^+$ transfer from RSB (Petrovskaya et al. 2015).

In this scheme, the strong candidate for the cytoplasmic (CP) proton donor is Lys96 present at the position of acidic proton donor in other typical proton pumps (they are mostly acidic residues, that is, Asp or Glu). The X-ray crystallographic structure suggests that Lys96 is mostly surrounded by hydrophobic residues except for Thr43 (Fig. 6.5b). The pKa of Lys96 is expected to be lowered in this hydrophobic environment resulting in the deprotonation (Balashov et al. 2013). Although the side chain of Lys96 shows different orientations in each molecule in the asymmetric crystal unit, one of them (chain A in PDB ID: 4HYJ) forms hydrogen-bonding network with the main chain of Lys225 via two water molecules (Fig. 6.5b). Compared to the proton donor in the structures of other proton pumping rhodopsins, Lys96 is located closer to the cytoplasmic surface of the protein, and it is separated from the bulk by only Thr43. The mutation of Lys96-to-alanine (ESR K96A) drastically decelerated the reprotonation process of RSB (the M-decay) by more than two orders of magnitude (Balashov et al. 2013). Furthermore, since the rate of M-decay of ESR K96A linearly depends on external $H^+$ concentration indicating direct $H^+$ binding to RSB bulk water in this mutant, Lys96 has been demonstrated as the CP-$H^+$ donor in ESR. The slope of pH dependence of the rate of M-decay of ESR K96A is less than 1 (~0.5). On the other hand, it is expected to be 1 if $H^+$ is directly taken up from the bulk to RSB. This deviation is proposed to be caused by the change in the surface charge at different pH (Dioumaev et al. 2013; Miller and Oesterhelt 1990). Based on the hydrophobic environment around Lys96 and the timing of $H^+$ uptake, this residue is considered to be deprotonated in the dark state and protonated after the formation of the M through putative opening of the CP side of protein as observed in several microbial rhodopsins immediately leading to the reprotonation of RSB (Radzwill et al. 2001; Wegener et al. 2000). The difference of Lys96 from acidic donors in other $H^+$ pumping rhodopsins results in the difference in the order of $H^+$ transfer. That is, whereas the $H^+$ transfer to RSB is faster than the $H^+$ uptake from CP milieu for the latter, the order is reverted for ESR which have initially deprotonated proton donor. However, although the expected large change in the pKa of Lys96 by the opening of hydrophobic cavity upon light activation strongly implies that it is directly related to the $H^+$ transfer, the possibility is not excluded that water molecule (s) around this residue act as proton donor without protonation change of Lys96. A recent study by the time-resolved measurement of light-induced electric potential ($\Delta\Psi$) suggested that ~90% of total $\Delta\Psi$ produced by $H^+$ transport by ESR WT is generated during the latter half of the photocycle ($M_{400} \leftrightharpoons N_{580} \leftrightharpoons N_{605} \leftrightharpoons N_{537}$ (O)→ESR)

which is consistent with the $H^+$ transfer processes observed by spectroscopic study at the same stage of the photocycle (Siletsky et al. 2019). In contrast, the large reduction of total $\Delta\Psi$ by the K96A mutation (~7–10 times smaller than that in the WT) suggests that the Lys96 mutation causes not only the M-decay deceleration but also back $H^+$ transfer from protonated Asp85 to RSB without generating membrane potential (Siletsky et al. 2019). Although the back $H^+$ transfer seemingly contradicts the linearly pH-dependent reprotonation of RSB and further study is required to unify them, this result indicates that Lys96 is important not only for fast reprotonation of RSB but also unidirectional $H^+$ transport in ESR.

### 6.2.4 Other Types of Proton Pumps

The diverse genomic and metagenomic analyses revealed more microbial rhodopsin groups not only from prokaryotes but also from many eukaryotes. The first eukaryotic microbial rhodopsin was identified in the genome in *Neurospora crassa*, and it was named *Neurospora* rhodopsin (NR) (Bieszke et al. 1999a). Based on the long photocycle whose turnover rate is several seconds, NR is considered to have a function of photo-sensor (Bieszke et al. 1999b; Brown et al. 2001). Another fungal rhodopsin gene, LR, was found in *Leptosphaeria maculans* (Idnurm and Howlett 2001), and it was expressed in *Pichia pastoris* and characterized (Waschuk et al. 2005). The photocycle of LR is significantly faster than that of NR, and LR reconstituted liposomes show an active proton transport. The transient absorption change of pH-indicating dye pyranine suggested LR first take up and then release an $H^+$ during the M- and O-decay, respectively. This is opposed to that of BR (Fig. 6.3) and same as bacterial $H^+$ pumps. Despite of this kinetic similarity to bacterial $H^+$ pumps, LR likely has homologous carboxylic residues at the positions of PRG of BR which is absent in eubacterial $H^+$ pumps (Glu194 and 204 in BR are replaced with Asp248 and Glu258 in LR). One of the structural origin of the large difference in the turnover rate between LR and NR is considered to be the difference in the type of $H^+$ donor at the BR's Asp96 position, which is occupied by Asp150 and Glu142 in LR and NR, respectively. Indeed, the mutation of LR Asp150 to a glutamic acid (corresponding to the motif conversion from DTD to DTE) decelerated the M decay ca. two orders of magnitude and made it rate-limiting step in the photocycle (Fan et al. 2007; Furutani et al. 2006b).

Now, several hundreds of rhodopsin-like proteins are identified in fungal species. Interestingly, significant part of them lost essential retinal binding lysine in the helix G, and they likely do not show visible absorption. These rhodopsin-like genes without the lysine are called "opsin-related proteins (ORPs)" (Bieszke et al. 1999a; Brown 2004). On the other hand, Dr. Brown and coworkers (2011) reported another type of fungal rhodopsin group different from the clade including NR and LR (Fan et al. 2011). Because most of the members of this new group are usually present with rhodopsins in different group, they are named "auxiliary" rhodopsins. The first biophysical study on auxiliary rhodopsin was conducted for the protein from *Phaeosphaeria nodorum*. *P. nodorum* has two rhodopsins, PhaeoRD1 and PhaeoRD2, which belong to the same group as NR and LR and auxiliary group, respectively. PhaeoRD1 and RD2 heterologously expressed in *Pichia pastoris* showed their absorption maxima at almost identical wavelength (540 and 530 nm, respectively, in DDM and 545 and 538 nm, respectively, in yeast membrane). Also, the photocycles of them are also similar to each other and both finish within 100 ms. Although the $H^+$ transport activity of auxiliary PhaeoRD2 has not been investigated yet, the fast photocycle implies it also pumps proton as LR. Interestingly, despite both of them conserving most functionally important residues in BR (e.g., Thr46, Tyr57, Arg82, Asp85, Thr89, Thr90, Asp96, Asp115, Trp182, Tyr185, Trp189, Glu204, Asp212) including the DTD motif, the rate of the M-decay corresponding to retinal reprotonation was almost linearly slowed down at higher pH. This implies direct proton uptake from the CP-side bulk solvent and lower pKa of

their proton donors (Asp145 and Asp126 in PhaeoRD1 and PhaeoRD2, respectively) compared to BR Asp96. The structural change upon photo-activation was investigated by FTIR spectroscopy (Fan et al. 2011; Ito et al. 2012). Although PhaeoR2 is phylogenetically almost equally separated from LR and BR (identities are 34.5 and 30.2% for PhaeoR2-LR and PhaeoR2-BR, respectively), the FTIR spectra of PhaeoRD2 representing structural change were identical to those of LR, but not to BR (Ito et al. 2012). Hence, regardless of the evolutionary distance, the PhaeoRD2 shares more identical structural features with LR and PhaeoRD1 than BR. Also, the FTIR spectra of the M-state are quite similar between PheaoRD1 and PhaeoRD2 (Fan et al. 2011). These results suggest that this auxiliary rhodopsin has almost identical molecular function and photochemical property as LR and PhaeoRD1. However, an interesting feature in their primary structure was found in the middle of the helix D where a characteristic glutamic acid is found, unique for the auxiliary rhodopsins. Since this glutamic acid (PhaeoRD2 Glu146) is just behind an aspartic acid corresponding to BR Asp115, it is expected to be oriented to lipid bilayer. Such conserved hydrophilic residue facing outside of TM part is reminiscent of conserved tyrosine in sensory rhodopsin II which forms an intermolecular hydrogen bond with cognate transducer (Gordeliy et al. 2002; Sudo et al. 2006), implying the possibility of the presence of unidentified interaction partner to auxiliary rhodopsin or the intermolecular interaction with rhodopsin in another group including LR and PhaeoRD1.

Plant pathogen *Fusarium fujikuroi* has NR-like (OpsA) and auxiliary (CarO) rhodopsins (García-Martínez et al. 2015). While OpsA does not show ion-transport activity, electrophysiology experiment indicated that CarO has outward $H^+$ pump function. Interestingly, the $H^+$ pump activity of CarO is increased in the presence of acetate or indole-3-acetic acid (IAA). Since IAA is a plant hormone, the increased $H^+$ pump activity of CarO would be related in the fungus–plant interaction (Adam et al. 2018). The CarO-deficient mutant of *F. fujikuroi* (*carO*$^-$) showed faster germination than that of *carO*$^+$ control strain, suggesting CarO has a physiological role to retard spore germination (García-Martínez et al. 2015).

While many cation and anion channels were reported in diverse algal species, the number of ion-pumping rhodopsins are not so high. Among them, the first algal $H^+$ pump rhodopsin was identified from marine giant unicellular green algae *Acetabularia acetabulum* in 2006 by Dr. Hegemann and coworkers (Tsunoda et al. 2006). The light-induced response of transmembrane voltage in *Acetabularia* cells was reported in 1968, and it was demonstrated that rhodopsin is related to the photo-response. In 2004, the cDNA library of juvenile phase of *A. acetabulum* was reported, and a putative microbial rhodopsin gene was included (Henry et al. 2004). The *Acetabularia* rhodopsin (AR) expressed in *Xenopus* oocyte showed robust outward photocurrent over wide membrane-potential range representing outward $H^+$ transport (Tsunoda et al. 2006). The first cloned AR was 279 amino acid protein ($AR_{1–279}$), and C-terminal truncated construct ($AR_{1–235}$) also pumps $H^+$. However, the further cloning taking into account of frame-shift correction in the C-terminal region and termination codon usage in *Acetabularia* (only TGA was used as termination codon) revealed one $H^+$ pumping *Acetabularia* rhodopsin (abbreviated as ARI) and another *Acetabularia* rhodopsin gene (ARII) (Lee et al. 2011; Wada et al. 2011). While the amino acid sequence of ARI is almost identical to $AR_{1–235}$ except for the 212th residue which is Val and Ile in $AR_{1–235}$ and ARI, respectively, and identical $H^+$ transport activity was observed (Lee et al. 2011), the sequence of ARII is significantly different from AR suggesting *A. acetabulum* has two different rhodopsin genes.

ARII was also revealed to have outward $H^+$ pump function in *Xenopus* oocytes and its crystallographic structure, which is the first structure of eukaryotic microbial rhodopsin, was solved in 2011 at 3.2 Å (Wada et al. 2011). The structure indicated that the orientation of Arg78 is opposed to that of homologous BR's Arg82. This difference in the orientation of the arginine and the loss of BR's Glu194 in ARII which is replaced with

Ser (ARII's Ser189) results in the putative absence of water molecules around Glu199 which is homologous to BR's Glu204 (Wada et al. 2011). The order of $H^+$ uptake and release of ARII depend on pH. That is, whereas the $H^+$ uptake occurs faster than the release at pH $< 7$, it is reversed at pH $> 7$ (the release precedes the uptake) (Kikukawa et al. 2011). The flash photolysis measurements and time-resolved observation of $H^+$ uptake and release over a wide pH range from pH 2.5 to 11.0 revealed several pKas of various residues: pKa 2.6, 5.6 (6.3), 8.4, 9.3, and 10.5 corresponding to pKa of Asp81 (homologous to BR Asp85) in the dark state, Asp92 in the N state, Glu199 in the M state, Glu199 in the dark state, unidentified proton releasing residue at the release, respectively, and the protein begins to denature at pH $> 11.3$ (Kikukawa et al. 2011). Interestingly, ARII has a cysteine (Cys218) at the position of BR's Leu223, and it forms an inter-helical hydrogen bond with proton donor Asp92 in the crystal structure (Wada et al. 2011). The disruption of this hydrogen bond by the mutations C218A and C218S resulted in the slower photocycle than that of the WT (Tamogami et al. 2018). Especially, the $H^+$-uptake in parallel with the N-decay is highly decelerated in these mutants. Therefore, the inter-helical interaction between Cys218 and Asp92 is demonstrated to be important for the efficient $H^+$ uptake in ARII.

The spectroscopic study of ARI was reported in 2015 for the protein which was expressed in *E. coli* with fused Mistic ("membrane-integrating sequence for translation of integral membrane protein constructs") protein on the both N- and C-terminal sides and regenerated after the cleavage of Mistic proteins by Factor X protease (Lee et al. 2015). The K, M, and O intermediates were observed in the ARI photocycle, and the M-decay was highly slowed at higher pH (pH 9.0) or upon the mutation of $H^+$ donor. Then, the flash photolysis measurement with higher time-resolution for ARI expressed by *P. pastoris* observed one order of magnitude faster M-formation compared to that in BR (Furuse et al. 2015). In 2015, the three-dimensional structure of ARI was solved at high resolution of 1.52–1.80 Å (Furuse et al. 2015). The high-resolution structure revealed the presence of many bound waters in ARI. In the active site, a pentagonal cluster consisting of three water molecules and two counterions (Asp89 and Asp214) is interacting with RSB as in BR (Luecke et al. 1999; Matsui et al. 2002). This suggests that ARI is closer to archaeal $H^+$ pumps than bacterial ones. A cytoplasmic inter-helical interaction is also present between the main-chain carbonyl of Leu97 (homologous to BR's Leu93) in helix C and Tyr221 (homologous to BR's Phe219) in helix G in ARI, but the position is different from the interaction between Asp92 and Cys218 in ARII. In contrast to the slower photocycle of Cys218 mutants of ARII compared to the WT, the disruption of the inter-helical interaction in ARII by the mutation of Tyr221-to-Phe three times accelerates the turnover rate of the photocycle. This indicates the different roles of inter-helical interaction in the photocycle turnover between ARI and ARII. Also, the pKa of proton donor (ARI's Asp100) is highly lowered in the ARI Y221F mutant, implying another role of the inter-helical interaction to regulate the pKa of Asp100 in the dark state (Furuse et al. 2015).

Another algal $H^+$ pump, CsR, was found in arctic Chlorophyta *Coccomyxa subellipsoidea* C-169 (Vogt et al. 2015). The amino acid sequence of CsR shows 37% homology with BR, and all residues in BR critical for the $H^+$ pump function are conserved. CsR, probably due to its eukaryotic origin, is better expressed in *Xenopus* oocytes and mammalian cells, and exhibits higher membrane transfer efficiency and extremely larger photo-currents compared to archaeal and bacterial $H^+$ pumps. The western blot analysis for the total cell lysate of *C. subellipsoidea* C-169 cells indicated that CsR is mostly present as dimer, and it is localized in the plasma membrane of the cells shown by the anti-CsR imaging (Ranjan and Kateriya 2018). Dr. Hegemann and coworkers found that the mutations of CsR's Arg83 (homologous to BR's Arg82)-to-Gln (CsR R83Q) convert the $H^+$ pump function to the inwardly rectified $H^+$ channel at outer pH ($pH_O$) 5.0. By contrasts, CsR's Tyr57 (homologous to BR's Tyr57)-to-Lys (CsR Y57K) mutant shows outwardly rectified $H^+$ channel at

$pH_O$ 10.0 (Vogt et al. 2015). The double mutant (CsR T57K/R83Q) shows inwardly and outwardly rectified $H^+$ current at $pH_O$ 5.0 and 10.0, respectively, but the conductance is smaller than those of single mutants. The X-ray crystallographic structure of CsR indicated that CsR's Arg83 forms a hydrogen bond with characteristic Tyr14 at the position of BR's Leu13. The mutation of Tyr14-to-Glu (CsR Y14E named "CySeR") guided by the structural insight led non-rectified photo-current at natural $pH_O$ (Fudim et al. 2019). These results suggest that the dynamic motion of CsR's Arg83 plays a role to prevent passive $H^+$ conductance during $H^+$ pumping photocycle.

While ARI, ARII, and CsR are phylogenetically close to fungal $H^+$ pumps (Fig. 6.1), dinoflagellates *Oxyrrhis marina* and *Karlodinium micrum* have other types of rhodopsins similar to XRs and PRs, respectively (Slamovits et al. 2011). One of XR-like rhodopsin in *O. marina* (OR1, Acc. No. ABV22426) conserves many characteristic residues in TM2 of XRs and indeed shows outward $H^+$ pump function (Janke et al. 2013). These XR and PR-like rhodopsins in dinoflagellates are thought to be acquired from marine bacteria by lateral gene transfers (Slamovits et al. 2011).

In all outward $H^+$ pumping rhodopsins, titratable residues (Asp, Glu or Lys) are present at the position of BR's Asp96. However, recently a new group conserving a glycine at this position was found. They were referred to as "DTG rhodopsins" (Harris et al. 2015; Sudo and Yoshizawa 2016). Although >30 bacterial species have the protein in this group (Harris et al. 2015), only three DTG rhodopsins from *Pseudomonas putida* (*Psp*R), *Pantoea ananatis* (*Pa*R), and *Pantoea vagans* (*Pv*R) were biophysically characterized (Harris et al. 2015; Sudo and Yoshizawa 2016). Despite the lack of the titratable donor, all of them showed outward $H^+$ pump activity in *E. coli* cells. However, the rate of reprotonation of RSB (the M-decay) was linearly slowed down as pH increased for *Psp*R and *Pv*R. This indicates direct protonation of RSB from the cytoplasmic bulk and looks consistent with the lack of general $H^+$ donor. However, all DTG rhodopsins have a highly conserved histidine, which possibly works as the $H^+$ donor, at the position of BR Thr46 on the cytoplasmic side of helix B along the putative $H^+$-uptake pathway. Although the mutation of this histidine in *Psp*R to arginine or tyrosine (*Psp*R H37R and H37Y) indeed highly slowed the M-decay compared to the WT (Harris et al. 2015), suggesting the importance of the histidine for the $H^+$-uptake, another mutation to a non-titratable residue such as asparagine (*Psp*R H37N) did not alter the M-decay. Therefore, the role of histidine as a new type $H^+$-donor is still controversial. To reveal how these histidines are related to the $H^+$-uptake process in DTG rhodopsins, their three-dimensional atomic structures should be revealed.

Recently, several giant viruses that infect algae and choanoflagellates were found to have distinct microbial rhodopsins, viral rhodopsins (VirR) different from the rhodopsins of cellular organisms (Needham et al. 2019; Philosof and Béjà 2013). In 2019, a VirR ($VirR_{DTS}$) derived from a genome of haptophyte algal species (*Phaeocystis globosa*) and having a DTS motif was shown to have an outward $H^+$ pumping function by the functional assay for heterologously expressed protein in *E. coli* (Needham et al. 2019). While the overall structure of $VirR_{DTS}$ is similar to other microbial rhodopsins (root-mean-square deviation (RMSD) from BR structure is 1.83 Å (Needham et al. 2019)), it has a short helix in the cytoplasmic loop between the helices C and D and no inter-helical β-sheet which is usually observed in other pumping rhodopsins (Fig. 6.2). The photocycle of $VirR_{DTS}$ shows large accumulation of the O intermediate, and the $H^+$ release occurring in the K-to-L transition precedes the $H^+$ uptake. This is significantly different from the photocycles of other $H^+$-pumping rhodopsins suggesting a new $H^+$ pumping mechanism by $VirR_{DTS}$.

### 6.2.5 Inward Proton Pumps: Xenorhodopsins

Most of ion-pumping rhodopsins transport cations and anions outward and inward,

respectively (Fig. 6.2). This rule is likely to be biologically beneficial since they hyperpolarize the membrane and provide chemical driving force for ATP synthesis and transport processes. In contrast, Kawanabe et al. found that an artificial mutant of *Anabaena* sensory rhodopsin (ASR) transports $H^+$ inwardly (Kawanabe et al. 2009). In this study, an aspartic acid in the helix G was replaced with a glutamic acid (ASR D217E). The natural function of ASR is suggested to be light-dependent regulation of expression of various light-harvesting proteins and proteins related to the circadian clock via cognate-soluble transducer protein ($ASR_T$) (Irieda et al. 2012; Jung 2007). ASR does not show regular photocyclic reaction as other microbial rhodopsins, but all-*trans* and 13-*cis* retinals are interconverted by photo-excitation of each of them (photochromism) (Kawanabe et al. 2007; Sineshchekov et al. 2005). Recently, many homologues close to ASR were identified, and this group is referred to as "xenorhodopsins (XeRs)" (Ugalde et al. 2011). XeRs are found not only in cyanobacteria but also in other bacterial phyla (Firmicutes, Bacteroidetes, and Tenericutes) and some archeal phyla such as Euryarchaeota and Nanohaloarchaea. XeRs can be distinguished by a proline at the position of Asp212 in BR, which is one of the most conserved residues in microbial rhodopsins (Ernst et al. 2014). Despite the similarity to ASR, the genes of most other XeRs do not form an operon with $ASR_T$ homolog. This suggests that the function of other XeRs might be different from ASR.

After a couple of years from the first proposal of XeRs as a new class, XeR from α-proteobacteria, *Parvularcula oceani*, (*Po*XeR) was revealed to have light-driven inward $H^+$ pump function (Inoue et al. 2016a). Dr. Sudo and coworkers also identified another XeR homolog from *Rubricoccus marinus* $SG29^T$ (*Rm*XeR) (Inoue et al. 2018b). Moreover, Dr. Gordeliy and coworkers also reported three other XeRs (*Ns*XeR, *Hrv*XeR, and *Alk*XeR), along with the crystallographic structure of *Ns*XeR (Shevchenko et al. 2017b). These results suggest that XeRs are a widely conserved family of light-driven inward $H^+$ pumps. Although ASR WT does not show any $H^+$ transport in *E. coli* cells (Jung et al. 2003) in contrast to XeRs, the functional conversion of it to the artificial inward $H^+$ pump with a single amino acid mutation (ASR D217E) implies that the dynamic structural changes and the most of $H^+$-translocating pathways are conserved between ASR and other XeRs without cognate-soluble transducer protein (Kawanabe et al. 2011).

The photocycles of several XeRs are compared with ASR in Fig. 6.6. They are composed of photo-intermediates similar to those in BR photocycle (K, L, M, and O). However, the N intermediate is not observed in the photocycles of ASR and XeRs. The most characteristic point of ASR and XeR's photocycles is the 15-*anti*-to-*syn* isomerization generating long-lived intermediate having 13-*cis*-15-*syn* retinal (ASR13C, $PoXeR_{13C}$, and $RmXeR_{13C}$), except for *Ns*XeR (Inoue et al. 2016a, 2018b; Shevchenko et al. 2017b; Sineshchekov et al. 2005). By the lack of 13-*cis*-15-*syn* state, *Ns*XeR shows remarkably fast turnover rate enabling a generation of large photo-current in mammalian cells. Also *Ns*XeR expressed in rat hippocampal neurons is able to induce high repetitive action potentials at 40 Hz showing its potential as a new type of excitatory tool in optogenetics (Shevchenko et al. 2017b).

The functional conversion of ASR by the D217E mutation suggests the importance of this residue for inward $H^+$ transport (Kawanabe et al. 2011). This aspartic acid is conserved in all XeRs (Shevchenko et al. 2017b), and homologous mutant of *Po*XeR (*Po*XeR D216E) showed about three times larger transport activity than the WT (Inoue et al. 2016a). FTIR spectroscopy and transient absorption measurement with pH-indicating dye (pyranine) revealed that an $H^+$ is transferred to Asp216 from RSB and then it is released into the cytoplasmic solvent upon the M-formation (Inoue et al. 2016a, 2018a). Similarly Glu217 in ASR D217E was also shown to receive an $H^+$ upon the M-formation (Kawanabe et al. 2011; Shi et al. 2006). Strongly hydrogen-bonded water (SHBW) was observed by FTIR spectroscopy for *Po*XeR, but it was not present in ASR (Ito et al. 2017). Kandori and coworkers reported SHBW is the structural

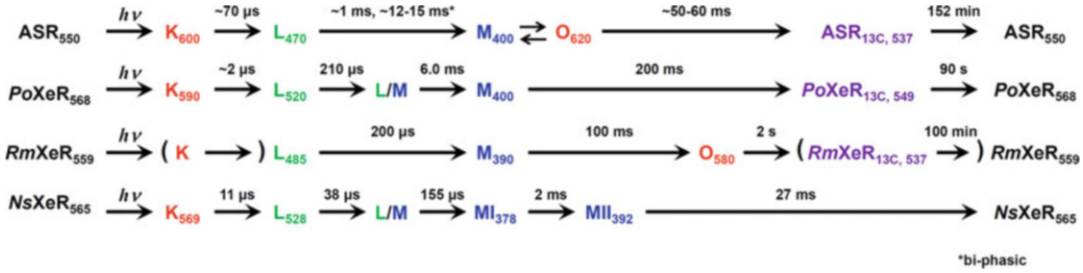


**Fig. 6.6** The photocycles of ASR and XeRs. The absorption wavelengths and lifetimes are based on Refs. (Inoue et al. 2016a, 2018b; Shevchenko et al. 2017b; Sineshchekov et al. 2005), and the former are shown as subscripts after the name of each state. Although the K intermediate of *Rm*XeR is not observed by flash photolysis measurement probably due to a faster decay than the time resolution (Inoue et al. 2018b), it is expected to be present in analogy to other XeRs and microbial rhodopsins. In addition, the direct recovery from $O_{580}$ to the initial state was suggested in the photocycle of *Rm*XeR (Inoue et al. 2018b). However, because a 13-*cis* form (*Rm*XeR$_{13C,\ 537}$) with long lifetime (100 min) was observed in the light-adapted protein, at least partly, $O_{580}$ is expected to be converted to *Rm*XeR$_{13C,\ 537}$ as in ASR and *Po*XeR

determinant for outward $H^+$ transport (Muroda et al. 2012), and the SHBW observed in *Po*XeR might be related to the functional difference between *Po*XeR and ASR.

In contrast to the $H^+$ release, the understanding of $H^+$-uptake process in XeRs is complicated. Based on the fact that the rate of RSB reprotonation (that is the decay of M) of *Po*XeR is pH-independent, the presence of unidentified proton donor was first suggested (Inoue et al. 2016a). However, any mutations of putative $H^+$-donating residues on the extracellular side (Glu3, Asp119, and Arg71 in *Po*XeR) does not substantially change the $H^+$ uptake process (Inoue et al. 2016a, 2018a), and the time evolution of the proton uptake from the outer solvent coincides with the M-decay representing protonation of RSB, indicating $H^+$ is directly transferred to RSB from the solvent (Inoue et al. 2018a). Interestingly, while the rate of $H^+$-release shows large (~8) kinetic isotope effect (KIE) between $H_2O$ and $D_2O$, it is smaller (~1.7) for $H^+$-uptake process and close to KIE of $H^+$ diffusion in bulk water (Inoue et al. 2018a). The pH-independent M-decay without $H^+$ donating residue implies that there is a rate-limiting process for the $H^+$-uptake from the outer solvent, and it is considered to be branched retinal isomerization to all-*trans*-15-*anti* and 13-*cis*-15-*syn* configurations which change the direction of lone electron pair of N atom of deprotonated RSB from the cytoplasmic to the extracellular side (Inoue et al. 2018a).

On the basis of these insights, the mechanism of inversion of vectorial $H^+$ transport between BR and XeR is explained as in Fig. 6.7. BR has two counterions, and they increase the probability of $H^+$ movement toward the extracellular side (arrow 1 in Fig. 6.7) compared with XeR in which Asp212 of BR is replaced with a proline. Furthermore, the crystal structure of ASR D217E (Dong et al. 2016) suggests that the cytoplasmic halves of XeRs are more hydrophilic than of BR, with several internal water molecules, which makes the conserved aspartic acid (*Po*XeR Asp216) deprotonated to work as the proton acceptor for RSB (arrow 3). Then, different proton uptake processes occur in BR and XeR. For the former, initially protonated Asp96 in the hydrophobic cytoplasmic region donates an $H^+$ to RSB via a transiently formed internal water chain (arrow 2) (Chen and Lanyi 2009; Weinert et al. 2019). In contrast, 13-*cis*-to-all-*trans* or 15-*anti*-to-15-*syn* isomerization occurs in XeR, changing the direction of RSB to accept an $H^+$ from the extracellular side (arrow 4). These mechanistic insights about the structural determinants of vectorial direction of ion transport would provide a new basis for the design of novel artificial optogenetic tools.

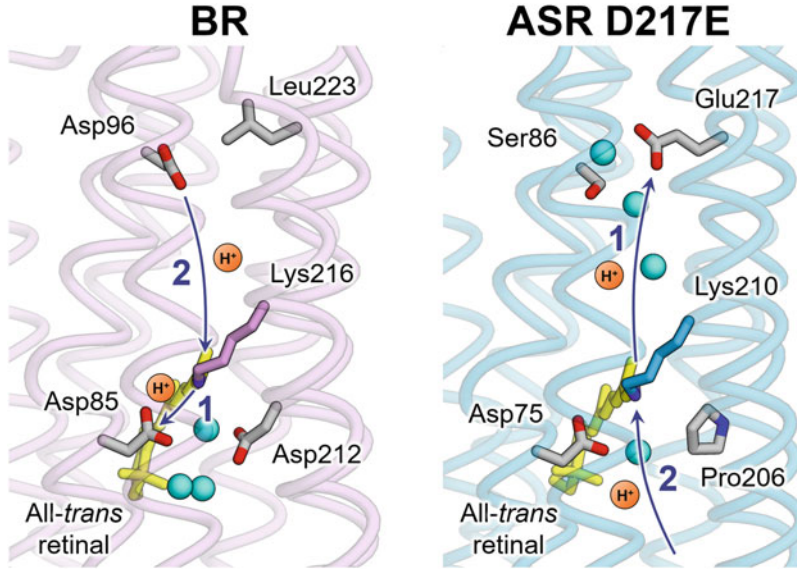


**Fig. 6.7** Schematic comparison between outward $H^+$ pumping by BR and inward $H^+$ pumping by XeR. The structure of XeR is based on the crystallographic structure of BR (PDB ID: 1IW6 (Matsui et al. 2002)) and ASR D217E (PDB ID: 4TL3 (Dong et al. 2016)). Arrows indicates the $H^+$ transfer between RSB and carboxylic residues or outer solvent

Recently, a new family of microbial rhodopsins, called schizorhodopsins (SzR), was found in the genome of Asgard archaea (Bulzu et al. 2019). Although SzR is phylogenetically distinct from other ion-transporting microbial rhodopsins, it functions as light-driven inward $H^+$ pump as XeR (Inoue et al. 2020). Also, a novel class of SzR, AntR, which also shows inward $H^+$ pump activity, was found in metagenomic sequences obtained in Antarctic freshwater lakes (Harris et al. 2020). Interestingly, SzR and AntR have a phenylalanine at the position homologous to BR Asp85 so that single counterion is present at the position of BR Asp212 in the helix G. Whereas XeR has the cytoplasmic $H^+$ acceptor in the helix G, mutational study on SzR suggested that Glu81 of SzR which is homologous to BR's Asp96 in the helix C accepts an $H^+$ from RSB. By contrast, the mutation of the same glutamate in AntR accelerated rather than inhibited $H^+$ release (Harris et al. 2020). These different effects of the mutation of the cytoplasmic glutamate suggest the different ion release mechanism between SzR and AntR despite of their sequential similarity (ca. 34% identity and 57% similarity). Although both XeR and SzR share a common architecture consisting of a single counterion and deprotonated cytoplasmic acceptor, their positions are swapped between the helices C and G.

## 6.3 Inward Chloride Pumps

### 6.3.1 Halorhodopsins

Since Dr. Engelhard et al. presented a comprehensive review on HR recently (Engelhard et al. 2018) and new types of rhodopsins are the main focus of this review, here the previous research on HR will be only briefly summarized to construct a basis for the comparison with the other inward $Cl^-$ pumps. HR was first identified in *H. salinarum* by Dr. Mukohata and coworkers in 1977 (Matsuno-Yagi and Mukohata 1977), and its light-driven inward chloride pump function was characterized by Drs. Lanyi and Schobert in 1982 (Schobert and Lanyi 1982). While halorhodopsin from *H. salinarum* (*Hs*HR) also transports $Br^-$ with efficiency almost equivalent to $Cl^-$ (Hazemoto et al. 1984), it shows negligible or weak transport of $NO_3^-$ (Duschl et al. 1990; Hazemoto et al. 1984; Schobert and Lanyi 1982). Homologous protein was also identified in another halophilic archaeon,

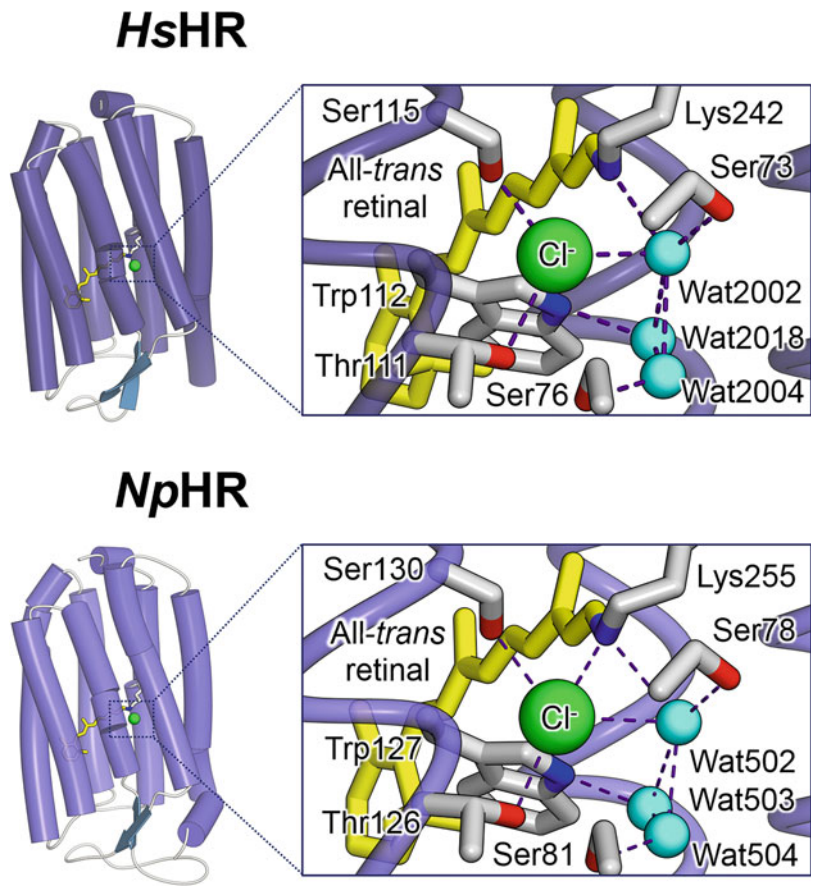


**Fig. 6.8** The crystallographic structures of *Hs*HR (upper, PDB ID: 5AHY (Schreiner et al. 2015)) and *Np*HR (lower, PDB ID: 3A7K (Kouyama et al. 2010)). The expanded view of $Cl^-$-binding sites near RSB is also shown. Putative hydrogen bonds whose distance is less than 3.5 Å are shown (indigo dash lines)

*Natronomonas pharaonis* (formally known as *Natronobacterium pharaonis*), and it is called *pharaonis* halorhodopsin (*p*HR or *Np*HR) (Lanyi et al. 1990). Although the identity of amino acid sequences between *Np*HR and *Hs*HR is high (52.4% identity), it shows $NO_3^-$ transport identical to that of $Cl^-$ (Duschl et al. 1990). Based on the transport ability for various anion species, HRs are referred as light-driven "anion" or "halide" pumps.

X-ray crystallographic structures of both *Hs*HR and *Np*HR were reported (Kolbe et al. 2000; Kouyama et al. 2010; Schreiner et al. 2015). Their structures are similar to each other, and $Cl^-$ is bound in identical position near RSB in both of them (Fig. 6.8). $Cl^-$ interacts with threonine and serine of the TSA motif (Thr112 and Ser115 in *Hs*HR and Thr126 and Ser 130 in *Np*HR) and a water molecule. These interactions are thought to be essential to capture $Cl^-$ from extracellular milieu, and dissociation constant of $Cl^-$ in *Np*HR was reported to be 1–3 mM (Scharf and Engelhard 1994; Váró et al. 1995a). Note that a different structure of *Hs*HR (PDB code: 1E12) in which the O–H group of Thr111 is not oriented toward $Cl^-$ was also reported (Kolbe et al. 2000), suggesting the structural flexibility of this residue. Dr. Kouyama and coworkers reported a crystallographic structure of *Np*HR in the membrane of HR-overexpressing mutant of *N. pharaonis* (strain KM-1) by membrane fusion method (Ihara et al. 2008; Kouyama et al. 2010). It showed trimetric assembly of *Np*HR with three carotenoid (bacterioruberin) molecules in crevices between adjacent *Np*HR protomers (Kouyama et al. 2010). This is reminiscent of the binding of salinixanthin in XR, but no efficient energy transfer is thought to occur between

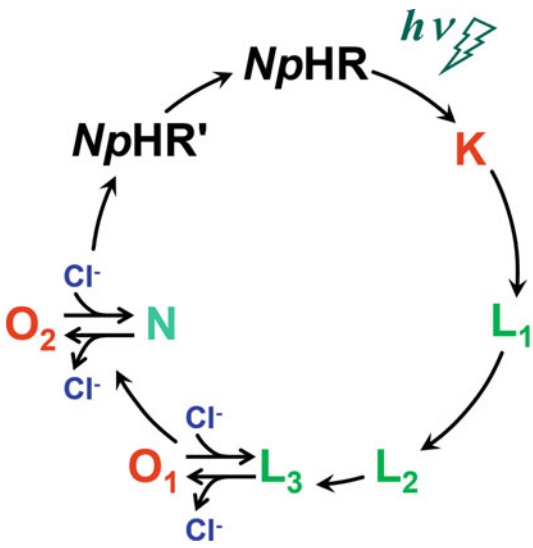


**Fig. 6.9** The photocycle of *Np*HR

the bacterioruberin and the retinal in *Np*HR (Kouyama et al. 2010).

The photocycles and their respective intermediates for *Hs*HR and *Np*HR were reported by several groups (Chizhov and Engelhard 2001; Duschl et al. 1990; Lanyi and Vodyanoy 1986; Oesterhelt et al. 1985; Sato et al. 2003, 2005; Schobert et al. 1983; Váró et al. 1995a, b, c; Zimányi et al. 1989), and the latter was more extensively studied because it shows no light–dark adaptation and is more easily expressed in *E. coli* cells. Although slight differences in the annotation of the photo-intermediates, absorption wavelengths, rate constants, and so on are present between each study, the overall photocycle of *Np*HR is summarized as shown in Fig. 6.9.

Three spectrally identical L intermediates ($L_1$, $L_2$, and $L_3$) are observed in many studies of the photocycle, and the $L_2$ is suggested to represent the state in which $Cl^-$ moved from the initial binding pocket to the cytoplasmic side (Shibata et al. 2005). X-ray crystallographic analysis for cryogenically trapped N intermediate (which shows blue-shifted absorption at ~520 nm and was suggested to be the same intermediate as $L_3$ (Engelhard et al. 2018)) revealed that a water channel is formed in the $Br^-$-transporting photocycle between $Br^-$ and the Lys215 in helix F in the cytoplasmic side (Kouyama et al. 2015). $Cl^-$ is considered to be released to the cytoplasmic milieu through this water channel. The structural change from the cytoplasmic-opened state to extracellular-opened state is thought to occur on $L_3 \leftrightharpoons O_1$ to $O_2 \leftrightharpoons N$ (Chizhov and Engelhard 2001; Engelhard et al. 2018).

The $Cl^-$ influx by HR hyperpolarizes the membrane, and *Np*HR expressed in hippocampal neurons can inhibit spiking in a light-dependent manner (Zhang et al. 2007). However, *Np*HR WT aggregates in endoplasmic reticulum (ER) when it is highly expressed. The *Np*HR fused with signal peptide derived from nicotinic acetylcholine receptor and ER-export signal from Kir2.1 on N- and C-termini, respectively (eNpHR), overcame this difficulty, and eNpHR is highly localized in the plasma membrane, enabling more efficient neuronal inhibition (Gradinaru et al. 2008). Since the $\lambda_{max}$ of *Np*HR is 577 nm, it can be activated by yellow light, and multimodal optogenetic control is possible in combination with blue-absorbing ChRs (Zhang et al. 2007). eNpHR was successfully applied for many animal systems such as mouse (Kaneda et al. 2011), zebrafish (Arrenberg et al. 2009), *Drosophila* larvae (Mattingly et al. 2018), and so on, and it is one of the most powerful inhibitory ion-pumping optogenetics tools which can work in vivo.

### 6.3.2 Bacterial Chloride Pumps

Although thousands of rhodopsins were identified in bacteria after the first report of PR, ion-transporting bacterial rhodopsin other than outward $H^+$ pumps were not found for more than a decade. However, Drs. Yoshizawa, DeLong, and coworkers reported three rhodopsin genes in the genome of marine flavobacterium *Nonlabens marinus* S1-08$^T$: the first and second ones were members of PR and outward $Na^+$ pump subfamilies (see Sect. 6.4) with DTE- and NDQ-motifs, respectively, and the third one (*Nm*ClR) had a new NTQ-motif (Yoshizawa et al. 2014). The ion-transport assay of the third NTQ-rhodopsin revealed its inward $Cl^-$ transport function. There are several homologues with the

same motif (Fig. 6.1), and they are classified as a new inward $Cl^-$ pump family referred "ClR." Other ClRs derived from *Fulvimarina pelagi* (FR) and *Parvularcula oceani* (*Po*ClR) are also reported to have similar $Cl^-$ transporting function (Inoue et al. 2014b, 2016a). The ion specificity of ClR is not so strict, and it transports other monovalent anions ($Br^-$, $I^-$ and $NO_3^-$) as HR (Inoue et al. 2014b; Yoshizawa et al. 2014).

ClRs exhibit a blue-shift of the absorption maximum ($\lambda_{max}$) in the presence of $Cl^-$, as compared to the absence. Based on the $Cl^-$ titration of the $\lambda_{max}$ shift, the dissociation constants of $Cl^-$ ($K_d$) were reported to be 24 and 84 mM for *Nm*ClR and FR, respectively (Inoue et al. 2014b; Tsukamoto et al. 2017). Despite the physiological $Cl^-$ levels for marine flavobacteria being lower (~500 mM) compared to those of halophilic archaea (saturating concentration), these values are higher than those of HRs ($K_d$ = 10 and 1–3 mM for *Hs*HR and *Np*HR (Scharf and Engelhard 1994; Schobert et al. 1986; Váró et al. 1995a), respectively). The photocycle of ClR was investigated for *Nm*ClR and FR so far (Inoue et al. 2014b; Tsukamoto et al. 2017). Both photocycles are basically similar to each other, and the K, L, O states are included. In contrast to the photocycles of *Hs*HR and *Np*HR in which the blue-shifted L intermediate is predominantly observed, large accumulation of the red-shifted intermediates (K and O) occurs in these ClR photocycles. At the last stage of these photocycles, the O is equilibrated with another intermediate (*Nm*ClR′ (also called NM-R3′ in the original paper) and FR′) having absorption identical to the dark state. Because the equilibration between the O and *Nm*ClR′ is shifted to the latter and the rates of O to O/*Nm*ClR′ or O/FR′ transitions increase at higher $Cl^-$ concentration, $Cl^-$ is likely to be taken up from the extracellular side in the O-to-ClR′ process. However, the rates of recovery of the initial state also increase at higher $Cl^-$ concentration, suggesting the existence of another $Cl^-$-uptake process (e.g., $Cl^-$ binding to the $Cl^-$-unbound ClR′).

The X-ray crystallographic structures of *Nm*ClR were reported by two groups in 2016 (Hosaka et al. 2016; Kim et al. 2016). A $Cl^-$ directly forming hydrogen bonds with the RSB and Thr102 (the "T" of the NTQ-motif) was observed in both structures. However, there is a difference in the interaction between $Cl^-$ and Asn98 (the "N" of the NTQ-motif). While the $Cl^-$ is likely to form a hydrogen bond with Asn98 in two structures obtained at pH 6.0 and 4.5 (PDB ID: 5G28 and 5G54, respectively), the distances between $Cl^-$ and Nδ atom of Asn98 are 3.1 and 2.9 Å, respectively (Kim et al. 2016), the distance is 4.0 Å, which is significantly longer than usual hydrogen-bonding length, in another structure (PDB ID: 5B2N (Hosaka et al. 2016)). The direct interaction between $Cl^-$ and RSB is different from *Hs*HR and *Np*HR in which a water molecule is present between $Cl^-$ and RSB (Kolbe et al. 2000; Kouyama et al. 2010) suggesting different ion-transport mechanism. By functional assay of mutant proteins, the several residues which are important for $Cl^-$ transport were identified. Despite the high conservation of the NTQ-motif, the mutants of Asn98 (*Nm*ClR N98A, N98D, N98L, and N98T) and Thr102 (*Nm*ClR T102D and T102V) showed loss of or much larger decrease in the transport activity compared to those of Gln109 (*Nm*ClR Q109E and Q109A) (Hosaka et al. 2016; Kim et al. 2016), suggesting the glutamine of this motif is less involved in the $Cl^-$-transport function than the other two residues.

In the crystallographic structure of *Nm*ClR, three internal cavities (IC1–3) are present (Fig. 6.10). IC1 is located on the extracellular side near the molecular surface (Kim et al. 2016). Five residues (Asn92, Tyr96, Gln143, Glu146, and Arg223) constitute hydrogen-bonding network with five internal water molecules (W601–605) in IC1. Furthermore, a hole-like structure consisting of Lys2, Ser91, and Q143 is present on the EC side connecting IC1 to the external solvent. The $Cl^-$ uptake presumably occurs through this part, and positively charged surface around the hole may help $Cl^-$-uptake. In fact, the mutants for the residues in the hole and IC1 (*Nm*ClR S91A, N92V in Ref. (Hosaka et al. 2016) and K2E, S91E, N92A, Q143E in Ref. (Kim et al. 2016)) show

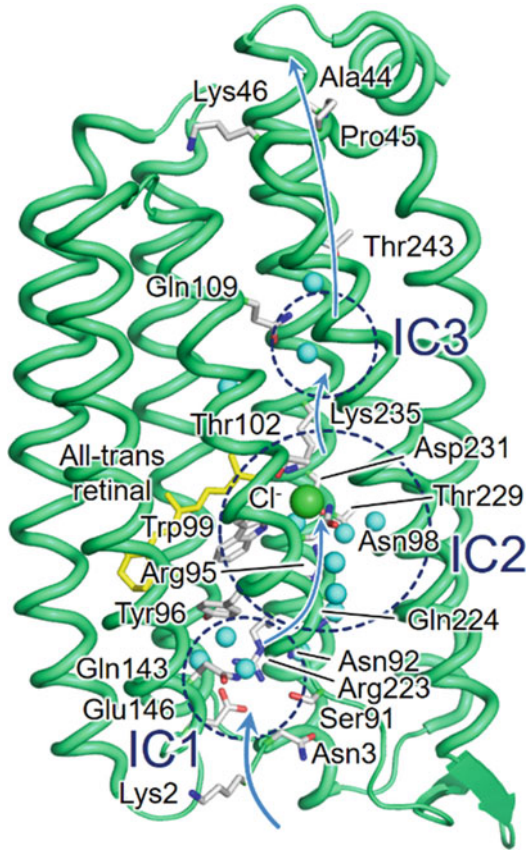


**Fig. 6.10** Three ICs in the crystallographic structure of *Nm*ClR (PDB ID: 5B2N (Kim et al. 2016))

significantly lowered or almost no transport activities. IC2 is the largest cavity in *Nm*ClR which includes RSB, a $Cl^-$, Arg95 (the homolog of BR's Arg82), Asn98, Thr102, Gln224, Thr229, Asp231 (the homolog of BR's Asp212), and several water molecules. In IC3, two water molecules connect Ser54, Gln109, Thr243, and main-chain carbonyl in retinal-binding Lys235. No cavity was observed on the cytoplasmic side of IC3, suggesting *Nm*ClR is cytoplasmically occluded in the dark state. Interestingly, the second $Cl^-$ binding site was observed in two *Nm*ClR structures (PDB ID: 5G28 and 5G54) on the cytoplasmic surface of the helix B. The cytoplasmic binding site composed of main chains of Ala44, Pro45, and Lys46. Although the physiological role of the $Cl^-$ in the second binding site is unclear because no significant difference was observed for the mutants of these residues, a possibility was suggested that it is related to the cytoplasmic transport pathway formed after photo-activation.

Recently, the crystallographic structure of *Nm*ClR at room temperature (294 K) was obtained by serial femtosecond X-ray crystallography (SFX) with an X-ray free-electron laser (XFEL) (Yun et al. 2019). While the comparison with the cryogenic (93 K) structure determined by an X-ray synchrotron showed basically identical structural features, slight but significant displacement of $Cl^-$ ions in both the first and the second binding sites was observed.

### 6.3.3 Bacterial Halorhodopsins

The carboxylic amino acids in the motifs of $H^+$ pump (homologous to BR's Asp85 and Asp96) are all replaced by non-carboxylic residues in TSA and NTQ-motifs of HR and ClR, respectively. However, recently Hasemi et al. reported a new type of chloride pump (*Mr*HR) with a TSD motif in cyanobacterium, *Mastigocladopsis repens* (Hasemi et al. 2016). *Mr*HR is also called MastR to distinguish it from haloarcheal HR (Harris et al. 2018). Although, despite its cyanobacterial origin, *Mr*HR is located in the archeal half of the phylogenic tree of microbial rhodopsin, it belongs to a new group distinct from BR and HR (Fig. 6.1b, here tentatively called "BacHR"). In this group, while about half of members have the TSD motif, the third aspartic acid is replaced with Ile, Leu, or Val in the others (Harris et al. 2018). *Mr*HR shows $\lambda_{max}$ at 537 nm in the $Cl^-$-binding form, and blue-shifts to 506 nm upon a removal of $Cl^-$ from the protein (Hasemi et al. 2016). The blue-shifting effect of the $Cl^-$ removal is similar to *Hs*HR and opposite to *Np*HR. The Kd of $Cl^-$-binding is 1.99 mM which is comparable to those of *Hs*HR and *Np*HR (Hasemi et al. 2016). The photocycle of *Mr*HR consists of similar photo-intermediates as those of HR: *Mr*HR $\xrightarrow{h\nu}$ $K_{540} \rightarrow L_{1,\ 460} \rightarrow L_{2,\ 460} \rightarrow N_{460}/O_{620} \rightarrow$ *Mr*HR′$_{540} \rightarrow$ *Mr*HR (Harris et al. 2018; Hasemi et al. 2016). $N_{460}/O_{620}$

represents a rapid equilibrium between N and O. The $Cl^-$-concentration dependence of the equilibrium showing the higher O-accumulation at the higher $Cl^-$ concentration suggests a $Cl^-$ uptake of *Mr*HR occurs in the N→O process, different from *Np*HR in which $Cl^-$ uptake occurs on O→*Np*HR (Harris et al. 2018). This suggests that, despite the similarity of visible absorption wavelength, the molecular properties of the O intermediate in *Mr*HR photocycle are significantly different from those of *Np*HR. Actually, it appears in the structure of chromophore. That is, while a retinal isomerization to all-*trans* form in *Np*HR occurs on the N→O process before the $Cl^-$ binding, it occurs on the final *Mr*HR′→*Mr*HR process for *Mr*HR (Hackmann et al. 2001; Harris et al. 2018). Interestingly, time-resolved and static FTIR spectroscopy observed a strong negative peak at 1755 $cm^{-1}$, suggesting transient deprotonation of *Mr*HR's Asp85 which is the third "D" in TSD-motif on the $L_1$→$L_2$ process (Harris et al. 2018). To our knowledge, this is the first example of deprotonation of a carboxylic residue in $Cl^-$ pump, and the recovery of $H^+$ to Asp85 is a rate-limiting process in the *Mr*HR′→*Mr*HR transition (Harris et al. 2018). While this aspartic acid is not completely conserved in BacHR, it is hypothesized that the transiently deprotonated Asp85 prevents back flow of transported $Cl^-$ from the cytoplasm (Harris et al. 2018).

The second BacHR with a TSD motif (*Sy*HR) was identified in a cyanobacterium *Synechocystis* sp. PCC 7509 by Drs. Sudo, Yoshizawa and coworkers in 2017 (Niho et al. 2017). While *Sy*HR is phylogenetically close to *Mr*HR, it was revealed to actively transport $SO_4^{2-}$. A redshift of visible absorption from anion-unbound state was also observed in the presence of $SO_4^{2-}$ with the $K_d = 5.81$ mM which is more than 50 times larger compared with the $K_d$ for $Cl^-$ (0.112 mM) (Niho et al. 2017). The protonated RSB is stabilized by the binding of $Cl^-$ or $SO_4^{2-}$ which results in one-unit elevation of $pK_a$ of RSB (Niho et al. 2017). Although the molecular mechanism and physiological significance of $SO_4^{2-}$ transport by *Sy*HR are not well understood, it has a potential to provide a new molecular basis for the development of molecular tools transporting various divalent anions by light.

## 6.4 Outward Sodium Pumps

While $H^+$ pump rhodopsins were found first and were subjects of numerous studies for a long time, no light-driven pump for non-proton cations such as $Na^+$ had been identified for about 40 years. However, a new rhodopsin (KR2 (Inoue et al. 2013), also called *De*NaR (da Silva et al. 2015)) with an NDQ-motif in flavobacterium, *Krokinobacter eikastus*, was revealed to have a light-driven outward $Na^+$ pump function in 2013. Since Dr. Kandori and coworkers presented a comprehensive review for most of studies on NaR and suggested the unique ion transport mechanism with the "Panama canal model" (Kandori et al. 2018), here more recent works and the potential of NaR for the optogenetic application will be focused on.

Although firstly the $Na^+$ pump activity of NaRs was reported for heterologously expressed protein in *E. coli* or mammalian cells, recently, it was observed in various cultured native bacterial species naturally possessing NaR genes (Kwon et al. 2016; Sorokin et al. 2018). While KR2 expressed in *E. coli* transports $Na^+$ and $Li^+$ in NaCl and LiCl solutions, outward $H^+$ pump function was observed in the presence of larger cations such as $K^+$, $Rb^+$, and $Cs^+$ (Inoue et al. 2013). Although many NaRs also exhibit similar outward $Na^+$ transport in the presence of sufficient amount of $Na^+$ as KR2 (Zhao et al. 2017), significant $H^+$ transport was not observed for some NaR members, such as *Nonlabens marinus* S1-08T, *Gillisia limnaea* (*Gl*NaR), *Dokdonia* sp. PRO95 (*Ds*NaR), *Flagellimonas* sp_DIK (*Fd*NaR), and *Nonlabens* sp. YIK_SED-11 (*Ny*NaR) (Balashov et al. 2014; Mamedov et al. 2016; Tsunoda et al. 2017; Yoshizawa et al. 2014) (but for *Gl*NaR, another group recently reported the $H^+$ transport in *E. coli* cells (Shevchenko et al. 2017a)). Recent study by Dr. Bogachev and coworkers based on the differences in primary structures of these NaRs and site-directed mutagenesis suggested that

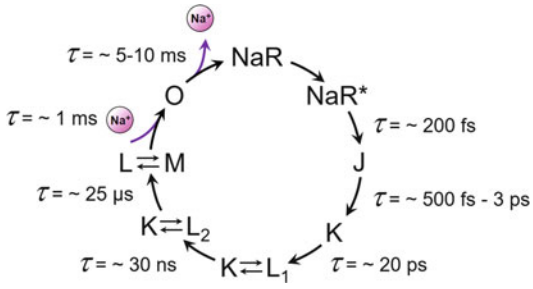


**Fig. 6.11** The photocycle of NaR. $Na^+$ is taken up in the L ⇋ M-to-O step from the cytoplasmic side, and it is released to the extracellular side in the O-to-NaR transition

Ser253 in KR2 is related to its $H^+$ pump function and a cysteine is conserved in non-$H^+$ pumping NaRs at the same position (except for NaR from *Nonlabens dokdonensis* DSW-6 in which the cysteine is conserved, but it transports $H^+$ (Zhao et al. 2017)). This is supported by the result that the mutation of the Cys at the same position in *Ds*NaR to Ser conferred $H^+$ pump ability (Mamedov et al. 2018).

The photocycles of NaRs were investigated in several studies (Balashov et al. 2014; Bogachev et al. 2016; Chen et al. 2018; Hontani et al. 2016; Inoue et al. 2013; Kajimoto et al. 2017; Tahara et al. 2015; Zhao et al. 2017), and all of them were found to have several photo-intermediate as shown in Fig. 6.11. The rates of decay of the L ⇋ M mixture and rise of the O intermediate are proportional to $Na^+$ concentration (Balashov et al. 2014; Inoue et al. 2013; Kato et al. 2015c), suggesting $Na^+$ is taken up from the cytoplasmic side in the (L ⇋ M)-to-O process. Because KR2 D116N mutant does not show the L ⇋ M intermediate, Asp116 is considered to accept an $H^+$ from the Schiff base (Inoue et al. 2013). The alteration of the orientation of the side chain of Asp116 was observed by X-ray crystallographic study in a pH-dependent manner (Kato et al. 2015a). This suggests a model in which side-chain flipping of protonated Asp116 opens the gate at RSB in the M state (Kato et al. 2015a, 2016). Furthermore, recent molecular dynamics (MD) simulation suggested that the side chain of Asp116 flips toward cytoplasmic side in the K ⇋ L intermediate before the deprotonation in the M state (Suomivuori et al. 2017). The negative electric potential on the cytoplasmic side induced by this flipping is likely to reduce the free-energy barrier of $Na^+$ uptake from the solvent. After the L ⇋ M intermediate, the O intermediate represents transiently $Na^+$-bound state, which was supported by the shift of absorption spectrum of the O state between $Na^+$ and $Li^+$ transporting photocycles (Kato et al. 2015a). Since the $\lambda_{max}$ of the O state is at ~600 nm, the $H^+$ is considered to return to the RSB from Asp116 in the (L ⇋ M)-to-O transition inhibiting the $Na^+$ backflow to the cytoplasmic side. In contrast to the O state of BR in which the retinal takes all-*trans* configuration, the O state of KR2 was shown to possess 13-*cis* retinal by low-temperature FTIR spectroscopy with 12,14-$D_2$ retinal-labeled protein (Chen et al. 2018). Because of the lack of atomic structure of the O, the precise position of the transient $Na^+$-binding site was unknown. However, the $Na^+$ binding near the Schiff base in the dark state of *Gl*NaR D251E and the inhibition of $Na^+$ uptake (that is (L ⇋ M)-to-O transition) by Asn112 to alanine mutation in KR2 suggest that the $Na^+$ binds in the space near Asn112, Asp251, and the Schiff base.

Recently, two X-ray crystallographic structures of the O intermediate of KR2 were reported independently from two groups (Kovalev et al. 2020; Skopintsev et al. 2020). In the first one obtained by cryo-trapping of the O intermediate accumulated under light illumination, substrate $Na^+$ is coordinated by Ser70, Asn112, Asp116, and main-chain carbonyl of Val63 (Kovalev et al. 2020). Another structure of the O intermediate which was determined by time-resolved serial femtosecond crystallography (TR-SFX) with an XFEL showed $Na^+$ binding between Asn112 and Asp254 (Skopintsev et al. 2020). These structures are well consistent with the idea based on preceding mutational and spectroscopic studies by several groups in which transient formation of $Na^+$ binding site near RSB was suggested.

All $H^+$ and $Cl^-$ pumping rhodopsins bind their substrate ions in the dark state (it is an $H^+$ of protonated Schiff base for the former). If one follows this rule, NaR is also expected to bind $Na^+$ in the dark. The bindings of substrate $H^+$ and

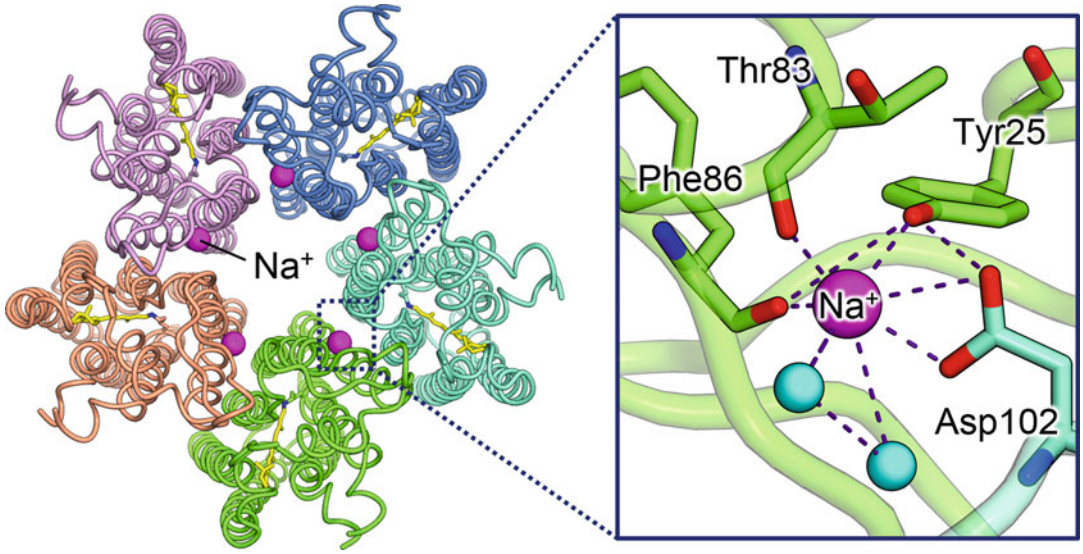


**Fig. 6.12** The structure of the extracellular $Na^+$ binding site in KR2 (PDB ID: 4XTL (Gushchin et al. 2015))

$Cl^-$ to $H^+$ and $Cl^-$ pumping rhodopsins alter their absorptions. In contrast, KR2 shows almost identical spectra in the absence and presence of $Na^+$ (da Silva et al. 2015; Inoue et al. 2013). This implies that no ion-binding occurs in the dark, or the $Na^+$ binding site is distant from the retinal. However, attenuated total reflection (ATR)-FTIR spectroscopy clearly observed IR-absorption change of KR2 between the presence and absence of $Na^+$ in the media, suggesting $Na^+$ binding at the position far from the chromophore (Inoue et al. 2013). Further mutational studies suggested that Tyr25, His30, Asp102, and Arg109, which are located on the extracellular side, are involved in the $Na^+$ binding (Inoue et al. 2013; Ito et al. 2018; Kato et al. 2015a). The atomic structure of $Na^+$ binding site was revealed by the X-ray crystallographic analysis of KR2 forming pentamer (Fig. 6.12) (Gushchin et al. 2015). The $Na^+$ binds in the interface between neighboring protomers, and it interacts with the –O–H group of Tyr25 and main-chain carbonyl of Thr83 and Phe86 in one protomer, carboxylic group of Asp102 in another protomer, and two water molecules. The direct interaction of $Na^+$ with Tyr25 and Asp102 is consistent with the result of ATR-FTIR spectroscopy. The wide-range ATR-FTIR spectroscopy covering 4000–1000 $cm^{-1}$ observed IR absorption peaks derived from extremely strongly hydrogen-bonded –O–H group of tyrosine at 2805, 2765, 2696, 2629, and 2512 $cm^{-1}$ in $Na^+$-bound form (Ito et al. 2018). Since these bands were abolished by the mutations of Tyr25 and Asp102 and the distance between the oxygen atoms of Tyr25 and Asp102 (2.5 Å) is shorter than that of normal hydrogen bond, Tyr25 is supposed to form the extremely strong hydrogen bond with Asp102. In contrast to $H^+$ and $Cl^-$ pumps which require the binding of substrate ions for the transport in the dark, the disruption of $Na^+$ binding site in the dark state does not affect the transport function of KR2 (Inoue et al. 2013; Kato et al. 2015a), indicating that the bound $Na^+$ is not related to the transport and the Panama canal model with the transient substrate $Na^+$ binding after photo-energization of protein was suggested for NaR (Kandori et al. 2018). Because KR2 WT without $Na^+$ and KR2 D102N mutant lacking $Na^+$ binding in the dark state show less thermal stability, the binding of $Na^+$ is considered to play a role in stabilizing the protein structure in the dark state (Kato et al. 2015a).

The outward active $Na^+$ transport by NaR induces hyperpolarization of membranes suggesting a usage as a new type of inhibitory optogenetic tool. Actually, the rat cortical

neurons expressing KR2 were shown to hyperpolarize and suppress action potentials (APs) upon illumination, and the locomotion behavior of *C. elegans* was inhibited by light if KR2 was expressed in neurons (Kato et al. 2015a). However, because KR2 WT exhibits significant accumulation in soma, higher membrane-targeting NaR is demanded for optogenetic control with lower excitation power. The NaR from *Indibacter alkaliphilus* (*Ia*NaR) exhibits higher membrane trafficking to the plasma membrane than KR2, and the small inactivation from peak ($I_p$) to stationary ($I_s$) current which is advantageous for stable neuronal control was observed for chimeric protein consisting of the helix A of *Ia*NaR and the helices B-G of KR2 ($I_1K_6$NaR) (Hoque et al. 2016). Also, high plasma membrane targeting was observed for several natural NaRs, such as *Fd*NaR and *Ny*NaR, which in ND7/23 cells show larger photo-current than that of KR2 (Tsunoda et al. 2017). In addition, the fusing N-terminal sequence of ChR to KR2 with C-terminal endoplasmic reticulum and the Golgi export sequences (called eKR2) highly increases membrane targeting of the protein and results in 65-fold higher photo-current than that of KR2 WT (Grimm et al. 2018). Since natural neuronal activity is regulated by $Na^+$ influx, these NaRs with improved properties would be more useful than $H^+$ or $Cl^-$ transporting inhibitory tools when the changes in pH or $Cl^-$ gradient cause unnatural cell behavior.

## 6.5 Summary/Future Perspectives

Only a few dozens of microbial rhodopsins were known in the twentieth century. However, they expanded more than 100 times in this century by the virtue of genomic and metagenomic analysis technologies (Pinhassi et al. 2016). Not only the number increased highly, but several types of new functional ion-pumping rhodopsins were discovered. Recently established single-cell metagenomics is expected to be able to further accelerate the speed of identifications of rhodopsin genes from uncultured species (Needham et al. 2019). The discovery of new functional rhodopsins will expand the range of applications in optogenetics.

One of the most critical problems of ion-pumping rhodopsins to solve is the lower efficiency of the trafficking toward plasma membrane. While a part of this problem can be solved by optimizing signaling sequences (Grimm et al. 2018), microbial rhodopsins from eukaryotes or giant viruses infecting them are expected to be more stably expressed in the plasma membrane in mammalian cells and tissues. For example, an $H^+$ pump (CsR) from arctic green alga *Coccomyxa subellipsoidea* showed surprisingly high membrane trafficking in HEK-293 cells and *Xenopus* oocytes (Vogt 2015). The single cellular metagenomics on uncultured eukaryotes and giant viruses are expected to provide more new eukaryotic pumps having ideal properties for optogenetic applications.

On the other hand, 3D structures of rhodopsins obtained by the X-ray crystallographic analysis bring the researches structural insights to design new artificial ion pumps. Especially, QM/MM calculation can predict $\lambda_{max}$ based on the 3D structures (Hayashi et al. 2001; Melaccio et al. 2016; Pedraza-González et al. 2019). Indeed, many types of color-shifted variants were designed by mutating the residues surrounding retinal chromophore (Inoue et al. 2019, 2015; Kato et al. 2015b; Sudo et al. 2013). The mutations of ion-transporting pathway can also alter ion species transported (Inoue et al. 2016b; Kato et al. 2015a; Konno et al. 2016), or even convert the function from pumps to channels (Fudim et al. 2019; Vogt 2015). Single particle analysis by cryo-electron microscopy (cryoEM) is expected to expand the target of structural analysis toward the molecules difficult to be crystallized (Gao et al. 2019). Time-resolved serial crystallography by XEFL or synchrotron light sources, or cryo-EM structural analysis for rapid frozen photo-activated protein would provide crucial insights on the structural dynamics during ion-transporting process (Müller et al. 2015; Nango et al. 2016; Skopintsev et al. 2020; Weinert et al. 2019). Furthermore, bioinformatic approaches based on machine-learning techniques were suggested to be able to

contribute to improving $\lambda_{max}$ and transport efficiency (Bedbrook et al. 2019; Karasuyama et al. 2018). The combination of these techniques will pave a way for the construction of new pumps having ideal molecular attributes as optogenetics tools.

**Acknowledgments** The author would like to thank Drs. Leonid S. Brown and Oded Béjà for their careful reading of the manuscript and insightful comments. I apologize to all authors whose research could not be cited because of space limitations. This work was supported by grants from the Japanese Ministry of Education, Culture, Sports, Science and Technology (17H03007), Takeda Science Foundation, The Mitsubishi Foundation, and Yamada Science Foundation.

## References

Adam A, Deimel S, Pardo-Medina J et al (2018) Protein activity of the *Fusarium fujikuroi* rhodopsins CarO and OpsA and their relation to fungus-plant interaction. Int J Mol Sci 19:215. https://doi.org/10.3390/ijms19010215

Arrenberg AB, Del Bene F, Baier H (2009) Optical control of zebrafish behavior with halorhodopsin. Proc Natl Acad Sci USA 106:17968–17973. https://doi.org/10.1073/pnas.0906252106

Balashov SP (2000) Protonation reactions and their coupling in bacteriorhodopsin. Biochim Biophys Acta 1460:75–94

Balashov SP, Imasheva ES, Boichenko VA et al (2005) Xanthorhodopsin: a proton pump with a light-harvesting carotenoid antenna. Science 309:2061–2064. https://doi.org/10.1126/science.1118046

Balashov SP, Imasheva ES, Lanyi JK (2006) Induced chirality of the light-harvesting carotenoid salinixanthin and its interaction with the retinal of xanthorhodopsin. Biochemistry 45:10998–11004. https://doi.org/10.1021/bi061098i

Balashov SP, Imasheva ES, Wang JM et al (2008) Excitation energy-transfer and the relative orientation of retinal and carotenoid in xanthorhodopsin. Biophys J 95:2402–2414. https://doi.org/10.1529/biophysj.108.132175

Balashov SP, Imasheva ES, Choi AR et al (2010) Reconstitution of *Gloeobacter* rhodopsin with echinenone: role of the 4-keto group. Biochemistry 49:9792–9799. https://doi.org/10.1021/bi1014166

Balashov SP, Petrovskaya LE, Lukashev EP et al (2012) Aspartate-histidine interaction in the retinal schiff base counterion of the light-driven proton pump of *Exiguobacterium sibiricum*. Biochemistry 51:5748–5762. https://doi.org/10.1021/bi300409m

Balashov SP, Petrovskaya LE, Imasheva ES et al (2013) Breaking the carboxyl rule: lysine 96 facilitates reprotonation of the Schiff base in the photocycle of a retinal protein from *Exiguobacterium sibiricum*. J Biol Chem 288:21254–21265. https://doi.org/10.1074/jbc.M113.465138

Balashov SP, Imasheva ES, Dioumaev AK et al (2014) Light-driven $Na^+$ pump from *Gillisia limnaea*: a high-affinity $Na^+$ binding site is formed transiently in the photocycle. Biochemistry 53:7549–7561. https://doi.org/10.1021/bi501064n

Bedbrook CN, Yang KK, Robinson JE et al (2019) Machine learning-guided channelrhodopsin engineering enables minimally invasive optogenetics. Nat Methods 16:1176–1184. https://doi.org/10.1038/s41592-019-0583-8

Béjà O, Lanyi JK (2014) Nature's toolkit for microbial rhodopsin ion pumps. Proc Natl Acad Sci USA 111:6538–6539. https://doi.org/10.1073/pnas.1405093111

Béjà O, Aravind L, Koonin EV et al (2000) Bacterial rhodopsin: evidence for a new type of phototrophy in the sea. Science 289:1902–1906

Béjà O, Spudich EN, Spudich JL et al (2001) Proteorhodopsin phototrophy in the ocean. Nature 411:786–789. https://doi.org/10.1038/35081051

Bergo VB, Sineshchekov OA, Kralj JM et al (2009) His-75 in proteorhodopsin, a novel component in light-driven proton translocation by primary pumps. J Biol Chem 284:2836–2843. https://doi.org/10.1074/jbc.M803792200

Bieszke JA, Braun EL, Bean LE et al (1999a) The *nop-1* gene of *Neurospora crassa* encodes a seven transmembrane helix retinal-binding protein homologous to archaeal rhodopsins. Proc Natl Acad Sci USA 96:8034–8039

Bieszke JA, Spudich EN, Scott KL et al (1999b) A eukaryotic protein, NOP-1, binds retinal to form an archaeal rhodopsin-like photochemically reactive pigment. Biochemistry 38:14138–14145

Birge RR (1981) Photophysics of light transduction in rhodopsin and bacteriorhodopsin. Annu Rev Biophys Bioeng 10:315–354. https://doi.org/10.1146/annurev.bb.10.060181.001531

Bogachev AV, Bertsova YV, Verkhovskaya ML et al (2016) Real-time kinetics of electrogenic $Na^+$ transport by rhodopsin from the marine flavobacterium *Dokdonia* sp. PRO95. Sci Rep 6:21397. https://doi.org/10.1038/srep21397

Bogomolni RA, Spudich JL (1982) Identification of a third rhodopsin-like pigment in phototactic *Halobacterium halobium*. Proc Natl Acad Sci USA 79:6250–6254

Boyden ES, Zhang F, Bamberg E et al (2005) Millisecond-timescale, genetically targeted optical control of neural activity. Nat Neurosci 8:1263–1268. https://doi.org/10.1038/nn1525

Braiman M, Mathies R (1980) Resonance Raman evidence for an all-*trans* to 13-*cis* isomerization in the proton-

pumping cycle of bacteriorhodopsin. Biochemistry 19:5421–5428
Bratanov D, Kovalev K, Machtens JP et al (2019) Unique structure and function of viral rhodopsins. Nat Commun 10:4939. https://doi.org/10.1038/s41467-019-12718-0
Brown LS (2004) Fungal rhodopsins and opsin-related proteins: eukaryotic homologues of bacteriorhodopsin with unknown functions. Photochem Photobiol Sci 3:555–565. https://doi.org/10.1039/b315527g
Brown LS, Sasaki J, Kandori H et al (1995) Glutamic acid 204 is the terminal proton release group at the extracellular surface of bacteriorhodopsin. J Biol Chem 270:27122–27126
Brown LS, Dioumaev AK, Lanyi JK et al (2001) Photochemical reaction cycle and proton transfers in *Neurospora* rhodopsin. J Biol Chem 276:32495–32505. https://doi.org/10.1074/jbc.M102652200
Bulzu PA, Andrei AS, Salcher MM et al (2019) Casting light on asgardarchaeota metabolism in a sunlit microoxic niche. Nat Microbiol 4:1129–1137. https://doi.org/10.1038/s41564-019-0404-y
Butt HJ, Fendler K, Bamberg E et al (1989) Aspartic acids 96 and 85 play a central role in the function of bacteriorhodopsin as a proton pump. EMBO J 8:1657–1663
Chen D, Lanyi JK (2009) Structural changes in the N and N' states of the bacteriorhodopsin photocycle. Biophys J 96:2779–2788. https://doi.org/10.1016/j.bpj.2008.12.3935
Chen HF, Inoue K, Ono H et al (2018) Time-resolved FTIR study of light-driven sodium pump rhodopsins. Phys Chem Chem Phys 20:17694–17704. https://doi.org/10.1039/c8cp02599a
Chizhov I, Engelhard M (2001) Temperature and halide dependence of the photocycle of halorhodopsin from *Natronobacterium pharaonis*. Biophys J 81:1600–1612. https://doi.org/10.1016/s0006-3495(01)75814-6
Chizhov I, Chernavskii DS, Engelhard M et al (1996) Spectrally silent transitions in the bacteriorhodopsin photocycle. Biophys J 71:2329–2345. https://doi.org/10.1016/s0006-3495(96)79475-4
Chou KC (1993) Conformational change during photocycle of bacteriorhodopsin and its proton-pumping mechanism. J Protein Chem 12:337–350
Chow BY, Han X, Dobry AS et al (2010) High-performance genetically targetable optical neural silencing by light-driven proton pumps. Nature 463:98–102. https://doi.org/10.1038/nature08652
da Silva GF, Goblirsch BR, Tsai AL et al (2015) Cation-specific conformations in a dual-function ion-pumping microbial rhodopsin. Biochemistry 54:3950–3959. https://doi.org/10.1021/bi501386d
de la Torre JR, Christianson LM, Beja O et al (2003) Proteorhodopsin genes are distributed among divergent marine bacterial taxa. Proc Natl Acad Sci USA 100:12830–12835. https://doi.org/10.1073/pnas.2133554100
Deisseroth K (2015) Optogenetics: 10 years of microbial opsins in neuroscience. Nat Neurosci 18:1213–1225. https://doi.org/10.1038/nn.4091
Deisseroth K, Hegemann P (2017) The form and function of channelrhodopsin. Science 357:eaan5544. https://doi.org/10.1126/science.aan5544
Dencher NA, Sass HJ, Buldt G (2000) Water and bacteriorhodopsin: structure, dynamics, and function. Biochim Biophys Acta 1460:192–203
Dioumaev AK, Brown LS, Needleman R et al (1999) Fourier transform infrared spectra of a late intermediate of the bacteriorhodopsin photocycle suggest transient protonation of Asp-212. Biochemistry 38:10070–10078. https://doi.org/10.1021/bi990873+
Dioumaev AK, Brown LS, Shih J et al (2002) Proton transfers in the photochemical reaction cycle of proteorhodopsin. Biochemistry 41:5348–5358
Dioumaev AK, Petrovskaya LE, Wang JM et al (2013) Photocycle of *Exiguobacterium sibiricum* rhodopsin characterized by low-temperature trapping in the IR and time-resolved studies in the visible. J Phys Chem B 117:7235–7253. https://doi.org/10.1021/jp402430w
Dong B, Sanchez-Magraner L, Luecke H (2016) Structure of an inward proton-transporting *Anabaena* sensory rhodopsin mutant: mechanistic insights. Biophys J 111:963–972. https://doi.org/10.1016/j.bpj.2016.04.055
Duschl A, Lanyi JK, Zimanyi L (1990) Properties and photochemistry of a halorhodopsin from the haloalkalophile, *Natronobacterium pharaonis*. J Biol Chem 265:1261–1267
Engelhard C, Chizhov I, Siebert F et al (2018) Microbial halorhodopsins: light-driven chloride pumps. Chem Rev 118:10629–10645. https://doi.org/10.1021/acs.chemrev.7b00715
Ernst OP, Lodowski DT, Elstner M et al (2014) Microbial and animal rhodopsins: structures, functions, and molecular mechanisms. Chem Rev 114:126–163. https://doi.org/10.1021/cr4003769
Eshel N, Bukwich M, Rao V et al (2015) Arithmetic and local circuitry underlying dopamine prediction errors. Nature 525:243–246. https://doi.org/10.1038/nature14855
Fan Y, Shi L, Brown LS (2007) Structural basis of diversification of fungal retinal proteins probed by site-directed mutagenesis of *Leptosphaeria* rhodopsin. FEBS Lett 581:2557–2561. https://doi.org/10.1016/j.febslet.2007.05.001
Fan Y, Solomon P, Oliver RP et al (2011) Photochemical characterization of a novel fungal rhodopsin from *Phaeosphaeria nodorum*. Biochim Biophys Acta 1807:1457–1466. https://doi.org/10.1016/j.bbabio.2011.07.005
Finkel OM, Béjà O, Belkin S (2013) Global abundance of microbial rhodopsins. ISME J 7:448–451. https://doi.org/10.1038/ismej.2012.112
Friedrich T, Geibel S, Kalmbach R et al (2002) Proteorhodopsin is a light-driven proton pump with variable vectoriality. J Mol Biol 321:821–838

Fudim R, Szczepek M, Vierock J et al (2019) Design of a light-gated proton channel based on the crystal structure of *Coccomyxa* rhodopsin. Sci Signal 12:eaav4203. https://doi.org/10.1126/scisignal.aav4203

Fujimoto KJ, Hayashi S (2009) Electronic Coulombic coupling of excitation-energy transfer in xanthorhodopsin. J Am Chem Soc 131:14152–14153. https://doi.org/10.1021/ja905697n

Furuse M, Tamogami J, Hosaka T et al (2015) Structural basis for the slow photocycle and late proton release in *Acetabularia* rhodopsin I from the marine plant *Acetabularia acetabulum*. Acta Crystallogr D Biol Crystallogr 71:2203–2216. https://doi.org/10.1107/S1399004715015722

Furutani Y, Ikeda D, Shibata M et al (2006a) Strongly hydrogen-bonded water molecule is observed only in the alkaline form of proteorhodopsin. Chem Phys 324:705–708. https://doi.org/10.1016/j.chemphys.2005.12.013

Furutani Y, Sumii M, Fan Y et al (2006b) Conformational coupling between the cytoplasmic carboxylic acid and the retinal in a fungal light-driven proton pump. Biochemistry 45:15349–15358. https://doi.org/10.1021/bi061864l

Gao Y, Hu H, Ramachandran S et al (2019) Structures of the rhodopsin-transducin complex: insights into G-protein activation. Mol Cell 75:781–790.e783. https://doi.org/10.1016/j.molcel.2019.06.007

García-Martínez J, Brunk M, Avalos J et al (2015) The CarO rhodopsin of the fungus *Fusarium fujikuroi* is a light-driven proton pump that retards spore germination. Sci Rep 5:7798. https://doi.org/10.1038/srep07798

Garczarek F, Gerwert K (2006) Functional waters in intraprotein proton transfer monitored by FTIR difference spectroscopy. Nature 439:109–112. https://doi.org/10.1038/nature04231

Garczarek F, Wang J, El-Sayed MA et al (2004) The assignment of the different infrared continuum absorbance changes observed in the 3000-1800-cm$^{-1}$ region during the bacteriorhodopsin photocycle. Biophys J 87:2676–2682. https://doi.org/10.1529/biophysj.104.046433

Gerwert K, Hess B, Soppa J et al (1989) Role of aspartate-96 in proton translocation by bacteriorhodopsin. Proc Natl Acad Sci USA 86:4943–4947

Gordeliy VI, Labahn J, Moukhametzianov R et al (2002) Molecular basis of transmembrane signalling by sensory rhodopsin II-transducer complex. Nature 419:484–487

Govorunova EG, Koppel LA (2016) The road to optogenetics: microbial rhodopsins. Biochemistry (Mosc) 81:928–940. https://doi.org/10.1134/S0006297916090029

Gradinaru V, Thompson KR, Deisseroth K (2008) eNpHR: a *Natronomonas* halorhodopsin enhanced for optogenetic applications. Brain Cell Biol 36:129–139. https://doi.org/10.1007/s11068-008-9027-6

Grimm C, Silapetere A, Vogt A et al (2018) Electrical properties, substrate specificity and optogenetic potential of the engineered light-driven sodium pump eKR2. Sci Rep 8:9316. https://doi.org/10.1038/s41598-018-27690-w

Gushchin I, Chervakov P, Kuzmichev P et al (2013) Structural insights into the proton pumping by unusual proteorhodopsin from nonmarine bacteria. Proc Natl Acad Sci USA 110:12631–12636. https://doi.org/10.1073/pnas.1221629110

Gushchin I, Shevchenko V, Polovinkin V et al (2015) Crystal structure of a light-driven sodium pump. Nat Struct Mol Biol 22:390–395. https://doi.org/10.1038/nsmb.3002

Hackmann C, Guijarro J, Chizhov I et al (2001) Static and time-resolved step-scan Fourier transform infrared investigations of the photoreaction of halorhodopsin from *Natronobacterium pharaonis*: consequences for models of the anion translocation mechanism. Biophys J 81:394–406. https://doi.org/10.1016/s0006-3495(01)75708-6

Han X, Chow BY, Zhou H et al (2011) A high-light sensitivity optical neural silencer: development and application to optogenetic control of non-human primate cortex. Front Syst Neurosci 5:18. https://doi.org/10.3389/fnsys.2011.00018

Harris A, Ljumovic M, Bondar AN et al (2015) A new group of eubacterial light-driven retinal-binding proton pumps with an unusual cytoplasmic proton donor. Biochim Biophys Acta 1847:1518–1529. https://doi.org/10.1016/j.bbabio.2015.08.003

Harris A, Saita M, Resler T et al (2018) Molecular details of the unique mechanism of chloride transport by a cyanobacterial rhodopsin. Phys Chem Chem Phys 20:3184–3199. https://doi.org/10.1039/c7cp06068h

Harris A, Lazaratos M, Siemers M et al (2020) Mechanism of inward proton transport in an antarctic microbial rhodopsin. J Phys Chem B https://doi.org/10.1021/acs.jpcb.0c02767

Hasemi T, Kikukawa T, Kamo N et al (2016) Characterization of a cyanobacterial chloride-pumping rhodopsin and its conversion into a proton pump. J Biol Chem 291:355–362. https://doi.org/10.1074/jbc.M115.688614

Haupts U, Tittor J, Oesterhelt D (1999) Closing in on bacteriorhodopsin: progress in understanding the molecule. Annu Rev Biophys Biomol Struct 28:367–399. https://doi.org/10.1146/annurev.biophys.28.1.367

Hayashi S, Tajkhorshid E, Pebay-Peyroula E et al (2001) Structural determinants of spectral tuning in retinal proteins-bacteriorhodopsin vs sensory rhodopsin II. J Phys Chem B 105:10124–10131

Hazemoto N, Kamo N, Kobatake Y et al (1984) Effect of salt on photocycle and ion-pumping of halorhodopsin and third rhodopsinlike pigment of *Halobacterium halobium*. Biophys J 45:1073–1077. https://doi.org/10.1016/s0006-3495(84)84254-x

Heberle J (2000) Proton transfer reactions across bacteriorhodopsin and along the membrane. Biochim Biophys Acta 1458:135–147

Hempelmann F, Holper S, Verhoefen MK et al (2011) His75-asp97 cluster in green proteorhodopsin. J Am Chem Soc 133:4645–4654. https://doi.org/10.1021/ja111116a

Henry IM, Wilkinson MD, Hernandez JM et al (2004) Comparison of ests from juvenile and adult phases of the giant unicellular green alga *Acetabularia acetabulum*. BMC Plant Biol 4:3. https://doi.org/10.1186/1471-2229-4-3

Hochbaum DR, Zhao Y, Farhi SL et al (2014) All-optical electrophysiology in mammalian neurons using engineered microbial rhodopsins. Nat Methods 11:825–833. https://doi.org/10.1038/nmeth.3000

Holz M, Drachev LA, Mogi T et al (1989) Replacement of aspartic acid-96 by asparagine in bacteriorhodopsin slows both the decay of the m intermediate and the associated proton movement. Proc Natl Acad Sci USA 86:2167–2171

Hontani Y, Inoue K, Kloz M et al (2016) The photochemistry of sodium ion pump rhodopsin observed by watermarked femto- to submillisecond stimulated Raman spectroscopy. Phys Chem Chem Phys 18:24729–24736. https://doi.org/10.1039/c6cp05240a

Hoque MR, Ishizuka T, Inoue K et al (2016) A chimera $Na^+$-pump rhodopsin as an effective optogenetic silencer. PLoS One 11:e0166820. https://doi.org/10.1371/journal.pone.0166820

Hosaka T, Yoshizawa S, Nakajima Y et al (2016) Structural mechanism for light-driven transport by a new type of chloride ion pump, *Nonlabens marinus* rhodopsin-3. J Biol Chem 291:17488–17495. https://doi.org/10.1074/jbc.M116.728220

Idnurm A, Howlett BJ (2001) Characterization of an opsin gene from the ascomycete *Leptosphaeria maculans*. Genome 44:167–171. https://doi.org/10.1139/g00-113

Ihara K, Narusawa A, Maruyama K et al (2008) A halorhodopsin-overproducing mutant isolated from an extremely haloalkaliphilic archaeon *Natronomonas pharaonis*. FEBS Lett 582:2931–2936. https://doi.org/10.1016/j.febslet.2008.07.030

Ikeda D, Furutani Y, Kandori H (2007) FTIR study of the retinal Schiff base and internal water molecules of proteorhodopsin. Biochemistry 46:5365–5373

Imasheva ES, Balashov SP, Choi AR et al (2009) Reconstitution of *Gloeobacter violaceus* rhodopsin with a light-harvesting carotenoid antenna. Biochemistry 48:10948–10955. https://doi.org/10.1021/bi901552x

Imasheva ES, Balashov SP, Wang JM et al (2011) Removal and reconstitution of the carotenoid antenna of xanthorhodopsin. J Mol Biol 239:95–104. https://doi.org/10.1007/s00232-010-9322-x

Inoue K, Ono H, Abe-Yoshizumi R et al (2013) A light-driven sodium ion pump in marine bacteria. Nat Commun 4:1678. https://doi.org/10.1038/ncomms2689

Inoue K, Kato Y, Kandori H (2014a) Light-driven ion-translocating rhodopsins in marine bacteria. Trends Microbiol 23:91–98. https://doi.org/10.1016/j.tim.2014.10.009

Inoue K, Koua FH, Kato Y et al (2014b) Spectroscopic study of a light-driven chloride ion pump from marine bacteria. J Phys Chem B 118:11190–11199. https://doi.org/10.1021/jp507219q

Inoue K, Tsukamoto T, Shimono K et al (2015) Converting a light-driven proton pump into a light-gated proton channel. J Am Chem Soc 137:3291–3299. https://doi.org/10.1021/ja511788f

Inoue K, Ito S, Kato Y et al (2016a) A natural light-driven inward proton pump. Nat Commun 7:13415. https://doi.org/10.1038/ncomms13415

Inoue K, Nomura Y, Kandori H (2016b) Asymmetric functional conversion of eubacterial light-driven ion pumps. J Biol Chem 291:9883–9893. https://doi.org/10.1074/jbc.M116.716498

Inoue K, Tahara S, Kato Y et al (2018a) Spectroscopic study of proton-transfer mechanism of inward proton-pump rhodopsin, *Parvularcula oceani* xenorhodopsin. J Phys Chem B 122:6453–6461. https://doi.org/10.1021/acs.jpcb.8b01279

Inoue S, Yoshizawa S, Nakajima Y et al (2018b) Spectroscopic characteristics of *Rubricoccus marinus* xenorhodopsin (*Rm*XeR) and a putative model for its inward $H^+$ transport mechanism. Phys Chem Chem Phys 20:3172–3183. https://doi.org/10.1039/c7cp05033j

Inoue K, Del Carmen Marin M, Tomida S et al (2019) Red-shifting mutation of light-driven sodium-pump rhodopsin. Nat Commun 10:1993. https://doi.org/10.1038/s41467-019-10000-x

Inoue K, Tsunoda SP, Singh M et al (2020) Schizorhodopsins: a family of rhodopsins from asgard archaea that function as light-driven inward $H^+$ pumps. Sci Adv 6:eaaz2441. https://doi.org/10.1126/sciadv.aaz2441

Irieda H, Morita T, Maki K et al (2012) Photo-induced regulation of the chromatic adaptive gene expression by *Anabaena* sensory rhodopsin. J Biol Chem 287:32485–32493. https://doi.org/10.1074/jbc.M112.390864

Ito H, Sumii M, Kawanabe A et al (2012) Comparative FTIR study of a new fungal rhodopsin. J Phys Chem B 116:11881–11889. https://doi.org/10.1021/jp306993a

Ito S, Sugita S, Inoue K et al (2017) FTIR analysis of a light-driven inward proton-pumping rhodopsin at 77 K. Photochem Photobiol 93:1381–1387. https://doi.org/10.1111/php.12771

Ito S, Iwaki M, Sugita S et al (2018) Unique hydrogen bonds in membrane protein monitored by whole mid-ir atr spectroscopy in aqueous solution. J Phys Chem B 122:165–170. https://doi.org/10.1021/acs.jpcb.7b11064

Janke C, Scholz F, Becker-Baldus J et al (2013) Photocycle and vectorial proton transfer in a rhodopsin

from the eukaryote *Oxyrrhis marina*. Biochemistry 52:2750–2763. https://doi.org/10.1021/bi301412n

Jennings JH, Rizzi G, Stamatakis AM et al (2013) The inhibitory circuit architecture of the lateral hypothalamus orchestrates feeding. Science 341:1517–1521. https://doi.org/10.1126/science.1241812

Jung KH (2007) The distinct signaling mechanisms of microbial sensory rhodopsins in archaea, eubacteria and eukarya. Photochem Photobiol 83:63–69. https://doi.org/10.1562/2006-03-20-IR-853

Jung KH, Trivedi VD, Spudich JL (2003) Demonstration of a sensory rhodopsin in eubacteria. Mol Microbiol 47:1513–1522. https://doi.org/10.1046/j.1365-2958.2003.03395.x

Kajimoto K, Kikukawa T, Nakashima H et al (2017) Transient resonance Raman spectroscopy of a light-driven sodium-ion-pump rhodopsin from *Indibacter alkaliphilus*. J Phys Chem B 121:4431–4437. https://doi.org/10.1021/acs.jpcb.7b02421

Kalaidzidis IV, Kaulen AD, Radionov AN et al (2001) Photoelectrochemical cycle of bacteriorhodopsin. Biochemistry (Mosc) 66:1220–1233

Kamo N, Hashiba T, Kikukawa T et al (2006) A light-driven proton pump from *Haloterrigena turkmenica*: functional expression in *Escherichia coli* membrane and coupling with a $H^+$ co-transporter. Biochem Biophys Res Commun 341:285–290. https://doi.org/10.1016/j.bbrc.2005.12.181

Kandori H (2000) Role of internal water molecules in bacteriorhodopsin. Biochim Biophys Acta 1460:177–191

Kandori H (2004) Hydration switch model for the proton transfer in the Schiff base region of bacteriorhodopsin. Biochim Biophys Acta 1658:72–79. https://doi.org/10.1016/j.bbabio.2004.03.015

Kandori H, Yamazaki Y, Hatanaka M et al (1997) Time-resolved Fourier transform infrared study of structural changes in the last steps of the photocycles of Glu-204 and Leu-93 mutants of bacteriorhodopsin. Biochemistry 36:5134–5141. https://doi.org/10.1021/bi9629788

Kandori H, Inoue K, Tsunoda SP (2018) Light-driven sodium-pumping rhodopsin: a new concept of active transport. Chem Rev 118:10646–10658. https://doi.org/10.1021/acs.chemrev.7b00548

Kaneda K, Kasahara H, Matsui R et al (2011) Selective optical control of synaptic transmission in the subcortical visual pathway by activation of viral vector-expressed halorhodopsin. PLoS One 6:e18452. https://doi.org/10.1371/journal.pone.0018452

Kanehara K, Yoshizawa S, Tsukamoto T et al (2017) A phylogenetically distinctive and extremely heat stable light-driven proton pump from the eubacterium *Rubrobacter xylanophilus* DSM $9941^T$. Sci Rep 7:44427. https://doi.org/10.1038/srep44427

Karasuyama M, Inoue K, Nakamura R et al (2018) Understanding colour tuning rules and predicting absorption wavelengths of microbial rhodopsins by data-driven machine-learning approach. Sci Rep 8:15580. https://doi.org/10.1038/s41598-018-33984-w

Kato HE, Inoue K, Abe-Yoshizumi R et al (2015a) Structural basis for $Na^+$ transport mechanism by a light-driven $Na^+$ pump. Nature 521:48–53

Kato HE, Kamiya M, Sugo S et al (2015b) Atomistic design of microbial opsin-based blue-shifted optogenetics tools. Nat Commun 6:7177. https://doi.org/10.1038/ncomms8177

Kato Y, Inoue K, Kandori H (2015c) Kinetic analysis of $H^+$-$Na^+$ selectivity in a light-driven $Na^+$-pumping rhodopsin. J Phys Chem Lett 6:5111–5115. https://doi.org/10.1021/acs.jpclett.5b02371

Kato HE, Inoue K, Kandori H et al (2016) The light-driven sodium ion pump: a new player in rhodopsin research. BioEssays 38:1274–1282. https://doi.org/10.1002/bies.201600065

Kawanabe A, Furutani Y, Jung KH et al (2007) Photochromism of *Anabaena* sensory rhodopsin. J Am Chem Soc 129:8644–8649. https://doi.org/10.1021/ja072085a

Kawanabe A, Furutani Y, Jung KH et al (2009) Engineering an inward proton transport from a bacterial sensor rhodopsin. J Am Chem Soc 131:16439–16444. https://doi.org/10.1021/ja904855g

Kawanabe A, Furutani Y, Jung KH et al (2011) An inward proton transport using *Anabaena* sensory rhodopsin. J Microbiol 49:1–6. https://doi.org/10.1007/s12275-011-0547-x

Khorana HG (1988) Bacteriorhodopsin, a membrane protein that uses light to translocate protons. J Biol Chem 263:7439–7442

Kikukawa T, Shimono K, Tamogami J et al (2011) Photochemistry of *Acetabularia* rhodopsin II from a marine plant, *Acetabularia acetabulum*. Biochemistry 50:8888–8898. https://doi.org/10.1021/bi2009932

Kim K, Kwon SK, Jun SH et al (2016) Crystal structure and functional characterization of a light-driven chloride pump having an NTQ motif. Nat Commun 7:12677. https://doi.org/10.1038/ncomms12677

Kitajima-Ihara T, Furutani Y, Suzuki D et al (2008) *Salinibacter* sensory rhodopsin: sensory rhodopsin I-like protein from a eubacterium. J Biol Chem 283:23533–23541. https://doi.org/10.1074/jbc.M802990200

Klyszejko AL, Shastri S, Mari SA et al (2008) Folding and assembly of proteorhodopsin. J Mol Biol 376:35–41. https://doi.org/10.1016/j.jmb.2007.11.030

Koh EY, Atamna-Ismaeel N, Martin A et al (2010) Proteorhodopsin-bearing bacteria in antarctic sea ice. Appl Environ Microbiol 76:5918–5925. https://doi.org/10.1128/aem.00562-10

Kolbe M, Besir H, Essen LO et al (2000) Structure of the light-driven chloride pump halorhodopsin at 1.8 Å resolution. Science 288:1390–1396. https://doi.org/10.1126/science.288.5470.1390

Konno M, Kato Y, Kato HE et al (2016) Mutant of a light-driven sodium ion pump can transport cesium ions. J Phys Chem Lett 7:51–55. https://doi.org/10.1021/acs.jpclett.5b02385

Kouyama T, Kinosita K Jr, Ikegami A (1988) Structure and function of bacteriorhodopsin. Adv Biophys 24:123–175

Kouyama T, Kanada S, Takeguchi Y et al (2010) Crystal structure of the light-driven chloride pump halorhodopsin from *Natronomonas pharaonis*. J Mol Biol 396:564–579. https://doi.org/10.1016/j.jmb.2009.11.061

Kouyama T, Kawaguchi H, Nakanishi T et al (2015) Crystal structures of the $L_1$, $L_2$, N, and O states of *pharaonis* halorhodopsin. Biophys J 108:2680–2690. https://doi.org/10.1016/j.bpj.2015.04.027

Kovalev K, Astashkin R, Gushchin I et al (2020) Molecular mechanism of light-driven sodium pumping. Nat Commun 11:2137. https://doi.org/10.1038/s41467-020-16032-y

Kralj JM, Douglass AD, Hochbaum DR et al (2011) Optical recording of action potentials in mammalian neurons using a microbial rhodopsin. Nat Methods 9:90–95. https://doi.org/10.1038/nmeth.1782

Krebs RA, Alexiev U, Partha R et al (2002) Detection of fast light-activated $H^+$ release and M intermediate formation from proteorhodopsin. BMC Physiol 2:5

Kwon YM, Kim SY, Jung KH et al (2016) Diversity and functional analysis of light-driven pumping rhodopsins in marine flavobacteria. Microbiol Open 5:212–223. https://doi.org/10.1002/mbo3.321

Lanyi JK (1992) Proton transfer and energy coupling in the bacteriorhodopsin photocycle. J Bioenerg Biomembr 24:169–179

Lanyi JK (1993) Proton translocation mechanism and energetics in the light-driven pump bacteriorhodopsin. Biochim Biophys Acta 1183:241–261

Lanyi JK (1998) Understanding structure and function in the light-driven proton pump bacteriorhodopsin. J Struct Biol 124:164–178. https://doi.org/10.1006/jsbi.1998.4044

Lanyi JK (2004) Bacteriorhodopsin. Annu Rev Physiol 66:665–688. https://doi.org/10.1146/annurev.physiol.66.032102.150049

Lanyi JK, Schobert B (2004) Local-global conformational coupling in a heptahelical membrane protein: transport mechanism from crystal structures of the nine states in the bacteriorhodopsin photocycle. Biochemistry 43:3–8. https://doi.org/10.1021/bi035843s

Lanyi JK, Vodyanoy V (1986) Flash spectroscopic studies of the kinetics of the halorhodopsin photocycle. Biochemistry 25:1465–1470

Lanyi JK, Duschl A, Hatfield GW et al (1990) The primary structure of a halorhodopsin from *Natronobacterium pharaonis*. Structural, functional and evolutionary implications for bacterial rhodopsins and halorhodopsins. J Biol Chem 265:1253–1260

Lee SS, Choi AR, Kim SY et al (2011) *Acetabularia* rhodopsin I is a light-stimulated proton pump. J Nanosci Nanotechnol 11:4596–4600

Lee KA, Lee SS, Kim SY et al (2015) Mistic-fused expression of algal rhodopsins in *Escherichia coli* and its photochemical properties. Biochim Biophys Acta 1850:1694–1703. https://doi.org/10.1016/j.bbagen.2015.04.002

Lórenz-Fonfría VA, Kandori H (2009) Spectroscopic and kinetic evidence on how bacteriorhodopsin accomplishes vectorial proton transport under functional conditions. J Am Chem Soc 131:5891–5901. https://doi.org/10.1021/ja900334c

Luck M, Mathes T, Bruun S et al (2012) A photochromic histidine kinase rhodopsin (HKR1) that is bimodally switched by ultraviolet and blue light. J Biol Chem 287:40083–40090. https://doi.org/10.1074/jbc.M112.401604

Luecke H (2000) Atomic resolution structures of bacteriorhodopsin photocycle intermediates: the role of discrete water molecules in the function of this light-driven ion pump. Biochim Biophys Acta 1460:133–156

Luecke H, Schobert B, Richter HT et al (1999) Structure of bacteriorhodopsin at 1.55 Å resolution. J Mol Biol 291:899–911. https://doi.org/10.1006/jmbi.1999.3027

Luecke H, Schobert B, Stagno J et al (2008) Crystallographic structure of xanthorhodopsin, the light-driven proton pump with a dual chromophore. Proc Natl Acad Sci USA 105:16561–16565. https://doi.org/10.1073/pnas.0807162105

Maciejko J, Mehler M, Kaur J et al (2015) Visualizing specific cross-protomer interactions in the homo-oligomeric membrane protein proteorhodopsin by dynamic-nuclear-polarization-enhanced solid-state NMR. J Am Chem Soc 137:9032–9043. https://doi.org/10.1021/jacs.5b03606

Maciejko J, Kaur J, Becker-Baldus J et al (2019) Photocycle-dependent conformational changes in the proteorhodopsin cross-protomer Asp-His-Trp triad revealed by DNP-enhanced MAS-NMR. Proc Natl Acad Sci USA 116:8342–8349. https://doi.org/10.1073/pnas.1817665116

Maeda A, Sasaki J, Shichida Y et al (1992) Structures of aspartic acid-96 in the L and N intermediates of bacteriorhodopsin: analysis by Fourier transform infrared spectroscopy. Biochemistry 31:4684–4690

Maeda A, Kandori H, Yamazaki Y et al (1997) Intramembrane signaling mediated by hydrogen-bonding of water and carboxyl groups in bacteriorhodopsin and rhodopsin. J Biochem 121:399–406

Mamedov MD, Mamedov AM, Bertsova YV et al (2016) A single mutation converts bacterial $Na^+$-transporting rhodopsin into an $H^+$ transporter. FEBS Lett 590:2827–2835. https://doi.org/10.1002/1873-3468.12324

Mamedov AM, Bertsova YV, Anashkin VA et al (2018) Identification of the key determinant of the transport promiscuity in $Na^+$-translocating rhodopsins. Biochem Biophys Res Commun 499:600–604. https://doi.org/10.1016/j.bbrc.2018.03.196

Man D, Wang W, Sabehi G et al (2003) Diversification and spectral tuning in marine proteorhodopsins. EMBO J 22:1725–1731. https://doi.org/10.1093/emboj/cdg183

Mathies RA, Brito Cruz CH, Pollard WT et al (1988) Direct observation of the femtosecond excited-state *cis-trans* isomerization in bacteriorhodopsin. Science 240:777–779

Matsui Y, Sakai K, Murakami M et al (2002) Specific damage induced by x-ray radiation and structural changes in the primary photoreaction of bacteriorhodopsin. J Mol Biol 324:469–481. https://doi.org/10.1016/S0022-2836(02)01110-5

Matsuno-Yagi A, Mukohata Y (1977) Two possible roles of bacteriorhodopsin; a comparative study of strains of *Halobacterium halobium* differing in pigmentation. Biochem Biophys Res Commun 78:237–243

Mattingly M, Weineck K, Costa J et al (2018) Hyperpolarization by activation of halorhodopsin results in enhanced synaptic transmission: Neuromuscular junction and CNS circuit. PLoS One 13:e0200107. https://doi.org/10.1371/journal.pone.0200107

Melaccio F, Del Carmen Marín M, Valentini A et al (2016) Toward automatic rhodopsin modeling as a tool for high-throughput computational photobiology. J Chem Theory Comput 12:6020–6034. https://doi.org/10.1021/acs.jctc.6b00367

Miller A, Oesterhelt D (1990) Kinetic optimization of bacteriorhodopsin by aspartic acid-96 as an internal proton donor. Biochim Biophys Acta Bioenerg 1020:57–64. https://doi.org/10.1016/0005-2728(90)90093-J

Misra R, Eliash T, Sudo Y et al (2019) Retinal-salinixanthin interactions in a thermophilic rhodopsin. J Phys Chem B 123(1):10–20. https://doi.org/10.1021/acs.jpcb.8b06795

Mogi T, Stern LJ, Marti T et al (1988) Aspartic acid substitutions affect proton translocation by bacteriorhodopsin. Proc Natl Acad Sci USA 85:4148–4152

Morizumi T, Ou WL, Van Eps N et al (2019) X-ray crystallographic structure and oligomerization of *Gloeobacter* rhodopsin. Sci Rep 9:11283. https://doi.org/10.1038/s41598-019-47445-5

Mukohata Y, Sugiyama Y, Ihara K et al (1988) An Australian halobacterium contains a novel proton pump retinal protein: archaerhodopsin. Biochem Biophys Res Commun 151:1339–1345

Mukohata Y, Ihara K, Uegaki K et al (1991) Australian *Halobacteria* and their retinal-protein ion pumps. Photochem Photobiol 54:1039–1045

Müller M, Bamann C, Bamberg E et al (2015) Light-induced helix movements in channelrhodopsin-2. J Mol Biol 427:341–349. https://doi.org/10.1016/j.jmb.2014.11.004

Muroda K, Nakashima K, Shibata M et al (2012) Protein-bound water as the determinant of asymmetric functional conversion between light-driven proton and chloride pumps. Biochemistry 51:4677–4684. https://doi.org/10.1021/bi300485r

Nango E, Royant A, Kubo M et al (2016) A three-dimensional movie of structural changes in bacteriorhodopsin. Science 354:1552–1557. https://doi.org/10.1126/science.aah3497

Needham DM, Yoshizawa S, Hosaka T et al (2019) A distinct lineage of giant viruses brings a rhodopsin photosystem to unicellular marine predators. Proc Natl Acad Sci USA 116:20574–20583. https://doi.org/10.1073/pnas.1907517116

Neutze R, Pebay-Peyroula E, Edman K et al (2002) Bacteriorhodopsin: a high-resolution structural view of vectorial proton transport. Biochim Biophys Acta 1565:144–167

Niho A, Yoshizawa S, Tsukamoto T et al (2017) Demonstration of a light-driven $SO_4^{2-}$ transporter and its spectroscopic characteristics. J. Am. Chem. Soc. https://doi.org/10.1021/jacs.6b12139

Oesterhelt D, Stoeckenius W (1971) Rhodopsin-like protein from the purple membrane of *Halobacterium halobium*. Nat New Biol 233:149–152

Oesterhelt D, Stoeckenius W (1973) Functions of a new photoreceptor membrane. Proc Natl Acad Sci USA 70:2853–2857

Oesterhelt D, Hegemann P, Tittor J (1985) The photocycle of the chloride pump halorhodopsin. II: quantum yields and a kinetic model. EMBO J 4:2351–2356

Oren A (2013) *Salinibacter*: an extremely halophilic bacterium with archaeal properties. FEMS Microbiol Lett 342:1–9. https://doi.org/10.1111/1574-6968.12094

Otto H, Marti T, Holz M et al (1989) Aspartic acid-96 is the internal proton donor in the reprotonation of the Schiff base of bacteriorhodopsin. Proc Natl Acad Sci USA 86:9228–9232

Pebay-Peyroula E, Rummel G, Rosenbusch JP et al (1997) X-ray structure of bacteriorhodopsin at 2.5 angstroms from microcrystals grown in lipidic cubic phases. Science 277:1676–1681

Pedraza-González L, De Vico L, Marι NM et al (2019) *a*-ARM: automatic rhodopsin modeling with chromophore cavity generation, ionization state selection, and external counterion placement. J Chem Theory Comput 15:3134–3152. https://doi.org/10.1021/acs.jctc.9b00061

Petrovskaya LE, Lukashev EP, Chupin VV et al (2010) Predicted bacteriorhodopsin from *Exiguobacterium sibiricum* is a functional proton pump. FEBS Lett 584:4193–4196. https://doi.org/10.1016/j.febslet.2010.09.005

Petrovskaya LE, Balashov SP, Lukashev EP et al (2015) ESR—a retinal protein with unusual properties from *Exiguobacterium sibiricum*. Biochemistry (Mosc) 80:688–700. https://doi.org/10.1134/S000629791506005X

Pettei MJ, Yudd AP, Nakanishi K et al (1977) Identification of retinal isomers isolated from bacteriorhodopsin. Biochemistry 16:1955–1959

Philosof A, Béjà O (2013) Bacterial, archaeal and viral-like rhodopsins from the red sea. Environ Microbiol Rep 5:475–482. https://doi.org/10.1111/1758-2229.12037

Piatkevich KD, Jung EE, Straub C et al (2018) A robotic multidimensional directed evolution approach applied to fluorescent voltage reporters. Nat Chem Biol

14:352–360. https://doi.org/10.1038/s41589-018-0004-9

Pinhassi J, DeLong EF, Béjà O et al (2016) Marine bacterial and archaeal ion-pumping rhodopsins: genetic diversity, physiology, and ecology. Microbiol Mol Biol Rev 80:929–954. https://doi.org/10.1128/mmbr.00003-16

Polívka T, Balashov SP, Chábera P et al (2009) Femtosecond carotenoid to retinal energy transfer in xanthorhodopsin. Biophys J 96:2268–2277. https://doi.org/10.1016/j.bpj.2009.01.004

Pushkarev A, Béjà O (2016) Functional metagenomic screen reveals new and diverse microbial rhodopsins. ISME J 10:2331–2335. https://doi.org/10.1038/ismej.2016.7

Radzwill N, Gerwert K, Steinhoff HJ (2001) Time-resolved detection of transient movement of helices F and G in doubly spin-labeled bacteriorhodopsin. Biophys J 80:2856–2866. https://doi.org/10.1016/S0006-3495(01)76252-2

Ramirez S, Liu X, MacDonald CJ et al (2015) Activating positive memory engrams suppresses depression-like behaviour. Nature 522:335–339. https://doi.org/10.1038/nature14514

Ran T, Ozorowski G, Gao Y et al (2013) Cross-protomer interaction with the photoactive site in oligomeric proteorhodopsin complexes. Acta Crystallogr D Biol Crystallogr 69:1965–1980. https://doi.org/10.1107/s0907444913017575

Ranjan P, Kateriya S (2018) Localization and dimer stability of a newly identified microbial rhodopsin from a polar, non-motile green algae. BMC Res Notes 11:65. https://doi.org/10.1186/s13104-018-3181-4

Reckel S, Gottstein D, Stehle J et al (2011) Solution nmr structure of proteorhodopsin. Angew Chem Int Ed Engl 50:11942–11946. https://doi.org/10.1002/anie.201105648

Rozenberg A, Oppermann J, Wietek J et al (2020) Lateral gene transfer of anion-conducting channelrhodopsins between green algae and giant viruses. Curr. Biol. 30:1-11. https://doi.org/10.1016/j.cub.2020.09.056

Rusch DB, Halpern AL, Sutton G et al (2007) The *Sorcerer II* Global Ocean Sampling expedition: Northwest Atlantic through eastern tropical Pacific. PLoS Biol 5:e77. https://doi.org/10.1371/journal.pbio.0050077

Sabehi G, Kirkup BC, Rozenberg M et al (2007) Adaptation and spectral tuning in divergent marine proteorhodopsins from the eastern Mediterranean and the Sargasso Seas. ISME J 1:48–55. https://doi.org/10.1038/ismej.2007.10

Saitou N, Nei M (1987) The neighbor-joining method: a new method for reconstructing phylogenetic trees. Mol Biol Evol 4:406–425

Sass HJ, Schachowa IW, Rapp G et al (1997) The tertiary structural changes in bacteriorhodopsin occur between M states: X-ray diffraction and Fourier transform infrared spectroscopy. EMBO J 16:1484–1491. https://doi.org/10.1093/emboj/16.7.1484

Sass HJ, Büldt G, Gessenich R et al (2000) Structural alterations for proton translocation in the m state of wild-type bacteriorhodopsin. Nature 406:649–653. https://doi.org/10.1038/35020607

Sato H, Takeda K, Tani K et al (1999) Specific lipid-protein interactions in a novel honeycomb lattice structure of bacteriorhodopsin. Acta Crystallogr D Biol Crystallogr 55:1251–1256

Sato M, Kikukawa T, Araiso T et al (2003) Roles of Ser130 and Thr126 in chloride binding and photocycle of *pharaonis* halorhodopsin. J Biochem 134:151–158

Sato M, Kubo M, Aizawa T et al (2005) Role of putative anion-binding sites in cytoplasmic and extracellular channels of *Natronomonas pharaonis* halorhodopsin. Biochemistry 44:4775–4784. https://doi.org/10.1021/bi047500f

Scharf B, Engelhard M (1994) Blue halorhodopsin from *Natronobacterium pharaonis*: wavelength regulation by anions. Biochemistry 33:6387–6393

Scheib U, Stehfest K, Gee CE et al (2015) The rhodopsin-guanylyl cyclase of the aquatic fungus *Blastocladiella emersonii* enables fast optical control of cGMP signaling. Sci Signal 8:rs8. https://doi.org/10.1126/scisignal.aab0611

Schneider F, Grimm C, Hegemann P (2015) Biophysics of channelrhodopsin. Annu Rev Biophys 44:167–186. https://doi.org/10.1146/annurev-biophys-060414-034014

Schobert B, Lanyi JK (1982) Halorhodopsin is a light-driven chloride pump. J Biol Chem 257:10306–10313

Schobert B, Lanyi JK, Cragoe EJ Jr (1983) Evidence for a halide-binding site in halorhodopsin. J Biol Chem 258:15158–15164

Schobert B, Lanyi JK, Oesterhelt D (1986) Effects of anion binding on the deprotonation reactions of halorhodopsin. J Biol Chem 261:2690–2696

Schreiner M, Schlesinger R, Heberle J et al (2015) Structure of halorhodopsin from *Halobacterium salinarum* in a new crystal form that imposes little restraint on the E-F loop. J Struct Biol 190:373–378. https://doi.org/10.1016/j.jsb.2015.04.010

Sharma AK, Spudich JL, Doolittle WF (2006) Microbial rhodopsins: functional versatility and genetic mobility. Trends Microbiol 14:463–469. https://doi.org/10.1016/j.tim.2006.09.006

Shevchenko V, Gushchin I, Polovinkin V et al (2017a) Sodium and engineered potassium light-driven pumps. In: Appasani K (ed) Optogenetics from neuronal function to mapping and disease biology. Cambridge University Press, Cambridge, pp 79–92. https://doi.org/10.1017/9781107281875.008

Shevchenko V, Mager T, Kovalev K et al (2017b) Inward $H^+$ pump xenorhodopsin: mechanism and alternative optogenetic approach. Sci Adv 3:e1603187. https://doi.org/10.1126/sciadv.1603187

Shi L, Yoon SR, Bezerra AG Jr et al (2006) Cytoplasmic shuttling of protons in *Anabaena* sensory rhodopsin: implications for signaling mechanism. J Mol Biol

358:686–700. https://doi.org/10.1016/j.jmb.2006.02.036

Shibata M, Muneda N, Sasaki T et al (2005) Hydrogen-bonding alterations of the protonated Schiff base and water molecule in the chloride pump of *Natronobacterium pharaonis*. Biochemistry 44:12279–12286. https://doi.org/10.1021/bi050726d

Shibata M, Yamashita H, Uchihashi T et al (2010) High-speed atomic force microscopy shows dynamic molecular processes in photoactivated bacteriorhodopsin. Nat Nanotechnol 5:208–212. https://doi.org/10.1038/nnano.2010.7

Shibata M, Inoue K, Ikeda K et al (2018) Oligomeric states of microbial rhodopsins determined by high-speed atomic force microscopy and circular dichroic spectroscopy. Sci Rep 8:8262. https://doi.org/10.1038/s41598-018-26606-y

Shichida Y, Yoshizawa T (2004) Photochemical aspect of rhodopsin. In: Horspool WM, Lenci F (eds) CRC handbook of organic photochemistry and photobiology. 2nd edn. CRC Press, Boca Raton, FL, pp 125–121–125–113

Shichida Y, Matuoka S, Hidaka Y et al (1983) Absorption-spectra of intermediates of bacteriorhodopsin measured by laser photolysis at room temperatures. Biochim Biophys Acta 723:240–246. https://doi.org/10.1016/0005-2728(83)90123-8

Siletsky SA, Mamedov MD, Lukashev EP et al (2019) Elimination of proton donor strongly affects directionality and efficiency of proton transport in ESR, a light-driven proton pump from *Exiguobacterium sibiricum*. Biochim Biophys Acta Bioenerg 1860:1–11. https://doi.org/10.1016/j.bbabio.2018.09.365

Sineshchekov OA, Trivedi VD, Sasaki J et al (2005) Photochromicity of *Anabaena* sensory rhodopsin, an atypical microbial receptor with a *cis*-retinal light-adapted form. J Biol Chem 280:14663–14668. https://doi.org/10.1074/jbc.M501416200

Skopintsev P, Ehrenberg D, Weinert T et al. (2020) Femtosecond-to-millisecond structural changes in a light-driven sodium pump. Nature 10.1038/s41586-020-2307-8:Published in the web. https://doi.org/10.1038/s41586-020-2307-8

Slamovits CH, Okamoto N, Burri L et al (2011) A bacterial proteorhodopsin proton pump in marine eukaryotes. Nat Commun 2:183. https://doi.org/10.1038/ncomms1188

Sorokin DY, Muntyan MS, Toshchakov SV et al (2018) Phenotypic and genomic properties of a novel deep-lineage haloalkaliphilic member of the phylum *Balneolaeota* from soda lakes possessing $Na^+$-translocating proteorhodopsin. Front Microbiol 9:2672. https://doi.org/10.3389/fmicb.2018.02672

Spudich JL, Jung K-H (2005) Microbial rhodopsin: phylogenetic and functional diversity. In: Briggs WR, Spudich JL (eds) Handbook of photosensory receptors. Wiley-VCH Verlag GmbH & Co. KGaA, Weinheim, pp 1–23

Spudich EN, Sundberg SA, Manor D et al (1986) Properties of a second sensory receptor protein in *Halobacterium halobium* phototaxis. Proteins 1:239–246. https://doi.org/10.1002/prot.340010306

Stingl U, Desiderio RA, Cho JC et al (2007a) The SAR92 clade: an abundant coastal clade of culturable marine bacteria possessing proteorhodopsin. Appl Environ Microbiol 73:2290–2296. https://doi.org/10.1128/aem.02559-06

Stingl U, Tripp HJ, Giovannoni SJ (2007b) Improvements of high-throughput culturing yielded novel SAR11 strains and other abundant marine bacteria from the Oregon coast and the Bermuda Atlantic time series study site. ISME J 1:361–371. https://doi.org/10.1038/ismej.2007.49

Subramaniam S, Henderson R (2000) Molecular mechanism of vectorial proton translocation by bacteriorhodopsin. Nature 406:653–657. https://doi.org/10.1038/35020614

Subramaniam S, Lindahl M, Bullough P et al (1999) Protein conformational changes in the bacteriorhodopsin photocycle. J Mol Biol 287:145–161. https://doi.org/10.1006/jmbi.1999.2589

Sudo Y, Yoshizawa S (2016) Functional and photochemical characterization of a light-driven proton pump from the gammaproteobacterium *Pantoea vagans*. Photochem Photobiol 92:420–427. https://doi.org/10.1111/php.12585

Sudo Y, Yamabi M, Kato S et al (2006) Importance of specific hydrogen bonds of archaeal rhodopsins for the binding to the transducer protein. J Mol Biol 357:1274–1282. https://doi.org/10.1016/j.jmb.2006.01.061

Sudo Y, Okazaki A, Ono H et al (2013) A blue-shifted light-driven proton pump for neural silencing. J Biol Chem 288:20624–20632. https://doi.org/10.1074/jbc.M113.475533

Suomivuori CM, Gamiz-Hernandez AP, Sundholm D et al (2017) Energetics and dynamics of a light-driven sodium-pumping rhodopsin. Proc Natl Acad Sci USA 114:7043–7048. https://doi.org/10.1073/pnas.1703625114

Tahara S, Takeuchi S, Abe-Yoshizumi R et al (2015) Ultrafast photoreaction dynamics of a light-driven sodium-ion-pumping retinal protein from *Krokinobacter eikastus* revealed by femtosecond time-resolved absorption spectroscopy. J Phys Chem Lett 6:4481–4486. https://doi.org/10.1021/acs.jpclett.5b01994

Tamogami J, Kikukawa T, Miyauchi S et al (2009) A tin oxide transparent electrode provides the means for rapid time-resolved pH measurements: application to photoinduced proton transfer of bacteriorhodopsin and proteorhodopsin. Photochem Photobiol 85:578–589. https://doi.org/10.1111/j.1751-1097.2008.00520.x

Tamogami J, Kikukawa T, Ohkawa K et al (2018) Interhelical interactions between D92 and C218 in the cytoplasmic domain regulate proton uptake upon N-decay in the proton transport of *Acetabularia*

rhodopsin II. J Photochem Photobiol B 183:35–45. https://doi.org/10.1016/j.jphotobiol.2018.04.012

Tamura K, Peterson D, Peterson N et al (2011) Mega5: molecular evolutionary genetics analysis using maximum likelihood, evolutionary distance, and maximum parsimony methods. Mol Biol Evol 28:2731–2739. https://doi.org/10.1093/molbev/msr121

Takahashi T, Tomioka H, Kamo N et al (1985) A photosystem other than PS370 also mediates the negative phototaxis of *Halobacterium halobium*. FEMS Microbiol Lett 28:161-165. https://doi.org/10.1111/j.1574-6968.1985.tb00784.x

Tateno M, Ihara K, Mukohata Y (1994) The novel ion pump rhodopsins from *Haloarcula* form a family independent from both the bacteriorhodopsin and archaerhodopsin families/tribes. Arch Biochem Biophys 315:127–132. https://doi.org/10.1006/abbi.1994.1480

Thorgeirsson TE, Milder SJ, Miercke LJ et al (1991) Effects of Asp-96 - Asn, Asp-85 - Asn, and Arg-82 - Gln single-site substitutions on the photocycle of bacteriorhodopsin. Biochemistry 30:9133–9142

Tomioka H, Takahashi T, Kamo N et al (1986) Flash spectrophotometric identification of a fourth rhodopsin-like pigment in *Halobacterium halobium*. Biochem Biophys Res Commun 139:389–395

Tsukamoto T, Inoue K, Kandori H et al (2013) Thermal and spectroscopic characterization of a proton pumping rhodopsin from an extreme thermophile. J Biol Chem 288:21581–21592. https://doi.org/10.1074/jbc.M113.479394

Tsukamoto T, Mizutani K, Hasegawa T et al (2016) X-ray crystallographic structure of thermophilic rhodopsin: implications for high thermal stability and optogenetic function. J Biol Chem 291:12223–12232. https://doi.org/10.1074/jbc.M116.719815

Tsukamoto T, Yoshizawa S, Kikukawa T et al (2017) Implications for the light-driven chloride ion transport mechanism of *Nonlabens marinus* rhodopsin 3 by its photochemical characteristics. J Phys Chem B 121:2027–2038. https://doi.org/10.1021/acs.jpcb.6b11101

Tsunoda SP, Ewers D, Gazzarrini S et al (2006) $H^+$-pumping rhodopsin from the marine alga *Acetabularia*. Biophys J 91:1471–1479. https://doi.org/10.1529/biophysj.106.086421

Tsunoda SP, Prigge M, Abe-Yoshizumi R et al (2017) Functional characterization of sodium-pumping rhodopsins with different pumping properties. PLoS One 12:e0179232. https://doi.org/10.1371/journal.pone.0179232

Ugalde JA, Podell S, Narasingarao P et al (2011) Xenorhodopsins, an enigmatic new class of microbial rhodopsins horizontally transferred between archaea and bacteria. Biol Direct 6:52. https://doi.org/10.1186/1745-6150-6-52

Váró G, Lanyi JK (1991) Kinetic and spectroscopic evidence for an irreversible step between deprotonation and reprotonation of the Schiff base in the bacteriorhodopsin photocycle. Biochemistry 30:5008–5015

Váró G, Brown LS, Sasaki J et al (1995a) Light-driven chloride ion transport by halorhodopsin from *Natronobacterium pharaonis*. 1. The photochemical cycle. Biochemistry 34:14490–14499

Váró G, Needleman R, Lanyi JK (1995b) Light-driven chloride ion transport by halorhodopsin from *Natronobacterium pharaonis*. 2. Chloride release and uptake, protein conformation change, and thermodynamics. Biochemistry 34:14500–14507

Váró G, Zimányi L, Fan X et al (1995c) Photocycle of halorhodopsin from *Halobacterium salinarium*. Biophys J 68:2062–2072

Venter JC, Remington K, Heidelberg JF et al (2004) Environmental genome shotgun sequencing of the Sargasso Sea. Science 304:66–74. https://doi.org/10.1126/science.1093857

Vogt N (2015) Neuroscience. Algae are the best engineers of optogenetic inhibitors. Nat Methods 12:806–807

Vogt A, Guo Y, Tsunoda SP et al (2015) Conversion of a light-driven proton pump into a light-gated ion channel. Sci Rep 5:16450. https://doi.org/10.1038/srep16450

Wada T, Shimono K, Kikukawa T et al (2011) Crystal structure of the eukaryotic light-driven proton-pumping rhodopsin, *Acetabularia* rhodopsin II, from marine alga. J Mol Biol 411:986–998. https://doi.org/10.1016/j.jmb.2011.06.028

Waschuk SA, Bezerra AG Jr, Shi L et al (2005) *Leptosphaeria* rhodopsin: bacteriorhodopsin-like proton pump from a eukaryote. Proc Natl Acad Sci USA 102:6879–6883. https://doi.org/10.1073/pnas.0409659102

Wegener AA, Chizhov I, Engelhard M et al (2000) Time-resolved detection of transient movement of helix F in spin-labelled pharaonis sensory rhodopsin II. J Mol Biol 301:881–891. https://doi.org/10.1006/jmbi.2000.4008

Weinert T, Skopintsev P, James D et al (2019) Proton uptake mechanism in bacteriorhodopsin captured by serial synchrotron crystallography. Science 365:61–65. https://doi.org/10.1126/science.aaw8634

Wickstrand C, Dods R, Royant A et al (2015) Bacteriorhodopsin: would the real structural intermediates please stand up? Biochim Biophys Acta 1850:536–553. https://doi.org/10.1016/j.bbagen.2014.05.021

Yoshida K, Yamashita T, Sasaki K et al (2017) Chimeric microbial rhodopsins for optical activation of Gs-proteins. Biophys Physicobiol 14:183–190. https://doi.org/10.2142/biophysico.14.0_183

Yoshizawa S, Kawanabe A, Ito H et al (2012) Diversity and functional analysis of proteorhodopsin in marine flavobacteria. Environ Microbiol 14:1240–1248. https://doi.org/10.1111/j.1462-2920.2012.02702.x

Yoshizawa S, Kumagai Y, Kim H et al (2014) Functional characterization of flavobacteria rhodopsins reveals a unique class of light-driven chloride pump in bacteria.

Proc Natl Acad Sci USA 111:6732–6737. https://doi.org/10.1073/pnas.1403051111

Yun JH, Li X, Park JH et al (2019) Non-cryogenic structure of a chloride pump provides crucial clues to temperature-dependent channel transport efficiency. J Biol Chem 294(3):794–804. https://doi.org/10.1074/jbc.RA118.004038

Zhang F, Wang LP, Brauner M et al (2007) Multimodal fast optical interrogation of neural circuitry. Nature 446:633–639. https://doi.org/10.1038/nature05744

Zhao H, Ma B, Ji L et al (2017) Coexistence of light-driven $Na^+$ and $H^+$ transport in a microbial rhodopsin from *Nonlabens dokdonensis*. J Photochem Photobiol B 172:70–76. https://doi.org/10.1016/j.jphotobiol.2017.05.004

Zhu JY, Gdor I, Smolensky E et al (2010) Photoselective ultrafast investigation of xanthorhodopsin and its carotenoid antenna salinixanthin. J Phys Chem B 114:3038–3045. https://doi.org/10.1021/jp910845h

Zimányi L, Keszthelyi L, Lanyi JK (1989) Transient spectroscopy of bacterial rhodopsins with an optical multichannel analyzer. 1. Comparison of the photocycles of bacteriorhodopsin and halorhodopsin. Biochemistry 28:5165–5172

Zscherp C, Schlesinger R, Heberle J (2001) Time-resolved FT-IR spectroscopic investigation of the pH-dependent proton transfer reactions in the E194Q mutant of bacteriorhodopsin. Biochem Biophys Res Commun 283:57–63. https://doi.org/10.1006/bbrc.2001.4730

Zuckerkandl E, Pauling L (1965) Evolutionary divergence and convergence in proteins. In: Bryson V, Vogel HJ (eds) Evolving genes and proteins. Academic Press, New York, pp 97–166. https://doi.org/10.1016/C2013-0-11981-2

# Part II

# Light-Sensitive Signaling Molecules

# 7 Photoactivated Adenylyl Cyclases: Fundamental Properties and Applications

Mineo Iseki and Sam-Yong Park

**Abstract**

Photoactivated adenylyl cyclase (PAC) was first discovered to be a sensor for photoavoidance in the flagellate *Euglena gracilis*. PAC is a flavoprotein that catalyzes the production of cAMP upon illumination with blue light, which enables us to optogenetically manipulate intracellular cAMP levels in various biological systems. Recent progress in genome sequencing has revealed several related proteins in bacteria and ameboflagellates. Among them, the PACs from sulfur bacterium *Beggiatoa* sp. and cyanobacterium *Oscillatoria acuminata* have been well characterized, including their crystalline structure. Although there have not been many reported optogenetic applications of PACs so far, they have the potential to be used in various fields within bioscience.

**Keywords**

Photoactivated adenylyl cyclase · BLUF domain · Flavin · cAMP · Photomovement · *Euglena* · X-ray crystallography · Optogenetics

## Abbreviations

| | |
|---|---|
| AppA | Activation of photopigment and *puc* expression A |
| ATP | Adenosine triphosphate |
| BlrP1 | Blue-light-regulated phosphodiesterase 1 |
| BLUF | Sensor of blue light using flavin adenine dinucleotide |
| bPAC (BlaC) | Photoactivated adenylyl cyclase from *Beggiatoa.* |
| cAMP | 3′,5′-cyclic adenosine monophosphate |
| CFTR | Cystic fibrosis transmembrane conductance regulator |
| CNG | Cyclic nucleotide-gated |
| cPAC | Cyanobacteriochrome-based photoswitchable adenylyl cyclase |
| cRNA | Complementary RNA |
| EAL | Glutamate (E)-alanine (A)-leucine (L) |
| FAD | Flavin adenine dinucleotide |
| FMN | Flavin mononucleotide |
| GAF | cGMP-specific phosphodiesterases, adenylyl cyclases and FhlA |
| GFP | Green fluorescent protein |
| GST | Glutathione-*S*-transferase |
| GTP | Guanosine triphosphate |

M. Iseki (✉)
Faculty of Pharmaceutical Sciences, Toho University, Tokyo, Japan
e-mail: mineo.iseki@phar.toho-u.ac.jp

S.-Y. Park
Drug Design Laboratory, Graduate School of Medical Life Science, Yokohama City University, Yokohama, Japan



H. Yawo et al. (eds.), *Optogenetics*, Advances in Experimental Medicine and Biology 1293,
https://doi.org/10.1007/978-981-15-8763-4_7

| | |
|---|---|
| LcPAC | Photoactivated adenyl cyclase from *Ilumatobacter coccineus* |
| LiPAC | Photoactivated adenylyl cyclase from *Leptonema illini* |
| LOV | Light, oxygen, and voltage |
| mPAC | Photoactivated adenylyl cyclase from *Microcoleus chthonoplastes* |
| NgPAC | Photoactivated adenylyl cyclase from *Naegleria gruberi* |
| OaPAC | Photoactivated adenylyl cyclase from *Oscillatoria acuminata* |
| PAB (PFB) | Paraxonemal body (Paraflagellar body) |
| PAC | Photoactivated adenylyl cyclase |
| PbPAC | Photoactivated adenylyl cyclase from *Pseudanabaena biceps* |
| PCK1 | Phosphoenolpyruvate carboxykinase 1 |
| RNAi | RNA interference |
| SthK | Cyclic nucleotide gated $K^+$ channel from *Spirochaeta thermophila* |

## 7.1 Introduction

The recent remarkable expansion of optogenetics has been brought about by the discovery of a wide variety of light-sensing proteins, such as channelrhodopsins (Nagel et al. 2002; Sineshchekov et al. 2002; Suzuki et al. 2003), light, oxygen, and voltage (LOV)-domain proteins (Huala et al. 1997), sensor of blue light using flavin adenine dinucleotide (BLUF)-domain proteins (Gomelsky and Klug 2002). These proteins have been discovered over the last two decades after a long struggle searching for sensors that lead to blue-light-induced responses in plants and microorganisms. It should be noted that the search for these light-sensing proteins was based on pure intellectual curiosity about biological phenomena without any expectations of technological applications. In this chapter, we introduce the history and recent progress of research concerning photoactivated adenylyl cyclase (PAC), a BLUF-domain protein that is considered to be a promising optogenetic tool, as well mentioning some examples of its application.

## 7.2 Photoactivated Cyclase from *Euglena*

### 7.2.1 Discovery of Photoactivated Adenylyl Cyclase

*Euglena*, a photosynthetic unicellular flagellate, responds to light stimuli to place itself in an environment that has appropriate light. Such a response has been known for over a century (Engelman 1882; see Häder and Iseki (2017) for an overview of photomovement in *Euglena*) and has attracted a great deal of interest as a primitive sensory perception system. Action spectra for the photoaccumulation and photoavoidance of *Euglena* showed peaks in the UV-A/blue region of the spectrum, which suggested that a flavin-based photoreceptor was involved as a photosensor for this organism (Checcucci et al. 1976; Diehn 1969; Matsunaga et al. 1998). *Euglena* has a small ellipsoidal structure near the base of its flagellum, the paraxonemal body (PAB, also called paraflagellar body, PFB), which was thought to be a light-sensing organelle (Colombetti et al. 1982; Lebert 2001) (Fig. 7.1). The PAB exhibits green autofluorescence under UV-A or blue excitation, which indicates the presence of flavin in the organelle and suggested the hypothesis that a flavoprotein located in the PAB acts as the photoreceptor molecule. Several attempts to identify the flavoprotein in the PAB had been made (Brodhun and Häder 1990, 1995), but the results were ambiguous, possibly due to low quality of their PAB preparations. Iseki et al. (2002) succeeded in isolating enough PABs for biochemical analysis and discovered a 400-kDa flavoprotein that binds to FAD from the isolated paraxonemal bodies. The 400-kDa flavoprotein showed significant adenylyl cyclase activity that was drastically elevated upon illumination with blue light. It was accordingly named photoactivated adenylyl cyclase (PAC) (Fig. 7.2). PAC is a heterotetramer of α- and β-subunits that contain two BLUF domains (F1,

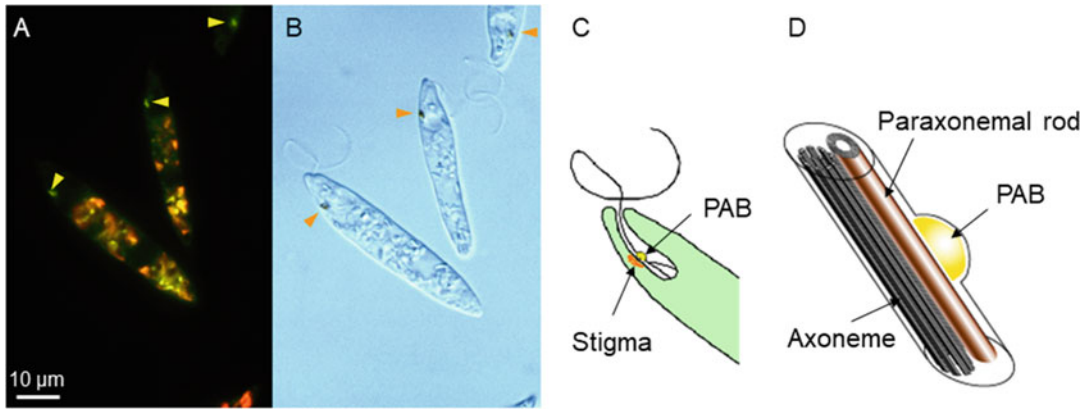


**Fig. 7.1** The paraxonemal body (PAB) and the stigma in *Euglena*. (**a**) The PAB (yellow arrowheads) exhibits green autofluorescence under UVA-blue excitation. (**b**) The stigma (orange arrowheads), an aggregates of carotenoid globules, can be observed in the bright field image of **a**. (**c**) Diagramatic representation of the position of the PAB and the stigma. (**d**) The PAB is attached to the paraxonemal rod that run parallel to the 9 + 2 axoneme within flagellar membrane

F2) each followed by an adenylyl cyclase catalytic domain (C1, C2) (Fig. 7.3). RNAi experiments have revealed that PAC acts as a sensor for photoavoidance in *Euglena* (Iseki et al. 2002). In the paper published in 2002, the authors discussed the possibility of the protein as a tool for the photomanipulation of the intracellular cAMP levels in heterologous cell systems.

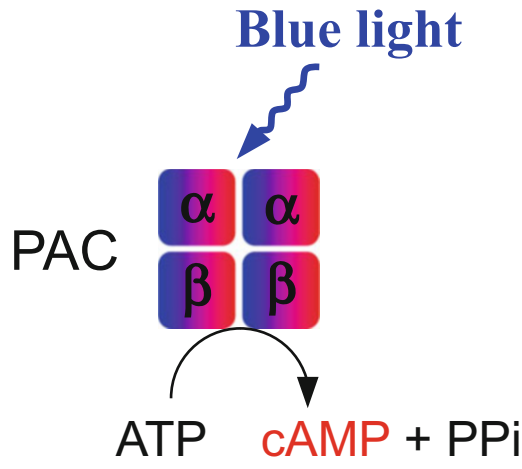


**Fig. 7.2** Illustrated image of PAC photoactivation. *Euglena* PAC is a heterotetramer with α- and β-subunits which produce cAMP when activated by blue light

### 7.2.2 Properties of Photoactivated Adenylyl Cyclase from *Euglena*

The photoactivation properties of PAC purified from *Euglena* were examined by Yoshikawa et al. (2005). The activity of PAC was dependent both on the photon fluence rate and the duration of illumination, the reciprocity of which held well in the range of 2–50 μmol $m^{-2}$ $s^{-1}$ (with a total fluence of 1200 μmol $m^{-2}$). Intermittent illumination also caused the activation of PAC, in a photon fluence-dependent manner, irrespective of cycle periods; this means that an elevation of PAC activity occurred only during the light period and that the elevated PAC activity fell off within 100 ms of the illumination ending (Yoshikawa et al. 2005). Such a sharp switching property seems suitable in the use of PAC as a tool to control the swift manipulation of intracellular cAMP levels.

Studies on the activation mechanism of PAC have not progressed well because difficulties in expressing PAC at full length in heterologous systems, while keeping its activity, have hampered efforts to obtain enough of the protein for a conventional spectroscopy or X-ray crystallography. Ito et al. (2005) obtained a soluble recombinant BLUF domain (F2) in PACα via

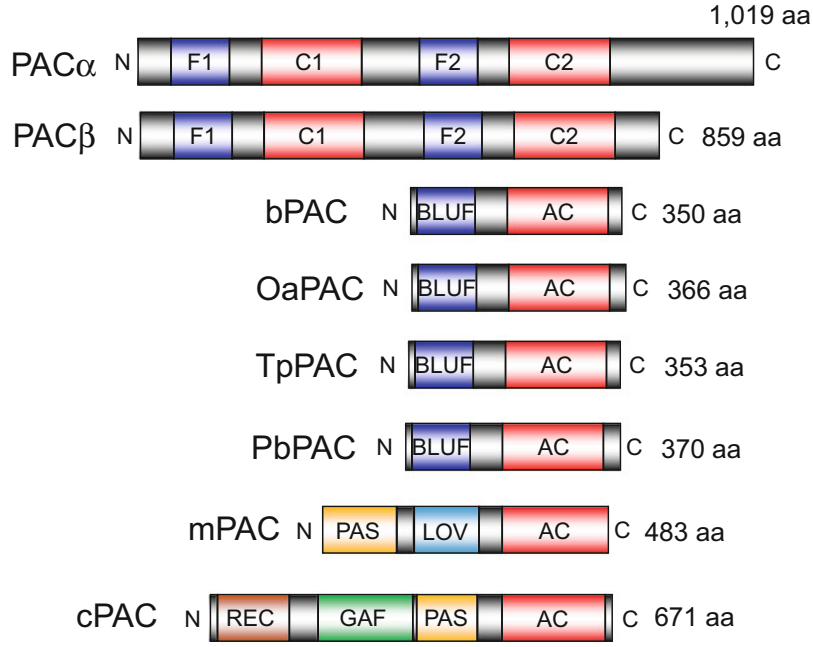


**Fig. 7.3** Domain organization of PACs. α- and β-subunits of *Euglena* PAC (PACα, PACβ), bPAC from *Beggiatoa* sp., OaPAC from *Oscillatoria acuminata* PCC 6304, TpPAC from *Turneriella parva* DSM 21527, PbPAC from *Pseudanabaena biceps* PCC 7429, mPAC from *Microcoleus chthonoplastes* PCC7420, and cPAC from *Microcoleus* sp. PCC7113 are presented

heterologous expression with fused glutathione-*S*-transferase (GST) in *E. coli*. The recombinant F2 protein contained both FAD and flavin mononucleotide (FMN) with trace amounts of riboflavin and showed a spectral red shift upon blue-light illumination followed by recovery in darkness. Such photoinduced spectral shifts were first reported in the BLUF domain of AppA, a photosensor for gene expression in *Rhodobacter sphaeroides* (Masuda and Bauer 2002), and have been regarded as a common feature of BLUF domains. The spectral red shift is caused by a rearrangement of the hydrogen bonding network around the chromophore flavin, where the glutamine (Gln63 in AppA) and the tyrosine (Tyl21 in AppA) residues play a crucial role (Gauden et al. 2006; Kita et al. 2005; Kraft et al. 2003; see reviews by Masuda 2013; Park and Tame, 2017). Ito et al. (2005) reported that the PACαF2 proteins that were point mutated at the conserved tyrosine (Tyr472), or glutamine (Gln514), residue showed no photoinduced spectral shift. Fujiyoshi et al. (2011) measured the fluorescence from a single PACαF2 molecule at 1.5 K and observed reversible spectral jumps of fluorescence that were attributed to a structural change around the hydrogen bonds at the FAD-binding site because the mutation in Gln514 suppressed these spectral jumps. Thus, the mechanism of photoactivation in PACαF2 seems essentially the same as that of the prokaryotic BLUF proteins, though their kinetic properties are different. Interestingly, the quantum efficiency of the phototransformation of PACβF2 (0.06–0.08) is lower than that of PACαF2 (0.28–0.32), whereas the half-life for the dark relaxation of PACβF2 (3–6 s) is shorter than that of PACαF2 (34–44 s) (Ito et al. 2010). Such photocyclic features of PACαF2 and PACβF2 may be useful in designing optogenetic tools to control cAMP levels with different sensitivities.

### 7.2.3 Optogenetic Application of Photoactivated Adenylyl Cyclase from *Euglena*

Schröder-Lang et al. (2007) reported the functional expression of PAC in various biological systems. They expressed PACα and/or PACβ with the human cystic fibrosis transmembrane

conductance regulator (CFTR) as a cAMP sensor in *Xenopus* oocytes and detected light-induced increases in conductance which indicates an increase in intracellular cAMP levels. They also expressed PACα in HEK293 cells with cyclic nucleotide-gated (CNG) channels and detected a light-induced $Ca^{2+}$ influx through CNG channels. Finally, they made transgenic fruit flies using the Gal4-UAS enhancer expression system to target the brain with PACs. Wild-type fruit flies displayed continuous grooming activity when covered with a fine powder, while the neuronal expression of PACα resulted in hyperactivity and a substantial decline in grooming activity under blue-light stimulation. This was the first demonstration of an optogenetic application of PAC to control animal behavior.

Nagahama et al. (2007) injected the PAC protein purified from *Euglena* into sensory neurons in *Aplysia* pleural ganglia and observed a blue-light-induced increase in spike width and a decrease in spike amplitude, which indicates the elevation of intracellular cAMP levels. The transient expression of PACs in the sensory neurons also induced a change in spike shape upon illumination with blue light (Nagahama et al. 2007). Hong et al. (2011) made a cRNA that coded PACα fused with mCherry and injected it into a *Xenopus* embryo to observe the circus movement of dissociated cells. Illumination with blue light arrested the circus movement of the cRNA injected cells, which is attributable to an increase in the concentration of cAMP within the cells. Weissenberger et al. (2011) generated transgenic strains of *Caenorhabditis elegans* expressing PACα with a GFP fusion in cholinergic motor neurons and observed their behavior. Illumination with blue-light-induced changes in swimming frequency, speed of locomotion, and the number of backward locomotion episodes that were caused by cAMP synthesis upon the photoactivation of PACα (Weissenberger et al. 2011). These are good demonstrations that PAC can be used as an optogenetic tool that directly affects intracellular signaling.

An application of PAC in axonal morphology, such as axonal guidance, has been expected since PAC was discovered. Nicol et al. (2011) observed that growth cones expressing mCherry-PACα turned their axons toward the stimulated side when illuminated with blue light. Zhou et al. (2016) transfected primary cultures of dentate granule cells with PACα and demonstrated that a short-term elevation of intracellular cAMP levels with 10 min of illumination-induced axonal branching but not elongation, whereas long-term cAMP elevation with 30 min of illumination induced both axonal branching and elongation. These studies demonstrate that PAC is a powerful tool for the spatiotemporal manipulation of intracellular cAMP levels, which may have a medical application in helping to clarify the mechanisms of diseases related to axonal morphogenesis, such as epilepsy.

## 7.3 Bacterial Photoactivated Adenylyl Cyclases

### 7.3.1 Diversity of PACs

In the early days, PACs were thought to be found only in *Euglena* species and their relatives (Koumura et al. 2004). However, a PAC-like gene was found in the genome sequence of the sulfur bacterium *Beggiatoa* (Losi and Gärtner 2008). The *Beggiatoa* PAC (hereinafter referred to as bPAC) has a BLUF domain and a cyclase domain showing high similarity to the C-terminal half of the α- and β-subunits of *Euglena* PAC (hereinafter referred to as euPAC) (Fig. 7.3). bPAC has been heterologously expressed in *E. coli* (Ryu et al. 2010), *Xenopus* oocytes, and mammalian neurons (Stierl et al. 2011), where it acts as a light-dependent adenylyl cyclase. In recent years, similar genes have been found in the genome sequences of bacteria, e. g., *Leptonema illini* (LiPAC) (Penzkofer et al. 2014b), *Turneriella parva* (TpPAC) (Penzkofer et al. 2015), *Oscillatoria acuminata* (OaPAC) (Ohki et al. 2016), *Pseudanabaena biceps* (PbPAC), and *Ilumatobacter coccineus* (LcPAC) (Tanwar et al. 2018). Other PAC-like genes were found in the genome sequence of the free-living amoeba *Naegleria gruberi* (Fritz-Laylin et al. 2010). The genes (encoding NgPAC1, NgPAC2,

and NgPAC3) were expressed in *E. coli* and their photochemical properties were recorded (Penzkofer et al. 2011, 2014a). Yasukawa et al. (2013) isolated similar genes from the potentially pathogenic *Naegleria* species *N. australiensis* and showed that its genes act as photoactivated adenylyl cyclases when expressed in *E. coli*. Genome screening of the cyanobacterium *Microcoleus chthonoplastes* PCC7420 identified a unique light-regulated adenylyl cyclase (mPAC) which has an LOV domain for chromophore binding instead of a BLUF domain (Fig. 7.3). mPAC was shown to have adenylyl cyclase activity in vivo and in vitro, which increased upon being subjected to illumination with blue light (Raffelberg et al. 2013). Recently, a light-regulated adenylyl cyclase with a GAF domain like that of cyanobacteriochrome was discovered in the genome sequence of *Microcoleus* sp. PCC7113 (Fig. 7.3). The protein, cPAC (cyanobacteriochrome-based photoswitchable adenylyl cyclase), showed a bistable photocycle whose adenylyl cyclase was reversibly activated and inactivated by blue and green light, respectively (Blain-Hartung et al. 2018).

### 7.3.2 Overall Structural Properties of OaPAC

Bacterial PACs seem suitable for crystallization for X-ray diffraction analysis due to their small size and prokaryotic origin. OaPAC was expressed in *E. coli*. and successfully analyzed by X-ray crystallography (Ohki et al. 2016).

Since BLUF domains were first discovered in 2002, they have been identified in a number of proteins, including YcgF in *E. coli* (Rajagopal et al. 2004) and BlrP1 in *Klebsiella pneumonia* (Tyagi et al. 2008). Both are homodimers with a single EAL domain (Schmidt et al. 2005) attached to an N-terminal BLUF domain. BlrP1 is a light-regulated cyclic nucleotide phosphodiesterase; the crystal structure of BlrP1 was the first experimental model showing how the flavin controls enzyme activity (Barends et al. 2009). The two copies of the protein associate in an anti-parallel fashion through conserved residues of the EAL domains so that the BLUF domains are held apart and act independently, each interacting with the EAL domain of the partner chain. Changes in the hydrogen bonding pattern around the flavin upon exposure to light affect the coordination of essential metal ions at the active site, thus triggering a fourfold rise in activity under suitable conditions.

OaPAC shows some similarities to BlrP1, being a homodimer formed from polypeptide chains carrying an N-terminal BLUF domain and C-terminal class-III adenylate cyclase (AC) domain. Cyclase activity is stimulated approximately 20-fold by light. The recently solved structure of dark-state OaPAC, a PAC from *Oscillatoria acuminata*, has the highest resolution of the models and is used for illustration (Ohki et al. 2016, 2017). At 1.8 Å resolution, the data allow the side-chain conformations around the flavin to be modeled with confidence, even if the hydrogen atoms are invisible, showing the tyrosine donates a hydrogen bond to the glutamine. bPAC from the sulfur bacterium *Beggiatoa* has a very similar sequence to that of OaPAC (Stierl et al. 2011).

The OaPAC dimer structure is completely different from BlrP1, with the monomers arranged in a parallel fashion, and the two BLUF domains sandwiching a pair of helices (α3 and its symmetry mate) that hold the AC domains distant from the flavins. The two FMN binding sites are on the opposite sides of the dimer, over 30 Å apart, yet they apparently act cooperatively on the active sites, which are themselves a similar distance from the light-sensing prosthetic groups (Fig. 7.4). The homologous protein bPAC responds very differently to mutations of conserved residues around the FMN binding site compared with other BLUF domains, and maintains an activated state of timescales in the order of 1–10 s. We have carried out functional studies of a number of OaPAC mutants to determine how the novel spatial arrangement and connector helices trigger enzyme activity in the light-activated state.

BLUF domains consist of a five-stranded β-sheet flanked by helices (Anderson et al. 2005;

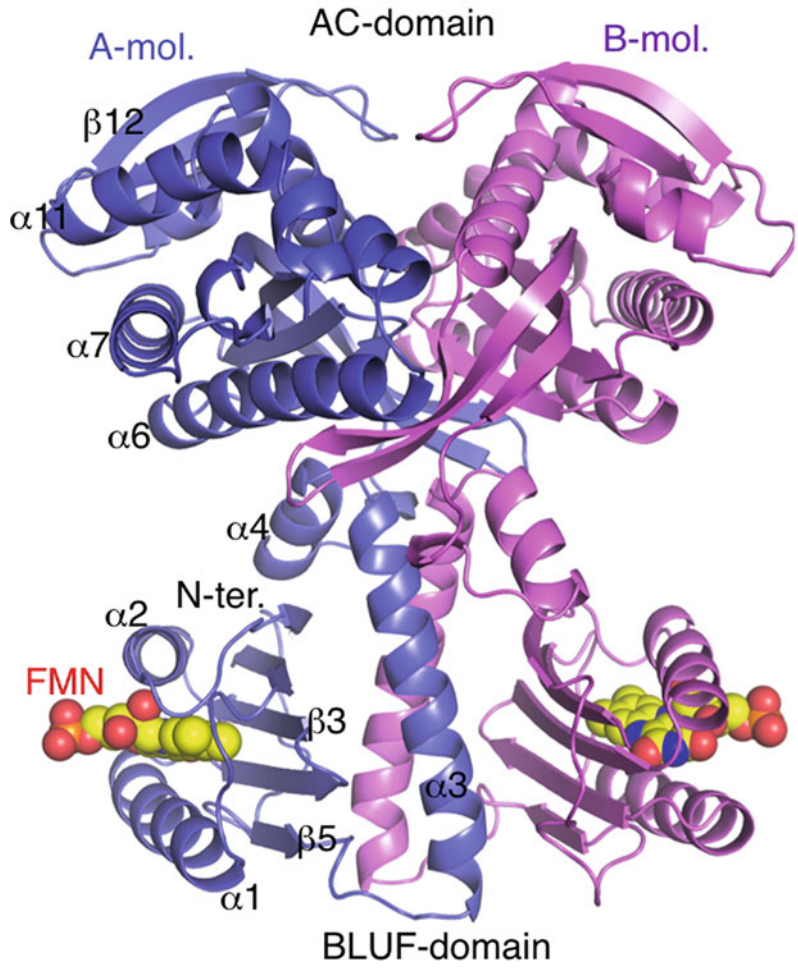


**Fig. 7.4** Crystallographic structure of dark-state OaPAC dimer. The chains are shown as Cα traces, with the dyad axis vertical and the BLUF domains at the bottom. One monomer is shown in pink, and the other in purple. The β5 strand of the β-sheet is connected to the N-terminus of the central α3 helix by a short loop region. The FMN chromophores are shown as space-filling models. Both domains contribute to the dimer interface; the BLUF domains do not directly contact the AC domain, but the C-terminal end of each α3 helix makes contact with the AC domain of the partner subunit

Kita et al. 2005), and use conserved tyrosine and glutamine residues adjacent to the bound FMN to sense light. Light exposure shifts the principal visible FMN absorption bands to longer wavelengths, and the carbonyl oxygen at C4 becomes a stronger hydrogen bond acceptor (Stelling et al. 2007). The maximum absorption difference (light state minus dark state) in OaPAC is seen at a wavelength of 492 nm. The simplest proposed sensing mechanism is a rotatory shift of the glutamine (Gln48), so that after stimulation this side chain donates a hydrogen bond to C4 = O carbonyl and accepts one from the tyrosine (Tyr6), whereas in the dark state the glutamine donates a hydrogen bond to the tyrosine (Anderson et al. 2005; Conrad et al. 2014). In BlrP1, these changes are accompanied by the movement of a nearby methionine (Met92) on the β5-strand of the BLUF domain, and both "$Met_{in}$" and "$Met_{out}$" arrangements have been described (Jung et al. 2006). The arrangement of Tyr6, Gln48, and Met92 in the two forms of OaPAC is presented in Fig. 7.5.

### 7.3.3 Optogenetic Application of Bacterial PACs

bPAC seemed advantageous in optogenetic application due to its smaller size, lower dark activity, and higher light activity than euPAC (Stierl et al. 2011). From the early demonstrations of the

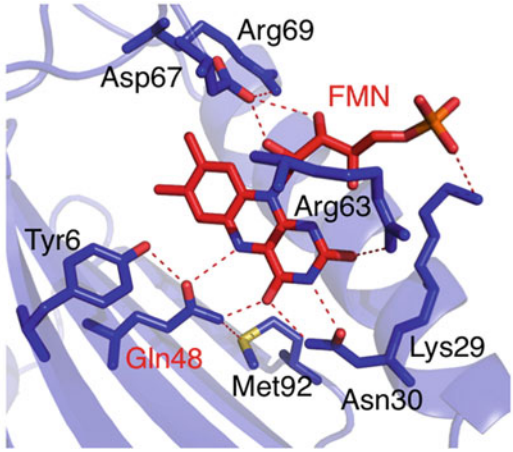


**Fig. 7.5** Structure of the FMN binding site in the BLUF domain. Hydrogen bonds formed by conserved residues with the flavin chromophore in the BLUF domain of OaPAC. The figure shows a ribbon diagram of the N-terminal of the protein. The FMN is shown as a stick model, with carbon atoms colored red, oxygen orange, and nitrogen blue. The O4 of the flavin receives hydrogen bonds from both Asn30 and Gln48, two absolutely conserved side chains in the BLUF family

optogenetic use of bPAC in *E. coli* (Ryu et al. 2010), *Xenopus* oocytes, rat hippocampal neurons, and adult fruit flies (Stierl et al. 2011), bPAC has been widely used as a tool to manipulate intracellular cAMP levels in various biological systems. Yasukawa et al. (2012) observed that light-dependent biofilm formation in *E. coli* transformed with an expression vector of bPAC (BsPAC). Tsvetanova and von Zastrow (2014) transfected bPAC into HEK293 cells and localized the expressed protein specifically to either the plasma membrane or the endosome-limiting membrane using targeting sequences. They showed that light stimulation of the plasma membrane bPAC did not lead to PCK1 (encoding phosphoenolpyruvate carboxykinase 1) induction, whereas the endosome-limiting membrane bPAC induced PCK1 upon light stimulation. Gutierrez-Triana et al. (2015) generated a stable transgenic line of zebrafish expressing bPAC and observed an increase in endogenous cortisol concentrations in a blue-light-dependent manner. Jansen et al. (2015) made a transgenic mouse model expressing bPAC in sperm and succeeded in restoring sperm motility and fertilization activity in vitro via light stimulation. Steuer Costa et al. (2017) reported that neurotransmitter release was promoted by bPAC stimulation in the cholinergic neurons of *C. elegans*. The optogenetic modulation of cAMP signaling that affects the starvation-induced developmental process in *Dictyostelium discoideum* using bPAC and NgPAC1 has also been reported (Tanwar et al. 2017).

### 7.3.4 Engineered Optogenetic Tools Based on Bacterial PACs

Since the catalytic domains of guanylyl cyclase and class-III adenylyl cyclase are closely related, the conversion of substrate specificity between these enzymes by site-directed mutagenesis has been successfully carried out in mammalian and cyanobacterial nucleotidyl cyclases (Kasahara et al. 2001; Liu et al. 1998; Sunahara et al. 1998). Ryu et al. (2010) attempted to change the substrate specificity of bPAC (BlaC) from ATP to GTP and succeeded in generating photoactivated guanylyl cyclase (BlgC) by substituting three amino acids (K197E/D265K/T267G). The same strategy of mutation was applied to several bacterial and *Naegleria* PACs, which brought about a variety of photoactivated guanylyl cyclases with different kinetic properties (Tanwar et al. 2018).

Since the spectral properties of cyanobacteriochromes are very diverse from near ultraviolet to the far-red region (Ikeuchi and Ishizuka 2008), cPAC was expected to change its spectral sensitivity by exchanging its GAF domain to that found in other cyanobacteriochromes. Blain-Hartung et al. (2018) succeeded in extending the wavelength-sensing specificity of cPAC into the near-IR range via domain exchange with the newly identified cyanobacteriochrome from *Leptolyngbya* sp. JSC1.

Beck et al. (2018) generated a light-gated $Ca^{2+}$-permeant channel by fusing bPAC to the bovine olfactory organ cyclic nucleotide-gated channel mutant T537S, which is a non-selective cation channel with high $Ca^{2+}$ permeability. They also generated a light-gated $K^+$ selective channel

by fusing bPAC to a cyclic nucleotide-gated $K^+$ channel from *Spirochaeta thermophila*, SthK. Using these constructs, they observed light-gated conductance in *Xenopus* oocytes and in rat hippocampal neurons. Moreover, they demonstrated that the constructs could be used to optogenetically control the motility of *Drosophila* larvae.

## 7.4 Perspectives

As mentioned above, reports on the optogenetic application of PACs in various biological systems have been increasing in the last decade. However, PACs have not yet gained a good standing, unlike channelrhodopsin, in the field of neuroscience. PACs have the potential to be used in various fields of bioscience because their product, cAMP, is a universal second messenger that is involved in a wide variety of biological processes, such as gene expression, hormonal control, olfaction, cell motility, and learning. Because cAMP is so ubiquitous, the fine-tuning of the cAMP concentration at a subcellular level would be necessary to realize actual optogenetic control of biological processes using PACs. In this sense, the subcellular targeting of PACs (O'Banion et al. 2019; Tsvetanova and von Zastrow 2014) is notable, and the use of light-dependent cyclic nucleotide phosphodiesterase (Yoshida et al. 2017) in combination with PACs may be helpful.

Both channelrhodopsin and PAC were first identified as a light sensor in microalgae. Since algae are a tremendously diverse group of organisms, there may be another embryo of optogenetic tools that awaits to be found. We would like to recall the saying: "*Study nature, not books*."

**Acknowledgments** Writing of this chapter was supported by JSPS KAKENHI Grant Numbers JP18K06166 and JP19H02672 to MI.

## References

Anderson S, Dragnea V, Masuda S, Ybe J, Moffat K, Bauer C (2005) Structure of a novel photoreceptor, the BLUF domain of AppA from *Rhodobacter sphaeroides*. Biochemistry 44:7998–8005

Barends TR, Hartmann E, Griese JJ, Beitlich T, Kirienko NV, Ryjenkov DA, Reinstein J, Shoeman RL, Gomelsky M, Schlichting I (2009) Structure and mechanism of a bacterial light-regulated cyclic nucleotide phosphodiesterase. Nature 459:1015–1018

Beck S, Yu-Strzelczyk J, Pauls D, Constantin OM, Gee CE, Ehmann N, Kittel RJ, Nagel G, Gao S (2018) Synthetic light-activated ion channels for optogenetic activation and inhibition. Front Neurosci 12:643

Blain-Hartung M, Rockwell NC, Moreno MV, Martin SS, Gan F, Bryant DA, Lagarias JC (2018) Cyanobacteriochrome-based photoswitchable adenylyl cyclases (cPACs) for broad spectrum light regulation of cAMP levels in cells. J Biol Chem 293:8473–8483

Brodhun B, Häder DP (1990) Photoreceptor proteins and pigments in the paraflagellar body of the flagellate *Euglena gracilis*. Photochem Photobiol 52:865–871

Brodhun B, Häder DP (1995) A novel procedure to isolate the chromoproteins in the paraflagellar body of the flagellate *Euglena gracilis*. J Photochem Photobiol B Biol 28:39–45

Checcucci A, Colombetti G, Ferrara R, Lenci F (1976) Action spectra for photoaccumulation of green and colorless *Euglena*: evidence for identification of receptor pigments. Photochem Photobiol 23:51–54

Colombetti G, Lenci F, Diehn B (1982) Responses to photic, chemical, and mechanical stimuli. In: Buetow DE (ed) The biology of *Euglena* III. Academic Press, New York, pp 169–195

Conrad KS, Manahan CC, Crane BR (2014) Photochemistry of flavoprotein light sensors. Nat Chem Biol 10:801–809

Diehn B (1969) Action spectra of the phototactic responses in *Euglena*. Biochim Biophys Acta 177:136–143

Engelman TW (1882) Über Licht- und Farbenperception niederster Organismen. Pflügers Arch Ges Physiol 29:387–400

Fritz-Laylin LK, Prochnik SE, Ginger ML, Dacks JB, Carpenter ML, Field MC, Kuo A, Paredez A, Chapman J, Pham J, Shu S, Neupane R, Cipriano M, Mancuso J, Tu H, Salamov A, Lindquist E, Shapiro H, Lucas S, Grigoriev IV, Cande WZ, Fulton C, Rokhsar DS, Dawson SC (2010) The genome of *Naegleria gruberi* illuminates early eukaryotic versatility. Cell 140:631–642

Fujiyoshi S, Hirano M, Matsushita M, Iseki M, Watanabe M (2011) Structural change of a cofactor binding site of flavoprotein detected by single-protein fluorescence spectroscopy at 1.5 K. Phys Rev Lett 106:078101

Gauden M, van Stokkum IH, Key JM, Luhrs D, van Grondelle R, Hegemann P, Kennis JT (2006) Hydrogen-bond switching through a radical pair mechanism in a flavin-binding photoreceptor. Proc Natl Acad Sci U S A 103:10895–10900

Gomelsky M, Klug G (2002) BLUF: a novel FAD-binding domain involved in sensory transduction in microorganisms. Trends Biochem Sci 27:497–500

Gutierrez-Triana JA, Herget U, Castillo-Ramirez LA, Lutz M, Yeh CM, De Marco RJ, Ryu S (2015) Manipulation of interrenal cell function in developing

zebrafish using genetically targeted ablation and an optogenetic tool. Endocrinology 156:3394–3401

Häder DP, Iseki M (2017) Photomovement in *Euglena*. In: Schwartzbach SD, Shigeoka S (eds) Advances in experimental medicine and biology 979: *Euglena*: biochemistry, cell and molecular biology. Springer, Berlin, pp 207–235

Hong KP, Spitzer NC, Nicol X (2011) Improved molecular toolkit for cAMP studies in live cells. BMC Res Notes 4:241

Huala E, Oeller PW, Liscum E, Han IS, Larsen E, Briggs WR (1997) *Arabidopsis* NPH1: a protein kinase with a putative redox-sensing domain. Science 278:2120–2123

Ikeuchi M, Ishizuka T (2008) Cyanobacteriochromes: a new superfamily of tetrapyrrole-binding photoreceptors in cyanobacteria. Photochem Photobiol Sci 7:1159–1167

Iseki M, Matsunaga S, Murakami A, Ohno K, Shiga K, Yoshida K, Sugai M, Takahashi T, Hori T, Watanabe M (2002) A blue-light-activated adenylyl cyclase mediates photoavoidance in *Euglena gracilis*. Nature 415:1047–1051

Ito S, Murakami A, Sato K, Nishina Y, Shiga K, Takahashi T, Higashi S, Iseki M, Watanabe M (2005) Photocycle features of heterologously expressed and assembled eukaryotic flavin-binding BLUF domains of photoactivated adenylyl cyclase (PAC), a blue-light receptor in *Euglena gracilis*. Photo Photo Sci 4:762–769

Ito S, Murakami A, Iseki M, Takahashi T, Higashi S, Watanabe M (2010) Differentiation of photocycle characteristics of flavin-binding BLUF domains of α-and β-subunits of photoactivated adenylyl cyclase of *Euglena gracilis*. Photo Photo Sci 9:1327–1335

Jansen V, Alvarez L, Balbach M, Strünker T, Hegemann P, Kaupp UB, Wachten D (2015) Controlling fertilization and cAMP signaling in sperm by optogenetics. Elife 4:e05161. https://doi.org/10.7554/eLife.05161

Jung A, Reinstein J, Domratcheva T, Shoeman RL, Schlichting I (2006) Crystal structures of the AppA BLUF domain photoreceptor provide insights into blue-light-mediated signal transduction. J Mol Biol 362:717–732

Kasahara M, Unno T, Yashiro K, Ohmori M (2001) CyaG, a novel cyanobacterial adenylyl cyclase and a possible ancestor of mammalian guanylyl cyclases. J Biol Chem 276:10564–10569

Kita A, Okajima K, Morimoto Y, Ikeuchi M, Miki K (2005) Structure of a cyanobacterial BLUF protein, Tll0078, containing a novel FAD-binding blue light sensor domain. J Mol Biol 349:1–9

Koumura Y, Suzuki T, Yoshikawa S, Watanabe M, Iseki M (2004) The origin of photoactivated adenylyl cyclase (PAC), the *Euglena* blue-light receptor: phylogenetic analysis of orthologues of PAC subunits from several euglenoids and trypanosome-type adenylyl cyclases from *Euglena gracilis*. Photochem Photobiol Sci 3:580–586

Kraft BJ, Masuda S, Kikuchi J, Dragnea V, Tollin G, Zaleski JM, Bauer CE (2003) Spectroscopic and mutational analysis of the blue-light photoreceptor AppA: a novel photocycle involving flavin stacking with an aromatic amino acid. Biochemistry 42:6726–6734

Lebert M (2001) Phototaxis of *Euglena gracilis*—flavins and pterins. In: Häder D-P (ed) Comprehensive series in photosciences 1: photomovement. Elsevier, Amsterdam, pp 297–341

Liu Y, Ruoho AE, Rao VD, Hurley JH (1998) Catalytic mechanism of the adenylyl and guanylyl cyclases: modeling and mutational analysis. Proc Natl Acad Sci U S A 94:13414–13419

Losi A, Gärtner W (2008) Bacterial bilin- and flavin-binding photoreceptors. Photochem Photobiol Sci 7:1168–1178

Masuda S (2013) Light detection and signal transduction in the BLUF photoreceptors. Plant Cell Physiol 54:171–179

Masuda S, Bauer CE (2002) AppA is a blue light photoreceptor that antirepresses photosynthesis gene expression in *Rhodobacter sphaeroides*. Cell 110:613–623

Matsunaga S, Hori T, Takahashi T, Kubota M, Watanabe M, Okamoto K, Masuda K, Sugai M (1998) Discovery of signaling effect of UV-B/C light in the extended UV-A/blue-type action spectra for stepdown and step-up photophobic responses in the unicellular flagellate alga *Euglena gracilis*. Protoplasma 201:45–52

Nagahama T, Suzuki T, Yoshikawa S, Iseki M (2007) Functional transplant of photoactivated adenylyl cyclase (PAC) into *Aplysia* sensory neurons. Neurosci Res 59:81–88

Nagel G, Ollig D, Fuhrmann M, Kateriya S, Musti AM, Bamberg E, Hegemann P (2002) Channelrhodopsin-1: a light-gated proton channel in green algae. Science 296:2395–2398

Nicol X, Hong KP, Spitzer NC (2011) Spatial and temporal second messenger codes for growth cone turning. Proc Natl Acad Sci U S A 108:13776–13781

O'Banion CP, Vickerman BM, Haar L, Lawrence DS (2019) Compartmentalized cAMP generation by engineered photoactivated adenylyl cyclases. Cell Chem Biol 26:1393–1406

Ohki M, Sugiyama K, Kawai F, Tanaka H, Nihei Y, Unzai S, Takebe M, Matsunaga S, Adachi S, Shibayama N, Zhou Z, Koyama R, Ikegaya Y, Takahashi T, Tame JR, Iseki M, Park SY (2016) Structural insight into photoactivation of an adenylate cyclase from a photosynthetic cyanobacterium. Proc Natl Acad Sci U S A 113:6659–6664

Ohki M, Sato-Tomita A, Matsunaga S, Iseki M, Tame JRH, Shibayama N, Park SY (2017) Molecular mechanism of photoactivation of a light-regulated adenylate cyclase. Proc Natl Acad Sci U S A 114:8562–8567

Park SY, Tame JRH (2017) Seeing the light with BLUF proteins. Biophys Rev 9:169–176

Penzkofer A, Stierl M, Hegemann P, Kateriya S (2011) Photo-dynamics of the BLUF domain containing solubule adenylyl cyclase (nPAC) from the

amoeboflagellate *Naegleria gruberi* NEG-M strain. Chem Phys 387:25–38

Penzkofer A, Tanwar M, Veetil SK, Kateriya S (2014a) Photo-dynamics of photoactivated adenylyl cyclase LiPAC from the spirochete bacterium *Leptonema illini* strain 3055. Trends Appl Spectrosc 11:39–62

Penzkofer A, Tanwar M, Veetil SK, Kateriya S, Stierl M, Hegemann P (2014b) Photo-dynamics of BLUF domain containing adenylyl cyclase NgPAC3 from the amoeboflagellate *Naegleria gruberi* NEG-M strain. J Photochem Photobiol A 287:19–29

Penzkofer A, Tanwar M, Veetil SK, Kateriya S (2015) Photo-dynamics of photoactivated adenylyl cyclase TpPAC from the spirochete bacterium *Turneriella parva* strain H(T). J Photochem Photobiol B 153:90–102

Raffelberg S, Wang L, Gao S, Losi A, Gärtner W, Nagel G (2013) A LOV-domain-mediated blue-light-activated adenylate (adenylyl) cyclase from the cyanobacterium *Microcoleus chthonoplastes* PCC 7420. Biochem J 55:359–365

Rajagopal S, Key JM, Purcell EB, Boerema DJ, Moffat K (2004) Purification and initial characterization of a putative blue-light-regulated phosphodiesterase from *Escherichia coli*. Photochem Photobiol 80:542–547

Ryu MH, Moskvin OV, Siltberg-Liberles J, Gomelsky M (2010) Natural and engineered photoactivated nucleotidyl cyclases for optogenetic applications. J Biol Chem 285:41501–41508

Schmidt AJ, Ryjenkov DA, Gomelsky M (2005) The ubiquitous protein domain EAL is a cyclic diguanylate-specific phosphodiesterase: enzymatically active and inactive EAL domains. J Bacteriol 187:4774–4781

Schröder-Lang S, Schwärzel M, Seifert R, Strünker T, Kateriya S, Looser J, Watanabe M, Kaupp UB, Hegemann P, Nagel G (2007) Fast manipulation of cellular cAMP level by light *in vivo*. Nat Methods 4:39–42

Sineshchekov OA, Jung KH, Spudich JL (2002) Two rhodopsins mediate phototaxis to low- and high-intensity light in *Chlamydomonas reinhardtii*. Proc Natl Acad Sci U S A 99:8689–8694

Stelling AL, Ronayne KL, Nappa J, Tonge PJ, Meech SR (2007) Ultrafast structural dynamics in BLUF domains: transient infrared spectroscopy of AppA and its mutants. J Am Chem Soc 129:15556–15564

Steuer Costa W, Yu SC, Liewald JF, Gottschalk A (2017) Fast cAMP modulation of neurotransmission via neuropeptide signals and vesicle loading. Curr Biol 27:495–507

Stierl M, Stumpf P, Udwari D, Gueta R, Hagedorn R, Losi A, Gärtner W, Petereit L, Efetova M, Schwarzel M, Oertner TG, Nagel G, Hegemann P (2011) Light modulation of cellular cAMP by a small bacterial photoactivated adenylyl cyclase, bPAC, of the soil bacterium *Beggiatoa*. J Biol Chem 286:1181–1188

Sunahara RK, Beuve A, Tesmer JJ, Sprang SR, Garbers DL, Gilman AG (1998) Exchange of substrate and inhibitor specificities between adenylyl and guanylyl cyclases. J Biol Chem 273:16332–16338

Suzuki T, Yamasaki K, Fujita S, Oda K, Iseki M, Yoshida K, Watanabe M, Daiyasu H, Toh H, Asamizu E, Tabata S, Miura K, Fukuzawa H, Nakamura S, Takahashi T (2003) Archaeal-type rhodopsins in *Chlamydomonas*: model structure and intracellular localization. Biochem Biophys Res Commun 301:711–717

Tanwar M, Khera L, Haokip N, Kaul R, Naorem A, Kateriya S (2017) Modulation of cyclic nucleotide-mediated cellular signaling and gene expression using photoactivated adenylyl cyclase as an optogenetic tool. Sci Rep 7:12048

Tanwar M, Sharma K, Moar P, Kateriya S (2018) Biochemical characterization of the engineered soluble photoactivated guanylate cyclases from microbes expands optogenetic tools. Appl Biochem Biotechnol 185:1014–1028

Tsvetanova NG, von Zastrow M (2014) Spatial encoding of cyclic AMP signaling specificity by GPCR endocytosis. Nat Chem Biol 10:1061–1065

Tyagi A, Penzkofer A, Griese J, Schlichting I, Kirienko NV, Gomelsky M (2008) Photodynamics of blue-light-regulated phosphodiesterase BlrP1 protein from *Klebsiella pneumoniae* and its photoreceptor BLUF domain. Chem Phys Lett 354:130–141

Weissenberger S, Schultheis C, Liewald JF, Erbguth K, Nagel G, Gottschalk A (2011) PACα—an optogenetic tool for in vivo manipulation of cellular cAMP levels, neurotransmitter release, and behavior in *Caenorhabditis elegans*. J Neurochem 116:616–625

Yasukawa H, Konno N, Haneda Y, Yamamori B, Iseki M, Shibusawa M, Ono Y, Kodaira K, Funada H, Watanabe M (2012) Photomanipulation of antibiotic susceptibility and biofilm formation of *Escherichia coli* heterologously expressing photoactivated adenylyl cyclase. J Gen Appl Microbiol 58:183–190

Yasukawa H, Sato A, Kita A, Kodaira K, Iseki M, Takahashi T, Shibusawa M, Watanabe M, Yagita K (2013) Identification of photoactivated adenylyl cyclases in *Naegleria australiensis* and BLUF-containing protein in *Naegleria fowleri*. J Gen Appl Microbiol 59:361–369

Yoshida K, Tsunoda SP, Brown LS, Kandori H (2017) A unique choanoflagellate enzyme rhodopsin exhibits light-dependent cyclic nucleotide phosphodiesterase activity. J Biol Chem 292:7531–7541

Yoshikawa S, Suzuki T, Watanabe M, Iseki M (2005) Kinetic analysis of the activation of photoactivated adenylyl cyclase (PAC), a blue-light receptor for photomovements of *Euglena*. Photochem Photobiol Sci 4:727–731

Zhou Z, Tanaka KF, Matsunaga S, Iseki M, Watanabe M, Matsuki N, Ikegaya Y, Koyama R (2016) Photoactivated adenylyl cyclase (PAC) reveals novel mechanisms underlying cAMP-dependent axonal morphogenesis. Sci Rep 5:19679

# Optogenetic Potentials of Diverse Animal Opsins: Parapinopsin, Peropsin, LWS Bistable Opsin

8

Mitsumasa Koyanagi, Tomoka Saito, Seiji Wada, Takashi Nagata, Emi Kawano-Yamashita, and Akihisa Terakita

**Abstract**

Animal opsin-based pigments are light-activated G-protein-coupled receptors (GPCRs), which drive signal transduction cascades via G-proteins. Thousands of animal opsins have been identified, and molecular phylogenetic and biochemical analyses have revealed the unexpected diversity in selectivity of G-protein activation and photochemical property. Here we discuss the optogenetic potentials of diverse animal opsins, particularly recently well-characterized three non-canonical opsins, parapinopsin, peropsin, and LWS bistable opsin. Unlike canonical opsins such as vertebrate visual opsins that have been conventionally used for optogenetic applications, these opsins are bistable; opsin-based pigments do not release the chromophore retinal after light absorption, and the stable photoproducts revert to their original dark states upon subsequent light absorption. Parapinopsins have a "complete photoregeneration ability," which allows a clear color-dependent regulation of signal transductions. On the other hand, peropsins serve as a "dark-active and light-inactivated" GPCR to regulate signal transductions in the opposite way compared with usual opsins. In addition, an LWS bistable opsin from a butterfly was revealed to be the longest wavelength-sensitive animal opsin with its absorption maximum at ~570 nm. The property-dependent optical regulations of signal transductions were demonstrated in mammalian cultured cells, showing potentials of new optogenetic tools.

**Keywords**

Animal rhodopsin · Opsin · Bistable pigment · Photoregeneration · G-protein-coupled receptor · Phototransduction · Second messenger · Cultured cells · Optogenetic potential

## Abbreviations

| | |
|---|---|
| cAMP | cyclic adenosine monophosphate |
| CNO | clozapine-*N*-oxide |
| DREADD | Designer receptor exclusively activated by designer drugs |
| GPCR | G-protein-coupled receptor |
| HEK293 | Human embryonic kidney cells 293 |
| KO | Knockout |
| LWS | Long wavelength-sensitive |
| PxRh3 | *Papilio xuthus* Rh3 |

Mitsumasa Koyanagi and Akihisa Terakita authors contributed equally to this work

M. Koyanagi · T. Saito · S. Wada · T. Nagata · E. Kawano-Yamashita · A. Terakita (✉)
Department of Biology and Geosciences, Graduate School of Science, Osaka City University, Osaka, Japan
e-mail: terakita@sci.osaka-cu.ac.jp



H. Yawo et al. (eds.), *Optogenetics*, Advances in Experimental Medicine and Biology 1293,
https://doi.org/10.1007/978-981-15-8763-4_8

| | |
|---|---|
| RGR | Retinal G-protein-coupled receptor |
| TMT | Teleost multiple tissue |
| UV | Ultraviolet |

## 8.1 Introduction

It is widely accepted that microbial rhodopsins are powerful tools for use in optogenetics: light-manipulating neural cells in which microbial rhodopsin genes are genetically expressed (Boyden 2011; Deisseroth 2011; Hegemann and Nagel 2013; Deisseroth and Hegemann 2017). Microbial rhodopsins basically function as ion channels and ion pumps upon light irradiation and thereby control the membrane potentials of targeted neural cells in a light-dependent manner. In addition, some microbial rhodopsins having enzyme domains (e.g., phosphodiesterase and guanylyl cyclase), called enzymerhodopsins, have recently been identified, and their optogenetic applications to light regulation of second messenger levels have been examined (Mukherjee et al. 2019). On the other hand, animal rhodopsins (opsin-based pigments) are light-activated G-protein-coupled receptors (GPCRs), which drive signal transduction cascades via G-proteins (Terakita 2005; Terakita et al. 2012; Koyanagi and Terakita 2014). To date, thousands of animal opsins have been identified, and molecular phylogenetic, biochemical, and spectroscopic analyses of them have revealed that opsin-based pigments have diversified in G-protein selectivity [Gs, Gq, Gi, Go, and transducin (Gt)] and photochemical properties including wavelength sensitivity (UV to red) (Terakita 2005; Koyanagi and Terakita 2014).

In general, GPCRs bind chemical signals, such as hormones and neurotransmitters, to activate G-protein-mediated cascades and modulate various aspects of cellular physiology. Therefore, application of diverse animal opsins to optogenetics could provide an opportunity to control various cellular functions using light. We have already summarized optogenetic potentials of jellyfish opsin, mosquito Opn3, and spider opsin, which activate Gs, Gi/Go, and Gq, respectively, in the previous review (Terakita et al. 2015). In this review, we discuss the diversity of the other animal opsins and their optogenetic potentials, particularly focusing on recently well-characterized bistable or bleach-resistant pigments.

## 8.2 Diversity of Animal Opsins

Animal visual pigments and related photosensitive pigments consist of a protein moiety (apo-) opsin and a chromophore retinal. Therefore, in this chapter, they are referred to as opsin-based pigments. To date, four different chromophore retinals (retinal, 3,4-dehydroretinal, 3-hydroxyretinal, and 4-hydroxyretinal) have been identified. Binding of each chromophore to an opsin basically forms a pigment that has a specific spectral sensitivity. On the other hand, thousands of opsins have been identified in a wide variety of animals thus far, and this variety of opsins is primarily responsible for the diversity of opsin-based "pigments."

Opsins have seven transmembrane helices as GPCRs, and a highly conserved lysine residue in the seventh helix binds to a retinal as a chromophore to form a pigment. Most opsins bind to the chromophore 11-*cis* retinal, which is isomerized to an all-*trans* form upon light irradiation. This isomerization triggers a structural change in opsins near the chromophore and subsequently in cytoplasmic regions, which interact with a G-protein. Therefore, the structural diversities of opsins near a chromophore and in the cytoplasmic region primarily contribute to the varying spectral sensitivities and selective activation of different G-protein-mediated signal transduction cascades, respectively.

Many animals possess multiple opsin genes, and the molecular phylogenetic tree of the opsin family reveals that animal opsins can be divided into eight groups (Koyanagi and Terakita 2014) (Fig. 8.1). For example, humans have nine opsin genes, each of which belongs to any one of six from these eight groups. The amino acid sequence identities are 20–25% among opsins that belong to individual groups. Interestingly, this classification also approximately corresponds to molecular functions. Members of six groups, Gt-coupled

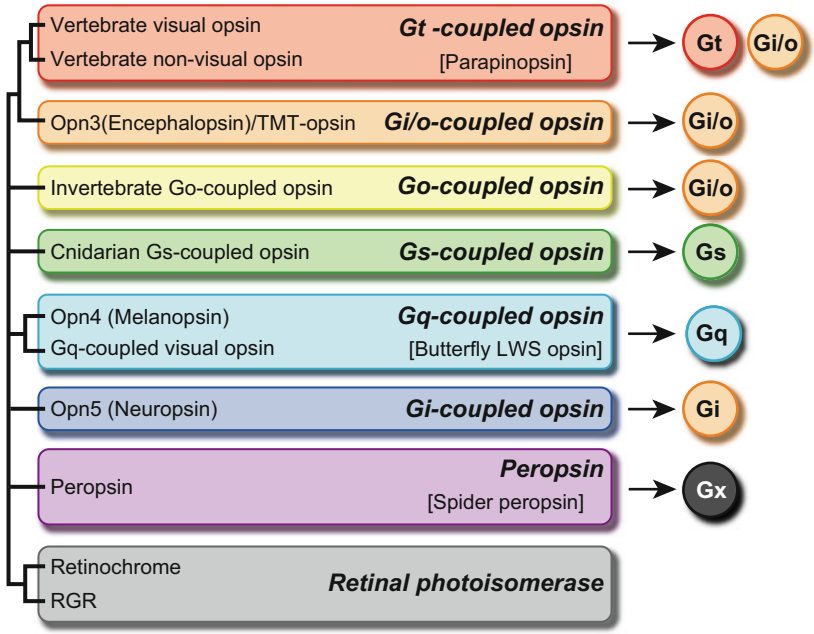


**Fig. 8.1** Eight opsin groups and the particular G-protein subtypes to which they are predominantly coupled. Note that peropsins have a potential to activate G-protein but not identified yet (indicated as Gx). Group names are designated after the G-protein coupling based on in vivo evidence; Gt-coupled opsin (Kuhn 1980), Gq-coupled opsin (Terakita et al. 1993; Lee et al. 1994; Koyanagi and Terakita 2008), and Go-coupled opsin (Kojima et al. 1997; Tsukamoto et al. 2005), and if it is not available, based on in vitro evidence, which is also indicated on right side of arrows from each group; Opn3 (Koyanagi et al. 2013), and Opn5 (Yamashita et al. 2010; Kojima et al. 2011)

opsins (vertebrate visual and non-visual opsins, including parapinopsin), Gq-coupled opsins [invertebrate Gq-coupled visual opsins and Opn4 (melanopsin)], invertebrate Go-coupled opsins, Gi/Go-coupled opsins [Opn3 (encephalopsin) and teleost multiple tissue (TMT) opsin], Gi-coupled Opn5 (neuropsin), and cnidarian Gs-coupled opsins have been shown to function as light-sensing GPCRs. Members of retinochrome/retinal G-protein-coupled receptor (RGR) are considered to be retinal photoisomerases that bind all-*trans* retinal to generate 11-*cis* retinal by light absorption. Another type of all-*trans* retinal binding opsin peropsin was recently revealed to serve as a "dark-active and light-inactivated" GPCR as introduced in this review (Nagata et al. 2018). In addition, xenopsins, which are found in several lophotrochozoans, could form a new Gi-coupled opsin group (Ramirez et al. 2016; Vocking et al. 2017).

## 8.3 Bistable or Bleach-Resistant Pigments

Vertebrate visual opsins that have been conventionally used as optogenetic tools belong to the Gt-coupled opsin group (Airan et al. 2009; Masseck et al. 2014) (Fig. 8.1). Bovine rhodopsin, which is one of the best studied members in this group, releases a retinal chromophore and bleaches (becomes colorless) after light activation (Fig. 8.2). In contrast, most opsins, including parapinopsin and peropsin as well as invertebrate visual opsins, form bleach-resistant pigments that do not release a chromophore after light absorption. Moreover, most of the photoproducts of bleach-resistant pigments revert to their original dark states upon subsequent light absorption. These opsin-based pigments that have two stable states, a dark state and a photoproduct that has

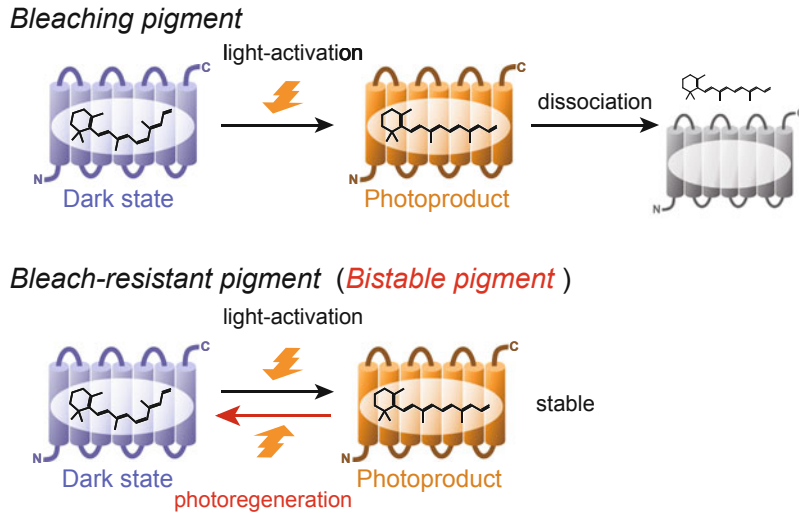


**Fig. 8.2** Photoreactions of bleaching pigments and bleach-resistant pigments. The photoproducts of bleaching pigments are thermally unstable and release their chromophores. Bleach-resistant pigments are photoconverted to stable photoproducts which do not release their chromophores. Opsin-based pigments of which photoproducts revert to their original dark state upon light absorption are called bistable pigments. Note that characteristics only for bistable pigments are indicated by red color

photoregeneration ability, are called bistable pigments (Fig. 8.2).

Opsins require a chromophore retinal in order to have a photoreceptive function (i.e., capture light information and subsequently activate a G-protein). As noted above, most opsin-based pigments bind to an 11-*cis* retinal as the chromophore. Tissues located outside eyes and pineal organs contain significantly less 11-*cis* retinal because these tissues do not express the enzymes that generate 11-*cis* retinoids, such as photoisomerases (RGR/retinochrome) and RPE65, which are specifically expressed in photoreceptor organs (Båvik et al. 1992; Jiang et al. 1993; Strauss 2005). The photoregeneration property of bistable pigments (i.e., reuse of a retinal chromophore) may allow an opsin to function in tissues located outside these photoreceptor organs. That is, the bistable nature of these particular pigments may be advantageous for their use as optogenetic tools.

## 8.4 Molecular Characteristics of Parapinopsin, Peropsin, and LWS Bistable Opsin

We have successfully obtained various functional opsins by expressing them in mammalian cultured cells and have characterized their opsin-based pigments spectroscopically and biochemically. Here we review the molecular properties of three non-canonical opsins: parapinopsin, peropsin, LWS bistable opsin, each of which has its own interesting characteristic(s) in addition to the bistable nature.

### 8.4.1 Parapinopsin

Parapinopsin was first identified in catfish pineal and parapineal organs (Blackshaw and Snyder 1997), and later, from lamprey, teleosts clawed frog and iguana (Koyanagi et al. 2004, 2015, 2017; Wada et al. 2012). By spectroscopic, immunohistochemical, and biochemical analyses mainly of lamprey and teleost parapinopsins, we revealed that parapinopsins serve as a Gt-coupled UV-sensitive pigment underlying UV reception in the pineal wavelength discrimination. Parapinopsins also activate Gi-type G-protein in vitro and in mammalian cultured cells (Terakita et al. 2004; Tsukamoto et al. 2009; Kawano-Yamashita et al. 2015; Wada et al. 2018). Interestingly although parapinopsins are closely related to vertebrate visual opsins (bleaching opsins), to form the Gt-coupled opsin group, parapinopsins are bistable opsins, like members

of other groups including invertebrate visual opsins. We emphasize that stable photoproducts of parapinopsins have its absorption maximum at ~500 nm, which are largely distant from that of the dark states (~360 nm). This difference in absorption spectrum enables the photoproduct to completely revert to the dark state by visible light absorption (Fig 8.3a). We also demonstrated that G-protein activations triggered by parapinopsin were up- and downregulated by UV and green light illumination, respectively, in vitro and in mammalian cultured cells (Kawano-Yamashita et al. 2015; Wada et al. 2018) (Fig. 8.3c). Furthermore, we recently revealed that parapinopsin alone can generate chromatic antagonistic cellular responses to UV and visible lights in pineal parapinopsin-expressing photoreceptor cells in zebrafish (Wada et al. 2018) (Fig. 8.3e). Since the gold fish UV cone opsin (bleaching pigments) exhibits only UV light-induced responses in vitro and in vivo, responses to visible light are originated from the photoregeneration ability based on bistable nature (Fig. 8.3b,d,f).

### 8.4.2 Peropsin

Peropsin, or retinal pigment epithelium-derived rhodopsin homolog, was first identified in the mouse retinal pigment epithelium (Sun et al. 1997) and is found in nearly all vertebrate classes (Davies et al. 2015). We have previously identified peropsins in an amphioxus, *Branchiostoma belcheri*, and a jumping spider, *Hasarius adansoni*, revealing that invertebrates also possess peropsins (Koyanagi et al. 2002; Nagata et al. 2010). We successfully obtained recombinant photopigment of amphioxus and jumping spider peropsins in mammalian cultured cells to reveal that peropsins are indeed bistable pigments, whereas no direct evidence is present showing that vertebrate peropsins form photosensitive pigments. Spectroscopic analysis of these invertebrate peropsins revealed that they bind all-*trans*-retinal as a chromophore and isomerize it to 11-*cis* form upon illumination as well as have a bistable nature (Koyanagi et al. 2002; Nagata et al. 2010) (Fig 8.4a). This all-*trans*-to-11-*cis* photoisomerization suggested previously that peropsins serve as a retinal photoisomerase similar to retinochrome. Interestingly, however, spider and amphioxus peropsin mutants in which the intracellular regions were replaced with that of a Gs-coupled opsin (sPeropsin-GsOpL3 and aPeropsin-GsOpL3) evoked a light-dependent decrease and an all-*trans*-retinal-dependent increase in cAMP levels in cultured cells expressing the peropsin mutants, indicating that the mutants could drive Gs signaling in the dark by binding to all-*trans* retinal and were inactivated by absorption of light (Nagata et al. 2018) (Fig. 8.4c). Similarly, the peropsin mutants with intracellular region(s) of a Gi-coupled opsin (sPeropsin-GiOpL3) were suggested to be active and drive Gi signaling in the dark (Fig. 8.4d). These findings suggest that wild-type peropsins might act as dark-active and light-inactivated GPCRs, whereas the G-proteins coupled to peropsins remain uncertain (Fig. 8.4b).

### 8.4.3 LWS Bistable Opsin

Both vertebrates and invertebrates possess long-wavelength-sensitive (LWS) opsins, which underlie color vision involving "red" sensing. Vertebrate LWS opsins, famous for primate LWS opsins including human "Red"-sensitive opsin (OPN1LW), are bleaching opsins in the Gt-coupled opsin group like other vertebrate visual opsins. On the other hand, invertebrate LWS opsins belong to the bistable Gq-coupled opsin group composed of invertebrate visual opsins and vertebrate melanopsins (Fig. 8.1). A butterfly, *Papilio xuthus*, has three LWS opsins. One of them, PxRh3 has been suggested to form a visual pigment having an absorption peak at 575 nm in electrophysiological recordings of PxRh3-expressing visual cells in the presence of the filtering effect of red screening pigments in the cells (Arikawa et al. 1999). Recently, we succeeded in estimating the absorption spectrum of recombinant PxRh3-based pigment and revealed that it has an absorption maximum at ~570 nm by analyzing heterologous action spectrum based on light-dependent changes in PxRh3-

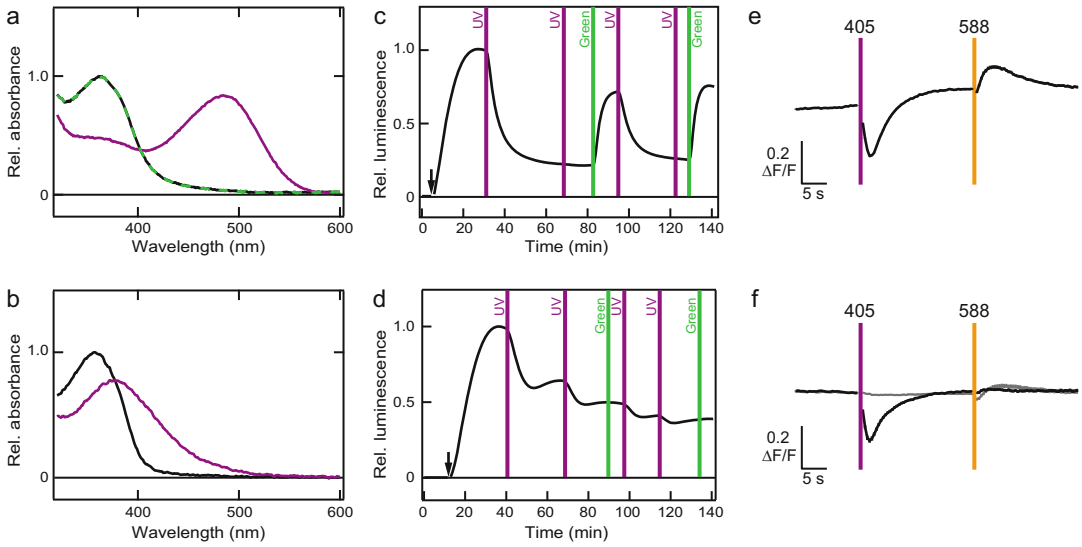


**Fig. 8.3** Parapinopsin photointerconvertibility. (**a**) Absorption spectra of the zebrafish parapinopsin in the dark state (black curve), after irradiation with UV light (purple curve), and after subsequent irradiation with green light (green-dotted curve), showing bistable nature and complete photoregeneration. (**b**) Absorption spectra of the goldfish UV cone opsin in the dark state (black curve), after irradiation with UV light (purple curve), showing bleaching nature. Light-induced changes of cAMP levels in HEK293 cells expressing lamprey parapinopsin or goldfish UV cone opsin. UV light-induced decreases of cAMP levels are observed in the parapinopsin-expressing (**c**) and the goldfish UV cone opsin-expressing (**d**) HEK293 cells. However, green light-induced increases (recovery) of cAMP level are observed only in the parapinopsin-expressing (**c**) but not in the goldfish UV cone opsin-expressing (**d**) HEK293 cells. The arrows and vertical lines indicate forskolin treatments and UV and green light irradiations, respectively. Calcium imagining in the zebrafish pineal photoreceptor cells expressing GCaMP6s by using two-photon microscope at 930 nm. Calcium level changes upon 405- or 588-nm light stimuli (vertical lines) in parapinopsin cells of WT zebrafish (**e**; $n = 41$), and goldfish UV cone opsin-expressing/parapinopsin-KO fish ($n = 27$, black) with just parapinopsin-KO fish ($n = 40$, grey) (**f**). Error bars indicate SE. ΔF/F values are change rates of normalized fluorescence intensity with the averaged intensity of 10 points before initial light stimuli

expressing cultured cells (Saito et al. 2019) (Fig. 8.5a). The result demonstrated that the butterfly LWS opsin has the longest wavelength sensitivity among known bistable opsins at present, which is achieved through a different spectral tuning mechanism involving the helix III during the insect LWS opsin evolution (Saito et al. 2019). In addition, the butterfly LWS opsin, which originally activates Gq-type G-protein, has been successfully engineered to activate Gs-type G-protein (Gs-coupled LWS bistable opsin) in the heterologous expression system when the third cytoplasmic loop region was replaced by that of a Gs-coupled jellyfish opsin (Koyanagi et al. 2008) (Fig. 8.5b).

## 8.5 Optogenetic Control of G-Protein Signaling by Animal Opsins

As summarized in the previous review (Terakita et al. 2015), jellyfish opsin, mosquito Opn3, and spider opsin, bleach-resistant or bistable pigments, activate Gq, Gs, and Gi/Go, respectively. In general, activating Gq, Gs, or Gi/Go results in changes in second messenger levels in cells, such as $Ca^{2+}$ and cAMP levels. In fact, we have demonstrated light-induced increase and decrease of intracellular cAMP level, and increase of intracellular $Ca^{2+}$ level in cultured cells expressing jellyfish opsin, mosquito Opn3, or spider opsin, respectively, showing their

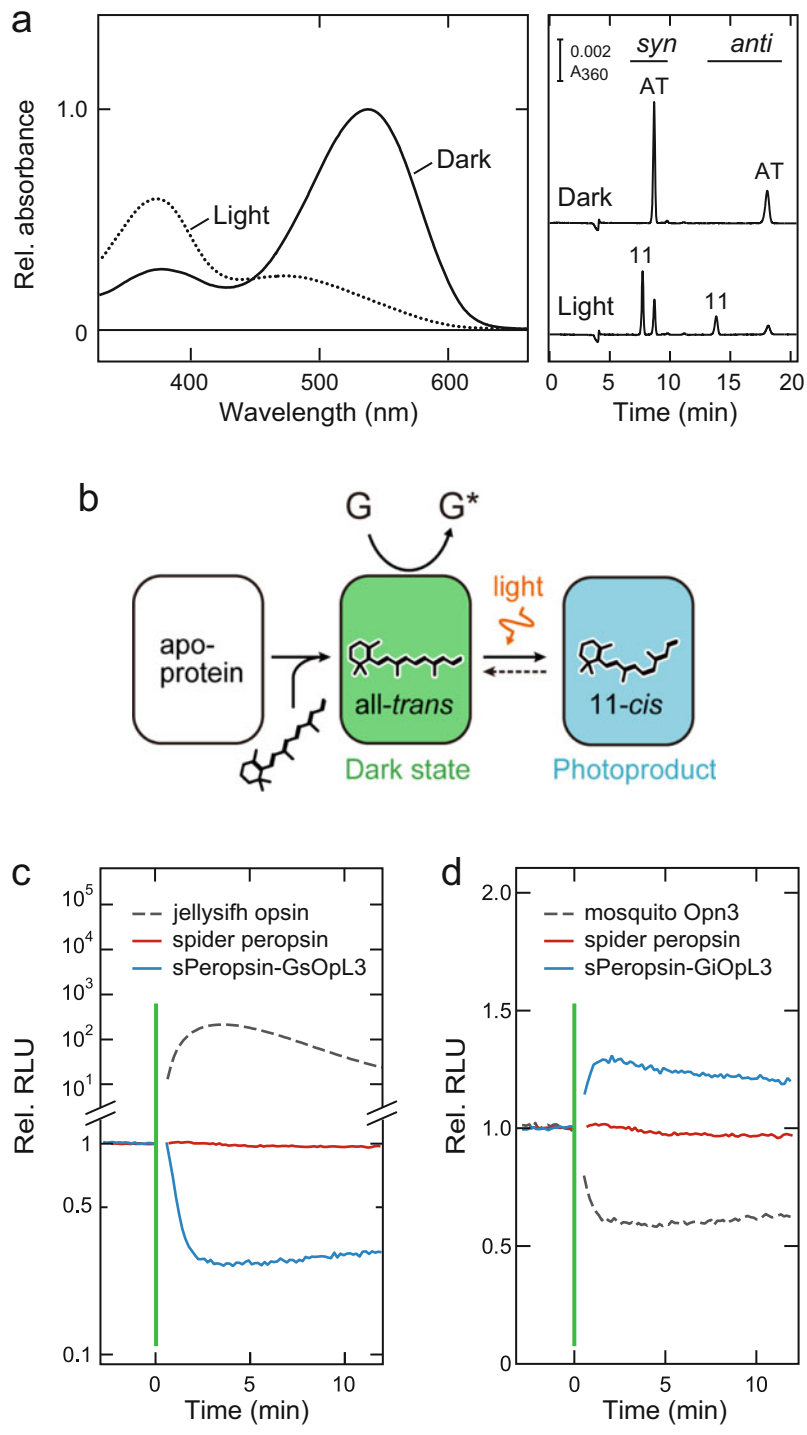


**Fig. 8.4** Peropsin as a "dark-active and light-inactivated" GPCR. (**a**) Absorption spectra of jumping spider peropsin in the dark state (solid curve) and after irradiation with orange light (dotted curve). Chromophore configurations of peropsin in the dark state (upper) and after irradiation with the orange light (lower) analyzed with HPLC as retinal oximes (*syn*- and *anti*-forms of 11-*cis* (11) and all-*trans* (AT) retinal oximes) are shown on the right. (**b**) A schematic model for G-protein activation by peropsin (hypothesis). $G^*$, the active form of G-protein. Apo-protein binds to all-*trans* retinal and forms the dark state that activates G-proteins. The dark state photoconverts to the photoproduct, or 11-*cis* retinal-binding form, which does not efficiently activate G-proteins. (**c**) GloSensor cAMP assay with HEK293 cells expressing jellyfish opsin, spider peropsin, or sPeropsin-GsOpL3 (spider peropsin mutant in which the third cytoplasmic loop was replaced with that of a Gs-coupled opsin). (**d**) GloSensor cAMP assay with HEK293 cells expressing mosquito Opn3, spider peropsin, or sPeropsin-GiOpL3. Cells were illuminated with green light (vertical lines)

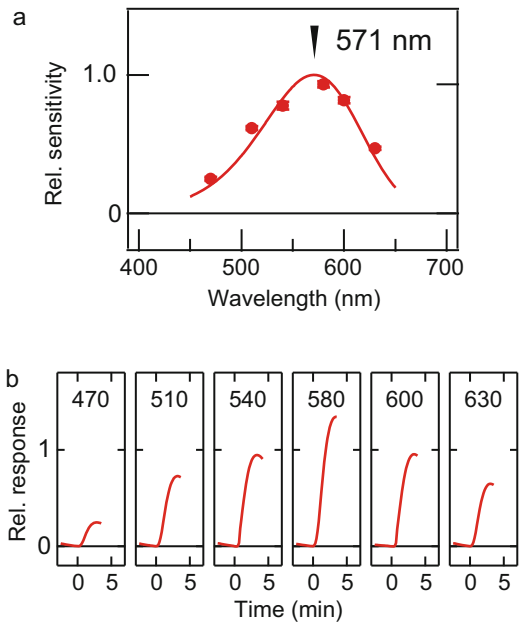


**Fig. 8.5** Butterfly LWS opsin PxRh3 as one of the longest wavelength-sensitive bistable opsins. (**a**) The absorption spectrum of PxRh3 estimated from the heterologous action spectrum with the cultured cells expressing the PxRh3 mutant. (**b**) The action spectrum was obtained based on color-dependent changes of cAMP levels in cultured cells expressing the PxRh3 mutant engineered to activate Gs-type G-protein by replacing the third cytoplasmic loop with that of the Gs-coupled jellyfish opsin

optogenetic potentials for optical control of some kinds of intracellular signaling. In addition, we have found potentials for further advanced optical control of cellular signalings using parapinopsin, peropsin, and LWS bistable opsin. As described above, by introducing parapinopsin, signal transductions and cellular responses can be controlled in a color-dependent manner, that is, UV light illumination induces decrease in intracellular cAMP levels via a Gi-mediated signaling, and visible light illumination terminates the signal transduction to recover the cAMP level based on the complete photoregeneration ability of parapinopsin (Fig. 8.3). The color-dependent regulation using parapinopsin as an optogenetic tool could allow temporally precise termination of signal transduction. The unique property of peropsin mutants as an all-*trans*-retinal-dependently dark-active and light-inactivated GPCR, which is an opposite activation manner compared with usual opsins, also shows the potential as a novel type of optogenetic tool (Fig. 8.4). Together with its photopigment formation ability with all-*trans* retinal, a ubiquitously present retinal isomer in animal body, peropsin mutants could be powerful optogenetic tools to drive G-protein signaling cascades spontaneously in the dark and be inactivated by light in vivo. It is well known that longer wavelength light can penetrate deeper into biological tissues. Therefore, long wavelength-sensitive tools have a big advantage for non-invasive as well as efficient optical controls of physiological responses at deeper tissues, such as deep brain regions. An LWS bistable opsin PxRh3, which has, to the best of our knowledge, the longest spectral sensitivity and the knowledge for the spectral tuning mechanism of bistable opsins could allow to develop highly efficient optogenetic tools to facilitate further advanced in vivo optical regulations of signal transductions (Fig. 8.5).

## 8.6 Optogenetic and Chemogenetic Control of G-Protein Signaling

In addition to optogenetic, chemogenetics using chemicals as stimuli are popular methods for artificially controlling physiological functions. In particular, in the case of G-protein signaling, chemogenetics using chemoreceptors such as DREADD (designer receptor exclusively activated by designer drugs) have been widely used (Armbruster et al. 2007; Conklin et al. 2008; Urban and Roth 2015), and optogenetics using mainly bleaching opsins have limitedly used. The low popularity is mainly due to the absence of effective tools for optogenetic control of G-protein signaling but now we have various promising tools based on bleach-resistant or bistable opsins as described above and in the previous review (Terakita et al. 2015), which would change the situation. Furthermore, temporally precise termination of G-protein signalings demonstrated by parapinopsin (Fig. 8.3) and peropsin (Fig. 8.4) as well as temporally precise

activation is never achieved by chemogenetics, showing a huge advantage of optogenetics. However, there are still advantages in chemogenetics. In chemogenetics, stimuli (chemicals) can be reliably delivered deep inside the body, but not or with insertion of light stimulation apparatus in optogenetics. The delivery problem might be overcome to some extent by using long wavelength-sensitive tools that are activated longer wavelength light, especially near infrared. In addition, DREADD is the most adopted technology for controlling G-protein signaling because they are designed to be exclusively activated by an inert drug (CNO, clozapine-*N*-oxide). Fortunately, since light does not activate any GPCRs other than endogenous opsin-based pigments, animal opsin-based tools can be used for exclusive activation of G-protein signalings involved in light-independent physiologies. DREADD also allows selective activation of Gq, Gi, or Gs-mediated signalings depending on template receptors of DREADDs. Furthermore, arrestin-signaling, which is triggered by several activated GPCRs, can be controlled by using ß-Arrestin DREADD created by removing the G-protein activation ability from Gq DREAD (Nakajima and Wess 2012). We have already succeeded in engineering bistable animal opsins to activate G-proteins different from native ones, but not evaluated their G-protein selectivity in detail. Further engineering of bistable animal opsins would be required to achieve elaborated control of GPCR signaling including G-protein signaling and arrestin signaling by light.

## 8.7 Conclusions

Animal opsin-based pigments having the bistable nature vary in photochemical properties including wavelength sensitivity as well as G-protein selectivity. Accordingly, chimera mutants for these diverse opsins would allow us to generate opsins that activate particular G-proteins on the basis of particular colors and patterns of light stimuli. The animal opsins, with their molecular-property-dependent optical regulations of cell signaling, should become powerful optogenetic tools to investigate various GPCR-involved physiology under high spatiotemporal precision.

**Acknowledgements** This work was supported by Japanese Ministry of Education, Culture, Sports, Science and Technology Grants-in-Aid for Scientific Research 15H05777 and 16K14778 (to A.T.) and 16KT0074 and 18H02482 (to M.K.); Japan Science and Technology Agency (JST) Core Research for Evolutional Science and Technology (CREST) Grant JPMJCR1753 (to A.T.) and JST Precursory Research for Embryonic Science and Technology (PRESTO) Grant JPMJPR13A2 (to M.K.).

## References

Airan RD, Thompson KR, Fenno LE, Bernstein H, Deisseroth K (2009) Temporally precise in vivo control of intracellular signalling. Nature 458 (7241):1025–1029. https://doi.org/10.1038/nature07926

Arikawa K, Scholten DGW, Kinoshita M, Stavenga DG (1999) Tuning of photoreceptor spectral sensitivities by red and yellow pigments in the butterfly Papilio xuthus. Zool Sci 16(1):17–24. https://doi.org/10.2108/Zsj.16.17

Armbruster BN, Li X, Pausch MH, Herlitze S, Roth BL (2007) Evolving the lock to fit the key to create a family of G protein-coupled receptors potently activated by an inert ligand. Proc Natl Acad Sci U S A 104(12):5163–5168. https://doi.org/10.1073/pnas.0700293104

Båvik CO, Busch C, Eriksson U (1992) Characterization of a plasma retinol-binding protein membrane receptor expressed in the retinal pigment epithelium. J Biol Chem 267(32):23035–23042

Blackshaw S, Snyder SH (1997) Parapinopsin, a novel catfish opsin localized to the parapineal organ, defines a new gene family. J Neurosci 17(21):8083–8092

Boyden ES (2011) A history of optogenetics: the development of tools for controlling brain circuits with light. F1000 Biol Rep 3:11. https://doi.org/10.3410/B3-11

Conklin BR, Hsiao EC, Claeysen S, Dumuis A, Srinivasan S, Forsayeth JR, Guettier JM, Chang WC, Pei Y, McCarthy KD, Nissenson RA, Wess J, Bockaert J, Roth BL (2008) Engineering GPCR signaling pathways with RASSLs. Nat Methods 5 (8):673–678. https://doi.org/10.1038/nmeth.1232

Davies WI, Tamai TK, Zheng L, Fu JK, Rihel J, Foster RG, Whitmore D, Hankins MW (2015) An extended family of novel vertebrate photopigments is widely expressed and displays a diversity of function. Genome Res 25(11):1666–1679. https://doi.org/10.1101/gr.189886.115

Deisseroth K (2011) Optogenetics. Nat Methods 8 (1):26–29. https://doi.org/10.1038/nmeth.f.324

Deisseroth K, Hegemann P (2017) The form and function of channelrhodopsin. Science 357(6356):eaan5544. https://doi.org/10.1126/science.aan5544

Hegemann P, Nagel G (2013) From channelrhodopsins to optogenetics. EMBO Mol Med 5(2):173–176. https://doi.org/10.1002/emmm.201202387

Jiang M, Pandey S, Fong HK (1993) An opsin homologue in the retina and pigment epithelium. Invest Ophthalmol Vis Sci 34(13):3669–3678

Kawano-Yamashita E, Koyanagi M, Wada S, Tsukamoto H, Nagata T, Terakita A (2015) Activation of transducin by bistable pigment parapinopsin in the pineal organ of lower vertebrates. PLoS One 10(10): e0141280. https://doi.org/10.1371/journal.pone.0141280

Kojima D, Terakita A, Ishikawa T, Tsukahara Y, Maeda A, Shichida Y (1997) A novel Go-mediated phototransduction cascade in scallop visual cells. J Biol Chem 272(37):22979–22982. https://doi.org/10.1074/jbc.272.37.22979

Kojima D, Mori S, Torii M, Wada A, Morishita R, Fukada Y (2011) UV-sensitive photoreceptor protein OPN5 in humans and mice. PLoS One 6(10):e26388. https://doi.org/10.1371/journal.pone.0026388

Koyanagi M, Terakita A (2008) Gq-coupled rhodopsin subfamily composed of invertebrate visual pigment and melanopsin. Photochem Photobiol 84 (4):1024–1030. https://doi.org/10.1111/j.1751-1097.2008.00369.x

Koyanagi M, Terakita A (2014) Diversity of animal opsin-based pigments and their optogenetic potential. Biochim Biophys Acta 1837(5):710–716. https://doi.org/10.1016/j.bbabio.2013.09.003

Koyanagi M, Terakita A, Kubokawa K, Shichida Y (2002) Amphioxus homologs of Go-coupled rhodopsin and peropsin having 11-cis- and all-trans-retinals as their chromophores. FEBS Lett 531(3):525–528. https://doi.org/10.1016/s0014-5793(02)03616-5

Koyanagi M, Kawano E, Kinugawa Y, Oishi T, Shichida Y, Tamotsu S, Terakita A (2004) Bistable UV pigment in the lamprey pineal. Proc Natl Acad Sci U S A 101(17):6687–6691. https://doi.org/10.1073/pnas.0400819101

Koyanagi M, Takano K, Tsukamoto H, Ohtsu K, Tokunaga F, Terakita A (2008) Jellyfish vision starts with cAMP signaling mediated by opsin-G(s) cascade. Proc Natl Acad Sci U S A 105(40):15576–15580. https://doi.org/10.1073/pnas.0806215105

Koyanagi M, Takada E, Nagata T, Tsukamoto H, Terakita A (2013) Homologs of vertebrate Opn3 potentially serve as a light sensor in nonphotoreceptive tissue. Proc Natl Acad Sci U S A 110(13):4998–5003. https://doi.org/10.1073/pnas.1219416110

Koyanagi M, Wada S, Kawano-Yamashita E, Hara Y, Kuraku S, Kosaka S, Kawakami K, Tamotsu S, Tsukamoto H, Shichida Y, Terakita A (2015) Diversification of non-visual photopigment parapinopsin in spectral sensitivity for diverse pineal functions. BMC Biol 13:73. https://doi.org/10.1186/s12915-015-0174-9

Koyanagi M, Kawano-Yamashita E, Wada S, Terakita A (2017) Vertebrate bistable pigment parapinopsin: implications for emergence of visual signaling and neofunctionalization of non-visual pigment. Front Ecol Evol 5:23. https://doi.org/10.3389/fevo.2017.00023

Kuhn H (1980) Light- and GTP-regulated interaction of GTPase and other proteins with bovine photoreceptor membranes. Nature 283(5747):587–589. https://doi.org/10.1038/283587a0

Lee YJ, Shah S, Suzuki E, Zars T, O'Day PM, Hyde DR (1994) The Drosophila dgq gene encodes a G alpha protein that mediates phototransduction. Neuron 13 (5):1143–1157. https://doi.org/10.1016/0896-6273(94)90052-3

Masseck OA, Spoida K, Dalkara D, Maejima T, Rubelowski JM, Wallhorn L, Deneris ES, Herlitze S (2014) Vertebrate cone opsins enable sustained and highly sensitive rapid control of Gi/o signaling in anxiety circuitry. Neuron 81(6):1263–1273. https://doi.org/10.1016/j.neuron.2014.01.041

Mukherjee S, Hegemann P, Broser M (2019) Enzymerhodopsins: novel photoregulated catalysts for optogenetics. Curr Opin Struct Biol 57:118–126. https://doi.org/10.1016/j.sbi.2019.02.003

Nagata T, Koyanagi M, Tsukamoto H, Terakita A (2010) Identification and characterization of a protostome homologue of peropsin from a jumping spider. J Comp Physiol A Neuroethol Sens Neural Behav Physiol 196(1):51–59. https://doi.org/10.1007/s00359-009-0493-9

Nagata T, Koyanagi M, Lucas R, Terakita A (2018) An all-trans-retinal-binding opsin peropsin as a potential dark-active and light-inactivated G protein-coupled receptor. Sci Rep 8(1):3535. https://doi.org/10.1038/s41598-018-21946-1

Nakajima K, Wess J (2012) Design and functional characterization of a novel, arrestin-biased designer G protein-coupled receptor. Mol Pharmacol 82 (4):575–582. https://doi.org/10.1124/mol.112.080358

Ramirez MD, Pairett AN, Pankey MS, Serb JM, Speiser DI, Swafford AJ, Oakley TH (2016) The last common ancestor of most bilaterian animals possessed at least nine opsins. Genome Biol Evol 8(12):3640–3652. https://doi.org/10.1093/gbe/evw248

Saito T, Koyanagi M, Sugihara T, Nagata T, Arikawa K, Terakita A (2019) Spectral tuning mediated by helix III in butterfly long wavelength-sensitive visual opsins revealed by heterologous action spectroscopy. Zool Lett 5:35. https://doi.org/10.1186/s40851-019-0150-2

Strauss O (2005) The retinal pigment epithelium in visual function. Physiol Rev 85(3):845–881. https://doi.org/10.1152/physrev.00021.2004

Sun H, Gilbert DJ, Copeland NG, Jenkins NA, Nathans J (1997) Peropsin, a novel visual pigment-like protein located in the apical microvilli of the retinal pigment epithelium. Proc Natl Acad Sci U S A 94 (18):9893–9898. https://doi.org/10.1073/pnas.94.18.9893

Terakita A (2005) The opsins. Genome Biol 6(3):213. https://doi.org/10.1186/gb-2005-6-3-213

Terakita A, Hariyama T, Tsukahara Y, Katsukura Y, Tashiro H (1993) Interaction of GTP-binding protein Gq with photoactivated rhodopsin in the photoreceptor membranes of crayfish. FEBS Lett 330(2):197–200. https://doi.org/10.1016/014-5793(93)80272-V

Terakita A, Koyanagi M, Tsukamoto H, Yamashita T, Miyata T, Shichida Y (2004) Counterion displacement in the molecular evolution of the rhodopsin family. Nat Struct Mol Biol 11(3):284–289. https://doi.org/10.1038/nsmb731

Terakita A, Kawano-Yamashita E, Koyanagi M (2012) Evolution and diversity of opsins. WIREs Membr Transport Signaling 1(1):104–111. https://doi.org/10.1002/wmts.6

Terakita A, Nagata T, Sugihara T, Koyanagi M (2015) Optogenetic potentials of diverse animal opsins. In: Yawo H, Kandori H, Koizumi A (eds) Optogenetics: light-sensing proteins and their applications. Springer, Berlin, pp 77–88. https://doi.org/10.1007/978-4-431-55516-2

Tsukamoto H, Terakita A, Shichida Y (2005) A rhodopsin exhibiting binding ability to agonist all-trans-retinal. Proc Natl Acad Sci U S A 102(18):6303–6308. https://doi.org/10.1073/pnas.0500378102

Tsukamoto H, Farrens DL, Koyanagi M, Terakita A (2009) The magnitude of the light-induced conformational change in different rhodopsins correlates with their ability to activate G proteins. J Biol Chem 284 (31):20676–20683. https://doi.org/10.1074/jbc.M109.016212

Urban DJ, Roth BL (2015) DREADDs (designer receptors exclusively activated by designer drugs): chemogenetic tools with therapeutic utility. Annu Rev Pharmacol Toxicol 55:399–417. https://doi.org/10.1146/annurev-pharmtox-010814-124803

Vocking O, Kourtesis I, Tumu SC, Hausen H (2017) Co-expression of xenopsin and rhabdomeric opsin in photoreceptors bearing microvilli and cilia. eLife 6: e23435. https://doi.org/10.7554/eLife.23435

Wada S, Kawano-Yamashita E, Koyanagi M, Terakita A (2012) Expression of UV-sensitive parapinopsin in the iguana parietal eyes and its implication in UV-sensitivity in vertebrate pineal-related organs. PLoS One 7(6):e39003. https://doi.org/10.1371/journal.pone.0039003

Wada S, Shen B, Kawano-Yamashita E, Nagata T, Hibi M, Tamotsu S, Koyanagi M, Terakita A (2018) Color opponency with a single kind of bistable opsin in the zebrafish pineal organ. Proc Natl Acad Sci U S A 115 (44):11310–11315. https://doi.org/10.1073/pnas.1802592115

Yamashita T, Ohuchi H, Tomonari S, Ikeda K, Sakai K, Shichida Y (2010) Opn5 is a UV-sensitive bistable pigment that couples with Gi subtype of G protein. Proc Natl Acad Sci U S A 107(51):22084–22089. https://doi.org/10.1073/pnas.1012498107

# Molecular Properties and Optogenetic Applications of Enzymerhodopsins

9

Satoshi P. Tsunoda, Masahiro Sugiura, and Hideki Kandori

**Abstract**

The cyclic nucleotides cAMP and cGMP are ubiquitous secondary messengers that regulate multiple biological functions including gene expression, differentiation, proliferation, and cell survival. In sensory neurons, cyclic nucleotides are responsible for signal modulation, amplification, and encoding. For spatial and temporal manipulation of cyclic nucleotide dynamics, optogenetics have a great advantage over pharmacological approaches. Enzymerhodopsins are a unique family of microbial rhodopsins. These molecules are made up of a membrane-embedded rhodopsin domain, which binds an all *trans*-retinal to form a chromophore, and a cytoplasmic water-soluble catalytic domain. To date, three kinds of molecules have been identified from lower eukaryotes such as fungi, algae, and flagellates. Among these, histidine kinase rhodopsin (HKR) is a light-inhibited guanylyl cyclase. Rhodopsin GC (Rh-GC) functions as a light-activated guanylyl cyclase, while rhodopsin PDE (Rh-PDE) functions as a light-activated phosphodiesterase that degrades cAMP and cGMP. These enzymerhodopsins have great potential in optogenetic applications for manipulating the intracellular cyclic nucleotide dynamics of living cells. Here we introduce the molecular function and applicability of these molecules.

**Keywords**

Microbial rhodopsin · Guanylate cyclase · Phosphodiesterase · Cyclic nucleotide · Signal transduction

## Abbreviations

| | |
|---|---|
| BLUF | Blue light using flavin |
| BR | Bacteriorhodopsin |
| cAMP | Adenosine, 3′5′-cyclic monophosphate |
| cGMP | Guanosine 3′5′-cyclic monophosphate |
| ChR2 | Channelrhodopsin2 |
| CNG channel | Cyclic nucleotide-gated channel |
| COP | Chlamydomonas opsin |
| CTE | Cyclase transducing element |
| GC | Guanylate cyclase |
| HCN channel | Hyperpolarization-activated cyclic nucleotide–gated channel |
| HK | Histidine kinase |

S. P. Tsunoda (✉)
Department of Life Science and Applied Chemistry, Nagoya Institute of Technology, Nagoya, Japan

JST PRESTO, Saitama, Japan
e-mail: tsunoda.satoshi@nitech.ac.jp

M. Sugiura · H. Kandori
Department of Life Science and Applied Chemistry, Nagoya Institute of Technology, Nagoya, Japan



H. Yawo et al. (eds.), *Optogenetics*, Advances in Experimental Medicine and Biology 1293,
https://doi.org/10.1007/978-981-15-8763-4_9

| | |
|---|---|
| HKR | Histidine kinase rhodopsin |
| LOV | Light-oxygen-voltage |
| PAC | Photoactivated adenylyl cyclase |
| PDE | Phosphodiesterase |
| Rh-GC | Rhodopsin guanylate cyclase |
| Rh-PDE | Rhodopsin phosphodiesterase |
| RR | Response regulator |
| TM | Transmembrane helix |

## 9.1 Introduction

### 9.1.1 General

Optogenetics is a growing technique that allows biological events to be manipulated simply by illumination at a high temporal and spatial resolution (Gradinaru et al. 2010; Mattis et al. 2012). The technique is appreciated, especially in neuroscience, because of its ability to control neuronal excitability. A light-gated cation channel, ChR2 from *Chlamydomonas reinhardtii*, is the first and most frequently applied to optogenetics for activating neuronal excitability (Boyden et al. 2005; Deisseroth and Hegemann 2017). In addition, the molecular mechanism of ChR2 has been intensively studied by electrophysiology, spectroscopy, X-ray structural studies, and other techniques (Zhang et al. 2011; Kato et al. 2012; Schneider et al. 2015; Govorunova et al. 2017; Volkov et al. 2017).

Rhodopsins, which are typically seven transmembrane proteins, are subdivided into a microbial type (type I) and an animal type (type II) (Ernst et al. 2014). Microbial-type rhodopsins found in archaea, bacteria, and lower eukaryotes covalently bind all *trans*-retinal as a chromophore via a conserved lysine residue in the seventh transmembrane (7-TM) helix to form a retinal Schiff base. The molecular functions of microbial rhodopsins are diverse, including light-driven cation and anion pumps, light-gated cation and anion channels, light sensors, and light-dependent enzymes. These are physiologically relevant for phototaxis and cellular energetics (i.e., ATP synthesis).

### 9.1.2 Optogenetics for Manipulating Cyclic Nucleotide Dynamics

Ion-transporting rhodopsins have been widely used to manipulate membrane potentials which cause neuronal excitation and inhibition (Zhang et al. 2011; Govorunova et al. 2017). These rhodopsins have also been used to control energy metabolism (Hara et al. 2013). On the other hand, optogenetic tools for controlling secondary messengers such as cyclic nucleotides have been found in nature or have been engineered. LOV (light-oxygen-voltage)-based or BLUF (blue light using flavin)-based photoactivated adenylyl cyclase (PAC) produce cAMP in a light-dependent manner (Iseki et al. 2002; Ryu et al. 2010; Stierl et al. 2011; Ohki et al. 2016; Zhou et al. 2016). These molecules and their derivatives have been applied to the control of cyclic nucleotide-dependent biological events (Jansen et al. 2015; Steuer Costa et al. 2017). Gasser et al. engineered a phytochrome-based phosphodiesterase (LAPD) which degrades cyclic nucleotides upon illumination with red light (Gasser et al. 2014). Optogenetics manipulation of cyclic nucleotide levels enables to study intracellular signaling mechanism in high spatial and temporal resolution. Although one has to introduce a genetically encoded molecule into cells of interest, it is feasible to trigger or silence the signaling in a second-scale by light, which is not the case of the pharmacological methods. As for spatial resolution, cell-type-specific delivery of optogenetics gene with an optical technique such as two-photon excitation microscopy allows stimulating subcellular domains such as small dendritic regions and individual spines, which was already demonstrated by using a channelrhodopsin (Prakash et al. 2012).

## 9.2 Enzymerhodopsins

Recent genomic studies revealed the existence of families of enzymerhodopsins which include a membrane-embedded rhodopsin moiety followed by an enzymatic catalytic domain. These

molecules exhibit light-dependent catalytic functions and thus have a great potential for optogenetic applications. Three families of enzymerhodopsins have been identified to date, namely histidine kinase rhodopsin (HKR), rhodopsin guanylyl cyclase (Rh-GC), and rhodopsin phosphodiesterase (Rh-PDE) (Fig. 9.1) (Luck et al. 2012; Avelar et al. 2014; Govorunova et al. 2017; Yoshida et al. 2017).

All these molecules contain a catalytic domain after the transmembrane rhodopsin moiety. An interesting structural feature of all enzymerhodopsins is an extra transmembrane helix prior to the usual 7-TM segments of microbial rhodopsins (Gao et al. 2015; Lamarche et al. 2017; Trieu et al. 2017; Tian et al. 2018a, b). Thus, both the N- and C-terminals of the protein are located on the cytoplasmic side. All three enzymerhodopsins form a dimer (Scheib et al. 2015; Yoshida et al. 2017; Tian et al. 2018a). The 7-TM rhodopsin part is well conserved compared to other microbial-type rhodopsins.

Figure 9.2a shows a phylogenetic tree of select microbial rhodopsins based on the amino acid sequences of their transmembrane domains. Enzyme rhodopsins form a cluster and are separated from ion transporters and sensory rhodopsins. Figure 9.2b shows select amino acid residues in the 7-TM rhodopsin domain. The number of common residues of microbial rhodopsins are conserved in the three enzymerhodopsins. Specifically, the residues making up the all-*trans*-retinal binding pocket of bacteriorhodopsin (BR), R82, W86, T89, and W182, are conserved in all three enzymerhodopsins. D85, the primary counterion of the protonated Schiff base in the light-driven proton pump BR, is conserved in Rh-GC and Rh-PDE, but not in HKR. Next, the molecular properties of each enzymerhodopsin are summarized and their applicability for optogenetics is discussed.

## 9.2.1 HKR (Histidine Kinase Rhodopsin)

HKR, histidine kinase rhodopsin, also known as two-component cyclase opsin, 2c-cyclop, was the first identified enzymerhodopsin from *C. reinhardtii* (Kateriya et al. 2004). The genes, which are markedly long, contain an opsin sequence followed by histidine kinase (HK), a response regulator (RR), and guanylyl cyclase domains (GC). Interestingly, the *C. reinhardtii* genome carries four HKR genes, previously named COP5–COP8 (chlamydomonas opsin 5–8) (Hegemann 2008). However, their light-dependent enzymatic function has yet to be demonstrated, despite the discovery of these genes in the early 2000s.

### 9.2.1.1 Molecular Function

In 2018, Tian et al. successfully demonstrated that HKRs are light-inhibited and ATP-dependent guanylyl cyclases regulated through a two-component-like phosphoryl transfer (Tian et al. 2018a). In darkness, HKR2 (2c-Cyclop) from *C. reinhardtii* and *Volvox carteri* exhibited guanylyl cyclase activity after phosphorylation and the transfer of phosphoryl from histidine kinase (HK) to the response regulator (RR). The absorption of light at the rhodopsin domain ($\lambda_{max}$ ~ 550 nm) resulted in a reduction of cyclase activity by inhibiting phosphoryl transfer. His352 in the HK domain was identified as the phosphorylation site. Phosphate is then transferred into D1092 in the RR domain (Fig. 9.1a).

The light–dark ratio of cyclase activity is ~35 in HKR2 from *C. reinhardtii* but about 5 in that from *Volvox carteri*. The light–dark ratio is larger than that of Rh-PDE (<~5), but less than that of Rh-GC (~5000). HKR2 shows high light sensitivity ($k_{0.5} = 0.2$ μW/mm$^2$), which is significantly higher than that of Rh-GC (BeGC1) (55 μW/mm$^2$), bPAC (4 μW/mm$^2$), and mPAC (6 μW/mm$^2$) (Stierl et al. 2011; Raffelberg et al. 2013; Gao et al. 2015).

HKR1 (COP5 from *C. reinhardtii*), a protein related to HKR2, shows a photochromic property in its photochemical reaction, in which the protein has two thermally stable intermediates absorbing blue (490 nm) and UV (380 nm) light (Luck et al. 2012; Penzkofer et al. 2014). These two states can be converted by switching illumination between blue and UV light. Such properties had already been reported in a sensory rhodopsin from

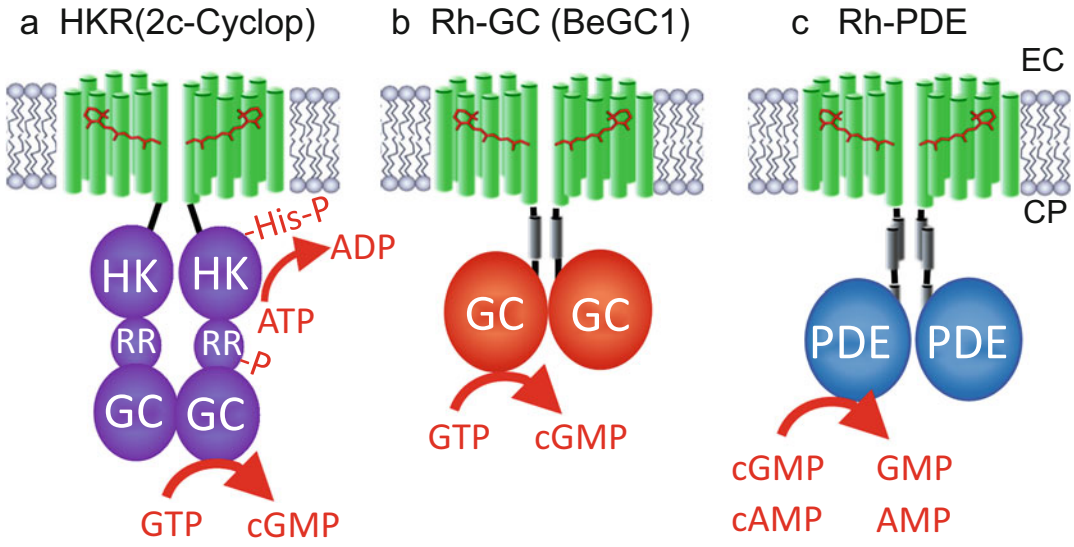


**Fig. 9.1** Schematic of three enzymerhodopsins. (**a**) *HKR* histidine kinase rhodopsin, also known as two-component cyclase opsin, 2c-cyclop; (**b**) *Rh-GC* rhodopsin guanylyl cyclase, also termed BeGC1; (**c**) *Rh-PDE* rhodopsin phosphodiesterase

*Anabaena* PCC7120, and in an inward-directed proton pump rhodopsin PoXeR from *Parvularcula oceani* (Kawanabe et al. 2007; Inoue et al. 2016). The photocycle of HKR2 has

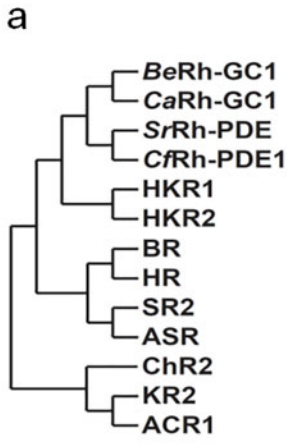


b

| No. in BR | 82 | 85 | 86 | 89 | 93 | 96 | 182 | 185 | 186 | 189 | 212 | 215 | 216 |
|---|---|---|---|---|---|---|---|---|---|---|---|---|---|
| Transmembrane Helix | 3 | 3 | 3 | 3 | 3 | 3 | 6 | 6 | 6 | 6 | 7 | 7 | 7 |
| BR | R | D | W | T | L | D | W | Y | P | W | D | A | K |
| HR | R | T | W | S | I | A | W | Y | P | W | D | A | K |
| KR2 | R | N | W | D | L | Q | W | Y | P | Y | D | S | K |
| ChR2 | R | E | W | T | I | H | W | F | P | F | D | S | K |
| ACR1 | R | S | W | T | M | L | W | Y | P | W | D | C | K |
| SR2 | R | D | W | T | I | F | W | Y | P | W | D | T | K |
| ASR | R | D | W | T | L | S | W | Y | P | W | P | S | K |
| HKR1 | R | M | W | T | M | L | W | F | P | W | D | G | K |
| HKR2 | R | Q | W | T | M | I | W | F | P | W | N | A | K |
| BeRh-GC1 | R | E | W | T | L | L | W | F | P | W | D | A | K |
| CaRh-GC | R | E | W | T | L | L | W | F | P | W | D | A | K |
| SrRh-PDE | R | E | W | T | L | W | W | F | P | E | D | A | K |
| CfRh-PDE1 | R | E | W | T | L | W | W | F | P | E | D | A | K |

**Fig. 9.2** Phylogenetic tree and amino acid alignment of selected microbial rhodopsins. (**a**) Three kinds of enzymerhodopsins and selected microbial rhodopsins are compared. (**b**) Selected amino acid residues in seven transmembrane rhodopsin domains are listed. *Be*Rh-GC and *Ca*Rh-GC Rh-GC from *Blastocladiella emersonii* and *Catanaria anguillulae*, *Sr*Rh-PDE and *Cf*Rh-PDE1 Rh-PDE from *Salpingoeca rosetta* and *Choanoeca flexa*, *HKR1 and HKR2* HKR from *Chlamydomonas reinhardtii*, *BR* proton pump rhodopsin from *Halobacterium salinarum*, *HR* chloride pump rhodopsin from *Natronobacterium pharaonis*, *SR2* sensory rhodopsin from *Halobacterium salinarum*, *ASR* sensory rhodopsin from *Anabaena* PCC7120, *ChR2* channelrhodopsin2 from *Chlamydomonas reinhardtii*, *KR2* sodium pump rhodopsin from *Krokinobacter eikastus*, *ACR1* anion channelrhodopsin1 from *Guillardia theta*

not been reported to date. However, it is estimated that it takes about 30 s based on the time course of enzymatic activity. Thus, the HKR2 photocycle would not show photochromism, but would rather return to the dark state.

#### 9.2.1.2 Physiology

In *V. carteri*, HKR2 is present in a development-dependent manner (Tian et al. 2018a). It is localized mainly in tiny vesicle-like structures around the nuclei of reproductive cells. This implies that HKR2 might be located in a lipid-raft within the endoplasmic reticulum (ER). It is proposed that the function of HKR2 is related to cell differentiation and development. In other algae, the involvement of HKRs in cell differentiation was also predicted (Kianianmomeni and Hallmann 2014). HKR could also be responsible for circadian rhythm (Pfeuty et al. 2012). In *C. reinhardtii*, HKR1 is present in the organism's eye spot (Luck et al. 2012). Interestingly, HKR4 (previously called COP8) has been shown to travel between the eye spot and flagellum by the intraflagellar transport machinery in a light-dependent manner. However, the physiological role(s) of HKR1 and HKR4 remain unknown.

### 9.2.2 Rh-GC (Rhodopsin Guanylyl Cyclase)

Rh-GC is a light-activated guanylyl cyclase and its molecular properties are the best characterized for an enzyme rhodopsin so far. The first Rh-GC (called BeGC1), found in the aquatic fungus *Blastocladiella emersonii*, is responsible for zoospore phototaxis in the organism (Avelar et al. 2014). Rh-GC might activate cyclic nucleotide-gated channels (CNG channels) to modulate membrane potentials, but the detailed mechanism of signal transduction remains to be studied.

#### 9.2.2.1 Basic Properties

A number of homologues and orthologues have been found in related fungi. For example, Rh-GC from *Catanaria anguillulae* (CaGC1) has 77% identity with the amino acid sequence. Gao et al. tested the functions of Rh-GCs from several organisms, one Rh-GC from *Blastocladiella emersonii*, and three genes encoding for Rh-GCs from *Allomyces macrogynus*, and one gene from *Catanaria anguillulae* after expression in *Xenopus laevis* oocytes (Gao et al. 2015). Even though the expression levels were comparable among all molecules, the activity and the light/dark ratio varied significantly. BeGC1 showed the highest activity with a markedly high light/dark ratio (5000-fold), while CaGC1 retained 28–54% of BeGC1 cGMP production with a reduced (230-fold) light/dark ratio. Notably, both Rh-GCs have highly specific GTP production (Gao et al. 2015; Scheib et al. 2015; Trieu et al. 2017). Introducing a double mutation, E497K/C566D, converted substrate specificity toward adenylyl cyclase, as was already known in mammalian cyclases (Sunahara et al. 1998; Tucker et al. 1998; Trieu et al. 2017; Scheib et al. 2018), but these mutations resulted in increased dark activity (Trieu et al. 2017; Scheib et al. 2018).

As already described above, Rh-GC contains eight transmembrane segments with N- and C-termini both located on the cytoplasmic side. The N-terminal cytoplasmic domain contains ~146 amino acid residues. Partial truncation of this domain resulted in higher dark activity and lower light-induced cGMP production (Gao et al. 2015). Further truncation up to 20 kDa of the N-terminal domain completely abolished cyclase activity, indicating that this domain is necessary for the tight light regulation of enzymatic activity (Trieu et al. 2017). Rhodopsin and the cyclase domain are connected by a linker made up of 45 amino acid residues, including 19 amino acids of a cyclase transducing element (CTE), which is widely conserved in class III cyclases (Ziegler et al. 2017).

#### 9.2.2.2 Enzymatic Properties

Rh-GC (BeGC1) shows higher activity in the presence of $Mn^{2+}$ than in $Mg^{2+}$, which is usually observed in type III GCs (Ziegler et al. 2017). The $K_m$ value of BeGC1 cyclase activity is 0.9 mM, consistent with physiological cGMP concentration. The crystal structure of the water-soluble enzyme domain (GC domain) was determined

by two groups in 2017 and 2018 (Kumar et al. 2017; Scheib et al. 2018). Kumar et al. and Scheib et al. revealed nonfunctional monomeric structures, that were made up of seven β-sheet strands and three α-helices. Scheib et al. further determined the structure of the cyclase domain of CaAC, which has the E479K/C566D double mutation and thus shows adenylyl cyclase activity. The structure forms an antiparallel dimer and binds ATPαS at the catalytic site, reflecting the functional state of a type III cyclase. The substrate binding site is similar to other ligand-bound ACs (Linder 2006; Steegborn 2014). Recently, Butryn et al. successfully determined the structure of the wild-type GC domain in the GTP-bound state at 1.7 Å resolution which also corresponded to its active conformation (Butryn et al. 2019). The structure provides insight into the detailed mechanism of substrate discrimination and activity regulation.

The Rh-GC photocycle was studied by time-resolved spectroscopy using a truncated rhodopsin and a full-length version (Scheib et al. 2015; Trieu et al. 2017). The dark-adapted state has a maximum absorption at 525 nm. After photoexcitation, Rh-GC (BeGC1) forms a deprotonated M intermediate (P380) within 12 ms, via a redshifted K intermediate (P580). From kinetics analysis of cyclase activity, it was suggested that the M intermediate corresponds to the catalytic active state. The M intermediate returns to the dark-adapted state with a time constant of 100 ms. The photocycle of the truncated form is similar to that of the full-length protein but with slightly faster kinetics probably due to the lack of an enzyme domain (Trieu et al. 2017). CaGC has a markedly long photocycle in which the M intermediate lasts 570 ms (Scheib et al. 2018).

#### 9.2.2.3 Activation Mechanism

How does light absorption trigger the activation of cyclase? In darkness, the catalytic site of the GC domain must be structurally constrained. The light signal then releases this constraint by conformational changes from the rhodopsin domain to the GC domain via the linker region. In OaPAC, photoactivated adenylyl cyclase (PAC) from the photosynthetic cyanobacterium *Oscillatoria acuminate*, it has been proposed that a central coiled coil of transmits changes from the light-sensing domains (BLUF domains) to the active sites of cyclase. However, the intermolecular signal transduction is based on protein vibration and structural rearrangement is minimal. In contrast, a structural study of bPAC demonstrated light-induced β4/5 loop movement for cyclase activation within the AC domain (Lindner et al. 2017).

Currently, details about the structure of rhodopsin and the linker region of Rh-GC are missing. Knowledge of the full-length structure of Rh-GC would be crucial to understand the activation mechanism in more detail.

#### 9.2.2.4 Optogenetics

Due to its excellent light–dark ratio of enzymatic activity, Rh-GC has great potential in optogenetic applications for elevating intracellular cGMP levels. Scheib et al. showed that Rh-GC could elevate intracellular cGMP levels in CHO K1 cells and in hippocampal neurons (Scheib et al. 2015). Furthermore, Gao et al. demonstrated it can be applied for controlling animal behavior (Gao et al. 2015). After the expression of Rh-GC together with CNG (cyclic nucleotide-gated) channels in the muscle cells of *C. elegans*, green light stimulation resulted in a reduced body length. They also demonstrated that the speed of *C. elegans* locomotion could be manipulated by illumination after introduction of Rh-GC into BAG neurons.

### 9.2.3 Rh-PDE (Rhodopsin Phosphodiesterase)

The genome of the choanoflagellate *Salpingoeca rosetta* contains an unusual gene encoding a rhodopsin fused to a C-terminal PDE domain (Rh-PDE). In 2017, Yoshida et al. and Lamarche et al. independently reported this novel type of enzymerhodopsin (Lamarche et al. 2017; Yoshida et al. 2017). It was proposed that Rh-PDE is a microbial rhodopsin that binds all *trans*-retinal as a chromophore, where light absorption triggers

protein structural changes to induce (or modulate) phosphodiesterase activity.

#### 9.2.3.1 Basic Properties

Sequence analysis implied that Rh-PDE is an 8-TM protein with an extra N-terminal transmembrane helix TM-0, which was experimentally demonstrated by an immune fluorescence method and fluorescent complementation (Lamarche et al. 2017; Tian et al. 2018b). The involvement of TM-0 is a unique feature of all enzyme rhodopsins known so far. In addition, Rh-PDE has an N-terminal cytoplasmic domain which is made up of ~60 amino acid residues. Although the role of this domain still needs to be investigated, it may be responsible for modulating enzymatic function. The catalytic PDE domain contains many conserved residues typical of the active centers of soluble PDEs, but it is not possible to predict the substrate specificity of Rh-PDE (cAMP, cGMP, or both) from its sequence (Yoshida et al. 2017).

#### 9.2.3.2 Molecular Function

The molecular function of Rh-PDE was investigated after expressing it in HEK293 cells and in *Xenopus laevis* oocytes (Lamarche et al. 2017; Yoshida et al. 2017; Tian et al. 2018b). Rh-PDE exhibits light-dependent phosphodiesterase activity toward cAMP and cGMP. Hydrolysis activity of cGMP is 10–100 times higher than that of cAMP. However, Rh-PDE was initially shown to have constitutive dark activity which means that the activity was enhanced by light only by 140% toward cGMP and by 160% toward cAMP (Yoshida et al. 2017). This is partially because of an additional fluorescent protein (GFP or YFP) tagged at the C-terminal which probably hampers proper conformation change for enzymatic activation. Placing YFP at the N-terminal of the protein instead resulted in an improvement of light activation by as much as 260% (Tian et al. 2018b). Furthermore, the light/dark ratio increased four- and fivefold for cGMP and cAMP, respectively, when the tagged protein was removed. These results indicate the importance of the N-terminal for light regulation of Rh-PDE activity. Interestingly, the light/dark ratio is also dependent on $Mg^{2+}$ concentration. The $K_m$ value for cGMP is decreased from 80 to 13 μM upon illumination, whereas the $V_{max}$ value only increased by 30%. A truncated PDE domain was isolated and was still active with a six- to ninefold reduction in hydrolysis rate compared to the full-length protein.

The spectroscopic properties of Rh-PDE were studied after isolating the full-length protein and truncating the rhodopsin moiety (Yoshida et al. 2017; Watari et al. 2019). In the dark-adapted state, Rh-PDE absorbed maximally at 492 nm and showed a photocycle. The *K* intermediate formed within 0.005 ms and converted into the deprotonated *M*-state with a time constant of 4 ms, with the latter returned to the original state within 4 s, which was significantly slower than the proton-pumping BR (Ernst et al. 2008). FTIR spectroscopy revealed that all-*trans* to 13-*cis* photoisomerization of retinal occurs as the primary event during which chromophore distortion is located in the middle of the polyene chain, allowing the Schiff base to form a stronger hydrogen bond (Watari et al. 2019). It was also revealed that the peptide backbone of the α-helix becomes deformed upon formation of the *M* intermediate.

From spectroscopic and biochemical experiments, the following reaction model was proposed (Yoshida et al. 2017; Watari et al. 2019). In the dark, Rh-PDE exhibits constitutive activity toward cGMP and cAMP, suggesting that the catalytic region is somewhat exposed to the cytoplasm in mammalian cells (Fig. 9.3a). Upon absorption of blue-green light by the rhodopsin domain, photoisomerization of the retinal chromophore from the all-*trans* to 13-*cis* form produces the *M* intermediate with a deprotonated Schiff base within 4 ms (rhodopsin domain Switch-ON), but the PDE domain has not changed yet (PDE domain Switch-OFF) (Fig. 9.3b). Next, the M intermediate decays to the parent spectral state in 4 s (Rh-domain Switch-OFF), accompanied by structural changes in the PDE domain (PDE domain Switch-ON) (Fig. 9.3c). The resulting increase in enzymatic activity is turned off within ~70 s (PDE domain Switch-OFF).

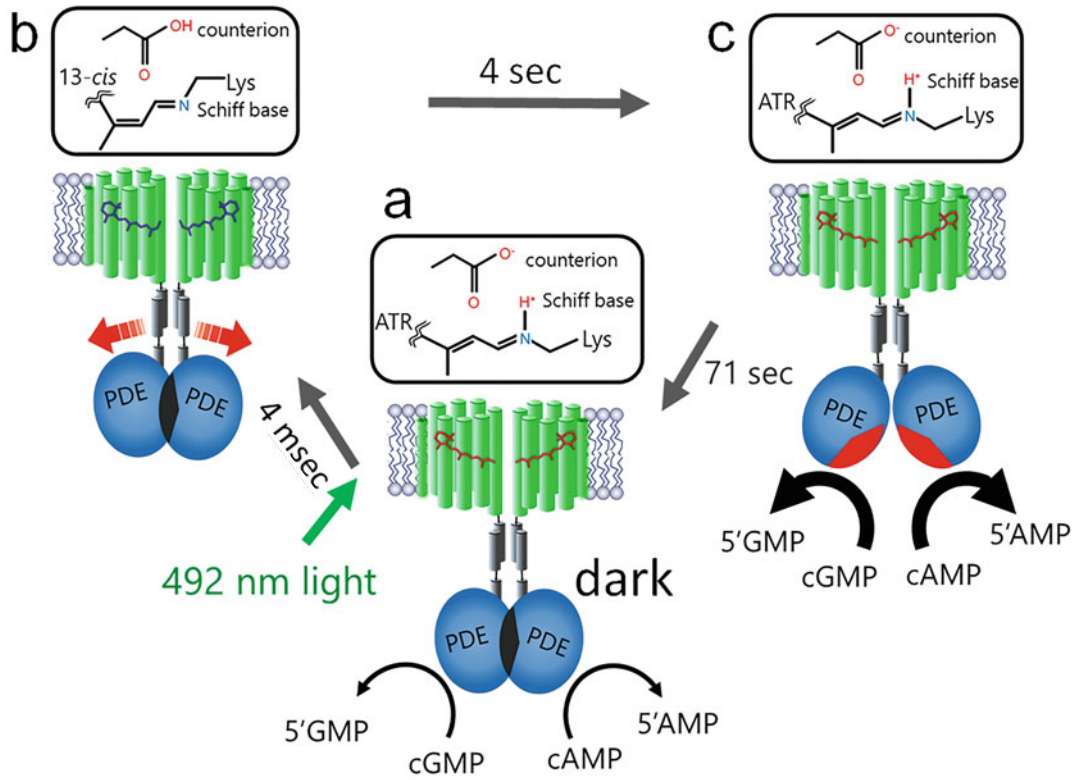


**Fig. 9.3** A proposed activation mechanism of Rh-PDE

#### 9.2.3.3 Structure of PDE Domain

Human PDEs are categorized into three groups based on their substrate specificities toward cAMP, cGMP, or both (Bender and Beavo 2006; Wang et al. 2007; Pandit et al. 2009). A comparison of amino acid sequences at the substrate binding domain did not indicate key residues for substrate specificity (Wang et al. 2007). This situation is different from cyclase in which substrate specificity was defined only by two residues (*E* and *C* for guanylyl cyclase and *K* and *D* for adenylyl cyclase at positions 497 and 566 based on Rh-GC numbering) (Sunahara et al. 1998; Tucker et al. 1998). The X-ray structure of the PDE domain of Rh-PDE showed a dimeric structure that was similar to human PDE9 (Lamarche et al. 2017).

#### 9.2.3.4 Orthologues and Physiological Relevance of Rh-PDE

Since the discovery of Rh-PDE from a choanoflagellate *Sarpingoeca rosetta* in 2017, it was predicted that light-triggered signal transduction by a cyclic nucleotide could be involved in the organism. It had already been reported that *S. rosetta* actually contains a homolog of HCN (hyperpolarization-activated cyclic nucleotide-gated) channels (Cai 2012), implying that an electric signaling could be triggered by light for physiological responses such as phototaxis or photophobic reactions.

In 2019, Brunet et al. identified eight orthologous genes encoding Rh-PDE from several chaonoflagellates related to *S. rosetta* (Brunet et al. 2019). Interestingly, four of them were found in one organism, *Choanoeca flexa*, a multicellular flagellate composed of ~100 single cells that together form a small sheet. They named them as *C. flexa* Rh-PDE1–4 (CfRh-PDE1–4). Two other genes were found in *Choanoeca perplexa* (CpRh-PDE1 and 2) which is evolutionally very close to *C. flexa*. The two remaining genes were found in *Micostomoeca ronanoka* and *Acanthoeca spectabilis*, one in

each. Interestingly, Rh-PDE from *Acanthoeca spectabilis* (AsRh-PDE) does not contain the retinal-binding Lys at TM7, implying no chromophore formation and thus no light-dependent enzymatic activity. Brunet et al. demonstrated that *C. flexa* senses light then changes its morphology, i.e., the sheet of cells was bent inward in the dark. However, it would invert this inward curvature upon illumination. They proposed that the Rh-PDE(s) reduced the intracellular cGMP level in a light-dependent manner to modulate the cGMP-signaling cascade for triggering actomyosin-mediated apical contractility. It remains unknown which of the Rh-PDE gene (s) are responsible for this behavior. Thus, direct validation will require targeted disruption of all four *C. flexa* Rh-PDE homologs. In addition, localization of Rh-PDE in the organism is still unknown. More physiological studies are needed to answer these questions.

Besides physiological studies, the enzymatic and molecular properties of novel eight Rh-PDEs have been investigated very recently after expression in HEK293 cells (Sugiura et al. 2020). Among CfRh-PDE1–4 from *C. flexa*, Cf Rh-PDE2 and Cf Rh-PDE3 exhibited no PDE activity when assessed in HEK293 cells and in vitro analysis. On the other hand, Cf Rh-PDE1 showed light-dependent PDE activity toward cGMP, which absorbed maximally at 491 nm. CfRh-PDE4 showed only small light-dependent activity toward cAMP. Thus, Cf Rh-PDE1 is presumably responsible for colony inversion in *C. flexa* by absorbing blue-green light. The molecular properties of MrRh-PDE were similar to those of SrRh-PDE, although the $\lambda_{max}$ of MrRh-PDE (516 nm) was redshifted from that of SrRh-PDE (492 nm). As mentioned above, AsRh-PDE did not contain the retinal-binding Lys at TM7. Despite luck of light dependency, AsRh-PDE showed cAMP-specific high PDE activity, a property that is in contrast to SrRh-PDE, which has PDE activity toward both cAMP and cGMP, the latter being stronger. These results provide mechanistic insight into rhodopsin-mediated enzymatic function and allow for engineering optogenetics tools.

#### 9.2.3.5 Optogenetics

Despite its high constitutive activity, the optogenetic applicability of Rh-PDE was assessed in HEK293 cells (Yoshida et al. 2017). After the expression of Rh-PDE, cAMP concentration was monitored in live cells by the GloSensor assay, which is based on a cyclic nucleotide-dependent luciferase. Figure 9.4 shows the activity of Rh-PDE toward cAMP. The level of cAMP gradually increased after the addition of forskolin, and reached a plateau after 40 min (Fig. 9.4a). At that time point, illumination at 510 nm resulted in a transient reduction of cAMP in cells expressing Rh-PDE (red line), but not with the empty vector (blue line) or a function-deficient mutant Rh-PDE D605A (yellow line) (Fig. 9.4a, b). Optical stimulation could be repeated many times (Fig. 9.4c). This result indicates that Rh-PDE is able to reduce cAMP level in living cells.

## 9.3 Conclusions

Here we summarized the current status of enzymerhodopsin research. Molecular functions have emerged following spectroscopic and structural studies together with biochemical studies. Crystal structures of the soluble domain have been revealed for Rh-GC and Rh-PDE. However, there are a number of questions that still need to be answered. For example, transducing light information from the rhodopsin domain to the enzyme function is still enigmatic. Further studies would be needed to understand a more detailed mechanism of these molecules. Especially, the molecular structure of the full-length protein would be a crucial study. These studies would be useful to apply and engineer molecules for optogenetics to modulate cyclic nucleotide levels for controlling biological functions. As optogenetic tools for modulating cyclic nucleotide dynamics, LOV- and BLUF-based cyclases such as bPAC are available. One of the advantages of enzymerhodopsins over LOV- and BLUF-based cyclases is the speed of turning-on and/or –off, i.e., the photocycle speed. For

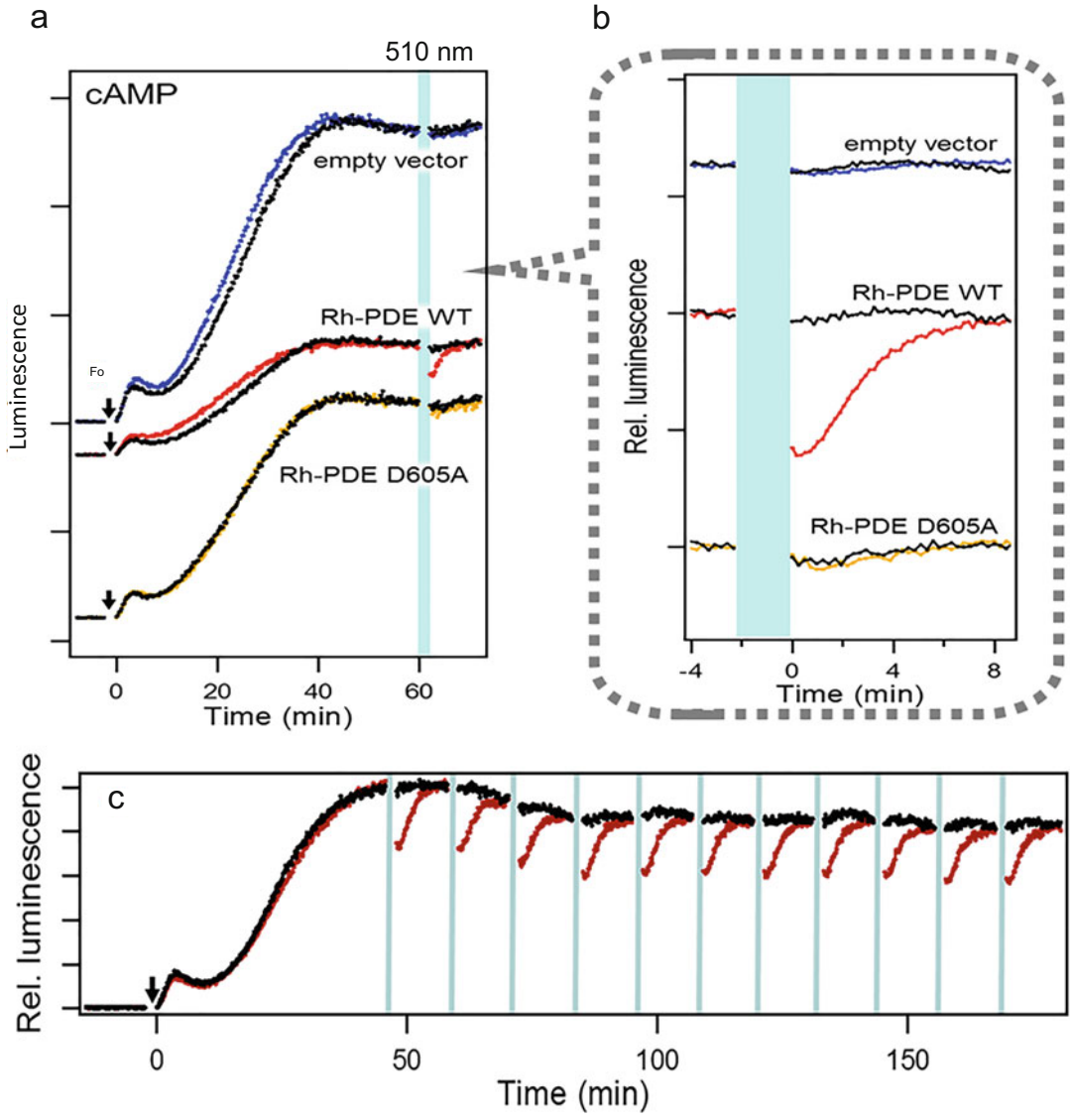


**Fig. 9.4** Optical manipulation of intracellular cAMP dynamics in HEK293 cells expressing Rh-PDE. (**a**) Intracellular cAMP dynamics was monitored by a luminescence-based cAMP indicator. Forskolin was added at 0 min to elevate cAMP level. Cells ware illuminated between 60 and 62 min as indicated by a bar in cyan. (**b**) Enlargement of traces in **a**. Cells were illuminated between −2 and 0 min as indicated by a bar in cyan. (**c**) Repetitive optical stimulation of Rh-PDE-expressing HEK293 cells. Cells were illuminated 11 times, as indicated by bars in cyan

instance, Rh-GC (BeGC1) exhibits the recovery kinetics of 100 ms (Scheib et al. 2015; Trieu et al. 2017), while that of euPAC was rather slow with $\tau_{off} = 12.3$ s (Stierl et al. 2011). The other advantage of enzymerhodopsin is that it can employ longer wavelengths of light. All three kinds of enzymerhdopsins have a $\lambda_{max}$ between 490 and 550 nm, blue to green light, while flavoproteins have shorter absorption maxima, usually from UV to 450 nm. Furthermore, the $\lambda_{max}$ of rhodopsins can be tuned to an even longer wavelength by an amino acid mutation around the

retinal pocket moiety. For optogenetic experiments, light with longer wavelengths can better penetrate into biological tissues, and are less invasive, e.g., cause less DNA damage. Another advantage of enzymerhodopsins is that they can be targeted in intracellular subcellular domains such as the ER and synaptic vesicles by fusing targeting signaling peptides. This allows for the optical manipulation of a local signaling event.

Finally, cGMP signaling plays a role in NO signaling cascade for smooth muscle relaxation, or even in animal vision, while concentrations of cAMP is elevated by β-adrenergic receptor signaling and is an important second messenger in regulating cardiac muscle. In neurons, the cAMP/PKA (cyclic-AMP-dependent protein kinase) signaling cascade controls various biological properties such as axonal growth, synaptic transmission, and regulation of excitability. Enzymerhodopsins would be applicable as optogenetics tools for these research fields for a better understanding of the detailed processes in signal transduction.

**Acknowledgments** This work was financially supported by the Japanese Ministry of Education, Culture, Sports, Science and Technology (25104009, 15H02391 to H.K and 18K06109 to S.P.T.), JST CREST grant (JPMJCR1753 to H.K.), JST PRESTO grant (JPMJPR1688 to S.P.T).

## References

Avelar GM, Schumacher RI, Zaini PA et al (2014) A rhodopsin-guanylyl cyclase gene fusion functions in visual perception in a fungus. Curr Biol 24:1234–1240. https://doi.org/10.1016/j.cub.2014.04.009

Bender AT, Beavo JA (2006) Cyclic nucleotide phosphodiesterases: molecular regulation to clinical use. Pharmacol Rev 58:488–520. https://doi.org/10.1124/pr.58.3.5

Boyden ES, Zhang F, Bamberg E et al (2005) Millisecond-timescale, genetically targeted optical control of neural activity. Nat Neurosci 8:1263–1268. https://doi.org/10.1038/nn1525

Brunet T, Larson BT, Linden TA et al (2019) Light-regulated collective contractility in a multicellular choanoflagellate. Science 366:326–334. https://doi.org/10.1126/science.aay2346

Butryn A, Raza H, Rada H et al (2019) Molecular basis for GTP recognition by light-activated guanylate cyclase RhGC. FEBS J 287:2797. https://doi.org/10.1111/febs.15167

Cai X (2012) Evolutionary genomics reveals the premetazoan origin of opposite gating polarity in animal-type voltage-gated ion channels. Genomics 99:241–245. https://doi.org/10.1016/j.ygeno.2012.01.007

Deisseroth K, Hegemann P (2017) The form and function of channelrhodopsin. Science 357(6356):eaan5544. https://doi.org/10.1126/science.aan5544

Ernst OP, Sánchez Murcia PA, Daldrop P et al (2008) Photoactivation of channelrhodopsin. J Biol Chem 283:1637–1643. https://doi.org/10.1074/jbc.M708039200

Ernst OP, Lodowski DT, Elstner M et al (2014) Microbial and animal rhodopsins: structures, functions, and molecular mechanisms. Chem Rev 114:126–163. https://doi.org/10.1021/cr4003769

Gao S, Nagpal J, Schneider MW et al (2015) Optogenetic manipulation of cGMP in cells and animals by the tightly light-regulated guanylyl-cyclase opsin CyclOp. Nat Commun 6:8046. https://doi.org/10.1038/ncomms9046

Gasser C, Taiber S, Yeh C-M et al (2014) Engineering of a red-light-activated human cAMP/cGMP-specific phosphodiesterase. Proc Natl Acad Sci U S A 111:8803–8808. https://doi.org/10.1073/pnas.1321600111

Govorunova EG, Sineshchekov OA, Li H, Spudich JL (2017) Microbial rhodopsins: diversity, mechanisms, and optogenetic applications. Annu Rev Biochem 86:845–872. https://doi.org/10.1146/annurev-biochem-101910-144233

Gradinaru V, Zhang F, Ramakrishnan C et al (2010) Molecular and cellular approaches for diversifying and extending optogenetics. Cell 141:154–165. https://doi.org/10.1016/j.cell.2010.02.037

Hara KY, Wada T, Kino K et al (2013) Construction of photoenergetic mitochondria in cultured mammalian cells. Sci Rep 3:1–4. https://doi.org/10.1038/srep01635

Hegemann P (2008) Algal sensory photoreceptors. Annu Rev Plant Biol 59:167. https://doi.org/10.1146/annurev.arplant.59.032607.092847

Inoue K, Ito S, Kato Y et al (2016) A natural light-driven inward proton pump. Nat Commun 7:13415. https://doi.org/10.1038/ncomms13415

Iseki M, Matsunaga S, Murakami A et al (2002) A blue-light-activated adenylyl cyclase mediates photoavoidance in Euglena gracilis. Nature 415:1047–1051. https://doi.org/10.1038/4151047a

Jansen V, Alvarez L, Balbach M et al (2015) Controlling fertilization and cAMP signaling in sperm by optogenetics. Elife 4:e05161. https://doi.org/10.7554/eLife.05161

Kateriya S, Nagel G, Bamberg E, Hegemann P (2004) "Vision" in single-celled algae. News Physiol Sci 19:133–137

Kato HE, Zhang F, Yizhar O et al (2012) Crystal structure of the channelrhodopsin light-gated cation channel. Nature 482:369–374. https://doi.org/10.1038/nature10870

Kawanabe A, Furutani Y, Jung KH, Kandori H (2007) Photochromism of Anabaena sensory rhodopsin. J Am Chem Soc 129:8644. https://doi.org/10.1021/ja072085a

Kianianmomeni A, Hallmann A (2014) Transcriptional analysis of Volvox photoreceptors suggests the existence of different cell-type specific light-signaling pathways. Curr Genet 61:3. https://doi.org/10.1007/s00294-014-0440-3

Kumar RP, Morehouse BR, Fofana J et al (2017) Structure and monomer/dimer equilibrium for the guanylyl cyclase domain of the optogenetics protein RhoGC. J Biol Chem 292:21578–21589. https://doi.org/10.1074/jbc.M117.812685

Lamarche LB, Kumar RP, Trieu MM et al (2017) Purification and characterization of RhoPDE, a retinylidene/phosphodiesterase fusion protein and potential optogenetic tool from the Choanoflagellate Salpingoeca rosetta. Biochemistry 56:5812–5822. https://doi.org/10.1021/acs.biochem.7b00519

Linder JU (2006) Class III adenylyl cyclases: molecular mechanisms of catalysis and regulation. Cell Mol Life Sci 63:1736

Lindner R, Hartmann E, Tarnawski M et al (2017) Photoactivation mechanism of a bacterial light-regulated adenylyl cyclase. J Mol Biol 429:1336. https://doi.org/10.1016/j.jmb.2017.03.020

Luck M, Mathes T, Bruun S et al (2012) A photochromic histidine kinase rhodopsin (HKR1) that is bimodally switched by ultraviolet and blue light. J Biol Chem 287:40083–40090. https://doi.org/10.1074/jbc.M112.401604

Mattis J, Tye KM, Ferenczi EA et al (2012) Principles for applying optogenetic tools derived from direct comparative analysis of microbial opsins. Nat Methods 9:159–172. https://doi.org/10.1038/nmeth.1808

Ohki M, Sugiyama K, Kawai F et al (2016) Structural insight into photoactivation of an adenylate cyclase from a photosynthetic cyanobacterium. Proc Natl Acad Sci U S A 113:6659–6664. https://doi.org/10.1073/pnas.1517520113

Pandit J, Forman MD, Fennell KF et al (2009) Mechanism for the allosteric regulation of phosphodiesterase 2A deduced from the X-ray structure of a near full-length construct. Proc Natl Acad Sci U S A 106:18225–18230. https://doi.org/10.1073/pnas.0907635106

Penzkofer A, Luck M, Mathes T, Hegemann P (2014) Bistable retinal Schiff base photodynamics of histidine kinase rhodopsin HKR1 from chlamydomonas reinhardtii. Photochem Photobiol 90:773–785. https://doi.org/10.1111/php.12246

Pfeuty B, Thommen Q, Corellou F et al (2012) Circadian clocks in changing weather and seasons: lessons from the picoalga ostreococcus tauri. BioEssays 34:781

Prakash R, Yizhar O, Grewe B et al (2012) Two-photon optogenetic toolbox for fast inhibition, excitation and bistable modulation. Nat Methods 9:1171. https://doi.org/10.1038/nmeth.2215

Raffelberg S, Wang L, Gao S et al (2013) A LOV-domain-mediated blue-light-activated adenylate (adenylyl) cyclase from the cyanobacterium Microcoleus chthonoplastes PCC 7420. Biochem J 455:359. https://doi.org/10.1042/BJ20130637

Ryu MH, Moskvin OV, Siltberg-Liberles J, Gomelsky M (2010) Natural and engineered photoactivated nucleotidyl cyclases for optogenetic applications. J Biol Chem 285:41501–41508. https://doi.org/10.1074/jbc.M110.177600

Scheib U, Stehfest K, Gee CE et al (2015) The rhodopsin – guanylyl cyclase of the aquatic fungus *Blastocladiella emersonii* enables fast optical control of cGMP signaling. Sci Signal 8:1–9

Scheib U, Broser M, Constantin OM, et al (2018) Rhodopsin-cyclases for photocontrol of cGMP/cAMP and 2.3 Å structure of the adenylyl cyclase domain. Nat Commun 9. https://doi.org/10.1038/s41467-018-04428-w

Schneider F, Grimm C, Hegemann P (2015) Biophysics of Channelrhodopsin. Annu Rev Biophys 44:167–186. https://doi.org/10.1146/annurev-biophys-060414-034014

Steegborn C (2014) Structure, mechanism, and regulation of soluble adenylyl cyclases—similarities and differences to transmembrane adenylyl cyclases. Biochim Biophys Acta Mol Basis Dis 1842:2535

Steuer Costa W, S chieh Y, Liewald JF, Gottschalk A (2017) Fast cAMP modulation of neurotransmission via neuropeptide signals and vesicle loading. Curr Biol 27:495. https://doi.org/10.1016/j.cub.2016.12.055

Stierl M, Stumpf P, Udwari D et al (2011) Light modulation of cellular cAMP by a small bacterial photoactivated adenylyl cyclase, bPAC, of the soil bacterium Beggiatoa. J Biol Chem 286:1181–1188. https://doi.org/10.1074/jbc.M110.185496

Sugiura M, Tsunoda SP, Hibi M, Kandori H (2020) Molecular properties of new enzyme rhodopsins with phosphodiesterase activity. https://doi.org/10.1021/acsomega.0c01113

Sunahara RK, Beuve A, Tesmer JJG et al (1998) Exchange of substrate and inhibitor specificities between adenylyl and guanylyl cyclases. J Biol Chem 273:16332. https://doi.org/10.1074/jbc.273.26.16332

Tian Y, Gao S, Heyde EL et al (2018a) Two-component cyclase opsins of green algae are ATP-dependent and light-inhibited guanylyl cyclases. BMC Biol 16:1–18. https://doi.org/10.1186/s12915-018-0613-5

Tian Y, Gao S, Yang S, Nagel G (2018b) A novel rhodopsin phosphodiesterase from Salpingoeca rosetta shows light-enhanced substrate affinity. Biochem J 475:1121. https://doi.org/10.1042/BCJ20180010

Trieu MM, Devine EL, Lamarche LB et al (2017) Expression, purification, and spectral tuning of RhoGC, a

retinylidene/guanylyl cyclase fusion protein and optogenetics tool from the aquatic fungus Blastocladiella emersonii. J Biol Chem 292:10379–10389. https://doi.org/10.1074/jbc.M117.789636

Tucker CL, Hurley JH, Miller TR, Hurley JB (1998) Two amino acid substitutions convert a guanylyl cyclase, RetGC-1, into an adenylyl cyclase. Proc Natl Acad Sci U S A 95:5993–5997. https://doi.org/10.1073/pnas.95.11.5993

Volkov O, Kovalev K, Polovinkin V et al (2017) Structural insights into ion conduction by channelrhodopsin 2. Science (80-) 358:eaan8862. https://doi.org/10.1126/science.aan8862

Wang H, Liu Y, Hou J et al (2007) Structural insight into substrate specificity of phosphodiesterase 10. Proc Natl Acad Sci U S A 104:5782–5787. https://doi.org/10.1073/pnas.0700279104

Watari M, Ikuta T, Yamada D et al (2019) Spectroscopic study of the transmembrane domain of a rhodopsin–phosphodiesterase fusion protein from a unicellular eukaryote. J Biol Chem 294:3432. https://doi.org/10.1074/jbc.RA118.006277

Yoshida K, Tsunoda SP, Brown LS, Kandori H (2017) A unique choanoflagellate enzyme rhodopsin exhibits lightdependent cyclic nucleotide phosphodiesterase activity. J Biol Chem 292:7531–7541. https://doi.org/10.1074/jbc.M117.775569

Zhang F, Vierock J, Yizhar O et al (2011) The microbial opsin family of optogenetic tools. Cell 147:1446–1457. https://doi.org/10.1016/j.cell.2011.12.004

Zhou Z, Tanaka KF, Matsunaga S et al (2016) Photoactivated adenylyl cyclase (PAC) reveals novel mechanisms underlying cAMP-dependent axonal morphogenesis. Sci Rep 5:19679. https://doi.org/10.1038/srep19679

Ziegler M, Bassler J, Beltz S et al (2017) Characterization of a novel signal transducer element intrinsic to class IIIa/b adenylate cyclases and guanylate cyclases. FEBS J 284:1204. https://doi.org/10.1111/febs.14047

# 10 Phytochromes and Cyanobacteriochromes: Photoreceptor Molecules Incorporating a Linear Tetrapyrrole Chromophore

Keiji Fushimi and Rei Narikawa

**Abstract**

In this chapter, we summarize the molecular mechanisms of the linear tetrapyrrole-binding photoreceptors, phytochromes, and cyanobacteriochromes. We especially focus on the color-tuning mechanisms and conformational changes during the photoconversion process. Furthermore, we introduce current status of development of the optogenetic tools based on these molecules. Huge repertoire of these photoreceptors with diverse spectral properties would contribute to development of multiplex optogenetic regulation. Among them, the photoreceptors incorporating the biliverdin IXα chromophore is advantageous for in vivo optogenetics because this is intrinsic in the mammalian cells, and absorbs far-red light penetrating into deep mammalian tissues.

**Keywords**

Tetrapyrrole · Bilin · Far-red · Phytochrome · Cyanobacteriochrome · GAF domain

## Abbreviations

| | |
|---|---|
| BR | Bilirubin |
| BV | Biliverdin IXα |
| CBCR | Cyanobacteriochrome |
| Chl. | Chlorophyll |
| DXCF | Asp-Xaa-Cys-Phe |
| DXCIP | Asp-Xaa-Cys-Ile-Pro |
| GAF | cGMP-phosphodiesterase/adenylate cyclase/FhlA |
| GOI | Gene of interest |
| PAS | Per/Arnt/Sim |
| PCB | Phycocyanobilin |
| PCM | Photosensory core module |
| PCR | Phycocyanorubin |
| phy | Phytochrome |
| PHY | Phytochrome-specific |
| PIF | Phytochrome interacting factor |
| POI | Protein of interest |
| PVB | Phycoviolobilin |
| PXB | Unknown chromophore |
| Pxx | violet- (Pv), blue- (Pb), teal- (Pt), green- (Pg), yellow- (Py), orange- (Po), red- (Pr) and far-red-absorbing form (Pfr) |
| PΦB | Phytochromobilin |
| PΦR | Phytochromorubin |

K. Fushimi
Graduate School of Integrated Science and Technology, Shizuoka University, Shizuoka, Japan

Core Research for Evolutional Science and Technology, Japan Science and Technology Agency, Saitama, Japan

R. Narikawa (✉)
Graduate School of Integrated Science and Technology, Shizuoka University, Shizuoka, Japan

Core Research for Evolutional Science and Technology, Japan Science and Technology Agency, Saitama, Japan

Research Institute of Green Science and Technology, Shizuoka University, Shizuoka, Japan
e-mail: narikawa.rei@shizuoka.ac.jp



H. Yawo et al. (eds.), *Optogenetics*, Advances in Experimental Medicine and Biology 1293,
https://doi.org/10.1007/978-981-15-8763-4_10

XRG Expanded red green

## 10.1 Introduction

Because light is one of the most important environmental signals not only for the photosynthetic organisms but also for the non-photosynthetic organisms, living organisms have evolved highly equipped photoresponsive systems by using specific photoreceptors to sense information on light color and intensity. To date, many photoreceptors such as UVR8, rhodopsins, cryptochromes, phototropins, phytochromes, and cyanobacteriochromes have been identified from various organisms (Fig. 10.1) (Ziegler and Möglich 2015). These photoreceptors except for the UVR8 bind the chromophore to sense the visible light. Light absorption by the chromophore triggers conformational changes of the protein and transfers the light signal to the other signals such as the phosphorylation and accumulation of second messengers, which finally alter the physiological processes to acclimate to the changing light environments.

On the other hand, optogenetic tools based on these photoreceptors have been extensively developed. Although many studies focus on the regulation of neural activities by using the channelrhodopsin at the initial phase of the optogenetic development (Rost et al. 2017), many optogenetic tools other than the channelrhodopsin-based ones have now been developed (Ziegler and Möglich 2015; Ueda and Sato 2018). Among them, the linear tetrapyrrole-binding photoreceptors, the phytochromes (Phys), and cyanobacteriochromes (CBCRs) exhibit huge repertoire with diverse spectral properties including far-red to near-infrared region (Rockwell and Lagarias 2017a, 2019; Fushimi and Narikawa 2019). This long wavelength region is called optical window, which is advantageous for in vivo application (Fig. 10.1) (Ziegler and Möglich 2015). This region can escape from absorption by hemoglobin and melanin, and so the energy penetrates into deep mammalian tissues. In this context, the Phys and CBCRs attract considerable attention in recent years. In this chapter, we summarize the molecular mechanisms of the Phys and CBCRs and introduce the current status of development of the optogenetic tools based on these molecules.

## 10.2 Linear Tetrapyrrole

Phytochromes (Phys) and cyanobacteriochromes (CBCRs) are photoreceptors that can autocatalytically form a covalent bond with a chromophore (Rockwell and Lagarias 2017a, 2019; Fushimi and Narikawa 2019). The binding chromophore has a variety of chemical structures of "linear" tetrapyrrole skeleton, which is supplied by oxidative cleavage of heme having a chemical structure of "cyclic" tetrapyrrole skeleton (Fig. 10.2). The linear tetrapyrrole chromophores are composed of four pyrrole rings (referred to as A, B, C, and D rings) connected with three carbon bridges (Fig. 10.2). In addition to the presence of various chromophore species having different lengths of the π-conjugated system, chromophore flexibility and modification by the surrounding protein enable wide repertoire of the Phys and CBCRs with various photochemical properties (Rockwell and Lagarias 2017a, 2019; Fushimi and Narikawa 2019).

The linear tetrapyrrole chromophores are also called bilin pigments because these pigments are originally found from mammalian bile. Biliverdin IXα (BV), a precursor of the various bilin pigments, exists in various organisms including mammals. BV has a longest π-conjugated system among natural bilin pigments. Phytochromobilin (PΦB) and phycocyanobilin (PCB) are enzymatically biosynthesized from BV in cyanobacteria, algae, and plants (Kohchi et al. 2001; Frankenberg et al. 2001; Dammeyer and Frankenberg-Dinkel 2008; Rockwell and Lagarias 2017b; Miyake et al. 2020). On the other hand, phycoviolobilin (PVB) is biosynthesized from PCB by autoisomerization activity of certain CBCRs (Ishizuka et al. 2007; Fushimi and Narikawa 2019). Notably, in vitro experiments have shown that biliverdin reductase can catabolize BV, PΦB, and PCB into bilirubin (BR), phytochromorubin (PΦR), and

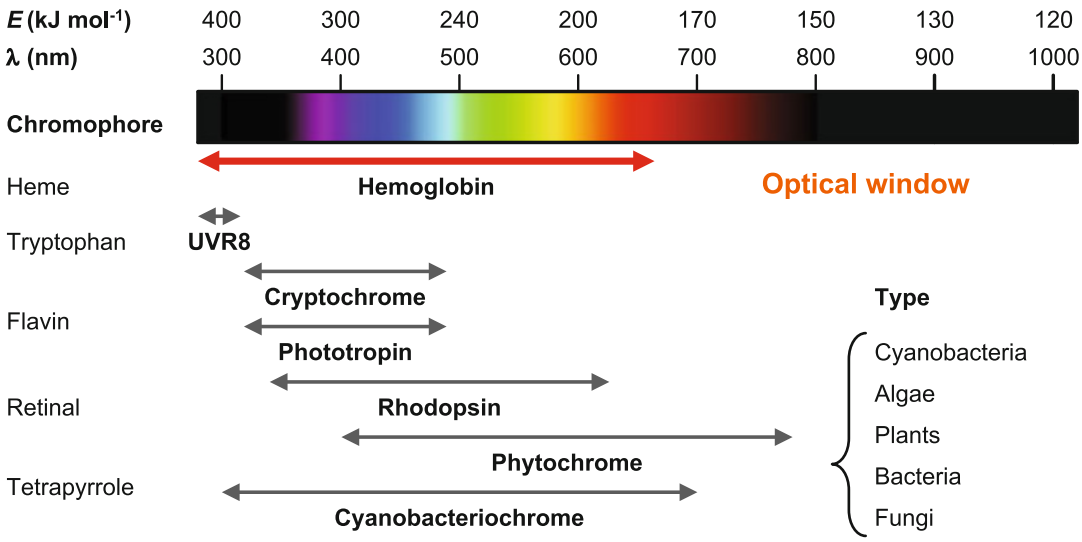


**Fig. 10.1** Absorption region of the various photoreceptors

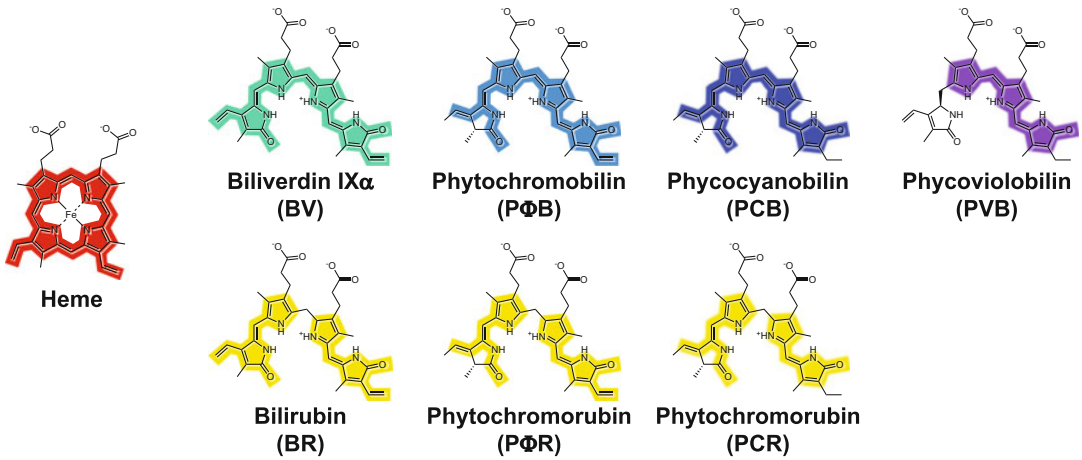


**Fig. 10.2** Chemical structures of tetrapyrroles. Heme, biliverdin IXα (BV), phytochromobilin (PΦB), phycocyanobilin (PCB), phycoviolobilin (PVB), bilirubin (BR), phytochromorubin (PΦR), and phycocyanorubin (PCR) are shown. Their π-conjugated systems are highlighted by each chromophore color

phycocyanorubin (PCR), respectively, as chromophores inactive for photoreceptors (Terry et al. 1993). Native chromophore species bound to the Phys and CBCRs in vivo are inferred from repertoire of the biosynthetic enzymes encoded by the organisms, but they have the potential to incorporate non-native chromophores (Kami et al. 2004; Mukougawa et al. 2006; Rockwell et al. 2012b; Fushimi et al. 2016b; Miyake et al. 2020). Such abilities are confirmed by experiments of in vivo complementation, in vitro reconstitution, or heterologous

co-expression in *E. coli*, which provide significant information on molecular basis of chromophore–protein interaction.

## 10.3 Photoconversion of the Phys and CBCRs

The Phys and CBCRs possess a Cys residue that stably form a covalent bond to the bilin pigments (Rockwell and Lagarias 2017a, 2019; Fushimi and Narikawa 2019). The Phys require Per/Arnt/Sim (PAS), cGMP-phosphodiesterase/adenylate cyclase/FhlA (GAF), and phytochrome-specific (PHY) domains as a photosensory core module (PCM) to incorporate the pigment into a chromophore binding pocket and serve as a photoreceptor. The cyanobacterial, algal, and plant Phys have the Cys residue within the GAF domain (canonical Cys) ligating to $C3^1$ position of PCB or PΦB, whereas the bacterial and fungal Phys have the Cys residue at N-terminal region of the PAS domain (N-terminal Cys) ligating to $C3^2$ position of BV (Figs. 10.3 and 10.4, left) (Lamparter et al. 2002; Wagner et al. 2005, 2007; Essen et al. 2008; Burgie et al. 2014). PCB and PΦB have double bond between C3 and $C3^1$, whereas BV has double bond between $C3^1$ and $C3^2$ (Fig. 10.2). This difference highly correlates with the position of the covalent-bonding Cys residue: inside of the GAF domain or N-terminus outside the PAS domain. Although the cyanobacterial and plant Phys can incorporate both PCB and PΦB in vitro, PCB and PΦB are native chromophores for the cyanobacterial and plant Phys, respectively. Furthermore, characteristic interdomain structural units, called "knot" and "tongue," are observed.

On the other hand, the PCM of the CBCRs consists of only the GAF domain (Fushimi and Narikawa 2019). Most CBCRs also retain the canonical Cys residue ligating to $C3^1$ position of the chromophore (Fig. 10.4, right). The CBCR GAF domains are highly diversified in their primary sequences and categorized into many lineages. Among them, expanded red green (XRG) and Asp-Xaa-Cys-Phe (DXCF) GAF domains have been extensively analyzed so far (Fushimi and Narikawa 2019). Most XRG GAF domains incorporate PCB (Narikawa et al. 2008a, 2014; Rockwell et al. 2011, 2012b; Chen et al. 2012), and exceptional molecules have been reported to incorporate not only PCB but also BV (Narikawa et al. 2015; Fushimi et al. 2016a, 2019). The DXCF GAF domains incorporate PCB, and some of them isomerize it into PVB by the isomerization activity of the GAF domain itself (Ishizuka et al. 2006, 2007; Rockwell et al. 2008, 2012a; Ma et al. 2012; Cho et al. 2015; Hasegawa et al. 2018). The DXCF GAF domains have not only the canonical Cys but also a second Cys in the DXCF motif. The second Cys can reversibly attach to C10 of the chromophore, contributing to large spectral shift (Fig. 10.3). Notably, recent study has revealed that exceptional GAF domains possessing only the second Cys within the Asp-Xaa-Cys-Ile-Pro (DXCIP) motif but not the canonical Cys function as a green light sensor (Fushimi et al. 2016b). In this case, the DXCIP GAF domain initially incorporates PCB and converts it into unknown chromophore (PXB).

The Phys and CBCRs consist of the N-terminal PCM and output module at the C-terminal region to transduce the signal to the downstream components (Fig. 10.4, details of their functions are described in the Sect. 10.6). The signal transduction activities are regulated by light-dependent structural changes called photoconversion. The bilin pigments incorporated in the Phy and CBCR GAF domains absorb various wavelength light corresponding to effective lengths of their π-conjugated systems. The photoconversion is triggered by the light absorption followed by *Z*/*E* isomerization of a double bond between C15 and C16 positions in the chromophore (Figs. 10.2 and 10.3) (Thümmler et al. 1983; Rüdiger et al. 1983; Wagner et al. 2005; Yang et al. 2008; Takala et al. 2014). Common to the Phys and CBCRs, rotation of the whole chromophore configuration occurs after the flip of the double bond. This

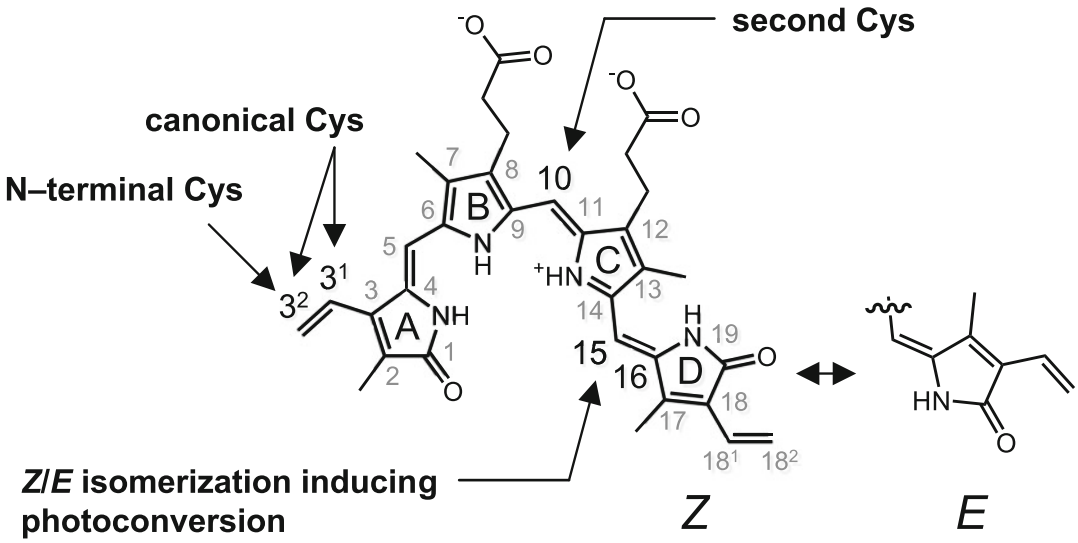


**Fig. 10.3** Numbering of carbons in the linear tetrapyrrole skeleton. Canonical Cys covalently bind to $C3^1$ or $C3^2$ position of the side chain of the A ring. Second Cys reversibly attach to the C10 position on the carbon bridge between the B and C rings. *Z*/*E* isomerization of the double bond between the C15 and C16 positions occurs upon light absorption, which induces photoconversion (details are described in the Sect. 10.3)

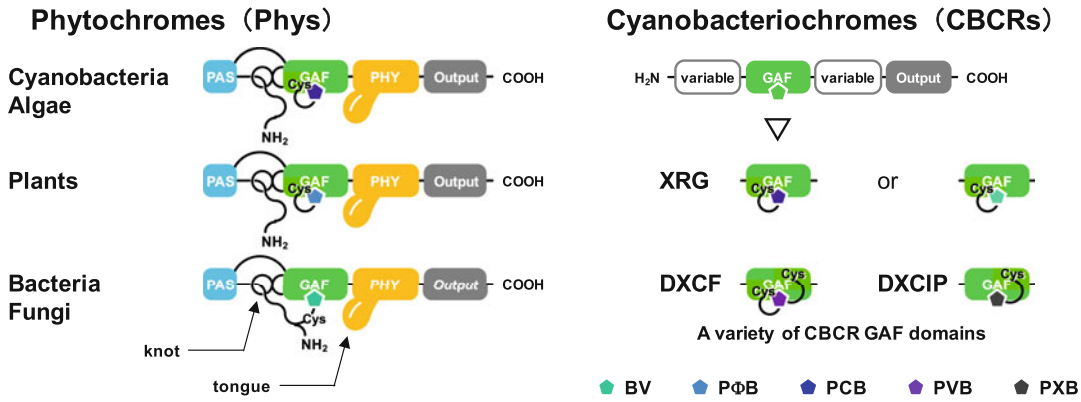


**Fig. 10.4** Simplified domain architectures of the Phys and CBCRs. Per/Arnt/Sim (PAS, cyan), cGMP-phosphodiesterase/adenylate cyclase/FhlA (GAF, green), and phytochrome-specific (PHY, yellow) domains and output modules (gray) in the Phys and CBCRs are shown with binding chromophores: BV (light green), PΦB (light blue), PCB (blue), PVB (purple), and PXB (dark gray). Characteristic structural units (knot and tongue) and conserved Cys (canonical Cys, N-terminal Cys, and second Cys) are depicted in each architecture

successive conformational change is called "flip and rotate" (Fushimi and Narikawa 2019). Recently, detailed molecular mechanisms of various Phys and CBCRs have been extensively revealed by analytical methods such as X-ray crystallography and various spectroscopy in combination with site-directed mutagenesis (Fig. 10.5) (Rockwell and Lagarias 2017a, 2019;

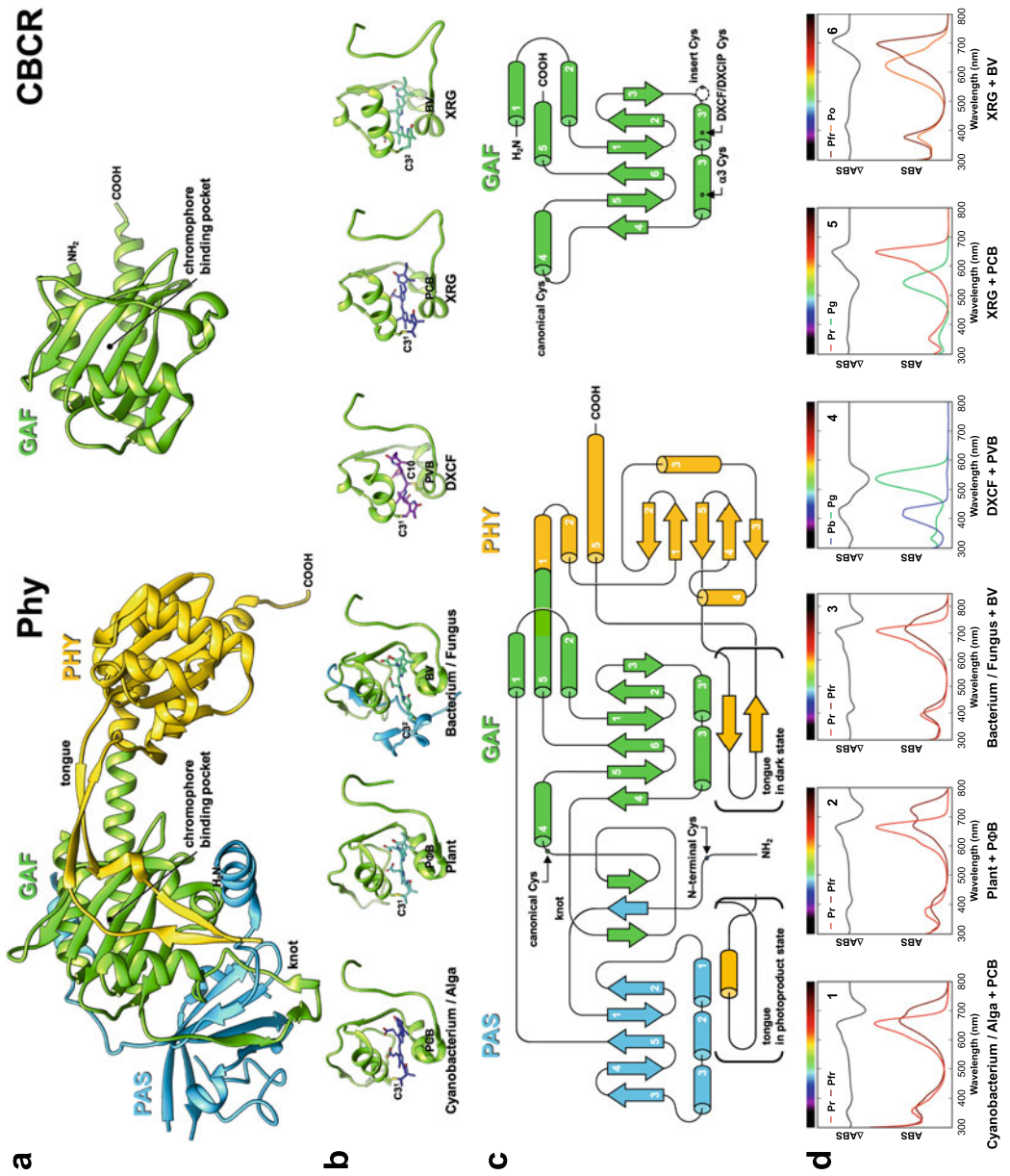
a
Phy
GAF
PHY
tongue
chromophore binding pocket
PAS
knot
COOH
CBCR
GAF
COOH
chromophore binding pocket
b
Cyanobacterium / Alga
PΦB
Plant
Bacterium / Fungus
BV
XRG
DXCF
PVB
c
PAS
GAF
PHY
canonical Cys
knot
N-terminal Cys
tongue in photoproduct state
tongue in dark state
COOH
insert Cys
α3 Cys
DXCF/DXCIP Cys
d
Pr – Pfr
Pr – Pg
Pfr – Po
ΔABS
ABS
Wavelength (nm)
Cyanobacterium / Alga + PCB
Plant + PΦB
Bacterium / Fungus + BV
DXCF + PVB
XRG + PCB
XRG + BV

**Fig. 10.5** Structures and photoconversions of the Phys and CBCRs. Tertiary structures of (**a**) the PCMs (PDB ID: 2VEA (Phy, SyCph1) and 3W2Z (CBCR, AnPixJg2)) and (**b**) chromophore binding regions in the Phys and CBCRs (PDB ID: 2VEA (SyCph1), 4OUR (AtPhyB), 4O0P (DrBphP), 4GLQ (TePixJg), 3W2Z (AnPixJg2), and 5ZOH (AnPixJg2_BV4)). (**c**) Topological structures of the PCMs in the Phys and CBCRs. Each domain and chromophore are shown in the same color as Fig. 10.4. (**d**) Absorption spectra and their difference spectra of the representative Phys and CBCRs showing various photoconversions between two absorbing forms; red/far-red- (d1-3, Pfr/Pr), blue/green- (d4, Pb/Pg), red/green- (d5, Pr/Pg), far-red/orange-absorbing (d6, Pfr/Po) forms. d1, d2, and d3 correspond to cyanobacterial, plant, and bacterial Phys, respectively

Fushimi and Narikawa 2019). The molecular details of the Phys and CBCRs were described in each section.

## 10.4 Biochemical and Photochemical Properties of the Phys

The Phys are conserved in various organisms covering not only the photosynthetic organisms, cyanobacteria, algae, and plants but also the non-photosynthetic organisms, bacteria and fungi (Rockwell and Lagarias 2017a, 2019). As described in the previous section, the PCMs of the Phys are composed of PAS, GAF, and PHY domains, most of which reversibly sense red and far-red light by showing photoconversion (Fig. 10.4, left and Fig. 10.5). The PCMs are roughly categorized into two types. One possesses the canonical Cys within the GAF domain and binds to PCB or PΦB, whereas the other possesses N-terminal Cys and binds to BV. Irrespective of this significant difference, they share common structural features possessing interdomain structural units, knot and tongue. The knot is formed by a strap structure of N-terminal region of the PAS domain passing through a loop of the GAF domain. This structural unit composed of an antiparallel β-sheet is apparently important for stable ligation of the N-terminal Cys with BV (Wagner et al. 2005). Because this structural unit is highly conserved among most Phys, this structural unit is likely to be also important for the canonical Cys-based Phys (Essen et al. 2008; Burgie et al. 2014). Nevertheless, knotless Phys lacking the PAS domain have been exceptionally identified from cyanobacteria (Anders et al. 2011, 2013; Gan et al. 2014b).

On the other hand, the tongue which is an extending region from the PHY domain to neighborhood of the chromophore binding pocket in the GAF domain is involved in conformational changes evoked by light absorption (Yang et al. 2008; Takala et al. 2014; Nagano 2016). A bacterial Phy, DrBphP from the bacterium *Deinococcus radiodurans*, exhibits reversible photoconversion between a red-absorbing form (Pr form) with 15*Z*–BV and a far-red-absorbing form (Pfr form) with 15*E*–BV. Its tertiary structures have been revealed in both forms by X-ray crystallography (Fig. 10.6) (Wagner et al. 2005; Takala et al. 2014). Both forms are present as a homodimer in the "back-to-back" manner, in which two subunits bind to each other via α-helix backbones connecting the GAF and PHY domains. A tongue structure in the Pr form has an antiparallel β-sheet composed of two β-strands connected with a β-hairpin, in which Arg466 on the hairpin forms hydrogen bonds with Asp207 and Tyr263 at entrance of the chromophore binding pocket (Fig. 10.6, left). Conversely, a tongue structure in the Pfr form is composed of one α-helix with a loop instead of the β-sheets, in which not Arg466 but Ser468 on the helical structure forms hydrogen bonds with the two residues on the pocket (Fig. 10.6, right). These interactions are involved in position adjustment of the tongue structures (a distance between the tongue and the GAF domain in the Pr form is 2.5 Å wider than that in the Pfr form). Resultantly, distance between the PHY domains of each subunit is dynamically modulated upon photoconversion. In conclusion, *Z*/*E* isomerization within the GAF domain results in dynamic conformational change between closed and open configurations of the PHY domains to transfer light signal to the output modules and to regulate various biological activities.

Typical Phys exhibit photoconversion between the 15*Z*–Pr dark state (or ground state) and the 15*E*–Pfr photoproduct state (or excited state) and show Pfr-to-Pr dark reversion regardless of the binding chromophore species. On the other hand, some bacterial Phys, called bathy phytochromes (Agp2, PaBphP1, and RpBphP1 identified from *Agrobacterium tume*faciens, *Pseudomonas aeruginosa*, and *Rhodopseudomonas palustris* genes, respectively), have 15*E*–Pfr forms as the dark state and 15*Z*–Pr forms as the photoproduct state and show Pr-to-Pfr dark reversion, which is opposite to typical Phys (Giraud et al. 2002; Lamparter et al. 2002; Karniol and Vierstra 2003; Lamparter and Michael 2005; Kojadinovic et al. 2008; Zienicke et al. 2013; Wang et al. 2019).

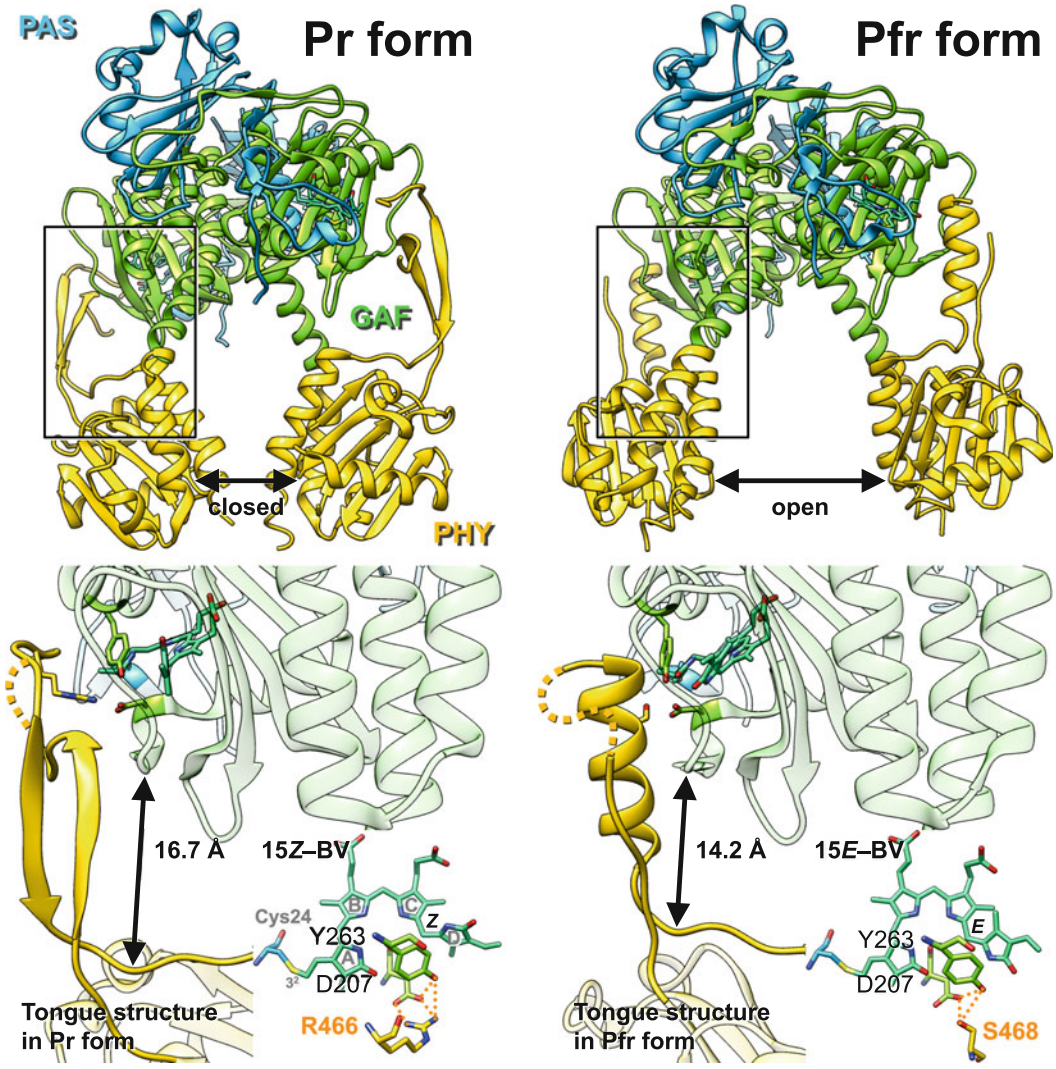


**Fig. 10.6** Molecular structures of the DrBphP PCMs in the Pr (dark state) and Pfr (photoproduct state) forms. Whole views (upper) and enlarged views focusing on the tongue structure (lower, enlarged views corresponding to the frames in the whole views) of the Pr (PDB ID: 4O0P) and the Pfr (PDB ID: 4O01) forms. Disordered areas on the tongue structures are shown by dashed line. Hydrogen bonds of the tongue residues with the chromophore are shown by orange dotted line. Each domain and chromophore are shown in the same color as Fig. 10.4

Furthermore, recent studies have revealed that algal Phys (CparGPS1, DtenPHY1, EsilPHL1, GwitGPS1, NpyrPHY1, PcolPHY1, TastPHY1, and DPH from *Cyanophora paradoxa*, *Dolichomastix tenuilepis*, *Ectocarpus siliculosus*, *Gloeochaete wittrockiana*, *Nephroselmis pyriformis*, *Prasinoderma coloniale*, *Tetraselmis astigmatica*, and *Phaeodactylum tricornutum*, respectively) show diverse spectral properties covering blue-to-far-red as the sensing light wavelength (Rockwell et al. 2014a, 2017b; Duanmu et al. 2014, 2017; Fortunato et al. 2016). Mechanisms behind these atypical properties have not yet been elucidated. Detailed analysis of these molecules should help understanding generality and diversity of the color-tuning mechanisms and would contribute to development of novel optogenetic tools.

## 10.5 Biochemical and Photochemical Properties of the CBCRs

In contrast to the Phys, the CBCRs are found only from cyanobacteria to date. The PCM of the CBCRs is composed of only the GAF domain needed for chromophore incorporation and proper photoconversion (Fushimi and Narikawa 2019). The GAF domains of the CBCRs are highly diversified and categorized into many lineages (Fig. 10.7a). Comprehensive spectroscopic studies have revealed extensive diversity of the spectral properties (Fig. 10.7b–j) (Yoshihara et al. 2004; Ishizuka et al. 2006; Rockwell et al. 2008, 2011, 2012a, 2015a, b, 2016, 2017a; Hirose et al. 2008; Narikawa et al. 2008a, b, 2011, 2014, 2015; Song et al. 2011; Enomoto et al. 2012; Ma et al. 2012; Cho et al. 2015; Fushimi et al. 2016b; Hasegawa et al. 2018). The representative photoconversions, violet/yellow, red/blue, red/green, far-red/orange, green/teal, blue/teal, blue/green, and blue/yellow reversible photoconversions, are shown in Fig. 10.7b–j. Furthermore, the structures of both absorbing forms for the red/green and blue/green reversible CBCRs have been revealed so far (Burgie et al. 2013; Narikawa et al. 2013; Cornilescu et al. 2014; Lim et al. 2018; Wiebeler et al. 2018). As mentioned above, "flip and rotate" process is commonly observed for these molecules (Fig. 10.8a, b) (Fushimi and Narikawa 2019).

It has been revealed that the combination of four color-tuning mechanisms results in such diversity (Fushimi and Narikawa 2019). First, the binding chromophore species roughly determine the sensing light wavelength region (Fig. 10.2). To date, PVB (Fig. 10.7f–h), PCB (Fig. 10.7b–d, i), and BV (Fig. 10.7e) have been identified for the chromophore of the CBCRs (Ishizuka et al. 2007; Narikawa et al. 2008a, 2015). In this order, the chromophore themselves absorbs shorter to longer wavelength, and the CBCRs incorporating these chromophores inherit this property. Second, a Cys residue distinct from the canonical Cys residue (second Cys residue) reversibly ligates to the C10 of the chromophore during the photoconversion (Rockwell et al. 2008, 2011, 2017a; Burgie et al. 2013; Narikawa et al. 2013, 2014) (Fig. 10.8c). Covalent bond formation with the C10 results in shortening of the π-conjugated system and large blue-shift of the absorbing light wavelength. The violet/yellow (Fig. 10.7b), red/blue (Fig. 10.7c), blue/teal (Fig. 10.7g), blue/green (Fig. 10.7h), and blue/yellow (Fig. 10.7i) molecules exhibit this reversible Cys adduct formation. Interestingly, since the second Cys residues (insert Cys, DXCF/DXCIP Cys, and α3 Cys) from these molecules are differently mapped on the structure (Fig. 10.5c, right), these second Cys residues have independently acquired during the evolutionary process. Third, some CBCR molecules show protochromic cycle during the photoconversion process (Fig. 10.8d), namely the CBCRs belonging to the green/red and blue/orange lineages exhibit protonation/deprotonation cycle (Hirose et al. 2013; Osoegawa et al. 2019; Sato et al. 2019). Protonation should stabilize the π-conjugated system, resulting in the red-shifted absorbance. Fourth, trapped-twist model explains blue-shifted absorbance, in which the ring D and/or ring A are highly twisted relative to the rings B–C plane (Narikawa et al. 2008a; Rockwell et al. 2012c, 2014b, 2015a; Lim et al. 2018; Wiebeler et al. 2018) (Fig. 10.8e). The green-absorbing forms of the red/green molecules (Fig. 10.7d) and the teal-absorbing forms of the blue/teal and green/teal molecules (Fig. 10.7f, g) adopt this system to absorb the short wavelength light. In fact, structural analyses of the green-absorbing forms of the red/green molecules have revealed the highly twisted A ring (Lim et al. 2018; Wiebeler et al. 2018). Based on the deep understanding of these natural color-tuning mechanisms, some trials for rational design to tune the spectral property have been succeeded (Fushimi et al. 2017a, b, 2019; Rockwell et al. 2017a; Kuwasaki et al. 2019).

Although the BV has not been considered to function as a chromophore for the CBCRs since the discovery of the CBCRs, we recently discovered the BV-binding CBCRs from the unique cyanobacterium *Acaryochloris marina* (Narikawa

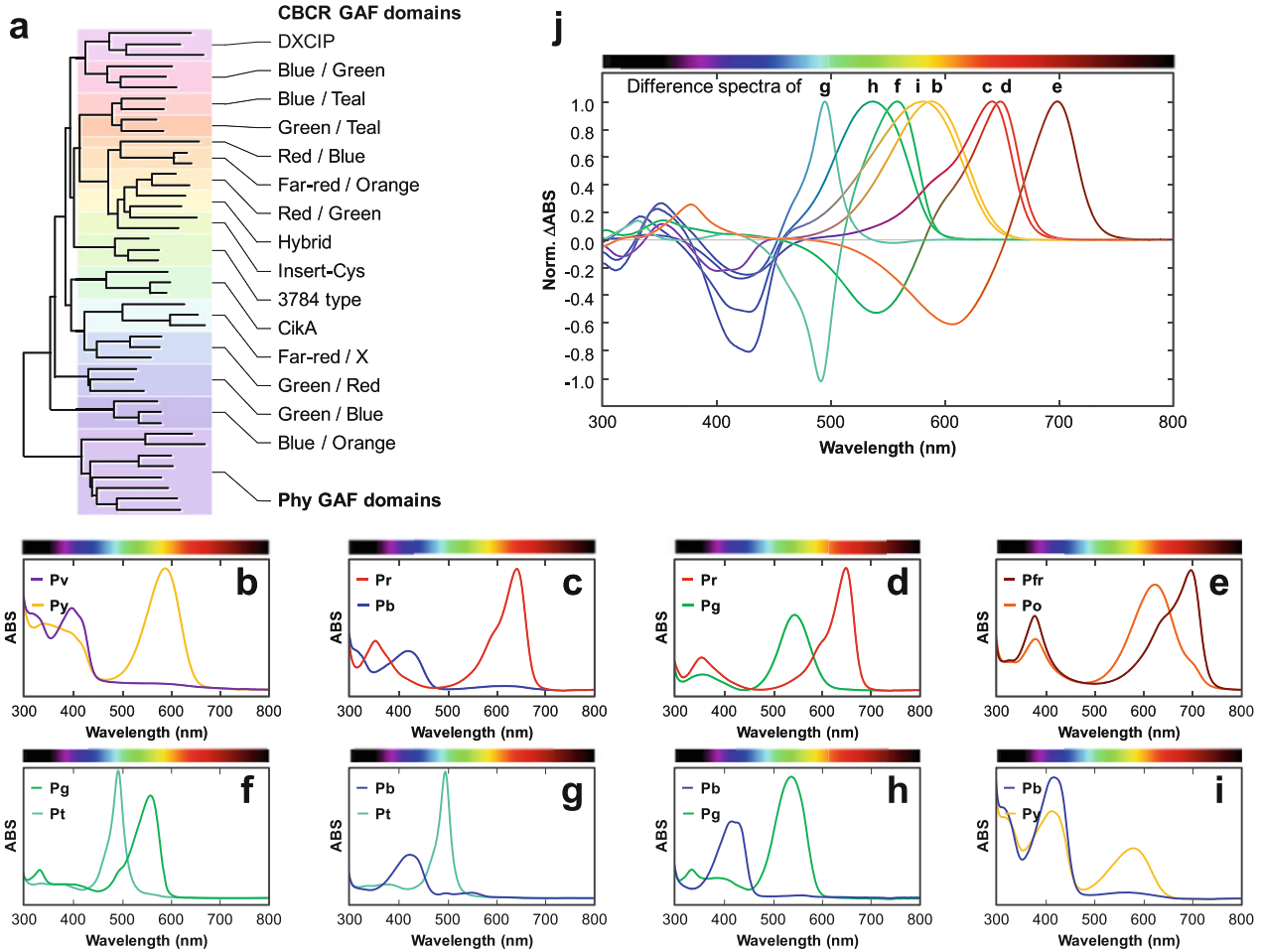


**Fig. 10.7** A variety of photoconversions observed for the CBCR PCMs. (**a**) Molecular phylogenetic tree of the CBCR GAF domains including the representative Phy GAF domains as the outgroup. (**b**–**i**) Absorption spectra of the representative CBCRs showing various photoconversions between two absorbing forms; violet/yellow- (**b**, Pv/Py), red/blue- (**c**, Pr/Pb), red/green- (**d**, Pr/Pg), far-red/orange- (**e**, Pfr/Po), green/teal- (**f**, Pg/Pt), blue/teal- (**g**, Pb/Pt), blue/green- (**h**, Pb/Pg), and blue/yellow-absorbing (**i**, Pb/Py) forms. (**j**) Difference spectra of the photoconversion of the representative CBCRs shown in (**b**–**i**)

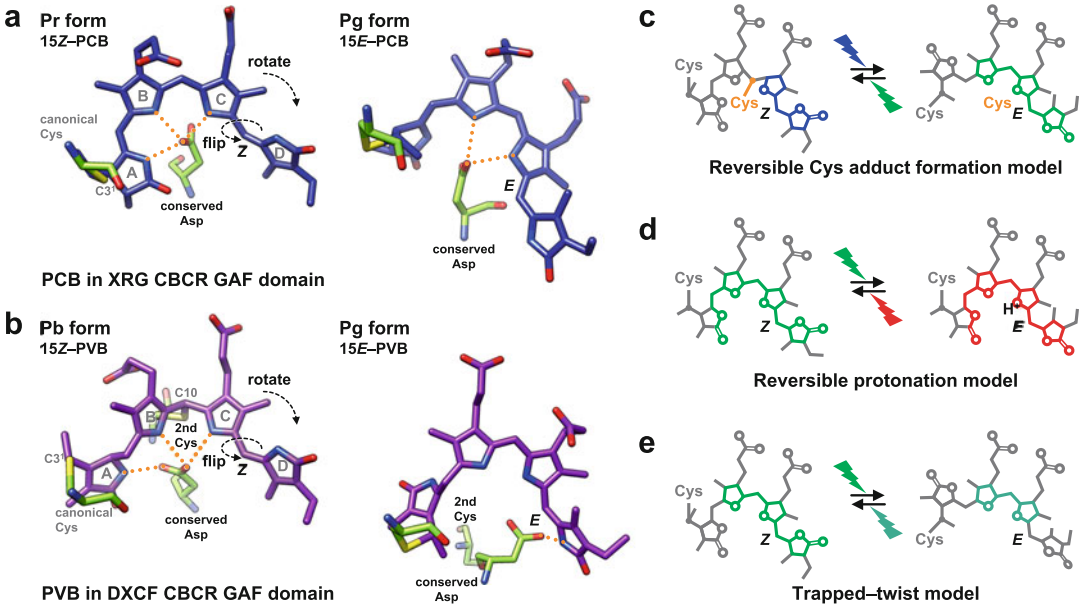


**Fig. 10.8** Photoconversion mechanisms of the CBCRs. (**a**) 15*Z* and 15*E*–PCB structures of the XRG CBCR GAF domains in the Pr and Pg forms, respectively (PDB ID: 6BHN (Pr form, NpR6012g4) and 6BHO (Pg form, NpR6012g4)). (**b**) 15*Z* and 15*E*–PVB structures of the DXCF CBCR GAF domains in the Pb and Pg forms, respectively (PDB ID: 4GLQ (Pb form, TePixJg) and 3VV4 (Pg form, TePixJg)). (**c**–**e**) Color-tuning mechanism models of (**c**) reversible Cys adduct formation, (**d**) reversible protonation, and (**e**) trapped-twist

et al. 2015; Fushimi et al. 2016a, 2019). We have further revealed the molecular mechanisms to incorporate the BV in detail and succeeded in conversion of the BV-rejective molecules into the BV-acceptable ones (Fushimi et al. 2019). As described below, the BV-binding CBCRs are promising platform to develop the in vivo optogenetic tools. Recent advancement of the genome sequencing technology has provided huge repertoire of novel natural CBCR molecules. In the future, it is expected that much more natural and artificial color variants should be provided, which would be useful for the development of the optogenetic tools.

## 10.6 Physiological Functions of the Phys and CBCRs

Physiologically, Phys and CBCRs are known to function as a kind of light-activated trigger which alters biological behavior. For example, plant Phys, such as AtPhyA and AtPhyB from *Arabidopsis thaliana*, induce biosynthesis of plant hormones, seed germination, stem growth, shade avoidance, and circadian clock, which are dependent on red:far-red light ratio (Leivar and Monte 2014). The Phys interact with phytochrome-interacting factors (PIFs), which serve as a transcription factor to regulate gene expression. A fungal Phy, FphA from *Aspergillus nidulans*, regulates alternation of generations between sexual and asexual phases; nurse cells (i.e., sexual phase) have been observed under red light condition, whereas conidia (i.e., asexual phase) have been observed under dark or far-red light condition (Blumenstein et al. 2005). Although physiological functions of bacterial Phys, such as AtBphP2 and PaBphP from *Agrobacterium tumefaciens* and *Pseudomonas aeruginosa*, respectively, have remained to be elucidated, they have His kinase domains in the C-terminal region of the whole molecules, and light-dependent phosphorylation reactions of the

PCM–His kinase domain units have been verified by comparing between the activities of the Pr and the Pfr forms (Bhoo et al. 2001; Karniol and Vierstra 2003). Although physiological roles of the cyanobacterial phytochromes have long been unknown, their roles have recently been elucidated in the cyanobacteria harboring chlorophyll *f* (Chl. *f*), which absorbs longer wavelength far-red light than chlorophyll *a* (Chl. *a*) (Gan et al. 2014a, b; Zhao et al. 2015). The Chl. *f*-harboring cyanobacteria accumulate only Chl. *a* under white light conditions, but accumulate Chl. *f* in addition to Chl. *a* under far-red light conditions, enabling efficient photosynthesis even under far-red light conditions (Gan et al. 2014a, b). It has been revealed that this acclimation process is regulated at the transcriptional level by the phytochrome called RfpA and the downstream factors RfpB and RfpC (Zhao et al. 2015).

In the case of CBCRs, it has been reported that SyCcaS and FdRcaE (green/red reversible CBCRs) from *Synechocystis* sp. PCC 6803 and *Fremyella diplosiphon*, respectively, regulate chromatic acclimation (Kehoe and Grossman 1996, 1997; Hirose et al. 2008, 2010, 2013). Chromatic acclimation is a photobiological response in cyanobacteria for optimization of light-harvesting antennae, phycobilisome, in response to the availability of light qualities (Gaidukov 1902; Hattori and Fujita 1959). On the other hand, SyUirS (also called SyPixA, violet/green reversible CBCR) and SyPixJ1 (blue/green reversible CBCR) have been revealed to regulate phototaxis in *S*. 6803 (Yoshihara et al. 2004; Song et al. 2011; Narikawa et al. 2011). PixJ homologs have been detected from the other cyanobacteria, some of which are also involved in the phototaxis regulation (Narikawa et al. 2008a; Campbell et al. 2015; Fushimi et al. 2016b; Yang et al. 2018). Notably, the photosensory GAF domains of some PixJ homologs belong not to blue/green type but to red/green type (Narikawa et al. 2008a; Campbell et al. 2015) or green power sensor type (Fushimi et al. 2016b). These CBCRs except for PixJ proteins have His kinase domains at the C-terminus. Photoconversion of the N-terminal GAF domains modulate His kinase activity and following phosphotransfer to the cognate response regulators, which finally result in light-dependent phenotypic responses; SyCcaS/SyCcaR, FdRcaE/FdRcaC/FdRcaF, and SyUirS/SyUirR systems. PixJ homologs have methyl-accepting domain at the C-terminus, homologous to that of well-known chemotaxis regulatory systems in many bacteria. Thus, signaling cascade of the phototaxis regulation would be analogous to that of the chemotaxis regulation.

Some CBCRs have other output domains that are involved in synthesis and breakdown of the second messengers such as cyclic-AMP and cyclic-di-GMP. Activity of these domains are also modulated by photoconversion of the N-terminal GAF domains. cPAC (or Mic7113_2205, blue/green reversible CBCR) from *Microcoleus* sp. PCC 7113 has adenylate cyclase domain to produce cyclic-AMP, and its activity is induced under blue light but repressed under green light (Blain-Hartung et al. 2018). TeSesA and TeSesC (blue/green reversible CBCRs) and TeSesB (blue/teal reversible CBCR) from *Thermosynechococcus vulcanus* regulate cyclic-di-GMP concentration via synthesis and breakdown of cyclic-di-GMP in response to blue-to-green light (Enomoto et al. 2014, 2015; Enomoto and Ikeuchi 2020). The synthetic activity of TeSesA is induced, and the breakdown activity of TeSesB is inhibited under blue light, whereas those activities are conversely regulated under green and teal light, respectively. TeSesC has both synthetic and breakdown domains to induce cyclic-di-GMP synthetic activity under blue light but induce its breakdown activity under green light. The cyclic-di-GMP further activates cellulose synthase, which results in cell aggregation. Such cooperative regulation of these three components enables light color-sensitive input system to regulate cell aggregation. In *S*. 6803, SyCph2 is a hybrid photoreceptor that comprises an N-terminal module for phytochrome and a C-terminal blue/green reversible CBCR, and the C-terminal part functions as blue-light-inducible cyclic-di-GMP synthase, which also contribute to cell aggregation (Savakis et al. 2012; Conradi et al. 2019).

## 10.7 Optogenetic Tools Based on the Phys and CBCRs

First identification and characterization of a Phy have been reported in 1959 (Butler et al. 1959), whereas those of a CBCR have been done in 2004 by Ikeuchi group (Yoshihara et al. 2004). Therefore, photobiological and photochemical reports of the Phys are much more than those of the CBCRs, and in the present situation, Phy-based optogenetic tools have been reported much more than CBCR-based ones.

The first Phy-based optogenetic tool has been reported in 2002 (Table 10.1) (Shimizu-Sato et al. 2002). The authors constructed a tool combined with the two-hybrid system (Fields and Song 1989) and PhyB/PIF system (Ni et al. 1998, 1999). This tool is composed of two chimeric proteins that are GAL4 DNA binding domain fused with AtPhyB from *Arabidopsis thaliana* and GAL4 activation domain fused with PIF3. Red light illumination results in association of PIF3 with AtPhyB and activation of GAL4 for transcriptional regulation. Conversely, far-red light illumination results in dissociation of PIF3 from AtPhyB and inactivation of GAL4. Since then, various optogenetic tools based on the PhyB/PIF system have been developed (Fig. 10.9a and Table 10.1) (Tyszkiewicz and Muir 2008; Levskaya et al. 2009; Toettcher et al. 2013; Ueda and Sato 2018; Bugaj et al. 2018; Yousefi et al. 2019). SyCph1 from *Synechocystis* sp. PCC 6803 has been used to regulate two-component systems by red light illumination (Fig. 10.9b and Table 10.1) (Levskaya et al. 2005; Reichhart et al. 2016). Because these systems applied the plant and cyanobacterial Phys, addition of PCB or introduction of biosynthetic pathway should be needed for the regulation in the organisms possessing no native biosynthetic pathway of PCB. Recently, mammalian cells harboring the PCB synthetic system and lacking the biliverdin reductase have been developed for better regulation (Uda et al. 2017). On the other hand, BV is an intrinsic chromophore in various organisms including mammals and has the long π-conjugated system enabling absorption of far-red-to-near-infrared light corresponding to the optical window region (Fig. 10.1). In this context, bacterial Phys incorporating the mammalian intrinsic chromophore and sensing far-red/near-infrared light should be advantageous for in vivo optogenetics. Until now, systems based on BphG1 (Ryu et al. 2014; Ryu and Gomelsky 2014; Shao et al. 2018), DrBphP (Fig. 10.9c and Table 10.1) (Gasser et al. 2014; Leopold et al. 2019) and BphP1/PpsR2 (Fig. 10.9d and Table 10.1) (Kaberniuk et al. 2016; Redchuk et al. 2017) have been developed for transcriptional regulation, kinase regulation, and synthesis and breakdown of the second messenger.

The first optogenetic tool based on the CBCR has been reported in 2011 (Table 10.1) (Tabor et al. 2011). The authors utilized the CcaS/CcaR system, which is a two-component system (SyCcaS and SyCcaR from *Synechocystis* sp. PCC 6803). SyCcaS possesses the CBCR GAF domain showing green/red reversible photoconversion and the His kinase domain to work as a green light sensor. SyCcaR is its cognate response regulator to work as a transcriptional regulator. In *S.* 6803 cells, green light activates transcription of the phycobilisome component gene, *cpcG2*, dependent on SyCcaS and SyCcaR (Fig. 10.9e and Table 10.1) (Hirose et al. 2008; Fernandez-Rodriguez et al. 2017; Castillo-Hair et al. 2019; Senoo et al. 2019). Furthermore, SyUirS/SyUirR two-component system has been also developed, in which violet light illumination activates transcription of the gene of interest (Fig. 10.9f and Table 10.1) (Song et al. 2011; Narikawa et al. 2011; Ramakrishnan and Tabor 2016). Although CBCR-based optogenetic tools are less than Phy-based ones for the present, multiplex optogenetic regulation has been established by combination of CBCRs, Phys, and the other photoreceptors (Tabor et al. 2011; Olson et al. 2017; Fernandez-Rodriguez et al. 2017). Because CBCRs are highly diversified in their sensing light qualities (Fig. 10.7), they can serve as "color palette" for development of the multiplex optogenetic regulation. Furthermore, the PCM of the CBCRs is much smaller than that of the Phys. In this context, the CBCRs are advantageous in comparison with the Phys as

**Table 10.1** Examples of optogenetic tools

| PCMs | Category | Chromophore | Photoconversion (dark state/ photoproduct state) | Input (regulation system) | Output (target gene, protein and signal) | Reference |
|---|---|---|---|---|---|---|
| **Phys** | | | | | | |
| AtphyB | Plant | PFB | Red/far-red | Fig. 10.9a | Yeast two-hybrid system | Shimizu-Sato, S. et al., *Nat Biotechnol.*, **20** (10), 1041–1044, 2002 |
| | | | | | Protein splicing | Tyszkiewicz, A. B. and Muir, T. W., *Nat. Methods*, **5**(4), 303–305, 2008 |
| | | | | | GTPase signaling | Levskaya A et al., *Nature*, **461**(7266), 997–1001, 2009 |
| | | | | | MAPK/ERK pathway | Toettcher, J. E. et al., *Cell*, **155** (6), 1422–1434, 2013 |
| | | | | | MAPK/ERK pathway | Bugaj, L. J. et al., *Science*, **361**(6405), 3048, 2018 |
| | | | | | T-cell receptor | Yousefi, O. S. et al., *eLife*, **8**, 42475, 2019 |
| SyCph1 | Cyanobacteria | PCB | Red/far-red | Fig. 10.9b | *lacZ* gene expression in *Escherichia coli* | Levskaya, A. et al., *Nature*, **438** (7067), 441–442, 2005 |
| | | | | | MAPK/ERK pathway | Reichhart, E. et al., *Angew Chem Int Ed Engl.*, **55**(21), 6339–6342, 2016 |
| DrBphP | Bacteria | BV | Red/far-red | Fig. 10.9c | cAMP/cGMP phosphodiesterase | Gasser, C. et al., *Proc. Natl. Acad. Sci. USA*. **111**(24), 8803–8808, 2014 |
| | | | | | MAPK/ERK pathway | Leopold, A. V. et al., *Nat. Commun.*, **10** (1), 1129, 2019 |

(continued)

**Table 10.1** (continued)

| PCMs | Category | Chromophore | Photoconversion (dark state/ photoproduct state) | Input (regulation system) | Output (target gene, protein and signal) | Reference |
|---|---|---|---|---|---|---|
| RpBphP1 | Bacteria | BV | Far-red/red | Fig. 10.9d | *SEAP* gene transcription in HeLa cells | Kaberniuk, A. A. et al., *Nat. Methods*, **13**(7):591–597, 2016 |
| | | | | | *EGFP* gene transcription in HeLa cells | Redchuk, T. A. et al., *Nat. Chem. Biol.*, **13** (6), 633–639, 2017 |
| **CBCRs** | | | | | | |
| CcaS | Cyanobacteria | PCB | Green/red | Fig. 10.9e | *lacZ* gene expression in *Escherichia coli* | Tabor, J. J. et al., *J. Mol. Biol.*, **405**(2), 315–324, 2011 |
| | | | | | *lacZ* gene expression in *Escherichia coli* | Fernandez-Rodriguez J., et al., *Nat. Chem. Biol.*, **13** (7), 706–708, 2017 |
| | | | | | *tipA* gene expression in *Escherichia coli* | Senoo, S. et al., *Biotechnol. Bioeng.* **116** (12), 3292–3300, 2019 |
| | | | | | *sfgfp* gene expression in *Bacillus subtilis* | Castillo-Hair S. M. et al., *Nat. Commun.*, **10**(1), 3099, 2019 |
| UirS | Cyanobacteria | PCB | Violet/green | Fig. 10.9f | *sfgfp* gene expression in *Escherichia coli* | Ramakrishnan P. and Tabor, J. J., ACS Synth. Biol., 5 (7), 733–740, 2016 |

optogenetic building unit. In addition, we recently identified the BV-binding CBCRs and revealed detailed molecular mechanism of protein–chromophore interaction (mentioned in the Sect. 10.5) (Narikawa et al. 2015; Fushimi et al. 2016a; Fushimi et al. 2019). We believe that these BV-binding CBCRs are promising molecular basis for development of in vivo optogenetic tools.

Development of the CBCR-based optogenetic tools are still in the midway because it has not been long since the CBCR discovery in comparison with the Phys. The CBCRs, however, show extensive diversity in the spectral property, and the molecular mechanisms have been steadily revealed in detail (Fushimi and Narikawa 2019). In the future, the increasing knowledge would promote to develop precise optogenetic tools

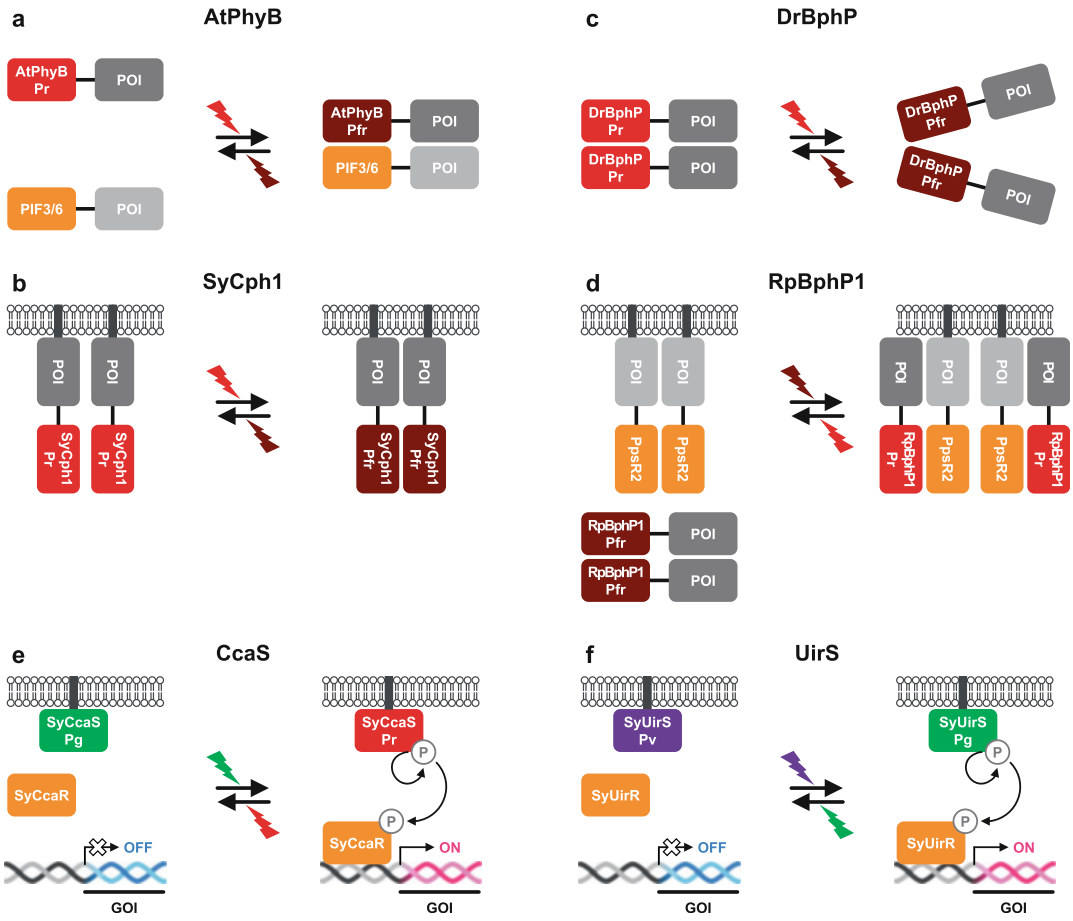


**Fig. 10.9** Optogenetic tool models based on the Phys and CBCRs. The optogenetic systems triggered by light-dependent intra/interprotein conformational change to regulate functions of protein or gene of interest (abbreviated as POI and GOI, respectively). (**a**) AtPhyB (plant Phy) attaches to and detaches from PIF3 or PIF6 in red/far-red light reversible manner. (**b**) SyCph1 (cyanobacterial Phy) shows conformational change between closed and open configurations between the dimer interface in red/far-red light reversible manner. (**c**) The PHY domain of DrBphP (bacterial Phy) shows conformational change between closed and open configurations between the dimer interface in red/far-red light reversible manner. (**d**) RpBphP1 (bathy Phy) attaches to and detaches from PpsR2 in far-red/red light reversible manner. (**e**) Autophosphorylation of SyCcaS (green/red CBCR) and phosphotransfer to SyCcaR followed by transcriptional activation of GOI are regulated in green/red light reversible manner. (**f**) Autophosphorylation of SyUirS (violet/green CBCR) and phosphotransfer to SyUirR followed by transcriptional activation of GOI are regulated in violet/green light reversible manner

based on the CBCRs, enabling broadband and taylormade optogenetics.

**Acknowledgments** This work was supported by grants from JST, CREST (JPMJCR1653 to R.N.).

## References

Anders K, von Stetten D, Mailliet J et al (2011) Spectroscopic and photochemical characterization of the red-light sensitive photosensory module of Cph2 from *Synechocystis* PCC 6803. Photochem Photobiol 87:160–173

Anders K, Daminelli-Widany G, Mroginski MA et al (2013) Structure of the cyanobacterial phytochrome

2 photosensor implies a tryptophan switch for phytochrome signaling. J Biol Chem 288:35714–35725
Bhoo SH, Davis SJ, Walker J et al (2001) Bacteriophytochromes are photochromic histidine kinases using a biliverdin chromophore. Nature 414:776–779
Blain-Hartung M, Rockwell NC, Moreno MV et al (2018) Correction: cyanobacteriochrome-based photoswitchable adenylyl cyclases (cPACs) for broad spectrum light regulation of cAMP levels in cells. J Biol Chem 293:13850
Blumenstein A, Vienken K, Tasler R et al (2005) The *Aspergillus nidulans* phytochrome FphA represses sexual development in red light. Curr Biol 15:1833–1838
Bugaj LJ, Sabnis AJ, Mitchell A et al (2018) Cancer mutations and targeted drugs can disrupt dynamic signal encoding by the Ras-Erk pathway. Science 361: eaao3048. https://doi.org/10.1126/science.aao3048
Burgie ES, Walker JM, Phillips GN Jr, Vierstra RD (2013) A photo-labile thioether linkage to phycoviolobilin provides the foundation for the blue/green photocycles in DXCF-cyanobacteriochromes. Structure 21:88–97
Burgie ES, Bussell AN, Walker JM et al (2014) Crystal structure of the photosensing module from a red/far-red light-absorbing plant phytochrome. Proc Natl Acad Sci U S A 111:10179–10184
Butler WL, Norris KH, Siegelman HW, Hendricks SB (1959) Detection, assay, and preliminary purification of the pigment controlling photoresponsive development of plants. Proc Natl Acad Sci U S A 45:1703–1708
Campbell EL, Hagen KD, Chen R et al (2015) Genetic analysis reveals the identity of the photoreceptor for phototaxis in hormogonium filaments of *Nostoc punctiforme*. J Bacteriol 197:782–791
Castillo-Hair SM, Baerman EA, Fujita M et al (2019) Optogenetic control of *Bacillus subtilis* gene expression. Nat Commun 10:3099
Chen Y, Zhang J, Luo J et al (2012) Photophysical diversity of two novel cyanobacteriochromes with phycocyanobilin chromophores: photochemistry and dark reversion kinetics. FEBS J 279:40–54
Cho SM, Jeoung SC, Song J-Y et al (2015) Genomic survey and biochemical analysis of recombinant candidate cyanobacteriochromes reveals enrichment for near UV/violet sensors in the halotolerant and alkaliphilic cyanobacterium *Microcoleus* IPPAS B353. J Biol Chem 290:28502–28514
Conradi FD, Zhou R-Q, Oeser S et al (2019) Factors controlling floc formation and structure in the cyanobacterium *Synechocystis* sp. strain PCC 6803. J Bacteriol 201. https://doi.org/10.1128/JB.00344-19
Cornilescu CC, Cornilescu G, Burgie ES et al (2014) Dynamic structural changes underpin photoconversion of a blue/green cyanobacteriochrome between its dark and photoactivated states. J Biol Chem 289:3055–3065
Dammeyer T, Frankenberg-Dinkel N (2008) Function and distribution of bilin biosynthesis enzymes in photosynthetic organisms. Photochem Photobiol Sci 7:1121–1130
Duanmu D, Bachy C, Sudek S et al (2014) Marine algae and land plants share conserved phytochrome signaling systems. Proc Natl Acad Sci U S A 111:15827–15832
Duanmu D, Rockwell NC, Lagarias JC (2017) Algal light sensing and photoacclimation in aquatic environments. Plant Cell Environ 40:2558–2570
Enomoto G, Ikeuchi M (2020) Blue-/green-light-responsive cyanobacteriochromes are cell shade sensors in red-light replete niches. iScience 23:100936
Enomoto G, Hirose Y, Narikawa R, Ikeuchi M (2012) Thiol-based photocycle of the blue and teal light-sensing cyanobacteriochrome Tlr1999. Biochemistry 51:3050–3058
Enomoto G, Nomura R, Shimada T et al (2014) Cyanobacteriochrome SesA is a diguanylate cyclase that induces cell aggregation in *Thermosynechococcus*. J Biol Chem 289:24801–24809
Enomoto G, Ni-Ni-Win, Narikawa R, Ikeuchi M (2015) Three cyanobacteriochromes work together to form a light color-sensitive input system for c-di-GMP signaling of cell aggregation. Proc Natl Acad Sci U S A 112:8082–8087
Essen L-O, Mailliet J, Hughes J (2008) The structure of a complete phytochrome sensory module in the Pr ground state. Proc Natl Acad Sci U S A 105:14709–14714
Fernandez-Rodriguez J, Moser F, Song M, Voigt CA (2017) Engineering RGB color vision into *Escherichia coli*. Nat Chem Biol 13:706–708
Fields S, Song O (1989) A novel genetic system to detect protein-protein interactions. Nature 340:245–246
Fortunato AE, Jaubert M, Enomoto G et al (2016) Diatom phytochromes reveal the existence of far-red-light-based sensing in the ocean. Plant Cell 28:616–628
Frankenberg N, Mukougawa K, Kohchi T, Lagarias JC (2001) Functional genomic analysis of the HY2 family of ferredoxin-dependent bilin reductases from oxygenic photosynthetic organisms. Plant Cell 13:965–978
Fushimi K, Narikawa R (2019) Cyanobacteriochromes: photoreceptors covering the entire UV-to-visible spectrum. Curr Opin Struct Biol 57:39–46
Fushimi K, Nakajima T, Aono Y et al (2016a) Photoconversion and fluorescence properties of a red/green-type cyanobacteriochrome AM1_C0023g2 that binds not only phycocyanobilin but also biliverdin. Front Microbiol 7:588
Fushimi K, Rockwell NC, Enomoto G et al (2016b) Cyanobacteriochrome photoreceptors lacking the canonical Cys residue. Biochemistry 55:6981–6995
Fushimi K, Enomoto G, Ikeuchi M, Narikawa R (2017a) Distinctive properties of dark reversion kinetics between two red/green-type cyanobacteriochromes and their application in the photoregulation of cAMP synthesis. Photochem Photobiol 93:681–691

Fushimi K, Ikeuchi M, Narikawa R (2017b) The expanded red/green cyanobacteriochrome lineage: an evolutionary hot spot. Photochem Photobiol 93:903–906

Fushimi K, Miyazaki T, Kuwasaki Y et al (2019) Rational conversion of chromophore selectivity of cyanobacteriochromes to accept mammalian intrinsic biliverdin. Proc Natl Acad Sci U S A 116:8301–8309

Gaidukov N (1902) Über den einfluss farbigen lichtes auf die färbung der Oscillarien. Abh Preuss Akad Wiss V:8–13

Gan F, Shen G, Bryant DA (2014a) Occurrence of far-red light photoacclimation (FaRLiP) in diverse cyanobacteria. Life 5:4–24

Gan F, Zhang S, Rockwell NC et al (2014b) Extensive remodeling of a cyanobacterial photosynthetic apparatus in far-red light. Science 345:1312–1317

Gasser C, Taiber S, Yeh C-M et al (2014) Engineering of a red-light-activated human cAMP/cGMP-specific phosphodiesterase. Proc Natl Acad Sci U S A 111:8803–8808

Giraud E, Fardoux J, Fourrier N et al (2002) Bacteriophytochrome controls photosystem synthesis in anoxygenic bacteria. Nature 417:202–205

Hasegawa M, Fushimi K, Miyake K et al (2018) Molecular characterization of DXCF cyanobacteriochromes from the cyanobacterium *Acaryochloris marina* identifies a blue-light power sensor. J Biol Chem 293:1713–1727

Hattori A, Fujita Y (1959) Formation of phycobilin pigments in a blue-green alga, *Tolypothrix tenuis*, as induced by illumination with colored lights. J Biochem 46:521–524

Hirose Y, Shimada T, Narikawa R et al (2008) Cyanobacteriochrome CcaS is the green light receptor that induces the expression of phycobilisome linker protein. Proc Natl Acad Sci U S A 105:9528–9533

Hirose Y, Narikawa R, Katayama M, Ikeuchi M (2010) Cyanobacteriochrome CcaS regulates phycoerythrin accumulation in *Nostoc punctiforme*, a group II chromatic adapter. Proc Natl Acad Sci U S A 107:8854–8859

Hirose Y, Rockwell NC, Nishiyama K et al (2013) Green/red cyanobacteriochromes regulate complementary chromatic acclimation via a protochromic photocycle. Proc Natl Acad Sci U S A 110:4974–4979

Ishizuka T, Shimada T, Okajima K et al (2006) Characterization of cyanobacteriochrome TePixJ from a thermophilic cyanobacterium *Thermosynechococcus elongatus* strain BP-1. Plant Cell Physiol 47:1251–1261

Ishizuka T, Narikawa R, Kohchi T et al (2007) Cyanobacteriochrome TePixJ of *Thermosynechococcus elongatus* harbors phycoviolobilin as a chromophore. Plant Cell Physiol 48:1385–1390

Kaberniuk AA, Shemetov AA, Verkhusha VV (2016) A bacterial phytochrome-based optogenetic system controllable with near-infrared light. Nat Methods 13:591–597

Kami C, Mukougawa K, Muramoto T et al (2004) Complementation of phytochrome chromophore-deficient *Arabidopsis* by expression of phycocyanobilin:ferredoxin oxidoreductase. Proc Natl Acad Sci U S A 101:1099–1104

Karniol B, Vierstra RD (2003) The pair of bacteriophytochromes from *Agrobacterium tumefaciens* are histidine kinases with opposing photobiological properties. Proc Natl Acad Sci U S A 100:2807–2812

Kehoe DM, Grossman AR (1996) Similarity of a chromatic adaptation sensor to phytochrome and ethylene receptors. Science 273:1409–1412

Kehoe DM, Grossman AR (1997) New classes of mutants in complementary chromatic adaptation provide evidence for a novel four-step phosphorelay system. J Bacteriol 179:3914–3921

Kohchi T, Mukougawa K, Frankenberg N et al (2001) The *Arabidopsis* HY2 gene encodes phytochromobilin synthase, a ferredoxin-dependent biliverdin reductase. Plant Cell 13:425–436

Kojadinovic M, Laugraud A, Vuillet L et al (2008) Dual role for a bacteriophytochrome in the bioenergetic control of *Rhodopseudomonas palustris*: enhancement of photosystem synthesis and limitation of respiration. Biochim Biophys Acta 1777:163–172

Kuwasaki Y, Miyake K, Fushimi K et al (2019) Protein engineering of dual-cys cyanobacteriochrome AM1_1186g2 for biliverdin incorporation and far-red/blue reversible photoconversion. Int J Mol Sci 20. https://doi.org/10.3390/ijms20122935

Lamparter T, Michael N (2005) *Agrobacterium* phytochrome as an enzyme for the production of *ZZE* bilins. Biochemistry 44:8461–8469

Lamparter T, Michael N, Mittmann F, Esteban B (2002) Phytochrome from *Agrobacterium tumefaciens* has unusual spectral properties and reveals an N-terminal chromophore attachment site. Proc Natl Acad Sci U S A 99:11628–11633

Leivar P, Monte E (2014) PIFs: systems integrators in plant development. Plant Cell 26:56–78

Leopold AV, Chernov KG, Shemetov AA, Verkhusha VV (2019) Neurotrophin receptor tyrosine kinases regulated with near-infrared light. Nat Commun 10:1129

Levskaya A, Chevalier AA, Tabor JJ et al (2005) Synthetic biology: engineering *Escherichia coli* to see light. Nature 438:441–442

Levskaya A, Weiner OD, Lim WA, Voigt CA (2009) Spatiotemporal control of cell signalling using a light-switchable protein interaction. Nature 461:997–1001

Lim S, Yu Q, Gottlieb SM et al (2018) Correlating structural and photochemical heterogeneity in cyanobacteriochrome NpR6012g4. Proc Natl Acad Sci U S A 115:4387–4392

Ma Q, Hua H-H, Chen Y et al (2012) A rising tide of blue-absorbing biliprotein photoreceptors: characterization of seven such bilin-binding GAF domains in *Nostoc* sp. PCC7120. FEBS J 279:4095–4108

Miyake K, Fushimi K, Kashimoto T et al (2020) Functional diversification of two bilin reductases for light perception and harvesting in unique cyanobacterium *Acaryochloris marina* MBIC 11017. FEBS J. https://doi.org/10.1111/febs.15230

Mukougawa K, Kanamoto H, Kobayashi T et al (2006) Metabolic engineering to produce phytochromes with phytochromobilin, phycocyanobilin, or phycoerythrobilin chromophore in *Escherichia coli*. FEBS Lett 580:1333–1338

Nagano S (2016) From photon to signal in phytochromes: similarities and differences between prokaryotic and plant phytochromes. J Plant Res 129:123–135

Narikawa R, Fukushima Y, Ishizuka T et al (2008a) A novel photoactive GAF domain of cyanobacteriochrome AnPixJ that shows reversible green/red photoconversion. J Mol Biol 380:844–855

Narikawa R, Kohchi T, Ikeuchi M (2008b) Characterization of the photoactive GAF domain of the CikA homolog (SyCikA, Slr1969) of the cyanobacterium *Synechocystis* sp. PCC 6803. Photochem Photobiol Sci 7:1253–1259

Narikawa R, Suzuki F, Yoshihara S et al (2011) Novel photosensory two-component system (PixA-NixB-NixC) involved in the regulation of positive and negative phototaxis of cyanobacterium *Synechocystis* sp. PCC 6803. Plant Cell Physiol 52:2214–2224

Narikawa R, Ishizuka T, Muraki N et al (2013) Structures of cyanobacteriochromes from phototaxis regulators AnPixJ and TePixJ reveal general and specific photoconversion mechanism. Proc Natl Acad Sci U S A 110:918–923

Narikawa R, Enomoto G, Ni-Ni-Win et al (2014) A new type of dual-Cys cyanobacteriochrome GAF domain found in cyanobacterium *Acaryochloris marina*, which has an unusual red/blue reversible photoconversion cycle. Biochemistry 53:5051–5059

Narikawa R, Nakajima T, Aono Y et al (2015) A biliverdin-binding cyanobacteriochrome from the chlorophyll *d*-bearing cyanobacterium *Acaryochloris marina*. Sci Rep 5:7950

Ni M, Tepperman JM, Quail PH (1998) PIF3, a phytochrome-interacting factor necessary for normal photoinduced signal transduction, is a novel basic helix-loop-helix protein. Cell 95:657–667

Ni M, Tepperman JM, Quail PH (1999) Binding of phytochrome B to its nuclear signalling partner PIF3 is reversibly induced by light. Nature 400:781–784

Olson EJ, Tzouanas CN, Tabor JJ (2017) A photoconversion model for full spectral programming and multiplexing of optogenetic systems. Mol Syst Biol 13:926

Osoegawa S, Miyoshi R, Watanabe K et al (2019) Identification of the deprotonated pyrrole nitrogen of the bilin-based photoreceptor by Raman spectroscopy with an advanced computational analysis. J Phys Chem B 123:3242–3247

Ramakrishnan P, Tabor JJ (2016) Repurposing *Synechocystis* PCC6803 UirS-UirR as a UV-violet/green photoreversible transcriptional regulatory tool in *E. coli*. ACS Synth Biol 5:733–740

Redchuk TA, Omelina ES, Chernov KG, Verkhusha VV (2017) Near-infrared optogenetic pair for protein regulation and spectral multiplexing. Nat Chem Biol 13:633–639

Reichhart E, Ingles-Prieto A, Tichy A-M et al (2016) A phytochrome sensory domain permits receptor activation by red light. Angew Chem Int Ed Engl 55:6339–6342

Rockwell NC, Lagarias JC (2017a) Phytochrome diversification in cyanobacteria and eukaryotic algae. Curr Opin Plant Biol 37:87–93

Rockwell NC, Lagarias JC (2017b) Ferredoxin-dependent bilin reductases in eukaryotic algae: ubiquity and diversity. J Plant Physiol 217:57–67

Rockwell NC, Lagarias JC (2019) Phytochrome evolution in 3D: deletion, duplication, and diversification. New Phytol. https://doi.org/10.1111/nph.16240

Rockwell NC, Njuguna SL, Roberts L et al (2008) A second conserved GAF domain cysteine is required for the blue/green photoreversibility of cyanobacteriochrome Tlr0924 from *Thermosynechococcus elongatus*. Biochemistry 47:7304–7316

Rockwell NC, Martin SS, Feoktistova K, Lagarias JC (2011) Diverse two-cysteine photocycles in phytochromes and cyanobacteriochromes. Proc Natl Acad Sci U S A 108:11854–11859

Rockwell NC, Martin SS, Gulevich AG, Lagarias JC (2012a) Phycoviolobilin formation and spectral tuning in the DXCF cyanobacteriochrome subfamily. Biochemistry 51:1449–1463

Rockwell NC, Martin SS, Lagarias JC (2012b) Red/green cyanobacteriochromes: sensors of color and power. Biochemistry 51:9667–9677

Rockwell NC, Martin SS, Lagarias JC (2012c) Mechanistic insight into the photosensory versatility of DXCF cyanobacteriochromes. Biochemistry 51:3576–3585

Rockwell NC, Duanmu D, Martin SS et al (2014a) Eukaryotic algal phytochromes span the visible spectrum. Proc Natl Acad Sci U S A 111:3871–3876

Rockwell NC, Martin SS, Gulevich AG, Lagarias JC (2014b) Conserved phenylalanine residues are required for blue-shifting of cyanobacteriochrome photoproducts. Biochemistry 53:3118–3130

Rockwell NC, Martin SS, Gan F et al (2015a) NpR3784 is the prototype for a distinctive group of red/green cyanobacteriochromes using alternative Phe residues for photoproduct tuning. Photochem Photobiol Sci 14:258–269

Rockwell NC, Martin SS, Lagarias JC (2015b) Identification of DXCF cyanobacteriochrome lineages with predictable photocycles. Photochem Photobiol Sci 14:929–941

Rockwell NC, Martin SS, Lagarias JC (2016) Identification of cyanobacteriochromes detecting far-red light. Biochemistry 55:3907–3919

Rockwell NC, Martin SS, Lagarias JC (2017a) There and back again: loss and reacquisition of two-Cys

photocycles in cyanobacteriochromes. Photochem Photobiol 93:741–754
Rockwell NC, Martin SS, Li F-W et al (2017b) The phycocyanobilin chromophore of streptophyte algal phytochromes is synthesized by HY2. New Phytol 214:1145–1157
Rost BR, Schneider-Warme F, Schmitz D, Hegemann P (2017) Optogenetic tools for subcellular applications in neuroscience. Neuron 96:572–603
Rüdiger W, Thümmler F, Cmiel E, Schneider S (1983) Chromophore structure of the physiologically active form (P(fr)) of phytochrome. Proc Natl Acad Sci U S A 80:6244–6248
Ryu M-H, Gomelsky M (2014) Near-infrared light responsive synthetic c-di-GMP module for optogenetic applications. ACS Synth Biol 3:802–810
Ryu M-H, Kang I-H, Nelson MD et al (2014) Engineering adenylate cyclases regulated by near-infrared window light. Proc Natl Acad Sci U S A 111:10167–10172
Sato T, Kikukawa T, Miyoshi R et al (2019) Protochromic absorption changes in the two-cysteine photocycle of a blue/orange cyanobacteriochrome. J Biol Chem 294:18909–18922
Savakis P, De Causmaecker S, Angerer V et al (2012) Light-induced alteration of c-di-GMP level controls motility of *Synechocystis* sp. PCC 6803. Mol Microbiol 85:239–251
Senoo S, Tandar ST, Kitamura S et al (2019) Light-inducible flux control of triosephosphate isomerase on glycolysis in Escherichia coli. Biotechnol Bioeng. https://doi.org/10.1002/bit.27148
Shao J, Wang M, Yu G et al (2018) Synthetic far-red light-mediated CRISPR-dCas9 device for inducing functional neuronal differentiation. Proc Natl Acad Sci U S A 115:E6722–E6730
Shimizu-Sato S, Huq E, Tepperman JM, Quail PH (2002) A light-switchable gene promoter system. Nat Biotechnol 20:1041–1044
Song J-Y, Cho HS, Cho J-I et al (2011) Near-UV cyanobacteriochrome signaling system elicits negative phototaxis in the cyanobacterium *Synechocystis* sp. PCC 6803. Proc Natl Acad Sci U S A 108:10780–10785
Tabor JJ, Levskaya A, Voigt CA (2011) Multichromatic control of gene expression in *Escherichia coli*. J Mol Biol 405:315–324
Takala H, Björling A, Berntsson O et al (2014) Signal amplification and transduction in phytochrome photosensors. Nature 509:245–248
Terry MJ, Maines MD, Lagarias JC (1993) Inactivation of phytochrome- and phycobiliprotein-chromophore precursors by rat liver biliverdin reductase. J Biol Chem 268:26099–26106
Thümmler F, Rüdiger W, Cmiel E, Schneider S (1983) Chromopeptides from phytochrome and phycocyanin. NMR studies of the Pfr and Pr chromophore of phytochrome and *E*, *Z* isomeric chromophores of phycocyanin. Z Naturforsch C 38:359–368
Toettcher JE, Weiner OD, Lim WA (2013) Using optogenetics to interrogate the dynamic control of signal transmission by the Ras/Erk module. Cell 155:1422–1434
Tyszkiewicz AB, Muir TW (2008) Activation of protein splicing with light in yeast. Nat Methods 5:303–305
Uda Y, Goto Y, Oda S et al (2017) Efficient synthesis of phycocyanobilin in mammalian cells for optogenetic control of cell signaling. Proc Natl Acad Sci U S A 114:11962–11967
Ueda Y, Sato M (2018) Induction of signal transduction by using non-channelrhodopsin-type optogenetic tools. Chembiochem 19:1217–1231
Wagner JR, Brunzelle JS, Forest KT, Vierstra RD (2005) A light-sensing knot revealed by the structure of the chromophore-binding domain of phytochrome. Nature 438:325–331
Wagner JR, Zhang J, Brunzelle JS et al (2007) High resolution structure of *Deinococcus* bacteriophytochrome yields new insights into phytochrome architecture and evolution. J Biol Chem 282:12298–12309
Wang D, Qin Y, Zhang S et al (2019) Elucidating the molecular mechanism of ultrafast Pfr-state photoisomerization in bathy bacteriophytochrome PaBphP. J Phys Chem Lett 10:6197–6201
Wiebeler C, Gopalakrishna Rao A, Gärtner W, Schapiro I (2018) The effective conjugation length is responsible for the red/green spectral tuning in the cyanobacteriochrome Slr1393g3. Angew Chem Int Ed Engl. https://doi.org/10.1002/anie.201810266
Yang X, Kuk J, Moffat K (2008) Crystal structure of *Pseudomonas aeruginosa* bacteriophytochrome: photoconversion and signal transduction. Proc Natl Acad Sci U S A 105:14715–14720
Yang Y, Lam V, Adomako M et al (2018) Phototaxis in a wild isolate of the cyanobacterium *Synechococcus elongatus*. Proc Natl Acad Sci U S A 115:E12378–E12387
Yoshihara S, Katayama M, Geng X, Ikeuchi M (2004) Cyanobacterial phytochrome-like PixJ1 holoprotein shows novel reversible photoconversion between blue- and green-absorbing forms. Plant Cell Physiol 45:1729–1737
Yousefi OS, Günther M, Hörner M et al (2019) Optogenetic control shows that kinetic proofreading regulates the activity of the T cell receptor. Elife 8. https://doi.org/10.7554/eLife.42475
Zhao C, Gan F, Shen G, Bryant DA (2015) RfpA, RfpB, and RfpC are the master control elements of far-red light photoacclimation (FaRLiP). Front Microbiol 6:1303
Ziegler T, Möglich A (2015) Photoreceptor engineering. Front Mol Biosci 2:30
Zienicke B, Molina I, Glenz R et al (2013) Unusual spectral properties of bacteriophytochrome Agp2 result from a deprotonation of the chromophore in the red-absorbing form Pr. J Biol Chem 288:31738–31751

# Photoreaction Mechanisms of Flavoprotein Photoreceptors and Their Applications

11

Tatsuya Iwata and Shinji Masuda

**Abstract**

Three classes of flavoprotein photoreceptors, cryptochromes (CRYs), light-oxygen-voltage (LOV)-domain proteins, and blue light using FAD (BLUF)-domain proteins, have been identified that control various physiological processes in multiple organisms. Accordingly, signaling activities of photoreceptors have been intensively studied and the related mechanisms have been exploited in numerous optogenetic tools. Herein, we summarize the current understanding of photoactivation mechanisms of the flavoprotein photoreceptors and review their applications.

**Keywords**

BLUF · Cryptochrome · Flavin · LOV · Optogenetics · Photocycle · Photoreceptor

## Abbreviations

| | |
|---|---|
| As | *Avena sativa* |
| At | *Arabidopsis thaliana* |
| AUREO | Aureochrome |
| Bc | *Botrytis cinereal* |
| B-LID | Blue-light-inducible degradation |
| BLUF | Blue light using FAD |
| BRET | Bioluminescence resonance energy transfer |
| bZIP | Basic leucine zipper |
| CCT | C-terminal extension |
| CIB1 | Cryptochrome-interacting basic-helix-loop-helix 1 |
| CIBN | CIB N-terminus |
| cLIPS1 | LOV inhibitor of protein synthesis 1 |
| CRY | Cryptochrome |
| dCas9 | Nuclease-dead Cas9 |
| FAD | Flavin adenine dinucleotide |
| FGFR1 | Fibroblast growth factor receptor 1 |
| FKF1 | Kelch repeat F-box |
| FLARE | Fast light- and activity-regulated expression |
| FTIR | Fourier transform infrared |
| GI | GIGANTEA |
| iLID | Light-induced dimer |
| LEXY | Light-inducible nuclear protein export system |
| LINuS | Light-induced nuclear localization signal |
| LINX | Light-induced-nuclear-export |
| LOV | Light-oxygen-voltage |
| nMag | Negatively charged Magnet |
| optoTrk | Photoactivatable tyrosine receptor kinase |

T. Iwata
Department of Pharmaceutical Sciences, Toho University, Funabashi, Chiba, Japan

S. Masuda (✉)
Department of Life Science and Technology, Tokyo Institute of Technology, Yokohama, Japan
e-mail: shmasuda@bio.titech.ac.jp



H. Yawo et al. (eds.), *Optogenetics*, Advances in Experimental Medicine and Biology 1293,
https://doi.org/10.1007/978-981-15-8763-4_11

| | |
|---|---|
| PAC | Photoactivated adenylyl cyclase |
| Phot | Phototropin |
| Photo-ECM | Photoswitchable extracellular matrix protein; |
| PICCORO, PHR | Photolyase homology region |
| PixD | Complex-dependent control |
| pMag | Positively charged Magnet |
| PL | Photolyase |
| psd | Photosensitive degron |
| REST | Repressor element 1-silencing transcription factor |
| Rs | *Rhodobacter sphaeroides* |
| SPARK | specific protein association tool that gives a transcriptional readout with rapid kinetics |
| TALEs | Transcription activator-like effectors; |
| TEVp | Tobacco-etch-virus protease |
| TULIPs | Tunable light-inducible dimerization tags |
| VVD | *Vivid* coloration |
| WC1 | White collar1 |

## 11.1 Photoactivation of Flavoprotein Photoreceptors

Flavins have been recognized as coenzymes in electron transfer reactions and various other reactions of flavin-binding enzymes (Macheroux et al. 2011; Massey 2000). It was first discovered in 1993 that flavins function as light-sensing antennas that activate proteins in cells (Macheroux et al. 2011). To date, three kinds of flavoprotein photoreceptors are known to have different structures and flavins' photoreactions: cryptochrome (CRY) (Ahmad and Cashmore 1993; Lin et al. 1995), the light-oxygen-voltage (LOV) domain (Huala et al. 1997), and the sensor of blue light using FAD (BLUF) domain (Gomelsky and Klug 2002; Iseki et al. 2002; Masuda and Bauer 2002) (Fig. 11.1).

In general, protein functions are accompanied by changes in their conformations following exposures to external stimuli. In photoreceptive proteins, light stimuli are received by chromophores that covalently or noncovalently bind to apoproteins. Photoinduced conformational changes of chromophores then mediate conformational and structural changes of these apoproteins. In the following section, we briefly outline the scientific history of the three flavopotein photoreceptors and the related structural changes in their chromophores and apoproteins. It is noteworthy that there are no reports on the photoreactions investigated using native proteins from original organisms. All photoreactions were investigated using proteins obtained through heterologous expression system in bacteria or insect cells.

### 11.1.1 Photoreactions of Cryptochromes

CRY is a flavoprotein photoreceptor that was firstly identified to be responsible for photomorphogenesis of plants (Ahmad and Cashmore 1993). Later, CRYs were discovered in insects and animals and were identified as components of the circadian clock (Cashmore et al. 1999; Todo et al. 1996). CRYs are also believed to be involved in magnetoreception in birds and insects (Gegear et al. 2008, 2010; Ritz et al. 2000). Their primary and tertiary structures are similar to those of DNA photolyases (PLs), and they are classified as the CRY/PL family (Ahmad and Cashmore 1993; Cashmore et al. 1999; Zoltowski et al. 2011).

Photoreactions of CRYs are initiated through light-induced reduction of the flavin adenine dinucleotide (FAD) chromophore (Fig. 11.1a). In *Arabidopsis* CRY1, the oxidized form of FAD ($FAD^{ox}$) was previously identified as the unphotolyzed state (Ahmad et al. 2002; Bouly et al. 2007). Under blue-light illumination, a neutral semiquinoid radical ($FADH^{\bullet}$) is formed by one-electron reduction and protonation of the bound FAD. In contrast, insect CRYs form an anionic radical state of FAD ($FAD^{\bullet-}$) (Bouly et al. 2007; Öztürk et al. 2008). In the case of CRY-DASHs, which form a distinct cluster in the CRY/PL family (Brudler et al. 2003; Hitomi et al.

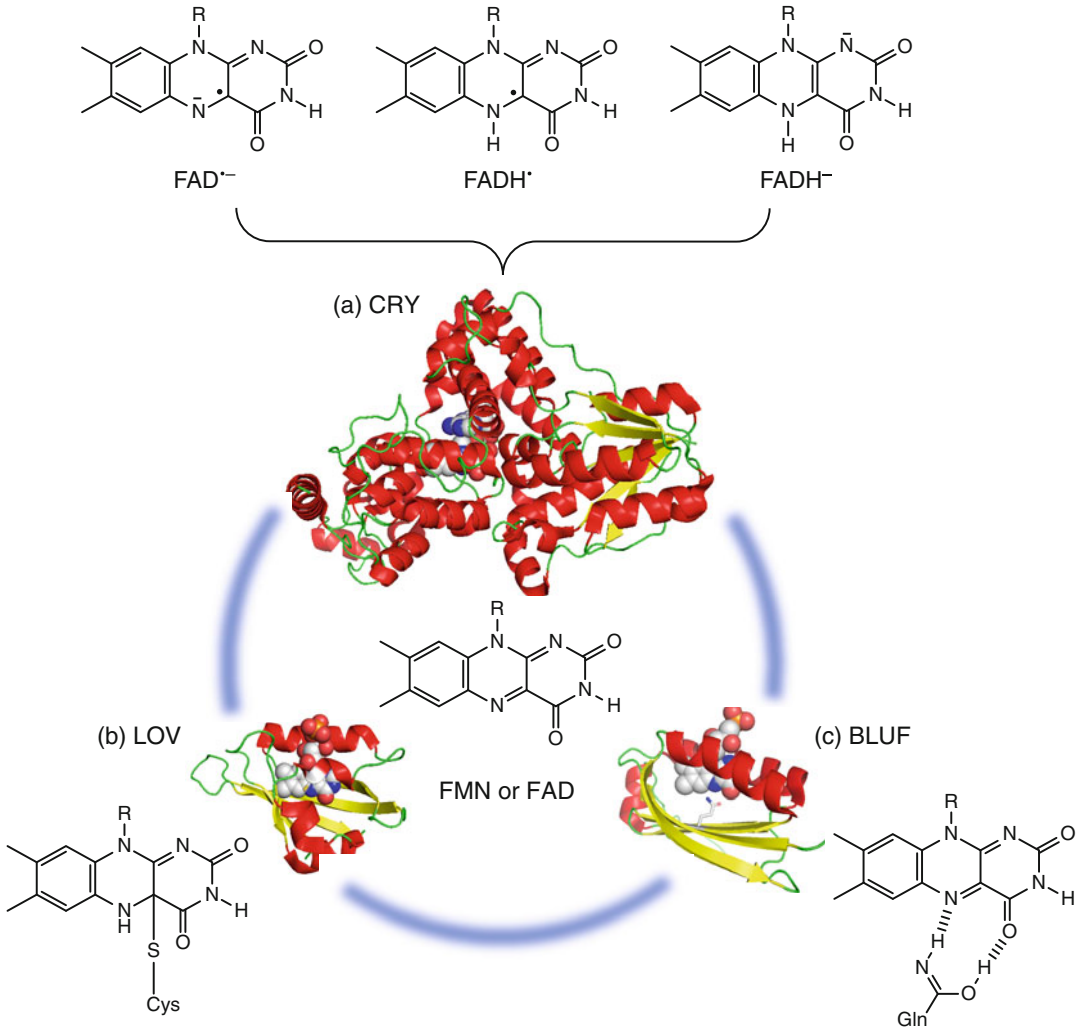


**Fig. 11.1** Structures and schematic of photochemical reactions of flavin in flavoprotein photoreceptors; In CRYs, FAD is reduced upon exposure to light (**a**). The resulting stable intermediates vary between species. In the LOV domain, a covalent bond is formed between the C4a atom of FMN and the sulfur atom of proximal cysteine residues (**b**). In BLUF domains, the chemical structure of FAD does not change in the intermediate state, but the side chain of a proximal glutamine isomerizes from keto to enol forms (**c**). Shown structures of flavoprotein photoreceptors are (**a**) PHR domain of *Arabidopsis* CRY1 (pdb ID: 1U3C) (Brautigam et al. 2004), (**b**) LOV domain of *Adiantum* neochrome1 (pdb ID: 1G28) (Crosson and Moffat 2001), and (**c**) BLUF domain of *R. sphaeroides* AppA (pdb ID: 1YRX) (Anderson et al. 2005)

2000), light illumination of $FAD^{ox}$ produces a stable two-electron reduced form ($FADH^{-}$) (Biskup et al. 2009; Damiani et al. 2009; Iwata et al. 2010; Zikihara et al. 2008). Stable reduced forms are believed to be regulated by specific amino acid residues surrounding the N5 position of FAD, including Asp in plant-type CRYs, Cys in insect CRY, and Asn in CRY-DASH (Balland et al. 2009; Iwata et al. 2010).

Among CRY family proteins, FAD is reduced by exogeneous electron donors, including conserved Trp residues that are proximal to FAD on the protein surface. These Trp residues form Trp triads or tetrads (Kao et al. 2008). In

*Arabidopsis* CRY1, an Asp residue near the N5 position of FAD was identified as a proton donor (Kottke et al. 2006), whereas in CRY-DASHs, Asn was showed to be present at the corresponding position, and failed to donate a proton to the bound FAD. Under these conditions, the proton may be donated by a water molecule, although no experimental evidence of this has been reported.

$FAD^{ox}$ is widely considered the resting state and reduced FAD, $FAD^{\bullet -}$, $FADH^{\bullet}$ and/or $FADH^{-}$ are generated during the formation of the signaling state. CRYs generally have an C-terminal extension (CCT) region in addition to the photolyase homology region (PHR) domain, and this region is thought to be involved in signal transduction (Yang et al. 2000). The mechanisms behind structural changes in CCT regions upon photoreduction of FAD have not been described. However, structural changes of the α/β region, which is distal from the FAD-binding region, was observed in *Chlamydomonas* CRY (Sommer et al. 2017). These structural changes of the PHR domain may be communicated to the CCT region.

### 11.1.2 Photoreactions of the LOV Domain

The LOV domain was originally described as a light-responsive domain of phototropins (phots) (Christie et al. 1999; Huala et al. 1997), which are plant blue-light receptors that mediate phototropic responses (Liscum and Briggs 1995). Phots were later identified as photoreceptors that control relocation of chloroplasts (Kagawa et al. 2001; Sakai et al. 2001) and stomata opening (Kinoshita et al. 2001). The phot isomers, phot1 and phot2, were then identified in vascular plants and were found to have differing light sensitivity. Phots comprise two LOV domains with kinase domains at N- and C-termini, respectively.

The LOV domain was named for its similarity of primary (Huala et al. 1997) and tertiary (Crosson and Moffat 2001) structures to those of the bacterial light-sensor PYP (Borgstahl et al. 1995), the oxygen sensor FixL (Miyatake et al. 2000), and the N-terminal domain of a voltage-gated potassium channel, HERG (Morais Cabral et al. 1998). The protein fold of the LOV domain also belongs to the Per-Arnt-Sim superfamily (Takahashi 1992). The LOV domain has been identified as a blue-light receptor domain in many proteins with highly diverse catalytic domains.

Photochemical reactions of LOV domains involve the formation of covalent bonds between FMN and a proximal Cys residue (Fig. 11.1b) (Crosson and Moffat 2002; Salomon et al. 2000, 2001; Swartz et al. 2001). When FMN is excited by light, intersystem crossing from singlet-excited to triplet-exited states of FMN occurs over nanoseconds (Kennis et al. 2003). A shorter-wavelength product (S390) is subsequently formed with a time constant of microseconds (Kottke et al. 2003; Swartz et al. 2001), during which the C4a atom of FMN and the sulfur atom of the conserved Cys are covalently bound.

An LOV2 domain from a plant phot was extensively investigated in a study of signaling from LOV domains, and the photoreaction was associated with the LOV2 domain rather than LOV1 domain. A specific α-helix, the Jα-helix, is located at the C-terminal region of the LOV2 domain, in which structural changes induce conformational perturbations of the Jα-helix and thereby activate the kinase domain (Balland et al. 2009; Christie et al. 1999; Kao et al. 2008; Kottke et al. 2006; Sommer et al. 2017; Yang et al. 2000).

LOV domains were found in blue-light photoreceptors other than phots, such as FKF1 in plants (Nelson et al. 2000) and aureochrome (AUREO) in stramenopile algae (Takahashi et al. 2007). In these organisms, LOV domains are located at the N-terminal side and regulate functional domains at the C-terminus, as in phots, except that in AUREO, the LOV domain and the effecter domain (DNA-binding domain) are located at C- and N-termini, respectively. This difference between AUREO and phot LOV domains suggests that differing intramolecular

signaling mechanisms regulate the respective effector domains.

### 11.1.3 Photoreactions of BLUF Domains

BLUF domains were most recently discovered as the third type of flavoprotein photoreceptors. Initially, BLUF domains were identified in *Euglena gracilis* and *Rhodobacter sphaeroides* as FAD-binding photoreceptor domains of the photoactivated adenylyl cyclase (PAC) and the anti-repressor AppA, respectively (Gomelsky and Klug 2002; Iseki et al. 2002; Masuda and Bauer 2002). Genes encoding BLUF-domain proteins have been found in sequenced genomes of many bacteria and in some eukaryotic microorganisms.

Photoexcitation of the BLUF domain leads to the formation of a 10-nm redshifted intermediate (Masuda and Bauer 2002). Absorption spectra of this BLUF domain indicate the presence of the oxidized form of FAD in both unphotolyzed and intermediate states, indicating that no apparent conformational changes take place in the chromophore. The redshift of absorption suggests strengthening of the hydrogen bond between amino acids and the C4=O group of FAD in the intermediate state (Masuda et al. 2004). Recent infrared spectroscopy and computational studies demonstrated keto–enol tautomerism in the conserved Gln residue, which then participated in hydrogen bonding with the C4=O group of FAD via newly formed O–H groups (Fig. 11.1c) (Domratcheva et al. 2016; Iwata et al. 2018). Isomerization of the Gln side chain during photoreactions of BLUF domains was first indicated by ultrafast infrared spectroscopy experiments (Haigney et al. 2011; Stelling et al. 2007).

During early stages of photoreactions, PixD and PapB from purple bacteria participate in electron-coupled proton transfer between conserved Tyr and Gln residues and FAD, followed by reverse transfer from FAD, leading to the formation of the redshifted intermediate (Fujisawa et al. 2014; Gauden et al. 2006). However, in ultrafast infrared spectroscopy experiments, this radical was not formed in BLUF domains from AppA and BlsA (Lukacs et al. 2014), leading to uncertainty regarding the early steps of photoreactions in BLUF domains.

How structural changes of BLUF domains activate other functional domains also remains unknown. BLUF domains from AppA exhibited structural changes of β-sheet regions in FTIR spectroscopy analyses (Masuda et al. 2005). But in X-ray crystallography analyses of the PAC from a cyanobacterium, only slight structural differences were found between dark and light forms (Ohki et al. 2016, 2017), indicating differences in signaling mechanisms among BLUF domains.

## 11.2 Optogenetic Applications of Flavoprotein Photoreceptors

Given that flavins are universal cofactors in cells, all three types of blue-light receptors (LOV, CRY, and BLUF) could be assembled in functional complexes if all apoprotein genes were present in heterologous expression systems. Such manipulations may allow the construction of tools for controlling cellular mechanisms in response to light in a highly spaciotemporal manner. Accordingly, light-dependent control of gene expression, protein degradation, neuronal differentiation, and cell-to-cell interactions has been exploited previously (Table 11.1). Below, we summarize optogenetic tools that have been developed using all three types of flavin-based photoreceptors. This area of investigation has been vigorously pursued, thus we limit our focus to recently established methods and related reviews that were published in recent years (Losi et al. 2018; Mansouri et al. 2019; Rost et al. 2017; Ziegler and Möglich 2015).

### 11.2.1 LOV Domain Applications

In early applications, LOV-based artificial photoreceptors were designed to control the activities of DNA-binding proteins, histidine

**Table 11.1** Flavoprotein photoreceptors and their optogenetic applications

| Application | Photoreceptor type | Origin of light-sensitive module | System | Reference(s) |
|---|---|---|---|---|
| Gene expression | LOV | VVD | Lighton | Ma et al. (2013) |
| | | | Magnets | Kawano et al. (2015) |
| | | AsLOV2 | REST | Paonessa et al. (2016) |
| | | | FLARE | Wang et al. (2017) |
| | | | SPARK | Kim et al. (2017) |
| | Cryptochrome | CRY2 | CRY2-CIBI1 | Kennedy et al. (2010); Liu et al. (2012) |
| | | | CRY2-GAL-VP16 | Pathak et al. (2017) |
| | | | CRY2-TALE | Konermann et al. (2013) |
| | BLUF | PixD | PICCORO | Masuda et al. (2013) |
| Protein interaction/ localization | LOV | AsLOV2 | iLID | Guntas et al. (2015) |
| | | | TULIPs | Strickland et al. (2012) |
| | | | LOVTRAP | Wang et al. (2016) |
| | | | LINuS/LIXY/ LINX | Niopek et al. (2014, 2016); Yumerefendi et al. (2015) |
| | | | Photo-ECM | Ricken et al. (2019) |
| | | VVD | Magnets | Yu et al. (2016) |
| | | AUREO | Opto-FGFRs | Grusch et al. (2014) |
| | Cryptochrome | CRY2 | optoTrk | Chang et al. (2014) |
| | | | CRY2-CIBI1 | Duan et al. (2015) |
| Genome editing | LOV | VVD | Magnets | Nihongaki et al. (2017) |
| | | RsLOV | RsLOV-Cas9 | Richter et al. (2016) |
| Protein degradation | LOV | AtLOV2 | psd | Renicke et al. (2013) |
| | | | B-LID | Bonger et al. (2014) |
| Second-messenger synthesis/hydrolysis | LOV | mPAC | cAMP syn[a] | Raffelberg et al. (2013) |
| | | SL2 | c-di-GMP hyd[b] | Cao et al. (2010) |
| | BLUF | PAC | cAMP syn | Iseki et al. (2002) |
| | | BlaC | cAMP syn | Ryu et al. (2010) |
| | | bPAC | cAMP syn | Stierl et al. (2011) |
| | | BlgC | cGMP syn | Ryu et al. (2010) |
| | | PapB-PapA | c-di-GMP hyd | Kanazawa et al. (2010) |
| | | BldP, EB1 | c-di-GMP hyd | Ryu et al. (2017) |

[a]*syn* synthesis
[b]*hyd* hydrolysis

kinases, and the small GTPase, Rac1, which controls cell motility (Pudasaini et al. 2015). Numerous subsequent applications have been reported, including those directed at light-dependent protein degradation, neuronal differentiation, and cell–cell interactions.

#### 11.2.1.1 Gene Regulation by LOV

To control gene expression through light-dependent mechanisms, chimeric transcription factors have been constructed by modifying DNA-binding proteins with several LOV domains, allowing binding to specific promoter regions of target genes. Early examples involved the use of the phot1 LOV2 domain (Strickland et al. 2008) and the LOV-containing FKF1 protein (Wang et al. 2012). In a later study, Yazawa et al. generated a light-activated transcription factor by fusing domains of the KFK1-interacting factor GIGANTEA (GI) to the DNA-binding domain of GAL4. These investigators also fused FKF1 to the transactivation domain of VP16, thus setting the stage for the development of light-regulated gene expression systems (Quejada

et al. 2017; Yazawa et al. 2009). These systems were further combined with synthetic zinc finger protein technology to engineer light regulation of DNA target sequences (Polstein and Gersbach 2012). Dimerization of the LOV-containing protein VVD from *Neurospora crassa* was also used to regulate the association of DNA-binding domains and their recognition sequences following exposure to light (designated as Lighton system) (Ma et al. 2013). Light-dependent dimerization reactions of VVD with WC1 from *N. crassa*, and with EL222 from the proteobacterium *Erythrobacter litoralis*, were also exploited in the GAL4-based light-induced gene activation system (Motta-Mena et al. 2014; Salinas et al. 2018). The resulting system was recently modified to control of transcription factor activity in living zebrafish (Reade et al. 2017).

Nihongaki et al. further engineered the VVD (Nihongaki et al. 2014) to establish an optogenetic system that efficiently controlled protein dimerization. In their Magnets system (Kawano et al. 2015), a homodimerization interface of VVD was engineered to produce distinct positively (pMag) and negatively charged (nMag) Magnet variants. Subsequently, these investigators fused pMag and nMag to the N- and C-terminal domains of nuclease-dead Cas9 (dCas9), respectively (Kawano et al. 2015). Upon expression in the presence of a specific single guided RNA (sgRNA) with MS2-binding sequences, target gene expression was upregulated by blue-light illumination. This system was used to induce neuronal differentiation in induced pluripotent stem cells (Kawano et al. 2015). The Magnets system was further applied to light-induced gene recombination by the Cre-loxP system. To this end, nMag and cMag were fused to N- and C-terminal domains of Cre, and enzyme activity was stimulated by low-intensity illumination or short-pulsed illumination (Kawano et al. 2015). Most recently, the Magnets system was used to efficiently orchestrate DNA recombination in specific organs of living mice (Jung et al. 2019), and to control DNA polymerase activity in mononegaviruses (Tahara et al. 2019) and T7 RNA polymerase activity following blue-light illumination (Baumschlager et al. 2017). Light control of T7 RNA polymerase was also achieved by inserting the *Avena sativa* phototropin 1 LOV2 domain (AsLOV2) with the Jα-helix at a specific position (Seifert et al. 2019).

Paonessa et al. used the AsLOV2 innovation to control repressor element 1 (RE1)-silencing transcription factor (REST), which is a master regulator of neural genes (Paonessa et al. 2016). In their manipulations, the AsLOV2 domain was fused to the minimal REST-interacting sequence of the corepressor mSin3a (AsLOV2-PAH1) or to the active domain of the REST inhibitor REST-interacting LIM domain protein. Both chimeric proteins inhibited REST activity under blue-light illumination, causing increased REST-dependent gene expression and enhanced firing activity of primary neurons (Paonessa et al. 2016).

Wang et al. designed a light- and calcium-gated transcription factor system called fast light- and activity-regulated expression (FLARE) (Wang et al. 2017). They fused a plasma membrane-anchoring trans-membrane helix and the calmodulin-binding peptide to the N-terminus of the *A. sativa* LOV2 domain using the tobacco-etch-virus protease (TEVp) recognition sequence. They also fused a transcription factor to the C-terminus of the LOV2 domain Jα-helix so that the fused TEVp-recognition sequence was masked by a strong interaction between the LOV domain and the Jα-helix under dark conditions. Subsequent application of blue-light illumination interrupted this interaction and thus exposed the TEVp-recognition sequence. Following expression of the recombinant gene in cultured tissues with another chimeric gene encoding the calmodulin-fused TEVp, the transcription factor was released only when blue-light irradiation was present and $Ca^{2+}$ concentrations were elevated. The FLARE system was also used to control opsin gene expression in selected neurons (Wang et al. 2017). This system was further developed in the design of specific protein association tool that gives a transcriptional readout with rapid kinetics (SPARK). SPARK achieves control of transcription factor release through blue-light illumination and the

application of a signaling molecule that disrupts the specific protein–protein interaction (Kim et al. 2017). Further modifications were recently made to generate SPARK2, in which excitation of the LOV domain is achieved through the incorporation of luciferase-dependent bioluminescence resonance energy transfer (BRET) component. In this technology, BRET signals provide a transcriptional readout with low background and improved specificity (Kim et al. 2019).

The LOV domain-containing protein family AUREO in stramenopile algae are uniquely light-sensitive DNA-binding transcription factors comprising single LOV domains with basic leucine zippers (bZIP) at C- and N-termini (Matiiv and Chekunova 2018; Takahashi 2016; Takahashi et al. 2007). DNA recognition sequences and light-dependent structural changes of AUREO have been characterized in biochemical, spectroscopic, and crystal structure studies (Heintz and Schlichting 2016; Takahashi et al. 2007). Yet despite the potential application of these structures for the construction of light-dependent gene expression systems, no light-dependent gene regulation system has yet been manifested using AUREO.

Under designed genetic screening conditions, Lu et al. identified a combination of a light-switchable LOV domain and the native inhibitor of translation eukaryotic initiation factor 4E binding protein 2 (4EBP2) (Lu et al. 2019). From their screen, they selected a fusion of a fragment of 4EBP2 with a circularly permuted version of a LOV2 domain from *A. sativa*, and designated the product LOV inhibitor of protein synthesis 1 (cLIPS1). Under light conditions, cLIPS1 inhibited translation in yeast harboring a human translation initiation factor 4E (eIF4E).

#### 11.2.1.2 Light-Dependent Control of Protein Localization and Activity by LOV

Guntas et al. designed a light-induced dimer (iLID) system for controlling the localization and activity of proteins (Guntas et al. 2015). They engineered the phot1 LOV2 domain from *A. sativa* with an *E. coli* SsrA peptide that specifically binds to the SspB peptide, which has a molecular mass of only 13-kDa. Interactions between LOV2-SspA and SspB were stimulated upon blue-light illumination, and the resulting iLID system was used to control light-mediated localization in mammalian cells and to reversibly control small GTPase signaling (Guntas et al. 2015). Recently, iLID was fused to the kinesin I motor protein, allowing optical control over aster formation, decay, and size through light-dependent induction of microtubule organization (Ross et al. 2019). Other photoswitchable peptides have been based on the *A. sativa* LOV2 domain. Among these, Lungu et al. combined the LOV2 domain with ipaA or SsrA peptides and stimulated interactions of LOV2–ipaA and/or LOV2–SsrA with their targets using light (Lungu et al. 2012). The *A. sativa* LOV domain and its interaction domain ePDZ were also used as tunable light-inducible dimerization tags (TULIPs) that recruit proteins to diverse structures in yeast and mammalian cells (Strickland et al. 2012). Most recently, this system enabled control of protein localization on plasma membranes in developing sea urchin embryos (Uchida and Yajima 2018). Wang et al. developed an optogenetic system for light-induced protein dissociation (Wang et al. 2016). Their LOVTRAP system was based on the *A. sativa* phot1 LOV2 domain and its interacting small protein Zdk, which was selected by library screening from the Z subunit of protein A. LOVTRAP enables reversible modulation of several target proteins toward cell edges.

In other studies, Niopek et al. used the *A. sativa* phot1 LOV2 domain to construct a light-induced nuclear localization signal (LINuS) (Niopek et al. 2014) with a peptide, and developed a light-inducible nuclear protein export system (LEXY) (Niopek et al. 2016). These systems were considered for light-induced control of localization of a synthetic repressor and human p53 transcriptional factor. Similar systems with the *A. sativa* phot1 LOV2 domain were developed independently by other groups, including light-activated-nuclear-shuttle and light-induced-nuclear-export (LINX) (Yumerefendi et al. 2015, 2016). These systems also achieved light-induced nuclear localization of target

proteins and consequent control of transcription and histone modifications in yeast and mammalian cells (Lerner et al. 2018). In an alternative application, *A. sativa* LOV2 was used as a photocage for a peroxisomal targeting sequence, and allowed light regulation of peroxisomal protein import (Spiltoir et al. 2016).

In an application of the Magnets system to control heterotrimeric G protein activity (Yu et al. 2016), the nMag variant was fused to a membrane-associated G protein receptor kinase, and the cMag variant was linked with its target Gα subunit, allowing optical control of assembly and disassembly of the G protein-coupled receptor and Gα activity. The Magnet system was also optimized to form an oligomeric complex that allows light-dependent control of protein self-assembly in cells (Furuya et al. 2017). To this end, the $Ca^{2+}$/calmodulin-dependent protein kinase IIα association domain (CAD) was fused to pMag domain variants. In combination with T-lymphoma invasion and metastasis 1 (Tiam1), this CAD-Magnet system regulated spatiotemporal formation of vertical ruffles on apical plasma membranes (Furuya et al. 2017). Moreover, with a 4D imaging technique, the CAD-Magnet system allowed observations of ruffle formation dynamics. In particular, time dependency of Magnets- and iLID-dependent localization of the target proteins to plasma membranes was well characterized (Benedetti et al. 2018).

Glantz et al. reported a new type of LOV-containing protein from *Botrytis cinerea* (*Bc*LOV4) and showed blue-light switchable and high-affinity interactions with anionic phospholipids and no preference for specific headgroups (Glantz et al. 2018). This development offers a new strategy for the design of new optogenetic tools with rapid membrane localization kinetics.

An artificial photoswitchable extracellular matrix protein (Photo-ECM) was recently developed (Ricken et al. 2019) by fusing the *A. sativa* phot1 LOV2 domain with an integrated cell-binding arginine, glycine, aspartic acid (RGD) sequence that can be reversibly exposed or hidden to control cell adhesion. Upon blue-light illumination, photo-ECM expressing cells show integrin binding, and promotes cell adhesion and spreading. This new method could be applied to tissue engineering and cell-based therapies.

Light-dependent stimulation of membrane-associated growth factor receptors was achieved through yet another LOV domain-based optogenetic approach (Csanaky et al. 2019; Grusch et al. 2014) in which the LOV domain from AUREO was incorporated into the catalytic domain of fibroblast growth factor receptor 1 (FGFR1). When the resulting opto-FGFRs were expressed in human cancer and endothelial cells, light-induced cellular signaling was achieved with spatial and temporal precision, and the consequent mitogenic cell behaviors resembled those induced by growth factors (Grusch et al. 2014). Opto-FGFRs expression in pheochromocytoma (PC12) similarly resulted in significantly longer and more numerous neurite extensions from cell bodies (Csanaky et al. 2019).

#### 11.2.1.3 Light Controllable Genome Editing Using LOV

To apply the Magnets system to spaciotemporal control of genome editing (Nihongaki et al. 2017), N- and C-terminal fragments of Cas9 were fused to pMag and nMag, respectively. These proteins then physically interacted upon light illumination and generated double strand breaks at specific sequences in human HEK293T cells (Nihongaki et al. 2017). Another light-switchable Cas9 was developed using recombinant Cas9 with a *R. sphaeroides* LOV domain (RsLOV) (Richter et al. 2016). In the dark, RsLOV formed homodimers that dissociated upon blue-light illumination. After fusion of RsLOV to Cas9, steric inhibition of Cas9 activity by dimerization in the dark was abolished upon blue-light illumination, leading to increased activity of the functional monomer. Temperature-sensitive variants of RsLOV-Cas9 were also isolated using genetic screening (Richter et al. 2016), and light- and temperature-inducible cleavage of genome sequences was demonstrated in *E. coli* (Richter et al. 2016).

#### 11.2.1.4 Light Control of Protein Degradation by LOV

Renicke et al. fused an *A. thaliana* phot1 LOV2 domain to a human ornithine decarboxylase sequence and constructed a photosensitive degron (psd) module (Renicke et al. 2013). Their psd comprises 37 unstructured amino acids with a cysteine-alanine motif at 19 amino acids from the C-terminus. Under dark conditions, the sequence is masked by the LOV2 domain, which exposes the sequence to solvent upon blue-light illumination, allowing association of the domain with the proteasome in a ubiquitin-independent manner (Renicke et al. 2013). After fusion with psd or its variants, any protein of interest could be degraded following exposure to blue light (Hasenjäger et al. 2019; Sun et al. 2017; Usherenko et al. 2014). The *A. sativa* phot1 LOV2 domain was also used to construct a blue-light-inducible degradation (B-LID) system (Bonger et al. 2014) by fusing the LOV2 domain to a small peptide from FK506- and rapamycin-binding protein (FKBP). This ubiquitin target was then degraded by the proteasome upon blue-light illumination. This B-LID system was functional in zebrafish (Bonger et al. 2014) and in the *Caenorhabditis elegans* nervous system (Hermann et al. 2015).

#### 11.2.1.5 Regulation of Nucleotide Second-Messenger Synthesis/Hydrolases by LOV

An LOV domain-containing light-activatable cAMP synthase was previously identified in the cyanobacterium *Microcoleus chthonoplastes* PCC 7420 (Raffelberg et al. 2013). This protein showed a typical LOV domain photocycle, and adenylyl cyclase activity was stimulated by a factor of 30 under blue-light illumination. Moreover, cAMP levels were significantly increased following expression of this protein in *Xenopus laevis* oocytes (Raffelberg et al. 2013), indicating functional potential in optogenetic applications with heterologous organisms. Cao et al. similarly found an LOV-containing light-activatable phosphodiesterase that hydrolases cyclic-dimeric GMP (c-di-GMP) (Cao et al. 2010). This protein may also have optogenetic applications, although its expression has not been demonstrated in many species.

### 11.2.2 CRY Applications

After the CRY2-interacting transcription factor CIB1 was identified (Liu et al. 2008), CRY2-CIB1 interactions were widely used to develop several optogenetic tools that control gene expression, protein localization, and various other cellular functions, as described below.

#### 11.2.2.1 Gene Regulation by CRY

The interaction between CRY2 and CIB1 (or its truncated version CIBN) has been used widely to achieve light-dependent gene expression. As for the LOV domain, CRY1–CIB1 interactions positively and/or negatively controlled GAL4-dependent transcription (Kennedy et al. 2010; Liu et al. 2012) and CRISPR-Cas9-based photoactivatable transcription in yeast, zebrafish, and mammalian cells (Nihongaki et al. 2015; Polstein and Gersbach 2015). Recently, light-dependent localization of a chimeric transcription factor comprising the DNA-binding domain of GAL4, CRY2, and the transcription activation domain of VP16 was designed to control specific genes with high signal-to-noise ratios. In the dark, the chimeric transcription factor (CRY2-GAL-VP16) accumulated in nuclei of mammalian cells and activated transcription of specific genes. After exposure to blue light, conformational changes of CRY2 resulted in export of the chimeric transcription factor from nuclei, resulting in ~40-fold reductions in expression over 24 h (Pathak et al. 2017).

Konermann et al. modified CRY2 and CIB1 to control gene expression and epigenetic states (Konermann et al. 2013). To this end, CRY2 was fused to a customizable DNA-binding domain, based on transcription activator-like effectors (TALEs) from *Xanthomonas* sp., and CIB1 was fused to the transcriptional activation domain of VP16. The CRY2–TALE construct constitutively binds target promoter sequences

and the CIB1-VP16 construct specifically interacts with CRY2-TALE upon blue-light illumination, resulting in specific activation of target transcription. To apply this method to the control of epigenetic states, CIB1 was fused to histone-modifying domains such as histone deacetylase and/or methyltransferase. After expressing the ensuing chimeric genes in neurons, blue-light-dependent alteration of histone modifications and related changes in transcriptional activity of target genes were observed (Konermann et al. 2013). In another CEY2–CIB1-based photoactivatable transcription system (Polstein and Gersbach 2015), CRY2 and CIB1 were fused to the transcription activation domains of VP16 and dCas9, respectively. In transfected human HEK293T cells carrying a specific guide RNA, the target gene was upregulated upon blue-light illumination.

#### 11.2.2.2 Light-Dependent Control of Protein and Cell Localization Using CRY

In a study by Benedetti et al., subcellular localization of a CRY2-fused target protein was controlled in blue-light-dependent manner (Benedetti et al. 2018). These investigators fused the CIBN domain to the cytosolic membrane-spanning domain and expressed the ensuing construct with a CRY2-fused mCherry construct. Under dark conditions, CRY2-mCherry diffused throughout the cell, and upon blue-light illumination, photoactivated CRY2-mCherry interacted with membrane-anchored CIBN and hence became localized to membranes.

Chang et al. designed a photoactivatable tyrosine receptor kinase (optoTrk) using CYR2 by exploiting the CYR2–CIBN interaction to regulate a cell-surface receptor kinase (Chang et al. 2014). Upon blue-light illumination of mammalian cells carrying the receptor kinase, dimerization of the kinases was stimulated and a signal was sent from the membrane fractions. Kim et al. also demonstrated that dimerization of the chimeric membrane protein, comprising fibroblast growth factor receptor and CRY2, could be controlled using light (Kim et al. 2014). These systems for controlling protein dimerization in membrane fractions provide novel experimental approaches for manipulating various biological processes.

In a further application of photoactivation, Duan et al. developed a system to control molecular motors and organelle distributions. They fused to the protein kinesis and localized CYR2 to organelle surfaces via cargo-specific membrane linkers. In cells expressing CIB1–kinesis, recruitment and transport of CRY2-labeled organelles could be controlled by blue-light illumination. In contrast with other studies, these authors demonstrated that mitochondria, peroxisomes, and lysosomes could be driven toward the cell periphery (Duan et al. 2015). In another study, light-dependent CRY2-CIB1 dimerization was used to influence cellular forces and mechanotransduction. Valon et al. fused CYR2 to the catalytic domain of RhoA and engineered CIB1 to maximize localization in plasma membranes or mitochondria. Upon blue-light illumination, the chimeric RhoA was targeted to plasma membranes and promoted cortical contractility. Moreover, after localization of chimeric RhoA to mitochondria, RhoA activity decreased and cell contractility was relaxed (Valon et al. 2017). These systems offer powerful tools for studying and controlling cellular processes.

CYR2-dependent optical control of protein–protein interactions has been used to control cell–matrix and/or cell–cell interactions. After expressing CRY2 on cell surfaces, Wegner and colleagues demonstrated binding of cells to CIBN-immobilizing substrates under blue-light illumination conditions (Yüz et al. 2019). These investigators also separately expressed CRY2 and CIBN on cell surfaces, and showed specific heterophilic interactions between the proteins that precisely controlled cell–cell interactions in space and time under blue-light conditions (Yüz et al. 2018). This system will facilitate studies of cell–cell interactions and the engineering of artificial tissues.

### 11.2.3 BLUF Applications

Optogenetic applications of BLUF are fewer than those with LOV and CRY, with only two reported examples. Nonetheless, BLUF was used to control gene expression and the synthesis of nucleotide second messengers such as cAMP and cGMP, as described below.

#### 11.2.3.1 Regulation of Gene Expression by BLUF

Upon dark adaptation, the cyanobacterial BLUF protein PixD forms a large oligomeric complex with the transcription factor-like protein PixE following interactions between decameric PixD and four ($PixD_{10}$–$PixE_4$) or five ($PixD_{10}$–$PixE_5$) monomeric PixE proteins. Under these conditions, PixE function is inhibited, but excitation with blue-light illumination results in disassembly of PixD–PixE complexes, and the release of active PixE, which inhibits phototaxis of the bacterium. Masuda et al. used this light-dependent PixD–PixE interaction to control gene expression in their studies; the system is designated as PixD-complex-dependent control (PICCORO) (Masuda et al. 2013; Masuda and Tanaka 2016). To this end, they fused the PixE N-terminus to the dominant negative version of the transcription factor No Tail (Ntl). Subsequent oligomerization of the chimeric transcription factor PixE–Ntl led to inhibition of transcription after transfection into zebrafish constitutively expressing PixD. Crucially, under dark conditions, the formation of PixD oligomers with PixE–Ntl prevented transcriptional inhibition by PixE–Ntl, which was released upon blue-light illumination and inhibited target transcription. Light-dependent interactions between PixD and PixE were also reportedly used to control the transcription factor GAL4 (Masuda et al. 2013).

#### 11.2.3.2 Regulation of Nucleotide Second-Messenger Synthesis/Hydrolases by BLUF

The BLUF protein was originally identified in *E. gracilis* as a PAC (Iseki et al. 2002). Later, many BLUF proteins were identified in bacterial species as multi-domain proteins that function as synthases and hydrolases of nucleotide second messengers, including cAMP and c-di-GMP (Barends et al. 2009; Kanazawa et al. 2010; Ryu et al. 2010, 2017; Stierl et al. 2011). Some of these enzymes have functions in multiple organisms (Hartmann et al. 2013; Nagahama et al. 2007; Ryu et al. 2010; Schröder-Lang et al. 2007; Stierl et al. 2011; Weissenberger et al. 2011), lending potential to their applications as optogenetic tools. Ryu et al. converted a BLUF-containing cAMP synthase to a photoactivatable cGMP synthase (Ryu et al. 2010), further demonstrating the use of BLUF proteins as molecular foundations for the construction of artificial photoactivatable nucleotide second-messenger synthase/hydrolases that control cellular signaling and function in various organisms following activation with blue light.

**Acknowledgments** Research on photoreceptor functions of the authors was partly supported by MEXT/JSPPS KAKENHI Grant Numbers 19H04719 and 19K22418.

## References

Ahmad M, Cashmore AR (1993) HY4 gene of *A. thaliana* encodes a protein with characteristics of a blue-light photoreceptor. Nature 366:162–166. https://doi.org/10.1038/366162a0

Ahmad M, Grancher N, Heil M, Black RC, Giovani B, Galland P, Lardemer D (2002) Action spectrum for cryptochrome-dependent hypocotyl growth inhibition in *Arabidopsis*. Plant Physiol 129:774–785. https://doi.org/10.1104/pp.010969

Anderson S, Dragnea V, Masuda S, Ybe J, Moffat K, Bauer C (2005) Structure of a novel photoreceptor, the BLUF domain of AppA from *Rhodobacter sphaeroides*. Biochemistry 44:7998. https://doi.org/10.1021/bi0502691

Balland V, Byrdin M, Eker APM, Ahmad M, Brettel K (2009) What makes the difference between a cryptochrome and DNA photolyase? A spectroelectrochemical comparison of the flavin redox transitions. J Am Chem Soc 131:426–427. https://doi.org/10.1021/ja806540j

Barends TRM, Hartmann E, Griese JJ, Beitlich T, Kirienko NV, Ryjenkov DA, Reinstein J, Shoeman RL, Gomelsky M, Schlichting I (2009) Structure and mechanism of a bacterial light-regulated cyclic nucleotide phosphodiesterase. Nature 459:1015–1018. https://doi.org/10.1038/nature07966

Baumschlager A, Aoki SK, Khammash M (2017) Dynamic blue light-inducible T7 RNA polymerases

(Opto-T7RNAPs) for precise spatiotemporal gene expression control. ACS Synth Biol 6:2157–2167. https://doi.org/10.1021/acssynbio.7b00169

Benedetti L, Barentine AES, Messa M, Wheeler H, Bewersdorf J, De Camilli P (2018) Light-activated protein interaction with high spatial subcellular confinement. Proc Natl Acad Sci U S A 115:E2238–E2245. https://doi.org/10.1073/pnas.1713845115

Biskup T, Schleicher E, Okafuji A, Link G, Hitomi K, Getzoff ED, Weber S (2009) Direct observation of a photoinduced radical pair in a cryptochrome blue-light photoreceptor. Angew Chem Int Ed 48:404–407. https://doi.org/10.1002/anie.200803102

Bonger KM, Rakhit R, Payumo AY, Chen JK, Wandless TJ (2014) General method for regulating protein stability with light. ACS Chem Biol 9:111–115. https://doi.org/10.1021/cb400755b

Borgstahl GEO, Williams DR, Getzoff ED (1995) 1.4 Å structure of photoactive zellow protein, a cytosolic photoreceptor: unusual fold, active site, and chromophore. Biochemistry 34:6278–6287. https://doi.org/10.1021/bi00019a004

Bouly J-P, Schleicher E, Dionisio-Sese M, Vandenbussche F, Van Der Straeten D, Bakrim N, Meier S, Batschauer A, Galland P, Bittl R, Ahmad M (2007) Cryptochrome blue light photoreceptors are activated through interconversion of flavin redox states. J Biol Chem 282:9383–9391. https://doi.org/10.1074/jbc.M609842200

Brautigam CA, Smith BS, Ma Z, Palnitkar M, Tomchick DR, Machius M, Deisenhofer J (2004) Structure of the photolyase-like domain of cryptochrome 1 from *Arabidopsis thaliana*. Proc Natl Acad Sci U S A 101:12142–12147. https://doi.org/10.1073/pnas.0404851101

Brudler R, Hitomi K, Daiyasu H, Toh H, Kucho K, Ishiura M, Kanehisa M, Roberts VA, Todo T, Tainer JA, Getzoff ED (2003) Identification of a new cryptochrome class. Structure, function, and evolution. Mol Cell 11:59–67. https://doi.org/10.1016/s1097-2765(03)00008-x

Cao Z, Livoti E, Losi A, Gärtner W (2010) A blue light-inducible phosphodiesterase activity in the cyanobacterium *Synechococcus elongatus*. Photochem Photobiol 86:606–611. https://doi.org/10.1111/j.1751-1097.2010.00724.x

Cashmore AR, Jarillo JA, Wu YJ, Liu D (1999) Cryptochromes: blue light receptors for plants and animals. Science 284:760–765. https://doi.org/10.1126/science.284.5415.760

Chang K-Y, Woo D, Jung H, Lee S, Kim S, Won J, Kyung T, Park H, Kim N, Yang HW, Park J-Y, Hwang EM, Kim D, Do Heo W (2014) Light-inducible receptor tyrosine kinases that regulate neurotrophin signalling. Nat Commun 5:4057. https://doi.org/10.1038/ncomms5057

Christie JM, Salomon M, Nozue K, Wada M, Briggs WR (1999) LOV (light, oxygen, or voltage) domains of the blue-light photoreceptor phototropin (nph1): binding sites for the chromophore flavin mononucleotide. Proc Natl Acad Sci 96:8779–8783. https://doi.org/10.1073/pnas.96.15.8779

Crosson S, Moffat K (2001) Structure of a flavin-binding plant photoreceptor domain: insights into light-mediated signal transduction. Proc Natl Acad Sci U S A 98:2995–3000. https://doi.org/10.1073/pnas.051520298

Crosson S, Moffat K (2002) Photoexcited structure of a plant photoreceptor domain reveals a light-driven molecular switch. Plant Cell 14:1067–1075. https://doi.org/10.1105/TPC.010475

Csanaky K, Hess MW, Klimaschewski L (2019) Membrane-associated, not cytoplasmic or nuclear, FGFR1 induces neuronal differentiation. Cells 8:243. https://doi.org/10.3390/cells8030243

Damiani MJ, Yalloway GN, Lu J, McLeod NR, O'Neill MA (2009) Kinetic stability of the flavin semiquinone in photolyase and cryptochrome-DASH. Biochemistry 48:11399–11411. https://doi.org/10.1021/bi901371s

Domratcheva T, Hartmann E, Schlichting I, Kottke T (2016) Evidence for tautomerisation of glutamine in BLUF blue light receptors by vibrational spectroscopy and computational chemistry. Sci Rep 6:22669. https://doi.org/10.1038/srep22669

Duan L, Che D, Zhang K, Ong Q, Guo S, Cui B (2015) Optogenetic control of molecular motors and organelle distributions in cells. Chem Biol 22:671–682. https://doi.org/10.1016/J.CHEMBIOL.2015.04.014

Fujisawa T, Takeuchi S, Masuda S, Tahara T (2014) Signaling-state formation mechanism of a BLUF protein PapB from the purple bacterium *Rhodopseudomonas palustris* studied by femtosecond time-resolved absorption spectroscopy. J Phys Chem B 118:14761–14773. https://doi.org/10.1021/jp5076252

Furuya A, Kawano F, Nakajima T, Ueda Y, Sato M (2017) Assembly domain-based optogenetic system for the efficient control of cellular signaling. ACS Synth Biol 6:1086–1095. https://doi.org/10.1021/acssynbio.7b00022

Gauden M, van Stokkum IHM, Key JM, Luhrs DC, van Grondelle R, Hegemann P, Kennis JTM (2006) Hydrogen-bond switching through a radical pair mechanism in a flavin-binding photoreceptor. Proc Natl Acad Sci 103:10895–10900. https://doi.org/10.1073/pnas.0600720103

Gegear RJ, Casselman A, Waddell S, Reppert SM (2008) Cryptochrome mediates light-dependent magnetosensitivity in *Drosophila*. Nature 454:1014–1018. https://doi.org/10.1038/nature07183

Gegear RJ, Foley LE, Casselman A, Reppert SM (2010) Animal cryptochromes mediate magnetoreception by an unconventional photochemical mechanism. Nature 463:804–807. https://doi.org/10.1038/nature08719

Glantz ST, Berlew EE, Jaber Z, Schuster BS, Gardner KH, Chow BY (2018) Directly light-regulated binding of RGS-LOV photoreceptors to anionic membrane phospholipids. Proc Natl Acad Sci U S A 115:E7720–E7727. https://doi.org/10.1073/pnas.1802832115

Gomelsky M, Klug G (2002) BLUF: a novel FAD-binding domain involved in sensory transduction in microorganisms. Trends Biochem Sci 27:497–500

Grusch M, Schelch K, Riedler R, Reichhart E, Differ C, Berger W, Inglés-Prieto Á, Janovjak H (2014) Spatio-temporally precise activation of engineered receptor tyrosine kinases by light. EMBO J 33:1713–1726. https://doi.org/10.15252/embj.201387695

Guntas G, Hallett RA, Zimmerman SP, Williams T, Yumerefendi H, Bear JE, Kuhlman B (2015) Engineering an improved light-induced dimer (iLID) for controlling the localization and activity of signaling proteins. Proc Natl Acad Sci 112:112–117. https://doi.org/10.1073/pnas.1417910112

Haigney A, Lukacs A, Zhao R-K, Stelling AL, Brust R, Kim R-R, Kondo M, Clark I, Towrie M, Greetham GM, Illarionov B, Bacher A, Römisch-Margl W, Fischer M, Meech SR, Tonge PJ (2011) Ultrafast infrared spectroscopy of an isotope-labeled photoactivatable flavoprotein. Biochemistry 50:1321–1328. https://doi.org/10.1021/bi101589a

Hartmann A, Arroyo-Olarte RD, Imkeller K, Hegemann P, Lucius R, Gupta N (2013) Optogenetic modulation of an adenylate cyclase in toxoplasma gondii demonstrates a requirement of the parasite cAMP for host-cell invasion and stage differentiation. J Biol Chem 288:13705–13717. https://doi.org/10.1074/jbc.M113.465583

Hasenjäger S, Trauth J, Hepp S, Goenrich J, Essen L-O, Taxis C (2019) Optogenetic downregulation of protein levels with an ultrasensitive switch. ACS Synth Biol 8:1026–1036. https://doi.org/10.1021/acssynbio.8b00471

Heintz U, Schlichting I (2016) Blue light-induced LOV domain dimerization enhances the affinity of Aureochrome 1a for its target DNA sequence. Elife 5: e11860. https://doi.org/10.7554/eLife.11860

Hermann A, Liewald JF, Gottschalk A (2015) A photosensitive degron enables acute light-induced protein degradation in the nervous system. Curr Biol 25: R749–R750. https://doi.org/10.1016/j.cub.2015.07.040

Hitomi K, Okamoto K, Daiyasu H, Miyashita H, Iwai S, Toh H, Ishiura M, Todo T (2000) Bacterial cryptochrome and photolyase: characterization of two photolyase-like genes of *Synechocystis* sp. PCC6803. Nucleic Acids Res 28:2353–2362. https://doi.org/10.1093/nar/28.12.2353

Huala E, Oeller PW, Liscum E, Han IS, Larsen E, Briggs WR (1997) *Arabidopsis* NPH1: a protein kinase with a putative redox-sensing domain. Science 278:2120–2123. https://doi.org/10.1126/science.278.5346.2120

Iseki M, Matsunaga S, Murakami A, Ohno K, Shiga K, Yoshida K, Sugai M, Takahashi T, Hori T, Watanabe M (2002) A blue-light-activated adenylyl cyclase mediates photoavoidance in *Euglena gracilis*. Nature 415:1047–1051. https://doi.org/10.1038/4151047a

Iwata T, Zhang Y, Hitomi K, Getzoff ED, Kandori H (2010) Key dynamics of conserved asparagine in a cryptochrome/photolyase family protein by Fourier transform infrared spectroscopy. Biochemistry 49:8882–8891. https://doi.org/10.1021/bi1009979

Iwata T, Nagai T, Ito S, Osoegawa S, Iseki M, Watanabe M, Unno M, Kitagawa S, Kandori H (2018) Hydrogen bonding environments in the photocycle process around the Flavin chromophore of the AppA-BLUF domain. J Am Chem Soc 140:11982–11991. https://doi.org/10.1021/jacs.8b05123

Jung H, Kim S-W, Kim M, Hong J, Yu D, Kim JH, Lee Y, Kim S, Woo D, Shin H-S, Park BO, Do Heo W (2019) Noninvasive optical activation of Flp recombinase for genetic manipulation in deep mouse brain regions. Nat Commun 10:314. https://doi.org/10.1038/s41467-018-08282-8

Kagawa T, Sakai T, Suetsugu N, Oikawa K, Ishiguro S, Kato T, Tabata S, Okada K, Wada M (2001) Arabidopsis NPL1: a phototropin homolog controlling the chloroplast high-light avoidance response. Science 291:2138–2141. https://doi.org/10.1126/science.291.5511.2138

Kanazawa T, Ren S, Maekawa M, Hasegawa K, Arisaka F, Hyodo M, Hayakawa Y, Ohta H, Masuda S (2010) Biochemical and physiological characterization of a BLUF protein-EAL protein complex involved in blue light-dependent degradation of cyclic diguanylate in the purple bacterium *Rhodopseudomonas palustris*. Biochemistry 49:10647–10655. https://doi.org/10.1021/bi101448t

Kao Y-T, Tan C, Song S-H, Öztürk N, Li J, Wang L, Sancar A, Zhong D (2008) Ultrafast dynamics and anionic active states of the flavin cofactor in cryptochrome and photolyase. J Am Chem Soc 130:7695–7701. https://doi.org/10.1021/ja801152h

Kawano F, Suzuki H, Furuya A, Sato M (2015) Engineered pairs of distinct photoswitches for optogenetic control of cellular proteins. Nat Commun 6:6256. https://doi.org/10.1038/ncomms7256

Kennedy MJ, Hughes RM, Peteya LA, Schwartz JW, Ehlers MD, Tucker CL (2010) Rapid blue-light–mediated induction of protein interactions in living cells. Nat Methods 7:973–975. https://doi.org/10.1038/nmeth.1524

Kennis JTM, Crosson S, Gauden M, van Stokkum IHM, Moffat K, van Grondelle R (2003) Primary reactions of the LOV2 domain of phototropin, a plant blue-light photoreceptor. Biochemistry 42:3385–3392. https://doi.org/10.1021/BI034022K

Kim N, Kim JM, Lee M, Kim CY, Chang K-Y, Heo WD (2014) Spatiotemporal control of fibroblast growth factor receptor signals by blue light. Chem Biol 21:903–912. https://doi.org/10.1016/J.CHEMBIOL.2014.05.013

Kim MW, Wang W, Sanchez MI, Coukos R, von Zastrow M, Ting AY (2017) Time-gated detection of

protein-protein interactions with transcriptional readout. Elife 6:e30233. https://doi.org/10.7554/eLife.30233

Kim CK, Cho KF, Kim MW, Ting AY (2019) Luciferase-LOV BRET enables versatile and specific transcriptional readout of cellular protein-protein interactions. Elife 8:e43826. https://doi.org/10.7554/eLife.43826

Kinoshita T, Doi M, Suetsugu N, Kagawa T, Wada M, Shimazaki K (2001) phot1 and phot2 mediate blue light regulation of stomatal opening. Nature 414:656–660. https://doi.org/10.1038/414656a

Konermann S, Brigham MD, Trevino AE, Hsu PD, Heidenreich M, Le Cong L, Platt RJ, Scott DA, Church GM, Zhang F (2013) Optical control of mammalian endogenous transcription and epigenetic states. Nature 500:472–476. https://doi.org/10.1038/nature12466

Kottke T, Heberle J, Hehn D, Dick B, Hegemann P (2003) Phot-LOV1: photocycle of a blue-light receptor domain from the green alga *Chlamydomonas reinhardtii*. Biophys J 84:1192–1201. https://doi.org/10.1016/S0006-3495(03)74933-9

Kottke T, Batschauer A, Ahmad M, Heberle J (2006) Blue-light-induced changes in Arabidopsis cryptochrome 1 probed by FTIR difference spectroscopy. Biochemistry 45:2472–2479. https://doi.org/10.1021/bi051964b

Lerner AM, Yumerefendi H, Goudy OJ, Strahl BD, Kuhlman B (2018) Engineering improved photoswitches for the control of nucleocytoplasmic distribution. ACS Synth Biol 7:2898–2907. https://doi.org/10.1021/acssynbio.8b00368

Lin C, Robertson D, Ahmad M, Raibekas A, Jorns M, Dutton P, Cashmore A (1995) Association of flavin adenine dinucleotide with the *Arabidopsis* blue light receptor CRY1. Science 269:968–970. https://doi.org/10.1126/science.7638620

Liscum E, Briggs WR (1995) Mutations in the NPH1 locus of Arabidopsis disrupt the perception of phototropic stimuli. Plant Cell 7:473–485. https://doi.org/10.1105/tpc.7.4.473

Liu H, Yu X, Li K, Klejnot J, Yang H, Lisiero D, Lin C (2008) Photoexcited CRY2 interacts with CIB1 to regulate transcription and floral initiation in *Arabidopsis*. Science 322:1535–1539. https://doi.org/10.1126/science.1163927

Liu H, Gomez G, Lin S, Lin S, Lin C (2012) Optogenetic control of transcription in Zebrafish. PLoS One 7:e50738. https://doi.org/10.1371/journal.pone.0050738

Losi A, Gardner KH, Möglich A (2018) Blue-light receptors for optogenetics. Chem Rev 118:10659–10709. https://doi.org/10.1021/acs.chemrev.8b00163

Lu H, Mazumder M, Jaikaran ASI, Kumar A, Leis EK, Xu X, Altmann M, Cochrane A, Woolley GA (2019) A yeast system for discovering optogenetic inhibitors of eukaryotic translation initiation. ACS Synth Biol 8:744–757. https://doi.org/10.1021/acssynbio.8b00386

Lukacs A, Brust R, Haigney A, Laptenok SP, Addison K, Gil A, Towrie M, Greetham GM, Tonge PJ, Meech SR (2014) BLUF domain function does not require a metastable radical intermediate state. J Am Chem Soc 136:4605–4615. https://doi.org/10.1021/ja4121082

Lungu OI, Hallett RA, Choi EJ, Aiken MJ, Hahn KM, Kuhlman B (2012) Designing photoswitchable peptides using the AsLOV2 domain. Chem Biol 19:507–517. https://doi.org/10.1016/j.chembiol.2012.02.006

Ma Z, Du Z, Chen X, Wang X, Yang Y (2013) Fine tuning the LightOn light-switchable transgene expression system. Biochem Biophys Res Commun 440:419–423. https://doi.org/10.1016/j.bbrc.2013.09.092

Macheroux P, Kappes B, Ealick SE (2011) Flavogenomics—a genomic and structural view of flavin-dependent proteins. FEBS J 278:2625–2634. https://doi.org/10.1111/j.1742-4658.2011.08202.x

Mansouri M, Strittmatter T, Fussenegger M (2019) Light-controlled mammalian cells and their therapeutic applications in synthetic biology. Adv Sci 6:1800952. https://doi.org/10.1002/advs.201800952

Massey V (2000) The chemical and biological versatility of riboflavin. Biochem Soc Trans 28:283–296

Masuda S, Bauer CE (2002) AppA is a blue light photoreceptor that antirepresses photosynthesis gene expression in *Rhodobacter sphaeroides*. Cell 110:613–623. https://doi.org/10.1016/S0092-8674(02)00876-0

Masuda S, Tanaka M (2016) PICCORO: a technique for manipulating the activity of transcription factors with blue light. Methods Cell Biol 135:289–295. https://doi.org/10.1016/bs.mcb.2016.03.009

Masuda S, Hasegawa K, Ishii A, Ono T-A (2004) Light-induced structural changes in a putative blue-light receptor with a novel FAD binding fold sensor of blue-light using FAD (BLUF); Slr1694 of *Synechocystis* sp. PCC6803. Biochemistry 43:5304–5313. https://doi.org/10.1021/bi049836v

Masuda S, Hasegawa K, Ono T-A (2005) Light-induced structural changes of apoprotein and chromophore in the sensor of blue light using FAD (BLUF) domain of AppA for a signaling state. Biochemistry 44:1215–1224. https://doi.org/10.1021/bi047876t

Masuda S, Nakatani Y, Ren S, Tanaka M (2013) Blue light-mediated manipulation of transcription factor activity in vivo. ACS Chem Biol 8:2649–2653. https://doi.org/10.1021/cb400174d

Matiiv AB, Chekunova EM (2018) Aureochromes—blue light receptors. Biochemist 83:662–673. https://doi.org/10.1134/S0006297918060044

Miyatake H, Mukai M, Park S-Y, Adachi S, Tamura K, Nakamura H, Nakamura K, Tsuchiya T, Iizuka T, Shiro Y (2000) Sensory mechanism of oxygen sensor FixL from *Rhizobium meliloti*: crystallographic, mutagenesis and resonance raman spectroscopic studies 1 1Edited by K. Nagai. J Mol Biol 301:415–431. https://doi.org/10.1006/jmbi.2000.3954

Morais Cabral JH, Lee A, Cohen SL, Chait BT, Li M, Mackinnon R (1998) Crystal structure and functional analysis of the HERG potassium channel N terminus: a eukaryotic PAS domain. Cell 95:649–655. https://doi.org/10.1016/s0092-8674(00)81635-9

Motta-Mena LB, Reade A, Mallory MJ, Glantz S, Weiner OD, Lynch KW, Gardner KH (2014) An optogenetic

gene expression system with rapid activation and deactivation kinetics. Nat Chem Biol 10:196–202. https://doi.org/10.1038/nchembio.1430

Nagahama T, Suzuki T, Yoshikawa S, Iseki M (2007) Functional transplant of photoactivated adenylyl cyclase (PAC) into Aplysia sensory neurons. Neurosci Res 59:81–88. https://doi.org/10.1016/j.neures.2007.05.015

Nelson DC, Lasswell J, Rogg LE, Cohen MA, Bartel B (2000) FKF1, a clock-controlled gene that regulates the transition to flowering in *Arabidopsis*. Cell 101:331–340. https://doi.org/10.1016/s0092-8674(00)80842-9

Nihongaki Y, Suzuki H, Kawano F, Sato M (2014) Genetically engineered photoinducible homodimerization system with improved dimer-forming efficiency. ACS Chem Biol 9:617–621. https://doi.org/10.1021/cb400836k

Nihongaki Y, Yamamoto S, Kawano F, Suzuki H, Sato M (2015) CRISPR-Cas9-based photoactivatable transcription system. Chem Biol 22:169–174. https://doi.org/10.1016/j.chembiol.2014.12.011

Nihongaki Y, Furuhata Y, Otabe T, Hasegawa S, Yoshimoto K, Sato M (2017) CRISPR–Cas9-based photoactivatable transcription systems to induce neuronal differentiation. Nat Methods 14:963–966. https://doi.org/10.1038/nmeth.4430

Niopek D, Benzinger D, Roensch J, Draebing T, Wehler P, Eils R, Di Ventura B (2014) Engineering light-inducible nuclear localization signals for precise spatiotemporal control of protein dynamics in living cells. Nat Commun 5:4404. https://doi.org/10.1038/ncomms5404

Niopek D, Wehler P, Roensch J, Eils R, Di Ventura B (2016) Optogenetic control of nuclear protein export. Nat Commun 7:10624. https://doi.org/10.1038/ncomms10624

Ohki M, Sugiyama K, Kawai F, Tanaka H, Nihei Y, Unzai S, Takebe M, Matsunaga S, Adachi S, Shibayama N, Zhou Z, Koyama R, Ikegaya Y, Takahashi T, Tame JRH, Iseki M, Park S-Y (2016) Structural insight into photoactivation of an adenylate cyclase from a photosynthetic cyanobacterium. Proc Natl Acad Sci 113:6659–6664. https://doi.org/10.1073/pnas.1517520113

Ohki M, Sato-Tomita A, Matsunaga S, Iseki M, Tame JRH, Shibayama N, Park S-Y (2017) Molecular mechanism of photoactivation of a light-regulated adenylate cyclase. Proc Natl Acad Sci 114:8562–8567. https://doi.org/10.1073/pnas.1704391114

Öztürk N, Song S-H, Selby CP, Sancar A (2008) Animal type 1 cryptochromes. J Biol Chem 283:3256–3263. https://doi.org/10.1074/jbc.M708612200

Paonessa F, Criscuolo S, Sacchetti S, Amoroso D, Scarongella H, Pecoraro Bisogni F, Carminati E, Pruzzo G, Maragliano L, Cesca F, Benfenati F (2016) Regulation of neural gene transcription by optogenetic inhibition of the RE1-silencing transcription factor. Proc Natl Acad Sci 113:E91–E100. https://doi.org/10.1073/pnas.1507355112

Pathak GP, Spiltoir JI, Höglund C, Polstein LR, Heine-Koskinen S, Gersbach CA, Rossi J, Tucker CL (2017) Bidirectional approaches for optogenetic regulation of gene expression in mammalian cells using *Arabidopsis* cryptochrome 2. Nucleic Acids Res 45:e167–e167. https://doi.org/10.1093/nar/gkx260

Polstein LR, Gersbach CA (2012) Light-inducible spatiotemporal control of gene activation by customizable zinc finger transcription factors. J Am Chem Soc 134:16480–16483. https://doi.org/10.1021/ja3065667

Polstein LR, Gersbach CA (2015) A light-inducible CRISPR-Cas9 system for control of endogenous gene activation. Nat Chem Biol 11:198–200. https://doi.org/10.1038/nchembio.1753

Pudasaini A, El-Arab KK, Zoltowski BD (2015) LOV-based optogenetic devices: light-driven modules to impart photoregulated control of cellular signaling. Front Mol Biosci 2:18. https://doi.org/10.3389/fmolb.2015.00018

Quejada JR, Park S-HE, Awari DW, Shi F, Yamamoto HE, Kawano F, Jung JC, Yazawa M (2017) Optimized light-inducible transcription in mammalian cells using Flavin Kelch-repeat F-box1/GIGANTEA and CRY2/CIB1. Nucleic Acids Res 45:e172. https://doi.org/10.1093/nar/gkx804

Raffelberg S, Wang L, Gao S, Losi A, Gärtner W, Nagel G (2013) A LOV-domain-mediated blue-light-activated adenylate (adenylyl) cyclase from the cyanobacterium *Microcoleus chthonoplastes* PCC 7420. Biochem J 455:359–365. https://doi.org/10.1042/BJ20130637

Reade A, Motta-Mena LB, Gardner KH, Stainier DY, Weiner OD, Woo S (2017) TAEL: a zebrafish-optimized optogenetic gene expression system with fine spatial and temporal control. Development 144:345–355. https://doi.org/10.1242/dev.139238

Renicke C, Schuster D, Usherenko S, Essen L-O, Taxis C (2013) A LOV2 domain-based optogenetic tool to control protein degradation and cellular function. Chem Biol 20:619–626. https://doi.org/10.1016/j.chembiol.2013.03.005

Richter F, Fonfara I, Bouazza B, Schumacher CH, Bratovič M, Charpentier E, Möglich A (2016) Engineering of temperature- and light-switchable Cas9 variants. Nucleic Acids Res 44:10003–10014. https://doi.org/10.1093/nar/gkw930

Ricken J, Medda R, Wegner SV (2019) Photo-ECM: a blue light photoswitchable synthetic extracellular matrix protein for reversible control over cell–matrix adhesion. Adv Biosyst 3:1800302. https://doi.org/10.1002/adbi.201800302

Ritz T, Adem S, Schulten K (2000) A model for photoreceptor-based magnetoreception in birds. Biophys J 78:707–718. https://doi.org/10.1016/S0006-3495(00)76629-X

Ross TD, Lee HJ, Qu Z, Banks RA, Phillips R, Thomson M (2019) Controlling organization and forces in active matter through optically defined boundaries. Nature 572:224–229. https://doi.org/10.1038/s41586-019-1447-1

Rost BR, Schneider-Warme F, Schmitz D, Hegemann P (2017) Optogenetic tools for subcellular applications in neuroscience. Neuron 96:572–603. https://doi.org/10.1016/j.neuron.2017.09.047

Ryu M-H, Moskvin OV, Siltberg-Liberles J, Gomelsky M (2010) Natural and engineered photoactivated nucleotidyl cyclases for optogenetic applications. J Biol Chem 285:41501–41508. https://doi.org/10.1074/jbc.M110.177600

Ryu M-H, Fomicheva A, Moskvin OV, Gomelsky M (2017) Optogenetic module for dichromatic control of c-di-GMP signaling. J Bacteriol 199:e00014–e00017. https://doi.org/10.1128/JB.00014-17

Sakai T, Kagawa T, Kasahara M, Swartz TE, Christie JM, Briggs WR, Wada M, Okada K (2001) *Arabidopsis* nph1 and npl1: blue light receptors that mediate both phototropism and chloroplast relocation. Proc Natl Acad Sci 98:6969–6974. https://doi.org/10.1073/pnas.101137598

Salinas F, Rojas V, Delgado V, López J, Agosin E, Larrondo LF (2018) Fungal light-oxygen-voltage domains for optogenetic control of gene expression and flocculation in yeast. MBio 9:e00626–e00618. https://doi.org/10.1128/mBio.00626-18

Salomon M, Christie JM, Knieb E, Lempert U, Briggs WR (2000) Photochemical and mutational analysis of the FMN-binding domains of the plant blue light receptor, phototropin. Biochemistry 39:9401–9410. https://doi.org/10.1021/bi000585+

Salomon M, Eisenreich W, Durr H, Schleicher E, Knieb E, Massey V, Rudiger W, Muller F, Bacher A, Richter G (2001) An optomechanical transducer in the blue light receptor phototropin from *Avena sativa*. Proc Natl Acad Sci 98:12357–12361. https://doi.org/10.1073/pnas.221455298

Schröder-Lang S, Schwärzel M, Seifert R, Strünker T, Kateriya S, Looser J, Watanabe M, Kaupp UB, Hegemann P, Nagel G (2007) Fast manipulation of cellular cAMP level by light in vivo. Nat Methods 4:39–42. https://doi.org/10.1038/nmeth975

Seifert S, Ehrt C, Lückfeldt L, Lubeck M, Schramm F, Brakmann S (2019) Optical control of transcription—genetically encoded photoswitchable variants of T7 RNA polymerase. ChemBioChem 20:2813–2817. https://doi.org/10.1002/cbic.201900298

Sommer C, Dietz MS, Patschkowski T, Mathes T, Kottke T (2017) Light-induced conformational changes in the plant cryptochrome photolyase homology region resolved by selective isotope labeling and infrared spectroscopy. Photochem Photobiol 93:881–887. https://doi.org/10.1111/php.12750

Spiltoir JI, Strickland D, Glotzer M, Tucker CL (2016) Optical control of peroxisomal trafficking. ACS Synth Biol 5:554–560. https://doi.org/10.1021/acssynbio.5b00144

Stelling AL, Ronayne KL, Nappa J, Tonge PJ, Meech SR (2007) Ultrafast structural dynamics in BLUF domains: transient infrared spectroscopy of AppA and its mutants. J Am Chem Soc 129:15556–15564. https://doi.org/10.1021/JA074074N

Stierl M, Stumpf P, Udwari D, Gueta R, Hagedorn R, Losi A, Gärtner W, Petereit L, Efetova M, Schwarzel M, Oertner TG, Nagel G, Hegemann P (2011) Light modulation of cellular cAMP by a small bacterial photoactivated adenylyl cyclase, bPAC, of the soil bacterium *Beggiatoa*. J Biol Chem 286:1181–1188. https://doi.org/10.1074/jbc.M110.185496

Strickland D, Moffat K, Sosnick TR (2008) Light-activated DNA binding in a designed allosteric protein. Proc Natl Acad Sci U S A 105:10709–10714. https://doi.org/10.1073/pnas.0709610105

Strickland D, Lin Y, Wagner E, Hope CM, Zayner J, Antoniou C, Sosnick TR, Weiss EL, Glotzer M (2012) TULIPs: tunable, light-controlled interacting protein tags for cell biology. Nat Methods 9:379–384. https://doi.org/10.1038/nmeth.1904

Sun W, Zhang W, Zhang C, Mao M, Zhao Y, Chen X, Yang Y (2017) Light-induced protein degradation in human-derived cells. Biochem Biophys Res Commun 487:241–246. https://doi.org/10.1016/J.BBRC.2017.04.041

Swartz TE, Corchnoy SB, Christie JM, Lewis JW, Szundi I, Briggs WR, Bogomolni RA (2001) The photocycle of a flavin-binding domain of the blue light photoreceptor phototropin. J Biol Chem 276:36493–36500. https://doi.org/10.1074/jbc.M103114200

Tahara M, Takishima Y, Miyamoto S, Nakatsu Y, Someya K, Sato M, Tani K, Takeda M (2019) Photocontrollable mononegaviruses. Proc Natl Acad Sci U S A 116:11587–11589. https://doi.org/10.1073/pnas.1906531116

Takahashi J (1992) Circadian clock genes are ticking. Science 258:238–240. https://doi.org/10.1126/science.1384127

Takahashi F (2016) Blue-light-regulated transcription factor, Aureochrome, in photosynthetic stramenopiles. J Plant Res 129:189–197. https://doi.org/10.1007/s10265-016-0784-5

Takahashi F, Yamagata D, Ishikawa M, Fukamatsu Y, Ogura Y, Kasahara M, Kiyosue T, Kikuyama M, Wada M, Kataoka H (2007) AUREOCHROME, a photoreceptor required for photomorphogenesis in stramenopiles. Proc Natl Acad Sci 104:19625–19630. https://doi.org/10.1073/pnas.0707692104

Todo T, Ryo H, Yamamoto K, Toh H, Inui T, Ayaki H, Nomura T, Ikenaga M (1996) Similarity among the Drosophila (6-4)photolyase, a human photolyase homolog, and the DNA photolyase-blue-light photoreceptor family. Science 272:109–112. https://doi.org/10.1126/science.272.5258.109

Uchida A, Yajima M (2018) An optogenetic approach to control protein localization during embryogenesis of the sea urchin. Dev Biol 441:19–30. https://doi.org/10.1016/J.YDBIO.2018.06.015

Usherenko S, Stibbe H, Muscó M, Essen L-O, Kostina EA, Taxis C (2014) Photo-sensitive degron variants for tuning protein stability by light. BMC Syst Biol 8:128. https://doi.org/10.1186/s12918-014-0128-9

Valon L, Marín-Llauradó A, Wyatt T, Charras G, Trepat X (2017) Optogenetic control of cellular forces and mechanotransduction. Nat Commun 8:14396. https://doi.org/10.1038/ncomms14396

Wang X, Chen X, Yang Y (2012) Spatiotemporal control of gene expression by a light-switchable transgene system. Nat Methods 9:266–269. https://doi.org/10.1038/nmeth.1892

Wang H, Vilela M, Winkler A, Tarnawski M, Schlichting I, Yumerefendi H, Kuhlman B, Liu R, Danuser G, Hahn KM (2016) LOVTRAP: an optogenetic system for photoinduced protein dissociation. Nat Methods 13:755–758. https://doi.org/10.1038/nmeth.3926

Wang W, Wildes CP, Pattarabanjird T, Sanchez MI, Glober GF, Matthews GA, Tye KM, Ting AY (2017) A light- and calcium-gated transcription factor for imaging and manipulating activated neurons. Nat Biotechnol 35:864–871. https://doi.org/10.1038/nbt.3909

Weissenberger S, Schultheis C, Liewald JF, Erbguth K, Nagel G, Gottschalk A (2011) PACα—an optogenetic tool for in vivo manipulation of cellular cAMP levels, neurotransmitter release, and behavior in *Caenorhabditis elegans*. J Neurochem 116:616–625. https://doi.org/10.1111/j.1471-4159.2010.07148.x

Yang HQ, Wu YJ, Tang RH, Liu D, Liu Y, Cashmore AR (2000) The C termini of *Arabidopsis* cryptochromes mediate a constitutive light response. Cell 103:815–827. https://doi.org/10.1016/s0092-8674(00)00184-7

Yazawa M, Sadaghiani AM, Hsueh B, Dolmetsch RE (2009) Induction of protein-protein interactions in live cells using light. Nat Biotechnol 27:941–945. https://doi.org/10.1038/nbt.1569

Yu G, Onodera H, Aono Y, Kawano F, Ueda Y, Furuya A, Suzuki H, Sato M (2016) Optical manipulation of the alpha subunits of heterotrimeric G proteins using photoswitchable dimerization systems. Sci Rep 6:35777. https://doi.org/10.1038/srep35777

Yumerefendi H, Dickinson DJ, Wang H, Zimmerman SP, Bear JE, Goldstein B, Hahn K, Kuhlman B (2015) Control of protein activity and cell fate specification via light-mediated nuclear translocation. PLoS One 10:e0128443. https://doi.org/10.1371/journal.pone.0128443

Yumerefendi H, Lerner AM, Zimmerman SP, Hahn K, Bear JE, Strahl BD, Kuhlman B (2016) Light-induced nuclear export reveals rapid dynamics of epigenetic modifications. Nat Chem Biol 12:399–401. https://doi.org/10.1038/nchembio.2068

Yüz SG, Ricken J, Wegner SV (2018) Independent control over multiple cell types in space and time using orthogonal blue and red light switchable cell interactions. Adv Sci 5:1800446. https://doi.org/10.1002/advs.201800446

Yüz SG, Rasoulinejad S, Mueller M, Wegner AE, Wegner SV (2019) Blue light switchable cell–cell interactions provide reversible and spatiotemporal control towards bottom-up tissue engineering. Adv Biosyst 3:1800310. https://doi.org/10.1002/adbi.201800310

Ziegler T, Möglich A (2015) Photoreceptor engineering. Front Mol Biosci 2:30. https://doi.org/10.3389/fmolb.2015.00030

Zikihara K, Ishikawa T, Todo T, Tokutomi S (2008) Involvement of electron transfer in the photoreaction of Zebrafish cryptochrome-DASH. Photochem Photobiol 84:1016–1023. https://doi.org/10.1111/j.1751-1097.2007.00364.x

Zoltowski BD, Vaidya AT, Top D, Widom J, Young MW, Crane BR (2011) Structure of full-length *Drosophila* cryptochrome. Nature 480:396–399. https://doi.org/10.1038/nature10618

# Part III

# Optogenetics in Biological Systems

# Genetically Encoded Voltage Indicators 12

Irene Mollinedo-Gajate, Chenchen Song, and Thomas Knöpfel

**Abstract**

Optogenetic approaches combine the power to allocate optogenetic tools (proteins) to specific cell populations (defined genetically or functionally) and the use of light-based interfaces between biological wetware (cells and tissues) and hardware (controllers and recorders). The optogenetic toolbox contains two main compartments: tools to interfere with cellular processes and tools to monitor cellular events. Among the latter are genetically encoded voltage indicators (GEVIs). This chapter outlines the development, current state of the art and prospects of emerging optical GEVI imaging technologies.

**Keywords**

Genetically encoded voltage indicators · Neuronal circuits · Fluorescent protein · Förster resonance energy transfer · Action potential · Brain · Heart

## Abbreviations

| | |
|---|---|
| 2p | Two-photon |
| AAV | Adeno-associated virus |
| AMBER | Autonomous molecular bioluminescent reporter |
| Arch | Archaerhodopsin |
| CGH | Computer-generated holography |
| CNS | Central nervous system |
| cpFP | Circularly permuted FP |
| DPA | Dipicrylamine |
| FP | Fluorescent protein |
| FRET | Förster resonance energy transfer |
| GECI | Genetically encoded calcium indicator |
| GEVI | Genetically encoded voltage indicator |
| GFP | Green fluorescent protein |
| GRIN | Gradient index |
| NIR | Near-infrared range |
| ROI | Region of interest |
| SNR | Signal-to-noise ratio |
| VSD | Voltage-sensing domain |
| VSFP | Voltage-sensitive fluorescent protein |

## 12.1 Introduction

Voltage across plasma membranes has many biological functions. In electrically excitable cells such as neurons and cardiomyocytes, fluctuations of membrane voltage (action potentials and synaptic potentials) are central to their physiological role. In the heart, electrical signals coordinate the heartbeat; and in the brain, electrical signals generate perception, cognition and emotions. The large number of neurons

I. Mollinedo-Gajate · C. Song · T. Knöpfel (✉)
Laboratory for Neuronal Circuit Dynamics, Imperial College London, London, UK
e-mail: tknopfel@knopfel-lab.net



H. Yawo et al. (eds.), *Optogenetics*, Advances in Experimental Medicine and Biology 1293,
https://doi.org/10.1007/978-981-15-8763-4_12

even in a relatively small brain such as that of a mouse (about $7 \times 10^7$ neurons as compared to about $8 \times 10^{10}$ neurons in humans), and their intricate synaptic connectivity, highlights some of the challenges towards understanding the neuronal circuit mechanism underlying complex brain functions (Markram et al. 2015; Seeman et al. 2018). Additional complications result from the diversity of classes of neurons, each class characterised by distinct integrative properties, connectivity patterns and sensitivity to neurotransmitters and neuromodulators. Although the functional properties of a single representative muscle cell tell us much about the function of the whole muscle (contraction when activated), brain functions are by far less deducible from the actions of a few representative neurons. Instead, elucidation of neuronal circuit mechanisms requires an experimental approach that gives access to the electrical activities of a large number of neurons with known cell class identity and with a temporal resolution consistent with the millisecond timescale of synaptic communication. The widely employed calcium imaging helps to identify the spatial distribution of recruited neurons but fails to faithfully track fast sequential activation of neurons during formation of an assembly. Moreover, calcium imaging provides little or no data on hyperpolarising (inhibitory) and subthreshold depolarising (excitatory) signals continuously occurring in most neurons.

Optical voltage imaging has the potential to overcome these limitations inherent to calcium imaging. Optical voltage imaging, as a tool to investigate neuronal circuits, has a history longer than calcium imaging approaches, but has suffered from a lack of suitable voltage indicators and a lack of fast multi-cell imaging technologies. Only recently, genetically encoded voltage indicators (GEVIs) and genetically targetable voltage indicators ('hybrid GEVIs') with the necessary performance properties have become available (Bando et al. 2019a; Knopfel and Song 2019). Improved GEVIs and advances in optical imaging instrumentation now expand the use of voltage imaging technologies from a small group of specialised laboratories to a broader range of brain researchers.

## 12.2 Molecular Structure and Currently Available GEVIs

GEVIs monitor membrane voltage by sensing the electrical field across the plasma membrane. For that purpose, these probes must reside within or in close proximity to the plasma membrane. The discovery of green fluorescent protein (GFP) together with a deeper understanding of the functioning of voltage-gated ion channels enabled the generation of the first fluorescent GEVIs (Siegel and Isacoff 1997; Sakai et al. 2001). The earliest versions of GEVIs that showed robust voltage reports in mammalian cells were based on the molecular fusion of coding sequences of fluorescent proteins (FPs) and of an isolated voltage-sensing domain (VSD) that is homologous to the voltage sensor of voltage-gated ion channels (Dimitrov et al. 2007). These early GEVIs (dubbed voltage-sensitive fluorescent proteins; VSFPs) have been the precursors of a large palette of subsequent VSD-based GEVIs, with emission wavelengths covering a broad range of the visible spectrum. Following the invention of VSD-based GEVIs, a second major class of GEVIs based on naturally occurring microbial opsins was discovered. The current set of available GEVIs also contains bioluminescent GEVIs as well as hybrid GEVIs, the latter of which are partially, but not fully, genetically encoded. Most of the currently available GEVIs are broadly known by their often creative acronyms, but knowing their principal structural design scaffolds helps to keep an overview (Fig. 12.1) (Knopfel and Song 2019).

### 12.2.1 Voltage-Sensing Domain-Based GEVIs

Voltage-sensing domain (VSD)-based GEVIs include a wide range of indicators, where a VSD (whose origin can be either the invertebrate basal chordate *Ciona intestinalis* or the vertebrate

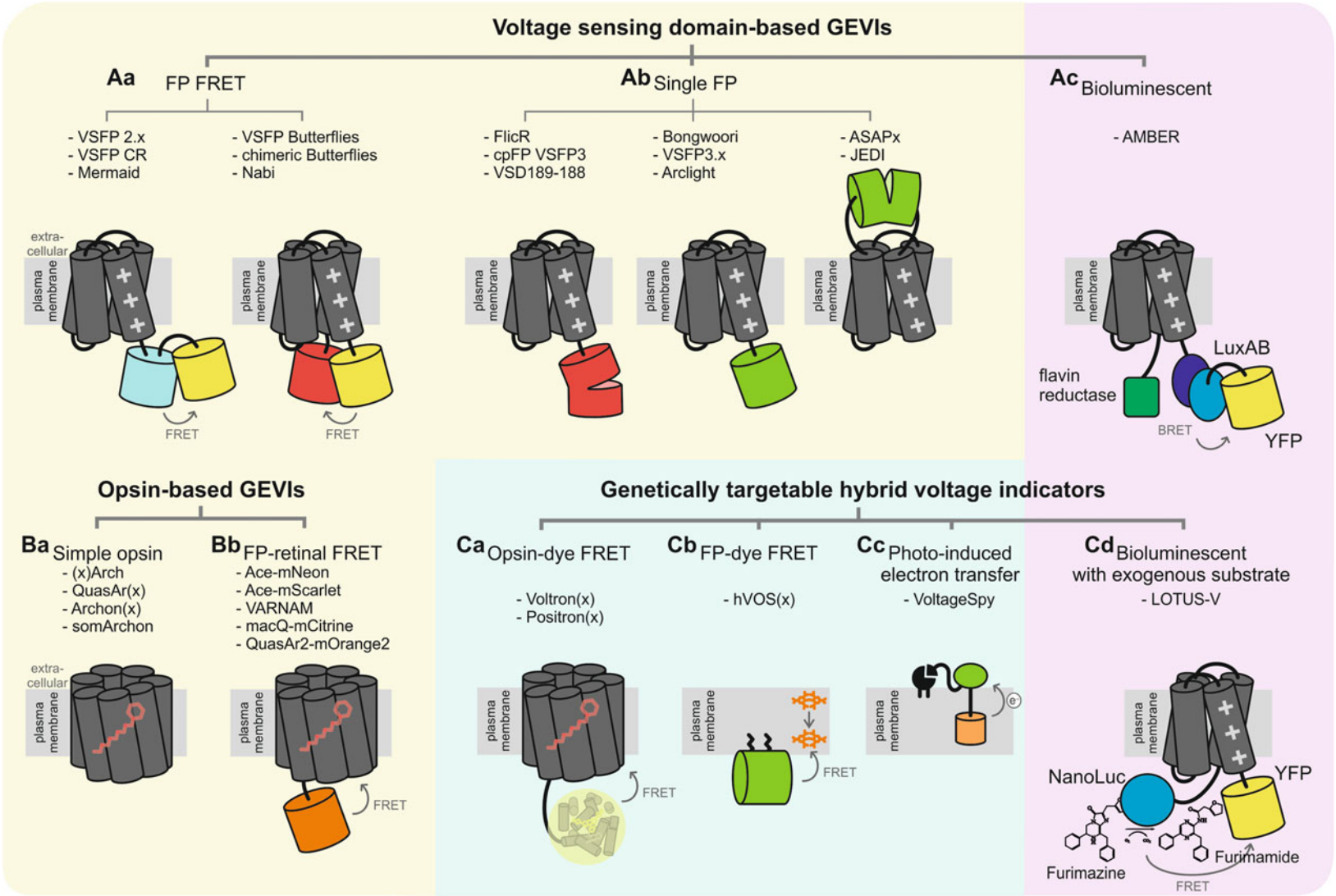
Voltage sensing domain-based GEVIs
Aa FP FRET
- VSFP 2.x
- VSFP CR
- Mermaid
- VSFP Butterflies
- chimeric Butterflies
- Nabi
Ab Single FP
- FlicR
- cpFP VSFP3
- VSD189-188
- Bongwoori
- VSFP3.x
- Arclight
- ASAPx
- JEDI
Ac Bioluminescent
- AMBER
extra-cellular
plasma membrane
FRET
LuxAB
flavin reductase
BRET
YFP
Opsin-based GEVIs
Ba Simple opsin
- (x)Arch
- QuasAr(x)
- Archon(x)
- somArchon
Bb FP-retinal FRET
- Ace-mNeon
- Ace-mScarlet
- VARNAM
- macQ-mCitrine
- QuasAr2-mOrange2
Genetically targetable hybrid voltage indicators
Ca Opsin-dye FRET
- Voltron(x)
- Positron(x)
Cb FP-dye FRET
- hVOS(x)
Cc Photo-induced electron transfer
- VoltageSpy
Cd Bioluminescent with exogenous substrate
- LOTUS-V
NanoLuc
YFP
Furimazine
Furimamide

**Fig. 12.1** Schematic depiction of GEVIs and hybrid GEVIs. (**Aa**) Fluorescent protein (FP) FRET-based GEVIs are engineered around a four transmembrane segment (S1–S4) voltage-sensing domain (dark grey) that spans in the plasma membrane. The efficacy of FRET increases upon plasma membrane depolarisation as the voltage sensor adopts its activated state. The FPs can be either in tandem configuration (e.g. VSFP2.x, Mermaid) or flanking the VSD (e.g. VSFP Butterflies). (**Ab**) Single FP GEVIs exhibit voltage-dependent fluorescence quenching. The FP can be in its native configuration (VSFP3x, ArcLight, Bongwoori) or in the form of a circularly permuted FP (cpFP indicated by opening of the FP structure) as, for example, in VSFP3 and FlicR. Both fusion of the FP to the C-terminus of the VSD (former examples) and insertion into the extracellular loop between transmembrane segments S3 and S4 (ASAPx, JEDI) have been successfully employed to develop GEVIs. (**Ac**) Autonomous bioluminescent GEVIs do not require fluorescence excitation and generate luminescence from an endogenous source of energy. (**Ba**) Simple opsin-based GEVIs exploit a voltage-dependent fluorescent state of their retinal chromophore. Prominent examples for this class are xArchs, QuasArs and Archons. (**Bb**) In order to address the dimness of simple opsin-based GEVIs, they have been combined with a bright FP that is quenched by the opsin in voltage-dependent fashion (e.g. Ace-mNeon, Ace-mScarlet, VARNAM, macQ-mCitrine, QuasarAr2-mOrange2). (**Ca**) Opsin-dye FRET hybrid GEVIs use an organic dye captured by a high affinity binding site engineered into the C-terminus of a voltage-dependent opsin (e.g. Voltron(x), Positron(x)). (**Cb**) FP-dye FRET GEVIs such as hVOS use a FP in combination with an exogenous organic quencher that distributes in the membrane in a voltage-dependent fashion, leading to voltage-dependent quenching of the FP. (**Cc**) Photoinduced electron transfer GEVIs exploit membrane voltage-dependent intramolecular quenching (e.g. VoltageSpy). (**Cd**) Bioluminescent hybrid GEVIs consume a substrate (luciferin or furimazine) that needs to be added to the system to induce luminescence. GEVIs named in the figure are as follows: VSFP2.x (Akemann et al. 2010); VSFP CR (Lam et al. 2012); Mermaid (Tsutsui et al. 2008); VSFP Butterflies (Akemann et al. 2012); Chimeric Butterflies (Mishina et al. 2014); Nabi (Sung et al. 2015); FlicR (Abdelfattah et al. 2016); cpFP VSFP3 (Gautam et al. 2009); VSD189–188 (Kost et al. 2017); Bongwoori (Lee et al. 2017); VSFP3(x) (Perron et al. 2009); Arclight (Jin et al. 2012); ASAP(x) (St-Pierre et al. 2014; Chamberland et al. 2017); (x)Arch (Kralj et al. 2011); QuasAr(x) (Hochbaum et al. 2014; Adam et al. 2019); Archon(x) (Piatkevich et al. 2018); Ace-mNeon (Gong et al. 2015); VARNAM (Kannan et al. 2018); Ace-mScarlet (Beck and Gong 2019) macQ-mCitrine (Gong et al. 2014); QuasAr2-mOrange2 (Zou et al. 2014); Voltron (Abdelfattah et al. 2019a); Positron (Abdelfattah et al. 2019b); hVOS(x) (Chanda et al. 2005; Bayguinov et al. 2017); VoltageSpy (Grenier et al. 2019); AMBER (Srinivasan et al. 2019); LOTUS-V (Inagaki et al. 2017)

*Gallus gallus*) is connected to one or more FPs (Fig. 12.1A). These indicators are further categorised into two families according to the number of attached FPs: FP FRET GEVIs, with two FPs and emission at two dissociable spectral bands; and single FP monochromatic GEVIs, which possess only one FP. In recent years, new VSD-based GEVIs have been generated with emission light covering not only the visible spectrum but also the near-infrared range.

#### 12.2.1.1 FP FRET GEVIs

These indicators (also termed ratiometric GEVIs) exploit the voltage-dependent Förster resonance energy transfer (FRET) between two FPs. Changes in membrane voltage modify the conformation of the VSD, and this is transduced into a change of the relative orientation of the two FPs, resulting in a modulation of FRET efficacy that, in turn, is read out as an anticorrelated change in donor and acceptor fluorescence. The emission fluorescence from both FPs is separated into two spectral channels, and detected by two different cameras or by two independent areas on the same detector when using a dual-view system.

The FP pair can either be attached to the VSD S4 in tandem (e.g. as in VSFP 2.3, VSFP CR and Mermaid (Sakai et al. 2001; Dimitrov et al. 2007; Tsutsui et al. 2008; Akemann et al. 2010; Lam et al. 2012)), or the two FPs can be sandwiching the VSD S1–S4 transmembrane segments (e.g. as in VSFP Butterflies, or Nabi (Akemann et al. 2012; Sung et al. 2015)). Generation of VSD chimeras via transplantation of segments from fast operating ion channels (e.g. Kv3.1 potassium channel) has been developed to improve kinetics in VSD-based GEVIs (e.g. chimeric VSFP Butterflies) (Mishina et al. 2012) (Fig. 12.1Aa).

Ratiometric GEVIs can be used for dual-emission imaging experiments since it is possible to capture both the acceptor and the donor emission wavelengths simultaneously. These indicators are of particular use for in vivo voltage imaging since voltage activity is reported by negatively correlated changes in donor and acceptor emission intensity, which can be separated from haemodynamic signals identified as correlated changes in donor and acceptor fluorescence (Akemann et al. 2010, 2012). However, for experiments using cultured cells or brain slices, imaging of only the acceptor or donor emission is likely to be sufficient for the reliable monitoring of voltage activity.

#### 12.2.1.2 Single FP GEVIs

Single FP GEVIs (also named monochromatic GEVIs) emit at a single spectral band, therefore may be less demanding in the optical imaging setup needed. These GEVIs allow to capture close to the full emission spectrum from the FP to maximise the sampling of useful photons. Nevertheless, when using these indicators for experiments in vivo in the mammalian brain, correction for haemodynamic and movement-related signals is more problematic than with ratiometric indicators. Multiplexing GEVI imaging with a reference signal or post hoc processing through subtraction of estimated haemodynamic signals may be used to overcome this issue (Borden et al. 2017).

The palette of monochromatic GEVIs includes variants of diverse colours by attaching FPs with different spectral properties to the fourth transmembrane domain of a VSD. The FP can be a FP in its native configuration (e.g. Arclight, Bongwoori, VSFP3x (Lundby et al. 2008; Perron et al. 2009; Jin et al. 2012; Lee et al. 2017)), or a circularly permuted FP (cpFP; e.g. cpFP-VSFP3x, FlicR (Gautam et al. 2009; Abdelfattah et al. 2016)). cpFP has also been fused extracellularly between the S3 and S4 transmembrane domains of *G. gallus* VSD to engineer the ASAPx family with high sensitivity and fast kinetics (St-Pierre et al. 2014; Chamberland et al. 2017; Villette et al. 2019) (Fig. 12.1Ab).

### 12.2.2 Opsin-Based GEVIs

The second main class of GEVIs (Fig. 12.1B) is designed utilising the native fluorescence of voltage-sensitive microbial opsins (Kralj et al. 2011), or by fusing the opsin to a bright FP. Several opsin-based GEVIs respond to changes in membrane voltage with large changes in fluorescence. The first members of this group

displayed dim fluorescence and hence required high excitation intensity and highly specific optical imaging setups to image (Kralj et al. 2011). A second potential caveat of these probes is the residual photocurrent that is observed even in nominally non-conducting channel mutants. However, the latest GEVIs that use rhodopsin fluorescence as readout have been successfully upgraded to improve brightness (Adam et al. 2019; Piatkevich et al. 2019).

An alternative strategy to address the brightness issue of early opsin-based GEVIs is to use a bright FP as readout while the opsin acts as a voltage-dependent quencher.

#### 12.2.2.1 Opsin GEVIs Using Rhodopsin Fluorescence

Protein engineering advances have recently made this group of GEVIs one of the leading candidates when reporting action potentials of individual cells in a population in vivo. These indicators report voltage fluctuations through voltage-dependent protonation of the Schiff base of the opsin retinal component that leads to chromophore absorption. The earliest example of this family used Archaerhodopsin (Arch). Although it operated at submillisecond scale, it suffered from dimness, thus required high excitation intensity, and it yielded an undesired photocurrent (Kralj et al. 2011). Later upgrades gave birth to the first generation QuasAr sensors (QuasAr1 and QuasAr2) (Hochbaum et al. 2014), and thereafter the second generation QuasAr indicators (QuasAr3, and photoactivated QuasAr—paQuasAr), with improved membrane targeting, small accompanying photocurrent and better signal-to-noise ratio (SNR) (Adam et al. 2019). Molecular modifications in Arch sensor led to the development of the Archon family of indicators (e.g. Archon1 (Piatkevich et al. 2018)), with several-fold higher brightness than its predecessor, while still displaying fast kinetics and sensitivity (Fig. 12.1Ba).

Indicators of this group are useful for all-optical electrophysiology approaches (Hochbaum et al. 2014) since they can be excited with wavelengths above 600 nm and emit in the near-infrared wavelength range. Therefore, they can be combined with blue-shifted optogenetic actuators within the same preparation with minimal spectral cross-talk, to both control and monitor membrane voltage.

#### 12.2.2.2 FRET-Opsin GEVIs

The molecular structure of these FRET-opsin GEVIs (also named FP-retinal FRET GEVIs) is based on the coupling of a rhodopsin protein to a bright FP. These sensors retain the opsin's fast kinetics and exploit the high quantum yield of the bright FP. In this case, the FP acts as the FRET donor, whereas the opsin acts as the FRET acceptor. These GEVIs are bright and fast enough to report action potentials in awake mice (Gong et al. 2015).

FPs such as the yellow FP mCitrine, the bright green FP mNeonGreen, or the orange FP mRuby3 and mScarlet, have been used to generate MacQ-mCitrine, Ace-mNeonGreen, VARNAM and Ace-mScarlet, respectively (Gong et al. 2014, 2015; Kannan et al. 2018; Beck and Gong 2019) (Fig. 12.1Bb).

### 12.2.3 Chemigenetic Hybrid GEVIs

GEVIs have the advantage of discriminating and targeting specific cells of interest within a population, but they can suffer from low brightness, poor photostability and sometimes slow kinetics. On the other hand, while the traditional small organic voltage-sensitive dyes are usually brighter than FPs, they cannot be targeted to specific cell types. Recently, these dyes have been tuned to precisely target the cells of interest using genetically encoded voltage protein tags (Sundukova et al. 2019). The structure of these probes encompasses two different components, the first one allows for targeting the indicator in defined cell types, whereas the second component is the fluorescent dye that needs to be delivered to the tissue, commonly via intravenous injection.

Chemigenetic or hybrid GEVIs (Fig. 12.1C) exploit genetically targetable proteins but require an exogenous chemical compound. In recent years, increasingly better performing GEVIs have been generated at a rapid pace. Newest

versions of GEVIs outperform organic voltage-sensitive dyes in many applications ranging from subcellular to circuit level. These probes may be good candidates for applications in vivo.

#### 12.2.3.1 Opsin-Dye FRET Chemigenetic Indicators

These probes combine the voltage sensitivity and fast kinetics (submillisecond scale) of microbial opsins, and the brightness and photostability of organic synthetic dyes. Genetic targeting of these hybrid indicators is achieved through genetic encoding of the voltage-sensing component, such as the opsin. Two of the most promising new series of GEVIs of this class are Voltron (Abdelfattah et al. 2019a) and Positron (Abdelfattah et al. 2019b) (Fig. 12.1Ca), where the opsin domain from the algae *Acetabularia acetabulum* is fused to a self-labelling protein tag that allows the covalent binding of a synthetic fluorophore dye ligand (e.g. Janelia Fluor dyes) (Grimm et al. 2015). Changes in membrane voltage modify the opsin absorption spectrum and thereby modulate fluorescence quenching of the dye component via FRET. Chemigenetic hybrid GEVIs have been successfully applied in in vivo voltage imaging in the mouse cortex, enabling recordings of spikes and subthreshold voltage signals from tens of neurons simultaneously with excellent SNR without trial averaging. Janelia Fluor dyes cover a wide range of the visible spectrum, allowing hence the development of Voltrons and Positrons in a variety of colours for multicolour imaging from different cell classes.

#### 12.2.3.2 FP-Dye FRET Hybrid Indicators

This class of hybrid dye indicators can also be led to specific cell types by genetic targeting of the fluorescent component (the FP), which is coupled to an exogenous chromophore (Chanda et al. 2005; Wang et al. 2010). This exogenous component (e.g. dipicrylamine, DPA; for the indicator hVOS) (Fig. 12.1Cb) needs to be applied to quench the FP fluorescence, with an efficacy that depends on the voltage-dependent distribution of DPA in the plasma membrane.

#### 12.2.3.3 Indicators Using Photoinduced Electron Transfer

Targeting of specific cell populations while still using fluorescein-based voltage-sensitive dyes can be achieved using fusion of the dye with the peptide SpyTag, which can covalently attach peptide-based cell surface receptors such as SpyCatcher (Grenier et al. 2019). Voltage sensing is achieved by photoinduced electron transfer through a synthetic molecular wire in the membrane to reversibly quench a synthetic fluorescent reporter (Fig. 12.1Cc).

### 12.2.4 Bioluminescent GEVIs

Bioluminescent GEVIs have recently been developed as promising candidates to overcome several limitations of FP-based GEVIs (Inagaki et al. 2017; Inagaki et al. 2019). The first set of bioluminescent voltage indicators consists of a VSD, a luciferase and an FP in a configuration analogous to FRET-based GEVIs. The luciferase produces light by chemical catalysis of an oxidative reaction of substrates (e.g. furimazine) that is administered externally (Fig. 12.1Cd). An increase in the membrane voltage produces a structural modification of the VSD, enhancing FRET between the light-emitting luciferase and the fluorescent protein. The main disadvantage of luciferase-based bioluminescent GEVIs is their requirement of exogenous substrate application. This issue has been addressed by recent advances in bioluminescent indicators that self-generate the energy-rich substrate (e.g. Autonomous Molecular BioluminEscent Reporter, AMBER) (Srinivasan et al. 2019) (Fig. 12.1Ac).

## 12.3 Biophysical Considerations of GEVIs

GEVIs and hybrid GEVIs, together with modern microscopy, have already begun to enable scientists to address basic research questions, beyond methodological proof of principle

experiments, in neuronal and cardiac systems (Scott et al. 2014; Fagerholm et al. 2016; Marshall et al. 2016; Quinn et al. 2016; Song et al. 2018; van Opbergen et al. 2018; Liu et al. 2019). In view of the broad variety of indicators currently available, prospective GEVI users would need to carefully select which indicator to use based on the research question, properties and available instrumentation. Over the last two decades, the chromatic palette of GEVIs has been expanded using fluorescent proteins with emission wavelengths covering from the visible to the infrared spectrum. Within these options, indicators that operate with longer wavelength light (red and near-infrared) are preferred, due to diminished light scattering in the tissue, decreased tissue autofluorescence and reduced absorption of fluorescence excitation and emission light by haemoglobin, thus facilitating imaging in deeper areas. The diverse spectral properties are particularly attractive for multicolour imaging, where the activity of distinct cell types can be optically monitored simultaneously through the expression of indicators of different colours. A number of GEVIs are compatible with two-photon (2p) microscopy, in which case the 2p cross section is a critical selection parameter.

Additional factors to consider are the GEVI photophysical and biophysical properties in the tissue of interest. GEVI imaging applications in intact brain tissue such as brain slices and living animals require the expression of the indicator over several weeks or months. Moreover, under these intact tissue conditions, SNR may be considerably lower (often by a factor of 10) than in cell culture systems (Akemann et al. 2010, 2012; Bando et al. 2019a, b; Quicke et al. 2019). Moving from imaging in brain slices to living animals comes with additional complications such as contamination of voltage signals by haemodynamic signals and movement artefacts that require particular attention (Akemann et al. 2010, 2012; Carandini et al. 2015).

## 12.4 Delivery of GEVI Genes

Classical organic voltage-sensitive dyes unselectively stain all cells within a preparation, hence are unable to distinguish between cell classes that have diverse circuit functions. GEVIs resolve this problem by enabling expression of the indicators in a cell-type-specific, and minimally invasive manner. Genetic targeting has the additional benefit of knowing the source of optical signals without acutely resolving the source. This allows imaging in living animals across defined population of neurons without single-cell level optical resolution. Genes encoding GEVIs need to be introduced into the preparation, and there are several widely employed approaches for GEVI gene delivery (Knopfel 2012).

*In utero electroporation*. Since its description in 2001, in utero electroporation has become a widely used standard tool for characterising optogenetic indicators and actuators in the rodent central nervous system (CNS) (Fukuchi-Shimogori and Grove 2001; Saito and Nakatsuji 2001; Tabata and Nakajima 2001). In a nutshell, the indicator gene along with an appropriate strong enhancer or promoter is contained in a plasmid which is injected into the lateral ventricle of an embryo through the uterus wall. The position of the electroporation electrodes and the embryonic stage will broadly determine the cell class that is targeted. For example, electroporation at mouse embryonic day 15.5 largely targets neural progenitor cells that develop into pyramidal neurons in cortical layers 2/3.

*Viral vectors*. The indicator gene is cloned into a virus plasmid to be packaged into a virus (often adeno-associated virus; AAV). Typically, the viruses are delivered through direct injection into the brain region of interest. The virus is taken up by cells near the injection area. Inside the cell, the virus releases its cargo, that is the expression construct for the indicator and, depending on the regulatory sequences, the indicator gene may be expressed. A promising recent

advance in viral delivery methods is based on virus capsids that pass the blood–brain barrier (e.g. *eB* serotype) (Chan et al. 2017). Using these novel capsids, AAVs for CNS neuronal transduction can be achieved by systemic injection of the AAVs into the peripheral blood stream, without damaging the CNS tissue of interest.

*Simple transgenesis*. The indicator gene, together with regulatory sequences from a cell-class-specific gene, is injected into a blastocyst (early stage embryo), which is then transplanted into a foster mouse. The offspring will randomly express the indicator with some having the gene integrated into the germline.

*Gene targeting and Cre-loxP system*. Gene targeting approaches allow for selection of a suitable (constitutively active) locus in the genome such as ROSA and TIGRE loci, (Zeng et al. 2008; Madisen et al. 2015). Specially useful are transgenic mice where the indicator gene expression is under inducible control (e.g. via a recombinase such as Cre). Along with appropriate Cre-driver mice, expression in specific cell types can be achieved by cross-breeding indicator mice and driver mice. Several inducible and conditional GEVI transgenic mouse lines are already available which capitalise on the rich and growing toolbox of driver lines using cell-class-specific promoters via the Cre-lox or transactivator systems to restrict indicator expression to specific cell types (Madisen et al. 2015).

*Combining Cre-driver mice and viral vectors*. The indicator gene can be present in a Cre-dependent configuration and delivered by a viral vector into Cre-driver transgenic mice. The indicator will be expressed where the virus infection and Cre-recombinase expression intersect.

## 12.5 Somatic and Sparse Targeting

GEVI signals are collected as photons emitted from regions of interest (ROIs). ROIs are typically not diffraction limited spots but volumes (defined by spatially extended indicator excitation and scattering of emitted photons) that usually contain a mixture of somata and processes from several or many neurons. Imaging of neuronal activities using genetically encoded calcium indicators (GECIs) yields movies of 'blinking' neuronal cell bodies caused by the calcium transients in the cytoplasm of the cells upon the occurrence of action potentials. Voltage signals, in contrast, are normally more spatially widespread throughout the neuronal processes. Because of this feature, voltage signals of individual cells are more susceptible to contamination by voltage signals of neighbouring cells and their processes imaged on the same pixels of detection.

Two conceptual approaches have been explored to reduce background noise associated with fluorescence from out-of-interest structures and improve the SNR in GEVI imaging: (1) limiting the expression of a GEVI to the cell body, and (2) expressing the GEVI sparsely. In somatic expression targeting, an amino acid motif derived from proteins that are naturally concentrated at the somatic plasma membrane (e.g. Kv2.1 potassium channels) is fused to the GEVI DNA sequence (Daigle et al. 2018; Piatkevich et al. 2019). This reduces the noise from optical signals originated from small processes not related to the cell of interest. Although somatic targeting facilitates the detection of single cells in vitro and in vivo, it compromises the detection of voltage changes in thin structures such as axons and dendrites, which is in fact one of the advantages of voltage imaging when compared to calcium imaging. Sparse expression of GEVIs in representative neurons within a dense population can be achieved by lowering the virus titre with the indicator gene. However, one should bear in mind that this approach can also diminish the expression levels of the indicator in the neurons of interest since mostly single copies would be delivered.

Fortunately, recent advances in intersectional expression approaches have enabled the sparse but strong expression of an indicator. This has been achieved by using two component systems, where a strong ubiquitous promoter (e.g. TET) drives strong GEVI expression (indicator expression component) but is itself under efficient control (e.g. via a transactivator) of a possibly weak but highly cell-class-specific promoter (cell selection component). Limiting the expression of the

transactivator (i.e. by using a virus at low titre or activation of the ttA expression cassette by limited recombination) reduces the number of expressing cells without affecting expression levels at the single-cell level (Chan et al. 2017; Song et al. 2017).

## 12.6 Imaging Approaches

Optical imaging of neuronal activity needs highly refined optical equipment. In fact, the use of GEVIs has been a driving force for tuning optical instrumentation for optimal performance. Voltage imaging experiments require high temporal resolution recording devices, efficient sampling of as many signalling photons as possible while limiting non-signalling photons. The use of optical filters to maximise excitation and emission intensity while minimising unblocked excitation light in the emission channel as well as the optimisation of collection of signal photons (large apertures, high detector quantum yield, etc.) are crucial aspects to optimise voltage signal readouts. Some of the instrumental approaches applied to GEVI imaging are summarised in the next sections.

### 12.6.1 Wide-Field Epifluorescence Imaging

Within this optical configuration, light of an appropriate wavelength is used to illuminate the whole field of view of an objective lens, and the emitted fluorescence signals are collected back through the same objective lens. Wide-field epifluorescence imaging is successfully used with high temporal resolution using the best performing GEVIs in cultured cells, brain slices and in vivo, owing to the large photon flux these GEVIs emit (Scott et al. 2014; Fagerholm et al. 2016; Marshall et al. 2016; Quinn et al. 2016; Song et al. 2018; van Opbergen et al. 2018; Liu et al. 2019). Although this technique is widely employed for cellular biology, scattered light from intact tissue strongly limits its applicability in deep tissue imaging conditions. Scattered light reduces spatial resolution and adds background noise to the signal, therefore it decreases the SNR.

Although single photon epifluorescence approach does not allow optical penetration much lower than 100 μm in mammalian brain tissues, deeper structures can be imaged by removing overlying tissue or by inserting optical components (e.g. microprisms or GRIN lenses; see Sect. 12.6.3) into the tissue.

### 12.6.2 Wide-Field Imaging with Patterned Illumination

Photons scattered from nearby areas can converge into the ROI at the image plane. This scattered light not only produces a background that reduces the contrast of the image but also produces shot noise that reduces the SNR. In order to overcome this issue, excitation light can be directed and limited specifically to an ROI. This can be achieved by the creation of a laser beam spot in the object plane ('spot illumination'), or using more complex equipment such as computer-generated holography (CGH) (Foust et al. 2015).

### 12.6.3 Deep Tissue Imaging Using GRIN Lenses

In imaging experiments in which the target region is inaccessible with a standard microscope objective, the implantation of a GRadient INdex (GRIN) lens may be necessary. These lenses can relay fluorescence emitted deep in the tissue. Their use is particularly convenient in combination with head-mounted microscopes (miniscopes), where they enable imaging of deep brain structures in freely moving animals. Such imaging configuration allows optical recordings of hundreds of neurons over a long timescale (e.g. weeks or months), for a better understanding of neural networks underlying behavioural patterns (Aharoni and Hoogland 2019; Barbera et al. 2019).

To date, this technique has been successfully performed using GECIs, as in general GECIs show larger and slower fluorescence variation (several milliseconds for onset, and several hundred milliseconds for decay). In contrast, GEVIs respond faster (millisecond-order) than GECIs,

making the detection of GEVI signals difficult with the sampling rate of the miniscopes available. However, promising preliminary studies envisage that in the near future miniscope-based voltage imaging will be also possible with implementation of faster cameras into miniscopes. This combination will enable advanced analysis of neuronal properties such as subthreshold voltage dynamics in awake, behaving animals.

### 12.6.4 Fibre Optic Imaging

Optical fibres allow imaging deeper into tissues at a high temporal resolution. In neuroscience, thin optical fibres are implanted into the brain in a minimally invasive manner to monitor neuronal activity in cortical and subcortical areas such as the hippocampus or the amygdala (Marshall et al. 2016; Miyamoto and Murayama 2016). This approach enables neuronal activity monitoring in head-fixed and freely moving behaving animals. These fibres consist of a core with a high refractive index covered by a lower refractive index material. Therefore, light beams are bidirectionally transmitted along both separate ends by internal reflections, resulting in faithful transmission of photons. Instead of a single fibre, fibre bundles have been used to obtain spatial resolution in combination with a CCD or CMOS camera that images the end of the fibre. But camera-based imaging systems have the disadvantage of imaging at a slower sampling rate. If voltage recordings at sub-milliseconds rate is required for particular research questions, then the use of a single fibre along with a photodiode or photomultiplier will be preferable.

### 12.6.5 Deep Tissue Imaging Using Two-Photon Excitation Fluorescence

Two-photon fluorescence microscopy is a widely adopted method for in vivo brain imaging that benefits from inherent optical sectioning properties to image in three dimensions. Laser scanning 2P microscopy combines efficient spot illumination with efficient collection of signal photons. Light scattering and absorption can impact imaging of deep tissues by decreasing both the excitation light and the emitted fluorescence, and thus decreasing the number of photons that reach the detector. However, infrared light is less phototoxic since native brain tissue has a relatively low infrared absorption and a low 2P cross section. For these reasons, two-photon line scanning microscopy is commonly used in neuroscience. This technique needs to balance between temporal resolution, spatial sampling and fluorescence excitation. Up to date, only a few GEVIs have been used for 2P imaging, such as the ratiometric VSFP Butterfly and the intensiometric ASAPs (Akemann et al. 2013; Chamberland et al. 2017). Recent instruments optimised for 2P voltage imaging are designed to excite small volumes rather than points using Bessel beam, light sheet illumination (Hillman et al. 2018; Kazemipour et al. 2019; Meng et al. 2019) or light-field microscopy (Nobauer et al. 2017; Skocek et al. 2018) to increase the flux of acquired emission photons.

## 12.7 GEVI Selection for a Particular Application

Selection of the most suitable GEVI for the application of interest is crucial to achieve best performance for the research at hand. Features like SNR, dynamic range, quantum yield, spectral properties, kinetics, selectivity and interference with blood changes and oxygenation, long-term stability, membrane targeting and localisation of the indicator are particularly important when carrying out in vivo or in vitro experiments.

*Dynamic range and signal-to-noise ratio.* This feature is one of the most crucial features when judging the performance of a GEVI. This dimensionless measurement states how many times brighter a GEVI in a depolarised state is when compared to the hyperpolarised state, under non-physiological conditions. In other words, how many times the maximal fluorescence intensity is compared to the minimal fluorescence intensity. However, more important

than the dynamic range is the SNR of an indicator in response to a physiological event (e.g. an action potential). This parameter is determined as the ratio between the fluorescence signal and the noise of the fluorescence baseline, $\Delta F/F = (F_{\text{signal}} - F_{\text{baseline}})/F_{\text{signal}}$.

*Optical output*. As mentioned in Sect. 12.2.1.2, instrumentation to image monochromatic GEVIs is less demanding than for ratiometric indicators (only one detector is needed), but the main caveat of monochromatic approaches is their incapacity to correctly separate optical signals that represent biological activities not related to membrane voltage changes, such as haemodynamic signals and movement artefacts. The former drawback is particularly problematic when performing conventional wide-field imaging, where population voltage signals are measured as rather small changes in fluorescence intensity. Sophisticated optics and data processing algorithms may be required to uniquely identify voltage-related signals while omitting the undesired external non-voltage-related responses in the optical signal. Another possible option is the use of ratiometric GEVIs, which allows for efficient separation of voltage signals and non-voltage-dependent signal sources (Akemann et al. 2012; Carandini et al. 2015). Some of the ratiometric GEVIs commonly used for this purpose include the VSFP Butterfly family, where the voltage-dependent VSD undergoes a conformational change as a result of voltage changes, which in turn alters FRET efficiency between the two FPs, resulting in anticorrelated fluorescence intensity changes between the FRET donor and acceptor FPs. VSFP Butterfly 1.2 contains a Ci-VSD flanked by a yellow (mCitrine; FRET donor) and a red (mKate2; FRET acceptor) FP (Akemann et al. 2012). This indicator consistently targets and localises within the membrane, and is capable of finely detecting subthreshold events. In vivo imaging experiments in awake mice have been successfully undertaken with this sensor (Akemann et al. 2012; Madisen et al. 2015). Further improvement of VSFP Butterfly 1.2 resulted in the chimeric VSFP Butterfly GEVIs, where the transplantation of a portion of the fast Kv3.1 potassium channel into Ci-VSD S4 transmembrane segment resulted in faster kinetic properties (Mishina et al. 2014).

*Spectral properties.* Regarding GEVI spectral variants, one should select a suitable indicator colour for the imaging approach and biological goal, considering that there could be a compromise between other indicator features such as response kinetics. The FPs of the currently available FP-based GEVIs offer an array of colours covering excitation and emission wavelengths over the entire visible spectrum (400–700 nm) and near-infrared range (NIR) (>700 nm). Nonetheless, opsin-based GEVIs (without a FP constituent) feature a more limited spectra (red/NIR band) although the inclusion of a FP component in their structure (hybrid FRET-opsin GEVIs) offers a wider spectral range coverage. The use of GEVIs able to operate within the NIR range is specially beneficial when working in deep tissue as they experience less tissue-related light scattering and autofluorescence, as well as less unwanted haemodynamic signals. Additionally, NIR GEVIs allow the combination of optical voltage imaging with opsin-based optogenetic manipulation, as well as combination with other optical probes, such as the green calcium indicator GCaMP6, for studies of neuronal circuits.

*Kinetics.* Kinetic properties are also features to consider when choosing an indicator. Recent variants of VSD- and opsin-based GEVIs respond to changes in voltage within milliseconds, and are successfully activated and deactivated during fast occurring action potentials (Kralj et al. 2011; St-Pierre et al. 2014; Gong et al. 2015). Fast activation of an indicator is required for sufficient activation during fast action potentials, but fast deactivation kinetics need the recording of fluorescence at a fast sampling rate (1 kHz or above). The ideal GEVI for resolving an action potential detection therefore activates very fast but deactivates only as fast as necessary. Hybrid GEVIs that exploit photoinduced electron transfer are very fast in their performance, and faithfully record rapid changes in the membrane electric field. To date, the fastest GEVIs exhibit response time constants around 1 ms, although many of the broadly used GEVIs display much slower time

constants a few ms (to 10 s of ms) (Antic et al. 2016). In order to record single action potentials, the use of GEVIs with time constants not larger than 1–2 ms, as well as well-optimised instrumentation able to record single-cell resolution in intact tissue is necessary.

So far, the majority of voltage imaging experiments record fluctuations in population membrane potentials that are dominated by volume averaged postsynaptic potentials. These voltage signals are much slower than those of single action potentials. For this approach, GEVIs with slower response time constants are the best choice. Therefore, although it is still necessary to continue developing faster GEVIs, many biological processes such as synaptic potentials and population up-down states do not naturally occur at such fast pace, and many of the currently existing GEVIs have sufficient kinetic features to monitor these processes.

## 12.8 Perspective

GEVI-based voltage imaging is advancing to a stage enabling a broader range of laboratories to address timely circuit-level neuroscience research questions. However, the journey of GEVI development is only midway. One important forthcoming task will be to perform a systematic unbiased side-by-side profiling and cross-validation of the most promising GEVIs. Also, voltage imaging remains methodologically more challenging than calcium imaging. For instance, there is no broadly distributed off-the-shelf equipment that is optimised for GEVI imaging. Another uncompleted task is related to the fact that GEVI imaging provides very rich data, but we are only at the beginning to develop analysis methods (algorithms and user interfaces) that can help experimentalists to extract circuit-level information such as population dynamics, criticality, entropy and attractor dynamics.

**Acknowledgements** Work in our laboratory is supported by grants from the BRAIN initiative (US National Institutes of Health, U01MH109091, U01NS099573).

## References

Abdelfattah AS, Farhi SL, Zhao Y, Brinks D, Zou P, Ruangkittisakul A, Platisa J, Pieribone VA, Ballanyi K, Cohen AE, Campbell RE (2016) A bright and fast red fluorescent protein voltage Indicator that reports neuronal activity in organotypic brain slices. J Neurosci 36:2458–2472

Abdelfattah AS, Kawashima T, Singh A, Novak O, Liu H, Shuai Y, Huang YC, Campagnola L, Seeman SC, Yu J, Zheng J, Grimm JB, Patel R, Friedrich J, Mensh BD, Paninski L, Macklin JJ, Murphy GJ, Podgorski K, Lin BJ, Chen TW, Turner GC, Liu Z, Koyama M, Svoboda K, Ahrens MB, Lavis LD, Schreiter ER (2019a) Bright and photostable chemigenetic indicators for extended in vivo voltage imaging. Science 365:699–704

Abdelfattah AS, Valenti R, Wong A, Koyama M, Kim DS, Schreiter ER (2019b) A general approach to engineer positive-going eFRET voltage indicators. bioRxiv 690925

Adam Y, Kim JJ, Lou S, Zhao Y, Xie ME, Brinks D, Wu H, Mostajo-Radji MA, Kheifets S, Parot V, Chettih S, Williams KJ, Gmeiner B, Farhi SL, Linda M, Kelly Buchanan E, Kinsella I, Zhou D, Paninski L, Harvey CD, Zeng H, Arlotta P, Campbell RE, Adam E. Cohen. (2019) Voltage imaging and optogenetics reveal behaviour-dependent changes in hippocampal dynamics. Nature 569:413–417

Aharoni D, Hoogland TM (2019) Circuit investigations with open-source miniaturized microscopes: past, present and future. Front Cell Neurosci 13:141

Akemann W, Mutoh H, Perron A, Rossier J, Knopfel T (2010) Imaging brain electric signals with genetically targeted voltage-sensitive fluorescent proteins. Nat Methods 7:643–649

Akemann W, Mutoh H, Perron A, Park YK, Iwamoto Y, Knopfel T (2012) Imaging neural circuit dynamics with a voltage-sensitive fluorescent protein. J Neurophysiol 108:2323–2337

Akemann W, Sasaki M, Mutoh H, Imamura T, Honkura N, Knopfel T (2013) Two-photon voltage imaging using a genetically encoded voltage indicator. Sci Rep 3:2231

Antic SD, Empson RM, Knopfel T (2016) Voltage imaging to understand connections and functions of neuronal circuits. J Neurophysiol 116:135–152

Bando Y, Grimm C, Cornejo VH, Yuste R (2019a) Genetic voltage indicators. BMC Biol 17:71

Bando Y, Sakamoto M, Kim S, Ayzenshtat I, Yuste R (2019b) Comparative evaluation of genetically encoded voltage indicators. Cell Rep 26:802–13.e4

Barbera G, Liang B, Zhang L, Li Y, Lin DT (2019) A wireless miniScope for deep brain imaging in freely moving mice. J Neurosci Methods 323:56–60

Bayguinov PO, Ma Y, Gao Y, Zhao X, Jackson MB (2017) Imaging voltage in genetically defined neuronal subpopulations with a Cre recombinase-targeted hybrid voltage sensor. J Neurosci 37:9305–9319

Beck C, Gong Y (2019) A high-speed, bright, red fluorescent voltage sensor to detect neural activity. Sci Rep 9:15878

Borden PY, Ortiz AD, Waiblinger C, Sederberg AJ, Morrissette AE, Forest CR, Jaeger D, Stanley GB (2017) Genetically expressed voltage sensor ArcLight for imaging large scale cortical activity in the anesthetized and awake mouse. Neurophotonics 4:031212

Carandini M, Shimaoka D, Rossi LF, Sato TK, Benucci A, Knopfel T (2015) Imaging the awake visual cortex with a genetically encoded voltage indicator. J Neurosci 35:53–63

Chamberland S, Yang HH, Pan MM, Evans SW, Guan S, Chavarha M, Yang Y, Salesse C, Wu H, Wu JC, Clandinin TR, Toth K, Lin MZ, St-Pierre F (2017) Fast two-photon imaging of subcellular voltage dynamics in neuronal tissue with genetically encoded indicators. Elife 6:e25690

Chan KY, Jang MJ, Yoo BB, Greenbaum A, Ravi N, Wu WL, Sanchez-Guardado L, Lois C, Mazmanian SK, Deverman BE, Gradinaru V (2017) Engineered AAVs for efficient noninvasive gene delivery to the central and peripheral nervous systems. Nat Neurosci 20:1172–1179

Chanda B, Blunck R, Faria LC, Schweizer FE, Mody I, Bezanilla F (2005) A hybrid approach to measuring electrical activity in genetically specified neurons. Nat Neurosci 8:1619–1626

Daigle TL, Madisen L, Hage TA, Valley MT, Knoblich U, Larsen RS, Takeno MM, Huang L, Gu H, Larsen R, Mills M, Bosma-Moody A, Siverts LA, Walker M, Graybuck LT, Yao Z, Fong O, Nguyen TN, Garren E, Lenz GH, Chavarha M, Pendergraft J, Harrington J, Hirokawa KE, Harris JA, Nicovich PR, McGraw MJ, Ollerenshaw DR, Smith KA, Baker CA, Ting JT, Sunkin SM, Lecoq J, Lin MZ, Boyden ES, Murphy GJ, da Costa NM, Waters J, Li L, Tasic B, Zeng H (2018) A suite of transgenic driver and reporter mouse lines with enhanced brain-cell-type targeting and functionality. Cell 174:465–80.e22

Dimitrov D, He Y, Mutoh H, Baker BJ, Cohen L, Akemann W, Knopfel T (2007) Engineering and characterization of an enhanced fluorescent protein voltage sensor. PLoS One 2:e440

Fagerholm ED, Scott G, Shew WL, Song C, Leech R, Knopfel T, Sharp DJ (2016) Cortical entropy, mutual information and scale-free dynamics in waking mice. Cereb Cortex 26:3945–3952

Foust AJ, Zampini V, Tanese D, Papagiakoumou E, Emiliani V (2015) Computer-generated holography enhances voltage dye fluorescence discrimination in adjacent neuronal structures. Neurophotonics 2:021007

Fukuchi-Shimogori T, Grove EA (2001) Neocortex patterning by the secreted signaling molecule FGF8. Science 294:1071–1074

Gautam SG, Perron A, Mutoh H, Knopfel T (2009) Exploration of fluorescent protein voltage probes based on circularly permuted fluorescent proteins. Front Neuroeng 2:14

Gong Y, Wagner MJ, Zhong Li J, Schnitzer MJ (2014) Imaging neural spiking in brain tissue using FRET-opsin protein voltage sensors. Nat Commun 5:3674

Gong Y, Huang C, Li JZ, Grewe BF, Zhang Y, Eismann S, Schnitzer MJ (2015) High-speed recording of neural spikes in awake mice and flies with a fluorescent voltage sensor. Science 350:1361–1366

Grenier V, Daws BR, Liu P, Miller EW (2019) Spying on neuronal membrane potential with genetically targetable voltage indicators. J Am Chem Soc 41 (3):1349–1358

Grimm JB, English BP, Chen J, Slaughter JP, Zhang Z, Revyakin A, Patel R, Macklin JJ, Normanno D, Singer RH, Lionnet T, Lavis LD (2015) A general method to improve fluorophores for live-cell and single-molecule microscopy. Nat Methods 12(3):244–250, 3 p following 50

Hillman EM, Voleti V, Patel K, Li W, Yu H, Perez-Campos C, Benezra SE, Bruno RM, Galwaduge PT (2018) High-speed 3D imaging of cellular activity in the brain using axially-extended beams and light sheets. Curr Opin Neurobiol 50:190–200

Hochbaum DR, Zhao Y, Farhi SL, Klapoetke N, Werley CA, Kapoor V, Zou P, Kralj JM, Maclaurin D, Smedemark-Margulies N, Saulnier JL, Boulting GL, Straub C, Cho YK, Melkonian M, Wong GK, Harrison DJ, Murthy VN, Sabatini BL, Boyden ES, Campbell RE, Cohen AE (2014) All-optical electrophysiology in mammalian neurons using engineered microbial rhodopsins. Nat Methods 11:825–833

Inagaki S, Tsutsui H, Suzuki K, Agetsuma M, Arai Y, Jinno Y, Bai G, Daniels MJ, Okamura Y, Matsuda T, Nagai T (2017) Genetically encoded bioluminescent voltage indicator for multi-purpose use in wide range of bioimaging. Sci Rep 7:42398

Inagaki S, Agetsuma M, Ohara S, Iijima T, Yokota H, Wazawa T, Arai Y, Nagai T (2019) Imaging local brain activity of multiple freely moving mice sharing the same environment. Sci Rep 9:7460

Jin L, Han Z, Platisa J, Wooltorton JRA, Cohen LB, Pieribone VA (2012) Single action potentials and subthreshold electrical events imaged in neurons with a fluorescent protein voltage probe. Neuron 75:779–785

Kannan M, Vasan G, Huang C, Haziza S, Li JZ, Inan H, Schnitzer MJ, Pieribone VA (2018) Fast, in vivo voltage imaging using a red fluorescent indicator. Nat Methods 15:1108–1116

Kazemipour A, Novak O, Flickinger D, Marvin JS, Abdelfattah AS, King J, Borden PM, Kim JJ, Al-Abdullatif SH, Deal PE, Miller EW, Schreiter ER, Druckmann S, Svoboda K, Looger LL, Podgorski K (2019) Kilohertz frame-rate two-photon tomography. Nat Methods 16:778–786

Knopfel T (2012) Genetically encoded optical indicators for the analysis of neuronal circuits. Nat Rev Neurosci 13:687–700

Knopfel T, Song C (2019) Optical voltage imaging in neurons: moving from technology development to practical tool. Nat Rev Neurosci 20:719–727

Kost LA, Nikitin ES, Ivanova VO, Sung U, Putintseva EV, Chudakov DM, Balaban PM, Lukyanov KA, Bogdanov AM (2017) Insertion of the voltage-sensitive domain into circularly permuted red fluorescent protein as a design for genetically encoded voltage sensor. PLoS One 12:e0184225

Kralj JM, Douglass AD, Hochbaum DR, Maclaurin D, Cohen AE (2011) Optical recording of action potentials in mammalian neurons using a microbial rhodopsin. Nat Methods 9:90–95

Lam AJ, St-Pierre F, Gong Y, Marshall JD, Cranfill PJ, Baird MA, McKeown MR, Wiedenmann J, Davidson MW, Schnitzer MJ, Tsien RY, Lin MZ (2012) Improving FRET dynamic range with bright green and red fluorescent proteins. Nat Methods 9:1005–1012

Lee S, Geiller T, Jung A, Nakajima R, Song YK, Baker BJ (2017) Improving a genetically encoded voltage indicator by modifying the cytoplasmic charge composition. Sci Rep 7:8286

Liu M, Song C, Liang Y, Knopfel T, Zhou C (2019) Assessing spatiotemporal variability of brain spontaneous activity by multiscale entropy and functional connectivity. Neuroimage 198:198–220

Lundby A, Mutoh H, Dimitrov D, Akemann W, Knopfel T (2008) Engineering of a genetically encodable fluorescent voltage sensor exploiting fast Ci-VSP voltage-sensing movements. PLoS One 3:e2514

Madisen L, Garner AR, Shimaoka D, Chuong AS, Klapoetke NC, Li L, van der Bourg A, Niino Y, Egolf L, Monetti C, Gu H, Mills M, Cheng A, Tasic B, Nguyen TN, Sunkin SM, Benucci A, Nagy A, Miyawaki A, Helmchen F, Empson RM, Knopfel T, Boyden ES, Reid RC, Carandini M, Zeng H (2015) Transgenic mice for intersectional targeting of neural sensors and effectors with high specificity and performance. Neuron 85:942–958

Markram H, Muller E, Ramaswamy S, Reimann MW, Abdellah M, Sanchez CA, Ailamaki A, Alonso-Nanclares L, Antille N, Arsever S, Kahou GA, Berger TK, Bilgili A, Buncic N, Chalimourda A, Chindemi G, Courcol JD, Delalondre F, Delattre V, Druckmann S, Dumusc R, Dynes J, Eilemann S, Gal E, Gevaert ME, Ghobril JP, Gidon A, Graham JW, Gupta A, Haenel V, Hay E, Heinis T, Hernando JB, Hines M, Kanari L, Keller D, Kenyon J, Khazen G, Kim Y, King JG, Kisvarday Z, Kumbhar P, Lasserre S, Le Be JV, Magalhaes BR, Merchan-Perez A, Meystre J, Morrice BR, Muller J, Munoz-Cespedes A, Muralidhar S, Muthurasa K, Nachbaur D, Newton TH, Nolte M, Ovcharenko A, Palacios J, Pastor L, Perin R, Ranjan R, Riachi I, Rodriguez JR, Riquelme JL, Rossert C, Sfyrakis K, Shi Y, Shillcock JC, Silberberg G, Silva R, Tauheed F, Telefont M, Toledo-Rodriguez M, Trankler T, Van Geit W, Diaz JV, Walker R, Wang Y, Zaninetta SM, DeFelipe J, Hill SL, Segev I, Schurmann F (2015) Reconstruction and simulation of neocortical microcircuitry. Cell 163:456–492

Marshall JD, Li JZ, Zhang Y, Gong Y, St-Pierre F, Lin MZ, Schnitzer MJ (2016) Cell-type-specific optical recording of membrane voltage dynamics in freely moving mice. Cell 167:1650–62.e15

Meng G, Liang Y, Sarsfield S, Jiang WC, Lu R, Dudman JT, Aponte Y, Ji N (2019) High-throughput synapse-resolving two-photon fluorescence microendoscopy for deep-brain volumetric imaging in vivo. eLife 8: e40805

Mishina Y, Mutoh H, Knopfel T (2012) Transfer of Kv3.1 voltage sensor features to the isolated Ci-VSP voltage-sensing domain. Biophys J 103:669–676

Mishina Y, Mutoh H, Song C, Knopfel T (2014) Exploration of genetically encoded voltage indicators based on a chimeric voltage sensing domain. Front Mol Neurosci 7:78

Miyamoto D, Murayama M (2016) The fiber-optic imaging and manipulation of neural activity during animal behavior. Neurosci Res 103:1–9

Nobauer T, Skocek O, Pernia-Andrade AJ, Weilguny L, Traub FM, Molodtsov MI, Vaziri A (2017) Video rate volumetric Ca2+ imaging across cortex using seeded iterative demixing (SID) microscopy. Nat Methods 14:811–818

Perron A, Mutoh H, Launey T, Knopfel T (2009) Red-shifted voltage-sensitive fluorescent proteins. Chem Biol 16:1268–1277

Piatkevich KD, Jung EE, Straub C, Linghu C, Park D, Suk HJ, Hochbaum DR, Goodwin D, Pnevmatikakis E, Pak N, Kawashima T, Yang CT, Rhoades JL, Shemesh O, Asano S, Yoon YG, Freifeld L, Saulnier JL, Riegler C, Engert F, Hughes T, Drobizhev M, Szabo B, Ahrens MB, Flavell SW, Sabatini BL, Boyden ES (2018) A robotic multidimensional directed evolution approach applied to fluorescent voltage reporters. Nat Chem Biol 14:352

Piatkevich KD, Bensussen S, Tseng HA, Shroff SN, Lopez-Huerta VG, Park D, Jung EE, Shemesh OA, Straub C, Gritton HJ, Romano MF, Costa E, Sabatini BL, Fu Z, Boyden ES, Han X (2019) Population imaging of neural activity in awake behaving mice. Nature 574:413–417

Quicke P, Song C, McKimm EJ, Milosevic MM, Howe CL, Neil M, Schultz SR, Antic SD, Foust AJ, Knopfel T (2019) Single-neuron level one-photon voltage imaging with sparsely targeted genetically encoded voltage indicators. Front Cell Neurosci 13:39

Quinn TA, Camelliti P, Rog-Zielinska EA, Siedlecka U, Poggioli T, O'Toole ET, Knopfel T, Kohl P (2016) Electrotonic coupling of excitable and nonexcitable cells in the heart revealed by optogenetics. Proc Natl Acad Sci U S A 113:14852–14857

Saito T, Nakatsuji N (2001) Efficient gene transfer into the embryonic mouse brain using in vivo electroporation. Dev Biol 240:237–246

Sakai R, Repunte-Canonigo V, Raj CD, Knopfel T (2001) Design and characterization of a DNA-encoded,

voltage-sensitive fluorescent protein. Eur J Neurosci 13:2314–2318

Scott G, Fagerholm ED, Mutoh H, Leech R, Sharp DJ, Shew WL, Knopfel T (2014) Voltage imaging of waking mouse cortex reveals emergence of critical neuronal dynamics. J Neurosci 34:16611–16620

Seeman SC, Campagnola L, Davoudian PA, Hoggarth A, Hage TA, Bosma-Moody A, Baker CA, Lee JH, Mihalas S, Teeter C, Ko AL, Ojemann JG, Gwinn RP, Silbergeld DL, Cobbs C, Phillips J, Lein E, Murphy G, Koch C, Zeng H, Jarsky T (2018) Sparse recurrent excitatory connectivity in the microcircuit of the adult mouse and human cortex. eLife 7:e37349

Siegel MS, Isacoff EY (1997) A genetically encoded optical probe of membrane voltage. Neuron 19:735–741

Skocek O, Nobauer T, Weilguny L, Traub FM, Xia CN, Molodtsov MI, Grama A, Yamagata M, Aharoni D, Cox DD, Golshani P, Vaziri A (2018) High-speed volumetric imaging of neuronal activity in freely moving rodents. Nat Methods 15:429–432

Song C, Do QB, Antic SD, Knopfel T (2017) Transgenic strategies for sparse but strong expression of genetically encoded voltage and calcium indicators. Int J Mol Sci 18:1461

Song C, Piscopo DM, Niell CM, Knopfel T (2018) Cortical signatures of wakeful somatosensory processing. Sci Rep 8:11977

Srinivasan P, Griffin NM, Joshi P, Thakur D, Nguyen-Le A, McCotter S, Jain A, Saeidi M, Kulkarni P, Eisdorfer J, Rothman J, Montell C, Theogarajan L 2019 An autonomous molecular bioluminescent reporter (AMBER) for voltage imaging in freely moving animals. bioRxiv, 845198

St-Pierre F, Marshall JD, Yang Y, Gong Y, Schnitzer MJ, Lin MZ (2014) High-fidelity optical reporting of neuronal electrical activity with an ultrafast fluorescent voltage sensor. Nat Neurosci 17:884–889

Sundukova M, Prifti E, Bucci A, Kirillova K, Serrao J, Reymond L, Umebayashi M, Hovius R, Riezman H, Johnsson K, Heppenstall PA (2019) A chemogenetic approach for the optical monitoring of voltage in neurons. Angew Chem Int Ed Engl 58:2341–2344

Sung U, Sepehri-Rad M, Piao HH, Jin L, Hughes T, Cohen LB, Baker BJ (2015) Developing fast fluorescent protein voltage sensors by optimizing FRET interactions. PLoS One 10:e0141585

Tabata H, Nakajima K (2001) Efficient in utero gene transfer system to the developing mouse brain using electroporation: visualization of neuronal migration in the developing cortex. Neuroscience 103:865–872

Tsutsui H, Karasawa S, Okamura Y, Miyawaki A (2008) Improving membrane voltage measurements using FRET with new fluorescent proteins. Nat Methods 5:683–685

van Opbergen CJM, Koopman CD, Kok BJM, Knopfel T, Renninger SL, Orger MB, Vos MA, van Veen TAB, Bakkers J, de Boer TP (2018) Optogenetic sensors in the zebrafish heart: a novel in vivo electrophysiological tool to study cardiac arrhythmogenesis. Theranostics 8:4750–4764

Villette V, Chavarha M, Dimov IK, Bradley J, Pradhan L, Mathieu B, Evans SW, Chamberland S, Shi D, Yang R, Kim BB, Ayon A, Jalil A, St-Pierre F, Schnitzer MJ, Bi G, Toth K, Ding J, Dieudonne S, Lin MZ (2019) Ultrafast two-photon imaging of a high-gain voltage Indicator in awake behaving mice. Cell 179:1590–608.e23

Wang D, Zhang Z, Chanda B, Jackson MB (2010) Improved probes for hybrid voltage sensor imaging. Biophys J 99:2355–2365

Zeng H, Horie K, Madisen L, Pavlova MN, Gragerova G, Rohde AD, Schimpf BA, Liang Y, Ojala E, Kramer F, Roth P, Slobodskaya O, Dolka I, Southon EA, Tessarollo L, Bornfeldt KE, Gragerov A, Pavlakis GN, Gaitanaris GA (2008) An inducible and reversible mouse genetic rescue system. PLoS Genet 4:e1000069

Zou P, Zhao Y, Douglass AD, Hochbaum DR, Brinks D, Werley CA, Harrison DJ, Campbell RE, Cohen AE (2014) Bright and fast multicoloured voltage reporters via electrochromic FRET. Nat Commun 5:4625

# Visualization and Manipulation of Intracellular Signaling

13

Yuhei Goto, Yohei Kondo, and Kazuhiro Aoki

**Abstract**

Cells respond to a wide range of extracellular stimuli, and process the input information through an intracellular signaling system comprised of biochemical and biophysical reactions, including enzymatic and protein–protein interactions. It is essential to understand the molecular mechanisms underlying intracellular signal transduction in order to clarify not only physiological cellular functions but also pathological processes such as tumorigenesis. Fluorescent proteins have revolutionized the field of life science, and brought the study of intracellular signaling to the single-cell and subcellular levels. Much effort has been devoted to developing genetically encoded fluorescent biosensors based on fluorescent proteins, which enable us to visualize the spatiotemporal dynamics of cell signaling. In addition, optogenetic techniques for controlling intracellular signal transduction systems have been developed and applied in recent years by regulating intracellular signaling in a light-dependent manner. Here, we outline the principles of biosensors for probing intracellular signaling and the optogenetic tools for manipulating them.

**Keywords**

Optogenetics · FRET · Cryptochrome · Phytochrome · ERK

## Abbreviations

| | |
|---|---|
| bNLS | Bipartite nuclear localization sequence |
| BVRA | Biliverdin reductase A |
| cpFP | Circularly permutated FP |
| CRY2 | Cryptochrome 2 |
| EGF | Epidermal growth factor |
| FAD | Flavin adenine dinucleotide |
| FMN | Flavin mononucleotide |
| FP | Fluorescent protein |
| FRET | Förster (or fluorescence) resonance energy transfer |
| iRFP | Infra-red FP |
| KTR | Kinase translocation reporter |
| LOV | Light-oxygen-voltage sensing |
| NES | Nuclear export signal |
| PCB | Phycocyanobilin |
| PhyB | Phytochrome B |
| PΦB | Phytochromobilin |

Y. Goto · Y. Kondo · K. Aoki (✉)
Quantitative Biology Research Group, Exploratory Research Center on Life and Living Systems (ExCELLS), National Institutes of Natural Sciences, Okazaki, Aichi, Japan

Division of Quantitative Biology, National Institute for Basic Biology, National Institutes of Natural Sciences, Okazaki, Aichi, Japan

Department of Basic Biology, School of Life Science, SOKENDAI (The Graduate University for Advanced Studies), Okazaki, Aichi, Japan
e-mail: k-aoki@nibb.ac.jp



H. Yawo et al. (eds.), *Optogenetics*, Advances in Experimental Medicine and Biology 1293,
https://doi.org/10.1007/978-981-15-8763-4_13

## 13.1 Introduction

Cells sense extracellular input signals via receptors on their membranes or receptors within the cells themselves. They then process the input information, such as the types and dose of input stimuli, by means of an intracellular signal transduction system, which is a network of a wide array of biophysical and biochemical reactions (Oda et al. 2005). Finally, the cells decide their own fates in order to best adapt to the change in the extracellular environment. Mutations in the signal transduction genes disrupt the cellular homeostasis and cause diseases such as malignant tumors (Hanahan and Weinberg 2011.

The discovery and development of fluorescent proteins (FPs) and biosensors have offered a unique opportunity to visualize the dynamics of intracellular signal transduction in space and time (Miyawaki 2011). Interestingly, single-cell analysis with fluorescence imaging is increasingly revealing the mechanisms by which the dynamics of intracellular signaling encodes the information for cellular decision-making (Purvis and Lahav 2013). For instance, stochastic and pulsatile activation of ERK MAP kinase is observed in many types of proliferating cells, which constitutes strong evidence that cell proliferation is modulated by ERK activity (Albeck et al. 2013; Aoki et al. 2013) (Fig. 13.1a). Furthermore, the ERK activation propagates to neighboring cells, and epithelial cells collectively migrate in the opposite direction of this intercellular propagation of ERK activation (Hiratsuka et al. 2015; Aoki et al. 2017) (Fig. 13.1b). p53 is another good example; p53 shows a variety of activation dynamics—such as oscillation and sustained activation—in a manner dependent on stress inputs, and its dynamics control cell fate (Purvis et al. 2012).

The exquisite complexity observed in these intracellular dynamics raises the question how the cells decode the information to yield distinct cellular phenotypes. Synthetic biology approaches such as optogenetics are of particular importance to directly address these questions by controlling the signaling and examining the relationship between the dynamics and phenotypic outcomes. For example, the aforementioned spatiotemporal ERK activation dynamics has been recapitulated by optogenetics, and the synthetic oscillation and intercellular propagation of ERK activation indeed induced cell proliferation (Aoki et al. 2013) and collective cell migration (Aoki et al. 2017), respectively.

In this chapter, we overview the recent progress in biosensors and optogenetic tools. For more information, readers are urged to consult the recently published databases for fluorescent proteins (FPbase), fluorescent protein-based biosensors (FPDB), and optogenetic tools (OptoBase) (Lambert 2019; Greenwald et al. 2018; Kolar et al. 2018).

## 13.2 Visualization of Cell Signaling by Fluorescent Biosensors

### 13.2.1 Single Fluorophore-Based Biosensors

#### 13.2.1.1 Translocation-Based Biosensors

The activation of intracellular signaling is often accompanied by changes in the subcellular localization of signaling molecules. The translocation of signaling molecules leads to an increase or decrease in the local concentration, and eventually turns signal transduction on or off. Plasma membrane recruitment, nuclear import/export, and aggregation/disaggregation are frequently observed in the context of intracellular signaling. These cellular events can be easily captured by live-cell fluorescence imaging; it is possible to visualize subcellular translocation upon stimulation with an FP fused with a signaling molecule (Fig. 13.2). For example, epidermal growth factor (EGF) activates EGF receptors, and initiates the recruitment of Shc, Grb2, and Sos to activate membrane-localized Ras, a small GTPase. The activated Ras then binds to Raf at the plasma membrane, followed by MEK activation. Finally, ERK is phosphorylated and activated by MEK in the cytoplasm, which in turn is imported into the nucleus to phosphorylate its substrates (Fig. 13.2a). Therefore, plasma membrane

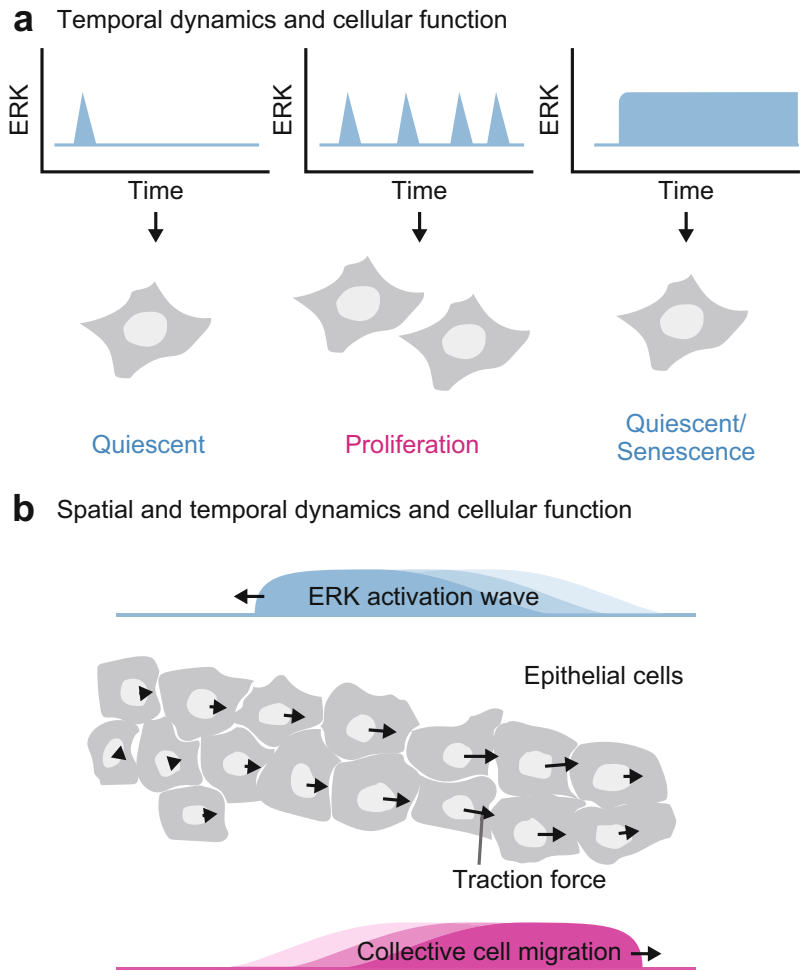


**Fig. 13.1** Spatiotemporal dynamics of cell signaling and cellular functions. (**a**) The frequency of ERK MAP kinase activation is involved in the control of cell proliferation. The middle frequency of ERK activation induces cell proliferation, while low or high frequency reads to quiescence or senescence. (**b**) Intercellular propagation of ERK activation plays a role in collective cell migration. Epithelial cells collectively migrate in the opposite direction of the ERK activation wave

recruitment of Raf and nuclear import of ERK can serve as a proxy for Ras and ERK activation (Rocks et al. 2005; Fujioka et al. 2006).

Regot et al. reported the kinase translocation reporter (KTR), a system for the rational design of translocation-based biosensors to detect kinase activity (Regot et al. 2014). The KTR system relies on a phosphorylation-induced increase in the nuclear export activity of the nuclear export signal (NES) and a phosphorylation-induced decrease in the nuclear import activity of the bipartite nuclear localization sequence (bNLS), which together lead to KTR translocation from the nucleus to the cytoplasm upon activation of that kinase (Fig. 13.2b). The specificity of the target kinase is ensured by adding a kinase docking sequence and/or substrate peptide sequence. Currently, JNK-, ERK-, p38-, PKA-, and Akt-KTRs are available (Regot et al. 2014; Maryu et al. 2016; Miura et al. 2018).

#### 13.2.1.2 Circularly Permuted Fluorescent Protein-Based Biosensors

In circularly permutated FPs (cpFPs), the original N- and C-termini are fused with a peptide linker, generating new N- and C-termini. If the new termini are formed in close proximity to the chromophore, the mutants are often sensitive to environmental changes such as changes in pH. By taking advantage of this property, cpFPs have

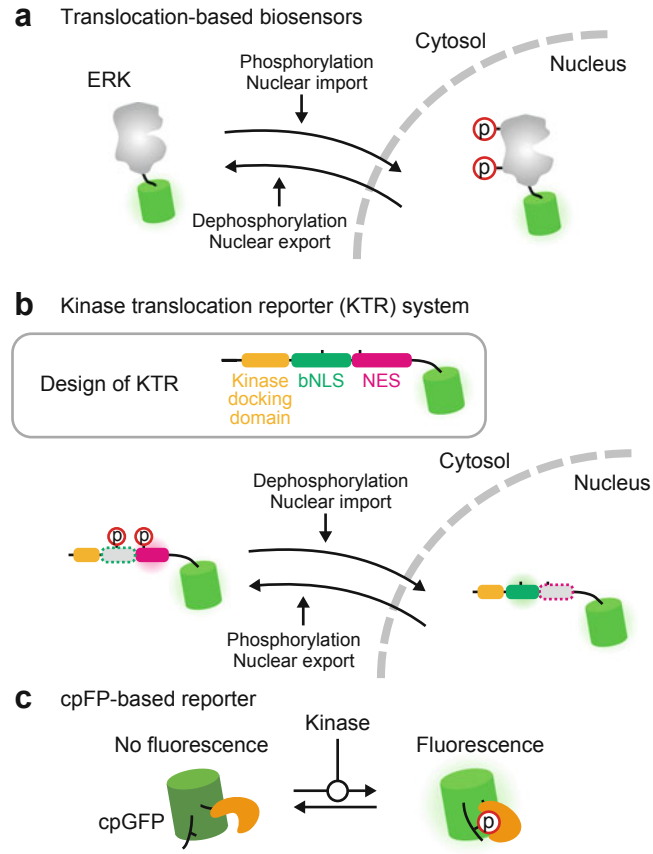


**Fig. 13.2** Single fluorophore-based biosensors. (**a**) Translocation of ERK from the cytoplasm to the nucleus is associated with phosphorylation and activation of ERK, thereby providing a good indicator for ERK activity. (**b**) The design and working model of kinase translocation reporter (KTR) are shown; a given kinase activation phosphorylates KTR, leading to the nuclear export of KTR. (**c**) A circular-permutated FP-based reporter shows an increase or decrease in fluorescence in a manner dependent on the conformation

been employed to develop genetically encoded fluorescent biosensors such as those for $Ca^{2+}$, voltage, and kinase activation (Kostyuk et al. 2019; Mehta et al. 2018) (Fig. 13.2c).

### 13.2.2 FRET-Based Biosensors

Förster (or fluorescence) resonance energy transfer (FRET) is a non-radiative process of excitation energy transfer from a donor fluorophore to an acceptor fluorophore (Jares-Erijman and Jovin 2003). FRET efficiency mainly depends on two factors: the relative distance and angle between the donor and acceptor fluorophore. Taking advantage of these properties, changes in molecular conformation and interaction have been detected as a change in the FRET signal.

Much effort has been devoted to developing genetically encoded FP-based FRET biosensors, enabling to visualize a wide range of cell signaling such as those involving ions, small GTPase, phospholipids, kinases, and metabolites (Miyawaki 2003; Greenwald et al. 2018; Kiyokawa et al. 2011; Maryu et al. 2016). This is mainly because FP-based FRET biosensors allow for the introduction of genes into cells and organisms through conventional gene delivery strategies. The FP-based FRET biosensors are classified into two types: intermolecular FRET biosensors and intramolecular FRET biosensors (Fig. 13.3a and b). The former are comprised of two separate proteins labeled with either donor or acceptor FP, while in the latter the donor and acceptor FPs are tethered as a single-chain protein. At present, many researchers prefer

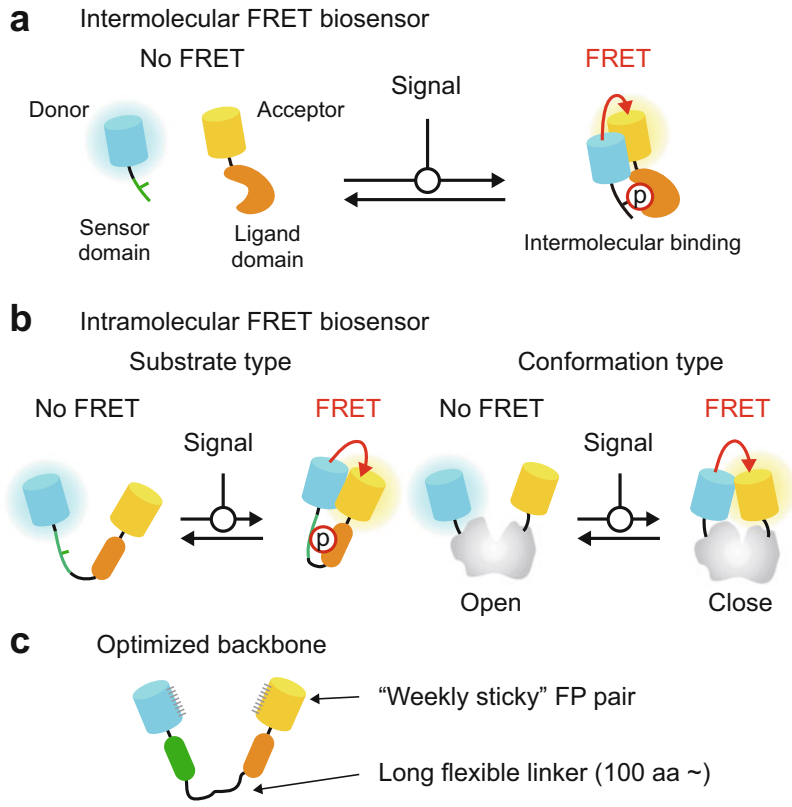


**Fig. 13.3** FRET-based biosensors. (**a**) An intermolecular FRET biosensor is comprised of separate donor and acceptor fluorophores, and FRET takes places when donor and acceptor fluorophores are located in close proximity. (**b**) An intramolecular FRET biosensor is classified into two types: substrate type (left) and conformation type (right). Substrate-type FRET biosensors act as a substrate of cell signaling, and therefore activation of an enzyme such as kinase can be quantified. Conformation-type FRET biosensors monitor conformational change of a target protein. (**c**) An optimized backbone for intramolecular FRET biosensor was proposed, called the *Extension for enhanced visualization by evading extraFRET* (Eevee) backbone

intramolecular FRET biosensors over intermolecular FRET biosensors. This is mainly due to the fact that the molar ratio of donor to acceptor of intramolecular FRET biosensor is 1:1, which greatly simplifies the quantification of FRET measurements (Aoki and Matsuda 2009). In addition, intramolecular FRET biosensors are usually more sensitive than intermolecular FRET biosensors.

The development of intramolecular FRET biosensors often requires a laborious trial-and-error approach because FRET is very sensitive to both the relative distance and angle between fluorophores. In order to develop these biosensors more efficiently, a rational backbone has been proposed for intramolecular FRET biosensors with a very long flexible linker, which renders the FRET distance-dependent and eliminates the influence of the relative angle (Komatsu et al. 2011) (Fig. 13.3c). Furthermore, under the condition with the long flexible linker, dimerization-prone FP pairs, e.g., YPet-ECFP, greatly increase FRET gain (Komatsu et al. 2011).

A significant difficulty arises when attempting to establish cell lines that stably express intramolecular FRET biosensors through linearized plasmid transfection and retroviral gene transfer; because of the high homology between YFP and CFP genes, which are the major FP pair used in intramolecular FRET biosensors, a gene

recombination between the FP pair occurs frequently (Aoki et al. 2012). Transposon-mediated gene transfer (Komatsu et al. 2011; Kamioka et al. 2012) and the use of lenti/retro-virus harboring codon-deoptimized YFP or CFP gene (Komatsubara et al. 2015) overcome this issue.

## 13.3 Optogenetic Manipulation of Cell Signaling

### 13.3.1 Blue Light-Responsive Optogenetic Tools for Cell Signaling

Optogenetics is a technique for manipulating protein and cellular functions by using light. Soon after the development of optogenetics in the field of neuroscience (Boyden et al. 2005), several groups reported techniques for optogenetic manipulation of intracellular signaling in non-neuronal cells (Wu et al. 2009; Levskaya et al. 2009; Kennedy et al. 2010). These studies made the best use of photo-responsive proteins from higher plants, cyanobacteria, molds, and fluorescent proteins (Fig. 13.4a). The photo-responsive proteins alter their structures upon exposure to light, resulting in a change in catalytic activity within a protein or homo- and/or hetero-dimerization (Kolar et al. 2018; Goglia and Toettcher 2019; Spiltoir and Tucker 2019). Such reactions are commonly found in the intracellular signal transduction system, thereby allowing the optical manipulation of cell signaling.

Currently, the light-oxygen-voltage sensing (LOV) domain and cryptochrome 2 (CRY2) are the most widely used blue light-responsive optogenetic tools (Kennedy et al. 2010; Guntas et al. 2015; Wu et al. 2009) (Fig. 13.4b). The LOV domain and CRY2 exploit flavin mononucleotide (FMN) and flavin adenine dinucleotide (FAD) as chromophores, respectively. The optogenetics system using LOV and CRY2 enables optical operations, such as intracellular signal transduction, lipid metabolism, gene expression, and transport of organelles (Aoki et al. 2013; Katsura et al. 2015; Kakumoto and Nakata 2013; Idevall-Hagren et al. 2012; Chan et al. 2015; Konermann et al. 2013; Duan et al. 2017). The chromophores of the respective systems, namely FMN and FAD, are abundant in many types of cells, and autocatalytically incorporated into CRY2 and the LOV domain, respectively. For this reason, the simple expression of CRY2 or LOV functions as an optogenetic tool. A drawback is that, since the LOV domain and CRY2 respond to blue light for photoactivation, imaging with GFP or many types of FRET biosensors is not compatible with CRY2- or LOV-based optogenetics. Recently, FPs emitting longer wavelengths, such as mCherry and infra-red FP (iRFP), have been made available for imaging combined with these optogenetic tools. The red-shifter FRET biosensors reported from several groups are also helpful for the visualization of cell signaling combined with optogenetics (Schaaf et al. 2018; Oliinyk et al. 2019).

### 13.3.2 Red/Far-Red-Light-Responsive Optogenetic Tools for Cell Signaling

Phytochrome B (PhyB) derived from higher plants has been utilized as an optogenetic tool responding to red/far-red light (Shimizu-Sato et al. 2002; Levskaya et al. 2009), thereby showing excellent compatibility with most of FRET biosensors. Apo-PhyB covalently attaches to a linear tetrapyrrole chromophore such as phycocyanobilin (PCB) and phytochromobilin (PΦB), and plays a central role in germination and flowering as a photoreceptor (Rockwell and Lagarias 2010). When PhyB absorbs red light, it binds to phytochrome interacting factors (PIFs), and exposure to far-red light quickly induces dissociation of the PhyB-PIF complex (Fig. 13.4c). Thus, PhyB has the unique feature that both binding and dissociation with PIFs can be controlled by light. Control of the spatial and temporal

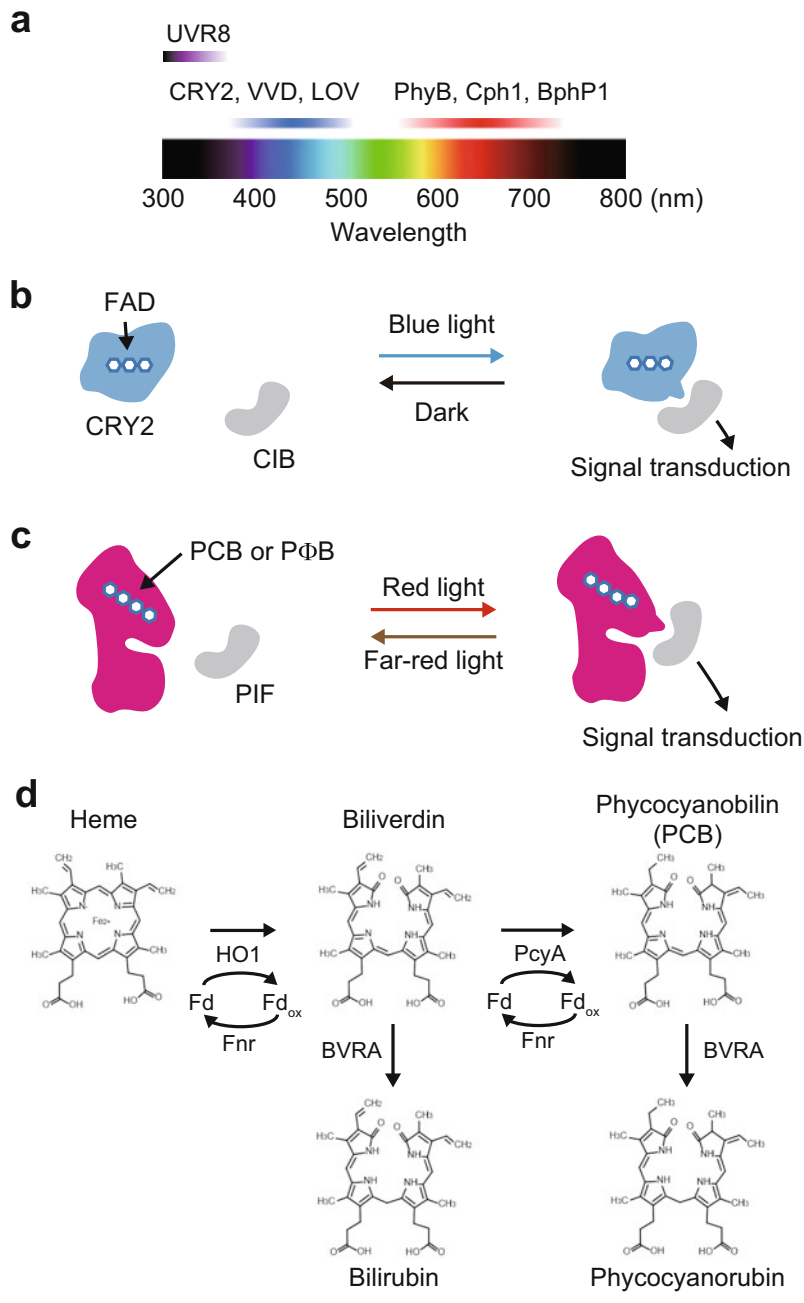


**Fig. 13.4** Optogenetic tool for optical manipulation of cell signaling. (**a**) Available optogenetic tools are listed with a range of responsible wavelengths. (**b**) CRY2 binds to CIB upon exposure to blue light and dissociates from CIB under the dark condition. Flavin adenine dinucleotide (FAD) is the chromophore of CRY2. (**c**) PhyB binds to PIF by red-light illumination, and dissociates from PIF by far-red-light exposure. Phycocyanobilin (PCB) or phytochromobilin (PΦB) is the chromophore of PhyB. (**d**) The metabolic pathway of PCB synthesis in cyanobacteria. Expression of PcyA, HO1, Fd, and Fnr at mitochondria is sufficient to synthesize PCB in mammalian cells and fission yeasts

dynamics of the intracellular signal transduction system was achieved by taking advantage of the PhyB-PIF system (Levskaya et al. 2009; Toettcher et al. 2011).

However, unlike the LOV domain and CRY2, chromophores of PhyB, namely PCB or PΦB, do not exist in many types of cells and organisms, except photosynthetic organisms. Therefore, it is necessary to purify PCB from cyanobacteria and add it to the culture media of cells prior to experiments, making it difficult to apply the PhyB-PIF system to higher organisms such as

mice. To overcome this issue, several groups have developed PCB synthesis systems by introducing a few genes involved in PCB synthesis in cyanobacteria. For instance, PcyA and HO1 genes suffice to produce PCB in bacteria (Mukougawa et al. 2006). On the other hand, fission yeast and mammalian cells require four genes (*PcyA*, *HO1*, *Fd*, and *Fnr*) for efficient PCB synthesis (Uda et al. 2017; Kyriakakis et al. 2018) (Fig. 13.4d). These systems allow the PhyB-PIF system to be fully genetically encoded, which is confirmed by red/far-red-light-induced PhyB-PIF formation (Uda et al. 2017). Knocking out biliverdin reductase A (BVRA) gene substantially increased PCB synthesis because BVRA is known to reduce both biliverdin and PCB levels. Interestingly, PCB synthesized in mammalian cells shows more efficient PhyB-PIF binding than crude PCB or PCB purified by HPCL, presumably because the latter PCBs are contaminated by nonfunctional tetrapyrroles that bind to PhyB and hamper its function (Oda et al. 2018).

## 13.4 Conclusion

Optogenetics with live-cell imaging have made it possible to reveal the direct link between cell signaling dynamics and cellular functions. It is expected that the development and improvement of both FRET-based biosensors and single fluorophore-based biosensors will continue, and more sensitive biosensors will be available in the future. Although optogenetics is a relatively new technology, its potential is virtually unlimited. For instance, the chromophores of CRY2 and LOV demonstrate few two-photon absorption cross sections, and therefore almost no excitation of CRY2 and LOV occurs by two-photon absorption. Recently, it was reported that CRY2 and LOV can be photoactivated by two-photon excitation assisted with FRET (Kinjo et al. 2019), enabling optogenetics in deeper tissue. In addition, optogenetics using nanobodies will be a powerful tool that can target almost any molecule with optogenetics in principle (Gil et al. 2020; Yu et al. 2019). We look forward to new approaches to address how the dynamics of the signal systems encode/decode information and how the systems are broken in pathogenesis.

**Acknowledgments** We thank all members of the Aoki Laboratories for helpful discussions and assistance. This work was supported by Japan Society for the Promotion of Science (JSPS) KAKENHI Grants (no.19K16050) (to Y. G.); JSPS KAKENHI Grants (no. 19K16207 and no. 19H05675) (to Y.K.); Core Research for Evolutional Science and Technology | Japan Society for the Promotion of Science (JPMJCR1654), JSPS KAKENHI Grants (no. 16KT0069, 16H01425 "Resonance Bio," 18H04754 "Resonance Bio," 18H02444, and 19H05798), and ONO Medical Research Foundation (to K.A.).

## References

Albeck JG et al (2013) Frequency-modulated pulses of ERK activity transmit quantitative proliferation signals. Mol Cell 49:249–261

Aoki K, Matsuda M (2009) Visualization of small GTPase activity with fluorescence resonance energy transfer-based biosensors. Nat Protoc 4:1623–1631

Aoki K et al (2012) Stable expression of FRET biosensors: a new light in cancer research. Cancer Sci 103:614–619

Aoki K et al (2013) Stochastic ERK activation induced by noise and cell-to-cell propagation regulates cell density-dependent proliferation. Mol Cell 52:529–540

Aoki K et al (2017) Propagating wave of ERK activation orients collective cell migration. Dev Cell 43:305–317. e5

Boyden ES et al (2005) Millisecond-timescale, genetically targeted optical control of neural activity. Nat Neurosci 8:1263–1268

Chan Y-B et al (2015) Optogenetic control of gene expression in Drosophila. PLoS One 10:e0138181

Duan L et al (2017) Understanding CRY2 interactions for optical control of intracellular signaling. Nat Commun 8:547

Fujioka A et al (2006) Dynamics of the Ras/ERK MAPK cascade as monitored by fluorescent probes. J Biol Chem 281:8917–8926

Gil AA et al (2020) Optogenetic control of protein binding using light-switchable nanobodies. Nat Commun 11:4044

Goglia AG, Toettcher JE (2019) A bright future: optogenetics to dissect the spatiotemporal control of cell behavior. Curr Opin Chem Biol 48:106–113

Greenwald EC et al (2018) Genetically encoded fluorescent biosensors illuminate the spatiotemporal

regulation of Signaling networks. Chem Rev 118:11707–11794
Guntas G et al (2015) Engineering an improved light-induced dimer (iLID) for controlling the localization and activity of signaling proteins. Proc Natl Acad Sci U S A 112:112–117
Hanahan D, Weinberg RA (2011) Hallmarks of cancer: the next generation. Cell 144:646–674
Hiratsuka T et al (2015) Intercellular propagation of extracellular signal-regulated kinase activation revealed by in vivo imaging of mouse skin. elife 4:e05178. https://doi.org/10.7554/eLife.05178
Idevall-Hagren O et al (2012) Optogenetic control of phosphoinositide metabolism. Proc Natl Acad Sci U S A 109:E2316–E2323
Jares-Erijman EA, Jovin TM (2003) FRET imaging. Nat Biotechnol 21:1387–1395
Kakumoto T, Nakata T (2013) Optogenetic control of PIP3: PIP3 is sufficient to induce the actin-based active part of growth cones and is regulated via endocytosis. PLoS One 8:e70861
Kamioka Y et al (2012) Live imaging of protein kinase activities in transgenic mice expressing FRET biosensors. Cell Struct Funct 37:65–73
Katsura Y et al (2015) An optogenetic system for interrogating the temporal dynamics of Akt. Sci Rep 5:14589
Kennedy MJ et al (2010) Rapid blue-light-mediated induction of protein interactions in living cells. Nat Methods 7:973–975
Kinjo T et al (2019) FRET-assisted photoactivation of flavoproteins for in vivo two-photon optogenetics. Nat Methods 16:1029–1036
Kiyokawa E et al (2011) Spatiotemporal regulation of small GTPases as revealed by probes based on the principle of Förster resonance energy transfer (FRET): implications for signaling and pharmacology. Annu Rev Pharmacol Toxicol 51:337–358
Kolar K et al (2018) OptoBase: a web platform for molecular optogenetics. ACS Synth Biol 7:1825–1828
Komatsu N et al (2011) Development of an optimized backbone of FRET biosensors for kinases and GTPases. Mol Biol Cell 22:4647–4656
Komatsubara AT et al (2015) Quantitative analysis of recombination between YFP and CFP genes of FRET biosensors introduced by lentiviral or retroviral gene transfer. Sci Rep 5:13283
Konermann S et al (2013) Optical control of mammalian endogenous transcription and epigenetic states. Nature 500:472–476
Kostyuk AI et al (2019) Circularly permuted fluorescent protein-based indicators: history, principles, and classification. Int J Mol Sci 20(17):4200. https://doi.org/10.3390/ijms20174200
Kyriakakis P et al (2018) Biosynthesis of orthogonal molecules using ferredoxin and ferredoxin-NADP+ reductase systems enables genetically encoded PhyB optogenetics. ACS Synth Biol 7:706–717
Lambert TJ (2019) FPbase: a community-editable fluorescent protein database. Nat Methods 16:277–278
Levskaya A et al (2009) Spatiotemporal control of cell signalling using a light-switchable protein interaction. Nature 461:997–1001
Maryu G et al (2016) Multiplexed fluorescence imaging of ERK and Akt activities and cell-cycle progression. Cell Struct Funct 41:81–92
Mehta S et al (2018) Single-fluorophore biosensors for sensitive and multiplexed detection of signalling activities. Nat Cell Biol 20(10):1215–1225. https://doi.org/10.1038/s41556-018-0200-6
Miura H et al (2018) Cell-to-cell heterogeneity in p38-mediated cross-inhibition of JNK causes stochastic cell death. Cell Rep 24:2658–2668
Miyawaki A (2003) Visualization of the spatial and temporal dynamics of intracellular signaling. Dev Cell 4:295–305
Miyawaki A (2011) Development of probes for cellular functions using fluorescent proteins and fluorescence resonance energy transfer. Annu Rev Biochem 80:357–373
Mukougawa K et al (2006) Metabolic engineering to produce phytochromes with phytochromobilin, phycocyanobilin, or phycoerythrobilin chromophore in Escherichia coli. FEBS Lett 580:1333–1338
Oda K et al (2005) A comprehensive pathway map of epidermal growth factor receptor signaling. Mol Syst Biol 1:E1–E17
Oda S et al (2018) Chapter 7: Optogenetic tools for quantitative biology: the genetically encoded PhyB–PIF light-inducible dimerization system and its application for controlling signal transduction. In: Optogenetics, pp 137–148
Oliinyk OS et al (2019) Smallest near-infrared fluorescent protein evolved from cyanobacteriochrome as versatile tag for spectral multiplexing. Nat Commun 10:279
Purvis JE, Lahav G (2013) Encoding and decoding cellular information through signaling dynamics. Cell 152:945–956
Purvis JE et al (2012) p53 dynamics control cell fate. Science 336:1440–1444
Regot S et al (2014) High-sensitivity measurements of multiple kinase activities in live single cells. Cell 157:1724–1734
Rocks O et al (2005) An acylation cycle regulates localization and activity of palmitoylated Ras isoforms. Science 307:1746–1752
Rockwell NC, Lagarias JC (2010) A brief history of phytochromes. ChemPhysChem 11:1172–1180
Schaaf TM et al (2018) Red-shifted FRET biosensors for high-throughput fluorescence lifetime screening. Biosensors 8:99. https://doi.org/10.3390/bios8040099
Shimizu-Sato S et al (2002) A light-switchable gene promoter system. Nat Biotechnol 20:1041–1044
Spiltoir JI, Tucker CL (2019) Photodimerization systems for regulating protein-protein interactions with light. Curr Opin Struct Biol 57:1–8

Toettcher JE et al (2011) Light-based feedback for controlling intracellular signaling dynamics. Nat Methods 8:837–839

Uda Y et al (2017) Efficient synthesis of phycocyanobilin in mammalian cells for optogenetic control of cell signaling. Proc Natl Acad Sci U S A 114:11962–11967

Wu YI et al (2009) A genetically encoded photoactivatable Rac controls the motility of living cells. Nature 461:104–108

Yu D et al (2019) Optogenetic activation of intracellular antibodies for direct modulation of endogenous proteins. Nat Methods 16(11):1095–1100. https://doi.org/10.1038/s41592-019-0592-7

# Light Control of Gene Expression Dynamics

14

Akihiro Isomura

**Abstract**

The progress in live-cell imaging technologies has revealed diverse dynamic patterns of transcriptional activity in various contexts. The discovery raised a next question of whether the gene expression patterns play causative roles in triggering specific biological events or not. Here, we introduce optogenetic methods that realize optical control of gene expression dynamics in mammalian cells and would be utilized for answering the question, by referring the past, the present, and the future.

**Keywords**

Genetic oscillation · Cell–cell communication · LOV proteins · GAVPO · Notch signaling

## Abbreviations

| | |
|---|---|
| *Dll1* | *Delta-like1* |
| FAD | Flavin adenine dinucleotide |
| *Lfng* | *Lunatic fringe* |
| LOV domains | Light-, oxygen-, and voltage-sensing domains |
| NICD | Notch intracellular domain |
| PSM | Presomitic mesoderm |
| UAS | Upstream activation sequence |
| VVD | Vivid |

## 14.1 Introduction

The transcription of genes is a ubiquitous, essential, and dynamic process in living organisms. Recent efforts to visualize biological activities in living cells have identified dynamic temporal patterns of gene expression in many contexts, including stochastic noisy patterns and regular oscillatory patterns (Isomura and Kageyama 2014; Levine et al. 2013; Purvis and Lahav 2013). For example, stress responses in yeast cells trigger pulsatile expression of the transcription factors Msn2 and Crz1 (Cai et al. 2008). In mammalian cells, DNA damage induced by γ-irradiation results in the oscillatory expression of the tumor suppressor p53 protein with a 4- to 5-h period (Lahav et al. 2004). Other oscillatory patterns have been found for transcription factors in mammalian cells, such as the cyclic shuttling of NF-κB in inflammatory responses (Nelson et al. 2004) and the oscillation of *Hes1* expression in proliferating neural stem cells (Shimojo et al. 2008). Interestingly, steady and sustained

A. Isomura (✉)
Institute for Integrated Cell-Material Sciences (WPI-iCeMS), Kyoto University, Kyoto, Japan

Japan Science and Technology Agency, PRESTO, Saitama, Japan

Institute for Frontier Life and Medical Sciences, Kyoto University, Kyoto, Japan
e-mail: aisomura@infront.kyoto-u.ac.jp



H. Yawo et al. (eds.), *Optogenetics*, Advances in Experimental Medicine and Biology 1293,
https://doi.org/10.1007/978-981-15-8763-4_14

expression patterns of these factors are observed in particular situations: NF-κB repeatedly shuttles from the cytosol to the nucleus in response to TNF-α, whereas it translocates to the nucleus in a sustained manner after LPS stimulation (Covert et al. 2005). These examples suggest that dynamic patterns in signaling activities can trigger specific cellular events. However, it is not known if dynamic patterns of transcriptional activities underlie specific biological functions or are simply collateral outcomes.

Oscillatory gene activity patterns are also prevalent in multicellular contexts. During the aggregation stage of *Dictyostelium discoideum*, cells produce chemo-attractant cAMP and release it to neighboring cells in a pulsatile manner. These pulses are relayed and propagated as traveling waves that trigger and orchestrate the collective movement of cells at the population level (Gregor et al. 2010). In vertebrate embryos, somites, which are future bone structures, are periodically produced; this periodicity is driven by genetic oscillators of the *Hes*/*Her* family. Transcriptional activities of *Hes*/*Her* are cyclically up- and downregulated in a synchronous manner at the tissue level (Hubaud and Pourquie 2014; Kageyama et al. 2012). The synchronized patterns propagate in a wave-like manner along the posterior-to-anterior (tail-to-head) directions. However, the minimum number of molecular architectures that are required to synchronize gene activities in tissues through dynamic intercellular communications has yet to be determined.

To address these issues, technologies that can perturb signaling patterns with high spatiotemporal precision are required. As light is highly tunable and noninvasive, optical methods offer a promising means of controlling cellular activities in living cells and tissues. In 2005, it was demonstrated that genetically encoded photosensitive proteins were useful for manipulating neuronal activities in mammalian cells (Boyden et al. 2005). The scope of this optogenetic approach has since been expanded to diverse biological functions, including enzymatic activities and gene expression. In this chapter, we describe optogenetic methods for controlling transcriptional activities, mainly in mammalian cells; we also discuss the dynamic features of an optogenetic gene expression system, including kinetics of switching; and finally, we show how optogenetic systems are applicable to studying dynamic functions of biomolecules in cell–cell communications.

## 14.2 Optogenetic Tools to Control Gene Expression Dynamics

Optogenetic technology is based on the use of naturally evolved photo-sensitive proteins whose activities are modulated by light inputs (Krueger et al. 2019; Losi et al. 2018). The majority of optogenetic methods harness proteins that can bind to photo-sensitive small organic molecules called chromophores. Upon light illumination, the protein–chromophore complex changes its conformation to initiate the appearance of functional interfaces in polypeptide chains that are linked to molecular function, such as dimerization. The first report of an optogenetic transcriptional system demonstrated that the hetero-dimerizer pair PhyB-PIF3 derived from plants can optically control gene expression in yeast cells (Shimizu-Sato et al. 2002). In this system, the binding of PhyB to the red-light-sensitive chromophore phycocyanobilin (PCB) triggers reconstitution of DNA binding (PhyB-Gal4DBD) and transactivation (PIF3-Gal4AD) domain-complexes upon red-light illumination (Fig. 14.1a). These reconstructed complexes can bind to UAS (upstream activation sequence) promoters and subsequently initiate the transcription of arbitrary genes controlled by a UAS promoter. The activation process is reversible; far-red-light illumination promotes the dissociation of the complexes, thereby inactivating red-light-induced gene expression in yeast and mammalian cells with the aid of externally supplied PCB (Müller et al. 2013). This reversible optogenetic switch enabled the development of a feedback control system in yeast cells in which transcriptional outputs of the optogenetic system could be monitored and simultaneously allow feedback to the system with red or far-red

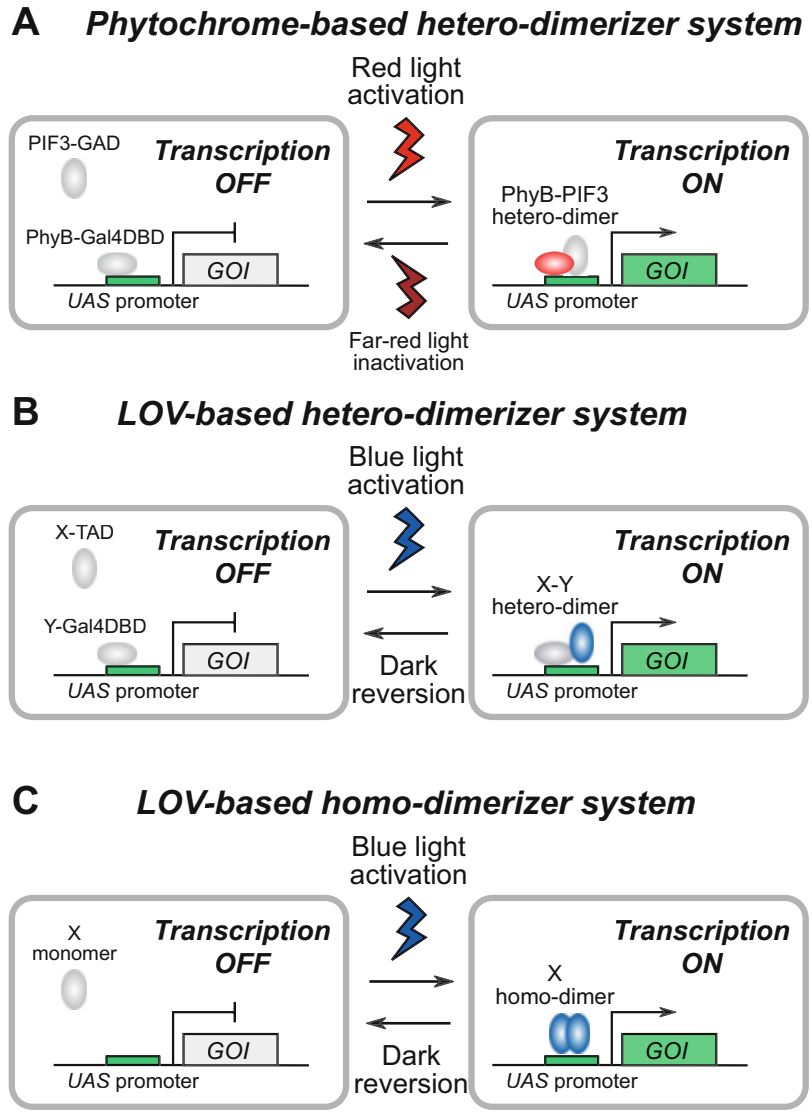


**Fig. 14.1** Optogenetic gene expression systems. (**a**) The red-light-sensitive PhyB-PIF3 system. (**b**) Blue-light-sensitive hetero-dimerizer systems, including the GIGANTEA-FKF1 and the CRY2-CIB1 systems. (**c**) Blue-light-sensitive homo-dimerizer systems, including the GAVPO (LightOn) and EL222 systems. GOI, gene of interest

illumination based on the monitored values of the outputs (Milias-Argeitis et al. 2011).

Blue-light-responsive optogenetic systems with hetero-dimerizers have also been developed (Fig. 14.1b). Yazawa et al. reported a mammalian optogenetic system in which blue-light illumination induces hetero-dimer pairs of GIGANTEA (GI) and the flavin-binding, Kelch repeat, F-box1 (FKF1) derived from *Arabidopsis thaliana*. The photo-sensitivity of this system is based on FKF1 containing light-, oxygen-, and voltage-sensing (LOV) domains; this amino acid motif can bind to blue-light-sensitive flavin molecules that are endogenous metabolic products in mammalian cells. By engineering the fusion proteins GI-Gal4 and FKF1-VP16, the authors showed photo-induced activation of UAS promoters in mammalian cells. The light-induced dimers of the FKF1-GIGANTEA pair dissociate in dark conditions due to the breakdown of the photo-adducts, and the decay proceeds very slowly, taking at least 1 day (Ito et al. 2012; Yazawa

et al. 2009). To overcome the slow kinetics of this process, Kennedy et al. created another blue-light optogenetic system, which uses hetero-dimers of CRY2-CIB1 with rapid association-dissociation kinetics (Kennedy et al. 2010). Similarly to LOV-domain proteins, CRY2 can bind to flavin adenine dinucleotide (FAD), and thereby does not require an external supply of chromophore molecules. This optogenetic switch is applied to control not only gene expression (Kennedy et al. 2010; Konermann et al. 2013; Quejada et al. 2017; Yamada et al. 2018) but also many other functions, including enzymatic activities (Losi et al. 2018).

Although hetero-dimerizer systems offer an intuitive and straightforward approach to creating a photo-sensitive transcriptional switch, homo-dimerizer systems may offer a simpler method in terms of the number of molecular components (Fig. 14.1c). Wang et al. generated the LightOn system that consists of the UAS promoter and a synthetic transcriptional factor GAVPO that is responsive to blue light (Wang et al. 2012). GAVPO is a fusion protein containing the Gal4 DNA binding domain, the photo-sensitive protein Vivid (VVD) derived from the fungus *Neurospora crassa*, and a p65 transactivation domain. As VVD can bind to FAD, this system works without an external supply of chromophore molecules. Upon blue-light illumination, GAVPO proteins form dimers and bind to UAS promoters, which initiate transcription of genes fused downstream of the promoters. The LightOn system can function in mammalian cells, and provide spatiotemporal control of transcriptional levels with dose dependency determined by photo-intensity. It was also demonstrated that a transient light illumination (2-h duration) was able to produce pulsatile patterns of gene expression; however, the timescale of the on–off kinetics was about a day and therefore very slow. To address issues about the kinetics of switching, Motta-Mena et al. developed another optogenetic homo-dimerizer by exploiting the blue-light-sensitive DNA-binding protein EL222 derived from the gram-negative bacterium *Erythrobacter litoralis* (Motta-Mena et al. 2014). They showed that blue light was able to induce pulsatile transcriptional activation in this system and estimated the timescale of on–off kinetics at $<10$ s and $<50$ s, respectively. These pioneering studies demonstrated the feasibility of controlling gene expression dynamics in a highly precise temporal manner.

## 14.3 Generation of Oscillatory Gene Expression by Periodic Light Illumination

Having validated the LightOn optogenetic system as a means of controlling gene expression, the system was then applied to analyzing the functional roles of gene expression dynamics in mammalian cells (Imayoshi et al. 2013; Isomura et al. 2017). Transiently photoactivated GAVPO proteins trigger the transcription of genes carrying stable 3′UTR sequences, such as SV40 polyA; the temporal patterns of gene expression were found to display a timescale of more than 10 h as originally reported (Fig. 14.2a and b) (Isomura et al. 2017; Wang et al. 2012). In sharp contrast, if target genes are fused to the 3′UTR sequences of the immediate early response genes *cFos*, *IL-2*, or *Hes1*, cyclic light illumination induces pulses of gene expression with periodicity of less than 2 h (Fig. 14.2c) (Isomura et al. 2017). These results are counter-intuitive because the photo-sensitive domain of GAVPO is the slow-cycling photoreceptor VVD; the half-life of the photo-adduct signaling state is about 5 h (Zoltowski et al. 2009). This raises the question of how GAVPO proteins generate rapid pulsatile dynamics in gene activation.

Here, we discuss a simple mathematical model that recapitulates gene expression patterns induced by photoactivated GAVPO proteins; this model includes a minimal number of assumptions. We hypothesize that the kinetics of photo-activation of GAVPO proteins is much faster than other processes such as dark-reversion of VVD domains, degradation of GAVPO, and molecular production of target mRNAs and proteins because the timescale of photo-adduct formation is typically at the order of $\sim$ μs (Ito

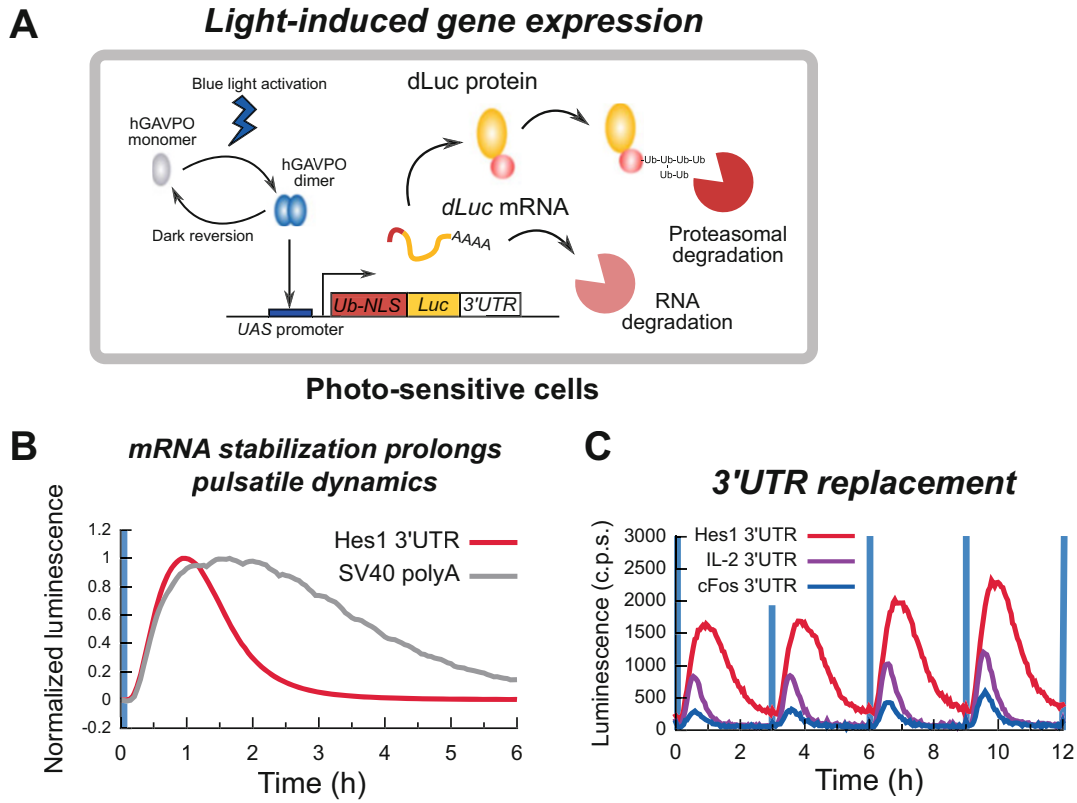


**Fig. 14.2** Generation of pulsatile gene expression patterns by the LightOn-hGAVPO system. (**a**) Schematic of the LightOn-hGAVPO system. (**b**, **c**) The effects of 3′UTR sequences on light-induced gene expression patterns. (c.p.s.) Counts per second. (Images are adapted from Isomura et al. (2017))

et al. 2012). Thus, a scheme of the reaction can be expressed as follows:

$$G \xrightarrow{k_1} M, \tag{14.1}$$

$$M \xrightarrow{k_2} P, \tag{14.2}$$

$$G \xrightarrow{\alpha} \varnothing, \tag{14.3}$$

$$M \xrightarrow{\beta} \varnothing, \tag{14.4}$$

$$P \xrightarrow{\gamma} \varnothing, \tag{14.5}$$

where $\varnothing$ indicates degradation of molecules. If transient light illumination produces activated GAVPO molecules with an initial number of $G(0)$ molecules, the temporal dynamics of molecular abundance can be expressed as follows:

$$\frac{dG(t)}{dt} = -\alpha G(t), \tag{14.6}$$

$$\frac{dM(t)}{dt} = k_1 G(t) - \beta M(t), \tag{14.7}$$

$$\frac{dP(t)}{dt} = k_2 M(t) - \gamma P(t), \tag{14.8}$$

where $G(t)$ is the number of DNA-binding active GAVPO proteins, $M(t)$ is the number of target mRNA molecules, and $P(t)$ is the number of target protein molecules. Equation (14.6) represents the decaying dynamics of the number of active GAVPO molecules bound to UAS promoters and initiating transcription of the target gene. Because light illumination is transient and absent after $t = 0$, a production term for $G(t)$ is not present. The parameter $\alpha$ indicates the decaying rate of activated GAVPO molecules, considering

multiple attenuating events: loss of binding with the UAS promoters, dissociation of the dimer forms due to photo-adduct decay, and proteasomal degradation (Fig. 14.3a). The parameters $k_1$ and $k_2$ are the production rates of target mRNAs and proteins, respectively. The parameters β and γ are the degradation rates of target mRNAs and proteins, respectively. Equations (14.7) and (14.8) describe the dynamics of mRNA transcription driven by the UAS promoter and proteins translated from the mRNAs, respectively.

These linear differential equations have an analytical solution:

$$G(t) = G_0 e^{-\alpha t}, \tag{14.9}$$

$$M(t) = \frac{k_1 G_0}{\beta - \alpha}\left(e^{-\alpha t} - e^{-\beta t}\right), \tag{14.10}$$

$$P(t) = \frac{k_1 k_2 G_0}{\beta - \alpha} e^{-\gamma t}\left(\frac{e^{(\gamma-\alpha)t} - 1}{\gamma - \alpha} - \frac{e^{(\gamma-\beta)t} - 1}{\gamma - \beta}\right), \tag{14.11}$$

where $G_0 = G(0)$ is the initial amount of photoactivated GAVPO protein and is expected to be proportional to the strength and time window of the transient light illumination. This mathematical description allows us to calculate the timing of the pulse peak, $\tau$. Setting $dP(t)/dt = 0$ in Eq. (14.8) leads to $k_2 M(\tau) = \gamma P(\tau)$. Combining this to Eqs. (14.10) and (14.11), we obtain the following:

$$k_2 \frac{k_1 G_0}{\beta - \alpha}\left(e^{-\alpha\tau} - e^{-\beta\tau}\right) = \gamma \frac{k_1 k_2 G_0}{\beta - \alpha} e^{-\gamma\tau}\left(\frac{e^{(\gamma-\alpha)\tau} - 1}{\gamma - \alpha} - \frac{e^{(\gamma-\beta)\tau} - 1}{\gamma - \beta}\right), \tag{14.12}$$

that is,

$$\frac{1}{\gamma}\left(e^{(\gamma-\alpha)\tau} - e^{(\gamma-\beta)\tau}\right) = \left(\frac{e^{(\gamma-\alpha)\tau} - 1}{\gamma - \alpha} - \frac{e^{(\gamma-\beta)\tau} - 1}{\gamma - \beta}\right). \tag{14.13}$$

Note that this equation is independent of parameters $G_0$, $k_1$, and $k_2$, and depends only on $\alpha$, $\beta$, and $\gamma$. This indicates that only the parameters of decay rates, $\alpha$, $\beta$, and $\gamma$, are responsible for the timing of pulsatile peaks in photo-induced gene expression pulses.

The mathematical model was compared with experimental data from a luminescence time series in reporter cells that carry pUAS-Ub-Luc-Hes1 3′UTR and hGAVPO expression cassette. For this comparison, we set parameter values of β and γ to the known half-lives of *Hes1* mRNA (24.1 min) and Ub-Luc signals (12.0 min), respectively (Masamizu et al. 2006). We also assumed 9 min time delay in the production process of Luciferase signals, because increasing of luminescence signals was detectable 9 min after light illumination in experiments, but the mathematical model allows infinitesimal time for increasing of the signals. This time delay would reflect the time required for transcription and translation, which was not taken into account in the above mathematical model. Curve fitting of the data by Eq. (14.11) with these parameters recapitulated the experimental results with an estimated decay half-life of activated GAVPO proteins, 12.4 min, that is much shorter than the lifetime of the photo-adduct of VVD (Fig. 14.3b and c). Numerical calculations with different parameters of functional half-life of activated GAVPO represented the diversity of timescale in output patterns (Fig. 14.3d), suggesting the critical roles of the deactivating process of GAVPO in accelerating the dynamic responses of optogenetic switches. Engineering of the degradation rate of GAVPO proteins and the dissociation kinetics of VVD might accelerate or decelerate the pulsatile dynamics. Taken together, these estimations provided insights into the mechanisms of light-induced gene expression, although more experimental tests are still required.

## 14.4 Applications of Optogenetics to the Analysis of Cell–Cell Communication by Oscillatory Gene Expression

During embryonic development, spatiotemporal patterns of gene expression are tightly scheduled, indicating mechanisms to coordinate the timings of gene activities in a clock-like manner. One of

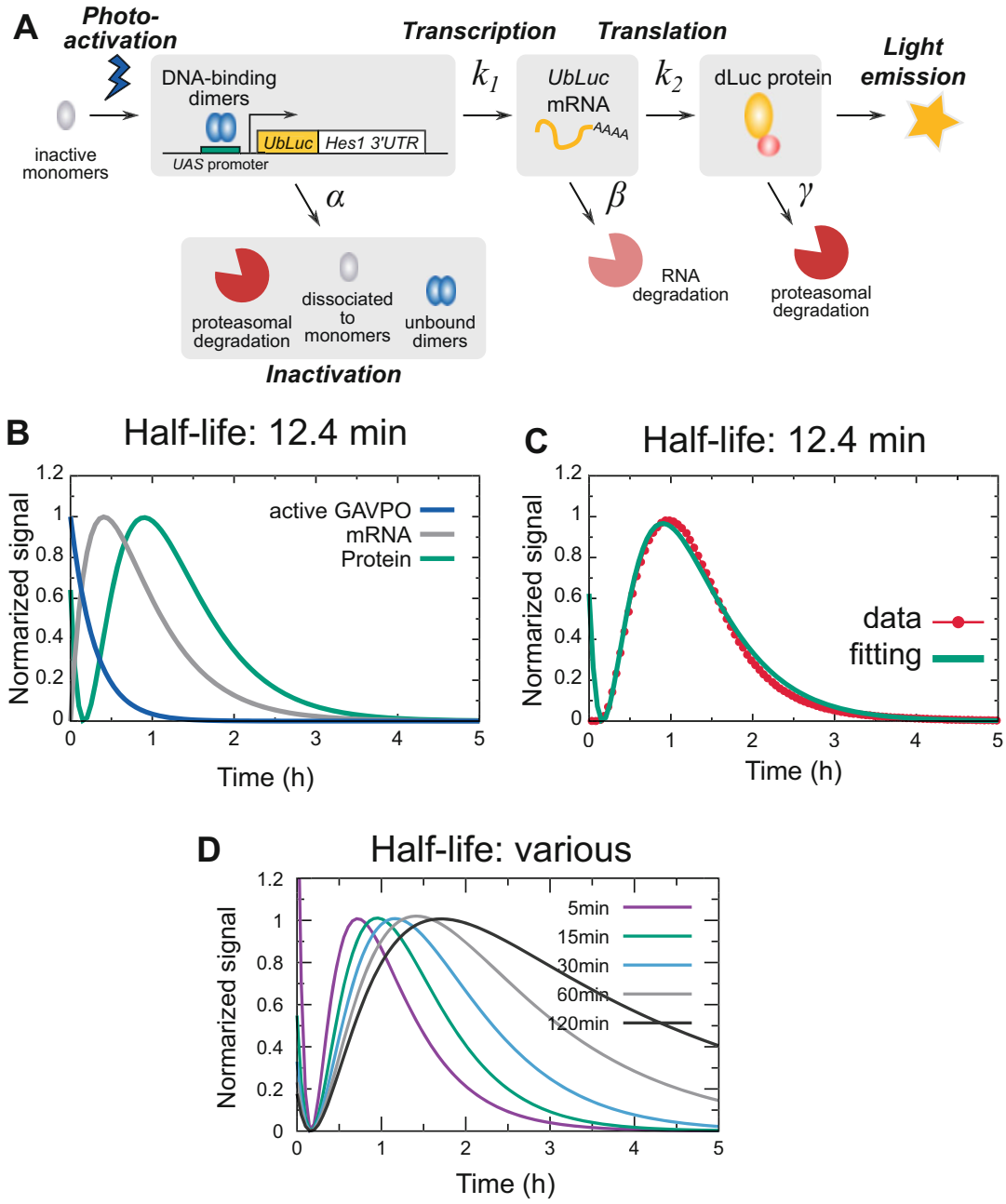


**Fig. 14.3** Mathematical modeling of gene expression patterns induced by the LightOn-hGAVPO system. (**a**) Schematic of the process of light-induced gene expression. Kinetic parameters of molecular production ($k_1$ and $k_2$) and degradation (α, β, and γ) are written. (**b**, **c**) Reproducing experimental data by a mathematical model. (**d**) Impact of inactivation kinetics of hGAVPO on light-induced gene expression patterns

the most striking examples is the segmentation clock in vertebrate embryos, which supports periodic formation of somites with regular spatial sizes (Hubaud and Pourquie 2014; Kageyama et al. 2012). This is achieved by synchronized differentiation of a group of presomitic mesoderm

(PSM) cells to somites under the control of the Notch, Wnt, and FGF signaling pathways. If the Notch signaling pathway is disrupted by inhibitor treatment or genetic perturbation, the regular somite structures are severely impaired due to the disappearance of synchronized expression patterns of oscillatory genes such as Notch effector genes *Hes7* in mice and *Her1/7* in zebrafish. These observations suggested the hypothesis that individual PSM cells can tick and communicate with each other by sending and receiving oscillatory information, such as periods, phases, and amplitudes, through the Notch signaling pathway (Jiang et al. 2000). Clock-like behaviors at the single-cell level was directly tested by live-imaging technologies in mice and zebrafish (Masamizu et al. 2006; Webb et al. 2016), but the mechanism that controls synchronization of individual clocks remains elusive.

Notch signaling is via a juxtacrine signaling pathway, which is conserved from fruit flies to mammals and is involved in diverse developmental contexts (Bray 2016; Kopan and Ilagan 2009). When Notch ligand–proteins on cell membranes of signal-sending cells interact with Notch receptors in neighboring receiver cells, the Notch receptors are activated and the intracellular domains of Notch (NICD: Notch intracellular domain) are cleaved by γ-secretases; the cleaved NICDs translocate into the nucleus and trigger the expression of the downstream target genes of the Notch signaling pathway. In mammalian PSM tissues, a Notch ligand *Delta-like 1* (*Dll1*) plays critical roles in normal tissue formation; Dll1 proteins show oscillatory expression patterns (Bone et al. 2014; Shimojo et al. 2016) and genetic manipulation to force sustained expression of Dll1 causes abnormal somite formation (Shimojo et al. 2016). These results indicated that Dll1 proteins might be an information carrier for oscillatory gene expression patterns in cell–cell communications. However, it is not clear whether and how cells can receive and transmit dynamic information through the Notch signaling pathway.

To address the issue of how cells might receive and transmit dynamic information, Isomura et al. developed an optogenetic sender–receiver assay that comprises two types of genetically engineered mammalian cells (Fig. 14.4a) (Isomura et al. 2017). One is a population of photo-sensitive sender cells that carry an optogenetic module and can produce ligand proteins of Dll1 upon blue-light illumination. Another is a population of photo-insensitive cells that carry a reporter system to detect the activity of Notch signaling and can produce luciferase proteins upon activation by Dll1 proteins from neighboring cells. In the assay, these two cell types are mixed and cocultured under dense conditions to enable sufficient cell–cell contacts between sender and receiver cells (Fig. 14.4b). When periodic illumination by blue light is applied to the coculture system, the photo-sensitive sender cells produced Dll1 proteins in an oscillatory manner. This oscillatory information is successfully transferred to neighboring cells as shown by the cyclic patterns of luminescence signals from the receiver cells (Fig. 14.4c). Interestingly, the number of sender cells can be smaller than that of receiver cells; even a 1:2 ratio of sender to receiver cells allowed transmission of oscillatory gene expression patterns. These results demonstrate that dynamic patterns of Dll1 protein abundance can synchronize gene expression dynamics in neighboring cells.

Although the optogenetic assays reconstituted synchronized oscillatory gene expression through Notch signaling, the efficiency of synchronization was lower than in natural PSM tissues, indicating that other mechanisms enhance cell–cell communications. It has been reported that *Lunatic fringe* (*Lfng*), a glycosyltransferase for DLL1 and Notch proteins, also plays indispensable roles in regular patterning in PSM tissues; however, the functional roles of *Lfng* in synchronization remain unknown. To investigate these roles, Yoshioka-Kobayashi et al. utilized the optogenetic sender–receiver assay (Yoshioka-Kobayashi et al. 2020). The authors prepared sender cells carrying the optogenetic module of Dll1 with or without the additional genetic module of *Lfng* for sustained overexpression. When pulsatile patterns of Dll1 were photo-induced in the sender cells without a *Lfng*-module, the receiver cells responded earlier than compared

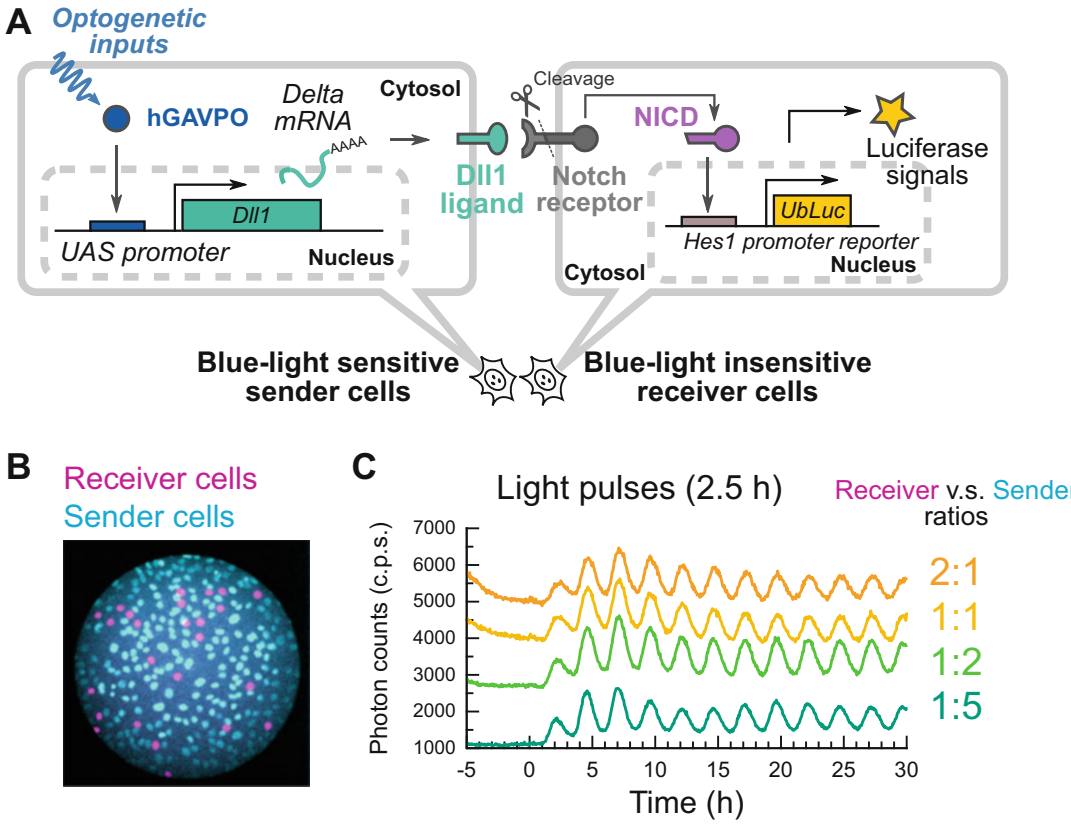


**Fig. 14.4** The optogenetic sender–receiver assay to analyze dynamic cell–cell interactions. (**a**) Schematic of sender and receiver cells used in the optogenetic assay. (**b**) A fluorescence image showing a mixed culture of reporter cells labeled with mCherry (magenta) and photosensitive sender cells labeled with iRFP713 (cyan) with a 1:5 mixing ratio. (**c**) Bioluminescence signals of coculture systems with a range of mixing ratios. Total cell numbers were fixed, but the ratios between the receivers and the senders ranged from 1:5 to 2:1. (Images are adapted from Isomura et al. (2017))

to when the sender cells carried the *Lfng*-module; moreover, the timings of signal transmission from sender to receiver cells was delayed when Lfng was expressed in the sender cells. Direct live imaging of the distribution of photo-induced Dll1 proteins showed that Lfng is involved in the signal-sending process and delays the translocation of Dll1 to the cellular membrane of sender cells. These results, taken together with single-cell imaging data of intact PSM cells, suggest that the dynamic function of Lfng is the production of time delays in cell–cell communication. Theoretical studies on synchronization in coupled oscillators have shown that the time delays required for communication between oscillators play critical roles in determining the modes of synchronization; there are parameter spaces of time delays that can realize anti-phase synchronization rather than in-phase synchronization. Lfng could modulate and lead to the correction of time delays for the emergence of in-phase synchronized oscillation, as observed in the PSM tissues.

## 14.5 Summary and Future Directions

In this chapter, we describe optogenetic systems that enable investigation of the dynamic control of gene expression patterns in mammalian cells. Although we focused on reversible systems,

irreversible switches have also been developed, such as photo-activatable Cre recombinase (paCre) (Meador et al. 2019; Taslimi et al. 2016), photo-activatable flippase (paFLP) (Jung et al. 2019), and photocleavable protein PhoCl (Zhang et al. 2017). These different approaches provide versatile tools for the optical control of gene expression.

A potential drawback of optogenetic transcription systems is the heterogeneity of photo-responses even in clonal cell populations. This might be due to fluctuation in the numbers of photo-sensitive proteins, also known as gene expression noise (Eldar and Elowitz 2010). Recent studies demonstrated that feedback systems can mitigate cell-to-cell variation in photo-induced gene expression (Guinn and Balázsi 2019; Rullan et al. 2018). Further improvements and engineering by sophisticated feedback mechanisms could provide the ideal optogenetic system for gene expression with homogeneous responses and precise tunability.

In many cases, synthetic gene expression systems are applied to artificial production of proteins; the applications shown in this chapter also utilized optogenetic systems to produce dynamic patterns of ligand–protein expression. Other methods to optically control protein expression patterns rather than gene expression might be more desirable tools for optogenetic experiments. Interestingly, recent studies reported photo-inducible translation systems (Weber et al. 2019) and photo-induced degradation systems based on photo-sensitive antibodies (Yu et al. 2019) in mammalian cells. The expanding range of the optogenetic toolbox is likely to produce sophisticated controllers for multicellular systems by manipulating proteins related to cell–cell communications and tissue formation.

**Acknowledgments** This work was supported by Precursory Research for Embryonic Science and Technology (JPMJPR15P1 to A.I.), Grant-in-Aid for Scientific Research on Innovative Areas (Ministry of Education, Culture, Sports, Science, and Technology (MEXT), Japan (18H04734 and 19H04960 to A.I.)).

**Competing Interests** The authors declare that they have no competing financial interests.

## References

Bone RA, Bailey CSL, Wiedermann G, Ferjentsik Z, Appleton PL, Murray PJ, Maroto M, Dale JK (2014) Spatiotemporal oscillations of Notch1, Dll1 and NICD are coordinated across the mouse PSM. Development 141:4806–4816

Boyden ES, Zhang F, Bamberg E, Nagel G, Deisseroth K (2005) Millisecond-timescale, genetically targeted optical control of neural activity. Nat Neurosci 8:1263–1268

Bray SJ (2016) Notch signalling in context. Nat Rev Mol Cell Biol 17:722–735

Cai L, Dalal CK, Elowitz MB (2008) Frequency-modulated nuclear localization bursts coordinate gene regulation. Nature 455:485–490

Covert MW, Leung TH, Gaston JE, Baltimore D (2005) Achieving stability of lipopolysaccharide-induced NF-κB activation. Science 309:1854–1857

Eldar A, Elowitz MB (2010) Functional roles for noise in genetic circuits. Nature 467:167–173

Gregor T, Fujimoto K, Masaki N, Sawai S (2010) The onset of collective behavior in social amoebae. Science 328:1021–1025

Guinn MT, Balázsi G (2019) Noise-reducing optogenetic negative-feedback gene circuits in human cells. Nucleic Acids Res 47:7703–7714

Hubaud A, Pourquie O (2014) Signalling dynamics in vertebrate segmentation. Nat Rev Mol Cell Biol 15:709–721

Imayoshi I, Isomura A, Harima Y, Kawaguchi K, Kori H, Miyachi H, Fujiwara T, Ishidate F, Kageyama R (2013) Oscillatory control of factors determining multipotency and fate in mouse neural progenitors. Science 342:1203–1208

Isomura A, Kageyama R (2014) Ultradian oscillations and pulses: coordinating cellular responses and cell fate decisions. Development 141:3627–3636

Isomura A, Ogushi F, Kori H, Kageyama R (2017) Optogenetic perturbation and bi-oluminescence imaging to analyze cell-to-cell transfer of oscillatory information. Genes Dev 31:524–535

Ito S, Song YH, Imaizumi T (2012) LOV domain-containing F-box proteins: light-dependent protein degradation modules in Arabidopsis. Mol Plant 5:573–582

Jiang Y-J, Aerne BL, Smithers L, Haddon C, Ish-Horowicz D, Lewis J (2000) Notch signalling and the synchronization of the somite segmentation clock. Nature 408:475–479

Jung H, Kim S-W, Kim M, Hong J, Yu D, Kim JH, Lee Y, Kim S, Woo D, Shin H-S, Park BO, Heo WD (2019) Noninvasive optical activation of Flp recombinase for genetic manipulation in deep mouse brain regions. Nat Commun 10:314

Kageyama R, Niwa Y, Isomura A, Gonzalez A, Harima Y (2012) Oscillatory gene expression and somitogenesis. WIREs Dev Biol 1:629–641

Kennedy MJ, Hughes RM, Peteya LA, Schwartz JW, Ehlers MD, Tucker CL (2010) Rapid blue-light-mediated induction of protein interactions in living cells. Nat Methods 7:973–975

Konermann S, Brigham MD, Trevino AE, Hsu PD, Heidenreich M, Cong L, Platt RJ, Scott DA, Church GM, Zhang F (2013) Optical control of mammalian endogenous transcription and epigenetic states. Nature 500:472–476

Kopan R, Ilagan MXG (2009) The canonical notch signaling pathway: unfolding the activation mechanism. Cell 137:216–233

Krueger D, Izquierdo E, Viswanathan R, Hartmann J, Pallares Cartes C, De Renzis S (2019) Principles and applications of optogenetics in developmental biology. Development 146:dev175067

Lahav G, Rosenfeld N, Sigal A, Geva-Zatorsky N, Levine AJ, Elowitz MB, Alon U (2004) Dynamics of the p53-Mdm2 feedback loop in individual cells. Nat Genet 36:147–150

Levine JH, Lin Y, Elowitz MB (2013) Functional roles of pulsing in genetic circuits. Science 342:1193–1200

Losi A, Gardner KH, Möglich A (2018) Blue-light receptors for optogenetics. Chem Rev 118:10659–10709

Masamizu Y, Ohtsuka T, Takashima Y, Nagahara H, Takenaka Y, Yoshikawa K, Okamura H, Kageyama R (2006) Real-time imaging of the somite segmentation clock: revelation of unstable oscillators in the individual presomitic mesoderm cells. Proc Natl Acad Sci U S A 103:1313–1318

Meador K, Wysoczynski CL, Norris AJ, Aoto J, Bruchas MR, Tucker CL (2019) Achieving tight control of a photoactivatable Cre recombinase gene switch: new design strategies and functional characterization in mammalian cells and rodent. Nucleic Acids Res 47:e97

Milias-Argeitis A, Summers S, Stewart-Ornstein J, Zuleta I, Pincus D, El-Samad H, Kham-mash M, Lygeros J (2011) In silico feedback for in vivo regulation of a gene expression circuit. Nat Biotechnol 29:1114–1116

Motta-Mena LB, Reade A, Mallory MJ, Glantz S, Weiner OD, Lynch KW, Gard-ner KH (2014) An optogenetic gene expression system with rapid activation and deactivation kinetics. Nat Chem Biol 10:196–202

Müller K, Engesser R, Metzger S, Schulz S, Kämpf MM, Busacker M, Steinberg T, Tomakidi P, Ehrbar M, Nagy F, Timmer J, Zubriggen MD, Weber W (2013) A red/far-red-light-responsive bi-stable toggle switch to control gene expression in mammalian cells. Nucleic Acids Res 41:e77

Nelson DE, Ihekwaba AEC, Elliott M, Johnson JR, Gibney CA, Foreman BE, Nelson G, See V, Horton CA, Spiller DG, Edwards SW, McDowell HP, Unitt JF, Sullivan E, Grimley R, Benson N, Broomhead D, Kell DB, White MRH (2004) Oscillations in NF-κB signaling control the dynamics of gene expression. Science 306:704–708

Purvis JE, Lahav G (2013) Encoding and decoding cellular information through signaling dynamics. Cell 152:945–956

Quejada JR, Park S-HE, Awari DW, Shi F, Yamamoto HE, Kawano F, Jung JC, Yazawa M (2017) Optimized light-inducible transcription in mammalian cells using Flavin Kelch-repeat F-box1/GIGANTEA and CRY2/CIB1. Nucleic Acids Res 45:e172

Rullan M, Benzinger D, Schmidt GW, Milias-Argeitis A, Khammash M (2018) An optogenetic platform for real-time, single-cell interrogation of stochastic transcriptional regulation. Mol Cell 70:745–756.e6

Shimizu-Sato S, Huq E, Tepperman JM, Quail PH (2002) A light-switchable gene promoter system. Nat Biotechnol 20:1041–1044

Shimojo H, Ohtsuka T, Kageyama R (2008) Oscillations in notch signaling regulate maintenance of neural progenitors. Neuron 58:52–64

Shimojo H, Isomura A, Ohtsuka T, Kori H, Miyachi H, Kageyama R (2016) Oscillatory control of Delta-like1 in cell interactions regulates dynamic gene expression and tissue morphogenesis. Genes Dev 30:102–116

Taslimi A, Zoltowski B, Miranda JG, Pathak GP, Hughes RM, Tucker CL (2016) Optimized second-generation CRY2–CIB dimerizers and photoactivatable Cre recombinase. Nat Chem Biol 12:425–430

Wang X, Chen X, Yang Y (2012) Spatiotemporal control of gene expression by a light-switchable transgene system. Nat Methods 9:266–269

Webb AB, Lengyel IM, Jörg DJ, Valentin G, Jülicher F, Morelli LG, Oates AC (2016) Persistence, period and precision of autonomous cellular oscillators from the zebrafish segmentation clock. eLife 5:e08438

Weber AM, Kaiser J, Ziegler T, Pilsl S, Renzl C, Sixt L, Pietruschka G, Moniot S, Kakoti A, Juraschitz M, Schrottke S, Lledo Bryant L, Steegborn C, Bittl R, Mayer G, Möglich A (2019) A blue light receptor that mediates RNA binding and translational regulation. Nat Chem Biol 15:1085–1092

Yamada M, Suzuki Y, Nagasaki SC, Okuno H, Imayoshi I (2018) Light control of the Tet gene expression system in mammalian cells. Cell Rep 25:487–500

Yazawa M, Sadaghiani AM, Hsueh B, Dolmetsch RE (2009) Induction of protein-protein interactions in live cells using light. Nat Biotechnol 27:941–945

Yoshioka-Kobayashi K, Matsumiya M, Niino Y, Isomura A, Kori H, Miyawaki A, Kageyama R (2020) Coupling delay controls synchronized oscillation in the segmentation clock. Nature 580:119–123

Yu D, Lee H, Hong J, Jung H, Jo Y, Oh B-H, Park BO, Heo WD (2019) Optogenetic activation of intracellular antibodies for direct modulation of endogenous proteins. Nat Methods 16:1095–1100

Zhang W, Lohman AW, Zhuravlova Y, Lu X, Wiens MD, Hoi H, Yaganoglu S, Mohr MA, Kitova EN, Klassen JS, Pantazis P, Thompson RJ, Campbell RE (2017) Optogenetic control with a photocleavable protein, PhoCl. Nat Methods 14:391–394

Zoltowski BD, Vaccaro B, Crane BR (2009) Mechanism-based tuning of a LOV domain photoreceptor. Nat Chem Biol 5:827–834

# Functional Modulation of Receptor Proteins on Cellular Interface with Optogenetic System

15

Mizuki Endo and Takeaki Ozawa

**Abstract**

In multicellular organisms, living cells cooperate with each other to exert coordinated complex functions by responding to extracellular chemical or physical stimuli via proteins on the plasma membrane. Conventionally, chemical signal transduction or mechano-transduction has been investigated by chemical, genetic, or physical perturbation; however, these methods cannot manipulate biomolecular reactions at high spatiotemporal resolution. In contrast, recent advances in optogenetic perturbation approaches have succeeded in controlling signal transduction with external light. The methods have enabled spatiotemporal perturbation of the signaling, providing functional roles of the specific proteins. In this chapter, we summarize recent advances in the optogenetic tools that modulate the function of a receptor protein. While most optogenetic systems have been devised for controlling ion channel conductivities, the present review focuses on the other membrane proteins involved in chemical transduction or mechano-transduction. We describe the properties of natural or artificial photoreceptor proteins used in optogenetic systems. Then, we discuss the strategies for controlling the receptor protein functions by external light. Future prospects of optogenetic tool development are discussed.

**Keywords**

GPCR · RTK · Mechano-transduction · Chemokine

## Abbreviations

| | |
|---|---|
| AdoCbl | 5′-Deoxyadenosylcobalamin |
| AsLOV2 | LOV2 from *Avena sativa* phototropin 1 |
| AU1 | Aureochrome 1 |
| BV | Biliverdin IXα |
| CBD | Cobalamin-binding domain |
| CIB1 | Cryptochrome interacting basic-helix-loop-helix protein 1 |
| CPH1 | Cyanobacterial phytochrome 1 |
| CRY2 | Cryptochrome 2 |
| DAG | Diacylglycerol |
| DCC | Deleted in colorectal carcinoma |
| DrBphP | Bacterial phytochrome photosensory domain from *Deinococcus radiodurans* |
| ECM | Extracellular matrix |
| EGFR | Epidermal growth factor receptor |
| EphB2 | Ephrin type-B receptor 2 |
| FAD | Flavin adenine nucleotide |
| FGFR | Fibroblast growth factor receptor |

M. Endo · T. Ozawa (✉)
Department of Chemistry, School of Science, The University of Tokyo, Tokyo, Japan
e-mail: ozawa@chem.s.u-tokyo.ac.jp



H. Yawo et al. (eds.), *Optogenetics*, Advances in Experimental Medicine and Biology 1293,
https://doi.org/10.1007/978-981-15-8763-4_15

| | |
|---|---|
| FMN | Flavin mononucleotide |
| GPCR | G-protein-coupled receptor |
| LOV | Light-oxygen-voltage sensing |
| LRP6 | Lipoprotein receptor-related protein 6 |
| MAPK | Mitogen-activated protein kinase |
| MxCBD | CBD of *Myxococcus xanthus* carh |
| PCB | Phycocyanobilin |
| PDGFRβ | Platelet-derived growth factor receptor β |
| PHR | Photolyase homology region |
| PhyB | Phytochrome B |
| PhyBt | Phyb tetramer |
| PIF6 | Phytochrome interacting factor 6 |
| pMHC | Peptide/major histocompatibility complex |
| PΦB | Phytochromobilin |
| RET | Rearranged during transfection |
| RGS4 | Regulator of G-protein signaling 4 |
| RTK | Receptor tyrosine kinase |
| SH2-N | N-terminal src-homology 2 domain from PLC-γ |
| TGF-β | Transforming growth factor beta |
| Trk | Tropomyosin receptor kinase |
| TtCBD | CBD of *Thermus thermophilus* carh |
| TβRI | TGF-β type I receptor |
| UVR8 | UV-B resistance 8 |
| VVD | Vivid |
| $\beta_2$AR | $\beta_2$-adrenergic receptor |

## 15.1 Introduction

The plasma membrane of a living cell contains proteins that mediate the signal transduction, where chemical or physical signals are transmitted through a cell as a series of biomolecular reactions. Chemical stimuli are conveyed by proteins, peptides, or other organic molecules, which are recognized by a receptor protein as ligands. The ligand-bound receptor subsequently triggers downstream signaling cascades, which elicit various cellular responses. Living cells are also able to respond to physical stimuli, which encompass heat, light, and mechanical cues. Especially, the process that converts mechanical stimuli into biochemical reactions is called mechano-transduction (Maurer and Lammerding 2019), which plays crucial roles in multicellular behaviors during tissue morphogenesis, cancer progression, etc. (Ladoux and Mège 2017). By responding to the dynamic extracellular stimuli, cells cooperate with each other to exert coordinated complex functions, which is indispensable in multicellular organisms.

In chemical signal transduction, ligands are recognized by various receptor proteins, including G-protein-coupled receptors (GPCRs), receptor tyrosine kinases (RTKs), and ligand-gated ion channels. GPCRs, or seven-transmembrane receptors, constitute the largest family of membrane receptor proteins in mammalian cells, which are also the most common target of therapeutic drugs. The ligand binding allosterically induces conformational changes in cytoplasmic surface, initiating G-protein- or arrestin-mediated signaling (Weis and Kobilka 2014). Most RTKs are single-pass transmembrane proteins, whose cytoplasmic domains have kinase activity that phosphorylates themselves and downstream molecules. The cytosolic domains are activated when they are brought into close proximity upon ligand binding. Similar activation mechanism also holds to other receptors. Ligand-gated ion channels, or ionotropic receptors, open a pore which allows regulated ion flux across the plasma membrane upon ligand-induced conformational changes. In all cases, extracellular biomolecules recognized by a receptor act as the first messengers to communicate intercellularly.

The major proteins engaged in the recognition of mechanical cues are mechano-receptors such as cadherins and integrins. Cadherin is a transmembrane protein that form adhesion complex at cell-to-cell interface. In the presence of calcium ion, the extracellular domain of cadherins expressed on different cells forms rigid contacts between cells. The intracellular domain is tethered to cytosolic structures such as actomyosin complex. The contractile force generated by the actomyosin assembly applies tension on the associating cadherins. The tension transmitted through the cadherin complex triggers biochemical responses in the adjacent cells. On the other hand, integrin expressed on the plasma membrane

forms rigid contact with extracellular matrix (ECM) via its extracellular domain. The stiffness of the surrounding ECM is transferred through integrins to downstream mechano-sensing proteins via the intracellular domain. Using these mechano-receptors, cell directly responds to the mechanical cues in the surrounding environments by mechano-transduction.

Conventionally, the roles of receptor proteins in chemical signal transduction have been examined by chemical or genetic perturbations. These approaches have identified a number of components in various signaling pathways by activating or inactivating the specific nodes in the signal network; however, these approaches are not suitable for analyzing the spatiotemporal dynamic behaviors of signaling systems due to their inherent technical difficulties. On the other hand, physical perturbations have also been used in examining the mechano-transduction: micropipette aspiration, optical traps, and laser ablation (Sung et al. 1986; Bambardekar et al. 2015; Roh-Johnson et al. 2012; Levayer and Lecuit 2013). However, these methods cannot provide biomolecular information, and sometimes destroy the plasma membrane integrity.

For the analysis of spatiotemporal dynamics in cellular signal transduction, optogenetic perturbation has gained wide attention recently. The approach requires expression of specifically designed proteins that modulate biomolecular reactions in response to light stimuli. Since the advent of light-gated ion channels, a number of optogenetic systems have been devised for the optical control of other proteins, including receptor proteins involved in chemical transduction or mechano-transduction. These systems have become powerful tools to dissect dynamic biological processes, and made a great impact on a wide range of biological research fields.

In this chapter, we summarize recent advances in the optogenetic tools that modulate the function of proteins on the plasma membrane. While most optogenetic systems have been devised for controlling ion channel conductivities, the present review focuses on receptor proteins responsible for chemical transduction or mechano-transduction. We describe the photoreaction characters of natural or artificial photoreceptor proteins used in optogenetic systems. Then, we discuss the molecular design for the generation of the optogenetic tools, which control the receptor protein functions with external light. Finally, we offer the conclusions and future prospects of the optogenetic tool development.

## 15.2 Light-Sensitive Modules Used in Optogenetic Systems

Optogenetic systems contain light-sensory modules, photoreceptor proteins, to convert light stimuli into biomolecular reactions (Tables 15.1, 15.2 and 15.3). Various photoreceptor proteins have been identified in mammals, plants, bacteria, and fungi, which absorbs light at specific wavelength ranging from UV to far-red. The light-absorbing unit in photoreceptor protein is called chromophore, usually an incorporated cofactor molecule (Fig. 15.1). The light-absorbed chromophore undergoes photochemical reaction and triggers subsequent conformational changes in photoreceptor proteins. The photo-activated photoreceptor proteins behave as conformational strain modules, light-dependent dimerization modules, or dissociation modules. In this section, we overview the characters of main photoreceptor proteins used in the optogenetic systems for controlling receptor proteins based on their photoreaction properties.

### 15.2.1 Light-Inducible Conformational Strain Modules

Opsins are light-sensitive seven-transmembrane ion channels or GPCRs found in various organisms. Some optogenetic tools utilize opsins as light-inducible conformational strain module (Fig. 15.2a, Table 15.1). Mammalian rhodopsin is an opsin expressed in retinal rod for dim light vision, which is composed of the protein opsin (~39 kDa) and covalently bound a cofactor molecule 11-*cis*-retinal (Fig. 15.1a) (Travis et al. 2007). Upon absorption of ~500 nm light, the 11-*cis*-retinal chromophore is converted to the

**Table 15.1** Opsins used for optoXRs

| Name | Origin | Size (kDa) | Cofactor | Activation/ deactivation (nm) | Fused GPCR | Ref |
|---|---|---|---|---|---|---|
| Rhodopsin | *Bos taurus* | 39 | 11-*Cis*-retinal | 500/dark | $\beta_2$AR, $\alpha_1$AR, 5-$HT_{1A}$, MOR, D1R, D2R, CXCR4, $A_2$AR, mAChR1–3, FFR3, Frizzled7 | Kim et al. (2005); Airan et al. (2009); Oh et al. (2010); Siuda et al. (2015a, b); Barish et al. (2013); Gunaydin et al. (2014); Morri et al. (2018); Xu et al. (2014); Li et al. (2015); Čapek et al. (2019) |
| mOpn4L | *Mus musculus* | 57 | 11-*Cis*-retinal | 470/560 | mGluR6 | van Wyk et al. (2015) |
| hOpn4L | *Homo sapiens* | 54 | 11-*Cis*-retinal | 470/560 | 5-$HT_{2A}$ | McGregor et al. (2016) |
| bOpsin | *Homo sapiens* | 39 | 11-*Cis*-retinal | 414/dark | Jellyfish opsin | Karunarathne et al. (2013) |
| OPN3 | *Danio rerio* | 20 | 11-*Cis*-retinal | 465/dark | Jellyfish opsin | Sugihara et al. (2016) |
| Peropsin | *Hasarius adansoni* | 38 | All-*Trans*-retinal | 540/dark | Jellyfish opsin, mosquito OPN3 | Nagata et al. (2018) |

all-*trans* isomer (Fig. 15.1b). The light-induced retinal isomerization triggers the motion of fifth and sixth transmembrane helices, which is similarly found in some ligand-induced GPCR activations. Regeneration of rhodopsin bound with 11-*cis*-retinal seems to require several enzymatic reactions, although the detailed mechanism is unclear.

Melanopsin is another retinal opsin, which is expressed in intrinsically photosensitive retinal ganglion cells. In contrast to rhodopsin, the chromophore of melanopsin remains attached after the photoactivation and shows a bistable photocycle

**Table 15.2** Photoreceptor proteins used for light-dependent interaction modules

| Name | Origin | Size (kDa) | Cofactor | Activation/ deactivation (nm) | Interacting partner | Ref |
|---|---|---|---|---|---|---|
| AU1 | *Vaucheria frigida* | 16 | FMN | 470/dark | – | Grusch et al. (2014); Sako et al. (2016); Khamo et al. (2019); Ingles-Prieto et al. (2015) |
| CPH1 | *Synechocystis* | 60 | PCB | 660/720 | – | Reichhart et al. (2016) |
| DrBphP | *Deinococcus radiodurans* | 80 | BV | 780/660 | – | Leopold et al. (2019) |
| CRY2[a] | *Arabidopsis thaliana* | 70 | FAD | 450/dark | CIB1 | Bugaj et al. (2013, 2015); Hannanta-anan and Chow (2018); Chang et al. (2014); Endo et al. (2016); Mao et al. (2018); Duan et al. (2018); Woo et al. (2019); Alapin et al. (2018); Deb Roy et al. (2017); Li et al. (2018); Nguyen et al. (2016); Takenouchi et al. (2018) |
| PhyB | *Arabiopsis thaliana* | 130 | PFB | 650/750 | PIF6 | Yu et al. (2016); Yousefi et al. (2019); Baaske et al. (2019) |
| pMag[a] | *Neurospora crassa* | 17 | FMN | 450/dark | nMag[a] | Yu et al. (2016, 2019) |

[a]Several variants are available

**Table 15.3** Photoreceptor proteins used for light-dependent dissociation modules

| Name | Origin | Size (kDa) | Cofactor | Activation/ deactivation (nm) | Interacting partner | Ref |
|---|---|---|---|---|---|---|
| UVR8 | *Arabidopsis thaliana* | 50 | None | 300/dark | – | Sarris et al. (2016) |
| MxCBD | *Myxococcus xanthus* | 23 | AdoCbl | 550/dark | – | Kainrath et al. (2017) |
| TtCBD | *Thermus thermophilus* | 22 | AdoCbl | 550/–[a] | – | Kainrath et al. (2017) |
| AsLOV2 | *Avena sativa* | 17 | FMN | 450/dark | Zdk1, Zdk2, Zdk3 | Tischer and Weiner (2019) |
| PhoCl | *Clavularia sp.* | 27 | None | 405/–[a] | – | Endo et al. (2019) |

[a]Reaction is irreversible

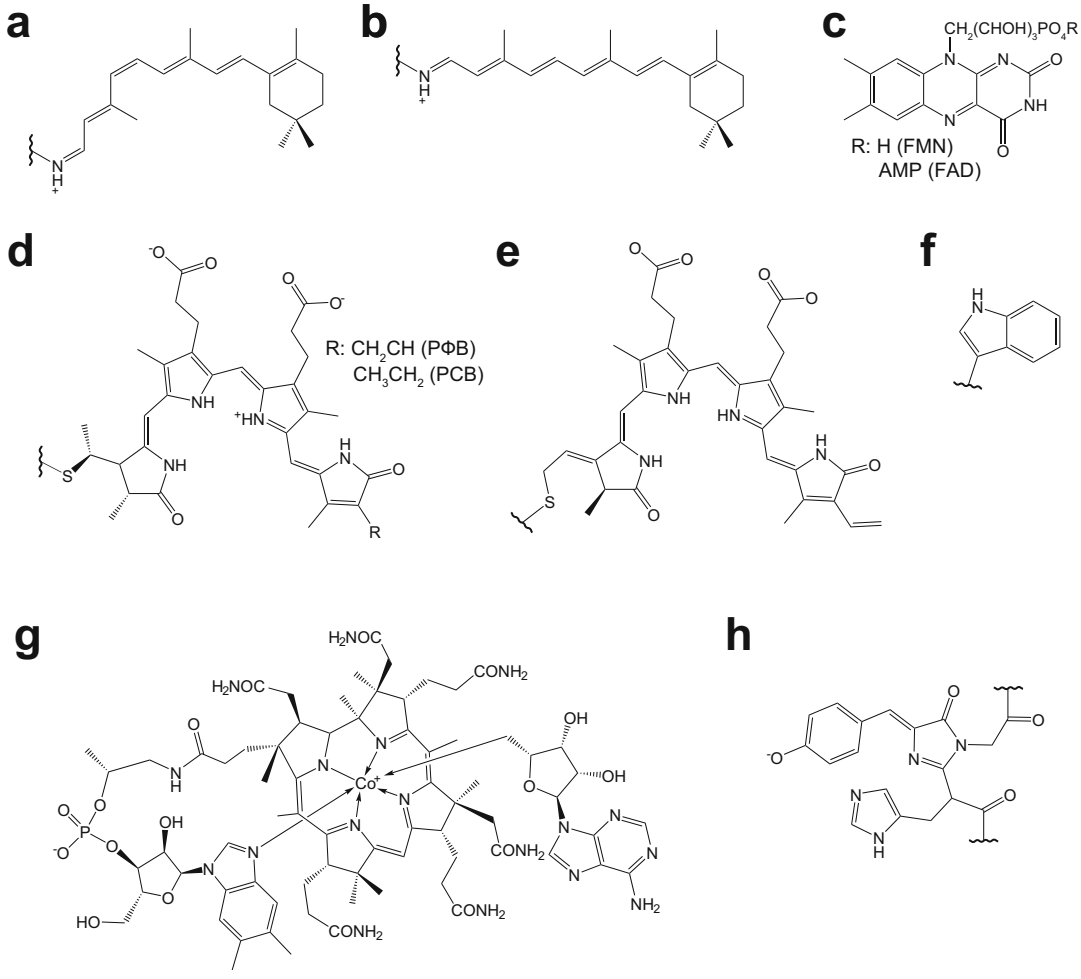


**Fig. 15.1** Chromophores in photoreceptor proteins. (**a**) 11-*Cis*-retinal. (**b**) All-*trans*-retinal. (**c**) Flavin molecule. (**d**) Phytochromobilin and phycocyanobilin. (**e**) Bilivertin IXα. (**f**) Tryptophan. (**g**) 5′-Deoxyadenosylcobalamin. (**h**) PhoCl chromophore

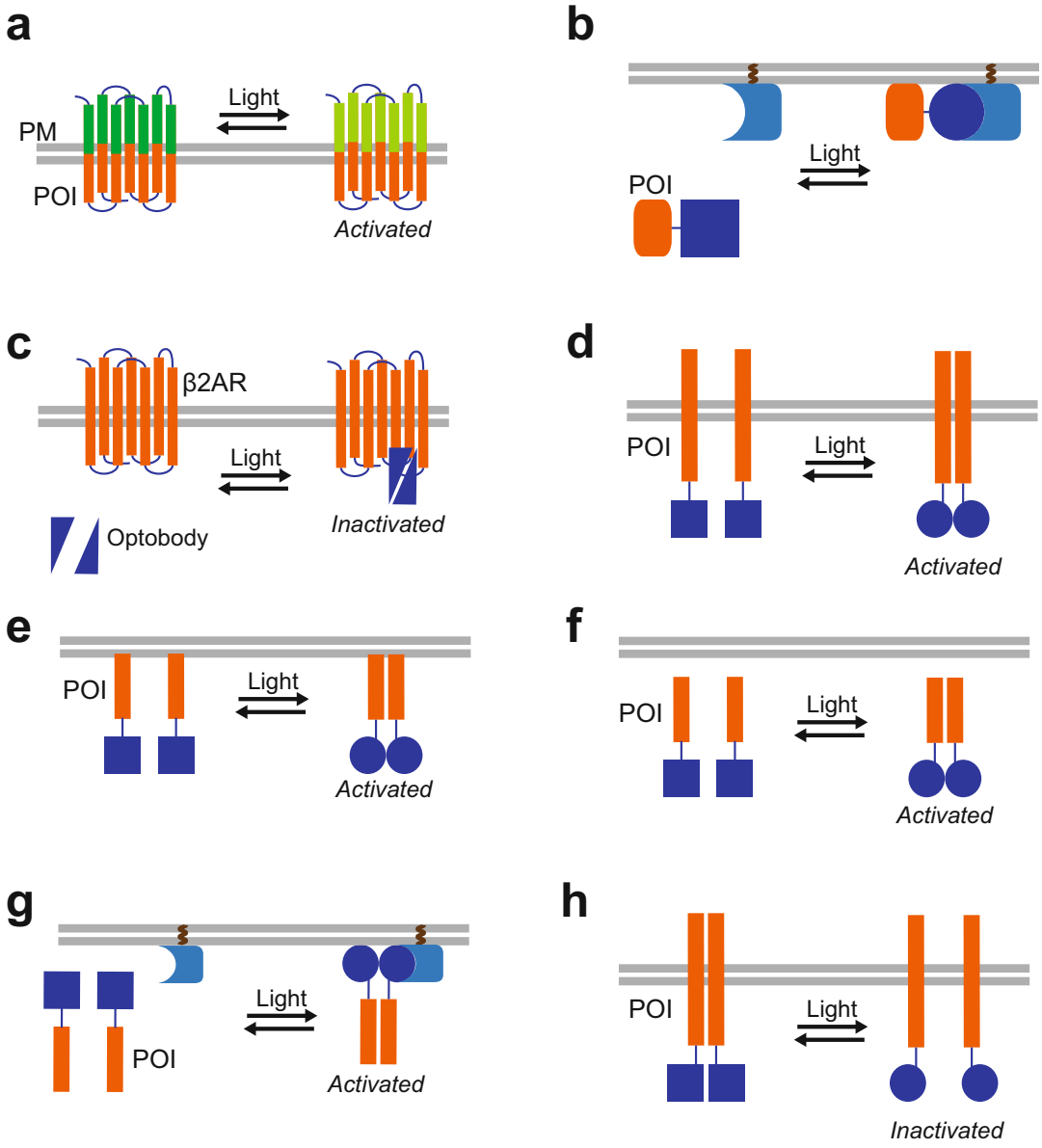


**Fig. 15.2** Molecular design for optogenetic tools. (**a**) optoXR. (**b**) Light-dependent protein recruitment. (**c**) Optical control of GPCR activity with optobody. (**d**) Photoactivation of full-length receptor. (**e**) Photo-activation of membrane-tethered receptor cytoplasmic domain. (**f**) Photo-activation of free receptor cytosolic domain. (**g**) Optical control of RTK with CLICR system. (**h**) Photoinactivation of RTK by light-dependent dissociation

(Sexton et al. 2012). Melanopsin is more resistant to bleach than rhodopsin, and usually photo-reverse at a different wavelength. For example, the long isoforms derived from mouse (mOpn4L) and human (hOpn4L) function as tristable pigments, which are activated by ~470 nm and inactivated by ~560 nm light (Spoida et al. 2016).

Opsins from different organisms are also used in optogenetic systems. Blue color opsin from human retina (bOpsin) responds to blue light

around 414 nm (Karunarathne et al. 2013). Zebrafish OPN3 is another light-sensitive opsin that absorbs blue light (~465 nm) (Sugihara et al. 2016). These bleach-resistant opsins bind 11-*cis*-retinal as a chromophore. In contrast, peropsin derived from a jumping spider *Hasarius adansoni* incorporates all-*trans*-retinal as a chromophore (Fig. 15.1b) (Nagata et al. 2018). In response to 540 nm light, spider peropsin forms thermally stable photoadduct with isomerized 11-*cis*-retinal, and does not release the chromophore retinal. The regeneration rate of spider peropsin (~10% in 8 min) is much slower than squid retinochrome (~100% in 1 min), a similar light-sensitive protein that binds all-*trans*-retinal chromophore.

### 15.2.2 Light-Dependent Dimerization Modules

Some photoreceptor proteins form homodimer or -oligomer, heterodimer with partner proteins upon light absorption (Table 15.2). Light-oxygen-voltage sensing (LOV) domain, a subfamily of the Per-aryl hydrocarbon receptor nuclear translocator-Sim family, is a blue-light-absorbing unit in various light-sensitive proteins. The LOV domain non-covalently incorporates flavin molecules as a chromophore (Fig. 15.1c). Upon blue light absorption, the photo-activated flavin forms a covalent adduct between the $C_{4a}$ of the flavin cofactor and the thiol moiety of a cysteine residue within the LOV core, leading to the conformational changes in the overall LOV domain. The lifetime of the covalent bond ranges from seconds to hours, depending on the LOV domain (Pudasaini et al. 2015). LOV domain of Aureochrome 1 from yellow-green alga *Vaucheria frigida* (AU1, ~16 kDa) forms homodimer upon blue light illumination (~470 nm) (Grusch et al. 2014). The lifetime of the photoadduct is 220 s at 37 °C. A circadian clock protein Vivid from filamentous fungus *Neurospora crassa* (VVD, ~17 kDa) also forms homodimer, whose lifetime is about 18,000 s (Zoltowski et al. 2009). The mutagenic engineering yielded light-dependent dimerizing pair named Magnets (pMag and nMag), whose lifetime ranges from 30 s to 9350 s, depending on the variants.

Cryptochrome is another blue-light-sensitive photoreceptor protein which contains flavin adenine nucleotide (FAD) in the photolyase homology region (PHR) as a chromophore (Fig. 15.1c). Cryptochrome 2 (CRY2, ~70 kDa) from flowering plant *Arabidopsis thaliana* is widely used as homo-oligomerizing or heterodimerizing module in various optogenetic systems. Upon blue light absorption (~450 nm), CRY2 reversibly forms homo-oligomer via the C-terminal surface of the PHR domain. The oligomerization efficiency can be modulated by E490G mutation (Bugaj et al. 2013; Duan et al. 2017), or by conjugating short peptide (ARDPPDLDN) or fluorescent protein at the C-terminus (Park et al. 2017). CRY2 also associates with cryptochrome-interacting basic-helix-loop-helix protein 1 (CIB1, ~40 kDa) via the N-terminal surface upon blue light absorption (Duan et al. 2017; Liu et al. 2008).

Phytochrome is a red- or far-red-sensitive photoreceptor protein, which incorporates bilin molecule as a chromophore (Fig. 15.1d, e): Phytochromobilin (PΦB) for plant phytochromes, phycocyanobilin (PCB) for cyanobacterial phytochromes, and biliverdin IXα (BV) for bacterial phytochrome. While PΦB and PCB are absent in mammalian cells, BV exists as a naturally degraded heme molecule in all cells. The photochemical transition between two conformational states is regulated by two wavelengths. Plant phytochrome B from *Arabidopsis thaliana* (PhyB, ~130 kDa) reversibly associates with N-terminal 100 amino acids of phytochrome interacting factor 6 (PIF6) upon red light (~650 nm) and dissociates upon far-red light (~750 nm) (Levskaya et al. 2009; Khanna et al. 2004). Cyanobacterial phytochrome 1 from *Synechocystis* (CPH1, ~60 kDa) forms homodimer upon 660 nm light, while monomerizes upon 720 nm light (Reichhart et al. 2016). Because their cofactors are not present in mammalian cells, these optogenetic systems require exogenous cofactor introduction, or genetic engineering on endogenous metabolic pathway (Uda et al. 2017). On the other hand, the

cofactor of bacterial phytochrome photosensory domain from *Deinococcus radiodurans* (DrBphP, ~80 kDa), BV, is available in mammalian cells. DrBphP serves as homodimerizing platform upon 780 nm illumination, which reverts to originally separated state under 660 nm illumination (Takala et al. 2014; Leopold et al. 2019).

### 15.2.3 Light-Dependent Dissociation Modules

Photoreceptor homodimer that dissociates upon illumination is used as a light-dependent dissociation module (Table 15.3). *Arabidopsis thaliana* UV-B resistance 8 (UVR8, ~50 kDa) was originally identified from mutant hypersensitive to UV-B light (~300 nm). The dimeric UVR8, which interact via arginine, glutamate, and aspartate residues at the dimer interface, absorbs UV-B light by intrinsic tryptophan residues (Fig. 15.1f), namely by Trp285 and Trp233 (Tilbrook et al. 2013). The excited tryptophan residues destabilize the dimer interface, resulting in the dissociation of UVR8 dimer into monomers (Binkert et al. 2016). Regeneration of the UVR8 dimer occurs in 1–2 h in plant; however, the dark reversion takes more than 8 h in mammalian cells (Chen et al. 2013). It is mostly because RUP1 and RUP2 help re-dimerization of UVR8 in plant cells (Tilbrook et al. 2013). In optogenetic system, UVR8 is used as almost irreversible dissociation module sensitive to UV-B light.

Cobalamin ($B_{12}$) is an essential vitamin in humans, which are synthesized by microorganisms (Zhang et al. 2009). Cobalamin-binding domain (CBD) of *Myxococcus xanthus* CarH (MxCBD, ~23 kDa) forms homo-tetramer upon incorporation of 5-′-deoxyadenosylcobalamin (AdoCbl, Fig. 15.1g) as a cofactor (Kainrath et al. 2017). Green-light (540–550 nm) illumination triggers photolytic cleavage of AdoCbl Co–C bond, resulting in reversible monomerization. Homo-tetrameric CBDs of *Thermus thermophilus* CarH (TtCBD, ~22 kDa) also dissociate into monomer upon green-light illumination; however, TtCBD stably exists as a monomer after illumination due to the stable conjugation between activated AdoCbl and the histidine residue.

Photo-dissociating pair between photoreceptor and its artificial binding partner was generated by protein engineering. LOV2 from *Avena sativa* phototropin 1 (AsLOV2, ~17 kDa), a widely used LOV domain in optogenetic systems, utilizes flavin mononucleotide (FMN, Fig. 15.1c) as a blue-light-absorbing (~450 nm) chromophore. Upon illumination, the formation of FMN-cysteine photoadduct causes reversible conformational change of AsLOV2. mRNA display screening based on the Z domain of immunoglobulin-binding staphylococcal protein A generated a small protein fragment Zdk, which selectively interacts with the dark state of AsLOV2 (Wang et al. 2016). Upon blue light illumination, the AsLOV2–Zdk heterodimer reversibly dissociates into monomers within a second, whose re-association kinetics can be tuned from <3 to ~500 s.

A photo-cleavable module named PhoCl (~27 kDa) was developed from a monomeric photo-convertible fluorescent protein, mMaple (Zhang et al. 2017). The chromophore of mMaple is generated by His, Tyr, and Gly residues (Fig. 15.1h), which absorbs ~490 nm light and emits green fluorescence (~505 nm). Blue light illumination (405 nm) triggers cleavage of the polypeptide chain through β-elimination of the residue immediately preceding the chromophore, yielding photo-converted chromophore, which emits red fluorescence (~580 nm) upon ~570 nm light absorption. PhoCl was developed by circular permutation and random mutagenesis on mMaple. Upon blue-light-induced cleavage of the protein backbone, PhoCl spontaneously dissociated into two fragments with loss of fluorescence.

## 15.3 Optogenetic Perturbation in Chemical Signal Transduction

The activation mechanisms of various receptors involved in chemical signal transduction have been unveiled by the intensive biochemical

analysis; activated GPCRs undergo dynamic conformational changes; ligand-bound RTKs form homodimer, which is a key step for the activation of cytoplasmic kinase domain. The incorporation of light-sensitive modules derived from photoreceptor proteins enabled optical control of the receptors. In this section, we summarize the recent advances in the generation of optogenetic tools that manipulate receptor functions, based on their regulatory strategies (Fig. 15.2).

### 15.3.1 Optical Modulation of GPCR Activities

GPCRs share similar three-dimensional structures: the N-terminal extracellular region, seven-transmembrane helices connected with three extracellular loops and three intracellular loops, and the C-terminal cytoplasmic tail. In most GPCRs, the N-terminus, transmembrane helices, and extracellular loops are involved in ligand binding and receptor activation, while intracellular loops and the C-terminus are responsible for the activation of downstream signaling. Photo-activatable chimeric GPCRs named "optoXRs" are generated by replacing the N-terminus, transmembrane helices and extracellular loops of the target GPCRs with those of opsins (Fig. 15.2a) (Tichy et al. 2019). Upon light absorption by retinal, the conformational changes in the fused opsin are transferred to the target GPCR cytoplasmic region, triggering the subsequent biomolecular signaling. The initial example of optoXR is the chimeric fusion between bovine rhodopsin and hamster $\beta_2$-adrenergic receptor ($\beta_2$AR) chimera (opto-$\beta_2$AR), which enabled photoactivation of $\beta_2$AR-dependent signaling (Kim et al. 2005). The subsequent application with human $\alpha_{1a}$-adrenergic receptor (opto-$\alpha_1$AR) in living mice demonstrated optical control of reward-related behavior (Airan et al. 2009). The optoXR strategy using bovine Rho was applied to other GPCRs, such as serotonergic receptor (5-$HT_{1A}$) (Oh et al. 2010), μ opioid receptor (MOR) (Siuda et al. 2015a; Barish et al. 2013), dopaminergic receptors (D1R, D2R) (Gunaydin et al. 2014; Morri et al. 2018), chemokine receptor (CXCR4) (Xu et al. 2014), adenosine receptor ($A_{2A}$R) (Li et al. 2015), muscarinic acetylcholine receptors (mAChR1, 2, and 3) (Barish et al. 2013), free fatty acid receptor (FFR3) (Barish et al. 2013), and Frizzled 7 (Čapek et al. 2019). The generation of optoXRs using orphan receptors, whose ligands and downstream signaling are unknown, provided biomolecular information on the receptor functions (Barish et al. 2013). Additional mutations on the fused GPCR intracellular loops enabled selective photoactivation of G-protein- or β-arrestin-mediated pathways (Siuda et al. 2015b).

Nonrhodopsin opsins have been exploited for the generation of optoXRs. The extracellular and transmembrane region of jellyfish opsin, which responds to ~500 nm light, was replaced with those of bOpsin or zebrafish OPN3, yielding the chimeric proteins that responds to 445 or 470 nm illumination (Karunarathne et al. 2013; Sugihara et al. 2016). The light-sensitive melanopsin core was used for the optical control of mGluR6 (van Wyk et al. 2015) or 5-$HT_{2A}$ (McGregor et al. 2016) functions. Because these opsins are resistant to bleach, they ensure repeatable photoactivation of the target GPCRs. In contrast, all-*trans*-retinal-binding peropsin is inactivated by illumination. The chimeric fusion with jellyfish opsin or mosquito OPN3 achieved dark-active, light-inactivated G-protein-mediated pathways (Nagata et al. 2018).

There are several other approaches for controlling the function of GPCRs. The light-dependent heterodimerization modules have been used for light-controlled protein translocation system, especially for plasma membrane recruitment of the target proteins (Fig. 15.2b) (Endo and Ozawa 2017). Magnet or PhyB/PIF6 translocates the constitutively active form of Gα to the plasma membrane upon illumination, subsequently triggering downstream signaling (Yu et al. 2016). The light-dependent recruitment of truncated regulator of G-protein signaling 4 (RGS4) or Gβγ-sequestering domain using CRY2/CIB1 results in the localized inhibition of G-protein-mediated signaling. Light-induced reconstitution of split RGS2 by CRY2/CIB1 enables direct analysis on the regulatory role of

RGS2 in the stochasticity of the $G\alpha_q$-mediated calcium spike timing (Hannanta-anan and Chow 2018). Recently, a single-chain antibody called nanobody against $\beta_2$AR was engineered into "optobody," whose antigen-binding ability was controllable with external light using Magnet (Fig. 15.2c) (Yu et al. 2019). $\beta_2$AR optobody achieved direct modulation of $\beta_2$AR functions by light-induced binding, demonstrating an innovative approach for future optogenetic engineering.

### 15.3.2 Photoactivation or Inactivation of Single-Pass Receptor Proteins

In general, ligand binding activates RTKs by inducing receptor dimerization, or oligomerization (Lemmon and Schlessinger 2010). Some other single-pass receptor proteins also share similar activation mechanisms. Due to their simple activation mechanisms, intensive efforts have been devoted to generate photo-activatable receptors using light-dependent heterodimerization or oligomerization modules.

The simplest molecular design is the genetic fusion between light-dependent oligomerization module CRY2 and full length of various receptors (Fig. 15.2d): tropomyosin receptor kinases (TrkA, B, C) (Chang et al. 2014), deleted in colorectal carcinoma (DCC) (Endo et al. 2016), and ephrin type-B receptor 2 (EphB2) (Mao et al. 2018). As for TrkA, a previous report suggests that the developed molecule using full-length TrkA cannot be fully activated by CRY2 oligomerization, partially due to the inhibitory effect by the extracellular and transmembrane domains (Duan et al. 2018).

In alternative molecular configuration, CRY2 is fused with the membrane-tethered intracellular kinase domain of the receptors (Fig. 15.2e), such as TrkA (Duan et al. 2018), TrkB (Woo et al. 2019), and EphB2 (Alapin et al. 2018). Light-dependent homodimerization module AU1 is also used for activating signaling downstream of RTKs: fibroblast growth factor receptor (FGFR), epidermal growth factor receptor (EGFR), rearranged during transfection (RET) (Grusch et al. 2014), Nodal receptors (Acvr1b and Acvr2b) (Sako et al. 2016), and TrkA (Khamo et al. 2019). The conjugation of AU1 to human ROS1 (hROS1), a proto-oncogene orphan RTK, enabled small-molecule screen without prior ligand information (Ingles-Prieto et al. 2015). The red photoreceptor CPH1 was used for activating FGFR1 or TrkB signaling upon 660 nm illumination (Reichhart et al. 2016). The far-red-sensitive photoreceptor DrBphP achieved optical control of TrkA or TrkB signaling at different wavelength (~780 nm), which require pre-illumination at 660 nm (Leopold et al. 2019).

Membrane-tethering of the receptor cytoplasmic domain is not necessarily required for the generation of photo-activatable receptor: the light-induced oligomerization of free cytosolic domain of lipoprotein receptor-related protein 6 (LRP6) using CRY2 triggered downstream signaling (Fig. 15.2f) (Bugaj et al. 2013). Combined with the plasma membrane recruitment based on the light-dependent interaction between the membrane-tethered CIB1 and receptor-fused CRY2 (Fig. 15.2e), TrkA and PlexinB1 were efficiently activated upon external light stimuli (Duan et al. 2018; Deb Roy et al. 2017). In some receptors, such as transforming growth factor beta (TGF-β) receptors, complex formation upon ligand binding is required for the signal activation. The light-induced association between membrane-tethered TGF-β type I receptor (TβRI) cytosolic domain and free TβRII cytosolic domain by CRY2/CIB triggered TGF-β signaling (Li et al. 2018).

Overexpression of receptor fusions sometimes increase the background activity: expression of full-length LRP6 fused with CRY2 exhibited high basal signaling (Bugaj et al. 2015). In CLICR system, CRY2 was fused with the N-terminal src-homology 2 domain from PLC-γ (SH2-N), which binds to FGFR1 and platelet-derived growth factor receptor β (PDGFRβ). Upon blue light illumination, co-expressed FGFR1 or PDGFRβ formed cluster via SH2-N clustering (Fig. 15.2g). Although SH2 domain typically does not bind unphosphorylated recognition site, SH2 domain clustering may enhance

association with unactivated or weakly activated receptors. In 3T3 fibroblasts, the blue-light-induced clustering of SH2-N induced activation of endogenous PDGFRβ signaling, without expressing the receptor fusions.

Light-induced dissociation modules were used for inactivating RTK with external light (Fig. 15.2h). The light-dependent dissociation modules, MxCBD or TtCBD, were fused with the membrane-tethered intracellular domain of FGFR1 (Kainrath et al. 2017). The addition of AdoCbl, cofactor of MxCBD and TtCBD, activated the FGFR1 signaling by CBD dimerization. After the onset of green-light illumination, fused FGFR1 and downstream substrate ERK underwent dephosphorylation. When cells were subsequently placed in the dark, the phosphorylation level of MxCBD-fused FGFR1 recovered to 86% of the original value within 60 min. In contrast, TtCBD-fused FGFR1 remained dephosphorylated due to the irreversibility of cofactor's photochemical reaction.

### 15.3.3 Optical Control of Receptor Protein Trafficking

The internalization of ligand-activated receptors plays a key role in the modulation of receptor-mediated signal transduction. Activated EGFR is internalized and delivered to Rab5-targeted early endosome, then to Rab7-targeted late compartment. In IM-LARIAT system, Rab5 fused with CIB1 was co-expressed with cytosolic CRY2 (Fig. 15.3a) (Nguyen et al. 2016). Upon blue light illumination, interaction between Rab5-fused CIB1 and CRY2 homo-oligomer induced aggregation of Rab5-targeted membrane. The Rab5 aggregation reduced the endocytosis rate of EGFR, which was monitored by dye-labeled EGF. On the other hand, the light-induced aggregation of Rab7 diminished the degradation of EGFR in the late compartment.

β-Arrestin is recruited to ligand-bound GPCRs, which promotes their endocytosis. In some GPCRs, the internalized GPCR-bound β-arrestin activates mitogen-activated protein kinases (MAPKs) pathway. The forced interaction between $\beta_2$AR and β-arrestin 2 by CRY2/CIB association with external light triggered clathrin-mediated $\beta_2$AR endocytosis (Fig. 15.3b) (Takenouchi et al. 2018). The prolonged illumination promoted lysosomal degradation of the internalized $\beta_2$AR. On the other hand, the light-dependent $\beta_2$AR/β-arrestin 2 interaction did not activate MAPK signaling, suggesting that β-arrestin 2 recruitment is not sufficient to trigger β-arrestin-mediated pathway.

### 15.3.4 Optogenetic Ligands

The light-induced interaction between photoreceptor protein and its partner is able to mimic ligand–receptor interaction. T-cell receptor on the T-cell surface is activated by the cognate peptide/major histocompatibility complex (pMHC) on the antigen-presenting cell. Conventionally, tetrameric pMHC based on streptavidin have been routinely used to stimulate TCR. In opto-ligand-TCR system, PhyB tetramer (PhyBt) was generated by streptavidin–biotin interaction, and TCR was fused with PIF6 (Fig. 15.4a) (Yousefi et al. 2019). Upon 660 nm illumination, the PhyBt interacted with PIF6-fused TCR and triggered calcium influx, which lead to T-cell activation. 740 nm illumination stopped the calcium signal, which ensured the bidirectional control of the opto-ligand-TCR system. Light-sensitive chimeric antigen receptor named Zdk-CAR was generated by the chimeric fusion between TCR and Zdk, which interacts with AsLOV2 in the dark (Fig. 15.4b) (Tischer and Weiner 2019). T cells expressing Zdk-CAR were exposed to supported lipid bilayer functionalized with AsLOV2. In the dark, AsLOV2 bound to Zdk-CAR and promoted the downstream biomolecular reaction, including ZAP70 recruitment and lipid diacylglycerol (DAG) accumulation. The blue-light-dependent dissociation between AsLOV2 and Zdk reversibly decreased the DAG accumulation.

The light-dependent dissociation module is applicable for triggering ligand release upon illumination (Fig. 15.4c). The C-termini of chemokines mouse Cxcl2 or zebrafish Cxcl8,

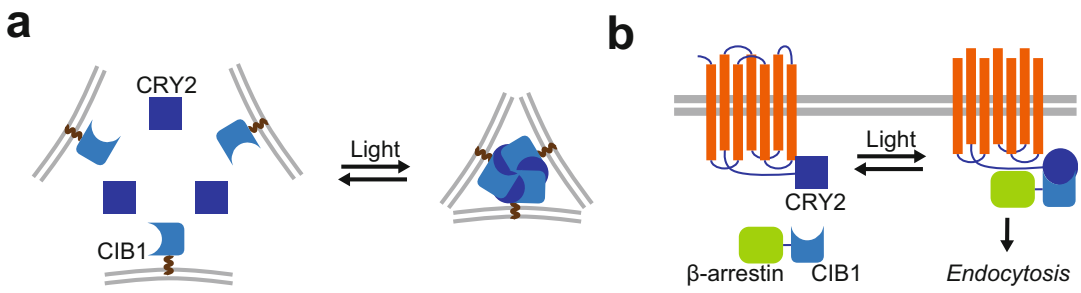


**Fig. 15.3** Optogenetic systems for controlling receptor trafficking. (**a**) IM-LARIAT system. (**b**) Light-dependent GPCR endocytosis

homologs of human CXCL8 (or interleukin-8), were fused with two UVR8 tandems via transmembrane region derived from VSVG and a cleavage site by furin, a Golgi-resident enzyme (Sarris et al. 2016). Due to the cluster formation by UVR8 repeat, fused chemokines were trapped in the endoplasmic reticulum. Upon UV irradiation, the dissociated chemokines were delivered to Golgi, where chemokines were cleaved off by furin. The light-induced chemokine secretion was confirmed in mouse and zebrafish tissues.

## 15.4 Optogenetic Perturbation in Mechano-Transduction

Cadherins and integrins are the major proteins that sense mechanical force at cell–cell or cell–ECM interface, respectively. There are emerging tools to control mechano-transduction mediated by these proteins with external light. In this section, we briefly introduce the optogenetic tools designed for the optical perturbation of cell–cell or cell–ECM mechano-transduction.

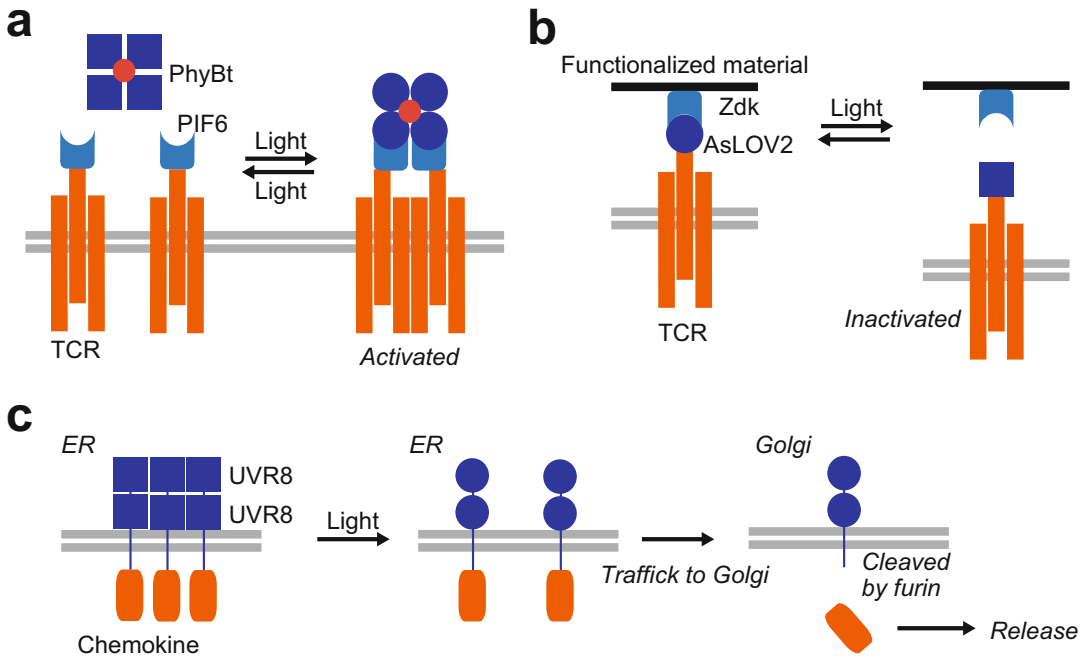


**Fig. 15.4** Optogenetic modulation of ligand–receptor reactions. (**a**) opto-ligand-TCR system. (**b**) Light-sensitive Zdk-CAR. (**c**) Light-dependent ligand release

Photo-cleavable protein is able to disrupt physical signal propagation in living cells. Intercellular E-cadherin complex is responsible for transmitting physical signals from cells to cells, especially as intercellular tension. To release intercellular contractile tension applied on E-cadherin complex, a photo-cleavable protein PhoCl was inserted into the cytoplasmic domain of E-cadherin, named PC-Cadherin (Fig. 15.5a) (Endo et al. 2019). Upon PhoCl photocleavage in response to blue light (405 nm), the PC-cadherin cleaved into two fragments. Dissociation of the C-terminal fragment attenuated intercellular tension transfer at intercellular junctions in living epithelial cells. The light-induced inhibition of the mechano-transduction perturbed the balance of contractile force among cells, resulting in expansion of the illuminated cell.

Light-dependent heterodimerization is able to mimic integrin–matrix interaction. OptoIntegrin was generated by inserting a PIF6 variant into the extracellular domain of the integrin αVβ3 β subunit (Fig. 15.5b) (Baaske et al. 2019). Purified PhyB was immobilized onto the glass surface, named OptoMatrix. Cells expressing OptoIngerin were seeded on the OptoMatrix. Under 660 nm light, OptoIntegrin–OptoMatrix interaction promoted cell adhesion on the functionalized surface; under 740 nm light, cells did not attach to the slide and formed large aggregates. The light-induced cell adhesion triggered downstream mechano-sensing pathways, including paxillin clustering and Erk or YAP1 activation.

## 15.5 Conclusions and Outlook

The emerging optogenetic technique drastically revolutionized the biological research field. It has achieved direct modulation of various signal transduction pathways in specific cell with external light, paving the way for unraveling the tangled cell–cell communications in multicellular organisms. There are several approaches to control chemical signal transduction: light-dependent control of ligand–receptor reactions, direct light regulation of receptor activities, and optical control of receptor trafficking. Because ligands are recognized by different receptors, and vice versa, different signaling pathways would be activated by photoactivation of ligands or receptors. Optical regulation of receptor trafficking (Nguyen et al. 2016; Takenouchi et al. 2018) will be helpful for the precise analysis of receptor functions, which is already demonstrated in the functional analysis of ionotropic receptor AMPA, for instance (Kakegawa et al. 2018). Depending on the target biological phenomena, the best optogenetic systems should be selected. As for mechano-transduction, there are few tools available for their optogenetic modulations. More intensive tool developments in this field will broaden the applicability of optogenetic approaches in deciphering cell–cell communications.

Light-sensitive single-pass receptors have been developed by several molecular designs: full-length receptor dimerization, membrane-tethered or free cytoplasmic domain dimerization, and translocation of the dimerized cytoplasmic domain. It seems difficult to predict which strategy works the best for controlling target receptor activities. Some receptors are activatable with full-length receptor dimerization approach (Chang et al. 2014; Endo et al. 2016; Mao et al. 2018). However, regarding TrkA-dependent neural outgrowth in PC12 cells, the approach was not able to activate the signal efficiently (Duan et al. 2018). Because a lot of optogenetic systems adopted the second strategy based on membrane-tethered cytoplasmic domain dimerization, it is tempting to speculate that the second strategy is the best; however, direct comparison among four approaches revealed that the last approach, which is based on translocation of the dimerized cytoplasmic domain, was the best for activating TrkA-dependent signaling. Therefore, it is encouraged to compare all molecular designs to develop optimal photoactivation system.

As described above, diverse photoreceptor proteins were utilized for modulating the signal transduction based on their photoreaction modes. Most of the developed optogenetic tools harnessed photoreceptor proteins which respond to blue to green light because they possess excellent photochemical properties and diverse

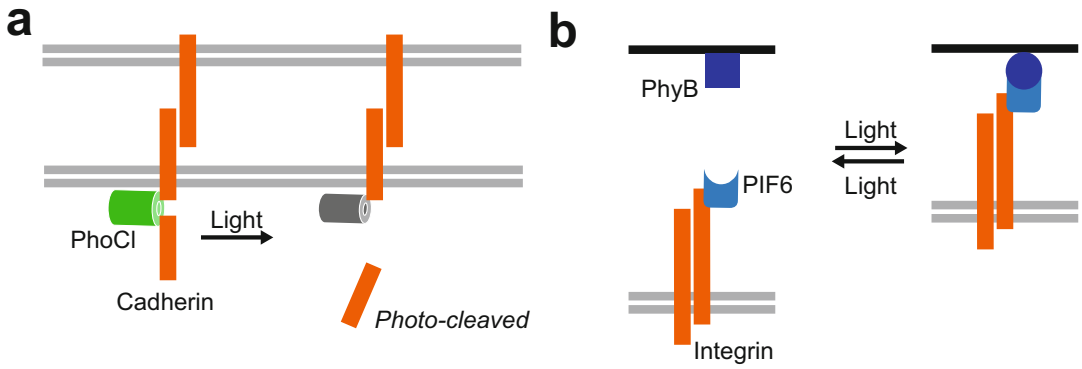


**Fig. 15.5** Optogenetic tools controlling mechano-transduction. (**a**) Photo-cleavable cadherin. (**b**) OptoIntegrin-OptoMatrix system

reaction modes, drastic conformational changes, heterodimerization, oligomerization, dissociation, and photocleavage. However, blue light is not suitable for the experiments in deep tissue, due to their poor tissue penetration. To overcome these difficulties, improvement on far-red-light-sensitive optogenetic modules is required.

Overexpression of optogenetic tools sometimes causes high basal activity in the dark, as seen in LRP6 fused with CRY2 (Bugaj et al. 2015). Direct gene engineering to establish stable cell line or transgenic mice is alternative solution to express light-sensitive receptor proteins, whose expression level can be comparable to that of endogenous proteins. Optical control of endogenous receptor proteins using nanobody (Yu et al. 2019) or adapter proteins (Bugaj et al. 2015) is another promising approach to solve the problem, although those modules are still limited. Further improvements on gene manipulation method or molecular recognition technique will expand the applicability of optogenetic tools in various biological contexts.

In summary, optical control of chemical- or mechano-transduction has paved the way for the precise analysis of dynamic cell–cell communication. Various molecular designs of optogenetic tools listed here will be helpful for future endeavors to achieve optical control of other signal pathways. Further improvements in photosensory modules, molecular design, or other related technologies will accelerate the various biological researches and deepen our understanding on highly sophisticated multicellular behaviors in living organisms.

**Acknowledgments** This work was supported by CREST (JPMJCR1752 to T.O.) from Japan Science and Technology (JST), and the Japan Society for the Promotion of Science (JSPS) KAKENHI (Grants-in-Aid for Scientific Research (A) 19H00900, Innovative Areas JP 18H04537 to T.O. and Grants-in-Aid for Scientific Research (C) 19K05538 to M.E.).

## References

Airan RD, Thompson KR, Fenno LE, Bernstein H, Deisseroth K (2009) Temporally precise *in vivo* control of intracellular signalling. Nature 458:1025–1029

Alapin JM, Dines M, Vassiliev M, Tamir T, Ram A, Locke C, Yu J, Lamprecht R (2018) Activation of EphB2 forward signaling enhances memory consolidation. Cell Rep 23:2014–2025

Baaske J, Mühlhäuser WWD, Yousefi OS, Zanner S, Radziwill G, Hörner M, Schamel WWA, Weber W (2019) Optogenetic control of integrin-matrix interaction. Commun Biol 2:15

Bambardekar K, Clément R, Blanc O, Chardès C, Lenne P-F (2015) Direct laser manipulation reveals the mechanics of cell contacts in vivo. Proc Natl Acad Sci U S A 112:1416–1421

Barish PA, Xu Y, Li J, Sun J, Jarajapu YPR, Ogle WO (2013) Design and functional evaluation of an optically active μ-opioid receptor. Eur J Pharmacol 705:42–48

Binkert M, Crocco CD, Ekundayo B, Lau K, Raffelberg S, Tilbrook K, Yin R, Chappuis R, Schalch T, Ulm R (2016) Revisiting chromatin binding of the *Arabidopsis* UV-B photoreceptor UVR8. BMC Plant Biol 16:1–11

Bugaj LJ, Choksi AT, Mesuda CK, Kane RS, Schaffer DV (2013) Optogenetic protein clustering and signaling activation in mammalian cells. Nat Methods 10:249–252

Bugaj LJ, Spelke DP, Mesuda CK, Varedi M, Kane RS, Schaffer DV (2015) Regulation of endogenous transmembrane receptors through optogenetic Cry2 clustering. Nat Commun 6:6898. https://doi.org/10.1038/ncomms7898

Čapek D, Smutny M, Tichy A-M, Morri M, Janovjak H, Heisenberg C-P (2019) Light-activated Frizzled7 reveals a permissive role of non-canonical wnt signaling in mesendoderm cell migration. eLife 8:e42093

Chang K-Y, Woo D, Jung H, Lee S, Kim S, Won J, Kyung T, Park H, Kim N, Yang HW, Park J-Y, Hwang EM, Kim D, Do Heo W (2014) Light-inducible receptor tyrosine kinases that regulate neurotrophin signalling. Nat Commun 5:4057. https://doi.org/10.1038/ncomms5057

Chen D, Gibson ES, Kennedy MJ (2013) A light-triggered protein secretion system. J Cell Biol 201:631–640

Deb Roy A, Yin T, Choudhary S, Rodionov V, Pilbeam CC, Wu YI (2017) Optogenetic activation of Plexin-B1 reveals contact repulsion between osteoclasts and osteoblasts. Nat Commun 8:15831

Duan L, Hope J, Ong Q, Lou H-Y, Kim N, McCarthy C, Acero V, Lin MZ, Cui B (2017) Understanding CRY2 interactions for optical control of intracellular signaling. Nat Commun 8:547

Duan L, Hope JM, Guo S, Ong Q, François A, Kaplan L, Scherrer G, Cui B (2018) Optical activation of TrkA signaling. ACS Synth Biol 7:1685–1693

Endo M, Ozawa T (2017) Strategies for development of optogenetic systems and their applications. J Photochem Photobiol C: Photochem Rev 30:10–23

Endo M, Hattori M, Toriyabe H, Ohno H, Kamiguchi H, Iino Y, Ozawa T (2016) Optogenetic activation of axon guidance receptors controls direction of neurite outgrowth. Sci Rep 6:23976

Endo M, Iwawaki T, Yoshimura H, Ozawa T (2019) Photocleavable cadherin inhibits cell-to-cell mechanotransduction by light. ACS Chem Biol 14:2206–2214

Grusch M, Schelch K, Riedler R, Reichhart E, Differ C, Berger W, Inglés-Prieto Á, Janovjak H (2014) Spatio-temporally precise activation of engineered receptor tyrosine kinases by light. EMBO J 33:1713–1726

Gunaydin LA, Grosenick L, Finkelstein JC, Kauvar IV, Fenno LE, Adhikari A, Lammel S, Mirzabekov JJ, Airan RD, Zalocusky KA, Tye KM, Anikeeva P, Malenka RC, Deisseroth K (2014) Natural neural projection dynamics underlying social behavior. Cell 157:1535–1551

Hannanta-anan P, Chow BY (2018) Optogenetic inhibition of Gαq protein signaling reduces calcium oscillation stochasticity. ACS Synth Biol 7:1488–1495

Ingles-Prieto A, Reichhart E, Muellner MK, Nowak M, Nijman SMB, Grusch M, Janovjak H (2015) Light-assisted small-molecule screening against protein kinases. Nat Chem Biol 11:952–954

Kainrath S, Stadler M, Reichhart E, Distel M, Janovjak H (2017) Green-light-induced inactivation of receptor signaling using cobalamin-binding domains. Angew Chem Int Ed 56:4608–4611

Kakegawa W, Katoh A, Narumi S, Miura E, Motohashi J, Takahashi A, Kohda K, Fukazawa Y, Yuzaki M, Matsuda S (2018) Optogenetic control of synaptic AMPA receptor endocytosis reveals roles of LTD in motor learning. Neuron 99:985–998.e986

Karunarathne WKA, Giri L, Kalyanaraman V, Gautam N (2013) Optically triggering spatiotemporally confined GPCR activity in a cell and programming neurite initiation and extension. Proc Natl Acad Sci U S A 110: E1565–E1574

Khamo JS, Krishnamurthy VV, Chen Q, Diao J, Zhang K (2019) Optogenetic delineation of receptor tyrosine kinase subcircuits in PC12 cell differentiation. Cell Chem Biol 26:400–410

Khanna R, Huq E, Kikis EA, Al-Sady B, Lanzatella C, Quail PH (2004) A novel molecular recognition motif necessary for targeting photoactivated phytochrome signaling to specific basic helix-loop-helix transcription factors. Plant Cell 16:3033–3044

Kim J-M, Hwa J, Garriga P, Reeves PJ, RajBhandary UL, Khorana HG (2005) Light-driven activation of β2-adrenergic receptor signaling by a chimeric rhodopsin containing the β2-adrenergic receptor cytoplasmic loops. Biochemistry 44:2284–2292

Ladoux B, Mège R-M (2017) Mechanobiology of collective cell behaviours. Nat Rev Mol Cell Biol 18:743–757

Lemmon MA, Schlessinger J (2010) Cell signaling by receptor tyrosine kinases. Cell 141:1117–1134

Leopold AV, Chernov KG, Shemetov AA, Verkhusha VV (2019) Neurotrophin receptor tyrosine kinases regulated with near-infrared light. Nat Commun 10:1129

Levayer R, Lecuit T (2013) Oscillation and polarity of E-cadherin asymmetries control actomyosin flow patterns during morphogenesis. Dev Cell 26:162–175

Levskaya A, Weiner OD, Lim WA, Voigt CA (2009) Spatiotemporal control of cell signalling using a light-switchable protein interaction. Nature 461:997–1001

Li P, Rial D, Canas PM, Yoo JH, Li W, Zhou X, Wang Y, van Westen GJP, Payen MP, Augusto E, Goncalves N, Tome AR, Li Z, Wu Z, Hou X, Zhou Y, Pijzerman A, Boyden ES, Cunha RA, Qu J, Chen JF (2015) Optogenetic activation of intracellular adenosine A2A receptor signaling in the hippocampus is sufficient to trigger CREB phosphorylation and impair memory. Mol Psychiatry 20:1339–1349

Li Y, Lee M, Kim N, Wu G, Deng D, Kim JM, Liu X, Heo WD, Zi Z (2018) Spatiotemporal control of TGF-β signaling with light. ACS Synth Biol 7:443–451

Liu H, Yu X, Li K, Klejnot J, Yang H, Lisiero D, Lin C (2008) Photoexcited CRY2 interacts with CIB1 to

regulate transcription and floral initiation in *Arabidopsis*. Science 322:1535–1539
Mao Y-T, Zhu JX, Hanamura K, Iurilli G, Datta SR, Dalva MB (2018) Filopodia conduct target selection in cortical neurons using differences in signal kinetics of a single kinase. Neuron 98:767–782
Maurer M, Lammerding J (2019) The driving force: nuclear mechanotransduction in cellular function, fate, and disease. Annu Rev Biomed Eng 21:443–468
McGregor KM, Bécamel C, Marin P, Andrade R (2016) Using melanopsin to study G protein signaling in cortical neurons. J Neurophysiol 116:1082–1092
Morri M, Sanchez-Romero I, Tichy A-M, Kainrath S, Gerrard EJ, Hirschfeld PP, Schwarz J, Janovjak H (2018) Optical functionalization of human Class A orphan G-protein-coupled receptors. Nat Commun 9:1950
Nagata T, Koyanagi M, Lucas R, Terakita A (2018) An all-trans-retinal-binding opsin peropsin as a potential dark-active and light-inactivated G protein-coupled receptor. Sci Rep 8:3535
Nguyen MK, Kim CY, Kim JM, Park BO, Lee S, Park H, Heo WD (2016) Optogenetic oligomerization of Rab GTPases regulates intracellular membrane trafficking. Nat Chem Biol 12:431–436
Oh E, Maejima T, Liu C, Deneris E, Herlitze S (2010) Substitution of 5-HT1A receptor signaling by a light-activated G protein-coupled receptor. J Biol Chem 285:30825–30836
Park H, Kim NY, Lee S, Kim N, Kim J, Heo WD (2017) Optogenetic protein clustering through fluorescent protein tagging and extension of CRY2. Nat Commun 8:30
Pudasaini A, El-Arab KK, Zoltowski BD (2015) LOV-based optogenetic devices: light-driven modules to impart photoregulated control of cellular signaling. Front Mol Biosci 2:18–18
Reichhart E, Ingles-Prieto A, Tichy A-M, McKenzie C, Janovjak H (2016) A phytochrome sensory domain permits receptor activation by red light. Angew Chem Int Ed 55:6339–6342
Roh-Johnson M, Shemer G, Higgins CD, McClellan JH, Werts AD, Tulu US, Gao L, Betzig E, Kiehart DP, Goldstein B (2012) Triggering a cell shape change by exploiting preexisting actomyosin contractions. Science 335:1232–1235
Sako K, Pradhan SJ, Barone V, Inglés-Prieto Á, Müller P, Ruprecht V, Čapek D, Galande S, Janovjak H, Heisenberg C-P (2016) Optogenetic control of nodal signaling reveals a temporal pattern of nodal signaling regulating cell fate specification during gastrulation. Cell Rep 16:866–877
Sarris M, Olekhnovitch R, Bousso P (2016) Manipulating leukocyte interactions *in vivo* through optogenetic chemokine release. Blood 127:e35–e41
Sexton TJ, Golczak M, Palczewski K, Van Gelder RN (2012) Melanopsin is highly resistant to light and chemical bleaching in vivo. J Biol Chem 287:20888–20897
Siuda ER, Copits BA, Schmidt MJ, Baird MA, Al-Hasani R, Planer WJ, Funderburk SC, McCall JG, Gereau RW, Bruchas MR (2015a) Spatiotemporal control of opioid signaling and behavior. Neuron 86:923–935
Siuda ER, McCall JG, Al-Hasani R, Shin G, Il Park S, Schmidt MJ, Anderson SL, Planer WJ, Rogers JA, Bruchas MR (2015b) Optodynamic simulation of b-adrenergic receptor signalling. Nat Commun 6:8480. https://doi.org/10.1038/ncomms9480
Spoida K, Eickelbeck D, Karapinar R, Eckhardt T, Mark MD, Jancke D, Ehinger BV, König P, Dalkara D, Herlitze S, Masseck OA (2016) Melanopsin variants as intrinsic optogenetic on and off switches for transient versus sustained activation of G protein pathways. Curr Biol 26:1206–1212
Sugihara T, Nagata T, Mason B, Koyanagi M, Terakita A (2016) Absorption characteristics of vertebrate non-visual opsin, Opn3. PLoS One 11:e0161215
Sung K, Sung L, Crimmins M, Burakoff S, Chien S (1986) Determination of junction avidity of cytolytic T cell and target cell. Science 234:1405–1408
Takala H, Björling A, Berntsson O, Lehtivuori H, Niebling S, Hoernke M, Kosheleva I, Henning R, Menzel A, Ihalainen JA, Westenhoff S (2014) Signal amplification and transduction in phytochrome photosensors. Nature 509:245–248
Takenouchi O, Yoshimura H, Ozawa T (2018) Unique roles of β-arrestin in GPCR trafficking revealed by photoinducible dimerizers. Sci Rep 8:677
Tichy A-M, Gerrard EJ, Sexton PM, Janovjak H (2019) Light-activated chimeric GPCRs: limitations and opportunities. Curr Opin Struct Biol 57:196–203
Tilbrook K, Arongaus AB, Binkert M, Heijde M, Yin R, Ulm R (2013) The UVR8 UV-B photoreceptor: perception, signaling and response. Arabidopsis Book 11: e0164–e0164
Tischer DK, Weiner OD (2019) Light-based tuning of ligand half-life supports kinetic proofreading model of T cell signaling. eLife 8:e42498
Travis GH, Golczak M, Moise AR, Palczewski K (2007) Diseases caused by defects in the visual cycle: retinoids as potential therapeutic agents. Annu Rev Pharmacol Toxicol 47:469–512
Uda Y, Goto Y, Oda S, Kohchi T, Matsuda M, Aoki K (2017) Efficient synthesis of phycocyanobilin in mammalian cells for optogenetic control of cell signaling. Proc Natl Acad Sci U S A 114:11962–11967
van Wyk M, Pielecka-Fortuna J, Löwel S, Kleinlogel S (2015) Restoring the ON switch in blind retinas: opto-mGluR6, a next-generation, cell-tailored optogenetic tool. PLoS Biol 13:e1002143
Wang H, Vilela M, Winkler A, Tarnawski M, Schlichting I, Yumerefendi H, Kuhlman B, Liu R, Danuser G, Hahn KM (2016) LOVTRAP: an optogenetic system for photoinduced protein dissociation. Nat Methods 13(9):755–758

Weis WI, Kobilka BK (2014) The molecular basis of G protein–coupled receptor activation. Annu Rev Biochem 87:897–919

Woo D, Seo Y, Jung H, Kim S, Kim N, Park S-M, Lee H, Lee S, Cho K-H, Heo WD (2019) Locally activating TrkB receptor generates actin waves and specifies axonal fate. Cell Chem Biol 26:1652

Xu Y, Hyun Y-M, Lim K, Lee H, Cummings RJ, Gerber SA, Bae S, Cho TY, Lord EM, Kim M (2014) Optogenetic control of chemokine receptor signal and T-cell migration. Proc Natl Acad Sci 111:6371–6376

Yousefi OS, Günther M, Hörner M, Chalupsky J, Wess M, Brandl SM, Smith RW, Fleck C, Kunkel T, Zurbriggen MD, Höfer T, Weber W, Schamel WWA (2019) Optogenetic control shows that kinetic proofreading regulates the activity of the T cell receptor. eLife 8: e42475

Yu G, Onodera H, Aono Y, Kawano F, Ueda Y, Furuya A, Suzuki H, Sato M (2016) Optical manipulation of the alpha subunits of heterotrimeric G proteins using photoswitchable dimerization systems. Sci Rep 6:35777

Yu D, Lee H, Hong J, Jung H, Jo Y, Oh B-H, Park BO, Do Heo W (2019) Optogenetic activation of intracellular antibodies for direct modulation of endogenous proteins. Nat Methods 16:1095. https://doi.org/10.1038/s41592-41019-40592-41597

Zhang Y, Rodionov DA, Gelfand MS, Gladyshev VN (2009) Comparative genomic analyses of nickel, cobalt and vitamin B12 utilization. BMC Genomics 10:78–78

Zhang W, Lohman AW, Zhuravlova Y, Lu X, Wiens MD, Hoi H, Yaganoglu S, Mohr MA, Kitova EN, Klassen JS, Pantazis P, Thompson RJ, Campbell RE (2017) Optogenetic control with a photocleavable protein, PhoCl. Nat Methods 14:391–394

Zoltowski BD, Vaccaro B, Crane BR (2009) Mechanism-based tuning of a LOV domain photoreceptor. Nat Chem Biol 5:827–834

# Genetically Encoded Photosensitizer for Destruction of Protein or Cell Function

16

Yemima Dani Riani, Tomoki Matsuda, and Takeharu Nagai

**Abstract**

There are several paths when excited molecules return to the ground state. In the case of fluorescent molecules, the dominant path is fluorescence emission that is greatly contributing to bioimaging. Meanwhile, photosensitizers transfer electron or energy from chromophore to the surrounding molecules, including molecular oxygen. Generated reactive oxygen species has potency to attack other molecules by oxidation. In this chapter, we introduce the chromophore-assisted light inactivation (CALI) method using a photosensitizer to inactivate proteins in a spatiotemporal manner and development of CALI tools, which is useful for investigation of protein functions and dynamics, by inactivation of the target molecules. Moreover, photosensitizers with high efficiency make it possible optogenetic control of cell ablation in living organisms and photodynamic therapy. Further development of photosensitizers with different excitation wavelengths will contribute to the investigation of multiple proteins or cell functions through inactivation in the different positions and timings.

**Keywords**

CALI · Photosensitizer · Reactive oxygen species (ROS) · Fluorescent protein · Protein destruction · Cell ablation

## Abbreviations

| | |
|---|---|
| $^1O^2$ | singlet oxygen |
| $^3O_2$ | Ground-state oxygen |
| CALI | chromophore-assisted light inactivation |
| CREM | correlative light and electron microscopy |
| FlAsH | fluorescein 4′,5′-bis(1,3,2-dithioarsolan-2-yl) fluorescein |
| FRAP | fluorescence recovery after photobleaching |
| GFP | Green Fluorescent Protein |
| GRASP | Golgi reassembly and stacking protein |
| KO | Knockout |
| NIR | Near infrared |
| $O_2^{\bullet-}$ | Superoxide anion |
| RNAi | RNA interference |
| ROS | reactive oxygen species |
| SIM | structured illumination microscopy |
| SOPP | singlet oxygen photosensitizing protein |
| Syt1 | synaptotagmin I |

Y. D. Riani · T. Matsuda · T. Nagai (✉)
The Institute of Scientific and Industrial Research (SANKEN), Osaka University, Osaka, Japan
e-mail: ng1@sanken.osaka-u.ac.jp



H. Yawo et al. (eds.), *Optogenetics*, Advances in Experimental Medicine and Biology 1293,
https://doi.org/10.1007/978-981-15-8763-4_16

## 16.1 Introduction

For understanding biological systems with constitutive approach, manipulation of the states of the system is an essential procedure. For this purpose, a diversity of the optogenetic tools based on the photoreceptors to regulate ion influx or induce protein structural change has been actively developed. They are applied to the wide-ranging research fields including neurobiology and developmental biology, as described in the other chapters in this book. Whereas if we look back on the era when the optogenetic tools had not yet become popular as in recent years, the principal way for perturbing biological systems was the induction of loss-of-function phenotypes by gene knockouts, RNA interference (RNAi), and the inhibitory drugs and antibodies. Although they have certainly contributed to give evidence to elucidate unexplained biological phenomena, they hold limitations to compromise analysis. Gene knockout, which produces knockout (KO) organisms by deletion or editing of target genes through embryonic stem cells, is inapplicable to destruction of genes essential for development or house-keeping due to embryonic lethality or lethality soon after birth. RNAi with controllability of timing is applicable to such genes. However, for completion of gene silencing, a period of time delay to degrade preexisting protein is required. Inhibitory drugs and antibodies have possibility to cause artifacts or side effects, depending on their specificity for the target protein.

As an alternative way to overcome these problems with higher spatiotemporal level, a technique to induce loss-of-function phenotypes by photocontrol was developed. It is known as a chromophore-assisted light inactivation (CALI) first reported by Daniel G. Jay in 1988, for which reactive oxygen species (ROS) is generated through photoirradiation of the chromophore in the photosensitizer to inactivate target molecules in the specific area and at specific timing (Jay 1988). Since ROS have high reactivity and their diffusible area in the cells is known to be limited within 6 nm, they can inflict oxidative damage to target proteins, DNA, and lipids that is located close enough to the photosensitizers (Jacobson et al. 2008). After the emergence of the protein-based genetically encoded photosensitizers, it is possible to create chimera with other proteins, the conjugation of the photosensitizers with target proteins become simple and easy. Meanwhile, by destructing proteins critical to maintaining cellular homeostasis, this technique is also applicable to the photoinduced cellular ablation of particular cells in the arbitral timing. That is useful to analyze cellular interactions, cell functions within tissues/organisms, and photodynamic therapy (targeted cancer treatment using light irradiation).

Here, mechanism of CALI and development of photosensitizer for protein and cellular inactivation are explained. In addition, future perspectives regarding this method are discussed.

## 16.2 The Molecular Mechanism of CALI

### 16.2.1 Discovery of CALI Phenomenon

Induction of cell death via light irradiation was conducted by a fluorescent dye, Lucifer yellow, in 1979. To achieve that, Miller and Selverston irradiated high-power laser with a wavelength of the absorption peak of the dye on a single neuron injected with the dye. Although there was no accepted notion about its mechanism at that time, two reasons caused by light irradiation were assumed. One of which was the heat generated, and the other was the conversion of the dye to the toxic substances (Miller and Selverston 1979).

About a decade later, D. G. Jay conducted an inactivation of the protein by fluorescent dye malachite green in 1988. Since the absorption peak at 620 nm does not overlap with the absorption spectrum of the most intracellular molecules, the dye was selected. Alkaline phosphatase and ß-galactosidase were labeled by its antibody conjugated with malachite green and specifically inactivated by pulse laser irradiation (Jay 1988). At this point, heat denaturation of the target

protein was assumed, however, later in 1994. Jay and colleagues concluded that it was not due to the photothermal effect. That was because the estimated 0.35 °C temperature increase at the target protein, which is 40 Å distant from the dye through the antibody, was insufficient to cause protein denaturation. They also indicated inconsistency of CALI process and photothermal mechanism by Arrhenius analysis. As an alternative mechanics, photochemical damage through the free radicals generated from excited chromophore was suggested and confirmed by the measurement to assess the influence of several ROS quenchers, such as sodium azide, mannitol, butylated hydroxytoluene, and vitamin E, on the inactivation of acetylcholinesterase and ß-galactosidase by malachite green. From the results, they concluded that malachite green-mediated CALI is attributed to the free radical species, specifically hydroxyl radicals generated by photoirradiation (Liao et al. 1994).

### 16.2.2 Photosensitization Mechanism

Prior to the acceptance of ROS-induced reaction as the principle of CALI, mechanism of the photosensitization had been well-investigated. By light absorption, chromophore in the photosensitizer is transit to the excitation states with several energy levels that are higher than the lowest excited level. That moves to the lowest excited singlet state through non-radiative transition mostly by generating heat and stays for several nanoseconds. There are following several pathways to return to the ground state, the fluorescence emission, energy transfer to the solvent, or transit to the long-lived excited triplet state having possibility to emit phosphorescence by intersystem crossing. Superoxide anion ($O_2^{\bullet -}$) is produced by one electron reduction of ground state oxygen ($^3O_2$). Most of the effective photosensitizers generate singlet oxygen ($^1O_2$), having paired electrons with opposite spins, by energy transfer from the chromophore in the triplet state to an oxygen molecule located nearby. The sensitization mechanisms categorized as Type I or Type II mechanisms are mechanisms generating superoxide anion or singlet oxygen, respectively (Fig. 16.1) (Jacobson et al. 2008; Laustriat 1986).

### 16.2.3 ROS Effects on Intracellular Molecules

During the diffusion of the ROS generated from the photosensitizers, ROS will attack nearby molecules due to their high reactivity. ROS attack DNA bonds, peroxidize lipids, and oxidize amino-acid side chain of cysteine, methionine, histidine, tyrosine, and tryptophan. Proteins affected by ROS are structurally and functionally disturbed and lead to intermolecular protein inactivation through protein–protein crosslinking and aggregation. The fragmentation of peptide bonds is also caused by ROS attack (Jacobson et al. 2008).

The specificity of CALI is determined by the lifetime of the generated ROS in solution that is related to the diffusible area. Assuming from the diffusion coefficient ~ 1000 $\mu m^2/s$ and lifetime 3 μs in water, approximate diffusion distances of singlet oxygen is approximately 130 nm (Jacobson et al. 2008). Hydrogen peroxide, which has long lifetime and approximate diffuse rate of 1000–2000 $\mu m^2/s$, may have several micrometers of intracellular diffusion distance in the absence of ROS scavenging enzyme (Winterbourn 2008). Hydroxyl radical, which has very short lifetime, have short diffusion distance 10 Å (Liao et al. 1994). Considering from average intermolecular distance within the cell (80 Å), hydroxyl radical is theoretically favorable to inactivate target proteins free from damage on the neighboring proteins (Linden et al. 1992). Meanwhile diffusion distance has not been assessed for the superoxide anion. Among these ROS species, singlet oxygen is suitable to cause universal damage including cell killing. The measured effective area for damaging surrounding molecules by CALI, which is helpful to consider the target specificity, is reported only for malachite green and fluorescein. In the case of malachite green, the half maximum radius from the dye moiety is 15 Å; there was no damage to

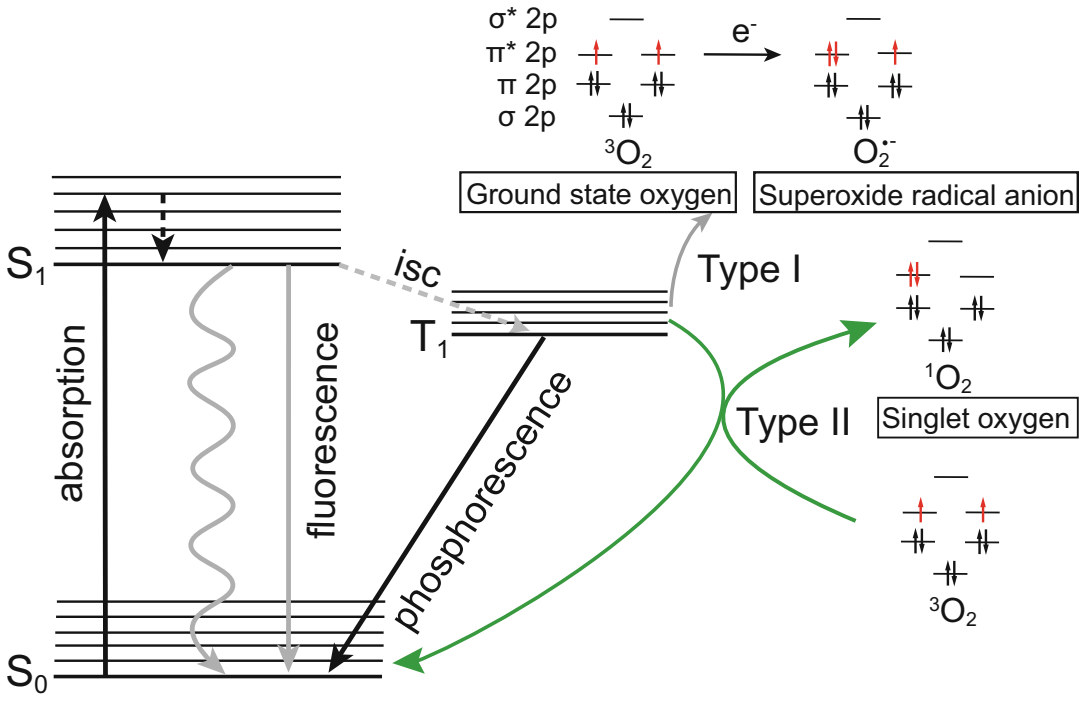


**Fig. 16.1** ROS generation mechanism in the Jablonski diagram. A photosensitizer at ground state ($S_0$) absorbs light and enters the excited state ($S_1$), or several higher states. It undergoes non-radiative transition (black dashed arrow) and remains in the lowest excited singlet state. After this state, the fluorescence emission or non-radiative transition (wavy arrow) happens. When intersystem crossing occurs, it enters a triplet state. In the presence of oxygen, through the electron transfer from photosensitizer to oxygen, superoxide anion species is generated (type I mechanism). Through the energy transfer from the photosensitizer to oxygen, singlet oxygen is generated (type II mechanism)

the distance over 60 Å (Linden et al. 1992). In another case of fluorescein by which singlet oxygen is generated, measured half damage radius ~ 4 nm was remarkably different from the estimated diffusion range in water. A possible explanation for this discrepancy is the quenching by scavenging molecule abundantly exists around chromophores.

Because of the lack of quantitative information for evaluation, it is difficult to organize experimental plan related to CALI. However, for better achievement of your research purpose, it is important to consider from the available information, such as the type of ROS generated, effective area, and efficiency of ROS generation. In the following section, we introduce the available photosensitizers in the aspect of their properties and practical achievements.

## 16.3 Development of Photosensitizers and its Application in Cell Biology

### 16.3.1 Chemical-Based Photosensitizers

#### 16.3.1.1 Application of Malachite Green on CALI

As mentioned in the previous section, the first attempt of CALI was conducted with malachite green as a photosensitizer. Alkaline phosphatase and ß-galactosidase were inactivated after 5 min irradiation of 25 mW/cm$^2$ of 620 nm pulsed laser in vitro (Jay 1988). Following this, malachite green has been commonly used for the investigation of the protein function in vivo. Its first

application was the elucidation of in vivo function of Fasciclin I in grasshopper embryos, for which only the mediation of homophilic adhesion in Drosophila S2 cell line was known. In the developmental stage of limb bug, Fasciclin I is expressed on the surface of Ti1 pioneer neurons. Growth cones are formed by the close mutual contact of these cells and their axons, which cross through epithelia with a process defined as fasciculation, and are extended toward the central nervous system. The separation of two axons, indicating defasciculation, was caused by CALI on Fasciclin I during this axonal projection process. With this result, the necessity of the Fasciclin I for the Ti1 pioneer neurons fasciculation was elucidated (Jay and Keshishian 1990).

#### 16.3.1.2 Micro-CALI by Chemical-Based Photosensitizers

A few years later, a more specific and targetable CALI was reported as micro-CALI. The method was performed by irradiating laser at a specific area to achiev fast and efficient chromophore bleaching. Micro-CALI was applied to the analysis of Fasciclin II, though having similarity with Fasciclin I and known to be concerned with the adhesion of Drosophila S2 cell lines, its in vivo functions were still unknown. Expression of Fasciclin II is chiefly on the longitudinal fascicles of the central nervous system and also in the periphery in grasshoppers. To investigate distinct roles of Fasciclin II at different times and locations during neurodevelopment, micro-CALI was performed on Ti1 neurons. From the results of micro-CALI on Fasciclin II for the different stages of axonogenesis, it was turned out that inhibition of axon outgrowth by Fasciclin II occurred only after the complete emergence of the Ti1 neurons from the epithelium, but before forming tear shape. Micro-CALI on post-axonogenic Ti1 neurons did not affect the length of axon growth. The requirement of a Fasciclin II in narrow temporal window during Ti1 development was suggested from these results. As another advantage of micro-CALI, the non-irradiated cells within the embryo could serve as internal controls due to the specificity of target cells (Diamond et al. 1993).

CALI was also applied to the investigation of cancer mechanisms through identification and validation of target proteins for drug discovery. To reveal proteins that might be involved in cancer metastasis, such as ezrin and pp60 c-src, malachite green has been used. Loss of membrane ruffling and pseudopodial retraction were caused by micro-CALI on ezrin in cultured rat fibroblasts that suggested requirement of pseudopodia-based extension during cancer metastasis (Lamb et al. 1997). Although it had already been known that proto-oncogene pp60 c-src has tyrosine kinase activity, its function in situ was not characterized. Any obvious effects in mice could not be revealed by the loss of function induced with a knockout-based method. On the other hand, growth cone motility and significant neurite extension were observed in developing chick neurons by conducting micro-CALI on pp60 c-src. That suggested usefulness of CALI for study of proto-oncogenes. It also reflects the advantage of spatiotemporal controllability of CALI advantage than knockout methods that have possibility to cause no phenotypic change due to the expression of other proteins compensating for loss of target protein (Hoffman-Kim et al. 2002). CALI applied to the *Drosophila* segment-polarity gene patched (*Ptc*) also exhibited the superiority of CALI over gene knockout methods. *Ptc* is essential for segmentation in the early embryo and fate determination of optic lobe primordia precursors at later stages. Since gene knockout of *Ptc* induced abnormal segmentation patterns, observation of its specific function became impossible. Meanwhile, CALI of Ptc made it possible to analyze specific functions after segmentation by discrimination of neural and epithelial cells in optic-lobe precursor cells (Schmucker et al. 1994).

#### 16.3.1.3 Labeling of Chemical-Based Photosensitizers with Genetically Encoded Tag

The first generation of the CALI method, for which target molecule is indirectly labeled with

malachite green via an antibody, has some practical limitations. First, The antibody must not influence on the function of target proteins by blocking active site. Second, to ensure proper targetability of the antibody to the intended target, checking process such as immunoblotting with immunocytochemistry is required. Another difficulty of CALI by antibody-conjugated photosensitizer is the delivery of the antibody into the cell through the plasma membrane. When the cells have larger size or number of cells for CALI are small, microinjection is conducted. While in the case of CALI for considerable of cells, techniques for bulk loading such as trituration, scrape loading, and electroporation are conducted (Li et al. 2012). Moreover, malachite green, which requires laser irradiation with high-power density, may have high risk of phototoxicity to the cells.

Following CALI by antibody-conjugated malachite green, techniques with higher ROS generation efficiency and lower illumination power were developed. For instance, 50 times higher efficiency was achieved by exchange the fluorescent dye from malachite green to fluorescein. ROS generated from fluorescein is singlet oxygen that is different from hydroxyl radicals in the case of malachite green (Surrey et al. 1998). To simplify the labeling of photosensitizers, attempts of genetically encoded tag-based techniques have been made in substitution for the antibody-based targeting. A biarsenical derivative of fluorescein 4′,5′-bis(1,3,2-dithioarsolan-2-yl) fluorescein (FlAsH) with membrane permeability and ability to bind to the tetracysteine motif was later developed. The tetracysteine motif could be genetically fused to the target protein. Synaptotagmin I (SytI), a major calcium sensor for transmitter release in a post-docking step of vesicle fusion, was labeled by FlAsH through tetracysteine motif, and the release of transmitter was decreased by irradiation of visible light in *Drosophila* (Marek and Davis 2002). Lower intensity light from a mercury lamp was applied for CALI on FlAsH-SytI (Marek and Davis 2002). After the emergence of FlAsH, its red derivative ReAsH with higher efficiency and preserved membrane permeability and binding capacity to the tetracysteine motif was developed. CALI on Connexin43 with ReAsH by irradiation of the 17 W/cm$^2$ light during 25 s caused inactivation of gap junction (Tour et al. 2003). However, FlAsH and ReAsH hold remaining issues of nonspecific binding with cysteine residue in endogenous proteins and high cytotoxicity (Hearps et al. 2007; Martin et al. 2005; Stroffekova et al. 2001).

For further improvement of the labeling efficiency, fusion of the target protein with protein tags such as SNAP tags and HaloTag, which having ability to bind with photosensitizer, has been used. CALI on fluorescein conjugated to the γ-tubulin with C-terminal SNAP-tag caused a failure in the nucleation and growth of microtubule which bring metaphase arrest (Keppler and Ellenberg 2009). By modification of haloalkane dehalogenase, protein tag to covalently bind to a variety of compounds with haloalkane was developed as the HaloTag protein. That enables haloalkane-conjugated photosensitizer to specifically target on the protein through fused HaloTag protein. Haloalkylated fluorescein and Ru(II)tris (bipyridyl) were tested as HaloTag ligands. To demonstrate superior performance of singlet oxygenation than fluorescein Ru(II)tris-bipyridyl di-cation was applied to CALI and succeeded in the efficient inactivation of Renilla luciferase (Lee et al. 2008). Nevertheless, near-ultraviolet (380 nm) excitation light for ruthenium has the possibility to cause cell phototoxicity. As another photosensitizer with higher efficiency than ruthenium, eosin with similar excitation wavelength (517 nm) and less toxic than UV excitation was found. Synthetized eosin-based HaloTag ligand diAc-eosin-AM was linked with a new HaloTag mutant HaloTag7, which has superior covalent bond formation with ligands. Cells for which Aurora-B was specifically targeted by HaloTag7-diAc-eosin-AM stopped cell division and formed a multinuclear structure after mitosis by conducting CALI (Takemoto et al. 2011). Eosin was also used to demonstrate CALI on synaptic AMPA receptors, and succeeded in the manipulation of mouse behavior by fear memory erase (Takemoto et al. 2016). Currently eosin can be considered as the most effective photosensitizer applied to CALI in mammalian cells and in vivo.

### 16.3.2 Genetically Encoded Photosensitizers

#### 16.3.2.1 GFP Based CALI

The discovery of green fluorescent protein (GFP) in 1962 has changed the way cell biology research conducted (Shimomura et al. 1962; Tsien 1998). Fusing this genetically encoded fluorescent marker to protein targets allows researchers to monitor biological processes in living systems. Since using GFP eliminates the necessity to add fluorescent dye exogenously, the concern that nonspecific inactivation caused by unbound chromophore or incomplete washing process would cause unwanted background could be neglected. In 1998, Surrey and colleagues made the first attempt to use GFP as CALI agent. GFP was fused beta-galactosidase, then with the same laser power as used for malachite green, GFP could inactivate the target. Using high-power laser approximately $10^6$ times stronger than typical confocal imaging, EGFP could cause retraction of stress fibers by inactivating alpha actinin, a key protein that require for cell adhesion (Rajfur et al. 2002). However, since such high-power laser was used, it became a concern that the light irradiation itself would cause artifact or phototoxicity. To overcome that, using less toxic excitation light at 850 nm, multiphoton excitation was actually useful to induce ROS production by EGFP as shown by inactivation of Connexin-43 that results in separation of the gap junctions of HeLa cells (Tanabe et al. 2005). Despite the promising result of multiphoton excitation, EGFP is still ineffective at generating ROS compared to the chemical-based photosensitizer. Later, with the new finding of other fluorescent proteins, genetically encoded photosensitizer could actually change the photosensitizer field (Table 16.1).

#### 16.3.2.2 KillerRed and its Derivatives

In 2006, Bulina and colleagues engineered the first effective genetically encoded photosensitizer from a red fluorescent protein that was previously cloned from Anthoathecata. After introducing several mutations into this protein, they found that this mutant could actually generate ROS at a high amount compared to EGFP, then named this mutant as KillerRed (Bulina et al. 2006). The engineering was done by introducing some mutations that hit the inner side of the beta barrel of the original protein, which then connects the chromophore to the outside environment with a big water channel. Based on KillerRed crystal structure, some further experiments showed that the channel functions to provide access for oxygen molecules to reach chromophore (Pletnev et al. 2009; Carpentier et al. 2009). Then when chromophore is excited, it would donate an electron to adjacent oxygen molecules. Further, the tunnel connecting the chromophore environment to the outside of the beta barrel would channel the superoxide to diffuse out of the protein. Some other experiments also suggested that when chromophore was excited, an electron was generated, then transferred to neighboring water molecules. Then these chain of water molecules inside the beta barrel would transfer the electron to external molecules near the opening of the beta barrel, which further generates ROS.

Since its emergence, KillerRed has shown to be useful to answer some biological questions. For example, KillerRed was used to clarify the role of Golgi reassembly and stacking protein (GRASP) 65 and 55 (Fig. 16.2). Originally, GRASP 65 and 55 were known to localize in cis and medial/trans cisternae, respectively. Knockout of either protein unlinks the Golgi ribbons, then caused failure in glycosylation. But it was still unclear why these two proteins are specifically sub-localized and what is their specific role in Golgi ribbon formation. Given that these two proteins are located very close to each other and the ribbon formation happens at a very short time, the authors exploited KillerRed advantages by fusing KillerRed to either of the protein then independently performed CALI upon these two proteins. Combined with fluorescence recovery after photobleaching (FRAP) to monitor the Golgi ribbon integrity after CALI and high-resolution structured illumination microscopy (SIM), it was revealed that GRASP65 mediates Golgi ribbon formation in early Golgi cisternae

**Table 16.1** List of photosensitizing protein and their properties

| Photosensitizing protein | Source organism | Oligomeric states | Excitation max | Emission max | Fluorescence quantum yield | Singlet oxygen quantum yield |
|---|---|---|---|---|---|---|
| **KillerRed-based photosensitizers** | | | | | | |
| KillerRed[a] | Anthoathecata | Dimer | 585 | 610 | 0.25 | 0.008[l] |
| KillerOrange[b,c] | Anthoathecata | Dimer | 455 | 555 | 0.42 | N.D. |
| mKillerOrange[b,c] | Anthoathecata | Monomer | 458 | 560 | 0.5 | N.D. |
| SuperNova Red[d] | Anthoathecata | Monomer | 579 | 610 | 0.3 | 0.02[l] |
| SuperNova Green[e] | Anthoathecata | Monomer | 440 | 510 | 0.23 | N.D. |
| **LOV-based photosensitizers** | | | | | | |
| miniSOG[f] | *A. thaliana* | Monomer | 488 | 500 | 0.37 | 0.03[m] |
| miniSOG2[g] | *A. thaliana* | Monomer | 429 | 507 | N.D. | N.D. |
| SOPP[h] | *A. thaliana* | Monomer | 440 | 490 | 0.32 | 0.04 |
| SOPP2[i] | *A. thaliana* | Monomer | 439 | 491 | 0.41 | 0.60 |
| SOPP3[h] | *A. thaliana* | Monomer | 439 | 490 | 0.41 | 0.60 |
| PP1FbFP[j] | *P. Putida* | Dimer | 450 | 496 | 0.27 | 0.23 |
| Pp2FbFP[j] | *P. Putida* | Dimer | 449 | 495 | 0.22 | 0.11 |
| Pp2FbFP L30M[j] | *P. Putida* | Dimer | 449 | 495 | 0.25 | 0.11 |
| DsFbFP [j] | *D. Shibae* | Dimer | 449 | 498 | 0.35 | 0.33 |
| DsFbFP M49I[j] | *D. Shibae* | Dimer | 450 | 498 | 0.36 | 0.42 |
| EcFbFP [j] | *B. subtilis* | N.D. | 448 | 496 | 0.44 | 0.07 |
| iLOV [j] | *A. thaliana* | Monomer | 450 | 497 | 0.33 | 0.05 |
| phiLOV2.1[j] | *A. thaliana* | Monomer | 450 | 497 | 0.20 | 0.01 |
| CreiLOV [j] | *C. reinhardtii* | N.D. | 449 | 497 | 0.32 | 0.04 |
| FMN[k] | | | 444 | 531 | 0.25 | 0.57 |

[a]Bulina et al. (2006), [b]Sarkisyan et al. (2015), [c]Pletneva et al. (2015), [d]Takemoto et al. (2013), [e]Riani et al. (2018), [f]Shu et al. (2011), [g]Makhijani et al. (2017), [h]Westberg et al. (2015). [i]Westberg et al. (2017). [j]Endres et al. (2018). [k]Baier et al. (2006). [l]Onukwufor et al. (2020), [m]Ruiz-González et al. (2013)

while GRASP 55 in the late cisternae (Jarvela and Linstedt 2014).

Not only in vitro applications, KillerRed was also capable for in vivo experiments from *C. elegans* to zebrafish. Targeting KillerRed to the plasma membranes of *Xenopus* embryos by mRNA microinjection could induce loss-of-function phenotype in developing eye and pronephric kidney (Jewhurst et al. 2014). In zebrafish, KillerRed was used to kill kidney and muscle cells. These experiments showed that KillerRed could be used to generate kidney and heart-failure animal model (Buckley et al. 2017; Teh and Korzh 2014). Moving further, KillerRed-induced cell ablation of AWA sensory neurons in *C. elegans* could manipulate its chemotaxis behavior (Kobayashi et al. 2013).

The broad application of KillerRed has drawn the protein engineers to further improve KillerRed properties. A monomeric version of KillerRed, SuperNova, was established to overcome the dimerization tendency of KillerRed that might hamper its localization or target fusion. Then the establishment of KillerRed color variants: KillerOrange (dimer), mKillerOrange (monomer) (Sarkisyan et al. 2015; Pletneva et al. 2015), KillerRed V44A (green, dimer) (De Rosny and Carpentier 2012), and SuperNova Green (dimer) (Riani et al. 2018) has expanded these genetically encoded color palette (Fig 16.3a,b). Having these color palettes in hand would be extremely helpful when a multiple spatiotemporally controlled inactivation of the two or three different proteins or cell ablation is needed. As the proof of concept, by using two monomeric variants of KillerRed, SuperNova Red and SuperNova Green, selective cell ablation of a mixed population of cells could be achieved in vitro

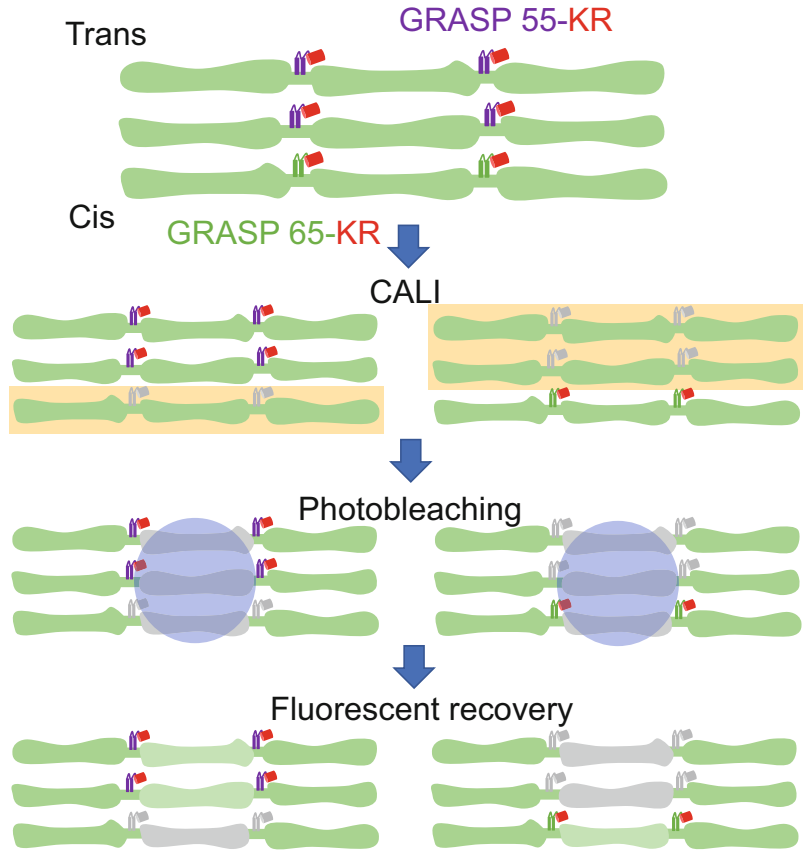


**Fig. 16.2** CALI for Golgi reassembly and stacking protein by KillerRed. GRASP65 and GRASP55 fused to KillerRed and localized only to the cis and trans cisternae, respectively. Inactivation of each GRASP protein was performed by orange light irradiation onto the corresponding area. Using FRAP, the recovery of Golgi ribbon formation was observed after GRASP 65 and 55 inactivation. Inactivation of GRASP65 and 55 showed that no ribbon formation occurs in cis and trans cisternae, respectively (Figure was adopted and modified based on Jarvela and Linstedt (2014) work)

using two different excitation wavelengths (Fig. 16.3c).

#### 16.3.2.3 LOV-Based Photosensitizer

Although the trend of genetically encoded photosensitizer originally emerged from KillerRed family, currently, the stronger and more applicable successor of the genetically encoded photosensitizer actually came from LOV (light, oxygen, or voltage) domain-based photoreceptor. The first LOV-domain-based photosensitizer to be developed was miniSOG from *Arabidopsis thaliana* phototropin 2. miniSOG, as other LOV domain, has FMN as the chromophore and excited at 440 nm (Shu et al. 2011). Some advanced studies have shown that miniSOG generates singlet oxygen when FMN was excited, then nearby oxygen received energy from FMN in its triplet state. The abundance of electron-rich side chains surrounding its chromophore also contributes to electron transfer and generates superoxide species (Ruiz-González et al. 2013; Pimenta et al. 2013). At first, miniSOG was shown to successfully advancing image resolution of correlative light and electron microscopy (CLEM) as: (1) it is targetable to specific subcellular structure; (2) it is fluorescence; (3) it promotes photo-oxidation of diaminobenzidine only in those targeted areas (Shu et al. 2011).

A method called InSynC (inhibition of synapses with CALI) has proven that miniSOG is also useful as optogenetic tools for neuroscience research. InSynC used miniSOG to inhibit signal transmission between neurons by fusing miniSOG to VAMP2 and synaptophysin, which are critical for presynaptic vesicular release (Fig. 16.4). In cultured neurons and hippocampal organotypic slices, fusion of miniSOG to the

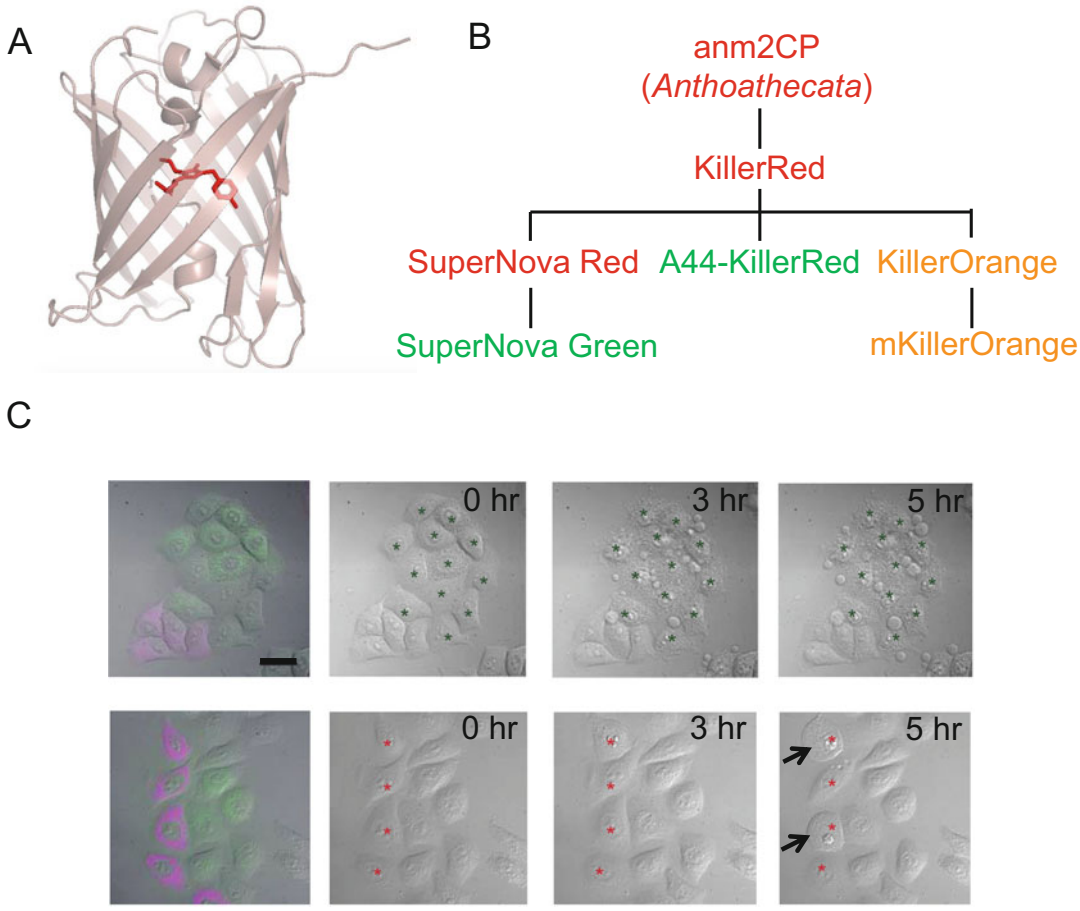


**Fig. 16.3** Development and application of KillerRed derivatives. (**a**) Crystal structure of KillerRed (PDB 3A8S). Similar to other GFP mimic fluorescent protein, KillerRed consists of 11 beta barrel (light pink) and chromophore inside (bright red). (**b**) KillerRed and its derivatives. KillerRed was derived from anm2CP protein cloned from Anthoathecata. The monomeric version of KillerRed is called SuperNova Red, which is further modified to be SuperNova Green. A mutant of KillerRed, A44 KillerRed also emits green color. The dimeric and monomeric orange version of KillerRed are called KillerOrange and mKillerOrange, respectively. (**c**) Coculture of HeLa cells expressing SuperNova Red (magenta) and SuperNova Green (green). The upper and lower panel shows cells that are irradiated with blue and orange light to activate SuperNova Green and Red, respectively. Five hours after irradiation, irradiation with blue light only killed cells expressing SuperNova Green while orange light killed cells expressing SuperNova Red (adapted from Riani et al. 2018)

C-terminal of synaptophysin followed by blue light irradiation could 100% reduce neurotransmitter release. Expression of miniSOG-VAMP2 in *C. elegans* has caused movement reduction and paralysis after light irradiation (Lin et al. 2013). miniSOG was also successfully revealed the detail function of respiratory complex II subunits in *C. elegans* mitochondria for which knockout approach would be impossible to achieve due to their lethality (Wojtovich et al. 2016).

Similar with KillerRed, the success of the first version of miniSOG has drawn protein engineers' attention. The ambition to make miniSOG a stronger ROS generator continues to the establishment of miniSOG2 and SOPP series. The first improvement was called SOPP (singlet oxygen photosensitizing protein), which contains Q102L

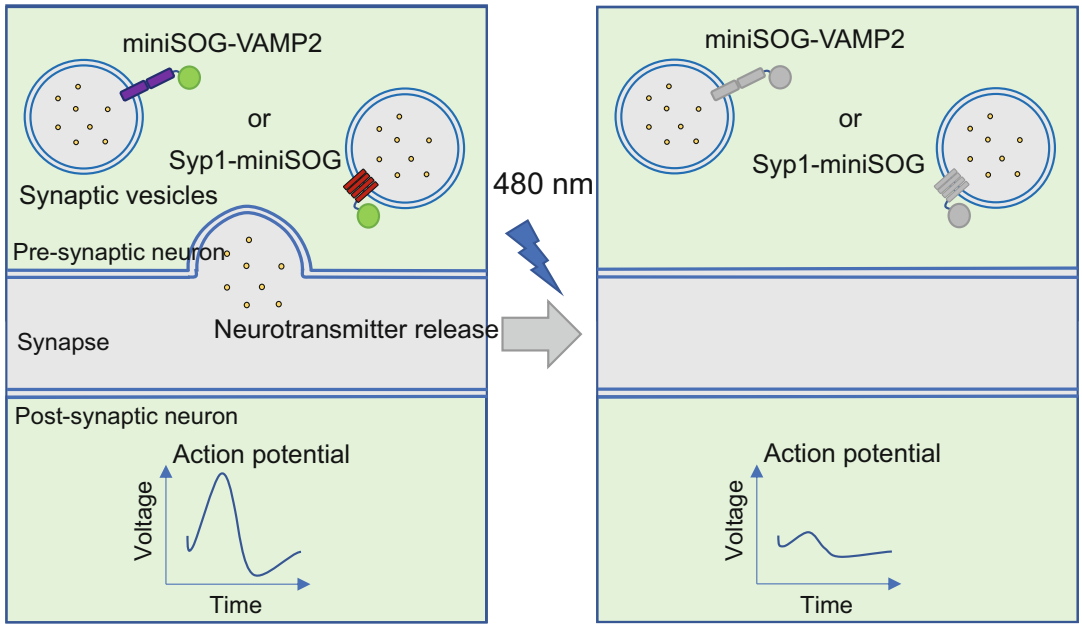


**Fig. 16.4** InSynC (Inhibition of Synapses with CALI). miniSOG fused to VAMP2 or Syp1 was successfully inhibited neurotransmitter release, resulting in inhibition of signal transmission to the post-synaptic neuron

mutation that reduces undesired photoinitiated electron transfer from the chromophore to its surrounding environment (Westberg et al. 2015). After SOPP, the establishment of miniSOG2 pushed cell killing application a more complex and well-known model organism, *Drosophila melanogaster*. Light irradiation on miniSOG expressing neurons and wing imaginal disc in *D. melanogaster* larvae showed apparent defect on its development (Makhijani et al. 2017).

Based on those early improvements of miniSOG, a new hypothesis suggests that steering the ROS generation by miniSOG from a half-singlet oxygen-half-superoxide species to a full singlet oxygen generation would make an even stronger miniSOG. Since the production of superoxide species was caused by electron transfer from FMN to electron-donating residues in the surrounding amino acids, introducing mutations on those amino acids increased the miniSOG singlet oxygen quantum yield to become closer to the original FMN. Following this hypothesis, Westberg and colleagues successfully developed highly efficient singlet oxygen photosensitizing proteins, which are called SOPP2 and SOPP3. SOPP3 has singlet oxygen quantum yield approximately 0.6 that is comparable to free FMN, which means that all the photons absorbed are channeled to produce singlet oxygen species only (Westberg et al. 2017).

Since LOV domain is present in a diverse range of photoreceptors from bacteria, fungi, and plants, recent publication analyzed several LOV-FP variants from other species. Some are derived from microbes (*Pseudomonas putida*, *Dinoroseobacter shibae*, *Bacillus subitilis*, and *Chlamydomonas reinhardtii*), and some are variants of *Arabidopsis thaliana* phototropin LOV2 domain (iLOV, phiLOV). This study examined the potentiality of those LOV domains to be the next generation of genetically encoded photosensitizer. Apparently, most of the LOV domain tested on its effectivity to kill bacteria showed potential results (Endres et al. 2018). However, if the singlet oxygen quantum yield of each kind of LOV-domain-based photosensitizer variants could not exceed FMN, which has been

achieved by SOPP3, then what is the point to explore other sources?

In the ideal situation, the encapsulation of the photosensitizing flavin chromophore by the LOV domain should guarantee that singlet oxygen generation is not affected by the chromophore surroundings (as achieved by SOPP3). However, this chromophore surrounding environment, which vary between each type of LOV domain, is also important for other parameters, such as the photostability property of the chromophore. Photostability, as is usually shown in photobleaching experiment, is often correlate to singlet oxygen production capacity and also determines light doses and exposure duration to produce desired results. Therefore, if these different FMN encapsulating variants have different photostability and other ROS generating properties, they could be useful for different purposes and application (Endres et al. 2018).

#### 16.3.2.4 Attempt of Photodynamic Therapy by Genetically Encoded Photosensitizers

Chemical photosensitizer to kill target cancer cells and for the bactericidal agents have been reported (Robertson et al. 2009; Junqueira et al. 2010; Ryskova et al. 2010). Development of genetically encoded photosensitizers with high efficiency motivates to expand its usage for such purposes. Some attempts to kill cancer cells by targeting genetically encoded photosensitizers have been conducted. One example is a genetically encoded immunophotosensitizer created by the fusion of an anti-receptor antibody-KillerRed/miniSOG. That succeeded in the efficient in vitro killing of cancer cells expressed p185 (HER-2-ECD) upon light irradiation (Serebrovskaya et al. 2009). Another type of attempts was performed by targeting genetically encoded photosensitizers to the inner and outer membranes of mitochondria, nuclei, plasma membranes, lysosomes, and peroxisomes, and achieved cell ablation in vitro and in vivo (Ryumina et al. 2013; Shirmanova et al. 2013; Serebrovskaya et al. 2014; Shirmanova et al. 2015; Liao et al. 2014; Ryumina et al. 2016).

However, applications of genetically encoded photosensitizers for photodynamic therapy have difficulty in the delivery of the photosensitizers to target cancer cells and reachability of CALI light to targets in deep tissue. To solve them, many efforts have been made. One example is an attempt to delivery of plasmids encoded KillerRed by polymeric micelle-encapsulating quantum dots to cancer cells. Although the authors proposed activation of KillerRed through the emission from quantum dot, it required excitation by near-ultraviolet light (Muthiah et al. 2014). Another attempt was the application of the upconversion nanoparticles, which can convert deep-penetrating near-infrared (NIR) light to green light, to deep-penetrating photodynamic therapies. It succeeded to ablated tumor cells by locally activated KillerRed in centimeter-thick tissue (Liang et al. 2017).

As an alternation of the development of complete near-infrared photosensitizers, the photosensitizer, for which targetability is conferred by protein, was developed. A targeted and activated photosensitizer (TAP), which produce singlet oxygen and emit fluorescence only when it binds with and is activated by fluorogen-activating protein (FAP) upon illumination by near-infrared light, was developed by using derivative of malachite green as incorporated chromophore. By this genetically targetable FAP-TAP approach targeted cell killing, and rapid targeted cell ablation in living larval and adult zebrafish was succeeded (He et al. 2016).

### 16.3.3 Future Direction of CALI by Genetically Encoded Photosensitizers

Since CALI is one of the techniques to control physiological function, it can be categorized in the optogenetic methods in a broad sense. Although control mechanism is limited to the destruction of the targets, CALI by photosensitizers is applicable for controlling similar and much broader targets than typical optogenetics tools. Ion channel activities are photo-controlled by channel-based optogenetic tools such as

channelrhodopsin-2 that penetrate several ions ($H^+$, $Na^+$, $K^+$, and $Ca^{2+}$) by blue light irradiation (Nagel et al. 2003). Nevertheless, type of photo-controllable channel is limited. For controlling the channel functions, for which suitable optogenetic channels have not yet developed, CALI by targeted photosensitizers could be an option of photo-controlling. CALI can also be applied to similar targets to the photoreceptor-based optogenetic tools for manipulation of protein interactions, such as LOV domains and CRY2, for which photoirradiation-dependent association dissociation between split targets or between actuators and target proteins is required. Compared with their complexity of molecular design, labeling with photosensitizer for CALI is quite direct and simple. Additionally, for the analysis of loss of function in longer term, irreversible destruction of targets by CALI is preferable.

To date, multicolor imaging and manipulation are required to analyze multicomponent of living systems by optical bioimaging. For catching up with this trend photosensitizers for CALI also necessary to be multicolored. Demonstration for proof of concept has already been made by combination of KillerRed and miniSOG on ablation of cholinergic motor neurons in *C. elegans*. CALI by miniSOG and KillerRed was conducted by the blue and green light irradiation, respectively, without cross talk. It indicated the inactivation of two different protein or cell species in independent spatiotemporal manner by CALI with different photosensitizers (Williams et al. 2013).

As it has already described, color variants of KillerRed have been developed. By using these three green, orange, and red color variants, inactivation of three independent molecules or cells with different timings can be achieved by irradiation of 440, 510, and 560 nm light, respectively.

**Acknowledgments** This work was partly supported by the Inamori Grants from the Inamori Foundation; a grant from the Naito Foundation; the Precursory Research for Embryonic Science and Technology (PRESTO) program from the Japan Science and Technology Agency (JST) (No. 113705), (No. 122168) (to T.N.); Japan Society for the Promotion of Science (JSPS) Grant-in-Aid for Scientific Research(A) (26251018) (to T.N.); the Ministry of Education, Culture, Sports, Science and Technology (MEXT) Grant-in-Aid for Scientific Research on Innovative Areas "Spying minority in biological phenomena" (No. JP23115003), "Singularity biology" (No. JP18H05410) (to T.N.), "Interplay of developmental clock and extracellular environment in brain formation" (No. JP16H06487) (to T.M.); and the Indonesia Endowment Fund for Education (to Y.D.R.).

## References

Baier J et al (2006) Singlet oxygen generation by UVA light exposure of endogenous photosensitizers. Biophys J 91:1452–1459

Buckley C et al (2017) Precise spatio-temporal control of rapid optogenetic cell ablation with mem-KillerRed in Zebrafish. Sci Rep 7:5096

Bulina ME et al (2006) A genetically encoded photosensitizer. Nat Biotechnol 24:95–99

Carpentier P, Violot S, Blanchoin L, Bourgeois D (2009) Structural basis for the phototoxicity of the fluorescent protein KillerRed. FEBS Lett 583:2839–2842

De Rosny E, Carpentier P (2012) GFP-like phototransformation mechanisms in the cytotoxic fluorescent protein KillerRed unraveled by structural and spectroscopic investigations. J Am Chem Soc 134:18015–18021

Diamond P et al (1993) Fasciclin I and II have distinct roles in the development of grasshopper pioneer neurons. Neuron 11:409–421

Endres S et al (2018) An optogenetic toolbox of LOV-based photosensitizers for light-driven killing of bacteria. Sci Rep 8:15021

He J et al (2016) A genetically targetable near-infrared photosensitizer. Nat Methods 13:263–268

Hearps AC et al (2007) The biarsenical dye Lumio exhibits a reduced ability to specifically detect tetracysteine-containing proteins within live cells. J Fluoresc 17:593–597

Hoffman-Kim D et al (2002) pp60(c-src) is a negative regulator of laminin-1-mediated neurite outgrowth in chick sensory neurons. Mol Cell Neurosci 21:81–93

Jacobson K, Rajfur Z, Vitriol E, Hahn K (2008) Chromophore-assisted laser inactivation in cell biology. Trends Cell Biol 18:443–450

Jarvela T, Linstedt AD (2014) Isoform-specific tethering links the Golgi ribbon to maintain compartmentalization. Mol Biol Cell 25:133–144

Jay DG (1988) Selective destruction of protein function by chromophore-assisted laser inactivation. Proc Natl Acad Sci 85:5454–5458

Jay DG, Keshishian H (1990) Laser inactivation of fasciclin I disrupts axon adhesion of grasshopper pioneer neurons. Nature 348:548–550

Jewhurst K, Levin M, McLaughlin KA (2014) Optogenetic control of apoptosis in targeted tissues of Xenopus laevis embryos. J Cell Death 7:25–31

Junqueira JC et al (2010) Antimicrobial photodynamic therapy: photodynamic antimicrobial effects of malachite green on staphylococcus, enterobacteriaceae, and Candida. Photomed Laser Surg 28:67–72

Keppler A, Ellenberg J (2009) Chromophore-assisted laser inactivation of alpha- and gamma-tubulin SNAP-tag fusion proteins inside living cells. ACS Chem Biol 4:127–138

Kobayashi J et al (2013) A method for selective ablation of neurons in *C. elegans* using the phototoxic fluorescent protein, KillerRed. Neurosci Lett 548:261–264

Lamb RF et al (1997) Essential functions of ezrin in maintenance of cell shape and lamellipodial extension in normal and transformed fibroblasts. Curr Biol 7:682–688

Laustriat G (1986) Molecular mechanisms of photosensitization. Biochimie 68:771–778

Lee J, Yu P, Xiao PX, Kodadek T (2008) A general system for evaluating the efficiency of chromophore-assisted light inactivation (CALI) of proteins reveals Ru(II) tris-bipyridyl as an unusually efficient "warhead". Mol BioSyst 4:59–65

Li W, Stuurman N, Ou G (2012) Chromophore-assisted laser inactivation in neural development. Neurosci Bull 28:333–341

Liang L et al (2017) Deep-penetrating photodynamic therapy with KillerRed mediated by upconversion nanoparticles. Acta Biomater 51:461–470

Liao JC, Roider J, Jay DG (1994) Chromophore-assisted laser inactivation of proteins is mediated by the photogeneration of free radicals. Proc Natl Acad Sci 91:2659–2663

Liao ZX, Li YC, Lu HM, Sung HW (2014) A genetically-encoded KillerRed protein as an intrinsically generated photosensitizer for photodynamic therapy. Biomaterials 35:500–508

Lin JY et al (2013) Optogenetic inhibition of synaptic release with chromophore-assisted light inactivation (CALI). Neuron 79:241–253

Linden KG, Liao JC, Jay DG (1992) Spatial specificity of chromophore assisted laser inactivation of protein function. Biophys J 61:956–962

Makhijani K et al (2017) Precision optogenetic tool for selective single- and multiple-cell ablation in a live animal model system. Cell Chem Biol 24:110–119

Marek KW, Davis GW (2002) Transgenically encoded protein photoinactivation (FlAsH-FALI): acute inactivation of synaptotagmin I. Neuron 36:805–813

Martin BR, Giepmans BN, Adams SR, Tsien RY (2005) Mammalian cell-based optimization of the biarsenical-binding tetracysteine motif for improved fluorescence and affinity. Nat Biotechnol 23:1308–1314

Miller JP, Selverston A (1979) Rapid killing of single neurons by irradiation of intracellularly injected dye. Science 206:702–704

Muthiah M et al (2014) Intracellular delivery and activation of the genetically encoded photosensitizer killer red by quantum dots encapsulated in polymeric micelles. Colloids Surf B Biointerfaces 116:284–294

Nagel G et al (2003) Channelrhodopsin-2, a directly light-gated cation-selective membrane channel. Proc Natl Acad Sci 100:13940–13945

Onukwufor JO et al (2020) Quantification of reactive oxygen species production by the red fluorescent proteins KillerRed, SuperNova and mCherry. Free Radic Biol Med 147:1–7

Pimenta FM et al (2013) Oxygen-dependent photochemistry and photophysics of "miniSOG," a protein-encased flavin. Photochem Photobiol 89:1116–1126

Pletnev S et al (2009) J Biol Chem 284:32028–32039

Pletneva NV et al (2015) Crystal structure of phototoxic orange fluorescent proteins with a tryptophan-based chromophore. PLoS One 10:e0145740

Rajfur Z, Roy P, Otey C, Romer L, Jacobson K (2002) Dissecting the link between stress fibres and focal adhesions by CALI with EGFP fusion proteins. Nat Cell Biol 4:286–293

Riani YD, Matsuda T, Takemoto K, Nagai T (2018) Green monomeric photosensitizing fluorescent protein for photo-inducible protein inactivation and cell ablation. BMC Biol 16:50

Robertson CA, Evans DH, Abrahamse H (2009) Photodynamic therapy (PDT): a short review on cellular mechanisms and cancer research applications for PDT. J Photochem Photobiol B Biol 96:1–8

Ruiz-González et al (2013) Singlet oxygen generation by the genetically encoded tag miniSOG. J Am Chem Soc 135:9564–9567

Ryskova L, Buchta V, Slezak R (2010) Photodynamic antimicrobial therapy. Cent Eur J Biol 5:400–406

Ryumina AP et al (2013) Flavoprotein miniSOG as a genetically encoded photosensitizer for cancer cells. Biochim Biophys Acta 1830:5059–5067

Ryumina AP et al (2016) Lysosome-associated miniSOG as a photosensitizer for mammalian cells. BioTechniques 61:92–94

Sarkisyan KS et al (2015) KillerOrange, a genetically encoded photosensitizer activated by blue and green light. PLoS One 10:e0145287

Schmucker D, Su AL, Beermann A, Jäckle H, Jay DG (1994) Chromophore-assisted laser inactivation of patched protein switches cell fate in the larval visual system of drosophila. Proc Natl Acad Sci U S A 91:2664–2668

Serebrovskaya EO et al (2009) Targeting cancer cells by using an antireceptor antibody-photosensitizer fusion protein. Proc Natl Acad Sci U S A 106:9221–9225

Serebrovskaya EO et al (2014) Phototoxic effects of lysosome-associated genetically encoded photosensitizer KillerRed. J Biomed Opt 19:071403

Shimomura O, Johnson FH, Saiga Y (1962) Extraction, purification and properties of aequorin, a bioluminescent protein from the luminous hydromedusan, Aequorea. J Cell Comp Physiol 59:223–239

Shirmanova M et al (2015) Towards PDT with genetically encoded photosensitizer KillerRed: a comparison of

continuous and pulsed laser regimens in an animal tumor model. PLoS One 10:e0144617

Shirmanova MV et al (2013) Phototoxic effects of fluorescent protein KillerRed on tumor cells in mice. J Biophotonics 6:283–290

Shu X et al (2011) A genetically encoded tag for correlated light and electron microscopy of intact cells, tissues, and organisms. PLoS Biol 9:e1001041

Stroffekova K, Proenza C, Beam KG (2001) The protein-labeling reagent FLASH-EDT2 binds not only to CCXXCC motifs but also non-specifically to endogenous cysteine-rich proteins. Pflugers Arch 442:859–866

Surrey T et al (1998) Chromophore-assisted light inactivation and self-organization of microtubules and motors. Proc Natl Acad Sci U S A 95:4293–4298

Takemoto K et al (2011) Chromophore-assisted light inactivation of HaloTag fusion proteins labeled with eosin in living cells. ACS Chem Biol 6:401–406

Takemoto K et al (2013) SuperNova, a monomeric photosensitizing fluorescent protein for chromophore-assisted light inactivation. Sci Rep 3:2629

Takemoto K et al (2016) Optical inactivation of synaptic AMPA receptors erases fear memory. Nat Biotechnol 35:38–47

Tanabe T et al (2005) Multiphoton excitation-evoked chromophore-assisted laser inactivation using green fluorescent protein. Nat Methods 2:503–505

Teh C, Korzh V (2014) *In vivo* optogenetics for light-induced oxidative stress in transgenic zebrafish expressing the KillerRed photosensitizer protein. Methods Mol Biol 1148:229–238

Tour O, Meijer RM, Zacharias DA, Adams SR, Tsien RY (2003) Genetically targeted chromophore-assisted light inactivation. Nat Biotechnol 21:1505–1508

Tsien RY (1998) The green fluorescent protein. Annu Rev Biochem 67:509–544

Westberg M, Bregnhøj M, Etzerodt M, Ogilby PR (2017) No photon wasted: an efficient and selective singlet oxygen photosensitizing protein. J Phys Chem B 121:9366–9371

Westberg M, Holmegaard L, Pimenta FM, Etzerodt M, Ogilby PR (2015) Rational design of an efficient, genetically encodable, protein-encased singlet oxygen photosensitizer. J Am Chem Soc 137:1632–1642

Williams DC et al (2013) Rapid and permanent neuronal inactivation in vivo via subcellular generation of reactive oxygen with the use of KillerRed. Cell Rep 5:553–563

Winterbourn CC (2008) Reconciling the chemistry and biology of reactive oxygen species. Nat Chem Biol 4:278–286

Wojtovich AP, Wei AY, Sherman TA, Foster TH, Nehrke K (2016) Chromophore-assisted light inactivation of mitochondrial electron transport chain complex II in Caenorhabditis elegans. Sci Rep 6:29695

# Bioluminescence-Optogenetics

17

Ken Berglund, Matthew A. Stern, and Robert E. Gross

**Abstract**

In this chapter, we introduce a relatively new, emerging method for molecular neuromodulation—bioluminescence-optogenetics. Bioluminescence-optogenetics is mediated by luminopsin fusion proteins—light-sensing opsins fused to light-emitting luciferases. We describe their structures and working mechanisms and discuss their unique benefits over conventional optogenetics and chemogenetics. We also summarize applications of bioluminescence-optogenetics in various neurological disease models in rodents.

**Keywords**

Chemogenetics · Luciferase · Luciferin · Channelrhodopsin · Halorhodopsin

## Abbreviations

| | |
|---|---|
| AAV | Adeno-associated virus |
| ANT | Anterior nucleus of the thalamus |
| BRET | Bioluminescence resonance energy transfer |
| CNO | Clozapine-*N*-oxide |
| *Cr*ChR2 | *Chlamydomonas* channelrhodopsin 2 |
| CTZ | Coelenterazine |
| DG | Dentate gyrus |
| DREADD | Designer receptors exclusively activated by designer drugs |
| eLMO | Enhanced luminopsin |
| FLuc | Firefly luciferase |
| GLuc | *Gaussia* luciferase |
| iLMO | Inhibitory luminopsin |
| LED | Light-emitting diode |
| LMO | Luminopsin |
| LOV | Light-oxygen-voltage sensing protein |
| *Np*HR | *Natronomonas pharaonis* halorhodopsin |
| PD | Parkinson's disease |
| PPI | Protein–protein interaction |
| PSAM | Pharmacologically selective actuator molecule |
| PTZ | Pentylenetetrazol |
| RLuc | *Renilla* luciferase |
| SFLMO | Step-function luminopsin |
| SFO | Step-function opsin |
| *V*ChR1 | *Volvox* channelrhodopsin 1 |

Genetic approaches to enable manipulation of neuronal activity constitute a fundamental class of methods in the basic neuroscientist's armamentarium. Furthermore, some of these methods may even hold potential for application in the clinical

K. Berglund (✉) · M. A. Stern · R. E. Gross
Department of Neurosurgery, Emory University School of Medicine, Atlanta, GA, USA
e-mail: ken.berglund@emory.edu; matthew.a.stern@emory.edu; rgross@emory.edu



H. Yawo et al. (eds.), *Optogenetics*, Advances in Experimental Medicine and Biology 1293,
https://doi.org/10.1007/978-981-15-8763-4_17

setting. Specifically, in the past decade, optogenetics and chemogenetics have become workhorses in many laboratories to control activity in genetically predefined populations of neurons. To this end, optogenetics utilizes targeted expression of light-sensitive ion channels and pumps, known as opsins, that allow for modulation of neuronal activity with high temporal and spatial precision, facilitated by highly controlled delivery of photostimulation. However, the application of optogenetics is limited in two critical ways. First the light used to excite most opsins (visible wavelength range) is highly scattered and absorbed in brain tissue, significantly limiting its ability to penetrate and disperse. Second, the light source is external, necessitating delivery to the targeted tissue (often through a fiber optic). Consequently, light dispersion, and hence, neuronal control, is confined to a relatively small number of neurons located at the tip of an optical fiber. Thus, it is challenging to manipulate neurons in multiple locations and/or large brain areas as this would require a cumbersome number of fibers to achieve sufficient coverage. Chemogenetics overcomes this limitation through targeted expression of artificial metabotropic (e.g., DREADDs; designer receptors exclusively activated by designer drugs) and ionotropic (e.g., PSAMs; pharmacologically selective actuator modules) receptors that were engineered to be activated by foreign ligands, which can be introduced systemically for brain-wide spread (Sternson and Roth 2014). Without the need for implanted hardware, simultaneous modulation of multiple brain regions can be more readily achieved. However, chemogenetics does not provide precise temporal or spatial control of neuronal activity, as the activation of the chemogenetic actuators depends on diffusion and clearance of the activating molecule in the brain, a passive process difficult to control. The focus of this chapter will be on an emerging genetic neuromodulatory approach, bioluminescence-optogenetics, which combines the benefits and advantages of these two mainstream genetic techniques for controlling neural activity.

## 17.1 Luminopsin Fusion Proteins

Bioluminescence-optogenetics utilizes luminopsin fusion proteins (LMOs), which are combinations of light-sensing opsins and light-emitting luciferases (Fig. 17.1). LMOs are activated by cognate substrates of the luciferase enzyme, luciferin, which cross the blood–brain barrier. They generate biological light or bioluminescence through an enzymatic reaction, thus providing an internal light source for opsins (Fig. 17.2, left). This approach solves the limitation of light delivery into the brain for opsin activation, as light is generated in the vicinity of the opsin internally, obviating the need for implanted hardware. Of note, LMOs retain the capability to be activated by external light, similar to the conventional optogenetic approach, as the opsin moiety is exactly the same as commonly used in optogenetic probes (Fig. 17.2, right).

Bioluminescence is an inherently dim light source compared to external light sources used for conventional optogenetics (e.g., lasers and LEDs). Since the first publication in 2013 (Berglund et al. 2013), the efficacy of LMOs has been progressively improved by combining luciferases with higher bioluminescence emission and opsins with higher light sensitivity (Fig. 17.3). To date, about a dozen LMOs have been created by combining various opsins with luciferases (Table 17.1), and the arsenal of bioluminescence-optogenetics is readily expandable through engineering of new LMOs, particularly with the continued discovery and development of novel opsins and luciferases. In theory, any luciferase can be coupled to any kind of opsin as long as there is sufficient light emission and spectral overlap between the two for bioluminescent activation. In practice, the currently available LMOs all utilize marine luciferases, either *Gaussia* luciferase (GLuc; Fig. 17.1, left) or *Renilla* luciferase (RLuc; Fig. 17.1, right), both of which catalyze marine luciferin, coelenterazine (CTZ). The polarity of the LMO action is determined by the electrophysiological properties of the coupled opsin and can be either excitatory (Fig. 17.1, left) or inhibitory

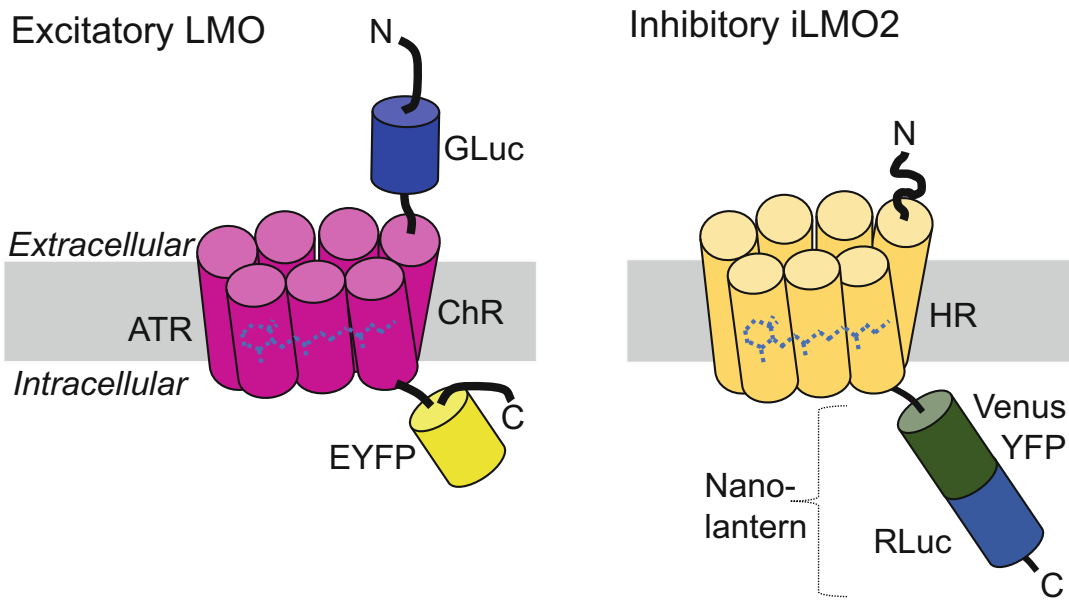


**Fig. 17.1** The molecular structure of luminopsins (LMOs). (Left) In excitatory LMOs, *Gaussia* luciferase (GLuc) is attached to the N-terminus of a light-gated cation channel, channelrhodopsin (ChR), placing the luciferase outside the cell. The channel is tagged with enhanced yellow fluorescent protein (EYFP) at the C-terminus for convenient identification of LMO-expressing cells. All-*trans*-retinal (ATR) is the chromophore within ChR. (Right) In inhibitory iLMO2, *Renilla* luciferase (RLuc)-based Nano-lantern is attached to the C-terminus of a light-driven chloride pump, halorhodopsin (HR), placing the luciferase inside the cell

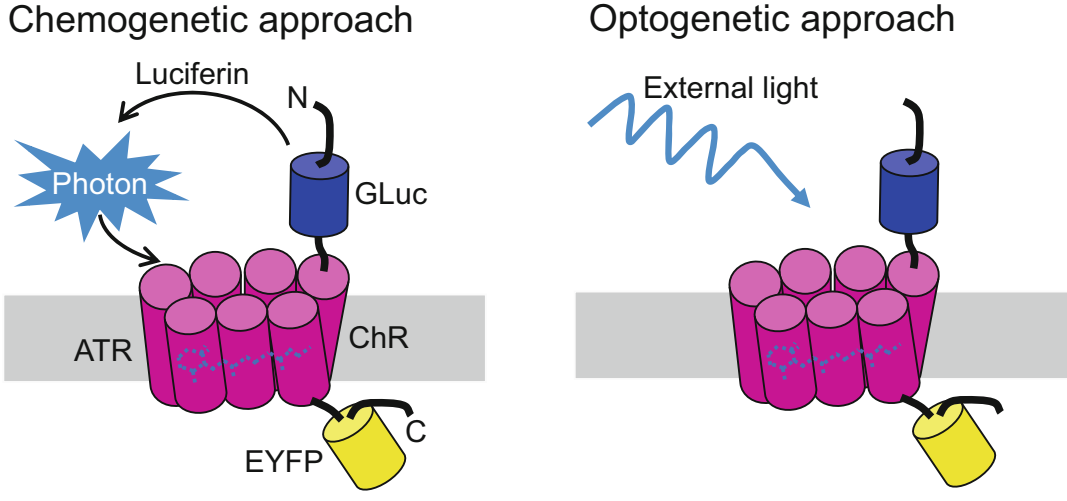


**Fig. 17.2** Bimodal luminopsins. Light needed for activation of LMOs is internally produced when a luciferase catalyzes its substrate, analogous to chemogenetics (left). The same molecule can be activated by external light, similar to conventional optogenetics (right)

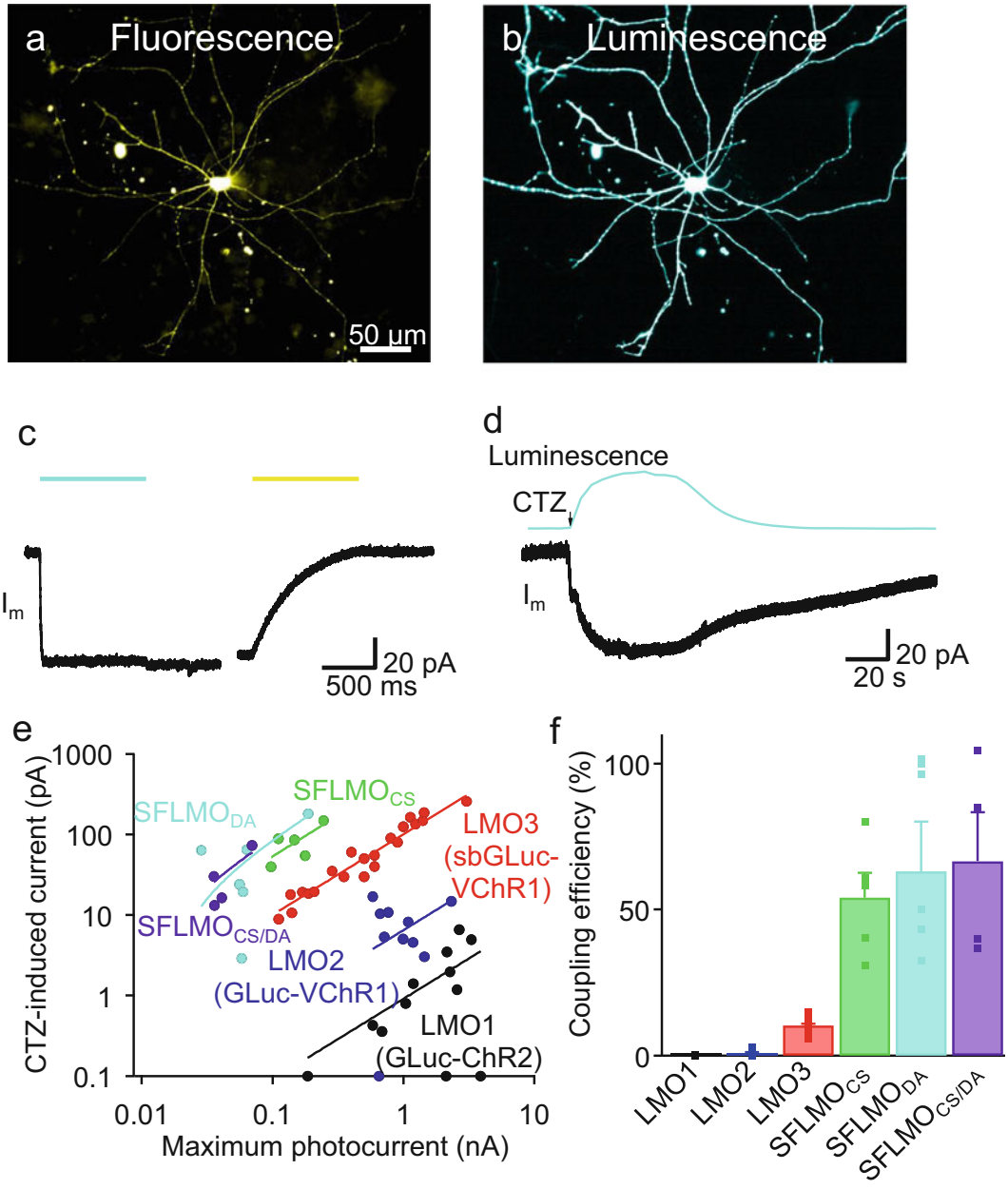


**Fig. 17.3** Bioluminescence-induced photocurrent and its efficiency in neurons. a and b. $SFLMO_{DA}$-transfected neurons in fluorescence (**a**) and bioluminescence (**b**). The EYFP tag in the LMO was imaged through a green filter cube in the microscope. Bioluminescence was induced by CTZ (100μM) and imaged without a filter cube. Exposure time was 100 ms and 1 s, respectively. (**c**, **d**) Representative photocurrents ($I_m$) in response to physical (**c**) and biological light (**d**). The $SFO_{DA}$ moiety in the LMO was activated by 480 nm light (422μW/mm$^2$; blue bar) and subsequently deactivated by 575 nm light (902μW/mm$^2$: yellow bar; **c**). CTZ (100μM; arrow) was bath-applied to the same cell, which induced bioluminescence and, in turn, bioluminescence-induced photocurrent (**d**). (**e**) Relationships between lamp-induced photocurrent and bioluminescence-induced photocurrent. Each cell was challenged by physical blue light from a lamp at a saturating intensity (> 2 mW/mm$^2$; 480 nm) and saturating concentration of CTZ (100μM) and the amplitudes of photocurrent induced in the two modes were plotted. $n = 12$ (LMO1), 10 (LMO2), 21 (LMO3), 5 ($SFLMO_{CS}$), 6 ($SFLMO_{DA}$), and 4 ($SFLMO_{CS/DA}$) cells. Data with SFLMOs were fitted with log-log linear regressions. (**f**) Coupling efficiency of SFLMOs. CTZ-induced photocurrent was divided by lamp-induced photocurrent in each cell and the means and SEMs were calculated for each variant of LMOs. $n = 12$ (LMO1), 10 (LMO2), 21 (LMO3), 5 ($SFLMO_{CS}$), 6 ($SFLMO_{DA}$), and 4 ($SFLMO_{CS/DA}$) cells. Data with LMO1, 2, and 3 were replotted from a previous publication (Berglund et al. 2016). The figure was reproduced from Berglund et al. (2020)

**Table 17.1** Currently available luminopsin variants

| Opsin \ Luciferase | | | GLuc | sbGLuc | GLuc/M23 | Nano-lantern |
|---|---|---|---|---|---|---|
| Inhibitory | $H^+$ pump | Mac | | iLMO[3] | | |
| | $Cl^-$ pump | NpHR | | | | iLMO2[2] |
| | $Cl^-$ channel | iChloC | | | iLMO4[4] | |
| Excitatory | Non-selective cation channel | ChR2 | LMO1[1] | | | |
| | | VChR1 | LMO2[1] | LMO3[3] | LMO4[4] | |
| | | $SFO_{CS}$ | | $SFLMO_{CS}$[5] | | |
| | | $SFO_{DA}$ | | $SFLMO_{DA}$[5] | | |
| | | $SFO_{CS/DA}$ | | $SFLMO_{CS/DA}$[5] | | |

The background color of luciferase and opsin moieties indicates emission and excitation spectra, respectively. Luminopsin molecules in black and red indicate inhibitory and excitatory ones, respectively. References: [1]Berglund et al. (2013); [2]Tung et al. (2015); [3]Berglund et al. (2016); [4]Park et al. (2020); [5]Berglund et al. (2020)

(Fig. 17.1, right). LMOs can be selectively expressed through targeted delivery of viruses (e.g., intracranial injection of adeno-associated virus; AAV) encoding the LMO construct under control of various promoters/enhancers, enabling neuromodulation of specific neuronal cell types.

## 17.2 Excitatory Luminopsins

In the first LMO (Berglund et al. 2013), wild-type GLuc was fused to *Chlamydomonas* channelrhodopsin 2 (*Cr*ChR2), based on the spectral overlap of blue emission in GLuc with blue excitation in *Cr*ChR2. The resulting molecule, LMO1, established the proof of concept for bioluminescence-optogenetics, namely activation of opsin by bioluminescence, albeit with dismissible efficacy: Only a fraction of the opsin moiety (~0.1%) was activatable by bioluminescence when CTZ was applied, compared to a saturating intensity of physical light from an arc lamp (defined as 100% efficacy). To improve efficacy, the authors employed a different opsin with superior light sensitivity, *Volvox* channelrhodopsin 1 (*V*ChR1), to create LMO2. Although *V*ChR1 is often times touted as redshifted *Cr*ChR2 due to its optimal excitation with green light, the authors capitalized on its superior sensitivity even in the blue spectrum and showed that *V*ChR1 could indeed improve efficacy up to 1%.

In a follow-up paper (Berglund et al. 2016), the same group generated the next LMO iteration, LMO3, by replacing the wild-type GLuc in LMO2 with a triple point mutated variant that is longer lasting and almost 10 times more bioluminescent (Welsh et al. 2009). The resulting LMO3 was 10 times more efficacious for bioluminescent activation than LMO2 and was able to elicit action potential firing in vitro and in vivo, when expressed in the rodent brains (Figs. 17.3b, c, d). Moreover, LMO3 activation was able to induce a specific behavioral change, namely rotational behavior, when expressed unilaterally in the substantia nigra.

Park et al. (2020) further bolstered this trend by coupling the brightest blue-emitting luciferase so far reported, the M23 variant of GLuc (Lindberg et al. 2013), with *V*ChR1, yielding LMO4. The authors showed that efficacy of activation by bioluminescence was improved in this new addition compared to previous iterations of the LMO family. Armed with this improved LMO, the authors showed that control of

neuronal activity was more efficient in vitro in cultured neurons (single unit activity) as well as in vivo in awake behaving rats (rotational behavior).

To improve efficacy and versatility of LMOs, Berglund et al. (2020) took a complementary approach as a workaround for inherently dim bioluminescence, instead replacing the opsin moiety with *Cr*ChR2 variants of enhanced light sensitivity and slower deactivation, step-function opsins (SFOs) and tested its efficacy in culture neurons in vitro (Figs. 17.3a, b). These longer lasting SFOs have the added ability of deactivation through application of longer wavelength light (Fig. 17.3c). The new luminopsins, termed step-function luminopsins (SFLMOs), were more efficiently activated by bioluminescence than previous LMO1–3 iterations (Figs. 17.3d–f). The authors further showed that SFLMOs could, as expected, control neuronal activity in vitro and rotational behavior in awake rats. In addition, SFLMOs offered an additional layer of controllability through deactivation by light of longer wavelength than generated by the luciferase, which can be applied using traditional optogenetic methods.

All aforementioned variants of LMOs are comprised of three transgenes, namely a marine luciferase for bioluminescence, a microbial opsin for photocurrent, and a hydrozoan fluorescent protein for fluorescent tagging of expressing cells. As in the case of opsins for conventional optogenetics, these foreign membrane proteins can be improperly processed in mammalian neurons and form cytosolic protein aggregates. To facilitate proper membrane targeting, Zhang et al. (2020) inserted the membrane trafficking signal found in a neuronal membrane protein, $K_{ir}2.1$, between the opsin and the fluorescent protein tag as previously used in enhancing expression of conventional optogenetic opsins (Gradinaru et al. 2008; Zhao et al. 2008). The resulting enhanced luminopsin 3 (eLMO3) demonstrated significantly reduced aggregation as well as significantly improved surface expression in vitro (primary mouse embryonic neuronal culture) and in vivo (AAV transduced mouse somatosensory cortex) as compared with its LMO3 predecessor. Additionally, in the same in vivo preparation, eLMO3 activation by CTZ more reliably elicited whisker-touching behavior.

## 17.3 Inhibitory Luminopsins

So far, four inhibitory luminopsins (iLMOs) based on hyperpolarizing opsins have been reported (Table 17.1, top). iLMO1 and iLMO2 (Fig. 17.1, right) (Tung et al. 2015) are fusion proteins of the light-driven chloride pump, *Natronomonas pharaonis* halorhodopsin (*Np*HR), with engineered RLucs, Tag red fluorescent protein (RFP)-RLuc and Nano-lantern (RLuc fused to Venus yellow fluorescent protein) (Saito et al. 2012), respectively. iLMO (without numbering) was a fusion protein of the slow-burn variant of GLuc with a light-driven proton pump from *Leptosphaeria maculans* (Berglund et al. 2016). iLMO4 (Park et al. 2020) contains the M23 variant of GLuc coupled with the improved chloride-conducting channelrhodopsin, iChloC (Wietek et al. 2015). These inhibitory LMOs have been demonstrated to induce neuronal inhibition in vitro and in vivo (both single unit activity and corresponding behavioral changes) in the presence of CTZ. A note on nomenclature: an iLMO3 variant was never published.

## 17.4 Fusion Vs. Co-Expression

The configuration of LMO as a single fusion protein provides convenience when expressing in cells (e.g., circumventing the need for coinfection with AAVs separately encoding the opsin and luciferase) as well as efficient activation of an opsin through bioluminescence, such as observed in SFLMOs. Multiple lines of evidence support that this highly efficient energy transfer from GLuc to SFO within the LMO molecule is mediated by radiationless bioluminescence resonance energy transfer (BRET), indicating that the fusion protein configuration is critical for bioluminescent activation of ChR-based LMOs (Berglund et al. 2020).

In contrast, *Np*HR has been demonstrated to be activated by a co-expressed luciferase without fusion, including firefly luciferase (FLuc) and RLuc (Land et al. 2014; Tung et al. 2015). While this energy transfer may not be as efficient, this functionality may offer the possibility for more flexible and creative usage of bioluminescence-optogenetics, such as transsynaptic activation by expressing a luciferase presynaptically and an opsin postsynaptically.

## 17.5 Luminopsin Substrate—Coelenterazine (CTZ)

Unlike DREADDs, which utilizes G-protein signaling, LMOs do not rely on any innate biochemical signaling cascades. Luciferins are completely foreign to mammals and other nonluminous species and do not have any distinct targets in the brain other than the exogenously expressed luciferase. However, luciferins, both CTZ for RLuc and GLuc and D-luciferin for FLuc, are known substrates for the ABC family transporters (Pichler et al. 2004; Zhang et al. 2007), whose activity may limit bioavailability of luciferins in the brain as they are expressed at the blood–brain barrier.

All the available toxicological data indicates that *CTZ poses no harm to mammals*; in contrast, clozapine-*N*-oxide (CNO)—the substrate for DREADDs—metabolizes to clozapine, an antipsychotic. No CTZ-induced cytotoxicity was observed in various mammalian cell lines (except for rat hepatocytes; Dubuisson et al. (2000)) at 100μM (Dubuisson et al. 2005), a concentration higher than estimated levels in the serum when systemically injected. Indeed, in addition to our publications, CTZ and luciferase have been widely used in oncological studies. Despite wide usage we are unaware of any documented adverse effects of CTZ administration. In fact, rodents treated with an excessively high dosage (>1 g/kg oral) of a CTZ derivative manifested no signs of acute or chronic toxicity (Dubuisson et al. 2005). Rather, therapeutic merits of CTZ, which is a natural antioxidant, have been suggested (Dubuisson et al. 2005), particularly as bioluminescence is an oxidation process.

CTZ is hydrophobic and therefore needs to be dissolved in a solvent first before diluting into aqueous solution for delivery. The resulting solution can be delivered to the brain systemically via various routes, including intraperitoneal, intravenous (jugular vein catheter or tail vein), intracortical, and intranasal injection. Among those, intranasal delivery is of special note. This rather inconspicuous route provides effectiveness and convenience for systemic administration of CTZ (Andreu et al. 2010). Yu et al. (2019) and Zhang et al. (2020) capitalized on the proximity of the nose and the brain for efficient delivery of CTZ to activate LMO3 in intracranial nervous tissue. While CTZ is expected to exert no significant off-target effects in the brain, certain solvents may affect the physiology of brain cells. Using neuronal firing recorded in a multi-electrode array in vitro as a readout, Prakash et al. (2020) systematically examined the effect of different preparations of CTZ in various solvents for a variety of LMOs. Their thorough study is a convenient guide for new luminopsin users to choose from different preparations of CTZ to avoid potential artifacts.

As there are many components to bioluminescence-optogenetics aside from the expression of the luminopsin—including the CTZ substrate and its metabolite (oxidized CTZ or coelenteramide), the solvents for CTZ, and resulting bioluminescence—it is possible that any component could impact neuronal activity indirectly through unexpected mechanisms, independent of the mechanism of bioluminescence-optogenetics. Therefore, to establish specificity of the approach, Gomez-Ramirez et al. (2020) tested each component systematically and demonstrated that neither CTZ, coelenteramide, nor solvent alone was sufficient to change neuronal activity. They further demonstrated that changes in neuronal activity were directly proportional to the amount of bioluminescence emitted. To rule out the effect of bioluminescence itself on neuronal activity, they employed a null mutated luminopsin with a point mutation that rendered the channel moiety nonfunctional. This elaborate negative control experiment utilizes opsins without phototransduction and perhaps should be more widely adopted in conventional

optogenetics. Thus, they provided strong evidence that the effect of LMOs was indeed caused by the changes in membrane potential induced by the opsin moiety gated by bioluminescence.

## 17.6 In Vivo Bioluminescence Imaging

One of the useful features of bioluminescence-optogenetics that is somewhat obvious, but nevertheless useful, is its byproduct bioluminescence. Bioluminescence emission can be used to noninvasively gauge expression of luminopsin molecules and/or pharmacodynamics of CTZ in vivo—a unique advantage of bioluminescence-optogenetics over conventional optogenetics and chemogenetics. Indeed bioluminescence emission from LMO molecules is strong enough to be observed through the intact skull and skin (Birkner et al. 2014; Tung et al. 2016). To illustrate this point, we expressed iLMO2 in the mouse primary visual cortex via AAV and observed transcranial/transcutaneous

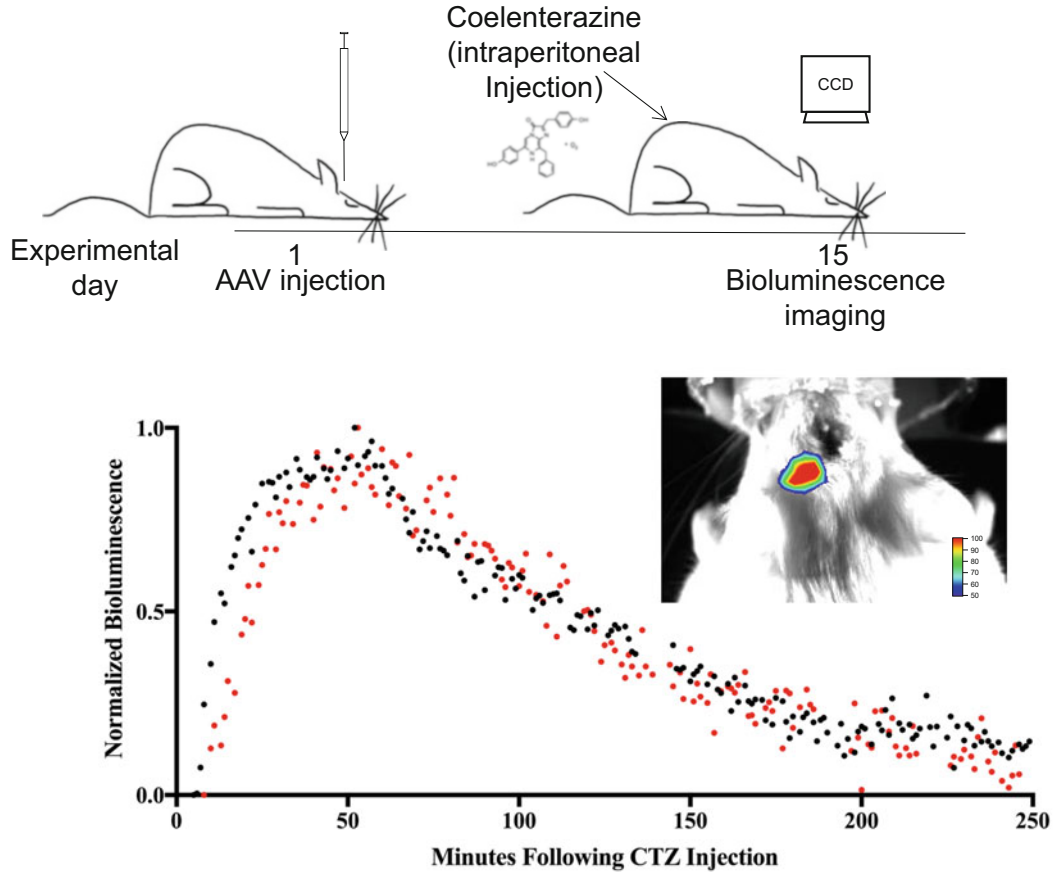


**Fig. 17.4** In vivo bioluminescence imaging using LMO. An AAV vector carrying the iLMO2 gene was injected into the adult mouse primary visual cortex. After a wait period to allow for sufficient gene expression (15 days), we conducted transcranial/transcutaneous in vivo bioluminescence imaging (top). CTZ was injected intraperitoneally (10 mg/kg) and bioluminescence was observed over 4 h (bottom). Peak luminescence occurred at 52.5 ± 0.5 min with luminescence greater than half of the maximum occurring from 18.5 ± 5.5 to 111.5 ± 3.5 min (mean ± standard error). Imaging was performed in separate subjects (n = 2; subject indicated by color). Bioluminescence was observed in the posterior brain where the visual cortex resides (inset)

**Table 17.2** Comparison of genetic neuromodulatory approaches

| Feature \ Method | Optogenetics | Chemogenetics | Bioluminescence-optogenetics |
|---|---|---|---|
| **Trigger** | External light | Exogenous chemical | External light or BRET |
| **Orthogonal multiplexing** | Wavelength | Substrate | Substrate |
| **Mechanism** | Ionotropic | Ionotropic or metabotropic | Ionotropic |
| **Hardware** | Required | Independent | Optional |
| **Region of Influence** | Small | Variable | Variable |
| **Kinetics** | Fast | Slow | Fast or slow |
| **Off-target effects** | Low | Possible | Low |
| **Intrinsic activation monitoring** | Inferred from light intensity and opacity of the tissue | None | Bioluminescence |

bioluminescence using a charge-coupled device camera after intraperitoneal injections of CTZ under anesthesia with isoflurane (Fig. 17.4). It took about 50 min for bioluminescence to reach its peak, with greater than half maximum luminescence occurring for 90 min (between 20 and 110 min postinjection) and with detectable luminescence observable for over 4 h. A repeat experiment in a separate animal resulted in almost identical bioluminescence, indicating reproducibility.

## 17.7 Comparison with Conventional Optogenetics and Chemogenetics

Bioluminescence-optogenetics was conceived to overcome the limitations of conventional optogenetics by leveraging a chemogenetic approach. Hence, a direct comparison of these three neuromodulatory modalities is warranted (Table 17.2). All three of these genetically encoded techniques enable highly specific neuromodulation when compared with conventional electrical stimulation, particularly with respect to their ability to target select cell types, facilitating circuit-informed modulation. Optogenetics has the advantage of temporal and spatial precision (i.e., control of the pattern and amount of light delivered and control of tissue modulated through placement of the fiber optics). However, optogenetics is limited for those same reasons, as external and implanted hardware are necessitated, which carries with it the risk for neural tissue injury, infection, hardware damage, and malfunction. Such limitations can constrain experimental design and limit its potential for translatability. Additionally, light dispersion is somewhat limited at sub-ablative power, making it difficult to conduct brain-wide and multiple-site neuromodulation as each brain region/nuclei would require a separate and/or multiple fiber placements to achieve adequate coverage.

Chemogenetics circumvents many of these limitations as it can be employed in a multinodal or even brain-wide fashion. Chemogenic substrates can be delivered systemically and will eventually disperse to all parts of the nervous

system; hence, wherever a chemogenetic receptor is present, the tissue can be modulated without the need for implanted hardware. However, herein lies a main limitation of chemogenetics: its temporal and spatial precision. The timing of neuromodulation is dependent on the dispersion and clearance of the substrate, a difficult process to control. Of course, one could consider more local delivery of substrate through cannulation and a pump, but that negates its advantage of hardware independence. Additionally, the most ubiquitously used chemogenic agents, DREADDs—which leverage endogenous metabotropic signaling cascades of which already exists in mammalian cells—can be confounded by endogenously occurring cellular processes and regulation. In a similar vein, these signaling cascades are also not exclusive to neuronal excitability and may have additional unintended downstream effects in some cell types. Furthermore, triggering activity through metabotropic receptors has slower response than ionotropic channels used in optogenetics. Moreover, the traditional substrate of DREADDs, CNO, metabolizes to the psychoactive molecule clozapine, which could lead to side effects.

Bioluminescence-optogenetics offers the advantages of both of these techniques, as LMOs can be activated through both approaches, activation of the opsin moiety directly through external light (in a traditional optogenetics sense) or activation of the opsin via BRET secondary to substrate binding (more akin to chemogenetics). Nevertheless, LMOs still have some of the same limitations as these other approaches, depending on the method chosen for activation. Importantly though, LMOs offer flexibility in experimental design to leverage the advantages of each system. In terms of key differences with DREADDs: LMOs are ionotropic which affords faster kinetics of activation than conventional chemogenetics; they do not rely on endogenous signaling cascades, so they are less likely to cause unintended effects; and the luminopsin substrate, CTZ, has not been demonstrated to have any toxicity or unwanted side effects. There are also several variants of effective luciferin, each with different kinetics, which offers more flexibility in experimental design. Moreover, LMOs enable users to spatiotemporally track their action through directly observing bioluminescence, the recording of which can be performed noninvasively.

## 17.8 Application in Neurological Disease Models in Rodents

Bioluminescence-optogenetics has been applied in various neurological disease models in rodents. To establish a mechanism of action for the therapeutic effects of physical exercise on peripheral nerve injury, Jaiswal et al. (2020) used iLMO2 (Fig. 17.1, right) to block the lower motor neuron activity thought to mediate the effect. Specifically, they injected an AAV carrying a Cre recombinase-dependent iLMO2 construct intramuscularly in the hindlimbs of transgenic mice expressing Cre under control of a motoneuron-specific promoter. The authors demonstrated that electrically evoked potentials in the muscles were reduced after application of CTZ in a time-dependent manner, confirming substrate-dependent inhibition of motoneurons by iLMO2. Using the same approach in a peripheral nerve injury model in mice, pretreatment with CTZ before each exercise session diminished functional recovery after the injury, suggesting a critical role of activity of motoneurons in this experimental paradigm. Their study exemplifies a simple but powerful approach using LMOs.

In an effort to lay the foundation for future treatments for epilepsy, Tung et al. (2018) utilized iLMO2 as a multi-nodal neuromodulatory therapeutic agent in a rat acute seizure model, induced by intraperitoneal injection of the chemoconvulsant pentylenetetrazol (PTZ). Targeting the circuit of Papez thought to mediate seizure generation in this model using AAV delivery, the authors expressed iLMO2 in multiple nuclei within this circuit, specifically granule cells in the dentate gyrus of the hippocampus (DG) and/or putative glutamatergic projection neurons in the anterior nucleus of the thalamus (ANT). iLMO2's efficacy in suppressing the induced seizures was assessed primarily through behavioral seizure outcomes. The authors observed a statistically significant decrease in

seizure duration compared with vehicle control when inhibiting a single nucleus bilaterally with iLMO2, either DG or ANT. Interestingly, when inhibiting both the DG and ANT with iLMO2 simultaneously, the authors observed a more pronounced seizure suppression than had been observed with inhibition of either nuclei alone. Seizure duration was decreased as well as Racine score, a measure of behavioral seizure severity. With iLMO2 in both DG and ANT, the majority of animals treated with CTZ showed the least severe form of seizure (Racine score 1), an effect not observed in control animals when vehicle was injected instead of CTZ. These results raise the prospect that better seizure suppression can be achieved using a circuit based multi-nodal neuromodulatory approach, exemplifying the advantage of multifocal targeting through the chemogenetic mode of bioluminescence-optogenetics.

As development of a potential therapeutic approach for Parkinson's disease (PD), Zenchak et al. (2020) used LMOs in conjunction with stem cell therapy in a genetic model of PD in mice. The authors first engineered mouse embryonic stem cells stably expressing LMO3. These cells were differentiated into neural precursors and then transplanted into the striatum of the mutant mice, which exhibit various neurological sequelae including motor deficits. When transplanted cells were chronically activated by daily injection of CTZ, the authors observed marked recovery of motor functions, indicating that increasing activity of neural precursors through LMO3 had therapeutic benefits in this rodent model of PD, while animals that received transplanted cells but did not receive CTZ failed to demonstrate a recovery of motor function.

Yu et al. (2019) took a similar combinatory stem cell/gene therapy for a mouse model of stroke. They first engineered induced pluripotent stem cells stably expressing LMO3, which they then differentiated into neuroprogenitor cells and transplanted into ischemic somatosensory cortex in mice. The transplanted cells were stimulated daily via intranasal delivery of CTZ. Using various physiological, biochemical, and histological assays, the authors demonstrated that neural circuits and connections were markedly repaired in the animals that received this combinatory treatment as compared with the control animals that received the cell transplantation but not CTZ. More importantly, those stroke model animals that received the transplanted cells and CTZ demonstrated significant improvements in behavioral tasks that require tactile sensation as compared with those that received neither or CTZ alone. The study suggests that chronic stimulation of neuroprogenitors through LMOs can provide pro-survival and pro-regenerative microenvironments that facilitate neural repair for the transplanted cells. Chemogenetic treatments of transplanted cells are an attractive alternative to optogenetic manipulations as transplanted cells may migrate and spread within the host brain, and thus may not be able to be targeted completely with conventional optogenetics, particularly given the limited spread of physical light within the tissue. Bioluminescence-optogenetics will ensure manipulation of transplanted cells even in such a scenario, as CTZ spreads brain-wide, far better than physical light delivered through fiber optics.

## 17.9 Potential beyond Rhodopsin-Based Optogenetics

It is important to note that, whereas we have focused our discussion specifically on bioluminescence-mediated activation of rhodopsins and their chromophore, retinal, there is great potential for bioluminescence to be employed in other optogenetic methods. We can imagine bioluminescent enzymes fused to photoactivated adenylyl cyclase to regulate intracellular cyclic adenosine monophosphate production (Schroder-Lang et al. 2007) as well as to various optogenetic systems that incorporate chromophores other than retinal, such as phycocyanobilin (Levskaya et al. 2009) and riboflavin-derived chromophores (Konermann et al. 2013). Phycocyanobilin-based systems are particularly interesting as they natively operate in the tissue-penetrating red/far-red spectrum (Tischer and Weiner 2014). Such systems may

be complemented by Akaluc (Iwano et al. 2018), a near-infrared emitting luciferase engineered from FLuc for bioluminescence-mediated activation.

Indeed, bioluminescence has already been deployed in one of these non-rhodopsin/non-retinal approaches. One such innovation is a variant on optogenetically gated transcriptional reporting of cellular protein–protein interaction (PPI) (Kim et al. 2019). The original use of this optogenetic method employed tagging a protein of interest with light-oxygen-voltage sensing protein (LOV) fused with a transcription factor for a reporter protein, separated by a proteolytic domain specific for a protease that would be tagged to another protein. This enables an AND logic for interaction of these two proteins of interest, for only in the presence of the correct wavelength of light to activate the LOV would the proteolytic domain be revealed such that it could be cleaved by the protease when the two proteins are close enough to interact. Thus, a researcher could regulate the precise timing of when this PPI would be reported. However, this method was prone to type 1 error: even without a PPI, if there was a high concentration of the protein tagged with the luciferase (during the light on phase), the proteolytic domain would be cleaved. Using a BRET gating mechanism researchers were able to overcome this limitation. Specifically, they added a luciferase tag to the protein they were already tagging with the protease, thus allowing the AND gate to be regulated by the presence of luciferin. The key advantage this afforded was that the proteins would need to be close enough not only for proteolytic cleavage to happen but also for BRET to occur. Thus, even if there were a high concentration of the protein tagged with the protease and luciferase (in the presence of luciferin), if a PPI were not occurring BRET could not occur, which greatly improved the reliability of this reporter system.

## 17.10 Concluding Remarks

This chapter provides an introduction to bioluminescence-optogenetics, specifically highlighting its versatility and advantages, from its potential for continued development to its growing application as a neuromodulatory approach to investigate disease and shed light on potential therapeutic avenues. As the field of bioluminescence-optogenetics continues to grow, we look forward to the innovative and creative uses the expanding user base will develop.

**Acknowledgments** This work was supported by NSF CBET-1512826 (KB/REG), NIH F31NS115479 (MAS), R21NS112948 (REG), DOD W81XWH1910776 (REG), and the Mirowski Family Foundation (REG).

## References

Andreu N, Zelmer A, Fletcher T, Elkington PT, Ward TH, Ripoll J, Parish T, Bancroft GJ, Schaible U, Robertson BD, Wiles S (2010) Optimisation of bioluminescent reporters for use with mycobacteria. PLoS One 5: e10777

Berglund K, Birkner E, Augustine GJ, Hochgeschwender U (2013) Light-emitting channelrhodopsins for combined optogenetic and chemical-genetic control of neurons. PLoS One 8:e59759

Berglund K, Clissold K, Li HE, Wen L, Park SY, Gleixner J, Klein ME, Lu D, Barter JW, Rossi MA, Augustine GJ, Yin HH, Hochgeschwender U (2016) Luminopsins integrate opto- and chemogenetics by using physical and biological light sources for opsin activation. Proc Natl Acad Sci 113:E358–E367

Berglund K, Fernandez AM, Gutekunst CN, Hochgeschwender U, Gross RE (2020) Step-function luminopsins for bimodal prolonged neuromodulation. J Neurosci Res 98:422–436

Birkner E, Berglund K, Klein ME, Augustine GJ, Hochgeschwender U (2014) Non-invasive activation of optogenetic actuators. SPIE

Dubuisson MLN, Bd W, Trouet A, Baguet F, Marchand-Brynaert J, Rees J-F (2000) Antioxidative properties of natural coelenterazine and synthetic methyl coelenterazine in rat hepatocytes subjected to tert-butyl hydroperoxide-induced oxidative stress. Biochem Pharmacol 60:471–478

Dubuisson MLN, Rees JF, Marchand-Brynaert J (2005) Coelenterazine (marine bioluminescent substrate): a source of inspiration for the discovery of novel antioxidants. Drug Dev Ind Pharm 31:827–849

Gomez-Ramirez M, More AI, Friedman NG, Hochgeschwender U, Moore CI (2020) The BioLuminescent-OptoGenetic in vivo response to coelenterazine is proportional, sensitive, and specific in neocortex. J Neurosci Res 98:471–480

Gradinaru V, Thompson KR, Deisseroth K (2008) eNpHR: a Natronomonas halorhodopsin enhanced for optogenetic applications. Brain Cell Biol 36:129–139

Iwano S et al (2018) Single-cell bioluminescence imaging of deep tissue in freely moving animals. Science 359:935–939

Jaiswal PB, Tung JK, Gross RE, English AW (2020) Motoneuron activity is required for enhancements in functional recovery after peripheral nerve injury in exercised female mice. J Neurosci Res 98:448–457

Kim CK, Cho KF, Kim MW, Ting AY (2019) Luciferase-LOV BRET enables versatile and specific transcriptional readout of cellular protein-protein interactions. elife 8:21

Konermann S, Brigham MD, Trevino AE, Hsu PD, Heidenreich M, Cong L, Platt RJ, Scott DA, Church GM, Zhang F (2013) Optical control of mammalian endogenous transcription and epigenetic states. Nature 500:472

Land B, Brayton C, Furman K, LaPalombara Z, DiLeone R (2014) Optogenetic inhibition of neurons by internal light production. Front Behav Neurosci 8

Levskaya A, Weiner OD, Lim WA, Voigt CA (2009) Spatiotemporal control of cell signalling using a light-switchable protein interaction. Nature 461:997–1001

Lindberg E, Mizukami S, Ibata K, Fukano T, Miyawaki A, Kikuchi K (2013) Development of cell-impermeable coelenterazine derivatives. Chem Sci 4:4395–4400

Park SY, Song S-H, Palmateer B, Pal A, Petersen ED, Shall GP, Welchko RM, Ibata K, Miyawaki A, Augustine GJ, Hochgeschwender U (2020) Novel luciferase–opsin combinations for improved luminopsins. J Neurosci Res 98:410–421

Pichler A, Prior JL, Piwnica-Worms D (2004) Imaging reversal of multidrug resistance in living mice with bioluminescence: *MDR1* P-glycoprotein transports coelenterazine. Proc Natl Acad Sci U S A 101:1702–1707

Prakash M, Medendorp WE, Hochgeschwender U (2020) Defining parameters of specificity for bioluminescent optogenetic activation of neurons using in vitro multi electrode arrays (MEA). J Neurosci Res 98:437–447

Saito K, Chang YF, Horikawa K, Hatsugai N, Higuchi Y, Hashida M, Yoshida Y, Matsuda T, Arai Y, Nagai T (2012) Luminescent proteins for high-speed single-cell and whole-body imaging. Nat Commun 3:1262

Schroder-Lang S, Schwarzel M, Seifert R, Strunker T, Kateriya S, Looser J, Watanabe M, Kaupp UB, Hegemann P, Nagel G (2007) Fast manipulation of cellular cAMP level by light in vivo. Nat Methods 4:39–42

Sternson SM, Roth BL (2014) Chemogenetic tools to interrogate brain functions. Annu Rev Neurosci 37:387–407

Tischer D, Weiner OD (2014) Illuminating cell signalling with optogenetic tools. Nat Rev Mol Cell Biol 15:551–558

Tung JK, Berglund K, Gutekunst C-A, Hochgeschwender U, Gross RE (2016) Bioluminescence imaging in live cells and animals. Neurophotonics 3:1–6. 6

Tung JK, Gutekunst C-A, Gross RE (2015) Inhibitory luminopsins: genetically-encoded bioluminescent opsins for versatile, scalable and hardware-independent optogenetic inhibition. Sci Rep 5:14366

Tung JK, Shiu FH, Ding K, Gross RE (2018) Chemically activated luminopsins allow optogenetic inhibition of distributed nodes in an epileptic network for non-invasive and multi-site suppression of seizure activity. Neurobiol Dis 109:1–10

Welsh JP, Patel KG, Manthiram K, Swartz JR (2009) Multiply mutated Gaussia luciferases provide prolonged and intense bioluminescence. Biochem Biophys Res Commun 389:563–568

Wietek J, Beltramo R, Scanziani M, Hegemann P, Oertner TG, Wiegert JS (2015) An improved chloride-conducting channelrhodopsin for light-induced inhibition of neuronal activity in vivo. Sci Rep 5:14807

Yu SP, Tung JK, Wei ZZ, Chen D, Berglund K, Zhong W, Zhang JY, Gu X, Song M, Gross RE, Lin SZ, Wei L (2019) Optochemogenetic stimulation of transplanted iPS-NPCs enhances neuronal repair and functional recovery after ischemic stroke. J Neurosci 39:6571–6594

Zenchak JR, Palmateer B, Dorka N, Brown TM, Wagner L-M, Medendorp WE, Petersen ED, Prakash M, Hochgeschwender U (2020) Bioluminescence-driven optogenetic activation of transplanted neural precursor cells improves motor deficits in a Parkinson's disease mouse model. J Neurosci Res 98:458–468

Zhang JY, Tung JK, Wang Z, Yu SP, Gross RE, Wei L, Berglund K (2020) Improved trafficking and expression of luminopsins for more efficient optical and pharmacological control of neuronal activity. J Neurosci Res 98:481–490

Zhang Y, Bressler JP, Neal J, Lal B, Bhang H-EC, Laterra J, Pomper MG (2007) ABCG2/BCRP expression modulates D-luciferin–based bioluminescence imaging. Cancer Res 67:9389–9397

Zhao S, Cunha C, Zhang F, Liu Q, Gloss B, Deisseroth K, Augustine GJ, Feng G (2008) Improved expression of halorhodopsin for light-induced silencing of neuronal activity. Brain Cell Biol 36:141–154

# Optogenetic Imaging of Protein Activity Using Two-Photon Fluorescence Lifetime Imaging Microscopy

18

Hideji Murakoshi

**Abstract**

Spatiotemporal dynamics of cellular proteins, including protein–protein interactions and conformational changes, is essential for understanding cellular functions such as synaptic plasticity, cell motility, and cell division. One of the best ways to understand the mechanisms of signal transduction is to visualize protein activity with high spatiotemporal resolution in living cells within tissues. Optogenetic probes such as fluorescent proteins, in combination with Förster Resonance Energy Transfer (FRET) techniques, enable the measurement of protein–protein interactions and conformational changes in response to signaling events in living cells. Of the various FRET detection systems, two-photon fluorescence lifetime imaging microscopy (2pFLIM) is one of the methods best suited to monitoring FRET in subcellular compartments of living cells located deep within tissues, such as brain slices. This review will introduce the principle of 2pFLIM-FRET and the use of chromoproteins for imaging intracellular protein activities and protein–protein interactions. Also, we will discuss two examples of 2pFLIM-FRET application: imaging actin polymerization in synapses of hippocampal neurons in brain sections and detecting small GTPase Cdc42 activity in astrocytes.

**Keywords**

2pFLIM · FRET · Fluorescent protein · Small GTPase · Cdc42 · Actin · Synapse · Neuron · Astrocyte

## Abbreviations

| | |
|---|---|
| 2pFLIM | Two-photon fluorescence lifetime imaging microscopy |
| AC | Adenylyl cyclase |
| ATP | Adenosine 5′-triphosphate |
| CNS | Central nervous system |
| F-actin | Filamentous actin |
| FRET | Förster resonance energy transfer |
| G-actin | Globular actin |
| GFP | Green fluorescent protein |
| LTP | Long-term potentiation |
| PLC | Phospholipase C |
| PMT | photomultiplier tube |
| REACh | Resonance energy-accepting chromoprotein |
| RFP | Red fluorescent protein |
| TCSPC | Time-correlated single photon counting |
| YFP | Yellow fluorescent protein |

H. Murakoshi (✉)
Supportive Center for Brain Research, National Institute for Physiological Science, Okazaki, Aichi, Japan

Department of Physiological Sciences, Graduate University for Advanced Studies, Okazaki, Aichi, Japan
e-mail: murakosh@nips.ac.jp



H. Yawo et al. (eds.), *Optogenetics*, Advances in Experimental Medicine and Biology 1293,
https://doi.org/10.1007/978-981-15-8763-4_18

## 18.1 Introduction

Intracellular signal transduction relies on signaling protein families such as kinases (Manning et al. 2002), small GTPase proteins (Wennerberg et al. 2005), and G-protein-coupled receptors (Bjarnadottir et al. 2006). These molecules interact with each other, forming complex signaling networks that play important roles in cellular functions, including synaptic plasticity, cell motility, and cell division. Thus, it is essential to understand the spatiotemporal regulatory mechanisms of intracellular signal transduction. One of the best ways to study protein dynamics such as diffusion and localization is to use fluorescent proteins. Since green fluorescent protein and its variants were discovered (Tsien 1998; Shaner et al. 2004), researchers have used them to visualize the dynamics of signaling molecules in living cells. Further, fluorescent proteins in combination with Förster Resonance Energy Transfer (FRET) phenomenon have allowed evaluating various protein activities including protein–protein interactions and conformational changes in living cells with high spatiotemporal resolution (Zhang et al. 2002; Miyawaki 2003; Newman et al. 2011; Ueda et al. 2013; Terai et al. 2019). The most widely used method is to use CFP as an energy donor and YFP as an energy acceptor, and takes the fluorescence intensity ratio of YFP and CFP (ratiometric imaging). This method has been used to measure the activity of various signaling proteins in living cells (Greenwald et al. 2018; Terai et al. 2019). Another way for the detection of FRET is fluorescence lifetime imaging microscopy (FLIM) (Lakowicz 2006). Because FLIM measures the fluorescence "lifetime" instead of fluorescence intensity, it has unique advantages when compared to ratiometric imaging such as insensitivity to photobleaching and quantitative measurement (Yasuda 2006). Furthermore, by using two-photon excitation with a near-infrared pulse laser (2pFLIM-FRET), we can detect FRET even in tissues, such as brain tissue. Recently, 2pFLIM-FRET has enabled the visualization of protein–protein interactions and protein conformational changes at the single-synapse level in deep tissues (Murakoshi and Yasuda 2012; Nishiyama and Yasuda 2015; Nakahata and Yasuda 2018). In this review, we will describe the principle of 2pFLIM-FRET, the use of chromoproteins, and their application in the detection of actin polymerization and small GTPase activity in dendritic spines of neurons and astrocytes.

## 18.2 Förster Resonance Energy Transfer (FRET)

FRET is a phenomenon that occurs when a donor fluorescent molecule is excited and there is an acceptor molecule within the Förster distance (<10 nm). The energy from the excited donor molecule is transferred to the acceptor molecule, producing a fluorescent emission from the acceptor molecule rather than the donor molecule (Miyawaki 2003; Lakowicz 2006; Lleres et al. 2007). For example, when GFP is excited, it emits green fluorescence. However, if red fluorescent protein (RFP) is located within 10 nm of the GFP molecule, the energy of excited GFP is transferred to the RFP, causing the RFP to emit red fluorescence. As a result, the GFP fluorescence intensity decreases while the RFP fluorescence intensity increases. FRET occurs when the following three criteria are satisfied: (1) The emission spectrum of the donor fluorophore overlaps with the excitation spectrum of the acceptor fluorophore (energy overlap), (2) the donor and acceptor fluorophores must be in close proximity (<10 nm), and (3) the relative orientation of the donor and acceptor fluorophores must be correct, i.e., FRET efficiency is maximized when the emission dipole moment of the donor and absorption dipole moment of the acceptor are parallel.

## 18.3 Fluorescence Lifetime

Fluorescent molecules, including synthetic organic fluorescent dyes and fluorescent proteins, have their unique fluorescence lifetime. It can be affected by environmental factors, like

temperature, pH, ionic strength, oxygen, and FRET. The fluorescence lifetime is the lag between fluorophore excitation and photon emission (i.e., the time spent in an excited state) (Lakowicz 2006). Using GFP as an example, blue light excites the GFP fluorophore, and this excited state lasts approximately 2.6 ns (fluorescence lifetime), after which GFP emits a photon as green fluorescence, and transitions back to its ground state (Fig. 18.2a, right). When a GFP molecule is continuously excited, the excitation and emission processes cycle until photobleaching occur as a result of the destruction of the fluorophore. In the case of GFP, photobleaching occurs after $10^5$ cycles of excitation/emission (photon budget) (Kubitscheck et al. 2000). Since fluorescence lifetime is affected by the local environment, it is beneficial in the measurement of changes to the intracellular state. Especially, fluorescence lifetime changes due to FRET can be used as a readout of protein–protein interactions and conformational changes. For example, when FRET occurs between GFP and RFP, the fluorescence lifetime of GFP (energy donor) shortens (see Box 18.1 for more detail). Quantification of the population of GFP that exhibits lifetime shortening enables us to detect and quantify FRET. Two major ways to measure lifetime are time-correlated single photon counting (TCSPC) (time-domain) and phase-delay methods (frequency domain) (Lakowicz 2006). Especially, the TCSPC method is highly compatible with a two-photon fluorescence microscope equipped with deep penetrating long-wavelength pulse lasers such as Ti-sapphire lasers, making it an ideal method for imaging neuronal activities occurring in tissues (Becker 2005; Yasuda 2006; Lleres et al. 2007).

**Box 18.1 Why Does the Fluorescence Lifetime of Donor Molecules Shorten during FRET?**

**–An explanation with an analogy with waterfall–**

As described in Sect. 18.3, when FRET occurs between a donor and an acceptor, the donor fluorescence lifetime shortens. Here is an analogy explain for lifetime shortening. If a blue-excitation photon hits the fluorophore of a single fluorescent molecule, it will place that molecule in an excited state. Usually, a cell expresses many GFP molecules, so blue light excites multiple GFP molecules at the same time. If we consider individual water molecules in a container with water to represent individual excited GFP molecules (Figure), this concept becomes easier to understand. If the container with the water molecules is raised and a hole made in the bottom of the container, all the water molecules will fall through the hole in 10 s ($\tau_D$) (Note that inverse of $\tau_D$ is $k_D$, which is proportional to the size of the hole). The same phenomenon is observed in the case of GFP molecules; the excited GFPs return to their ground state at a rate constant ($k_D$), but when FRET occurs, the second rate constant ($k_{FRET}$) appears. It is like adding a second hole in the bottom of the water container described above. If the two holes in this container are the same size, water will flow through each hole at the same rate (e.g., in 5 s) ($\tau_{DFRET}$) because two paths to the ground are now available. Similarly, when FRET occurs (i.e., two pathways, $k_D$ and $k_{FRET}$ are available for GFP to return to its ground state), the lifetime of the GFP signal shortens, just like the lifetime of the containment of water in the container with two holes.

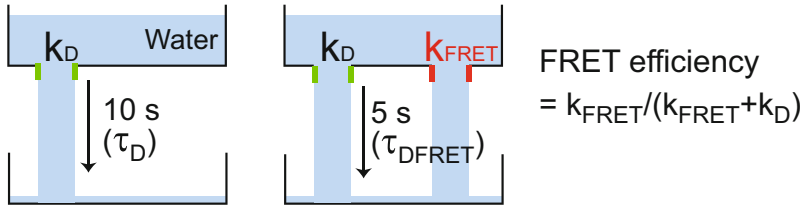


## 18.4 Advantages of Fluorescence Lifetime Imaging

FLIM has two advantages over ratiometric imaging. (1) In ratiometric imaging, CFP and YFP variants are commonly used as the energy donor and acceptor, respectively. This is because YFP has superior chromophore maturation and absorption/emission properties, promoting a strong FRET signal. When FRET occurs, CFP fluorescence intensity decreases while YFP fluorescence intensity increases. YFP fluorescence is then divided by CFP fluorescence to get a measure of FRET. However, this means that this method is very sensitive to photobleaching of CFP and YFP. During measurement, photobleaching of CFP or YFP can affect the ratio of YFP and CFP fluorescence intensities, resulting in artificial changes to the YFP/CFP ratio. In contrast, because FLIM measures the fluorescence lifetime of the donor but not its intensity, donor photobleaching does not affect FRET measurement. (2) Because CFP and YFP variants have quite a large spectral overlap (the excitation wavelength for CFP also excites YFP), it is difficult to separate the CFP and YFP emissions. It means that FRET-independent localization changes of CFP and YFP disturb the YFP/CFP ratio, resulting in experimental artifacts. Thus, it is necessary to use single-molecule type FRET probes or fuse CFP and YFP to the same protein to circumvent these issues. In contrast, FLIM uses GFP and RFPs (like mCherry), which are spectrally well separated. Thus, FRET-independent localization changes in a cell do not affect measurements. Although the quantum yield of mCherry is very low, this is not a disadvantage because FLIM does not require acceptor fluorescence to evaluate FRET events. Also, while CFP requires violet donor excitation, GFP requires low phototoxic blue light excitation, making it more accessible to most researchers. Also, most GFP variants have higher extinction coefficients and quantum yields than CFP variants (Tsien 1998; Cranfill et al. 2016; Bajar et al. 2016), making it robust FRET measurement.

## 18.5 Chromoproteins as FLIM-FRET Acceptors

Because acceptor absorption but not emission is only required for FLIM measurement, one can use chromoproteins as FLIM acceptors. The chromoprotein optimized for FLIM was first developed using EYFP as a template. Mutations (Y145W, V148W) around the chromophore led to selective decreases in the quantum yield rather than those in the extinction coefficient. This nonradiative yellow fluorescent protein, called resonance energy-accepting chromoprotein (REACh), was used as a FLIM acceptor and paired with EGFP (Ganesan et al. 2006). Since EGFP and EYFP have a spectral overlap in their emissions, contamination with EYFP fluorescence disturbs the measurement of EGFP fluorescence. However, since REACh does not have fluorescence, EGFP fluorescence can be measured without yellow fluorescence contamination. This pairing has two advantages. (1) EGFP emission and REACh excitation spectra have a large spectral overlap; Förster distance is large (5.4–5.9 nm). (2) Because the EGFP/REACh pair only occupies wavelengths of

500–580 nm, other fluorescent proteins such as mRFP and mCherry, with emission wavelengths of 600–700 nm, can be observed simultaneously. Similarly, dim fluorescent proteins/chromoproteins, which have large extinction coefficients but low quantum yields, have been developed and used for FLIM-FRET experiments (Murakoshi et al. 2008; Pettikiriarachchi et al. 2012; Don Paul et al. 2013; Murakoshi et al. 2015; Nakahata et al. 2016; Li et al. 2016; Murakoshi and Shibata 2017; Murakoshi et al. 2019).

## 18.6 Fluorescence Lifetime Measurement and Curve Fitting

TCSPC-based two-photon fluorescence lifetime imaging microscopy (2pFLIM) is often used to monitor and quantify protein–protein interactions or protein conformational changes in living cells within tissues (Becker 2005). The typical setup for 2pFLIM is described in Fig. 18.1. GFP is repeatedly subjected to pulses of two-photon excitation at a rate of 80 MHz. The laser intensity is adjusted so that only one GFP photon is detected in the photomultiplier tube during the 10–1000 excitation pulses. To determine the fluorescence lifetime, the time lag between the arrival time of GFP fluorescence photons and the excitation laser pulses are repeatedly measured using a single photon counting FLIM board (Becker 2005) while running a two-dimensional image acquisition. After repeating this process approximately 20 times with the laser focused in the sample plane, the lifetime histogram for each pixel is constructed from the assembled time-lag measurements (Fig. 18.1). To create the fluorescence lifetime image, the mean values ($\tau_m$), Eq. (18.1) from the constructed histograms at each pixel were calculated and used to generate a color-coded image (Fig. 18.1). Typically, a few seconds are required for single-plane image acquisitions.

$$\tau_m = \frac{\sum_i t_i F(t_i)}{\sum_i F(t_i)} \tag{18.1}$$

For the quantification of free GFP and GFP undergoing FRET in any region of interest (ROI), a histogram is first constructed from the time-lag ($t_i$) measurements for each ROI, and the decay time values are calculated by fitting with two exponentials. Since the instrument response function (IRF) is Gaussian-shaped (Yasuda et al. 2006), mainly as a result of the temporal profile of the laser pulse, two exponentially modified Gaussian functions (Eq. 18.2) are better for curve fitting of these data (Kalambet et al. 2011).

$$F(t) = P_D \exp\left(\frac{\sigma_G^2}{2\tau_D{}^2} - \frac{t-t_0}{\tau_D}\right) \operatorname{erfc}\left(\frac{\sigma_G^2 - \tau_D(t-t_0)}{\sqrt{2}\tau_D\sigma_G}\right) + P_{DFRET} \exp\left(\frac{\sigma_G^2}{2\tau_{DFRET}{}^2} - \frac{t-t_0}{\tau_{DFRET}}\right) \operatorname{erfc}\left(\frac{\sigma_G^2 - \tau_{DFRET}(t-t_0)}{\sqrt{2}\tau_{DFRET}\sigma_G}\right) \tag{18.2}$$

In Eq. (18.2), erfc is the complementary error function, $t_0$ is the time offset, $\sigma_G$ is the standard deviation of the IRF, and $\tau_D$ and $\tau_{DFRET}$ are the decay time constants of free donor (GFP) and donor undergoing FRET, respectively. $P_D$ and $P_{DFRET}$ are the coefficients for free donor and donor undergoing FRET, respectively. Thus, the binding fraction of donor, i.e., donor undergoing FRET, can be calculated as $P_{DFRET}/(P_D + P_{DFRET})$. For more details, please refer to Yasuda et al. (2006) (Yasuda 2012).

Here, to simply explain the relationships between FRET and fluorescence lifetime curves, a simplified (Eq. 18.3) form was used instead of (Eq. 18.2) in the following.

$$F(t) = P_D e^{-k_D t} + P_{DFRET} e^{-(k_D + k_{DFRET})t} \tag{18.3}$$

In Eq. (18.3), $k_D$ and $k_{FRET}$ are the rate constants for donor and FRET, respectively ($k_D = 1/\tau_D$, $k_D + k_{FRET} = 1/\tau_{DFRET}$). As the

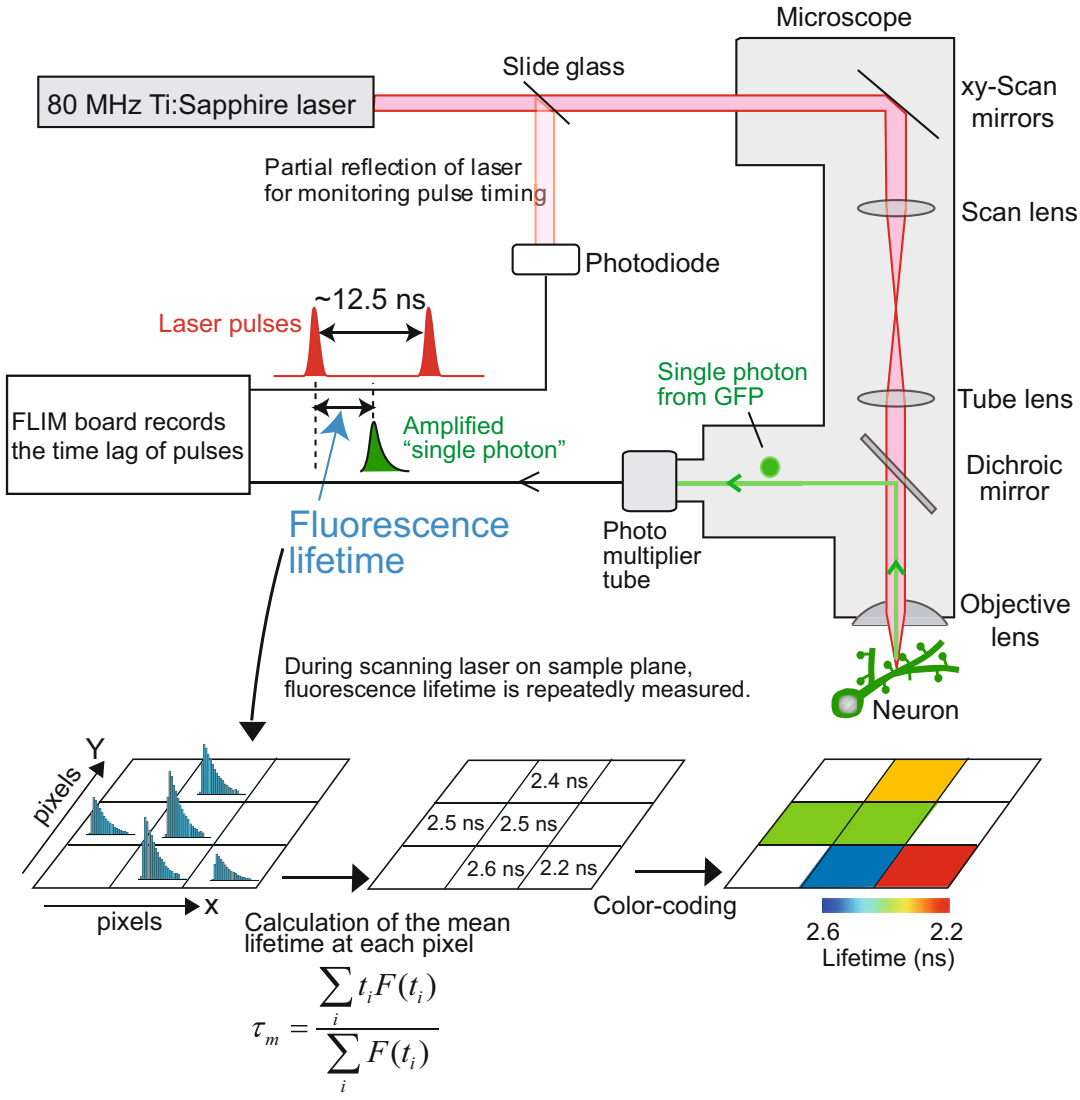


**Fig. 18.1** Setup for 2-photon fluorescence lifetime imaging microscope. An Olympus BX51WI microscope is often used as a base, and a hole is punctured through the microscope's side body near the fluorescence cube turret. Fluorescent signals are detected by the photomultiplier tube (PMT). The custom mirror cube is used to allow the side entry of GFP photons into the PMT. A Ti:sapphire laser tuned to 920 nm is used for two-photon GFP excitation with xy-galvano scan mirrors operated by ScanImage (Pologruto et al. 2003). For FLIM measurements, a minor fraction of the laser light is split by a slide glass to detect the reference pulses and to compare the arrival time of fluorescence photon from the sample. The difference in arrival time between the laser pulse and the fluorescence photon is measured by a FLIM board (Becker 2005). After repeated lifetime measurements, the mean lifetime of each pixel is calculated and translated to the corresponding color with custom (Yasuda 2012) or commercially available software (Becker 2005)

fluorescence lifetime of the GFP expressed in a cell is measured, its lifetime histogram can be fitted to a single-exponential function with a decay rate of $k_D$ (Fig. 18.2a). In contrast, when GFP and RFP are equally co-expressed and bound each other with a 1:1 stoichiometry (i.e., FRET occurs), and the fluorescence lifetime of GFP shorten because of a result of the addition of

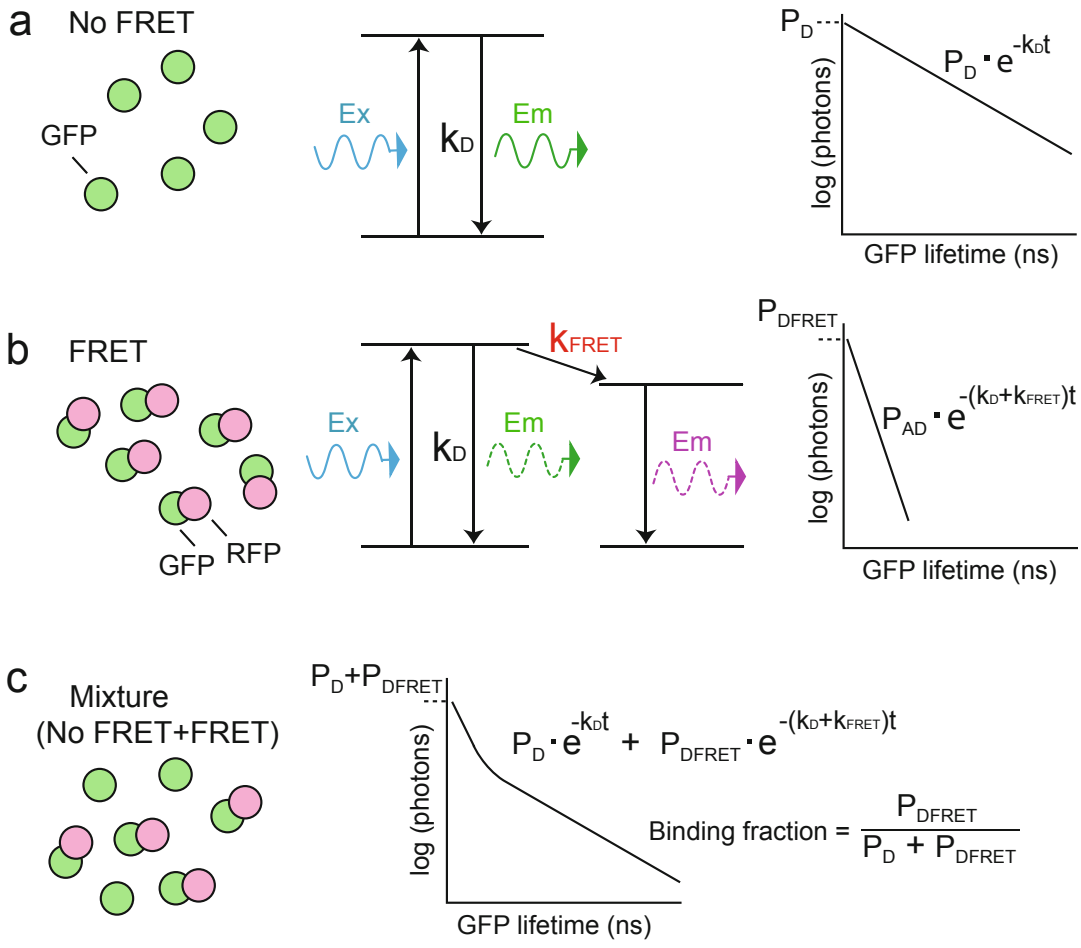


**Fig. 18.2** Fluorescence lifetime curve fitting. (**a**) (left) GFP molecules in the absence of FRET acceptor molecules. (middle) Jablonski diagram showing that, after a flash of light, the GFP molecule is excited, emits a photon, and then returns to its ground state. (right) When a number of GFP molecules ($P_D$) are excited, the fluorescence decay is fit to a single exponential decay curve since the photon emission occurs stochastically. (**b**) (left) All GFP molecules bind to the RFP molecules (FRET acceptors). (middle) Jablonski diagram showing that after a GFP molecule is excited by a flash of light, photon emission or FRET occurs with the rate constants, $k_D$ and $k_{FRET}$, respectively. Since the photon emission and FRET occur competitively, the fluorescence decay can be fitted to a single exponential curve, like that of the GFP lifetime plot when examined in the absence of FRET acceptors. Note that the fluorescence lifetime is shorter than that of free GFP because of the two extinction pathways ($k_D$ and $k_{FRET}$). See also Box 18.1. (**c**) (left) The mixture of free GFP and GFP bound to RFP with a ratio of $P_D$ and $P_{DFRET}$. (right) Since the two populations coexist, the fluorescence lifetime of GFP can be fitted with two exponential curves, and the binding fraction can be calculated as $P_{DFRET}/(P_D + P_{DFRET})$

a second decay rate $k_{FRET}$ (Fig. 18.2b, Box 18.1). Here, FRET efficiency is expressed as $k_{FRET}/(k_D + k_{FRET})$ or, in other words, $1 - \tau_{DFRET}/\tau_D$. In reality, free GFP and GFP undergoing FRET are usually both present at the same time in cells. Thus, the fluorescence lifetime should be fitted with two exponential functions (Fig. 18.2c), where the binding fraction is estimated as $P_{DFRET}/(P_D + P_{DFRET})$.

This fitting model can be quantitative when a strong enough signal is acquired. When the signal emitted from only a single synapse is analyzed, the curve fitting can fail as a result of the relatively small signal-to-noise ratio. Therefore, the

non-fitting method (Eq. 18.4) is also used for the estimation of the binding fraction (Yasuda 2012). Note that $\tau_D$, $\tau_{DFRET}$ can be determined by independent experiments (Yasuda et al. 2006). Therefore, once the mean lifetime $\tau_m$ of the ROI is determined, $P_{DFRET}$ is calculated directly without curve fitting.

$$P_{DFRET} = \frac{\tau_D(\tau_D - \tau_m)}{(\tau_D - \tau_{DFRET})(\tau_D + \tau_{DFRET} - \tau_m)} \quad (18.4)$$

## 18.7 Imaging Actin Polymerization in Synapses

Inter-neuronal connections occur at synapses, where electrical signals in the presynaptic neuron trigger the release of chemical transmitter signals into the synaptic cleft, which then produces an electrical signal in the postsynaptic neuron (Vitureira et al. 2012; Lynch 2004). In the central nervous system, excitatory synapses are generally formed on postsynaptic structures called spines, which are approximately 300 nm in diameter and often have a mushroom-like shape (Harris and Stevens 1989) working as the container of postsynaptic components (Fig. 18.3a). One of the characteristics of spines is their plasticity, which can be classified into two main types, long-term potentiation (LTP) and long-term depression (LTD). In hippocampal neurons, the mechanisms underlying LTP have been extensively studied using electrophysiological and biochemical methods. These studies have led to a deep understanding of plasticity, with one of the key findings being that AMPA receptors are recruited to the postsynaptic density (PSD), which is critical for their increased sensitivity to the glutamate released from the presynaptic neuron (Lynch 2004).

Actin is a main cytoskeletal component in cells and plays central roles in cell migration, cell division, and cell shape maintenance. Actin exists in two states, filamentous actin (F-actin) and globular actin (G-actin), which coexist within a cell, and local modulation of the equilibrium between F- and G-actin (actin polymerization–depolymerization) is essential to its function. In neurons, actin is highly enriched in dendritic spines and filopodia (Fig. 18.3a) and regulates their shape during both structural plasticity and development (Matus 2000; Krucker et al. 2000; Okamoto et al. 2004; Sekino et al. 2007; Honkura et al. 2008; Cingolani and Goda 2008).

One of the strategies used to visualize the extent of actin polymerization is to fuse actin molecules to donor and acceptor fluorescent proteins, respectively. For example, monomeric enhanced GFP (mEGFP) as a donor molecule and an improved version of REACh (sREACh) (Murakoshi et al. 2008) as an acceptor are both fused to the N-terminal of actin molecules, respectively (Fig. 18.3a). When these molecules (i.e., mEGFP-actin and sREACh-actin) are polymerized, FRET will occur as the size of actin is 5.5 nm (Holmes et al. 1990), which brings the mEGFP-sREACh pair within the Förster distance (Ganesan et al. 2006). In Fig. 18.3b, a neuron expressing mEGFP-actin/sREACh-actin was imaged using conventional two-photon fluorescence microscopy and 2pFLIM. FRET probe was sparsely transfected into a neuron of cultured hippocampal slices using ballistic gene transfer (McAllister 2000). The expression pattern of mEGFP-actin, when imaged by two-photon microscopy, shows the distribution of actin molecules in both the dendrites and the spines (Fig. 18.3b, top left), but G-actin cannot be discriminated from F-actin. In contrast, the 2pFLIM image shows the color-coded FRET signals, which acts as a readout of the level of F-actin polymerization (Fig. 18.3b, bottom left). These data clearly show that actin is highly polymerized in the spines rather compared to the dendrites. Treatment with jasplakinolide, which stabilizes and promotes actin polymerization, greatly increased the level of actin polymerization in the spines (Fig. 18.3b, top right and bottom right). These data confirm that FRET (indicated by reduced fluorescence lifetime) can be used as a quantitative measure of actin polymerization (Fig. 18.3c). Using Eq. (18.4), the binding fraction of mEGFP-actin in an individual spine can be

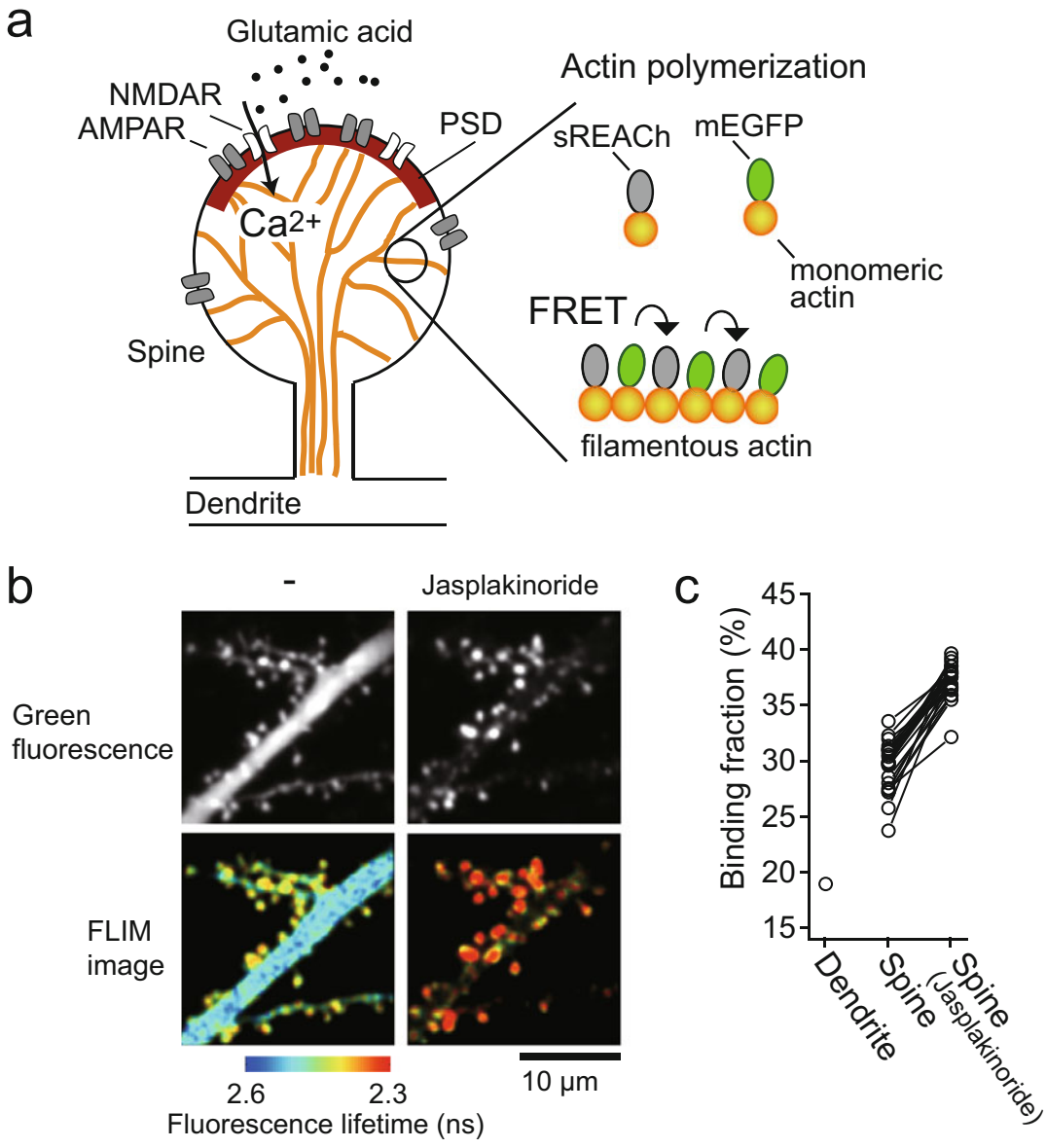


**Fig. 18.3** Imaging actin polymerization by mEGFP-actin/sREACh-actin FRET sensor. (**a**) The mushroom-like structure of the dendritic spine is maintained by actin filaments (orange). The binding of glutamate to the NMDA receptors induces $Ca^{2+}$ influx into the spine, which triggers the activation of various signaling proteins, resulting in spine enlargement and LTP due to actin polymerization and the recruitment of the AMPA receptors to the PSD. To detect actin polymerization. mEGFP-actin and sREACh-actin constructs can be used as FRET donor and acceptor, respectively. (**b**) Imaging actin polymerization in dendritic spines (Murakoshi et al. 2008). (Top left) The fluorescence intensity image of mEGFP-actin. (Bottom left) The fluorescence lifetime image for mEGFP-actin. (Top right) The fluorescence intensity image after jasplakinolide treatment. Note that almost all actin molecules are localized in the spines following this treatment. (Bottom left) The fluorescence lifetime image after jasplakinolide treatment. (**c**) The binding fraction (%) in individual spines before and after jasplakinolide treatment

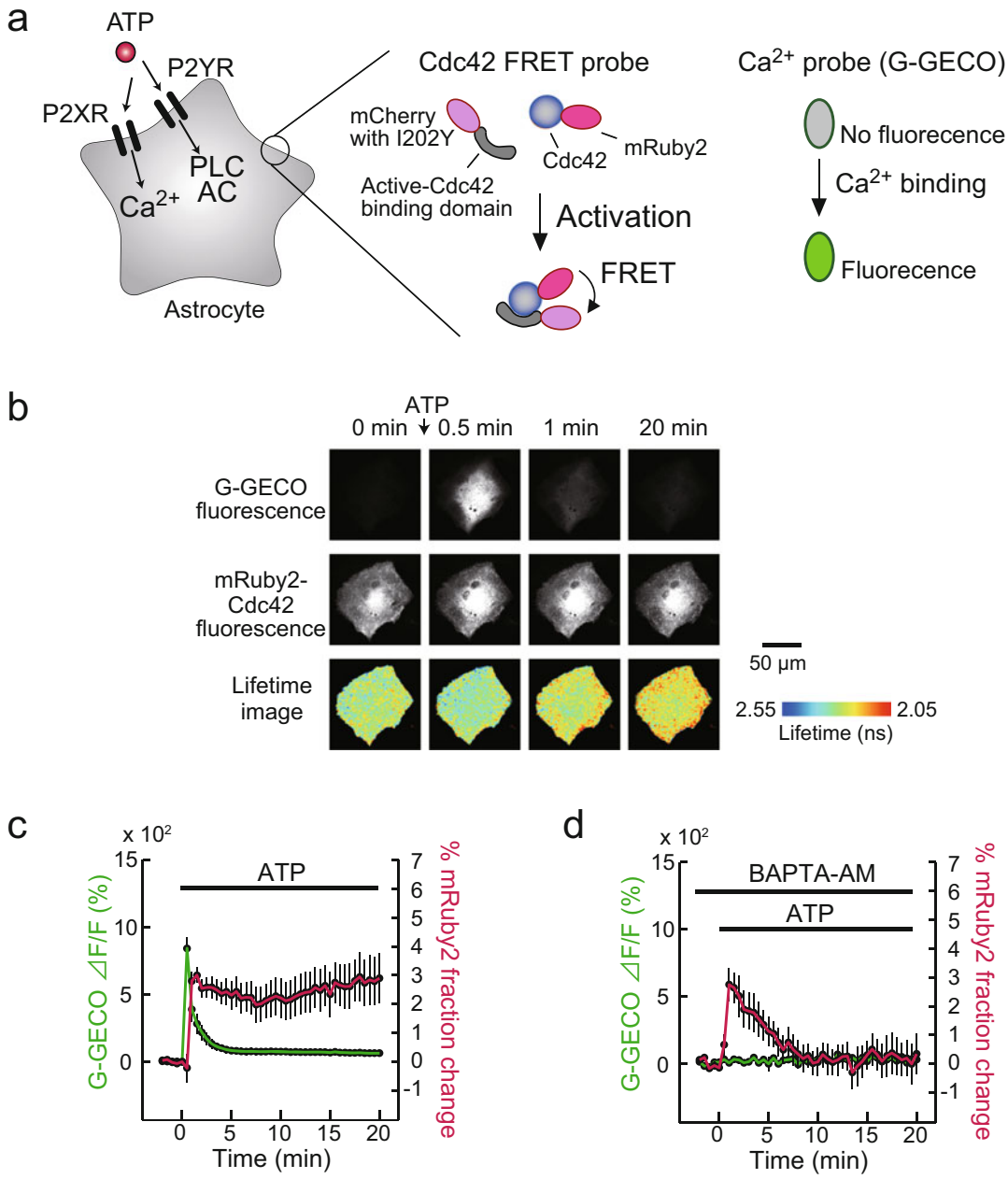


**Fig. 18.4** Dual observation of $Ca^{2+}$ transient and Cdc42 activation in cultured astrocytes. (**a**) Astrocytes express purinergic receptors such as P2X and P2Y receptors on plasma membrane so that they can receive extracellular ATP. As the P2X receptor is an ATP-gated cation channel, ATP binding induces $Ca^{2+}$ influx into the cytosol. In contrast, P2Y is a G-protein-coupled receptor that transmits signals to phospholipase C (PLC) or adenylyl cyclase (AC). (Right panel) Schematic representation of the G-GECO and Cdc42 FRET sensor. (**b**) Time-lapse images of G-GECO fluorescence (top), mRuby2-Cdc42 fluorescence (middle), and the fluorescence lifetime images of mRuby2-Cdc42 (bottom) before and after 100 μM ATP stimulation. (**c**, **d**) Time course analyses of the $Ca^{2+}$ response (green) and Cdc42 activation (magenta; the change in the mRuby2-Cdc42 binding fraction as calculated by using Eq. (18.4) (See Nakahata et al. 2016 for details) after addition of ATP in the absence (**c**) or presence of BAPTA (**d**). (**b–d** from Nakahata et al. (2016) with permission)

quantified (Fig. 18.3c). The binding fraction in spines increased by approximately 7% after jasplakinolide treatment. This shows that 2pFLIM is a sensitive, selective, and quantitative measure of protein–protein interactions.

## 18.8 Imaging Cdc42 Activity in Astrocytes

In the central nervous system (CNS), several types of glial cells such as oligodendrocytes, astrocytes, and microglia exist. Among these glial cell types, astrocytes are the most abundant and play essential roles in structural maintenance, metabolism, and synaptic function (Halassa and Haydon 2010; Sofroniew and Vinters 2010). Extracellular signals such as adenosine 5-′-triphosphate (ATP) and glutamate induce an increase in intracellular $Ca^{2+}$ concentration which activates astrocytes (Fig. 18.4a) (Volterra and Meldolesi 2005). However, the downstream signaling of $Ca^{2+}$ has remained elusive. Here, we introduce a dual imaging system to study the interactions of the cell division cycle 42 (Cdc42) and $Ca^{2+}$ increase using a chromoprotein-based Cdc42 FRET probe (Fig. 18.4a) (Nakahata et al. 2016). Cdc42 is a member of the Rho family small GTPases and is known to play important roles in actin polymerization/depolymerization associated with various cellular functions such as morphological changes and cell migration (Takai et al. 2001). Recently a FRET probe using mRuby2 as a donor and $mCherry_{I202Y}$ (mCherry with I202Y mutation to reduce emission while maintaining absorption) as an acceptor was developed and applied to Cdc42 FRET probe (Nakahata et al. 2016). The Cdc42 FRET probe consists of two components; mRuby2 was fused to the N-terminal of Cdc42 and dark mCherry was fused to the N-terminal of the Cdc42-binding domain (CBD, amino acid residues 60–113) of Pak3 (Fig. 18.4a) (Murakoshi et al. 2011). When mRuby2-Cdc42 is activated, $mCherry_{I202Y}$-CBD can bind to it, which results in FRET from mRuby2 to $mCherry_{I202Y}$. One of the disadvantages of two components type of FRET probe is that the expression levels of donor and acceptor may be variable in cells, which may disturb the measurement due to the increased variability of FRET responses in individual cells. To minimize the variability of FRET response as a result of imbalanced expression of donor and acceptor, Nakahata et al. equally expressed mRuby2-Cdc42 and $mCherry_{I202Y}$-CBD using a P2A sequence (Donnelly et al. 2001). Because mRuby2 and $mCherry_{I202Y}$ pair requires a fairly narrow band (550–650 nm) for FLIM-FRET measurements, additional fluorescent protein-based sensors such as a genetically encoded calcium sensor such as G-GECO (green fluorescent genetically encoded $Ca^{2+}$ indicators for optical imaging) (Zhao et al. 2011) (Fig. 18.4a), which requires the bandwidth (500–550 nm) for observation, can be used. To visualize Cdc42 and $Ca^{2+}$ dynamics, DNA encoding the Cdc42 FRET probes and G-GECO were transfected into cultured astrocytes using electroporation and observed under a two-photon fluorescence lifetime imaging microscope (Fig. 18.4b). Since ATP is a well-known extracellular ligand of P2 receptors (James and Butt 2002), which induce $Ca^{2+}$ transient in astrocytes (Fig. 18.4a), Nakahata et al. bath-applied ATP to cultured astrocytes and tested if $Ca^{2+}$ transient resulted in activation of Cdc42. ATP application triggered $Ca^{2+}$ transient within a few minutes (Fig. 18.4c) which was followed by the sustained activation of Cdc42 over 20 min (Fig. 18.4b, c). To further evaluate the effect of $Ca^{2+}$ on Cdc42 activation, cells were pretreated with a cell-permeable calcium chelator (200 μM BAPTA-AM) in combination with the removal of extracellular $Ca^{2+}$ and stimulated with ATP. Inhibition of $Ca^{2+}$ transient was confirmed by no G-GECO fluorescence (Fig. 18.4d). In the absence of $Ca^{2+}$ transient, ATP sill triggered Cdc42 activation, but the sustained activity of Cdc42 (10–20 min) backed to the baseline (Fig. 18.4d). This suggests that $Ca^{2+}$ transient is required for sustained Cdc42 activity, but not for the transient activity.

## 18.9 Conclusion

The optogenetic FRET sensors and methods described in this chapter can be combined to provide valuable information about the spatiotemporal profiles of biochemical reactions in subcellular structures, such as synapses. In addition, the use of optogenetic manipulation tools such as blue light-responsive photoactivatable proteins has gained popularity in recent years (Tye and Deisseroth 2012). The use of these tools in combination with 2pFLIM will allow us to obtain more detailed information about spatiotemporally regulated signal transduction in the future.

**Acknowledgments** This work was supported in part by a Grant-in-Aid for Scientific Research in Innovative Areas (18H02708, 18K19382, 18H04748 Resonance Bio, 19H05434 Singularity Biology, JP16H06280 Advanced Bioimaging Support to H.M.) from MEXT/Japan Society for the Promotion of Sciences (JSPS), Core Research for Evolutional Science and Technology (CREST) (to H.M.).

## References

Bajar BT, Wang ES, Zhang S, Lin MZ, Chu J (2016) A guide to fluorescent protein FRET pairs. Sensors (Basel) 16:9. https://doi.org/10.3390/s16091488

Becker W (2005) In: Castleman AW, Toennies JP, Zinth W (eds) Advanced time-correlated single photon counting techniques, vol 81. Springer

Bjarnadottir TK, Gloriam DE, Hellstrand SH, Kristiansson H, Fredriksson R, Schioth HB (2006) Comprehensive repertoire and phylogenetic analysis of the G protein-coupled receptors in human and mouse. Genomics 88(3):263–273. https://doi.org/10.1016/j.ygeno.2006.04.001

Cingolani LA, Goda Y (2008) Actin in action: the interplay between the actin cytoskeleton and synaptic efficacy. Nat Rev Neurosci 9(5):344–356

Cranfill PJ, Sell BR, Baird MA, Allen JR, Lavagnino Z, de Gruiter HM, Kremers GJ, Davidson MW, Ustione A, Piston DW (2016) Quantitative assessment of fluorescent proteins. Nat Methods 13(7):557–562. https://doi.org/10.1038/nmeth.3891

Don Paul C, Kiss C, Traore DA, Gong L, Wilce MC, Devenish RJ, Bradbury A, Prescott M (2013) Phanta: a non-fluorescent photochromic acceptor for pcFRET. PLoS One 8(9):e75835. https://doi.org/10.1371/journal.pone.0075835

Donnelly ML, Luke G, Mehrotra A, Li X, Hughes LE, Gani D, Ryan MD (2001) Analysis of the aphthovirus 2A/2B polyprotein 'cleavage' mechanism indicates not a proteolytic reaction, but a novel translational effect: a putative ribosomal 'skip'. J Gen Virol 82 (Pt 5):1013–1025. https://doi.org/10.1099/0022-1317-82-5-1013

Ganesan S, Ameer-Beg SM, Ng TT, Vojnovic B, Wouters FS (2006) A dark yellow fluorescent protein (YFP)-based Resonance Energy-Accepting Chromoprotein (REACh) for Forster resonance energy transfer with GFP. Proc Natl Acad Sci U S A 103(11):4089–4094. https://doi.org/10.1073/pnas.0509922103

Greenwald EC, Mehta S, Zhang J (2018) Genetically encoded fluorescent biosensors illuminate the spatiotemporal regulation of signaling networks. Chem Rev 118(24):11707–11794. https://doi.org/10.1021/acs.chemrev.8b00333

Halassa MM, Haydon PG (2010) Integrated brain circuits: astrocytic networks modulate neuronal activity and behavior. Annu Rev Physiol 72:335–355. https://doi.org/10.1146/annurev-physiol-021909-135843

Harris KM, Stevens JK (1989) Dendritic spines of CA 1 pyramidal cells in the rat hippocampus: serial electron microscopy with reference to their biophysical characteristics. J Neurosci 9(8):2982–2997

Holmes KC, Popp D, Gebhard W, Kabsch W (1990) Atomic model of the actin filament. Nature 347 (6288):44–49. https://doi.org/10.1038/347044a0

Honkura N, Matsuzaki M, Noguchi J, Ellis-Davies GC, Kasai H (2008) The subspine organization of actin fibers regulates the structure and plasticity of dendritic spines. Neuron 57(5):719–729

James G, Butt AM (2002) P2Y and P2X purinoceptor mediated $Ca^{2+}$ signalling in glial cell pathology in the central nervous system. Eur J Pharmacol 447 (2–3):247–260

Kalambet Y, Kozmin Y, Mikhailova K, Nagaev I, Tikhonov P (2011) Reconstruction of chromatographic peaks using the exponentially modified Gaussian function. J Chemom 25(7):352–356. https://doi.org/10.1002/Cem.1343

Krucker T, Siggins GR, Halpain S (2000) Dynamic actin filaments are required for stable long-term potentiation (LTP) in area CA1 of the hippocampus. Proc Natl Acad Sci U S A 97(12):6856–6861

Kubitscheck U, Kuckmann O, Kues T, Peters R (2000) Imaging and tracking of single GFP molecules in solution. Biophys J 78(4):2170–2179. https://doi.org/10.1016/S0006-3495(00)76764-6

Lakowicz JR (2006) Principles of fluorescence spectroscopy. Springer

Li Y, Forbrich A, Wu J, Shao P, Campbell RE, Zemp R (2016) Engineering dark chromoprotein reporters for photoacoustic microscopy and FRET imaging. Sci Rep 6:22129. https://doi.org/10.1038/srep22129

Lleres D, Swift S, Lamond AI (2007) Detecting protein-protein interactions in vivo with FRET using multiphoton fluorescence lifetime imaging microscopy (FLIM). Current protocols in cytometry/editorial board, J Paul

Robinson, managing editor [et al] Chapter 12:Unit12 10. doi:https://doi.org/10.1002/0471142956.cy1210s42

Lynch MA (2004) Long-term potentiation and memory. Physiol Rev 84(1):87–136. https://doi.org/10.1152/physrev.00014.2003

Manning G, Whyte DB, Martinez R, Hunter T, Sudarsanam S (2002) The protein kinase complement of the human genome. Science 298(5600):1912–1934. https://doi.org/10.1126/science.1075762

Matus A (2000) Actin-based plasticity in dendritic spines. Science 290(5492):754–758

McAllister AK (2000) Biolistic transfection of neurons. Sci STKE 2000(51):pl1

Miyawaki A (2003) Visualization of the spatial and temporal dynamics of intracellular signaling. Dev Cell 4 (3):295–305

Murakoshi H, Horiuchi H, Kosugi T, Onda M, Sato A, Koga N, Nabekura J (2019) ShadowR: a novel chromoprotein with reduced non-specific binding and improved expression in living cells. Sci Rep 9 (1):12072. https://doi.org/10.1038/s41598-019-48604-4

Murakoshi H, Lee SJ, Yasuda R (2008) Highly sensitive and quantitative FRET-FLIM imaging in single dendritic spines using improved non-radiative YFP. Brain Cell Biol 36(1–4):31–42. https://doi.org/10.1007/s11068-008-9024-9

Murakoshi H, Shibata AC, Nakahata Y, Nabekura J (2015) A dark green fluorescent protein as an acceptor for measurement of Forster resonance energy transfer. Sci Rep 5:15334. https://doi.org/10.1038/srep15334

Murakoshi H, Shibata ACE (2017) ShadowY: a dark yellow fluorescent protein for FLIM-based FRET measurement. Sci Rep 7(1):6791. https://doi.org/10.1038/s41598-017-07002-4

Murakoshi H, Wang H, Yasuda R (2011) Local, persistent activation of Rho GTPases during plasticity of single dendritic spines. Nature 472(7341):100–104

Murakoshi H, Yasuda R (2012) Postsynaptic signaling during plasticity of dendritic spines. Trends Neurosci 35(2):135–143. https://doi.org/10.1016/j.tins.2011.12.002

Nakahata Y, Nabekura J, Murakoshi H (2016) Dual observation of the ATP-evoked small GTPase activation and $Ca^{2+}$ transient in astrocytes using a dark red fluorescent protein. Sci Rep 6:39564. https://doi.org/10.1038/srep39564

Nakahata Y, Yasuda R (2018) Plasticity of spine structure: local signaling, translation and cytoskeletal reorganization. Front Synaptic Neurosci 10:29. https://doi.org/10.3389/fnsyn.2018.00029

Newman RH, Fosbrink MD, Zhang J (2011) Genetically encodable fluorescent biosensors for tracking signaling dynamics in living cells. Chem Rev 111 (5):3614–3666. https://doi.org/10.1021/cr100002u

Nishiyama J, Yasuda R (2015) Biochemical computation for spine structural plasticity. Neuron 87(1):63–75. https://doi.org/10.1016/j.neuron.2015.05.043

Okamoto K, Nagai T, Miyawaki A, Hayashi Y (2004) Rapid and persistent modulation of actin dynamics regulates postsynaptic reorganization underlying bidirectional plasticity. Nat Neurosci 7(10):1104–1112

Pettikiriarachchi A, Gong L, Perugini MA, Devenish RJ, Prescott M (2012) Ultramarine, a chromoprotein acceptor for Forster resonance energy transfer. PLoS One 7(7):e41028. https://doi.org/10.1371/journal.pone.0041028

Pologruto TA, Sabatini BL, Svoboda K (2003) ScanImage: flexible software for operating laser scanning microscopes. Biomed Eng Online 2:13. https://doi.org/10.1186/1475-925X-2-13

Sekino Y, Kojima N, Shirao T (2007) Role of actin cytoskeleton in dendritic spine morphogenesis. Neurochem Int 51(2–4):92–104. https://doi.org/10.1016/j.neuint.2007.04.029

Shaner NC, Campbell RE, Steinbach PA, Giepmans BN, Palmer AE, Tsien RY (2004) Improved monomeric red, orange and yellow fluorescent proteins derived from Discosoma sp. red fluorescent protein. Nat Biotechnol 22(12):1567–1572

Sofroniew MV, Vinters HV (2010) Astrocytes: biology and pathology. Acta Neuropathol 119(1):7–35. https://doi.org/10.1007/s00401-009-0619-8

Takai Y, Sasaki T, Matozaki T (2001) Small GTP-binding proteins. Physiol Rev 81(1):153–208

Terai K, Imanishi A, Li C, Matsuda M (2019) Two decades of genetically encoded biosensors based on Forster resonance energy transfer. Cell Struct Funct 44(2):153–169. https://doi.org/10.1247/csf.18035

Tsien RY (1998) The green fluorescent protein. Annu Rev Biochem 67:509–544. https://doi.org/10.1146/annurev.biochem.67.1.509

Tye KM, Deisseroth K (2012) Optogenetic investigation of neural circuits underlying brain disease in animal models. Nat Rev Neurosci 13(4):251–266. https://doi.org/10.1038/nrn3171

Ueda Y, Kwok S, Hayashi Y (2013) Application of FRET probes in the analysis of neuronal plasticity. Front Neural Circuits 7:163. https://doi.org/10.3389/fncir.2013.00163

Vitureira N, Letellier M, Goda Y (2012) Homeostatic synaptic plasticity: from single synapses to neural circuits. Curr Opin Neurobiol 22(3):516–521. https://doi.org/10.1016/j.conb.2011.09.006

Volterra A, Meldolesi J (2005) Astrocytes, from brain glue to communication elements: the revolution continues. Nat Rev Neurosci 6(8):626–640. https://doi.org/10.1038/nrn1722

Wennerberg K, Rossman KL, Der CJ (2005) The Ras superfamily at a glance. J Cell Sci 118 (Pt 5):843–846. https://doi.org/10.1242/jcs.01660

Yasuda R (2006) Imaging spatiotemporal dynamics of neuronal signaling using fluorescence resonance energy transfer and fluorescence lifetime imaging microscopy. Curr Opin Neurobiol 16(5):551–561

Yasuda R (2012) Studying signal transduction in single dendritic spines. Cold Spring Harb Perspect Biol 4

(10):1121–1128. https://doi.org/10.1101/cshperspect.a005611

Yasuda R, Harvey CD, Zhong H, Sobczyk A, van Aelst L, Svoboda K (2006) Supersensitive Ras activation in dendrites and spines revealed by two-photon fluorescence lifetime imaging. Nat Neurosci 9(2):283–291. https://doi.org/10.1038/nn1635

Zhang J, Campbell RE, Ting AY, Tsien RY (2002) Creating new fluorescent probes for cell biology. Nat Rev Mol Cell Biol 3(12):906–918. https://doi.org/10.1038/nrm976

Zhao Y, Araki S, Wu J, Teramoto T, Chang YF, Nakano M, Abdelfattah AS, Fujiwara M, Ishihara T, Nagai T, Campbell RE (2011) An expanded palette of genetically encoded Ca(2)(+) indicators. Science 333 (6051):1888–1891. https://doi.org/10.1126/science.1208592

# Optogenetics in *Drosophila*

19

Hiroshi Kohsaka and Akinao Nose

**Abstract**

The fruit fly *Drosophila melanogaster*, an insect 4 mm long, has served as the experimental subject in a wide range of biological research, including neuroscience. In this chapter, we briefly introduce optogenetic applications in *Drosophila* neuroscience research. First, we describe the development of *Drosophila* from egg to adult. In fly neuroscience, temperature-controlled perturbation of neural activity, sometimes called "thermogenetics," has been an invaluable tool that predates the advent of optogenetics. After briefly introducing this perturbation technique, we describe the process of generating transgenic flies that express optogenetic probes in a specific group of cells. Transgenic techniques are crucial in the application of optogenetics in *Drosophila* neuroscience; here we introduce the transposon P-elements, ϕC31 integrase, and CRISPR-Cas9 methods. As for cell-specific gene expression techniques, the binary expression systems utilizing Gal4-UAS, LexA-lexAop, and Q-system are described. We also present a short and basic optogenetic experiment with *Drosophila* larvae as a practical example. Finally, we review a few recent studies in *Drosophila* neuroscience that made use of optogenetics. In this overview of fly development, transgenic methods, and applications of optogenetics, we present an introductory background to optogenetics in *Drosophila*.

**Keywords**

*Drosophila* · Thermogenetics · Transgenic fly · P-element · φC31 integrase · CRISPR-Cas9 locomotion · Motor circuits

## Abbreviations

| | |
|---|---|
| ATR | All-Trans Retinal |
| attB | the Bacterial attachment site |
| attP | the Phage attachment site |
| Cas9 | CRISPR Associated protein 9 |
| ChR2 | Channelrhodopsin 2 |
| CRISPR | Clustered Regularly Interspaced Short Palindromic Repeats |
| FRT | Flippase Recognition Target |
| GDLs | GABAergic DorsoLateral neurons |
| GFP | Green Fluorescent Protein |
| PMSIs | Period-positive Median Segmental Interneurons |

H. Kohsaka (✉)
Department of Complexity Science and Engineering, University of Tokyo, Kashiwanoha, Chiba, Japan
e-mail: kohsaka@edu.k.u-tokyo.ac.jp

A. Nose
Department of Complexity Science and Engineering, University of Tokyo, Kashiwanoha, Chiba, Japan

Department of Physics, Graduate School of Science, University of Tokyo, Bunkyo-ku, Tokyo, Japan



H. Yawo et al. (eds.), *Optogenetics*, Advances in Experimental Medicine and Biology 1293,
https://doi.org/10.1007/978-981-15-8763-4_19

| | |
|---|---|
| TRP | Transient Receptor Potential |
| UAS | the Upstream Activation Sequence |

## 19.1 Drosophila

Drosophila *melanogaster*, a member of the guild of "cosmopolitan" fruit flies, is a useful model organism in a wide range of biology research, from genetics to ecology. *Drosophila* lives in many regions of the world. With their small body size (~5 mm), rapid reproduction rate, and no special food requirements, they are easy to rear in laboratories and use as model organisms in biology research. The use of *Drosophila* in neuroscience has been key to the large amount of accumulated knowledge and powerful techniques in genetics and developmental biology over the past century (Bellen et al. 2010). We begin this review with a brief introduction to the development of *Drosophila melanogaster* (hereafter, *Drosophila*).

### 19.1.1 Overview of *Drosophila* Development

A single female fly lays about 1000 eggs in a lifetime. Embryogenesis is completed in a day, then the first instar larva hatches. It takes 1 day for the first instar, 1 day for the second instar, and 2 days for the third instar (they molt between instars). After 5 days of the pupal stage, an adult fly emerges from the pupa case (eclosion) (Fig. 19.1).

*Drosophila* are holometabolous insects, which means they go through a pupal stage. Although larvae (before pupariation) and adults (after eclosion) are both the same individual animals, the behavioral repertoires are quite different between the two stages. Larvae spend a significant amount of time eating (the body lengthens ten-fold in the 4 days after hatching), so feeding and locomotion behaviors are prominent. In the adult stage, reproduction is of paramount importance. Adult flies search for and recognize potential mates, and then execute stereotypical courtship behavior. Both larvae and adults have sensory systems that detect environmental information, including visual (object and circadian recognition), chemical (odor and taste), and physical (vibration, gravity, and touch) cues. Based on environmental information, combined with individual experiences stored in the brain as memories, they exhibit adaptive behaviors. Using a vast amount of accumulated knowledge and techniques in genetic and developmental research, *Drosophila* researchers have untangled neural networks at the cellular and molecular level for a variety of behaviors (Simpson and Looger 2018; Venken et al. 2011).

### 19.1.2 Manipulation of Neural Activity in *Drosophila*

Optogenetics quickly spread throughout neuroscience research, starting in 2005. In *Drosophila* neuroscience before the advent of optogenetics, temperature-sensitive proteins had been used to manipulate neural activity. Here we briefly introduce this method, which is sometimes called thermogenetics. Shibire$^{ts}$ protein is a temperature-sensitive mutant of the dynamin protein. The *Shibire* gene was cloned (Chen et al. 1991; Van Der Bliek and Meyerowrtz 1991) by the analyses of a mutant (Grigliatti et al. 1973) that is paralyzed at high temperatures ("Shibire" means paralysis in Japanese). Shibire$^{ts}$ blocks endocytosis at temperatures higher than 30 °C ("restrictive temperatures"), but has no effect on endocytosis at lower temperatures ("permissive temperatures") (Kitamoto 2001). This change is reversible (Thum et al. 2006). Since the protein works in a dominant-negative manner, one can block neurotransmission by overexpressing this gene in neurons. In restrictive temperatures, Shibire$^{ts}$ blocks secretion of synaptic vesicles (Kosaka and Ikeda 1983), so it is used as a temporal blocker of neural activity. In its application, one should keep in mind that Shibire$^{ts}$ cannot block electrical synapses because the target of Shibire$^{ts}$ is dynamin-dependent vesicular neurotransmission, not gap junction communication.

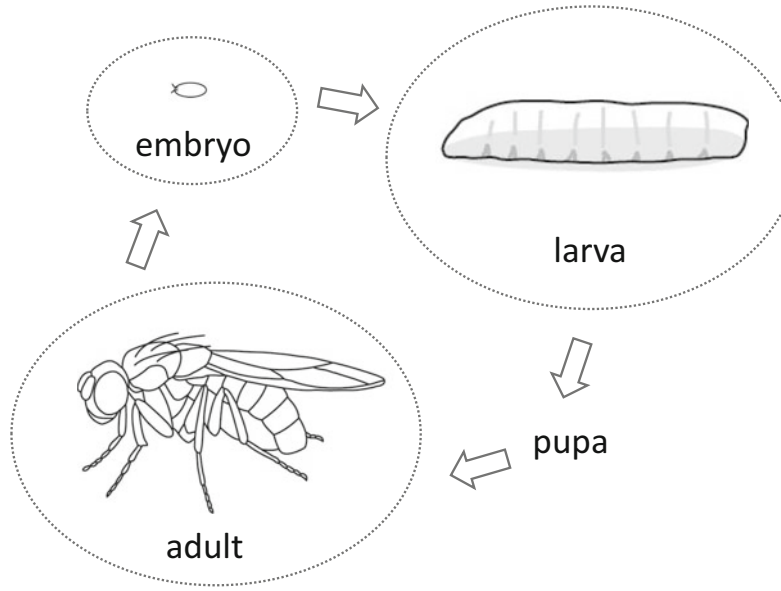


**Fig. 19.1** Life cycle of *Drosophila*. Embryos are about 0.5 mm long; larvae and adults are about 4 mm long

While Shibire$^{ts}$ is used to block neural activity, dTRPA1, a member of the TRP (Transient Receptor Potential) channel family is an ion channel activated at >25 °C that can be used to activate neurons by temperature control (Hamada et al. 2008; Pulver et al. 2009). TRPM8 is a cation channel that remains open below 25 °C and that also can be used as a neuron exciter (McKemy et al. 2002; Peabody et al. 2009). In *Drosophila* neuroscience, these temperature-controlled neuronal activity manipulations (thermogenetics) can be used in conjunction with optogenetics, depending on the experimental design.

## 19.2 Transgenic Methods in *Drosophila*

Optogenetics requires cell-specific gene expression to manipulate neural activity in a specific group of neurons. In *Drosophila*, transgenic methods are widely used for this purpose. There are three methods for generating transgenic flies: using a transposon P-element, ϕC31 integrase, and CRISPR-Cas9 endonuclease. As for exogenous gene expression techniques, binary expression systems utilizing Gal4-UAS, LexA-lexAop, and Q-system are commonly used. These methods are summarized in the following (Fig. 19.2).

### 19.2.1 Making Transgenic Flies Using P-Element Transposons

A P-element is a *Drosophila*-specific transposon that is used for mutagenesis, as it possesses inverted repeats of 31 base pairs at both ends. It also contains a DNA sequence that encodes the transposase enzyme, which recognizes the 31-pair sequences and can incise and insert the DNA in between the ends into a region of the genome. Using this system, one can insert any DNA sequence into the *Drosophila* genome through the following procedure. First, one prepares a vector including the DNA sequence to be inserted ("exogenous gene") sandwiched between the 31 base-pair inverted repeats. Then a vector possessing a gene encoding the transposase enzyme ("helper DNA") is injected into fertilized eggs of a strain lacking the endogenous P-element transposon. In the embryos, the exogenous DNA is inserted into the genome of some cells in a random manner by the function of

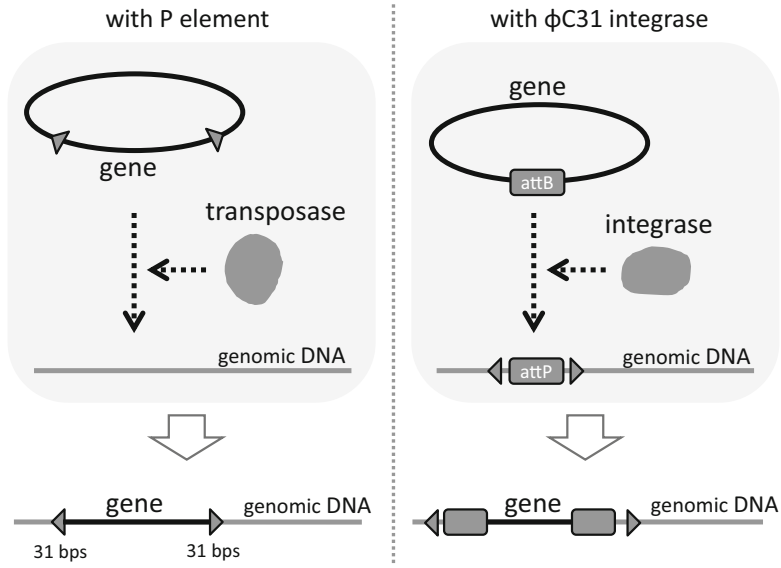


**Fig. 19.2** Methods of transgenic fly generation. Vectors are used to insert genes into genomic DNA by enzymes (transposase or integrase)

transposase, which is transcribed and translated from the helper DNA. In early stages of *Drosophila* embryogenesis, embryos undergo nuclear division without cell division. So DNA injected into embryos just within 1 h of egg laying diffuses throughout the whole embryo and can be integrated into any nuclei, including those of the presumptive germ cells. Thus, transgenic animals that stably possess the exogenous genes in all cells can be obtained in the progeny of the germ cells that underwent the integration process (Rubin and Spradling 1982). Note that the exogenous gene no longer remobilizes because the progeny lacks transposase.

During the above procedures, the P-element is inserted into random positions in chromosomes (but with a tendency to be inserted into regions near the promoter of genes (Bellen et al. 2011)). This property bears advantages and disadvantages. The expression pattern of the exogenously introduced gene depends on the location of P-element insertion (called the "position effect" (Levis et al. 1985)). Accordingly, one can obtain transgenic lines with a range of expression levels of the exogenously introduced gene, and, in particular, those with a high expression level. The disadvantage, however, is that expression of the exogenous gene may be influenced by the regulatory elements of nearby genes, potentially yielding unwanted ectopic expression. Moreover, P-element insertion may affect the expression and function of the endogenous genes near the insertion site. Accordingly, one has to be careful about these caveats and perform appropriate control experiments when assessing the phenotype of the transgenic animals.

### 19.2.2 Making Transgenic Flies with ϕC31 Integrase or CRISPR-Cas9 Endonuclease

Whereas an exogenous gene is inserted at random positions in the genome in the P-element system, the ϕC31 integrase system allows one to control the location of insertion (site-directed insertion). ϕC31 is the name of a phage that infects bacteria. Integrase, an enzyme produced by this phage, recognizes both a phage attachment site (attP DNA sequence) and a bacterial attachment site (attB DNA sequence) and induces DNA recombination between them. As a result, phage DNA can be inserted into the genome of host bacteria ("lysogenization"). This phenomenon has been used to generate transgenic lines of *Drosophila* (Groth et al. 2004). A collection of attP lines, in

which a single attP sequence is inserted in various locations in the genome, has been generated. Since the location of the attP insertion sites in these lines is determined, one can insert an exogenous gene in a desirable position in the genome by cloning the gene in a vector with an attB sequence and injecting the vector with messenger RNA encoding integrase into embryos of the appropriate attP line. Thus, we can design transgenic animals with an exogenous gene inserted in a genomic location determined in advance (Markstein et al. 2008).

In the ϕC31 method, the attP sequence should be inserted by the P-element method in advance. In contrast, the CRISPR-Cas9 method enables us to target specific loci in the genome for gene insertion. The Cas9 nuclease cleaves a specific locus in the genomic DNA. The specificity relies on the sequence of the guide RNA (Wiedenheft et al. 2012). If the Cas9 protein, the guide RNA, and a donor plasmid vector encoding a gene to be inserted and a homologous sequence around the cleavage coexisted in a cell, after Cas9-induced cleavage of the genomic DNA targeted by gRNA, the gene is integrated at the locus by homology-directed DNA repair. By harnessing this process, transgenes, including Gal4 and UAS-effector genes, are inserted into specific genomic loci (Gratz et al. 2013; Katow et al. 2019; Kondo and Ueda 2013; Li-Kroeger et al. 2018; Mohr et al. 2016). Both the site-directed transgene insertion methods (ϕC31 and CRISPR-Cas9) and the P-element method have been widely used to generate transgenic animals.

### 19.2.3 Gal4-UAS, LexA-lexAop, and Q System

Cell-specific expression of exogenous genes is required in optogenetics. In *Drosophila*, the Gal4-UAS system is widely used for artificial gene expression (Brand and Perrimon 1993) (Fig. 19.3). The yeast transcription factor Gal4 binds to a DNA sequence known as the upstream activation sequence (UAS) and drives expression of a gene downstream of the UAS. By utilizing this mechanism, expression of genes can be induced in specific cells in *Drosophila*. A collection of Gal4 lines, in which Gal4 is expressed in specific cells, and UAS lines, which can be used to express various reporters and optogenetic tools, have been established. Both Gal4 lines and UAS lines are made by the P-element, ϕC31 integrase, or CRISPR-Cas9 method, described above. Gal4 lines are generated by (1) inserting a vector containing the Gal4 gene sequence and the enhancer element that drives expression of Gal4 in specific cells (enhancer-Gal4 lines), (2) screening P-element-mediated Gal4 insertions in random positions in the genome for those in which Gal4 is expressed, by influence of the nearby enhancers, in the cells of interest (enhancer-trap lines), (3) knocking-in a vector containing the Gal4 gene to a specific genomic region of interest. By crossing a Gal4 line and a UAS line, one can obtain progenies that express an exogenous gene in specific cells. For example, by crossing "motoneuron-Gal4" with "UAS-ChR2," one can obtain animals expressing ChR2 in motor neurons. Currently, thousands of Gal4 lines have been established and are publicly available (Pfeiffer et al. 2008). Several UAS lines for expression of optogenetic probes have also been generated (Shearin et al. 2013). Moreover several genetic techniques to control spatiotemporal expression patterns have been developed using Gal80 repressor, split-Gal4, the recombinase Cre-loxP, and the recombinase flippase-FRT (Venken et al. 2011).

The LexA-lexAop system has been developed following the Gal4-UAS system (Lai and Lee 2006) (Fig. 19.3). The *E. coli* protein LexA works as a repressor by binding to the lexA operator (lexAop). A fusion protein of LexA and a transcription activator (such as the activator domain of Gal4) can induce expression of the gene downstream of the lexAop sequence. By using LexA transgenic lines, in which LexA is expressed in specific cells, exogenous genes can be expressed in specific cells with the LexA-lexAop system. To narrow down the number of labeled cells, the split-LexA system has been developed (Ting et al. 2011). Combinatorial use of the Gal4-UAS system and the LexA-lexAop

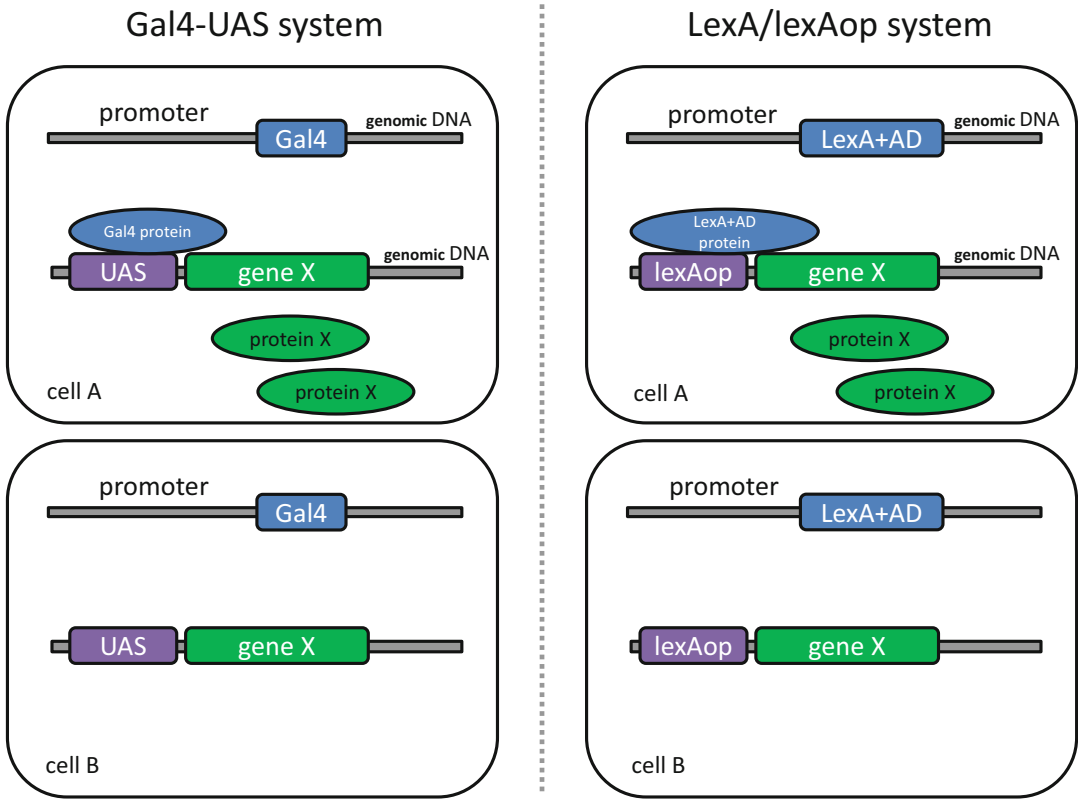


**Fig. 19.3** Gene expression systems. In cell A, Gal4 or lexA+AD is expressed by the promoter, then in turn gene X is expressed by Gal4 or lexA+AD proteins. In cell B, since neither Gal4 nor lexA+AD is expressed, gene X is not expressed. *AD* activation domain

system allows one to express different genes in distinct subsets of cells in the same animals and widens the range of optogenetic applications. For example, by using the Gal4-UAS system to express ChR2 in cells A and LexA-lexAop system to express GCaMP in cells B, one can study the effects of activating cells A on the activity of cells B.

The Q-system is another powerful tool in the fly genetic arsenal. The transcription activator QF induces expression of a gene following the QUAS sequence (Potter et al. 2010; Riabinina et al. 2015). This QF-dependent expression is suppressed by its suppressor QS. Furthermore, to narrow down the number of labeled cells, the split-LexA system has been developed (Riabinina et al. 2019).

### 19.2.4 Generate/Obtain Transgenic Lines

To establish new transgenic lines, one can design and generate a transgene vector as described above, inject the vector into fertilized eggs, select the animals that integrate the transgene and keep them as stocks. Solution containing the transgene is injected into embryos using a micro glass pipette. The injection process can be outsourced to some companies. Transgenic lines that are reported in published papers are in principle shared among fly researchers. They can be obtained by requesting them from individual researchers or from the stock centers in the United States (the Bloomington *Drosophila* Stock Center), Europe (Vienna *Drosophila* Resource

Center), and Japan (Kyoto Stock Center), which maintain and supply valuable transgenic lines.

## 19.3 Example Optogenetics Experiment in *Drosophila* Larvae

We have described how to generate transgenic animals in *Drosophila*. Next, we describe an example of an optogenetic experiment using *Drosophila* larvae (Fig. 19.4). We expressed ChR2 in motor neurons, expecting muscles that are innervated by those motor neurons to contract when excited with blue light. (*Drosophila* motor neurons form excitatory synapses on muscle.)

First, we crossed a "motoneuron-Gal4" line that drives gene expression in motor neurons (OK6-Gal4; (Aberle et al. 2002)) with a "UAS-ChR2" line for expression of ChR2 (Pulver et al. 2009). This generates larvae that express ChR2 in motor neurons. Blue light illumination on the larvae (OK6-Gal4 + UAS-ChR2), however, cannot activate motor neurons because ATR (all-trans-retinal) is missing. Unfortunately, *Drosophila* do not synthesize sufficient amounts of ATR for optogenetics, so it is necessary to feed larvae with ATR. As *Drosophila* larvae have a large appetite, a sufficient amount of ATR can be supplied by feeding a mixture of normal food and ATR. We simply spread yeast paste containing ATR (final concentration 1 mM) on agar gel and reared the larvae overnight on the gel. The motor neurons were ready to be activated the next day (Matsunaga et al. 2013). The excitation light for imaging green fluorescent protein (GFP) in fluorescence microscopy is suitable for the excitation of ChR2. Upon illuminating the freely moving larva on an agar plate with blue light, body wall muscles of the larva contract simultaneously.

Can we conclude from this observation that activating motor neurons with ChR2 leads to muscle contraction? Not without control groups. The experiment has three components: motoneurons-Gal4, UAS-ChR2, and ATR, and we tested combinations of these to find out if blue light illumination induces muscle contraction in each case. Thus, the required control groups are motoneuron-Gal4 + UAS-ChR2 (lacking ATR), UAS-ChR2 + ATR (lacking motoneurons-Gal4), and motoneurons-Gal4 + ATR (lacking UAS-ChR2). None of these larvae showed the muscle contraction was that seen in the experimental group, and so we can conclude that muscles contracted as a result of ChR2 activation of motor neurons. In these three control groups, UAS-ChR2 + ATR is especially important, since UAS lines sometimes induce gene expression even without Gal4 protein due to a position effect called "leak" (B. D. Pfeiffer et al. 2010). To avoid misinterpretation of the results, a "no Gal4" control must be included.

Efficacy of neural activation with ChR2 depends on several factors, including the expression level of ChR2, the amount of ATR, and the intensity of the light stimulation. We tested how the amount of ATR and light intensity affect the efficacy of activation of larval motor neurons. We reared larvae with three levels of ATR concentration (10 μM, 100 μM, and 1 mM) overnight, and then illuminated them with various intensities of blue light (20–360 $\mu W/mm^2$) and measured body contractions (Fig. 19.4). We found that the higher ATR concentration we fed the larvae, the more they exhibited contraction. And, in a low-ATR concentration condition, the stronger the light we applied to larvae, the more the larvae showed body contractions. Although this observation seems to suggest that we should use blue light at maximum power, in practice we should pay attention to the innate photophobic behavior of larvae. Larvae have eyes on the head (actually, they also have photoreceptors over the whole surface of the body (Xiang et al. 2010)) and exhibit photophobic response behavior upon being illuminated with strong blue light. To reduce the photophobic response in optogenetic experiments, the light intensity for stimulation should be minimized. Accordingly, the light intensity is determined by a trade-off between the efficiency of ChR2 excitation and the larval photophobic response. Larvae are less sensitive to longer wavelengths of light. Accordingly, redshifted ChR2 (Klapoetke et al. 2014; Lin et al. 2013) can be used to activate larval neurons while avoiding innate photophobic responses.

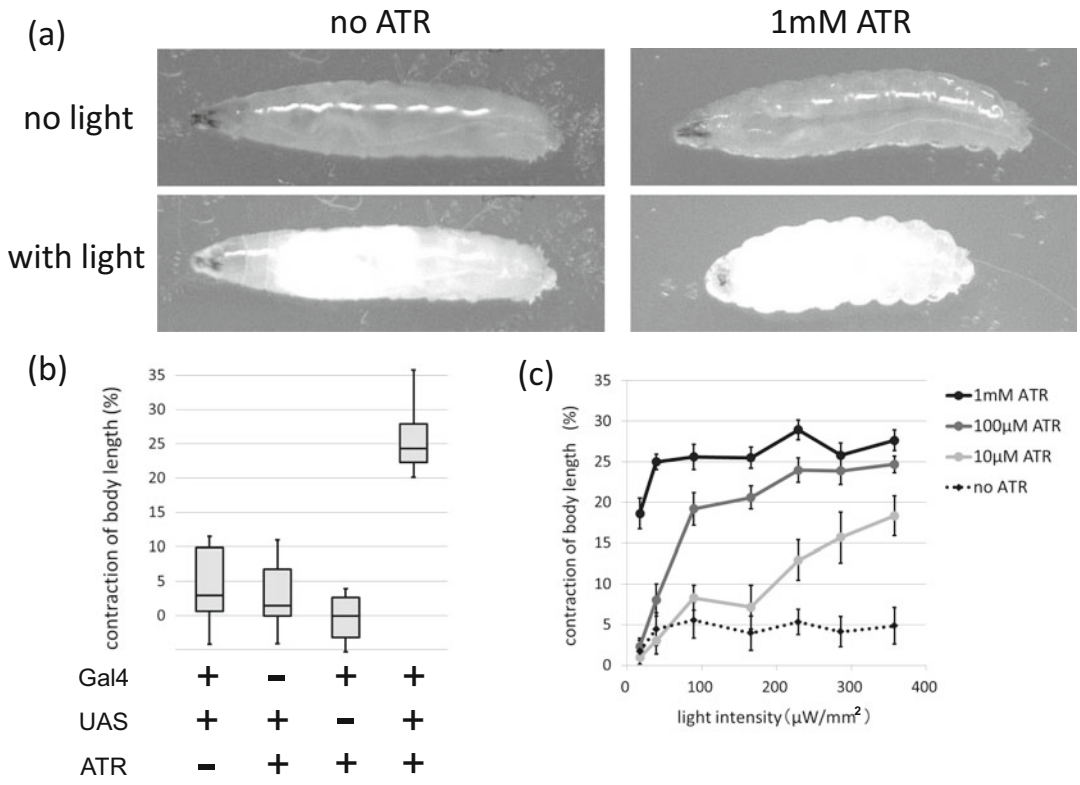


**Fig. 19.4** Optogenetic activation of larval motor neurons. (**a**) Snapshots of optogenetic activation of larval motor neurons with 285 μW/mm$^2$ blue light. (**b**) Quantification of body contraction of experimental and control groups. (**c**) Dependence of efficiency of optogenetic stimulation on amounts of ATR and intensities of stimulation light

## 19.4 Examples of Optogenetic Research in *Drosophila*

Finally, we briefly review some recent applications of optogenetics in *Drosophila*, which have been growing quickly over the past several years. Specifically, combining cell-specific gene expression by *Drosophila* genetics and spatiotemporal manipulation of neural activity by optogenetics allows us to study circuit principles of animal behavior.

As shown in Fig. 19.5, in typical larval behavior forward peristaltic locomotion is generated by propagation of body segment contraction from posterior to anterior (Kohsaka et al. 2012). This propagative activity is one example of axial locomotion, a form of animal motion that includes swimming, crawling, and walking. By local laser illumination of specific segments in the nervous system, we can perturb local neural activity during ongoing activity propagation and assess the spatiotemporal dynamics of motor circuits (Matsunaga et al. 2013). During the axial propagation of the motor activity, activating inhibitory premotor interneurons PMSIs (*period*-positive median segmental interneurons) (Kohsaka et al. 2014) or inhibitory second-order premotor interneurons GDLs (GABAergic dorsolateral neurons) (Fushiki et al. 2016) in a wave front arrests the propagation of the axial waves (Fig. 19.6). Operability of spatiotemporal activation with optogenetics allows us to study circuit activity dynamics, which is especially critical in motor function.

By temporal manipulation of neural activity by optogenetics, computational processes for

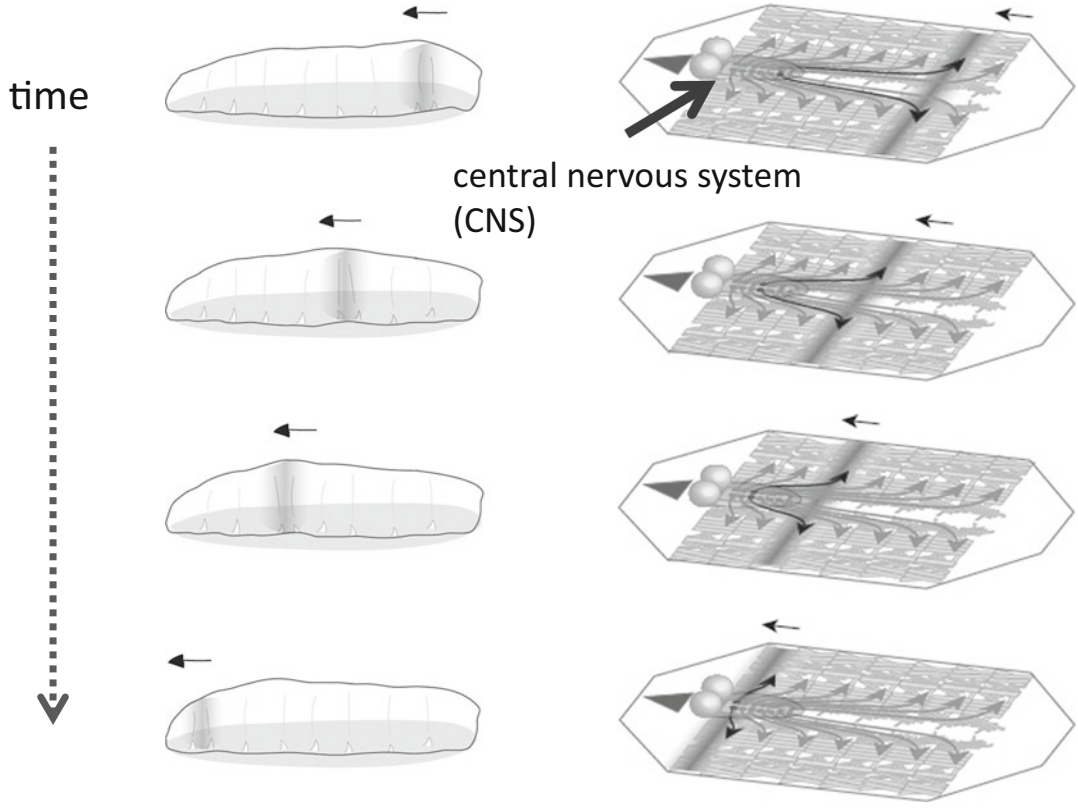


**Fig. 19.5** Peristaltic locomotion of intact (left) or dissected (right) larvae. In forward locomotion, local segmental contraction is propagated from the posterior (right) to the anterior segment (left). Arrows in left panels show motor neuronal projection to muscles. (From Kohsaka et al. (2012))

behavioral decision-making can be analyzed. Sensory-motor transformation in larval chemotactic behavior was quantitatively analyzed by random patterns of optogenetic activation and a statistical analysis named reverse-correlation analysis (Hernandez-Nunez et al. 2015). The authors succeeded in establishing a mathematical model to describe navigational dynamics in chemotactic behavior. Dynamic computation of multi-sensory integration of visual and olfactory cues has also been studied using the powerful optogenetic tools (Gepner et al. 2015). By reverse-correlation analysis and linear–nonlinear-Poisson model, the authors showed that olfactory and visual signals are linearly combined before the decision to change locomotion direction. These studies clearly showed the power of optogenetics in studying dynamic processes in neural computation.

The cell-specific activation in living organisms by optogenetics allows us to study plasticity in neural circuits. Fly larvae have been used as a suitable model to study associative olfactory learning and memory. To further increase the efficiency in the larval experiments, a fully automated optogenetic activation device called the Maggot Instructor was developed (Tomasiunaite et al. 2018). This device can train multiple groups of larvae in parallel and establish an olfactory memory. Combination of the fly genetics and optogenetics enables this high-throughput memory study and will give extensive insights on neural mechanisms in humans.

The swift switching properties of optogenetics enable virtual reality stimulation. To analyze the

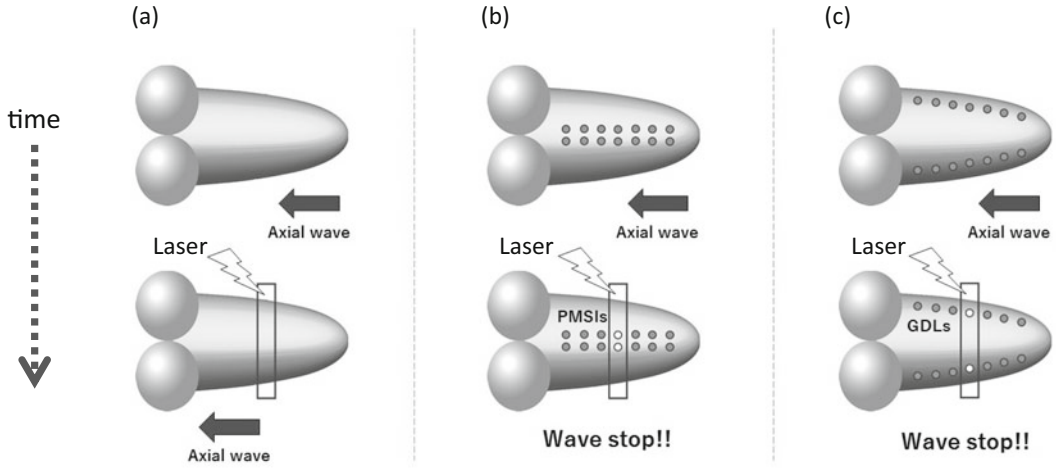


**Fig. 19.6** Local optogenetic stimulation in larval motor circuits. (**a**) The normal propagation of motor output within the CNS. (**b**) Local activation of inhibitory premotor interneuron PMSIs arrests the propagation of the motor outputs. (**c**) Local activation of second-order inhibitory premotor interneurons GDLs arrests the propagation of the motor outputs. Spatiotemporal control of optogenetic manipulation allows us to analyze cellular mechanisms in dynamic propagation of neural activity

dynamic process in feeding behavior of the adult fly, a closed-loop optogenetic device, named optoPAD, was developed (Moreira et al. 2019). Upon detection of feeding behavior, optogenetic stimulus is given to the fly. By hijacking the downstream neurons by optogenetics, the authors can change the gustatory sensation from appetitive to aversive or vice versa. This sophisticated device will dissect spatiotemporal dynamics in animal sensation and adaptation under changing environments.

## 19.5 Conclusion

The history of powerful genetic approaches in *Drosophila* neuroscience has laid a foundation for widespread application of optogenetics in fly research. Comprehensive developments of Gal4 lines, LexA lines, and QF lines, which target specific cells, are ongoing in several institutions. UAS lines, lexAop lines, and QUAS lines that encode optogenetic or Ca imaging probes are also being established in parallel with improvements of the probes. Implementation of complicated but accessible neuronal circuits encoding multiple neural functions including sensory processing and motor controls, combined with established methods for gene expression, make *Drosophila* an invaluable model system for untangling the functions of neural circuits.

**Acknowledgments** We thank Ms. Kasumi Shibahara for help with preparing the figures. This work was supported by MEXT/JSPS KAKENHI grants (22115002, 15H04255, 221S0003 to A.N. and 26430004, 17 K07042, 20 K06908 to H.K.).

## References

Aberle H, Haghighi AP, Fetter RD, McCabe BD, Magalhães TR, Goodman CS (2002) Wishful thinking encodes a BMP type II receptor that regulates synaptic growth in drosophila. Neuron 33(4):545–558. https://doi.org/10.1016/S0896-6273(02)00589-5

Bellen HJ, Levis RW, He Y, Carlson JW, Evans-Holm M, Bae E, Kim J, Metaxakis A, Savakis C, Schulze KL, Hoskins RA, Spradling AC (2011) The drosophila gene disruption project: progress using transposons with distinctive site specificities. Genetics 188 (3):731–743. https://doi.org/10.1534/genetics.111.126995

Bellen HJ, Tong C, Tsuda H (2010) A history lesson for the future. Neuroscience 11(juLy):514–522. https://doi.org/10.1038/nrn2839

Brand AH, Perrimon N (1993) Targeted gene expression as a means of altering cell fates and generating dominant phenotypes. Development 118(2):401–415

Chen M, Obar R, Schroeder C (1991) Multiple forms of dynamin are encoded by shibire, a Drosophila gene involved in endocytosis. Nature 351(6327):583–586. https://www.nature.com/articles/382731a0.pdf

Fushiki A, Zwart MF, Kohsaka H, Fetter RD, Cardona A, Nose A (2016) A circuit mechanism for the propagation of waves of muscle contraction in Drosophila. elife 5:1–23. https://doi.org/10.7554/elife.13253

Gepner R, Skanata MM, Bernat NM, Kaplow M, Gershow M (2015) Computations underlying Drosophila phototaxis, odor-taxis, and multi-sensory integration. elife 4:1–21. https://doi.org/10.7554/eLife.06229

Gratz SJ, Cummings AM, Nguyen JN, Hamm DC, Donohue LK, Harrison MM, Wildonger J, O'connor-Giles KM (2013) Genome engineering of Drosophila with the CRISPR RNA-guided Cas9 nuclease. Genetics 194(4):1029–1035. https://doi.org/10.1534/genetics.113.152710

Grigliatti T, Hall L, Rosenbluth R, Suzuki D (1973) Temperature-sensitive mutations in Drosophila melanogaster. Mol Gen Genomics 120:107–114. https://doi.org/10.1126/science.170.3959.695

Groth AC, Fish M, Nusse R, Calos MP (2004) Construction of transgenic drosophila by using the site-specific integrase from phage φC31. Genetics 166 (4):1775–1782. https://doi.org/10.1534/genetics.166.4.1775

Hamada FN, Rosenzweig M, Kang K, Pulver SR, Ghezzi A, Jegla TJ, Garrity PA (2008) An internal thermal sensor controlling temperature preference in Drosophila. Nature 454(7201):217–220. https://doi.org/10.1038/nature07001

Hernandez-Nunez L, Belina J, Klein M, Si G, Claus L, Carlson JR, Samuel ADT (2015) Reverse-correlation analysis of navigation dynamics in Drosophila larva using optogenetics. elife 4:1–16. https://doi.org/10.7554/eLife.06225

Katow H, Takahashi T, Saito K, Tanimoto H, Kondo S (2019) Tango knock-ins visualize endogenous activity of G protein-coupled receptors in Drosophila. J Neurogenet 33(2):44–51. https://doi.org/10.1080/01677063.2019.1611806

Kitamoto T (2001) Conditional modification of behavior in drosophila by targeted expression of a temperature-sensitive shibire allele in defined neurons. J Neurobiol 47(2):81–92. https://doi.org/10.1002/neu.1018

Klapoetke NC, Murata Y, Kim SS, Pulver SR, Birdsey-Benson A, Cho YK, Morimoto TK, Chuong AS, Carpenter EJ, Tian Z, Wang J, Xie Y, Yan Z, Zhang Y, Chow BY, Surek B, Melkonian M, Jayaraman V, Constantine-Paton M et al (2014) Independent optical excitation of distinct neural populations. Nat Methods 11(3):338–346. https://doi.org/10.1038/nmeth.2836

Kohsaka H, Okusawa S, Itakura Y, Fushiki A, Nose A (2012) Development of larval motor circuits in Drosophila. Dev Growth Differ 54(3):408–419. https://doi.org/10.1111/j.1440-169X.2012.01347.x

Kohsaka H, Takasu E, Morimoto T, Nose A (2014) A group of segmental premotor interneurons regulates the speed of axial locomotion in drosophila larvae. Curr Biol 24(22):2632–2642. https://doi.org/10.1016/j.cub.2014.09.026

Kondo S, Ueda R (2013) Highly improved gene targeting by germline-specific Cas9 expression in Drosophila. Genetics 195(3):715–721. https://doi.org/10.1534/genetics.113.156737

Kosaka T, Ikeda K (1983) Possible temperature-dependent blockage of synaptic vesicle recycling induced by a single gene mutation in drosophila. J Neurobiol 14 (3):207–225. https://doi.org/10.1002/neu.480140305

Lai SL, Lee T (2006) Genetic mosaic with dual binary transcriptional systems in drosophila. Nat Neurosci 9 (5):703–709. https://doi.org/10.1038/nn1681

Levis R, Hazelrigg T, Rubin GM (1985) Effects of genomic position on the expression of transduced copies of the white gene of Drosophila. Science 229 (4713):558–561. https://doi.org/10.1126/science.2992080

Li-Kroeger D, Kanca O, Lee PT, Cowan S, Lee MT, Jaiswal M, Salazar JL, He Y, Zuo Z, Bellen HJ (2018) An expanded toolkit for gene tagging based on MiMIC and scarless CRISPR tagging in Drosophila. elife 7:1–27. https://doi.org/10.7554/eLife.38709

Lin JY, Knutsen PM, Muller A, Kleinfeld D, Tsien RY (2013) ReaChR: a red-shifted variant of channelrhodopsin enables deep transcranial optogenetic excitation. Nat Neurosci 16(10):1499–1508. https://doi.org/10.1038/nn.3502

Markstein M, Pitsouli C, Villalta C, Celniker SE, Perrimon N (2008) Exploiting position effects and the gypsy retrovirus insulator to engineer precisely expressed transgenes. Nat Genet 40(4):476–483. https://doi.org/10.1038/ng.101

Matsunaga T, Fushiki A, Nose A, Kohsaka H (2013) Optogenetic perturbation of neural activity with laser illumination in semi-intact drosophila larvae in motion. J Vis Exp 77:1–5. https://doi.org/10.3791/50513

McKemy DD, Neuhausser WM, Julius D (2002) Identification of a cold receptor reveals a general role for TRP channels in thermosensation. Nature 416(6876):52–58. https://doi.org/10.1038/nature719

Mohr SE, Hu Y, Ewen-Campen B, Housden BE, Viswanatha R, Perrimon N (2016) CRISPR guide RNA design for research applications. FEBS J 283:3232–3238. https://doi.org/10.1111/febs.13777

Moreira JM, Itskov PM, Goldschmidt D, Baltazar C, Steck K, Tastekin I, Walker SJ, Ribeiro C (2019) optoPAD, a closed-loop optogenetics system to study the circuit basis of feeding behaviors. elife 8:1–19. https://doi.org/10.7554/eLife.43924

Peabody NC, Pohl JB, Diao F, Vreede AP, Sandstrom DJ, Wang H, Zelensky PK, White BH (2009) Characterization of the decision network for wing expansion in drosophila using targeted expression of the TRPM8

channel. J Neurosci 29(11):3343–3353. https://doi.org/10.1523/JNEUROSCI.4241-08.2009

Pfeiffer B, Jenett A, Hammonds A, Ngo T, Misra S, Murphy C, Scully A, Carlson J, Wan K, Laverty T, Mungall C, Svirskas R, Kadonaga J, Doe C, Eisen M, Rubin G, Janelia (2008) Tools for neuroanatomy and neurogenetics in drosophila. Proc Natl Acad Sci 105 (28):9715–9720. https://doi.org/10.5694/j.1326-5377.1975.tb111372.x

Pfeiffer BD, Ngo TTB, Hibbard KL, Murphy C, Jenett A, Truman JW, Rubin GM (2010) Refinement of tools for targeted gene expression in drosophila. Genetics 186 (2):735–755. https://doi.org/10.1534/genetics.110.119917

Potter CJ, Tasic B, Russler EV, Liang L, Luo L (2010) The Q system: a repressible binary system for transgene expression, lineage tracing, and mosaic analysis. Cell 141(3):536–548. https://doi.org/10.1016/j.cell.2010.02.025

Pulver SR, Pashkovski SL, Hornstein NJ, Garrity PA, Griffith LC (2009) Temporal dynamics of neuronal activation by channelrhodopsin-2 and TRPA1 determine behavioral output in Drosophila larvae. J Neurophysiol 101(6):3075–3088. https://doi.org/10.1152/jn.00071.2009

Riabinina O, Luginbuhl D, Marr E, Liu S, Wu MN, Luo L, Potter CJ (2015) Improved and expanded Q-system reagents for genetic manipulations. Nat Methods 12 (3):219–222. https://doi.org/10.1038/nmeth.3250

Riabinina O, Vernon SW, Dickson BJ, Baines RA (2019) Split-QF system for fine-tuned transgene expression in Drosophila. Genetics 212(1):53–63. https://doi.org/10.1534/genetics.119.302034

Rubin GM, Spradling AC (1982) Genetic transformation of Drosophila with transposable element vectors. Science 218(4570):348–353. https://doi.org/10.1126/science.6289436

Shearin HK, Dvarishkis AR, Kozeluh CD, Stowers RS (2013) Expansion of the Gateway MultiSite Recombination Cloning Toolkit. PLoS One 8(10):1–14. https://doi.org/10.1371/journal.pone.0077724

Simpson JH, Looger LL (2018) Functional imaging and optogenetics in Drosophila. Genetics 208:1291–1309

Thum A, Knapek S, Rister J, Dierichs-Schmitt E, Heisenberg M, Tanimoto H (2006) Differential potencies of effector genes in adult Drosophila. Comp Gen Pharmacol 498:194–2003. https://doi.org/10.1002/cne

Ting CY, Gu S, Guttikonda S, Lin TY, White BH, Lee CH (2011) Focusing transgene expression in drosophila by coupling Gal4 with a Novel Split-Lex A expression system. Genetics 188(1):229–233. https://doi.org/10.1534/genetics.110.126193

Tomasiunaite U, Widmann A, Thum AS (2018) Maggot instructor: semi-automated analysis of learning and memory in Drosophila larvae. Front Psychol 9:1–18. https://doi.org/10.3389/fpsyg.2018.01010

Van Der Bliek AM, Meyerowrtz EM (1991) Dynamin-like protein encoded by the Drosophila shibire gene associated with vesicular traffic. Nature 351 (6325):411–414. https://doi.org/10.1038/351411a0

Venken KJT, Simpson JH, Bellen HJ (2011) Genetic manipulation of genes and cells in the nervous system of the fruit fly. Neuron 72(2):202–230. https://doi.org/10.1016/j.neuron.2011.09.021

Wiedenheft B, Sternberg SH, Doudna JA (2012) RNA-guided genetic silencing systems in bacteria and archaea. Nature 482(7385):331–338. https://doi.org/10.1038/nature10886

Xiang Y, Yuan Q, Vogt N, Looger LL, Jan LY, Jan YN (2010) Light-avoidance-mediating photoreceptors tile the Drosophila larval body wall. Nature 468 (7326):921–926. https://doi.org/10.1038/nature09576

# Optogenetics in *Caenorhabditis elegans* 20

Yuki Tsukada and Ikue Mori

**Abstract**

With a compact neural circuit consisting of entirely mapped 302 neurons, *Caenorhabditis elegans* plays an important role in the development and application of optogenetics. Optogenetics in *C. elegans* offers the opportunity that drastically changes experimental designs with increasing accessibility for neural activity and various cellular processes, thereby accelerating the studies on the functions of neural circuits and multicellular systems. Combining optogenetics with other approaches such as electrophysiology increases the resolution of elucidation. In particular, technologies like patterned illumination specifically developed in combination with optogenetics provide new tools to interrogate neural functions. In this chapter, we introduce the reasons to use optogenetics in *C. elegans*, and discuss the technical issues raised, especially for *C. elegans* by revisiting our chapter in the first edition of this book. Throughout the chapter, we review early and recent milestone works using optogenetics to investigate a variety of biological systems including neural and behavioral regulation.

**Keywords**

*Caenorhabditis elegans* · *C. elegans* · Neural circuit · Behavioral analysis · Photoelectrophysiology · Tracking · Patterned illumination

## Abbreviations

| | |
|---|---|
| ATR | All-Trans Retinal |
| CALI | Chromophore-Assisted Light Inactivation |
| CGC | *C. elegans* Genetic Center |
| ChR | channelrhodopsin |
| ChRGR | channelrhodopsin green receiver |
| CoLBeRT | Control Locomotion and Behavior in Real Time |
| DMD | Digital micro-mirror devices |
| FRET | Förster resonance energy transfer |
| GECI | genetically encoded calcium indicators |
| GEIs | genetically encoded indicators |
| InSynC | Inhibition of Synapses with CALI |
| LCD | liquid crystal display |
| LED | light-emitting diode |
| NGM | nematode growth medium |
| NIR | near-inferred |
| NpHR | halorhodopsin from *Natronomonas pharaonis* |
| PMT | photomultiplier tube |
| PSC | postsynaptic current |

Y. Tsukada (✉) · I. Mori
Nagoya University, Neuroscience Institute of the Graduate School of Science, Nagoya, Japan
e-mail: tsukada.yuki@nucc.cc.nagoya-u.ac.jp



H. Yawo et al. (eds.), *Optogenetics*, Advances in Experimental Medicine and Biology 1293,
https://doi.org/10.1007/978-981-15-8763-4_20

| | |
|---|---|
| PSP | postsynaptic potential |
| ROS | Reactive Oxygen Species |
| RyRs | ryanodine receptors |
| UV | ultraviolet |
| VGCCs | voltage-gated $Ca^{2+}$ channels |

## 20.1 Introduction: Reasons to Use *Caenorhabditis elegans*

Tiny nematode *Caenorhabditis elegans* (Fig. 20.1) has been used as an important model organism for various kinds of biological research for about 50 years (Brenner 1974). Abundant advantages for scientific studies such as a short life cycle, a transparent body, and the convenience of genetic analysis have been pushing various fields of research, including genomics, cell biology, development, aging, and neuroscience. Optogenetics is actively and naturally introduced into work with *C. elegans* from the beginning, not only because neuroscience is a prominent region in *C. elegans* research but also because the characteristics of *C. elegans* are amenable to optogenetics. In this section, we overview the advantages of *C. elegans* as a platform for optogenetic research, especially for neuroscience.

### 20.1.1 Transparent Body

Optical manipulation requires the conveyance of specific light stimulus to target molecules. The transparent body of *C. elegans* renders it suitable for optogenetic manipulation with the supply of enough light to the opsins or fluorescent proteins in a body. Thus, in vivo analysis with optogenetic tools is convenient in *C. elegans* because of its transparency and tiny body size. These characteristics are even more useful in optogenetics with behavioral assays in the case of freely migrating animals, since noninvasive and of a low power of photostimulus is sufficient to drive optogenetic tools inside the body of target animals without altering their natural behavior.

### 20.1.2 Abundant Promoters

Specific expression of opsins or genetically encoded indicators (GEIs) is a key technology in optogenetics. There are abundant annotated promoters for *C. elegans*, so expression of optogenetic tools in most targeted neurons is promising. Convenient sites exist for searching expression patterns of annotated promoters (Wormbase: http://www.wormbase.org/) or services providing transgenic animals (*C. elegans* Genetic Center (CGC): http://www.cbs.umn.edu/cgc/) and plasmids (plasmid search: http://hokatsu-nou.biochem.s.u-tokyo.ac.jp/index.html [only in Japanese]). Genetic manipulation, such as the generation of transgenic animals, keeping strains as frozen stock, and crossbreeding, is established and the short life cycle helps to generate transgenic lines quickly. Testing a new optogenetic tool related to membrane potential is practical by using myo-3 promoter for body muscles because the apparent phenotype is measurable with muscle contraction (Zhang et al. 2007).

### 20.1.3 The Connectome Has Been Produced

Fully annotated anatomical information for *C. elegans*, including a neural circuit map, is beneficial when planning effective experiments to study neural circuits using optogenetics. Represented by the completely identified cell lineage, details of developmental and anatomical information about *C. elegans* are fully described and available on some web databases (wormatlas: http://www.wormatlas.org/, wormbook: http://www.wormbook.org/). Electron microscopic analysis elucidated whole connections among 302 neurons of the entire neural network in hermaphrodites (White et al. 1986) and 383 neurons in males (Jarrell et al. 2012; Cook et al. 2019). Connectomes including the positions of chemical synapses and gap junctions are mapped out and include the strength of each connection. Furthermore, many visual online

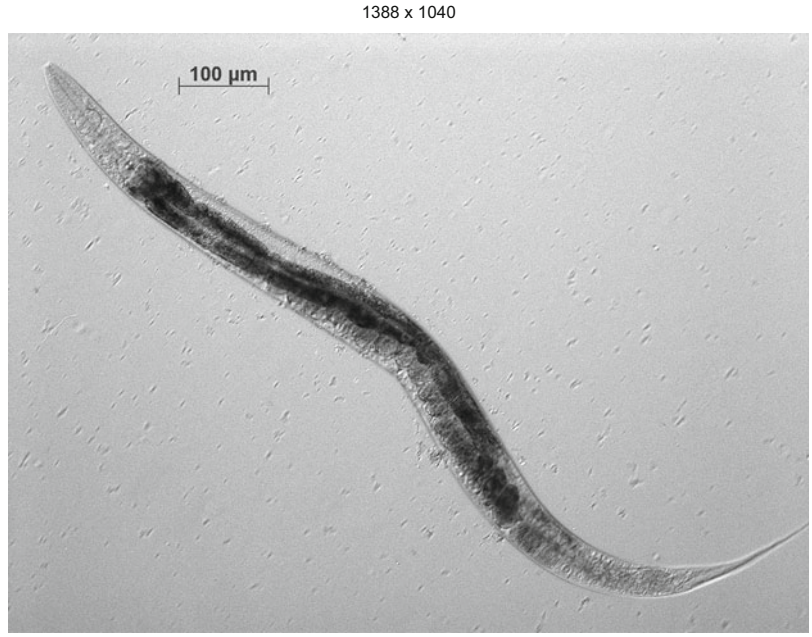


**Fig. 20.1** DIC image of adult hermaphrodite *C. elegans*

databases are available to help in the understanding of circuit properties in the compact neural system of *C. elegans* (*C. elegans* neural net: http://wormweb.org/neuralnet, worm wiring project: http://wormwiring.org/, Database of Synaptic Connectivity of *C. elegans* for computation: http://ims.dse.ibaraki.ac.jp/ccep-tool/).

Based on these annotated neural maps and information about the function of each neuron, one can conduct optogenetics to explore deep into the principles of neural circuits. Noninvasive perturbation and monitoring of each neural activity using opsins and genetically encoded calcium or voltage indicators take advantage of the complete neural map and should shed light on its functional properties.

### 20.1.4 Preserving High-Order Functions with a Compact Neural Circuit

The simple neural circuit of *C. elegans* preserves high-order functions such as sensation of environmental stimuli, learning, and memory that regulate apparent quantifiable behavior like chemotaxis or thermotaxis. Therefore, the essential mechanisms of such functions can be investigated using abundant and powerful tools in *C. elegans* research. In addition to classical genetics or physiology, optogenetic tools offer the ability to dissect neural circuit properties by providing perturbation or monitoring tools for individual neurons.

Because of the above, *C. elegans* is regarded as an effective model organism for the study of neural circuits using optogenetics.

## 20.2 Protocols and Notes

This section describes how to introduce optogenetics into *C. elegans* work. The section includes both worm-specific tips and general topics in optogenetics.

### 20.2.1 Transfection of Optogenetic Genes

To conduct optogenetics with *C. elegans*, one must have transgenic animals. The published strains expressing optogenetic proteins may be available directly from researchers, or the CGC,

which carries out the collection, maintenance, and distribution of *C. elegans* strains. Transgenic animals can be generated via conventional procedures with microinjection to gonads or other methods (Boulin and Hobert 2012). The online protocols, including the creation of transgenic animals, are available on wormbook (wormbook: http://www.wormbook.org/). Although there is no optimized protocol for the generation of transgenic animals expressing optogenetic genes in *C. elegans*, it would be better to have a high enough number of candidates for the transgenic lines because expression of opsin protein itself does not guarantee it will drive neural or cellular functional manipulation. An appropriate quantity of expressed opsins is critical in some cases.

### 20.2.2 Supplying all-Trans Retinal (ATR)

The expressed opsin proteins such as channelrhodopsin (ChR-2) and halorhodopsin from *Natronomonas pharaonis* (NpHR) need a cofactor, all-trans retinal (ATR), to work with photoactivation. Because nematodes do not generate ATR, exogenous supplementation with ATR in the nematode growth medium (NGM) agar or bacterial lawn with ethanol is necessary throughout the development. Note that ATR solution decomposes in about 10 days in room temperature; fresh NGM plates should be used for light-induced neural manipulation. Conversely, NGM plates without ATR serve as a good negative control for transgenic lines as mentioned in the later parts of this chapter.

### 20.2.3 Notes for Illumination

#### 20.2.3.1 Illumination Devices and Light Paths

Illumination devices have a critical role in optogenetic experiments. Nevertheless, a standard epifluorescence microscope system (Fig. 20.2a) is usually sufficient for illuminating opsins expressed in worms. The requirements of an illumination system for opsins are similar to those for fluorescence probes: to effectively provide an appropriate wavelength, strength, and timing of light to an object. Yet, the purposes of both systems differ slightly in that one is needed for visualization of fluorescence and the other for stimulation of opsins. An illumination system for fluorescence probes focuses on collecting fluorescence light, while illumination for opsins mainly focuses on maximizing light power to supply enough energy to drive opsins.

A complex optogenetic illumination system is necessary when simultaneously monitoring and manipulating neural activity. The selection of dichroic mirrors and filters depends on the combination of absorption and emission spectrums of both fluorescence probes and opsins. A prospective example is the use of genetically encoded calcium indicators (GECIs) and ChR2 (Akerboom et al. 2013). Some approaches exist to avoid interventions between the excitation of florescence probes and the stimulation of opsins: dividing the given light stimuli based on wavelength, strength, location, and timing. Avoiding overlapping absorption wavelengths and/or using different light strengths of fluorescence probes and opsins is critical for the simultaneous monitoring and manipulation of neural activity. Specially designed devices for multicolor or multilocation illumination support simultaneous monitoring and manipulation with optogenetics. Spatial and temporal division of photostimulation using patterned illumination is described in later sections.

Another approach independently illuminates opsins without a microscope or epifluorescence system. Kawazoe et al. used a customized high-power light-emitting diode (LED) ring to regulate improved ChR, called channelrhodopsin green receiver (ChRGR) expressed in body wall muscle (Fig. 20.2b) (Kawazoe et al. 2012). An independent illumination device is free of the restrictions of epifluorescence and microscope systems. The application of such an illuminating device for opsins extends the possible experimental variations, for example, conditioning for the population of worms in specific timing with optogenetics. The application of optogenetics is

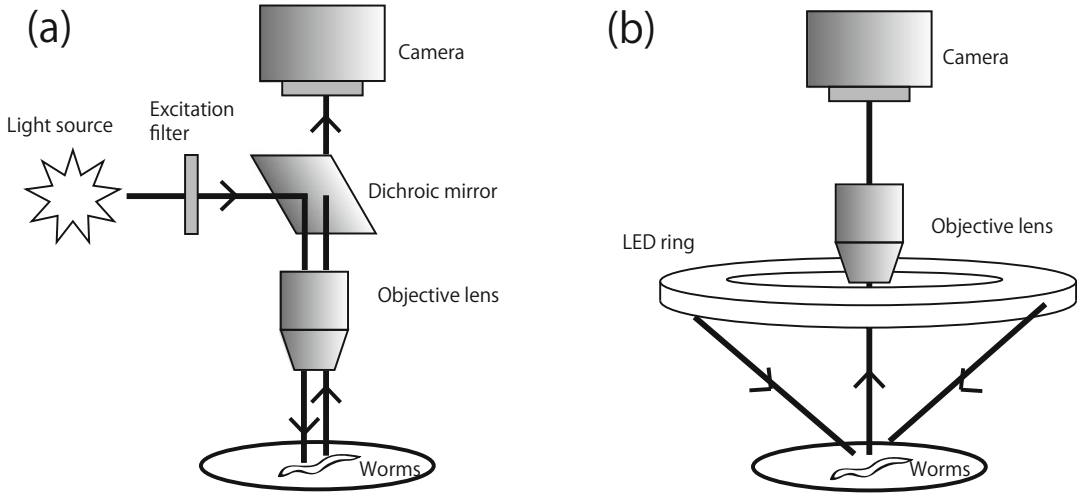


**Fig. 20.2** Examples of optogenetic illumination applicable for *C. elegans*. (**a**) Schematic of a standard epifluorescence illumination system. Light source, excitation filter, and dichroic mirror are especially important for optogenetic photostimulus. Choice of light source or filters is critical for optogenetic manipulation. (**b**) LED ring illumination: An external illumination frees a limitation of epifluorescence illumination or even a limitation of microscope. Of course, combination of epifluorescence and LED ring is feasible

thus expanded in combination with suitable illuminating devices.

#### 20.2.3.2 Avoiding Heat from Illumination

Opsins often need several mW/mm$^2$ of high-power illumination to drive their functions in neurons. The heat caused by the illumination per se will be a problem for dealing with small volumes of *C. elegans*. In particular, it will be critical for behavioral experiments because a known behavior of worms is heat avoidance. Some approaches solve or reduce the effects of heat: shortening the illumination exposure time and/or using an external cooling device such as a metal plate or Peltier device are valuable to consider. To ensure that the heat generated by light stimulation does not induce any artifacts, it is useful to show whether the events could be induced only in the presence of ATR and not in the absence of ATR.

#### 20.2.3.3 Light Toxicity in Short Wave Length

Wild-type *C. elegans* exhibits apparent avoidance behavior to ultraviolet (UV), violet, and blue light. Moreover, continuous UV lighting even causes death to *C. elegans* in 10 min. For these reasons, it is important to discern optogenetic manipulation of neural activity from light-induced responses in *C. elegans*. An eight-transmembrane protein, LITE-1, is identified as a main regulator of the avoidance behavior evoked by light (Edwards et al. 2008) although *C. elegans* lacks a photoreceptive organ or eye. Therefore, lite-1 mutant strains are commonly used for behavioral optogenetics, as the lite-1 mutants reduce light-induced avoidance behavior. It should be noted that there is lite-1-independent light-evoked behavior, and the use of the lite-1 background strain does not assure the complete suppression of light avoidance (Edwards et al. 2008). Also, similar to the heat problem, a negative control experiment without ATR is useful to judge whether observed phenomenon is caused by opsins or not.

#### 20.2.3.4 Regulation of Illumination

The regulation of illumination is one of the most important factors for successful optogenetic experiments. Synchronization of the illumination device and camera is critical for fluorescence imaging, especially in combination with neural

activity manipulation because the light power used in imaging and in optical manipulation is quite different. Also, precise control of illumination timing and power is necessary to find the optimum light stimulation for neural manipulation, and ON/OFF states of illumination timestamps validate the correlation between a given optogenetic manipulation and its outcome. In addition, the millisecond order control of illumination has the potential to improve the efficiency of long-term optogenetic manipulation of neural activity. NpHR shows a decrease in efficiency when continuous light stimulation is used to evoke neural inhibition (Zhang et al. 2007). However, millisecond order pulsed light restores (Zhang et al. 2007) or prevents (Kuhara et al. 2011) this decrease, and thus regulation of illumination increases the performance of opsins.

## 20.3 Applications of Optogenetics in *C. elegans* Research

This section introduces the applications of optogenetics in *C. elegans* studies, and discusses the present situation and prospects.

### 20.3.1 *C. elegans* Optogenetics as Pioneering Works

As mentioned in the beginning of this chapter, *C. elegans* provides many advantageous characteristics to investigate multicellular organisms, and many important pioneering works have emerged with *C. elegans*. The pioneering works with GFP, the whole genome project, and the complete connectome of neural circuits clearly illustrate the significance of *C. elegans* as a model animal serving as a platform for studies on living systems. In terms of the use of opsin proteins for neural manipulation, *C. elegans* was the first multicellular organism in which behavioral regulation by a ChR was investigated (Nagel et al. 2005). This was in the same year as the first neural manipulation using hippocampal cell culture (Boyden et al. 2005).

Nagel et al. expressed a gain-of-function mutant of ChR2, the histidine of which at position 134 was altered to an arginine residue (H134R) in order to have high depolarization by illumination, into the body wall and egg-laying muscle using myo-3 promoter. Transgenic worms with ATR show muscle contraction at 500 ms of illumination, showing that exogenous ATR works on transgenic strains expressing ChR2. With the advantage of many available mutants, Nagel et al. also elucidated that L-type voltage-gated $Ca^{2+}$-channels (VGCCs) and ryanodine receptors (RyRs) regulate this ChR2-mediated muscle contraction. Further, light-evoked expression of ChR2 (H134R) in mechanosensory neurons ALML, ALMR, PLML, PLMR, AVM, and PVM using mec-4 promoter (Fig. 20.3a) induced withdrawal behavior in a similar way to mechanical stimulation.

This study clearly showed temporal- and cell-specific manipulation of neural or muscular activity in a living multicellular organism using optogenetics. This first optogenetic study of *C. elegans* symbolically shows the good compatibility of optogenetics with *C. elegans*. The study thoroughly used the merits of *C. elegans*, such as identifying the neurons required for withdrawal behavior, and promoters that regulate gene expression in the identified neurons and muscles. As shown here, accumulation of genetic, cellular, and behavioral levels of information and technologies enables the effective use of optogenetics.

### 20.3.2 Combination of Electrophysiology and Optogenetics

The complete identification of *C. elegans* neural circuit connectivity is pushing neuroscience research to the new challenge of a functional connectome. The combination of electrophysiology and optogenetics, "photo-electrophysiology," provides a powerful toolbox to elucidate functional relationships among neurons on the complete neural map (Husson et al. 2013). Photo-electrophysiology extends

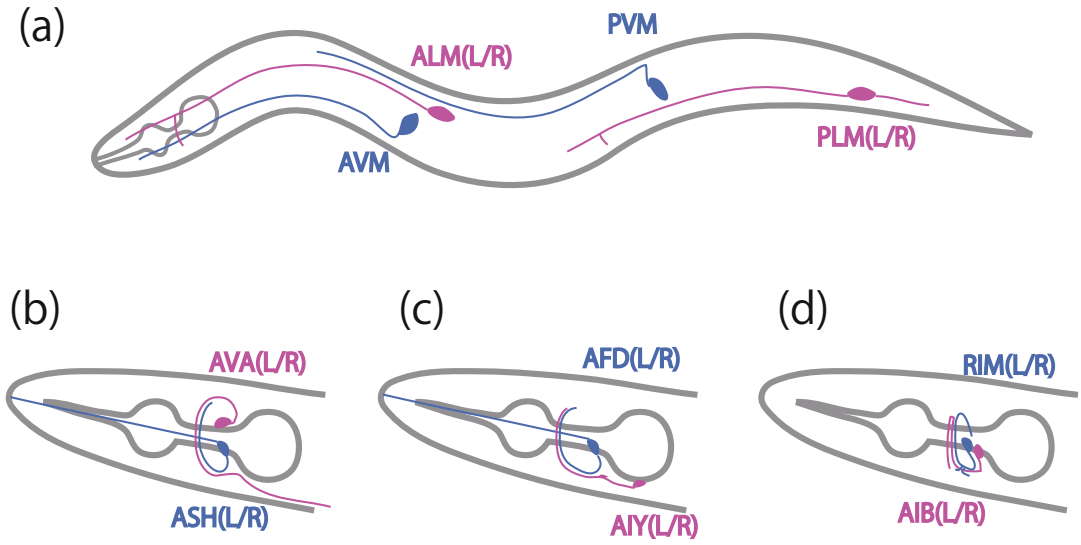


**Fig. 20.3** Positions and projections of neurons. All figures show heads in left. Blue and red colors are used to discriminate closely located individual neurons. (L/R) denotes left and right pair of neurons; however, one is omitted for legibility. (**a**) Mechanosensitive nociceptive neurons labeled by mec-4 promoter regulated expression. (**b**) Nociceptive sensory neuron ASH and interneuron AVA. (**c**) Thermosensory neuron AFD and interneuron AIY. (**d**) Interneuron AIB and motor neuron RIM

electrophysiological dissection by arbitrary selection of a neuron to manipulate activity and thus examine the functional properties between target neural connections.

As an example of the target of photo-electrophysiology, ASH sensory neurons and AVA interneurons are known to work as part of the nociceptive neural network (Fig. 20.3b). The functional relationship between these neurons, i.e., how the sensory signal received at ASH transmits to AVA, was unclear. For this problem, to access multiple neurons for electrophysiology is technically challenging due to the difficulty of surgery with hard cuticle and the small size of the neurons in *C. elegans*.

Lindsay et al. expressed ChR2 in presynaptic ASH neurons using an sra-6 promoter, and recorded postsynaptic AVA neural activity with electrodes during light-evoked ASH activation (Fig. 20.4a). The results showed gradual synaptic transmission between these two types of neurons and a graded probabilistic change of reversal behavior by photostimulation (Lindsay et al. 2011). The combination of electrophysiology, behavioral analysis, and molecular genetics delivered the conclusion that stronger aversive stimulus elicits a greater number of escape responses and depends on a glutamate signal. This approach clearly shows the power of photo-electrophysiology to dissect neural circuit mechanisms.

Graded synaptic transmission is not only found in severe aversive stimulus but also in relatively mild environmental sensory systems, such as thermosensation. A sensory neuron, AFD is known to work as a main thermosensory neuron and is connected to AIY interneurons; both types of neurons are known to play important roles in thermotaxis (Fig. 20.3c) (Mori and Ohshima 1995). Narayan et al. (2011) showed graded transmission between AFD and AIY by expressing ChR2 in AFD using gcy-8 promoter, and they recorded postsynaptic current (PSC) and postsynaptic potential (PSP) in AIY (Fig. 20.4b). AFD thermosensory neurons sense temperature differences at least as small as 0.05 °C (Clark

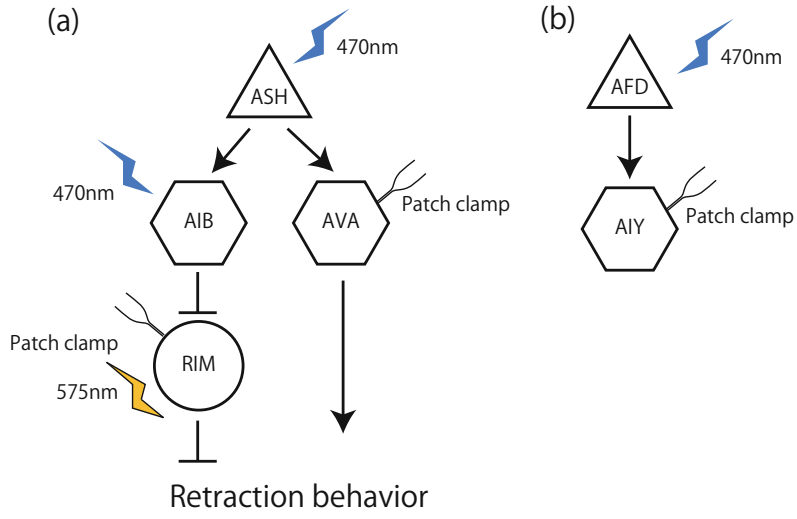


**Fig. 20.4** Neural network diagrams and schemes of the photo-electrophysiologies. Triangles, hexagons, and circles indicate for sensory, inter-, and motor neurons, respectively. (**a**) Photo-electrophysiology for nociceptive neural circuit. Photostimulation of upstream neurons (ASH and AIB) evokes activity of downstream neurons (AVA and RIM). Piggot et al. quantified reversal behavior when they stimulated RIM with photostimulation. (**b**) Photo-electrophysiology for thermosensory neural circuit. The synaptic connection between AFD sensory neuron and AIY interneuron was measured by stimulating AFD with light, and conducting whole cell patch clamp with AIY

et al. 2006), and such faint signals received by AFD might be amplified in AFD. The graded signal transmission between AFD and AIY implies that the amplified signal in AFD is scaled in a quantitative manner. The graded transmissions in two different sensory circuits suggest the general scaling mechanism between sensory and inter neurons for information integration of different sensory inputs.

Photo-electrophysiology is also applicable to the output of neural information processing such as motor circuits. A backward regulatory neural circuit consists of AIB interneuron and RIM motor neuron under several sensory neurons (Fig. 20.3d). Piggot et al. expressed ChR2 and NpHR in AIB and RIM, respectively; they uncovered an inhibitory pathway between AIB and RIM using photo-manipulation of these neurons with tracking and photo-electrophysiology (Fig. 20.4a). This study also used a tracking system to analyze free behavioral animals as described in the next section.

### 20.3.3 Combination with Tracking System

The application of noninvasive manipulation of neural activity expands to studies of behavioral regulation when it is combined with a tracking microscope. The transparent body and slow migration speed of *C. elegans* are suitable characteristics for such experiments. However, microscopes are required to be able to effectively observe or illuminate the small body of *C. elegans*. Then, the tracking system is required to keep a target animal within a microscopic field during neural manipulation and observation. Accordingly, several laboratories have developed various tracking systems for *C. elegans* for dissecting neural circuits responsible for behavioral regulation (Faumont et al. 2011; Kuhara et al. 2011; Piggott et al. 2011; Kocabas et al. 2012).

Thermotaxis of *C. elegans* is an intriguing behavior that includes the mechanism of learning

and memory: worms store cultivated temperature when they were previously cultivated for a few hours at a certain temperature with plenty of food, and these conditioned worms move to the cultivated temperature when they are on a thermal gradient without food. Although the neural circuit related to the thermotaxis is already identified (Mori and Ohshima 1995), how the information processing occurs inside the thermotaxis neural circuit is still unknown. Kuhara et al. attenuated the activity of the AFD thermosensory neuron by expressing NpHR in AFD, and then showed behavioral change that depended on the strength of AFD neuronal activity (Kuhara et al. 2011). Using the automated tracking system with feedback regulation of a motorized microscopic stage, Kuhara et al. analyzed the tracks of freely migrating *C. elegans* on an agar plate for 1 h (Fig. 20.5). This system enables the recording of behavioral status during free movement, and also allows for long periods of photostimulation. The records of motorized-stage regulation provide traces of migrating worms as behavioral data. This approach is generally applicable to any other behavioral analysis.

Faumont et al. adopted a four-quadrant photomultiplier tube (PMT) as a tracking system instead of cameras (Faumont et al. 2011). PMT reduces exposure, data reading, and image processing time, thereby enabling a tracking system to quickly track a moving worm under high-magnification objective lens. The tracking system captures fluorescence signals of a target neuron in a freely moving *C. elegans* using 63× objective lens. Photo-manipulation of ASH neuron with this tracking system showed imitating osmotic avoidance behavior caused by ASH activity. In addition, the tracking system enabled the quantification of the activities of reverse command neuron AVA and forward command neuron AVB by expressing ratiometric calcium sensors (TN-XL or YC3.60) in AVA and AVB. The combination of tracking systems and optogenetics should expand the ability of the methodology, and shed light on the neural mechanism related to behavioral regulation.

### 20.3.4 Calcium Imaging and Neural Manipulation

In the same way as optogenetic neural activity manipulation, GECIs are impacting on neuroscience studies. Förster resonance energy transfer (FRET)-based calcium sensors called cameleons (Miyawaki et al. 1997) and circular permutated-based GCaMPs (Nakai et al. 2001) are remarkable examples of genetically encoded neural activity sensors that are popular in neuroscience. *C. elegans* is compatible with these fluorescent probes as discussed in the beginning of this chapter. Because calcium imaging and optogenetic operation realize complete noninvasive monitoring and manipulation of neural activity, a method of combining these approaches is valuable for behavioral neuroscience. Moreover, such noninvasive approaches expand the targets to freely moving animals in combination with the tracking system described above. Although these approaches have technological or engineering difficulties that remain unsolved, they are unveiling functional meanings of neural activities.

A tracking and calcium imaging approach obtains quantitative data, and thus expands the scope of analysis to continuous phenomena. Kocabas et al. focused on the mechanism of navigation during chemotaxis, and found that AIY interneurons control gradual curves in navigation (Kocabas et al. 2012). They expressed ChR2 and GCaMP3 in AIY neurons, and confirmed the increase of AIY activity using photostimulation with calcium imaging. They then manipulated navigation behavior by activating AIY with ChR2. Although the experiments did not show the relationship between the intact activity of AIY and behavior, the results did show that the manipulated activity of AIY neurons is sufficient to navigate migrating *C. elegans*.

Representing a good combination of calcium imaging and optogenetic manipulation, some of the studies discussed in this chapter have also used calcium imaging with optogenetic manipulation (Faumont et al. 2011; Piggott et al. 2011).

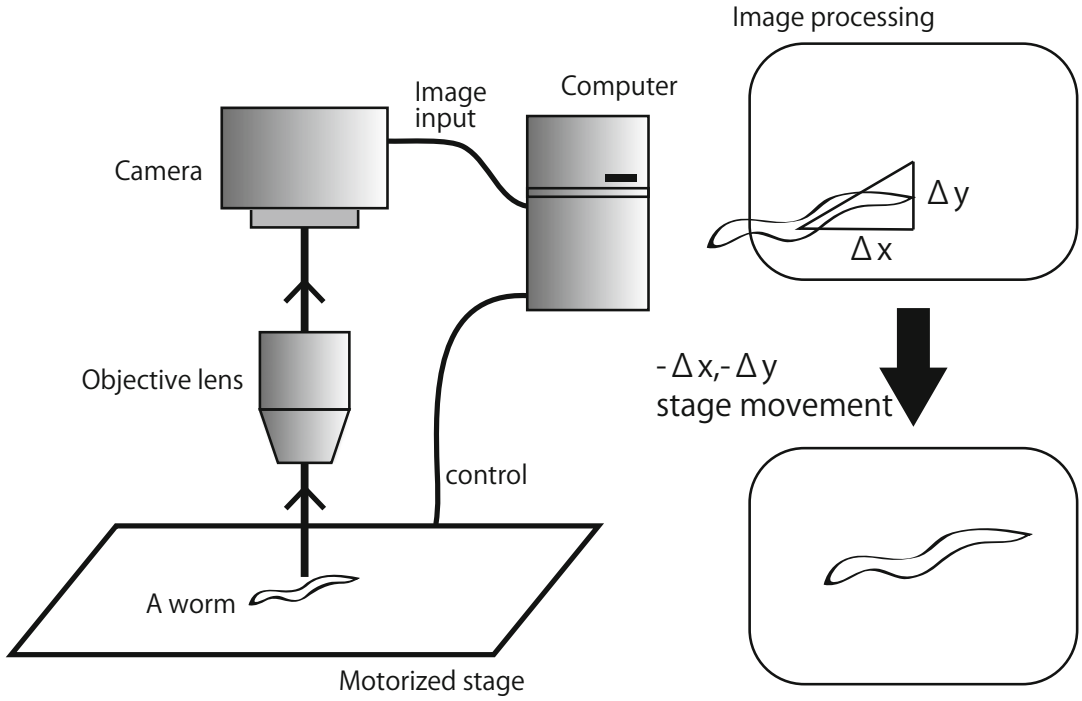


**Fig. 20.5** An example of tracking system. Real-time feedback regulation using camera and motorized stage enable to track individual *C. elegans*. Coordinates of the center of mass for binary image of worm body or a target neuron is convenient variable to keep the tracking animal in microscopic field. A record of stage regulation denotes a trace of migrating history of tracking worm. Combination with a movie acquired by camera input help to further behavioral analysis

Since the combination of multiple technologies often provides solutions to overcome technical difficulties, the multi-technological approach serves as a driving force to elucidate remaining problems in modern neuroscience. Fluorescence imaging and optogenetic manipulation offer combinatorial components to monitor or manipulate neural activity by providing several options for probes and opsins that have different characteristics (Yizhar et al. 2011). The flourishing development of new probes and opsins should continue to expand their abilities.

### 20.3.5 Patterned Illumination Devices

Patterned illumination expands the application of optogenetics by illuminating multiple objects with different wavelengths in a specific spatio-temporal pattern. A hurdle to making pattern illumination systems has lowered because the popularization of digital projectors increased the performance of the components and decreased its cost. Digital micro-mirror devices (DMDs) and liquid crystal display (LCDs) were used as a pattern illumination device for optogenetics (Guo et al. 2009; Leifer et al. 2011; Stirman et al. 2011). These devices enabled the simultaneous illumination of multiple neurons or muscles of spatially different positions, and thus the system complements the specificity of optogenetic manipulation beyond promoter-dependent regulation of gene localization.

Leifer et al. developed a system called Control Locomotion and Behavior in Real Time (CoLBeRT), which performs patterned light stimulus to a freely migrating worm with DMD (Leifer et al. 2011). The worms expressing ChR2 and NpHR in body wall muscles, motor neurons, and mechanosensory neurons were used

to validate the performance of the CoLBeRT system. Patterned illumination discriminates opsins in different locations and, consequently, enables to interrogate specific cells. Similarly to that described above, they used mec-4 promoter to express ChR2 in ALM (L/R), PLM (L/R), AVM, and PVM neurons. Patterned illumination distinguished different roles in these neurons by selectively activating opsins in each neuron: PLM promotes forward movement, AVM and ALM promotes backward movement, and AVM and ALM adapt to stimulus as shown previously (Chalfie et al. 1985).

Stirman et al. used an LCD to provide patterned illumination in a relatively easy and less expensive manner (Stirman et al. 2011). Similar to the study with CoLBeRT, mec-4 promoter-driven opsin protein expression was dissected via patterned illumination. A mechanism of integration of localized neural input for mechanosensory avoidance behavior was thus examined. Moreover, Stirman et al. established the simultaneous activation of different opsins such as ChR2 and Mac, which have different excitation peaks, with simultaneous illumination of different wavelengths at different places. This study provides a good example of optogenetic neural manipulation in multiple colors and positions. Thus, the combination of optogenetics and these light manipulation technologies promotes studies for a functional connectome.

## 20.4 Expansion of Optogenetic Manipulation

### 20.4.1 Expansion of Spectrum

Expanding the spectrum of optogenetic actuators is an important progress of optogenetic tools. The light absorption peak of the commonly used channel rhodopsin (ChR2) is 470 nm, and phototoxicity of the short wavelength of light hampers proper investigation for living cells. As mentioned in Sect. 20.2.3.3, phototoxicity also affects the behavior. To avoid the phototoxicity to cellular mechanisms and behavior, longer wavelength versions of opsins are valuable. Diligent works for expanding the color palette of optogenetic tools are producing useful outcomes.

Redshifted channel rhodopsin called Chrimson is a prominent product which enables to reduce phototoxicity and to conduct multiple executions of optogenetic regulation of neural activity (Klapoetke et al. 2014; Schild and Glauser 2015). Even more, Ao et al. designed and synthesized nanoparticles to upconvert near-inferred (NIR) light to green light that is compatible to activate Chrimson so that NIR light can be used to regulate neural activity through Chrimson (Ao et al. 2019). Decreasing phototoxicity reduces the risk of artifacts derived from light stimuli. Multicolor regulation of neural activity allows a complex pattern of photostimulus for multiple targets. Thus, these expansions are contributing to uncovering the mechanisms of neural circuits.

### 20.4.2 Expansion of Function

In addition to neuronal activity, various optogenetic tools allow one to target a variety of intracellular mechanisms. Photoreceptors such as opsins act as membrane-bound pumps and channels that consequently regulate neural activity. Same as the opsins, different types of photoactivated molecules enable to target specific proteins or molecules that consequently regulate intracellular processes. Genetically encoded reactive oxygen species (ROS) generators are valuable optogenetic tools that provide different approaches from opsins. Since ROS plays diverse roles in cells and organisms such as damaging, changing enzyme activity, gene transcription, metabolism, and signal transduction (Wojtovich and Foster 2014), photosensitive ROS generators enable to regulate those intracellular processes by light.

Cell ablation is a key methodology to understand multicellular systems such as neural circuits. Instead of laser surgery, optogenetic ROS generation provides a highly selective ablation system by genetic tools. Moreover, optimized photosensitive ROS generators can scale in application from single neurons to entire

tissues in single or population of animals. KillerRed and miniSOG are both prevalent photosensitive ROS generators. A dimeric red fluorescent protein KillerRed is a photosensitizer that generates superoxide by 540–585 nm light excitation. Williams et al. demonstrated that KillerRed sufficiently evokes the ablation of various types of neurons and subcellular inactivation with light stimulation (Williams et al. 2013). Moreover, they showed that *sod-1*, a mutant of a superoxide detoxifying enzyme, improved the efficiency of KillerRed-derived neuronal death. The result of *sod-1* mutant confirmed the mechanism of KillerRed that causes ROS damage, and thus provides an efficient protocol for cell ablation using the ROS generator. Another type of ROS generator, miniSOG consists of 106 amino acid, and it generates singlet oxygen by light stimulation (Xu and Chisholm 2016). Although miniSOG requires a flavin mononucleotide cofactor, it is endogenously present in cells and therefore an exogenous supplement of the cofactor is not necessary.

Cell ablation is not the only application of ROS generators, and chromophore-assisted light inactivation (CALI) is a powerful approach to probe a function of a specific compartment or protein. Both KillerRed and miniSOG are used for CALI, and particularly inhibition of synapses with CALI (InSynC) is available with miniSOG (Lin et al. 2013; Liu et al. 2018). InSynC directly causes a perturbation of synaptic vesicles in a specific neuron by making a fusion protein of miniSOG and a synaptic vesicular protein such as synaptobrevin. Inhibition of specific synapses by InSynC induced stereotyped behavior (Lin et al. 2013). Besides, targeted illumination of a specific compartment of an interneuron caused distinct behavior (Liu et al. 2018). Thus, optogenetic inhibition and ablation tools provide valuable methodologies the same as opsins.

### 20.4.3 Expansion of Application

Optogenetics flourish not only in the neuroscience but also burgeon into various fields in biology. A variety of optogenetic actuators allow one to approach various types of cellular mechanisms (Rost et al. 2017). One of the prominent examples is a study for mitotic spindle positioning (Fielmich et al. 2018). A lot of *C. elegans* studies contributed to understanding the mechanisms of cell division, and key molecular players of regulating mitotic spindle are identified by molecular genetics. To understand the dynamic regulation of identified molecules, optogenetic tools are indispensable. Fielmich et al. took an approach to regulate the localization of mitotic spindle-related proteins by using ePDZ-LOV system. In this system, blue light rapidly induces the recruitment of ePDZ fused protein to LOV components so that one can study the outcome of the interaction between two proteins. The results of ePDZ-LOV system showed LIN-5 is intrinsically required for dynein-dependent pulling force generation. These results exhibited how optogenetic regulation of molecular localization helps to understand an important question of a dynamic process in cell biology.

As a good tool for genetics, Noma and Jin established optogenetic mutagenesis by making a fusion protein of miniSOG and histone H3.3 variant, *C. elegans* HIS-72 (Noma and Jin 2015). This approach provides a toxic chemical-free protocol for mutagenesis, and light-induced mutagenesis produces a wide variety of DNA changes such as single-nucleotide variations, deletions, and insertion of extrachromosomal transgenes. Since mutagenesis is a fundamental methodology for laboratory genetics, this unique protocol allows one for a reliable option to progress genetic approach.

## 20.5 Conclusion

Studies using the convenient characteristics of *C. elegans* have greatly contributed to the establishment of optogenetics. At the same time, optogenetics has become one of the general tools in *C. elegans* neuroscience (Fang-Yen et al. 2015; Kimura and Busch 2017; Fischer et al. 2018). Synergistic effects accelerate the development of upcoming new technologies and consolidate the basis of optogenetic

methodologies (Yu et al. 2019). These methodological progresses continue to support pioneering research in neural circuits and behavioral regulation.

**Acknowledgments** This work was supported by Japan Society for the Promotion of Science (JSPS) Grant-in-Aid for Scientific Research Grant Numbers 26560459 and 19H05644.

## References

Akerboom J, Carreras Calderón N, Tian L, Wabnig S, Prigge M, Tolö J, Gordus A, Orger MB, Severi KE, Macklin JJ, Patel R, Pulver SR, Wardill TJ, Fischer E, Schüler C, Chen T-W, Sarkisyan KS, Marvin JS, Bargmann CI, Kim DS, Kügler S, Lagnado L, Hegemann P, Gottschalk A, Schreiter ER, Looger LL (2013) Genetically encoded calcium indicators for multi-color neural activity imaging and combination with optogenetics. Front Mol Neurosci 6:2. https://doi.org/10.3389/fnmol.2013.00002

Ao Y, Zeng K, Yu B, Miao Y, Hung W, Yu Z, Xue Y, Tan TTY, Xu T, Zhen M, Yang X, Zhang Y, Gao S (2019) An upconversion nanoparticle enables near infrared-optogenetic manipulation of the Caenorhabditis elegans motor circuit. ACS Nano 13:3373–3386. https://doi.org/10.1021/acsnano.8b09270

Boulin T, Hobert O (2012) From genes to function: the C. elegans genetic toolbox. WIREs Dev Biol 1:114–137. https://doi.org/10.1002/wdev.1.FROM

Boyden ES, Zhang F, Bamberg E, Nagel G, Deisseroth K (2005) Millisecond-timescale, genetically targeted optical control of neural activity. Nat Neurosci 8:1263–1268. https://doi.org/10.1038/nn1525

Brenner S (1974) The genetics of Caenorhabditis elegans. Genetics 77:71–94

Chalfie M, Sulston JE, White JG, Southgate E, Thomson JN, Brenner S (1985) The neural circuit for touch sensitivity in Caenorhabditis elegans. J Neurosci 5:956–964

Clark DA, Biron D, Sengupta P, Samuel ADT (2006) The AFD sensory neurons encode multiple functions underlying thermotactic behavior in Caenorhabditis elegans. J Neurosci 26:7444–7451. https://doi.org/10.1523/JNEUROSCI.1137-06.2006

Cook SJ, Jarrell TA, Brittin CA, Wang Y, Bloniarz AE, Yakovlev MA, Nguyen KCQ, Tang LTH, Bayer EA, Duerr JS, Bülow HE, Hobert O, Hall DH, Emmons SW (2019) Whole-animal connectomes of both Caenorhabditis elegans sexes. Nature 571:63–71. https://doi.org/10.1038/s41586-019-1352-7

Edwards SL, Charlie NK, Milfort MC, Brown BS, Gravlin CN, Knecht JE, Miller KG (2008) A novel molecular solution for ultraviolet light detection in Caenorhabditis elegans. PLoS Biol 6. https://doi.org/10.1371/journal.pbio.0060198

Fang-Yen C, Alkema MJ, Samuel ADT (2015) Illuminating neural circuits and behaviour in caenorhabditis elegans with optogenetics. Philos Trans R Soc B Biol Sci 370. https://doi.org/10.1098/rstb.2014.0212

Faumont S, Rondeau G, Thiele TR, Lawton KJ, McCormick KE, Sottile M, Griesbeck O, Heckscher ES, Roberts WM, Doe CQ, Lockery SR (2011) An image-free opto-mechanical system for creating virtual environments and imaging neuronal activity in freely moving Caenorhabditis elegans. PLoS One 6:e24666. https://doi.org/10.1371/journal.pone.0024666

Fielmich LE, Schmidt R, Dickinson DJ, Goldstein B, Akhmanova A, Van Den Heuvel S (2018) Optogenetic dissection of mitotic spindle positioning in vivo. elife 7:1–31. https://doi.org/10.7554/eLife.38198

Fischer KE, Vladis NA, Busch KE (2018) Optogenetic applications in the nematode Caenorhabditis elegans. NeuroMethods 133:89–116. https://doi.org/10.1007/978-1-4939-7417-7_6

Guo Z, Hart AC, Ramanathan S (2009) Optical interrogation of neural circuits in Caenorhabditis elegans. Nat Methods 6:891–896. https://doi.org/10.1038/nmeth.1397

Husson SJ, Gottschalk A, Leifer AM (2013) Optogenetic manipulation of neural activity in C. elegans: from synapse to circuits and behaviour. Biol Cell 105:235–250. https://doi.org/10.1111/boc.201200069

Jarrell TA, Wang Y, Bloniarz AE, Brittin CA, Xu M, Thomson JN, Albertson DG, Hall DH, Emmons SW (2012) The connectome of a decision-making neural network. Science (New York, NY) 337:437–444. https://doi.org/10.1126/science.1221762

Kawazoe Y, Yawo H, Kimura KD (2012) A simple optogenetic system for behavioral analysis of freely moving small animals. Neurosci Res 75:65–68. https://doi.org/10.1016/j.neures.2012.04.011

Kimura KD, Busch KE (2017) From connectome to function: using optogenetics to shed light on the Caenorhabditis elegans nervous system. In: Optogenetics. Cambridge University Press, pp 37–54

Klapoetke NC, Murata Y, Kim SS, Pulver SR, Birdsey-Benson A, Cho YK, Morimoto TK, Chuong AS, Carpenter EJ, Tian Z, Wang J, Xie Y, Yan Z, Zhang Y, Chow BY, Surek B, Melkonian M, Jayaraman V, Constantine-Paton M, Wong GK-S, Boyden ES (2014) Independent optical excitation of distinct neural populations. Nat Methods 11:338–346. https://doi.org/10.1038/nmeth.2836

Kocabas A, Shen C-H, Guo Z, Ramanathan S (2012) Controlling interneuron activity in Caenorhabditis elegans to evoke chemotactic behaviour. Nature:3–8. https://doi.org/10.1038/nature11431

Kuhara A, Ohnishi N, Shimowada T, Mori I (2011) Neural coding in a single sensory neuron controlling opposite seeking behaviours in Caenorhabditis elegans. Nat Commun 2:355. https://doi.org/10.1038/ncomms1352

Leifer AM, Fang-Yen C, Gershow M, Alkema MJ, Samuel ADT (2011) Optogenetic manipulation of neural activity in freely moving Caenorhabditis elegans. Nat Methods 8:147–152. https://doi.org/10.1038/nmeth.1554

Lin J, Sann S, Zhou K, Nabavi S, Proulx C, Malinow R, Jin Y, Tsien R (2013) Optogenetic inhibition of synaptic release with chromophore-assisted light inactivation (CALI). Neuron 79:241–253. https://doi.org/10.1016/j.neuron.2013.05.022

Lindsay TH, Thiele TR, Lockery SR (2011) Optogenetic analysis of synaptic transmission in the central nervous system of the nematode Caenorhabditis elegans. Nat Commun 2:306. https://doi.org/10.1038/ncomms1304

Liu H, Yang W, Wu T, Duan F, Soucy E, Jin X, Zhang Y (2018) Cholinergic sensorimotor integration regulates olfactory steering. Neuron:1–16. https://doi.org/10.1016/j.neuron.2017.12.003

Miyawaki A, Llopis J, Heim R, Mccaffery JM, Adams JA, Ikurak M, Tsien RY (1997) Fluorescent indicators for Ca 2 + based on green fluorescent proteins and calmodulin. Nature 388:882–887

Mori I, Ohshima Y (1995) Neural regulation of thermotaxis in Caenorhabditis elegans. Nature 376:344–348

Narayan AL, Sternberg G, Paul W (2011) Transfer characteristics of a thermosensory synapse in Caenorhabditis elegans. Proc Natl Acad Sci U S A 108(23):9667–9672

Nagel G, Brauner M, Liewald JF, Adeishvili N, Bamberg E, Gottschalk A (2005) Light activation of channelrhodopsin-2 in excitable cells of Caenorhabditis elegans triggers rapid behavioral responses. Curr Biol 15:2279–2284. https://doi.org/10.1016/j.cub.2005.11.032

Nakai J, Ohkura M, Imoto K (2001) A high signal-to-noise Ca(2+) probe composed of a single green fluorescent protein. Nat Biotechnol 19:137–141. https://doi.org/10.1038/84397

Noma K, Jin Y (2015) Optogenetic mutagenesis in Caenorhabditis elegans. Nat Commun 6. https://doi.org/10.1038/ncomms9868

Piggott BJ, Liu J, Feng Z, Wescott SA, Xu XZS (2011) The neural circuits and synaptic mechanisms underlying motor initiation in C. elegans. Cell 147:922–933. https://doi.org/10.1016/j.cell.2011.08.053

Rost BR, Schneider-warme F, Schmitz D, Hegemann P (2017) Primer optogenetic tools for subcellular applications in neuroscience. Neuron 96:572–603. https://doi.org/10.1016/j.neuron.2017.09.047

Schild LC, Glauser DA (2015) Dual color neural activation and behavior control with chrimson and CoChR in Caenorhabditis elegans. Genetics 200:1029–1034. https://doi.org/10.1534/genetics.115.177956

Stirman JN, Crane MM, Husson SJ, Wabnig S, Schultheis C, Gottschalk A, Lu H (2011) Real-time multimodal optical control of neurons and muscles in freely behaving Caenorhabditis elegans. Nat Methods 8:153–158. https://doi.org/10.1038/nmeth.1555

White JG, Southgate E, Thomson JN, Brenner S (1986) The structure of the nervous system of the nematode Caenorhabditis elegans. Philos Trans R Soc Lond Ser B Biol Sci 314:1–340

Williams DC, ElBejjani R, Ramirez PM, Coakley S, Kim SA, Lee H, Wen Q, Samuel A, Lu H, Hilliard MA, Hammarlund M (2013) Rapid and permanent neuronal inactivation InVivo via subcellular generation of reactive oxygen with the use of KillerRed. Cell Rep 5:553–563. https://doi.org/10.1016/j.celrep.2013.09.023

Wojtovich AP, Foster TH (2014) Optogenetic control of ROS production. Redox Biol 2:368–376. https://doi.org/10.1016/j.redox.2014.01.019

Xu S, Chisholm AD (2016) Highly efficient optogenetic cell ablation in C. Elegans using membrane-targeted miniSOG. Sci Rep 6:1–13. https://doi.org/10.1038/srep21271

Yizhar O, Fenno LE, Davidson TJ, Mogri M, Deisseroth K (2011) Primer optogenetics in neural systems. Neuron 71:9–34. https://doi.org/10.1016/j.neuron.2011.06.004

Yu AJ, McDiarmid TA, Ardiel EL, Rankin CH (2019) High-throughput analysis of behavior under the control of optogenetics in Caenorhabditis elegans. Curr Protoc Neurosci 86:1–17. https://doi.org/10.1002/cpns.57

Zhang F, Wang L-P, Brauner M, Liewald JF, Kay K, Watzke N, Wood PG, Bamberg E, Nagel G, Gottschalk A, Deisseroth K (2007) Multimodal fast optical interrogation of neural circuitry. Nature 446:633–639. https://doi.org/10.1038/nature05744

# Optogenetics on Zebrafish

# 21

Wataru Shoji

**Abstract**

Optogenetics brought noninvasive neural activation in living organisms. Transparent zebrafish larva is one of the suitable animal models that receive the full benefit of this technique and provides behavioral studies based on intact individual nervous system. In this chapter, we describe methods to introduce optogenetic genes into zebrafish, and desirable apparatus for photostimulation and motion analysis with an example from our studies.

**Keywords**

Zebrafish · Optogenetics · Behavior · Tol2 · Knock-in

## Abbreviations

| | |
|---|---|
| CiD neuron | Circumferential ipsilateral descending neuron |
| CoPA neuron | Commissural primary ascending neuron |
| DLF | Dorsal longitudinal fascicule |
| dpf | Days postfertilization |
| IC neuron | Ipsilateral projecting neuron |
| PTU | Phenylthiourea |
| RB neuron | Rohon-Beard neuron |
| RS neuron | Reticulospinal neuron |

## 21.1 Transparent Organism that Conserves Vertebrate Neural Architecture

Zebrafish larva grows 1–4 mm body length between one and five dpf (days postfertilization). Its neural circuits are evolutionally conserved among vertebrates and are optically imaged under microscopes with a living whole-mount preparation. The larva is perfectly transparent at first dpf, then gradually blocked by pigment cells after hatching. PTU (phenylthiourea) is commonly used to decrease pigmentation by inhibiting tyrosinase that catalyzes melanin production. Pigmentation mutants are another excellent solution for keeping larval transparency. Casper is a viable double mutant for nacre ($mitfa^{-/-}$) lacking melanophores and roy ($mpv17^{-/-}$) lacking iridophores (White et al. 2008), which is widely used as a background strain for optogenetic and imaging analysis. The mutant fish are available from International bioresource association; Zebrafish International Resource Center (https://zebrafish.org/home/guide.php).

W. Shoji (✉)
Frontier Research Institute for Interdisciplinary Sciences, Tohoku University, Sendai, Japan
e-mail: wshoji@idac.tohoku.ac.jp



H. Yawo et al. (eds.), *Optogenetics*, Advances in Experimental Medicine and Biology 1293,
https://doi.org/10.1007/978-981-15-8763-4_21

## 21.2 Genetic Manipulation for Optogenetic Tools

To manipulate gene expression, RNA/DNA microinjection into fertilized eggs is an easy and reliable method (Fig. 21.1). Ubiquitous expression is obtained by injecting arbitrary mRNA, but it decreases by dilution and degradation in growing embryos. When DNA expression construct (cDNA linked with expression promoter) is injected, chromosomal integration of the exogenous DNA occurs randomly at low frequency. Then mosaic expression in small number of cells lasts throughout life. Although prescreening of desirable expression is required, it is useful to restrict optogenetic activation in preferred cells. Various tissue-specific and neuron subtype promoters were isolated and are currently available to increase probability of optogenetic gene expression.

To establish stable transgenic strains, adult fish raised from DNA-injected eggs are screened to find germline transmitting founders. Tol2-based transposon vector was developed to enhance DNA integration to chromosome (Fig. 21.2). On average, 50% of DNA-injected fish becomes germline transmitting founders, which produce F1 transgenic offspring at 3–100% frequency (Kawakami 2007). This method enabled researchers to raise transgenic zebrafish with less effort, so facilitated to create useful tools to manipulate gene expression. Tol2-incorporated Gateway vector system is one of such tools which allows rapid subcloning of DNA expression constructs (Villefranc et al. 2007). GAL4 library is a powerful tool, which is a pool of zebrafish insertion strains with a yeast gene encoding transcription activator GAL4. GAL4 expression pattern which depends on inserted genome position is determined and listed in each strain, so researchers get desirable driver strains and cross with effector strains which carry UAS promoter with the genes of interest (e.g., optogenetic channelrhodopsin or halorhodopsin).

CRISPR/Cas9 system is being standard method for gene disruption (Hwang et al. 2013; Li et al. 2016) and is also available for inserting exogenous DNA at desirable genomic position (Kimura et al. 2014). Methods using CRISPR/Cas9 are currently updated in efficiency and accuracy, so it would be widely applicable to introducing the genes of interest under an endogenous promoter appropriate for optogenetic studies.

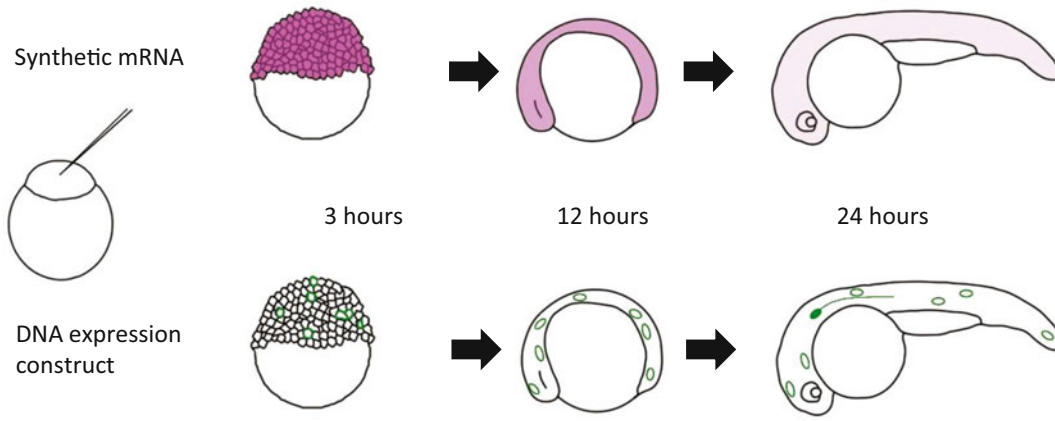


**Fig. 21.1** Basic expression study by RNA/DNA microinjection into fertilized eggs. Upper: Injected mRNA is rapidly translated to express protein. Its expression is ubiquitous and high level, but decreases by dilution and degradation in growing embryos. Lower: Injected DNA is integrated into chromosomes at low frequency, and its mosaic expression lasts throughout life in small number of cells

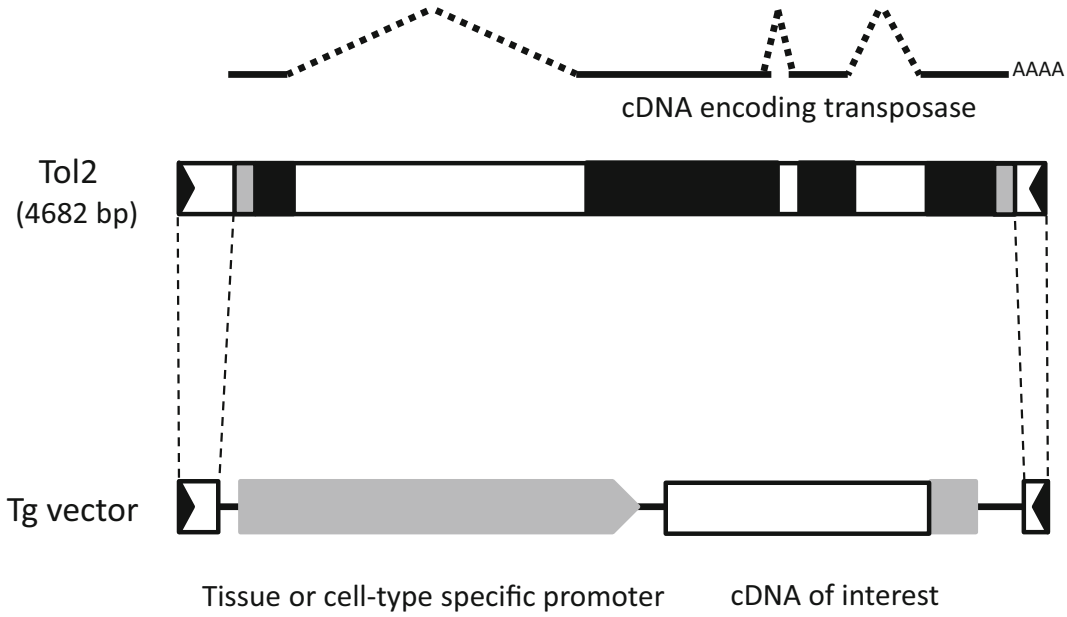


**Fig. 21.2** Original Tol2 and a transgenic vector construct (modified from (Kawakami 2007). Upper: Tol2 was identified as autonomously active transposon element in Medaka fish genome. It contains a gene encoding transposase within terminal inverted repeats at its both ends. Lower: For a transgenic vector construction, transposase cDNA is replaced to an expression construct. Terminal region of the vector was minimized to 200 bp (5′) and 150 bp (3′) with keeping genetic mobility. The vector DNA and transposase mRNA is co-injected into fertilized eggs, which expects germline mosaic in founder candidates

## 21.3 Photostimulation Apparatus for Optogenetic Analysis

When applying optogenetic manipulation on living zebrafish, it is crucial to find an appropriate way of specimen holding in each case. Commonly, an anesthetized larva is pinned on a silicon elastomer (e.g., Sylgard 184 from The Dow Chemical Company) coated chamber where the specimen can be exposed to microscopic fluorescent path or external photostimulation devices. This way is also suited for other microscopic experiment, so combined optogenetic studies with electrophysiology, pharmacology, or fluorescent imaging analysis could be assisted. Another holding way is partial body mounting within agarose block, which allows motion studies under optogenetic neural activation. Anesthetized zebrafish larva is sunk under fluid low-melting point agarose at phase transition temperature (usually 35–38 °C), which rapidly solidifies at room temperature. Then taking agarose off from a motile organ of interest and removal of anesthetic agent allows free motion analysis.

As for photostimulation apparatus, conventional fluorescent microscopes work well in most cases, while additional electromagnetic shutter set may be required to control duration of fluorescent illumination. Confocal laser microscopes that equip photobleaching mode are appropriate for photostimulating small region of interest at a single neuron level. If laser wavelength matches with target gene products, two-photon laser should be powerful tools as it penetrates into deep region of intact brain. External light source loading digital projection devices (Digital mirror device or Liquid crystal on silicon) developed for optogenetic studies are available for major maker's microscopes. These devices allow free assignment of photostimulating region within a monitoring visual field (Fig. 21.3: upper light source).

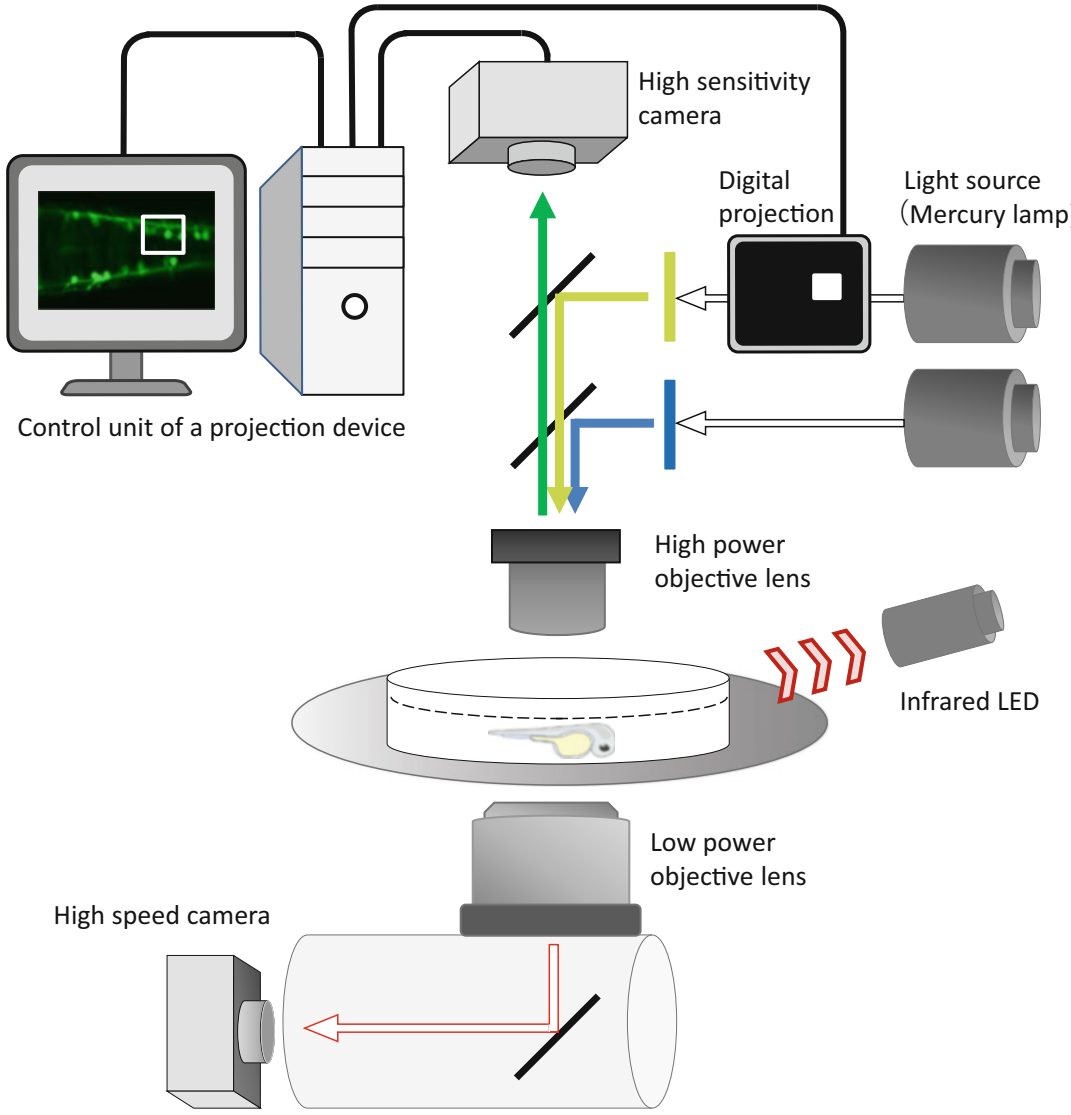


**Fig. 21.3** Digital projection device for targeted photostimulation and imaging light path for capturing zebrafish behavior. Neurons that express optogenetic genes are identified by fluorescent tag protein, and region of photostimulation is selected on a computer monitor that synchronizes a digital projection device (the apparatus over the sample stage). In order to capture behaviors triggered by photostimulation, the light condenser at the bottom of the stage is replaced to optical barrel that connects a low power lens and a camera. When high-speed recording over 300 fps is required, continuous illumination by infrared LED would be helpful

## 21.4 Modulated Reflex Action Triggered by Optogenetic Neural Activation

Studies on intact motile response on the basis of neural manipulation are one of intriguing scopes that are facilitated by optogenetics, while it is often crucial to focus neurons and motile organs within a same microscopic visual field. Use of a medium power objective lens (10–20×) with high numerical aperture (NA ~ 1.0) brings excellent resolution with relatively broad visual fields, so

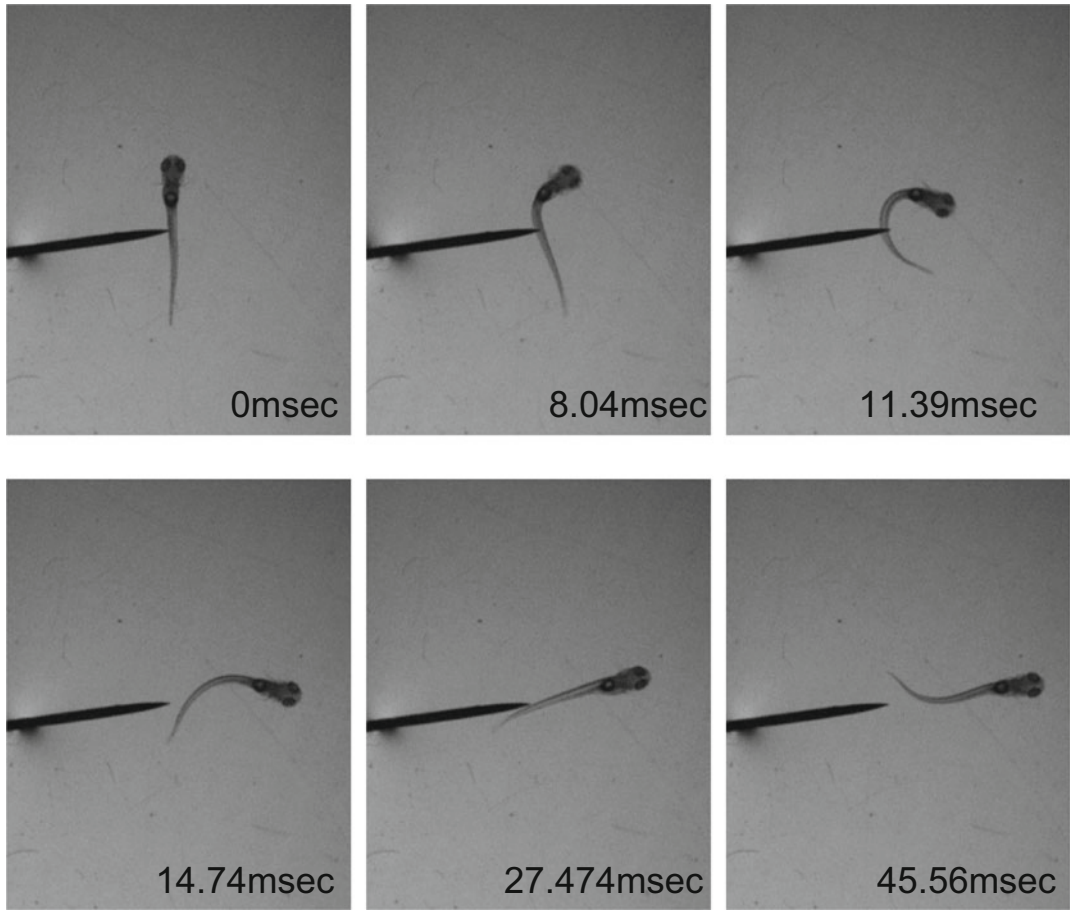


**Fig. 21.4** Escape reflex of zebrafish larva. Tactile stimulation of tungsten needle elicits C-shaped body curvature to swim away from the stimulus. Strength of the first curvature is a key factor for choosing the direction of escape

works well in some cases. Otherwise, additional optical pathway to capture low power field image is required. We replaced a light condenser below the upright microscope stage to a custom-made optical barrel and enabled to record whole-body motion of zebrafish larva (Fig. 21.3: optical path below the specimen).

Using the modified microscope, we recorded escape reflex behavior evoked by optogenetic neural stimulation. Aquatic vertebrates react to water vibration from an oncoming threat and begin C-shaped body curvature with various strengths (Fig. 21.4). For example, sensory stimulus from the front evokes a large turning curvature to move toward the side opposite the threat, while stimulus from the back elicits small changes in direction to swim forward. This strength modulation was observed by targeted optogenetic activation of mechanosensory RB (Rohon-Beard) neurons that innervate trunk surface of zebrafish larvae. Statistically larger turn angle was elicited when more anterior RB neurons were stimulated (Fig. 21.5). The numbers of stimulated neurons did not affect turning strength; however, it did switch turning laterality. Stimulation of multiple RB neurons produced contralateral turn, which corresponds to the appropriate escape behavior from the threat. On the other hand, stimulation of a single RB neuron produced ipsilateral turn to the same side of stimulus (Fig. 21.6).

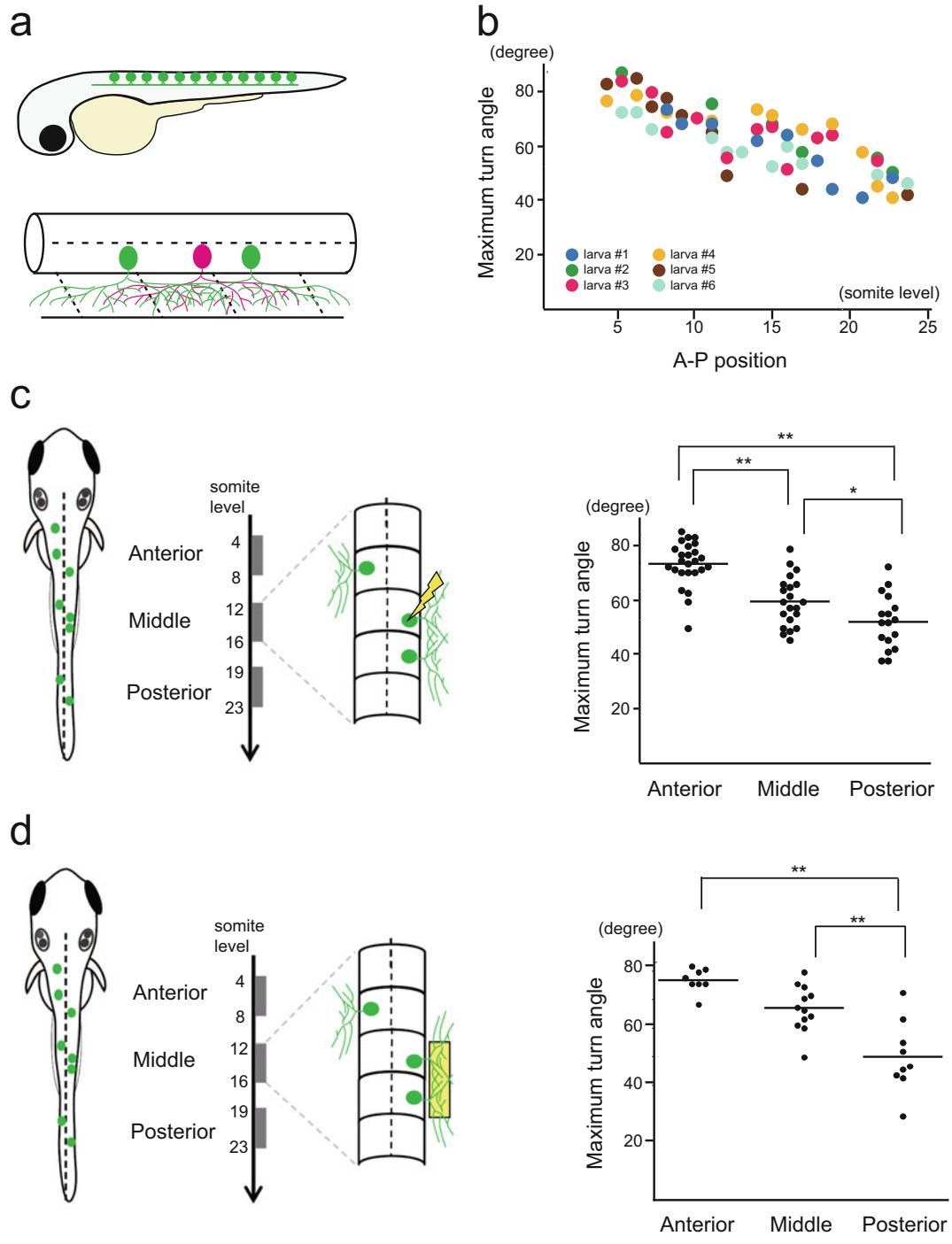


**Fig. 21.5** Strength of the first turning response correlates with the A–P position of RB neurons. (**a**) Upper panel shows RB neurons forming longitudinal column in dorsal spinal cord (green circles). Lower panel shows three RB neurons in spinal cord (white rod) from dorsal view. Only neurons on the left side are schemed with their peripheral arbors on the epidermal region. Dashed oblique lines indicate somite segment borders. (**b**) RB neurons expressing optimized Channelrhodopsin (ChRWR-GFP) is photostimulated to elicit turning behavior, and maximum turn angles are plotted along A–P position of stimulated neurons from six individual larvae in different colors. The change in the degree was graded depending on the position. (**c**) (left) RB neurons expressing ChRWR-

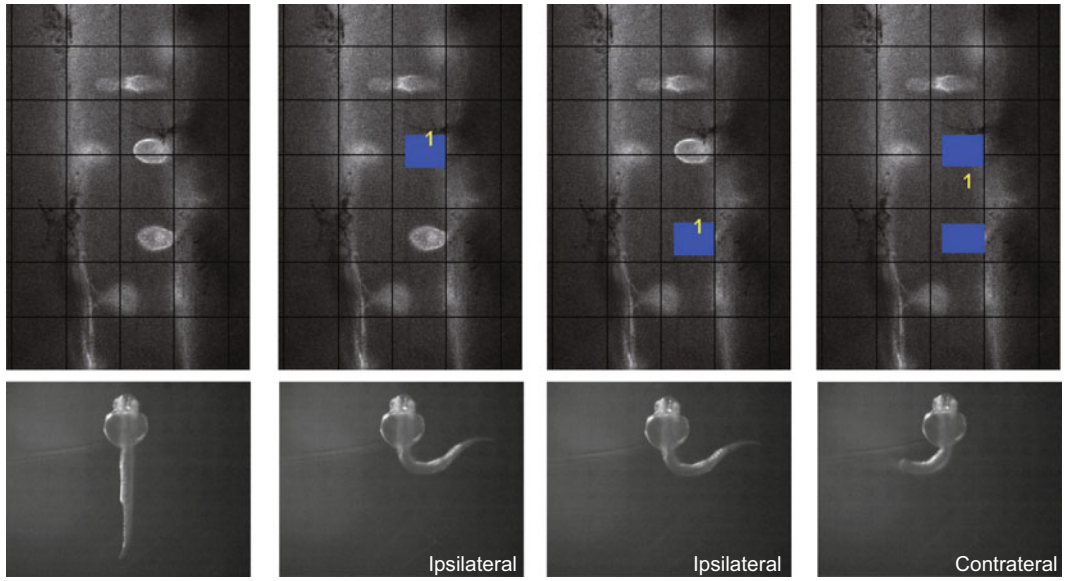


**Fig. 21.6** Different laterality is evoked in response to the quantity of stimulated neurons. (Upper panels) RB neurons captured from dorsal view using a digital projection device. Two neurons on the right side were targeted. Photostimulated areas are marked by blue rectangles in three images on the right. Grid intervals, 24 μm. (Lower panels) Elicited turning responses corresponding to the upper panels. Single-cell photostimulation on its cell body elicited ipsilateral turning, while the same neurons produced the contralateral response by simultaneous stimulation of both two cells

This difference of the laterality was based on divided neural pathways: intraspinal versus supraspinal circuits. The contralateral response by the multicell stimulation was maintained after surgical microdissection between the spinal cord and the hindbrain, so it appears to be produced by an intraspinal circuit. Importantly, the strength modulation along anterior–posterior perception was affected by the dissection, which indicates the modulation depends on supraspinal circuits. While current studies are limited in specifying all the neural components involved, a subset of spinal neurons called CoPA (commissural primary ascending) serves as sensory interneurons whose dendrites form glutamatergic synapses with RB axons (Gleason et al. 2003; Pietri et al. 2009). Their axons run ventral to cross the midline, then ascend along the opposite side of a neural tract called DLF (dorsal longitudinal fasciicule). On the opposite side of the spinal cord, synchronous motor excitation can be triggered by premotor interneurons such as CiD (circumferential ipsilateral descending) and IC (ipsilateral projecting), whose axons descend within the

**Fig. 21.5** (continued) GFP in a mosaic manner (green circles) were categorized into three groups by their A–P position; anterior (4–8 somite level), middle (12–16 somite), and posterior (19–23 somite), and were subjected to photostimulation (right). Analysis of variance in maximum turn angle elicited by single-cell stimulation. More anterior RB neurons elicited larger turning than middle and posterior. Differences in mean values were assessed by the Bonferroni multiple comparison test. * and **denote $P < 0.05$ and $P < 0.01$, respectively. (**d**) (left) Overlapping peripheral arbors from RB neurons were subjected to photostimulation. In a 96 × 12 μm rectangle from the dorsal view, axons from two or three ChRWR-GFP neurons were included, and the stimulated area was categorized into three groups by their A–P position (right). Analysis of variance in maximum turn angle with multicell stimulation. The anterior and middle neurons elicited larger turning angles than the posterior neurons. **$P < 0.01$ by the Bonferroni multiple comparison test (**b**, **c**, and **d** from Umeda et al. 2016)

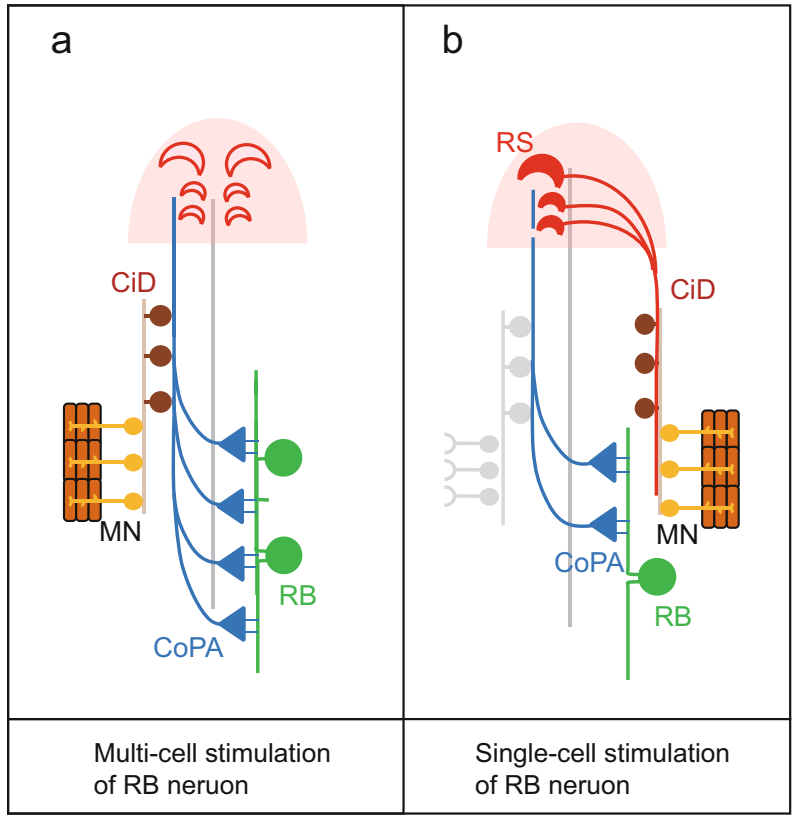


**Fig. 21.7** Diagram of neural circuits that produce contra- and ipsilateral turning depending on the input quantity. (**a**) Contralateral turning by RB multicell stimulation is triggered by an intraspinal reflex circuit. RB neurons form synapses with CoPA neurons, and their commissural axons send sensory signal to the opposite side of the spinal cord. Descending interneurons such as CiD were shown to excite motor neurons for escape, and CoPA axons were suggested to provide sensory signal to these descending interneurons, although it remains unclear how these pathways are connected. (**b**) The ipsilateral response requires supraspinal neural circuits. Single-cell RB input activates CoPA neurons as in a, but is proposed to be fewer than with the multicell input. If small numbers of CoPA neurons do not launch the intraspinal reflex, yet transmit the signal beyond the spinal cord through the contralateral DLF, hindbrain RS neurons might trigger turning behavior by driving motor neurons on the stimulated side. (Modified from Umeda et al. 2016)

ventral spinal cord. These neurons are persuasive candidates that constitute the intraspinal reflex circuit for the contralateral response (Fig. 21.7a). On the other hand, the ipsilateral response by the single-cell stimulation did disappear by the dissection between the spinal cord and hindbrain, suggesting supraspinal neurons are required for the response. Specific disconnection of the contralateral DLF also abolished the response, which indicates RB-CoPA pathway transmits the sensory information to activate a supraspinal circuit. Thus, both in the ipsi- and contralateral turning, a sensory signal takes a common RB-CoPA pathway. Meanwhile, the single-cell stimulation presumably activates fewer numbers of CoPA neurons than the multicell, which would be insufficient for launching the intraspinal circuits, but be further transmitted beyond the spinal cord through the opposite side of the DLF (Fig. 21.7b). In zebrafish hindbrain, Mauthner and its homologous RS (reticulospinal) neurons send descending axons to the opposite side of the spinal cord. If sensory signal is transmitted to these neurons, they would bring excitation of

spinal motor neurons on the stimulated side. Fish escape behavior is an urgent and robust startle reflex to a significant threat, while harmless minor sensation or irrelevant noise should be filtered. In this regard, the requirement of multi-cell input for the contralateral turning by intraspinal reflex makes sense in achieving robust escape. On the other hand, biological relevance of the ipsilateral turning remains an open question. It may be useful to capture small planktonic organisms for food, or may be masked or suppressed by voluntary behaviors in matured neural circuits, since it is elicited by a minor sensation and is processed in supraspinal level. Further studies are necessary to evaluate these possibilities, whereas the optogenetic study indicates zebrafish larva is an excellent model to investigate neural circuits that implement sensory-motor coordination of stereotypical animal behaviors.

## 21.5 Perspective/Conclusion

Useful genetic tools have been developed over last decade, and transparent zebrafish is ready to receive the full benefit of optogenetic technique. Zebrafish is also suitable to study intact motile response on the basis of a single or a group of neurons. Our study described here is an example that would uncover prototypical neural circuits that may also underlie in complex vertebrate neural networks. Recent improvement of optogenetic genes in activation efficiency and long-shifted excitation wavelength expand applicable neurons to the midbrain and the forebrain, which should facilitate studies of supraspinal network using this animal model.

**Acknowledgments** The studies described here were supported by FRIS promoted research grant. I thank to the National Bioresource Project (NBRP), Japan for supplying a transgenic zebrafish strain in the work.

## References

Gleason MR, Higashijima S, Dallman J, Liu K, Mandel G, Fetcho JR (2003) Translocation of CaM kinase II to synaptic sites in vivo. Nat Neurosci 6:217–218

Hwang WY, Fu Y, Reyon D, Maeder ML, Tsai SQ, Sander JD, Peterson RT, Yeh JR, Joung JK (2013) Efficient genome editing in zebrafish using a CRISPR-Cas system. Nat Biotechnol 31:227–229

Kawakami K (2007) Tol2: a versatile gene transfer vector in vertebrates. Genome Biol 8(Suppl 1):S7

Kimura Y, Hisano Y, Kawahara A, Higashijima S (2014) Efficient generation of knock-in transgenic zebrafish carrying reporter/driver genes by CRISPR/Cas9-mediated genome engineering. Sci Rep 4:6545

Li M, Zhao L, Page-McCaw PS, Chen W (2016) Zebrafish genome engineering using the CRISPR-Cas9 system. Trends Genet 32:815–827

Pietri T, Manalo E, Ryan J, Saint-Amant L, Washbourne P (2009) Glutamate drives the touch response through a rostral loop in the spinal cord of zebrafish embryos. Dev Neurobiol 69:780–795

Umeda K, Ishizuka T, Yawo H, Shoji W (2016) Position- and quantity-dependent responses in zebrafish turning behavior. Sci Rep 6:27888

Villefranc JA, Amigo J, Lawson ND (2007) Gateway compatible vectors for analysis of gene function in the zebrafish. Dev Dyn 236:3077–3087

White RM, Sessa A, Burke C, Bowman T, LeBlanc J, Ceol C, Bourque C, Dovey M, Goessling W, Burns CE, Zon LI (2008) Transparent adult zebrafish as a tool for in vivo transplantation analysis. Cell Stem Cell 2:183–189

# Nonhuman Primate Optogenetics: Current Status and Future Prospects

22

Ken-ichi Inoue, Masayuki Matsumoto, and Masahiko Takada

**Abstract**

Nonhuman primates (NHPs) have widely and crucially been utilized as model animals for understanding various higher brain functions and neurological disorders since their behavioral actions mimic both normal and disease states in humans. To know about how such behaviors emerge from the functions and dysfunctions of complex neural networks, it is essential to define the role of a particular pathway or neuron-type constituting these networks. Optogenetics is a potential technique that enables analyses of network functions. However, because of the large size of the NHP brain and the difficulty in creating genetically modified animal models, this technique is currently still hard to apply effectively and efficiently to NHP neuroscience. In this article, we focus on the issues that should be overcome for the development of NHP optogenetics, with special reference to the gene introduction strategy. We review the recent breakthroughs that have been made in NHP optogenetics to address these issues and discuss future prospects regarding more effective and efficient approaches to successful optogenetic manipulation in NHPs.

**Keywords**

Nonhuman primates · Optogenetics · Behavioral manipulation · Viral vectors · Cell type-specific manipulation · Pathway-selective manipulation

## Abbreviations

| | |
|---|---|
| AAV | Adeno-associated virus |
| BBB | Blood–brain barrier |
| BSL | Biosafety level |
| CED | Convention-enhanced delivery |
| ChR2 | Channelrhodopsin 2 |
| CT | Computed tomography |
| DREADD | Designer receptors exclusively activated by designer drugs |
| FEF | Frontal eye field |
| MRI | Magnetic resonance imaging |

K.-i. Inoue (✉)
Systems Neuroscience Section, Primate Research Institute, Kyoto University, Inuyama, Aichi, Japan

PRESTO, Japan Science and Technology Agency, Kawaguchi, Saitama, Japan
e-mail: inoue.kenichi.6z@kyoto-u.ac.jp

M. Matsumoto
Faculty of Medicine, Division of Biomedical Science, University of Tsukuba, Tsukuba, Ibaraki, Japan

Graduate School of Comprehensive Human Sciences, University of Tsukuba, Tsukuba, Ibaraki, Japan

Transborder Medical Research Center, University of Tsukuba, Tsukuba, Ibaraki, Japan

M. Takada
Systems Neuroscience Section, Primate Research Institute, Kyoto University, Inuyama, Aichi, Japan



H. Yawo et al. (eds.), *Optogenetics*, Advances in Experimental Medicine and Biology 1293,
https://doi.org/10.1007/978-981-15-8763-4_22

| | |
|---|---|
| NHP | Nonhuman primate |
| PET | Positron emission tomography |
| V1 | Primary visual cortex |

## 22.1 Introduction

Research works using nonhuman primates (NHPs) play vital roles in the progress in medical and life sciences, because they are the evolutionarily closest to humans among the animals used for invasive experiments and they resemble humans in terms of body structure and function. For example, it is thought that a structural basis for dexterous finger movements in humans lies in the corticospinal tract originating from the motor cortex of the frontal lobe and reaching the anterior horn of the spinal cord. However, such connectivity that large pyramidal neurons in the motor cortex project directly to spinal motoneurons is characteristic of higher NHP animals, including macaque monkeys (Lemon 2008). Since they have the excellent ability to learn and perform various motor and cognitive tasks, macaque monkeys are useful not only for elucidating higher brain functions but also for revealing the pathophysiology of psychiatric and neurological disorders and establishing innovative therapeutic approaches for these disorders. So far, considerable lines of anatomical and physiological knowledge have been accumulated about sensory and motor functions, and further, about various higher brain functions (learning, memory, cognition, etc.), especially in macaques monkeys. However, in order to understand the mechanisms underlying various functions achieved by complex brain networks, it is important to elucidate the functions of individual neural pathways constituting networks and to verify the symptoms of disorders caused by dysfunctions of these pathways. For such researches, techniques that can manipulate the activity of individual neural pathways in NHPs are required.

Optogenetics is a potential tool that allows such approaches. As a result of the recent development in engineered photoreceptors (opsins) (Deisseroth 2015; Govorunova et al. 2017), this technique enables us to (1) target specific cell populations by controlling the expression of opsins, (2) control neuronal activity in either an excitatory or an inhibitory fashion by selecting opsins as well as control intracellular signals, (3) control the manipulation period by selecting opsins and changing the duration of light irradiation, and (4) control the stimulation area at the subcellular to whole-brain level. These features make it possible to accurately manipulate the activity of a particular neuron type or neural circuit with high temporal and spatial resolutions, and allow this technique to utilize as a standard tool for understanding the causal link between neuronal activity and animal behavior, especially in small model animals such as rodents (Kim et al. 2017).

An attempt to apply optogenetic manipulation to NHPs has been made since optogenetics became available in rodents. Han et al. (2009) introduced channelrhodopsin 2 (ChR2) into neurons of the monkey cerebral cortex and demonstrated that blue light laser stimulation could increase neuronal activity at the level of milliseconds. Several years later, the use of an inhibitory opsin and a step-function opsin, which could control neuronal activity over a long-term period, was shown in NHPs (Diester et al. 2011). Although no behavioral effects were clearly observed in these studies, Gerits et al. (2012) reported that optical stimulation of frontal eye field (FEF) neurons expressing ChR2 affected the reaction time of visually guided saccades, and Jazayeri et al. (2012) also showed that optical stimulation of V1 neurons expressing ChR2 increased the frequency of saccades toward the receptive fields of the stimulation sites. Furthermore, Cavanaugh et al. (2012) introduced an inhibitory opsin, Arch-T, into the superior colliculus and showed that light-stimulated inhibition of collicular neuron activity altered the end point of saccades, reduced the peak velocity, and prolonged the reaction time. Since then, many behavioral changes caused by the optical stimulation have been reported, which targeted the oculomotor, visual, somatosensory, and reward systems (Deng et al. 2017; El-Shamayleh and Horwitz 2019; Galvan et al. 2017). However,

**Table 22.1** Problematic issues on effective and efficient optogenetics in NHPs

| Differences from rodent experiments | Difficulties in NHP optogenetics experiments |
|---|---|
| Limited number of experiments | Relatively poor information about vector/promoter characteristics |
| Large brain size | Undesired side effects or tissue damage caused by multiple or large-volume vector injections<br>Limited behavioral effects due to less spread of optical stimulation (also due to brain opaqueness) |
| Complex immune system | Higher risk of neuroinflammation or immune response |
| Long duration of individual experiments | Too much time for validity of vector injections or gene expression |
| Lack of inbred lines | Greater individual differences in brain coordinates and immune response |
| Limited productivity of transgenic/knock-in animals | Lack of cell type-specific Cre-expressing animal resources |

with a few exceptions, behavioral changes reported in these studies were modest, and these studies could not fully exploit the benefits of optogenetics described above. This is because there are many problems that prevent the effective and efficient use of optogenetics in NHPs, for example, large brain size and difficulty in producing transgenic or knock-in animals (Chan 2013) (Table 22.1). For these reasons, the application of optogenetics to NHPs has lagged far behind in comparison with small model animals, such as *C*aenorhabditis *elegans*, drosophila, zebrafish, and mice. In recent years, however, a series of studies have attempted to overcome technical hurdles in applying optogenetics to NHPs. In this article, we review these studies, with special reference to gene introduction strategy, and discuss future perspectives regarding challenges that accelerate the effective and efficient application of this technique to NHP neuroscience.

## 22.2 Viral Vectors

In optogenetic experiments, it is essential to introduce opsins into a target cell population. At present, it is not realistic to use gene-manipulated animals with the opsin gene introduced for NHP optogenetics, because the production of transgenic animals through reproductive engineering in NHPs is limited to those expressing marker genes and disease-related genes (Chan 2013; Liu et al. 2016). Thus, the use of viral vectors is the only way that introduces opsins into NHPs.

### 22.2.1 Viral Vectors Utilized for NHP Optogenetics

Two kinds of virus vectors have been mainly utilized in NHP optogenetics. The lentiviral vector was firstly used for optogenetic experiments in NHPs (Han et al. 2009). This single-stranded RNA (+) vector integrates a portion of its own genome into the host's genome after infection to achieve gene expression, resulting in a stable and permanent expression of the introduced gene (Cockrell and Kafri 2007; Naldini et al. 1996). The alternative is the adeno-associated virus (AAV) vector, which originates from single-stranded DNA virus that can efficiently infect both dividing and nondividing cells. Currently, AAV vectors are widely used as gene transfer vectors not only for basic research works but also for preclinical trials for gene therapy (Grimm and Büning 2017). These vectors have been adopted as opsin-expressing vectors in many laboratories for the following reasons: (1) the original virus itself is not pathogenic and can be treated as biosafety level (BSL) 1, and, therefore, AAV vectors can be used with a lower physical containment criterion than lentiviral vectors in many countries; (2) the AAV is a non-enveloped (capsid-encased) virus, and, therefore, AAV vectors are physicochemically stable as compared to enveloped lentiviral vectors, such that degradation in the laboratory environment is almost negligible; and (3) high levels of opsin gene expression required for efficient optogenetic manipulation are relatively easily obtained with these vectors. Multiple serotypes of AAV have

been reported to have different infectious properties (El-Shamayleh et al. 2016; Gerits et al. 2015; Markakis et al. 2010; Watakabe et al. 2015). To date, a variety of serotypes have been used for NHP optogenetics (Deng et al. 2017), and this situation raises a serious question as to which serotype is the best for each experiment. To address this issue, it is crucial to develop new AAV serotypes (or other viral vector species) that can be used universally for various purposes or to establish a database about the efficiency of opsin introduction and side effects in NHPs.

### 22.2.2 Immune Response to Viral Vector Injections

An ideal universal vector for optogenetics is needed to have the ability to effectively express genes, which are essential for successful optogenetic experiments, as well as to exhibit a low probability of causing neuroinflammation due to vector infection and/or gene expression. This requirement is more important in macaque monkeys than in mice because the monkey brain is about 200 times larger than the mouse brain, and thus more viral particles must be introduced to transfer genes into a given brain region. For sufficient infection efficiency in the target region, the amount of AAV vector injected in each penetration will increase in macaques, and more viral particles are contained at the center of the injection site, resulting in a greater possibility of neuroinflammation. Moreover, the immune system of monkeys is known to be more complex than that of mice (Bjornson-Hooper et al. 2019). These facts suggest that a vector that works well in mice will not necessarily suffice in monkeys. The induction of immune response differs among the AAV serotypes, probably due to some differences in neurotropism or glial infectivity (Ciesielska et al. 2013; Samaranch et al. 2014; Yazdan-Shahmorad et al. 2018). Given that no serotypes that possess all of high neurotropism, low immune response, and high exogenous gene expression have been available, the development of modified serotypes with such properties is indispensable for increasing the success rate of optogenetic experiments in NHPs (Kimura et al. 2019; Tordo et al. 2018). It has also been indicated that AAV injection causes an immune response that results in a significant reduction in infection efficiency in subsequent injection of the same serotype, although antibodies cannot normally pass through the blood–brain barrier (BBB), nor can enter the brain (Mendoza et al. 2017). Although the mechanism of this reduction has not yet been understood, we have experienced that the second injection of the highly neurotropic AAV2 vector, which expresses a DREADD receptor for chemogenetics obtained a successful result in macaque monkeys (Nagai et al. 2016). In this regard, an attempt has been made to use drugs such as steroids that suppress the immune response, but no marked effects have been shown to date.

### 22.2.3 Variability of Gene Expression Efficiency and Undesired Side Effects

The efforts described above are expected to lead to a reduction in the number of test injections prior to the main experiment and, further, to a reduction in the number of experiments in which the expected effect is not obtained. In addition, it is important to reduce the variation of expression efficiency and side effects for each experiment in NHP studies in which the number of animals is limited and each experiment takes a long time. In NHP experiments where inbred lines with identical gene backgrounds cannot be used, individual differences are likely to occur for a variety of reasons. For example, in gene transfer using AAV vectors, which are isolated from humans or macaque monkeys, it has been suggested that endogenous anti-AAV neutralizing antibodies might affect infection efficiency (Calcedo et al. 2018). In this case, the effect on infection efficiency can be estimated to some extent by checking the amount of endogenous anti-AAV neutralizing antibody before the experiment, but it is not clear whether the endogenous neutralizing antibody shows protective effects on a small amount of AAV vector injection into

the brain. In our experience, the amount of endogenous anti-AAV neutralizing antibody has a significant effect on the efficiency of gene introduction when injected intravenously as well as in other reports (Wang et al. 2011), but no animals showed significant reductions in the transduction efficiency after intracerebral injection. The age of the monkeys may also affect the infection efficiency, but no details have been examined.

On the other hand, certain differences in the quality and quantity among AAV vector lots may cause the diversity of transduction efficiency and side effects from experiment to experiment (Dai et al. 2015). It is less likely to use the same lot across multiple monkeys because their large brain size requires more AAV vectors for NHP experiments than for rodent experiments. Therefore, it is recommended to perform quality checks such as protein staining and in vitro infectivity checks before the injection experiments of the vectors.

## 22.3 Injection Methods and Assessment of Gene Expression

As noted earlier in this review, since the monkey brain is about 200 times larger than the mouse brain, it is necessary to introduce more AAV vectors to transfer genes to specific functional units. Moreover, since there is no inbred line in monkeys, the shape and size of the brain vary among individuals. Thus, vector injections based on a brain atlas are not strongly recommended in NHPs. Various injection methods have been attempted to prevent the failure of each experiment due to injection error in valuable animals.

### 22.3.1 Injections After Electrophysiological Mapping or Under Visual Guidance

One of the most reliable methods is to use an injectrode, an electrode attached to an injection cannula, which allows a virus solution to be accurately injected into the site with the expected neuronal activity (Maeda et al. 2020). When targeting the cortex close to the surface of the brain, it is also effective to perform injections following electrophysiological mapping using an ordinary electrode (Inoue et al. 2015). In this case, for accurate injection, it would be better to use the same insertion method for both the electrode and the injection needle (i.e., use of the grid). Moreover, if the dura is replaced with a transparent artificial dura, the injection point can be visually confirmed, so that the injection can be made in a more effective position (Ruiz et al. 2013). Sometimes, researchers would inject visually without mapping after dura removal and prior to covering the brain surface with an artificial dura.

### 22.3.2 Injections Based on Brain Imaging

On the other hand, there are increasing reports on the vector injection using brain imaging, such as magnetic resonance imaging (MRI) and computed tomography (CT). These include a method for estimating the position of the needle tip in the brain using a navigation system with a physical marker, a method of matching the visual information with the MRI structure information by the MRI imaging including blood vessel imaging and a combined method of the real-time imaging by CT scan with the MRI structure information (Nagai et al. 2016; Tanabe et al. 2019). In these methods, injection needle or cannula insertion can be performed outside the MRI apparatus. In contrast, a method of inserting cannula and injecting a viral vector while performing real-time imaging in an MRI apparatus by using an MR-compatible cylinder and cannula has recently been reported (Yazdan-Shahmorad et al. 2016, 2018). This procedure can visualize not only the position of the cannula but also the spread of a vector solution in the brain by using an MRI contrast agent. Visualization of the spread of the vector solution using a contrast agent is also possible by performing MRI imaging immediately after the injection, which

provides the important information for determining whether the injection site may be appropriate.

### 22.3.3 Volume and Locus of Vector Injections

At present, there is little consensus regarding the number of injection points, the injection volume of per point, or the concentration of the vector solution. It is desirable that appropriate values can be determined for each target area through database construction. In general, however, it is better to inject a small amount of the viral vector at many points because injecting a large amount of the vector at one point will have unexpected damage from a high concentration of the vector especially at the injection center. It has been reported that the spread of the viral vector varies depending on the vector type (Diester et al. 2011; Lerchner et al. 2014), and it is desirable to inject the vector at certain intervals such that the concentration of a vector solution is as uniform as possible. On the other hand, it has recently been reported that by injecting a large amount of the viral vector solution with a high pressure at a single injection locus by convention-enhanced delivery (CED) technique, opsin can be introduced relatively uniformly over a very wide range (Yazdan-Shahmorad et al. 2016, 2018). Although this method is not suitable for precise control of a transducing area, it is very promising as a method that allows gene transfer over a wide area in large monkey brains. Whole-brain gene transfer with a systemic delivery of a capsid-modified AAV vector is also attractive. Recently, capsid-modified AAV vectors (AAV-PHP.B and AAV-PHP.eB) generated by an in vivo directed evolution method has been shown to achieve widespread neuronal gene transduction in rodents through intravenous injection of the vectors (Chan et al. 2017; Deverman et al. 2016). Unfortunately, the AAV-PHP.B vector does not exhibit similar properties in monkeys, but if a vector capable of transferring genes into extensive brain regions by the intravenous injection in monkeys is developed in the near future, it may be applied to optogenetic experiments (Hordeaux et al. 2018; Matsuzaki et al. 2018).

### 22.3.4 Assessment of Vector Spread and Gene Expression

As mentioned above, spread of a viral vector solution after the injection via a needle or a cannula can be detected during or immediately after the injection by using a contrast agent (gadolinium or magnesium) that is contained in the injection solution. However, the spread of the vector solution does not guarantee the gene expression. In NHP optogenetics, in which experiments are often conducted over a long period of time, it is preferable to confirm whether sufficient gene expression may occur at the target site prior to conducting stimulation experiments. If the target is a cortex close to the surface of the brain, it is possible to obtain useful information for selecting a stimulation target by observing the expression of fluorescent protein bound to opsin through a transparent artificial dura (Ruiz et al. 2013; Ju et al. 2018; Yazdan-Shahmorad et al. 2016). When the target is located deep in the brain, the amount of fluorescence at the tip of the optical fiber can be measured using a fiber for optical stimulation in the same manner as fiber photometry. This also leads to the confirmation of gene expression condition at the target site and the selection of an effective stimulation point (Diester et al. 2011; Tamura et al. 2017). In chemogenetic approaches, on the other hand, the recent development of PET ligands that recognize DREADD receptors has achieved in vivo imaging of the expression kinetics of DREADD receptors (Nagai et al. 2016). This technique is very useful because the DREADD expression in the whole brain can be confirmed noninvasively before starting the stimulation experiment, and the necessity of an additional injection can be considered. More recently, it is also possible to identify the brain regions receiving the projection from the gene introduction site by visualizing the DREADD receptor expressed on axons of the transduced neurons located around the injection site (Nagai et al. 2019a). This is considered to be

very useful for neural network analyses in NHPs because the brain regions that are likely to change neural activity by stimulation of the target site can be accurately detected before electrophysiological recording experiments. Unfortunately, since opsins are not receptors, the same technique cannot be used in optogenetics. However, it is strongly hopeful that similar imaging techniques will be established by combining opsins with PET-detectable molecules or by expressing both opsins and PET-detectable molecules via vectors. In addition, the development of a detection method using MRI is necessary for the extensive use of these assessment techniques.

## 22.4 Opsins

A variety of novel photoreceptors have been discovered and developed for multiple purposes (Govorunova et al. 2017; Kim et al. 2017). Details of these opsins are described in other chapters. The first and most commonly used opsin in NHPs was ChR2, an excitatory opsin activated with blue light, but the recent interest in NHP optogenetics has focused on the use of red light-activated opsins, which are C1V1, Chrimson, and ChRmine as excitatory opsins, and eNpHR 3.0 and Jaws as inhibitory opsins. Because the brain is a nontransparent material, the light emitted from optical fibers is absorbed and diffused in the brain and rapidly decays (Acker et al. 2016; Robles et al. 2010). This phenomenon is not only problematic in small model animals such as mice when irradiated from the outside of the brain but also in the opaque primate brain in which optical stimulation is necessary to cover a large area to induce behavioral changes. It is, therefore, considered that the use of opsins, which are activated with light having a long wavelength with a high transmittance, greatly contributes to the expansion of the stimulation area. In fact, behavioral changes induced by optical stimulation using C1V1 and Jaws have already been reported in NHPs (Acker et al. 2016; Dai et al. 2014). Introducing both blue light-activated and red light-activated opsins into different cell populations in the same animal is an intriguing strategy for NHP optogenetics where the number of animals used is limited.

## 22.5 Cell Type-Specific Opsin Expression

One of the major reasons for the rapid development of optogenetics from early 2000s to date is the ability of this technique to target specific cell populations by regulating opsin expression. This property has made it possible to verify the functions of specific cell populations causally and has been used to elucidate the mechanisms underlying various brain functions. Many researchers use cell type-specific Cre-expressing mice, and the compatibility with abundant cell-type-specific Cre-expressing mouse resources is one of the great advantages of optogenetics. However, there are no cell-type-specific Cre expression models in NHPs. Recently, the production of genetically modified animals by reproductive engineering has been reported in NHPs (Chan 2013; Liu et al. 2016; Zhou et al. 2019). At present, however, the production of genetically modified NHPs is limited to individuals expressing marker proteins as a proof of concept or those with the introduction or deletion of disease-causing genes (Jennings et al. 2016). Considering the effort and cost involved in production and maintenance, it can be said that the possibility of developing cell-type-specific Cre-expressing monkey resources is extremely low. Thus, in NHPs, the cell type-specific gene transfer relies on the control of promoters carried by viral vectors.

### 22.5.1 Promoters Used for NHP Optogenetics

Several promoters have been tested in primate optogenetics. Among these, ubiquitous promoters that are not cell-type-specific, such as CMV and CAG, induce strong opsin expression (El-Shamayleh et al. 2016). However, since their expression is extremely potent in glial cells, the selection of these promoters can be recommended

only when used in combination with viral vectors with extremely high neurotropism, such as AAV2, to avoid serious side effects. Pan-neuronal promoters, such as the hSyn promoter, have the ability to express genes in various neuronal populations and are used in many cases as ubiquitous promoters that are restricted to neurons. However, they cannot be used for neuron type-specific optogenetic manipulation. Currently, the most successful neuron type-specific optogenetic approach in NHPs is to use promoters that have already been well established in mice, such as the CaMKIIα promoter for selective expression of excitatory neurons in the cortex and the L7 promoter for selective expression of cerebellar Purkinje cells (Deng et al. 2017; El-Shamayleh et al. 2016; Klein et al. 2016). Exceptionally, the TH (tyrosine hydroxylase) promoter has been used to achieve selective stimulation of dopamine neurons in the macaque monkey (Stauffer et al. 2016). Such a restricted promoter application is ascribed to the issue that for gene expression control using AAV or lentiviral vectors, the promoter sequence to be incorporated must be shortened due to the limited length of the sequence inserted into the vectors, and the selectivity that has been confirmed in transgenic or knock-in animals is not necessarily obtained.

### 22.5.2 Recent Technical Improvement in Cell-Type-Specific Gene Expression

Recently, however, a variety of promoter sequences have been reported, reflecting the increasing demand for expression control by viral vectors alone, and some of them have already been found to be successful in cell type-specific gene expression in NHPs (Dimidschstein et al. 2016; Jüttner et al. 2019; Knobloch et al. 2012; Nagai et al. 2019b). It is noteworthy that many enhancer sequences have been identified with the remarkable development of genome analysis methods in recent years, and cell type-specific gene expression has been achieved by combining these enhancer sequences with minimal promoters (Graybuck et al. 2019; Hrvatin et al. 2019; Nair et al. 2019). Although it should be noted that there are cases in which functional expression control sequences confirmed in mice, and sometimes even those from macaque monkeys, do not function in the monkeys, it is expected that the cell type-specific gene expression in NHPs and the consequent selective optogenetic manipulation will become widespread based on these improvements (Jüttner et al. 2019). Thus, to promote the cell type-specific optogenetic manipulation in NHPs, each candidate for the expression control sequence should be tested in NHPs prior to the main experiment, and it is desirable that the results are accumulated and published in a database or a similar medium.

## 22.6 Pathway-Selective Manipulation

In addition to cell type-specific optogenetic manipulation, pathway-selective optogenetic manipulation is quite useful for understanding the mechanisms of various brain functions. To selectively stimulate a particular neural pathway or a neuronal population with a certain projection can be considered the most direct method for investigating the causal relationship between the functional role and the information processing of a target neural network. There are two major approaches to pathway-selective optogenetics as described below.

### 22.6.1 Pathway-Selective Optogenetics Through Axonal Stimulation

The first approach is to inject a virus vector that infects neurons at the injection site, irradiate one of the projection targets of the infected neurons, and control the activity of a particular projection by axonal stimulation (Fig. 22.1a). This is an effective strategy for elucidating neural network functions, especially in the case where individual collaterals of a bifurcating axon need to be

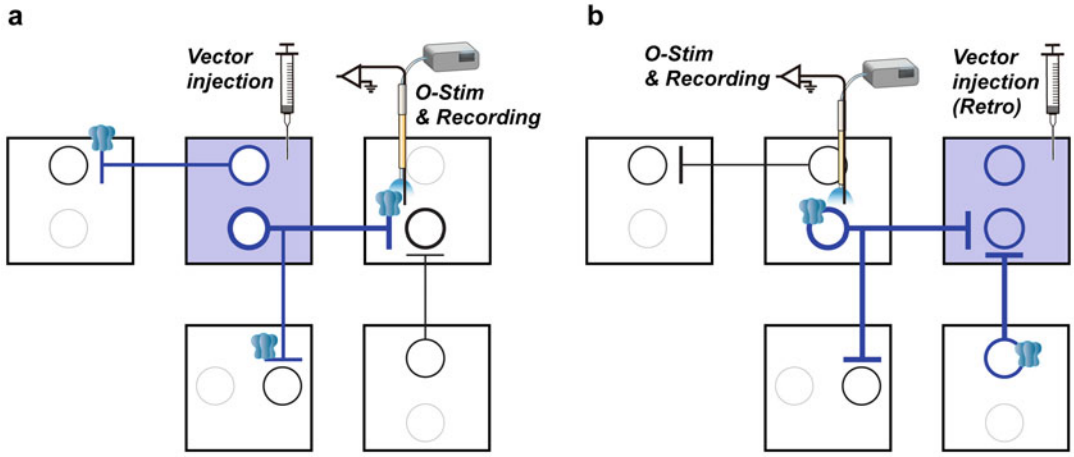


**Fig. 22.1** Pathway-selective optogenetics. Schematic diagram showing the experimental strategies for two types of pathway-selective optogenetics. Squares represent regions of the brain. (**a**) Pathway-selective optogenetics by axonal stimulation. In this approach, a viral vector is injected into a region from which the target pathway originates, and the optical stimulation is done in a region in which the target pathway terminates. This strategy is effective for elucidating neural network functions by controlling the activity of a particular pathway by axonal stimulation, especially in the case where individual axon collaterals need to be differentiated. (**b**) Pathway-selective optogenetics by somal stimulation via retrograde gene transfer. In this approach, a viral vector with retrograde infectivity is injected into a region in which the target pathway ends, and the optical stimulation is carried out in a region from which the target pathway arises. This strategy is useful for identifying the type of neurons giving rise to the target pathway because the occurrence of direct responses evoked by the optical stimulation confirms that the recorded neuron sends projection fibers to the injection site of the vector

distinguished, and has so far been used for many network function analyses in rodents. Recently, we have shown that this technique can be applied to primates (Inoue et al. 2015). In this study, an AAV vector expressing ChR2 was injected into the frontal eye field (FEF) of macaque monkeys, and axon terminals of the ChR2-expressing FEF neurons in the superior colliculus, one of the major targets of the FEF, were light-stimulated (Fig. 22.2a, b). As a result, an increase in collicular neuron activity was observed (Fig. 22.2c). Moreover, the generation of an unintended saccade in a fixation task and the change in the reaction time in a visually guided saccade task were induced by the axonal optical stimulation (Fig. 22.2d). Notably, much stronger behavioral effects were exerted than the effects shown in previous studies with gene transfer into the FEF and optical stimulation in the FEF (Han et al. 2009; Ohayon et al. 2013). This suggests that selective stimulation targeting a neuronal population playing a peculiar functional role is effective. The same strategy is also applicable to other neural pathways, such as the corticothalamic pathway and the direct pathway of the basal ganglia (Amita et al. 2020; Galvan et al. 2016). Although not evident in our experiments, some effects of antidromic stimulation must be considered in the case of excitatory opsin-based axonal stimulation. In several studies using rodents, antidromic spikes have been observed in response to optical stimulation of opsin-introduced axons and have occasionally been used for identifying the target sites of recorded neurons (Jennings et al. 2013; Sato et al. 2014). In other cases, including our study (Inoue et al. 2015), however, antidromic spikes have not been observed (Adhikari et al. 2015; Tye et al. 2011), suggesting that it may depend on the intensity and parameter of the stimulation and, perhaps, the target neural system.

Axonal optical stimulation of inhibitory opsins may also be a very effective way to elucidate the function of a given neural pathway. The neuronal and behavioral effects have been reported in

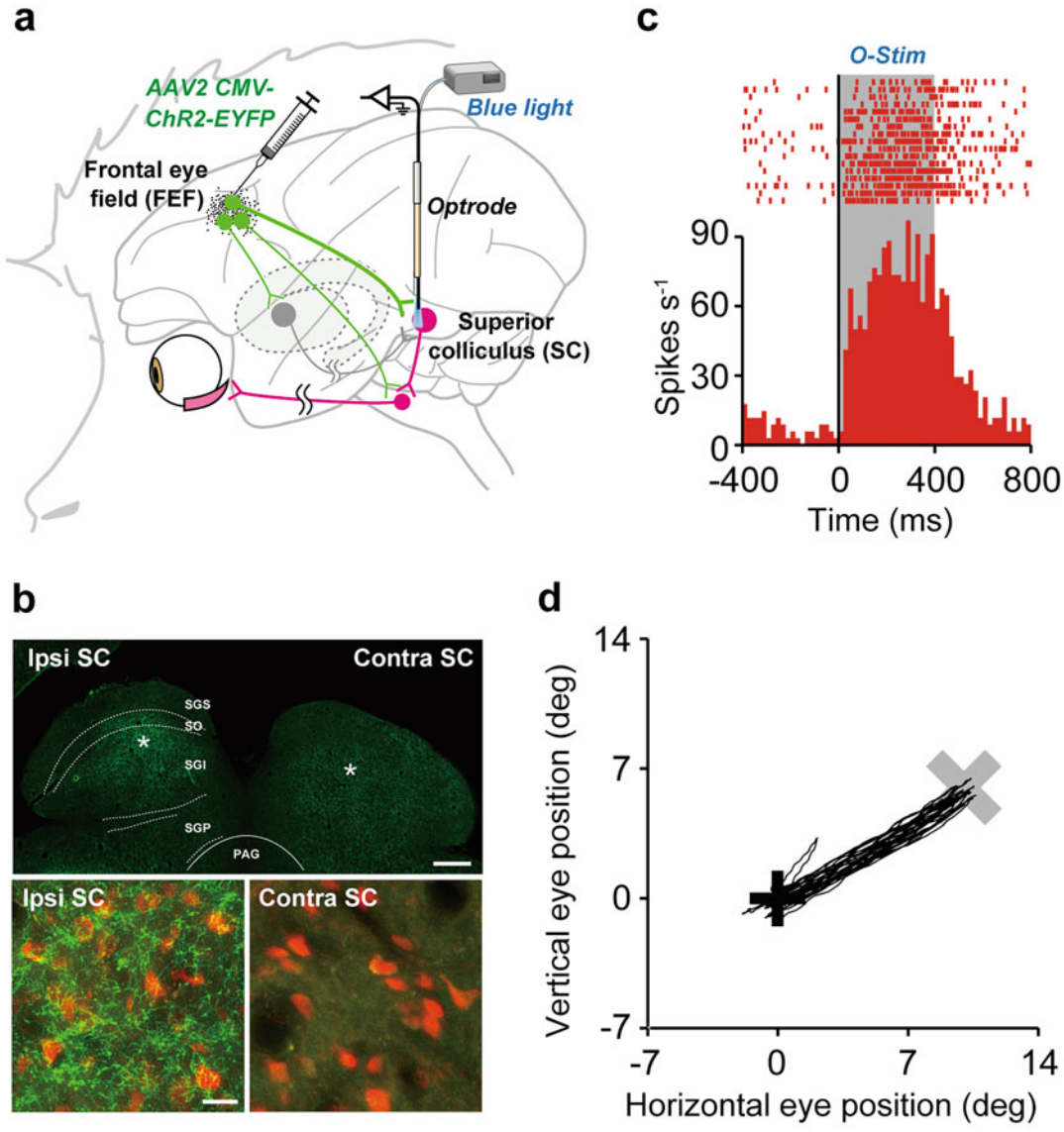


**Fig. 22.2** Optical stimulation of the pathway from the frontal eye field (FEF) to the superior colliculus (SC). (**a**) Schema of experimental configuration. AAV2 vector expressing ChR2 was injected into the FEF. Then, single-unit activity was recorded while the blue light was emitted into the SC by using optrodes. (**b**) ChR2-EYFP expression in the SC. Top, wide-field immunofluorescent image of a coronal section through the SC. Bottom, immunofluorescence of YFP-expressing axons in the ipsilateral and contralateral SC. NeuN-expressing SC neurons are shown in red. Scale bars, 1 mm for the top panel and 20 μm for the bottom panels. *PAG* periaqueductal gray, *SGI* stratum griseum intermediale, *SGP* stratum griseum profundum, *SGS* stratum griseum superficiale, *SO* stratum opticum. (**c**) Representative neuronal responses to laser light emission in the ipsilateral SC. Gray areas indicate the period of laser light emission. (**d**) Saccadic eye movements evoked by optical stimulation at a representative site in the ipsilateral SC. Trajectories of eye positions are shown. Black and gray crosses indicate the fixation point and the center of the response field at the stimulation site in the SC, respectively. Adapted from Inoue et al. (2015)

response to optical stimulation of axons that express the inhibitory opsin in rodents and NHPs (Carta et al. 2019; Nurminen et al. 2018). However, it should be noted here that ion flow with the optical stimulation of currently available inhibitory opsins may have different effects on cell bodies and axon terminals and may not have a simple inhibitory effect on axon terminals (Mahn et al. 2016). In the future, the development of opsins related to potassium channels and sodium efflux pumps is expected for this purpose.

### 22.6.2 Pathway-Selective Optogenetics Through Retrograde Gene Transfer

The second approach is to utilize retrograde infective viral vectors (Fig. 22.1b). In this approach, injection of a retrograde vector which infects from the axon terminal results that a neuronal population giving rise to a particular projection can be singled out for optical stimulation. This technique is very useful for differentially controlling or recording the activity of target neurons, especially in NHPs in which cell type-specific gene transfer is not so easy. In recent years, retrograde infective viral vectors have been developed for lentiviral and AAV vectors, and these vectors may be used for pathway-selective optogenetic manipulation in NHPs (Davidsson et al. 2019; Tanabe et al. 2019; Tervo et al. 2016). Since it is suggested that the expression ability and infection specificity of these vectors may differ from vector to vector (Chatterjee et al. 2018), it might be expected that their detailed characterization will be carried out in different projection systems to permit vector selection appropriate for the target system. In particular, for the retrograde vectors, which generally require injections at high titers for efficient retrograde infection, the infectivity from neuronal cell bodies and, also, to glial cells at their injection sites may cause undesirable side effects, such as triggering an immune response (Tanabe et al. 2019).

### 22.6.3 Pathway-Selective Optogenetics Combined with Cell-Type-Specific Gene Transfer

The two types of pathway-selective optogenetics described above can be combined with cell-type-specific gene transfer techniques and such combinations have indeed been demonstrated in rodents (Adhikari et al. 2015; Tye et al. 2011). It might be expected that more selective stimulation of a particular neural pathway will be achieved in NHPs through the development of promoters that work prominently in the NHP brain. By combining a propagation-deficient rabies virus vector and cell type-specific gene transfer, it becomes possible to introduce a target gene selectively into a given neuronal population that sends projection fibers to a certain type of neurons, and such an approach has already been tested in rodents (Luo et al. 2018). However, unlike the lentiviral and AAV vectors, this rabies virus vector requires viral gene expression for expression of foreign genes, which makes the same method unsuitable for long-term NHP studies because of presumed cytotoxicity (Nassi et al. 2015; Wickersham et al. 2007). Currently, propagation-deficient rabies virus vectors with reduced cytotoxicity are being developed (Chatterjee et al. 2018; Ciabatti et al. 2017). However, since these vectors have a low gene expression capacity and require the application of Cre-loxP recombination technique for the expression of enough amounts of foreign genes, it is called for to develop the vectors with a reduced cytotoxicity and a higher foreign gene expression capability in the near future.

## 22.7 Conclusion

In addition to the topics discussed in this chapter, many problems still exist that hinder the effective and efficient use of optogenetics in NHPs (Table 22.1). Considering the large monkey brain and long-lasting monkey experiments, methodological improvement and unique

ingenuity should be required with respect to optical stimulation and measurement of neuronal activity in response to the stimulation. In fact, some progress has recently been made in these technical issues (for reviews, see Deng et al. 2017; El-Shamayleh and Horwitz 2019; Galvan et al. 2017). Although many of the early optogenetic works in NHPs were rather focused on the methodological development, more refined studies are now being conducted to investigate higher brain functions. By further developing elemental technologies leading to establishment of applied optogenetics using NHPs, this novel technique is expected to become a very powerful tool for dissecting complex neural networks and elucidating their functional roles. Moreover, such an advance will contribute to the development of therapeutic strategies for neurological and psychiatric disorders based on the outcome derived from NHPs.

**Acknowledgments** This work was supported by MEXT/JSPS (15H05879 and 19H03335 to K.I.), by JST (JPMJPR1683 to K.I. and JPMJCR1853 to M.T.), and by AMED (JP18dm0307021 to K.I. and JP19dm0207077 to M.T.).

## References

Acker L, Pino EN, Boyden ES et al (2016) FEF inactivation with improved optogenetic methods. Proc Natl Acad Sci U S A 113:E7297–E7306

Adhikari A, Lerner TN, Finkelstein J et al (2015) Basomedial amygdala mediates top-down control of anxiety and fear. Nature 527:179–185

Amita H, Kim HF, Inoue K et al (2020) Optogenetic manipulation of a value-coding pathway from the primate caudate tail facilitates saccadic gaze shift. Nat Commun 11:1876

Bjornson-Hooper ZB, Fragiadakis GK, Spitzer MH et al (2019) A comprehensive atlas of immunological differences between humans, mice and non-human primates. bioRxiv 574160

Calcedo R, Chichester JA, Wilson JM (2018) Assessment of humoral, innate, and t-cell immune responses to adeno-associated virus vectors. Hum Gene Ther Meth 29:86–95

Carta I, Chen CH, Schott AL (2019) Cerebellar modulation of the reward circuitry and social behavior. Science 363:eaav0581

Cavanaugh J, Monosov IE, McAlonan K et al (2012) Optogenetic inactivation modifies monkey visuomotor behavior. Neuron 76:901–907

Chan AW (2013) Progress and prospects for genetic modification of nonhuman primate models in biomedical research. ILAR J 54:211–223

Chan KY, Jang MJ, Yoo BB (2017) Engineered AAVs for efficient noninvasive gene delivery to the central and peripheral nervous systems. Nat Neurosci 20:1172–1179

Chatterjee S, Sullivan HA, MacLennan BJ (2018) Nontoxic, double-deletion-mutant rabies viral vectors for retrograde targeting of projection neurons. Nat Neurosci 21:638–646

Ciabatti E, Gonza'lez-Rueda A, Mariotti L (2017) Lifelong genetic and functional access to neural circuits using self-inactivating rabies virus. Cell 170:1–11

Ciesielska A, Hadaczek P, Mittermeyer G et al (2013) Cerebral infusion of AAV9 vector-encoding non-self proteins can elicit cell-mediated immune responses. Mol Ther 21:158–166

Cockrell AS, Kafri T (2007) Gene delivery by lentivirus vectors. Mol Biotechnol 36:184–204

Dai J, Brooks DI, Sheinberg DL (2014) Optogenetic and electrical microstimulation systematically bias visuospatial choice in primates. Curr Biol 24:63–69

Dai J, Ozden I, Brooks DI (2015) Modified toolbox for optogenetics in the nonhuman primate. Neurophotonics 2:031202

Davidsson M, Wang G, Aldrin-Kirk P (2019) A systematic capsid evolution approach performed in vivo for the design of AAV vectors with tailored properties and tropism. Proc Natl Acad Sci U S A 116:27053–27062

Deisseroth K (2015) Optogenetics: 10 years of microbial opsins in neuroscience. Nat Neurosci 18:1213–1225

Deng C, Yuan H, Dai J (2017) Behavioral manipulation by optogenetics in the nonhuman primate. Neuroscientist 24:526–539

Deverman BE, Pravdo PL, Simpson BP et al (2016) Cre-dependent selection yields AAV variants for widespread gene transfer to the adult brain. Nat Biotechnol 34:204–209

Diester I, Kaufman MT, Mogri M et al (2011) An optogenetic toolbox designed for primates. Nat Neurosci 14:387–397

Dimidschstein J, Chen Q, Tremblay R et al (2016) A viral strategy for targeting and manipulating interneurons across vertebrate species. Nat Neurosci 19:1743–1749

El-Shamayleh Y, Horwitz GD (2019) Primate optogenetics: progress and prognosis. Proc Natl Acad Sci U S A 116:26195–26203

El-Shamayleh Y, Ni AM, Horwitz GD (2016) Strategies for targeting primate neural circuits with viral vectors. J Neurophysiol 116:122–134

Galvan A, Hu X, Smith Y et al (2016) Effects of optogenetic activation of corticothalamic terminals in the motor thalamus of awake monkeys. J Neurosci 36:3519–3530

Galvan A, Stauffer WR, Acker L et al (2017) Nonhuman primate optogenetics: recent advances and future directions. J Neurosci 37:10894–10903

Gerits A, Farivar R, Rosen BR et al (2012) Optogenetically induced behavioral and functional network changes in primates. Curr Biol 22:1722–1726

Gerits A, Vancraeyenest P, Vreysen S et al (2015) Serotype-dependent transduction efficiencies of recombinant adeno-associated viral vectors in monkey neocortex. Neurophotonics 2:031209

Govorunova EG, Sineshchekov OA, Li H et al (2017) Microbial rhodopsins: diversity, mechanisms, and optogenetic applications. Annu Rev Biochem 86:845–872

Graybuck LT, Sedeño-Cortés AE, Nguyen TN et al (2019) Prospective, brain-wide labeling of neuronal subclasses with enhancer-driven AAVs. bioRxiv 525014

Grimm D, Büning H (2017) Small but increasingly mighty: latest advances in AAV vector research, design, and evolution. Hum Gene Ther 28:1075–1086

Han X, Qian X, Bernstein JG et al (2009) Millisecond-timescale optical control of neural dynamics in the nonhuman primate brain. Neuron 62:191–198

Hordeaux J, Wang Q, Katz N et al (2018) The neurotropic properties of AAV-PHP.B are limited to C57BL/6J mice. Mol Ther 26:664–688

Hrvatin S, Tzeng CP, Nagy MA et al (2019) A scalable platform for the development of cell-type-specific viral drivers. elife 8:e48089

Inoue K, Takada M, Matsumoto M (2015) Neuronal and behavioral modulations by pathway-selective optogenetic stimulation of the primate oculomotor system. Nat Commun 6:8378

Jazayeri M, Lindbloom-Brown Z, Horwitz GD (2012) Saccadic eye movements evoked by optogenetic activation of primate V1. Nat Neurosci 15:1368–1370

Jennings JH, Sparta DR, Stamatakis AM et al (2013) Distinct extended amygdala circuits for divergent motivational states. Nature 496:224–228

Jennings CG, Landman R, Zhou Y et al (2016) Opportunities and challenges in modeling human brain disorders in transgenic primates. Nat Neurosci 19:1123–1130

Ju N, Jiang R, Macknik SL et al (2018) Long-term all-optical interrogation of cortical neurons in awake-behaving nonhuman primates. PLoS Biol 16:e2005839

Jüttner J, Szabo A, Gross-Scherf B (2019) Targeting neuronal and glial cell types with synthetic promoter AAVs in mice, non-human primates and humans. Nat Neurosci 22:1345–1356

Kim CK, Adhikari A, Deisseroth K (2017) Integration of optogenetics with complementary methodologies in systems neuroscience. Nat Rev Neurosci 18:222–235

Kimura K, Nagai Y, Tanabe S et al (2019) The modified adeno associated virus vectors enable neuron specific efficient gene transduction in the primate brain. Abstract for Neuroscience 2019, Chicago, 433.09

Klein C, Evrard HC, Shapcott KA et al (2016) Cell-targeted optogenetics and electrical microstimulation reveal the primate koniocellular projection to supragranular visual cortex. Neuron 90:143–151

Knobloch HS, Charlet A, Hoffmann LC et al (2012) Evoked axonal oxytocin release in the central amygdala attenuates fear response. Neuron 73:553–566

Lemon RN (2008) Descending pathways in motor control. Annu Rev Neurosci 31:195–218

Lerchner W, Corgiat B, Der-Minassian V et al (2014) Injection parameters and virus dependent choice of promoters to improve neuron targeting in the nonhuman primate brain. Gene Ther 21:233–241

Liu Z, Li X, Zhang JT et al (2016) Autism-like behaviours and germline transmission in transgenic monkeys overexpressing MeCP2. Nature 530:98–102

Luo L, Callaway EM, Svoboda K (2018) Genetic dissection of neural circuits: a decade of progress. Neuron 98:256–281

Maeda K, Inoue K, Kunimatsu J et al (2020) Primate amygdalo-nigral pathway for boosting oculomotor action in motivating situations. iScience in press

Mahn M, Prigge M, Ron S et al (2016) Biophysical constraints of optogenetic inhibition at presynaptic terminals. Nat Neurosci 19:554–556

Markakis EA, Vives KP, Bober J et al (2010) Comparative transduction efficiency of AAV vector serotypes 1-6 in the substantia nigra and striatum of the primate brain. Mol Ther 18:588–593

Matsuzaki Y, Konno A, Mochizuki R et al (2018) Intravenous administration of the adeno-associated virus-PHP.B capsid fails to upregulate transduction efficiency in the marmoset brain. Neurosci Lett 665:182–188

Mendoza SD, El-Shamayleh Y, Horwitz GD (2017) AAVmediated delivery of optogenetic constructs to the macaque brain triggers humoral immune responses. J Neurophysiol 117:2004–2013

Nagai Y, Kikuchi E, Lerchner W et al (2016) PET imaging-guided chemogenetic silencing reveals a critical role of primate rostromedial caudate in reward evaluation. Nat Commun 7:13605

Nagai Y, Miyakawa N, Takuwa H (2019a) Deschloroclozapine: a potent and selective chemogenetic actuator enables rapid neuronal and behavioral modulations in mice and monkeys. bioRxiv 854513

Nagai Y, Nishitani N, Yasuda M et al (2019b) Identification of neuron-type specific promoters in monkey genome and their functional validation in mice. Biochem Biophys Res Commun 518:619–624

Nair RR, Blankvoort S, Lagartos MJ et al (2019) Generation of viral vectors specific to neuronal subtypes of targeted brain regions by Enhancer-Driven Gene Expression (EDGE). bioRxiv 606467

Naldini L, Blömer U, Gage FH et al (1996) Efficient transfer, integration, and sustained long-term expression of the transgene in adult rat brains injected with a lentiviral vector. Proc Natl Acad Sci U S A 93:11382–11388

Nassi JJ, Cepko CL, Born RT et al (2015) Neuroanatomy goes viral! Front Neuroanat 9:80

Nurminen L, Merlin S, Bijanzadeh M et al (2018) Top-down feedback controls spatial summation and response amplitude in primate visual cortex. Nat Commun 9:2281

Ohayon S, Grimaldi P, Schweers N et al (2013) Saccade modulation by optical and electrical stimulation in the macaque frontal eye field. J Neurosci 33:16684–16697

Robles FE, Chowdhury S, Wax A (2010) Assessing hemoglobin concentration using spectroscopic optical coherence tomography for feasibility of tissue diagnostics. Biomed Opt Express 1:310–317

Ruiz O, Lustig BR, Nassi JJ et al (2013) Optogenetics through windows on the brain in the nonhuman primate. J Neurophysiol 110:1455–1467

Samaranch L, Sebastian WS, Kells AP et al (2014) AAV9-Mediated expression of a non-self protein in nonhuman primate central nervous system triggers widespread neuroinflammation driven by antigen-presenting cell transduction. Mol Ther 22:329–337

Sato TK, Häusser M, Carandini M (2014) Distal connectivity causes summation and division across mouse visual cortex. Nat Neurosci 17:30–32

Stauffer WR, Lak A, Yang A et al (2016) Dopamine neuron-specific optogenetic stimulation in rhesus macaques. Cell 166:1564–1571

Tamura K, Takeda M, Setsuie R et al (2017) Conversion of object identity to object-general semantic value in the primate temporal cortex. Science 357:687–692

Tanabe S, Uezono S, Tsuge H et al (2019) A note on retrograde gene transfer efficiency and inflammatory response of lentiviral vectors pseudotyped with FuG-E vs. FuG-B2 glycoproteins. Sci Rep 9:3567

Tervo DGR, Hwang BY, Viswanathan S (2016) A designer AAV variant permits efficient retrograde access to projection neurons. Neuron 92:372–382

Tordo J, O'Leary C, Antunes ASLM et al (2018) A novel adeno-associated virus capsid with enhanced neurotropism corrects a lysosomal transmembrane enzyme deficiency. Brain 141:2014–2031

Tye KM, Prakash R, Kim SY et al (2011) Amygdala circuitry mediating reversible and bidirectional control of anxiety. Nature 471:358–362

Wang L, Calcedo R, Bell P et al (2011) Impact of pre-existing immunity on gene transfer to nonhuman primate liver with adeno-associated virus 8 vectors. Hum Gene Ther 22:1389–1401

Watakabe A, Ohtsuka M, Kinoshita M et al (2015) Comparative analyses of adeno-associated viral vector serotypes 1, 2, 5, 8 and 9 in marmoset, mouse and macaque cerebral cortex. Neurosci Res 93:144–157

Wickersham IR, Lyon DC, Barnard RJ et al (2007) Monosynaptic restriction of transsynaptic tracing from single, genetically targeted neurons. Neuron 53:639–647

Yazdan-Shahmorad A, Diaz-Botia C, Hanson TL et al (2016) A large-scale interface for optogenetic stimulation and recording in nonhuman primates. Neuron 89:927–939

Yazdan-Shahmorad A, Tian N, Kharazia V et al (2018) Widespread optogenetic expression in macaque cortex obtained with MR-guided, convection enhanced delivery (CED) of AAV vector to the thalamus. J Neurosci Methods 293:347–358

Zhou Y, Sharma J, Ke Q et al (2019) Atypical behaviour and connectivity in SHANK3-mutant macaques. Nature 570:326–331

# Application of Optogenetics for Muscle Cells and Stem Cells

23

Toshifumi Asano, Daniel Boon Loong Teh, and Hiromu Yawo

**Abstract**

This chapter describes the current progress of basic research, and potential therapeutic applications primarily focused on the optical manipulation of muscle cells and neural stem cells using microbial rhodopsin as a light-sensitive molecule. Since the contractions of skeletal, cardiac, and smooth muscle cells are mainly regulated through their membrane potential, several studies have been demonstrated to up- or downregulate the muscle contraction directly or indirectly using optogenetic actuators or silencers with defined stimulation patterns and intensities. Light-dependent oscillation of membrane potential also facilitates the maturation of myocytes with the development of T tubules and sarcomere structures, tandem arrays of minimum contractile units consists of contractile proteins and cytoskeletal proteins. Optogenetics has been applied to various stem cells and multipotent/pluripotent cells such as embryonic stem cells (ESCs) and induced pluripotent stem cells (iPSCs) to generate light-sensitive neurons and to facilitate neuroscience. The chronic optical stimulation of the channelrhodopsin-expressing neural stem cells facilitates their neural differentiation. There are potential therapeutic applications of optogenetics in cardiac pacemaking, muscle regeneration/maintenance, locomotion recovery for the treatment of muscle paralysis due to motor neuron diseases such as amyotrophic lateral sclerosis (ALS). Optogenetics would also facilitate maturation, network integration of grafted neurons, and improve the microenvironment around them when applied to stem cells.

**Keywords**

Cardiac muscle · Smooth muscle · Skeletal muscle · Myoblast · Myocyte · EC coupling · T tubule · Sarcomere · Cardiac pacemaker · Spinal cord injury · Amyotrophic lateral sclerosis · ALS · Stem cell · iPSC · ESC · NSC · Neural graft · Neurogenesis · Microenvironment · $Ca^{2+}$

T. Asano
Graduate School of Medical and Dental Sciences, Tokyo Medical and Dental University, Bunkyo-ku, Tokyo, Japan
e-mail: asano.cbio@tmd.ac.jp

D. B. L. Teh
Department of Biochemistry, Yong Loo Lin School of Medicine, National University of Singapore, Singapore, Singapore
e-mail: danielteh@nus.edu.sg

H. Yawo (✉)
The Institute for Solid State Physics, The University of Tokyo, Kashiwa, Japan
e-mail: yawo_hrm.277-8581@issp.u-tokyo.ac.jp



H. Yawo et al. (eds.), *Optogenetics*, Advances in Experimental Medicine and Biology 1293,
https://doi.org/10.1007/978-981-15-8763-4_23

## Abbreviations

| | |
|---|---|
| ALS | Amyotrophic lateral sclerosis |
| DA | Dopaminergic |
| EFS | Electrical field stimulation |
| ESC | Embryonic stem cell |
| fMRI | Functional magnetic resonance imaging |
| iPSC | Induced pluripotent stem cell |
| NSC | Neural stem cell |
| OS | Optical stimulation |
| SFO | Step-function opsin |

## 23.1 Introduction

Over a decade many researches benefited from optogenetics, both optical manipulation and functional imaging, in the field of neuroscience with three technical improvements: (1) generation and selection of the optimal molecular tools for neuroscience, (2) targeted expression of such molecular tools in a specific group of neurons, and (3) targeted illumination/imaging of multiple neurons in parallel with high spatiotemporal precision. These novel techniques brought a revolution in neuroscience that could not be attained previously, e.g., the activation/inhibition of an individual neuron to reveal the cause–result relationship between neural activity and behavior, the orchestration of multiple neurons in the brain to the complex inputs (Deisseroth 2015). No doubt, the neural mechanisms underlying mind and consciousness will be revealed in the future using optogenetics with computer sciences. Numbers of neural disabilities can be attributed to the loss of functional connectivity between the central nervous system and the peripheral organs. Optogenetics may connect these two parts by light to be applied for the treatments of spinal cord injury and muscle atrophy as well as artificial retina and cochlear implants. Similarly, the brain and machine or computer will be connected by light using optogenetics, that is, the brain–machine interface (BMI) and the brain-computer interface (BCI). Neurodegenerative diseases, such as Parkinson's disease and Alzheimer's disease, are attributed to the loss of function of neurons in the brain. On the other hand, psychiatric diseases, such as schizophrenia, bipolar disorders, and autism spectrum disorders, are thought to be caused by dysfunction of the neural network. Therefore, optogenetics will reveal the functional disorders underlying these diseases and correct them by the optical tuning of neural network activities.

Recently, optogenetics has expanded beyond neuroscience to nonneuronal cells, such as muscle cells (Arrenberg et al. 2010; Asano et al. 2012), glial cells (Jung et al. 2019), and stem cells (Steinbeck et al. 2015). Nonetheless, despite these expansions, optogenetic toolbox remains as an explorative technology to elucidate the loss or gain functions of a specific activity-dependent event in a single cell or a group of cells in neural circuitry. This chapter describes the current progress of basic research and with potential therapeutic applications, especially focused on the optical manipulation of muscle cells and neural stem cells using microbial rhodopsin as a light-sensitive molecule. The non-rhodopsin light-sensitive molecules and their application for cell physiology are considered in Chapters 10, 11, and 13–16.

## 23.2 Muscle Optogenetics

The innovative optogenetics using genetically encoded light-sensitive molecules has been extensively employed to observe and control cellular functions in the living cell. Notably, this technique is well suited to investigate the local and transient dynamics of materials, energy, and information in a cell or tissue, which has been hard to resolve using electrophysiological, pharmacological, and biochemical methods. One of the widely used optogenetic tools is channelrhodopsin-2 (ChR2), a light-driven cation channel from the green alga *Chlamydomonas reinhardti* (Nagel et al. 2003). So far there have been developed various variants of rhodopsin-based optogenetic actuators/silencers with improvements of membrane expression, photosensitivity, wavelength specificity, ion selectivity, and kinetics by genome mining

and/or molecular engineering approaches, such as point mutation and chimeric fusion of domains from different photosensitive protein (Yawo et al. 2013; Schneider et al. 2015; Deisseroth and Hegemann 2017). Since the contraction of skeletal, cardiac, and smooth muscle cells is mainly regulated through their membrane potential, several studies have been demonstrated to up- or downregulate the muscle contraction directly or indirectly using optogenetic actuators or silencers with defined stimulation patterns and intensities.

### 23.2.1 Optogenetic Stimulation of Cardiac and Smooth Muscles

The electrophysiological properties of cardiac muscles were reported to be remarkably modulated by light. Bruegmann et al. (2010) have shown the light-induced depolarization and $Ca^{2+}$ transient in vitro in the cardiomyocytes derived from a stable transgenic embryonic stem cell (ESC) line expressing one of ChR2 variants, ChR2 (H134R), and the optical pacing of the heartbeat in vivo in the transgenic mice generated from ChR2 (H134R)-expressing ESCs. Arrenberg et al. (2010) achieved to modulate cardiac pacemaker activities in a heart expressing ChR2 (H134R) or chloride pump halorhodopsin (NpHR) from transgenic zebrafishes with patterned illumination using light-sheet microscopy. Thus large-scale and three-dimensional mapping of regions triggering the cardiac rhythm was made with high spatial–temporal resolution.

Optogenetic pacing using a cell delivery strategy has been explored using the donor cells expressing ChR2, such as HEK cells (Jia et al. 2011), 3T3 cells (Nussinovitch et al. 2014), and human ESC-derived cardiomyocyte (Abilez et al. 2011), which form coupling electrically with host natural cardiomyocytes through gap junctions. The light-dependent activity of the donor cells was conducted to the native cardiomyocytes and, eventually, regulated the cardiac rhythm. Using a model mouse expressing the light-driven proton pump ArchT in cardiomyocytes, ventricular arrhythmia was terminated by the epicardial illumination of green light (Funken et al. 2019).

The contractility of smooth muscles was also regulated by optogenetics. Wu et al. (2015) generated a transgenic mouse strain that expresses ChR2 (H134R) in the vascular smooth muscle cells of various tissues, of which optical stimulation induced vasoconstrictions of arterial walls. At the low intensity of light, the contraction was induced by $Ca^{2+}$ entry through voltage-gated $Ca^{2+}$ channels with subsequent involvement of plasmalemmal depolarizing channels (TMEM16A and TRPM) and intracellular IP3 receptors. In contrast, the higher intensity evoked a significant $Ca^{2+}$ influx directly through channelrhodopsins (Rorsman et al. 2018). Otherwise, either ChR2 (H134R), ChR2 (C128S/D156A), a stable step-function opsin (SSFO), or NpHR was expressed in the bladder smooth muscles (Park et al. 2017). A blue light pulse (1 s) elevated the pressure of the bladder expressing SSFO for up to 60 s until illumination with a yellow light. On the other hand, the NpHR-expressing bladder was relaxed by yellow light even under overactivation by prostaglandin E2 (PGE2).

### 23.2.2 Optogentic Stimulation *Via* Motor Neurons

Electrical field stimulation (EFS) is frequently used for the control of muscle contraction indirectly through the excitation of motor nerves innervating the muscle as well as directly through excitation of the muscle fibers themselves. However, this method is usually accompanied by nonselective excitation of other motor, sensory, and autonomic nerves in the vicinity of electrodes, particularly the large and thick motor nerves innervating fatigable fast muscles. It is also unsuitable for the treatment of muscle weakness caused by motor neuron dysfunction such as amyotrophic lateral sclerosis (ALS).

In contrast, optogenetic stimulation of motor systems generally overcomes rapid muscle fatigue, lack of specificity for the cell types, and imprecision of the number and spatial location of target cells. Indeed, light-controlled motor activities of whisker deflection were demonstrated by stimulation of the ChR2-

expressing motor cortex through implanted optical fiber in the brain (Aravanis et al. 2007). The optical stimulation of muscle-specific spinal motor neurons expressing ChR2 enabled controlled muscle contractions so as recruitment of motor units proceeds in the physiological recruitment sequence from smaller, fatigue-resistant motor units to larger, fatigable motor units being dependent on light intensities given on the sciatic nerve (Llewellyn et al. 2010). Alternatively, the ESC-derived motor neurons that express ChR2 were transplanted into the injured sciatic nerve in an adult mouse (Bryson et al. 2014). Several weeks after, the grafted neurons extended axons through nerve branches to innervate the hind–limb muscles which were previously denervated. Optical stimulation of engrafted ChR2 motor neurons in vivo restored muscle function, once paralyzed, in a controlled manner. Optical stimulation *via* motor neurons has significant advantages of high selectivity that allows limiting the activation only in the target cells genetically encoded light-sensitive proteins without activating sensory neurons as caused by EFS. However, it is generally accepted that skeletal muscles remain unrecoverable of their motor functions after complete and permanent denervation because they become resistant to reinnervation over time.

### 23.2.3 Optogenetic Stimulation of Skeletal Muscle

Skeletal muscles play essential roles in the movement, postural retention, heat production, and metabolic regulation for maintaining homeostasis and physical activities. The motor input depolarizes the plasma membrane (sarcolemma) at the neuromuscular junction to evoke an action potential in a manner dependent on the voltage-gated $Na^+$ channels. The action potential is conducted along sarcolemma and depolarizes the membrane of transverse tubules (T tubules), sarcolemmal invagination penetrating radially in the muscle at regular intervals. Although the T tubule membrane does not have the voltage-gated $Na^+$ channels, its depolarization is sensed by the dihydropyridine receptors (DHPRs), $Ca_v1.1$ calcium channels on it. Finally, the muscle contraction is achieved via excitation–contraction (EC) coupling (Numa et al. 1990). That is, the depolarization-induced conformational changes of DHPRs are coupled to the gating of the ryanodine receptor, which is responsible for the rapid release of $Ca^{2+}$ from the sarcoplasmic reticulum (SR) to the cytoplasm, an event that triggers subsequent muscle contraction. Therefore, optogenetics enables the direct depolarization of sarcolemma/T tubule membrane to evoke muscle contraction associated with light stimulation even without neural inputs.

The direct optogenetic stimulation of mammalian skeletal muscle cells in vitro was firstly shown in murine skeletal muscle C2C12 myoblasts expressing ChR2 (Asano et al. 2012). These genetically engineered C2C12 cells were fused with non-engineered C2C12 cells to form a multinucleated myotube, which expressed ChR2 uniformly throughout in the sarcolemma. Illumination of pulsed blue LED light evoked an action potential and eventually generated the contraction synchronized with the illumination in a manner dependent on the intensity and duration of light pulses, although it possibly activated EC coupling directly through depolarization of T tubule membrane (Asano et al. 2015). These photosensitive myocytes responded twitch-like contractions at low frequency (1–4 Hz) and tetanus-like sustained contractions at high frequency (5–10 Hz) of illumination patterns like those by the electrical stimulation.

The optical control of skeletal muscle tissue was also tested in intact muscle from transgenic mice, which were genetically engineered to express ChR2 (H134R) in all skeletal muscle cells (Bruegmann et al. 2015; Magown et al. 2015). These studies confirmed the feasibility of generating light-induced muscle contraction in isolated fibers of the flexor digitorum brevis muscle and in the hind limb, respectively, and to transmit enough light through muscle to evoke activations of multiple muscle fibers. The amplitude of twitch and tetanic contraction force was modulated by varying duration and intensity of the light pulse.

### 23.2.4 Optogenetic Control of Myogenesis

During development/regeneration of a skeletal muscle, the fusion of proliferated myoblasts generates primary myotubes and then immature myocytes without innervation of motor neurons. However, full maturation of myocytes with the development of T tubules and sarcomere structures, tandem arrays of minimum contractile units consist of contractile and cytoskeletal proteins, is dependent on a motor nerve supply in birds and mammals (Jacobson 1991). In addition to the trophic influences from innervating motor nerves, the development and maintenance of muscle contractility are dependent on the activity of neuromuscular synapse. Indeed, muscle fiber stimulation with electrical, mechanical, or pharmacological methods, which mimic motor neuron inputs, facilitate the maturation of developing muscles as well as the maintenance of contractility. It is thus hypothesized that the oscillation of membrane potential with a particular pattern facilitates the T tubules formation and sarcomere assembly to form mature muscle fibers (Fig. 23.1).

The above hypothesis was tested by direct depolarization of sarcolemma using optogenetics (Asano et al. 2015). In this experiment, photosensitive myotubes were made from the C2C12 myoblasts expressing a chimeric channelrhodopsin variant, ChRGR, which is sensitive to cyan light. Cyclic optical stimulation (OS) by cyan LED flash at about 1 Hz effectively induced the morphological maturation, T tubules formation, and sarcomere assembly, as well as contractility of myocytes in 2 h. The OS-dependent myogenesis was not affected by (*S*)-(−)-Bay K 8644, an agonist of L-type $Ca^{2+}$ channels (LTCCs), but inhibited by nifedipine, an antagonist of LTCCs and an inhibitor of EC coupling. It was also strongly inhibited by the removal of extracellular $Ca^{2+}$ and thapsigargin, an inhibitor of $Ca^{2+}$ ATPase in sarcoplasmic/endoplasmic reticulum (SERCA) whereas not enhanced by the increase of extracellular $Ca^{2+}$ (Fig. 23.2).

Probably, T tubule invagination, EC coupling mechanism, and sarcomere assembly proceed coordinately during activity-dependent myogenesis (Fig. 23.3). The depolarization of the primary T tubule membrane, either directly by light or indirectly by the conducting action potential in sarcolemma, triggers the mobilization of $Ca^{2+}$ from SR through the EC coupling mechanism. The resultant rise of cytoplasmic $Ca^{2+}$ promotes the self-organization of sarcomere as well as the further invagination of the T tubule system with the maturation of EC coupling mechanism, while the intraluminal $Ca^{2+}$ is recovered through $Ca^{2+}$ uptake by SERCA and store-operated $Ca^{2+}$ entry (SOCE) by Stim1-Orai system (Prakriya and Lewis 2015). It is possible that the SOCE-dependent $Ca^{2+}$ entry from extracellular milieu is also involved in the myogenesis. The depletion–refilling cycle of the intracellular $Ca^{2+}$ store may be one of the determinants of the optimal frequency of membrane potential oscillation. This scheme would be tested in the future with optogenetics manipulating intracellular $Ca^{2+}$ under spatiotemporal precision (Asano et al. 2018).

### 23.2.5 Potential Therapeutic Applications of Muscular Optogenetics

Optogenetics technology also has the potential for future translational applications that allow specific targeting to the tissue/cell type or the locations with minimal invasiveness and energy in principle. Researchers have verified the feasibility of optogenetics as a novel therapeutic candidate for cardiac and skeletal muscle dysfunctions to overcome limitations of electrical stimulation. Optogenetically multisite pacing of rat heart was attained at different beating frequencies in vivo and ex vivo (Nussinovitch and Gepstein 2015). A further experiment has shown optogenetic pacing of mouse heart by expressing ChR2 in cardiomyocytes using adeno-associated virus (AAV)-based gene delivery (Vogt et al. 2015). In this work, ChR2 was detected with high selectivity in cardiomyocytes of interest with minimal expression in other organs, such as diaphragm and liver.

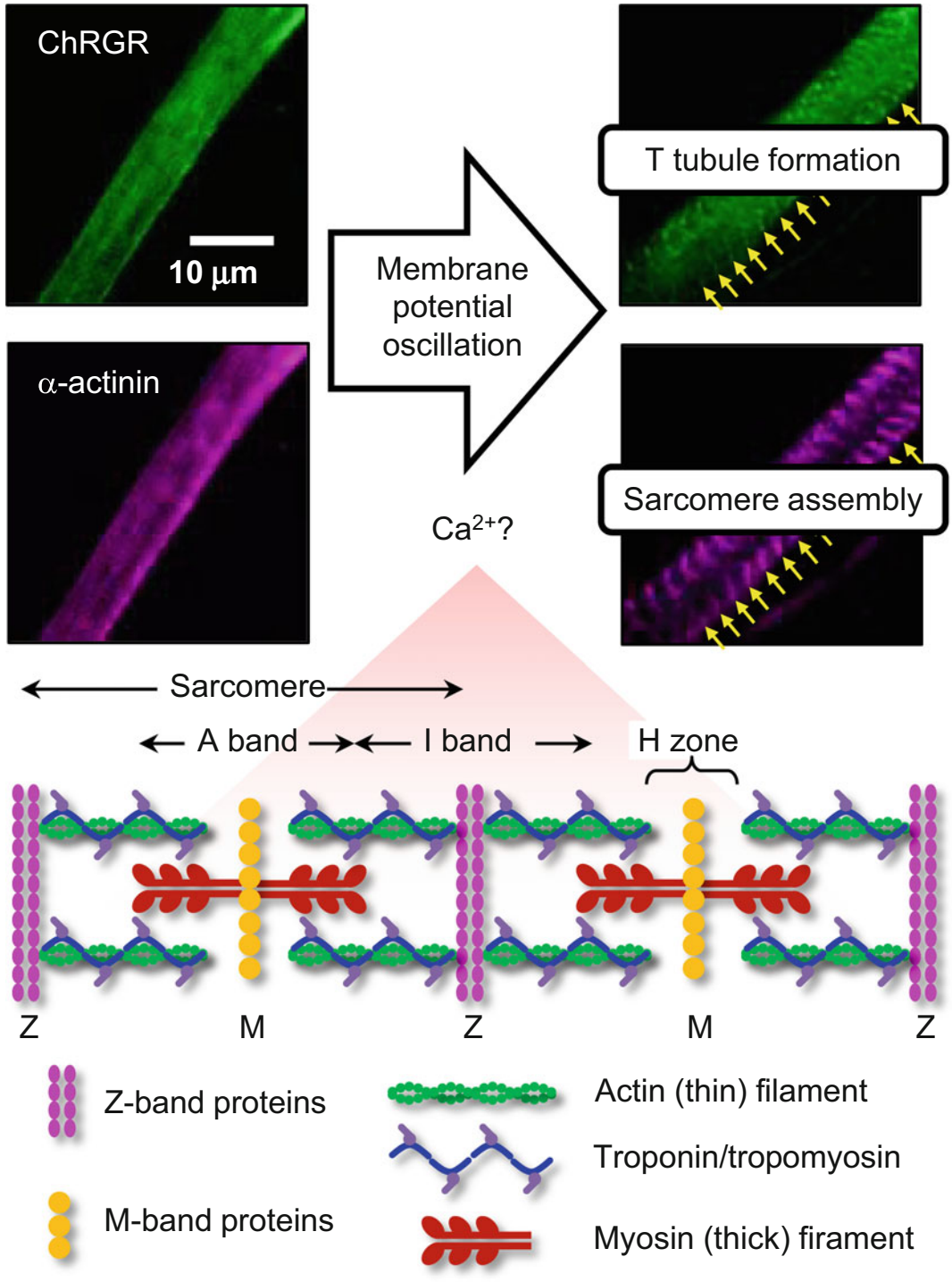


**Fig. 23.1** Activity-dependent maturation of skeletal muscle cells. Optogenetics was applied to generate the oscillation of membrane potential and facilitated T tubule formation and sarcomere assembly (Upper panels). It is hypothesized that the rise of intracellular $Ca^{2+}$ triggers these processes

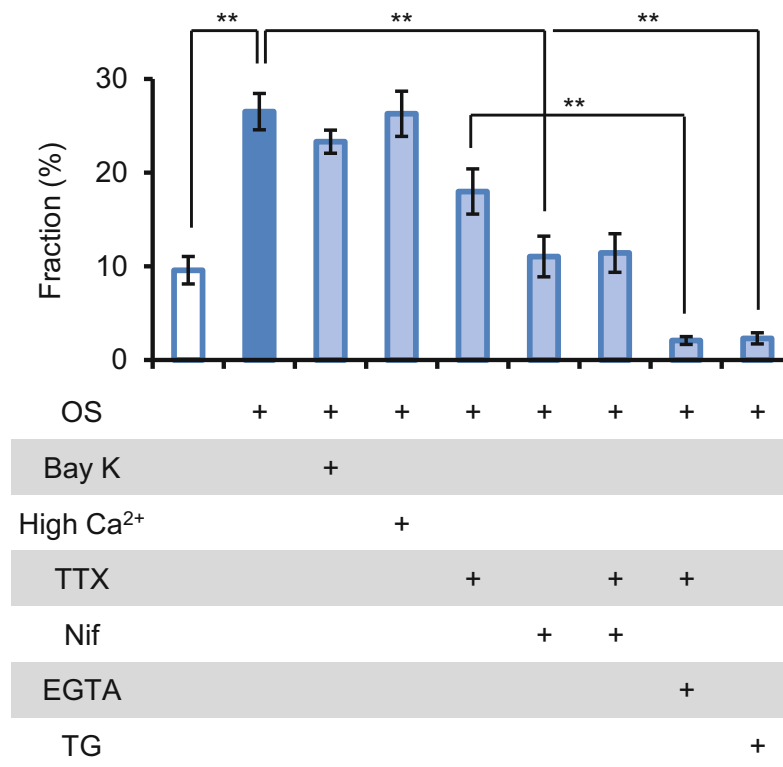


**Fig. 23.2** Involvement of EC coupling for the sarcomere self-organization. The fraction (%) of C2C12 myocytes with sarcomere structure was compared. $^{**}p < 0.01$, one-way ANOVA. Abbreviations: *OS* optical stimulation, *Bay K* (*S*)-(−)-Bay K 8644 (an agonist of L-type $Ca^{2+}$ channels), *High* $Ca^{2+}$ high extracellular $Ca^{2+}$ (10 mM), *TTX* tetrodotoxin (a $Na^{+}$ channel blocker), *Nif* nifedipine (an antagonist of L-type $Ca^{2+}$ channels and EC coupling), *EGTA* 10 mM (a chelator of $Ca^{2+}$), *TG* thapsigargin (an inhibitor of sarcoplasmic/endoplasmic reticulum $Ca^{2+}$ ATPase, SERCA)

Denervation of skeletal muscle causes atrophy with a reduction in muscle mass due to physical inactivity and results in paralysis and loss of motor function in the denervated muscle. Electrical stimulation can produce muscle activation for maintaining the mass and maximum force generation. Unfortunately, electrical stimulation is usually ineffective for the recruitment of motor functions when the peripheral nerve is injured or dysfunctional, rather it simultaneously stimulates nearby sensory nerves to generate unpleasant sense such as pain. On the other hand, it is possible to discriminate motor nerves from other groups by illuminating the defined stimulation region precisely. For example, the localized illumination of individual intralaryngeal muscle, which expressed ChR2, was demonstrated to lead selectively opening and closing of the vocal cord, which is essential for breathing, protection from aspiration as well as producing voices (Bruegmann et al. 2015). Furthermore, daily stimulation through transcutaneous illumination of hindlimb muscle fibers expressing ChR2 within the sarcolemma and T tubules was sufficient to attenuate the denervation atrophy and to maintain the contractile force even after sciatic nerve lesion (Magown et al. 2015). Thus, for the restoration of muscle motor functions, direct skeletal muscle activation using optogenetics could have advantages over EFS, such as the pain-free stimulation and the requisition of reinnervation with motor nerves. If the light-sensitive actuators of different spectral sensitivity are specifically expressed in the different types of muscle fibers such as slow and fast muscle fibers, the precise control of muscle contraction would be enabled with mimicking the physiological pattern. Also, optogenetic silencing would be able to prevent muscle activities from spasticity through overactivation of spindle afferents.

Motor nerve inputs affect the innervating muscle cells with two major roles, the maturation/maintenance of structure/molecular organization and the signals for muscle contraction. These

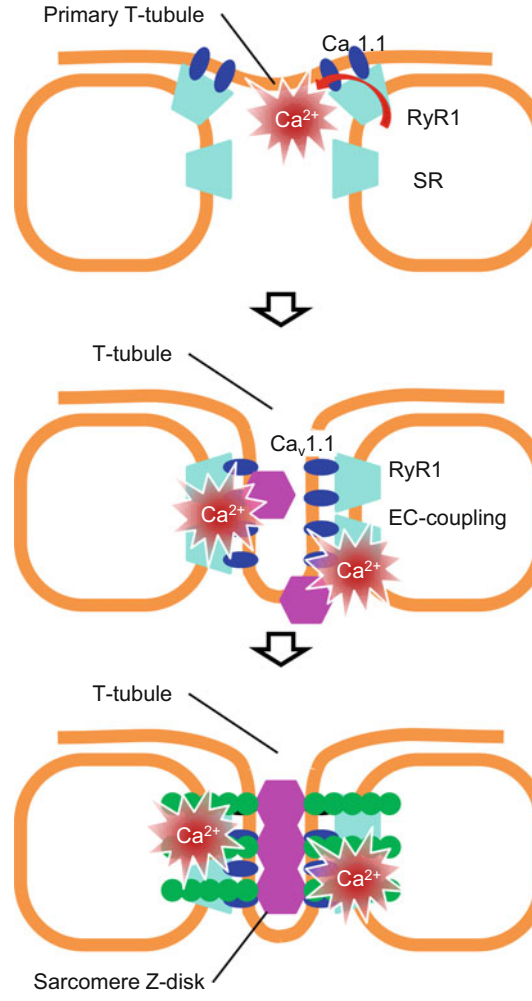


**Fig. 23.3** $Ca^{2+}$-dependent coordination of T tubule invagination, EC coupling mechanism, and sarcomere assembly (hypothesis). The depolarization of primary T tubule membrane triggers the mobilization of $Ca^{2+}$ from SR through EC coupling mechanism (top). The resultant rise of cytoplasmic $Ca^{2+}$ promotes the formation of T tubule system with the maturation of EC coupling mechanism (middle) and induces the self-organization of sarcomere (bottom)

roles can be replaced by the all-optical approach (Fig. 23.4) without further physical and biochemical treatments if optogenetics is applied for the myoblasts since light-sensitive muscle cells with contractile ability were effectively generated by light (Asano et al. 2015). Therefore, the optogenetics of myoblasts/satellite cells is promising for the treatment of muscle paralysis with atrophy due to peripheral nerve/spinal cord injury, motor neuron diseases such as ALS, myasthenia gravis, and so forth. The cultured muscle cells, either cardiac, skeletal, or smooth, may become an obviously useful experimental model system in combination with optogenetics for both primary and development researches of bioproduction, drug development, toxicology test, and differentiation and regeneration mechanisms.

### 23.2.6 Future Perspectives of Muscle Optogenetics

Muscular optogenetics has significant advantages in selective modulation of the activity of cells/tissues with the high temporal, spatial, and genetic specification. The use of this technology enables bidirectional manipulation of muscle fiber physiology such as the sarcolemmal membrane potential and subsequent EC coupling with

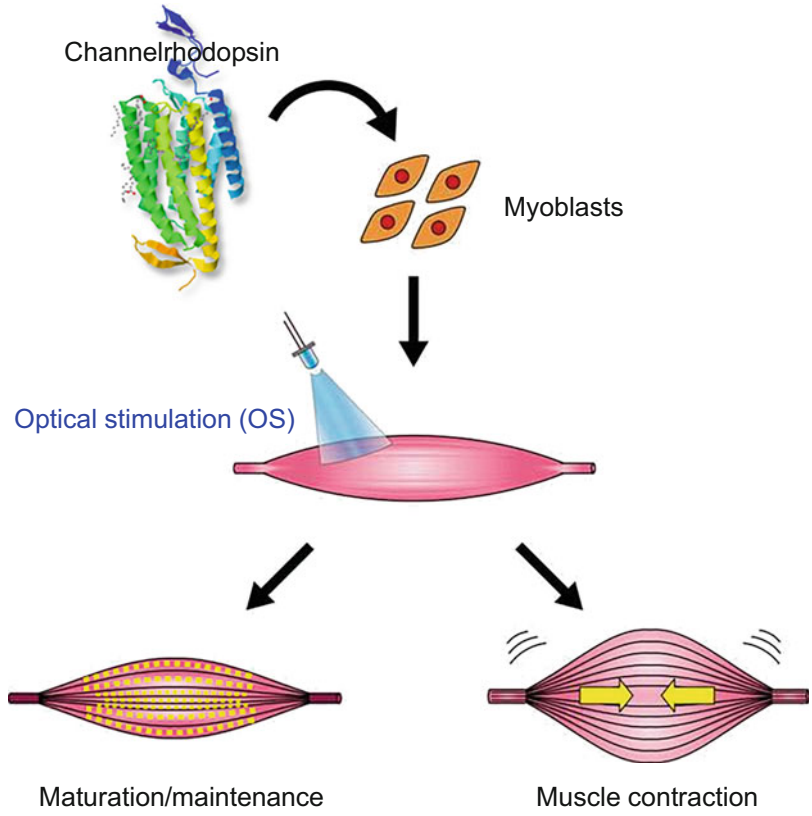


**Fig. 23.4** All-optical reconstruction of skeletal muscles. Light-sensitive immature muscle cells are generated from the myoblasts which are engineered to harbor channelrhodopsin gene. The optical stimulation (OS) both facilitates their maturation/maintenance and becomes the signals for muscle contraction

several potential medical applications. Moreover, intracellular signaling cascades, metabolism, and gene expression could also become the targets of optogenetic manipulation by using light-sensitive molecular switches and/or by localized expression into specific subcellular compartments. Indeed, several optogenetic tools have been provided to study specific intracellular signals using photosensitive proteins targeted to subcellular compartments (Rost et al. 2017). Retrograde information from a muscle cell to the innervating neuron could also be studied in the future using optogenetics.

Asano et al. (2018) recently developed novel organelle optogenetics that allows specific and light-dependent regulation of $Ca^{2+}$ release from endoplasmic/sarcoplasmic reticulum (ER/SR), a major intracellular $Ca^{2+}$ store. This ER/SR optogenetics, in combination with plasma membrane optogenetics should overcome the technical limitations in differentiating between two significant sources of $Ca^{2+}$ mobilization, the extracellular milieu, and the internal $Ca^{2+}$ stores to promote cell physiology involved in the spatiotemporal dynamics of intracellular $Ca^{2+}$ (Iino 2010). Simultaneous optical measurement of intracellular/intraluminal $Ca^{2+}$, membrane potentials of sarcolemma, T tubules, and organelles under spatiotemporal precision will no doubt open a new field of muscle physiology and pathophysiology (Toettcher et al. 2011). Such interrogation is also necessary to control the delicate muscle activity such as tension, stretch, and flexor–extensor balance under the loss of feedback by the neural network.

Once technical advancement of gene delivery and light delivery can be addressed, in the future, the optogenetic strategy may be provided a clinical option for cardiac, skeletal, and smooth muscle dysfunctions. However, it has been reported

that long-term and high-level expression of ChR2 in neocortex potentially has a risk of detrimental effects on axonal structure, axonal targeting, and cortical circuits (Miyashita et al. 2013). Therefore, careful regulation of opsin expression is necessary to exploit optogenetics for experimental researches and therapeutic applications.

Challenges have been made to engineer devices integrated with and powered by biological components (bio-actuators) that convert energy into motion using skeletal/cardiac muscle to understand the design rules that govern the structure and function of natural biological systems to develop artificial human organ and reduce stiffness and energy consumption (Ricotti and Menciassi 2012). The wireless drive of muscle-powered actuators/microdevices has been developed using the light-sensitive muscle fibers derived from C2C12 myoblasts expressing ChR2 (Sakar et al. 2012; Raman et al. 2016).

## 23.3 Stem Cell Optogenetics

Similar to the myoblasts, optogenetics has been applied to various stem cells, which are destined to generate the specific tissues and cells, and multipotent/pluripotent cells such as embryonic stem cells (ESCs) and induced pluripotent stem cells (iPSCs). Probably, the first known optogenetics application in stem cell research was the transplanted ChR2-expressing neurons derived from human ESCs of which functional integration and plasticity were investigated by light under spatiotemporal precision (Weick et al. 2010). An expansion of this concept was used to study the bidirectional synaptic connectivity between host and grafted dopaminergic (DA) neurons derived from the neural stem cells in the ventral midbrain of embryonic mice (Tønnesen et al. 2011). When the host striatal neurons expressing ChR2 were excited by light, no direct synaptic responses were observed in the grafted DA neurons. However, when the activity of host striatal neurons expressing halorhodopsin was suppressed by light, the frequency of spontaneous excitatory inputs was increased in grafted DA neurons. On the other hand, activation of grafted ChR2-expressing DA neurons suggested intra-graft excitatory connections through the constant increase in spontaneous excitatory signals. This phenomenon may be attributed to the potential existence of direct cortical excitatory inputs to the grafted neurons, which are minimized by the inhibitory collateral inputs from striatal neurons. Silencing of the host striatal neurons, therefore, increased the excitatory cortical inputs from the host to the DA neuron transplants. Optogenetics thus elucidated a complex interplay of connectivity between the grafted DA neurons and the host striatal neurocircuitry. Alternatively, graft-to-host connectivity was directly confirmed using the neurons derived from ChR2-engineered human ESCs, which were transplanted to the ex vivo model of brain slices. Then, the grafted neurons were selectively excited by light without affecting the host neurons. In this manner, the establishment of graft-to-host connectivity was revealed by multi-electrode array recordings from hippocampal slice culture (Piña-Crespo et al. 2012). In the above studies, ChR2/NpHR was not expressed in the undifferentiated cells because its transcription was under regulation by pan-neuronal synapsin I promotor, which is only activated at fate determined stage or later of differentiation.

In an animal model of Parkinson's disease, mesencephalic dopaminergic (DA) neurons were made from human ESCs expressing NpHR (Steinbeck et al. 2015). Although the grafted DA neurons recovered motor functional deficit in the behavioral outcome, their silencing by light reintroduced motor deficit phenotype in these mice. These human-derived grafted neurons innervated their axons into the mouse striatum to modify the glutamatergic transmission like endogenous mesencephalic DA neurons.

The significance of functional neurocircuitry made by grafted neurons was investigated in a larger scale imaging using functional MRI (fMRI) in combination with optogenetics (Byers et al. 2015). fMRI provided an additional noninvasive paradigm that can be used to directly observe brain's activity upon excitation or inhibition of grafted neurons by light. Although ChR2 was expressed in the human ESCs early on the stem

cell stage because of the use of *EF1α* promoter, the effectiveness of grafts was mainly investigated after their differentiation.

### 23.3.1 Neural Stem Cell Optogenetics

Critically though, many of the earlier works using optogenetic stem cells were aimed to regulate the activity of differentiated neurons derived from them as the expression of exogenous genes was driven by neuronal promoter such as synapsin I promoter. On the other hand, with the use of *EF1α* promoter, which can drive expression of transgene stably even in the undifferentiated cells, allows the potential control of physiological function in the stem cell itself by light. Indeed, the ChR2-expressing neural stem cells (NSCs) can be depolarized in membrane potential by blue light even at undifferentiated stages to modify its fate (Stroh et al. 2011; Daadi et al. 2016), probably through activation of L-type $Ca^{2+}$ channels (D'Ascenzo et al. 2006). However, the magnitude of light-dependent depolarization of NSCs varies over differentiation stages and among individual cells, even in the same stage.

What is the consequence of light-dependent depolarization of membrane potential? Chronic optical stimulation (OS) over days facilitated the neural differentiation of ChR2-expressed ESCs with the increased production of neuronal cells (Stroh et al. 2011). Animal model grafted with ChR2-expressing NSCs also showed that neurogenesis and differentiation of NSCs could be enhanced even in vivo with blue light excitation (Daadi et al. 2016). Critically, it was suggested that optical stimulation of these grafted ChR2-expressing NSCs reduced the expression of inflammatory genes, which could modulate viable microenvironment to incorporate the grafted cells in host neural networks and to help tissue repair. Therefore, optogenetic stimulation of NSCs may modulate the microenvironment, such as the extracellular matrix through an autocrine, paracrine, or both since the survival and differentiation of NSCs are dependent on the host's cue for development, such as the network activity and chemical stimuli. It has been shown that the microenvironment critically regulates the repair conditions and often is the primary reason for the failure of repairs or axon regrowth (Anderson et al. 2016). Optogenetic stimulation can also control the physical characteristics of developing stem cells. Repetitive OS reduced the migratory activity of ChR2-expressing NSCs, as observed with the advancement of neuronal differentiation (Köhidi et al. 2017).

The direct depolarization of stem cells by chemical for instance, through the L-type $Ca^{2+}$ channel agonists or high $K^+$, has differential effects on NSCs: increase of neuronal fraction over other cell types through enhanced survival and maturation with minimal or no effects on the NSC proliferation (Teh et al. 2014). Consistently, in the dentate gyrus of the hippocampus in vivo, chronic OS during neurogenesis was shown to enhance the survival and maturation of the ChR2-expressing newborn neurons in a manner dependent on L-type $Ca^{2+}$ channels with recovery from cognitive deficits (Zhao et al. 2018). Optogenetic direct stimulation also disrupted the self-renewal capability and inhibited stem cell proliferation (Wang et al. 2019) as well as facilitated the neurogenesis (Teh et al. 2020), probably due to the early exit of the mitotic stem cell phase to immature fate-determining neuronal phenotypes with upregulation of genes involved in neural phenotype in an activity-dependent fashion. Furthermore, not only neurons but glial cells, astrocytes, and oligodendrocytes are differentiated from NSCs (Fig. 23.5). These developing glial cells may interact with the neuronal population of the host tissue and grafted stem cells to help neurogenesis. It is also possible that the grafting of the mixture of glial progenitors and neurons could better support the survival and development of transplants in host tissue. Are these functions of glial cells also regulated by its membrane potential? Such an issue will be studied in the future with optogenetics using NSCs such as those shown in Fig. 23.5.

Graft to host neural circuitry connectivity can also be achieved using iPSC at undifferentiated stages. However, human iPSCs, when grafted in

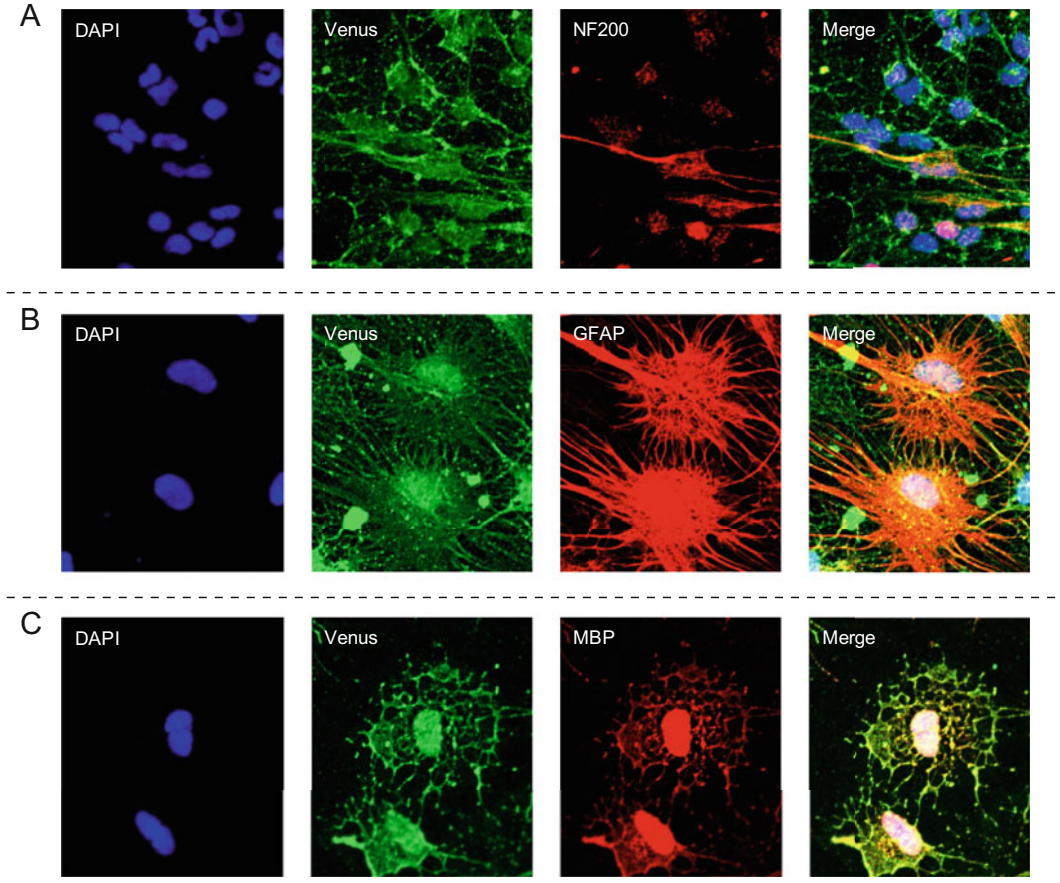


**Fig. 23.5** Generation of light-sensitive glia as well as neurons from neural stem cells (NSCs), which were optogenetically modified to express ChRFR (C167A), one of the step-function opsins, conjugated with a green fluorescent protein, Venus, under CAG promoter. (**a**) Neurons immunoreactive to a neuronal marker, neurofilament (NF) 200 (red). (**b**) Astrocytes immunoreactive to glial fibrillary acidic protein (GFAP, red). (**c**) Oligodendrocytes immunoreactive to myelin basic protein (MBP, red)

rodent at self-renewing neuroepithelial stem cell stage, require an extended time for maturation and afferent synaptogenesis for the establishment of neurocircuitry (Avaliani et al. 2014). Although the afferent synapses were scant within 5 months after transplantation, its number increased significantly in the following months. Thus the presence of a critical window period of sensitivity and integration is suggested in between these two periods. Most of the transplants were differentiated into GABAergic neurons innervated by the afferent synapses, suggesting that host circuitry can regulate the activity of iPSC-derived GABAergic neurons.

### 23.3.2 Associate Techniques for Stem Cell Optogenetics

Although conventional optogenetic light excitation system is available in electrophysiology setup, this system will have to be modified to cater to lighting technologies more suited for in vitro chronic optogenetics in incubation condition. Stroh et al. (2011) reported the first work on stem cell optogenetics using a robotic system attached to a microscope incubation system that can deliver customized excitation to a specific region of interest in multi-well plates. There are also other publications on the in vitro

optogenetics excitation model, one being applied in compartmentalized culture system of primary neurons where their soma and axons were separated in light impermeable microchambers (Lee et al. 2017; Blasiak et al. 2018). Optogenetic stimulations of these neurons enhanced the formation of myelinated fragments from engrafted oligodendrocyte precursor cells (OPCs) in their axons (Blasiak et al. 2018). Moreover, the focal illumination on either soma or axon was sufficient to enhance myelination, which may provide insight on how optogenetics can be potentially applied to promote the activity-dependent remyelination process (Gibson et al. 2014). Wide-field optical stimulation (OS) system for in vitro setting can also be achieved by LED arrays in combination with a diffuser lens, which illuminate the culture plate from a certain distance although the power density is not homogenous at the bottom of culture plate (Asano et al. 2015; Jung et al. 2019).

Since the bicolor step-function opsins (SFOs) are highly sensitive to light (Berndt et al. 2009; Hososhima et al. 2015; Sineshchekov et al. 2016), they are more feasible to stem cell optogenetics than conventional ChR2 both in vitro and in vivo by the reasons: (1) the low irradiance reduces potential phototoxicity and heating, (2) the SFO-expressing stem cells can be manipulated by light even transplanted deep in the tissue, and (3) the same energy can photostimulate transplants of a larger volume (Sidor et al. 2015). Usually, the dual-wavelength optical system, one for activation and another for deactivation, is employed. However, it is not absolutely necessary for stimulating cells at a low frequency determined by the photocycle period of SFO (Igarashi et al. 2018).

A virus-dependent gene delivery could not eliminate the possibility for proliferating cells such as ESCs, iPSCs, and NSCs to become carcinogenic because of the viral components (Karra and Dahm 2010). Therefore, nonviral transfection methods might be ideal for cell transplantation therapy in the future. On the other hand, several drawbacks also arise when a foreign gene is inserted into the host cell genome to enable stable expression of the transgene (Woodard and Wilson 2015). For example, some integration methods, such as spontaneous integration, are associated with transcription variation as a result of position effects. The integrated transgene is often silenced, particularly when multiplicated in sequence. The excessive and uncontrolled insertion of transgenes often induces mutations in the host genome. Among various nonviral transfection methods, the *piggyBac* transposon system has several advantages, such as no limit in cargo size, footprint-free delivery, and reversible removal of transgenes. Indeed, a gene coding one of SFO variants of channelrhodopsin was stably inserted in a genome of an NSC culture cell line using a *piggyBac* transposon system without affecting cell proliferation and differentiation (Teh et al. 2020).

### 23.3.3 Potential Therapeutic Applications of Stem Cell Optogenetics

It was not until 2015 that two major critical events vastly influence optogenetics translation from bench to bedside directly and indirectly. Firstly, the FDA approval being given to RST-001, which is an AAV2-based vector carrying ChR2 gene, for the safety and efficacy studies of potential optogenetics therapeutics in patients with retinitis pigmentosa (Adamantidis et al. 2015; Gordon et al. 2019). Secondary, the first clinical trial for iPSC to treat Parkinson's disease, which began recruiting in Japan since 2018 (Takahashi 2019). A year prior, the same team reported the breakthrough of transplanted human iPSC-derived DA neurons in primate Parkinson's disease model by showing improved locomotor activities in primates and histological evidence of mature transplanted DA neurons connectivity to host striatum (Kikuchi et al. 2017). The impact of this research suggests that the feasibility of functional motor recovery in the primates' model, which is translatable to humans.

Accumulating evidence obtained from in vitro and in vivo experiments strongly suggest that the stem cell-based therapy can be better improved with optogenetics in combination than alone (Mirzapour Delavar et al. 2016). Subtle manipulation of transplanted cells would be enabled by light to adjust their activity to the physiological

requirements of the patient, such as the cardiac pacemaker (Boyle et al. 2018). Furthermore, stem cell optogenetics will elucidate how the transplanted cells were working in the patient in combination with other techniques, e.g., the study of interconnectivity between grafted neurons and host brain using fMRI.

### 23.3.4 Future Perspectives of Stem Cell Optogenetics

Stem cells, such as iPSCs, differentiate to form a 3D culture model in vitro, in which complex and dynamic synaptic connections are made. It also provides better surface interaction between cells

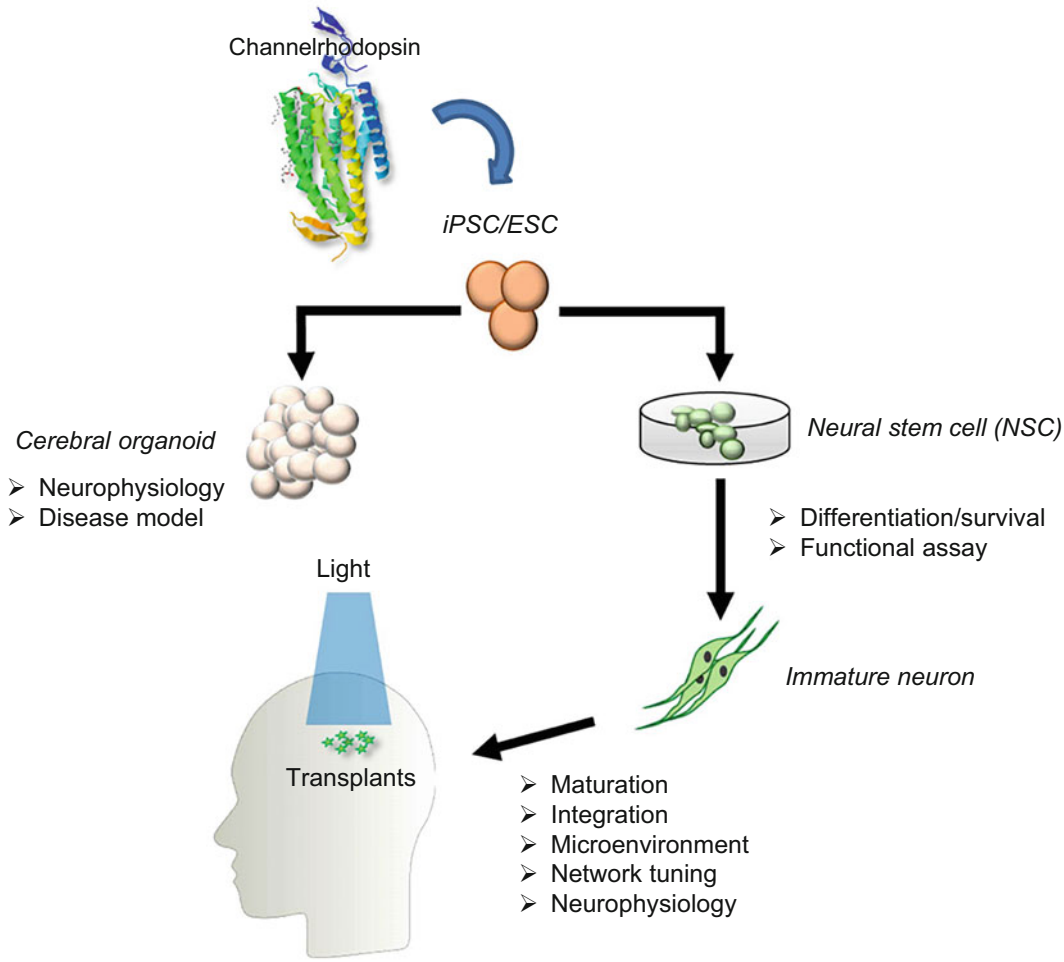


**Fig. 23.6** Potential application of optogenetics in neuroscience using stem cells. Cerebral organoids are made from induced pluripotential cells (eg. iPSCs) or embryonic stem cells (ESCs) which are engineered to harbor optogenetic molecular tools such as channelrhodopsin. This generates in vitro 3D model system for neurophysiology and neural dysfunction (left). These stem cells are also differentiated to the neural stem cells (NSCs) which generate light-sensitive neurons and are transplanted in the brain as grafts (right). Optogenetics facilitates the studies on mechanisms of neurogenesis and the assay of functionality in the pre-grafting stage. It also facilitates maturation, network integration of grafted neurons, and improves the microenvironment around them in post-grafting stage. It is applied for correcting the abnormal neural network to be normal (network-tuning) as well as neurophysiological studies in the human brain

and extracellular milieu. An example of such a culture system is the cerebral organoids, which have spatial architecture close to an actual human brain. Organoids also mimic young brain tissue. Optogenetics, both manipulation, and recording, will be applied to investigate the network dynamics in the cerebral organoids (Garita-Hernandez et al. 2018). To manipulate neuronal activity deep in 3D culture or mini-brains, the 800-nm light-based source, which has deeper tissue penetration than visible light and less heating effect than other bands of near-infrared light, would be useful in combination with the implantable miniaturized upconversion probes that emit visible light (Ding et al. 2018). Recently, retinal organoids were made from human iPSCs, and the cone photoreceptors, which were transfected with a halorhodopsin (Jaws), were implanted in the retina of blind mice (Garita-Hernandez et al. 2019). The grafted cells were responsive to light with hyperpolarization and generated a visual response in the retina.

In conclusion, with the breakthrough in stem cell technologies, the functional role of optogenetics is expected to be expanded directly to the clinical setting in both pre- and post-grafting stages (Fig. 23.6). Optogenetic manipulation in membrane potential, probably through the mobilization of intracellular $Ca^{2+}$ and $Ca^{2+}$-dependent signaling cascades, such as CREB-dependent gene regulation and autocrine/paracrine exocytosis, would regulate the fate, apoptosis/survival, and maturation during differentiation. Similarly, other intracellular signals would be directly regulated by light at optimal time and place to tune the stem cells to the niche. Immature neurons should be correctly involved in the network if they would be optically depolarized in synchronous to the signals derived from the network (Lisman and Spruston 2005). In fact, the dendritic spine of a ChR2-expressing hippocampal neuron induced LTP with translocation of αCaMKII when the light-dependent depolarization was paired with glutamate uncaging (Zhang et al. 2008).

**Acknowledgments** This work was supported by a JSPS (Japan Society for the Promotion of Science) Grant-in-Aid for Scientific Research (17KK0164 and 19K12777 to TA), a National University of Singapore Start-up Grant (R-183-000-413-733 and R-185-000-363-733 to DT), Grants-in-Aid for Scientific Research (KAKENHI) from the Ministry of Education, Culture, Sports, Science, and Technology (MEXT), Japan (15H01413, 25250001 and 15K15025 to HY), a Strategic International Collaborative Research Program (SICORP) from Japan Science and Technology Agency (JST) to HY as well as Research Foundation for Opto-Science and Technology to HY.

## References

Abilez OJ, Wong J, Prakash R et al (2011) Multiscale computational models for optogenetic control of cardiac function. Biophys J 101:1326–1334

Adamantidis A, Arber S, Bains JS et al (2015) Optogenetics: 10 years after ChR2 in neurons--views from the community. Nat Neurosci 18:1202–1212

Anderson MA, Burda JE, Ren Y et al (2016) Astrocyte scar formation aids central nervous system axon regeneration. Nature 532:195–200

Aravanis AM, Wang LP, Zhang F et al (2007) An optical neural interface: *in vivo* control of rodent motor cortex with integrated fiberoptic and optogenetic technology. J Neural Eng 4:S143–S156

Arrenberg AB, Stainier DY, Baier H et al (2010) Optogenetic control of cardiac function. Science 330:971–974

Asano T, Ishizuka T, Yawo H (2012) Optically controlled contraction of photosensitive skeletal muscle cells. Biotechnol Bioeng 109:199–204

Asano T, Ishizuka T, Morishima K et al (2015) Optogenetic induction of contractile ability in immature C2C12 myotubes. Sci Rep 5:8317

Asano T, Igarashi H, Ishizuka T et al (2018) Organelle optogenetics: direct manipulation of intracellular $Ca^{2+}$ dynamics by light. Front Neurosci 12:561

Avaliani N, Sørensen AT, Ledri M et al (2014) Optogenetics reveal delayed afferent synaptogenesis on grafted human-induced pluripotent stem cell-derived neural progenitors. Stem Cells 32:3088–3098

Berndt A, Yizhar O, Gunaydin LA et al (2009) Bi-stable neural state switches. Nat Neurosci 12:229–234

Blasiak A, Nag S, Yang IH (2018) Subcellular optogenetic stimulation platform for studying activity-dependent axon myelination *in vitro*. Methods Mol Biol 1791:207–224

Boyle PM, Karathanos TV, Trayanova NA (2018) Cardiac optogenetics: 2018. JACC Clin Electrophysiol 4:155–167

Bruegmann T, Malan D, Hesse M et al (2010) Optogenetic control of heart muscle *in vitro* and *in vivo*. Nat Methods 7:897–900

Bruegmann T, van Bremen T, Vogt CC et al (2015) Optogenetic control of contractile function in skeletal muscle. Nat Commun 6:7153

Bryson JB, Barcellos Machado C, Crossley M et al (2014) Optical control of muscle function by transplantation of stem cell-derived motor neurons in mice. Science 344:94–97

Byers B, Lee HJ, Liu J et al (2015) Direct *in vivo* assessment of human stem cell graft-host neural circuits. NeuroImage 114:328–337

Daadi MM, Klausner JQ, Bajar B et al (2016) Optogenetic stimulation of neural grafts enhances neurotransmission and downregulates the inflammatory response in experimental stroke model. Cell Transplant 25:1371–1380

D'Ascenzo M, Piacentini R, Casalbore P et al (2006) Role of L-type $Ca^{2+}$ channels in neural stem/progenitor cell differentiation. Eur J Neurosci 23:935–944

Deisseroth K (2015) Optogenetics: 10 years of microbial opsins in neuroscience. Nat Neurosci 18:1213–1225

Deisseroth K, Hegemann P (2017) The form and function of channelrhodopsin. Science 357:eaan5544

Ding H, Lu L, Shi Z et al (2018) Microscale optoelectronic infrared-to-visible upconversion devices and their use as injectable light sources. Proc Natl Acad Sci U S A 115:6632–6637

Funken M, Malan D, Sasse P et al (2019) Optogenetic hyperpolarization of cardiomyocytes terminates ventricular arrhythmia. Front Physiol 10:498

Garita-Hernandez M, Guibbal L, Toualbi L et al (2018) Optogenetic light sensors in human retinal organoids. Front Neurosci 12:789

Garita-Hernandez M, Lampič M, Chaffiol A et al (2019) Restoration of visual function by transplantation of optogenetically engineered photoreceptors. Nat Commun 10:4524

Gibson EM, Purger D, Mount CW et al (2014) Neuronal activity promotes oligodendrogenesis and adaptive myelination in the mammalian brain. Science 344:1252304

Gordon K, Del Medico A, Sander I et al (2019) Gene therapies in ophthalmic disease. Nat Rev Drug Discov 18:415–416

Hososhima S, Sakai S, Ishizuka T et al (2015) Kinetic evaluation of photosensitivity in bi-stable variants of chimeric channelrhodopsins. PLoS One 10:e0119558

Igarashi H, Ikeda K, Onimaru H et al (2018) Targeted expression of step-function opsins in transgenic rats for optogenetic studies. Sci Rep 8:5435

Iino M (2010) Spatiotemporal dynamics of $Ca^{2+}$ signaling and its physiological roles. Proc Jpn Acad Ser B Phys Biol Sci 86:244–256

Jacobson M (1991) Developmental neurobiology, 3rd edn. Plenum Press, New York

Jia Z, Valiunas V, Lu Z et al (2011) Stimulating cardiac muscle by light: cardiac optogenetics by cell delivery. Circ Arrhythm Electrophysiol 4:753–760

Jung K, Park JH, Kim SY et al (2019) Optogenetic stimulation promotes Schwann cell proliferation, differentiation, and myelination *in vitro*. Sci Rep 9:3487

Karra D, Dahm R (2010) Transfection techniques for neuronal cells. J Neurosci 30:6171–6177

Kikuchi T, Morizane A, Doi D et al (2017) Human iPS cell-derived dopaminergic neurons function in a primate Parkinson's disease model. Nature 548:592–596

Köhidi T, Jády AG, Markó K et al (2017) Differentiation-dependent motility-responses of developing neural progenitors to optogenetic stimulation. Front Cell Neurosci 11:401

Lee HU, Blasiak A, Agrawal DR et al (2017) Subcellular electrical stimulation of neurons enhances the myelination of axons by oligodendrocytes. PLoS One 12:e0179642

Lisman J, Spruston N (2005) Postsynaptic depolarization requirements for LTP and LTD: a critique of spike timing-dependent plasticity. Nat Neurosci 8:839–841

Llewellyn ME, Thompson KR, Deisseroth K et al (2010) Orderly recruitment of motor units under optical control *in vivo*. Nat Med 16:1161–1165

Magown P, Shettar B, Zhang Y et al (2015) Direct optical activation of skeletal muscle fibres efficiently controls muscle contraction and attenuates denervation atrophy. Nat Commun 6:8506

Mirzapour Delavar H, Karamzadeh A, Pahlavanneshan S (2016) Shining light on the sprout of life: optogenetics applications in stem cell research and therapy. J Membr Biol 249:215–220

Miyashita T, Shao Y, Chung J et al (2013) Long-term channelrhodopsin-2 (ChR2) expression can induce abnormal axonal morphology and targeting in cerebral cortex. Front Neural Circuits 7:8

Nagel G, Szellas T, Huhn W et al (2003) Channelrhodopsin-2, a directly light-gated cation-selective membrane channel. Proc Natl Acad Sci U S A 100:13940–13945

Numa S, Tanabe T, Takeshima H et al (1990) Molecular insights into excitation-contraction coupling. Cold Spring Harb Symp Quant Biol 55:1–7

Nussinovitch U, Gepstein L (2015) Optogenetics for *in vivo* cardiac pacing and resynchronization therapies. Nat Biotechnol 33:750–754

Nussinovitch U, Shinnawi R, Gepstein L (2014) Modulation of cardiac tissue electrophysiological properties with light-sensitive proteins. Cardiovasc Res 102:176–187

Park JH, Hong JK, Jang JY et al (2017) Optogenetic modulation of urinary bladder contraction for lower urinary tract dysfunction. Sci Rep 7:40872

Piña-Crespo JC, Talantova M, Cho EG et al (2012) High-frequency hippocampal oscillations activated by optogenetic stimulation of transplanted human ESC-derived neurons. J Neurosci 32:15837–15842

Prakriya M, Lewis RS (2015) Store-operated calcium channels. Physiol Rev 95:1383–1436

Raman R, Cvetkovic C, Uzel SG et al (2016) Optogenetic skeletal muscle-powered adaptive biological machines. Proc Natl Acad Sci U S A 113:3497–3502

Ricotti L, Menciassi A (2012) Bio-hybrid muscle cell-based actuators. Biomed Microdevices 14:987–998

Rorsman NJG, Ta CM, Garnett H et al (2018) Defining the ionic mechanisms of optogenetic control of vascular tone by channelrhodopsin-2. Br J Pharmacol 175:2028–2045

Rost BR, Schneider-Warme F, Schmitz D et al (2017) Optogenetic tools for subcellular applications in neuroscience. Neuron 96:572–603

Sakar MS, Neal D, Boudou T et al (2012) Formation and optogenetic control of engineered 3D skeletal muscle bioactuators. Lab Chip 12:4976–4985

Schneider F, Grimm C, Hegemann P (2015) Biophysics of channelrhodopsin. Annu Rev Biophys 44:167–186

Sidor MM, Davidson TJ, Tye KM et al (2015) *In vivo* optogenetic stimulation of the rodent central nervous system. J Vis Exp 95:e51483

Sineshchekov OA, Li H, Govorunova EG et al (2016) Photochemical reaction cycle transitions during anion channelrhodopsin gating. Proc Natl Acad Sci U S A 113:E1993–E2000

Steinbeck JA, Choi SJ, Mrejeru A et al (2015) Optogenetics enables functional analysis of human embryonic stem cell-derived grafts in a Parkinson's disease model. Nat Biotechnol 33:204–209

Stroh A, Tsai HC, Wang LP et al (2011) Tracking stem cell differentiation in the setting of automated optogenetic stimulation. Stem Cells 29:78–88

Takahashi J (2019) Preparing for first human trial of induced pluripotent stem cell-derived cells for Parkinson's disease: an interview with Jun Takahashi. Regen Med 14:93–95

Teh DB, Ishizuka T, Yawo H (2014) Regulation of later neurogenic stages of adult-derived neural stem/progenitor cells by L-type $Ca^{2+}$ channels. Develop Growth Differ 56:583–594

Teh DBL, Prasad A, Jiang W et al (2020) Driving neurogenesis in neural stem cells with high sensitivity optogenetics. Neuromolecular Med 22:139–149

Toettcher JE, Voigt CA, Weiner OD et al (2011) The promise of optogenetics in cell biology: interrogating molecular circuits in space and time. Nat Methods 8:35–38

Tønnesen J, Parish CL, Sørensen AT et al (2011) Functional integration of grafted neural stem cell-derived dopaminergic neurons monitored by optogenetics in an *in vitro* Parkinson model. PLoS One 6:e17560

Vogt CC, Bruegmann T, Malan D et al (2015) Systemic gene transfer enables optogenetic pacing of mouse hearts. Cardiovasc Res 106:338–343

Wang S, Du L, Peng GH (2019) Optogenetic stimulation inhibits the self-renewal of mouse embryonic stem cells. Cell Biosci 9:73

Weick JP, Johnson MA, Skroch SP et al (2010) Functional control of transplantable human ESC-derived neurons via optogenetic targeting. Stem Cells 28:2008–2016

Woodard LE, Wilson MH (2015) *piggyBac*-ing models and new therapeutic strategies. Trends Biotechnol 33:525–533

Wu Y, Li SS, Jin X et al (2015) Optogenetic approach for functional assays of the cardiovascular system by light activation of the vascular smooth muscle. Vasc Pharmacol 71:192–200

Yawo H, Asano T, Sakai S et al (2013) Optogenetic manipulation of neural and non-neural functions. Develop Growth Differ 55:474–490

Zhang YP, Holbro N, Oertner TG (2008) Optical induction of plasticity at single synapses reveals input-specific accumulation of αCaMKII. Proc Natl Acad Sci U S A 105:12039–12044

Zhao ML, Chen SJ, Li XH et al (2018) Optical depolarization of DCX-expressing cells promoted cognitive recovery and maturation of newborn neurons via the Wnt/β-catenin pathway. J Alzheimers Dis 63: 303–318

# Observing and Manipulating Cell-Specific Cardiac Function with Light

24

Callum M. Zgierski-Johnston and Franziska Schneider-Warme

**Abstract**

The heart is a complex multicellular organ comprising both cardiomyocytes (CM), which make up the majority of the cardiac volume, and non-myocytes (NM), which represent the majority of cardiac cells. CM drive the pumping action of the heart, triggered via rhythmic electrical activity. NM, on the other hand, have many essential functions including generating extracellular matrix, regulating CM activity, and aiding in repair following injury. NM include neurons and interstitial, immune, and endothelial cells. Understanding the role of specific cell types and their interactions with one another may be key to developing new therapies with minimal side effects to treat cardiac disease. However, assessing cell-type-specific behavior in situ using standard techniques is challenging. Optogenetics enables population-specific observation and control, facilitating studies into the role of specific cell types and subtypes. Optogenetic models targeting the most important cardiac cell types have been generated and used to investigate non-canonical roles of those cell populations, e.g., to better understand how cardiac pacing occurs and to assess potential translational possibilities of optogenetics. So far, cardiac optogenetic studies have primarily focused on validating models and tools in the healthy heart. The field is now in a position where animal models and tools should be utilized to improve our understanding of the complex heterocellular nature of the heart, how this changes in disease, and from there to enable the development of cell-specific therapies and improved treatments.

**Keywords**

Cardiac optogenetics · Interstitial cells · Immune cells · Endothelial cells · Neurons · Heterocellular interactions

## Abbreviations

| | |
|---|---|
| AAV | Adeno-associated viral [particles] |
| ACR | Anion channelrhodopsins |
| AV | Atrioventricular |
| ChR2 | *Chlamyodomonas reinhardtii* channelrhodopsin-2 |
| CM | Cardiomyocytes |
| ECG | Electrocardiogram |
| ICNS | Intrinsic cardiac nervous system |
| NM | Non-myocytes |

C. M. Zgierski-Johnston · F. Schneider-Warme (✉)
Institute for Experimental Cardiovascular Medicine, University Heart Center Freiburg—Bad Krozingen, Medical Center—University of Freiburg, Freiburg, Germany

Faculty of Medicine, University of Freiburg, Freiburg, Germany
e-mail: franziska.schneider@universitaets-herzzentrum.de



H. Yawo et al. (eds.), *Optogenetics*, Advances in Experimental Medicine and Biology 1293,
https://doi.org/10.1007/978-981-15-8763-4_24

| | |
|---|---|
| NpHR | *Natromonas pharaonis* halorhodopsin |
| PN | Parasympathetic neurons |
| RA | Right atrial |
| SN | Sympathetic neurons |
| VSFP | Voltage-sensitive fluorescent protein |

## 24.1 Introduction

The vertebrate heart is the central muscular organ maintaining blood flow throughout an organism's entire lifespan. Coordinated contraction–relaxation cycles are achieved by concerted electrical activation from the sinus node via the atria, the atrioventricular (AV) node, and the ventricular conduction system to the working myocardium of the ventricles. Cardiomyocytes (CM) are the predominant cell type driving the electromechanical activity of the heart. CM form a functional syncytium that enables depolarization-induced activation of cellular action potentials, leading to $Ca^{2+}$-induced $Ca^{2+}$ release, which in turn triggers CM contraction. CM are not only crucial for heart function but also occupy the majority of the heart volume. However, they are embedded in a complex and intricate network of other cells, non-myocytes (NM), including cardiac endothelial cells, fibroblasts, immune cells, and neurons. In fact, NM are significantly more numerous than CM in the healthy heart and the NM to CM ratio is further increased in cardiac disease. NM have diverse functions ranging from structural support and regulation of CM activity to driving repair following cardiac injury. Thus, in order to understand cardiac function in health and disease, we need to not only unravel the role of each individual cardiac cell type but also to understand how these cell types interact with one another.

Classically, cardiac electrical activity has been monitored with body surface electrodes, which report overall atrial and ventricular depolarization–repolarization cycles (the electrocardiogram—ECG). In basic research, ECG recordings have been complemented by dye-based optical mapping of membrane voltage, providing time-resolved, near-epicardial conduction maps of isolated Langendorff-perfused hearts. Modulation of electrical activity has been performed via implantable electrodes, e.g., electrical pacemakers for cardiac pacing and implantable cardioverter–defibrillators for electrical shock–based restoration of heart rhythm (defibrillation). Thus, classic cardiac monitoring and intervention tools report/modulate overall electrical activity that is dominated by CM, without the possibility to target cell-specific behavior of CM or NM.

Cell-specific targeting is possible, however, by combining advanced optical methods and state-of-the-art genetic engineering. The underlying optogenetic approaches enable manipulation and/or monitoring of the activity of specific cells, cell populations, or cell types. Cardiac optogenetics thus represents an emerging method in basic research for deciphering cell-specific functions and heterocellular interactions in intact myocardium, laying the foundation for future development of cell-specific therapies to treat cardiac diseases.

## 24.2 Introduction to Cardiac Optogenetics

Eight years after the discovery of directly light-gated ion channels in motile green algae (Nagel et al. 2002, 2003; Sineshchekov et al. 2002; Suzuki et al. 2003), and five years after groundbreaking experiments using channelrhodopsins in neurons and brain tissue (Li et al. 2005; Nagel et al. 2005; Boyden et al. 2005; Ishizuka et al. 2006), channelrhodopsin-2 (ChR2) and halorhodopsin from *Natromonas pharaonis* (NpHR) were first applied for contact-free alteration of cardiac electrophysiology by illumination (Arrenberg et al. 2010; Bruegmann et al. 2010). However, optogenetics includes both observation and control of cell function with light (Miesenböck 2009). Therefore, first cardiac optogenetic experiments were performed as early as in 2006, when Tallini et al. used the genetically encoded $Ca^{2+}$ sensor GCaMP2 to measure CM $Ca^{2+}$ transients in murine hearts in vivo (Tallini et al. 2006).

In the last decade, a handful of optogenetic actuators and reporters have been applied to the study of cardiac electrophysiology. Actuators used include ChR2 and the red-shifted channelrhodopsin chimera ReaChR, the chloride pump NpHR and the proton pump ArchT as well as the more recently found anion channelrhodopsins (ACR) (Arrenberg et al. 2010; Bruegmann et al. 2010; Govorunova et al. 2016; Nyns et al. 2017; Kopton et al. 2018; Funken et al. 2019). Established reporters are $Ca^{2+}$ sensors of the GCaMP family and genetically encoded voltage sensors such as the voltage-sensitive fluorescent protein (VSFP), which have been used to image $Ca^{2+}$ and voltage dynamics in cardiac cells and tissue (Tallini et al. 2006, 2007; Liao et al. 2015).

Proof-of-principle optogenetic studies were initially focused on overall cardiac function, showing the feasibility of optical pacing, atrial and ventricular defibrillation, as well as cardiac resynchronization (Bruegmann et al. 2010, 2016, 2018; Nussinovitch and Gepstein 2015; Nyns et al. 2017). Similarly, optical reporters have primarily been used to study CM function, in particular examining cardiac development (Chi et al. 2008, 2010; Hou et al. 2014; Weber et al. 2017) and, using subcellular targeting of sensors, $Ca^{2+}$-induced $Ca^{2+}$ release (Lu et al. 2013; Despa et al. 2014; Ljubojevic et al. 2014; Shang et al. 2014). Global activation of optogenetic sensors or actuators expressed in CM thus enables testing optogenetic approaches to study and/or steer overall cardiac electrophysiology with light. However, it provides limited insight into the role of CM subpopulations or other electrophysiologically relevant cell types. This book chapter focuses on optogenetic studies aiming to unravel basic research questions regarding cell-type-specific functions and interactions in the vertebrate heart in situ. We outline strategies to target different classes of cells and how these attempts have already widened our understanding of the heterocellular heart (Fig. 24.1).

## 24.3 Targeting CM Subpopulations

### 24.3.1 Global Expression and Localized Illumination

Arrenberg et al. combined global overexpression of either NpHR or ChR2 in CM with *patterned illumination*, generated with a digital micromirror device, to identify pacemaker cells of the developing zebrafish heart, and to optically induce cardiac rhythm disturbances such as AV block, tachycardia, and bradycardia (Arrenberg et al. 2010). Similarly, Crocini et al. developed an optical platform capable of simultaneously mapping and controlling the electrical activity of CM subsets within whole murine hearts at sub-millisecond temporal resolution (Crocini et al. 2016). Their optical stimulation setup consisted of a macroscope equipped with a laser scanning system based on acousto-optic deflectors. This platform enabled testing different geometric patterns for light activation of ChR2, with the aim of identifying optimal patterns of CM depolarization to terminate ventricular reentrant arrhythmias. In follow-up research, the system was further refined, allowing for closed-loop control of cardiac electrical activity, e.g., to restore normal conduction after AV block and to manipulate intraventricular wavefront propagation (Scardigli et al. 2018).

Complementary to patterned illumination for ChR activation, Weber et al. developed an imaging system for *cell-accurate* recording of $Ca^{2+}$ dynamics of the entire developing zebrafish heart over extended time frames (here 36–52 h postfertilization) (Weber et al. 2017). To this end, they combined GCaMP5G expression in CM with nucleus-targeted mCherry labeling for identification of single cells. A custom-built light-sheet microscope enabled fast (400 Hz) high-resolution (0.5μm × 0.5μm × 1μm voxels) imaging of reporter fluorescence, and post-acquisition synchronization was used to visualize $Ca^{2+}$ transients in CM across the embryonic myocardium.

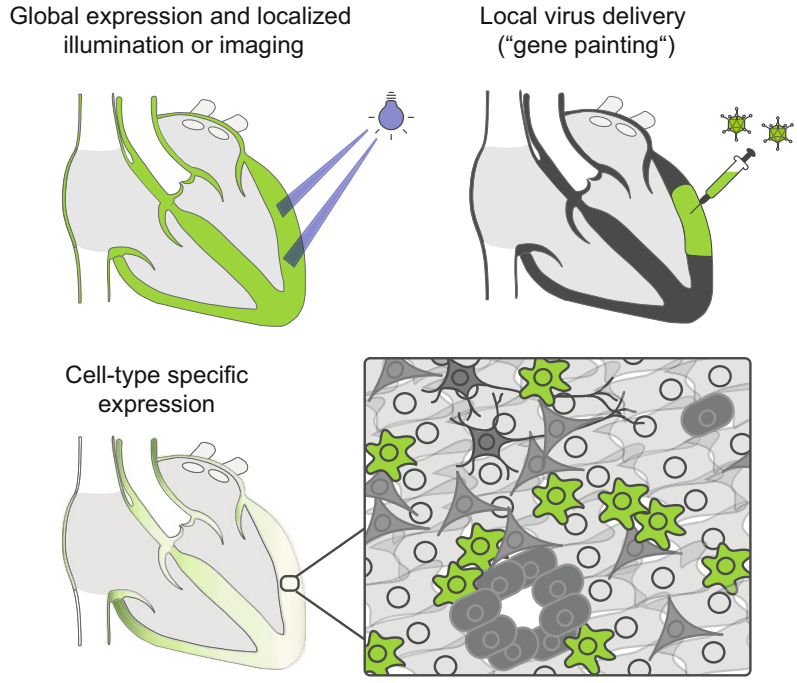


**Fig. 24.1** Strategies to optogenetically target different cardiac cell populations. (This figure is based on one kindly supplied by Professor Lutz Hein, Freiburg)

### 24.3.2 Local Virus Delivery or Cell-Type-Specific Viral Serotypes

An alternative strategy for spatially defined, optogenetic activation was recently presented by Nyns et al. (2019). ReaChR-encoding adeno-associated viral (AAV) particles were *locally* applied to the right atrial (RA) epicardium of rat hearts ("gene painting"), resulting in efficient transmural transduction of RA myocytes, with minimal off-target expression in other cardiac compartments. Accordingly, RA illumination enabled optical pacing, as well as termination of atrial tachyarrhythmias, while illumination of non-RA areas did not affect heart rhythm.

Localized illumination or viral delivery allows for activation or recording from spatially restricted subsets of cells, but they do not necessarily enable targeting of specific cell classes within a region. With the advent of high-throughput single-cell sequencing approaches, the range of subtypes within each cell population is increasingly being recognized, and the functional relevance of each subpopulation needs to be elucidated.

The use of viral shuttles by itself may open up the possibility to target specific cell types, as certain viral serotypes preferentially transduce different cell populations (viral tropism), even upon systemic application. For example, the adeno-associated virus 2/9 has been shown to be cardiotropic, and CM specificity can be further increased by the use of a CM-specific promoter to drive transgene expression (Pacak et al. 2006; Bish et al. 2008; Prasad et al. 2011). In line, Vogt et al. showed that AAV2/9-mediated systemic delivery of Cop4 (coding for ChR2) ensured efficient and stable ChR2 expression in CM, allowing for blue-light triggered pacing of murine hearts (Vogt et al. 2015).

### 24.3.3 Genetic Targeting of Cardiomyocyte Subsets

Cell populations can be *genetically* targeted either by expressing transgenes under direct control of

cell-specific promoters or using recombination systems such as the Cre-LoxP system. The latter approach was used by Zaglia et al. to drive ChR2 expression in CM (using α-myosin heavy chain-Cre) or in the specialized cells of the conduction system (using connexin-40-Cre) to probe the minimal cell number that needs to be simultaneously depolarized to induce ventricular extrasystoles (Zaglia et al. 2015). They found that focal ectopy requires depolarization of 1300–1800 working CM, supporting earlier computational predictions that inhibition of the $Na^+/K^+$ ATPase in approximately 1000 atrial CM would be sufficient to cause spontaneous ectopic beats (Winslow et al. 1993). In contrast, optogenetic depolarization of only 90–160 Purkinje fibers was sufficient to elicit focal ectopies in the murine ventricle. A Cre recombinase-based mouse model was also used by Wang et al. to elucidate the morphology and electromechanical function of phenylethanolamine N-methyltransferase (pnmt)-positive cells, a subset of CM able to convert noradrenaline to adrenaline, as well as their descendants (Wang et al. 2017).

As mentioned previously, NM constitute the majority of cardiac cells and play important roles in preserving and regulating cardiac structure and function—yet they were long regarded as "inert," in as far as cardiac electrophysiology is concerned (acting as barriers, but not as active players). In recent years, a steadily rising number of studies have used optogenetic tools to target-specific NM populations, including interstitial cells, resident cardiac immune cells, cells forming the vasculature, and, last but not least, intracardiac neurons.

## 24.4 Interstitial Cells and Resident Cardiac Immune Cells

Interstitial fibroblasts not only generate the scaffold of the myocardium, but have been implicated in regulating cardiac function, both via biochemical and biophysical signaling (Gourdie et al. 2016). In vitro studies indicated direct electrotonic coupling between fibroblasts and CM as early as 50 years ago (Goshima and Tonomura 1969). However, only recently have optogenetic approaches provided direct evidence of such coupling in *native* myocardium. By selectively expressing VSFP in cardiac NM (using the Wilm's tumor protein 1-Cre driver line) Quinn et al. observed action potential like depolarizations in NM of ventricular scar border zone tissue, indicating that these NM follow rhythmic de- and repolarization of electrotonically coupled CM in murine hearts after cryoinjury (Quinn et al. 2016). Similar findings were described for myofibroblasts, where combined myofibroblast-specific expression of the fluorescent reporter Zsgreen (driven by Periostin-Cre) and global loading with a red-shifted, voltage-sensitive dye, allowed for visualization of CM-myofibroblast coupling in the infarct border zone of mouse hearts (Rubart et al. 2017).

Resident macrophages constitute the most abundant immune cell type in the heart, with distinct functions in steady state and during myocardial remodeling following cardiac injury (Hulsmans et al. 2016). Notably, cardiac macrophages express connexin-43, indicating that they might be coupled to adjacent CM (Hulsmans et al. 2017). To assess functional macrophage-CM coupling, Hulsmans et al. expressed ChR2 specifically in resident cardiac macrophages (using the Cx3Cr1-Cre mouse line). Upon ChR2-mediated depolarization of macrophages, they observed improved AV node conduction at high-pacing frequencies, supporting the hypothesis that changes in the membrane potential of macrophages could potentially impact normal cardiac function even in healthy murine myocardium.

The above-described studies show how cell-specific optogenetic approaches can be used to probe the existence and functional relevance of heterocellular electrotonic coupling, both in healthy and remodeled mouse hearts.

## 24.5 Optogenetic Manipulation of the Cardiac Vasculature

The cardiac circulatory system provides oxygen and nutrients to the heart and facilitates the

transport of immune and other circulatory cells to the four heart chambers. The principal cellular components of coronary vessels are endothelial and perivascular cells (vascular smooth muscle cells and pericytes), together providing the structure and regulating the development, stability, and contractile function of the vessels (Kapuria et al. 2018). Cardiac endothelial cells were optogenetically targeted by CreLoxP recombination of Cre-dependent ChR2 mice, bred with the cadherin (Cdh5)-Cre driver line (Zhang et al. 2015). Interestingly, blue-light mediated ChR2 activation in vascular endothelial cells led to vasoconstriction, thereby increasing the perfusion pressure of the Langendorff-perfused mouse heart. Vasoconstriction was also observed when activating ChR2 in cardiac vascular smooth muscle cells (driven by transgelin [Tagln]-Cre), with increasing constriction during sustained ChR2 activation, potentially indicating depolarization-induced changes in transmembrane ionic gradients (e.g., cellular $Ca^{2+}$ overload) (Wu et al. 2015). Sustained ChR2 activation also elicited severe ventricular arrhythmias, suggesting insufficient myocardial blood perfusion.

## 24.6 Intrinsic Cardiac Nervous System

On top of centrally derived sympathetic and parasympathetic innervation of the heart, the heart has a complex intrinsic network of neurons, termed the intrinsic cardiac nervous system (ICNS). Traditionally, it was assumed that the ICNS acted as a relay system for the central nervous system, however, a number of subsequent studies confirmed that the ICNS plays a distinct and significant independent role in cardiac physiology in both health and disease (for a full review, see Wake and Brack 2016). However, probing the exact pathways and mechanisms by which the ICNS affects cardiac physiology using standard electrical stimulation techniques, presents with the difficulty of ensuring that only the specific neuron population of interest is excited. Optogenetics overcomes this issue by enabling cell-type-specific stimulation and recording, thus allowing the assessment of the role and interactions of different neuronal populations in the heart.

Studies using optogenetic tools to assess cardiac innervation initially focused on cardiac effects of optical activation of neurons in the central nervous system (Mastitskaya et al. 2012; Marina et al. 2013; Yu et al. 2017). Wengrowski et al. (2015) performed the first study looking directly at the role of the ICNS (Wengrowski et al. 2015). They expressed ChR2 in sympathetic neurons (SN; using the tyrosine hydroxylase-Cre driver line) and assessed how optical excitation of SN altered force production, heart rate, action potential duration, and arrhythmia susceptibility in Langendorff-perfused hearts. This study demonstrated that isolated hearts can be utilized to characterize cardiac responses to intracardiac neural activation through the use of optogenetics, simplifying experimental models, and opening up the path to a better understanding of cardiac innervation.

Prando et al. (2018) subsequently investigated the mechanisms underlying communication between SN and CM (Prando et al. 2018). Confocal microscopy demonstrated close contacts between SN and CM, and electron microscopy revealed sympathetic varicosities at an intermembrane distance of 70 nm from CM, and clustering of norepinephrine-containing vesicles in the SN close to the SN–CM interface. To test whether these points of contact act as spatially restricted domains for communication, an optogenetic sensor for cAMP (H187) was used in vitro, confirming that only the directly innervated cell was excited in response to SN stimulation. They further assessed the in vivo response to optogenetic activation of ChR2 in SN. By combining functional optogenetic experiments with same-site histological analysis, they identified a subset of SN that forms quasi-synaptic clefts with sinoatrial node CM. Presence of such quasi-synaptic junctions alters our understanding of cell–cell communication in the heart, a prerequisite for developing novel therapies, e.g., for treating atrial and ventricular fibrillation, both of which have been linked to abnormal nerve

activity (Scherlag and Po 2006; Lu et al. 2009; He et al. 2013).

In 2019, the first reports targeting parasympathetic neurons (PN) were published. Moreno et al. expressed ChR2 in PN (using choline acetyltransferase-Cre mice) and demonstrated optically induced changes in heart rate and conduction (Moreno et al. 2019). Rajendran et al. took this a step further by examining both PN and SN innervation of the sinoatrial node (Rajendran et al. 2019). They demonstrated the ability to accurately trace cardiac innervation through the use of optical clearing, immunostaining, and genetic labeling, providing a high-resolution map of the murine ICNS. They further compared optical stimulation of PN to SN in terms of its effects on cardiac electrophysiology and confirmed the utility of optogenetics by comparing optical to electrical stimulation of the vagus nerve. Their data suggest that electrical stimulation affects both afferent and efferent fibers in the vagus nerve, whereas optical stimulation, due to genetic expression of probes in particular neuronal subsets, can be used to only stimulate efferent fibers.

The above studies exemplify how optogenetic approaches can greatly facilitate probing the roles of different cardiac cell types, including CM, fibroblasts, macrophages, endothelial cells, smooth muscle cells, and intracardiac neurons, and subpopulations thereof. In the following paragraphs, we will discuss several challenges of cardiac optogenetics at present, and propose how they might be overcome in the near future.

## 24.7 Current Challenges and Future Directions

A range of optogenetic sensors and actuators have been applied to record and modulate cell-type-specific cardiac activity. Despite genetically targetable optogenetic sensors first being used in the heart in 2006, and actuators in 2010, cardiac optogenetics research has primarily utilized CM-specific expression in healthy hearts. The ability to target-specific cell types, subtypes, and intracellular compartments has been shown, but primarily as a part of proof-of-principle studies. Thus far, the use of optogenetics to address fundamental scientific questions in the cardiac field is lagging behind neurosciences, with only a handful of published reports, largely focusing on the healthy heart (Quinn et al. 2016; Hulsmans et al. 2017; Prando et al. 2018; Rajendran et al. 2019). The advent of new models, and demonstration of their utility for assessing the specific roles of cardiac endothelial cells, smooth muscle cells, neurons, and interstitial cells in recent years, will hopefully encourage addressing more fundamental questions regarding cardiac biology in health and disease.

In particular, optogenetics could be used to modulate different NM populations in the diseased heart to help understand their role in cardiac homeostasis and repair and how these differ between localized lesions (e.g., those occurring due to myocardial infarction or ablation therapy) and global remodeling (e.g., as occurs in atrial fibrillation or cardiac hypertrophy). Potentially exciting applications of cardiac optogenetics—such as for defibrillation—have been explored in "healthy" hearts. These may not apply equally to a diseased heart, where cells die (e.g., CM), proliferate (e.g., interstitial cells), and/or invade from external sources (e.g., immune cells), changing tissue electrophysiological properties. Resulting spatial heterogeneities may act as organizing centers for arrhythmias, making them more difficult to be terminated. Furthermore, poor cell health may affect ion distributions, so that optogenetic activation of ion channels may have different effects in diseased, compared to healthy myocardium. In regard to optogenetic defibrilliation, it would be most interesting to explore which cell type(s) might be best suited to terminate arrhythmias with light, as targeting NM might be a safer option than directly targeting CM, and may allow for targeting lesion-specific activated cell populations. A further key issue with the application of optogenetics for treating cardiac disease is that no study has shown the ability to perform long-term cardiac optical stimulation or observation on vertebrates in vivo. Weber et al. recorded calcium transients in zebrafish embryos over 16 h (Weber et al.

2017), and no group has exceeded this period to our knowledge. A number of groups have demonstrated optical pacing or resynchronization in vivo with open-chest models (Bruegmann et al. 2010; Nussinovitch and Gepstein 2015; Vogt et al. 2015), and Nyns et al. recently demonstrated the ability to pace and defibrillate in a closed-chest model (Nyns et al. 2017). However, transitioning from using optogenetics in an anesthetized to a freely moving animal remains challenging, due to continuous motion (heartbeat, respiration) of the heart, and its location in the body.

The use of larger animals would potentially lower the technical threshold to implementing chronic studies by offering more space for implanting flexible light sources. Furthermore, larger mammals such as rabbits or pigs are considered more suitable models of the human heart compared to rodent species. This is especially true for cardiac electrophysiology, with large interspecies differences, e.g., in action potential shape and heart rate. However, taking cardiac optogenetics to non-rodent hearts poses additional challenges. One of the main hurdles is limited light penetration into tissue, as blue light is attenuated by 80% within 1–2 mm of the myocardial surface (Baxter et al. 2001; Zaglia et al. 2015). Tissue-penetrating light sources, which allow transmural illumination, are available, but their use would still be restricted by light penetration in 3D (Zgierski-Johnston et al. 2019). Alternatively, developments in the field of nanoparticles offer the possibility for exciting deeper tissue layers through either photo-upconversion (see review by All et al. 2019, where long-wavelength light is used to excite nanoparticles which emit lower wavelengths), or ultrasound-triggered light emission (Wu et al. 2019). However, the need to produce such nanoparticles limits their widespread adoption and their application and turnover pose nontrivial problems for research and development. A further approach would be the use of ultralight-sensitive optogenetic tools, such as the recently presented optogenetic $Ca^{2+}$ modulator monSTIM1, which can be noninvasively activated by illuminating the animal with blue light of moderate intensity (Kim et al. 2020). Finally, newly developed genetically encoded infrared reporters (Monakhov et al. 2019) or red-shifted actuators (Oda et al. 2018) are set to enable the use of longer wavelength light for excitation, thereby opening up the possibility for transmural observation and steering in larger hearts. Red-shifted proteins offer the additional advantage of allowing for combined use of optogenetic tools, an area that has traditionally been challenging due to spectral overlap.

Utilizing newly generated optogenetic tools remains difficult. The majority of researchers using cardiac optogenetics—including ourselves—still utilize ChR2; despite the available repertoire of ChR variants with improved/tuned properties, including action spectra, photocycle kinetics, ion selectivity, and channel membrane targeting (Prigge et al. 2012; Schneider et al. 2015; Rost et al. 2017). This is largely due to the availability of floxed ChR2 mouse lines and ChR2-encoding viral vectors, while the development of new transgenic mouse lines is both cost- and time-consuming. We still encourage researchers to identify the optogenetic probe most suitable for each specific experimental design, as this may reduce unwanted side effects of optogenetic activation. For example, ChR2 has been shown to effectively silence CM activity during prolonged illumination, but at the cost of depolarizing CM to the reversal potential of ChR2 (near 0 mV), activating secondary voltage-gated ion channels. This may, in particular in diseased myocardium, aggravate the conditions (such as $Ca^{2+}$-overload-induced arrhythmogenesis) that one might hope to control or treat. Other tools might be better suited to arrest cardiac excitation, in particular, hyperpolarizing light-driven pumps and light-gated $Cl^-$ and $K^+$ channels (Arrenberg et al. 2010; Govorunova et al. 2016; Kopton et al. 2018; Bernal Sierra et al. 2018; Funken et al. 2019).

An alternative model system is zebrafish, as the effort involved in generating transgenic fish is much lower than for mammals. Furthermore, a number of recent publications suggest that fish may even be a more suitable cardiac model than mice (see editorial by Stoyek and Quinn 2018). A

major advantage is the speed and relative simplicity of gene manipulation in zebrafish. Zebrafish are, of course, not suitable for all studies, due to their small size and different biology (e.g., two-chamber heart, potential to regenerate heart tissue), but they can serve as a good model for generating hypotheses and for testing novel optogenetic tools.

## 24.8 Summary

Experiments targeting a range of different cardiac cell types and subtypes have demonstrated the utility of optogenetics for teasing apart the role of specific cell populations in the heterocellular heart. The studies discussed above lay the groundwork for future research, focusing on understanding the interactions between different cell populations, and their role in development, homeostasis, disease, and therapy.

**Acknowledgments** We thank all members of the Institute of Experimental Cardiovascular Medicine for critical discussion of the manuscript. This research was funded by the German Research Foundation DFG (SPP1926: FS1486/1-2, ZG58/1-1, and an Emmy-Noether-Fellowship: FS1486/2-1). Both authors are members of the DFG-funded Collaborative Research Centre 1425.

## References

All AH, Zeng X, Teh DBL et al (2019) Expanding the toolbox of upconversion nanoparticles for in vivo optogenetics and neuromodulation. Adv Mater 31:1–15. https://doi.org/10.1002/adma.201803474

Arrenberg AB, Stainier DYR, Baier H, Huisken J (2010) Optogenetic control of cardiac function. Science 330:971–974. https://doi.org/10.1126/science.1195929

Baxter WT, Mironov SF, Zaitsev AV et al (2001) Visualizing excitation waves inside cardiac muscle using transillumination. Biophys J 80:516–530. https://doi.org/10.1016/S0006-3495(01)76034-1

Bernal Sierra YA, Rost BR, Pofahl M et al (2018) Potassium channel-based optogenetic silencing. Nat Commun 9:4611. https://doi.org/10.1038/s41467-018-07038-8

Bish LT, Morine K, Sleeper MM et al (2008) Adeno-associated virus (AAV) serotype 9 provides global cardiac gene transfer superior to AAV1, AAV6, AAV7, and AAV8 in the mouse and rat. Hum Gene Ther 19:1359–1368. https://doi.org/10.1089/hum.2008.123

Boyden ES, Zhang F, Bamberg E et al (2005) Millisecond-timescale, genetically targeted optical control of neural activity. Nat Neurosci 8:1263–1268. https://doi.org/10.1038/nn1525

Bruegmann T, Malan D, Hesse M et al (2010) Optogenetic control of heart muscle in vitro and in vivo. Nat Methods 7:897–900. https://doi.org/10.1038/nmeth.1512

Bruegmann T, Boyle PM, Vogt CC et al (2016) Optogenetic defibrillation terminates ventricular arrhythmia in mouse hearts and human simulations. J Clin Invest 126:3894–3904. https://doi.org/10.1172/JCI88950

Bruegmann T, Beiert T, Vogt CC et al (2018) Optogenetic termination of atrial fibrillation in mice. Cardiovasc Res 114:713–723. https://doi.org/10.1093/cvr/cvx250

Chi NC, Shaw RM, Jungblut B et al (2008) Genetic and physiologic dissection of the vertebrate cardiac conduction system. PLoS Biol 6:1006–1019. https://doi.org/10.1371/journal.pbio.0060109

Chi NC, Bussen M, Brand-Arzamendi K et al (2010) Cardiac conduction is required to preserve cardiac chamber morphology. Proc Natl Acad Sci U S A 107:14662–14667. https://doi.org/10.1073/pnas.0909432107

Crocini C, Ferrantini C, Coppini R et al (2016) Optogenetics design of mechanistically-based stimulation patterns for cardiac defibrillation. Sci Rep 6:1–7. https://doi.org/10.1038/srep35628

Despa S, Shui B, Bossuyt J et al (2014) Junctional cleft [Ca2+]i measurements using novel cleft-targeted Ca2+ sensors. Circ Res 115:339–347. https://doi.org/10.1161/CIRCRESAHA.115.303582

Funken M, Malan D, Sasse P, Bruegmann T (2019) Optogenetic hyperpolarization of cardiomyocytes terminates ventricular arrhythmia. Front Physiol 10:1–7. https://doi.org/10.3389/fphys.2019.00498

Goshima K, Tonomura Y (1969) Synchronized beating of embryonic mouse myocardial cells mediated by FL cells in monolayer culture. Exp Cell Res 56:387–392. https://doi.org/10.1016/0014-4827(69)90029-9

Gourdie RG, Dimmeler S, Kohl P (2016) Novel therapeutic strategies targeting fibroblasts and fibrosis in heart disease. Nat Rev Drug Discov 15(9):620–638. https://www.nature.com/articles/nrd.2016.89. Accessed 10 Jan 2020

Govorunova EG, Cunha SR, Sineshchekov OA, Spudich JL (2016) Anion channelrhodopsins for inhibitory cardiac optogenetics. Sci Rep 6:33530. https://doi.org/10.1038/srep33530

He B, Lu Z, He W et al (2013) The effects of atrial ganglionated plexi stimulation on ventricular electrophysiology in a normal canine heart. J Interv Card Electrophysiol 37:1–8. https://doi.org/10.1007/s10840-012-9774-2

Hou JH, Kralj JM, Douglass AD et al (2014) Simultaneous mapping of membrane voltage and calcium in

zebrafish heart in vivo reveals chamber-specific developmental transitions in ionic currents. Front Physiol 5:344. https://doi.org/10.3389/fphys.2014.00344

Hulsmans M, Sam F, Nahrendorf M (2016) Monocyte and macrophage contributions to cardiac remodeling. J Mol Cell Cardiol 93:149–155. https://doi.org/10.1016/j.yjmcc.2015.11.015

Hulsmans M, Clauss S, Xiao L et al (2017) Macrophages facilitate electrical conduction in the heart. Cell 169:510–522.e20. https://doi.org/10.1016/j.cell.2017.03.050

Ishizuka T, Kakuda M, Araki R, Yawo H (2006) Kinetic evaluation of photosensitivity in genetically engineered neurons expressing green algae light-gated channels. Neurosci Res 54:85–94. https://doi.org/10.1016/j.neures.2005.10.009

Kapuria S, Yoshida T, Lien C-L (2018) Coronary Vasculature in Cardiac Development and Regeneration. J Cardiovasc Dev Dis 5:59. https://doi.org/10.3390/jcdd5040059

Kim S, Kyung T, Chung J et al (2020) Non-invasive optical control of endogenous Ca2+ channels in awake mice. Nat Commun 11:210. https://doi.org/10.1038/s41467-019-14005-4

Kopton RA, Baillie JS, Rafferty SA et al (2018) Cardiac electrophysiological effects of light-activated chloride channels. Front Physiol 9:1806. https://doi.org/10.3389/FPHYS.2018.01806

Li X, Gutierrez DV, Hanson MG et al (2005) Fast noninvasive activation and inhibition of neural and network activity by vertebrate rhodopsin and green algae channelrhodopsin. Proc Natl Acad Sci 102:17816–17821. https://doi.org/10.1073/pnas.0509030102

Liao MLC, De Boer TP, Mutoh H et al (2015) Sensing cardiac electrical activity with a cardiac myocyte-targeted optogenetic voltage indicator. Circ Res 117:401–412. https://doi.org/10.1161/CIRCRESAHA.117.306143

Ljubojevic S, Radulovic S, Leitinger G et al (2014) Early remodeling of perinuclear Ca2+ stores and nucleoplasmic Ca2+ signaling during the development of hypertrophy and heart failure. Circulation 130:244–255. https://doi.org/10.1161/CIRCULATIONAHA.114.008927

Lu Z, Scherlag BJ, Lin J et al (2009) Autonomic mechanism for initiation of rapid firing from atria and pulmonary veins: evidence by ablation of ganglionated plexi. Cardiovasc Res 84:245–252. https://doi.org/10.1093/cvr/cvp194

Lu X, Ginsburg KS, Kettlewell S et al (2013) Measuring local gradients of intramitochondrial [Ca2+] in cardiac myocytes during sarcoplasmic reticulum Ca2+ release. Circ Res 112:424–431. https://doi.org/10.1161/CIRCRESAHA.111.300501

Marina N, Tang F, Figueiredo M et al (2013) Purinergic signalling in the rostral ventro-lateral medulla controls sympathetic drive and contributes to the progression of heart failure following myocardial infarction in rats. Basic Res Cardiol 108:1–10. https://doi.org/10.1007/s00395-012-0317-x

Mastitskaya S, Marina N, Gourine A et al (2012) Cardioprotection evoked by remote ischaemic preconditioning is critically dependent on the activity of vagal pre-ganglionic neurones. Cardiovasc Res 95:487–494. https://doi.org/10.1093/cvr/cvs212

Miesenböck G (2009) The optogenetic catechism. Science 326:395–399

Monakhov M, Matlashov M, Colavita M, et al (2019) Bright near-infrared genetically encoded voltage indicator for all-optical electrophysiology. bioRxiv 536359. https://doi.org/10.1101/536359

Moreno A, Endicott K, Skancke M et al (2019) Sudden heart rate reduction upon optogenetic release of acetylcholine from cardiac parasympathetic neurons in perfused hearts. Front Physiol 10:16. https://doi.org/10.3389/fphys.2019.00016

Nagel G, Ollig D, Fuhrmann M et al (2002) Channelrhodopsin-1: a light-gated proton channel in green algae. Science 296:2395–2398. https://doi.org/10.1126/science.1072068

Nagel G, Szellas T, Huhn W et al (2003) Channelrhodopsin-2, a directly light-gated cation-selective membrane channel. Proc Natl Acad Sci U S A 100:13940–13945. https://doi.org/10.1073/pnas.1936192100

Nagel G, Brauner M, Liewald JF et al (2005) Light activation of Channelrhodopsin-2 in excitable cells of caenorhabditis elegans triggers rapid behavioral responses. Curr Biol 15:2279–2284. https://doi.org/10.1016/j.cub.2005.11.032

Nussinovitch U, Gepstein L (2015) Optogenetics for in vivo cardiac pacing and resynchronization therapies. Nat Biotechnol 33:750–754. https://doi.org/10.1038/nbt.3268

Nyns ECA, Kip A, Bart CI et al (2017) Optogenetic termination of ventricular arrhythmias in the whole heart: towards biological cardiac rhythm management. Eur Heart J 38:2132–2136. https://doi.org/10.1093/eurheartj/ehw574

Nyns ECA, Poelma RH, Volkers L et al (2019) An automated hybrid bioelectronic system for autogenous restoration of sinus rhythm in atrial fibrillation. Sci Transl Med 11:1–12. https://doi.org/10.1126/scitranslmed.aau6447

Oda K, Vierock J, Oishi S et al (2018) Crystal structure of the red light-activated channelrhodopsin Chrimson. Nat Commun 9:1–11. https://doi.org/10.1038/s41467-018-06421-9

Pacak CA, Mah CS, Thattaliyath BD et al (2006) Recombinant adeno-associated virus serotype 9 leads to preferential cardiac transduction in vivo. Circ Res 99:e3–e9. https://doi.org/10.1161/01.RES.0000237661.18885.f6

Prando V, Da Broi F, Franzoso M et al (2018) Dynamics of neuroeffector coupling at cardiac sympathetic synapses. J Physiol 596:2055–2075. https://doi.org/10.1113/JP275693

Prasad K-MR, Xu Y, Yang Z et al (2011) Robust cardiomyocyte-specific gene expression following systemic injection of AAV: in vivo gene delivery follows a Poisson distribution. Gene Ther 18:43–52. https://doi.org/10.1038/gt.2010.105

Prigge M, Schneider F, Tsunoda SP et al (2012) Color-tuned channelrhodopsins for multiwavelength optogenetics. J Biol Chem 287:31804–31812. https://doi.org/10.1074/jbc.M112.391185

Quinn TA, Camelliti P, Rog-Zielinska EA et al (2016) Electrotonic coupling of excitable and nonexcitable cells in the heart revealed by optogenetics. Proc Natl Acad Sci 113:14852–14857. https://doi.org/10.1073/pnas.1611184114

Rajendran PS, Challis RC, Fowlkes CC et al (2019) Identification of peripheral neural circuits that regulate heart rate using optogenetic and viral vector strategies. Nat Commun 10:1–13. https://doi.org/10.1038/s41467-019-09770-1

Rost BR, Schneider-Warme F, Schmitz D, Hegemann P (2017) Optogenetic tools for subcellular applications in neuroscience. Neuron 96:572–603. https://doi.org/10.1016/j.neuron.2017.09.047

Rubart M, Tao W, Lu X-L et al (2017) Electrical coupling between ventricular myocytes and myofibroblasts in the infarcted mouse heart. Cardiovasc Res 107:1011–1020. https://doi.org/10.1093/cvr/cvx163

Scardigli M, Müllenbroich C, Margoni E et al (2018) Real-time optical manipulation of cardiac conduction in intact hearts. J Physiol 596:3841–3858. https://doi.org/10.1113/JP276283

Scherlag BJ, Po S (2006) The intrinsic cardiac nervous system and atrial fibrillation. Curr Opin Cardiol 21:51–54. https://doi.org/10.1097/01.hco.0000198980.40390.e4

Schneider F, Grimm C, Hegemann P (2015) Biophysics of channelrhodopsin. Annu Rev Biophys 44:167–186. https://doi.org/10.1146/annurev-biophys-060414-034014

Shang W, Lu F, Sun T et al (2014) Imaging Ca2+ nanosparks in heart with a new targeted biosensor. Circ Res 114:412–420. https://doi.org/10.1161/CIRCRESAHA.114.302938

Sineshchekov OA, Jung K-H, Spudich JL (2002) Two rhodopsins mediate phototaxis to low- and high-intensity light in Chlamydomonas reinhardtii. Proc Natl Acad Sci U S A 99:8689–8694. https://doi.org/10.1073/pnas.122243399

Stoyek MR, Quinn TA (2018) One fish, two fish, red fish, blue fish*: zebrafish as a model for cardiac research. Prog Biophys Mol Biol 138:1–2. https://doi.org/10.1016/j.pbiomolbio.2018.11.003

Suzuki T, Yamasaki K, Fujita S et al (2003) Archaeal-type rhodopsins in chlamydomonas: model structure and intracellular localization. Biochem Biophys Res Commun 301:711–717. https://doi.org/10.1016/S0006-291X(02)03079-6

Tallini YN, Ohkura M, Choi B-R et al (2006) Imaging cellular signals in the heart in vivo: cardiac expression of the high-signal Ca2+ indicator GCaMP2. Proc Natl Acad Sci U S A 103:4753–4758. https://doi.org/10.1073/pnas.0509378103

Tallini YN, Brekke JF, Shui B et al (2007) Propagated endothelial Ca2+ waves and arteriolar dilation in vivo: measurements in Cx40BAC-GCaMP2 transgenic mice. Circ Res 101:1300–1309. https://doi.org/10.1161/CIRCRESAHA.107.149484

Vogt CC, Bruegmann T, Malan D et al (2015) Systemic gene transfer enables optogenetic pacing of mouse hearts. Cardiovasc Res 106:338–343. https://doi.org/10.1093/cvr/cvv004

Wake E, Brack K (2016) Characterization of the intrinsic cardiac nervous system. Auton Neurosci Basic Clin 199:3–16. https://doi.org/10.1016/j.autneu.2016.08.006

Wang Y, Lin WK, Crawford W et al (2017) Optogenetic control of heart rhythm by selective stimulation of cardiomyocytes derived from pnmt + cells in murine heart. Sci Rep 7:40687. https://doi.org/10.1038/srep40687

Weber M, Scherf N, Meyer AM et al (2017) Cell-accurate optical mapping across the entire developing heart. elife 6:1–23. https://doi.org/10.7554/eLife.28307

Wengrowski AM, Wang X, Tapa S et al (2015) Optogenetic release of norepinephrine from cardiac sympathetic neurons alters mechanical and electrical function. Cardiovasc Res 105:143–150. https://doi.org/10.1093/cvr/cvu258

Winslow RL, Varghese A, Noble D et al (1993) Generation and propagation of ectopic beats induced by spatially localized Na-K pump inhibition in atrial network models. Proc R Soc B Biol Sci 253:55–61. https://doi.org/10.1098/rspb.1993.0126

Wu Y, Li SS, Jin X et al (2015) Optogenetic approach for functional assays of the cardiovascular system by light activation of the vascular smooth muscle. Vasc Pharmacol 71:192–200. https://doi.org/10.1016/j.vph.2015.03.006

Wu X, Zhu X, Chong P et al (2019) Sono-optogenetics facilitated by a circulation delivered rechargeable light source for minimally invasive optogenetics. Proc Natl Acad Sci U S A 116:26332–26342. https://doi.org/10.1073/pnas.1914387116

Yu L, Zhou L, Cao G et al (2017) Optogenetic modulation of cardiac sympathetic nerve activity to prevent ventricular arrhythmias. J Am Coll Cardiol 70:2778–2790. https://doi.org/10.1016/j.jacc.2017.09.1107

Zaglia T, Pianca N, Borile G et al (2015) Optogenetic determination of the myocardial requirements for extrasystoles by cell type-specific targeting of Channel Rhodopsin-2. Proc Natl Acad Sci 112:E4495–E4504. https://doi.org/10.1073/pnas.1509380112

Zgierski-Johnston CM, Ayub S, Fernández MC et al (2019) Cardiac pacing using transmural multi-LED probes in channelrhodopsin-expressing mouse hearts. Prog Biophys Mol Biol 154:51–61. https://doi.org/10.1016/j.pbiomolbio.2019.11.004

Zhang S, Cui N, Wu Y et al (2015) Optogenetic intervention to the vascular endothelium. Vasc Pharmacol 74:122–129. https://doi.org/10.1016/j.vph.2015.05.009

# Part IV

# Optogenetics in Neuroscience

# Elucidation of Neural Circuits Involved in the Regulation of Sleep/Wakefulness Using Optogenetics

25

Tomomi Tsunematsu

**Abstract**

Although sleep is an absolutely essential physiological phenomenon for maintaining normal health in animals, little is known about its function to date. In this section, I introduce the application of optogenetics to freely behaving animals for the purpose of characterizing neural circuits involved in the regulation of sleep/wakefulness. Applying optogenetics to the specific neurons involved in sleep/wakefulness regulation enabled the precise control of the sleep/wakefulness states between wakefulness, non-rapid eye movement (NREM) sleep, and REM sleep states. For example, selective activation of orexin neurons using channelrhodopsin-2 and melanopsin induced a transition from sleep to wakefulness. In contrast, suppression of these neurons using halorhodopsin and archaerhodopsin induced a transition from wakefulness to NREM sleep and increased the time spent in NREM sleep. Selective activation of melanin-concentrating hormone (MCH) neurons induced a transition from NREM sleep to REM sleep and prolonged the time spent in REM sleep, which was accompanied by a decrease in NREM sleep time. Optogenetics was first introduced to orexin neurons in 2007 and has since rapidly spread throughout the field of neuroscience. In the last 13 years or so, neural nuclei and the cell types that control sleep/wakefulness have been identified. The use of optogenetic studies has greatly contributed to the elucidation of the neural circuits involved in the regulation of sleep/wakefulness.

**Keywords**

Orexin · Melanin-concentrating hormone · Wakefulness · Non-rapid eye movement (NREM) sleep · Rapid eye movement (REM) sleep

## Abbreviations

| | |
|---|---|
| AAV | Adeno-associated virus |
| ArchR | Archaerhodopsin-3 |
| ArchT | Archaerhodopsin TP009 |
| ChR2 | Channelrhodopsin-2 |
| dDpMe | Deep mesencephalic nucleus |
| DR | Dorsal raphe |
| EEGs | Electroencephalograms |
| EMGs | Electromyograms |
| GPCR | G Protein-coupled receptor |
| HaloR | Halorhodopsin |
| LC | Locus coeruleus |

T. Tsunematsu (✉)
Graduate School of Life Sciences, Tohoku University, Sendai, Japan

Frontier Research Institute for Interdisciplinary Sciences, Tohoku University, Sendai, Japan

JST, PRESTO, Kawaguchi, Japan
e-mail: tsune@tohoku.ac.jp



H. Yawo et al. (eds.), *Optogenetics*, Advances in Experimental Medicine and Biology 1293,
https://doi.org/10.1007/978-981-15-8763-4_25

| | |
|---|---|
| LDT | Laterodorsal tegmental nucleus |
| MCH | Melanin-concentrating hormone |
| MnPO | Median preoptic nucleus |
| NA | Numerical aperture |
| NREM | Non-rapid eye movement |
| OPN4 | Melanopsin |
| OX1R | Orexin 1 receptor |
| OX2R | Orexin 2 receptor |
| PAG | Periaqueductal gray |
| PBN | Parabrachial nucleus |
| PPT | Pedunculopontine tegmental nucleus |
| REM | Rapid eye movement |
| SLD | Sublaterodorsal nucleus |
| TMN | Tuberomammillary nucleus |
| VLPO | Ventrolateral preoptic area |

## 25.1 Introduction of Sleep/Wakefulness: Wakefulness, Non-rapid Eye Movement (NREM) Sleep, and REM Sleep

I will first introduce the concepts of sleep and wakefulness before discussing the regulation of sleep/wakefulness using optogenetics. Sleeping is one of the most instinctive behaviors and is a universal physiological phenomenon conserved in insects and vertebrates. If a person sleeps for 8 h/day, they will have spent a third of their lifetime sleeping. When animals such as rats or dogs are deprived of sleep, they show notable reductions in body weight while increasing their food intake. Animals will eventually die if they are maintained in a sleep-deprived state for 2 weeks due to the development of opportunistic infections (Rechtschaffen et al. 1983). These reports suggest that sleep is an absolutely essential physiological activity that maintains normal health in animals.

There are two completely different states of sleep: rapid eye movement (REM) sleep and non-REM (NREM) sleep. To evaluate these distinct states (wakefulness, NREM sleep, and REM sleep), recordings such as electroencephalograms (EEGs) and electromyograms (EMGs) are typically used. There are also functional differences in the autonomic activity between these states. During wakefulness, EEGs show low-amplitude and EMGs show high-amplitude patterns due to muscle contraction (Fig. 25.1). When NREM sleep begins, EEGs show slow-wave patterns with high amplitude, and EMGs show lower amplitudes than the patterns observed during wakefulness (Fig. 25.1). In contrast, during REM sleep, EEGs have a relatively low-amplitude pattern which, at first glance, appears similar to the EEGs recorded during wakefulness. However, the main component of EEG frequency in this case is predominantly theta waves (6–10 Hz), and EMG activity is barely observed due to the relaxation of voluntary muscles (Fig. 25.1). If we look at the EEG power spectra that are calculated by fast-Fourier transformation, it is easy to visually understand the type of EEG frequency that comprises each vigilance state and it greatly aids in determining the vigilance state (Fig. 25.1).

## 25.2 Flip-Flop Circuit Regulating the Timing of Sleep/Wakefulness: Sleep Center and Arousal Center

What controls the sleep/wakefulness state in the brain and how is it regulated? It had been generally accepted that sleep is a passive phenomenon to alleviate tiredness caused by continuous wakefulness. However, this might represent a big misunderstanding regarding sleep. A portion of the brain actively promotes quiescence throughout the entire brain and body, that is, there exists a "sleep center" in the brain. This sleep center is located in the anterior part of the hypothalamus, called the ventrolateral preoptic area (VLPO), and contains GABAergic neurons. These GABAergic neurons are activated during sleep. The longer the time spent in wakefulness, the greater the increase in sleep pressure (sleepiness). As a result, sleep pressure increases the activity of GABAergic neurons in the VLPO.

In comparison, the "arousal centers," which induce wakefulness, are located in the brainstem and posterior part of the hypothalamus. Monoaminergic neurons, such as the histaminergic

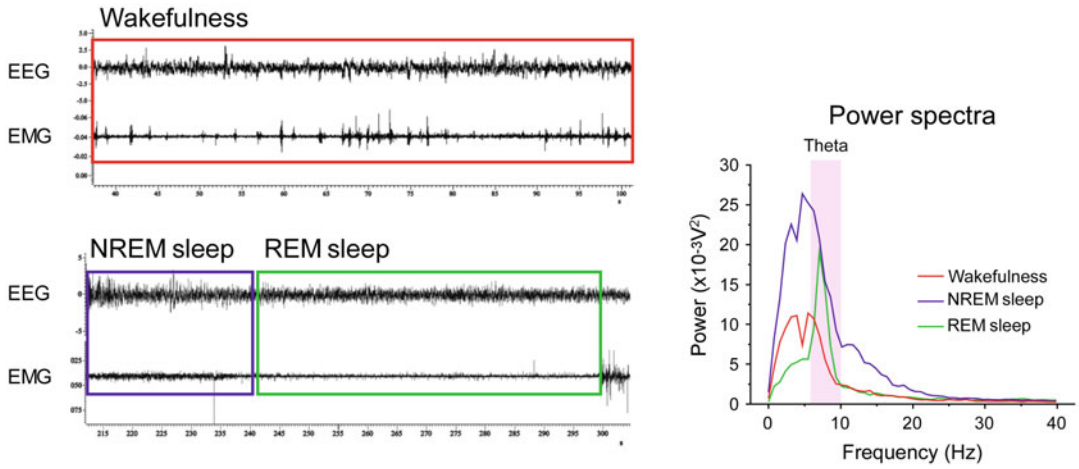


**Fig. 25.1** EEG and EMG during wakefulness, NREM sleep, and REM sleep

neurons in the tuberomammillary nucleus (TMN), serotonergic neurons in the raphe nucleus, and noradrenergic neurons in the locus coeruleus (LC), are the major contributors to the generation of arousal, comprising the arousal centers. The activity of monoaminergic neurons is synchronized and strongly associated with sleep/wakefulness states (Hobson et al. 1975; Trulson and Jacobs 1979; Foote et al. 1980; Szymusiak et al. 1989; Portas et al. 1998). These neurons exhibit tonic firing during wakefulness, decreased firing during NREM sleep, and are mostly electrically quiescent during REM sleep. Monoaminergic neurons project axons broadly throughout the brain, not only to the brainstem and posterior part of the hypothalamus but also to the cerebral cortex to activate whole-brain regions. This activation results in the promotion of arousal.

Sleep and arousal centers share mutually inhibitory circuitry; that is, sleep centers inhibit arousal centers and vice versa. Sleep and arousal centers function in a seesaw relationship, which is known as a flip-flop circuit (Fig. 25.2). Sleep or wakefulness is determined by the balance of activity between sleep and arousal centers. For example, if sleep center activity overcomes arousal center activity, sleep is initiated (Fig. 25.2). The sensation that promotes sleep after an all-nighter might imply the sudden flipping of a switch within the flip-flop circuit.

## 25.3 Orexin/Hypocretin and Narcolepsy

Narcolepsy is one type of sleep disorders. Narcolepsy typically begins in adolescence with the primary symptom of excessive daytime sleepiness. Patients tend to fall asleep even at an inappropriate time or place. In the context of a boring lecture, even a healthy person may fall asleep (as they might not make an effort to maintain wakefulness). However, narcolepsy patients fall asleep even if they are doing critical things such

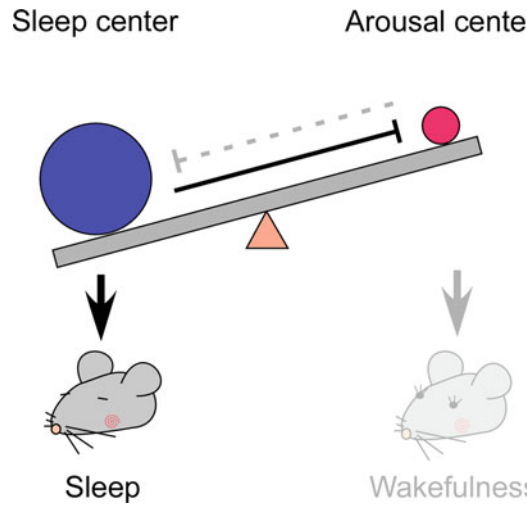


**Fig. 25.2** Flip-flop circuit which regulates the timing of sleep/wakefulness

as giving a lecture. Cataplexy is a specific symptom of narcolepsy. Cataplexy is the sudden relaxation of muscles triggered by strong emotions such as surprise, anger, and humor. In addition to sleepiness and cataplexy, narcoleptic patients exhibit a direct transition from wakefulness to REM sleep, in comparison to normal subjects that display a marked transit from wakefulness to REM sleep via NREM sleep. As a result, narcoleptic patients frequently experience sleep paralysis.

Narcolepsy had remained a disease of unknown etiology for a long time. The discovery of the neuropeptide orexin (also known as hypocretin) in 1998 opened the door to understanding the etiology of narcolepsy (Sakurai et al. 1998). Orexin-producing neurons (orexin neurons) are specifically and sparsely located in the lateral hypothalamic area, which is a well-known feeding center, and projects their axons to almost all regions of the brain (Fig. 25.3). Orexin actually consists of two peptides, orexin A and B, which are enzymatically processed from a common precursor peptide, prepro-orexin. Orexin acts physiologically by binding two kinds of G protein-coupled receptors, orexin 1 (OX1R) and orexin 2 (OX2R) receptors (Fig. 25.3). Orexin was initially described as a regulator of feeding behavior based on results showing that intracerebroventricular injections of orexin induce feeding behavior in rats and mice. Subsequently, *prepro-orexin* knockout mice, *OX2R* knockout mice, and orexin neuron-ablated mice displayed narcolepsy-like phenotypes, specifically a fragmentation of sleep/wakefulness (or a frequent repetition of sleep and wakefulness). These mice were unable to maintain wakefulness and thus behavior was commonly arrested (Chemelli et al. 1999; Hara et al. 2001; Willie et al. 2003; Tabuchi et al. 2014). In addition, a postmortem study of human narcolepsy patients revealed a degeneration of orexin neurons in the hypothalamus (Peyron et al. 2000). These studies support the idea that degeneration of orexin neurons by unknown causes (possibly autoimmune disease) leads to narcolepsy.

While orexin neurons project their axons to almost all regions of the brain, they project to the arousal centers, such as the TMN, raphe nucleus, and LC, at much higher density. Orexin neurons activate the monoaminergic neurons in the arousal centers. Orexin neurons are thought to be phasically active during wakefulness and almost silent during NREM and REM sleep. Therefore, it seems that orexin neurons contribute to the stabilization of the flip-flop circuit as an activator of arousal centers, especially for the maintenance of wakefulness (Fig. 25.4). In contrast, in narcolepsy patients, the balance between sleep and arousal centers may be unstable due to the specific degeneration of orexin neurons. This would cause the fragmentation of sleep/wakefulness states as a result of the frequent transition within the flip-flop circuit (Fig. 25.4). It can thus be hypothesized that orexin neurons play a crucial role in the stabilization of arousal states.

We have previously presented evidence supporting this hypothesis using genetically modified mice. However, these mice likely compensate for their genetic modifications with the activity of other neurons during development, since the regulation of sleep/wakefulness is essential to the physiological maintenance of life. Thus, the question remains, how does the activity of orexin neurons drive behavior, particularly the regulation of sleep/wakefulness? Optogenetics represents a powerful tool that could be used to address this question.

## 25.4 Wired Optogenetic System for Freely Moving Mice

Here, I will introduce the wired optogenetic system for freely moving mice, which was developed by Prof. Akihiro Yamanaka's group at Nagoya University, to which I previously belonged. To determine the sleep/wakefulness states in mice, both EEG and EMG must be used, while simultaneously illuminating orexin neurons, which are located in the lateral hypothalamic area. After many trials and errors over several years, we were able to successfully design a wired system

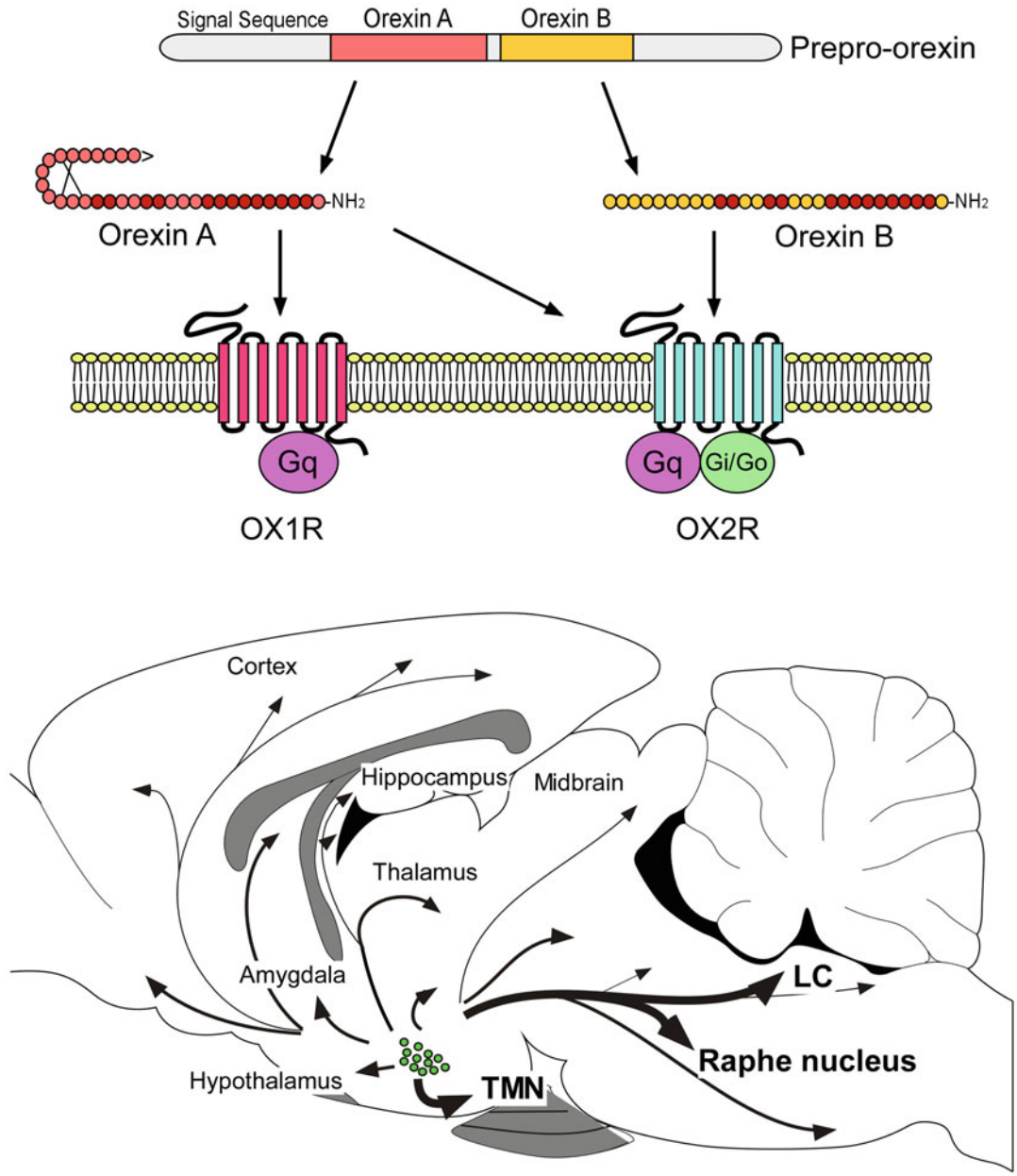


**Fig. 25.3** Orexin and orexin receptors

that fulfills the above requirements (Fig. 25.5) (Yamanaka 2012).

A high-power LED or laser is used as the light source. On and off switching of the light source is regulated by a TTL signal connected to an electrical stimulator (or a pulse generator). The light is guided through quartz fiber optics (diameter of 1 mm), which are connected to a light source. Flexible plastic fiber optics (diameter of 0.5 mm) is inserted bilaterally into the brain. The tips of the fibers are located 1 mm above the targeted neurons. Quartz and plastic fibers are connected via a light slip ring, which is a rotatable devise that maintains high

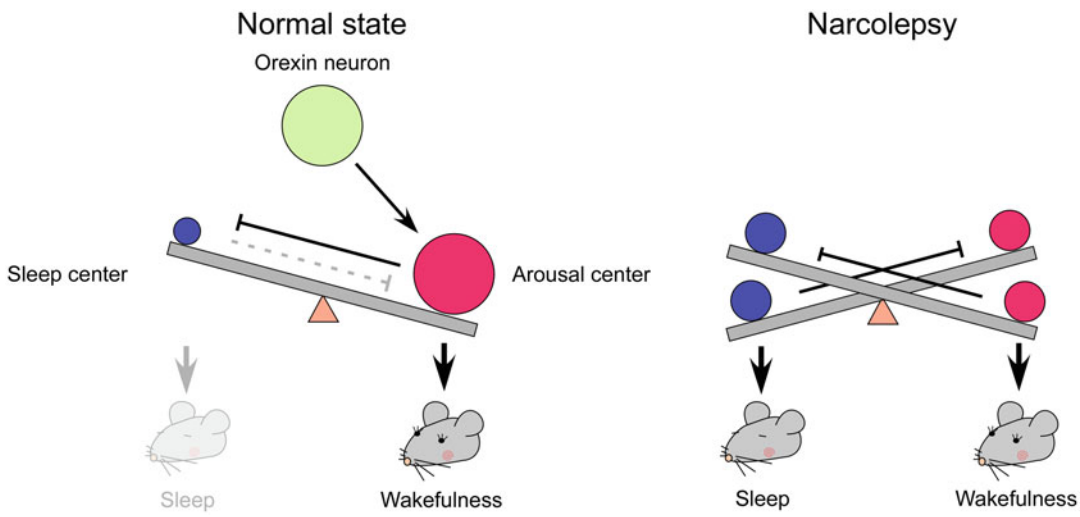


**Fig. 25.4** Orexin and narcolepsy

light-coupling efficacy. The device enables mice to move freely without twisting the optical fibers. The position of the inserted fiber optics is determined by the location of target cells, the three-dimensional range of their distribution, and the numerical aperture (NA) of the fiber optics. In our setup, the fiber optics was positioned 1 mm above the location of the target cells with an NA of 0.5, and with the assumption that orexin neurons are distributed within a range of approximately 1 $mm^3$ cube.

To determine the sleep/wakefulness states concurrent with the illumination, EEGs and EMGs are simultaneously recorded. EEGs are

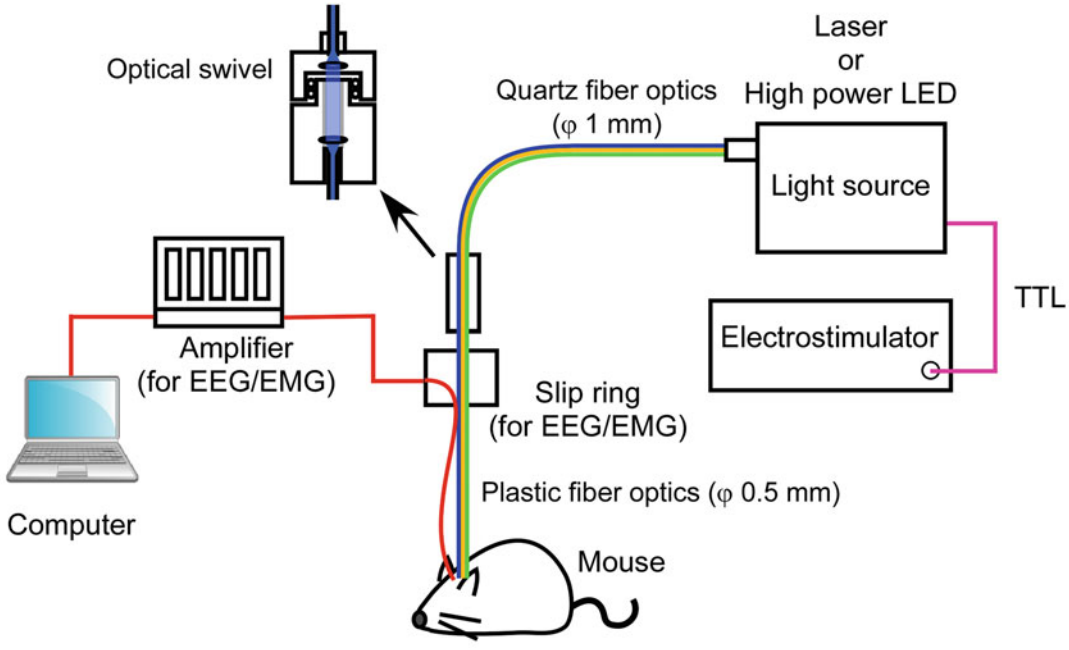


**Fig. 25.5** Schematic of the wired optogenetic system for freely moving mice

recorded from the surface of the cortex using screw electrodes and EMGs are recorded from the neck muscle using wire electrodes. The signals from EEG/EMG are continuously recorded via a slip ring. The signals are amplified and then data are acquired and analyzed using computer software.

## 25.5 Induction of Wakefulness Via Activation of Orexin Neurons

In 2007, the group of Prof. Deisseroth and Prof. de Lecea at Stanford University applied optogenetics to freely behaving animals and successfully controlled sleep/wakefulness by targeting orexin neurons in the hypothalamus (Adamantidis et al. 2007). To selectively activate orexin neurons with light, channelrhodopsin-2 (ChR2) was exclusively expressed in orexin neurons using a viral vector. They generated mice in which orexin neurons specifically expressed ChR2 using a lentivirus vector containing the 3.1-kb upstream region of the mouse *prepro-orexin* gene as a promoter. To confirm the function of ChR2 expression in orexin neurons, slice patch-clamp recordings were performed and blue illumination-induced depolarization of the ChR2-expressing orexin neurons. It was discovered that both continuous and pulse illumination could induce depolarization and increase firing frequency.

As mentioned above, orexin neurons phasically fire during wakefulness and are almost silent during sleep. This raised the question: Can wakefulness be artificially induced in mice via activation of orexin neurons during sleep? Prof. Deisseroth and Prof. de Lecea were the first to provide the answer. Blue illumination was applied in vivo to freely moving mice that displayed spontaneous sleep or wakefulness states. During spontaneous sleep, continuous or pulsative illumination of greater than 5 Hz in frequency induced a transition to wakefulness after a delay of approximately 30 s from the initiation of illumination. This effect was observed not only during NREM sleep but also during REM sleep, suggesting that the upregulation of orexin neural activity is sufficient to promote the initiation of arousal (Adamantidis et al. 2007). This study was the first successful report linking activation of specific types of neurons in mice to behavior through the use of optogenetics. In addition, this study established that optogenetics is a powerful tool for regulating neural activity. Since the publication of this report, optogenetic approaches have been applied to the study of many neural populations and various behaviors.

Another independent attempt was made by our group using transgenic mice in which orexin neurons specifically expressed melanopsin (OPN4) under control of the tet-off system (*Orexin-tTA; BitetO human OPN4/mCherry* bigenic mice) (Tsunematsu et al. 2013b). OPN4 is a blue light-driven Gq-coupling G protein-coupled receptor (GPCR) normally expressed in retinal ganglion cells. Blue illumination depolarizes OPN4-expressing neurons via activation of the Gq signal transduction cascade. The advantage of using OPN4 is that the application of even short light pulses induces long-lasting depolarization since GPCR signaling is relatively long lasting. In addition, another advantage of our study was the use of a bigenic mouse strain which enabled reliable and reproducible expression of OPN4 in orexin neurons compared to the use of a viral vector. This study also confirmed continuous light-evoked depolarization after blue light cessation using slice-patch clamp. Similarly, blue light pulses induced the transition from NREM sleep to wakefulness in bigenic mice.

## 25.6 Induction of NREM Sleep Via Acute Inhibition of Orexin Neurons

The reports using ChR2 and OPN4 demonstrated that the acute activation of orexin neural activity induces the transition from sleep to wakefulness in mice. The next question is thus whether the inhibition of orexin neural activity induces sleep and/or a narcolepsy-like phenotype in the opposite manner.

To inhibit orexin neural activity, we employed an orange light-driven chloride pump,

halorhodopsin (HaloR). To express HaloR in orexin neurons, the 3.2-kb upstream sequence of the human prepro-orexin gene was used as a promoter to generate new transgenic mice (*orexin/HaloR* transgenic mice). Immunohistochemical analyses revealed that 94% of orexin neurons expressed HaloR in the *orexin/HaloR* mice.

First, to confirm the function of HaloR expression in orexin neurons in the transgenic mouse brain, slice patch-clamp analysis was performed using brain slice preparations from *orexin/HaloR* mice. Orange illumination immediately hyperpolarized HaloR-expressing orexin neurons and completely inhibited the generation of action potentials. In addition, we determined the length over which orexin neural activity could be inhibited. Firing was completely inhibited for approximately 1 min from the initiation of orange illumination. However, firing gradually recovered, likely due to the desensitization of HaloR or the accelerated outward transport of chloride ions. Based on the results of these in vitro experiments, we attempted to acutely silence orexin neurons for 1 min in freely moving *orexin/HaloR* mice.

Using the wired optogenetic system for freely moving mice described above, orexin neural activity was inhibited for 1 min via continuous orange illumination. Illumination was applied when mice were in a state of arousal. To determine the sleep/wakefulness states, EEGs and EMGs were simultaneously recorded. Mice maintained a wakefulness state for a few seconds after the initiation of orange illumination. EMG power gradually decreased, and the slow-wave component of the EEGs increased. This indicates an induction of NREM sleep. It has been suggested that the acute inhibition of orexin neural activity is sufficient to promote the initiation of NREM sleep or that the activation of orexin neurons is necessary to maintain an arousal state. However, a narcolepsy-like phenotype, such as cataplexy, and a direct transition from wakefulness to REM sleep was not observed.

To further study the physiological significance of orexin neural activity in sleep/wakefulness regulation in conjunction with other arousal centers, EEG and EMG activity and the activity of dorsal raphe (DR) serotonergic neurons were simultaneously recorded. In vivo single-unit extracellular recordings were performed using conscious, head-fixed *orexin/HaloR* mice. The firing of serotonergic neurons in the DR was recorded when orexin neural activity was inhibited by illumination via fiber optics located in the hypothalamus. Serotonergic neurons in the DR are densely innervated by orexin neurons and are activated by orexin either directly or indirectly. During orange illumination, the firing frequency of serotonergic neurons in the DR gradually decreased in conjunction with an EEG delta power increase (Fig. 25.6). This suggests that acute silencing of orexin neural activity by orange illumination into the hypothalamus decreased the firing frequency of serotonergic neurons in the DR and induced NREM sleep in mice. This study provided the first example that the selective inhibition of orexin neurons is sufficient to induce a transition from wakefulness to NREM sleep (Tsunematsu et al. 2011).

## 25.7 Increased Total NREM Sleep Time Via Long-Lasting Inhibition of Orexin Neurons

The study using *orexin/HaloR* mice revealed that acute inhibition of orexin neural activity functions as the switch to initiate NREM sleep. However, to completely understand the regulatory circuitry and the mechanisms of sleep/wakefulness under physiological conditions, silencing for more than 1 min is essential. However, as described above, it is difficult to inhibit neural activity for longer durations, at least in orexin neurons, likely due to the desensitization of HaloR or the accelerated outward transport of chloride ions. To address this issue, a green light-driven proton pump, Archaerhodopsin-3 (ArchR) and Archaerhodopsin TP009 (ArchT) (Tsunematsu et al. 2013a; Williams et al. 2019), were employed. The authors generated two transgenic mice in which orexin neurons specifically express ArchR or ArchT using the human prepro-orexin promoter in the case of ArchR *(orexin/*

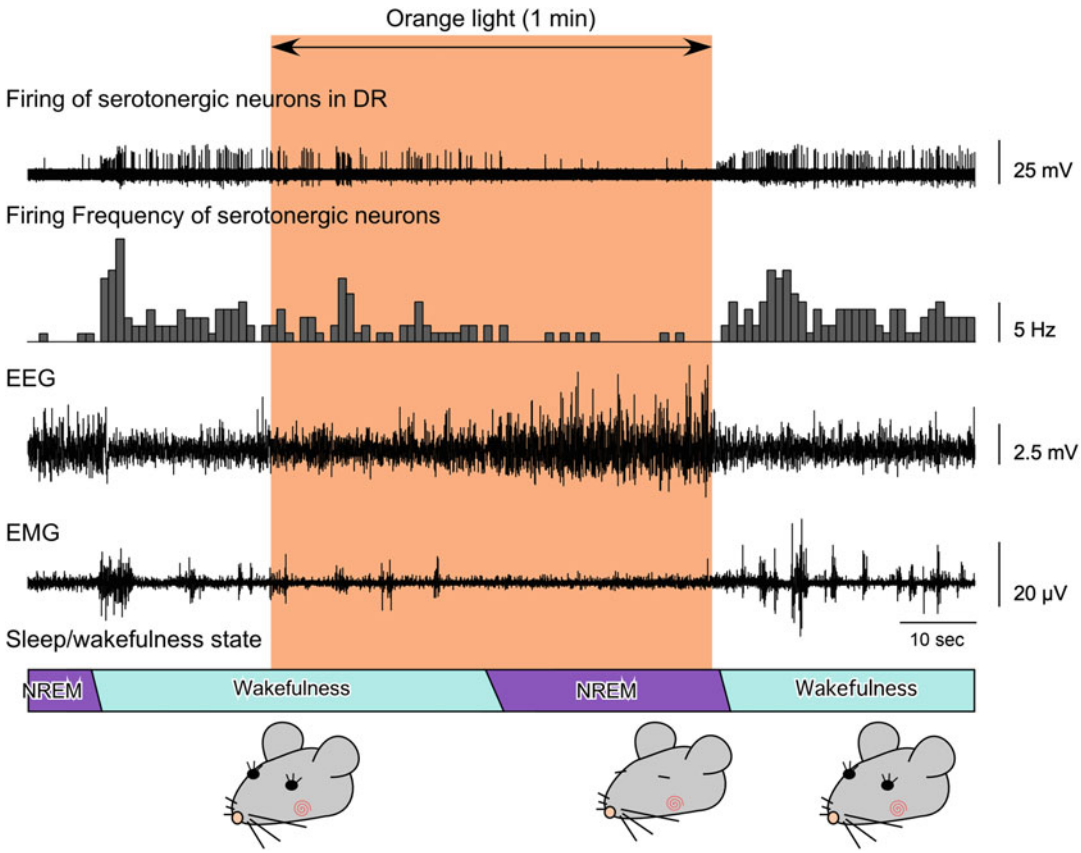


**Fig. 25.6** Transition from wakefulness to NREM sleep and inhibition of serotonergic neural activity by illumination of orexin neurons

*ArchR* mice) and the tet-off system in the case of ArchT (*orexin-tTA; TetO ArchT* mice). The expression rate of ArchR and ArchT in orexin neurons of *Orexin/ArchR* mice and *orexin-tTA; TetO ArchT* mice was 80% and 72%, respectively.

Light-induced responses of HaloR-expressing, ArchR-expressing, or ArchT-expressing orexin neurons were evaluated using slice-patch clamp. As shown in Fig. 25.7, ArchR and ArchT induced stronger inhibition of activity in terms of light-induced current, hyperpolarization, and the duration of inhibition compared to HaloR (at least in orexin neurons). It seems that ArchR and ArchT are suitable for longer duration inhibition due to their limited desensitization. Moreover, using both slice-patch clamp and immunohistochemical measurement of c-Fos, a marker of activated neurons, it was possible to detect a significant inhibition of orexin neurons over at least 1 h.

Using novel transgenic mouse lines, the effects of 1-h illumination on the sleep/wakefulness state were examined during both the subjective day and subjective night. Inhibition of orexin neurons by application of continuous green illumination induced a significant increase in total NREM sleep time during the subjective night (the active period for nocturnal mice; Fig. 25.8). Mice underwent several repeated bouts of approximately 10 min of NREM sleep and could not maintain wakefulness but continued to sleep during illumination. This can be interpreted as a fragmentation of sleep/wakefulness, such as seen in the narcolepsy phenotype. In contrast, illumination had little effect on sleep/wakefulness patterns during the subjective day (the inactive

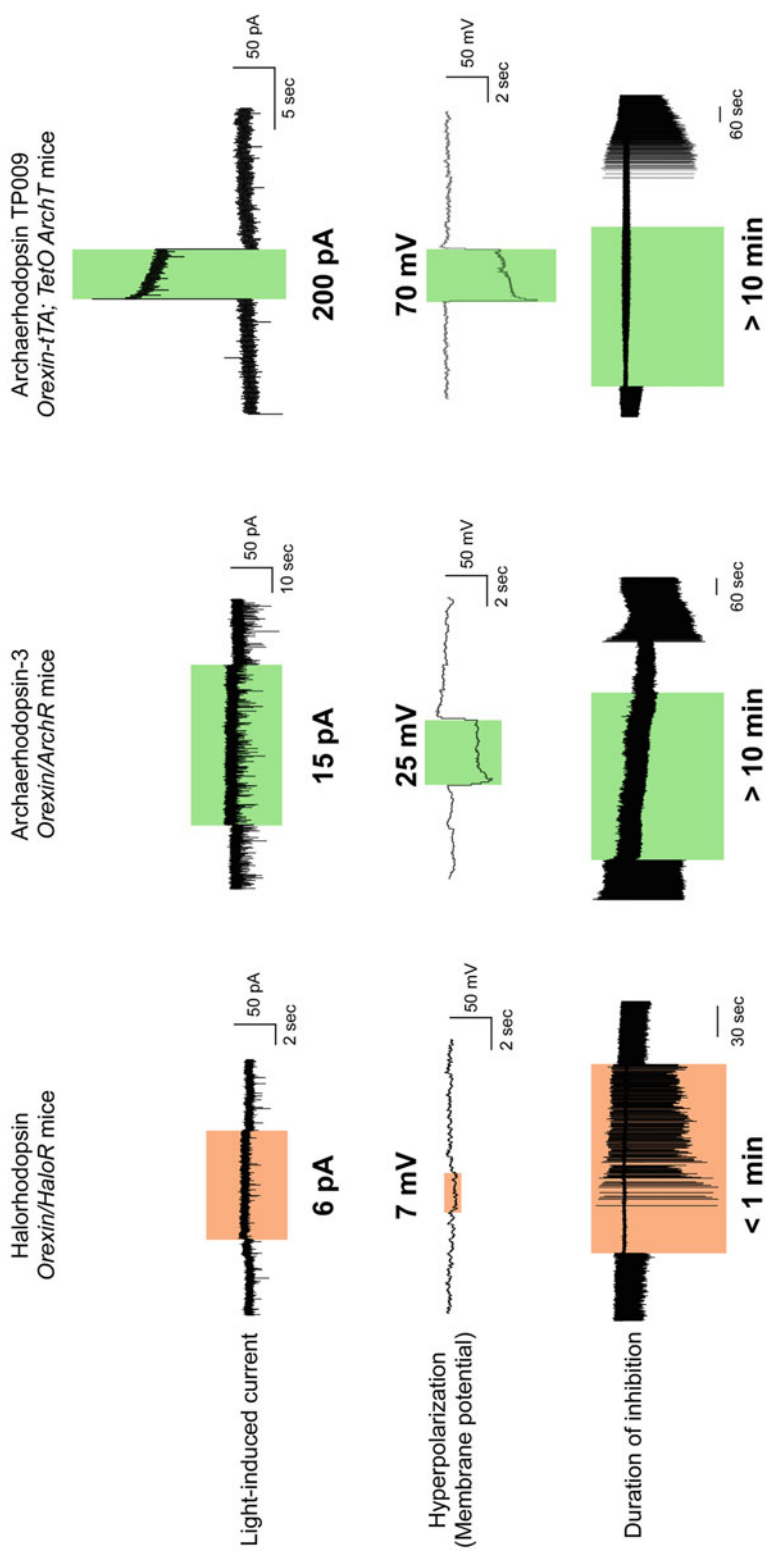


**Fig. 25.7** Comparison of light-evoked responses via light-driven pumps in orexin neurons

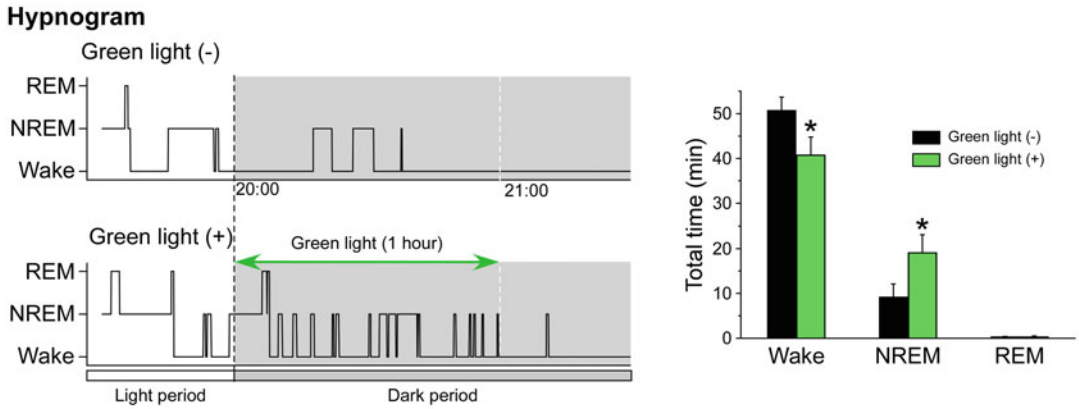


**Fig. 25.8** Sustained silencing of orexin neurons induces an increase in total NREM sleep time

period for nocturnal mice). These results suggest that orexin neural activity contributes to the maintenance of wakefulness during the active phase (Tsunematsu et al. 2013a; Williams et al. 2019).

## 25.8 Other Neuronal Types Involved in the Arousal Switch

Thus far, I have introduced the concept of sleep/wakefulness regulation via orexin neural activity. Orexin neurons contribute to the stabilization of the flip-flop circuitry, which is composed of mutual inhibitory circuits between the sleep centers and arousal centers in the brain. In addition to optogenetic control of orexin neurons, optogenetic strategies directly applied to neurons within the sleep, and arousal centers would be expected to control sleep/wakefulness states.

As discussed above, monoaminergic neurons, such as the histaminergic neurons in the TMN, serotonergic neurons in the raphe nucleus, and noradrenergic neurons in the LC, play an important role in wakefulness, serving as arousal centers. These monoaminergic neurons, which are responsible for the activity of the arousal center, project axons from the brainstem and hypothalamus to the cerebral cortex, and enhance activity throughout the entire brain and maintain arousal. In 2010, the group of Prof. Deisseroth and Prof. de Lecea at Stanford University introduced the optogenetic neural control of noradrenergic neurons in the LC. Noradrenergic neurons in mice specifically express ChR2 or HaloR. A 5 Hz frequency of blue light pulse for 5 s was applied to ChR2-expressing mice during the subjective day. This illumination induced transition from both NREM sleep and REM sleep to wakefulness within 5 s from the initiation of illumination. They also evaluated the effect of 1-h illumination on the sleep/wakefulness cycle using HaloR-expressing freely moving mice. Results showed that yellow illumination significantly increased total NREM sleep time and decreased total wakefulness time during the subjective night (active period) (Carter et al. 2010). Similarly, using optogenetic techniques, activation of raphe nucleus serotonergic neurons induced an increase in wakefulness and fragmentation of NREM sleep (Ito et al. 2013). Other groups have reported that activation of histaminergic neurons in the TMN using chemogenetic techniques not only increases the time spent in wakefulness but also locomotor activity (Yu et al. 2015). These results support the physiological function of monoaminergic neurons as components of an arousal center, which was postulated for some time ago.

It has been reported that glutamatergic neurons localized in the parabrachial nucleus (PBN), and cholinergic neurons localized in the laterodorsal tegmental nucleus (LDT) and pedunculopontine tegmental nucleus (PPT) show high expression levels of cFos and high firing frequency during

both wakefulness and REM sleep. The physiological function of cholinergic neurons in the basal forebrain has also been investigated through the application of optogenetics. Inhibition of neural activity by light induced an increase in the slow-wave component of the EEG and decreased the transition from NREM sleep to wakefulness. Conversely, photoactivation showed a completely opposite phenotype (Irmak and de Lecea 2014; Xu et al. 2015). In conclusion, cholinergic neurons in the basal forebrain, as well as in the PPT and LDT, are mainly involved in the control of cortical neural activity. The question remains, however, as to whether these neurons are necessary for wakefulness itself. Optogenetic activation of GABAergic neurons located in the basal forebrain induces wakefulness. This is because cortical activity can be increased by reducing the activity of inhibitory cortical interneurons. GABAergic neurons are an anatomically and functionally heterogeneous group, and parvalbumin-positive neurons seem to be responsible for arousal (Xu et al. 2015).

## 25.9 Neurons Involved in the NREM Sleep Switch

The sleep center is driven by GABAergic neurons localized in the preoptic area and functions as a switch for NREM sleep. The peak in firing frequency and cFos expression of these neurons occurs during sleep. In particular, the GABAergic neurons of the ventrolateral preoptic area (VLPO) strongly innervate and inhibit the arousal-promoting brain regions, including the TMN, LC, raphe nuclei, periaqueductal gray (PAG), PBN, and hypothalamus. Conversely, the VLPO is innervated by arousal-promoting neurons. In vitro brain slice preparation experiments have shown that VLPO GABAergic neurons are inhibited by acetylcholine, noradrenaline, dopamine, and serotonin. However, GABAergic neurons are not inhibited by histamine but have been shown to be inhibited by endomorphin, which colocalizes with histamine neurons. This reciprocal inhibition makes up the flip-flop circuit of the sleep and wake centers.

In addition to the VLPO, 75% of neurons localized to the median preoptic nucleus (MnPO) increase firing frequency during sleep. Many of these neurons are characterized by an increase in firing prior to the onset of sleep. Additionally, MnPO neurons strongly innervate the VLPO. These results suggest that MnPO neurons are involved in the perception of sleep pressure (sleepiness), and transmit the information to the NREM neurons in the VLPO responsible for the switch.

However, it has been reported that total sleep time is reduced to only about 50% after lesioning the VLPO, indicating the potential presence of other sleep centers. In 2014, a combination of chemogenetic and lesion studies revealed that GABAergic/glycinergic neurons located in the parafacial zone in the medulla are NREM sleep switches. Chemogenetic activation of these neurons increased the time spent in NREM sleep and decreased the time spent in wakefulness and REM sleep. Moreover, it has been reported that this effect inhibits the transition to arousal by suppressing the glutamatergic neurons located in the PBN (Anaclet et al. 2014).

## 25.10 Neurons Involved in the REM Sleep Switch

It has been hypothesized that cholinergic neurons in the LDT and PPT are responsible for the REM sleep switch since administration of the cholinergic agonist carbachol induced an increase in REM sleep. However, lesion studies in the LDT and PPT had no effect on the REM sleep state, suggesting that these are seen as modulators rather than the central REM switch itself. So where are the REM sleep switch neurons located? Possible candidates include the neurons which localize to the sublaterodorsal nucleus (SLD) or subcoeruleus. cFos expression in these neurons increases during REM sleep, and SLD lesions can shorten the episode duration of REM sleep and reduce total REM sleep time (Krenzer et al. 2011). The SLD controls REM sleep by mutual inhibition with GABAergic neurons in the PAG and deep mesencephalic nucleus (dDpMe) in

which neurons strongly inhibit REM sleep. In this way, the neural circuit for turning REM sleep on or off also forms a flip-flop circuit. Therefore, the neural circuit which controls the stage of sleep/wakefulness is a double flip-flop circuit of wake/NREM and REM sleep on/off (Fig. 25.9). Animals with lesions in the SLD show REM sleep without atonia. Animals will twitch, jump, and sometimes show motor behaviors (possibly related to the contents of a dream) during REM sleep suggesting the involvement of muscle atonia. It appears that neurons which play an important role in inhibition of REM sleep strongly disturb the direct transition from wakefulness to REM sleep, which is normally not possible.

Melanin-concentrating hormone (MCH) neurons in the lateral hypothalamus also play a role in transiting to REM sleep. Previous reports revealed that MCH neurons are important in the regulation of feeding behavior, energy metabolism, and locomotor activity. In comparison, in vivo studies involving extracellular recordings in rats demonstrated that MCH neurons are silent during wakefulness, discharge during sleep, and are maximally active during REM sleep. This firing pattern is reciprocal to that of orexin neurons, implying that the MCH neurons may be involved in REM sleep regulation.

In 2013, the research group of Prof. Adamantidis at McGill University, and our group in 2014, independently published reports in which optogenetics was applied to the study of MCH neurons. Jego et al. (2013) injected adeno-associated virus (AAV) into transgenic mice in which MCH neurons expressed Cre recombinase. In the brains of these mice, either ChR2, HaloR, or ArchR was expressed in MCH neurons. In contrast, in our study, we generated transgenic mice in which MCH neurons specifically expressed ChR2 or ArchT using the tet-off system (*MCH-tTA; TetO ChR2* bigenic mice and *MCH-tTA; TetO ArchT* bigenic mice).

In the Jego et al. study, in vivo optogenetic activation of MCH neurons was performed in freely moving mice. They reported that optogenetic stimulation of MCH neurons at a frequency of 20 Hz at the onset of NREM sleep had little effect on the duration of NREM sleep, although it increased the probability of NREM to REM sleep transitions. Comparatively, at the onset of REM sleep, activation of MCH neurons significantly extended REM sleep duration. Conversely, optogenetic silencing of MCH neurons during REM sleep did not reduce the duration but induced a shift in the dominant theta wave peak frequencies toward slower oscillations (Jego et al. 2013). Our group also described optogenetic manipulation of MCH neurons using transgenic mice. Optical activation of MCH neurons using a 10 Hz frequency of blue light pulses for 3 h in *MCH-tTA; TetO ChR2* mice resulted in an increase in time spent in REM sleep accompanied by a decrease in time spent in NREM sleep without affecting total wakefulness time. In addition, an acute 1-min activation of MCH neurons at a 10 Hz frequency during the NREM sleep state induced a transition to REM sleep. In comparison, silencing MCH neurons by continuous green illumination for 3 h using *MCH-tTA; TetO ArchT* mice had little effect on vigilance state (Tsunematsu et al. 2014). The combined results from these two reports suggest that MCH neural activity is sufficient to induce REM sleep but is not necessary for the occurrence of REM sleep.

## 25.11 Perspective

With the introduction of optogenetic technology, the neural circuits responsible for the regulation of sleep/wakefulness states have been identified in turn. However, the identity of the "finger" that flips the switch remains unknown. Several possibilities have been discussed, from external factors such as the environment, to internal factors such as circadian rhythms. As an example of an external factor, it is known that the total time of wakefulness increases in situations where food and water are not available because it is necessary to explore the environment in search of them in order to live. In these situations, it has been reported that an increase in locomotor activity and maintenance of arousal occur via activation of orexin neurons (Yamanaka et al. 2003; Tsunematsu et al. 2008).

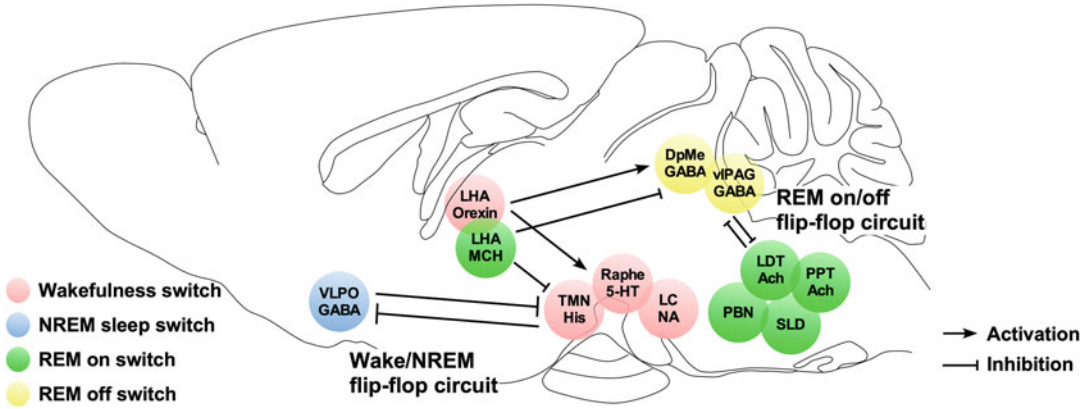


**Fig. 25.9** Double flip-flop circuits regulating REM/NREM/wakefulness states

In another example, sleep deprivation increases the time spent in sleep. When cerebrospinal fluid collected from sleep-deprived dogs was administered to other dogs, they fell asleep immediately despite not having sleep deprivation. This suggests that humoral factors contribute to sleep pressure (sleepiness). Subsequent studies identified these factors to be adenosine and prostaglandin D2. Interestingly, it has been reported that astrocytes, a type of glial cell, release adenosine, a sleep-inducing substance. ATP is released from astrocytes and is rapidly hydrolyzed to adenosine outside of the cell. It has been found that mice with specific disruptions in the exocytosis of astrocytes do not show increased sleep after sleep deprivation (Halassa et al. 2009).

In astrocytes, gene expression patterns differ between arousal and sleep. Gene expression related to metabolism and process elongation is particularly enhanced during sleep. Thus, during wakefulness, these patterns might contribute to the clearance of neurotransmitters such as glutamate. Conversely, during sleep, this might contribute to the promotion of glutamate spillover. It is expected that this effect might be involved in the synchronization of neural activity during NREM sleep (Bellesi et al. 2015). Individual astrocytes are thought to span 90,000 synapses and may be involved in the periodicity and synchrony of neural activity in sleep/wakefulness states. The causal and correlative relationship between astrocytes and the neurons responsible for the sleep switch remain a topic for future research.

Another issue that remains in sleep research is the elucidation of physiological functions of sleep. Although part of the physiological functions of sleep has been elucidated by optogenetical manipulation of field potential oscillations characteristic during sleep, neural circuit, and specific type of neurons in recent years (Boyce et al. 2016; Miyamoto et al. 2016; Ghandour et al. 2019; Izawa et al. 2019), it is necessary to approach its function using optogenetics furthermore.

**Acknowledgments** T.T. is supported by PRESTO from JST (JPMJPR1887), JSPS Grant-in-Aid for Research Activity Start-up (17H06520), and JSPS Grant-in-Aid for Scientific Research on Innovative Areas (20H05047).

## References

Adamantidis AR, Zhang F, Aravanis AM, Deisseroth K, de Lecea L (2007) Neural substrates of awakening probed with optogenetic control of hypocretin neurons. Nature 450(7168):420–424

Anaclet C, Ferrari L, Arrigoni E, Bass CE, Saper CB, Lu J, Fuller PM (2014) The GABAergic parafacial zone is a medullary slow wave sleep–promoting center. Nat Neurosci 17(9):1217–1224

Bellesi M, de Vivo L, Tononi G, Cirelli C (2015) Effects of sleep and wake on astrocytes: clues from molecular and ultrastructural studies. BMC Biol 13:66

Boyce R, Glasgow SD, Williams S (2016) Causal evidence for the role of REM sleep theta rhythm in contextual memory consolidation. Science 352:812–816

Carter ME, Yizhar O, Chikahisa S, Nguyen H, Adamantidis A, Nishino S, Deisseroth K, de Lecea L (2010) Tuning arousal with optogenetic modulation of locus coeruleus neurons. Nat Neurosci 13:1526–1533

Chemelli RM, Willie JT, Sinton CM, Elmquist JK, Scammell T, Lee C, Richardson JA, Williams SC, Xiong Y, Kisanuki Y, Fitch TE, Nakazato M, Hammer RE, Saper CB, Yanagisawa M (1999) Narcolepsy in orexin knockout mice: molecular genetics of sleep regulation. Cell 98:437–451

Foote SL, Aston-Jones G, Bloom FE (1980) Impulse activity of locus coeruleus neurons in awake rats and monkeys is a function of sensory stimulation and arousal. Proc Natl Acad Sci U S A 77(5):3033–3037

Ghandour K, Ohkawa N, Fung CCA, Asai H, Saitoh Y, Takekawa T, Okubo-Suzuki R, Soya S, Nishizono H, Matsuo M, Osanai M, Sato M, Ohkura M, Nakai J, Hayashi Y, Sakurai T, Kitamura T, Fukai T, Inokuchi K (2019) Orchestrated ensemble activities constitute a hippocampal memory engram. Nat Commun 10 (1):2637

Halassa MM, Florian C, Fellin T, Munoz JR, Abel T, Haydon PG, Frank MG (2009) Astrocytic modulation of sleep homeostasis and cognitive consequences of sleep loss. Neuron 61:213–219

Hara J, Beuckmann CT, Nambu T, Willie JT, Chemelli RM, Sinton CM, Sugiyama F, Yagami KI, Goto K, Yanagisawa M, Sakurai T (2001) Genetic ablation of orexin neurons in mice results in narcolepsy, hypophagia, and obesity. Neuron 30:345–354

Hobson JA, McCarley RW, Wyzinski PW (1975) Sleep cycle oscillation: reciprocal discharge by two brainstem neuronal groups. Science 189:55–58

Irmak SO, de Lecea L (2014) Basal forebrain cholinergic modulation of sleep transitions. Sleep 37 (12):1941–1951

Ito H, Yanase M, Yamashita A, Kitabatake C, Hamada A, Suhara Y, Narita M, Ikegami D, Sakai H, Yamazaki M, Narita M (2013) Analysis of sleep disorders under pain using an optogenetic tool: possible involvement of the activation of dorsal raphe nucleus-serotonergic neurons. Mol Brain 6:59

Izawa S, Chowdhury S, Miyazaki T, Mukai Y, Ono D, Inoue R, Ohmura Y, Mizoguchi H, Kimura K, Yoshioka M, Terao A, Kilduff TS, Yamanaka A (2019) REM sleep-active MCH neurons are involved in forgetting hippocampus-dependent memories. Science 365(6459):1308–1313

Jego S, Glasgow SD, Herrera CG, Ekstrand M, Reed SJ, Boyce R, Friedman J, Burdakov D, Adamantidis AR (2013) Optogenetic identification of a rapid eye movement sleep modulatory circuit in the hypothalamus. Nat Neurosci 16(11):1637–1643

Krenzer M, Anaclet C, Vetrivelan R, Wang N, Vong L, Lowell BB, Fuller PM, Lu J (2011) Brainstem and spinal cord circuitry regulating REM sleep and muscle atonia. PLoS One 6(10):e24998

Miyamoto D, Hirai D, Fung CCA, Inutsuka A, Odagawa M, Suzuki T, Boehringer R, Adaikkan C, Matsubara C, Matsuki N, Fukai T, Mchugh TJ, Yamanaka A, Murayama M (2016) Top-down cortical input during NREM sleep consolidates perceptual memory. Science 352:1315–1318

Peyron C, Faraco J, Rogers W, Ripley B, Overeem S, Charnay Y, Nevsimalova S, Aldrich M, Reynolds D, Albin R, Li R, Hungs M, Pedrazzoli M, Padigaru M, Kucherlapati M, Fan J, Maki R, Lammers GJ, Bouras C, Kucherlapati R, Nishino S, Mignot E (2000) A mutation in a case of early onset narcolepsy and a generalized absence of hypocretin peptides in human narcoleptic brains. Nat Med 6:991–997

Portas CM, Bjorvatn B, Fagerland S, Gronli J, Mundal V, Sorensen E, Ursin R (1998) On-line detection of extracellular levels of serotonin in dorsal raphe nucleus and frontal cortex over the sleep/wake cycle in the freely moving rat. Neuroscience 83(3):807–814

Rechtschaffen A, Gilliland MA, Bergmann BM, Winter JB (1983) Physiological correlates of prolonged sleep deprivation in rats. Science 221:182–184

Sakurai T, Amemiya A, Ishii M, Matsuzaki I, Chemelli RM, Tanaka H, Williams SC, Richardson JA, Kozlowski GP, Wilson S, Arch JRS, Buckingham RE, Haynes AC, Carr SA, Annan RS, Mcnulty DE, Liu W-s, Terrett JA, Elshourbagy NA, Bergsma DJ, Yanagisawa M (1998) Orexins and orexin receptors: a family of hypothalamic neuropeptides and G protein-coupled receptors that regulate feeding behavior. Cell 92:573–585

Szymusiak R, Iriye T, McGinty D (1989) Sleep-waking discharge of neurons in the posterior lateral hypothalamic area of cats. Brain Res Bull 23(1–2):111–120

Tabuchi S, Tsunematsu T, Black SW, Tominaga M, Maruyama M, Takagi K, Minokoshi Y, Sakurai T, Kilduff TS, Yamanaka A (2014) Conditional ablation of orexin/hypocretin neurons: a new mouse model for the study of narcolepsy and orexin system function. J Neurosci 34:6495–6509

Trulson ME, Jacobs BL (1979) Raphe unit activity in freely moving cats: correlation with level of behavioral arousal. Brain Res 163(1):135–150

Tsunematsu T, Fu L-Y, Yamanaka A, Ichiki K, Tanoue A, Sakurai T, van den Pol AN (2008) Vasopressin increases locomotion through a V1a receptor in orexin/hypocretin neurons: implications for water homeostasis. J Neurosci 28:228–238

Tsunematsu T, Kilduff TS, Boyden ES, Takahashi S, Tominaga M, Yamanaka A (2011) Acute optogenetic silencing of orexin/hypocretin neurons induces slow-wave sleep in mice. J Neurosci 31(29):10529–10539

Tsunematsu T, Tabuchi S, Tanaka KF, Boyden ES, Tominaga M, Yamanaka A (2013a) Long-lasting silencing of orexin/hypocretin neurons using archaerhodopsin induces slow-wave sleep in mice. Behav Brain Res 255:64–74

Tsunematsu T, Tanaka KF, Yamanaka A, Koizumi A (2013b) Ectopic expression of melanopsin in orexin/hypocretin neurons enables control of wakefulness of mice in vivo by blue light. Neurosci Res 75:23–28

Tsunematsu T, Ueno T, Tabuchi S, Inutsuka A, Tanaka KF, Hasuwa H, Kilduff TS, Terao A, Yamanaka A (2014) Optogenetic manipulation of activity and temporally controlled cell-specific ablation reveal a role for MCH neurons in sleep/wake regulation. J Neurosci 34 (20):6896–6909

Williams RH, Tsunematsu T, Thomas AM, Bogyo K, Yamanaka A, Kilduff TS (2019) Transgenic archaerhodopsin-3 expression in hypocretin/orexin neurons engenders cellular dysfunction and features of type 2 narcolepsy. J Neurosci 39(47):9435–9452

Willie JT, Chemelli RM, Sinton CM, Tokita S, Williams SC, Kisanuki YY, Marcus JN, Lee C, Elmquist JK, Kohlmeier KA, Leonard CS, Richardson JA, Hammer RE, Yanagisawa M (2003) Distinct narcolepsy syndromes in orexin receptor-2 and orexin null mice: molecular genetic dissection of non-REM and REM sleep regulatory processes. Neuron 38:715–730

Xu M, Chung S, Zhang S, Zhong P, Ma C, Chang W-C, Weissbourd B, Sakai N, Luo L, Nishino S, Dan Y (2015) Basal forebrain circuit for sleep-wake control. Nat Neurosci 18:1641–1647

Yamanaka A (2012) Optogenetical approach to control the activity of specific types of neurons in vivo. Nihon Yakurigaku Zasshi 140(6):280–284

Yamanaka A, Beuckmann CT, Willie JT, Hara J, Tsujino N, Mieda M, Tominaga M, Yagami KI, Sugiyama F, Goto K, Yanagisawa M, Sakurai T (2003) Hypothalamic orexin neurons regulate arousal according to energy balance in mice. Neuron 38:701–713

Yu X, Ye Z, Houston CM, Zecharia AY, Ma Y, Zhang Z, Uygun DS, Parker S, Vyssotski AL, Yustos R, Franks NP, Brickley SG, Wisden W (2015) Wakefulness is governed by GABA and histamine cotransmission. Neuron 87:1–15

# Fiberless Optogenetics

# 26

Srikanta Chowdhury and Akihiro Yamanaka

**Abstract**

Optogenetics, which relies on the use of photons to manipulate cellular and subcellular processes, has emerged as an important tool that has transformed several fields including neuroscience. Improvement of optogenetic topographies, together with integration with complementary tools such as electrophysiology, imaging, anatomical and behavioral analysis, facilitated this transformation. However, an inherent challenge associated with optogenetic manipulation of neurons in living organisms, such as rodents, is the requirement for implanting light-delivering optical fibers. This is partly because the current repertoires of light-sensitive opsins are activated only by visible light, which cannot effectively penetrate biological tissues. Insertion of optical fibers and subsequent photo-stimulation inherently damages brain tissue, and fiber tethering can constrain animal behavior. To overcome these technical limitations, we and other research groups recently developed minimally invasive "fiberless optogenetics," which uses particles that can emit visible light through up-conversion luminescence in response to irradiation with tissue-penetrating near-infrared light. Fiberless optogenetics also offers the opportunity to control neural function over longer time frames in freely behaving animals. In this chapter, we discuss the development of fiberless optogenetics and its application in neuroscience and beyond.

**Keywords**

Fiberless optogenetics · Opsins · Up-conversion · Near-infrared light · Lanthanides

## Abbreviations

| | |
|---|---|
| ACR1 | Anion channelrhodopsin-1 |
| AuNP | Gold nanoparticle |
| C1V1 | ChR1/VChR1 chimera |
| ChR | Channelrhodopsin |
| ChR2 | Channelrhodopsin-2 |
| CNT | Carbon nanotube |
| GlyR | Glycine receptor |
| IR | Infrared |

S. Chowdhury
Department of Biochemistry and Molecular Biology, University of Chittagong, Chittagong, Bangladesh

Eukaryotic Gene Expression and Function (EuGEF) Research Group, Chittagong, Bangladesh

A. Yamanaka (✉)
Department of Neuroscience II, Research Institute of Environmental Medicine, Nagoya University, Nagoya, Japan

Department of Neural Regulation, Nagoya University Graduate School of Medicine, Nagoya, Japan

Core Research for Evolutional Science and Technology (CREST), Japan Science and Technology Agency (JST), Honcho Kawaguchi, Saitama, Japan
e-mail: yamank@riem.nagoya-u.ac.jp



H. Yawo et al. (eds.), *Optogenetics*, Advances in Experimental Medicine and Biology 1293,
https://doi.org/10.1007/978-981-15-8763-4_26

| | |
|---|---|
| LED | Light-emitting diode |
| LMP | Lanthanide micro-particle |
| NIR | Near-infrared |
| Opto-CRAC | Near-infrared-stimulable optogenetic platform using the $Ca^{2+}$ release-activated $Ca^{2+}$ |
| PL | Photoluminescence |
| QD | Quantum dot |
| UCNP | Up-conversion nanoparticle |

## 26.1 Optogenetics and Current Limitations

There are two distinct opsin gene superfamilies, namely type I (microbial origin) and type II (animal origin) (Spudich et al. 2000). Optogenetics typically employs the use of microbial opsins. Upon light activation, microbial opsins enable modulation of molecular events in living cells or organisms in a targeted manner, as well as with high spatiotemporal precision (Boyden et al. 2005; Deisseroth 2011). Microbial opsins include proton pumps (e.g., bacteriorhodopsins), ion pumps (e.g., halorhodopsins), ion channels (e.g., channelrhodopsins), and sensory rhodopsins (e.g., histidine kinase rhodopsins) (Zhang et al. 2011). Among the ion channel opsins, channelrhodopsins (ChRs) are the only class of light-activated ion channels identified to date that are capable of conducting passive nonselective cation flow across the cell membrane, all on the timescale of milliseconds. Like other opsins, the backbone of ChRs is the familiar 7-transmembrane protein structure that is common in the G-protein coupled receptor family of proteins (Josselyn 2018). One of the most common light-sensitive proteins in use today is the algal protein from *Chlamydomonas reinhardtii* known as channelrhodopsin-2 (ChR2). However, all of the previously mentioned classes of light-sensing proteins share a common property, namely that they are only activated by light in the visible spectrum (~400–700 nm).

Neurons express multiple types of ion channels that can be either ligand-gated, voltage-gated, temperature-sensitive, or mechanosensitive (Zheng and Trudeau 2015). These ion channels play crucial roles in modulating the membrane potential of neurons and eventually their signal processing and plasticity (Koch and Segev 2000; Sjostrom and Nelson 2002). Therefore, modifying neurons to express light-sensitive opsin proteins can allow for light to open ion channels and, eventually, activate or silence neurons (Deisseroth 2011). However, as noted above, use of microbial opsins requires visible light for activation, which limits their biomedical application. In vivo applications of optogenetics, particularly in rodents and larger animals, are hindered by very low penetration of visible light into biological tissues. Short-wavelength photons attenuate significantly along the optical path through tissues due to scattering and absorption (Zonios et al. 2001). For instance, by illuminating high-power green laser light (550 nm, 300 mW) above brain slices of varying thicknesses, it was found that more than 80% of the light was absorbed within only 1 mm of the brain slices, and this value approached 0% in a brain slice with a thickness of 3 mm (Miyazaki et al. 2019). Moreover, considering that the skin, scalp, and skull of a rodent absorb more energy, it is highly unlikely that visible light can be used to directly activate neurons via external laser illumination. Therefore, use of cannula-based optical fibers surgically implanted into the brain with stereotactic guidance has become a very common method for in vivo light delivery (Aravanis et al. 2007; Yizhar et al. 2011a).

However, insertion of fiber optics for light delivery can cause damage to brain tissue, infection, and sometimes inflammation at the site of insertion. Chronic high-frequency optogenetic stimulation also generates heat and may cause phototoxicity (Allen et al. 2015). Moreover, displacement of the inserted fiber optic tip by natural animal movements may lead to off-target light delivery, as well as additional damage to brain tissue. Furthermore, tethering optical fibers with a light source can cause behavioral restriction by limiting the range of movements.

## 26.2 Fiberless Optogenetics

Fortunately, several of the obstacles associated within conventional optogenetics discussed above have been overcome by the advent of a newly developed technique known as fiberless (or wireless) optogenetics (Fig. 26.1) (Chen et al. 2018; Miyazaki et al. 2019). As the name suggests, the technique evolved to eliminate the need for a wired light-delivering system. By employing the use of miniaturized light-emitting diodes (LEDs) to activate opsin proteins, researchers developed an improved light delivery system that eliminates the need for tethers by delivering light via wireless head-mounted systems, which can be powered either wirelessly (Wentz et al. 2011; Kwon et al. 2015; Montgomery et al. 2015) or with a battery (Iwai et al. 2011; Hashimoto et al. 2014). While earlier attempts mostly focused on light delivery to the surface of the mouse brain with an LED, the development of a flexible and implantable LED system has allowed for targeting deeper brain regions (Kim et al. 2013; McCall et al. 2013). Devices like "Teleopto®" were also developed, whereby a remote controller accepts trigger signals from a stimulator and sends the signals to the receiver, which allows for both pulse and continuous light delivery using infrared (IR) emitters (Sato et al. 2015; Izawa et al. 2019). However, even these miniaturized fiberless devices cannot overcome the limitations of tissue penetration noted above. Moreover, the sizes and weights of the devices may inhibit the natural movements of animals and may also prevent the ability to target neurons in the peripheral nervous system. In addition to these limitations, the battery run time in such miniaturized LED devices is typically on the order of several hours, so that chronic studies may require the need for battery replacement or wireless power charging system that can disturb the natural behaviors of experimental animals.

More recently, a less invasive fiberless optogenetics technique was developed using either light of shorter wavelengths than that of the visible spectrum, like ultraviolet or X-ray light with wavelengths <450 nm (Pansare et al. 2012; Matsubara et al. 2019), or light of higher wavelengths, like IR light with wavelengths >650 nm (Pansare et al. 2012; Chen et al. 2018; Miyazaki et al. 2019). Employing inorganic scintillators, X-ray-mediated optogenetics has been used to bidirectionally modulate midbrain dopamine neurons of freely moving mice (Matsubara et al. 2019). This method is useful for the application of fiberless optogenetics to deeper brain areas where IR cannot be reached. Although a low dose of X-rays, which is a type of ionizing radiation, is not thought to cause any immediate health effects, exposure to high levels of radiation poses a number of health threats, including possible damage to DNA, the immune system, intestinal epithelial cells, etc. (Shi and Tashiro 2018). In contrast, while high doses of IR radiation can result in heat generation (Miyazaki et al. 2019), lanthanide-doped materials that can up-convert near-infrared (NIR) light to visible light (Zhou et al. 2015) offer significant potential for use in fiberless optogenetics.

## 26.3 How NIR-Mediated Fiberless Optogenetics Works

NIR-mediated fiberless optogenetics relies on optical up-conversion of NIR to visible light using lanthanide-doped materials (Auzel 2004; Chen et al. 2018; Miyazaki et al. 2019). NIR light can penetrate through biological tissues, such as the brain, with less scattering of photons and is minimally absorbed by melanin in the skin and hemoglobin in the red blood cells (Zonios et al. 2001). Therefore, NIR can be efficiently delivered to targeted neurons, even to deeper regions in the brain that cannot be reached by visible light. As NIR-responsive opsins have not yet been discovered or developed, it is possible to circumvent the technological challenges by employing materials that convert NIR irradiation into emission of visible light via an up-conversion process with high efficiency (Auzel 2004). Currently, one of the most effective approaches to achieve photon up-conversion within the region

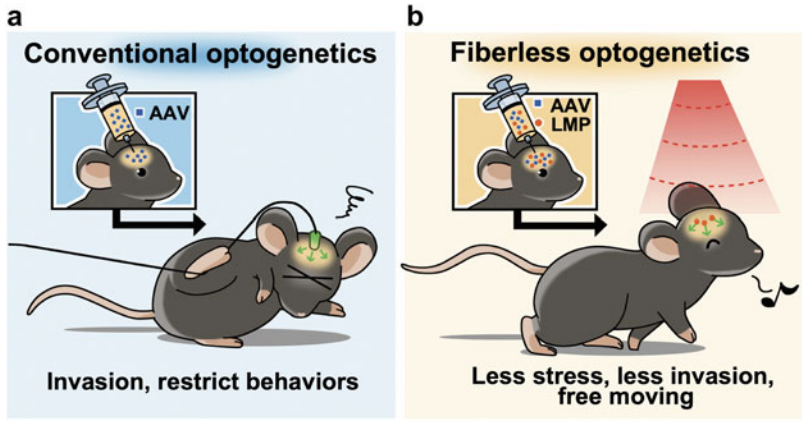


**Fig. 26.1** Neuronal manipulation using NIR and lanthanide-based up-conversion optogenetics in freely behaving animals (e.g., mouse). (**a**) Conventional optogenetics requires delivery of light-sensitive opsins (blue rectangles) either via lentivirus and adeno-associated virus (AAV) vectors or via transgenic technology. Light-delivering fibers result in restriction of natural behaviors of animals. (**b**) NIR and lanthanide-based fiberless optogenetics requires administration of lanthanide particles (red closed circles) along with the opsins. Irradiation with NIR causes up-conversion luminescence of lanthanide particles, which, in turn, causes activation of light-sensitive proteins to manipulate neuronal function

of interest is by injection of up-conversion nanoparticles (UCNPs) (Wang et al. 2010; Chen et al. 2018). Initially applied exclusively as luminescent contrast agents, UCNPs are luminescent nanomaterials that, upon excitation in the NIR region, emit stable, bright visible luminescence at a variety of selectable wavelengths (Auzel 2004; Heer et al. 2004; Sivakumar et al. 2005; Wang et al. 2010). Moreover, a micrometer-scale optoelectronic up-conversion device for IR-to-visible photon up-conversion was recently developed, which exhibited higher quantum yield, broadband absorption, wide-emission spectral tunability (red, yellow, and blue), and faster dynamics (Ding et al. 2018). These encapsulated miniaturized devices can be implanted into subdermal tissues and provide stable operation in behaving animals. Upon excitation at 810 nm, these encapsulated implants with biocompatible surfaces led to an enhanced local field potential in mouse model (Ding et al. 2018). Blue- and green light-emitting nanoparticles comprised of $NaYF_4$:$Yb^{3+}$/$Tm^{3+}$ and $NaYF_4$:$Yb^{3+}$/$Er^{3+}$ can be used to activate opsin-expressing neurons both in vitro and ex vivo (Hososhima et al. 2015; Shah et al. 2015; Wu et al. 2016). More recently, it was shown that this technique could be used for activation and inhibition of neurons within deep regions of the brain of both anesthetized and awake mice (Lin et al. 2017, 2018; Chen et al. 2018). In addition, up-conversion luminescence emitted by lanthanide micro-particles (LMPs, Fig. 26.2) can be used for manipulation of neuronal activities (Miyazaki et al. 2019). These LMPs, originally developed for printing applications, are made of lanthanide-doped $NaYF_4$ and are larger in size than nanoparticles used in similar applications. Recently, Miyazaki et al. found that up-conversion luminescence from green light-emitting LMPs was intense enough to actuate excitatory (ChR1/VChR1 chimera, C1V1 (Yizhar et al. 2011b)) and inhibitory opsins (anion channelrhodopsin-1, ACR1 (Govorunova et al. 2016)) and could thereby modulate neuronal activity both in vitro and in vivo (Miyazaki et al. 2019). Using these LMP–opsin combinations, locomotor activity of mice was shown to be able to be controlled remotely by bidirectionally regulating neuronal functions in the dorsal striatum without the need for fiber insertion. Moreover, injected LMPs were found to be functional in the brain for more than 8 weeks, suggesting that LMPs exhibit the potential to be used for

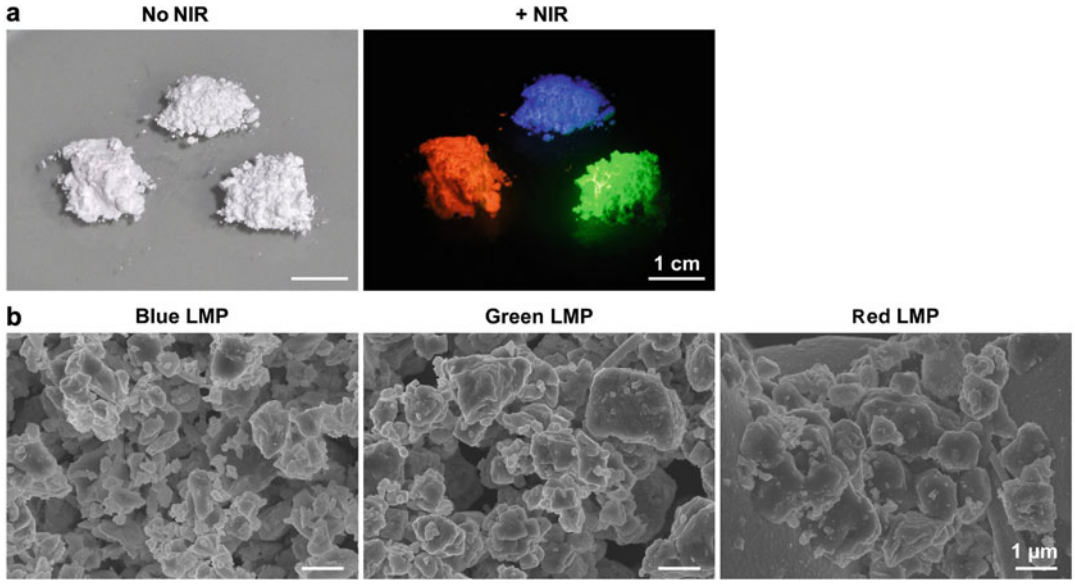


**Fig. 26.2** Lanthanide microparticles (LMPs) observed by the naked eye and with a scanning electron microscope (SEM). (**a**) Blue-, green-, and red-light-emitting LMPs are crystalline powders that are impossible to differentiate by the naked eye. However, upon irradiation with NIR, the LMPs luminesce with different colors allowing them to be easily distinguished. (**b**) SEM images of blue-, green-, and red-light-emitting LMPs. While the shapes of the particles were relatively random (**b**), their sizes were estimated to be around 1.0 μm in diameter on average. This figure is modified from Miyazaki et al. Cell Reports (Miyazaki et al. 2019)

long-term behavioral tests involving complex body movements (Miyazaki et al. 2019).

## 26.4 Other Fiberless Approaches to Regulate Neuronal Function

Other fiberless noninvasive approaches that are used in neuroscience to bidirectionally modulate neuronal activity include electromagnetic regulation and sonogenetics. Electromagnetic regulation employs ferritin-fused, heat-sensitive ion channels (Stanley et al. 2012, 2015, 2016; Wheeler et al. 2016), while sonogenetics uses ultrasound-responsive proteins (Ibsen et al. 2015), to remotely regulate neuronal activity by a magnetic field or ultrasound pulse, respectively. However, there is a convincing argument that the use of magnetic fields for the activation of ferritin-tagged ion channels conflicts with the basic laws of physics (Meister 2016). This is in contrast to up-conversion-mediated fiberless optogenetics, which follows a relatively straightforward principle, whereby light energy is used to activate light-sensitive protein molecules. Although electromagnetic regulation and sonogenetics do not use photons in their mechanism, they do provide fiberless approaches to regulate cellular activity, and ultimately add to the repertoire of available techniques.

Other nanomaterials, such as quantum dots (QDs), gold nanoparticles (AuNPs), and carbon nanotubes (CNTs), can also facilitate fiberless strategies, and even eliminate the need for genetic manipulation. QDs are nanometer-sized light-sensitive semiconductors (Efros and Rosen 2000; Dahan et al. 2003; Lugo et al. 2012; Rowland et al. 2015). Upon optical excitation, QDs can either emit photoluminescence (PL) (Efros and Rosen 2000) or generate a dipole-induced electric field (Lugo et al. 2012). While QDs were initially used to track individual glycine receptors (GlyRs) expressed on the neuronal membrane (Dahan et al. 2003), their PL quenching phenomenon in the presence of an electric field allows for their use in monitoring

the firing profiles of neurons (Rowland et al. 2015). Moreover, by culturing cortical neurons on QD films, researchers were able to manipulate the membrane properties of neurons (Lugo et al. 2012). However, QD-induced neuronal manipulations depend on both the proximity of the QDs to the membrane, as well as the identity of ion channels in the vicinity of the QDs, which hinders their applications in this field. As mentioned earlier, ligand-conjugated AuNPs have also been employed to remotely manipulate neuronal activity (Carvalho-de-Souza João et al. 2015). In response to NIR pulses, AuNP-targeted cells cause rapid increases in membrane temperature, which changes the membrane capacitance and induces depolarization (Carvalho-de-Souza João et al. 2015). However, one study revealed a severe, complex, and cell-type independent stress response following laser irradiation, suggesting the need for a thorough reassessment of the AuNP approach (Johannsmeier et al. 2018). Pyramidally microstructured biomaterial sensors composed of a CNT composite have also been used to modulate neuronal functions in a fiberless manner; this method exhibits distinct promise, albeit with some drawbacks (Tee et al. 2015).

## 26.5 Applications of Fiberless Optogenetics Beyond Neuroscience

While fiberless optogenetics has become an extremely useful tool in neuroscience, it has also demonstrated utility in various other research applications, including immunomodulation, autophagy, and cancer biology, among others. Fiberless optogenetics also offers the potential to support the development of more innovative therapies for diseases such as cancer, cardiovascular diseases, etc.

Cancer biologists are eagerly seeking new antitumor therapies as alternatives to chemotherapy. In a recent study, He and coworkers demonstrated a UCNP-based NIR-stimulable optogenetic platform ($Ca^{2+}$ release-activated $Ca^{2+}$, termed "Opto-CRAC") that selectively and remotely controls $Ca^{2+}$ oscillations and $Ca^{2+}$-responsive gene expression, which ultimately regulates the function of non-excitable cells, including T-lymphocytes, macrophages, and dendritic cells (He et al. 2015). Opto-CRAC was shown to specifically destroy tumor cells by acting as a genetically encoded "photoactivatable adjuvant" that improved antigen-specific immune response (He et al. 2015). Recently, a fiberless optogenetic nano system was shown to achieve autophagy upregulation with spatiotemporal precision both in vitro and in vivo (Pan et al. 2019). As autophagy plays critical roles in intracellular signaling pathways and is correlated with diverse pathological conditions, the implantable, recyclable, and biocompatible fiberless optogenetic technique in the Opto-CRAC platform is expected to be useful for various fundamental and clinical applications. NIR-mediated fiberless optogenetics was also used to control the apoptotic signaling pathway of cancer cells both in mammalian cells and in mice, implying significant potential for use in clinical applications (Zheng et al. 2017).

Biologists are also seeking alternative methods to address some of the limitations associated with current treatments for cardiovascular diseases, such as optical pacing, defibrillation, and resynchronization. While optogenetics has already been demonstrated as a novel and useful method for cardiac control using optical energy (Arrenberg et al. 2010; Bruegmann et al. 2010), application of fiberless optogenetics was also recently shown to be a reliable and reproducible tissue-penetrating method for cardiac optical pacing in a rat model, and thus holds promise as an improved treatment option for cardiovascular diseases (Rao et al. 2020).

## 26.6 Limitations, Promise, and Future Perspectives of Fiberless Optogenetics

Application of upconversion fiberless optogenetics is currently limited by two greatly debated issues: biocompatibility and heat generation (Chen et al. 2018; Miyazaki et al. 2019). This technology is also still facing challenges associated with the efficiency of photon

conversion (Huang et al. 2016; Liang et al. 2019). As up-conversion materials exhibit inherently weak photon responses, achieving practical luminescence requires a laser beam with coherent pump intensities above a certain threshold range (Zheng et al. 2013; Liang et al. 2019). Another limitation lies in the target-selecting capability of UCNPs for remote regulation of cell-type/tissue-specific ion channels, as the UCNPs are randomly biodistributed (Yadav et al. 2017). Therefore, further improvement of the up-conversion system is essential for improved biocompatibility, high emission efficiency, and long-term utility. In addition, systematic optimization of the dose of UCNP injection, and the parameters of NIR stimulation, will be critical for improved accuracy and safety.

Despite these limitations, the fiberless optogenetic technique offers promise for applications in nearly all sectors of biology. Fiberless optogenetics can be used to interrogate specific cell types in complex tissues and can be applied to a broad range of research questions related to behavior and physiology. Moreover, with the potential development of opsins that are compatible with human immune systems, fiberless optogenetics may help to treat a myriad of neurological disorders, such as deafness, blindness, migraines, spinal cord injury, nerve disorders, or epilepsy. Fiberless optogenetics may also be used for modulation of other electrically excitable cells, including cardiac and skeletal muscle cells (Arrenberg et al. 2010; Llewellyn et al. 2010). Combinations of fiberless optogenetics and stem cell biology may offer an exciting means of solving the problem of how to deliver light and light-sensitive opsins to the human brain without the use of viruses.

## 26.7 Conclusion

The world is currently facing an increasing demand for improved strategies for the diagnosis and treatment of neurological disorders. Optogenetics, which combines optics and genetics, has emerged as a powerful tool for interrogating complex neuronal networks by enabling selective control of neural activity and casual manipulation of specific neural circuits. While conventional optogenetics has been hindered by the availability of suitable light delivery approaches, material scientists have developed up-conversion materials that offer the possibility of delivering visible light into the brain in an effective, minimally invasive, and fiberless manner. In vitro and in vivo studies yielded promising results indicating that nanoparticles present little or no toxicity. Despite the lack of acute toxic effects, very few animal studies have evaluated possible long-term effects of nanoparticles in living organisms. The physicochemical properties of nanomaterials ultimately regulate their fate in living systems. A complete characterization of the biodistribution pathways and clearance mechanisms of nanoparticles following systemic administration will help to determine the requirements and properties needed to fulfill safe in vivo applications. This is also a prerequisite for the use of such nanoparticles in clinical applications. Therefore, continuous advancements in the field of materials science, nanotechnology, chemistry, and optics are required for the successful application of fiberless optogenetics in neuroscience and beyond.

**Acknowledgments** This work was supported by a grant from the Core Research for Evolutional Science and Technology (CREST), Japan Science and Technology Agency (JST) (JPMJCR1656) to A.Y., KAKENHI grants (26293046, 26640041, 16H01271, 17H05563, 18H05124, 18KK0223, and 18H02523) to A.Y., and Grant-in-Aid for Scientific Research from Bangladesh Medical Research Council (BMRC/HPNSP-569(1-60)) to S.C.

**Declaration of Interests** The authors declare no competing financial interests.

## References

Allen BD, Singer AC, Boyden ES (2015) Principles of designing interpretable optogenetic behavior experiments. Learn Mem 22:232–238

Aravanis AM, Wang LP, Zhang F, Meltzer LA, Mogri MZ, Schneider MB, Deisseroth K (2007) An optical neural interface: in vivo control of rodent motor cortex

with integrated fiberoptic and optogenetic technology. J Neural Eng 4:S143–S156
Arrenberg AB, Stainier DYR, Baier H, Huisken J (2010) Optogenetic Control of Cardiac Function. Science 330:971
Auzel F (2004) Upconversion and anti-Stokes processes with f and d ions in solids. Chem Rev 104:139–173
Boyden ES, Zhang F, Bamberg E, Nagel G, Deisseroth K (2005) Millisecond-timescale, genetically targeted optical control of neural activity. Nat Neurosci 8:1263–1268
Bruegmann T, Malan D, Hesse M, Beiert T, Fuegemann CJ, Fleischmann BK, Sasse P (2010) Optogenetic control of heart muscle in vitro and in vivo. Nat Methods 7:897–900
Carvalho-de-Souza João L, Treger Jeremy S, Dang B, Kent Stephen BH, Pepperberg David R, Bezanilla F (2015) Photosensitivity of neurons enabled by cell-targeted gold nanoparticles. Neuron 86:207–217
Chen S, Weitemier AZ, Zeng X, He L, Wang X, Tao Y, Huang AJY, Hashimotodani Y, Kano M, Iwasaki H, Parajuli LK, Okabe S, Teh DBL, All AH, Tsutsui-Kimura I, Tanaka KF, Liu X, McHugh TJ (2018) Near-infrared deep brain stimulation via upconversion nanoparticle–mediated optogenetics. Science 359:679
Dahan M, Lévi S, Luccardini C, Rostaing P, Riveau B, Triller A (2003) Diffusion dynamics of glycine receptors revealed by single-quantum dot tracking. Science 302:442
Deisseroth K (2011) Optogenetics. Nat Methods 8:26–29
Ding H, Lu L, Shi Z, Wang D, Li L, Li X, Ren Y, Liu C, Cheng D, Kim H, Giebink NC, Wang X, Yin L, Zhao L, Luo M, Sheng X (2018) Microscale optoelectronic infrared-to-visible upconversion devices and their use as injectable light sources. Proc Natl Acad Sci 115:6632
Efros AL, Rosen M (2000) The electronic structure of semiconductor nanocrystals. Annu Rev Mater Sci 30:475–521
Govorunova EG, Sineshchekov OA, Spudich JL (2016) Proteomonas sulcata ACR1: a fast anion channelrhodopsin. Photochem Photobiol 92:257–263
Hashimoto M, Hata A, Miyata T, Hirase H (2014) Programmable wireless light-emitting diode stimulator for chronic stimulation of optogenetic molecules in freely moving mice. Neurophotonics 1:011002
He L, Zhang Y, Ma G, Tan P, Li Z, Zang S, Wu X, Jing J, Fang S, Zhou L, Wang Y, Huang Y, Hogan PG, Han G, Zhou Y (2015) Near-infrared photoactivatable control of Ca2+ signaling and optogenetic immunomodulation. elife 4:e10024
Heer S, Kömpe K, Güdel HU, Haase M (2004) Highly efficient multicolour upconversion emission in transparent colloids of lanthanide-doped NaYF4 nanocrystals. Adv Mater 16:2102–2105
Hososhima S, Yuasa H, Ishizuka T, Hoque MR, Yamashita T, Yamanaka A, Sugano E, Tomita H, Yawo H (2015) Near-infrared (NIR) up-conversion optogenetics. Sci Rep 5:16533
Huang K, Dou Q, Loh XJ (2016) Nanomaterial mediated optogenetics: opportunities and challenges. RSC Adv 6:60896–60906
Ibsen S, Tong A, Schutt C, Esener S, Chalasani SH (2015) Sonogenetics is a non-invasive approach to activating neurons in Caenorhabditis elegans. Nat Commun 6:8264
Iwai Y, Honda S, Ozeki H, Hashimoto M, Hirase H (2011) A simple head-mountable LED device for chronic stimulation of optogenetic molecules in freely moving mice. Neurosci Res 70:124–127
Izawa S, Chowdhury S, Miyazaki T, Mukai Y, Ono D, Inoue R, Ohmura Y, Mizoguchi H, Kimura K, Yoshioka M, Terao A, Kilduff TS, Yamanaka A (2019) REM sleep–active MCH neurons are involved in forgetting hippocampus-dependent memories. Science 365:1308
Johannsmeier S, Heeger P, Terakawa M, Kalies S, Heisterkamp A, Ripken T, Heinemann D (2018) Gold nanoparticle-mediated laser stimulation induces a complex stress response in neuronal cells. Sci Rep 8:6533
Josselyn SA (2018) The past, present and future of light-gated ion channels and optogenetics. elife 7:e42367
Kim TI et al (2013) Injectable, cellular-scale optoelectronics with applications for wireless optogenetics. Science 340:211–216
Koch C, Segev I (2000) The role of single neurons in information processing. Nat Neurosci 3 (Suppl):1171–1177
Kwon KY, Lee HM, Ghovanloo M, Weber A, Li W (2015) Design, fabrication, and packaging of an integrated, wirelessly-powered optrode array for optogenetics application. Front Syst Neurosci 9:69
Liang L, Teh DBL, Dinh N-D, Chen W, Chen Q, Wu Y, Chowdhury S, Yamanaka A, Sum TC, Chen C-H, Thakor NV, All AH, Liu X (2019) Upconversion amplification through dielectric superlensing modulation. Nat Commun 10:1391
Lin X, Wang Y, Chen X, Yang R, Wang Z, Feng J, Wang H, Lai KWC, He J, Wang F, Shi P (2017) Multiplexed optogenetic stimulation of neurons with spectrum-selective upconversion nanoparticles. Adv Healthc Mater 6:17
Lin X, Chen X, Zhang W, Sun T, Fang P, Liao Q, Chen X, He J, Liu M, Wang F, Shi P (2018) Core-shell-shell upconversion nanoparticles with enhanced emission for wireless optogenetic inhibition. Nano Lett 18:948–956
Llewellyn ME, Thompson KR, Deisseroth K, Delp SL (2010) Orderly recruitment of motor units under optical control in vivo. Nat Med 16:1161–1165
Lugo K, Miao X, Rieke F, Lin LY (2012) Remote switching of cellular activity and cell signaling using light in conjunction with quantum dots. Biomed Opt Express 3:447–454
Matsubara T, Yanagida T, Kawaguchi N, Nakano T, Yoshimoto J, Tsunoda SP, Horigane S-I, Ueda S, Takemoto-Kimura S, Kandori H, Yamanaka A,

Yamashita T (2019) Remote control of neural function by X-ray-induced scintillation. bioRxiv:798702
McCall JG, Kim TI, Shin G, Huang X, Jung YH, Al-Hasani R, Omenetto FG, Bruchas MR, Rogers JA (2013) Fabrication and application of flexible, multimodal light-emitting devices for wireless optogenetics. Nat Protoc 8:2413–2428
Meister M (2016) Physical limits to magnetogenetics. elife 5:e17210
Miyazaki T, Chowdhury S, Yamashita T, Matsubara T, Yawo H, Yuasa H, Yamanaka A (2019) Large timescale interrogation of neuronal function by fiberless optogenetics using lanthanide micro-particles. Cell Rep 26:1033–1043.e1035
Montgomery KL, Yeh AJ, Ho JS, Tsao V, Mohan Iyer S, Grosenick L, Ferenczi EA, Tanabe Y, Deisseroth K, Delp SL, Poon AS (2015) Wirelessly powered, fully internal optogenetics for brain, spinal and peripheral circuits in mice. Nat Methods 12:969–974
Pan H, Wang H, Yu J, Huang X, Hao Y, Zhang C, Ji W, Yang M, Gong X, Wu X, Chang J (2019) Near-infrared light remotely up-regulate autophagy with spatiotemporal precision via upconversion optogenetic nanosystem. Biomaterials 199:22–31
Pansare V, Hejazi S, Faenza W, Prud'homme RK (2012) Review of long-wavelength optical and NIR imaging materials: contrast agents, fluorophores and multifunctional nano carriers. Chem Mater 24:812–827
Rao P, Wang L, Cheng Y, Wang X, Li H, Zheng G, Li Z, Jiang C, Zhou Q, Huang C (2020) Near-infrared light driven tissue-penetrating cardiac optogenetics via upconversion nanoparticles in vivo. Biomed Opt Express 11:1401–1416
Rowland CE, Susumu K, Stewart MH, Oh E, Mäkinen AJ, O'Shaughnessy TJ, Kushto G, Wolak MA, Erickson JS, Efros L, Huston AL, Delehanty JB (2015) Electric field modulation of semiconductor quantum dot photoluminescence: insights into the design of robust voltage-sensitive cellular imaging probes. Nano Lett 15:6848–6854
Sato M, Ito M, Nagase M, Sugimura YK, Takahashi Y, Watabe AM, Kato F (2015) The lateral parabrachial nucleus is actively involved in the acquisition of fear memory in mice. Mol Brain 8:22
Shah S, Liu JJ, Pasquale N, Lai J, McGowan H, Pang ZP, Lee KB (2015) Hybrid upconversion nanomaterials for optogenetic neuronal control. Nanoscale 7:16571–16577
Shi L, Tashiro S (2018) Estimation of the effects of medical diagnostic radiation exposure based on DNA damage. J Radiat Res 59:ii121–ii129
Sivakumar S, van Veggel FC, Raudsepp M (2005) Bright white light through up-conversion of a single NIR source from sol-gel-derived thin film made with Ln3 +−doped LaF3 nanoparticles. J Am Chem Soc 127:12464–12465
Sjostrom PJ, Nelson SB (2002) Spike timing, calcium signals and synaptic plasticity. Curr Opin Neurobiol 12:305–314
Spudich JL, Yang CS, Jung KH, Spudich EN (2000) Retinylidene proteins: structures and functions from archaea to humans. Annu Rev Cell Dev Biol 16:365–392
Stanley SA, Gagner JE, Damanpour S, Yoshida M, Dordick JS, Friedman JM (2012) Radio-wave heating of iron oxide nanoparticles can regulate plasma glucose in mice. Science 336:604–608
Stanley SA, Sauer J, Kane RS, Dordick JS, Friedman JM (2015) Remote regulation of glucose homeostasis in mice using genetically encoded nanoparticles. Nat Med 21:92–98
Stanley SA, Kelly L, Latcha KN, Schmidt SF, Yu X, Nectow AR, Sauer J, Dyke JP, Dordick JS, Friedman JM (2016) Bidirectional electromagnetic control of the hypothalamus regulates feeding and metabolism. Nature 531:647–650
Tee BC, Chortos A, Berndt A, Nguyen AK, Tom A, McGuire A, Lin ZC, Tien K, Bae WG, Wang H, Mei P, Chou HH, Cui B, Deisseroth K, Ng TN, Bao Z (2015) A skin-inspired organic digital mechanoreceptor. Science 350:313–316
Wang F, Han Y, Lim CS, Lu Y, Wang J, Xu J, Chen H, Zhang C, Hong M, Liu X (2010) Simultaneous phase and size control of upconversion nanocrystals through lanthanide doping. Nature 463:1061–1065
Wentz CT, Bernstein JG, Monahan P, Guerra A, Rodriguez A, Boyden ES (2011) A wirelessly powered and controlled device for optical neural control of freely-behaving animals. J Neural Eng 8:046021
Wheeler MA, Smith CJ, Ottolini M, Barker BS, Purohit AM, Grippo RM, Gaykema RP, Spano AJ, Beenhakker MP, Kucenas S, Patel MK, Deppmann CD, Guler AD (2016) Genetically targeted magnetic control of the nervous system. Nat Neurosci 19:756–761
Wu X, Zhang Y, Takle K, Bilsel O, Li Z, Lee H, Zhang Z, Li D, Fan W, Duan C, Chan EM, Lois C, Xiang Y, Han G (2016) Dye-sensitized core/active shell upconversion nanoparticles for optogenetics and bioimaging applications. ACS Nano 10:1060–1066
Yadav K, Chou AC, Ulaganathan RK, Gao HD, Lee HM, Pan CY, Chen YT (2017) Targeted and efficient activation of channelrhodopsins expressed in living cells via specifically-bound upconversion nanoparticles. Nanoscale 9:9457–9466
Yizhar O, Fenno LE, Davidson TJ, Mogri M, Deisseroth K (2011a) Optogenetics in neural systems. Neuron 71:9–34
Yizhar O, Fenno LE, Prigge M, Schneider F, Davidson TJ, O'Shea DJ, Sohal VS, Goshen I, Finkelstein J, Paz JT, Stehfest K, Fudim R, Ramakrishnan C, Huguenard JR, Hegemann P, Deisseroth K (2011b) Neocortical excitation/inhibition balance in information processing and social dysfunction. Nature 477:171–178
Zhang F, Vierock J, Yizhar O, Fenno LE, Tsunoda S, Kianianmomeni A, Prigge M, Berndt A, Cushman J, Polle J, Magnuson J, Hegemann P, Deisseroth K

(2011) The microbial opsin family of optogenetic tools. Cell 147:1446–1457
Zheng J, Trudeau MC (2015) Handbook of ion channels. CRC Press, Boca Raton
Zheng Q, Zhu H, Chen S-C, Tang C, Ma E, Chen X (2013) Frequency-upconverted stimulated emission by simultaneous five-photon absorption. Nat Photonics 7:234–239
Zheng B, Wang H, Pan H, Liang C, Ji W, Zhao L, Chen H, Gong X, Wu X, Chang J (2017) Near-infrared light triggered upconversion optogenetic nanosystem for cancer therapy. ACS Nano 11:11898–11907
Zhou J, Liu Q, Feng W, Sun Y, Li F (2015) Upconversion luminescent materials: advances and applications. Chem Rev 115:395–465
Zonios G, Bykowski J, Kollias N (2001) Skin melanin, hemoglobin, and light scattering properties can be quantitatively assessed in vivo using diffuse reflectance spectroscopy. J Investig Dermatol 117:1452–1457

# Functional Connectome Analysis of the Striatum with Optogenetics

27

Nao Chuhma

**Abstract**

Neural circuit function is determined not only by anatomical connections but also by the strength and nature of the connections, that is functional or physiological connectivity. To elucidate functional connectivity, selective stimulation of presynaptic terminals of an identified neuronal population is crucial. However, in the central nervous system, intermingled input fibers make selective electrical stimulation impossible. With optogenetics, this becomes possible, and enables the comprehensive study of functional synaptic connections between an identified population of neurons and defined postsynaptic targets to determine the functional connectome. By stimulating convergent synaptic inputs impinging on individual postsynaptic neurons, low frequency and small amplitude synaptic connections can be detected. Further, the optogenetic approach enables the measurement of cotransmission and its relative strength. Recently, optogenetic methods have been more widely used to study synaptic connectivity and revealed novel synaptic connections and revised connectivity of known projections. In this chapter, I focus on functional synaptic connectivity in the striatum, the main input structure of the basal ganglia, involved in the motivated behavior, cognition, and motor control, and its disruption in a range of neuropsychiatric disorders.

**Keywords**

Nucleus accumbens · Spiny projection neurons · Cholinergic interneurons · GABA interneurons · Channelrhodopsin · Synaptic responses

## Abbreviations

| | |
|---|---|
| ACh | Acetylcholine |
| BLA | Basolateral amygdala |
| ChAT | Choline acetyltransferase |
| ChI | Cholinergic interneuron |
| ChR2 | Channelrhodopsin 2 |
| CR | Calretinin-expressing interneurons |
| Ctx | Cortex |
| DA | Dopamine |
| dSPN | Direct-pathway spiny projection neuron |
| dStr | Dorsal striatum |
| FAI | Fast-adapting interneurons |
| FSI | Fast-spiking interneuron |
| GP | Globus pallidus |
| Hipp | Hippocampus |

N. Chuhma (✉)
Department of Psychiatry, Columbia University, New York, NY, USA

Department of Molecular Therapeutics, New York State Psychiatric Institute, New York, NY, USA
e-mail: nc2027@cumc.columbia.edu



H. Yawo et al. (eds.), *Optogenetics*, Advances in Experimental Medicine and Biology 1293,
https://doi.org/10.1007/978-981-15-8763-4_27

| | |
|---|---|
| iSPN | Indirect-pathway spiny projection neuron |
| LTSI | Low-threshold spike interneuron |
| M1 | Primary motor area of the cortex |
| M2 | Secondary motor area of the cortex |
| NAc | Nucleus accumbens |
| NGF | Neurogliaform interneuron |
| PFC | Prefrontal cortex |
| PPN | Pedunculopontine nucleus |
| PV | Parvalbumin |
| SABI | Spontaneously active bursting interneurons |
| SN | Substantia nigra |
| SNc | Substantia nigra pars compacta |
| SNr | Substantia nigra pars reticulata |
| SOM | Somatostatin |
| Str | Striatum |
| TH | Tyrosine hydroxylase |
| Thal | Thalamus |
| THIN | Tyrosine hydroxylase-positive interneuron |
| VGLUT | Vesicular glutamate transporter |
| vHipp | Ventral hippocampus |
| VP | Ventral pallidum |
| VTA | Ventral tegmental area |

## 27.1 Introduction

The mammalian brain contains billions of neurons and the majority of its functions are determined by their connectivity. Since the identification of synapses as the connections between neurons by Sherrington (Shepherd 1994), determining the wiring diagram of the brain has been a central interest of neuroscientists in order to understand brain function. Neuronal connectivity is evaluated in two ways: the physical wiring diagram, that is anatomical connectivity, and the strength and nature of the connection, that is physiological or functional connectivity. Anatomical connectivity is typically determined using retrograde and orthograde tracers, including viruses with reporter proteins. Synaptic connections can be identified by trans-synaptic tracers (e.g., pseudorabies virus), green fluorescent protein (GFP) reconstitution across synaptic partners (GRASP) (Feinberg et al. 2008), or observation with electron microscopy. However, the functional strength of a particular synaptic connection is not revealed by these methods. Direct measurement of synaptic responses in identified populations of neurons is crucial for determining functional (physiological) connectivity.

### 27.1.1 Functional Connectome

We introduced the concept of the *functional connectome* to describe comprehensive studies of functional (physiological) connectivity (Chuhma et al. 2011). The word "connectome" was used by Sporns in 2005 to describe the wiring diagram of the human brain (Sporns et al. 2005). The current definition of connectome is the comprehensive mapping of wiring in a brain (not limited to human) or a brain region (Lichtman and Sanes 2008; Seung 2009). In contrast to connectome, defined as the comprehensive study of anatomical connections of neurons, functional connectome can be defined as the comprehensive study of the physiological strength and nature (e.g., kinds of transmitters) of monosynaptic connections between two identified populations of neurons. It should be noted that the concept of functional connectivity used in the functional connectome approach is different from the functional connectivity used in brain imaging, which refers to temporally associated activity of two or more brain regions during a certain brain state (Friston et al. 1993). Functional connectivity in brain imaging is not necessarily relevant to direct synaptic connections among recorded regions, while the functional connectome is restricted to direct synaptic connections from an identified population of neurons to their defined postsynaptic target neurons.

### 27.1.2 Why the Optogenetic Approach is Suitable for Functional Connectome Studies

For a functional connectome study, selective and reliable stimulation of an identified population of neurons and recording from identified target neurons is crucial. Although identification of postsynaptic neurons is possible in vivo, intracellular recording from brain slices has advantages. In contrast to multiple ways of identifying postsynaptic neurons, selective stimulation of identified presynaptic neurons has been hard to achieve. Particularly in the basal ganglia, where cell architecture is not layered and input fibers from multiple structures are intermingled, population-selective stimulation with electrical stimulation is almost impossible. The advent of optogenetics has enabled selective activation of identified neuronal populations by genetically limited expression of photoactivatable proteins. Optogenetic activation enables convergent stimulation of inputs to a single neuron and detection of low-frequency small-amplitude responses (Eskenazi et al. 2020). The optogenetic approach also enables measurement of cotransmission. Immunohistochemistry or gene-expression studies may indicate the potential for cotransmission; however, the functional contribution of any cotransmitter is difficult to discern without physiological measurement.

For functional connectome studies, fast-on fast-off excitation current generation is necessary. Suitable photoactivatable proteins are nonselective cation channel channelrhodopsin (ChR)-2 and its mutants with faster kinetics and/or higher light sensitivity (Wietek and Prigge 2016; Yizhar et al. 2011). Because of its membrane-targeted nature, ChR2 can also be used as a genetically controlled axonal tracer. Although this makes coordinated anatomical studies feasible, this chapter focuses on excitation of genetically identified axon terminals to reveal functional connectivity. In the following section, I focus on the striatum (Str) and its intrinsic and extrinsic connectivity. The Str is one of the most suitable locations to apply the optogenetic approach to the functional connectome, because of intermingled inputs and existence of genetic drivers for conditional expression of ChR2. In this chapter, "functional connectivity" is used as physiologically confirmed direct synaptic connection from an identified cell population to a single identified neuron.

## 27.2 Functional Connectome of the Striatum with Optogenetics

### 27.2.1 Basics of Striatal Circuits

The rodent Str comprises the nucleus accumbens (NAc) and dorsal or neostriatum (dStr). The NAc corresponds to the ventral striatum in primates. Although the striatal region corresponding to the primate caudate or putamen is not clear in rodent, the ventromedial dStr is regarded as roughly homologous to the caudate and dorsolateral dStr roughly homologous to the putamen (Graybiel 2008). Both the NAc and dStr share similar cytoarchitectures: about 95% GABAergic spiny projection neurons (SPNs) and about 5% interneurons (Wilson 2004). SPNs are the sole population of output neurons and their major projection sites are the globus pallidus (GP)/ventral pallidum (VP) and ventral midbrain (Wilson 2004). Striatal interneurons comprise cholinergic and GABAergic interneurons. Cholinergic interneurons (ChIs) are a single population and makeup about 1% of striatal neurons, while GABAergic interneurons comprise several different types, namely fast-spiking interneurons (FSIs), low-threshold spike interneurons (LTSIs), and neurogliaform interneurons (Kreitzer 2009; Tepper et al. 2010). A subset of GABA interneurons expresses tyrosine hydroxylase (TH), although they do not release dopamine (DA) (Tepper et al. 2018). While interneurons make up small minority populations, they exert strong control of SPN excitability and modulate DA neuron afferents axo-axonally (Exley and Cragg 2008; Nelson et al. 2014; Oldenburg and Ding 2011; Tepper et al. 2004).

Both the dStr and NAc receive inputs from the cortex (Ctx), thalamus (Thal), and ventral midbrain (Yin and Knowlton 2006). The NAc is distinguished by inputs from limbic structures: the hippocampus (Hipp) and basolateral amygdala (BLA) (Belujon and Grace 2011; Pennartz et al. 2009). Those inputs show a topographic projection pattern. Ventral midbrain DA neurons in the medial ventral tegmental area (VTA) project to the NAc medial shell, the most ventromedial subregion of the Str, while more lateral DA neurons in the substantia nigra pars compacta (SNc) project to dorsolateral subregion of the Str (Haber et al. 2000; Ikemoto 2007). These connections modulate Ctx-basal ganglia-Thal loops that run in parallel from the ventral "limbic loop" to the dorsal "sensorimotor loop" (Pennartz et al. 2009; Yin and Knowlton 2006).

### 27.2.2 Connectivity Between Str Neurons and Extra Str Regions

Functional connectome studies have proceeded from examination of connectivity between principal neurons to more subregion-specific and cell-type-specific functional connectivity. Now the input–output connectivity in each Str neuron type has been examined.

#### 27.2.2.1 Spiny Projection Neurons

SPNs are divided into two populations based on their projections to the output nuclei of the basal ganglia, directly (the direct pathway), or via the GP/VP (the indirect pathway). The output nuclei comprise the VTA/SN and entopeduncular nucleus, the rodent counterpart of the internal segment of the GP in primates, which in turn projects to the Thal (Gerfen and Surmeier 2011). Direct pathway SPNs (dSPNs) express DA D1 receptors and enkephalin, while indirect pathway SPNs (iSPNs) express DA D2 receptors and substance P (Gerfen and Surmeier 2011). These two populations of SPNs are almost completely segregated in the dStr and NAc core in adult rodents (Bertran-Gonzalez et al. 2008). In the NAc shell, 17–38% of SPNs express both D1 and D2 receptors (Bertran-Gonzalez et al. 2008; Gangarossa et al. 2013).

**Direct Pathway Spiny Projection Neurons**

dSPNs receive glutamatergic synaptic connection from the Ctx and Thal, both in the dStr and NAc (Choi et al. 2019; Ding et al. 2012; Ellender et al. 2013; Parker et al. 2016; Zhu et al. 2016). In the medial dStr, inputs from the anterior cingulate Ctx are stronger than those from parafascicular nucleus of the Thal, which rarely fire dSPNs even after blockade of $GABA_A$ receptors (Choi et al. 2019) (Fig. 27.1a). There are direct inputs to the Str from somatostatin (SOM)-positive and parvalbumin (PV)-positive GABA neurons in the primary (M1) and secondary (M2) motor areas of the Ctx (Melzer et al. 2017). dSPNs receive strong input from M1 PV and M2 SOM GABA neurons and weaker inputs from M1 SOM GABA neurons. M2 PV GABA neurons make only weak connections to Str GABA interneurons (Fig. 27.1a). dSPNs receive direct synaptic inputs from ventral midbrain DA neurons, though the connection was by glutamate and GABA cotransmission, not DA (Chuhma et al. 2018; Kim et al. 2015; Tritsch et al. 2012) (Fig. 27.1a). Although GABA cotransmission appears to be more widely observed in dStr subregions, glutamate cotransmission to SPNs is limited to the lateral dStr (Chuhma et al. 2018). The dStr and GP make reciprocal GABAergic connections (Kita 2007). Pallidal neurons make direct synaptic connections to both dSPNs and iSPNs, primarily from neuronal PAS domain protein (Npas)1-positive neurons, and inputs to iSPNs are consistently larger than those to dSPNs (Glajch et al. 2016) (Fig. 27.1a).

In the NAc, the Hipp and BLA make glutamatergic connections in addition to the Ctx and Thal (Belujon and Grace 2011; Pennartz et al. 2009; Sesack and Grace 2010). Optical stimulation of ventral Hipp (vHipp) generates monosynaptic glutamate currents in dSPN and iSPNs in the NAc medial shell, while most strong inputs are on FSIs (Scudder et al. 2018) (Fig. 27.1b). The BLA also makes glutamatergic inputs on NAc SPNs with the same strength in dSPNs and iSPNs (Zhu et al. 2016) (Fig. 27.1b). Among these glutamate

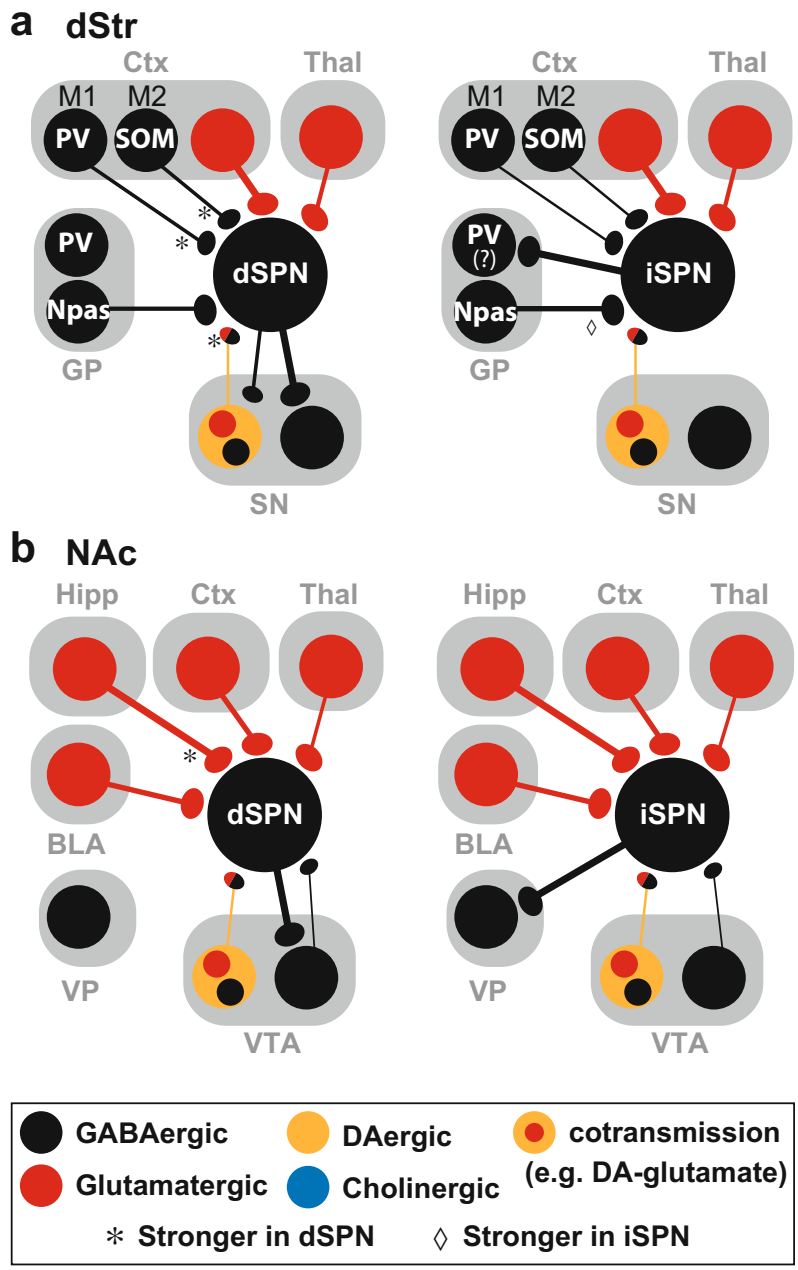


**Fig. 27.1** Optogenetically confirmed connections between striatal spiny projection neurons (SPNs) and extra-striatal neurons, in the dStr (**a**) and NAc (**b**). Direct pathway SPNs (dSPNs; *left*) and indirect pathway SPNs (iSPNs; *right*) are shown separately. Soma (*circles*) colors indicate the neurons' transmitter. The color of axon terminals (*small ovals*) indicates the released transmitter from the terminal. Connection strength is indicated by the thickness of the axons (*lines*)

inputs, the strongest are from the vHipp, and inputs from the BLA and PFC are the same strength but significantly weaker than those from the vHipp (Britt et al. 2012). Both glutamate and GABA cotransmission of DA neurons is observed in NAc SPNs, although the subtypes of SPNs were not specified (Chuhma et al. 2014; Mingote et al. 2015; Stuber et al. 2010; Tecuapetla et al. 2010; Tritsch et al. 2014) (Fig. 27.1b).

Retrograde tracer injections show that dSPNs send axons to both DA neurons in the SNc and GABA neurons in the SN pars reticulata (SNr) (Fujiyama et al. 2011; Gerfen 1985). Early

studies of output to the ventral midbrain with transgenic expression of ChR2 in the dStr (Chuhma et al. 2011) or viral injection in the NAc (Xia et al. 2011) showed $GABA_A$ responses in only non-DA neurons, but not DA neurons. In subsequent studies using viral transfection, SPN GABAergic connections to DA neurons were seen in the VTA (Bocklisch et al. 2013) and SNc (Lerner et al. 2015); however, the GABAergic input to GABA neurons was much stronger (Fig. 27.1a). The dStr is comprised of two chemically distinct compartments; striosome with prominent μ-opioid receptor expression and matrix with choline acetyltransferase (ChAT) expression (Crittenden and Graybiel 2011). A recent study revealed that SPNs innervating DA neurons were in striosome (Mcgregor et al. 2019). NAc dSPNs make direct connection to VTA neurons, preferentially to non-DA neurons (Xia et al. 2011) (Fig. 27.1b).

Most dSPNs also send collaterals to the GP (Fujiyama et al. 2011), which comprise about one-third of Str inputs to the region (Kita 2007). In vivo activation of dSPN collaterals inhibits GP neuron firing (Cazorla et al. 2014). Although the inhibition was likely mediated by direct collateral connections activating $GABA_A$ receptors, direct synaptic connections have not been confirmed.

#### Indirect Pathway Spiny Projection Neurons

iSPNs receive inputs from the same populations as dSPNs, however, strengths differ in some inputs. Weaker connections to iSPNs are from M2 SOM and M1 PV GABA neurons (Melzer et al. 2017), the vHipp (Scudder et al. 2018), and glutamate cotransmission from DA neurons in the lateral dStr (Chuhma et al. 2018), while stronger connections to iSPNs are from Npas1-positive pallidal GABAergic neurons (Glajch et al. 2016) (Fig. 27.1a, b).

iSPNs project to the GP/VP. Selective activation of striatal inputs, with expression of ChR2 in SPNs, evoked $GABA_A$ response in GP neurons (Chuhma et al. 2011). More than 98% of GP neurons are GABAergic projection neurons. Pallidal neurons can be classified by expression of Npas1, PV, Lim homeobox 6 (Lhx6), and transcription factor Fox P2 (Abrahao and Lovinger 2018). We observed two types of electrophysiologically distinguishable populations; slower firing high-input impedance neurons and faster firing low-input impedance neurons (Chuhma et al. 2011). The former population shares the nature of Cooper–Stanford type A neurons (Cooper and Stanford 2000) and Lhx6/Npas1 positive neurons (Abrahao and Lovinger 2018; Mastro et al. 2014); the latter shares the nature of Cooper–Stanford type B and C neurons (Cooper and Stanford 2000) and parvalbumin (PV)-positive neurons (Abrahao and Lovinger 2018, Mastro et al. 2014). Str $GABA_A$ input is stronger in type B/C-like neurons and very weak in type A-like neurons (Chuhma et al. 2011). Although the target neuron type was not specified, NAc core iSPNs make GABAergic connections to VP neurons as well (Dobbs Lauren et al. 2016).

#### 27.2.2.2 Cholinergic Interneurons

Cholinergic interneurons receive direct synaptic inputs from the Ctx, Thal, GP, and ventral midbrain (Guo et al. 2015). Although all studies report strong glutamatergic inputs from the Thal and relatively weak inputs from the Ctx to ChIs (Assous et al. 2019), the difference between these two inputs varies. This was likely due to differences in origins of inputs in the Ctx or Thal, recording protocols, recording locations, and short-term plasticity. A recent study showed that glutamate synaptic currents evoked by single-pulse photostimulation were not different between inputs from M1 and parafascicular nucleus of the Thal, while effects on ChI firing were different (Mamaligas et al. 2019) (Fig. 27.2). ChIs receive GABA inputs from the motor Ctx as well (Melzer et al. 2017). Inputs are primarily from M1 SOM GABA neurons, with weaker inputs from M1 PV and M2 SOM GABA neurons. ChIs receive direct synaptic connection from ventral midbrain DA neurons (Fig. 27.2a). In addition to fast glutamate and GABA

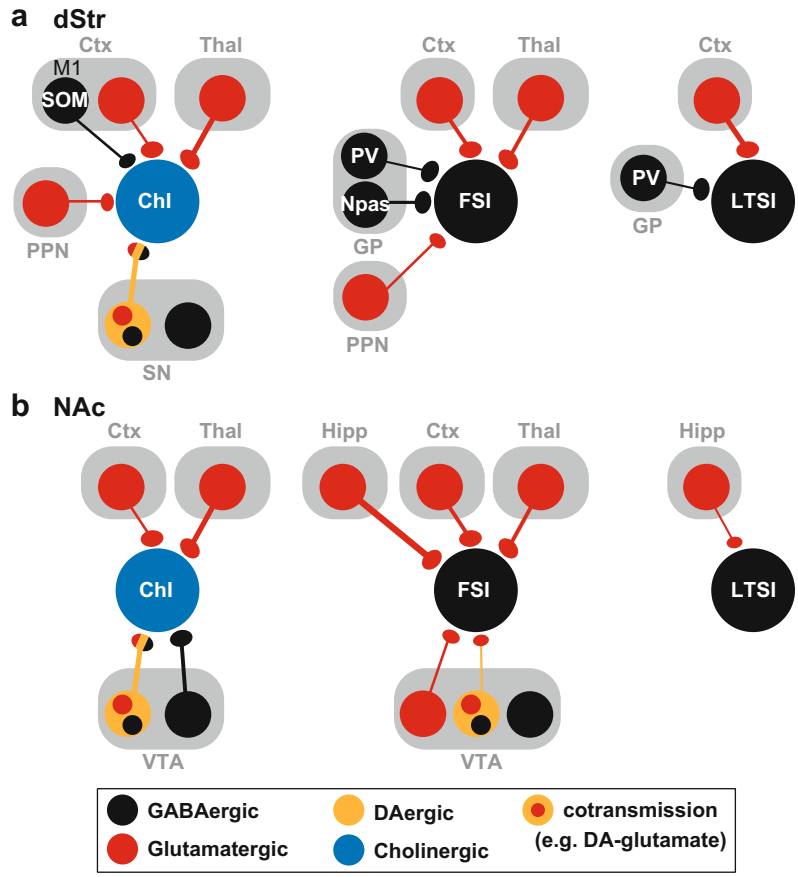


**Fig. 27.2** Optogenetically confirmed extra-striatal inputs to striatal cholinergic interneurons (ChI; *left*), fast-spiking interneurons (FSI; *middle*), and low-threshold spike interneurons (LTSI; *right*), in the dStr (**a**) and the NAc (**b**)

cotransmission, ChIs show D2-mediated IPSCs, D1/5-mediated delayed EPSCs, and mGluR1-mediated delayed EPSCs (Chuhma et al. 2014, 2018; Straub et al. 2014) (Fig. 27.2). The DA neuron synaptic responses showed regionally different blends of transmitters, e.g., dominant fast glutamate responses in the NAc dorsal medial shell, strong D2 and GABA responses in the medial dStr, and weak D2 responses and strong D1/5 and mGluR1 responses in the lateral dStr (Chuhma et al. 2014, 2018). The VTA contains GABA neurons projecting to the NAc (Van Bockstaele and Pickel 1995). The VTA GABA neurons generate large amplitude responses in all recorded ChIs (Brown et al. 2013) (Fig. 27.2b), and modest responses in SPNs. Recently, direct glutamatergic inputs from the pedunculopontine nucleus (PPN) to ChIs were reported (Assous et al. 2019) (Fig. 27.2a).

### 27.2.2.3 GABAergic Interneurons

#### Fast-Spiking Interneurons

FSIs receive inputs from both the Ctx and Thal. Optogenetic stimulation of the Ctx and Thal evokes about the same strength of glutamate responses in FSIs (Sciamanna et al. 2015) (Fig. 27.2). GP neurons, likely to be Npas1-positive, make direct synaptic connections to FSIs (Glajch et al. 2016) (Fig. 27.2a). Although it is not as prominent as in Npas1-positive neurons, PV-positive GP neurons make connections to FSIs as well (Glajch et al. 2016; Saunders et al. 2016). Glutamate inputs from PPN make direct connections to FSIs, which are as strong as to ChIs (Assous et al. 2019) (Fig. 27.2a).

In the NAc, FSIs receive glutamatergic input from the vHipp that is substantially stronger than input to SPNs (Scudder et al. 2018) (Fig. 27.2b).

VTA glutamate neurons, including DA-glutamate neurons, make direct synaptic connection to FSIs in the NAc medial shell (Chuhma et al. 2014, Zhang et al. 2016: 725–733) (Fig. 27.2b).

#### Low-Threshold Spike Interneurons

Although LTSIs receive strong glutamatergic inputs from the Ctx, they appear not to receive inputs from the parafascicular nucleus of the Thal, which sends projections to other types of Str neurons (Assous et al. 2017). PV-positive GP neurons make connections to LTSIs, but they are weaker than those to FSIs (Saunders et al. 2016). In the NAc, the vHipp makes weak inputs to LTSIs (Scudder et al. 2018) (Fig. 27.2).

#### Other GABA Interneurons

In addition to FSIs and LTSIs, several classes of GABA interneurons have been described: neurogliaform interneurons (NGFs), TH-positive interneurons (THINs), calretinin-expressing interneurons (CRs), fast-adapting interneurons (FAIs), and spontaneously active bursting interneurons (SABIs) (Tepper et al. 2018). NGFs received strong inputs from the Thal and moderate subthreshold inputs from the Ctx (Assous et al. 2017). THINs received strong glutamatergic inputs from the Ctx and Thal (Assous et al. 2017). However, input sources to CRs, FAIs, and SABIs have not been clearly identified.

### 27.2.3 Intra Striatum Connectivity

Str neurons make direct synaptic connections within the Str. Since Str neurons are GABAergic except for ChIs and ChIs exert inhibitory effects through muscarinic acetylcholine (ACh) receptors, the intrinsic connections are predominantly inhibitory. Possible excitatory transmission in local Str connections is limited to nicotinic ACh receptor-mediated responses and VGLUT3-mediated ChI glutamate cotransmission. Because of physical proximity, paired recordings are possible between identified Str neurons. However, paired recordings will miss weak or lower probability connections. Optogenetic stimulation of an identified neuronal population activates convergent inputs and is more likely to detect low probability synaptic connections.

#### 27.2.3.1 Interneuron to Projection Neuron Connections

SPNs are under strong control of interneurons, and received direct synaptic inputs from GABAergic interneurons, besides SABIs (Assous and Tepper 2019; Tepper et al. 2018). Both dSPNs and iSPNs receive strong inputs from FSIs and LTSIs in the dStr (Straub et al. 2016; Szydlowski et al. 2013) and NAc medial shell (Scudder et al. 2018) (Fig. 27.3). Although the strength of inputs does not differ in dSPNs and iSPNs, inputs from FSIs are significantly stronger than those from LTSIs (Straub et al. 2016). NGFs also made direct inputs to SPNs in the dStr with very high incidence even in slices (Assous et al. 2017; English et al. 2012) (Fig. 27.3). ChIs make fast glutamate responses to SPNs through VGLUT3-mediated cotransmission (Higley et al. 2011) (Fig. 27.3).

#### 27.2.3.2 Projection Neuron to Projection Neuron Connections

Most studies of collateral connections among SPNs have been done with simultaneous whole-cell recordings. An early study with transgenic

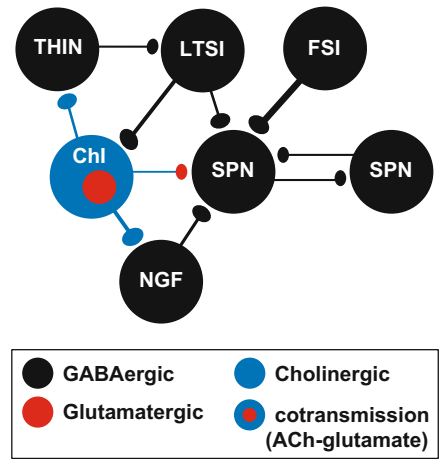


**Fig. 27.3** Optogenetically confirmed intrinsic striatal connections

expression of ChR2 in ~10% of SPNs in the dStr revealed a higher incidence of GABAergic connection among SPNs (Chuhma et al. 2011). In the NAc core, iSPN to dSPN collateral GABAergic connections are reliably elicited by ChR2 activation expressed in iSPNs (Dobbs Lauren et al. 2016) (Fig. 27.3).

#### 27.2.3.3 Interneuron to Interneuron Connections

SPNs have been regarded to be the sole targets of FSI synaptic connections, and this was confirmed using optogenetics showing only negligible connections between FSIs and other interneurons (Straub et al. 2016, Szydlowski et al. 2013) (Fig. 27.3). Other GABAergic interneurons made connections to interneurons: LTSIs to ChIs (Straub et al. 2016), NGFs to ChIs (English et al. 2012), and THINs to LTSIs (Assous et al. 2017). ChIs excited NGFs and THINs through nicotinic ACh receptors (Assous et al. 2017; Assous and Tepper 2019; English et al. 2012) (Fig. 27.3).

## 27.3 Future Directions

Optogenetics enables selective stimulation of identified populations of neurons with intermingled inputs in the basal ganglia, making functional connectome studies possible. Functional connectome studies add information to anatomical connectome studies regarding both the strength of synaptic connections and the transmitters used. The optogenetic approach is also a powerful tool for studies of cotransmission, not only proving existence and function, but also showing relative strength of the cotransmission. The combination of genetic fluorescent markers in postsynaptic neurons and ChR2 expression in presynaptic identified neuronal populations allows the study of cell-type-specific connectivities, particularly connection to and from interneurons.

New optogenetic tools will enable refined functional connectome studies. ChR2 can be expressed with "boolean" logic by combining two types of recombinases (e.g., Cre-loxP and Flp-FRT). This system is termed INTRSECT, for "INTRonic Recombinase Sites Enabling Combinatorial Targeting" (Fenno et al. 2014). INTRSECT can be used to target specific subpopulations of neurons; e.g., those capable of cotransmission (Mingote et al. 2019; Poulin et al. 2018). Synaptic connectivity can be determined using optical recording. Postsynaptic recording can be done either genetic $Ca^{2+}$ indicators (Farhi et al. 2019; Mollinedo-Gajate et al. 2019; Shen et al. 2020) or genetic voltage indicators (Bando et al. 2019; Mollinedo-Gajate et al. 2019; Shen et al. 2020; Yang and St-Pierre 2016). Genetically encoded indicators allow recording from identified populations of neurons without electrophysiological identification (Mollinedo-Gajate et al. 2019).

There are certain limitations in functional connectome studies with optogenetics. ChR2 expression depends on the strength of cell-specific promoters. If the promoter is not strong enough, expression of ChR2 may not be enough to activate presynaptic axons limiting detection of synaptic connections. Because of expression efficacy and limits in penetration of blue light through tissue (Aravanis et al. 2007; Yizhar et al. 2011), all synaptic inputs may not be activated with photostimulation. Light penetration issues can be minimized by using longer wavelength photostimulation, which penetrates deeper into tissue, with longer wavelength sensitive ChR2 variants (Yizhar et al. 2011). Another potential confound is in the interpretation of results of optogenetics experiments. Since ChR2 is activated by blue laser or high-power LED, it may activate terminals more synchronously than happens under normal physiological conditions in vivo (Kravitz and Bonci 2013: 169). Therefore, what is observed in optogenetic functional connectome studies may not be physiological; it should be interpreted as the maximum input strength of the synapses. Another potential problem is the distortion of membrane properties by expression of high levels of ectopic proteins (Zimmermann et al. 2008). ChR2 has very small single-channel conductance (Feldbauer et al. 2009; Wietek and Prigge 2016), and high expression is required for fast depolarization. A recent

comparison between conditional heterozygous and homozygous expression of ChR2 in cochlea revealed only minor effects on intrinsic membrane properties (Meng et al. 2019), minimizing this concern.

Although the anatomical connectome is fundamental, anatomical information alone does not elucidate functional connectivity. It is essential to evaluate the relative strength and physiological nature of connections, for a full description of neural connectivity. Gaining information about connectivity of identified populations of neurons is crucial for understanding how neuronal wiring diagrams correlate with function. Functional connectome is one of the ways to explore how our brain works, with optogenetics shining the light to show the direction.

**Acknowledgments** The author thanks Mihran Bakalian and Stephen Rayport for helpful comments and discussion. Writing of this chapter was supported by NIH grant MH117128 and DA038966.

## References

Abrahao KP, Lovinger DM (2018) Classification of GABAergic neuron subtypes from the globus pallidus using wild-type and transgenic mice. J Physiol 596:4219–4235

Aravanis AM, Wang L-P, Zhang F et al (2007) An optical neural interface: in vivo control of rodent motor cortex with integrated fiberoptic and optogenetic technology. J Neural Eng 4:S143–S156

Assous M, Tepper JM (2019) Excitatory extrinsic afferents to striatal interneurons and interactions with striatal microcircuitry. Eur J Neurosci 49:593–603

Assous M, Kaminer J, Shah F et al (2017) Differential processing of thalamic information via distinct striatal interneuron circuits. Nat Commun 8:15860

Assous M, Dautan D, Tepper JM et al (2019) Pedunculopontine glutamatergic neurons provide a novel source of feedforward inhibition in the striatum by selectively targeting interneurons. J Neurosci 39:4727–4473

Bando Y, Grimm C, Cornejo VH et al (2019) Genetic voltage indicators. BMC Biol 17:71

Belujon P, Grace AA (2011) Hippocampus, amygdala, and stress: interacting systems that affect susceptibility to addiction. Ann N Y Acad Sci 1216:114–121

Bertran-Gonzalez J, Bosch C, Maroteaux M et al (2008) Opposing patterns of signaling activation in dopamine D1 and D2 receptor-expressing striatal neurons in response to cocaine and haloperidol. J Neurosci 28:5671–5685

Bocklisch C, Pascoli V, Wong JCY et al (2013) Cocaine disinhibits dopamine neurons by potentiation of GABA transmission in the ventral tegmental area. Science (New York, NY) 341:1521–1525

Britt JP, Benaliouad F, Mcdevitt RA et al (2012) Synaptic and behavioral profile of multiple glutamatergic inputs to the nucleus accumbens. Neuron 76:790–803

Brown MTC, Tan KR, O'connor EC et al (2013) Ventral tegmental area GABA projections pause accumbal cholinergic interneurons to enhance associative learning. Nature 492:452–456

Cazorla M, De Carvalho FD, Chohan MO et al (2014) Dopamine D2 receptors regulate the anatomical and functional balance of basal ganglia circuitry. Neuron 81:153–164

Choi K, Holly EN, Davatolhagh MF et al (2019) Integrated anatomical and physiological mapping of striatal afferent projections. Eur J Neurosci 49:623–636

Chuhma N, Tanaka KF, Hen R et al (2011) Functional connectome of the striatal medium spiny neuron. J Neurosci 31:1183–1192

Chuhma N, Mingote S, Moore H et al (2014) Dopamine neurons control striatal cholinergic neurons via regionally heterogeneous dopamine and glutamate signaling. Neuron 81:901–912

Chuhma N, Mingote S, Yetnikoff L et al (2018) Dopamine neuron glutamate cotransmission evokes a delayed excitation in lateral dorsal striatal cholinergic interneurons. Elife 7:e39786

Cooper AJ, Stanford IM (2000) Electrophysiological and morphological characteristics of three subtypes of rat globus pallidus neurone in vitro. J Physiol 527 (Pt 2):291–304

Crittenden JR, Graybiel AM (2011) Basal ganglia disorders associated with imbalances in the striatal striosome and matrix compartments. Front Neuroanat 5:59

Ding JB, Oh W-J, Sabatini BL et al (2012) Semaphorin 3E-Plexin-D1 signaling controls pathway-specific synapse formation in the striatum. Nat Neurosci 15:215–223

Dobbs Lauren K, Kaplan Alanna R, Lemos Julia C et al (2016) Dopamine regulation of lateral inhibition between striatal neurons gates the stimulant actions of cocaine. Neuron 90:1100–1113

Ellender TJ, Harwood J, Kosillo P et al (2013) Heterogeneous properties of central lateral and parafascicular thalamic synapses in the striatum. J Physiol 591:257–272

English DF, Ibanez-Sandoval O, Stark E et al (2012) GABAergic circuits mediate the reinforcement-related signals of striatal cholinergic interneurons. Nat Neurosci 15:123–130

Eskenazi D, Chuhma N, Mingote S et al (2020) Functional connectome mapping. In: Wilson GS, Michael AC (eds) Compendium of in-vivo monitoring in real-time molecular neuroscience. World Scientific, Singapore

Exley R, Cragg SJ (2008) Presynaptic nicotinic receptors: a dynamic and diverse cholinergic filter of striatal dopamine neurotransmission. Br J Pharmacol 153: S283–S297

Farhi SL, Parot VJ, Grama A et al (2019) Wide-area all-optical neurophysiology in acute brain slices. J Neurosci 39:4889–4908

Feinberg EH, Vanhoven MK, Bendesky A et al (2008) GFP reconstitution across synaptic partners (GRASP) defines cell contacts and synapses in living nervous systems. Neuron 57:353–363

Feldbauer K, Zimmermann D, Pintschovius V et al (2009) Channelrhodopsin-2 is a leaky proton pump. Proc Natl Acad Sci U S A 106:12317–12322

Fenno LE, Mattis J, Ramakrishnan C et al (2014) Targeting cells with single vectors using multiple-feature Boolean logic. Nat Methods 11:763–772

Friston KJ, Frith CD, Liddle PF et al (1993) Functional connectivity: the principal-component analysis of large (PET) data sets. J Cereb Blood Flow Metab 13:5–14

Fujiyama F, Sohn J, Nakano T et al (2011) Exclusive and common targets of neostriatofugal projections of rat striosome neurons: a single neuron-tracing study using a viral vector. Eur J Neurosci 33:668–677

Gangarossa G, Espallergues J, De Kerchove D'e A et al (2013) Distribution and compartmental organization of GABAergic medium-sized spiny neurons in the mouse nucleus accumbens. Front Neural Circuit 7:22

Gerfen CR (1985) The neostriatal mosaic. I Compartmental organization of projections from the striatum to the substantia nigra in the rat. J Comp Neurol 236:454–476

Gerfen CR, Surmeier DJ (2011) Modulation of striatal projection systems by dopamine. Annu Rev Neurosci 34:441–466

Glajch KE, Kelver DA, Hegeman DJ et al (2016) Npas1+ pallidal neurons target striatal projection neurons. J Neurosci 36:5472–5488

Graybiel AM (2008) Habits, rituals, and the evaluative brain. Annu Rev Neurosci 31:359–387

Guo Q, Wang D, He X et al (2015) Whole-brain mapping of inputs to projection neurons and cholinergic interneurons in the dorsal striatum. PLoS One 10: e0123381

Haber SN, Fudge JL, Mcfarland NR (2000) Striatonigrostriatal pathways in primates form an ascending spiral from the shell to the dorsolateral striatum. J Neurosci 20:2369–2382

Higley MJ, Gittis AH, Oldenburg IA et al (2011) Cholinergic interneurons mediate fast VGluT3-dependent glutamatergic transmission in the striatum. PLoS One 6:e19155

Ikemoto S (2007) Dopamine reward circuitry: two projection systems from the ventral midbrain to the nucleus accumbens-olfactory tubercle complex. Brain Res Rev 56:27–78

Kim J-I, Ganesan S, Luo SX et al (2015) Aldehyde dehydrogenase 1a1 mediates a GABA synthesis pathway in midbrain dopaminergic neurons. Science (New York, NY) 350:102–106

Kita H (2007) Globus pallidus external segment. Prog Brain Res 160:111–133

Kravitz AV, Bonci A (2013) Optogenetics, physiology, and emotions. Front Behav Neurosci 7:169

Kreitzer AC (2009) Physiology and pharmacology of striatal neurons. Annu Rev Neurosci 32:127–147

Lerner TN, Shilyansky C, Davidson TJ et al (2015) Intact-brain analyses reveal distinct information carried by SNc dopamine subcircuits. Cell 162:635–647

Lichtman JW, Sanes JR (2008) Ome sweet ome: what can the genome tell us about the connectome? Curr Opin Neurobiol 18:346–353

Mamaligas AA, Barcomb K, Ford CP (2019) Cholinergic transmission at muscarinic synapses in the striatum is driven equally by cortical and thalamic inputs. Cell Rep 28:1003–1014.e3

Mastro KJ, Bouchard RS, Holt HAK et al (2014) Transgenic mouse lines subdivide external segment of the globus pallidus (GPe) neurons and reveal distinct GPe output pathways. J Neurosci 34:2087–2099

Mcgregor MM, Mckinsey GL, Girasole AE et al (2019) Functionally distinct connectivity of developmentally targeted striosome neurons. Cell Rep 29:1419–1428.e5

Melzer S, Gil M, Koser DE et al (2017) Distinct corticostriatal GABAergic neurons modulate striatal output neurons and motor activity. Cell Rep 19:1045–1055

Meng X, Murali S, Cheng Y-F et al (2019) Increasing the expression level of ChR2 enhances the optogenetic excitability of cochlear neurons. J Neurophysiol 122:1962–1974

Mingote S, Chuhma N, Kusnoor SV et al (2015) Functional connectome analysis of dopamine neuron glutamatergic connections in forebrain regions. J Neurosci 35:16259–16271

Mingote S, Amsellem A, Kempf A et al (2019) Dopamine-glutamate neuron projections to the nucleus accumbens medial shell and behavioral switching. Neurochem Int 129:104482

Mollinedo-Gajate I, Song C, Knöpfel T (2019) Genetically encoded fluorescent calcium and voltage indicators. In: Barrett JE, Page CP, Michel MC (eds) Concepts and principles of pharmacology: 100 years of the handbook of experimental pharmacology. Springer International Publishing, Cham

Nelson AB, Bussert TG, Kreitzer AC et al (2014) Striatal cholinergic neurotransmission requires VGLUT3. J Neurosci 34:8772–8777

Oldenburg IA, Ding JB (2011) Cholinergic modulation of synaptic integration and dendritic excitability in the striatum. Curr Opin Neurobiol 21:425–432

Parker PRL, Lalive AL, Kreitzer AC (2016) Pathway-specific remodeling of thalamostriatal synapses in parkinsonian mice. Neuron 89:734–740

Pennartz CMA, Berke JD, Graybiel AM et al (2009) Corticostriatal interactions during learning, memory processing, and decision making. J Neurosci 29:12831–12838

Poulin J-F, Caronia G, Hofer C et al (2018) Mapping projections of molecularly defined dopamine neuron

subtypes using intersectional genetic approaches. Nat Neurosci 21:1260–1271
Qi J, Zhang S, Wang H-L et al (2016) VTA glutamatergic inputs to nucleus accumbens drive aversion by acting on GABAergic interneurons. Nat Neurosci 19:725–733
Saunders A, Huang KW, Sabatini BL (2016) Globus pallidus externus neurons expressing parvalbumin interconnect the subthalamic nucleus and striatal interneurons. PLoS One 11:e0149798
Sciamanna G, Ponterio G, Mandolesi G et al (2015) Optogenetic stimulation reveals distinct modulatory properties of thalamostriatal vs corticostriatal glutamatergic inputs to fast-spiking interneurons. Sci Rep 5:16742
Scudder SL, Baimel C, Macdonald EE et al (2018) Hippocampal-evoked feedforward inhibition in the nucleus accumbens. J Neurosci 38:9091–9104
Sesack SR, Grace AA (2010) Cortico-Basal Ganglia reward network: microcircuitry. Neuropsychopharmacology 35:27–47
Seung HS (2009) Reading the book of memory: sparse sampling versus dense mapping of connectomes. Neuron 62:17–29
Shen Y, Nasu Y, Shkolnikov I et al (2020) Engineering genetically encoded fluorescent indicators for imaging of neuronal activity: progress and prospects. Neurosci Res 152:3–14
Shepherd G (1994) Neurobiology. Oxford University Press, Oxford
Sporns O, Tononi G, Kötter R (2005) The human connectome: a structural description of the human brain. PLoS Comput Biol 1:e42
Straub C, Tritsch NX, Hagan NA et al (2014) Multiphasic modulation of cholinergic interneurons by nigrostriatal afferents. J Neurosci 34:8557–8569
Straub C, Saulnier JL, Bègue A et al (2016) Principles of synaptic organization of GABAergic interneurons in the striatum. Neuron 92:84–92
Stuber GD, Hnasko TS, Britt JP et al (2010) Dopaminergic terminals in the nucleus accumbens but not the dorsal striatum corelease glutamate. J Neurosci 30:8229–8233
Szydlowski SN, Pollak Dorocic I, Planert H et al (2013) Target selectivity of feedforward inhibition by striatal fast-spiking interneurons. J Neurosci 33:1678–1683
Tecuapetla F, Patel JC, Xenias H et al (2010) Glutamatergic signaling by mesolimbic dopamine neurons in the nucleus accumbens. J Neurosci 30:7105–7110
Tepper JM, Koós T, Wilson CJ (2004) GABAergic microcircuits in the neostriatum. Trends Neurosci 27:662–669
Tepper JM, Tecuapetla F, Koos T et al (2010) Heterogeneity and diversity of striatal GABAergic interneurons. Front Neuroanat 4:150
Tepper JM, Koós T, Ibanez-Sandoval O et al (2018) Heterogeneity and diversity of striatal GABAergic interneurons: update 2018. Front Neuroanat 12:91
Tritsch NX, Ding JB, Sabatini BL (2012) Dopaminergic neurons inhibit striatal output through non-canonical release of GABA. Nature 490:262–266
Tritsch NX, Oh WJ, Gu C et al (2014) Midbrain dopamine neurons sustain inhibitory transmission using plasma membrane uptake of GABA, not synthesis. Elife 3:e01936
Van Bockstaele EJ, Pickel VM (1995) GABA-containing neurons in the ventral tegmental area project to the nucleus accumbens in rat brain. Brain Res 682:215–221
Wietek J, Prigge M (2016) Enhancing channelrhodopsins: an overview. In: Kianianmomeni A (ed) Optogenetics. Humana Press, New York, NY
Wilson CJ (2004) The basal ganglia. In: Shepherd G (ed) The synaptic organization of the brain, 5th edn. Oxford University Press, Oxford
Xia Y, Driscoll JR, Wilbrecht L et al (2011) Nucleus accumbens medium spiny neurons target non-dopaminergic neurons in the ventral tegmental area. J Neurosci 31:7811–7816
Yang HH, St-Pierre F (2016) Genetically encoded voltage indicators: opportunities and challenges. J Neurosci 36:9977–9989
Yin HH, Knowlton BJ (2006) The role of the basal ganglia in habit formation. Nat Rev Neurosci 7:464–476
Yizhar O, Fenno LE, Davidson TJ et al (2011) Optogenetics in neural systems. Neuron 71:9–34
Zhu Y, Wienecke CFR, Nachtrab G et al (2016) A thalamic input to the nucleus accumbens mediates opiate dependence. Nature 530:219–222
Zimmermann D, Zhou A, Kiesel M et al (2008) Effects on capacitance by overexpression of membrane proteins. Biochem Biophys Res Commun 369:1022–1026

# Cell-Type-Specific Optogenetic Techniques Reveal Neural Circuits Crucial for Episodic Memories

28

Naoki Yamamoto, William D. Marks, and Takashi Kitamura

**Abstract**

The formation and maintenance of episodic memories are important for our daily life. Accumulating evidence from extensive studies with pharmacological, electrophysiological, and molecular biological approaches has shown that both entorhinal cortex (EC) and hippocampus (HPC) are crucial for the formation and recall of episodic memory. However, to further understand the neural mechanisms of episodic memory processes in the EC-HPC network, cell-type-specific manipulation of neural activity with high temporal resolution during memory process has become necessary. Recently, the technological innovation of optogenetics combined with pharmacological, molecular biological, and electrophysiological approaches has significantly advanced our understanding of the circuit mechanisms for learning and memory. Optogenetic techniques with transgenic mice and/or viral vectors enable us to manipulate the neural activity of specific cell populations as well as specific neural projections with millisecond-scale temporal control during animal behavior. Integrating optogenetics with drug-regulatable activity-dependent gene expression systems has identified memory engram cells, which are a subpopulation of cells that encode a specific episode. Finally, millisecond pulse stimulation of neural activity by optogenetics has further achieved (a) identification of synaptic connectivity between targeted pairs of neural populations, (b) cell-type-specific single-unit electrophysiological recordings, and (c) artificial induction and modification of synaptic plasticity in targeted synapses. In this chapter, we summarize technological and conceptual advancements in the field of neurobiology of learning and memory as revealed by optogenetic approaches in the rodent EC-HPC network for episodic memories.

**Keywords**

Optogenetics · Hippocampus · Entorhinal cortex · Episodic memory · Neural circuit · Memory engram · Synaptic plasticity · Systems consolidation of memory

## Abbreviations

| | |
|---|---|
| AAV | Adeno-associated virus |
| Arch | Archaerhodopsin |

N. Yamamoto · W. D. Marks
Department of Psychiatry, University of Texas Southwestern Medical Center, Dallas, TX, USA

T. Kitamura (✉)
Department of Psychiatry, University of Texas Southwestern Medical Center, Dallas, TX, USA

Department of Neuroscience, University of Texas Southwestern Medical Center, Dallas, TX, USA
e-mail: Takashi.Kitamura@UTSouthwestern.edu



H. Yawo et al. (eds.), *Optogenetics*, Advances in Experimental Medicine and Biology 1293,
https://doi.org/10.1007/978-981-15-8763-4_28

| | |
|---|---|
| CFC | Contextual fear conditioning |
| ChR2 | Channelrhdopsin-2 |
| CS | Conditioned stimulus |
| DG | Dentate gyrus |
| dSub | Dorsal subiculum |
| EC | Entorhinal cortex |
| EC2 | Layer II of entorhinal cortex |
| EC3 | Layer III of entorhinal cortex |
| EC5 | Layer V of entorhinal cortex |
| HPC | Hippocampus |
| IEG | Immediate early gene |
| LTD | Long-term depression |
| LTP | Long-term potentiation |
| mPFC | Medial prefrontal cortex |
| MTT | Multiple Trace Theory |
| NMDA | *N*-methyl-D-aspartate |
| NpHR | Halorhodopsin |
| NR1 | *N*-methyl-D-aspartate receptor |
| Reelin+ cells | Reelin-positive stellate cells |
| SCT | Standard consolidation theory |
| SL | Stratum lacunosum |
| SL-IN | Stratum lacunosum interneuron (GABAergic) |
| SWR | Sharp-wave ripples |
| TeTX | Tetanus-toxin (light chain) |
| TFC | Trace fear conditioning |
| US | Unconditioned stimulus |
| Wfs1 | Wolfram syndrome 1 |
| Wfs1+ cell | Wolfram syndrome 1-positive (pyramidal) cell |

## 28.1 Introduction

In the mammalian brain, massive amounts of multisensory stimulation are combined and stored as a series of experienced events for acquiring and remembering episodes. Learning and memory processes affect a wide variety of adaptive behaviors and contribute to higher cognitive function. In humans and rodents, the entorhinal cortical (EC)–hippocampal (HPC) circuit is required for the formation and recall of episodic memory, which extends into the spatial/contextual, object/individual, and temporal domains (Eichenbaum 2000; Tulving 2002). Episodic memory can be formed as an integration between multiple elements individually remembered and linked to form a singular memory unit (Fortin et al. 2002; Naya and Suzuki 2011; MacDonald et al. 2011, 2013; Kitamura et al. 2014; Sakon et al. 2014; Allen et al. 2016; Aronov et al. 2017). These individual components include the "what" in the form of objects, the "where" representing spatial orientation, navigation, and context (Moser et al. 2008; Smith and Bulkin 2014), the "when" indicated by timing sequencing of events and linking of events across time (Kitamura et al. 2014), and the "who," or social memory involving recall of individual conspecifics and relationships (Allsop et al. 2014). Furthermore, while memory acquisition initially requires the EC-HPC network, the acquired memory is gradually consolidated in neocortical networks for permanent storage (Frankland and Bontempi 2005; Tonegawa et al. 2018). To further understand the neural mechanisms by which the brain stores each component (what, where, who, and when) of episodic memories in the EC-HPC network and how each component is integrated to complete an episodic memory, we need to understand neural circuits and their activity during the formation, recall, and consolidation (Box 28.1) of episodic memories.

**Box 28.1: Memory Consolidation**

The process of transforming a newly acquired memory into a more long-lasting stable state is referred as memory consolidation (Squire 1986; Eichenbaum 2000). Several theories have attempted to explain the neurobiological mechanisms that underlie this process. The most commonly accepted theory is the Standard Consolidation Theory (SCT). Beginning with Scoville and Milner's study of patients with hippocampal lesions (Scoville and Milner 1957), many studies of memory-impaired patients and animals have provided strong evidence that our memories are initially stored within HPC and, with the passage of time, slowly

(continued)

**Box 28.1** (continued)

consolidated in extra-hippocampal (neocortical) structures (Squire 1986; Zola-Morgan and Squire 1990; Kim and Fanselow 1992). For example, rats receiving electrolytic lesions to HPC 1 day after a contextual fear memory task do not retain the memory, whereas rats receiving a lesion 4 weeks later retain the memory (Kim and Fanselow 1992). However, there are conflicting reports about the role of HPC on the remote memories (Squire 1992; Nadel and Moscovitch 1997; Bayley et al. 2005). For example, HPC damage not only disrupts recently acquired memory but also impairs recall of long-term memory in human studies (Nadel and Moscovitch 1997). These contrary pieces of evidence have led to a new theoretical formulation; the Multiple Trace Theory (MTT). According to MTT, reactivation of a memory creates additional memory traces in HPC, and these multiple traces of a particular memory give greater robustness against partial HPC disruption (Nadel and Moscovitch 1997; Winocur and Moscovitch 2011). These conflicts had not been resolved until the emergence of new technologies enabled examination of the functionality of memory traces of a particular memory in a specific area (Kitamura et al. 2017).

In 2005, a novel technology termed optogenetics was invented. The light-responsive cation channel, channelrhdopsin-2 (ChR2), chloride, and proton pumps such as halorhodopsin (NpHR) and archaerhodopsin (Arch) have revolutionized the way that neuroscientists can interrogate the roles of neural circuits on learning and memory process by temporally and reversibly manipulating neural activity during animal behavior (Fig. 28.1b) (Boyden et al. 2005; Zhang et al. 2006; Chow et al. 2010; Yizhar et al. 2011). These opsin proteins can be expressed in selective brain regions by injection of viral vectors under the control of cell-type-specific promoters (Sohal et al. 2009; Stuber et al. 2011). Furthermore, transgenic animals expressing Cre-recombinase in a specific cell population with the virus-mediated delivery of vectors encoding a Cre-inducible opsin allows us to manipulate neural activity in specific cell populations in the brain (Fig. 28.1a) (Cardin et al. 2010; Cohen et al. 2012; Kitamura et al. 2014). Retrograde transport of replication-deficient rabies virus (Wickersham et al. 2007; Chatterjee et al. 2018) and adeno-associated viruses (AAVs) (Tervo et al. 2016) can be utilized for selective labeling of a defined neural population projecting to a virus-injected area (Fig. 28.1a) (Zhang et al. 2013; Kitamura et al. 2015b). Selective light delivery to axon terminals can be also used as an projection-specific neural activity control (Fig. 28.1a) (Tye et al. 2011). Activity-dependent cell labeling with optogenetic stimulation has identified memory engram cells, which are a subpopulation of cells that encode a specific episode (Box 28.2; Fig. 28.1c[iv]) (Reijmers et al. 2007; Liu et al. 2012). Finally, millisecond–timescale control of neural stimulation by optogenetics enables us to examine (a) identification of synaptic connectivity between targeted pairs of neurons, (b) cell-type-specific single-unit electrophysiological activity, and (c) artificial induction and modification of synaptic plasticity in targeted synapses (Fig. 28.1c). In this chapter, we focus on recent advances in our understanding of neural circuits and the neural processes underlying the formation, recall, and consolidation of episodic memory with emphasis on cell-type-specific optogenetic approaches.

**Box 28.2: Memory Engram**

In 1904, German scientist Richard Semon coined the term "engram" to conceptualize the physical substrate of memory, which he defined as "the enduring though primarily latent modification in the irritable substance produced by a stimulus" (Semon 1904, 1921). The term engram is equivalent to another commonly used term, "memory

(continued)

**Box 28.2** (continued)

trace." In order to be considered as such, an engram must meet three criteria: it is an enduring physical and/or chemical change that occurs in a neural network in the brain (criterion 1) as a result of activation of neuronal subpopulations by episodic stimuli (criterion 2) and can be subsequently reactivated by stimuli that were part of the original set of encoded stimuli, resulting in the recall of the original memory (criterion 3). The current conception is that individual neurons act as the substrate of engram formation, becoming "engram cells" (Josselyn 2010; Tonegawa et al. 2015). Over a century later, rapid development of molecular genetics and biological technologies allows us to examine Semon's theory by labeling specific neuronal subpopulations activated during defined periods and manipulating or recording their activities (Reijmers et al. 2007; Han et al. 2009; Liu et al. 2012). Reijmers et al. found that a subpopulation of neurons activated during the acquisition of a fear memory is preferentially reactivated during the recall of that memory in the amygdala of the mouse brain by examining the expression of the immediate–early gene (IEG), c-Fos (Reijmers et al. 2007). Han et al. found that a subpopulation of neurons artificially overexpressing the cAMP response element-binding (CREB) protein was preferentially activated during a subsequent contextual fear-conditioning training and became a part of the putative array of engram cells (Han et al. 2007). They also demonstrated that selective ablation of these putative engram cells impairs the recall of the associated fear memory in mice, but ablation of a random population of neurons in the same region does not (Han et al. 2009). Finally, Liu et al. showed that optogenetic reactivation of a subpopulation of dentate gyrus granule cells which were previously activated during the acquisition of a contextual fear memory is sufficient to induce memory recall (Liu et al. 2012). This phenomenon, identified in the dentate gyrus granule cells, which stores a contextual fear memory meets all three of the criteria for a true engram (Josselyn 2010; Tonegawa et al. 2015).

## 28.2 Identification of Novel Hippocampal Neural Circuit by Optogenetics

EC-HPC neuronal networks contain two major feed-forward excitatory pathways. One is called the hippocampal tri-synaptic pathway; it runs from EC layer II (EC2) to granule cells in the dentate gyrus (DG) to CA3 and CA1 pyramidal cells, and the other pathway is called the hippocampal direct pathway from EC layer III (EC3) to CA1 pyramidal cells (Fig. 28.2) (Amaral and Witter 1989; Witter et al. 2000; Nakazawa et al. 2003). In both pathways, glutamatergic inputs from EC eventually converge onto the CA1 region. The CA1 directly projects to other neocortical areas or indirectly connects through subiculum and EC layer V (EC5) to various brain structures (Steward and Scoville 1976; Amaral and Witter 1989). Patch-clamp recordings with electrical stimulation in an acute brain slice have identified many synaptic connections in the EC-HPC networks (Andersen et al. 1966; Winson and Abzug 1977; McNaughton and Barnes 1977; Empson and Heinemann 1995; Scharfman 1995; Chevaleyre and Siegelbaum 2010; Masurkar et al. 2017; Hashimotodani et al. 2017). However, electrical stimulation of afferent fibers in acute brain slices may activate any afferent fibers passing through the area; there is no specificity of stimulation to distinguish individual components present within the tract. Expressing ChR2 in a specific neural population allows us to optically stimulate targeted-afferent fibers expressing ChR2 in the brain (Fig. 28.1a). Using patch-clamp recording paired with optogenetic light-pulse stimulation of

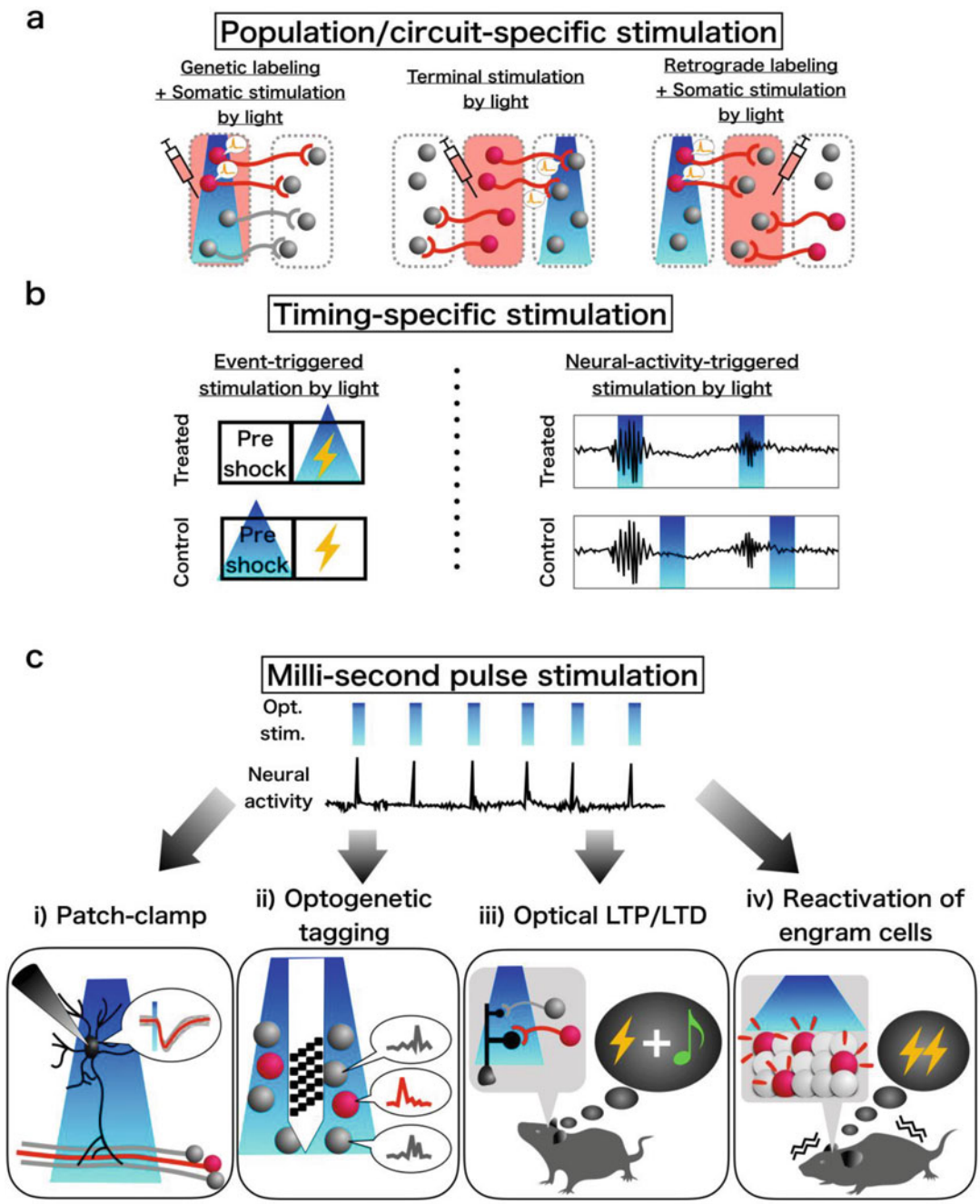


**Fig. 28.1** Advantages of optogenetic stimulation for learning and memory studies. (**a**) Left panel; population-specific opsin expression enables population-specific manipulation of neural activity by local light delivery. Each area surrounded by a dotted line represents a brain region. Red area represents a virus-injected brain area. Middle panel; projection-specific light illumination enables selective manipulation of the neural activity at axon terminals (manipulating neural output). Right panel; retrograde transport of virus enables labeling of specific neural population projecting to the virus-injected brain area. (**b**) Left panel; specific neural activities in a defined period of behavioral paradigms can be optically manipulated. Figure is an example of the event-triggered optogenetic stimulation in a fear-conditioning paradigm. Right panel; neural activity-triggered stimulation by light enables us to examine the functional roles of neural activities during the photo-stimulating period. Figure is an example of the burst-firing-triggered optogenetic stimulation and its control optogenetic stimulation. (**c**)

specific neural fibers, it has become possible to assess the existence and/or strength of synaptic connections between targeted pairs of neurons (Fig. 28.1c[i]) (Petreanu et al. 2007). For example, using cell-type-specific Cre transgenic mouse lines, Kohara et al. discovered a new monosynaptic pathway from DG cells to CA2 pyramidal cells through abundant longitudinal projections. They expressed ChR2 in DG granule cells and conducted patch-clamp recordings in CA2 neurons with optogenetic pulse stimulation of DG granule cells. This resulted in the observation of monosynaptic responses from CA2 neurons after a brief pulse of blue light (460 nm) was delivered to the brain slice (Kohara et al. 2014), indicating that DG granule cells directly project to CA2 pyramidal neurons (Fig. 28.2). In addition, contrary to previous observations made with electrical stimulation (Chevaleyre and Siegelbaum 2010; Jones and McHugh 2011), Kohara et al. observed there is no direct input from EC3 to CA2 (Kohara et al. 2014), indicating that CA2 mainly receives input coming from the tri-synaptic pathway (Fig. 28.2). In 2014, Kitamura et al. discovered a novel direct projection from Wolfram syndrome 1 (Wfs1) positive pyramidal cells ($Wfs1^+$ cells) in EC2 to GABAergic interneurons in stratum lacunosum (SL-INs) of hippocampal CA1 (Fig. 28.2) (Kitamura et al. 2014). Optogenetic terminal stimulation of ChR2-expressing $Wfs1^+$ cells in EC2 with in vitro patch-clamp recordings revealed a monosynaptic glutamatergic input onto SL-INs. Furthermore, simultaneous recordings of CA1 pyramidal cells and SL-INs paired with optogenetic axonal stimulation from EC3 cells demonstrated the existence of a novel gating circuit in CA1 controlled by the $Wfs1^+$ cells of EC2 (Kitamura et al. 2014). Similarly, Basu et al. found long-range projecting GABAergic interneurons in EC, which mediate gating mechanisms in CA1 (Basu et al. 2016). Utilizing cell-type-specific optogenetic manipulation, Leão et al. discovered that hippocampal oriens lacunosum–moleculare cells differentially modulate inputs coming from CA3 and EC3/EC2 (Leão et al. 2012). These results demonstrate that patch-clamp electrophysiology combined with the millisecond pulse stimulation of neural activity with optogenetics enables the discovery of novel neural circuits, even in the well-known EC-HPC network.

## 28.3 Neural Circuit Mechanisms for Episodic Memory by Optogenetics

### 28.3.1 Neural Circuits for Contextual Memory

#### 28.3.1.1 Loss-of-Function Analysis by Optogenetics

Contextual memory is comprised of multimodal information including spatial cues, sound, odor, texture, and more (Spear 1973; Maren et al. 2013). A common behavioral test in animal studies is contextual fear conditioning (CFC), in which an animal is given aversive footshocks paired with a specific context (Pavlov 1927; Phillips and LeDoux 1992; Kim and Fanselow 1992; Kim et al. 1993; Frankland et al. 1998; Sutherland et al. 2008; Goshen et al. 2011; Maren et al. 2013; Kitamura et al. 2017). During the conditioning

**Fig. 28.1** (continued) Advantages of millisecond pulse stimulation of neural activity by optogenetics. (*i*) Patch-clamp recording with millisecond pulse stimulation by optogenetics enables examination of the synaptic connectivity between targeted pairs of neural populations (Petreanu et al. 2007). (*ii*) in vivo electrophysiology with millisecond pulse stimulation to specific neural populations expressing opsin enables examination of cell-type-specific single-unit electrophysiological recording (Cohen et al. 2012). (*iii*) Artificial induction and modification of synaptic plasticity in targeted-synapses by high-frequency light-pulse optogenetic stimulation (Nabavi et al. 2014). (*iv*) Activity-dependent cell labeling with millisecond pulse stimulation by optogenetics enables induction of artificial memory recall by optogenetic activation of memory engram cells (Liu et al. 2012). (**a**–**c**) Red or gray neurons represent opsin-expressing or non-expressing cells. Blue tetragons or squares represent light-delivered periods/areas

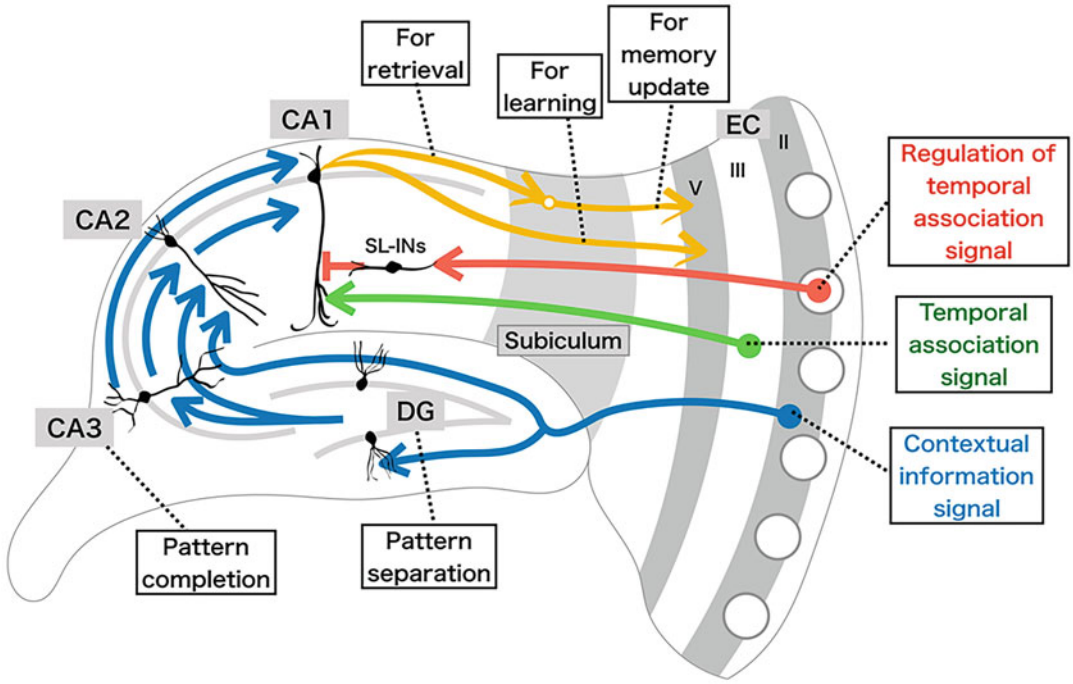


**Fig. 28.2** EC-HPC neural circuits for episodic memory. EC2 contains two populations of excitatory neurons, Reelin$^+$ stellate cells, and Wfs1$^+$ pyramidal cells. Reelin+ cells project to hippocampal DG, CA3, and CA2, while Wfs1$^+$ cells project to GABAergic interneurons in SL (SL-INs) of hippocampal CA1 region. Pyramidal cells in EC3 directly project to CA1 pyramidal cells. Hippocampal DG granule cells project to CA3 and CA2. Hippocampal CA3 project to CA2 and CA1. CA2 projects to CA1. CA1 projects to subiculum as well as EC5. Reelin$^+$ stellate cells in EC2 drive contextual information to hippocampal DG and CA3 circuits to form contextual memory (blue). In the tri-synaptic circuits, DG contributes to the pattern separation process, while CA3 contributes to the pattern completion. Temporal association signals from EC3 cells to CA1 contribute to temporal association learning (green). On the other hand, Wfs1$^+$ pyramidal cells in EC2 project to GABAergic interneurons in CA1, which gate inputs from EC3 to CA1 (red), and inhibit temporal association learning. While the pathway from CA1 to EC5 via dorsal subiculum is involved in the memory recall as well as update, the direct pathway from CA1 to EC5 is crucial for memory encoding (yellow)

and recall of CFC, contextual information has been thought to proceed through the hippocampal tri-synaptic circuit from EC2 to DG to CA3 and then to CA1 (Marr 1971; O'Reilly and McClelland 1994; Treves and Rolls 1994; Dudchenko et al. 2000; Gilbert et al. 2001; Nakazawa et al. 2003; Leutgeb et al. 2004, 2007; McHugh et al. 2007; Nakashiba et al. 2008, 2009). Accumulating evidence from theoretical (Marr 1971; McNaughton and Morris 1987), anatomical (Marr 1971; O'Reilly and McClelland 1994; Treves and Rolls 1994), physiological (Leutgeb et al. 2004, 2007; McHugh et al. 2007), and behavioral studies using loss-of-function animals (Dudchenko et al. 2000; Gilbert et al. 2001; Nakazawa et al. 2003; McHugh et al. 2007; Nakashiba et al. 2008, 2009) indicates that the functional role of the EC2-DG-CA3 feed-forward excitatory pathway is pattern separation; a process allowing discrimination of overlapping inputs, and that the functional role of the recurrent connections in CA3 is pattern completion; a process for recall of complete memories on the basis of incomplete sets of cues (Box 28.3). Furthermore, Kitamura et al. found that the Reelin$^+$ stellate cells (Reelin$^+$

cells) in EC2 show context-specific neural activity during exploration of distinct contexts (Kitamura et al. 2015b) by using in vivo calcium imaging, indicating that the entorhinal cortex drives contextual information to the hippocampal circuit. To examine the role of EC2 input into the DG (and subsequently CA3) on contextual memory, they expressed ArchT (Han et al. 2011) in the Reelin$^+$ cells of EC2 by retrograde AAV infection from the axon terminals in DG and inhibited the neural activity of Reelin$^+$ cells in EC2 with green light illumination (561 nm) in EC during either conditioning or testing (Fig. 28.1b). They found that optogenetic inhibition of the Reelin$^+$ cells during conditioning or testing in CFC impaired contextual fear memory and reduced context-specific neural activation in CA3 pyramidal cells (Kitamura et al. 2015b). These results indicate that contextual information is already encoded by the Reelin$^+$ cells in EC2 and neural input from Reelin$^+$ cells in EC2 to the DG and CA3 is crucial for the formation and recall of contextual fear memory.

**Box 28.3: Pattern Separation and Pattern Completion**

As a memory system, HPC must be able to generate distinct patterns of activation of neural networks, even from highly similar cues, at the time of storage, and HPC must be able to retrieve the full stored patterns of activation of neural networks from noisy and partial cues at the time of recall. The process of transforming overlapping or similar inputs into more distinct outputs is called pattern separation. The process of reconstructing incomplete or partial sets of inputs into complete stored representations is called pattern completion. Earlier theoretical studies provide an insightful theoretical framework for associating functional properties of memory with the mechanisms of pattern separation and pattern completion (McNaughton and Morris 1987; O'Reilly and McClelland 1994). Based on the anatomical organization of the hippocampal tri-synaptic pathway, in which a large number of granule cells in DG project to a smaller number of recurrently connected CA3 cells and form powerful synaptic connection with large synapses located very close to the soma of CA3 cells, these studies predicted that the EC2–DG–CA3 feed-forward excitatory pathway works as the pattern separator, and the recurrent connections in CA3 work as the pattern completer (Marr 1971; McNaughton and Morris 1987; O'Reilly and McClelland 1994; Treves and Rolls 1994). These theories were supported by physiological observations a within each hippocampal subregion in awake, behaving animals (Leutgeb et al. 2004, 2007; McHugh et al. 2007), and by the behavioral performance of mice with genetic/pharmacological inactivation or lesion of discrete components of the EC-HPC network (Dudchenko et al. 2000; Gilbert et al. 2001; Nakazawa et al. 2003; McHugh et al. 2007; Nakashiba et al. 2008, 2009). For example, McHugh et al. examined the role of the granule cells in the DG using a transgenic mouse line in which synaptic plasticity in EC2-DG synapses was attenuated by the DG-specific conditional knockout of N-methyl-D-aspartate (NMDA) receptor NR1. They found that the mutant mice showed impairment in the discrimination of similar contexts and reduced the context-specific activities of CA3 pyramidal cells (McHugh et al. 2007).

While the EC2-DG-CA3 circuit processes contextual memory and sends it to hippocampal CA1 pyramidal cells, how does contextual information further proceed from hippocampal CA1 pyramidal cells to basolateral amygdala for the formation and recall of contextual fear memory? CA1 pyramidal cells in dorsal HPC directly project to EC5 as well as dorsal subiculum (dSub) (Amaral and Witter 1989). Excitatory neurons in dorsal subiculum project to EC5 and other

cortical and subcortical brain regions including amygdala (Ding 2013) (Fig. 28.2). EC5 neurons have also extensive projections to the neocortex as well as basolateral amygdala (Sürmeli et al. 2015; Kitamura et al. 2017). Studies with functional magnetic resonance imaging of human subjects suggested that the DG and CA subfields are activated during episodic memory formation, whereas dSub is more active during memory recall (Gabrieli et al. 1997; Eldridge et al. 2005). On the other hand, in rodents, chemical lesions of the CA1 or dSub caused impairment in the acquisition of place navigation (Morris et al. 1990). However, given the close anatomical proximity between CA1 and dSub in rodents, lesions might be difficult to target to a specific hippocampal subregion. With transgenic mice expressing Cre recombinase in excitatory neurons of dSub or CA1 combined with the injection of Cre-dependent AAV expressing Arch, Roy et al. examined the role of dSub and CA1 neurons and their circuits in the formation and recall of CFC (Roy et al. 2017). First, optogenetic cell body inhibition of dSub neurons impaired the recall of CFC but not learning. Axonal terminal inhibition of dSub neurons at EC5 targeted by the implantation of optic fibers also impaired the recall of CFC but not learning. Similarly, optogenetic terminal inhibition of CA1 neurons at dSub inhibited the recall of CFC but not learning. In contrast, optogenetic terminal inhibition of CA1 neurons at EC5 during testing of CFC did not impair the recall of CFC memory, while optogenetic terminal inhibition of CA1 neurons at EC5 during CFC acquisition resulted in inability to recall CFC memory. In addition, selective optogenetic terminal inhibition of dSub terminals at EC5 impaired the updating of CFC memory (Roy et al. 2017). These results showed that the di-synaptic pathway from CA1 to EC5 via dSub is selectively required for memory recall and updating, whereas the direct pathway from CA1 to EC5 is essential for memory formation. Furthermore, by using optogenetic terminal inhibition of EC5 neurons at basolateral amygdala, Kitamura et al. showed that the EC5 to basolateral amygdala pathway is crucial for the formation and recall of CFC (Kitamura et al. 2017). In summary, cell-type-specific and/or projection-specific optogenetic manipulation of neural activity revealed that Reelin$^{+}$ cells in EC2 drive contextual information to HPC, and contextual memory is formed in EC2-DG-CA3 circuits (Fig. 28.2). However, after EC2-DG-CA3 circuits processed contextual memory to hippocampal CA1 pyramidal cells, two distinct neural pathways (CA1–dSub–EC5 pathway or CA1-EC5 pathway) to basolateral amygdala are differentially involved in the formation or recall of contextual fear memory.

#### 28.3.1.2 Gain-of-Function Analysis by Optogenetics

The previous section discussed the identification of specific neural circuits crucial for the formation and recall of contextual fear memory. However, these studies did not provide direct evidence as to whether these circuits store memory traces for CFC. In the early nineteenth century, Richard Semon proposed that our brains retain traces for a specific memory, which are generated by and endure through modification produced by a stimulus. These long-term memory traces are referred to as an engram (Box 28.2). Until recently, biological basis of a true engram as defined by Semon's theory, a stably maintained neural subpopulation which is activated during acquisition of specific memory and reactivated during memory recall, had not been identified. In 2012, optogenetic technology combined with activity-dependent cell labeling using immediate–early gene promoters to drive opsin expression in cells activated during an episode made it possible to identify engram cells for a specific episode (Reijmers et al. 2007; Liu et al. 2012). As a first demonstration of engram cells, Liu et al. labeled hippocampal DG cells activated during CFC with ChR2 in doxycycline-dependent manner. They found that optogenetic reactivation of these cells in DG by 20 Hz pulse stimulation of blue light via optic fibers implanted into the brain is sufficient to induce memory recall without natural recall cues but optogenetic reactivation of cells labeled in a context not associated with fear did not (Fig. 28.1c[iv]) (Liu et al. 2012). These results demonstrate that artificial optogenetic reactivation of a selective neural subset activated during

learning is sufficient for the recall of specific episodic memory, indicating a direct evidence for the existence of memory engram for CFC in the hippocampal DG cells. Subsequent studies also showed that memory engram cells can be formed in various brain regions for different types of memories, however, the optimal frequency of light pulse stimulation for artificial memory recall is different in each brain region, indicating that the temporal pattern of neural activity in engram cells is also important for memory recall (Fig. 28.1c[iv]) (Ramirez et al. 2013; Redondo et al. 2014; Cowansage et al. 2014; Ohkawa et al. 2015; Ryan et al. 2015; Okuyama et al. 2016; Kitamura et al. 2017; Abdou et al. 2018).

#### 28.3.1.3 Optogenetic Manipulation of Synaptic Plasticity

Since we now are able to optogenetically activate targeted-neural projections with high-frequency light-pulse stimulation (Fig. 28.1a) (Lin et al. 2009), it has become possible to artificially induce and modulate synaptic plasticity to directly address causality between long-term potentiation (LTP) or long-term depression (LTD)-mediated synaptic plasticity (Box 28.4) and memory expression (Fig. 28.1c[iii]). Nabavi et al. demonstrated that high-frequency (100 Hz) or low-frequency (1 Hz) light pulse stimulation of axon terminals expressing mammalian codon-optimized ChiEF (oChIEF) (Lin et al. 2009, 2013), a ChR2 variant that can respond to high-frequency optical stimuli, induced LTP or LTD in the brain of behaving animals. By using the optical LTP/LTD protocol, they found that induction of optical LTD at synapses of auditory cortex neurons onto lateral amygdala after auditory fear conditioning disrupted the recall of auditory fear memory. Furthermore, induction of optical LTP restored the conditioned fear response which had been disrupted by optical LTD (Nabavi et al. 2014). By using optical LTD protocols combined with activity-dependent cell labeling in auditory cortex and amygdala, Abdou et al. also found that induction of optical LTP by stimulating axon terminals from auditory cortical neurons activated during tone fear conditioning disrupted the recall of the auditory fear memory, but did not affect other auditory fear memory associated with a different tone frequency, indicating the recall of two distinct auditory fear memories required synapse-specific activation (Abdou et al. 2018). These studies demonstrated that LTP/LTD-mediated synaptic plasticity directly links with memory formation and memory expression.

**Box 28.4: Long-Term Potentiation and Long-Term Depression**

In 1949, Canadian psychologist Donald Hebb proposed an elegant model explaining how the function of neurons contributed to learning and memory processes (Hebb 1949). In this model, he postulated a synaptic modification for learning and memory that occurs as a consequence of coincidence between pre- and postsynaptic activity. However, experimental evidence showing plasticity of synapses in the mammalian brain predicted from the model was lacking. In 1966, Lomo found that brief, high-frequency electric stimulation of the perforant path fibers to the hippocampal DG caused a rapid and long-lasting increase in the strength of these synapses (Lomo 1966). This long-lasting strengthening of synapses and the response of a postsynaptic nerve cell to stimulation is called long-term potentiation (LTP) (Bliss and Lomo 1973). By contrast, prolonged, low-frequency electric stimulation of the Schaffer collateral to the hippocampal CA1 caused long-lasting decrease in the strength of these synapses (Dudek and Bear 1992). This long-lasting weakening of synapses and the response of a postsynaptic nerve cell to stimulation called long-term depression (LTD). This LTP/LTD-mediated synaptic plasticity is a prevailing cellular model for learning and memory.

#### 28.3.1.4 Optogenetic Tagging for In Vivo Electrophysiology

In vivo electrophysiology in behaving animals is useful to investigate the behavioral correlates of

the activity patterns of individual neurons. The combination of optogenetics and in vivo electrophysiology with single-unit recording has emerged as a versatile method for identifying specific neuronal populations within blind extracellular recordings in behaving animals by expressing ChR2 in a specific neuronal population and inferring the light-responsive cell population from its reaction to the stimulus, referred to as "optogenetic tagging" (Fig. 28.1c[ii]) (Cohen et al. 2012). By combining transgenic mice expressing Cre recombinase under the control of cell-specific promoter and in vivo electrophysiology, Cohen et al. labeled dopaminergic and GABAergic neurons in ventral tegmental area with ChR2, and then identified their cell types based on their responses to optical stimulation during in vivo single-unit recording (Cohen et al. 2012). Ciocchi et al. combined optogenetic tagging with optogenetic terminal stimulation of light-responsive cells and found that the ventral CA1 routes anxiety-related information preferentially to the prefrontal cortex and goal-related information preferentially to the nucleus accumbens (Ciocchi et al. 2015). Tanaka et al. applied optogenetic tagging combined with activity-dependent cell labeling to examine the electrophysiological profile of memory engram cells in hippocampal CA1 (Tanaka et al. 2018). These studies demonstrated cell-type-specific single-unit electrophysiological recording by optogenetic in behaving animals.

### 28.3.2 Neural Circuits for Temporal Association Memory

Remembering the timing of distinct events and associating temporally discontinuous events are crucial processes for the formation of episodic memories. We refer to this aspect of memory encoding as temporal association learning to engage a diverse set of temporally segregated information as an episode. Great progress in our understanding of temporal association learning has been made by using classical Pavlovian conditioning (Solomon et al. 1986; Maren 2001). In animal studies, a trace fear-conditioning paradigm has been widely used to assess the associative learning of temporally discontinuous events (Solomon et al. 1986; Moyer et al. 1990; McEchron et al. 1998; Suh et al. 2011). The training session of classical trace fear conditioning (TFC) consists of a 20-s tone as conditioned stimulus (CS) followed by a 20-s delay, after which a foot shock as unconditioned stimulus (US) is delivered to the animal subject. In test sessions, the extent of association of two experiences, CS and a shock, was assessed by duration of freezing after delivery of the tone without shock. A number of studies with lesions as well as pharmacological and genetic manipulations showed that the EC-HPC network is necessary for establishing CS–US associations across the temporal gap (Solomon et al. 1986; Moyer et al. 1990; McEchron et al. 1998; Hasselmo and Stern 2006; Kitamura et al. 2015a; Kitamura 2017). Suh et al. examined the roles of the EC3-CA1 direct pathway for bridging two events across the temporal gap by using mutant mice in which glutamatergic synaptic transmission from EC3 cells to CA1 pyramidal cells is blocked by tetanus toxin (TeTX) (Suh et al. 2011). They found that the mutant mice showed deficits in association of temporally discontinuous events in TFC, but they associated concurrently experienced events. On the other hand, inhibition of the CA3-CA1 pathway with TeTX did not affect TFC. In 2014, Kitamura et al. optogenetically manipulated the direct pathway from EC3 to CA1 during TFC. They found that optogenetic inhibition of the pathway during conditioning (tone+trace+shock) caused deficits in TFC, while optogenetic activation of the direct pathway from EC3 to CA1 by ChR2 stimulation enhanced TFC, indicating that the EC3 to CA1 direct pathway during TFC is crucial for driving temporal association learning (Kitamura et al. 2014).

Like most cognitive and motor phenomena, temporal association should be regulated for optimal adaptive benefit in animals. In 2014, Kitamura et al. discovered a novel excitatory input from $Wfs1^{+}$ cells in EC2 to GABAergic neurons in SL which gates excitatory EC3 input onto CA1 pyramidal cells (Kitamura et al. 2014)

as mentioned above (Sect. 28.2). They examined the role of the excitatory input from Wfs1$^+$ cells in EC2 into CA1 on TFC and found that optogenetic terminal activation of EC2 input in CA1 during the entire training period and the delay plus foot-shock period inhibited TFC, whereas activation of the same pathway during only CS period had no effect (Kitamura et al. 2014). On the other hand, optogenetic terminal inhibition of EC2 input in CA1 during TFC enhanced TFC. Optogenetic light activation/inactivation with temporal control identified the functional role of two direct glutamatergic inputs from EC to CA1 for specific moment during temporal association learning.

### 28.3.3 Neural Circuits and Neural Process for Memory Consolidation

Memory consolidation is a process by which a newly acquired memory is transformed into a more long-lasting stable state (Box 28.1) (Lechner et al. 1999). Memories are thought to be initially stored within the EC-HPC network (recent memory) and, over time, slowly consolidated within the neocortex for permanent storage (remote memory) (Marr 1971; Squire 1986; Kim et al. 1993). This process is known as systems consolidation of memory. Several theories have attempted to explain the neurobiological mechanisms that underlie consolidation of episodic memories. The Standard Consolidation Theory (SCT) argues that newly acquired episodic memories are initially stored in the HPC and are then transferred to the cortex for long-term storage (Squire 1986). While there is much evidence to support SCT, comparably strong evidence refutes SCT (Squire 1992; Nadel and Moscovitch 1997; Bayley et al. 2005). These inconsistencies have led to the Multiple Trace Theory (MTT). Unlike SCT, MTT argues that the HPC is always required for the recall of episodic memory that initially required the HPC for the formation. Furthermore, memory stored in the neocortex might be important for the recall of generalized semantic memory, whereas memory stored in the HPC might be important for the recall of detailed memory (Nadel and Moscovitch 1997). A possible mechanism that can explain these results is that there are memory traces in both the HPC and neocortex and that either trace can be used for memory recall depending on an individual's situation and condition (Kitamura and Inokuchi 2014; Tonegawa et al. 2018; Terranova et al. 2019). Goshen et al. showed that the acute optogenetic inhibition of the hippocampal CA1 neurons timed to the onset of recall impaired the recall of CFC in both recent and remote memory tests, whereas pharmacological hippocampal inhibition (tested 30 min after drug infusion) or prolonged optogenetic inhibition before and during memory recall impaired only recent memory recall (Goshen et al. 2011). These results could be explained if memory traces coexist in both the hippocampus and neocortex and that either memory trace can be used for memory recall depending on the animal's situation and condition during recall. By using activity-dependent cell labeling with ChR2 to identify memory engram cells as mentioned above (Sect. 28.3.1.2), Kitamura et al. examined the existence of memory engrams in the HPC and medial prefrontal cortex (mPFC) at recent and remote time points after CFC (Kitamura et al. 2017). They identified that mPFC engram cells are rapidly generated during the acquisition phase of contextual fear conditioning, however, mPFC engram cells are not reactivated during recent memory recall and are not necessary for the recall of recent memory. The memory engram cells in this state are referred to as silent engrams (Tonegawa et al. 2018; Terranova et al. 2019). After contextual fear conditioning, the mPFC silent engram cells mature over time with support from HPC engram cells. On the other hand, HPC engram cells rapidly generate as active state, which is reactivated during memory recall and necessary for memory recall. However, HPC engram cells gradually become "silent," such that they can be only reactivated by artificial optogenetic stimuli but not by using natural recall cues. These data provide new evidence for a unified theory of memory consolidation between SCT and MTT. In summary, the systems consolidation process consists

of two major steps: generation of silent memory engram in the PFC during learning and following functional maturation of the memory engram network by inputs from engram cells in EC-HPC network lasting a couple of weeks (Kitamura et al. 2017; Tonegawa et al. 2018; Terranova et al. 2019). However, even at remote time points, HPC engram cells still exist but in a silent state. These recent studies with optogenetic neural activation in engram cells revealed that responsible neural circuits and their engrams for a specific memory are functionally organized during the systems consolidation process.

Accumulating physiological evidence has suggested that high-frequency field oscillations, referred to as sharp-waves ripples (SWR), which are spontaneously observed in the hippocampal CA1 during slow-wave sleep and immobile quiet awake state, may contribute to the memory consolidation process (O'Keefe 1976; Buzsáki et al. 1983, 1992). Discovery of the sequential reactivation of the firing sequences that represents recently acquired memory during sleep SWR events in hippocampal CA1 further supports the idea (Wilson and McNaughton 1994; Skaggs and McNaughton 1996; Karlsson and Frank 2009). Several groups examined the role of SWR on memory consolidation and found that the disruption of SWR with electric stimulation showed the causal behavioral relevance of hippocampal SWR on the stabilization of recently acquired memory (Girardeau et al. 2009; Ego-Stengel and Wilson 2010; Jadhav et al. 2012). Nakashiba et al. also tested the effect of the inhibition of CA3 to CA1 output with TeTX (Nakashiba et al. 2009). Although the chronic blockade of CA3 output with TeTX did not alter the number of SWR events, the blockade reduced the intrinsic frequency of SWR in CA1 and impaired the remote memory formation of CFC (Nakashiba et al. 2009). However, two recent studies applied optogenetics to acutely inactivate the CA3 to CA1 pathway to reexamine the role of the tri-synaptic pathway on SWRs. An acute optogenetic silencing of CA3 terminals in CA1 drastically suppresses SWR incidence in both awake and sleep state in mice and rats (Yamamoto and Tonegawa 2017; Davoudi and Foster 2019), suggesting that the compensatory changes by prolonged suppression with TeTX underscored the importance of CA3 output on the generation of SWRs. The real-time optogenetic manipulation triggered by SWR occurrence in behaving animals and acute brain slices further showed that hippocampal SWRs in quiet awake and slow-wave states stabilize newly learned memory by downregulation of unrelated synaptic weight (Fig. 28.1b) (Norimoto et al. 2018). These studies indicate that hippocampal SWRs are crucial for memory consolidation and may contribute to the generation and maturation of PFC engram cells as well as silencing hippocampal engram cells for the formation of neocortical remote memory.

## 28.4 Conclusion

In this chapter, we have reviewed recent updates about neural circuit mechanisms of episodic memory revealed by cell-type-specific optogenetic approach. Reelin$^{+}$ cells in EC2 drive contextual information to HPC, and contextual memory is formed in EC2-DG-CA3 circuits (Fig. 28.2). During CFC, subpopulations of DG granule cells are activated as memory engrams and the activated cells during CFC are necessary and sufficient for recall of a CFC memory. However, after EC2-DG-CA3 circuits deliver processed contextual memory information to hippocampal CA1 pyramidal cells, two distinct neural pathways (CA1–dSub–EC5 pathway or CA1–EC5 pathway) to basolateral amygdala are differentially involved in the formation or recall of contextual fear memory. While memory engram cells are rapidly generated after CFC, memory engram cells are also formed in mPFC, but they are not responsible for memory recall by natural recall cues. Rather, mPFC engram cells gradually mature with time to form remote CFC memories. On the other hand, the tri-synaptic pathway is dispensable for temporal association learning. The direct pathway from EC3 to CA1 is necessary for TFC, and other direct pathway from Wfs1$^{+}$ cells in EC2 into CA1 inhibits TFC by the suppression of the EC3 input into the CA1 pyramidal

cells through feed-forward inhibition. These studies suggest that each subregion and projection in the EC-HPC networks may have distinct functional roles in the formation, recall, and consolidation of episodic memory. As a technical development, millisecond–timescale control of neural stimulation by optogenetics has facilitated (a) identification of synaptic connectivity between targeted paired of neurons, (b) cell-type-specific single-unit electrophysiological recording, (c) identification of memory engram cells, and (d) artificial induction and modification of synaptic plasticity in targeted synapses.

While optogenetics has significantly advanced the field of neurobiology of learning and memory, there are several issues which need to be improved. For example, excitation of ChR2 in high-expressing neurons triggers firing with relatively high reliability, whereas low-expressing neurons need longer exposure of blue light to acquire reliable neuronal firing, and that longer exposure can result in phototoxicity (Wade et al. 1988; Lin 2011; Kravitz and Kreitzer 2011; Yizhar et al. 2011; Owen et al. 2019). However, high levels of opsin expression have been also linked to neuronal defects and toxicity (Zimmermann et al. 2008; Zhao et al. 2008; Lin 2011; Yizhar et al. 2011; Miyashita et al. 2013). Another issue is a misidentification error due to the variety of spike latency between directly excited cells and indirectly excited cells (Kravitz et al. 2013). It might be difficult to separate direct or indirect light-responsive cells by latency parameter criteria in combination with use of in vivo electrophysiology (Kravitz et al. 2013; Buzsáki et al. 2015). The silencing of neural activities also suffers from the same technical issue due to the reduction of firing rate of their connected partners (Senzai and Buzsáki 2017). Another issue is the production of heat with light illumination. Because optogenetic inactivation needs to continuously illuminate green light to inhibit neuronal activity, the light that is emitted from the optical fibers can cause heating. In fact, Owen et al. showed that neural firing rates were reduced by continuous illumination in correlation with the extent of temperature increase (Owen et al. 2019). Importantly, they showed that continuous illumination without expression of opsin affected animal behavior as well as neural firing rates. Thus, it is crucial to consider light-delivery parameters without the expression of opsins.

Nevertheless, optogenetic approaches have been significantly advancing day by day. For example, an activity-dependent cell labeling technique with doxycycline control, which was mentioned above in Sect. 28.3.1.2., has low temporal resolution (a couple of days) to label activated cells due to the control by doxycycline diet. However, newly developed technologies enable the labeling neurons with increasing intracellular calcium concentration by the delivery of blue light (Lee et al. 2017; Moeyaert et al. 2018), which would produce higher temporal resolution for labeling cells activated during a specific moment. Although their sensitivity and stability should be tested in vivo, the development of these light- and activity-dependent cell labeling techniques will enable us to examine neural mechanisms of the formation, recall, and consolidation of episodic memory with higher spatial–temporal resolution.

**Acknowledgments** This work was supported by grants from Endowed Scholar Program to T.K., Human Frontier Science Program to T.K. (RGY0072/2018), Brain Research Foundation to T.K. (BRFSG-2018-04), Faculty Science and Technology Acquisition and Retention Program to T.K., the Brain & Behavior Research Foundation to T.K. (26391), The Whitehall Foundation to T.K. (2019-05-38), National Institute of Mental Health to T.K. (R01MH120134), and W.D.M. (T32MH076690-10), and Japan Society for the Promotion of Science to N.Y. (201860573).

## References

Abdou K, Shehata M, Choko K et al (2018) Synapse-specific representation of the identity of overlapping memory engrams. Science 360:1227–1231. https://doi.org/10.1126/science.aat3810

Allen TA, Salz DM, McKenzie S, Fortin NJ (2016) Nonspatial sequence coding in CA1 neurons. J Neurosci 36:1547–1563. https://doi.org/10.1523/JNEUROSCI.2874-15.2016

Allsop SA, Vander Weele CM, Wichmann R, Tye KM (2014) Optogenetic insights on the relationship between anxiety-related behaviors and social deficits.

Front Behav Neurosci 8:241. https://doi.org/10.3389/fnbeh.2014.00241

Amaral DG, Witter MP (1989) The three-dimensional organization of the hippocampal formation: a review of anatomical data. Neuroscience 31:571–591. https://doi.org/10.1016/0306-4522(89)90424-7

Andersen P, Holmqvist B, Voorhoeve PE (1966) Entorhinal activation of dentate granule cells. Acta Physiol Scand 66:448–460. https://doi.org/10.1111/j.1748-1716.1966.tb03223.x

Aronov D, Nevers R, Tank DW (2017) Mapping of a non-spatial dimension by the hippocampal–entorhinal circuit. Nature 543:719–722. https://doi.org/10.1038/nature21692

Basu J, Zaremba JD, Cheung SK et al (2016) Gating of hippocampal activity, plasticity, and memory by entorhinal cortex long-range inhibition. Science 351:aaa5694. https://doi.org/10.1126/science.aaa5694

Bayley PJ, Gold JJ, Hopkins RO, Squire LR (2005) The neuroanatomy of remote memory. Neuron 46:799–810. https://doi.org/10.1016/j.neuron.2005.04.034

Bliss TV, Lomo T (1973) Long-lasting potentiation of synaptic transmission in the dentate area of the anaesthetized rabbit following stimulation of the perforant path. J Physiol Lond 232:331–356. https://doi.org/10.1113/jphysiol.1973.sp010273

Boyden ES, Zhang F, Bamberg E et al (2005) Millisecond-timescale, genetically targeted optical control of neural activity. Nat Neurosci 8:1263–1268. https://doi.org/10.1038/nn1525

Buzsáki G, Leung LW, Vanderwolf CH (1983) Cellular bases of hippocampal EEG in the behaving rat. Brain Res 287:139–171. https://doi.org/10.1016/0165-0173(83)90037-1

Buzsáki G, Horvath Z, Urioste R et al (1992) High-frequency network oscillation in the hippocampus. Science 256:1025–1027. https://doi.org/10.1126/science.1589772

Buzsáki G, Stark E, Berényi A et al (2015) Tools for probing local circuits: high-density silicon probes combined with optogenetics. Neuron 86:92–105. https://doi.org/10.1016/j.neuron.2015.01.028

Cardin JA, Carlén M, Meletis K et al (2010) Targeted optogenetic stimulation and recording of neurons in vivo using cell-type-specific expression of Channelrhodopsin-2. Nat Protoc 5:247–254. https://doi.org/10.1038/nprot.2009.228

Chatterjee S, Sullivan HA, MacLennan BJ et al (2018) Nontoxic, double-deletion-mutant rabies viral vectors for retrograde targeting of projection neurons. Nat Neurosci 21:638–646. https://doi.org/10.1038/s41593-018-0091-7

Chevaleyre V, Siegelbaum SA (2010) Strong CA2 pyramidal neuron synapses define a powerful disynaptic cortico-hippocampal loop. Neuron 66:560–572. https://doi.org/10.1016/j.neuron.2010.04.013

Chow BY, Han X, Dobry AS et al (2010) High-performance genetically targetable optical neural silencing by light-driven proton pumps. Nature 463:98–102. https://doi.org/10.1038/nature08652

Ciocchi S, Passecker J, Malagon-Vina H et al (2015) Brain computation. Selective information routing by ventral hippocampal CA1 projection neurons. Science 348:560–563. https://doi.org/10.1126/science.aaa3245

Cohen JY, Haesler S, Vong L et al (2012) Neuron-type-specific signals for reward and punishment in the ventral tegmental area. Nature 482:85–88. https://doi.org/10.1038/nature10754

Cowansage KK, Shuman T, Dillingham BC et al (2014) Direct reactivation of a coherent neocortical memory of context. Neuron 84:432–441. https://doi.org/10.1016/j.neuron.2014.09.022

Davoudi H, Foster DJ (2019) Acute silencing of hippocampal CA3 reveals a dominant role in place field responses. Nat Neurosci 22:337–342. https://doi.org/10.1038/s41593-018-0321-z

Ding SL (2013) Comparative anatomy of the prosubiculum, subiculum, presubiculum, postsubiculum, and parasubiculum in human, monkey, and rodent. J Comp Neurol 521:4145–4162. https://doi.org/10.1002/cne.23416

Dudchenko PA, Wood ER, Eichenbaum H (2000) Neurotoxic hippocampal lesions have no effect on odor span and little effect on odor recognition memory but produce significant impairments on spatial span, recognition, and alternation. J Neurosci 20:2964–2977. https://doi.org/10.1523/JNEUROSCI.20-08-02964.2000

Dudek SM, Bear MF (1992) Homosynaptic long-term depression in area CA1 of hippocampus and effects of N-methyl-D-aspartate receptor blockade. Proc Natl Acad Sci U S A 89:4363–4367. https://doi.org/10.1073/pnas.89.10.4363

Ego-Stengel V, Wilson MA (2010) Disruption of ripple-associated hippocampal activity during rest impairs spatial learning in the rat. Hippocampus 20:1–10. https://doi.org/10.1002/hipo.20707

Eichenbaum H (2000) A cortical-hippocampal system for declarative memory. Nat Rev Neurosci 1:41–50. https://doi.org/10.1038/35036213

Eldridge LL, Engel SA, Zeineh MM et al (2005) A dissociation of encoding and retrieval processes in the human hippocampus. J Neurosci 25:3280–3286. https://doi.org/10.1523/JNEUROSCI.3420-04.2005

Empson RM, Heinemann U (1995) Perforant path connections to area CA1 are predominantly inhibitory in the rat hippocampal-entorhinal cortex combined slice preparation. Hippocampus 5:104–107. https://doi.org/10.1002/hipo.450050203

Fortin NJ, Agster KL, Eichenbaum HB (2002) Critical role of the hippocampus in memory for sequences of events. Nat Neurosci 5:458–462. https://doi.org/10.1038/nn834

Frankland PW, Bontempi B (2005) The organization of recent and remote memories. Nat Rev Neurosci 6:119–130. https://doi.org/10.1038/nrn1607

Frankland PW, Cestari V, Filipkowski RK et al (1998) The dorsal hippocampus is essential for context

discrimination but not for contextual conditioning. Behav Neurosci 112:863–874. https://doi.org/10.1037//0735-7044.112.4.863

Gabrieli JD, Brewer JB, Desmond JE, Glover GH (1997) Separate neural bases of two fundamental memory processes in the human medial temporal lobe. Science 276:264–266. https://doi.org/10.1126/science.276.5310.264

Gilbert PE, Kesner RP, Lee I (2001) Dissociating hippocampal subregions: a double dissociation between dentate gyrus and CA1. Hippocampus 11:626–636. https://doi.org/10.1002/hipo.1077

Girardeau G, Benchenane K, Wiener SI et al (2009) Selective suppression of hippocampal ripples impairs spatial memory. Nat Neurosci 12:1222–1223. https://doi.org/10.1038/nn.2384

Goshen I, Brodsky M, Prakash R et al (2011) Dynamics of retrieval strategies for remote memories. Cell 147:678–689. https://doi.org/10.1016/j.cell.2011.09.033

Han J-H, Kushner SA, Yiu AP et al (2007) Neuronal competition and selection during memory formation. Science 316:457–460. https://doi.org/10.1126/science.1139438

Han J-H, Kushner SA, Yiu AP et al (2009) Selective erasure of a fear memory. Science 323:1492–1496. https://doi.org/10.1126/science.1164139

Han X, Chow BY, Zhou H et al (2011) A high-light sensitivity optical neural silencer: development and application to optogenetic control of non-human primate cortex. Front Syst Neurosci 5:18. https://doi.org/10.3389/fnsys.2011.00018

Hashimotodani Y, Nasrallah K, Jensen KR et al (2017) LTP at Hilar Mossy cell-dentate granule cell synapses modulates dentate gyrus output by increasing excitation/inhibition balance. Neuron 95:928–943.e3. https://doi.org/10.1016/j.neuron.2017.07.028

Hasselmo ME, Stern CE (2006) Mechanisms underlying working memory for novel information. Trends Cogn Sci (Regul Ed) 10:487–493. https://doi.org/10.1016/j.tics.2006.09.005

Hebb DO (1949) The organization of behavior. 1–365

Jadhav SP, Kemere C, German PW, Frank LM (2012) Awake hippocampal sharp-wave ripples support spatial memory. Science 336:1454–1458. https://doi.org/10.1126/science.1217230

Jones MW, McHugh TJ (2011) Updating hippocampal representations: CA2 joins the circuit. Trends Neurosci 34:526–535. https://doi.org/10.1016/j.tins.2011.07.007

Josselyn SA (2010) Continuing the search for the engram: examining the mechanism of fear memories. J Psychiatry Neurosci 35:221–228. https://doi.org/10.1503/jpn.100015

Karlsson MP, Frank LM (2009) Awake replay of remote experiences in the hippocampus. Nat Neurosci 12:913–918. https://doi.org/10.1038/nn.2344

Kim JJ, Fanselow MS (1992) Modality-specific retrograde amnesia of fear. Science 256:675–677. https://doi.org/10.1126/science.1585183

Kim JJ, Rison RA, Fanselow MS (1993) Effects of amygdala, hippocampus, and periaqueductal gray lesions on short- and long-term contextual fear. Behav Neurosci 107:1093–1098. https://doi.org/10.1037//0735-7044.107.6.1093

Kitamura T (2017) Driving and regulating temporal association learning coordinated by entorhinal-hippocampal network. Neurosci Res 121:1–6. https://doi.org/10.1016/j.neures.2017.04.005

Kitamura T, Inokuchi K (2014) Role of adult neurogenesis in hippocampal-cortical memory consolidation. Molecul Brain 7:13. https://doi.org/10.1186/1756-6606-7-13

Kitamura T, Pignatelli M, Suh J et al (2014) Island cells control temporal association memory. Science 343:896–901. https://doi.org/10.1126/science.1244634

Kitamura T, MacDonald CJ, Tonegawa S (2015a) Entorhinal-hippocampal neuronal circuits bridge temporally discontiguous events. Learn Mem 22:438–443. https://doi.org/10.1101/lm.038687.115

Kitamura T, Sun C, Martin J et al (2015b) Entorhinal cortical ocean cells encode specific contexts and drive context-specific fear memory. Neuron 87:1317–1331. https://doi.org/10.1016/j.neuron.2015.08.036

Kitamura T, Ogawa SK, Roy DS et al (2017) Engrams and circuits crucial for systems consolidation of a memory. Science 356:73–78. https://doi.org/10.1126/science.aam6808

Kohara K, Pignatelli M, Rivest AJ et al (2014) Cell type-specific genetic and optogenetic tools reveal hippocampal CA2 circuits. Nat Neurosci 17:269–279. https://doi.org/10.1038/nn.3614

Kravitz AV, Kreitzer AC (2011) Optogenetic manipulation of neural circuitry in vivo. Curr Opin Neurobiol 21:433–439. https://doi.org/10.1016/j.conb.2011.02.010

Kravitz AV, Owen SF, Kreitzer AC (2013) Optogenetic identification of striatal projection neuron subtypes during in vivo recordings. Brain Res 1511:21–32. https://doi.org/10.1016/j.brainres.2012.11.018

Leão RN, Mikulovic S, Leão KE et al (2012) OLM interneurons differentially modulate CA3 and entorhinal inputs to hippocampal CA1 neurons. Nat Neurosci 15:1524–1530. https://doi.org/10.1038/nn.3235

Lechner HA, Squire LR, Byrne JH (1999) 100 Years of consolidation—remembering Muller and Pilzecker. Learn Mem 6:77–87

Lee D, Hyun JH, Jung K et al (2017) A calcium- and light-gated switch to induce gene expression in activated neurons. Nat Biotechnol 35:858–863. https://doi.org/10.1038/nbt.3902

Leutgeb S, Leutgeb JK, Treves A et al (2004) Distinct ensemble codes in hippocampal areas CA3 and CA1. Science 305:1295–1298. https://doi.org/10.1126/science.1100265

Leutgeb JK, Leutgeb S, Moser M-B, Moser EI (2007) Pattern separation in the dentate gyrus and CA3 of the hippocampus. Science 315:961–966. https://doi.org/10.1126/science.1135801

Lin JY (2011) A user's guide to channelrhodopsin variants: features, limitations and future developments. Exp Physiol 96:19–25. https://doi.org/10.1113/expphysiol.2009.051961

Lin JY, Lin MZ, Steinbach P, Tsien RY (2009) Characterization of engineered channelrhodopsin variants with improved properties and kinetics. Biophys J 96:1803–1814. https://doi.org/10.1016/j.bpj.2008.11.034

Lin JY, Knutsen PM, Muller A et al (2013) ReaChR: a red-shifted variant of channelrhodopsin enables deep transcranial optogenetic excitation. Nat Neurosci 16:1499–1508. https://doi.org/10.1038/nn.3502

Liu X, Ramirez S, Pang PT et al (2012) Optogenetic stimulation of a hippocampal engram activates fear memory recall. Nature 484:381–385. https://doi.org/10.1038/nature11028

Lomo T (1966) Frequency potentiation of excitatory synaptic activity in dentate area of hippocampal formation. Blackwell Science Ltd, Oxford, England, p 128

MacDonald CJ, Lepage KQ, Eden UT, Eichenbaum H (2011) Hippocampal "time cells" bridge the gap in memory for discontiguous events. Neuron 71:737–749. https://doi.org/10.1016/j.neuron.2011.07.012

MacDonald CJ, Carrow S, Place R, Eichenbaum H (2013) Distinct hippocampal time cell sequences represent odor memories in immobilized rats. J Neurosci 33:14607–14616. https://doi.org/10.1523/JNEUROSCI.1537-13.2013

Maren S (2001) Neurobiology of Pavlovian fear conditioning. Annu Rev Neurosci 24:897–931. https://doi.org/10.1146/annurev.neuro.24.1.897

Maren S, Phan KL, Liberzon I (2013) The contextual brain: implications for fear conditioning, extinction and psychopathology. Nat Rev Neurosci 14:417–428. https://doi.org/10.1038/nrn3492

Marr D (1971) Simple memory: a theory for archicortex. Philos Trans R Soc Lond Ser B Biol Sci 262:23–81

Masurkar AV, Srinivas KV, Brann DH et al (2017) Medial and lateral entorhinal cortex differentially excite deep versus superficial CA1 pyramidal neurons. Cell Rep 18:148–160. https://doi.org/10.1016/j.celrep.2016.12.012

McEchron MD, Bouwmeester H, Tseng W et al (1998) Hippocampectomy disrupts auditory trace fear conditioning and contextual fear conditioning in the rat. Hippocampus 8:638–646. https://doi.org/10.1002/(SICI)1098-1063(1998)8:6<638::AID-HIPO6>3.0.CO;2-Q

McHugh TJ, Jones MW, Quinn JJ et al (2007) Dentate gyrus NMDA receptors mediate rapid pattern separation in the hippocampal network. Science 317:94–99. https://doi.org/10.1126/science.1140263

McNaughton BL, Barnes CA (1977) Physiological identification and analysis of dentate granule cell responses to stimulation of the medial and lateral perforant pathways in the rat. J Comp Neurol 175:439–454. https://doi.org/10.1002/cne.901750404

McNaughton BL, Morris RGM (1987) Hippocampal synaptic enhancement and information storage within a distributed memory system. Trends Neurosci 10:408–415. https://doi.org/10.1016/0166-2236(87)90011-7

Miyashita T, Shao R, Chung J et al (2013) Long-term channelrhodopsin-2 (ChR2) expression can induce abnormal axonal morphology and targeting in cerebral cortex. Front Neural Circuits 7:8. https://doi.org/10.3389/fncir.2013.00008

Moeyaert B, Holt G, Madangopal R et al (2018) Improved methods for marking active neuron populations. Nat Commun 9:4440. https://doi.org/10.1038/s41467-018-06935-2

Morris RGM, Schenk F, Tweedie F, Jarrard LE (1990) Ibotenate lesions of hippocampus and/or subiculum: dissociating components of allocentric spatial learning. Eur J Neurosci 2:1016–1028. https://doi.org/10.1111/j.1460-9568.1990.tb00014.x

Moser EI, Kropff E, Moser M-B (2008) Place cells, grid cells, and the brain's spatial representation system. Annu Rev Neurosci 31:69–89. https://doi.org/10.1146/annurev.neuro.31.061307.090723

Moyer JR, Deyo RA, Disterhoft JF (1990) Hippocampectomy disrupts trace eye-blink conditioning in rabbits. Behav Neurosci 104:243–252. https://doi.org/10.1037/0735-7044.104.2.243

Nabavi S, Fox R, Proulx CD et al (2014) Engineering a memory with LTD and LTP. Nature 511:348–352. https://doi.org/10.1038/nature13294

Nadel L, Moscovitch M (1997) Memory consolidation, retrograde amnesia and the hippocampal complex. Curr Opin Neurobiol 7:217–227. https://doi.org/10.1016/s0959-4388(97)80010-4

Nakashiba T, Young JZ, McHugh TJ et al (2008) Transgenic inhibition of synaptic transmission reveals role of CA3 output in hippocampal learning. Science 319:1260–1264. https://doi.org/10.1126/science.1151120

Nakashiba T, Buhl DL, McHugh TJ, Tonegawa S (2009) Hippocampal CA3 output is crucial for ripple-associated reactivation and consolidation of memory. Neuron 62:781–787. https://doi.org/10.1016/j.neuron.2009.05.013

Nakazawa K, Sun LD, Quirk MC et al (2003) Hippocampal CA3 NMDA receptors are crucial for memory acquisition of one-time experience. Neuron 38:305–315. https://doi.org/10.1016/S0896-6273(03)00165-X

Naya Y, Suzuki WA (2011) Integrating what and when across the primate medial temporal lobe. Science 333:773–776. https://doi.org/10.1126/science.1206773

Norimoto H, Makino K, Gao M et al (2018) Hippocampal ripples down-regulate synapses. Science 359:1524–1527. https://doi.org/10.1126/science.aao0702

Ohkawa N, Saitoh Y, Suzuki A et al (2015) Artificial association of pre-stored information to generate a qualitatively new memory. Cell Rep 11:261–269. https://doi.org/10.1016/j.celrep.2015.03.017

O'Keefe J (1976) Place units in the hippocampus of the freely moving rat. Exp Neurol 51:78–109. https://doi.org/10.1016/0014-4886(76)90055-8

Okuyama T, Kitamura T, Roy DS et al (2016) Ventral CA1 neurons store social memory. Science 353:1536–1541. https://doi.org/10.1126/science.aaf7003

O'Reilly RC, McClelland JL (1994) Hippocampal conjunctive encoding, storage, and recall: Avoiding a trade-off. Hippocampus 4:661–682. https://doi.org/10.1002/hipo.450040605

Owen SF, Liu MH, Kreitzer AC (2019) Thermal constraints on in vivo optogenetic manipulations. Nat Neurosci 22:1061–1065. https://doi.org/10.1038/s41593-019-0422-3

Pavlov IP (1927) Conditioned reflexes: an investigation of the physiological activity of the cerebral cortex. Oxford University Press, Oxford, England

Petreanu L, Huber D, Sobczyk A, Svoboda K (2007) Channelrhodopsin-2-assisted circuit mapping of long-range callosal projections. Nat Neurosci 10:663–668

Phillips RG, LeDoux JE (1992) Differential contribution of amygdala and hippocampus to cued and contextual fear conditioning. Behav Neurosci 106:274–285. https://doi.org/10.1037//0735-7044.106.2.274

Ramirez S, Liu X, Lin P-A et al (2013) Creating a false memory in the hippocampus. Science 341:387–391. https://doi.org/10.1126/science.1239073

Redondo RL, Kim J, Arons AL et al (2014) Bidirectional switch of the valence associated with a hippocampal contextual memory engram. Nature 513:426–430. https://doi.org/10.1038/nature13725

Reijmers LG, Perkins BL, Matsuo N, Mayford M (2007) Localization of a stable neural correlate of associative memory. Science 317:1230–1233. https://doi.org/10.1126/science.1143839

Roy DS, Kitamura T, Okuyama T et al (2017) Distinct neural circuits for the formation and retrieval of episodic memories. Cell 170:1000–1012.e19. https://doi.org/10.1016/j.cell.2017.07.013

Ryan TJ, Roy DS, Pignatelli M et al (2015) Engram cells retain memory under retrograde amnesia. Science 348:1007–1013. https://doi.org/10.1126/science.aaa5542

Sakon JJ, Naya Y, Wirth S, Suzuki WA (2014) Context-dependent incremental timing cells in the primate hippocampus. Proc Natl Acad Sci U S A 111:18351–18356. https://doi.org/10.1073/pnas.1417827111

Scharfman HE (1995) Electrophysiological evidence that dentate hilar mossy cells are excitatory and innervate both granule cells and interneurons. J Neurophysiol 74:179–194. https://doi.org/10.1152/jn.1995.74.1.179

Scoville WB, Milner B (1957) Loss of recent memory after bilateral hippocampal lesions. J Neurol Neurosurg Psychiatry 20:11–21. https://doi.org/10.1136/jnnp.20.1.11

Semon RW (1904) Die Mneme als erhaltendes Prinzip im Wechsel des organischen Geschehens

Semon RW (1921) The Mneme

Senzai Y, Buzsáki G (2017) Physiological properties and behavioral correlates of hippocampal granule cells and mossy cells. Neuron 93:691–704.e5. https://doi.org/10.1016/j.neuron.2016.12.011

Skaggs WE, McNaughton BL (1996) Replay of neuronal firing sequences in rat hippocampus during sleep following spatial experience. Science 271:1870–1873. https://doi.org/10.1126/science.271.5257.1870

Smith DM, Bulkin DA (2014) The form and function of hippocampal context representations. Neurosci Biobehav Rev 40:52–61. https://doi.org/10.1016/j.neubiorev.2014.01.005

Sohal VS, Zhang F, Yizhar O, Deisseroth K (2009) Parvalbumin neurons and gamma rhythms enhance cortical circuit performance. Nature 459:698–702. https://doi.org/10.1038/nature07991

Solomon PR, Vander Schaaf ER, Thompson RF, Weisz DJ (1986) Hippocampus and trace conditioning of the rabbit's classically conditioned nictitating membrane response. Behav Neurosci 100:729–744. https://doi.org/10.1037/0735-7044.100.5.729

Spear NE (1973) Retrieval of memory in animals. Psychol Rev 80:163–194. https://doi.org/10.1037/h0034326

Squire LR (1986) Mechanisms of memory. Science 232:1612–1619. https://doi.org/10.1126/science.3086978

Squire LR (1992) Memory and the hippocampus: a synthesis from findings with rats, monkeys, and humans. Psychol Rev 99:195–231. https://doi.org/10.1037/0033-295X.99.2.195

Steward O, Scoville SA (1976) Cells of origin of entorhinal cortical afferents to the hippocampus and fascia dentata of the rat. J Comp Neurol 169:347–370. https://doi.org/10.1002/cne.901690306

Stuber GD, Sparta DR, Stamatakis AM et al (2011) Excitatory transmission from the amygdala to nucleus accumbens facilitates reward seeking. Nature 475:377–380. https://doi.org/10.1038/nature10194

Suh J, Rivest AJ, Nakashiba T et al (2011) Entorhinal cortex layer III input to the hippocampus is crucial for temporal association memory. Science 334:1415–1420. https://doi.org/10.1126/science.1210125

Sürmeli G, Marcu DC, McClure C et al (2015) Molecularly defined circuitry reveals input-output segregation in deep layers of the medial entorhinal cortex. Neuron 88:1040–1053. https://doi.org/10.1016/j.neuron.2015.10.041

Sutherland RJ, O'Brien J, Lehmann H (2008) Absence of systems consolidation of fear memories after dorsal,

ventral, or complete hippocampal damage. Hippocampus 18:710–718. https://doi.org/10.1002/hipo.20431
Tanaka KZ, He H, Tomar A et al (2018) The hippocampal engram maps experience but not place. Science 361:392–397. https://doi.org/10.1126/science.aat5397
Terranova JI, Ogawa SK, Kitamura T (2019) Adult hippocampal neurogenesis for systems consolidation of memory. Behav Brain Res 372:112035. https://doi.org/10.1016/j.bbr.2019.112035
Tervo DGR, Hwang B-Y, Viswanathan S et al (2016) A designer AAV variant permits efficient retrograde access to projection neurons. Neuron 92:372–382. https://doi.org/10.1016/j.neuron.2016.09.021
Tonegawa S, Liu X, Ramirez S, Redondo R (2015) Memory engram cells have come of age. Neuron 87:918–931. https://doi.org/10.1016/j.neuron.2015.08.002
Tonegawa S, Morrissey MD, Kitamura T (2018) The role of engram cells in the systems consolidation of memory. Nat Rev Neurosci 19:485–498. https://doi.org/10.1038/s41583-018-0031-2
Treves A, Rolls ET (1994) Computational analysis of the role of the hippocampus in memory. Hippocampus 4:374–391. https://doi.org/10.1002/hipo.450040319
Tulving E (2002) Episodic memory: from mind to brain. Annu Rev Psychol 53:1–25. https://doi.org/10.1146/annurev.psych.53.100901.135114
Tye KM, Prakash R, Kim S-Y et al (2011) Amygdala circuitry mediating reversible and bidirectional control of anxiety. Nature 471:358–362. https://doi.org/10.1038/nature09820
Wade PD, Taylor J, Siekevitz P (1988) Mammalian cerebral cortical tissue responds to low-intensity visible light. Proc Natl Acad Sci U S A 85:9322–9326. https://doi.org/10.1073/pnas.85.23.9322
Wickersham IR, Lyon DC, Barnard RJO et al (2007) Monosynaptic restriction of transsynaptic tracing from single, genetically targeted neurons. Neuron 53:639–647. https://doi.org/10.1016/j.neuron.2007.01.033
Wilson MA, McNaughton BL (1994) Reactivation of hippocampal ensemble memories during sleep. Science 265:676–679. https://doi.org/10.1126/science.8036517
Winocur G, Moscovitch M (2011) Memory transformation and systems consolidation. J Int Neuropsychol Soc 17:766–780. https://doi.org/10.1017/S1355617711000683
Winson J, Abzug C (1977) Gating of neuronal transmission in the hippocampus: efficacy of transmission varies with behavioral state. Science 196:1223–1225. https://doi.org/10.1126/science.193192
Witter MP, Wouterlood FG, Naber PA, Van Haeften T (2000) Anatomical organization of the parahippocampal-hippocampal network. Ann N Y Acad Sci 911:1–24. https://doi.org/10.1111/j.1749-6632.2000.tb06716.x
Yamamoto J, Tonegawa S (2017) Direct medial entorhinal cortex input to hippocampal Ca1 is crucial for extended quiet awake replay. Neuron 96:217–227.e4. https://doi.org/10.1016/j.neuron.2017.09.017
Yizhar O, Fenno LE, Davidson TJ et al (2011) Optogenetics in neural systems. Neuron 71:9–34. https://doi.org/10.1016/j.neuron.2011.06.004
Zhang F, Wang L-P, Boyden ES, Deisseroth K (2006) Channelrhodopsin-2 and optical control of excitable cells. Nat Methods 3:785–792. https://doi.org/10.1038/nmeth936
Zhang S-J, Ye J, Miao C et al (2013) Optogenetic dissection of entorhinal-hippocampal functional connectivity. Science 340:1232627. https://doi.org/10.1126/science.1232627
Zhao S, Cunha C, Zhang F et al (2008) Improved expression of halorhodopsin for light-induced silencing of neuronal activity. Brain Cell Biol 36:141–154. https://doi.org/10.1007/s11068-008-9034-7
Zimmermann D, Zhou A, Kiesel M et al (2008) Effects on capacitance by overexpression of membrane proteins. Biochem Biophys Res Commun 369:1022–1026. https://doi.org/10.1016/j.bbrc.2008.02.153
Zola-Morgan SM, Squire LR (1990) The primate hippocampal formation: evidence for a time-limited role in memory storage. Science 250:288–290. https://doi.org/10.1126/science.2218534

# Optogenetic Approach to Local Neuron Network Analysis of the Medullary Respiratory Center

29

Hiroshi Onimaru and Keiko Ikeda

**Abstract**

Using an optogenetic approach, we analyzed a local neuron network of the respiratory center in the medulla of a brainstem–spinal cord preparation isolated from neonatal rat. We developed a transgenic (Tg) rat line in which Phox2b-positive cells expressed archaerhodopsin-3 (Arch) or one of the step-function channelrhodopsin variants (ChRFR) under the control of Phox2b promoter-enhancer regions. Then, in en bloc preparations from 0- to 2-day-old Tg neonatal rats, we analyzed membrane potential changes of medullary respiratory-related neurons in response to photostimulation of the rostral ventral medulla. The photostimulation-induced inhibition or facilitation of the respiratory rhythm in Arch-expressing or ChRFR-expressing Tg rat preparations, respectively. Selective photoactivation of Phox2b-positive neurons expressing ChRFR in the rostral ventrolateral medulla of a neonatal rat en bloc preparation induced membrane potential changes of respiratory-related neurons that were dependent on heterogeneous properties of synaptic connections in the respiratory center. We concluded that the optogenetic approach is a powerful method of verifying a hypothetical model of local networks among respiratory-related neurons in the rostral ventrolateral medulla of neonatal rat.

**Keywords**

Phox2b · Parafacial respiratory group · Respiratory networks · Optogenetics · Transgenic rat · Medulla

## Abbreviations

| | |
|---|---|
| AICA | Anterior inferior cerebellar artery |
| Arch | Archaerhodopsin-3 |
| C4 | Fourth cervical ventral root |
| ChRFR | Step-function channelrhodopsin variants |
| Exp | Expiratory |
| EYFP | Enhanced yellow fluorescent protein |
| FN | Facial nucleus |
| Insp | Inspiratory |
| LED | Light-emitting diode |
| pFRG | Parafacial respiratory group |
| preBötC | preBötzinger complex |
| Pre-I | Preinspiratory |
| RTN | Retrotrapezoid nucleus |
| Tg | Transgenic |

H. Onimaru (✉)
Department of Physiology, Showa University School of Medicine, Tokyo, Japan
e-mail: oni@med.showa-u.ac.jp

K. Ikeda
Clinical Research Department, National Hospital Organization Murayama Medical Center, Tokyo, Japan
e-mail: ikeda-k@murayama-hosp.jp



H. Yawo et al. (eds.), *Optogenetics*, Advances in Experimental Medicine and Biology 1293,
https://doi.org/10.1007/978-981-15-8763-4_29

TH Tyrosine hydroxylase
TTX Tetrodotoxin

## 29.1 Introduction

Optogenetics provides a powerful tool in the neurophysiological analysis of respiratory control. We recently applied this method to local network analysis of the respiratory center in the medulla (Ikeda et al. 2019a, b). In this chapter, we summarize the basic strategy of the application of optogenetics together with findings from the respiratory neural network.

## 29.2 Respiratory Rhythm Generator, Phox2b, Chemoreceptors

The central pattern generator of respiration resides in the lower brainstem, and respiratory-related neurons in the ventral medulla play an important role in rhythm and pattern generation (Ballanyi et al. 1999; Ikeda et al. 2017; Onimaru et al. 1997). Respiratory-related neurons in a brainstem-spinal cord preparation from the newborn rat (see below) are divided basically into three subgroups: preinspiratory (Pre-I), inspiratory (Insp), and expiratory (Exp) neurons (Ballanyi et al. 1999; Onimaru et al. 1997). We have hypothesized that Pre-I neurons periodically trigger burst generation of Insp neurons to produce the basic respiratory rhythm in the newborn rat preparation (Onimaru et al. 1988; Onimaru and Homma 1987). The parafacial respiratory group (pFRG) composed predominantly of Pre-I neurons was identified initially by optical recordings of respiratory neuron activity in the rostral ventrolateral medulla (Onimaru and Homma 2003). The pFRG is a medullary cluster of respiratory-related neurons surrounding the facial motor nucleus and is one of the respiratory rhythm generators that function through its interaction with the pre-Bötzinger complex (preBötC) that locates in the more caudal ventrolateral medulla in the newborn rat (Ikeda et al. 2017; Mellen et al. 2003; Onimaru and Homma 2003; Smith et al. 1991). Anatomically, the pFRG overlaps at least partly with the retrotrapezoid nucleus (RTN), which has been characterized in adult mammals (Ellenberger and Feldman 1990; Guyenet et al. 2009; Onimaru and Homma 2003; Smith et al. 1989). Both the pFRG and RTN contain neuronal groups that express a transcription factor called Phox2b (Dubreuil et al. 2008; Onimaru et al. 2008; Stornetta et al. 2006).

The paired-like homeobox gene Phox2b encodes a transcription factor and is essential for the development of not only the peripheral autonomic nervous system and a subset of cranial nerves but also lower brainstem nuclei (Pattyn et al. 1997, 1999). Particularly, a substantial number of neurons in the pFRG/RTN of rodents express Phox2b (Dubreuil et al. 2008; Onimaru et al. 2008, 2012a, b; Stornetta et al. 2006). One of the highest densities of Phox2b-positive cell clusters is found at the level of the caudal end of the facial nucleus (caudal pFRG), in which Pre-I neurons show heterogeneous properties: some express Phox2b and exhibit $CO_2$ sensitivity in the presence of tetrodotoxin (TTX), and others are Phox2b negative and $CO_2$ insensitive (Onimaru et al. 2008). In contrast, most of the Pre-I neurons in the rostral pFRG express Phox2b and are intrinsically $CO_2$ sensitive (Onimaru et al. 2008, 2012a). We recently analyzed the activity of Phox2b-positive cells by calcium imaging with confocal laser microscopy in transgenic (Tg) rats in which Phox2b-positive cells expressed enhanced yellow fluorescent protein (EYFP) (Ikeda et al. 2015). We found that more than 60% of the EYFP/Phox2b-positive cells in the parafacial region showed Pre-I neuron-like rhythmic burst activity in neonatal rat (Onimaru et al. 2018). These data indicate that Phox2b-expressing cells in the pFRG/RTN are involved not only in central chemoreception but also in respiratory rhythm generation. Thus, Phox2b could be a key genetic marker of the pFRG/RTN neurons for optogenetic analysis.

## 29.3 Brainstem–Spinal Cord Preparation from Transgenic Rat

A brainstem–spinal cord preparation isolated from a neonatal rat (Suzue 1984) has been used for analyses of brainstem function including respiratory rhythm generation (Ballanyi et al. 1999; Onimaru et al. 1997) (Fig. 29.1). This en bloc preparation preserves more intact medullary neuron networks than those in the slice preparation. The optogenetic approach could be a powerful method for the analysis of detailed neural connections in the local circuit of the respiratory center. For this purpose, it is essential to analyze membrane potential changes of different types of respiratory-related neurons induced by selective photoactivation of Phox2b-positive cells in the rostral ventrolateral medulla, where the respiratory rhythm generation center resides. However, such analysis is hampered by technical difficulty in experiments using in vivo preparations. The brainstem–spinal cord preparation is most suitable for such detailed analysis of membrane potentials of various types of respiratory-related neurons.

Several optogenetic analyses have been conducted in in vivo preparations of adult rats in which genes of photosensitive ion channels (or pumps) were introduced by viral infection: e.g., inhibitory manipulation by archaerhodopsin (Basting et al. 2015; Wenker et al. 2017) and excitatory manipulation by channelrhodopsin-2- (Abbott et al. 2009; Kanbar et al. 2010; Malheiros-Lima et al. 2018). However, viral strategies have moderately specific targeting (Lawlor et al. 2009; Lee et al. 2010; Nathanson et al. 2009) and are not practical for intrauterine surgery to perform targeted injection of viruses to a specific fetal brain region (i.e., ventral medulla). Therefore, experiments in the in vitro newborn rat en bloc preparation that are useful during postnatal days 0–4 would be impossible. To overcome these limitations and apply optogenetics, we developed a Tg rat line in which Phox2b-positive cells expressed archaerhodopsin-3 (Arch) or one of the step-function channelrhodopsin variants (ChRFR) under the control of Phox2b promoter–enhancer regions (Igarashi et al. 2018) and used en bloc preparations from 0- to 2-day-old Tg neonatal rats.

## 29.4 Optogenetic Manipulation of Respiratory Rhythm

Photoactivation of Arch was performed by continuous photostimulation of the ventral medulla for up to 90 s using green laser light (532 nm, 10 mW/mm$^2$) (COME2-LG532/100-SA, Lucir Inc., Tsukuba, Japan) through an optic fiber with 1-mm outer diameter. For this experiment, the right half of the pFRG was removed (Fig. 29.1a) because previous studies have shown that the unilateral pFRG was adequate for producing rhythmic Pre-I neuron bursts and inspiratory burst activity (Onimaru and Homma 2003; Onimaru et al. 2015). Indeed, photostimulation on the left (unilateral) side of the pFRG was not effective when the medulla was intact (Ikeda et al. 2019b). For photoactivation of ChRFR, photostimulation was performed with a blue light-emitting diode (LED) (460–470 nm, 0.1–0.2 mW/mm$^2$; LED5W-B; Brain Vision, Tsukuba, Japan) via an optic fiber with 0.2-mm outer diameter for up to 43 s (mostly 22.5 s) (50-ms duration/150-ms interval) (Igarashi et al. 2018; Ikeda et al. 2019a). The tip of the optic fiber was set at 0.5–0.8 mm above the tissue surface of the rostral medulla to avoid interference with electrode insertion of the whole-cell patch-clamp recording. Thus, the illuminated area covered the whole ipsilateral rostral ventrolateral medulla including the pFRG.

We confirmed specific expression of reporter fluorescence proteins for Arch or ChRFR expression in cell soma and neuronal processes (dendrites and axons) in Phox2b-positive cells in the rostral ventrolateral medulla (Ikeda et al. 2019a, b). The photostimulation induced inhibition or facilitation of respiratory rhythm in Arch-expressing or ChRFR-expressing Tg rat preparations, respectively. In both cases, the effects of photostimulation appeared with the maximum change of respiratory frequency and

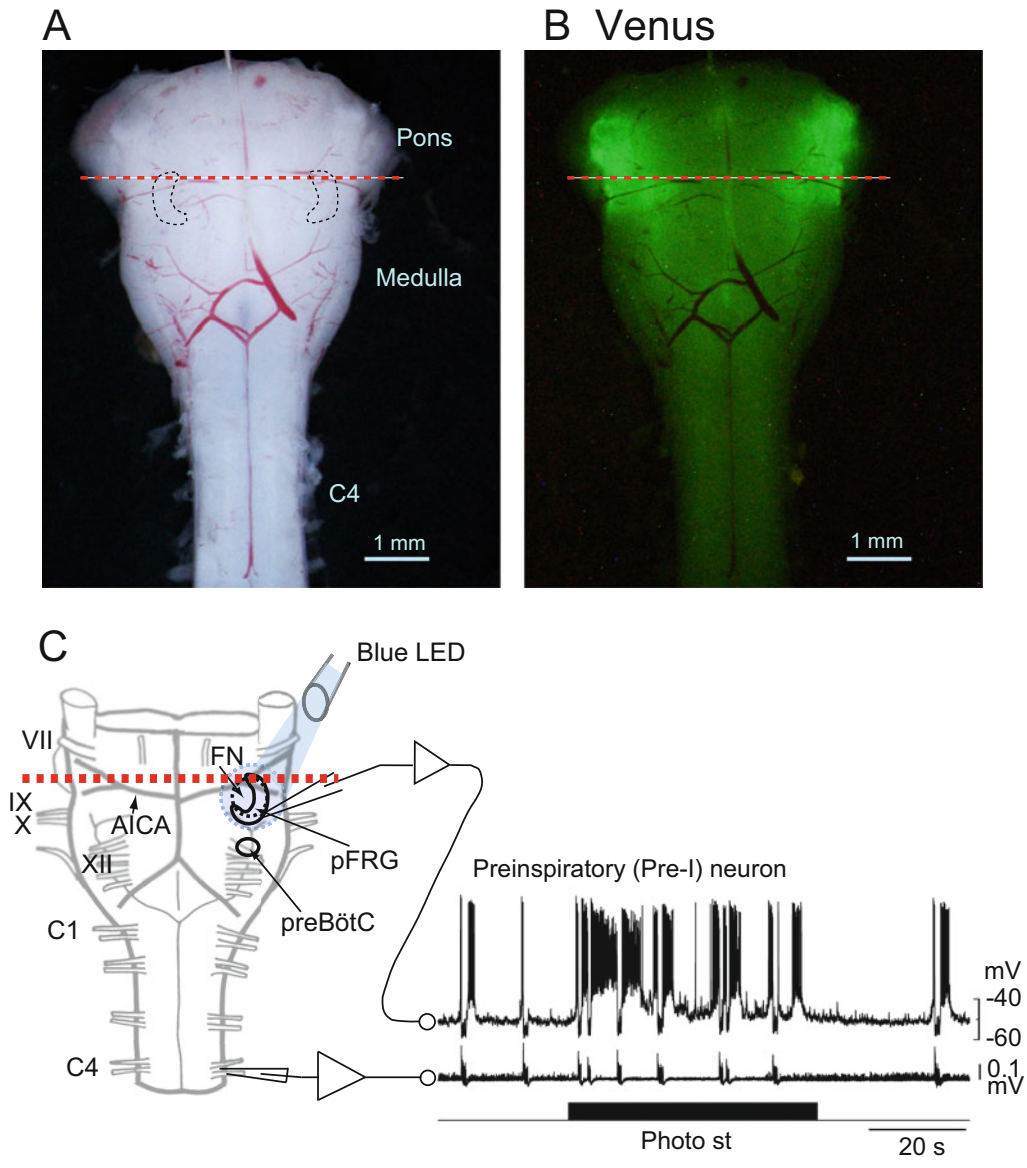


**Fig. 29.1** The ventral view of a Phox2b-ChRFR-expressing transgenic rat by fluorescence microscopy. (**a**) Bright field mode. (**b**) Fluorescence mode. Dashed red lines denote the level of transverse section. The preparation is from a newborn rat on postnatal day 1. Note that clear expression of Venus (reporter for ChRFR) in the rostral ventrolateral medulla including the parafacial respiratory group (pFRG) (dotted black line area in **a**). (**c**) Schematic presentation of the experimental arrangement. The brainstem–spinal cord preparation from a transgenic rat was cut at the level of the dashed red line. Inspiratory motor neuron activity was monitored from the fourth cervical ventral root (C4). Respiratory-related neurons in the rostral ventrolateral medulla were recorded from the pFRG or more caudal medulla including the preBötzinger complex (preBötC) by whole-cell patch clamp. The example is from a preinspiratory (Pre-I) neuron. The ipsilateral ventral medulla was photostimulated by a blue light-emitting diode (LED) in this case (Phox2b-ChRFR-expressing transgenic rat). The photostimulation (Photo st) induced membrane depolarization of the Pre-I neuron and facilitated the C4 burst rate. VII, IX, X, XII; cranial nerves. C1, C4; cervical ventral roots. *AICA* anterior inferior cerebellar artery, *FN* facial nucleus

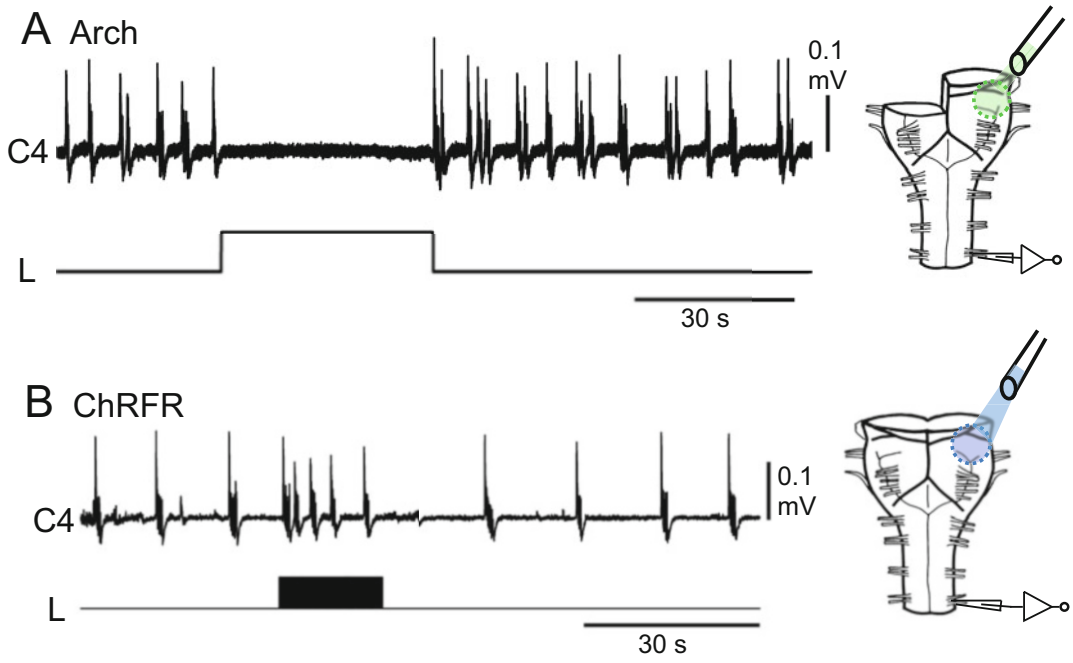


**Fig. 29.2** Effects of photostimulation on the unilateral side of the pFRG. (**a**) Response in the preparation from Arch-positive pups. The medulla was cut to remove the right half of the pFRG. Continuous photostimulation of the ventral medulla was performed with green laser light (532 nm) through an optic fiber with 1-mm outer diameter. Note that the photostimulation depressed C4 inspiratory rhythm. (**b**) Response in the preparation from ChRFR-positive pups. Train pulse photostimulation (50-ms duration/150-ms interval) was performed by a blue light-emitting diode (LED) (460–470 nm) via an optic fiber with 0.2-mm outer diameter. Note that photostimulation increased the C4 inspiratory rate

tended to be weakened during the stimulation (Fig. 29.2).

## 29.5 Local Network Analysis by Optogenetic Approach

Analyses of local network connections among respiratory neurons in the rostral ventral medulla were mainly performed in ChRFR-expressing rat. Phox2b-positive (i.e., ChRFR-expressing) respiratory neurons are composed mainly of Pre-I neurons and respiratory-modulated tonically firing neurons. Phox2b-negative respiratory neurons are composed of Pre-I, Insp, and Exp neurons. We recorded membrane potentials from all types of respiratory-related neurons by whole-cell patch-clamp methods and examined the responses to photostimulation in the absence and presence of TTX. Regardless of the neuronal subtypes, in the presence of TTX, photostimulation depolarized the Phox2b-positive cells but induced no significant change in the membrane potential of the Phox2b-negative cells. We concluded that photostimulation in our experimental condition mainly targeted postsynaptic (i.e., cell soma) membranes in the Phox2b-positive cells but not presynaptic terminals derived from Phox2b-positive neurons (Ikeda et al. 2019a).

In the absence of TTX (i.e., control condition), membrane potential responses to photostimulation were variable depending on neuronal subtypes. Photostimulation induced membrane depolarization of all types of Phox2b-positive neurons (Pre-I, Insp, and respiratory-modulated tonic neurons) in the pFRG and Phox2b-negative Pre-I neurons. In contrast, membrane potential

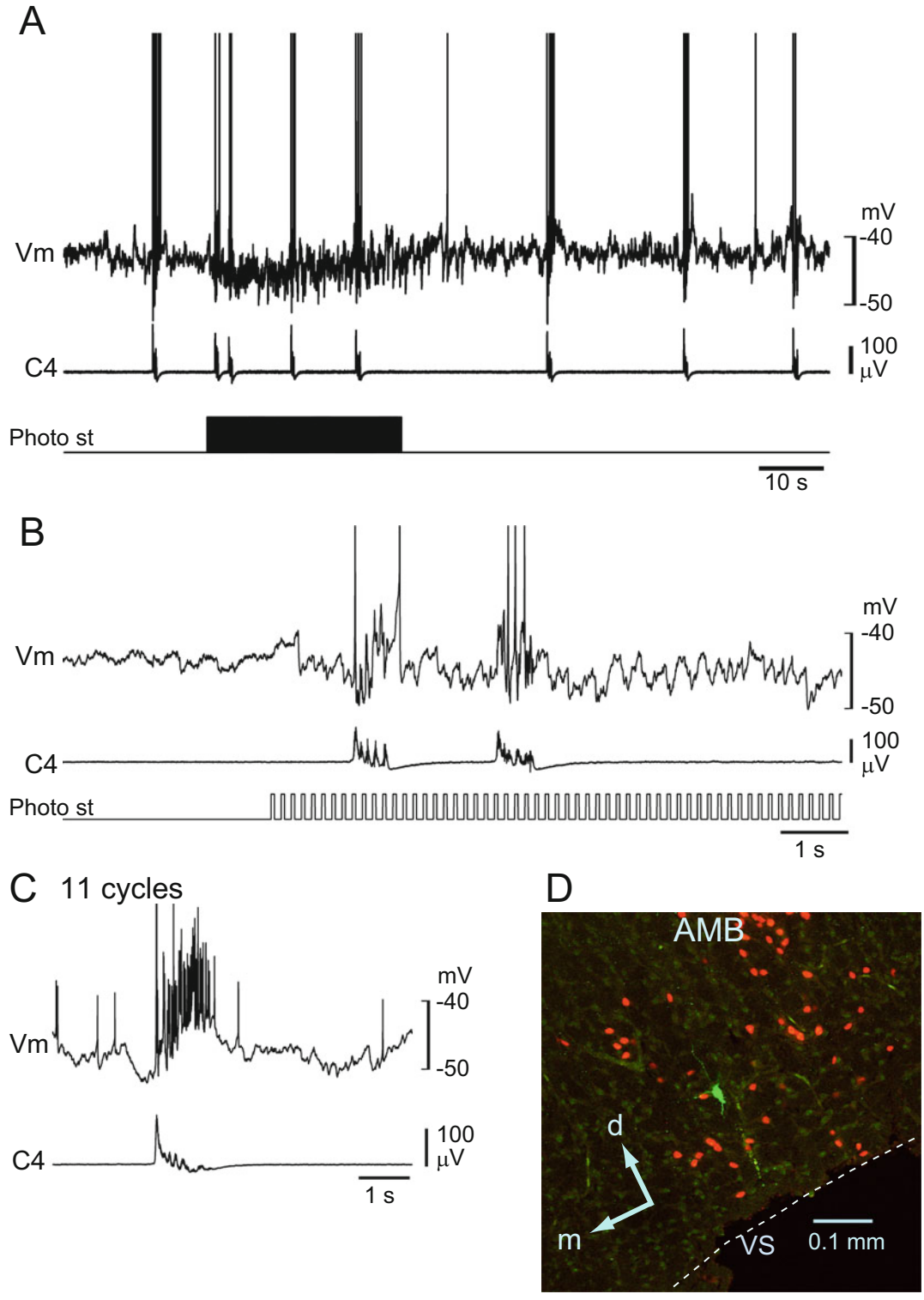


**Fig. 29.3** An example of a subtype of inspiratory neuron that receives inhibitory postsynaptic potentials (IPSPs) from a Pre-I neuron. (**a**) Photostimulation (Photo st) induced membrane hyperpolarization during the interburst phases due to photoactivation of Pre-I neurons. (**b**) Faster sweep representations around the start of

changes of Phox2b-negative Insp and Exp neurons induced by photostimulation were either depolarization or hyperpolarization and dependent on the subtypes of neurons.

The subtypes of Phox2b-negative Insp neurons were previously characterized based on periodic synaptic inputs from Pre-I neurons in control respiratory cycles: excitatory (type I), inhibitory (type III), and no obvious input (type II) (Ballanyi et al. 1999; Onimaru and Homma 1992). Thus, it was predictable that the membrane potential changes of Phox2b-negative Insp neurons depended on photoactivation of Pre-I neurons that made synaptic connections to targeted Insp neurons: depolarization in type I, hyperpolarization in type III, and no change in type II neurons. Indeed, our findings confirmed these predicted membrane potential changes in Phox2b-negative Insp neurons during photostimulation (Fig. 29.3). A subtype of Exp neurons (Exp-pi) that received inhibitory synaptic inputs from Pre-I (and Insp) neurons was hyperpolarized by photostimulation. Therefore, type III Insp and Exp-pi neurons should receive inhibitory synaptic inputs from Phox2b-negative (inhibitory) Pre-I neurons that were activated by Phox2b-positive (excitatory) neurons during photostimulation. Thus, our findings clearly indicated that the membrane potential changes occurring in Phox2b-negative respiratory neurons during photostimulation depended on the characteristics of the specific ongoing synaptic connections in local respiratory networks in the rostral medulla (Fig. 29.4) (Ikeda et al. 2019a).

It should be noted that membrane potential changes in the Phox2b-negative neurons during photostimulation without TTX were largest in the Pre-I neurons (+9.1 mV) and were comparable to those of Phox2b-positive neurons and were smallest in the Insp neurons (+2.6 mV in type I and −2.0 in type III Insp). These results suggested that Phox2b-negative Pre-I neurons receive synaptic inputs from a greater number of Phox2b-positive (and/or indirectly Phox2b-negative) neurons than do Phox2b-negative Insp neurons that receive synaptic inputs from a more limited number of neurons (Ikeda et al. 2019a).

## 29.6 Limitations and Perspective

The brainstem–spinal cord preparation is useful only during the early postnatal period (P0–P4). Therefore, developmental changes of respiratory neuron networks during postnatal to adult periods should be studied in different types of preparation, e.g., arterially perfused in situ preparation (Paton 1996) or in vivo preparation. Indeed, comparison of drug effects between the neonatal rat in vitro preparation and the juvenile rat in situ preparation suggested that the cellular and/or network properties of the respiratory neurons changed during postnatal development (Kotani et al. 2019). Although the detailed process of developmental changes of the neonatal pFRG to the adult pFRG/RTN is not yet clarified, some of the neonatal pFRG neurons may develop into adult pFRG neurons that produce active expiration (Pagliardini et al. 2011), and others may develop into adult RTN neurons that show a more tonic firing pattern with respiratory modulation and are sensitive to hypercapnia (Guyenet et al. 2005; Stornetta et al. 2006). Our Tg rat model may also be useful for optogenetic analysis of respiratory neuron networks in later developmental stages.

In the pFRG/RTN region, Phox2b-positive neurons are predominantly glutamatergic and tyrosine hydroxylase (TH) negative, whereas TH-positive cells (i.e., A1/C1 [nor]adrenergic neurons) in the similar or more caudal ventrolateral medulla are Phox2b positive (Basting et al.

**Fig. 29.3** (continued) photostimulation. Note that IPSPs appeared in the trace of the membrane potential because this inspiratory neuron received inhibitory input from photoactivated Pre-I neurons. (**c**) Membrane potential trajectory by cycle-triggered averaging (11 cycles) in control. Note hyperpolarization during the preinspiratory phase. (**d**) Location of the neurobiotin-labeled (green) neuron recorded. This cell was Phox2b (red) negative. *d* dorsal, *m* medial, *AMB* nucleus ambiguous, *VS* ventral surface

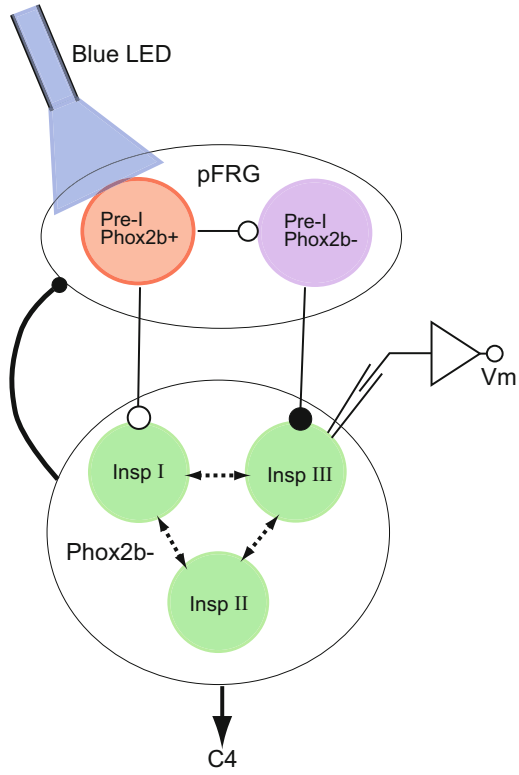


**Fig. 29.4** Simplified model of neuronal organization of the central pattern generator of respiration in the brainstem–spinal cord preparation and the basic experimental strategy of optogenetic analysis. Synaptic connections among neuron groups (Ballanyi et al. 2009; Mellen et al. 2003; Onimaru et al. 1997, 2008; Onimaru and Homma 1992) are indicated by straight lines with open circles (excitatory synaptic connection) or closed circles (inhibitory synaptic connection). The Pre-inspiratory (Pre-I) neuron network is composed of Phox2b-positive and Phox2b-negative Pre-I neurons in the rostral ventrolateral medulla including the parafacial respiratory group (pFRG). At least some of the Phox2b-negative Pre-I neurons are inhibitory (Onimaru et al. 2014) and are located in the caudal pFRG or more caudal ventral medulla including the Bötzinger complex and preBötzinger complex and interact with Phox2b-positive Pre-I neurons. The inspiratory (Insp) neuron (Phox2b negative) network is composed of three types of Insp neurons: type I (Insp I), receiving excitatory synaptic inputs from the Pre-I neurons; type II (Insp II), not receiving synaptic inputs from the Pre-I neurons, and type III (Insp III), receiving inhibitory synaptic inputs from the Pre-I neurons (Onimaru and Homma 1992). These Insp neurons interact with mutual synaptic connections (dashed line with double-headed arrows). One of the motor outputs derived from Insp neurons can be recorded from the fourth cervical ventral root (C4). Photostimulation by blue LED excited Phox2b-positive Pre-I neurons and facilitated C4 inspiratory rhythm via burst rhythm facilitation of type I Insp neurons. Photostimulation also indirectly excited Phox2b-negative Pre-I neurons that sent inhibitory synaptic inputs to type III Insp neurons. Thus, photostimulation induced an increase of inhibitory postsynaptic potentials and membrane hyperpolarization in the type III Insp neurons as shown in Fig. 29.3 (see Ikeda et al. 2019a for details)

2015; Kang et al. 2007; Malheiros-Lima et al. 2018; Wenker et al. 2017). Therefore, photostimulation could activate TH-positive cells in addition to Phox2b-positive/TH-negative cells in the ventrolateral medulla and could modulate respiratory frequency via tonic excitatory synaptic inputs (Basting et al. 2015; Burke et al. 2014; Malheiros-Lima et al. 2018). In our preliminary experiments, typical respiratory-related neurons (Pre-I and Insp neurons) seemed to be largely TH-negative (unpublished observation). Future discovery of different genetic markers that are

expressed more specifically in respiratory-related neurons may help to resolve the above problems experienced with an optogenetic approach.

## 29.7 Conclusion

Photostimulation of the pFRG induced inhibition or facilitation of respiratory rhythm in Arch-expressing or ChRFR-expressing Tg rat preparations, respectively. Selective photoactivation of Phox2b-positive neurons expressing ChRFR in the rostral ventrolateral medulla of a neonatal rat en bloc preparation induced membrane potential changes of respiratory-related neurons that were dependent on heterogeneous properties of synaptic connections in the respiratory center. The optogenetic approach made possible the further reinforcement of a hypothetical model of local networks among respiratory-related neurons in the rostral ventrolateral medulla of neonatal rat, as proposed in previous studies (Ballanyi et al. 1999; Onimaru et al. 1997), suggesting that Phox2b-positive Pre-I neurons play a central role in respiratory rhythm generation in neonatal rats. In addition, we emphasize that the method used here is a powerful means of analysis of local circuits of respiratory rhythm generation especially in the en bloc newborn rat preparation.

**Acknowledgments** This research was supported by Scientific Research on Innovative Areas (Comprehensive Brain Science Network) from the Ministry of Education, Culture, Sports, Science and Technology (MEXT) of Japan, and JSPS KAKENHI (16K07003, 25430012), and by the Program for the Strategic Research Foundation at Private Universities 2016–2017 (Showa University School of Medicine and Jichi Medical University).

## References

Abbott SB, Stornetta RL, Fortuna MG et al (2009) Photostimulation of retrotrapezoid nucleus phox2b-expressing neurons in vivo produces long-lasting activation of breathing in rats. J Neurosci 29:5806–5819

Ballanyi K, Onimaru H, Homma I (1999) Respiratory network function in the isolated brainstem-spinal cord of newborn rats. Prog Neurobiol 59:583–634

Ballanyi K, Ruangkittisakul A, Onimaru H (2009) Opioids prolong and anoxia shortens delay between onset of preinspiratory (pFRG) and inspiratory (preBotC) network bursting in newborn rat brainstems. Pflugers Arch 458:571–587

Basting TM, Burke PG, Kanbar R et al (2015) Hypoxia silences retrotrapezoid nucleus respiratory chemoreceptors via alkalosis. J Neurosci 35:527–543

Burke PG, Abbott SB, Coates MB et al (2014) Optogenetic stimulation of adrenergic C1 neurons causes sleep state-dependent cardiorespiratory stimulation and arousal with sighs in rats. Am J Respir Crit Care Med 190:1301–1310

Dubreuil V, Ramanantsoa N, Trochet D et al (2008) A human mutation in Phox2b causes lack of CO2 chemosensitivity, fatal central apnea, and specific loss of parafacial neurons. Proc Natl Acad Sci U S A 105:1067–1072

Ellenberger HH, Feldman JL (1990) Brainstem connections of the rostral ventral respiratory group of the rat. Brain Res 513:35–42

Guyenet PG, Mulkey DK, Stornetta RL et al (2005) Regulation of ventral surface chemoreceptors by the central respiratory pattern generator. J Neurosci 25:8938–8947

Guyenet PG, Bayliss DA, Stornetta RL et al (2009) Retrotrapezoid nucleus, respiratory chemosensitivity and breathing automaticity. Respir Physiol Neurobiol 168:59–68

Igarashi H, Ikeda K, Onimaru H et al (2018) Targeted expression of step-function opsins in transgenic rats for optogenetic studies. Sci Rep 8:5435

Ikeda K, Takahashi M, Sato S et al (2015) A Phox2b BAC transgenic rat line useful for understanding respiratory rhythm generator neural circuitry. PLoS One 10: e0132475

Ikeda K, Kawakami K, Onimaru H et al (2017) The respiratory control mechanisms in the brainstem and spinal cord: integrative views of the neuroanatomy and neurophysiology. J Physiol Sci 67:45–62

Ikeda K, Igarashi H, Yawo H et al (2019a) Optogenetic analysis of respiratory neuronal networks in the ventral medulla of neonatal rats producing channelrhodopsin in Phox2b-positive cells. Pflugers Arch 471:1419–1439

Ikeda K, Kaneko R, Yanagawa Y et al (2019b) Analysis of the neuronal network of the medullary respiratory center in transgenic rats expressing archaerhodopsin-3 in Phox2b-expressing cells. Brain Res Bull 144:39–45

Kanbar R, Stornetta RL, Cash DR et al (2010) Photostimulation of Phox2b medullary neurons activates cardiorespiratory function in conscious rats. Am J Respir Crit Care Med 182:1184–1194

Kang BJ, Chang DA, Mackay DD et al (2007) Central nervous system distribution of the transcription factor Phox2b in the adult rat. J Comp Neurol 503:627–641

Kotani S, Yazawa I, Onimaru H et al (2019) An aromatic substance, eugenol induces distinct depressant effects on respiratory activity in different postnatal

developmental stages of the rat. Neurosci Res S0168-0102(19):30170–30171

Lawlor PA, Bland RJ, Mouravlev A et al (2009) Efficient gene delivery and selective transduction of glial cells in the mammalian brain by AAV serotypes isolated from nonhuman primates. Mol Ther 17:1692–1702

Lee JH, Durand R, Gradinaru V et al (2010) Global and local fMRI signals driven by neurons defined optogenetically by type and wiring. Nature 465:788–792

Malheiros-Lima MR, Totola LT, Lana MVG et al (2018) Breathing responses produced by optogenetic stimulation of adrenergic C1 neurons are dependent on the connection with preBotzinger complex in rats. Pflugers Arch 470:1659–1672

Mellen NM, Janczewski WA, Bocchiaro CM et al (2003) Opioid-induced quantal slowing reveals dual networks for respiratory rhythm generation. Neuron 37:821–826

Nathanson JL, Jappelli R, Scheeff ED et al (2009) Short promoters in viral vectors drive selective expression in mammalian inhibitory neurons, but do not restrict activity to specific inhibitory cell-types. Front Neural Circuits 3:19

Onimaru H, Homma I (1987) Respiratory rhythm generator neurons in medulla of brainstem-spinal cord preparation from newborn rat. Brain Res 403:380–384

Onimaru H, Homma I (1992) Whole cell recordings from respiratory neurons in the medulla of brainstem-spinal cord preparations isolated from newborn rats. Pflugers Arch 420:399–406

Onimaru H, Homma I (2003) A novel functional neuron group for respiratory rhythm generation in the ventral medulla. J Neurosci 23:1478–1486

Onimaru H, Arata A, Homma I (1988) Primary respiratory rhythm generator in the medulla of brainstem-spinal cord preparation from newborn rat. Brain Res 445:314–324

Onimaru H, Arata A, Homma I (1997) Neuronal mechanisms of respiratory rhythm generation: an approach using in vitro preparation. Jpn J Physiol 47:385–403

Onimaru H, Ikeda K, Kawakami K (2008) CO2-sensitive preinspiratory neurons of the parafacial respiratory group express Phox2b in the neonatal rat. J Neurosci 28:12845–12850

Onimaru H, Ikeda K, Kawakami K (2012a) Postsynaptic mechanisms of CO(2) responses in parafacial respiratory neurons of newborn rats. J Physiol 590:1615–1624

Onimaru H, Ikeda K, Kawakami K (2012b) Relationship between the distribution of the paired-like homeobox gene (Phox2b) expressing cells and blood vessels in the parafacial region of the ventral medulla of neonatal rats. Neuroscience 212:131–139

Onimaru H, Ikeda K, Mariho T et al (2014) Cytoarchitecture and CO(2) sensitivity of Phox2b-positive parafacial neurons in the newborn rat medulla. Prog Brain Res 209:57–71

Onimaru H, Tsuzawa K, Nakazono Y et al (2015) Midline section of the medulla abolishes inspiratory activity and desynchronizes pre-inspiratory neuron rhythm on both sides of the medulla in newborn rats. J Neurophysiol 113:2871–2878

Onimaru H, Nakamura S, Ikeda K et al (2018) Confocal calcium imaging analysis of respiratory-related burst activity in the parafacial region. Brain Res Bull 139:16–20

Pagliardini S, Janczewski WA, Tan W et al (2011) Active expiration induced by excitation of ventral medulla in adult anesthetized rats. J Neurosci 31:2895–2905

Paton JF (1996) The ventral medullary respiratory network of the mature mouse studied in a working heart-brainstem preparation. J Physiol 493(Pt 3):819–831

Pattyn A, Morin X, Cremer H et al (1997) Expression and interactions of the two closely related homeobox genes Phox2a and Phox2b during neurogenesis. Development 124:4065–4075

Pattyn A, Morin X, Cremer H et al (1999) The homeobox gene Phox2b is essential for the development of autonomic neural crest derivatives. Nature 399:366–370

Smith JC, Morrison DE, Ellenberger HH et al (1989) Brainstem projections to the major respiratory neuron populations in the medulla of the cat. J Comp Neurol 281:69–96

Smith JC, Ellenberger HH, Ballanyi K et al (1991) Pre-Botzinger complex: a brainstem region that may generate respiratory rhythm in mammals. Science 254:726–729

Stornetta RL, Moreira TS, Takakura AC et al (2006) Expression of Phox2b by brainstem neurons involved in chemosensory integration in the adult rat. J Neurosci 26:10305–10314

Suzue T (1984) Respiratory rhythm generation in the in vitro brain stem-spinal cord preparation of the neonatal rat. J Physiol 354:173–183

Wenker IC, Abe C, Viar KE et al (2017) Blood pressure regulation by the rostral ventrolateral medulla in conscious rats: effects of hypoxia, hypercapnia, baroreceptor denervation, and anesthesia. J Neurosci 37:4565–4583

# Optogenetic Manipulation of the Vagus Nerve

30

Toya Okonogi and Takuya Sasaki

**Abstract**

The vagus nerve plays a pivotal role in communication between the brain and peripheral organs involved in the sensory detection and the autonomic control of visceral activity. While the lack of appropriate experimental techniques to manipulate the physiological activity of the vagus nerve has been a long-standing problem, recent advancements in optogenetic tools, including viral vectors and photostimulation devices, during the late 2010s have begun to overcome this technical hurdle. Furthermore, identifying promoters for expressing transgenes in a cell-type-specific subpopulation of vagal neurons enables the selective photoactivation of afferent/efferent vagal neurons and specific visceral organ-innervating vagal neurons. In this chapter, we describe recent optogenetic approaches to study vagus nerve physiology and describe how these approaches have provided novel findings on the roles of vagus nerve signals in the cardiac, respiratory, and gastrointestinal systems. Compared with studies of the central nervous system, there are still few insights into vagus nerve physiology. Further studies with optogenetic tools will be useful for understanding the fundamental characteristics of vagus nerve signals transferred throughout the body.

**Keywords**

Optogenetics · Vagus nerve · Virus · Cardiac system · Respiratory system · Digestive system · Gut–brain axis · Interoception

## Abbreviations

| | |
|---|---|
| ChAT | Choline acetyltransferase |
| ChR2 | Channelrhodopsin2 |
| GLP1R | Glucagon-like peptide-1 receptor |
| GPR65 | G-protein-coupled receptor 65 |
| iDISCO | Immunolabeling-enabled three-dimensional imaging of solvent-cleared organs |
| NPY2R | Neuropeptide Y receptor Y2 |
| NTS | The nucleus of the solitary tract |
| P2RY1 | Purinergic receptor P2Y1 |
| TRE | Proteins from the tetracycline-responsive element |
| TRPV1 | Transient receptor potential vanilloid 1 |
| tTA | Tetracycline transactivator |
| VGluT2 | Vesicular glutamate transporter 2 |

T. Okonogi · T. Sasaki (✉)
Laboratory of Chemical Pharmacology, Graduate School of Pharmaceutical Sciences, The University of Tokyo, Tokyo, Japan
e-mail: tsasaki@mol.f.u-tokyo.ac.jp



H. Yawo et al. (eds.), *Optogenetics*, Advances in Experimental Medicine and Biology 1293,
https://doi.org/10.1007/978-981-15-8763-4_30

## 30.1 Introduction

Optogenetic tools, including both devices and molecular tools, have greatly advanced our understanding of how neuronal networks in the brain cooperatively regulate complex brain functions since the 2000s. After approximately 10 years, they began to be introduced into studies of the vagus nerve, a major autonomic pathway for communication between the central nervous system and peripheral organs. Similar to neuronal cells in the brain, pulses of visible light on vagus fibers expressing foreign photosensitive proteins, such as channelrhodopsin 2 (ChR2) (Boyden et al. 2005), can selectively activate these fibers. As the vagal nervous system regulates many internal organs, including the heart, lungs, and intestines (Fig. 30.1a), optogenetic manipulations of vagus nerve fibers have the potential to activate/inhibit the internal organs innervated by these fibers. In addition, cell-type-specific expressions of optogenetic molecular tools in the vagus nerve are advantageous over existing electrical stimulation or pharmacological techniques because these methods can more precisely reproduce unidirectional and cell-type-specific vagal nerve transduction.

Here, we summarize recent advancement in optogenetics molecular tools, including viral vectors, transgenic animals, promoters, and photosensitive proteins, applied to the vagus nerve. The vagal nervous system consists of multiple fiber types that innervate multiple internal organs. It remains largely unknown how these various vagus nerve fibers cooperate and transmit signals to maintain internal organ functions. Optogenetic approaches are a promising method to address these long-standing questions because they are

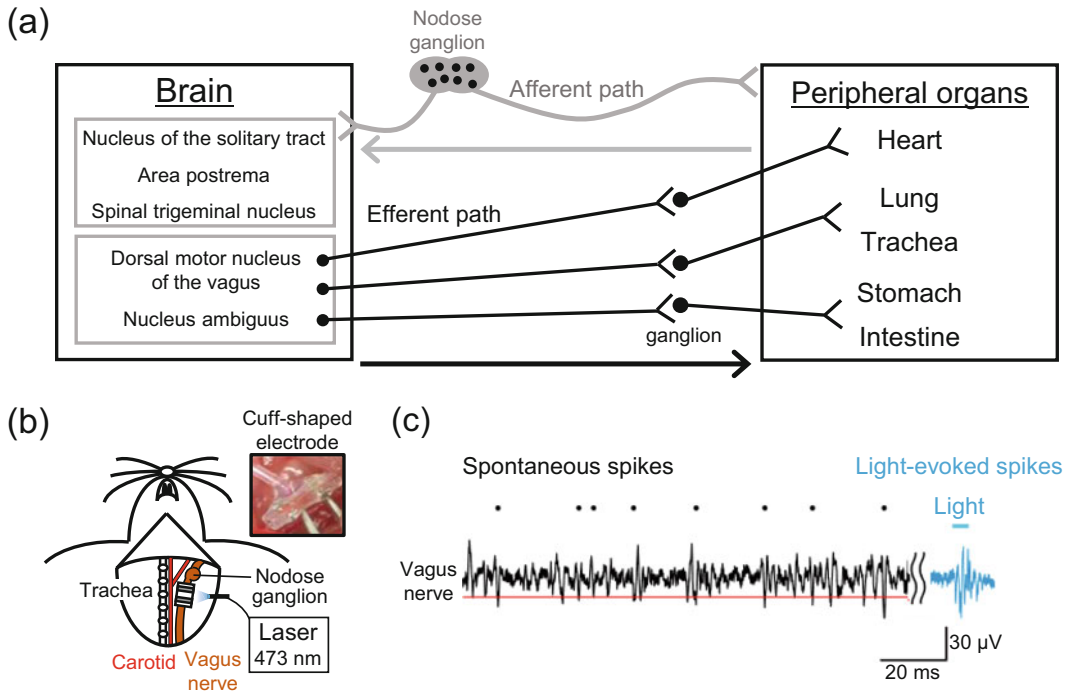


**Fig. 30.1** In vivo vagus nerve recording. (**a**) Schematic illustration of the vagal nervous system and related organs. Filled circles represent cell bodies of vagal neurons. (**b**) A vagus nerve recording in which vagus nerve fibers were covered with a cuff-shaped electrode. (**c**) Extracellular voltage traces recorded from an anesthetized *Vglut2-ires-Cre; lox-ChR2* mouse. The left trace represents spontaneously occurring spikes, and the right blue trace represents a photostimulation-induced spike recorded from the same mouse. The timing of blue light illumination of the recorded site is indicated by a blue tick above the trace

able to label and activate specific vagus nerve fibers. In this chapter we introduce several recent pioneering studies, describing which optogenetic molecular tools are currently available and how the recruitment of these tools could contribute to novel findings.

## 30.2 Application of Optogenetic Tools to the Vagus Nerve

### 30.2.1 Basic Structures of the Vagus Nerve

The vagus nerve is one of the most crucial pathways for interactions between the brain and other peripheral organs (Fig. 30.1a). In general, a well-known role of the vagus nerve is to efferently send parasympathetic cholinergic signals to control the circulatory, respiratory, and digestive systems (Evans and Murray 1954; Agostoni et al. 1957; Prechtl and Powley 1990; Cailotto et al. 2014). The soma of the efferent vagus nerve originates in the nucleus ambiguus and the dorsal motor nucleus in the brain. Notably, this efferent vagus nerve pathway is only a subcomponent of the vagal nerve system. A larger proportion of the vagus nerve forms afferent pathways that transmit ascending information to the nucleus of the solitary tract (NTS), area postrema, and spinal trigeminal nucleus in the brain from visceral organs, such as the heart (Hayakawa et al. 2011), the digestive organs (Czaja et al. 2006; Campos et al. 2012), and the lungs (Weijs et al. 2015; Han et al. 2018). The soma of the afferent vagus nerve is located at the nodose ganglion, and the number of soma has been estimated to be approximately 2300 in mice (Fox et al. 2001). The major afferent pathway utilizes glutamatergic transmission and is considered to convey information of the activity states of the internal organs to the brain, so-called interoception, a neurophysiological process by which the brain monitors the internal physiological states of the peripheral organs (Garfinkel and Critchley 2016; Pfeifer et al. 2017), which could potentially affect cognition and emotion. Moreover, vagus nerve stimulation has been shown to alter brain electrical activity (Usami et al. 2013; Cao et al. 2016; Larsen et al. 2016; Alexander et al. 2017), stop seizures (Woodbury and Woodbury 1990) and refractory epilepsy (Ben-Menachem et al. 1994; Takaya et al. 1996), and ameliorate treatment-resistant depression (Nemeroff et al. 2006; Wani et al. 2013).

### 30.2.2 Electrophysiological Recordings of Optogenetically Induced Vagus Nerve Spikes

While the importance of the vagus nerve has long been advocated, the precise physiological dynamics of nerve signals transmitted through the vagus nerve remains to be elucidated due to technical limitations related to directly recording electrical action potential signals from the vagus nerve. Recently, some studies have succeeded in performing vagus nerve recordings that monitored vagus nerve spikes in anesthetized animals (Harreby et al. 2011; Caravaca et al. 2017; McCallum et al. 2017; Silverman et al. 2018; Nishimura et al. 2020) by utilizing cuff-shaped or hook-shaped electrodes (Fig. 30.1b). More recently, we established a novel vagus nerve recording method that is applicable in freely moving animals (Shikano et al. 2019).

In parallel, the application of optogenetic molecular tools in the vagus nerve is spreading. By utilizing several gene delivery methods, described later, some researchers have achieved the selective expression of ChR2 in the vagus nerve. The development of electrophysiological vagus nerve recordings enables direct verification that the vagus nerve expressing ChR2 surely emits action potentials in response to blue light illumination at the recording site (Fig. 30.1b, c) (Chang et al. 2015; Williams et al. 2016; Nonomura et al. 2017; Han et al. 2018; Tsaava et al. 2019). In the next sections, we summarize the currently available optogenetic molecular tools for the manipulation of various types of the vagus nerve.

### 30.2.3 Expression of Photosensitive Proteins in the Vagus Nerve

#### 30.2.3.1 Bigenic Mouse Line

The selective expression of ChR2 in defined subpopulations of the vagus nerve can be achieved by the Cre–Lox recombination system using bigenic mouse lines (Fig. 30.2). In this system, two mouse lines are crossbred: one transgenic mouse line, in which Cre recombinase is expressed under the control of a cell-type-specific promoter, and another reporter mouse line, in which ChR2-EYFP is expressed in a Cre-dependent manner. A crucial advantage of bigenic mouse lines is that they provide stable levels of transgene expression without mature experimental techniques, such as virus injection into the vagus nerve. Table 30.1 summarizes the repertoire of bigenic mouse lines for vagus nerve optogenetics published to date. The afferent- and efferent-selective manipulation of vagus nerve spikes is possible in *Vglut2-ires-Cre; lox-ChR2* mice (Chang et al. 2015; Han et al. 2018) and *Chat-ires-Cre; lox-ChR2* mice (Chang et al. 2015; Rajendran et al. 2019), respectively. More specifically, cell-type-specific promoters have been identified for the optogenetic manipulation of the vagus nerve innervating individual organs (applications are described in the following sessions).

A similar Cre–loxP system is applicable for the expression of fluorescent calcium indicator proteins such as GCaMPs in specific subcomponents of the vagus nerve. For example, calcium imaging from the cell bodies of subpopulations of afferent vagal neurons have been performed using *Glp1r-ires-Cre; lox-GCaMP3* and *Gpr65-ires-Cre; lox-GCaMP3* mice (Williams et al. 2016) and *P2ry1-ires-Cre; ROSA26-GCaMP3* and Piezo2-ires-Cre; *ROSA26-GCaMP3* mice (Prescott et al. 2020).

Currently, transcriptional profiles of vagal neurons are publicly available and were obtained from comprehensive transcriptomic analysis using single-cell RNA sequencing (Bai et al. 2019; Kupari et al. 2019; Prescott et al. 2020). These profiles identified diverse subclasses of vagal neurons expressing specific molecules. Information on such molecular profiles will be helpful in designing new optogenetic molecular tools for the vagus nerve and in systematically elucidating the detailed physiological characteristics of the vagus nerve.

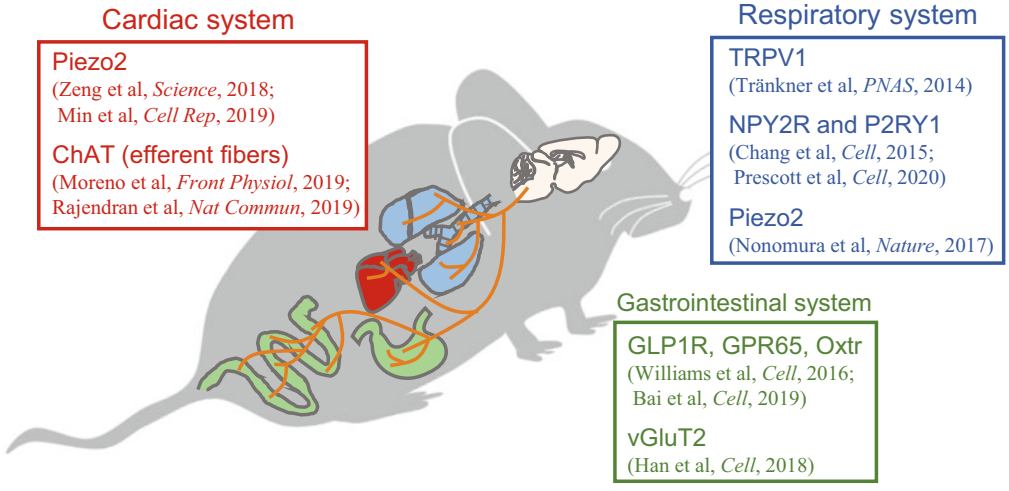


**Fig. 30.2** Optogenetics studies in individual organ systems. In each box, specific promoters for the expression of ChR2 are shown for each organ (reported until April 2020)

**Table 30.1** The repertoire of bigenic mouse lines for the optogenetic photostimulation of the vagus nerve (reported until April 2020)

| Mouse lines | Fiber type (organ) | Effects | Refs. |
|---|---|---|---|
| *Chat-ires-Cre; lox-ChR2* | Efferent fibers | HR ↓<br>RR → | Chang et al. (2015)<br>Moreno et al. (2019)<br>Rajendran et al. (2019)<br>Tsaava et al. (2019)<br>Prescott et al. (2020) |
| *Vglut2-ires-Cre; lox-ChR2* | Afferent fibers | GP ↓<br>HR ↓<br>RR ↓ | Chang et al. (2015)<br>Williams et al. (2016)<br>Min et al. (2019)<br>Prescott et al. (2020) |
| *Mc4r-2a-Cre; loxP-ChR2* | Afferent fibers | BP→<br>HR→ | Min et al. (2019) |
| *Npy2r-ires-Cre; lox-ChR2* | Afferent C fibers (airway and lungs) | GP ↓<br>HR ↓<br>RR ↑ | Chang et al. (2015) |
| *P2ry1-ires-Cre; lox-ChR2* | Afferent A fibers (airway and lungs) | GP →<br>HR →<br>RR ↓ | Chang et al. (2015)<br>Williams et al. (2016)<br>Prescott et al. (2020) |
| *Glp1r-ires-Cre; lox-ChR2* | Afferent C fibers (intestine and stomach) | GP ↑<br>HR ↓<br>RR ↑ | Williams et al. (2016) |
| *Gpr65-ires-Cre; lox-ChR2* | Afferent C fibers (duodenum) | GP ↓<br>HR →<br>RR → | Williams et al. (2016) |
| *Piezo2(GFP)-ires-Cre; lox-ChR2* | Afferent A and C fibers (airway and aorta) | BP ↓<br>HR ↓<br>RR ↓ | Nonomura et al. (2017)<br>Zeng et al. (2018)<br>Min et al. (2019)<br>Prescott et al. (2020) |
| *Trpv1-ires-Cre; lox-ChR2* | Afferent A and C fibers | N/A | Tränkner et al. (2014)<br>Tsaava et al. (2019) |

Transgenic Cre-expressing mice are crossed with reporter mice containing a Cre-dependent ChR2 allele
*BP* blood pressure, *GP* gastric pressure, *HR* heart rate, *RR* respiratory rate

#### 30.2.3.2 Viral Vector

Viral vectors are an alternative approach for introducing photosensitive proteins into the vagus nerve. The advantage of viral vectors, compared with bigenic mice, is that the focal administration of a virus solution into a specific organ leads to a more selective expression of targeted genes in the organ-innervating vagus nerve. A widely utilized strategy is to inject Cre-inducible viral constructs into Cre-expressing mouse lines. For example, labeling specific cell types of afferent vagus nerves with transgenes such as eGFP and tdTomato is achieved by the injection of Cre-inducible *AAV-eGFP* and *AAV-flex-tdTomato*, respectively, into the nodose/jugular complex (Chang et al. 2015; Williams et al. 2016). Recent reports with similar methods are summarized in Table 30.2. For more organ-specific labeling, an alternative strategy is to introduce a viral vector carrying Cre recombinase into targeted tissue along with a Cre-dependent viral construct. Han et al. (2018) succeeded in establishing this combinatorial viral strategy to selectively label the gut vagal sensory nerve in wild-type mice.

Another advantage of viral vectors is that the titer and the amount of virus are flexibly adjustable for individual research purposes. Rajendran et al. (2019) performed sparse labeling of the efferent vagus nerve innervating the heart in *Chat-ires-Cre* mice by co-administrating two viruses: a low-concentration vector expressing

**Table 30.2** The repertoire of mouse lines and viral vectors for the optogenetic photostimulation of the vagus nerve (reported until April 2020)

| Mouse lines | Viral vector lines (injection site) | Fiber type (organs) | Refs. |
|---|---|---|---|
| WT | *AAV-eGFP* (nodose ganglion) | Afferent fibers | Chang et al. (2015) Williams et al. (2016) Min et al. (2019) Prescott et al. (2020) |
| *Vglut2-ires-Cre* | *AAV-flex-tdTomato* (nodose ganglion) | Afferent fibers | |
| *Npy2r-ires-Cre* | | Afferent C fibers (airway and lungs) | |
| *P2ry1-ires-Cre* | | Afferent A fibers (airway and lungs) | |
| *Glp1r-ires-Cre* | | Afferent C fibers (intestine and stomach) | |
| *Gpr65-ires-Cre* | | Afferent C fibers (duodenum) | |
| *Piezo2-ires-Cre* | | Afferent A and C fibers (aortic arch) | |
| *Oxtr-T2A-Cre-D* | *AAV-EF1(or CAG)-DIO-ChR2-mCherry* (nodose ganglion) | Afferent fibers (stomach) | Bai et al. (2019) |
| *Vip-ires-Cre* | | Afferent fibers (intestine) | |
| *Nav1.8-Cre* | *AAV-CAG-DIO-tdTomato* (nodose ganglion) | Afferent fibers | |
| *Calca-Cre$^{ER}$* | | Afferent fibers (intestine and stomach) | |
| *Sst-ires-Cre* | | | |
| *Uts2b-2A-Cre* | | Afferent fibers (intestine) | |
| *Chat-ires-Cre* | *AAV-PHP.S:CAG-DIO-XFPs* (retro-orbital) | Efferent fibers | Rajendran et al. (2019) |
| | (1) *AAV-PHP.S:ihSyn1-DIO-tTA*[a] (2) *AAV-PHP.S:TRE-DIO-XFPs*[a] (retro-orbital) | | |
| WT | (1) *AAV-EF1a-DIO-hChR2(H134R)-EYFP* (nodose ganglion) (2) *AAVrg-pmSyn1-EBFP-Cre* (stomach, duodenum, proximal jejunum) | Afferent fibers (stomach, duodenum, proximal jejunum) | Han et al. (2018) |
| WT | (1) *AAV-hSyn-DIO-rM3D(Gs)-mCherry* (nodose ganglion) (2) *CAV2-Cre-GFP* (stomach, duodenum, proximal jejunum) | | |
| WT | (1) *AAV-CAG-lox-tdTomato-2A-cmHTK* (nodose ganglion) (2) *AAVrg-pmSyn1-EBFP-Cre* (stomach, duodenum, proximal jejunum) | | |

[a]These viral vectors are used for sparse neuronal labeling by the tTA–TRE system

the tetracycline transactivator (tTA) and a high-concentration vector expressing fluorescent proteins from the tetracycline-responsive element (TRE) promoter in a Cre-dependent manner (*ihSyn1-DIO-tTA* and *TRE-DIO-XFPs*). Compared with a general labeling method, low-density labeling by the tTA/TRE expression system enabled more efficient tracing of vagus nerve morphology. This vector tool will also be helpful to finely manipulate the vagus nerve.

In addition, a novel capsid variant, *ssAAV-PHP.S*, which enables more efficient transduction

of transgenes to peripheral visceral organs was recently developed (Chan et al. 2017). In the efferent vagal nervous system, this viral vector can selectively label postganglionic neurons closer to effector organs, rather than preganglionic neurons. Rajendran et al. (2019) performed the intravenous administration of a viral vector, *ssAAV-PHP. S:CAG-DIO-ChR2-eYFP*, through the retro-orbital venous sinus and confirmed a pronounced decrease in heart rate induced by the photoactivation of postganglionic cholinergic neurons in the inferior pulmonary vein–ganglionated plexus.

## 30.3 Optogenetic Manipulation of the Vagus Nerve Innervating Visceral Organs

In this section, we describe novel optogenetic approaches for vagal nerve control of individual visceral organs.

### 30.3.1 Optogenetic Manipulation in the Cardiac System

Classic physiological and pharmacological studies have thoroughly established that the efferent vagus nerve innervating the heart sends parasympathetic cholinergic signals to lower the heart rate via the activation of heart muscarinic receptors. However, appropriate experimental techniques to selectively visualize and manipulate the parasympathetic pathway have been absent. Rajendran et al. (2019) overcame this technical limitation using bigenic mouse lines and viral vectors, as described in the previous session. They visualized the 3D anatomical structures of parasympathetic cholinergic nerve projections that control mouse heart rate by the iDISCO heart clearing method (Renier et al. 2014). Moreover, they could reduce the heart rate by the photostimulation of the ChR2-expressing efferent vagus nerve both in vivo and ex vivo in *Chat-ires-Cre; lox-ChR2* mice and AAV-PHP. S-infected mice (Moreno et al. 2019; Rajendran et al. 2019). Such optogenetic photostimulation could replicate the heartbeat reduction effect more precisely than with conventional vagus nerve electrical stimulation, in which both afferent and efferent pathways are nonselectively activated, highlighting the advantage of utilizing optogenetic molecular tools to selectively activate the efferent vagus nerve. In addition to parasympathetic nerves, Rajendran et al. (2019) induced heartbeat increases by the focal illumination of ChR2-expressing noradrenergic sympathetic neurons above the craniomedial right stellate ganglia or right T2 ganglion in *TH-ires-Cre; lox-ChR2* mice. The studies demonstrated that the application of optogenetic molecular tools is effective in functionally dissecting parasympathetic and sympathetic neural circuits involved in heart rate regulation. (Zeng et al. 2018) and (Min et al. 2019) showed that the optogenetic activation of the afferent vagal nerve expressing Piezo2, a mechanically activated ion channel, induced bradycardia and decreased blood pressure through baroreflex in *Piezo2GFP-ires-Cre; lox-ChR2* mice. Further physiological experiments using such optogenetic molecular tools are needed to understand the relative contributions of vagal efferent and afferent fibers to cardiac function.

### 30.3.2 Optogenetic Manipulation in the Respiratory System

Vagal sensory nerve fibers innervating the respiratory system are essential to maintain normal breathing. Tränkner et al. (2014) first reported an optogenetic approach to regulate vagus nerve-induced respiration by engineering a bigenic mouse line, *transient receptor potential vanilloid 1 (TRPV1)-ires-Cre; lox-ChR2* mice. They showed that the photoactivation of ChR2 in TRPV1-expressing vagal ganglia that had been immune-sensitized with ovalbumin caused airway hyperreactivity. Chang et al. (2015) studied two distinct types of lung-innervating vagal sensory neurons, P2ry1 neurons terminating in the lateral NTS and Npy2r neurons terminating in the medial posterior NTS. They demonstrated that the optogenetic activation of Npy2r neurons elevated respiration rates in *Npy2r-ires-Cre; lox-ChR2*

mice, whereas that of P2ry1 neurons transiently inhibited respiration in *P2ry1-ires-Cre; lox-ChR2* mice. Similarly, Nonomura et al. (2017) showed that the photoactivation of airway-innervating Piezo2-expressing vagal nerve trunk led to apnea. More recently, with a combination of mouse lines *Vglut2-ires-Cre; loxP-ChR2, Chat-ires-Cre; loxP-ChR2, and P2ry1-ires-Cre; loxP-ChR2* mice, Prescott et al. (2020) discovered a novel type of vagal afferent neurons to prevent infiltration and injury within the respiratory tract. These studies suggest that the effects of vagal nerve activation are more complicated than expected. Future applications of optogenetic molecular tools are expected to further unveil the detailed physiology of the respiratory system.

### 30.3.3 Optogenetic Manipulation in the Gastrointestinal System

Afferent vagal neurons in the gastrointestinal tract play a central role in the gut–brain axis (Box 30.1 and Fig. 30.3) by surveying and controlling the physiological states of the digestive system. In particular, vagus nerve fibers expressing GLP1R and GPR65 are both C fibers innervating the stomach and intestinal villi, respectively. Using calcium imaging techniques in *Glp1r-ires-Cre; lox-GCaMP3* and *Gpr65-ires-Cre; lox-GCaMP3* mice described in Sect. 30.2.3.1, Williams et al. (2016) revealed that GLP1R vagal neurons respond to mechanical stretch in stomach and intestine muscles, whereas GPR65 vagal neurons respond to intestinal nutrients. They next expressed ChR2 in these subclasses of neurons by creating *Glp1r-ires-Cre; lox-ChR2* and *Gpr65-ires-Cre; lox-ChR2* mice. The selective activation of GLP1R neurons and GPR65 neurons by the photostimulation of the bundle of the left vagus nerve in these mice resulted in pronounced increases and decreases in gastric pressure, respectively, with minor changes in instantaneous heart rates and respiratory rates. Furthermore, Bai et al. (2019) showed that selective optogenetic activation of GLP1R neurons, not GPR65 neurons, reduced food intake. These studies are good state-of-the-art examples achieving the cell-type-specific monitoring and manipulation of the vagus nerve, demonstrating the anatomical and functional segregation of two distinct subtypes of vagal neurons innervating the gut.

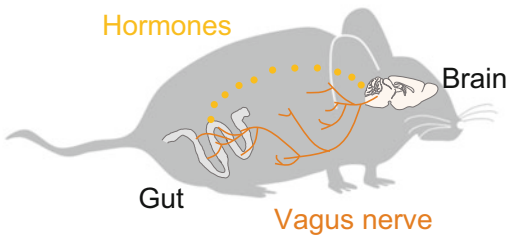


**Fig. 30.3** The gut–brain axis connecting between the brain and peripheral the gastrointestinal tract via neural and humoral processes

**Box 30.1: The Gut–Brain Axis and the Vagus Nerve**

The gut–brain axis refers to a bidirectional communication between the brain and the gastrointestinal tract (Fig. 30.3). In the axis, the afferent vagus nerve innervating the gut is a central pathway to transfer information regarding digestive states in the organs to the brain and influence psychiatric states such as cognition, reinforcement, and emotion, which are typical mechanisms of so-called interoception (Garfinkel and Critchley 2016). While the detailed neuronal circuit and physiological mechanisms for the gut-innervating vagus nerve have been fully identified, recent studies begin to unveil how they anatomically innervate the brain and how transferred viscerosensory information physiologically affect brain neural circuits underlying emotion and arousal (Bravo et al. 2011; Han et al. 2018; Nishimura et al. 2020). Furthermore, it has been reported that changes in intestinal bacteria by an oral gavage of bacteria strains can ameliorate several symptoms of autism spectrum disorders via the vagus nerve (Sgritta et al. 2019),

(continued)

**Box 30.1** (continued)

highlighting a therapeutic target to treat some psychiatric disorders. As an experimental tool to selectively manipulate specific vagus nerve, optogenetic molecular tools will be useful to further elucidate novel physiological mechanisms in the gut–brain axis.

The final destination of the afferent vagus nerve innervating the gastrointestinal system is the NTS in the brain, i.e., the so-called the gut–brain axis. To examine how gut-derived afferent vagus nerve signals affect motivational and emotional behavior, Han et al. (2018) expressed ChR2 in upper gut-innervating vagal sensory neurons in wild-type mice using a combinatorial viral strategy (see Sect. 30.2.3.2). They showed that the photoactivation of these vagal sensory neurons evoked increased self-stimulation behavior and place preference, both of which represent reward behavior, in freely moving conditions through dopamine release in the brain. This study is a direct demonstration that the afferent vagus nerve is actually involved in interoception (Garfinkel and Critchley 2016; Pfeifer et al. 2017).

Furthermore, a recent study has demonstrated that optogenetic manipulation is applicable to not only the vagus nerve but also gut epithelial sensory cells, cell populations that detect nutrients and send signals to the afferent vagus nerve (Kaelberer et al. 2018).

## 30.4 Future Perspectives

As shown in this review, optogenetic molecular tools have enabled us to examine the physiological significance of vagus nerve signals that have not been tested with the existing methods. As the vagus nerve innervates many visceral organs, including the cardiac system, respiratory system, and gastrointestinal system, the application of these experimental tools is not restricted within a single organ but will be useful to study interactions across multiple organs.

Especially, the afferent vagus nerve is crucially related to interoception in which the brain senses the activity states of the peripheral organs (Garfinkel and Critchley 2016; Pfeifer et al. 2017). The idea of interoception recently attracts considerable attention as it is a unique neurophysiological process from peripheral organs to influence brain functions such as cognition, arousal, and emotion. In other words, brain information processing is not simply initiated within the brain but also induced by the peripheral body. However, as interoception is a result of complex integration of different types of sensory information such as hormonal, nociceptive, thermal, and visceromotor information to the central nervous system (Quadt et al. 2018), traditional physiological studies could not easily examine the contribution of single pathways to interoception due to the lack of experimental techniques to dissect and extract each pathway, including specific organ-innervating vagus nerves. As reviewed in this paper, optogenetic molecular tools have a great potential to overcome this issue. For example, as shown by Han et al. (2018), the cell-type-specific photoactivation of upper gut-innervating vagal neurons could induce reward behavior. These reports are still the beginning of new studies of interoception and further extensive applications of optogenetic molecular tools will be helpful to understand the exact contribution of the vagus nerve to interoception. Interesting questions include whether the observations reported in these papers actually work under natural conditions and whether the afferent vagus nerve innervating other organs induces similar or different effects on the brain functions.

Another interesting topic related to the vagus nerve is the therapeutic effect of vagus nerve stimulation. Clinical studies have demonstrated that electrical vagus nerve stimulation can inhibit refractory epilepsy (Ben-Menachem et al. 1994; Takaya et al. 1996) and treatment-resistant depression (Nemeroff et al. 2006; Wani et al. 2013). However, such nonselective electrical stimulation affects all vagal neuron cell types, and the detailed mechanisms underlying these

therapeutic effects, thus, remain unknown. Cell-type specificity provided by optogenetic molecular tools will enable the functional dissection of vagal nerve subpopulations that are related or unrelated to vagus nerve-derived therapy for diseases in the brain.

While the insights obtained from these studies have been relatively few and sparse compared with those from studies in the central nervous system, accumulating evidence from future enduring research will potentially open new avenues in the study of the vagal nervous system.

**Acknowledgments** This work was supported by Kakenhi (19H04897; 20H03545) from the Japan Society for the Promotion of Science (JSPS) and Precursory Research for Embryonic Science and Technology (JPMJPR1785) from the Japan Science and Technology Agency (JST).

## References

Agostoni E, Chinnock JE, De Daly MB, Murray JG (1957) Functional and histological studies of the vagus nerve and its branches to the heart, lungs and abdominal viscera in the cat. J Physiol 135:182–205

Alexander GM, Huang Y, Soderblom EJ, He XP, Moseley AM, McNamara JO (2017) Vagal nerve stimulation modifies neuronal activity and the proteome of excitatory synapses of amygdala/piriform cortex. J Neurochem 140:629–644. https://doi.org/10.1111/jnc.13931

Bai L, Mesgarzadeh S, Ramesh KS, Huey EL, Liu Y, Gray LA, Aitken TJ, Chen Y, Beutler LR, Ahn JS, Madisen L, Zeng H, Krasnow MA, Knight ZA (2019) Genetic Identification of Vagal Sensory Neurons That Control Feeding. Cell 179:1129–1143. e1123. https://doi.org/10.1016/j.cell.2019.10.031

Ben-Menachem E, Manon-Espaillat R, Ristanovic R, Wilder BJ, Stefan H, Mirza W, Tarver WB, Wernicke JF (1994) Vagus nerve stimulation for treatment of partial seizures: 1. A controlled study of effect on seizures. First International Vagus Nerve Stimulation Study Group. Epilepsia 35:616–626

Boyden ES, Zhang F, Bamberg E, Nagel G, Deisseroth K (2005) Millisecond-timescale, genetically targeted optical control of neural activity. Nat Neurosci 8:1263–1268. https://doi.org/10.1038/nn1525

Bravo JA, Forsythe P, Chew MV, Escaravage E, Savignac HM, Dinan TG, Bienenstock J, Cryan JF (2011) Ingestion of Lactobacillus strain regulates emotional behavior and central GABA receptor expression in a mouse via the vagus nerve. Proc Natl Acad Sci U S A 108:16050–16055. https://doi.org/10.1073/pnas.1102999108

Cailotto C, Gomez-Pinilla PJ, Costes LM, van der Vliet J, Di Giovangiulio M, Nemethova A, Matteoli G, Boeckxstaens GE (2014) Neuro-anatomical evidence indicating indirect modulation of macrophages by vagal efferents in the intestine but not in the spleen. PLoS One 9:e87785. https://doi.org/10.1371/journal.pone.0087785

Campos CA, Wright JS, Czaja K, Ritter RC (2012) CCK-induced reduction of food intake and hindbrain MAPK signaling are mediated by NMDA receptor activation. Endocrinology 153:2633–2646. https://doi.org/10.1210/en.2012-1025

Cao B, Wang J, Shahed M, Jelfs B, Chan RHM, Li Y (2016) Vagus Nerve Stimulation Alters Phase Synchrony of the Anterior Cingulate Cortex and Facilitates Decision Making in Rats. Sci Rep 6:35135. https://doi.org/10.1038/srep35135

Caravaca AS, Tsaava T, Goldman L, Silverman H, Riggott G, Chavan SS, Bouton C, Tracey KJ, Desimone R, Boyden ES, Sohal HS, Olofsson PS (2017) A novel flexible cuff-like microelectrode for dual purpose, acute and chronic electrical interfacing with the mouse cervical vagus nerve. J Neural Eng 14:066005. https://doi.org/10.1088/1741-2552/aa7a42

Chan KY, Jang MJ, Yoo BB, Greenbaum A, Ravi N, Wu WL, Sanchez-Guardado L, Lois C, Mazmanian SK, Deverman BE, Gradinaru V (2017) Engineered AAVs for efficient noninvasive gene delivery to the central and peripheral nervous systems. Nat Neurosci 20:1172–1179. https://doi.org/10.1038/nn.4593

Chang RB, Strochlic DE, Williams EK, Umans BD, Liberles SD (2015) Vagal Sensory Neuron Subtypes that Differentially Control Breathing. Cell 161:622–633. https://doi.org/10.1016/j.cell.2015.03.022

Czaja K, Ritter RC, Burns GA (2006) Vagal afferent neurons projecting to the stomach and small intestine exhibit multiple N-methyl-D-aspartate receptor subunit phenotypes. Brain Res 1119:86–93. https://doi.org/10.1016/j.brainres.2006.08.042

Evans DH, Murray JG (1954) Histological and functional studies on the fibre composition of the vagus nerve of the rabbit. J Anat 88:320–337

Fox EA, Phillips RJ, Baronowsky EA, Byerly MS, Jones S, Powley TL (2001) Neurotrophin-4 deficient mice have a loss of vagal intraganglionic mechanoreceptors from the small intestine and a disruption of short-term satiety. J Neurosci 21:8602–8615

Garfinkel SN, Critchley HD (2016) Threat and the body: how the heart supports fear processing. Trends Cogn Sci 20:34–46. https://doi.org/10.1016/j.tics.2015.10.005

Han W, Tellez LA, Perkins MH, Perez IO, Qu T, Ferreira J, Ferreira TL, Quinn D, Liu ZW, Gao XB, Kaelberer MM, Bohorquez DV, Shammah-Lagnado SJ, de Lartigue G, de Araujo IE (2018) A neural circuit for gut-induced reward. Cell 175:665–678.e23. https://doi.org/10.1016/j.cell.2018.08.049

Harreby KR, Sevcencu C, Struijk JJ (2011) Early seizure detection in rats based on vagus nerve activity. Med Biol Eng Comput 49:143–151. https://doi.org/10.1007/s11517-010-0683-1

Hayakawa T, Kuwahara-Otani S, Maeda S, Tanaka K, Seki M (2011) Projections of calcitonin gene-related peptide immunoreactive neurons in the vagal ganglia of the rat. J Chem Neuroanat 41:55–62. https://doi.org/10.1016/j.jchemneu.2010.11.003

Kaelberer MM, Buchanan KL, Klein ME, Barth BB, Montoya MM, Shen X, Bohorquez DV (2018) A gut-brain neural circuit for nutrient sensory transduction. Science 361:eaat5236. https://doi.org/10.1126/science.aat5236

Kupari J, Haring M, Agirre E, Castelo-Branco G, Ernfors P (2019) An atlas of vagal sensory neurons and their molecular specialization. Cell Rep 27:2508–2523. e2504. https://doi.org/10.1016/j.celrep.2019.04.096

Larsen L, Wadman W, van Mierlo P, Delbeke J, Grimonprez A, Nieuwenhuyse B, Portelli J, Boon P, Vonck K, Raedt R (2016) Modulation of hippocampal activity by vagus nerve stimulation in freely moving rats. Brain Stimul 9:124–132. https://doi.org/10.1016/j.brs.2015.09.009

McCallum GA, Sui X, Qiu C, Marmerstein J, Zheng Y, Eggers TE, Hu C, Dai L, Durand DM (2017) Chronic interfacing with the autonomic nervous system using carbon nanotube (CNT) yarn electrodes. Sci Rep 7:11723. https://doi.org/10.1038/s41598-017-10639-w

Min S, Chang RB, Prescott SL, Beeler B, Joshi NR, Strochlic DE, Liberles SD (2019) Arterial baroreceptors sense blood pressure through decorated aortic claws. Cell Rep 29:2192–2201.e2193. https://doi.org/10.1016/j.celrep.2019.10.040

Moreno A, Endicott K, Skancke M, Dwyer MK, Brennan J, Efimov IR, Trachiotis G, Mendelowitz D, Kay MW (2019) Sudden heart rate reduction upon optogenetic release of acetylcholine from cardiac parasympathetic neurons in perfused hearts. Front Physiol 10:16. https://doi.org/10.3389/fphys.2019.00016

Nemeroff CB, Mayberg HS, Krahl SE, McNamara J, Frazer A, Henry TR, George MS, Charney DS, Brannan SK (2006) VNS therapy in treatment-resistant depression: clinical evidence and putative neurobiological mechanisms. Neuropsychopharmacology 31:1345–1355. https://doi.org/10.1038/sj.npp.1301082

Nishimura Y, Fukuda Y, Okonogi T, Yoshikawa S, Karasuyama H, Osakabe N, Ikegaya Y, Sasaki T, Adachi T (2020) Dual real-time in vivo monitoring system of the brain-gut axis. Biochem Biophys Res Commun 524:340–345. https://doi.org/10.1016/j.bbrc.2020.01.090

Nonomura K, Woo SH, Chang RB, Gillich A, Qiu Z, Francisco AG, Ranade SS, Liberles SD, Patapoutian A (2017) Piezo2 senses airway stretch and mediates lung inflation-induced apnoea. Nature 541:176–181. https://doi.org/10.1038/nature20793

Pfeifer G, Garfinkel SN, van Praag CD, Sahota K, Betka S, Critchley HD (2017) Feedback from the heart: emotional learning and memory is controlled by cardiac cycle, interoceptive accuracy and personality. Biol Psychol 126:19–29. https://doi.org/10.1016/j.biopsycho.2017.04.001

Prechtl JC, Powley TL (1990) The fiber composition of the abdominal vagus of the rat. Anat Embryol (Berl) 181:101–115

Prescott SL, Umans BD, Williams EK, Brust RD, Liberles SD (2020) An airway protection program revealed by sweeping genetic control of vagal afferents. Cell 181:574–589.e514. https://doi.org/10.1016/j.cell.2020.03.004

Quadt L, Critchley HD, Garfinkel SN (2018) The neurobiology of interoception in health and disease. Ann N Y Acad Sci 1428:112–128. https://doi.org/10.1111/nyas.13915

Rajendran PS, Challis RC, Fowlkes CC, Hanna P, Tompkins JD, Jordan MC, Hiyari S, Gabris-Weber BA, Greenbaum A, Chan KY, Deverman BE, Munzberg H, Ardell JL, Salama G, Gradinaru V, Shivkumar K (2019) Identification of peripheral neural circuits that regulate heart rate using optogenetic and viral vector strategies. Nat Commun 10:1944. https://doi.org/10.1038/s41467-019-09770-1

Renier N, Wu Z, Simon DJ, Yang J, Ariel P, Tessier-Lavigne M (2014) iDISCO: a simple, rapid method to immunolabel large tissue samples for volume imaging. Cell 159:896–910. https://doi.org/10.1016/j.cell.2014.10.010

Sgritta M, Dooling SW, Buffington SA, Momin EN, Francis MB, Britton RA, Costa-Mattioli M (2019) Mechanisms underlying microbial-mediated changes in social behavior in mouse models of autism spectrum disorder. Neuron 101:246–259.e246. https://doi.org/10.1016/j.neuron.2018.11.018

Shikano Y, Nishimura Y, Okonogi T, Ikegaya Y, Sasaki T (2019) Vagus nerve spiking activity associated with locomotion and cortical arousal states in a freely moving rat. Eur J Neurosci 49:1298–1312. https://doi.org/10.1111/ejn.14275

Silverman HA, Stiegler A, Tsaava T, Newman J, Steinberg BE, Battinelli Masi E, Robbiati S, Bouton C, Huerta PT, Chavan SS, Tracey KJ (2018) Standardization of methods to record Vagus nerve activity in mice. Bioelectron Med 4:3

Takaya M, Terry WJ, Naritoku DK (1996) Vagus nerve stimulation induces a sustained anticonvulsant effect. Epilepsia 37:1111–1116

Tränkner D, Hahne N, Sugino K, Hoon MA, Zuker C (2014) Population of sensory neurons essential for asthmatic hyperreactivity of inflamed airways. Proc Natl Acad Sci U S A 111:11515–11520. https://doi.org/10.1073/pnas.1411032111

Tsaava T, Kressel AM, Uryu K, Chavan SS, Tracey KJ, Chang EH (2019) Optogenetic activation of fiber-specific compound action potentials in the mouse

vagus nerve. 2019 9th International IEEE/EMBS Conference on Neural Engineering (NER). pp 867–870

Usami K, Kano R, Kawai K, Noda T, Ishiramatsu T, Saito N, Takahashi H (2013) Modulation of Cortical Synchrony by Vagus Nerve Stimulation in Adult Rats. 2013 35th Annual International Conference of the IEEE Engineering in Medicine and Biology Society (EMBC). 1:5348–5351. https://doi.org/10.1109/EMBC.2013.6610757

Wani A, Trevino K, Marnell P, Husain MM (2013) Advances in brain stimulation for depression. Ann Clin Psychiatry 25:217–224

Weijs TJ, Ruurda JP, Luyer MD, Nieuwenhuijzen GA, van Hillegersberg R, Bleys RL (2015) Topography and extent of pulmonary vagus nerve supply with respect to transthoracic oesophagectomy. J Anat 227:431–439. https://doi.org/10.1111/joa.12366

Williams EK, Chang RB, Strochlic DE, Umans BD, Lowell BB, Liberles SD (2016) Sensory neurons that detect stretch and nutrients in the digestive system. Cell 166:209–221. https://doi.org/10.1016/j.cell.2016.05.011

Woodbury DM, Woodbury JW (1990) Effects of vagal stimulation on experimentally induced seizures in rats. Epilepsia 31(Suppl 2):S7–S19

Zeng WZ, Marshall KL, Min S, Daou I, Chapleau MW, Abboud FM, Liberles SD, Patapoutian A (2018) PIEZOs mediate neuronal sensing of blood pressure and the baroreceptor reflex. Science 362:464–467. https://doi.org/10.1126/science.aau6324

# 31 Multimodal Functional Analysis Platform: 1. Ultrathin Fluorescence Endoscope Imaging System Enables Flexible Functional Brain Imaging

Makoto Osanai, Hideki Miwa, Atsushi Tamura, Satomi Kikuta, Yoshio Iguchi, Yuchio Yanagawa, Kazuto Kobayashi, Norihiro Katayama, Tetsu Tanaka, and Hajime Mushiake

**Abstract**

To elucidate the expression mechanisms of brain functions, we have developed an ultrathin fluorescence endoscope imaging system (U-FEIS) that can image cells in the brain at any depth while minimizing the invasion. The endoscope part of U-FEIS consists of a GRIN lens and a 10,000-pixel image fiber with a diameter of 450 μm. The specialized microscope of U-FEIS is within 30 cm square and includes lenses and optical filters optimized for the endoscope. Using U-FEIS, we successfully visualized neurons expressing GFP with single-cell resolution and recorded the multineuronal activities in vitro and in vivo. U-FEIS can also perform imaging and optical stimulation simultaneously.

M. Osanai (✉)
Laboratory for Physiological Functional Imaging, Department of Medical Physics and Engineering, Division of Health Sciences, Osaka University Graduate School of Medicine, Suita, Japan

Department of Physiology, Tohoku University Graduate School of Medicine, Sendai, Japan

Department of Radiological Imaging and Informatics, Tohoku University Graduate School of Medicine, Sendai, Japan
e-mail: osanai@sahs.med.osaka-u.ac.jp

H. Miwa
Department of Genetic and Behavioral Neuroscience, Gunma University Graduate School of Medicine, Maebashi, Japan

Department of Neuropsychopharmacology, National Institute of Mental Health, National Center of Neurology and Psychiatry, Tokyo, Japan

A. Tamura
Department of Radiological Imaging and Informatics, Tohoku University Graduate School of Medicine, Sendai, Japan

Neurobiology Research Unit, Okinawa Institute of Science and Technology Graduate University, Okinawa, Japan

S. Kikuta
Department of Radiological Imaging and Informatics, Tohoku University Graduate School of Medicine, Sendai, Japan

Systems Neuroscience Section, Primate Research Institute, Kyoto University, Inuyama, Japan

Y. Iguchi · K. Kobayashi
Department of Molecular Genetics, Institute of Biomedical Sciences, Fukushima Medical University School of Medicine, Fukushima, Japan

Y. Yanagawa
Department of Genetic and Behavioral Neuroscience, Gunma University Graduate School of Medicine, Maebashi, Japan

N. Katayama
Biomodeling Laboratory, Department of Applied Information Sciences, Graduate School of Information Sciences, Tohoku University, Sendai, Japan

T. Tanaka
Medical Nanosystem Engineering, Graduate School of Biomedical Engineering, Tohoku University, Sendai, Japan

H. Mushiake
Department of Physiology, Tohoku University Graduate School of Medicine, Sendai, Japan



H. Yawo et al. (eds.), *Optogenetics*, Advances in Experimental Medicine and Biology 1293,
https://doi.org/10.1007/978-981-15-8763-4_31

Therefore, U-FEIS should be a powerful optical tool in neuroscience research.

**Keywords**

Multicellular imaging · Activity imaging · Imaging system · Endoscope · Image fiber · GRIN lens

## Abbreviations

| | |
|---|---|
| GABA | γ-Aminobutyric acid |
| GFP | Green fluorescent protein |
| GRIN lens | Gradient index lens |
| U-FEIS | Ultrathin fluorescence endoscope imaging system |

## 31.1 Multimodal Functional Analysis Platform

To better understand the brain, it is essential to elucidate the function expression mechanisms of brain neural networks. To address this problem, we propose bidirectional research strategies, in which intervention and multimodal neuronal activity measurements of neural circuits are performed on the same animal. Optogenetics is a suitable intervention approach for manipulating neuronal circuits. Multimodal measurements include optical imaging with a specialized endoscope (Osanai et al. this chapter), electrophysiological recording with a multimodal multielectrode array (Tanaka et al. Chap. 32), and behavioral analysis with a spherical treadmill (Katayama et al. Chap. 33) (Fig. 31.1).

By measuring neural circuit activity and behavioral phenotypes using these methods while simultaneously manipulating neural circuits by optogenetic stimulation, one can clarify dynamic changes in neuronal circuits (Mushiake et al. Chap. 34) (Fig. 31.2). We call this strategy for elucidating the expression mechanisms of brain function "Dynamic reverse engineering neuroscience" and call this measurement platform the "Multimodal functional analysis platform." In the following section, we introduce the development philosophy of these measurement systems, the measurement systems developed, and the practical results of dynamic reverse engineering utilizing the "Multimodal functional analysis platform."

## 31.2 Backgrounds

To reveal the mechanisms of function expression mechanisms of the brain as well as those underlying information processing in the brain, we must grasp the dynamics of neuronal circuits by characterizing multicellular and/or multiregional neuronal activities. Multielectrode recordings were often used as a direct approach to revealing circuit dynamics (Nicholson and Llinás 1975; Norman et al. 1999; Kindlundh et al. 2004; Ferguson et al. 2009; Desai et al. 2010; for review see Seymour et al. 2017). Although multielectrode arrays can simultaneously record action potentials or local field potentials from an ensemble of neurons, this approach has the disadvantage of sampling only a small population of neurons and lacks anatomical and cell-type information about the cells that were activated.

To overcome these problems, optical imaging is feasible with fluorescent calcium ($Ca^{2+}$) indicators. Because they produce large signals (more than several percent changes in fluorescence), it is possible to detect the responses of single neurons or some cellular process (e.g., the presynaptic terminal and the dendrite), and the signals of a large population of brain cells can be measured simultaneously (Smetters et al. 1999; Helmchen and Waters 2002; Ikegaya et al. 2005; Osanai et al. 2010). Moreover, when this method is combined with the use of transgenic animals expressing fluorescence proteins or genetically encoded $Ca^{2+}$ indicators in a specific cell type, it is also possible to identify the cell types and cell morphologies (Tian et al. 2012). Intracellular $Ca^{2+}$ concentration ($[Ca^{2+}]_i$) can be increased by subthreshold postsynaptic potentials in the dendritic spine, by sodium or calcium action potentials in entire the cell, or by $Ca^{2+}$-

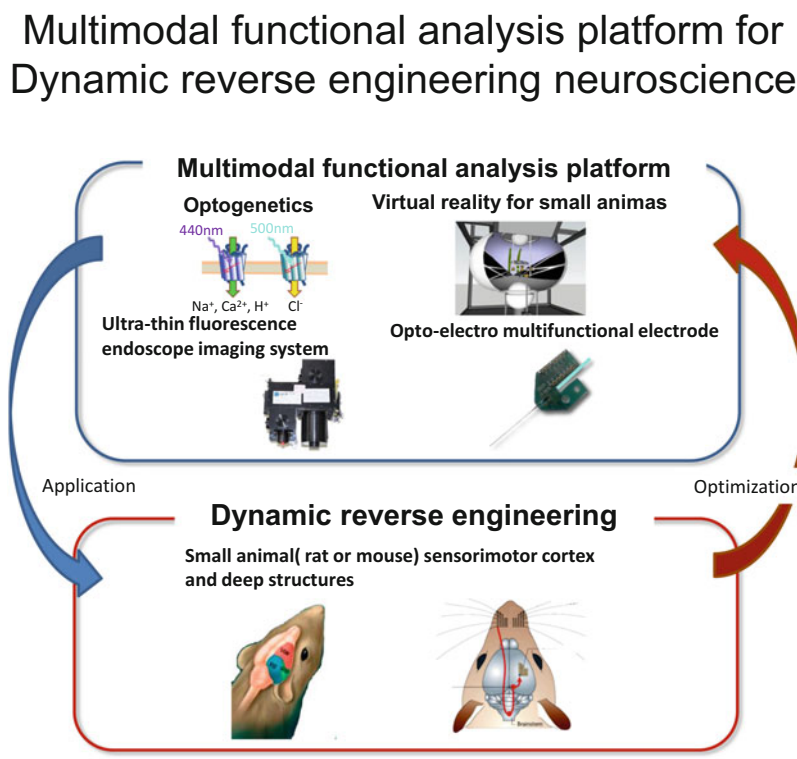


**Fig. 31.1** Conceptual diagram of the multimodal functional analysis platform for dynamic reverse engineering neuroscience

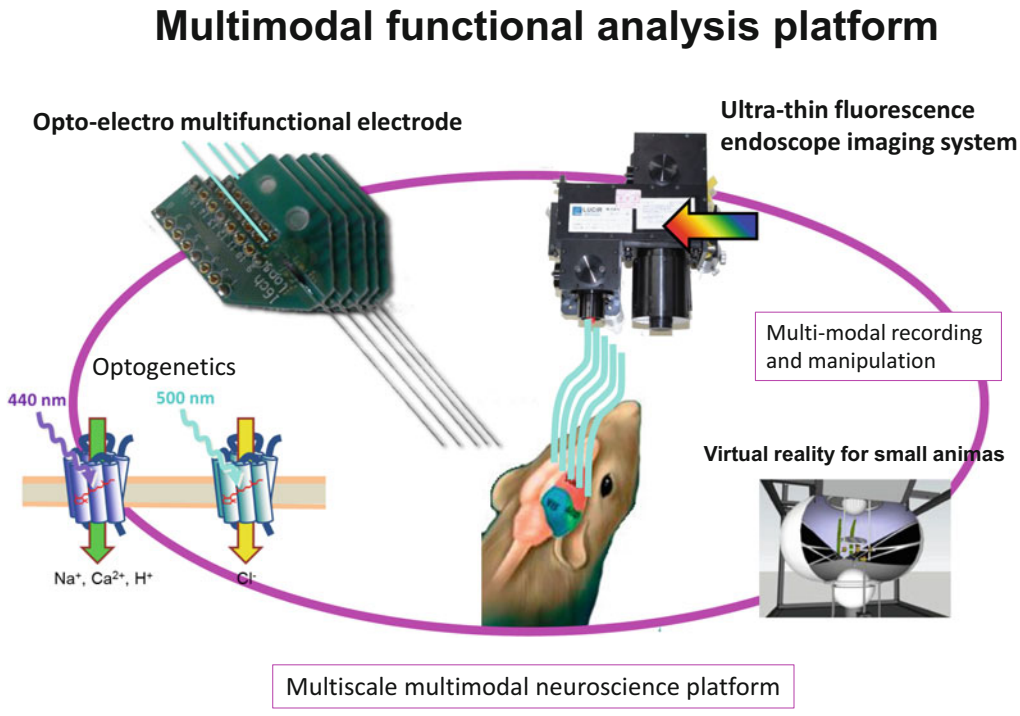


**Fig. 31.2** Multimodal functional analysis platform for neuroscience

release from intracellular $Ca^{2+}$ stores, such as the endoplasmic reticulum (Smetters et al. 1999; Tamura et al. 2014). Therefore, depending on the situation, the $Ca^{2+}$ imaging method can be used to detect many types of neuronal signals.

As an alternative optical recording method, it is also possible to measure intrinsic optical signals, such as changes in flavoprotein fluorescence (Shibuki et al. 2003) and absorption changes due to hemodynamics (Grinvald et al. 1986). Although the monitoring of the intrinsic signals does not afford high spatial resolution and the signals change slowly compared to the dynamics of neuronal activities, it does enable label-free imaging and recording of activity from whole brain.

Optical imaging studies have been performed using in vitro preparations (Smetters et al. 1999; Osanai et al. 2010; Kikuta et al. 2019). However, in vivo studies are needed to elucidate the expression mechanisms of brain functions. Toward this aim, multiphoton imaging studies that record the multicellular neuronal activity in vivo were conducted (Svoboda et al. 1997). However, although multiphoton microscopes can observe deeper brain regions that conventional epifluorescence microscopes, much deeper brain regions, such as the subcortical areas, can hardly be observed with this technique. Moreover, it is difficult to apply multiphoton microscopy to a freely moving animal.

Many attempts at in vivo optical imaging with a specialized microscope have been made (Llewellyn et al. 2008; Murayama and Larkum 2009; Piyawattanmetha et al. 2009; Engelbrecht et al. 2010; Ghosh et al. 2011; Hayashi et al. 2012; Jennings and Stuber 2014). Among them, the small, head-mounted microscope made by Schnitzer and colleagues (Ghosh et al. 2011) can record the multicellular neuronal activities in freely moving animals (Ziv et al. 2013; Ziv and Ghosh 2015) and is already commercially available (nVista, Inscopix; UCLA miniscope). To date, many studies have been conducted using this microscope (Berdyyeva et al. 2014; Harrison et al. 2016; Eisenstein 2019). However, the excitation and emission wavelengths of this microscope are fixed, its size makes it difficult to record activity from multiple regions, and the issue of invasiveness has to be considered.

To resolve these issues, we designed and developed the low-cost Ultrathin Fluorescence Endoscope Imaging System (U-FEIS, Lucir Inc.; Osanai and Mushiake 2017) for functional deep brain imaging. Using U-FEIS, we can less invasively observe the fluorescence of cells at any depth in the brain. In this chapter, we introduce the configuration of U-FEIS, describe the signals that can be observed, and its compatibility with optogenetic studies.

## 31.3 Configuration of U-FEIS

A schematic diagram of U-FEIS is shown in Fig. 31.3. U-FEIS consists of an endoscope and

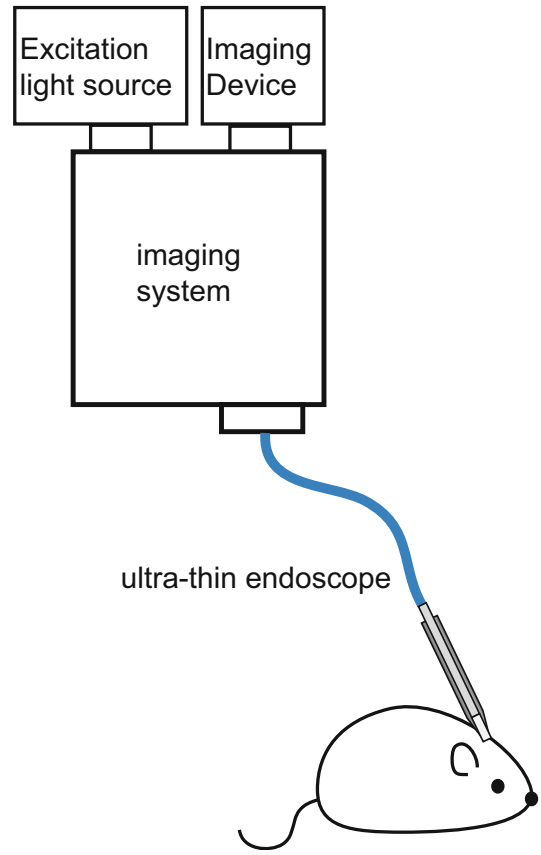


**Fig. 31.3** Schematic diagram of U-FEIS

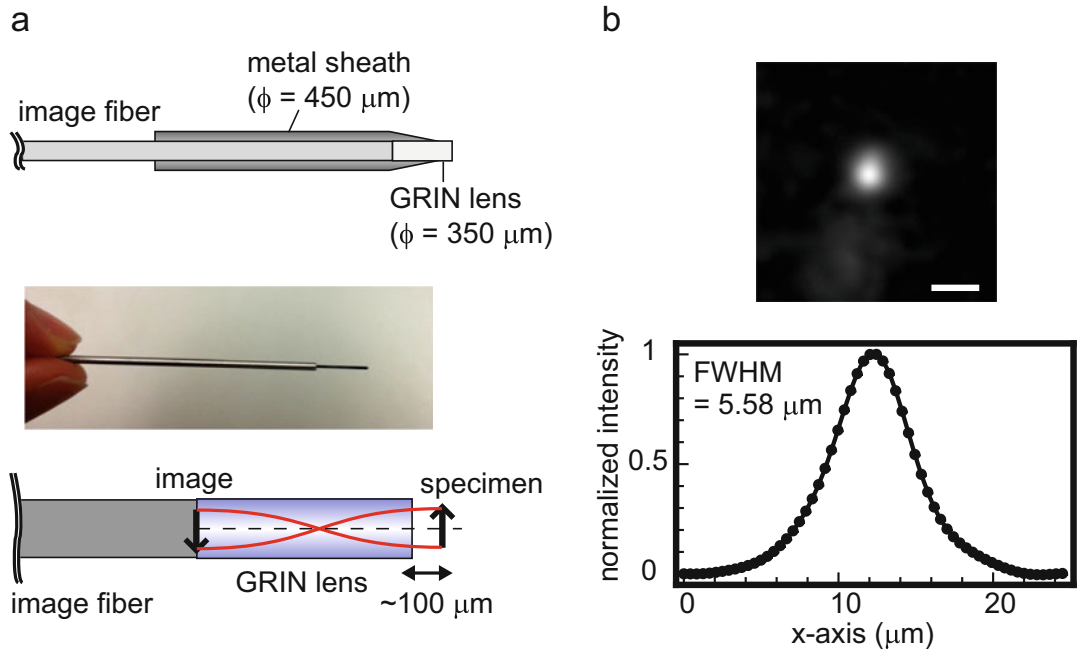


**Fig. 31.4** The U-FEIS endoscope. (**a**) Illustration and photograph of the structure of the ultra-thin endoscope. The endoscope is composed of a 350-μm-diameter GRIN lens and a 350-μm-diameter (without coating), 10,000-pixels image fiber. (**b**) The resolution of the ultra-thin endoscope. Filtered images of a fluorescent, 4-μm microsphere and the *x*–*y* profile of the fluorescence intensity obtained from the filtered image. Scale bar = 10 μm. (Reproduced from Osanai et al. 2013)

a specialized optical system. The endoscope consists of a 350-μm-diameter GRIN lens and a 450-μm-diameter, 10,000-pixel image fiber (FIGH-10-350-S, Fujikura) with a spatial resolution of about 2 μm (Osanai et al. 2013) (Fig. 31.4). This endoscope has a smaller diameter and a higher spatial resolution than traditional endoscopes, making it less invasive and able to visualize individual cells in deep brain regions.

We have also developed a specialized optical system for the endoscope that is within 30 cm square and includes lenses and optical filters optimized for the endoscope (Fig. 31.5). This optical system can be used with any imaging device and any light source as well as with any type of mirror and any type of optical filter. This allows the user to freely select the excitation and the emission wavelengths.

## 31.4 What Signals Can be Observed with U-FEIS

What kind of signal can be measured with U-FEIS? We have tried many types of fluorescence imaging with U-FEIS. To ascertain whether the endoscope is suitable for functional brain imaging, we conducted $Ca^{2+}$ imaging in a striatal slice preparation as a model. Figure 31.6 shows $[Ca^{2+}]_i$ transients evoked by a puff application of high-$K^+$ solution recorded by the endoscope (Osanai et al. 2013). Patchy clusters of high $[Ca^{2+}]_i$ regions were observed with a high signal-to-noise ratio (Fig. 31.6). These responses demonstrate that the endoscope can detect cellular activities. U-FEIS can image the fluorescence from fluorescence-protein-expressing cells in vivo brain. As shown in Fig. 31.7, U-FEIS

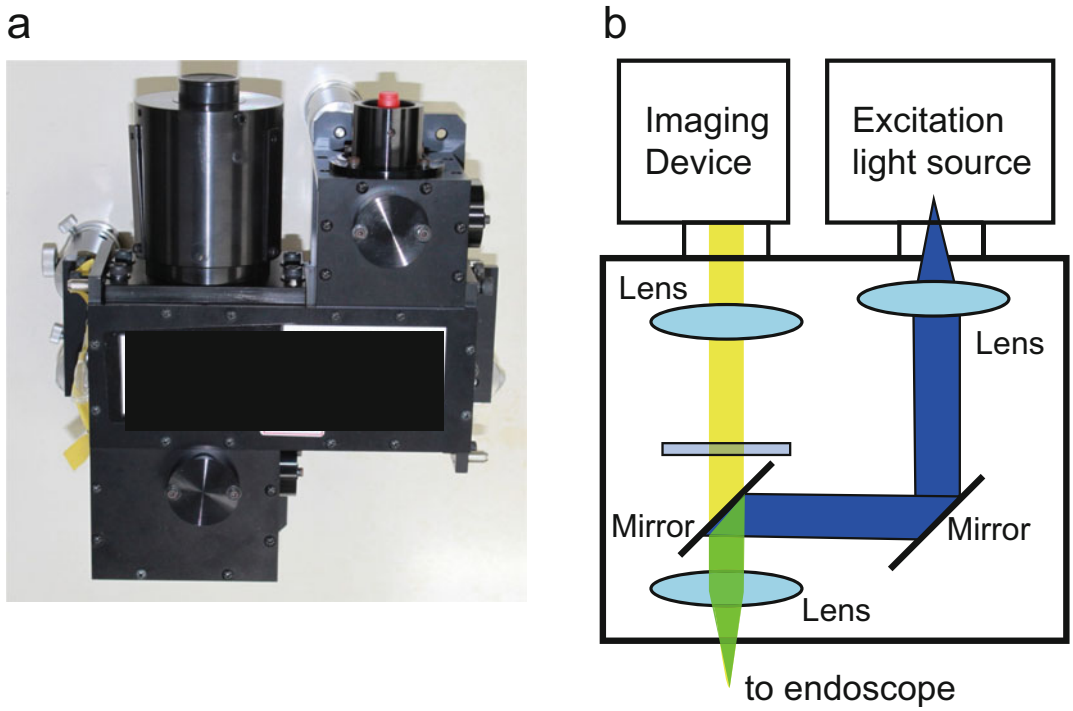


**Fig. 31.5** Photograph (**a**) and optical diagram (**b**) of the specialized optical system for U-FEIS

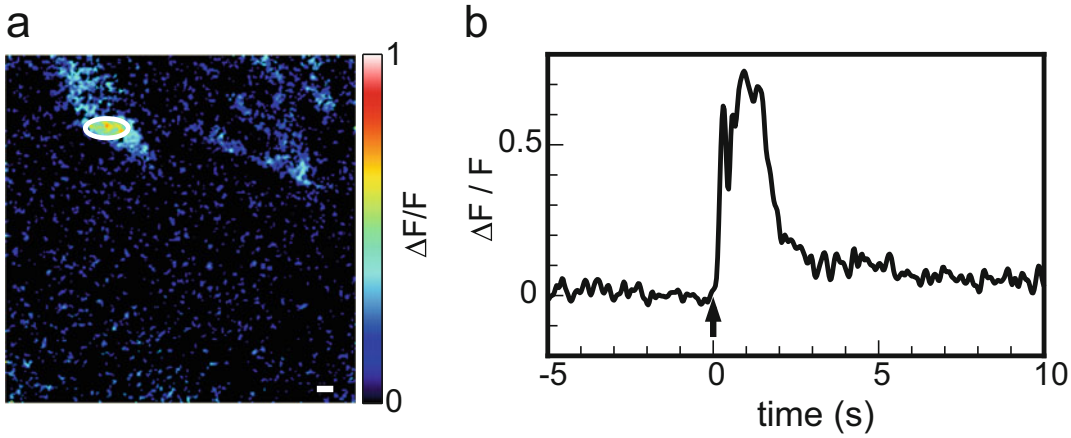


**Fig. 31.6** Cellular $Ca^{2+}$ dynamics were visualized using the endoscope. (**a**) Pseudocolor image of the peak amplitudes of $[Ca^{2+}]_i$ transients evoked with a puff application of high-$K^+$ solution. The peak ΔF/F values in each pixel are indicated by a pseudo-colored scale. Scale bar = 10 μm. (**b**) The time course of $[Ca^{2+}]_i$ transients within the region of interest indicated with a white dashed circle in (**a**). The arrow indicates the time of the high-$K^+$ solution application. (Reproduced from Osanai et al. 2013)

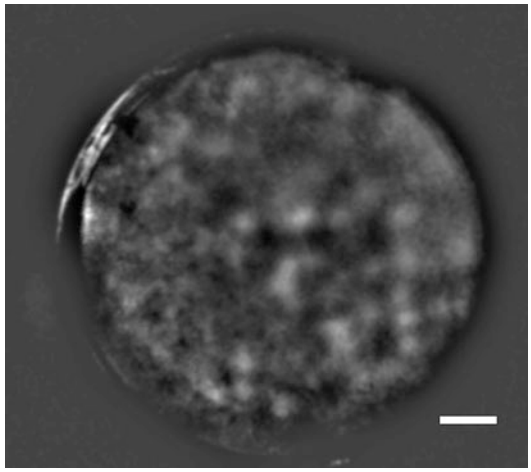

**Fig. 31.7** GFP fluorescence in cortical GABA neurons of GAD67-GFP knock-in mice visualized by U-FEIS. Scale bar = 50 μm

visualized the cortical GFP-positive GABAergic neurons of a GAD67-GFP knock-in mouse (Tamamaki et al. 2003) with single-cell resolution, in vivo.

U-FEIS can also be used for intrinsic signal imaging. The endoscope was inserted into the primary visual cortex and fluorescence was monitored when a contralateral eye was exposed to 10-Hz flashing light (Fig. 31.8). As shown in Fig. 31.8c, a transient change in fluorescence that might be related to the fluorescence of flavoprotein was observed in response to the flashing light, suggesting that the visual response in the mouse visual cortex was detected by U-FEIS in a label-free manner.

To elucidate the mechanisms by which brain functions are expressed, it is necessary to analyze the relationship between the dynamics of neuronal circuit activities and phenotypic behaviors. Thus, neuronal activity must be imaged on animals in action. We are now developing jigs for fixing the endoscope to the head so that the U-FEIS can be used on freely moving animals (Fig. 31.9).

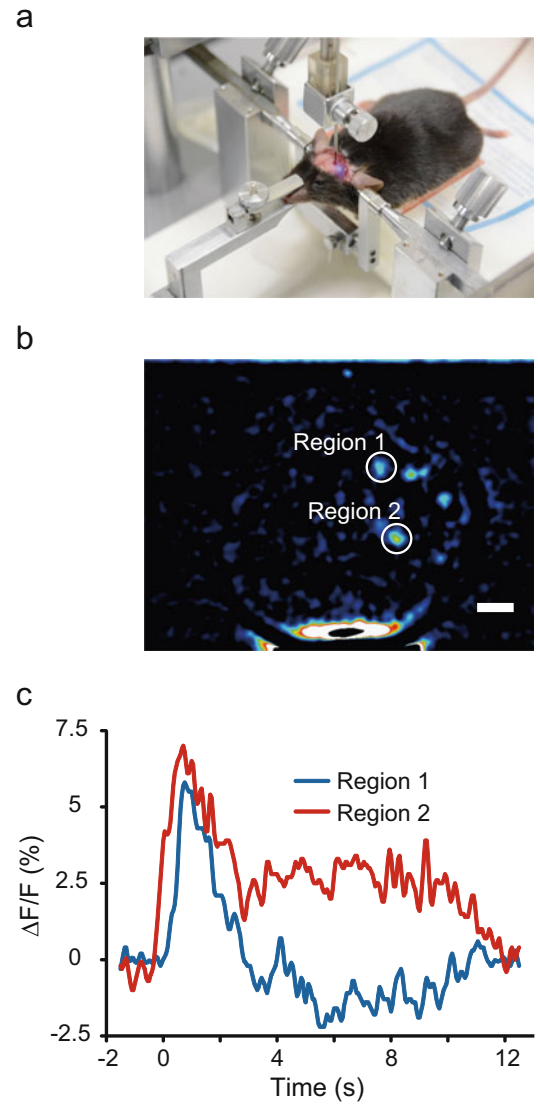


**Fig. 31.8** Cortical response evoked by visual stimuli recorded as an intrinsic fluorescence change (flavoprotein fluorescence) using U-FEIS. (**a**) Photograph of the experimental setup. (**b**) Pseudo color image of the peak amplitudes of the fluorescence change in the visual cortex caused by flashlight stimuli to the contralateral eye. Scale bar = 50 μm. (**c**) Time courses of the fluorescence in the regions of interests indicated with white circles in (**b**)

## 31.5 Optogenetic Experiments with U-FEIS

Optogenetics is a promising tool for understanding the brain. As mentioned above, the U-FEIS can be equipped with any type of light source. By choosing different wavelengths for imaging and for photostimulation to excite optogenetic proteins, the U-FEIS can record changes in neuronal ensemble activity in vivo simultaneously with photostimulation to excite light-sensitive

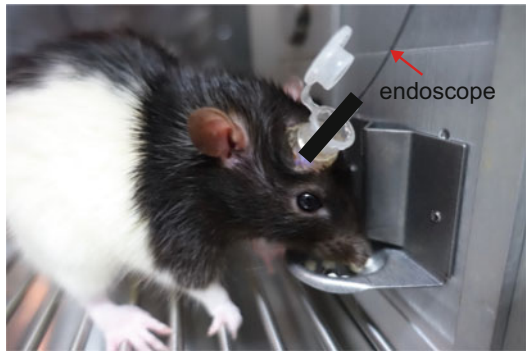


**Fig. 31.9** U-FEIS can be applied to the freely moving animals. Photograph of a freely moving rat in a chamber during $Ca^{2+}$ imaging with U-FEIS

proteins such as channelrhodopsin. Thus, U-FEIS can simultaneously record changes in animal behavior and neuronal circuit dynamics caused by optogenetic manipulation.

## 31.6 Concluding Remarks

We have been developing the U-FEIS for functional brain imaging. It enables us to visualize cellular fluorescence at any depth of the brain and to record multicellular activities in neuronal circuits in vivo. U-FEIS achieves flexible imaging, can record many types of fluorescence and absorption signals, and enables simultaneous optical imaging and optogenetic stimulation. Therefore, U-FEIS is highly suitable for functional cellular imaging in vivo and we hope it will pave the way for significant progress in neuroscience research.

**Acknowledgments** This work was supported by MEXT KAKENHI (Non-linear Neuro-oscillology) JP18H04931 (to MO), JP15H05872 (to YY); MEXT KAKENHI [JP16H06276 (AdAMS); to MO, YY, KK, NK, TT, and HM]; Brain/MINDS [Mapping by Integrated Neurotechnologies for Disease Studies (JP19dm0207001)], AMED (to MO, KK, HM); Program for Revitalization Promotion, JST (to MO); the Matching Planner Program, JST (to MO); "Innovation Inspired by Nature" Research Support Program, SEKISUI CHEMICAL CO. LTD (to MO). We thank Yuji Kohmura, Taro Kojima, and Takehiko Nagai of Lucir Inc. and Daisuke Komada of KYOCERA Corporation for technical assistance.

**Conflict of Interest** The following patent concerning the configuration of U-FEIS is pending: Osanai M, Mushiake H (2017). Optical imaging device. PCT/JP2017/12850, JP2018-508134, US16/089662, CN201780019699.8. Author MO received research support fees from SEKISUI CHEMICAL CO. LTD.

## References

Berdyyeva T, Otte S, Aluisio L, Ziv Y, Burns LD, Dugovic C, Yun S, Ghosh KK, Schnitzer MJ, Lovenberg T, Bonaventure P (2014) Zolpidem reduces hippocampal neuronal activity in freely behaving mice: a large scale calcium imaging study with miniaturized fluorescence microscope. PLoS One 9(11):e112068. https://doi.org/10.1371/journal.pone.0112068

Desai SA, Rolston JD, Guo L, Potter SM (2010) Improving impedance of implantable microwire multielectrode arrays by ultrasonic electroplating of durable platinum black. Front Neuroeng 3:1. https://doi.org/10.3389/fneng.2010.00005

Eisenstein M (2019) On their best behavior. Nat Methods 16:5–8. https://doi.org/10.1038/s41592-018-0277-7

Engelbrecht CJ, Voigt F, Helmchen F (2010) Miniaturized selective plane illumination microscopy for high-contrast in vivo fluorescence imaging. Opt Lett 35:1413–1415

Ferguson JE, Boldt C, Redish AD (2009) Creating low-impedance tetrodes by electroplating with additives. Sens Actuators A Phys 156:388–393. https://doi.org/10.1016/j.sna.2009.10.001

Ghosh KK, Burns LD, Cocker ED, Nimmerjahn A, Ziv Y, El Gamal A, Schnitzer MJ (2011) Miniaturized integration of a fluorescence microscope. Nat Methods 8:871–878

Grinvald A, Lieke E, Frostig RD, Gilbert CD, Wiesel TN (1986) Functional architecture of cortex revealed by optical imaging of intrinsic signals. Nature 324:361–364. https://doi.org/10.1038/324361a0

Harrison TC, Pinto L, Brock JR, Dan Y (2016) Calcium imaging of basal forebrain activity during innate and learned behaviors. Front Neural Circuits 10:36. https://doi.org/10.3389/fncir.2016.00036

Hayashi Y, Tagawa Y, Yawata S, Nakanishi S, Funabiki K (2012) Spatio-temporal control of neural activity in vivo using fluorescence microendoscopy. Eur J Neurosci 36:2722–2732. https://doi.org/10.1111/j.1460-9568.2012.08191.x

Helmchen F, Waters J (2002) $Ca^{2+}$ imaging in the mammalian brain in vivo. Eur J Pharmacol 447:119–129. https://doi.org/10.1016/S0014-2999(02)01836-8

Ikegaya Y, Le Bon-Jego M, Yuste R (2005) Large-scale imaging of cortical network activity with calcium indicators. Neurosci Res 52:132–138

Jennings JH, Stuber GD (2014) Tools for resolving functional activity and connectivity within intact neural

circuits. Curr Biol 24:R41–R50. https://doi.org/10.1016/j.cub.2013.11.042

Kikuta S, Iguchi Y, Kakizaki T, Kobayashi K, Yanagawa Y, Takada M, Osanai M (2019) Store-operated calcium channels are involved in spontaneous slow calcium oscillations in striatal neurons. Front Cell Neurosci 13:547. https://doi.org/10.3389/fncel.2019.00547

Kindlundh M, Norlin P, Hofmann UG (2004) A neural probe process enabling variable electrode configurations. Sensors Actuators B Chem 102:51–58. https://doi.org/10.1016/j.snb.2003.10.009

Llewellyn ME, Barretto RPJ, Delp SL, Scnitzer MJ (2008) Minimally invasive high-speed imaging of sarcomere contractile dynamics in mice and humans. Nature 454:784–788

Murayama M, Larkum ME (2009) In vivo dendritic calcium imaging with a fiberoptic periscope system. Nat Protoc 4:1551–1559

Nicholson C, Llinás R (1975) Real time current source-density analysis using multi-electrode array in cat cerebellum. Brain Res 100:418–424. https://doi.org/10.1016/0006-8993(75)90494-1

Norman RA, Maynard EM, Rousche PJ, Warren DJ (1999) A neural interface for a cortical vision prosthesis. Vis Res 39:2577–2587. https://doi.org/10.1016/S0042-6989(99)00040-1

Osanai M, Mushiake H (2017) Optical imaging device. Patent Application PCT/JP2017/12850, JP 2018-508134, US 16/089662, CN 2017800196998, 29 March 2017

Osanai M, Tanaka S, Takeno Y, Takimoto S, Yagi T (2010) Spatiotemporal properties of the action potential propagation in the mouse visual cortical slice analyzed by calcium imaging. PLoS One 5(10): e13738. https://doi.org/10.1371/journal.pone.0013738

Osanai M, Suzuki T, Tamura A, Yonemura T, Mori I, Yanagawa Y, Yawo H, Mushiake H (2013) Development of a micro-imaging probe for functional brain imaging. Neurosci Res 75:46–52. https://doi.org/10.1016/j.neures.2012.10.008

Piyawattanmetha W, Cocker ED, Burns LD, Baretto RPJ, Jung CJ, Ra H, Solgaard O, Schnitzer MJ (2009) In vivo brain imaging using a portable 2.9 g two-photon microscope based on a microelectromechanical systems scanning mirror. Opt Lett 34:2309–2311

Seymour JP, Wu F, Wise KD, Yoon E (2017) State-of-the-art MEMS and microsystem tools for brain research. Microsyst Nanoeng 3:16066. https://doi.org/10.1038/micronano.2016.66

Shibuki K, Hishida R, Murakami H, Kudoh M, Kawaguchi T, Watanabe M, Watanabe S, Kouuchi T, Tanaka R (2003) Dynamic imaging of somatosensory cortical activity in the rat visualized by flavoprotein autofluorescence. J Physiol 549(3):919–927. https://doi.org/10.1113/jphysiol.2003.040709

Smetters D, Majewska A, Yuste R (1999) Detecting action potentials in neuronal populations with calcium imaging. Methods 18:215–221

Svoboda K, Denk W, Kleinfeld D, Tank DW (1997) In vivo dendritic calcium dynamics in neocortical pyramidal neurons. Nature 385:161–165

Tamamaki N, Yanagawa Y, Tomioka R, Miyazaki J, Obata K, Kaneko T (2003) Green fluorescent protein expression and colocalization with calretinin, parvalbumin, and somatostatin in the GAD67-GFP knock-in mouse. J Comp Neurol 467:60–79

Tamura A, Yamada N, Yaguchi Y, Machida Y, Mori I, Osanai M (2014) Both neurons and astrocytes exhibited tetrodotoxin-resistant metabotropic glutamate receptor-dependent spontaneous slow $Ca^{2+}$ oscillations in striatum. PLoS One 9(1):e85351. https://doi.org/10.1371/journal.pone.0085351

Tian L, Akerboom A, Schreiter ER, Looger LL (2012) Neural activity imaging with genetically encoded calcium indicators. Prog Brain Res 196:79–94. https://doi.org/10.1016/B978-0-444-59426-6.00005-7

Ziv Y, Ghosh KK (2015) Miniature microscopes for large-scale imaging of neuronal activity in freely behaving rodents. Curr Opin Neurobiol 32:141–147. https://doi.org/10.1016/j.conb.2015.04.001

Ziv Y, Burns LD, Cocker ED, Hamel EO, Ghosh KK, Kitch LJ, El Gamal A, Schnitzer MJ (2013) Long-term dynamics of CA1 hippocampal place codes. Nat Neurosci 16:264–266. https://doi.org/10.1038/nn.3329

# 32

# Multimodal Functional Analysis Platform: 2. Development of Si Opto-Electro Multifunctional Neural Probe with Multiple Optical Waveguides and Embedded Optical Fiber for Optogenetics

Tetsu Tanaka, Norihiro Katayama, Kazuhiro Sakamoto, Makoto Osanai, and Hajime Mushiake

**Abstract**

We have developed a Si opt-electro multifunctional neural probe with multiple waveguides and embedded optical fiber for highly accurate optical stimulation. The Si opt-electro multifunctional neural probe had 16 recording sites, three optical waveguides, and metal cover for suppressing light leakage. The other opt-electro multifunctional neural probe had an optical fiber in the trench of the probe shank, which leads to fewer damages to tissues. We evaluated the electrochemical properties of the recording sites and confirmed that the neural probe had suitable characteristics for neural recording. We also demonstrated the optical stimulation to the neurons expressing ChR2 using our probe. As a result, we succeeded in multisite optical stimulation and observed that no light leakage from the optical waveguides because of the metal cover. From in vivo experiments, we successfully recorded optically modulated local field potential using the fabricated Si neural probe with optical waveguides. Moreover, we applied current source density analysis to the recorded LFPs. As a result, we confirmed that the light-induced membrane current sinks in the locally stimulated area. The Si opto-electro multifunctional neural probe is one of the most versatile tools for optogenetics.

**Keywords**

Neural probe · Opto-electro multifunctional · Optical fiber · Optical waveguide

T. Tanaka (✉)
Medical Nanosystem Engineering Laboratory, Graduate School of Biomedical Engineering, Tohoku University, Sendai, Japan
e-mail: ttanaka@bme.tohoku.ac.jp

N. Katayama
Biomodeling Laboratory, Department of Applied Information Sciences, Graduate School of Information Sciences, Tohoku University, Sendai, Japan
e-mail: katayama@ecei.tohoku.ac.jp

K. Sakamoto
Faculty of Medicine, Department of Neuroscience, Tohoku Medical and Pharmaceutical University, Sendai, Japan
e-mail: sakamoto@tohoku-mpu.ac.jp

M. Osanai
Laboratory for Physiological Functional Imaging, Division of Health Sciences, Department of Medical Physics and Engineering, Osaka University Graduate School of Medicine, Suita, Japan
e-mail: osanai@sahs.med.osaka-u.ac.jp

H. Mushiake
Department of Physiology, Tohoku University Graduate School of Medicine, Sendai, Japan
e-mail: hmushiak@med.tohoku.ac.jp



H. Yawo et al. (eds.), *Optogenetics*, Advances in Experimental Medicine and Biology 1293,
https://doi.org/10.1007/978-981-15-8763-4_32

## Abbreviations

| | |
|---|---|
| BMI | Brain–machine interface |
| CSD | Current source density |
| LED | Light-emitting diode |
| LFP | Local field potential |
| LSI | Large-scale integrated circuit |
| MEMS | Microelectromechanical systems |
| PCB | Printed circuit board |
| PECVD | Plasma-enhanced chemical vapor deposition |
| RIE | Reactive-ion etching |
| SiN | Silicon nitride |

## 32.1 Introduction

Recently, lots of researches have dedicated themselves to developing medical treatments for brain diseases, analyzing brain functions, and realizing brain–machine interface (BMI). In this researches, various kinds of neural probes were developed and used for recording neuronal action potentials and other brain activities. Especially, Si neural probe was one of the essential tools. As the Si neural probe was fabricated by micro and nanotechnologies used for MEMS and LSI fabrication, it was possible to realize high-density recording (Sodagar et al. 2009; Du et al. 2009; Harimoto et al. 2011). We also proposed an intelligent Si neural probe system that had multifunctional properties (Kobayashi et al. 2009a, b; Kanno et al. 2009). Figure 32.1 shows a conceptual drawing of the intelligent Si neural probe system. The crucial part of this system was the Si neural probe with high-density recording sites and various sensors. By mounting electrical and chemical sensors on the Si probe, we can record neural activities electrically and chemically. At the other end of the intelligent Si neural probe, electronic circuits such as low-noise amplifiers, multiplexers, and analog-to-digital converters were integrated. The neuronal signals recorded from the brain were amplified while keeping a lower noise level. After that, the recorded neuronal signals from the brain were transmitted to the external recording apparatus by wireless connection. Therefore, once the intelligent Si neural probe system was embedded in freely moving animals, neural recording from the animal brain can be immediately achieved. We reported in vitro and in vivo high-density recording with the double-sided Si neural probes. We successfully recorded neuronal action potentials from the brains of a guinea pig and a macaque (Kobayashi et al. 2009a, b). The Si neural probe with a microfluidic channel was also fabricated and successfully demonstrated fluid delivery into the brain with a microfluidic channel (Kanno et al. 2009).

In this chapter, we described a novel Si opto-electro multifunctional neural probe with multiple optical waveguides and embedded optical fiber for optical stimulation of neurons. We fabricated the Si opto-electro multifunctional neural probe and evaluated the electrochemical and optical characteristics. Additionally, we demonstrated the optical stimulation for neurons expressing ChR2 using the fabricated probe.

## 32.2 Silicon Opto-Electro Multifunctional Neural Probe with Multiple Optical Waveguides and Metal Cover

Direct optical stimulation is an effective method to realize a precise stimulation of neurons. In this method, the gene transfer technology was used, and neurons expressed a light-sensitive channel protein such as Channelrhodopsin-2 (ChR2) (Boyden et al. 2005; Wang et al. 2009; Gradinaru et al. 2009). High spatial and time resolutions and less invasive tissue can be realized with the light for neural stimulation. Moreover, we can electrically record neural reactions simultaneously during the optical stimulation (Sakai et al. 2012).

To realize the optical stimulation to neurons, several kinds of probes capable of delivering light were reported (Zhang et al. 2007, 2009; Royer et al. 2010).

To accurately stimulate the neurons, we proposed the novel Si opto-electro multifunctional neural probe with micromachined optical waveguides for the optical stimulation

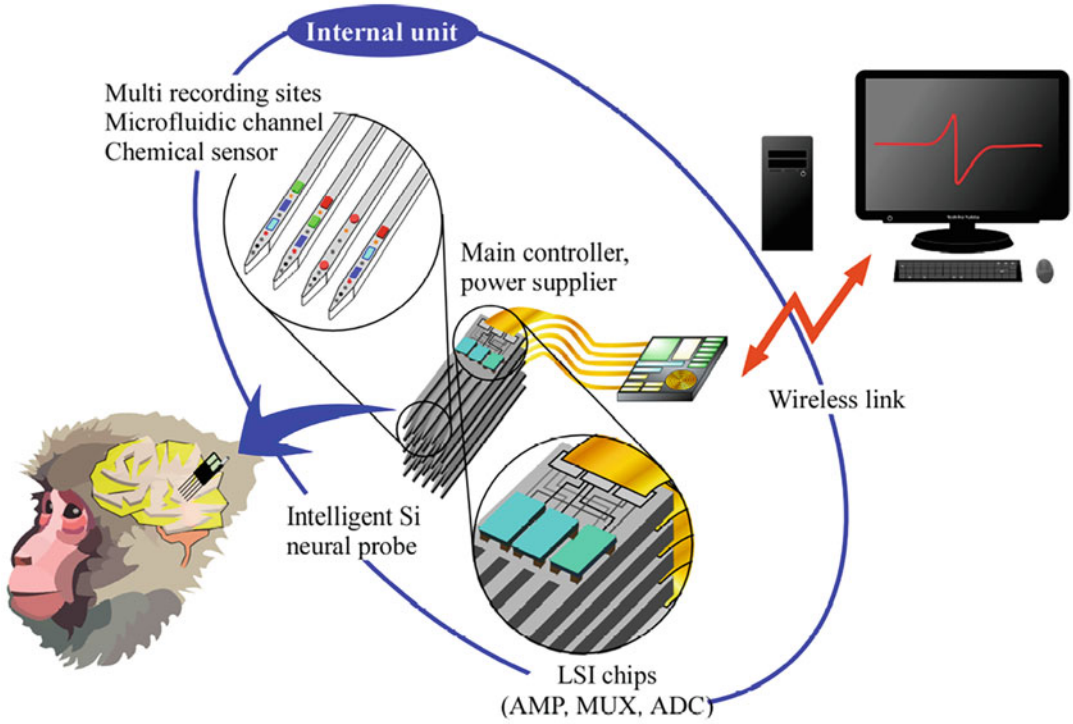


**Fig. 32.1** Conceptual drawing of the Si opto-electro multifunctional neural probe system

(Kobayashi et al. 2011; Kanno et al. 2013). Figure 32.2 shows a conceptual drawing of the Si opto-electro multifunctional neural probe, which has optical waveguides fabricated by micromachining process on the Si probe. Therefore, optical stimulation sites were formed on the probe precisely. As recording electrodes were also formed on the probe, we can record the neural reactions elicited by the optical stimulation simultaneously. The size of the optical waveguide was generally 100th times smaller than that of optical fiber. Thus, we can form several optical waveguides on the same probe and decrease an insertion injury caused by waveguides.

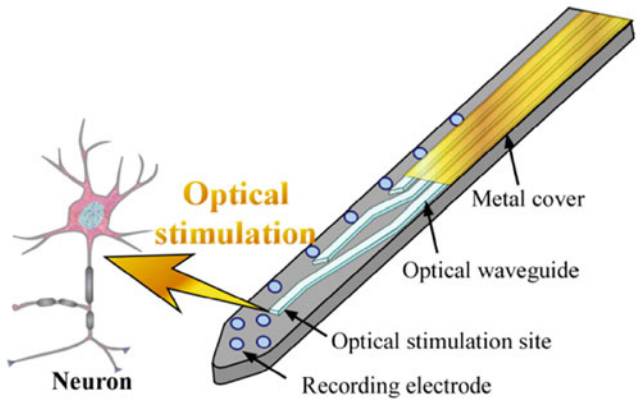


**Fig. 32.2** Si opto-electro multifunctional neural probe with optical waveguides and metal cover

## 32.3 Fabrication of Silicon Opto-Electro Multifunctional Neural Probe with Multiple Optical Waveguides and Metal Cover

A fabrication sequence of our Si opto-neural probe is shown in Fig. 32.3. A 100-μm-thick Si wafer was used as the substrate of the probe. First, a 1-μm-thick $SiO_2$ layer was formed by thermal oxidation. Then, a 1-μm-thick SiN layer for the waveguide core was formed by plasma-enhanced chemical vapor deposition (PECVD). Next, the SiN layer was patterned for optical waveguide shape using reactive-ion etching (RIE) with $CHF_3$ gases. Next, a 1-μm-thick $SiO_2$ layer for waveguide clad was also formed by PECVD. From these processes, optical waveguides were formed. Then, Au/Ti wirings were formed on the surface of the wafer by sputtering and wet etching with an iodine etchant and a dilute HF solution. Then, a 1-μm-thick $SiO_2$ layer was deposited by PECVD for isolation of the wirings. After that, contact holes were opened by RIE with $CHF_3$. Next, both Au recording electrodes and metal covers of optical waveguides were formed using a liftoff process. The metal cover prevented a light leakage from optical waveguides except for light outlets. Finally, the probe shape was formed by deep RIE with $SF_6$ and $C_4F_8$ gases. Using this method, we successfully fabricated the Si opto-electro multifunctional neural probe having three optical waveguides and metal cover.

Figure 32.4a shows the fabricated neural probe with multiple optical waveguides and metal cover. The neural probe was assembled on a printed circuit board (PCB), and optical fibers were connected to the neural probe. Using the optical fibers, it became possible to inject lights into optical waveguides of the neural probe. Figure 32.4b, c shows enlarged views of the probe tip. From these figures, we confirmed that Au recording electrodes, three optical waveguides, and metal covers were well formed on the Si neural probe.

## 32.4 Silicon Opto-Electro Multifunctional Neural Probe with Embedded Optical Fiber

Although several kinds of the Si neural probes which have optical stimulation device/structure such as micro-LED and optical waveguides have been developed, these neural probes have complicated structures and resultant high fabrication costs. In these situations, a neural probe that has a chemically thinned optical fiber has been developed (Royer et al. 2010) and it can be easily used in many experiments owing to its simple structure. However, such a neural probe induces damage to the brain tissues during probe insertion due to protrusion of optical fiber and the resultant large cross section of the probe. In this chapter, we have proposed the Si opto-electro multifunctional neural probe with embedded optical fiber in probe shank (Morikawa et al. 2017). Since a chemically thinned optical fiber was fully embedded in the probe shank, this neural probe can be inserted into the brain without injuring tissues and can optically stimulate the tissues.

## 32.5 Fabrication of Silicon Opto-Electro Multifunctional Neural Probe with Embedded Optical Fiber

Figure 32.5 shows a fabrication process flow of the Si opto-neural probe. A 100-μm-thick Si wafer was used as the substrate of the probe. First, a 1-μm-thick $SiO_2$ layer was formed by thermal oxidation. Then, the base polyimide layer was spin-coated on the silicon substrate. Ti/Au/Ti wirings were formed on the surface of the base polyimide layer by sputtering and wet-etched by an iodine etchant and HF solution. Then, the insulation polyimide layer was also spin-coated and contact holes were formed. Next, Au recording electrodes were formed on the insulation polyimide layer by sputtering and wet-etching. Finally, the probe shape with a

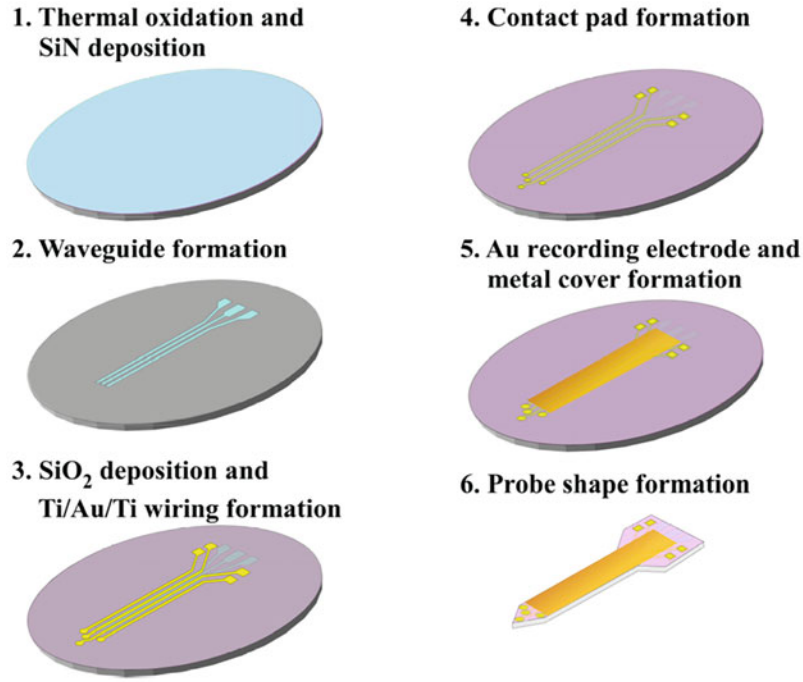


**Fig. 32.3** Fabrication process of the Si opto-electro multifunctional neural probe with optical waveguides and metal cover

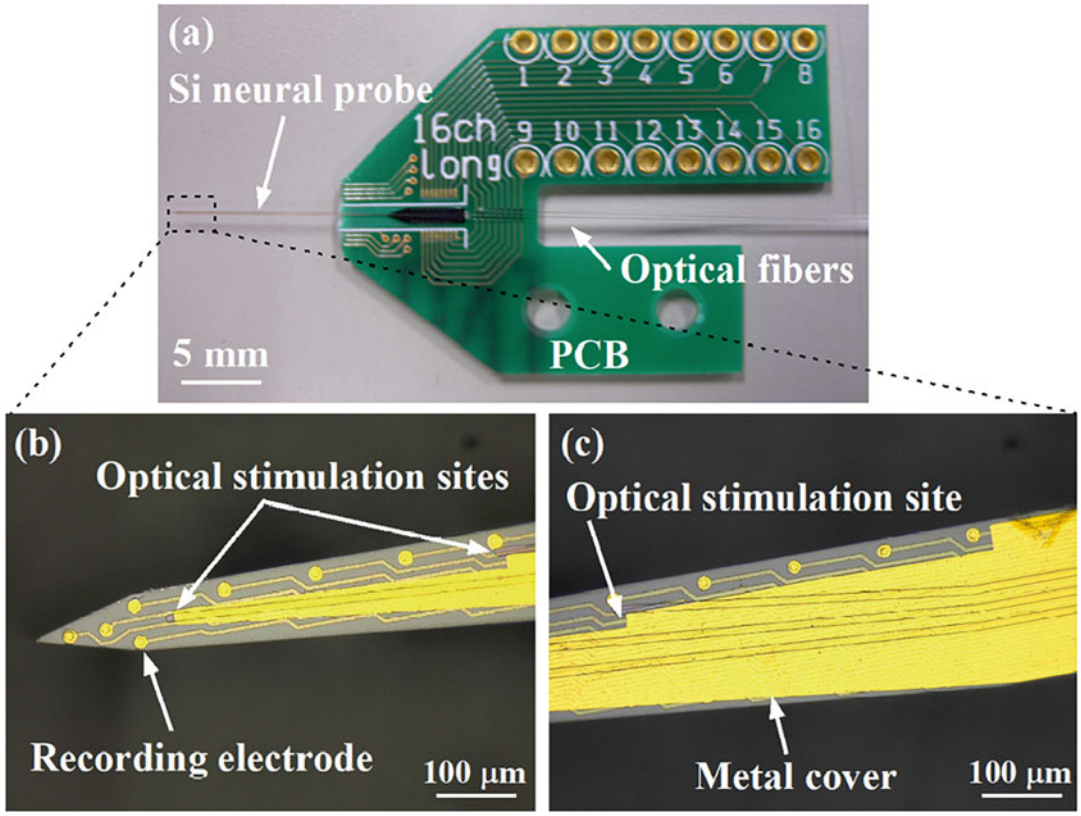


**Fig. 32.4** Fabricated Si opto-electro multifunctional neural probe with three optical waveguides and metal cover

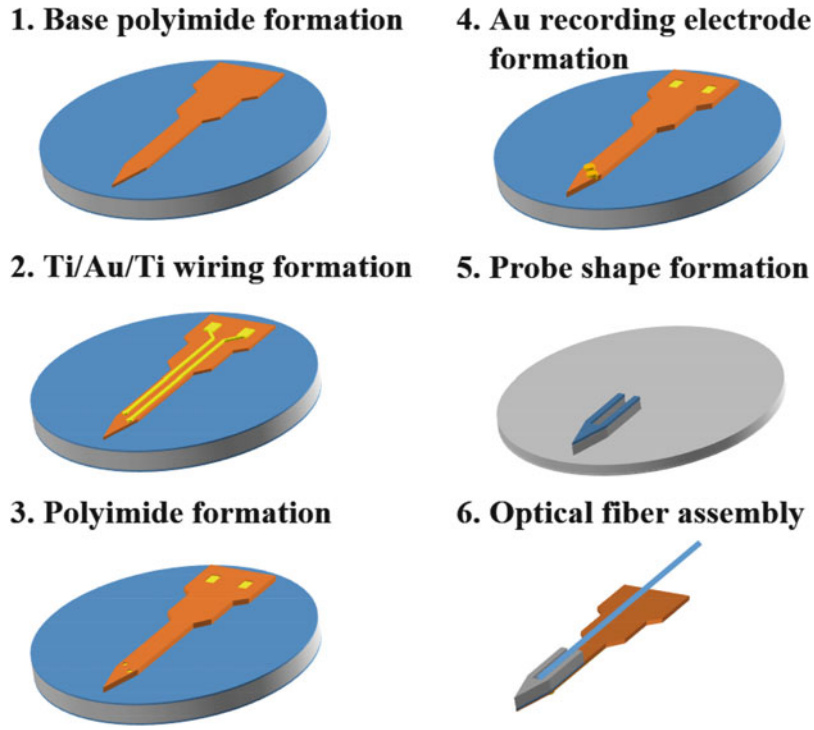


**Fig. 32.5** Fabrication process of the Si opto-electro multifunctional neural probe with embedded optical fiber in the trench of the probe shank

trench for embedding was formed by deep reactive-ion etching with $SF_6$ and $C_4F_8$ gases. Besides, an optical fiber was etched by HF dipping. Figure 32.6 shows a laser micrograph of the fabricated Si probe with the 60-μm-depth trench in the Si probe shank. The optical fibers adhered to the Si neural probe with UV curable epoxy. Figure 32.7 shows the fabricated Si neural probes with the chemically thinned optical fiber.

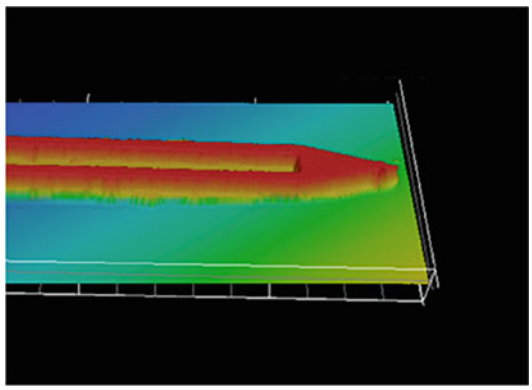

**Fig. 32.6** Laser micrograph of the neural probe with a 60-μm-depth trench in the Si probe shank

## 32.6 Evaluation of Silicon Opto-Electro Multifunctional Neural Probe with Multiple Optical Waveguides and Metal Cover

### 32.6.1 Electrochemical Characteristics

At first, to confirm the capability of neural recording, we evaluated the electrochemical characteristics of the fabricated probe. We measured electrochemical impedance of recording electrodes in an electrolyte with the 10 mV AC signal and the frequency ranging from 100 Hz to 10 kHz in phosphate-buffered saline. In the measurement, we used the Pt electrode as the counter electrode and Ag/AgCl electrode to reference one. Figure 32.8 shows the electrochemical impedance spectroscopy of the Si

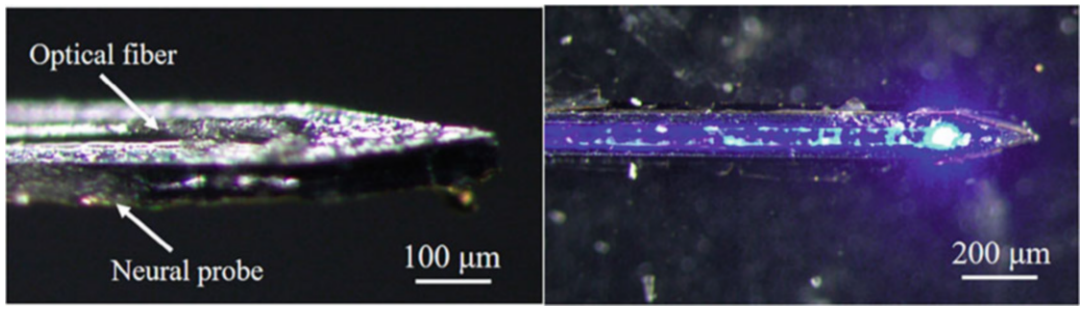


**Fig. 32.7** Photographs of Si opto-electro multifunctional neural probe with an optical fiber embedded in a 60-μm-depth trench of the Si probe shank (left) and under light irradiation (right)

opto-electro multifunctional neural probe. The impedance value was about 1.5 Mohm at a frequency of 1 kHz. From this result, we confirmed that this probe had a suitable impedance value for neuronal recording.

### 32.6.2 Optical Characteristics

We confirmed the optical characteristics of the Si opto-electro multifunctional neural probe. We performed the optical stimulation to neurons expressing the ChR2. Since sensitive wavelengths of a cell expressing ChR2 were 400–560 nm (Wang et al. 2009), a light source was a blue laser with a wavelength of 452 nm. The Si opto-electro multifunctional neural probe was connected with laser sources via optical fibers. Using this setup, we injected light into optical waveguides independently. Figure 32.9 shows light outputs from the multiple optical stimulation sites. Figure 32.9a shows the probe tip and three optical stimulation sites were observed. Figure 32.9b–d shows the light output from the three optical stimulation sites, respectively. From this result, we confirmed that it was entirely possible to optically and independently stimulate multi-points in the brain.

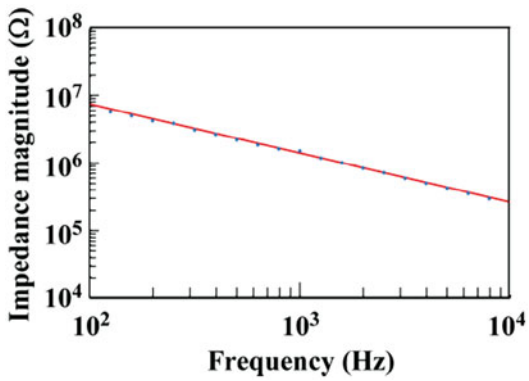


**Fig. 32.8** Measured electrochemical impedance values of the recording electrode on the neural probe

### 32.6.3 In Vivo Experiments

In this chapter, we demonstrated the optical stimulation for neurons using the fabricated neural probe. All the animal experiments were approved by the Tohoku University Committee for Animal Experiments. They were carried out following the Guidelines for Animal Experiments and Related Activities in Tohoku University as well as the guiding principles of the Physiological Society of Japan and the National Institutes of Health. In this experiment, we used the transgenic rat, which expressed the ChR2 in the neural tissue of the whole body. We also used a 452-nm wavelength laser diode as the light source. The neural probe was connected with this laser diode by an optical fiber. Figure 32.10 shows the insertion of the neural probe into the rat brain. The rat was in an anesthetized condition, and the neural probe was inserted in an M1 area of the rat brain. The stimulation light exposed from the optical stimulation site 3, shown in Fig. 32.9a. Then, we optically stimulated neurons and recorded local field

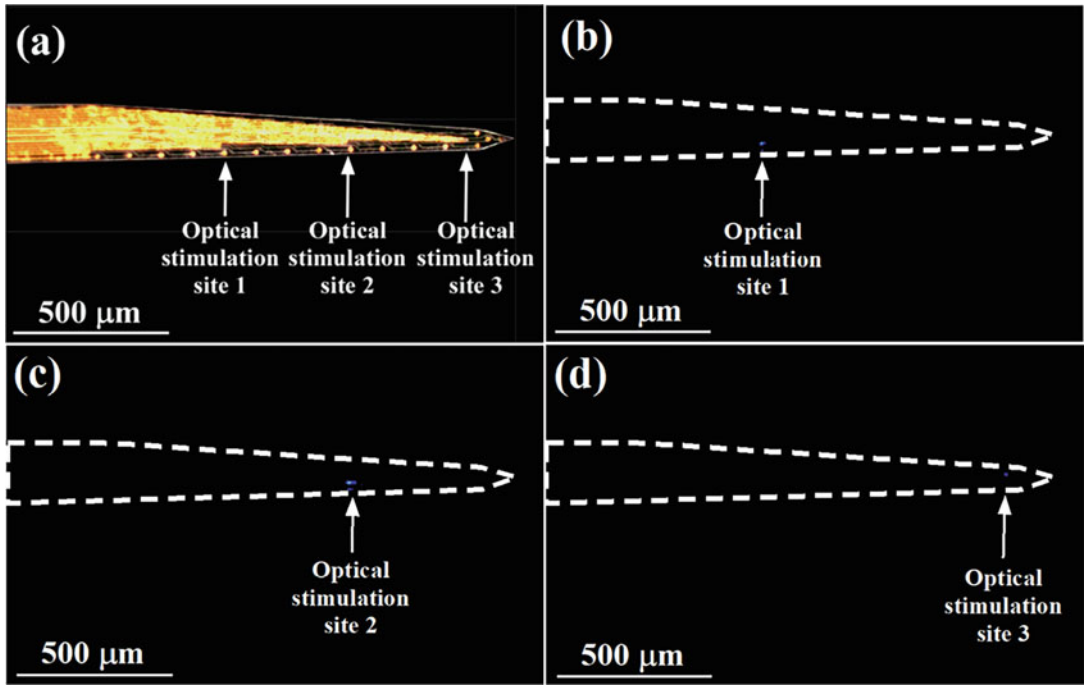


**Fig. 32.9** Multisite optical outputs using three optical waveguides with metal cover

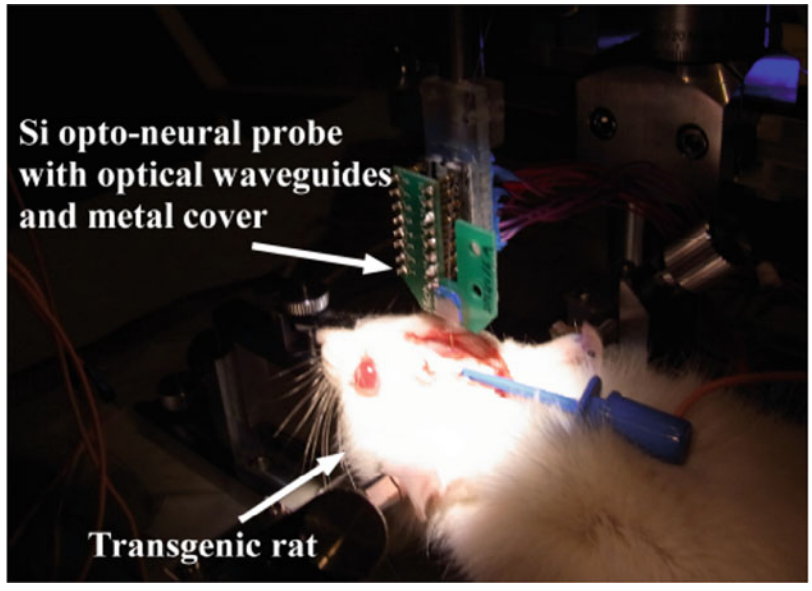


**Fig. 32.10** Insertion of the Si opto-electro multifunctional neural probe with three optical waveguides and metal cover into the rat brain

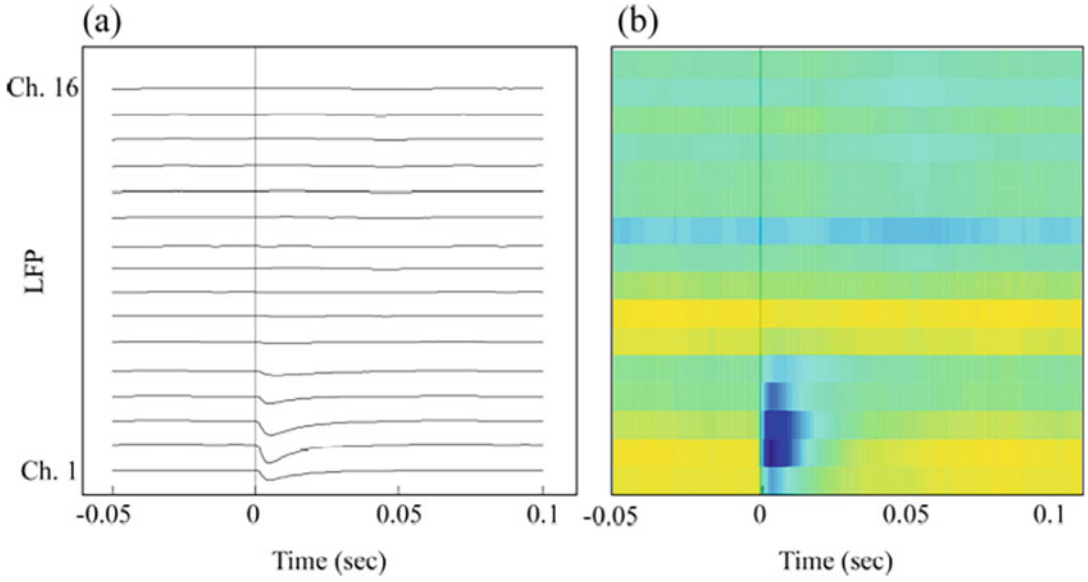


**Fig. 32.11** Recorded LFP induced by optical stimulation using the fabricated neural probe with optical waveguides and metal cover

potentials (LFPs) using the fabricated neural probe.

Figure 32.11a shows the averaged LFPs recorded by 16 recording electrodes and Fig. 32.11b shows the electric potential distribution expressed by color. The blue color indicated low potentials. We optically stimulated at a time of 0 s in this graph. In Fig. 32.11, light-induced LFP changes were observed in Chapters 1–4. These recording sites were formed around the optical stimulation site 3. Next, to identify current sources and current sinks of the neurons around the opto-neural probe, we adopted a current source density (CSD) analysis for the recorded LFPs (Mitzdorf 1985). Figure 32.12a, b shows the averaged membrane currents and the membrane current distribution expressed by color, respectively. Blue color regions indicated the current sink. Neurons were stimulated at the time of 0 s. From this analysis, the current sink occurred only around the light-exposed area. From in vivo experiments, we succeeded that the local control of neural activity by the light stimulation using the Si opto-electro multifunctional neural probe with optical waveguides.

## 32.7 Conclusion

We successfully fabricated the Si opto-electro multifunctional neural probe with multiple waveguides and embedded optical fiber for optogenetics application. The Si neural probe with optical waveguides was well fabricated and had 16 recording sites, three optical waveguides, and metal cover for suppressing light leakage. The Si opto-electro multifunctional neural probe with embedded optical fiber was also successfully fabricated. A chemically-thinned optical fiber was embedded entirely in the trench of the probe shank, which leads to less damage to tissues. From electrical experiments, it became clear that our probe had a suitable impedance for neuronal recording. Using the neural probe with three optical waveguides, we successfully demonstrated the multiple optical stimulations. Finally, we demonstrated the optical stimulation for neurons expressing the ChR2. We succeeded in the recording of the light-induced LFP changes and confirmed the optically induced membrane current by the CSD analysis. From this experiment,

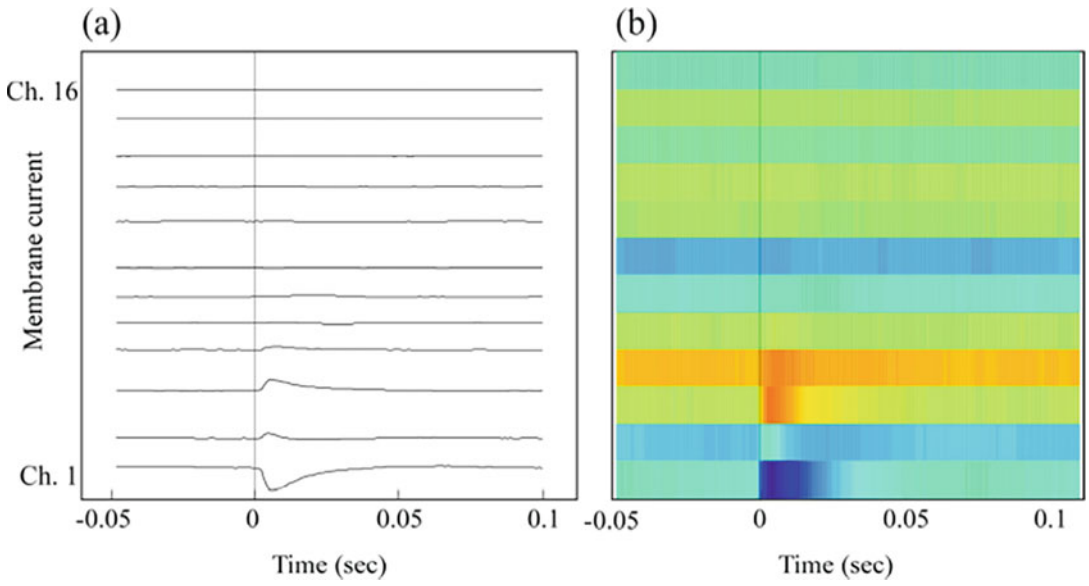


**Fig. 32.12** Results of the current source density (CSD) analysis extracted from recorded LFPs data

we achieved the neural activity recording with higher spatial and time resolutions using the Si neural probe. The Si opto-electro multifunctional neural probe is one of the most versatile tools for optogenetics.

**Acknowledgments** A Grant-in-Aid for Scientific Research partially supported this work on Priority Areas "Integrative Brain Research" from the Ministry of Education, Culture, Sports, Science, and Technology-Japan, and the device was fabricated in Micro/Nano-Machining Research and Education Center, Tohoku University, Japan.

## References

Boyden ES, Zhang F, Bamberg E, Nagel G, Deisseroth K (2005) Millisecond-timescale genetically targeted optical control of neural activity. Nat Neurosci 8:1263–1268

Du J, Roukes ML, Masmanidis SC (2009) Dual-side and three-dimensional microelectrode arrays fabricated from ultra-thin silicon substrates. J Micromech Microeng 19:1–7

Gradinaru V, Mogri M, Thompson KR, Henderson JM, Deisseroth K (2009) Optical deconstruction of parkinsonian neural circuitry. Science 324:354–359

Harimoto T, Takei K, Kawano T, Ishihara A, Kawashima T, Kaneko H, Ishida M, Usui S (2011) Enlarged gold-tipped silicon microprobe arrays and signal compensation for multi-site electroretinogram recordings in the isolated carp retina. Biosens Bioelectron 26:2368–2375

Kanno S, Kobayashi R, Lee S, Bea J, Fukushima T, Sakamoto K, Katayama N, Mushiake H, Koyanagi M, Tanaka T (2009) Development of Si neural probe with microfluidic channel fabricated using wafer direct bonding. Jpn J Appl Phys 48:1–5

Kanno S, Lee S, Harashima T, Kuki T, Kino H, Mushiake H, Yawo H, Tanaka T (2013) Multiple optical stimulation to neuron using Si opto-neural probe with multiple optical waveguides and metal-cover for optogenetics. 35th Annual International Conference of the IEEE EMBS. pp 253–256

Kobayashi R, Kanno S, Lee S, Bea J, Fukushima T, Sakamoto K, Katayama N, Mushiake H, Koyanagi M, Tanaka T (2009a) Development of Si double-sided microelectrode for platform of brain signal processing system. Jpn J Appl Phys 48:1–5

Kobayashi R, Kanno S, Lee S, Fukushima T, Sakamoto K, Matsuzaka Y, Katayama N, Mushiake H, Koyanagi M, Tanaka T (2009b) Development of double-sided Si neural probe with microfluidic channels using wafer direct bonding technique. Proc 4th International IEEE EMBS Conf on Neural Eng. pp 96–99

Kobayashi R, Kanno S, Sakai S, Lee S, Koyanagi M, Yawo H, Tanaka T (2011) Development of Si neural probe with optical waveguide for highly accurate optical stimulation of neuron. Proc 5th International IEEE EMBS Conf on Neural Eng, pp 294–297

Mitzdorf U (1985) Current source-density method and application in cat cerebral cortex: investigation of

evoked potentials and EEG phenomena. Physiol Rev 65:37–100

Morikawa T, Harashima T, Kino H, Fukushima T, Tanaka T (2017) Evaluation of insertion characteristics of less invasive Si opto-neural probe with embedded optical fiber. Jpn J Appl Phys 56:4S

Royer S, Zemelman BV, Barbic M, Losonczy A, Buzsáki G, Magee JC (2010) Multi-array silicon probes with integrated optical fibers: light-assisted perturbation and recording of local neural circuits in the behaving animal. Eur J Neurosci 31:2279–2291

Sakai S, Ueno K, Ishizuka T, Yawo H (2012) Parallel and patterned optogenetic manipulation of neurons in the brain slice using a DMD-based projector. Neurosci Res 75:59–64

Sodagar AM, Wise KD, Najafi K (2009) A wireless implantable microsystem for multichannel neural recording. IEEE Trans Microwave Theory Techniq 57:2565–2573

Wang H, Sugiyama Y, Hikima T, Sugano E, Tomita T, Takahashi T, Ishizuka T, Yawo H (2009) Molecular determinants differentiating photocurrent properties of two channelrhodopsins from chlamydomonas. J Biol Chem 284:5685–5696

Zhang F, Aravanis AM, Adamantidis A, Lecea L, Deisseroth K (2007) Circuit-breakers: optical technologies for probing neural signals and systems. Nat Rev Neurosci 8:577–581

Zhang J, Laiwalla F, Kim JA, Urabe H, Van Wagenen R, Song YK, Connors BW, Zhang F, Deisseroth K, Nurmikko AV (2009) Integrated device for optical stimulation and spatiotemporal electrical recording of neural activity in light-sensitized brain tissue. J Neural Eng 6:1–13

# Multimodal Functional Analysis Platform: 3. Spherical Treadmill System for Small Animals

33

Norihiro Katayama, Mitsuyuki Nakao, Tetsu Tanaka, Makoto Osanai, and Hajime Mushiake

**Abstract**

In the application of advanced neuroscience techniques including optogenetics to small awake animals, it is often necessary to restrict the animal's movements. A spherical treadmill is a beneficial option that enables virtual locomotion of body- or head-restrained small animals. Besides, it has a wide application range, including virtual reality experiments. This chapter describes the fundamentals of a spherical treadmill for researchers who want to start experiments with it. First, we describe the physical aspect of a spherical treadmill based on the simple mechanical analysis. Next, we explain the basics of data logging and preprocessing for behavioral analysis. We also provide simple computer programs that work for the purpose.

**Keywords**

Spherical treadmill · Passive treadmill · Effective mass · Behavioral analysis · Virtual reality · Data logger · Resampling · Smoothing · Processing · Python

All the figures appeared in this manuscript are original materials.

All the programs and lists appeared in this manuscript are original materials.

N. Katayama (✉) · M. Nakao
Biomodeling Laboratory, Department of Applied Information Sciences, Graduate School of Information Sciences, Tohoku University, Sendai, Japan
e-mail: katayama@ecei.tohoku.ac.jp; nakao@ecei.tohoku.ac.jp

T. Tanaka
Medical Nanosystem Engineering Laboratory, Graduate School of Biomedical Engineering, Tohoku University, Sendai, Japan
e-mail: ttanaka@lbc.mech.tohoku.ac.jp

M. Osanai
Laboratory for Physiological Functional Imaging, Department of Medical Physics and Engineering, Division of Health Sciences, Osaka University Graduate School of Medicine, Suita, Japan

Department of Physiology, Tohoku University Graduate School of Medicine, Sendai, Japan
e-mail: osanai@sahs.med.osaka-u.ac.jp

H. Mushiake
Department of Physiology, Tohoku University Graduate School of Medicine, Sendai, Japan
e-mail: hmushiak@med.tohoku.ac.jp

## Abbreviations

| | |
|---|---|
| CSV | Comma-separated values |
| PC | Personal computer |
| USB | Universal serial bus |

## 33.1 Introduction

In the application of advanced neuroscience techniques including optogenetics (Kuki et al. 2015; Osawa et al. 2013), optical imaging (Dombeck et al. 2007; Osanai et al. 2013;



H. Yawo et al. (eds.), *Optogenetics*, Advances in Experimental Medicine and Biology 1293,
https://doi.org/10.1007/978-981-15-8763-4_33

Yoshida et al. 2018), electrical stimulation (Kobayashi et al. 2009; Ueno et al. 2012), and electrophysiological recordings (Harvey et al. 2009; Niell and Stryker 2010) to small awake animals, it is often necessary to restrict the animal's movements. A spherical treadmill is a beneficial option that enables virtual locomotion of body- or head-restrained small animals (Niell and Stryker 2010; Reimer et al. 2014). Besides, it has a wide application range, including virtual reality experiments (Dombeck et al. 2010; Harvey et al. 2009; Hölscher et al. 2005; Katayama et al. 2012). In the present chapter, we explain the outline of the spherical treadmill system for small animals and the points to notice in its utilization in neuroscience experiments.

## 33.2 Hardware

### 33.2.1 Structure of the Spherical Treadmill

The spherical (ball) treadmill is classified into passive and active types by the driving force rotating the sphere. In the case of the active type, to keep the animal on the apex of the ball, the servomotor built into the treadmill system turns the ball in the opposite direction to the animal's motion monitored by the motion sensors (Götz and Gambke 1968; Kaupert et al. 2017). In the case of the passive treadmill system, the kicking force by the walking motion of the animal, whose body or head is physically restrained on the apex of the treadmill ball, rotates the ball (Dahmen 1980; Dombeck et al. 2007, 2010; Hölscher et al. 2005; Katayama et al. 2012). The walking motion is acquired by measuring the movement of a ball. As the passive type does not require a servomechanism, it can be manufactured and used easily. Thus, in the following, we focus on the passive spherical treadmill.

The typical structure of a passive spherical treadmill is shown in Fig. 33.1. The treadmill consists of a light ball, a bowl fitting the ball, and optical sensors for measurement of the ball rotation. Air pressure is applied from the bottom of the bowl to keep the ball floating. The subject animal in an animal jacket is placed on the apex of the treadmill ball and held in place by securing the jacket (Hölscher et al. 2005). Alternatively, to fix the head of the animal on the apparatus, a plastic or metal plate adhered to the skull by surgery and held with a fitting device is also adopted (Dombeck et al. 2007, 2010).

The rotation of the sphere has three directions, pitch, yaw, and roll (Fig. 33.1b), corresponding to an animal's forward and backward movements, right and left turns, and lateral sliding movements. With the arrangement shown in Fig. 33.1, the pitch and yaw rotation can be measured by sensor 1, and that of yaw and roll can be measured by sensor 2. Because rodents have little lateral shifting movement, the sensor 2 is often omitted.

For use as a motion sensor of the ball, high speed and precise tracking performance are required. Computer mice manufactured for action games (gaming mice) are suitable for the treadmill because they are readily available, and the manufacturers provide the software for setting the communication and measurement conditions in detail, which allows optimization of the sensor parameters to the experimental conditions.

### 33.2.2 Dynamics of the Spherical Treadmill

Before examining the dynamical property of walking motion on the treadmill, we first express the action and reaction of an animal locomoting on the stationary ground (Fig. 33.2a). If an unrestrained animal kicks the stationary ground with force $f$, it moves in the opposite direction of the force vector (law of action and reaction). The reaction motion of the animal is described as follows.

$$m_{\mathrm{a}}\dot{v}_{\mathrm{a}} = f, \tag{33.1}$$

where $t$ represents time, $m_{\mathrm{a}}$ represents the bodyweight of the animal, $v_{\mathrm{a}}$ represents the moving velocity of the animal, and $\dot{v}_{\mathrm{a}}$ represents differentiation of $v_{\mathrm{a}}$ with respect to time. For

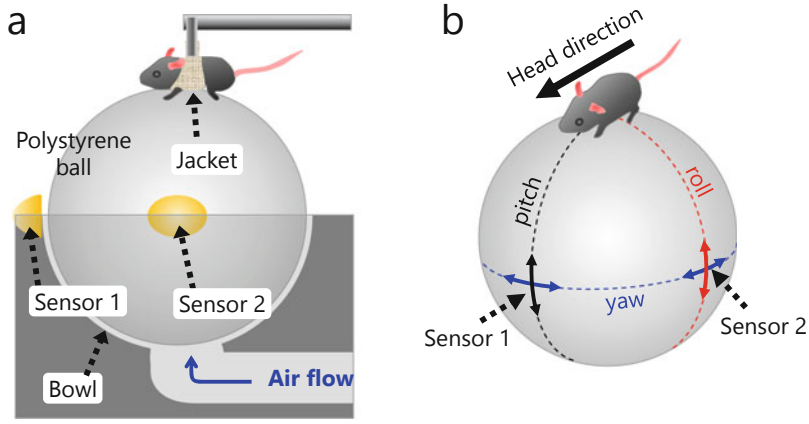


**Fig. 33.1** (**a**) Typical construction of a spherical treadmill. A body- or head-restrained animal is placed at the apex of an air-supported polystyrene ball in the bowl. The ball can freely rotate in any direction with little friction. The ball's rotational movements caused by the walking motion of the animal are measured by an optical sensor placed at the equator of the ball. (**b**) The placement of motion sensors to measure the rotation of the ball. Sensor 1 measures the pitch and yaw rotations, and sensor 2 measures the yaw and roll rotations of the ball. See the text for details

simplicity, we assume that air resistance is negligible.

Then, we consider locomotion on a treadmill ball (Fig. 33.2b), assuming that the body-restrained animal kicks the surface of the ball of the treadmill backward with the same force $f$ as in the case on the ground. As a result, the ball rotates around the axis passing through the center of the ball in the bowl of the treadmill. Equation (33.2) represents the motion.

$$I\dot{\omega} = fr, \tag{33.2}$$

where $\omega$, $I$, and $r$ are the rotational angular velocity, the moment of inertia, and the radius of the sphere, respectively. The air resistance is assumed to be negligible as well. The surface velocity $v_b$ of the ball is given by $v_b = r\omega$. Therefore, (Eq. 33.2) can be rewritten as follows:

$$M\dot{v}_b = f. \tag{33.3}$$

Thus, we set $M = Ir^{-2}$, which is called *the effective mass* of the ball.

Equations (33.1) and (33.3) show that when $M = m$, we obtain $\dot{v}_a = \dot{v}_b$. It indicates that the relative motion between the animal and the surface of the treadmill ball coincides with that of the animal and the ground. If the treadmill ball is heavier than this, the inertial force of the ball

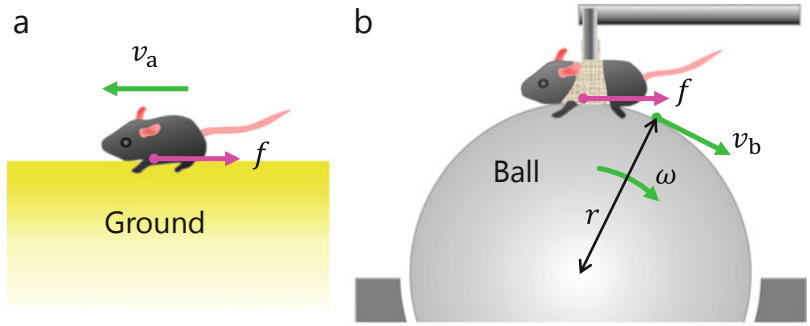


**Fig. 33.2** (**a**) If an unrestrained animal kicks the stationary ground, it moves to the opposite direction of the force vector (law of action and reaction). (**b**) If a body-fixed animal kicks the surface of the treadmill ball, the ball rotates in the same direction as the force vector

exceeds the leg force, hindering the control of the ball movement by the animals. The movement will be slower than the animal intended. Even if the animal tries to stop, it will be swayed by the inertial force of the sphere, and there is a possibility of unintended rotational motion.

The particular conditions on the actual treadmill are also examined. In the case in which the treadmill ball is a uniform solid sphere with radius $r$, the moment of inertia of the sphere is given by the expression $I = \frac{2}{5} M_{\text{solid}} r^2$, where $M_{\text{solid}}$ is the mass of the solid sphere. The effective mass is given by $M = Ir^{-2} = 0.4 M_{\text{solid}}$. For example, when the weight of an animal is $m = 30$ g, the weight of the solid ball that balances is given by $M_{\text{solid}} = 2.5m = 75$ g. In the case of a thin hollow sphere, the moment of inertia is given by $I = \frac{2}{3} M_{\text{hollow}} r^2$, where $M_{\text{hollow}}$ is the mass of the hollow sphere. Therefore, the mass of the hollow sphere that balances with the animal is calculated as $M_{\text{hollow}} = 45$ g.

## 33.3 Data Acquisition and Analysis

### 33.3.1 Logging the History of the Ball Movement

A simple setup to record the movement of a treadmill ball is the combination of an optical USB mouse, which works as the sensor 1 in Fig. 33.1, and a consumer PC. This setup has been widely used because it is effortless and useful (Dahmen 1980; Dombeck et al. 2007, 2010; Harvey et al. 2009; Hölscher et al. 2005; Katayama et al. 2012). However, the sampling interval is not equal, and the output of the sensor is noisy. Thus, it is necessary for an artifice to resolve these problems. In the following, we show a simple logger program for the setup, actual data obtained by the logger, and we share the data-processing techniques to resolve the problems.

The source program of the logger used is shown in List 33.1 (SimpleLogger). This program is written in the Processing 3 language (Reas and Fry 2014; Processing Foundation 2001), which is an open-source programming language, and includes the integrated development environment. The readers can probably find the software on the Internet, install and use it on personal devices. When the logger program runs, it opens a full-size gray window containing simple messages on the PC screen. At the same time, it starts to record the movement history of the PC mouse in the file named "data.csv.," which can be found in the same folder as the program source code. When the PC mouse is moved, the cursor on the screen slightly tracks the movement, but it is forced to the center the position of the screen immediately. By left-clicking the PC mouse, the timing is recorded in the log, and by right-clicking, logging is quit.

**List 33.1: A Processor 3 Code for Logging the Mouse Movement**

```
1  // A simple mouse movement logger (SimpleLogger.pde)
2  // Processing 3.5.3
3  // Programmed by: Norihiro Katayama, Tohoku Univ., Japan
4  // Date: Jan, 4, 2020
5
6  import java.awt.Robot;
7  Robot robot;
8
9  PrintWriter writer;
10 String fname = "data.csv";
11 int cx, cy, x=0, y=0, marker=0;
12 enum State {Logging, Quit};
13 State state;
14
15 void setup () {
16   frameRate(100); fullScreen();
17   cx = displayWidth/2; cy = displayHeight/2;
18   try { robot = new Robot(); }
19   catch (Throwable e) { e.printStackTrace(); }
20   fill(0); textSize(24);
21   text("Log data file: "+fname+"\n"
22     +"Left-click to set a marker\n"
23     +"Right-click to quit", 100, 100);
24
```

(continued)

**List 33.1** (continued)

```
25    writer = createWriter(fname); state = State.Logging;
26    print("Now data logging.\n");
27  }
28
29  void mousePressed() {
30    if (mouseButton == LEFT) marker=1;
31    else if (mouseButton == RIGHT) state=State.Quit;
32  }
33
34  void draw() {
35    if (State.Logging == state) {
36      int ctime=millis(), dx=mouseX-cx, dy=mouseY-cy;
37      robot.mouseMove(cx, cy);
38      x += dx; y += dy;
39      if (marker==1) print("Marker: "+str(ctime)+" ms\n");
40      String s = str(ctime)+","+str(dx)+","+str(dy)+","
41        +str(x)+","+str(y)+","+str(marker);
42      writer.println(s); marker = 0;
43    } else if (State.Quit == state){
44      writer.flush(); writer.close();
45      print("Finished.\n");
46      exit();
47    }
48  }
```

List 33.2 shows a part of a log file. The log file is a comma-separated-value (CSV) type text file, in which each line has six data fields that are sampled at the same time. The first data field is the elapsed time from the time the program started ($t_n$; in ms, $n$ is the sample number). The second and third fields are movement distances of the object monitored by the sensor in x and y directions, respectively, between the sampling times ($\Delta x_n$, $\Delta y_n$; in pixel). The fourth and fifth fields are cumulative movement distances of x and y, respectively, from the program start point ($x_n$, $y_n$; in pixel), and the sixth column is a timing marker (0 or 1), where "1" is stored at the time of left-clicking. As it is not possible to obtain correct data for several hundred of seconds after starting the program, it is necessary to exclude it from the analysis.

**List 33.2: Example of a Part of Log Data**

| $n$ | $t_n$, $\Delta x_n$, $\Delta y_n$, $x_n$, $y_n$, Marker |
|---|---|
| ⋮ | ⋮ |
| 104 | 1260, -1, -1, 1430, -54, 0 |
| 105 | 1271, 1, -1, 1431, -55, 0 |
| 106 | 1280, 5, -1, 1436, -56, 0 |
| 107 | 1289, 7, -3, 1443, -59, 0 |
| 108 | 1299, 14, -3, 1457, -62, 0 |
| 109 | 1311, 23, -5, 1480, -67, 0 |
| 110 | 1320, 100, -14, 1580, -81, 0 |
| 111 | 1329, 47, -7, 1627, -88, 0 |
| 112 | 1339, 74, -8, 1701, -96, 0 |
| 113 | 1350, 81, -6, 1782, -102, 0 |
| 114 | 1363, 206, -10, 1988, -112, 0 |
| ⋮ | ⋮ |

### 33.3.2 Resampling and Smoothing Data

Figure 33.3a shows an example of the data collected using the SimpleLogger program (List 33.1) in the Processing 3.5.3 environment. The experiment was performed with a laptop PC (CF-LV 73, Panasonic Corp., Japan) with Windows 10 Pro OS (Microsoft Corp. USA) installed. In the program, the sampling period was set to 10 ms (Frame rate of 100 Hz, Line 16 in List 33.1), but the actual sampling interval $T_S$ was 10.3 ± 1.4 ms (mean ± standard deviation). Besides, large variations were also observed in the sampled movement distance ($\Delta x_n$).

Before the analysis of the relationship between the treadmill data and the simultaneously recorded biological signals, it is necessary to resample at appropriate equal intervals and smooth the data before postprocessing. We usually perform the preprocessing procedure as follows.

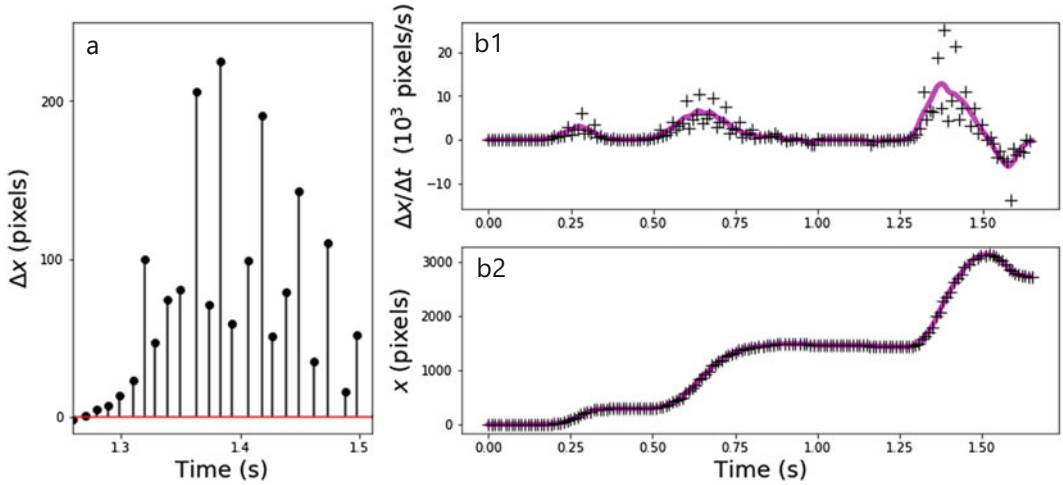


**Fig. 33.3** (**a**) Example of raw data of mouse movements acquired by the logger program. Note that the sampling interval was unequal, and the fluctuation of the displacements ($\Delta x$) was considerable. (**b1**) The time course of the moving speed. (**b2**) The time course of the travel distance. Cross marks (+) indicate raw data, and magenta curves show filtered waveforms. See the text for details of filtering methods

(1) Calculate the travel distance from the start of recording at each sampling time

$$(x_n,\ y_n) = \left(\sum_{i=1}^{n} \Delta x_i, \sum_{i=1}^{n} \Delta y_i\right) \tag{33.4}$$

(2) Linearly interpolate $(x_n, y_n)$ at the adjacent sampling times and up-sample it at equal intervals: $(x(mT_{\mathrm{UP}}), y(mT_{\mathrm{UP}}))$, where $m$ is the index number of up-sampling, $T_{\mathrm{UP}}$ is the up-sampling interval that satisfies $T_{\mathrm{UP}} \leq \mathrm{mean}(T_{\mathrm{S}})/k$. We usually adopt the value of the factor $k$ in the range of 5–10.

(3) Smooth the $(x(mT_{\mathrm{UP}}), y(mT_{\mathrm{UP}}))$ by low pass filtering to obtain $(\widehat{x}(mT_{\mathrm{UP}}), \widehat{y}(mT_{\mathrm{UP.}}))$

(4) Consider time-difference to estimate the moving velocity by the following:

$$\left(\frac{\Delta x}{\Delta t}, \frac{\Delta y}{\Delta t}\right) = \left(\frac{\Delta \widehat{x}(mT_{\mathrm{UP}})}{T_{\mathrm{UP}}}, \frac{\Delta \widehat{y}(mT_{\mathrm{UP}})}{T_{\mathrm{UP}}}\right). \tag{33.5}$$

An implementation of this algorithm in the Python 3.6 (Van Rossum and Drake 2009), which is also an open-source programming language, is shown in List 33.3. The results of the processing are shown in Fig. 33.3b. Cross marks represent raw data, and magenta curves represent processed waveforms. It is confirmed that the processing reduces noise. Besides, it is also easy to examine the relationship with other biological signals because the sampling timing can be freely set.

**List 33.3: A Python Code for Resampling and Smoothing the Logger Data**

```
1  ''' InterpolAndSmooth.py (for Python 3.6 or later)
2  Programmed by: Norihiro Katayama, Tohoku Univ., Japan
3  Date: Jan, 5, 2020
4  '''
5  import numpy as np
6  from scipy import signal
7  from scipy import interpolate
8  import matplotlib.pyplot as plt
9
10 # Data loading (recorded by SimpleLogger.pde)
11 d = np.loadtxt('data.csv', delimiter=',',skiprows=1)
12 d[:,0] *= 1e-3 # change time-scale (ms -> s)
```

(continued)

**List 33.3** (continued)

```
13
14  # (2) Linear interpolation
15  fs_res = 200.0 # (Hz) resampling rate
16  fn = fs_res/2 # (Hz) Nyquist frequency
17  t_res = np.arange(d[0,0],d[-1,0], 1./fs_res)
18  d1 = np.zeros([t_res.shape[0],5])
19  d1[:,0] = t_res
20  for k in range(1,5):
21      f = interpolate.interp1d(d[:,0],d[:,k])
22      d1[:,k] = f(t_res) # interpolating data
23
24  # (3) Smoothing
25  fp = 10 # (Hz) Passband edge frequency
26  fs = 25 # (Hz) Stopband edge frequency
27  gpass = 1 # (dB) Maximum loss through the domain
28  gstop = 10 # (dB) Stopband minimum attenuation
29  N, Wn = signal.buttord(fp/fn, fs/fn, gpass, gstop)
30  b, a = signal.butter(N, Wn, "low")
31  d2 = np.zeros(d1.shape)
32  d2[:,0] = d1[:,0]
33  for k in [3, 4]:
34      d2[:,k] = signal.filtfilt(b, a, d1[:,k])
35      d2[1:,k-2] = np.diff(d2[:,k])
36
37  # Graph plotting
38  fig, ax = plt.subplots(2,1, sharex=True, figsize=(10,8))
39  ax[0].plot(d2[:,0], d2[:,1]*fs_res)
40  ax[0].scatter(d[:-1,0], d[:-1,1]/np.diff(d[:,0]))
41  ax[0].set_ylabel('Speed\n$\Delta{}x/\Delta{}t$ (pixels/s)')
42  ax[1].plot(d2[:,0], d2[:,3])
43  ax[1].scatter(d[:,0], d[:,3])
```

**List 33.3** (continued)

```
44  ax[1].set_ylabel('Travel distance\n$x$ (pixels)')
45  ax[1].set_xlabel('Time (s)')
```

## 33.4 Concluding Remarks

This section explained the essentials on hardware and software of a spherical treadmill system for small animals. Although an actual treadmill ball rotates in three axes, our description was limited to a one-axial analysis. It is also necessary to train the animals used in the experiment, enabling them to locomote on the treadmill as they intend. We will further explain these issues in other articles. We hope that this text helps the readers to start experiments using a spherical treadmill in practice.

**Acknowledgments** This research was partly supported by the MEXT/JSPS KAKENHI Grant Numbers JP16H06276 (AdAMS) (H.M., N.K.), JP15K01276 (N.K.), JP18H04103 (N.K.), and JP19K12773 (N.K.).

## References

Dahmen HJ (1980) A simple apparatus to investigate the orientation of walking insects. Experientia 36 (6):685–687. https://doi.org/10.1007/BF01970140

Dombeck DA, Khabbaz AN, Collman F et al (2007) Imaging large-scale neural activity with cellular resolution in awake, mobile mice. Neuron 56(1):43–57. https://doi.org/10.1016/j.neuron.2007.08.003

Dombeck DA, Harvey CD, Tian L et al (2010) Functional imaging of hippocampal place cells at cellular resolution during virtual navigation. Nat Neurosci 13 (11):1433–1440. https://doi.org/10.1038/nn.2648

Götz KG, Gambke C (1968) Zum Bewegungssehen des Mehlkäfers Tenebrio molitor. Kybernetika 4 (6):225–228. https://doi.org/10.1007/BF00272520

Harvey CD, Collman F, Dombeck DA et al (2009) Intracellular dynamics of hippocampal place cells during virtual navigation. Nature 461(7266):941–946. https://doi.org/10.1038/nature08499

Hölscher C, Schnee A, Dahmen H et al (2005) Rats are able to navigate in virtual environments. J Exp Biol 208(3):561–569. https://doi.org/10.1242/jeb.01371

Katayama N, Hidaka K, Karashima A, et al (2012) Development of an immersive virtual reality system for mice. In: Proceedings of the SICE Annual Conference (SICE), 2012, pp 791–794. https://ieeexplore.ieee.org/document/6318548

Kaupert U, Thurley K, Frei K et al (2017) Spatial cognition in a virtual reality home-cage extension for freely moving rodents. J Neurophysiol 117(4):1736–1748. https://doi.org/10.1152/jn.00630.2016

Kobayashi R, Kanno S, Lee S, et al. (2009). Development of double-sided Si neural probe with microfluidic channels using wafer direct bonding technique. In: Proceedings of the 4th International IEEE EMBS Conference on Neural Engineering, pp 96–99. https://doi.org/10.1109/NER.2009.5109243

Kuki T, Fujihara K, Miwa H et al (2015) Contribution of parvalbumin and somatostatin-expressing GABAergic neurons to slow oscillations and the balance in beta-gamma oscillations across cortical layers. Front Neural Circuit 9:3. https://doi.org/10.3389/fncir.2015.00006

Niell CM, Stryker MP (2010) Modulation of visual responses by behavioral state in mouse visual cortex. Neuron 65(4):472–479. https://doi.org/10.1016/j.neuron.2010.01.033

Osanai M, Suzuki T, Tamura A et al (2013) Development of a micro-imaging probe for functional brain imaging. Neurosci Res 75(1):46–52. https://doi.org/10.1016/j.neures.2012.10.008

Osawa S, Iwasaki M, Hosaka R et al (2013) Optogenetically induced seizure and the longitudinal hippocampal network dynamics. PLoS One 8(4):e60928. https://doi.org/10.1371/journal.pone.0060928

Reas C, Fry B (2014) Processing: a programming handbook for visual designers and artists, 2nd edn. The MIT Press, Cambridge, MA, USA

Reimer J, Froudarakis E, Cadwell CR et al (2014) Pupil fluctuations track fast switching of cortical states during quiet wakefulness. Neuron 84(2):355–362. https://doi.org/10.1016/j.neuron.2014.09.033

Ueno A, Katayama N, Karashima A et al (2012) Improvement of diameter selectivity in nerve recruitment using multi-cuff electrodes. Adv Biomed Eng 1:36–42. https://doi.org/10.14326/abe.1.36

Van Rossum G, Drake FL (2009) Python 3 reference manual. CreateSpace. Processing Foundation, Scotts Valley, CA. https://processing.org/

Yoshida Y, Nakao M, Katayama N (2018) Resting-state functional connectivity analysis of the mouse brain using intrinsic optical signal imaging of cerebral blood volume dynamics. Physiol Meas 39 (054003):1–9. https://doi.org/10.1088/1361-6579/aac033

# 34 Multimodal Functional Analysis Platform: 4. Optogenetics-Induced Oscillatory Activation to Explore Neural Circuits

Hajime Mushiake, Tomokazu Ohshiro, Shin-ichiro Osawa, Ryosuke Hosaka, Norihiro Katayama, Tetsu Tanaka, Hiromu Yawo, and Makoto Osanai

**Abstract**

To elucidate neural mechanisms underlying oscillatory phenomena in brain function, we have developed optogenetic tools and statistical methods. Specifically, opto-current-clamp induced oscillation reveals intrinsic frequency preferences in the neural circuits by oscillatory resonance. Furthermore, resonance or entrainment to intrinsic frequency is state-dependent. When resonance phenomena go beyond a certain range, it could even induce epileptic seizure in highly reproducible manner. We are able to study how seizures start, develop, and stop in neural circuits. Therefore, the optogenetics-induced oscillatory activation is a powerful tool in neuroscience research

**Keywords**

Opto-current clamp · Resonance · Entrainment · Barrel cortex · Hippocampus · Seizure

H. Mushiake (✉) · T. Ohshiro
Department of Physiology, Tohoku University Graduate School of Medicine, Sendai, Japan
e-mail: hmushiak@med.tohoku.ac.jp

S.-i. Osawa
Department of Neurosurgery, Tohoku University Graduate School of Medicine, Sendai, Japan

R. Hosaka
Department of Applied mathematics, Fukuoka University, Fukuoka, Japan

N. Katayama
Department of Applied Information Sciences, Graduate School of Information Sciences, Tohoku University, Sendai, Japan

T. Tanaka
Graduate School of Biomedical Engineering, Tohoku University, Sendai, Japan

H. Yawo
Institute for Solid State Physics (ISSP), The University of Tokyo, Kashiwa, Japan

M. Osanai
Department of Physiology, Tohoku University Graduate School of Medicine, Sendai, Japan

Laboratory for Physiological Functional Imaging, Division of Health Sciences, Department of Medical Physics and Engineering, Osaka University Graduate School of Medicine, Suita, Japan

## Abbreviations

| | |
|---|---|
| GAD | Glutamic acid decarboxylase |
| MI | Caudal motor area |
| MII | Rostral motor area |
| PV | Parvalbumin |
| RSSL | Rectified sinusoidal sweep of light |
| SOM | Somatostatin |

## 34.1 Introduction

To understand how the brain works, we propose a bidirectional research in which the intervention and multimodal neuronal activity measurements



H. Yawo et al. (eds.), *Optogenetics*, Advances in Experimental Medicine and Biology 1293,
https://doi.org/10.1007/978-981-15-8763-4_34

of the neural circuit are performed on the same animal. As the fourth session of introduction of our multimodal measurements system, we will focus on methods of the optogenetics-induced oscillatory activation to explore neural circuits.

Neuronal oscillations are a fundamental physiological brain function. Networks are built from both excitatory and inhibitory elements and balance of these opposing forces often gives rise to rhythmic behavior (Buzsáki 2006). Neuronal oscillations are derived from intrinsic properties of neuronal networks and extrinsic stimulations. To manipulate neural oscillation directly by electrical stimulation, however, stimulations cause electrical artifacts in recording system. Since optogenetics is techniques involving the use of light to control the activity of neurons that have been genetically modified, optogenetics allows us to manipulate neural oscillation without electrical artifacts. In this chapter, we introduced examples of Optogenetics-induced oscillatory activation and discussed significance of this technique to study neural cuircuits from the perspective of neural oscillations.

## 34.2 Opto-Current Resonance Method Reveals Intrinsic Frequency Preferences in the Neural Circuits

With its kinetic advantages, the use of channelrhodopsin would enable one to inject a current into a neuron by the time course as predicted by the intensity of the shedding light (opto-current clamp). A variety of neurons and circuits shows a maximal response at a preferred frequency, generally considered to be important in tuning network activity. To investigate intrinsic frequency preferences, we have developed opto-current resonance method by applying an oscillatory photocurrent. We first generated an oscillatory LED light from 0.1 and 100 Hz using ZAP function. ZAP (chirp) function is as follows, sweeping through many frequencies over time.

The oscillatory LED light was generated according to the following voltage change (Puil et al. 1986)

$$V(t) = V_{\min} + V_{\max} \sin\left[2\pi f(t)t\right] \tag{34.1}$$

where $V_{\min}$ and $V_{\max}$ are the minimal and the maximal voltages driving the LED. The oscillation frequency is swept from the minimal frequency, $f_{\min}$, to the maximal frequency, $f_{\max}$, following the equation (Tohidi and Nadim 2009)

$$f(\mathrm{t}) = f_{\min}\left(\mathrm{e}^{\mathrm{Lt}} - 1\right)/L, \tag{34.2}$$

where

$$L = \log\left(\frac{f_{\max}}{f_{\min}}\right) \tag{34.3}$$

However, since the LED light power density was 0 during $V < V_{\min}$, only a positive range of the above function was employed (the rectified sinusoidal sweep of light).

The rectified sinusoidal sweep of light from 0.1 to 100 Hz was used to evoke photocurrent in the cortex. The photocurrent response of an L5 pyramidal neuron under voltage clamp was examined to calculate the trial-to-trial responses of the membrane potential under current clamp and average the evoked membrane potential. Then, wavelet analysis of voltage-clamp response to evaluate the relative level of power of each frequency in response to different frequencies of photostimulation.

We analyzed the time–frequency energy distribution of the stimulation-evoked response by continuous wavelet transformation (Sutoh et al. 2000) We used the following equation:

$$\mathrm{Gw}(b,a) = \int \frac{1}{\sqrt{\mathrm{a}}}\,\overline{\Psi\left(\frac{t-b}{a}\right)x(t)dt} \tag{34.4}$$

$$\Psi(\mathrm{t}) = \frac{1}{2\sqrt{\pi\sigma}}\mathrm{e}^{-\frac{t^2}{\sigma^2}}\mathrm{e}^{-jt} \tag{34.5}$$

where $x(t)$ is the evoked response in time ($t$) domain, $\Psi(t)$ is the mother wavelet, $a$ and $b$ are the scaling factor and translation, respectively. For the mother wavelet, we used the Gabor function in equation with s being the central frequency of 2 Hz. We varied the scaling factor $a$ to explore frequencies ranging from 1 to 100 Hz. The above Eq. (34.1) yielded a series of coefficients that represent the temporal evolution of the frequency

content, which were plotted on a pseudocolored 2D graph. If stimulating frequency resonates with intrinsic preferred frequency, energy coefficient is indicated by the pseudocolor scaling. Figure 34.1 shows an example of optogenetics-induced oscillatory activation.

We applied the opto-current resonance method to examine intrinsic frequency preferences in the cortical neural circuits. When an oscillatory LED light signal was applied sweeping through frequencies, it robustly evoked action potentials synchronized to the oscillatory light at 3–10 Hz in layer 5 pyramidal cells in the cortical slice (Fig. 34.2) (Wen et al. 2010).

Opto-current resonance method reveals intrinsic frequency preferences in the neural circuits. However, the preferred frequency is dependent on behavioral state. In the next chapter, we show entrainment phenomena of slow oscillation of the cortex of rats under anesthesia.

## 34.3 Frequency-Dependent Entrainment of Neocortical Slow Oscillation

During sleep or while under anesthesia, slow oscillation (<1 Hz) is typically observed in the cortex and reflects synchronous activation/inactivation of the cortical neuron population. We optically stimulated rostral motor area (MII) in the rat and recorded from the caudal motor area (MI). We found that the local field potentials (LFPs) could be effectively entrained to repeated optical stimulation at 1 Hz in deep layers. We next systematically changed stimulus frequencies and explored effective stimulus conditions. We found that optical stimulation that caused a local peak in the spectrum was near 1 Hz. These results suggest that the anesthetized rat cortex has an intrinsic mechanism that leads to oscillation near 1 Hz; effective entrainment to the 1 Hz stimulation reflects the resonated state of the cortex to that stimulus (Fig. 34.3) (Kuki et al. 2013; Kanno et al. 2013).

We also found the resonated state is dependent on phase of intrinsic oscillation. Optical stimulation primarily induced the transition from the cortical up to down state. Optical stimulation to MII area may be transmitted to the recording site (MI) through a direct cortico–cortical connection or through a complex interaction between the excitatory and the local inhibitory circuits and it forces the transition from up state to down state. These findings suggest that there is state-dependent preference in frequency and phase in cortical circuits in opto-current resonance.

We used mice lacking glutamate decarboxylase 67, primarily in PV cells (PV-GAD67 mice) or in SOM cells (SOM-GAD67 mice). We then compared LFPs between PV-GAD67 mice and SOM-GAD67 mice. PV cells target the proximal regions of pyramidal cells, whereas SOM cells are dendrite-preferring interneurons. We found that the upstate as shortened in duration in the PV-GAD 67 mice, but tended to be longer in SOM-GAD67 mice. Our findings suggested that intrinsic oscillation is dependent on the excitatory-inhibitory balance and controlled by various types of inhibitory and excitatory neurons in the cortex (Kuki et al. 2015).

## 34.4 Optogenetic Patterning of Whisker-Barrel Cortical System

Optical stimulations to the retina are used for mapping receptive field in the visual system with very high precision of spatiotemporal parameters. However, other sensory systems such as tactile system are optimized to mechanical stimulation. To study somatosensory system with optogenetics, we generated several transgenic lines of rat which express channelrhodopsin-2 (ChR2) under the control of thy1.2 promoter (Tomita et al. 2009). In one of them, W-TChR2V4, ChR2 was exclusively expressed in a subpopulation of large mechanoreceptive neurons in the dorsal root ganglion (DRG) but not in the small-sized neurons, which are involved in nociception.

Now optogenetics allows us to investigate the relationship between whisker mechanoreceptive inputs and the neural responses of the barrel cortex with optical precision (Fig. 34.4) (Honjoh

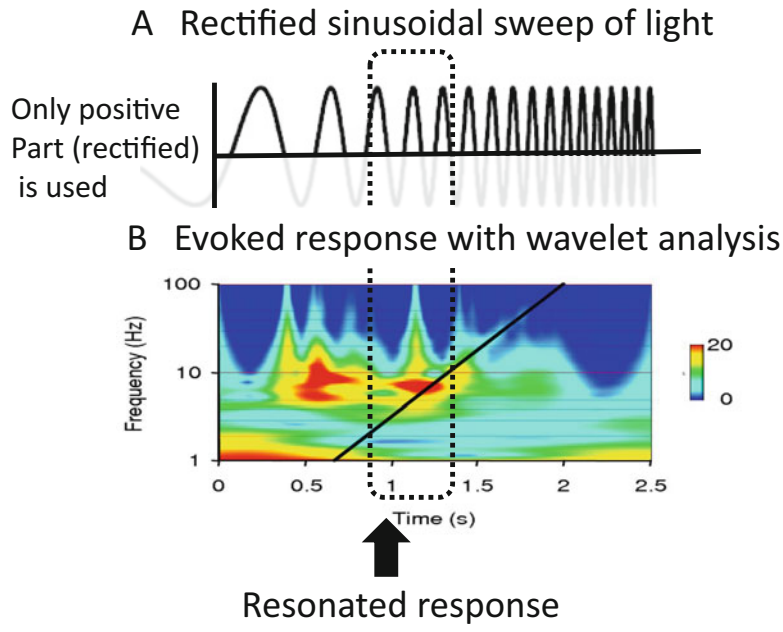


**Fig. 34.1** Opto-current resonance method. (**a**) The rectified sinusoidal sweep of light. We generated an oscillatory LED light signal that sweeps through frequencies between 0.1 and 100 Hz over 2 s. (**b**) Wavelet analysis of the oscillatory photocurrent response evoked by the rectified sinusoidal sweep of light Wavelet analysis of evoked response reveals resonance phenomena around 5–10 Hz

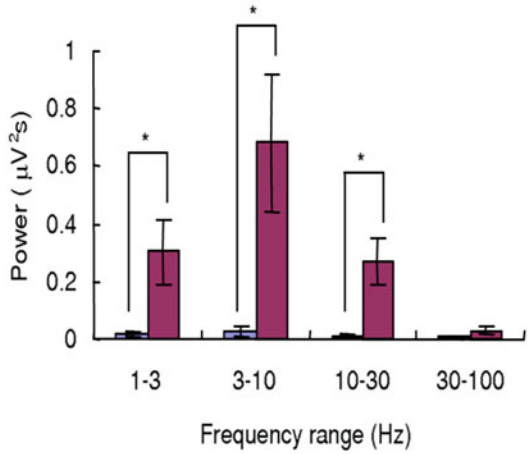


**Fig. 34.2** Summary of the LFP power spectrum analysis of (Wen et al. 2010 Fig. 5): control (non-injected side of the hemisphere, blue columns, left) and test (ChR2-expressing side of the hemisphere, crimson column, right). Asterisks indicate statistical significances (P,0.05, Wilcoxon signed-ranks test) (from Fig. 5F. Wen L, Wang H, Tanimoto S, Egawa R, Matsuzaka Y, Mushiake H, Ishizuka T, Yawo H. Opto-current-clamp actuation of cortical neurons using a strategically designed channelrhodopsin. PLoS One. 2010 Sep 23;5(9):e12893)

et al. 2014). The spatiotemporal pattern of whisker irradiation thus produced a barrel-cortical response with a specific spatiotemporal pattern.

We investigated the relationship between whisker mechanoreceptive inputs and the neural responses to optical stimulation in the barrel cortex using optogenetics. The peripheral nerve endings surrounding the whisker follicles were respectively connected one-by-one with 16 LED-coupled optical fibers. Then we illuminated the targets according to a certain spatial pattern in order to evaluate interactions among the inputs in the upper layer of the barrel cortex using optogenetics (Liu et al. 2019). The whisker photostimulation evoked spindle-burst like oscillatory activities of the cortical neurons. The bursts occurred rhythmically with 10–20 Hz (alpha–beta band) but did not continue over 1 s. Similar spindle-burst oscillatory activities also occurred spontaneously and are reminiscent of the spontaneous burst clusters prominent during non-REM sleep and anesthesia.

Our optical stimulation suggested that the neurons in the barrel cortex have intrinsic tendency of oscillation of slow oscillation range

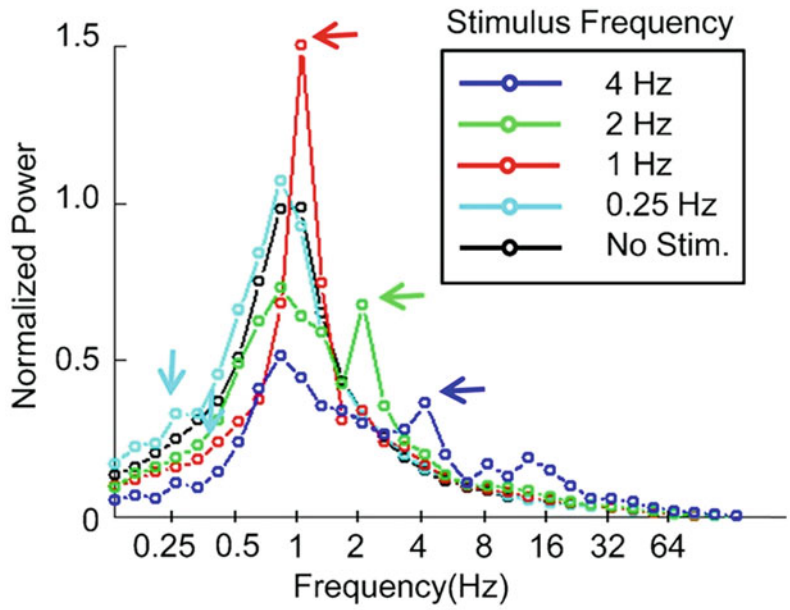


**Fig. 34.3** The frequency power spectrum of the LFP recordings in the cortex, stimulated at different stimulus frequencies. Optical stimulation caused a local peak in the spectrum at the frequency corresponding to the stimulus frequency (colored arrow heads). Note the exclusive amplification of the power at 1 Hz by the 1 Hz stimulation. Also, notice that the persistence of the slow oscillation components peaked at 0.8 Hz for all other stimulus conditions (from Fig. 5D Kuki T, Ohshiro T, Ito S, Ji ZG, Fukazawa Y, Matsuzaka Y, Yawo H, Mushiake H. Frequency-dependent entrainment of neocortical slow oscillation to repeated optogenetic stimulation in the anesthetized rat. Neurosci Res. 2013 Jan;75(1):35–45)

and alpha–beta band range. We were able to use this intrinsic property of oscillation to study how spatiotemporal pattern of whisker irradiation produced a barrel-cortical response with a specific spatiotemporal pattern. In short, we found center-surround organization in the barrel cortex. Specifically, we found clear suppressions of the major afferent inputs response by additional surrounding stimulation at whiskers that were ineffective when presented alone. Thus the optogenetic approach would still be suitable for revealing principles of afferent integration in the cortex.

## 34.5 Optogenetically Induced Seizure Model

Epileptic seizure is a paroxysmal and self-limited phenomenon characterized by abnormal hypersynchrony of a large population of neurons. However, our current understanding of seizure dynamics is still limited. To study seizure dynamics, we proposed a novel in vivo model of seizure-like afterdischarges using optogenetics. Specifically, repetitive pulse photostimulation was applied to the rodent hippocampus, in which channelrhodopsin-2 (ChR2) was expressed, under simultaneous recording of LFPs. Seizure-like afterdischarges were successfully induced and we report on investigation of directional network dynamics during seizure along the septo-temporal (ST) axis of hippocampus (Osawa et al. 2013). A novel in vivo model of seizure-like afterdischarge was developed using optogenetics, which was advantageous in its reproducibility and artifact-free electrophysiological observations (see Chap. 39).

According to Osawa's study, when seizure activity is initiated, focal seizure activity is propagated along not only the transverse but

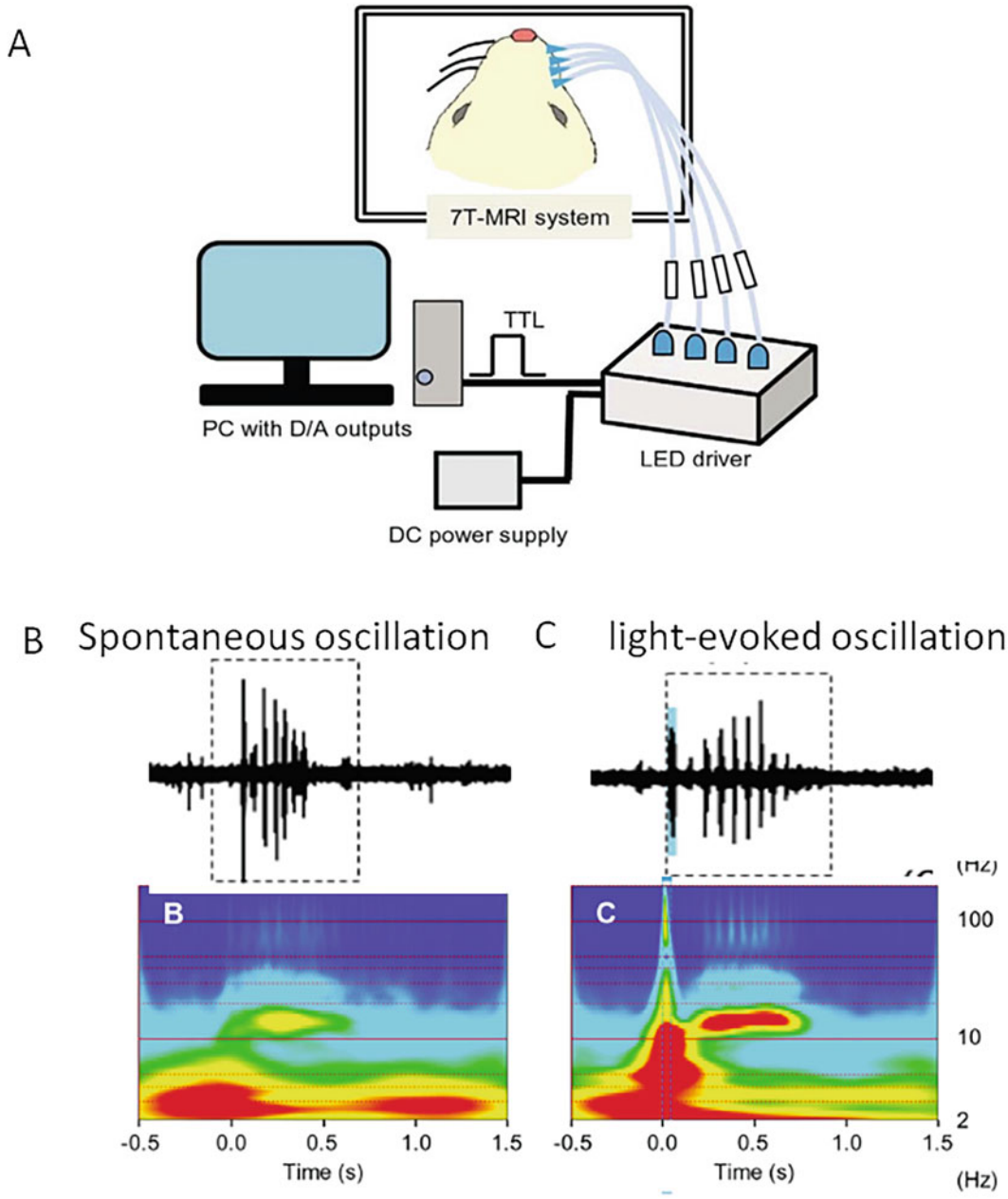


**Fig. 34.4** (**a**) System setup for optogenetic tactile sense mapping. (**b**) Spontaneous LFP oscillation with wavelet analysis. (**c**) Light-evoked LFP oscillation with wavelet analysis (from Fig. 6A,7B, C and 9A Honjoh T, Ji ZG, Yokoyama Y, Sumiyoshi A, Shibuya Y, Matsuzaka Y, Kawashima R, Mushiake H, Ishizuka T, Yawo H. Optogenetic patterning of whisker-barrel cortical system in transgenic rat expressing channelrhodopsin-2. PLoS One. 2014 Apr 2;9(4):e93706)

also the septo-temporal (longitudinal) direction of the hippocampus, and the propagation direction flipped to the opposite direction. We evaluate propagation, flow of signal, and synchronization among signals recorded from multichannel electrodes (Osawa et al. 2013).

### 34.5.1 Information Flow Among Signals by Granger Causality

Degree of information flow was evaluated by Granger causality (GC) (Osawa et al. 2013), where X1 and X2 are two zero-mean stationary signals whose time observations are $x_1(t)$ and $x_2(t)$, with $t = 1.\ldots.T$. If the temporal dynamics of $x_1(t)$ and $x_2(t)$ could be written by a univariate autoregressive model of order $p$, the model would be

$$x_1(t) = \sum_{k=1}^{p} a_{1.1}(k)x_1(t-k) + u_1(t) \quad (34.6)$$

$$x_2(t) = \sum_{k=1}^{p} a_{2.2}(k)x_2(t-k) + u_2(t) \quad (34.7)$$

where prediction error $u_1(t)$ and $u_2(t)$ for a signal depend only on its own past. $x_1(t)$ and $x_2(t)$ can be assumed to be represented by the following multivariate auto-regressive model of order $p$,

$$X_1(t) = \sum_{k=1}^{p} a_{1.1}(k)x_1(t-k) + \sum_{k'=1}^{p} a_{1.2}(k')x_2(t-k') + w_1(t) \quad (34.8)$$

$$X_2(t) = \sum_{k=1}^{p} a_{2.1}(k)x_1(t-k) + \sum_{k'=1}^{p} a_{2.2}(k')x_2(t-k') + w_2(t) \quad (34.9)$$

where prediction error $w_1(t)$ and $w_2(t)$ depend on the past of the two signals. So in the model above, if $w_1(t)$ were smaller than $u_1(t)$, then we could conclude that X2 caused X1. Similarly, if $w_2(t) < u_2(t)$, then X1 caused X2. In short, if knowing time series X2 helped to predict the future of the other time series X1 and X2 "Granger caused" X1. The magnitude of the GC was quantified by the log ratio of the prediction error variance

$$G_{2\to1} = \ln\left(\frac{\mathrm{var}(u_1)}{\mathrm{var}(w_1)}\right) \quad (34.10)$$

The model order was chosen using Akaike's information criterion (AIC) and Bayesian information criterion (BIC). Dominance of the information flow, from septal side to temporal side or its opposite direction, was evaluated by an index, we called the "Granger index," defined by

$$\text{Granger Index} = \frac{G_{s\to t} - G_{t\to s}}{G_{s\to t} + G_{t\to s}} \quad (34.11)$$

where $G_{s\to t}$ and $G_{t\to s}$ denote the GC from septal to temporal sides and the GC from temporal to septal sides, respectively. The Granger index was positive if $G_{s\to t} > G_{t\to s}$, otherwise it was negative. GC indicates positive values when the septal-to-temporal causality is larger than the opposite direction. Otherwise, it is negative.

### 34.5.2 Synchronization of Signals by Coherence

Coherence was introduced to evaluate the synchronization of signals in the frequency domain. The coherence of signals $x_m(t)$ and $x_n(t)$ was calculated as follows

$$\mathrm{Coh}_{mm}(f) = \sqrt{\frac{|S_{mn}(f)|^2}{S_{mm}(f)S_{nn((f)}}} \quad (34.12)$$

$$S_{mn}(f) = \frac{1}{2\pi}\int_{-\infty}^{\infty} C_{mn}(\tau)\exp(-if\tau)d\tau \quad (34.13)$$

$$C_{mn}(\tau) = \overline{x_m(t)x_n(t-\tau)} \quad (34.14)$$

where overline $x$ represents a temporal averaging operation, and $S_{mn}(f)$ and $C_{mn}(t)$ are the cross-spectrum and cross-correlation, respectively. The coherence is essentially the square of the correlation coefficient between the corresponding frequency component of $x_m(t)$ and $x_n(t)$.

State-space plots of Granger index (flow) and coherence (synchrony) revealed three distinct states: (1) resting state in which causality and synchrony were both low (black); (2) early

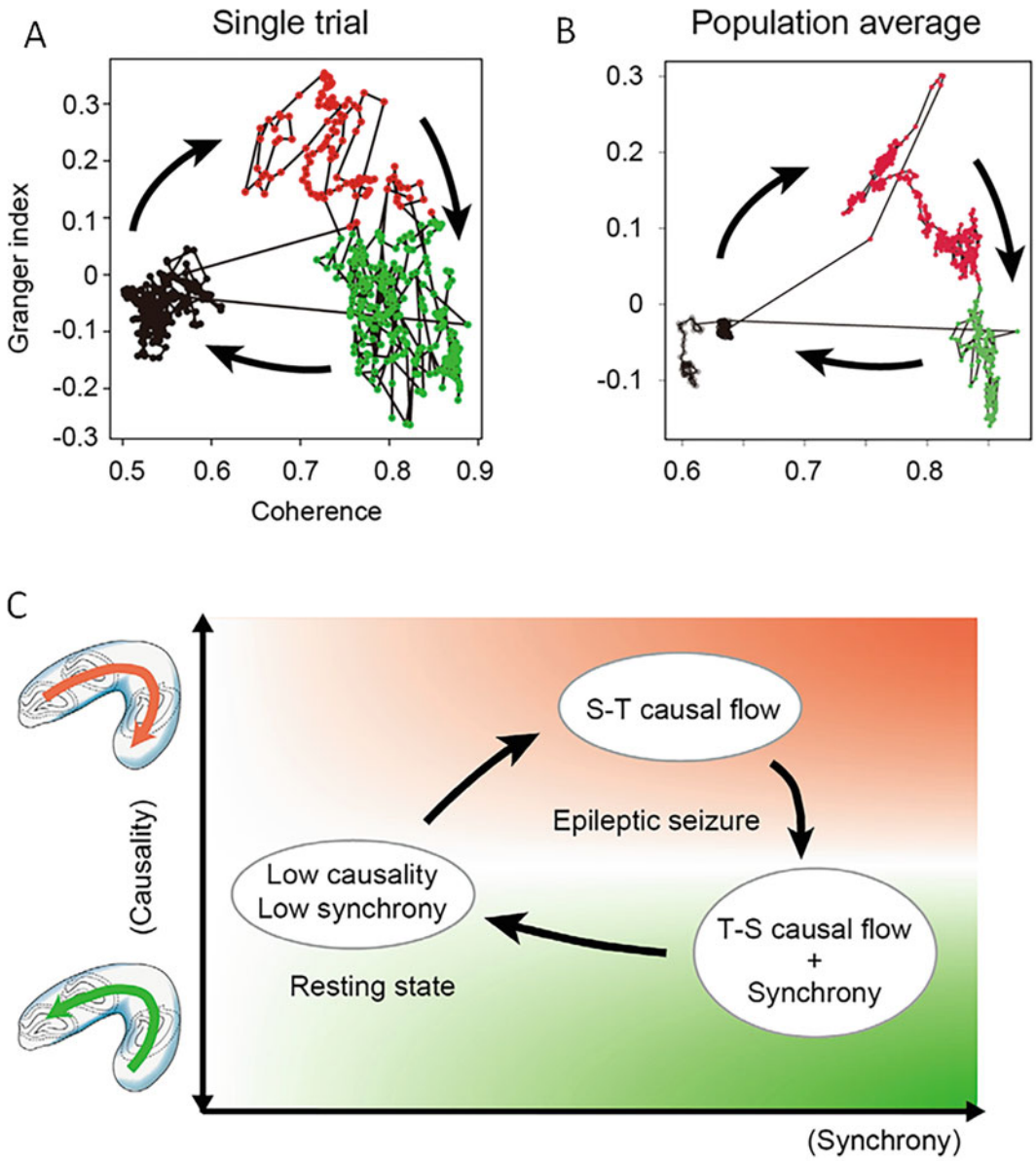


**Fig. 34.5** State transitions during hippocampal seizure-like afterdischarges. Three discrete states are illustrated by means of causality and coherence. (**a**) Single trial. (**b**) Population average. (**c**) Scheme of state transition and direction of propagation. Bidirectional networks along the longitudinal hippocampus work hierarchically in the genesis and termination of seizure-like afterdischarges (from Fig. 6C, Fig. 8. Osawa S, Iwasaki M, Hosaka R, Matsuzaka Y, Tomita H, Ishizuka T, Sugano E, Okumura E, Yawo H, Nakasato N, Tominaga T, Mushiake H. Optogenetically induced seizure and the longitudinal hippocampal network dynamics. PLoS One. 2013 Apr 10;8(4):e60928)

phase of afterdischarge characterized by dominant septo-temporal causality (flow) and increase in coherence (red); and (3) late phase of afterdischarge characterized by reversal of causality index to the temporo-septal direction and increase in coherence (green). Although flow of

signals fluctuates along septo-temporal axis, coherence among electrodes gradually built up, and the epileptic seizures stop suddenly like quenching (Fig. 34.5) (Osawa et al. 2013).

Combination of optogenetics and electrical monitoring techniques are suitable for understanding functions of neural network through spatio-temporal manipulation of neural circuits.

## 34.6 Concluding Remarks

We have been developing multimodal approaches to study functions of neural circuits by optogenetics-induced neural oscillations. It enables us to manipulate neural oscillations without electrical artifacts. Thus combination of optical stimulation and electrical monitoring will offer various approaches to study functions of neural circuits. Optogenetics-induced neural oscillations revealed resonance properties of neural circuits and entrained global neural network and eventually evoked state transitions of neural circuits such as seizure. We could study somatosensory system with optical precision of time and space by stimulating somatosensory system expressing light-gated ion channels with blue light. Therefore, multimodal functional analysis platform will provide significant progress in research on the neuroscience.

**Acknowledgments** This work was supported by JSPS KAKENHI Grant Number JP16H06276 (Platform of Advanced Animal Model Support) and MEXT KAKENHI Grant Number 15H05879 (Non-linear Neuro-oscillology) and this research was supported by AMED under Grant Number JP19dm0207001.

## References

Buzsáki G (2006) Rhythms of the brain. Oxford University Press, Oxford

Honjoh T, Ji ZG, Yokoyama Y, Sumiyoshi A, Shibuya Y, Matsuzaka Y, Kawashima R, Mushiake H, Ishizuka T, Yawo H (2014) Optogenetic patterning of whisker-barrel corticalsystem in transgenic rat expressing channelrhodopsin-2. PLoS One 9(4):e93706

Kanno S, Lee S, Harashima T, Kuki T, Kino H, Mushiake H, Yao H, Tanaka T (2013) Multiple optical stimulation to neuron using Si opto-neural probe with multiple optical waveguides and metal-cover for optogenetics. Conf Proc IEEE Eng Med Biol Soc 2013:253–256

Kuki T, Ohshiro T, Ito S, Ji ZG, Fukazawa Y, Matsuzaka Y, Yawo H, Mushiake H (2013) Frequency-dependent entrainment of neocortical slow oscillation to repeated optogenetic stimulation in the anesthetized rat. Neurosci Res 75(1):35–45

Kuki T, Fujihara K, Miwa H, Tamamaki N, Yanagawa Y, Mushiake H (2015) Contribution of parvalbumin and somatostatin-expressing GABAergic neurons to slow oscillations and the balance in beta-gamma oscillations across cortical layers. Front Neural Circuits 9:6

Liu Y, Ohshiro T, Sakuragi S, Koizumi K, Mushiake H, Ishizuka T, Yawo H (2019) Optogenetic study of the response interaction among multi-afferent inputs in the barrel cortex of rats. Sci Rep 9(1):3917

Osawa S, Iwasaki M, Hosaka R, Matsuzaka Y, Tomita H, Ishizuka T, Sugano E, Okumura E, Yawo H, Nakasato N, Tominaga T, Mushiake H (2013) Optogenetically induced seizure and the longitudinal hippocampal network dynamics. PLoS One 8(4): e60928

Puil E, Gimbarzevsky B, Miura RM (1986) Quantification of membrane properties of trigeminal root ganglion neurons in guinea pigs. J Neurophysiol 55:995–1016

Sutoh T, Yabe H, Sato Y, Hiruma T, Kaneko S (2000) Event-related desynchronization during an auditory oddball task. Clin Neurophysiol 111:858–862

Tohidi V, Nadim F (2009) Membrane resonance in bursting pacemaker neurons of an oscillatory network is correlated with network frequency. J Neurosci 29:6427–6435

Tomita H, Sugano E, Fukazawa Y, Isago H, Sugiyama Y et al (2009) Visual properties of transgenic rats harboring the channelrhodopsin-2 gene regulated by the thy-1.2 promoter. PLoS One 4:e7679

Wen L, Wang H, Tanimoto S, Egawa R, Matsuzaka Y, Mushiake H, Ishizuka T, Yawo H (2010) Opto-current-clamp actuation of cortical neurons using a strategically designed channelrhodopsin. PLoS One 5 (9):e12893

# Part V

# Medical Optogenetics

# Current Topics of Optogenetics for Medical Applications Toward Therapy

35

Toshihiro Kushibiki

**Abstract**

The optogenetics approach uses a combination of genetic and optical methods to initiate and control functions in specific cells of biological tissues. Since the high-speed control of neuronal activity by irradiating channelrhodopsin-2 with blue light was reported in 2005, tremendous advancement and application of optogenetics in the field of neuroscience, such as in studies that associate neuronal activity with behaviors, have been initiated. Optogenetics is not only used as a research tool, but is also started to apply in the diagnosis of a disease or as therapy in various studies. Here, I summarize current reports on therapy using a typical photopigment used in optogenetics, channelrhodopsin-2.

**Keywords**

Optogenetics · Channnelrhodopsin-2 · Gene therapy · Neuroscience · Cardiac resynchronization · Insulin · Diabetes

## Abbreviations

ChR Channelrhodopsin

ChR2 Channelrhodopsin-2

## 35.1 Introduction

The optogenetics approach uses optical methods to modulate the cellular expression of molecules, which are activated by irradiation with light energy, by genetic engineering to control/regulate cellular function or intracellular signal transduction (Miesenbock 2009, 2011; Fehrentz et al. 2011; Plaiasu 2011; Izquierdo-Serra et al. 2013). Advances in optogenetics enabled the precise control of specific cells on the millisecond timescale. Numerous studies have been reported that associate neuronal activity with behaviors, particularly where channelrhodopsin (ChR) is introduced into neurons as a photopigment (Wyart et al. 2009; Pastrana 2010; Deisseroth 2011; Kauwe and Isacoff 2013; Kramer et al. 2013). Neuroscientists have wished to control the neuronal activity at will, which remained a dream until the development of optogenetics. Since the development of the use of electricity at the end of the eighteenth century, electrical stimulation has been mainly employed for induction of muscle contraction and artificial induction of neuronal activity. However, electrical stimulation causes physical aggression; the cells and neuroaxis near an electrode are also stimulated, which hinders stimulation of only specific cells. In contrast, light irradiation allows focused irradiation at a site with multicolor control. The longer

T. Kushibiki (✉)
Department of Medical Engineering, National Defense Medical College, Tokorozawa, Saitama, Japan
e-mail: toshi@ndmc.ac.jp



H. Yawo et al. (eds.), *Optogenetics*, Advances in Experimental Medicine and Biology 1293,
https://doi.org/10.1007/978-981-15-8763-4_35

the wavelength is, the deeper the light reaches. In organisms, light irradiation is less aggressive than electrical stimulation. However, since neurons, other than photopigment cells, do not respond to light irradiation alone, a technology for introduction of photo-reactive molecules, neurons, or extracellular fluid had been desired. ChR was reported as an ancient cell-type rhodopsin based on the cDNA sequence database of the green algae *Chlamydomonas* (Nagel et al. 2002; Sineshchekov et al. 2002; Suzuki et al. 2003), and in 2003, channelrhodopsin-2 (ChR2) was reported to be a channel allowing direct permeation of cations, such as $Na^+$ and $K^+$, on irradiation with blue light (Nagel et al. 2003). ChR2 is a membrane protein with seven transmembrane domains and uses retinal as a chromophore. Retinal is covalently bound to the protein through the formation of a linkage between a Schiff base and a lysine residue conserved in the seventh helix of ChR2. When a photon of blue light is absorbed by retinal, it is converted from the all-trans form to the 13-cis form, causing a change in the protein structure and increasing its permeability to cations. This structural change is similar to that of ancient cell-type rhodopsin. Subsequently, ChR2 reverts to an inactive state and retinal converts back to the all-trans form to return to a resting state. In vertebrates, once retinal dissociates from rhodopsin upon absorbing light, it again rebinds to rhodopsin; however, ChR2 does not exhibit such a process. Thus, ChR2 was revealed to be a remarkable molecule that continues to function in the presence of retinal. Light irradiation of the neuronal membrane expressing ChR2 allows hyperpolarized neurons to depolarize mainly by the influx of extracellular $Na^+$ due to an electrochemical gradient and to induce an action potential when the influx is sufficient. In 2005, the expression of ChR2 in mammalian and nematode neurons was first reported by Deisseroth et al. and Nagel et al., respectively, along with the optical induction of the neuronal activity (Boyden et al. 2005; Nagel et al. 2005). Their studies demonstrated a very rapid activity, in which the period of activation was approximately 1 ms and the period after termination of light irradiation until the disappearance of ChR2 activity was 10–20 ms, and light at approximately 10–20 Hz was capable of inducing neuronal activity. Currently, modified ChR2 variants possessing various channel open states have been developed for use in studies. In 2007, Boyden et al. reported that halorhodopsin derived from ancient extreme halophile *Natronomonas pharaonis* (NpHR) was expressed in neurons and irradiation with yellow light enabled hyperpolarization of the neurons (Han and Boyden 2007; Zhang et al. 2007). In addition, they demonstrated that ChR2 and NpHR were simultaneously expressed in the same neurons, and blue and yellow light were capable of turning ON/OFF the neuronal activity. Optogenetic applications have now expanded rapidly to encompass studies on neural circuits, brain diseases, and nonneuronal systems, such as stem cells, cardiac tissues, and skeletal muscles. Accordingly, based on its increasing importance as a paradigm in many fields of biomedical research, optogenetics was selected as the "Method of the Year" in 2010 by *Nature Methods*.

The use of optogenetics has answered the question of whether memories are recorded in neurons of the hippocampus, which had been unresolved for years (Liu et al. 2012). Optogenetics has significantly contributed toward the exploration of the possibility of answering the questions of whether glial cells are associated with respiratory function (Gourine et al. 2010) and of elucidating the function of the neural circuits in the amygdala causing anxiety (Tye et al. 2011). To control intracellular signal transduction pathways, chimeric proteins, OptoXRs, were reported in which the intracellular loop of rhodopsin is replaced with that of adrenergic receptor, a G-protein-coupled receptor (Airan et al. 2009). Furthermore, light-switchable transgene systems (Wang et al. 2012; Chen et al. 2013; Ma et al. 2013) (Wu et al. 2009) (Konermann et al. 2013), which switch protein expression ON/OFF by light irradiation and photopigments that use scavengers other than retinal, such as photoactivated adenylyl cyclase (PAC) (Iseki et al. 2002; Yoshikawa et al. 2005) (Schroder-Lang et al. 2007; Looser et al. 2009), LiGluR

(Volgraf et al. 2006) (Szobota et al. 2007), and HyLighter (Janovjak et al. 2010), were reported; thus, photopigments used in optogenetics have progressively developed and their applications have been reported. Studies in which such rapidly developing optogenetics is not only used as a research tool, but is also applied in the diagnosis or treatment of a disease are increasingly reported. Here, we present our recent study and summarize the reports on therapy with a typical photopigment, ChR2, used in optogenetics.

## 35.2 Application of Optogenetics in Therapy

Optogenetics has been mainly used as a technique to study the control of cellular and behavioral functions. Since optogenetics can be used to control not only neuronal functions but also the functions of various other cells with light, there is high possibility of applying optogenetics to studies elucidating cellular function and the resultant physiological phenomena. Therefore, the use of optogenetics as a treatment method for disease, in addition to its use as a research tool, is inevitable. Table 35.1 shows the diseases and physiological functions targeted by treatment using optogenetics.

### 35.2.1 Brain Disease

Even greater experimental power has been achieved by targeting the expression of ChR2 in specific subsets of neurons within the brain. Such targeting is often achieved by restricting channel expression both anatomically, by precise delivery of ChR2-encoding viral vectors to specific brain regions, or genetically, by placing ChR2 under the control of a promoter specifically activated in a cell type of interest. Genetic targeting can itself be achieved by multiple means, e.g., by transgenesis or by the use of viruses encoding channels driven by cell-type-specific promoters.

Electronic systems that integrate with the body provide powerful diagnostic and therapeutic capabilities for basic research and clinical medicine. Recent research establishes materials and mechanical constructs for electronic circuits, light-emitting diodes (LEDs), sensors, and other components. In optogenetics, the use of fiber optic devices restricts opportunities for in vivo use and widespread biological application. As a solution, the groups lead by Bruchas and Rogers developed mechanically compliant, ultrathin, multifunctional optoelectronic systems that mount on releasable injection needles for insertion into the depths of the soft tissue (Kim et al. 2013; McCall et al. 2013). These devices incorporate cellular-scale components ranging from independently addressable multicolored microscale, precision optical, thermal, and electrophysiological sensors and actuators. In addition, Tamura et al. reported a tungsten microelectrode-based optical probe, or an optrode, which encloses optical fibers within its insulation glass (Tamura et al. 2012). This smooth glass-coated optrode is a promising tool for long-term in vivo experiments with various research targets, including the deep brain structures in behaving monkeys. These types of custom devices represent a significant step toward the use of optogenetics in clinical applications, allowing multiple bright excitation sites along the length of a minimally invasive probe.

#### 35.2.1.1 Alzheimer's Disease

Etter et al. reported that optogenetic stimulation of medial septal parvalbumin neurons at 40 Hz could provide a novel strategy for treating memory deficits in Alzheimer's disease (Etter et al. 2019). They showed that optogenetic stimulation of parvalbumin neurons at 40 Hz (but not 80 Hz) restores hippocampal slow gamma oscillations amplitude and phase-amplitude coupling of the J20 Alzheimer's disease mouse model. Restoration of slow gamma oscillations during retrieval rescued spatial memory in mice despite significant plaque deposition. In addition, Bostancikliogl et al. reported how serotonin affects the pathogenesis of Alzheimer's disease in a comprehensive perspective and they suggested that the optogenetics manipulation of serotonin nuclei retrieves the lost memory by closing the inward-rectifier potassium channel

**Table 35.1** Representative diseases and physiological functions targeted in therapy using channelrhodopsin for optogenetics

| Organ | Target of treatment | References |
|---|---|---|
| Brain | Alzheimer's disease | Etter et al. (2019), Bostancikliogl u (2020) |
| | Parkinson's disease | Kravitz et al. (2010), Chen et al. (2015) |
| | Depression | Ramirez et al. (2015), Biselli et al. (2019) |
| | Functional recovery and regeneration | Bryson et al. (2014), Cheng et al. (2014) |
| Eye | Reconstructing vision | Lagali et al. (2008), Tomita et al. (2010), Isago et al. (2012), Osawa et al. (2013), Garita-Hernandez et al. (2019) |
| Ear | Inner ear reconstruction | Duarte et al. (2018), Dombrowski et al. (2019) |
| Heart | Cardiac pacing | Bingen et al. (2014), Nussinovitch and Gepstein (2015), Dwenger et al. (2019), Sasse et al. (2019), Zgierski-Johnston et al. (2019) |
| Pancreas | Insulin secretion | Kushibiki et al. (2015) |

Kir2 on the memory engram cells (Bostancikliogl u 2020). Also, they raised the possible effects of serotonin on the memory engram cells and the interactions between the amyloid-centric hypothesis of Alzheimer's disease and the memory engram hypothesis to explain the pathophysiology of memory loss in Alzheimer's disease.

#### 35.2.1.2 Parkinson's Disease

Kravitz et al. demonstrated that when ChR2 is expressed only under the transcriptional control of dopamine D1 receptor, which is expressed in the medium spiny neurons of the striatal direct pathway, and when light irradiation is conducted using an optical fiber, symptoms can be relieved in a mouse model of Parkinson's disease (Kravitz et al. 2010). In their study, freezing, bradykinesia, and abnormal motion at the beginning of movement were remitted in the conscious mice by activation of the direct pathway. This study confirmed that basal ganglia circuits play an extremely important role in the bidirectional regulation of motor behavior and demonstrated that the regulation of the circuits of direct pathway is a potential epoch-making therapy for improving dyskinesia in Parkinson's disease. This technique is considered to allow more precise neuronal stimulation compared to that by deep brain stimulation, which is currently used in therapy for Parkinson's disease. Previously, a report clarified the mechanism underlying an important function of dopaminergic pathways, in which the dopaminergic pathway projecting from the substantia nigra to the striatum regulates excitatory glutamatergic inputs from the cerebral cortex and thalamus by controlling transplanted dopaminergic neurons with light (Chen et al. 2015). In this report, stimulation of the adjacent tissue, callosum, induced dopamine release from the grafts in the striatal GABAergic neurons, and excitatory postsynaptic potential was blocked by a D1 receptor antagonist (Chen et al. 2015).

#### 35.2.1.3 Depression

Biselli et al. reviewed that optogenetics and chemogenetics are driving major depressive disorder (MDD) research forward by unveiling causal relations between cell-type-specific control of neurons and depressive-like behavior in rodents (Biselli et al. 2019). A complex interacting network of relevant structures, in which central circuitries causally related to depressive-like behavior are implicated, has been identified. As most relevant structures emerge: medial prefrontal cortex, anterior cingulate cortex, amygdala, nucleus accumbens, ventral tegmental area, hippocampus, and raphe nuclei. They described that comparability of studies is partly limited since even small deviations in methodological approaches lead to different outcomes. Factors influencing study outcomes were identified and need to be considered in future studies. Ramirez et al. successfully improved depression in mice by artificially activating the cells in the hippocampal dentate

gyrus that had been active in memorization during the pleasant period in depressed mice (Ramirez et al. 2015).

#### 35.2.1.4 Functional Recovery and Regeneration

In recent years, numerous studies on therapies in the field of neuroscience, where optogenetics has progressed, have been reported. Among them, Cheng et al. presented a successful acceleration in restoring neuronal function after stroke by neuronal stimulation with optogenetics (Cheng et al. 2014), and Bryson et al. demonstrated the optical control of muscle function by transplanting differentiated motor neurons derived from the embryonic stem (ES) cells expressing ChR2 into mice (Bryson et al. 2014). Xie et al. described the possibility whether optogenetics could be used to control the release of gliotransmitters and regulate astrocytic membrane channels (Xie et al. 2020). The capability of modulating the bidirectional interactions between astrocytes and neurons in both synaptic and neuronal networks via optogenetics is evaluated. Furthermore, they described that manipulating astrocytes via optogenetics might be an effective way to investigate the potential therapeutic strategy for neurodegenerative diseases.

### 35.2.2 Reconstructing Vision

Application of photoreceptors to the photoresponse system and the retina in humans, i.e., a possibility of reconstructing vision, has been reported. Electrical stimulation of the artificial retina has been studied in degenerated photoreceptors resulting from retinitis pigmentosa or age-related maculopathy, where neurons are active after degeneration. However, the number of stimulating electrodes is limited in the artificial retina and the resolution is not sufficient. Some groups have attempted to reconstruct vision by targeted expression of ChR2 in the remaining retinal ganglion cells (Lagali et al. 2008; Tomita et al. 2010; Isago et al. 2012; Osawa et al. 2013). These studies suggest that introducing ChR2 into the retinal ganglion cells may lead to a much higher resolution than that obtained by the use of the artificial retina. Garita-Hernandez et al. reported that a hyperpolarizing microbial opsin into photoreceptor precursors from newborn mice, and transplant them into blind mice lacking the photoreceptor layer for a retinal pigment epithelium (RPE)-independent treatment approach (Garita-Hernandez et al. 2019). Those optogenetically transformed photoreceptors are light-responsive and their transplantation leads to the recovery of visual function, as shown by ganglion cell recordings and behavioral tests. Subsequently, they generated cone photoreceptors from human-induced pluripotent stem cells, expressing the chloride pump. After transplantation into blind mice, they observed light-driven responses at the photoreceptor and ganglion cell levels. Those results demonstrated that structural and functional retinal repair is possible by combining stem cell therapy and optogenetics.

### 35.2.3 Inner Ear Reconstruction

Dombrowski et al. reported the optical cochlear implants (CIs) (Dombrowski et al. 2019). When hearing fails, CIs provide open speech perception to most of the currently half a million CI users. CIs bypass the defective sensory organ and stimulate the auditory nerve electrically. The major bottleneck of current CIs is the poor coding of spectral information, which results from wide current spread from each electrode contact. As light can be more conveniently confined, optical stimulation of the auditory nerve presents a promising perspective for a fundamental advance of CIs. Moreover, given the improved frequency resolution of optical excitation and its versatility for arbitrary stimulation patterns, the approach also bears the potential for auditory research. Duarte et al. reported the first to describe robust SGN transduction, opsin expression, and optically evoked auditory electrophysiology in neonatal mice (Duarte et al. 2018). That work may provide the basis for a new generation of cochlear implant based on light.

### 35.2.4 Cardiac Pacing

Optogenetic methods enable selective de- and hyperpolarization of cardiomyocytes expressing light-sensitive proteins within the myocardium. By using light, this technology provides very high spatial and temporal precision, which is in clear contrast to electrical stimulation. In addition, cardiomyocyte-specific expression would allow pain-free stimulation. In light of these intrinsic technical advantages, optogenetic methods provide an intriguing opportunity to understand and improve current strategies to terminate cardiac arrhythmia as well as for possible pain-free arrhythmia termination in patients in the future (Sasse et al. 2019). Zgierski-Johnston et al. reported that the utility of an implantable multi light-emitting diode (LED) optical probe (IMLOP) for intramural pacing of mouse hearts expressing cardiac-specific ChR2 (Zgierski-Johnston et al. 2019). They demonstrated IMLOP-based intramural optical pacing of the heart. Those probes cause locally constrained tissue damage in the acute setting and require low-light intensities for pacing. Bingen et al. first demonstrated the efficacy of optogenetics for defibrillation in a model where atrial fibrillation was induced in a cardiomyocyte sheet; this report revealed a potential therapy for patients with atrial fibrillation (Bingen et al. 2014). Dwenger et al. transfected ChR2 into human-induced pluripotent stem cell-derived engineered cardiac tissues with a desensitization resistant, chimeric channelrhodopsin protein, and then optically paced engineered cardiac tissues to accelerate maturation (Dwenger et al. 2019). Engineered cardiac tissues were then chronically optically paced above their intrinsic beat rates in vitro from day 7 to 14. Chronically optically paced resulted in improved engineered cardiac tissue electrophysiological properties and subtle changes in the expression of some cardiac relevant genes, though active force generation and histology were unchanged. These results validate the feasibility of a novel chronically optically paced paradigm to explore noninvasive and scalable optically paced-induced engineered cardiac tissue maturation strategies. Nussinovitch et al. succeeded in in vivo cardiac resynchronization therapy, where ChR2 was delivered to the rat myocardium with an adeno-associated virus vector and ventricular pacing was performed by light irradiation to improve the pumping function of the heart (Nussinovitch and Gepstein 2015).

### 35.2.5 Regenerative Medicine

Studies not only on optogenetics as a research tool for understanding the control of cellular and behavioral functions but also on applied research to medicine, particularly, regenerative medicine has been increasingly reported in recent years. A study showed that light irradiation of ES cells with incorporated ChR2-induced differentiation by depolarization of the cell membrane (Stroh et al. 2011), and studies have been conducted with a focus on application in regenerative medicine. Hu et al. reviewed optogenetic tools are a promising method for elucidating and simulating developmental processes, thus providing vast prospects for tissue engineering and regenerative medicine applications (Hu et al. 2020). They summarize potential applications of optogenetics for tissue engineering are discussed, including light-controlled genetic engineering and regulation of signaling pathways. Furthermore, they reported how emerging biomaterials and photoelectric technologies have greatly promoted the clinical application of optogenetics and inspired new concepts for optically controlled therapies. That review seems to be a very well-organized article describing the future of optogenetics. We controlled insulin secretion with light irradiation in a mouse pancreatic β cell line (MIN6) expressing ChR2 (Kushibiki et al. 2015). In the mechanism underlying insulin secretion from the normal pancreatic β cells, the ATP level increases when glucose is metabolized in the pancreatic β cells and the potential of the cell membrane elevates due to closing of the ATP-sensitive potassium channels, followed by opening of voltage-dependent calcium channels and influx of $Ca^{2+}$ into the cells, which initiates insulin secretion. The forced expression of ChR2 in the

pancreatic β cells and laser irradiation enabled us to facilitate insulin secretion from the pancreatic β cells without contribution of glycolysis As shown in our studies, stimulation of transplanted cells and improvement in the function of regenerated tissues with optogenetics can be expected in the field where the functional substitution of cells/tissues by conventional regenerative medicine or cell transplantation therapy alone has not been sufficient. We are continuing our research with an aim to utilize optogenetics for the control of cellular and tissue functions with optical techniques in the field of medicine.

## 35.3 Future Perspectives

A growing number of studies have been reported to use the optogenetics approach, with over 800 such studies being conducted annually in recent years. Two steps—expression of sufficient number of photo-reactive protein molecules in the cells to be controlled and sufficient energy light irradiation of these cells—are necessary for successful studies using optogenetics. If these steps can be carried out, any function within cells can be controlled at a given time. Although optogenetics was first expected to advance in the field of neurophysiology, the optical control of intracellular signal transduction has become possible and the range of its applications has expanded to the study of almost all species and tissues. Furthermore, optogenetics is useful for elucidating mechanisms underlying various diseases and actions of drugs. Since foreign genes are introduced into the target cells to be treated, therapy with optogenetics falls under gene therapy. There is no doubt that optogenetics will become a useful tool for therapy if some regulations are cleared. We expect that not only optogenetics will become a major research tool for analyzing cellular and behavioral functions, but the world of optical medicine/optical biology will also expand with optogenetics as a diagnostic/therapeutic method in the near future.

## References


Airan RD, Thompson KR, Fenno LE et al (2009) Temporally precise in vivo control of intracellular signalling. Nature 458:1025–1029

Bingen BO, Engels MC, Schalij MJ et al (2014) Light-induced termination of spiral wave arrhythmias by optogenetic engineering of atrial cardiomyocytes. Cardiovasc Res 104:194–205

Biselli T, Lange SS, Sablottny L et al (2019) Optogenetic and chemogenetic insights into the neurocircuitry of depression-like behaviour: a systematic review. Eur J Neurosci. https://doi.org/10.1111/ejn.14603

Bostancikli oglu M (2020) Optogenetic stimulation of serotonin nuclei retrieve the lost memory in Alzheimer's disease. J Cell Physiol 235:836–847

Boyden ES, Zhang F, Bamberg E et al (2005) Millisecond-timescale, genetically targeted optical control of neural activity. Nat Neurosci 8:1263–1268

Bryson JB, Machado CB, Crossley M et al (2014) Optical control of muscle function by transplantation of stem cell-derived motor neurons in mice. Science 344:94–97

Chen X, Wang X, Du Z et al (2013) Spatiotemporal control of gene expression in mammalian cells and in mice using the LightOn system. Curr Protoc Chem Biol 5:111–129

Chen Y, Xiong M, Zhang SC (2015) Illuminating Parkinson's therapy with optogenetics. Nat Biotechnol 33:149–150

Cheng MY, Wang EH, Woodson WJ et al (2014) Optogenetic neuronal stimulation promotes functional recovery after stroke. Proc Natl Acad Sci U S A 111:12913–12918

Deisseroth K (2011) Optogenetics. Nat Methods 8:26–29

Dombrowski T, Rankovic V, Moser T (2019) Toward the optical Cochlear implant. Cold Spring Harb Perspect Med 9:a033225

Duarte MJ, Kanumuri VV, Landegger LD et al (2018) Ancestral adeno-associated virus vector delivery of opsins to spiral ganglion neurons: implications for optogenetic cochlear implants. Mol Ther 26:1931–1939

Dwenger M, Kowalski WJ, Ye F et al (2019) Chronic optical pacing conditioning of h-iPSC engineered cardiac tissues. J Tissue Eng 10:2041731419841748

Etter G, van der Veldt S, Manseau F et al (2019) Optogenetic gamma stimulation rescues memory impairments in an Alzheimer's disease mouse model. Nat Commun 10:5322

Fehrentz T, Schonberger M, Trauner D (2011) Optochemical genetics. Angew Chem Int Ed Engl 50:12156–12182

Garita-Hernandez M, Lampic M, Chaffiol A et al (2019) Restoration of visual function by transplantation of optogenetically engineered photoreceptors. Nat Commun 10:4524

Gourine AV, Kasymov V, Marina N et al (2010) Astrocytes control breathing through pH-dependent release of ATP. Science 329:571–575

Han X, Boyden ES (2007) Multiple-color optical activation, silencing, and desynchronization of neural activity, with single-spike temporal resolution. PLoS One 2: e299

Hu W, Li Q, Li B et al (2020) Optogenetics sheds new light on tissue engineering and regenerative medicine. Biomaterials 227:119,546

Isago H, Sugano E, Wang Z et al (2012) Age-dependent differences in recovered visual responses in Royal College of surgeons rats transduced with the Channelrhodopsin-2 gene. J Mol Neurosci 46:393–400

Iseki M, Matsunaga S, Murakami A et al (2002) A blue-light-activated adenylyl cyclase mediates photoavoidance in Euglena gracilis. Nature 415:1047–1051

Izquierdo-Serra M, Trauner D, Llobet A et al (2013) Optical modulation of neurotransmission using calcium photocurrents through the ion channel LiGluR. Front Mol Neurosci 6:3

Janovjak H, Szobota S, Wyart C et al (2010) A light-gated, potassium-selective glutamate receptor for the optical inhibition of neuronal firing. Nat Neurosci 13:1027–1032

Kauwe G, Isacoff EY (2013) Rapid feedback regulation of synaptic efficacy during high-frequency activity at the Drosophila larval neuromuscular junction. Proc Natl Acad Sci U S A 110:9142–9147

Kim TI, McCall JG, Jung YH et al (2013) Injectable, cellular-scale optoelectronics with applications for wireless optogenetics. Science 340:211–216

Konermann S, Brigham MD, Trevino A et al (2013) Optical control of mammalian endogenous transcription and epigenetic states. Nature 500:472–476

Kramer RH, Mourot A, Adesnik H (2013) Optogenetic pharmacology for control of native neuronal signaling proteins. Nat Neurosci 16:816–823

Kravitz AV, Freeze BS, Parker PR et al (2010) Regulation of parkinsonian motor behaviours by optogenetic control of basal ganglia circuitry. Nature 466:622–626

Kushibiki T, Okawa S, Hirasawa T et al (2015) Optogenetic control of insulin secretion by pancreatic beta-cells in vitro and in vivo. Gene Ther 22:553–559

Lagali PS, Balya D, Awatramani GB et al (2008) Light-activated channels targeted to ON bipolar cells restore visual function in retinal degeneration. Nat Neurosci 11:667–675

Liu X, Ramirez S, Pang PT et al (2012) Optogenetic stimulation of a hippocampal engram activates fear memory recall. Nature 484:381–385

Looser J, Schroder-Lang S, Hegemann P et al (2009) Mechanistic insights in light-induced cAMP production by photoactivated adenylyl cyclase alpha (PACalpha). Biol Chem 390:1105–1111

Ma Z, Du Z, Chen X et al (2013) Fine tuning the LightOn light-switchable transgene expression system. Biochem Biophys Res Commun 440:419–423

McCall JG, Kim TI, Shin G et al (2013) Fabrication and application of flexible, multimodal light-emitting devices for wireless optogenetics. Nat Protoc 8:2413–2428

Miesenbock G (2009) The optogenetic catechism. Science 326:395–399

Miesenbock G (2011) Optogenetic control of cells and circuits. Annu Rev Cell Dev Biol 27:731–758

Nagel G, Ollig D, Fuhrmann M et al (2002) Channelrhodopsin-1: a light-gated proton channel in green algae. Science 296:2395–2398

Nagel G, Szellas T, Huhn W et al (2003) Channelrhodopsin-2, a directly light-gated cation-selective membrane channel. Proc Natl Acad Sci U S A 100:13940–13945

Nagel G, Brauner M, Liewald JF et al (2005) Light activation of channelrhodopsin-2 in excitable cells of Caenorhabditis elegans triggers rapid behavioral responses. Curr Biol 15:2279–2284

Nussinovitch U, Gepstein L (2015) Optogenetics for in vivo cardiac pacing and resynchronization therapies. Nat Biotechnol 33:750–754

Osawa S, Iwasaki M, Hosaka R et al (2013) Optogenetically induced seizure and the longitudinal hippocampal network dynamics. PLoS One 8:e60928

Pastrana E (2010) Optogenetics: controlling cell function with light. Nat Methods 8:24–25

Plaiasu V (2011) Update in genetics. Maedica (Buchar) 6:70

Ramirez S, Liu X, MacDonald CJ et al (2015) Activating positive memory engrams suppresses depression-like behaviour. Nature 522:335–339

Sasse P, Funken M, Beiert T et al (2019) Optogenetic termination of cardiac arrhythmia: mechanistic enlightenment and therapeutic application? Front Physiol 10:675

Schroder-Lang S, Schwarzel M, Seifert R et al (2007) Fast manipulation of cellular cAMP level by light in vivo. Nat Methods 4:39–42

Sineshchekov OA, Jung KH, Spudich JL (2002) Two rhodopsins mediate phototaxis to low- and high-intensity light in Chlamydomonas reinhardtii. Proc Natl Acad Sci U S A 99:8689–8694

Stroh A, Tsai HC, Wang LP et al (2011) Tracking stem cell differentiation in the setting of automated optogenetic stimulation. Stem Cells 29:78–88

Suzuki T, Yamasaki K, Fujita S et al (2003) Archaeal-type rhodopsins in Chlamydomonas: model structure and intracellular localization. Biochem Biophys Res Commun 301:711–717

Szobota S, Gorostiza P, Del Bene F et al (2007) Remote control of neuronal activity with a light-gated glutamate receptor. Neuron 54:535–545

Tamura K, Ohashi Y, Tsubota T et al (2012) A glass-coated tungsten microelectrode enclosing optical fibers for optogenetic exploration in primate deep brain structures. J Neurosci Methods 211:49–57

Tomita H, Sugano E, Isago H et al (2010) Channelrhodopsin-2 gene transduced into retinal

ganglion cells restores functional vision in genetically blind rats. Exp Eye Res 90:429–436

Tye KM, Prakash R, Kim SY et al (2011) Amygdala circuitry mediating reversible and bidirectional control of anxiety. Nature 471:358–362

Volgraf M, Gorostiza P, Numano R et al (2006) Allosteric control of an ionotropic glutamate receptor with an optical switch. Nat Chem Biol 2:47–52

Wang X, Chen X, Yang Y (2012) Spatiotemporal control of gene expression by a light-switchable transgene system. Nat Methods 9:266–269

Wu YI, Frey D, Lungu OI et al (2009) A genetically encoded photoactivatable Rac controls the motility of living cells. Nature 461:104–108

Wyart C, Del Bene F, Warp E et al (2009) Optogenetic dissection of a behavioural module in the vertebrate spinal cord. Nature 461:407–410

Xie Z, Yang Q, Song D et al (2020) Optogenetic manipulation of astrocytes from synapses to neuronal networks: a potential therapeutic strategy for neurodegenerative diseases. Glia 68:215–226

Yoshikawa S, Suzuki T, Watanabe M et al (2005) Kinetic analysis of the activation of photoactivated adenylyl cyclase (PAC), a blue-light receptor for photomovements of Euglena. Photochem Photobiol Sci 4:727–731

Zgierski-Johnston CM, Ayub S, Fernandez MC et al (2019) Cardiac pacing using transmural multi-LED probes in channelrhodopsin-expressing mouse hearts. Prog Biophys Mol Biol. https://doi.org/10.1016/j.pbiomolbio.2019.11.004

Zhang F, Wang LP, Brauner M et al (2007) Multimodal fast optical interrogation of neural circuitry. Nature 446:633–639

# Optogenetic Approaches to Understand the Neural Circuit Mechanism of Social Deficits Seen in Autism Spectrum Disorders

36

Nobuhiro Nakai, Eric T. N. Overton, and Toru Takumi

**Abstract**

Individuals with neurodevelopmental disorders, such as autism spectrum disorders (ASDs), are diagnosed based on nonquantitative objective parameters such as behavioral phenotypes. It is still unclear how any neural mechanism affects such behavioral phenotypes in these patients. In human genetics, a large number of genetic abnormalities including single nucleotide variation (SNV) and copy number variation (CNV) have been found in individuals with ASDs. It is thought that influence of such variations converges on dysfunction of neural circuit resulting in common behavioral phenotypes of ASDs such as deficits in social communication and interaction. Recent studies suggest that an excitatory/inhibitory (E/I) imbalanced state, which induces disruption of neural circuit activities, is one of the pathophysiological abnormalities in ASD brains. To assess the causal relationship between brain abnormalities and behavioral deficits, we can take advantage of optogenetics with animal models of ASDs that recapitulate human genetic mutations. Here, we review optogenetics studies being utilized to dissect neural circuit mechanisms associated with social deficits in model mice of ASD. Optogenetic manipulation of disrupted neural activities would help us understand how neural circuits affect behavioral deficits observed in ASDs.

**Keywords**

ASD · E/I balance · Medial prefrontal cortex · Animal model · Social behavior

## Abbreviations

| | |
|---|---|
| 5-HT | 5-Hydroxytryptamine (serotonin) |
| ACC | Anterior cingulate cortex |
| ASD | Autism spectrum disorder |
| CMS | Chronic mild stress |
| CNV | Copy number variation |
| DBS | Deep brain stimulation |
| DRN | Dorsal raphe nucleus |
| E/I | Excitatory/inhibitory |
| EEG | Electroencephalography |
| GABA | γ-Aminobutyric acid |
| GAD | Glutamic acid decarboxylase |
| KI | Knockin |
| KO | Knockout |
| LFP | Long-term potentiation |
| MEG | Magnetoencephalography |
| mPFC | Medial prefrontal cortex |

N. Nakai · T. Takumi (✉)
RIKEN Brain Science Institute, Wako, Saitama, Japan

Department of Physiology and Cell Biology, Kobe University School of Medicine, Kobe, Japan
e-mail: takumit@med.kobe-u.ac.jp

E. T. N. Overton
RIKEN Brain Science Institute, Wako, Saitama, Japan



H. Yawo et al. (eds.), *Optogenetics*, Advances in Experimental Medicine and Biology 1293,
https://doi.org/10.1007/978-981-15-8763-4_36

| | |
|---|---|
| NAc | Nucleus accumbens |
| NMDAR | N-methyl-D-aspartate receptor |
| NS | Narrow-spiking |
| PL | Prelimbic area |
| PV | Parvalbumin |
| SDS | Social defeat stress |
| SNV | Single-nucleotide variation |
| SSFO | Stable step-function opsin |
| VTA | Ventral tegmental area |
| WS | Wide-spiking |

## 36.1 Utilization of Animal Models for ASDs

Genetic or biological markers in neurodevelopmental and psychiatric disorders, such as autism spectrum disorders (ASDs), schizophrenia, and major depressive disorder, are still not available. Diagnosis for such disorders is conventionally performed via interviews with patients by clinical experts. Although it is well known that patients with such disorders commonly have deficits in social behavior, we have few information on the pathophysiology and functional mechanisms of the brain in these patients. Functional brain studies in human subjects using noninvasive methods (e.g., functional magnetic resonance imaging, near-infrared spectroscopy, electroencephalography (EEG), and magnetoencephalography (MEG)) are one way to understand human social behaviors at neural circuit levels under the condition of social-related tasks. While such noninvasive measurements are useful in discovering correlations between neural activities and social-related tasks, it is difficult to investigate the causal relationship of neural circuits which contribute to social behavior by manipulating neural activities due to ethical issues for living subjects. Usage of animal models is another option in understanding deficits in social behaviors. Modeling genetic and behavioral abnormalities that resemble neurodevelopmental and psychiatric disorders is an initial step in understanding the underlying neural mechanisms of such disorders. By using animal models that replicate disorder-like behaviors in combination with optogenetic tools, we can assess how their neural circuit abnormalities link to their behavioral abnormalities, which is an advantage of animal model studies.

Recently, a large number of genetic and genomic mutations have been found in individuals with ASDs (Liu and Takumi 2014; Malhotra and Sebat 2012; Sullivan et al. 2012). In the human genome, it is estimated that 10–20% of ASD cases have pathogenic genome abnormalities including single nucleotide variations (SNVs) and copy number variations (CNVs) which may perturb typical development of brain function (Cross-Disorder Group of the Psychiatric Genomics Consortium et al. 2013; Marshall and Scherer 2012; Schaaf and Zoghbi 2011; Takumi and Tamada 2018). SNVs and CNVs induce alteration of gene expression in cells and affect cellular physiological functions that potentially contribute to changes in neural function. However, the relationship between SNVs/CNVs and neural abnormalities is not well understood due to the heterogeneity in these pathogenic genome abnormalities. Chromosome-engineering techniques which generate chromosomal abnormalities in animals provide models for ASD with CNVs, which satisfies their construct validity (Nakatani et al. 2009). Currently, the CRISPR-Cas9 system, a genome editing tool, greatly contributes in quickly and easily generating model animals with SNVs or CNVs (Nakanishi et al. 2017). The models additionally need to satisfy face validity, which means that a model should have behavioral phenotypes similar to symptoms observed in human patients. Although ASD model mice exhibit variations in their behavioral phenotypes, there is a common trend of deficits in sociability (Blundell et al. 2009; Chao et al. 2010; Dani et al. 2005; Etherton et al. 2011; Gibson et al. 2008; Gkogkas et al. 2013; Han et al. 2012; Hines et al. 2008; Nakai et al. 2017; Peça et al. 2011; Poulopoulos et al. 2009; Schmeisser et al. 2012; Tabuchi et al. 2007; Wallace et al. 2012; Won et al. 2012; Yang et al. 2012). Finding common characteristics at not only the behavioral but also at the physiological levels in these genetic models by meta-analysis

would help our understanding of the pathophysiology in ASD brains.

## 36.2 Excitatory/Inhibitory Imbalance in ASD and Schizophrenia

Neural synchrony is regulated by well-organized excitatory and inhibitory (E/I) transmissions and controls behavioral responses to external stimuli from the environment. It is hypothesized that patients with ASDs (and also schizophrenia) have alterations in E/I balance in their brain (Gao and Penzes 2015; Nelson and Valakh 2015; Rubenstein and Merzenich 2003), suggested by the fact that about 30% of ASD patients have seizure-related symptoms. In a postmortem study of human patients with ASD, the expression of glutamic acid decarboxylase 65 and 67 (GAD65/67), which synthesize γ-aminobutyric acid (GABA), is decreased in parietal and cerebellar cortices (Fatemi et al. 2002). EEG and MEG studies also show abnormalities in the synchronized oscillatory activity in cortical regions of patients with ASD and schizophrenia (Uhlhaas and Singer 2010). These abnormalities may arise from dysfunction in inhibitory systems, as evidenced by the decreased number of parvalbumin (PV) positive interneurons in the cortex, which is consistently reported in studies of ASD model mice, suggesting that dysfunction in the inhibitory system enhances the excitatory state and directly or indirectly induce autistic behavioral phenotypes (Gogolla et al. 2009). Such reduced expression of GAD65/67 or disruption of PV interneurons may elicit profound impairments in homeostasis of neural excitability, resulting in dysfunction of information processing and decision-making in ASDs.

Recent optogenetic studies indicate that inhibitory neural activities along with excitatory activities contribute to the generation of beta and gamma oscillations (Buzsáki and Wang 2012; Cardin et al. 2009; Chen et al. 2017; Sohal et al. 2009). For example, gamma oscillations on local neural circuits in the somatosensory cortex were able to be generated by optogenetically stimulating PV interneurons at 30–50 Hz, while photoactivation of pyramidal neurons was unable to induce gamma oscillations at the same stimulation frequency (Cardin et al. 2009). The gamma oscillations in local neural circuits generated by the activity of PV interneurons may be controlled by function of N-methyl-D-aspartate receptor (NMDAR). PV neuron-specific NMDAR subunit 1-deficient mice (PV-cre/NR1$^{f/f}$) show upregulation of gamma oscillation at resting state (Carlén et al. 2012). Optogenetic stimulation of PV interneurons at gamma-range frequency induces the enhancement of gamma oscillations of the somatosensory cortex in control mice but induces reduction of gamma oscillations in PV-cre/NR1$^{f/f}$ mice. This PV-specific NR1 knockout does not affect spatial memory in the water maze test but decreases working memory in the T-maze test.

Furthermore, it is suggested that hypofunction of NMDAR is associated with cortical oscillatory abnormalities in schizophrenia, which is induced by weakened excitability of GABAergic interneurons and disinhibition of pyramidal neurons (Frohlich and Van Horn 2014). Mice administered with NMDAR antagonists (phencyclidine (PCP), dizocilpine (MK-801), ketamine) exhibit schizophrenia-like behavior (Homayoun and Moghaddam 2007). NMDARs preferentially drive the activity of cortical interneurons (Seillier and Giuffrida 2009) and are considered to be strongly associated with the emergence of gamma oscillations (Wang and Carlén 2012). PV neuron activity via NMDA receptor is also sufficient to enhance gamma oscillations and its hypoactivity is implicated in the deficit in information processing underlying cognitive dysfunction in schizophrenia.

These findings indicate that inhibitory inputs, mainly by the activity of fast-spiking interneurons, are a key regulator of high-frequency oscillation in the cortical area, and supports the hypothesis that E/I imbalance due to inhibitory dysfunction may cause ASD and schizophrenia.

## 36.3 Optogenetic Studies in Social Behavior

Deficits in social behavior are broadly observed in individuals with ASDs. By optogenetically controlling a specific neural function in animal models, we may understand the brain mechanism associated with social behavioral abnormalities in ASDs. Recent studies utilizing optogenetics demonstrate the underlying mechanisms of the relationship between neural functions at the brain circuit level and social behavior (e.g., social interaction and social novelty) with higher spatiotemporal resolution.

As mentioned before, in rodent studies, cortical E/I imbalance may be a probable cause of autistic behavior such as social deficits. Yizhar et al. reported that enhanced excitability in the medial prefrontal cortex (mPFC) induced social dysfunction but not exploratory behavior (Yizhar et al. 2011). To regulate neural excitability during behavior tests, an optogenetic tool, stable step-function opsin (SSFO), was used. SSFO can depolarize neurons for periods of over 30 min, which allows for behavioral tests in freely moving mice by detaching the optical fibers after a single photostimulation. The activation of SSFO in pyramidal neurons of the mPFC increases high-frequency power of gamma oscillation in local field potentials (LFPs). The elevated cellular E/I balance induces deficits in social interaction behavior in the mPFC, but not in the primary visual area, suggesting that the balanced E/I state in the mPFC is associated with normal social behavior. Altered E/I ratio also affects learning and memory, where mice with elevated E/I in the mPFC show reduction in freezing rate during contextual conditioning tasks and tone stimuli after fear conditioning. It is assumed that the increased E/I ratio in the mPFC can be suppressed by activation of inhibitory neurons in the same area. To rebalance the E/I ratio in the mPFC expressing SSFO in excitatory cells, C1V1 (E122T/E162T), a redshifted variant of channelrhodopsin, is used to activate inhibitory cells. The independent photostimulation of C1V1(E122T/E162T) expressed in PV neurons in the mPFC does not change social behavior. On the other hand, in the case of co-activation of SSFO and C1V1(E122T/E162T), social deficits seen in mice with elevated E/I in the mPFC are partially ameliorated by restoring balance with increased inhibition (Fig. 36.1). These results suggest that the balanced E/I state of neural activity in the prefrontal area is important to express social behaviors.

Mutations in synaptic molecule genes such as neuroligins and neurexins are suggested to be highly associated with ASDs. A point mutation in *NLGN3* resulting in an amino acid change from arginine to cysteine at residue 451 (R451C) of Neuroligin-3 has been found in ASD patients. *Nlgn3* R451C knockin (KI) mouse is a model for the *NLGN3* mutation and shows impaired social novelty, hyperactivity, and repetitive behaviors (Rothwell et al. 2014; Tabuchi et al. 2007). The KI mice exhibit enhanced inhibitory transmissions with no change in the number of PV- and somatostatin-positive interneurons in the somatosensory cortex (Speed et al. 2015). Given that altered E/I balance in the cortex affects social behavior of the KI mice, functional study of the sociability-associated cortical area is worthwhile. Cao et al. found that the reduced excitability of fast-spiking interneurons and the resulting dysfunction of gamma oscillations in the mPFC caused social deficits in KI mice (Cao et al. 2018). Alterations of phase-coding (reduced low gamma (30–50 Hz) with theta phase (4–12 Hz) and increased high gamma (55–90 Hz) with theta phase) in the KI mice are also observed during social interaction periods. Optogenetic stimulation of PV neurons in the mPFC at 40 Hz nested at 8 Hz rescues social novelty deficits in the KI mice (Fig. 36.1). The 40 Hz stimulation alone and the combination of 20 and 8 Hz have no effect on the social behavior of KI mice. The 80 Hz stimulation worsens social novelty behavior of wild-type mice as well as the KI mice. On the other hand, these stimulations do not affect total distance traveled and the percentage of time spent in the center during an open-field test. These results suggest that oscillation-coupled excitation of PV neurons in the mPFC plays a critical role in social novelty behavior.

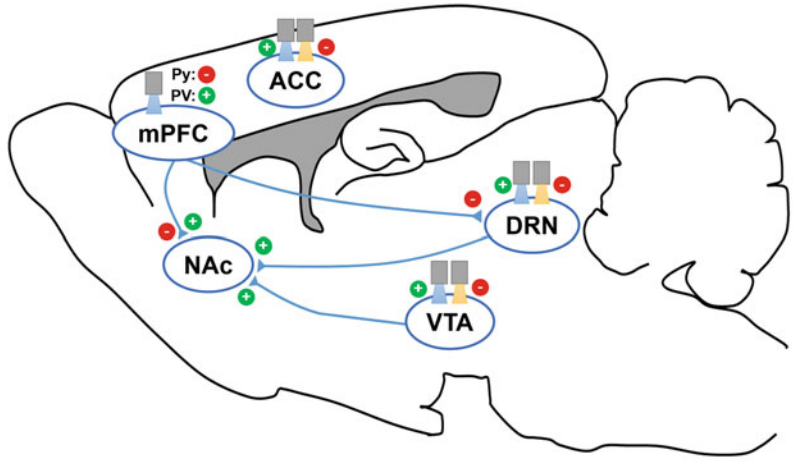


**Fig. 36.1** Optogenetic manipulation of neural circuits diversely affects social behavior. Optogenetic activation of pyramidal neurons in the mPFC induces antisocial effect, and the co-activation of PV neurons partially improves sociability in wild-type mice (Yizhar et al. 2011). Optogenetic PV activation in the mPFC rescues social behavior of *Nlgn3* R451C KI mice and *Cntnap2* KO mice (Cao et al. 2018; Selimbeyoglu et al. 2017). Optogenetic activation of pyramidal neurons in the ACC improves sociability of *Shank3* KO mice while optogenetic inhibition in same area impairs social behavior of wild-type mice (Guo et al. 2019). Optogenetic activation of the DRN 5-HT neurons or DRN-NAc projections improves social behavior of 16p11.2 deletion model mice while inhibition of the DRN 5-HT neurons decreases sociability (Walsh et al. 2018). The optogenetic manipulation of the VTA shows bidirectional effect on the sociability (Gunaydin et al. 2014). The input pathways to NAc basically induce pro-social effect by optogenetically activating the circuits. Blue and yellow lights indicate photostimulation with ChR2 or its variants and photoinhibition with NpHR within a brain area, respectively. Blue projections indicate pathway-specific photostimulation. "+" indicates pro-social effect. "−" indicates antisocial effect. *mPFC* Medial prefrontal cortex, *ACC* Anterior cingulate cortex, *NAc* Nucleus accumbens, *VTA* Ventral tegmental area, *DRN* Dorsal raphe nucleus, *Py* Pyramidal neuron, *PV* Parvalbumin-positive interneuron

Loss-of-function and polymorphic variants of *CNTNAP2* gene have been associated with increased risk of ASDs. Contactin-associated protein-like 2 encoded in *CNTNAP2* is one of the neurexin superfamily proteins involved in neuron-glia interactions and clustering of voltage-gated potassium channels at the nodes of Ranvier (Poliak et al. 1999, 2003). *Cntnap2* knockout (KO) mice show social behavior deficits as well as hyperactivity and epileptic seizures (Peñagarikano et al. 2011). The KO mice have reduced interneuron density in the cortical and striatal brain regions, indicating dysfunction of inhibitory networks in the brain. Selimbeyoglu et al. reported that reduction of E/I balance in the mPFC either by optogenetically increasing the excitability of PV interneurons by selectively expressing SSFO or by decreasing the excitability of pyramidal neurons by selectively expressing SwiChR++, a step-function inhibitory opsin, rescued deficits in social behavior and hyperactivity of the KO mice (Selimbeyoglu et al. 2017) (Fig. 36.1). On the other hand, these optogenetic manipulations of E/I balance in the mPFC do not affect the behaviors of wild-type mice. It is assumed that abnormal but not normal E/I balance can be modified by increasing inhibition or decreasing excitation in the mPFC. An electrophysiology study reported the reduction of excitatory and inhibitory synaptic inputs onto L2/3 pyramidal neurons of the mPFC brain slices from KO mice, concurrent with reduced spines and synapses, despite normal dendritic complexity and intrinsic excitability (Lazaro et al. 2019). However, E/I balance in individual neurons of the KO mice is not altered. Firing rates of

wide-spiking (WS, putative excitatory neuron) units are compatible, but narrow-spiking (NS, putative interneurons) units from the KO mice fire at a significantly higher rate. The averaged power of LFP in delta, theta oscillations, or even higher frequencies (beta, slow gamma, or high gamma) during either locomotion or immobility is not different from wild-type mice, while there is a significant decrease in the strength of phase locking of WS units to delta oscillations and NS units to delta and theta oscillations in the KO mice. Decreased phase locking of individual units to LFP oscillations suggests a reduction in coordinated population activity in the KO mice. These abnormalities in network oscillations derived from the decrease in functional synapses in the mPFC may underlie ASD-related phenotypes in KO mice.

Neurons in the mPFC compose reciprocal networks with many brain regions including other cortical and subcortical areas (e.g. nucleus accumbens (NAc), amygdala, ventral tegmental area (VTA), and raphe nucleus). Murugan et al. demonstrated that one of the mPFC descending projections specifically contributes to social preference (Murugan et al. 2017). The prelimbic area (PL) in the mPFC contains distinct subpopulations that project to the NAc, VTA, and amygdala where social behavior has been implicated. Continuous activation of ChR2 expressing pyramidal neurons at 20 Hz in PL-NAc, but not PL-VTA or PL-amygdala projection, decreases social preference behavior in the three-chamber test (Murugan et al. 2017). The PL-NAc neurons also bidirectionally modulate social–spatial learning. By conditionally activating the PL-NAc projection when the subject mouse enters the stranger mouse zone, the subject shows social preference toward the stimulated side stranger compared to the non-stimulated side stranger mouse. Conversely, inhibition of PL-NAc by NpHR decreases the preference for the stimulated side stranger mouse. These results suggest that PL-NAc neurons encode a conjunction of social–spatial information (Fig. 36.1). The outputs from the mPFC selectively affect social behavioral expression. The VTA dopamine neurons projecting to NAc also bidirectionally regulate social behavior. Gunaydin et al. reported that phasic optical stimulation of VTA dopamine neurons with 30 Hz bursts of 473 nm light (8 pulses, 5 ms duration) every 5 s increases but continuous optical inhibition with eNpHR3.0 decreases investigation of the novel mouse in the home-cage social interaction assay. This result demonstrates that phasic activity of VTA dopamine neurons is sufficient to enhance social interaction, and that suppression of the neuronal activity impairs social behavior (Gunaydin et al. 2014). Gunaydin et al. selectively manipulated the terminals of VTA dopamine neurons at mPFC or NAc and found that the VTA-NAc, but not VTA-mPFC projection is involved in social interaction behavior (Fig. 36.1). Taken together, the NAc activity regulated by mPFC excitatory inputs, VTA dopaminergic inputs or both of them is necessary for the expression of normal social behavior.

The raphe nucleus is a core of serotonergic neurons, where its dysfunction is suggested to be related with ASD phenotypes in mice and humans (Nakai et al. 2017; Walsh et al. 2018). A CNV model mice for human 16p11.2 deletion exhibit deficits in social behavior and decreased DRN 5-HT neuronal activity during social contact (Walsh et al. 2018). Optogenetic activation of DRN 5-HT neurons, especially the DRN-NAc projecting neurons, induces pro-social effect but inhibition induces antisocial effect (Fig. 36.1). In this way, optogenetic activation of 5-HT neurons rescues the social deficits in 16p11.2 deletion mice. Such dysfunction of 5-HT neurons in the DRN is also found in another CNV model mice for human 15q11-13 duplication and the pharmacological intervention of 5-HT system rescues social behavior of the model mice (Nakai et al. 2017). Thus, the 5-HT system can be a strong candidate therapeutic target in ASDs. The DRN 5-HT neurons receive excitatory inputs from the ventromedial PFC (vmPFC). The manipulation of vmPFC-DRN projections indicates divergent effects on social behavior in the chronic social defeat paradigm (Challis et al. 2014). Optogenetic activation of the vmPFC-DRN projections in the undefeated mice decreases the number of entries and time spent in the interaction zone with

aggressors although inhibition has no effect. In the defeated mice, however, optogenetic inhibition improves sociability in the paradigm, suggesting that chronic stress modifies the responsiveness of the DRN area to excitatory inputs from the vmPFC. The excitatory projections from the vmPFC primarily localize to GABA-rich areas of the DRN. Thus, the GABAergic pathway in the DRN may modulate or filter the vmPFC inputs for behavioral expression of sociability (Challis et al. 2014).

The anterior cingulate cortex (ACC) is implicated in a broad range of behaviors and cognitive processes (Apps et al. 2016) and its activity has been suggested to be linked with social anxiety disorder (Amir et al. 2005; Klumpp et al. 2017). The morphological change in neuron density and decreased functional connectivity in the ACC are found in individuals with ASDs (Simms et al. 2009; Zhou et al. 2016). A recent study reported that the ACC dysfunction is associated with social deficits in mice with a mutation in *Shank3*, a high-confident candidate ASD gene (Guo et al. 2019). *Shank3* KO mice exhibit less branches and spine density of pyramidal neurons and weakened excitatory transmissions in the ACC. Optogenetic activation of the ACC pyramidal neurons at 10–20 Hz but not at 5 Hz stimulation rescues social interaction and anxiety-like behavior in the KO mice (Fig. 36.1). On the other hand, optogenetic inhibition of the ACC pyramidal neurons in wild-type mice with NpHR induces impairments in social interaction and social preference but does not affect anxiety-like behavior (Guo et al. 2019). As excessive increase of mPFC activity decreases social interaction behavior in wild-type mice (Yizhar et al. 2011), ACC activity may also be maintained in a precise balance of excitation and inhibition to exhibit normal social behavior.

## 36.4 Optogenetic Studies in Depression-Related Behavior

Chronic exposure to stress is implicated as a risk factor of depressive disorder. Depression causes a persistent feeling of sadness and/or a lack of interest or pleasure. According to the WHO Global Health Estimates, the total number of people living with depression in the world is over 300 million. Given its high prevalence, advances in understanding the neurological mechanism and treatment of depression are strongly desired. Advantages of optogenetics in cell-type- and pathway-specific manipulation have been utilized in approaching the neural mechanisms in animal models for depression. A chronic mild stress (CMS) paradigm in which the subject mouse received unpredictable mild stressors for 8–12 weeks induces a depressive-like state (e.g., anhedonia, less locomotor activity, and reduced sucrose preference). Phasic photoactivation (eight times 5 ms duration pulses at 30 Hz, every 5 s) of VTA dopamine neurons rescues the CMS-induced depression-like phenotype (Tye et al. 2013). On the other hand, optogenetic inhibition of the VTA dopamine neurons itself induces depression-like phenotypes in non-stressed mice in the tail-suspension test and sucrose-preference test (Tye et al. 2013). Social defeat stress (SDS) is also used to generate a reliable mouse model for depression. A subpopulation of chronic SDS-conditioned mice is susceptible to stress and exhibits depression-like behaviors including low sociability and decreased locomotion, whereas the other subpopulation of mice exhibits resilient behavior to stress (Krishnan et al. 2007). This behavioral difference between susceptible and resilient mice is modulated by optogenetically stimulating the dopaminergic projections from the VTA to NAc. The VTA dopamine neurons show two firing patterns: low-frequency tonic and high-frequency phasic firing, where phasic firing is upregulated by SDS. Optogenetic phasic activation, but not tonic activation of the VTA-NAc pathway, induces a susceptible phenotype in the SDS paradigm, while optogenetic suppression of this pathway using NpHR induces resilience (Chaudhury et al. 2013). In the VTA-mPFC pathway, optogenetic activation does not change the susceptibility but optogenetic inhibition of this pathway increases the socially defeated state. These results suggest that neural circuit-specific mechanisms are involved in stress-induced

depression. Optogenetic manipulation of the VTA dopamine neurons bidirectionally modulates depression-like behavior as well as social behavior (Gunaydin et al. 2014). Since the primary reward circuit includes dopaminergic projections from the VTA to the NAc (Russo and Nestler 2013), dopamine release at the NAc may positively change the emotional state in depression by enhancing the motivation for rewards. Optogenetic activation of D2 type dopamine receptor-expressing pyramidal neurons in the mPFC disrupts normal social behavior (Brumback et al. 2018) and the continuous activation of glutamatergic projections in the mPFC-NAc pathway decreases social interaction behavior (Murugan et al. 2017). Thus, dopamine release in the mPFC may not necessarily induce emotionally positive change. The reduction in expression of immediate early genes in the mPFC is found in both susceptible mice and human patients with depression (Covington et al. 2010), suggesting that endogenous activity of the mPFC in a depressive state is low. Interestingly, increased mPFC activity by robust optogenetic stimulation at 100 Hz is able to recover the sociability of the susceptible mice. Such findings on the antidepressive effects on mouse behavior using optogenetic stimulation might be applied to human studies. Deep-brain stimulation (DBS), which electrically stimulates deep nuclei of the brain, has also been applied to human patients. As an example, DBS of the subcallosal cingulate gyrus shows effective results for treatment-resistant depression (Lozano et al. 2008). Further development of studies using animal models is desired to improve the quality of DBS, such as targeting brain regions and conditions for stimulation strength or frequency.

## 36.5 Concluding Remarks

By taking advantage of optogenetic technology, cell type- and/or neural circuit-specific modulation of brain activity can be achieved. Such selectivity contributes to the identification of neural mechanisms of social deficits or depression-related behavior in neurodevelopmental and psychiatric disorders. Optogenetic manipulation of social behavior-related circuits rescues sociability of model mice for ASDs. Currently, it is still difficult to use optogenetics in human clinical studies, since it requires accurate gene delivery systems to express the opsins in the target cells and small light-emitting implant systems to minimize brain damage. Nonspecific effects such as light illumination producing heat and causing photodamage to neurons should also be considered. But unlike DBS, optogenetic approach can suppress neural activities if the target brain area exhibits excess excitability in patients. Bidirectional control of brain activity by optogenetics will become an option in future therapeutic methods for neurodevelopmental and psychiatric disorders. Furthermore, optogenetics provides light-dependent control systems for modulation of gene expression and epigenetic states in neurons (e.g., a light-inducible transcriptional effector (LITE) system, a light-activated CRISPR-Cas9 effector (LACE) system, a photoactivatable-Tet-OFF/ON system, and a far-red light-activated CRISPR-dCas9 effector (FACE) system (Konermann et al. 2013; Polstein and Gersbach 2015; Shao et al. 2018; Yamada et al. 2018)). These methods induce transcription of endogenous genes in a blue or far-red light-dependent manner by using the light-inducible heterodimerizing proteins CRY2 and CIB1 fused to transcription activators or chromatin-modifying enzymes. As mentioned above, genomic abnormalities like SNVs and CNVs induce alteration of gene expression, which is thought to affect cellular physiological functions in ASD brains. Optogenetic modification of gene expression and epigenetic states may help restore appropriate gene dosage to recover physiological functions of cells with genomic mutations. To date, we use animal models of ASD in combination with optogenetics to study the neural circuit mechanism. However, advances in optogenetic research will be invaluable in developing therapeutic methods for human patients.

**Acknowledgments** This work was supported in part by KAKENHI (16H06316, 16H06463, 19K16886), Japan Society of Promotion of Science and Ministry of

Education, Culture, Sports, Science, and Technology, Intramural Research Grant for Neurological and Psychiatric Disorders of NCNP, the Takeda Science Foundation, and the Smoking Science Foundation.

## References

Amir N, Klumpp H, Elias J, Bedwell JS, Yanasak N, Miller LS (2005) Increased activation of the anterior cingulate cortex during processing of disgust faces in individuals with social phobia. Biol Psychiatry 57:975–981

Apps MAJ, Rushworth MFS, Chang SWC (2016) The anterior cingulate gyrus and social cognition: tracking the motivation of others. Neuron 90:692–707

Blundell J, Tabuchi K, Bolliger MF, Blaiss CA, Brose N, Liu X, Südhof TC, Powell CM (2009) Increased anxiety-like behavior in mice lacking the inhibitory synapse cell adhesion molecule neuroligin 2. Genes Brain Behav 8:114–126

Brumback AC, Ellwood IT, Kjaerby C, Iafrati J, Robinson S, Lee AT, Patel T, Nagaraj S, Davatolhagh F, Sohal VS (2018) Identifying specific prefrontal neurons that contribute to autism-associated abnormalities in physiology and social behavior. Mol Psychiatry 23:2078–2089

Buzsáki G, Wang X-J (2012) Mechanisms of gamma oscillations. Annu Rev Neurosci 35:203–225

Cao W, Lin S, Xia Q-Q, Du Y-L, Yang Q, Zhang M-Y, Lu Y-Q, Xu J, Duan S-M, Xia J et al (2018) Gamma oscillation dysfunction in mPFC leads to social deficits in Neuroligin 3 R451C Knockin mice. Neuron 97:1253–1260.e7

Cardin JA, Carlén M, Meletis K, Knoblich U, Zhang F, Deisseroth K, Tsai L-H, Moore CI (2009) Driving fast-spiking cells induces gamma rhythm and controls sensory responses. Nature 459:663–667

Carlén M, Meletis K, Siegle JH, Cardin JA, Futai K, Vierling-Claassen D, Rühlmann C, Jones SR, Deisseroth K, Sheng M et al (2012) A critical role for NMDA receptors in parvalbumin interneurons for gamma rhythm induction and behavior. Mol Psychiatry 17:537–548

Challis C, Beck SG, Berton O (2014) Optogenetic modulation of descending prefrontocortical inputs to the dorsal raphe bidirectionally bias socioaffective choices after social defeat. Front Behav Neurosci 8:43

Chao H-T, Chen H, Samaco RC, Xue M, Chahrour M, Yoo J, Neul JL, Gong S, Lu H-C, Heintz N et al (2010) Dysfunction in GABA signalling mediates autism-like stereotypies and Rett syndrome phenotypes. Nature 468:263–269

Chaudhury D, Walsh JJ, Friedman AK, Juarez B, Ku SM, Koo JW, Ferguson D, Tsai H-C, Pomeranz L, Christoffel DJ et al (2013) Rapid regulation of depression-related behaviours by control of midbrain dopamine neurons. Nature 493:532–536

Chen G, Zhang Y, Li X, Zhao X, Ye Q, Lin Y, Tao HW, Rasch MJ, Zhang X (2017) Distinct inhibitory circuits orchestrate cortical beta and gamma band oscillations. Neuron 96:1403–1418.e6

Covington HE, Lobo MK, Maze I, Vialou V, Hyman JM, Zaman S, LaPlant Q, Mouzon E, Ghose S, Tamminga CA et al (2010) Antidepressant effect of optogenetic stimulation of the medial prefrontal cortex. J Neurosci 30:16,082–16,090

Cross-Disorder Group of the Psychiatric Genomics Consortium, Lee SH, Ripke S, Neale BM, Faraone SV, Purcell SM, Perlis RH, Mowry BJ, Thapar A, Goddard ME et al (2013) Genetic relationship between five psychiatric disorders estimated from genome-wide SNPs. Nat Genet 45:984–994

Dani VS, Chang Q, Maffei A, Turrigiano GG, Jaenisch R, Nelson SB (2005) Reduced cortical activity due to a shift in the balance between excitation and inhibition in a mouse model of Rett syndrome. Proc Natl Acad Sci U S A 102:12560–12565

Etherton M, Földy C, Sharma M, Tabuchi K, Liu X, Shamloo M, Malenka RC, Südhof TC (2011) Autism-linked neuroligin-3 R451C mutation differentially alters hippocampal and cortical synaptic function. Proc Natl Acad Sci U S A 108:13,764–13,769

Fatemi SH, Halt AR, Stary JM, Kanodia R, Schulz SC, Realmuto GR (2002) Glutamic acid decarboxylase 65 and 67 kDa proteins are reduced in autistic parietal and cerebellar cortices. Biol Psychiatry 52:805–810

Frohlich J, Van Horn JD (2014) Reviewing the ketamine model for schizophrenia. J Psychopharmacol 28:287–302

Gao R, Penzes P (2015) Common mechanisms of excitatory and inhibitory imbalance in schizophrenia and autism spectrum disorders. Curr Mol Med 15:146–167

Gibson JR, Bartley AF, Hays SA, Huber KM (2008) Imbalance of neocortical excitation and inhibition and altered UP states reflect network hyperexcitability in the mouse model of fragile X syndrome. J Neurophysiol 100:2615–2626

Gkogkas CG, Khoutorsky A, Ran I, Rampakakis E, Nevarko T, Weatherill DB, Vasuta C, Yee S, Truitt M, Dallaire P et al (2013) Autism-related deficits via dysregulated eIF4E-dependent translational control. Nature 493:371–377

Gogolla N, Leblanc JJ, Quast KB, Südhof TC, Fagiolini M, Hensch TK (2009) Common circuit defect of excitatory-inhibitory balance in mouse models of autism. J Neurodev Disord 1:172–181

Gunaydin LA, Grosenick L, Finkelstein JC, Kauvar IV, Fenno LE, Adhikari A, Lammel S, Mirzabekov JJ, Airan RD, Zalocusky KA et al (2014) Natural neural projection dynamics underlying social behavior. Cell 157:1535–1551

Guo B, Chen J, Chen Q, Ren K, Feng D, Mao H, Yao H, Yang J, Liu H, Liu Y et al (2019) Anterior cingulate cortex dysfunction underlies social deficits in Shank3 mutant mice. Nat Neurosci 22:1223–1234

Han S, Tai C, Westenbroek RE, Yu FH, Cheah CS, Potter GB, Rubenstein JL, Scheuer T, de la Iglesia HO, Catterall WA (2012) Autistic-like behaviour in Scn1a +/− mice and rescue by enhanced GABA-mediated neurotransmission. Nature 489:385–390

Hines RM, Wu L, Hines DJ, Steenland H, Mansour S, Dahlhaus R, Singaraja RR, Cao X, Sammler E, Hormuzdi SG et al (2008) Synaptic imbalance, stereotypies, and impaired social interactions in mice with altered neuroligin 2 expression. J Neurosci 28:6055–6067

Homayoun H, Moghaddam B (2007) NMDA receptor hypofunction produces opposite effects on prefrontal cortex interneurons and pyramidal neurons. J Neurosci 27:11,496–11,500

Klumpp H, Fitzgerald JM, Kinney KL, Kennedy AE, Shankman SA, Langenecker SA, Phan KL (2017) Predicting cognitive behavioral therapy response in social anxiety disorder with anterior cingulate cortex and amygdala during emotion regulation. NeuroImage Clin 15:25–34

Konermann S, Brigham MD, Trevino A, Hsu PD, Heidenreich M, Cong L, Platt RJ, Scott DA, Church GM, Zhang F (2013) Optical control of mammalian endogenous transcription and epigenetic states. Nature 500:472–476

Krishnan V, Han M-H, Graham DL, Berton O, Renthal W, Russo SJ, Laplant Q, Graham A, Lutter M, Lagace DC et al (2007) Molecular adaptations underlying susceptibility and resistance to social defeat in brain reward regions. Cell 131:391–404

Lazaro MT, Taxidis J, Shuman T, Bachmutsky I, Ikrar T, Santos R, Marcello GM, Mylavarapu A, Chandra S, Foreman A et al (2019) Reduced prefrontal synaptic connectivity and disturbed oscillatory population dynamics in the CNTNAP2 model of autism. Cell Rep 27:2567–2578.e6

Liu X, Takumi T (2014) Genomic and genetic aspects of autism spectrum disorder. Biochem Biophys Res Commun 452:244–253

Lozano AM, Mayberg HS, Giacobbe P, Hamani C, Craddock RC, Kennedy SH (2008) Subcallosal cingulate gyrus deep brain stimulation for treatment-resistant depression. Biol Psychiatry 64:461–467

Malhotra D, Sebat J (2012) CNVs: harbingers of a rare variant revolution in psychiatric genetics. Cell 148:1223–1241

Marshall CR, Scherer SW (2012) Detection and characterization of copy number variation in autism spectrum disorder. Methods Mol Biol 838:115–135

Murugan M, Jang HJ, Park M, Miller EM, Cox J, Taliaferro JP, Parker NF, Bhave V, Hur H, Liang Y et al (2017) Combined social and spatial coding in a descending projection from the prefrontal cortex. Cell 171:1663–1677.e16

Nakai N, Nagano M, Saitow F, Watanabe Y, Kawamura Y, Kawamoto A, Tamada K, Mizuma H, Onoe H, Watanabe Y et al (2017) Serotonin rebalances cortical tuning and behavior linked to autism symptoms in 15q11-13 CNV mice. Sci Adv 3: e1603001

Nakanishi M, Nomura J, Ji X, Tamada K, Arai T, Takahashi E, Bućan M, Takumi T (2017) Functional significance of rare neuroligin 1 variants found in autism. PLoS Genet 13:e1006940

Nakatani J, Tamada K, Hatanaka F, Ise S, Ohta H, Inoue K, Tomonaga S, Watanabe Y, Chung YJ, Banerjee R et al (2009) Abnormal behavior in a chromosome-engineered mouse model for human 15q11-13 duplication seen in autism. Cell 137:1235–1246

Nelson SB, Valakh V (2015) Excitatory/inhibitory balance and circuit homeostasis in autism spectrum disorders. Neuron 87:684–698

Peça J, Feliciano C, Ting JT, Wang W, Wells MF, Venkatraman TN, Lascola CD, Fu Z, Feng G (2011) Shank3 mutant mice display autistic-like behaviours and striatal dysfunction. Nature 472:437–442

Peñagarikano O, Abrahams BS, Herman EI, Winden KD, Gdalyahu A, Dong H, Sonnenblick LI, Gruver R, Almajano J, Bragin A et al (2011) Absence of CNTNAP2 leads to epilepsy, neuronal migration abnormalities, and core autism-related deficits. Cell 147:235–246

Poliak S, Gollan L, Martinez R, Custer A, Einheber S, Salzer JL, Trimmer JS, Shrager P, Peles E (1999) Caspr2, a new member of the neurexin superfamily, is localized at the juxtaparanodes of myelinated axons and associates with K+ channels. Neuron 24:1037–1047

Poliak S, Salomon D, Elhanany H, Sabanay H, Kiernan B, Pevny L, Stewart CL, Xu X, Chiu S-Y, Shrager P et al (2003) Juxtaparanodal clustering of shaker-like K+ channels in myelinated axons depends on Caspr2 and TAG-1. J Cell Biol 162:1149–1160

Polstein LR, Gersbach CA (2015) A light-inducible CRISPR-Cas9 system for control of endogenous gene activation. Nat Chem Biol 11:198–200

Poulopoulos A, Aramuni G, Meyer G, Soykan T, Hoon M, Papadopoulos T, Zhang M, Paarmann I, Fuchs C, Harvey K et al (2009) Neuroligin 2 drives postsynaptic assembly at perisomatic inhibitory synapses through gephyrin and collybistin. Neuron 63:628–642

Rothwell PE, Fuccillo MV, Maxeiner S, Hayton SJ, Gokce O, Lim BK, Fowler SC, Malenka RC, Südhof TC (2014) Autism-associated neuroligin-3 mutations commonly impair striatal circuits to boost repetitive behaviors. Cell 158:198–212

Rubenstein JLR, Merzenich MM (2003) Model of autism: increased ratio of excitation/inhibition in key neural systems. Genes Brain Behav 2:255–267

Russo SJ, Nestler EJ (2013) The brain reward circuitry in mood disorders. Nat Rev Neurosci 14:609–625

Schaaf CP, Zoghbi HY (2011) Solving the autism puzzle a few pieces at a time. Neuron 70:806–808

Schmeisser MJ, Ey E, Wegener S, Bockmann J, Stempel AV, Kuebler A, Janssen A-L, Udvardi PT, Shiban E, Spilker C et al (2012) Autistic-like behaviours and

hyperactivity in mice lacking ProSAP1/Shank2. Nature 486:256–260
Seillier A, Giuffrida A (2009) Evaluation of NMDA receptor models of schizophrenia: divergences in the behavioral effects of sub-chronic PCP and MK-801. Behav Brain Res 204:410–415
Selimbeyoglu A, Kim CK, Inoue M, Lee SY, Hong ASO, Kauvar I, Ramakrishnan C, Fenno LE, Davidson TJ, Wright M et al (2017) Modulation of prefrontal cortex excitation/inhibition balance rescues social behavior in CNTNAP2-deficient mice. Sci Transl Med 9:eaah6733
Shao J, Wang M, Yu G, Zhu S, Yu Y, Heng BC, Wu J, Ye H (2018) Synthetic far-red light-mediated CRISPR-dCas9 device for inducing functional neuronal differentiation. Proc Natl Acad Sci U S A 115:E6722–E6730
Simms ML, Kemper TL, Timbie CM, Bauman ML, Blatt GJ (2009) The anterior cingulate cortex in autism: heterogeneity of qualitative and quantitative cytoarchitectonic features suggests possible subgroups. Acta Neuropathol 118:673–684
Sohal VS, Zhang F, Yizhar O, Deisseroth K (2009) Parvalbumin neurons and gamma rhythms enhance cortical circuit performance. Nature 459:698–702
Speed HE, Masiulis I, Gibson JR, Powell CM (2015) Increased cortical inhibition in autism-linked Neuroligin-3R451C mice is due in part to loss of endocannabinoid signaling. PLoS One 10:e0140638
Sullivan PF, Daly MJ, O'Donovan M (2012) Genetic architectures of psychiatric disorders: the emerging picture and its implications. Nat Rev Genet 13:537–551
Tabuchi K, Blundell J, Etherton MR, Hammer RE, Liu X, Powell CM, Südhof TC (2007) A neuroligin-3 mutation implicated in autism increases inhibitory synaptic transmission in mice. Science 318:71–76
Takumi T, Tamada K (2018) CNV biology in neurodevelopmental disorders. Curr Opin Neurobiol 48:183–192
Tye KM, Mirzabekov JJ, Warden MR, Ferenczi EA, Tsai H-C, Finkelstein J, Kim S-Y, Adhikari A, Thompson KR, Andalman AS et al (2013) Dopamine neurons modulate neural encoding and expression of depression-related behaviour. Nature 493:537–541
Uhlhaas PJ, Singer W (2010) Abnormal neural oscillations and synchrony in schizophrenia. Nat Rev Neurosci 11:100–113
Wallace ML, Burette AC, Weinberg RJ, Philpot BD (2012) Maternal loss of Ube3a produces an excitatory/inhibitory imbalance through neuron type-specific synaptic defects. Neuron 74:793–800
Walsh JJ, Christoffel DJ, Heifets BD, Ben-Dor GA, Selimbeyoglu A, Hung LW, Deisseroth K, Malenka RC (2018) 5-HT release in nucleus accumbens rescues social deficits in mouse autism model. Nature 560:589–594
Wang X, Carlén M (2012) Optogenetic dissection of cortical information processing-shining light on schizophrenia. Brain Res 1476:31–37
Won H, Lee H-R, Gee HY, Mah W, Kim J-I, Lee J, Ha S, Chung C, Jung ES, Cho YS et al (2012) Autistic-like social behaviour in Shank2-mutant mice improved by restoring NMDA receptor function. Nature 486:261–265
Yamada M, Suzuki Y, Nagasaki SC, Okuno H, Imayoshi I (2018) Light control of the Tet gene expression system in mammalian cells. Cell Rep 25:487–500.e6
Yang M, Bozdagi O, Scattoni ML, Wohr M, Roullet FI, Katz AM, Abrams DN, Kalikhman D, Simon H, Woldeyohannes L et al (2012) Reduced excitatory neurotransmission and mild autism-relevant phenotypes in adolescent Shank3 null mutant mice. J Neurosci 32:6525–6541
Yizhar O, Fenno LE, Prigge M, Schneider F, Davidson TJ, O'Shea DJ, Sohal VS, Goshen I, Finkelstein J, Paz JT et al (2011) Neocortical excitation/inhibition balance in information processing and social dysfunction. Nature 477:171–178
Zhou Y, Shi L, Cui X, Wang S, Luo X (2016) Functional connectivity of the caudal anterior cingulate cortex is decreased in autism. PLoS One 11:e0151879

# Optogenetics-Mediated Gene Therapy for Retinal Diseases

37

Hiroshi Tomita and Eriko Sugano

**Abstract**

The visual system consists of various types of neurons and a single-nucleotide mutation can sometimes lead to blindness. The phototransduction pathway in the retina starts from the first-order neurons, the photoreceptor cells, and transmits the signals to second-order neurons. Finally, the output signal from third-order neurons, the ganglion cells, is carried to the brain. The photoreceptor cells are the only neurons in the retina that can respond to a light signal; they are hyperpolarised when they receive light, and the ganglion cells carry the signals to the brain following the depolarization. Recently, various types of channelrhodopsins have been found and developed. It is expected that the gene therapies using the cation channel as well as anion channelrhodopsin genes would be effective against diseases that cause severe destruction of visual function, such as the retinitis pigmentosa and age-related macular degeneration. In this review, we mainly describe mVChR1-mediated gene therapy for retinitis pigmentosa and the future application of optogenetic genes in retinal diseases.

**Keywords**

Retina · Photoreceptor degeneration · Gene therapy · Retinitis pigmentosa

## Abbreviations

| | |
|---|---|
| AMD | Age-related macular degeneration |
| ChR2 | Chlamydomonas-derived channelrhodopsin-2 |
| GPCR | G-protein coupled receptor |
| mVChR1 | Modified volvox-derived channelrhodopsin-1 |
| PDE6B | 3′,5′-Cyclic phosphodiesterase subunit beta |
| RCS rat | Royal college surgeons rat |
| RP | Retinitis pigmentosa |
| RPE cells | Retinal pigment epithelial cells |
| VEPs | Visually evoked potentials |

## 37.1 Retinal Architecture and the Phototransduction Pathway

The retina consists of various types of neurons that play different roles in the phototransduction pathway. Light passing through the cornea and lens is first received by the photoreceptors located at the bottom of the retinal layer. There are two types of photoreceptor cells in the mammalian

H. Tomita (✉) · E. Sugano
Laboratory of Visual Neuroscience, Department of Chemistry and Biological Sciences, Faculty of Science and Engineering, Iwate University, Morioka, Iwate, Japan
e-mail: htomita@iwate-u.ac.jp



H. Yawo et al. (eds.), *Optogenetics*, Advances in Experimental Medicine and Biology 1293,
https://doi.org/10.1007/978-981-15-8763-4_37

retina: rods and cones. The cones are classified into three types based on the wavelength sensitivity of photosensitive proteins. They need brighter light to produce the signals as compared to the rods. The cones are responsible for color vision during daytime. On the contrary, rods are extremely sensitive to light and can detect even a single photon (Baylor et al. 1979, Rieke and Baylor 1998). The human retina contains about 120 million rod cells and 6 million cone cells. The distribution of rods and cones is not uniform in the retina. The cones concentrate in the fovea and rods are in the peripheral retina (Fig. 37.1a).

The phototransduction in the photoreceptor cells is initiated from the absorption of light by a G-protein coupled receptor (GPCR), rhodopsin, in the rods. The chromophore, 11-cis-retinal, bound to rhodopsin undergoes photoisomerization to all-trans-retinal by light and induces the conformational change of rhodopsin along with the initiation of the G-protein coupled signaling. Finally, photoreceptor cells are hyperpolarised by closing the cGMP-dependent sodium channels. The same changes are effected in opsin of the cones. Thus, the first-order neurons, the photoreceptor cells, are depolarised in the dark and the neurotransmitter, glutamate, is continuously released. The photoreceptor cells by the absorption of light cause the hyperpolarisation and stop the glutamate release (Fig. 37.1b). The second-order neurons, ON- and OFF- bipolar cells, respond differently to the change in glutamate concentrations. The ON-bipolar cells, having the metabotropic glutamate receptor, and the OFF-bipolar cells, having the ionotropic glutamate receptor, are depolarized and hyperpolarized, respectively, with decreasing glutamate release. Other retinal neurons, such as the horizontal cells and amacrine cells, play a role in the modification of produced signals from the photoreceptor cells and the bipolar cells, and finally, the signals as action potentials are output from the ganglion cells to the brain.

## 37.2 Retinal Degenerative Diseases

Retinitis pigmentosa (RP) is one of the major diseases resulting in blindness. It affects roughly 1 in 4000 people, both in the United States and worldwide (www.nei.nih.gov/learn-about-eye-health/eye-conditions-and-diseases/retinitis-pigmentosa). Therefore, a knowledge of the direct and indirect aetiologies of RP is essential. Pathologically/histologically, the second and third neurons are preserved, while the first neurons degenerate in the early stages of RP. It has been reported that various types of gene mutations are related to the phototransduction pathways in the retina (https://sph.uth.edu/retnet/). Some gene mutations directly affect the light perception in the photoreceptor cells resulting in functional loss followed by photoreceptor cell death. Therefore, individuals with the gene mutation become blind because the photoreceptor cells are the only cells to receive light related to the visual function. Age-related macular degeneration (AMD) is also a major disease to cause blindness resulting from photoreceptor degeneration. It accounts for 8.7% of all blindness worldwide, particularly in people older than 60 years. The prevalence is expected to increase as a consequence of the increasing aging society (Wong et al. 2014). The first sign of AMD is a gradual or sudden change in the quality of vision, such as straight lines appearing distorted. Development of AMD leads to loss of central vision. There are no effective treatment options for both diseases. It has been reported that the inner retinal layer was well-preserved after severe destruction of the photoreceptors in RP (Santos et al. 1997, Stone et al. 1992) and AMD patients (Kim et al. 2002). One possible method to restore vision is to use the surviving neurons in the inner retinal layer.

## 37.3 ChR2-Gene Therapy for RP

Bi et al. first reported that the expression of Chlamydomonas-derived channelrhodopsin-2 (ChR2) in the retinal ganglion cells restored visual responses in rd1 mice with photoreceptor degeneration (Bi et al. 2006). The rd1 mice have an early-onset severe retinal degeneration (Farber and Lolley 1974) due to the mutation of rod cGMP-specific 3′,5′-cyclic phosphodiesterase subunit beta (PDE6B) gene related to the hydrolysis of cGMP (Fig. 37.1b). Mutations in cGMP-

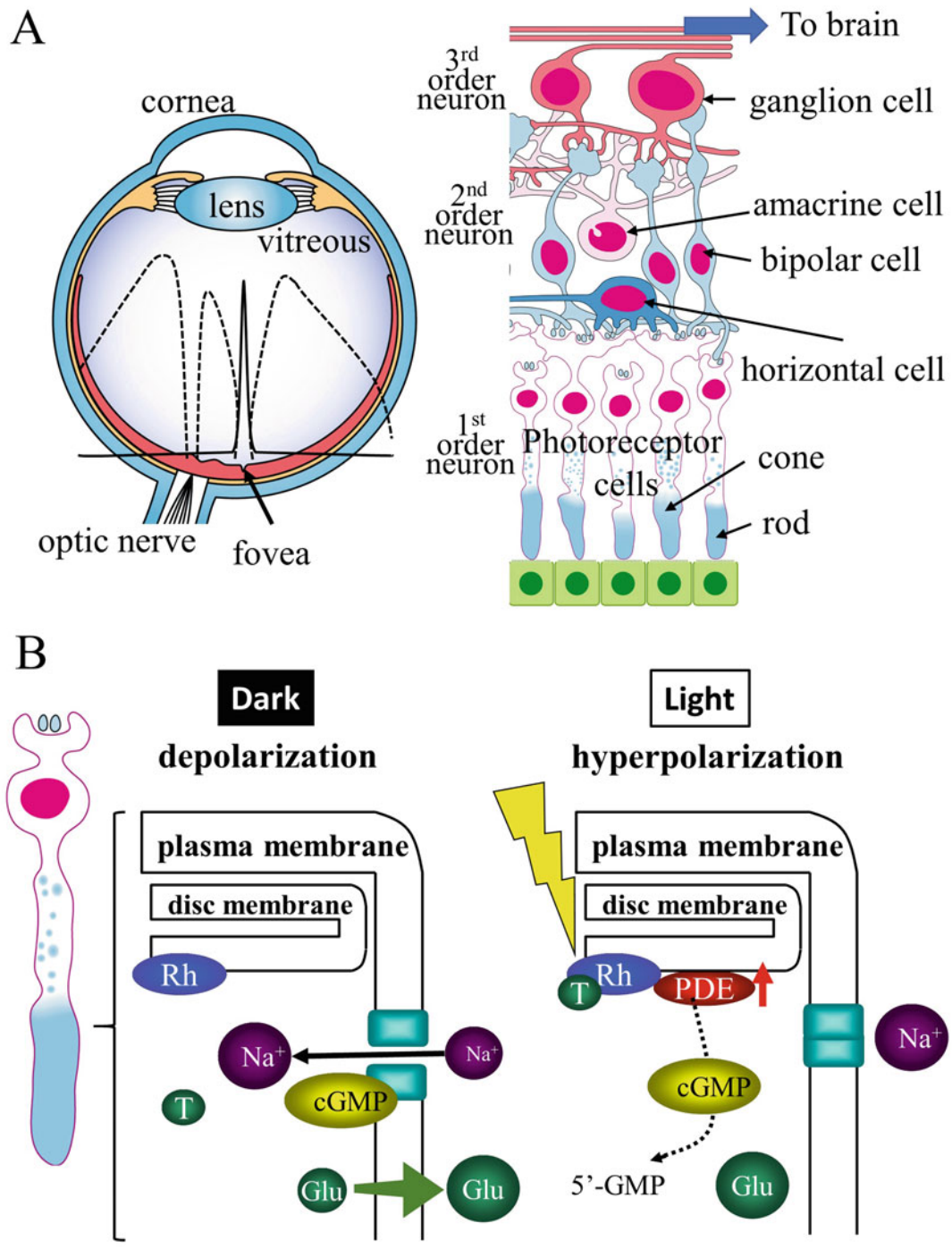


**Fig. 37.1** Retinal architecture and the phototransduction pathway. (**a**) Eyeball and retinal neurons. A broken and filled line is respectively drawn in proportion to the number of rods and cones in the whole retina. Cones are in high numbers in the fovea, and rods are in high numbers in the peripheral retina. The first-order neurons, the photoreceptor cells, are rods and cones. Amacrine cells, bipolar cells, and horizontal cells belong to the second-order neurons. The ganglion cells are classified as the third-order neurons. (**b**) Phototransduction in rods. In the dark state, cGMP-dependent sodium channel is opened and the excitatory amino acid, glutamate, is continuously released during depolarisation. Hydrolysis of the membrane-bound cGMP by the light-induced activation of cGMP phosphodiesterase closes the sodium channel. Cells are hyperpolarised and the glutamate release is decreased

PDE have been found in human patients suffering from autosomal recessive RP (McLaughlin et al. 1993). We also reported visual (Tomita et al. 2007) and behavioral responses (Tomita et al. 2010) in Royal College Surgeons (RCS) rats by an adeno-associated virus vector-mediated ChR2 gene transfer in the retinal ganglion cells (Fig. 37.2a–e). RCS rats have MertK mutation (Audo et al. 2018, D'Cruz et al. 2000) in the retinal pigment epithelial (RPE) cells but not in the photoreceptor cells as in rd1 mice. The ganglion cells are targeted in ChR2-mediated gene therapy in these reports. On the other hand, Lagali PS et al. reported that the restoration of vision in rd1 mice by the ChR2 gene was transduced into the second-order neurons, ON-bipolar cells, in rd1 mice. Thus, if the third-order neurons, the ganglion cells, survived, the visual function could be restored by the transduction of the optogenetic gene into any of the surviving retinal neurons, independent of the causes of photoreceptor degeneration. The gene therapy using ChR2 for the RP patients is currently in clinical trials in the United States (NCT02556736 and NCT03326336).

## 37.4 mVChR1-Gene Therapy for RP

There are some limitations to the restoration of vision by ChR2 transduction. One of the limitations is the light sensitivity. We found in the behavioral study that at least 500 lux of the blue light (Tomita et al. 2010) was needed to elicit the optomoter response (Fig. 37.2a–d). Another limitation is the wavelength sensitivity. The visually evoked potentials (VEPs) in ChR2-transduced rats could not be recorded over a stimuli with 550 nm of light (Nagel et al. 2003, Tomita et al. 2010) although it could be recorded in the non-dystrophic rat (Fig. 37.2e). These are thought to be big problems that need to be taken into consideration for the clinical trials. It is well-known that an intense light shows a toxic effect on the photoreceptor cells (Tomita et al. 2005, 2016). If the patients still retain the native photoreceptor cells, they cannot use the intense light to activate the ChR2-transduced cells. In regard to the wavelength sensitivities, if the patients receiving ChR2-gene therapy would recover their vision, they would see the objects corresponding below 550 nm as blue colored objects. However, if there are objects that are out of the ChR2-sensitive wavelength range, they would not only see them but also the defect of the visual field.

In contrast to ChR2, it has been reported that Volvox-derived ChR1 (VChR1) has a broader, red-shifted action spectrum (Zhang et al. 2008). Considering the human visual spectrum, VChR1 might be more useful for restoring vision in blind patients. However, the light sensitivity of the native VChR1 is quite low owing to the inappropriate localization in the mammalian cells (Fig. 37.3a). The expression of VChR1 was mainly observed in the cytoplasm. We modified VChR1 by the addition of the N-terminal signal of Chlamydomonas ChR1 (Genbank acc#: LC315678). The expression of mVChR1 was clearly localized in the membrane (Fig. 37.3b) and the photocurrents increased upto 30 times higher than that in VChR1 (Fig. 37.3c, d). After the transduction of mVChR1 by using an AAV vector (Fig. 37.3e), VEPs in genetically blind rats recorded at a stimuli with 468–640 nm of LED (Fig. 37.3f) (Tomita et al. 2014). These results indicate that patients who received mVChR1 but not ChR2 could see broader range of colored objects. The mVChR1-gene therapy for patients with RP is now on preparatory stages of the clinical trial in Japan.

## 37.5 Effect of Two Different Types of Channelrhodpsin Expression on Visual Properties

Various types of ChRs are considered to be effective against diseases that cause blindness and the development of new types of ChRs continues to be explored. From the patient's perspective, it would be difficult to decide when or which gene would be suitable for treatment. One of the ways for treatment is the possibility of adding ChR with a different character even if the patient has already undergone gene therapy. We investigated the visual properties in the retina co-expressing

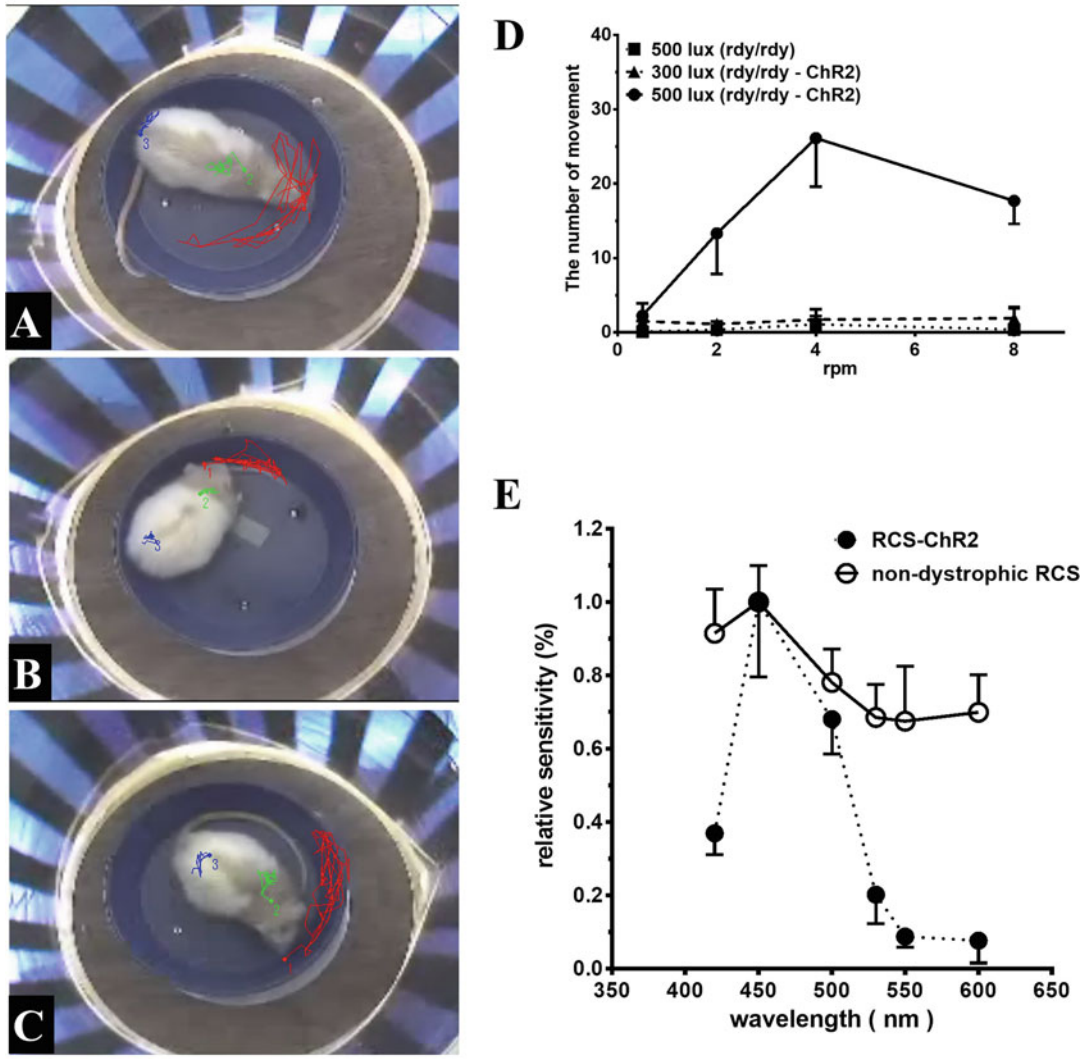


**Fig. 37.2** Behavioral and visual responses in RCS rats transduced with ChR2 gene. The traces of each marked point in control (**a**), RCS (**b**; blind), and ChR2 gene-transduced RCS (**c**) rats during a test at 4 rpm. The red, green, and blue lines correspond to the marks on the nose, the neck, and the waist, respectively. Each score was calculated by subtracting the number of movements at 0 rpm. The luminosity at the center of the holding chamber affected the movement. The score of the non-dystrophic rats increased with increasing light intensities (**d**). Amplitudes of VEPs elicited at different wavelengths at the intensity of 1 mW/cm$^2$ (**e**)

two different characters of two ChR genes (Sato et al. 2017). In this experiment, we used ChR2 transgenic rats. In ChR2-TG rats (Tomita et al. 2009), ChR2 transgene is driven by Thy-1.2 promoter, an effective regulator in the RGCs (Barnstable and Drager 1984, Kerrison et al. 2005). The native photoreceptor cells were made to undergo degeneration by an intraperitoneal N-Methyl-N-Nitrosourea (Sugano et al. 2019) injection so as to inhibit the native photoreceptor function. In ChR2-TG rat, the ChR2 expressions were about 63% among all the RGCs. After mVChR1 transduction by an AAV vector, the ratio of mVChR1-expressing ganglion cells was about 17% of all the RGCs, and co-expressing RGCs with ChR2 and mVChR1 were about 12%

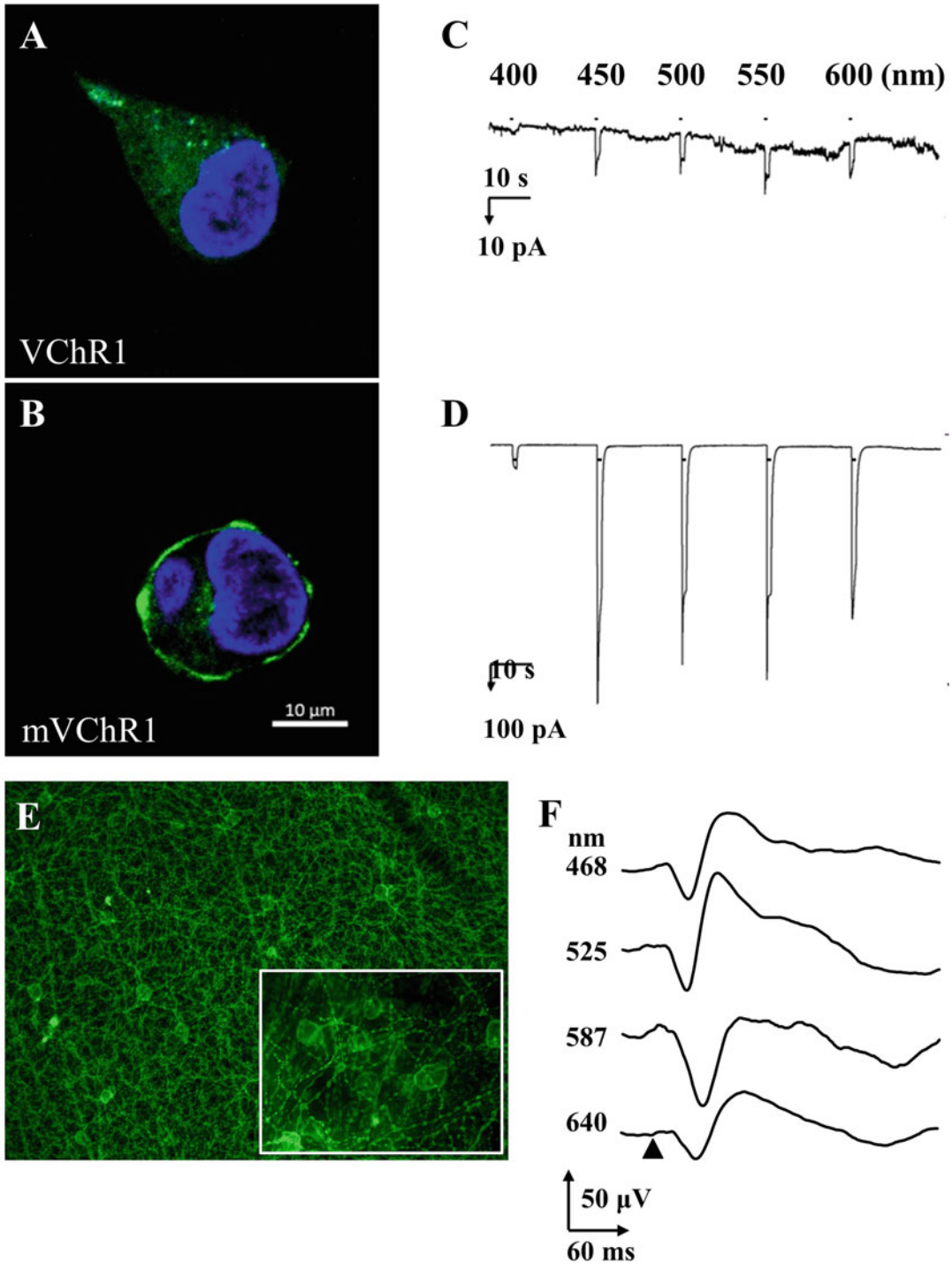


**Fig. 37.3** Expression profiles of modified Volvox channelrhodopsin-1 (mVChR1) in HEK 293 cells and Royal College of Surgeons rat retinas. The plasmids including the VChR1 (**a**) or mVChR1 (**b**) gene were electroporated into HEK 293 cells. VChR1 expression was observed in the cytoplasm. The localization of mVChR1 protein is clearly seen on the cell membrane. Typical waveforms from patch clamp recordings were shown in **c** and **d**. Photocurrents induced by various wavelengths of light in VChR1-HEK 293 cells were about 30 times lower than those in mVChR1-HEK 293 cells. Expression of mVChR1 was observed in the entire retina (**e**) and visually evoked potentials were recorded at a stimulus of 468–640 nm of LEDs (**f**)

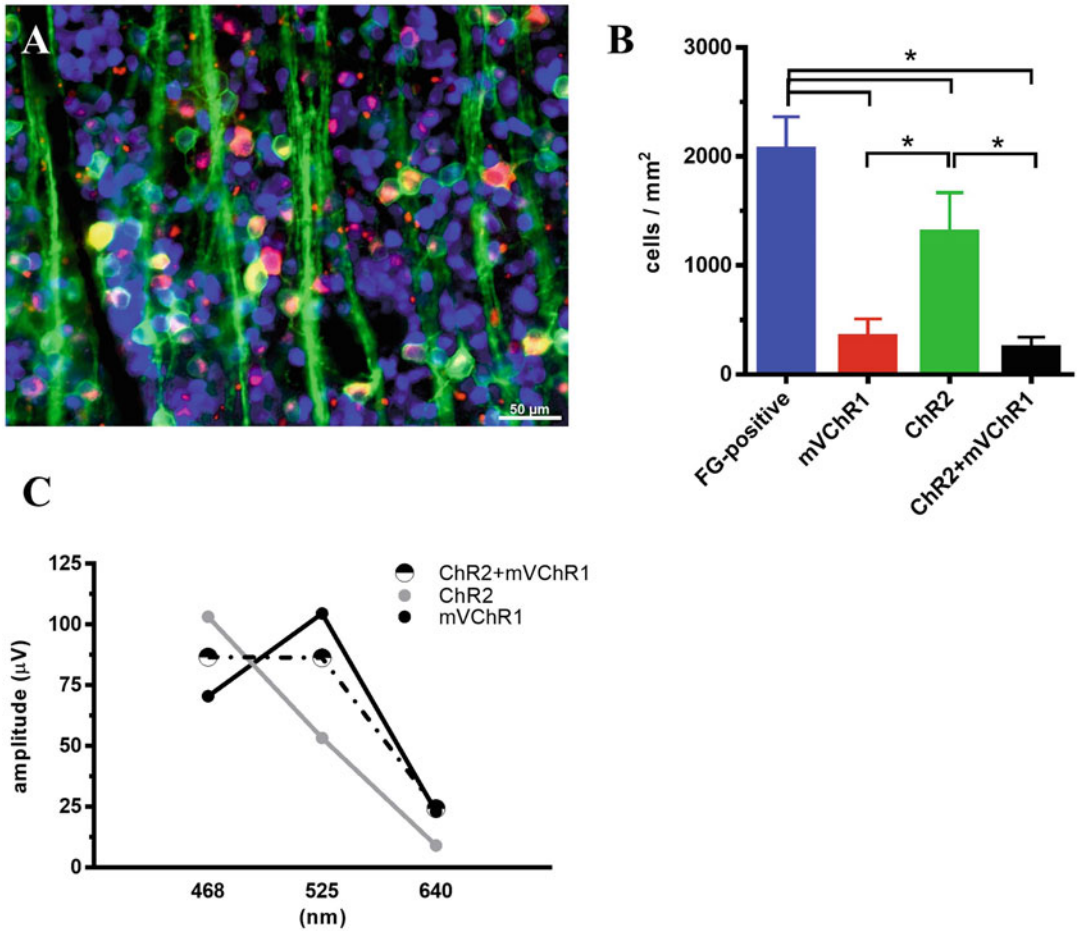


**Fig. 37.4** mVChR1 expression in photoreceptor degenerated ChR2-TG rat retina after AAV-mediated mVChR1 gene transduction. The green and red color corresponds to the ChR2 and mVChR1 expression, respectively. To identify the RGCs, RGCs were retrograde labeled with fluorogold (Blue) (**a**). The number of ChR2-, mVChR1-, and both expressing cells was shown in the graph (**b**). Visually evoked potentials in the photoreceptor degenerated-mVChR1 transduced rat, the photoreceptor degenerated-mVChR1 transduced ChR2 TG rat, and the photoreceptor degenerated ChR2-TG rat were recorded with blue-, green-, and red-LEDs (**c**)

(Fig. 37.4b). Before the AAV-mVChR1 injection, the VEPs could be detected at a stimulus of 468 and 525 nm of LEDs corresponding to the ChR2-sensitive wavelength but not 640 nm of LEDs (Fig. 37.4b). After the transduction of mVChR1, the VEPs in ChR2-TG rats with photoreceptor degeneration could respond at a stimulus of 640 nm of LEDs and the increased responses with a stimulus of 525 nm of LEDs compared to the photoreceptor degenerated ChR2-TG rats. These results indicate that the additional ChR gene transduction having a different wavelength sensitivity could expand the wavelength sensitivity. However, both VEP amplitudes in 468 and 525 nm stimuli slightly declined in the ChR2 rats and mVChR1-transduced rats.

## 37.6 Difference Between the Native Vision and the Optogenetic Vision

Cation-selective ion channels, such as ChR2 and mVChR1, have been considered for their applicative potential in the treatment of RP. However,

there is a big difference between the native vision produced by photoreceptor cells and the optogenetic vision. With regard to the light sensitivity, taking mVChR1 as an example, at least 0.1 μW/mm$^2$ is needed to activate the cell in patch-clamp recordings. The light intensity seemed to be quite low compared to other channelrhodopsins and the intensity corresponded to the room light. However, the fact that the photoreceptor cells can detect a single photon indicates the big difference in the light sensitivity. The other is color vision. Patients cannot get color vision although mVChR1 has a broad spectrum. The human retina has three types of color opsins that are independently expressed in the cells as blue-, green-, and red-cone. If it is possible to transduce optogenetic genes with different wavelength properties into specific cell types, patients could get color vision. As future initiatives, it is important to develop cell-type specific promoters.

## 37.7 Perspective

We focused here on the restoration of vision using cation channelrhodopsins. Retinal prostheses, for restoring vision, have already been approved as a treatment option in the United States (Farvardin et al. 2018). However, patients need to undergo a complicated surgery for the implantation of the electric device into the eye. In addition, the number of electrodes corresponding to the resolution remains small (60 electrodes). Conversely, in the case of gene therapy using optogenetics, the treatment is accomplished by only a single intravitreous injection of an AAV vector and 0.3 million retinal ganglion cells become photosensitive. When compared to retinal prostheses, the most important difference is that cellular depolarization occurs because of cation influx into the neuronal cells responding to light stimuli. Recently, anion channelrhodopsins have also been studied for the reactivation of surviving photoreceptor cells, but not for the treatment of complete blindness (Busskamp et al. 2010, Khabou et al. 2018). The application of optogenetic gene therapy in humans has faced a lot of difficulties because the optogenetic genes did not originate from humans at the start of the optogenetic gene therapy. We have performed some safety studies on rats (Sugano et al. 2011, 2016) and monkeys (data not shown) and shown that the optogenetic gene therapy was applicable for humans.

In the future, the therapeutic application of optogenetics will include not only the treatment of retinal diseases but also other organ disorders, with the development of medical devices that stimulate the internal organs with light.

**Acknowledgments** This work was partly supported by Grants-in-Aid for Scientific Research from the Ministry of Education, Culture, Sports, Science, and Technology of Japan (Grant Nos. 16H05485, 16K15729, 16K11314, and 17H06330).

## References

Audo I, Mohand-Said S, Boulanger-Scemama E et al (2018) MERTK mutation update in inherited retinal diseases. Hum Mutat 39:887–913

Barnstable CJ, Drager UC (1984) Thy-1 antigen: a ganglion cell specific marker in rodent retina. Neuroscience 11:847–855

Baylor DA, Lamb TD, Yau KW (1979) Responses of retinal rods to single photons. J Physiol 288:613–634

Bi A, Cui J, Ma YP et al (2006) Ectopic expression of a microbial-type rhodopsin restores visual responses in mice with photoreceptor degeneration. Neuron 50:23–33

Busskamp V, Duebel J, Balya D et al (2010) Genetic reactivation of cone photoreceptors restores visual responses in retinitis pigmentosa. Science 329:413–417

D'Cruz PM, Yasumura D, Weir J et al (2000) Mutation of the receptor tyrosine kinase gene Mertk in the retinal dystrophic RCS rat. Hum Mol Genet 9:645–651

Farber DB, Lolley RN (1974) Cyclic guanosine monophosphate: elevation in degenerating photoreceptor cells of the C3H mouse retina. Science 186:449–451

Farvardin M, Afarid M, Attarzadeh A et al (2018) The Argus-II retinal prosthesis implantation; from the global to local successful experience. Front Neurosci 12:584

Kerrison JB, Duh EJ, Yu Y et al (2005) A system for inducible gene expression in retinal ganglion cells. Invest Ophthalmol Vis Sci 46:2932–2939

Khabou H, Garita-Hernandez M, Chaffiol A et al (2018) Noninvasive gene delivery to foveal cones for vision restoration. JCI Insight 3:e96029

Kim SY, Sadda S, Pearlman J et al (2002) Morphometric analysis of the macula in eyes with disciform age-related macular degeneration. Retina 22:471–477

McLaughlin ME, Sandberg MA, Berson EL et al (1993) Recessive mutations in the gene encoding the beta-subunit of rod phosphodiesterase in patients with retinitis pigmentosa. Nat Genet 4:130–134

Nagel G, Szellas T, Huhn W et al (2003) Channelrhodopsin-2, a directly light-gated cation-selective membrane channel. Proc Natl Acad Sci U S A 100:13,940–13,945

Rieke F, Baylor DA (1998) Origin of reproducibility in the responses of retinal rods to single photons. Biophys J 75:1836–1857

Santos A, Humayun MS, de Juan E Jr et al (1997) Preservation of the inner retina in retinitis pigmentosa. A morphometric analysis. Arch Ophthalmol 115:511–515

Sato M, Sugano E, Tabata K et al (2017) Visual responses of photoreceptor-degenerated rats expressing two different types of Channelrhodopsin genes. Sci Rep 7:41,210

Stone JL, Barlow WE, Humayun MS et al (1992) Morphometric analysis of macular photoreceptors and ganglion cells in retinas with retinitis pigmentosa. Arch Ophthalmol 110:1634–1639

Sugano E, Isago H, Wang Z et al (2011) Immune responses to adeno-associated virus type 2 encoding channelrhodopsin-2 in a genetically blind rat model for gene therapy. Gene Ther 18:266–274

Sugano E, Tabata K, Takahashi M et al (2016) Local and systemic responses following intravitreous injection of AAV2-encoded modified Volvox channelrhodopsin-1 in a genetically blind rat model. Gene Ther 23:158–166

Sugano E, Tabata K, Takezawa T et al (2019) N-methyl-N-nitrosourea-induced photoreceptor degeneration is inhibited by nicotinamide via the blockade of upstream events before the phosphorylation of signalling proteins. Biomed Res Int 2019:3238719

Tomita H, Kotake Y, Anderson RE (2005) Mechanism of protection from light-induced retinal degeneration by the synthetic antioxidant phenyl-N-tert-butylnitrone. Invest Ophthalmol Vis Sci 46:427–434

Tomita H, Sugano E, Yawo H et al (2007) Restoration of visual response in aged dystrophic RCS rats using AAV-mediated channelopsin-2 gene transfer. Invest Ophthalmol Vis Sci 48:3821–3826

Tomita H, Sugano E, Fukazawa Y et al (2009) Visual properties of transgenic rats harboring the channelrhodopsin-2 gene regulated by the thy-1.2 promoter. PLoS One 4:e7679

Tomita H, Sugano E, Isago H et al (2010) Channelrhodopsin-2 gene transduced into retinal ganglion cells restores functional vision in genetically blind rats. Exp Eye Res 90:429–436

Tomita H, Sugano E, Murayama N et al (2014) Restoration of the majority of the visual spectrum by using modified Volvox channelrhodopsin-1. Mol Ther 22:1434–1440

Tomita H, Tabata K, Takahashi M et al (2016) Light induces translocation of NF-kappaB p65 to the mitochondria and suppresses expression of cytochrome c oxidase subunit III (COX III) in the rat retina. Biochem Biophys Res Commun 473:1013–1018

Wong WL, Su X, Li X et al (2014) Global prevalence of age-related macular degeneration and disease burden projection for 2020 and 2040: a systematic review and meta-analysis. Lancet Glob Health 2:e106–e116

Zhang F, Prigge M, Beyriere F et al (2008) Red-shifted optogenetic excitation: a tool for fast neural control derived from Volvox carteri. Nat Neurosci 11:631–633

# Optogenetic Strategies for Vision Restoration

38

Qi Lu and Zhuo-Hua Pan

**Abstract**

The loss of photoreceptor cells caused by retinal degenerative diseases leads to blindness. The optogenetic approach for restoring vision involves converting the surviving inner retinal neurons into photosensitive cells, thus imparting light sensitivity to the retina following the loss of photoreceptor cells. Our first demonstration of the feasibility of such an approach involved expressing ChR2 in the retinal ganglion cells of blind mice; since then, optogenetic vision restoration has been demonstrated by using a variety of optogenetic tools, especially microbial channelrhodopsins (ChRs). A ChR-based optogenetic therapy for treating blindness has advanced to clinical trials. In this chapter, we review our early proof-of-concept study of optogenetic vision restoration. We also discuss our studies for developing better ChR tools and for restoring intrinsic visual processing features in retinas with degenerated photoreceptors.

**Keywords**

Optogenetics · Retinal degeneration · Microbial rhodopsin · Channelrhodopsins · Adeno-associated virus · ON and OFF response · Center-surround receptive field · Sustained and transient response

## Abbreviations

| | |
|---|---|
| AAV | Adeno-associated virus |
| AIS | Axon initial segment |
| CAG | CMV early enhancer/chicken β actin |
| ChR | Channelrhodopsin |
| ChR2 | Channelrhodopsin-2 |
| CMV | Cytomegalovirus |
| CoChR | Channelrhodopsin variant from *Chloromonas oogama* |
| GFP | Green fluorescent protein |
| GtACR | Chloride-conducting channel from *Guillardia theta* |
| Kv2.1 | Voltage-gated $K^+$ channel 2.1 |
| NLG1 | Neuroligin-1 |
| NpHR | Halorhodopsin |
| RGC | Retinal ganglion cell |
| RP | Retinitis pigmentosa |
| YFP | Yellow fluorescent protein |

## 38.1 Introduction

Vision begins in the retina when rod and cone photoreceptor cells respond to light and convert changing light levels into electrical signals, which are then transmitted through second-order (bipolar cells and horizontal cells) and third-order

Q. Lu · Z.-H. Pan (✉)
Department of Ophthalmology, Visual and Anatomical Sciences, Wayne State University School of Medicine, Detroit, MI, USA
e-mail: qlu@med.wayne.edu; zhpan@med.wayne.edu



H. Yawo et al. (eds.), *Optogenetics*, Advances in Experimental Medicine and Biology 1293,
https://doi.org/10.1007/978-981-15-8763-4_38

(amacrine cells and ganglion cells) retinal neurons to higher visual centers in the brain. The severe loss of photoreceptor cells that occurs in inherited and acquired retinal degenerative diseases, such as retinitis pigmentosa (RP) and aged-related macular degeneration (AMD), leads to partial or complete blindness. At present, no effective treatment is available for restoring vision once the photoreceptor cells have been lost. Optogenetics is a promising approach that has the potential to restore significant useful vision to the blind.

The principle behind the optogenetic approach for treating blindness involves imparting light sensitivity to light-insensitive second- or third-order retinal neurons by ectopically expressing genetically encoded light sensors. The discovery of light-gated microbial channelrhodopsins (ChRs) (Nagel et al. 2002, 2003), particularly channelrhodopsin-2 (ChR2), prompted the exploration of this novel approach for vision restoration.

## 38.2 Early Proof-of-Concept Studies

Immediately following the report of ChR2 (Nagel et al. 2003), we began to investigate the feasibility of functional expression of ChR2 in inner retinal neurons in vivo (Bi et al. 2006). The experiments were conducted both in rats and mice, and we especially used a retinal degenerative mouse model, *rd1* mice. Because retinal neurons do not divide, a viral-based delivery was found to be the most effective way to express ChR2 in inner retinal neurons in vivo. Specifically, AAV2 vectors were used to deliver a ChR2–GFP fusion construct driven by a ubiquitous CAG promoter. One month after the viral vectors were injected into the intravitreal space of the eyes, robust ChR2–GFP expression was observed in inner retinal neurons, and it was predominantly observed in retinal ganglion cells (RGCs) (Fig. 38.1). ChR2-mediated spike activities were recorded from ChR2–GFP-expressing RGCs from *rd1* mice in the absence of an exogenous supply of the chromophore all-*trans* retinal (Fig. 38.2). Furthermore, ChR2 expression also restored visually evoked potentials in the visual cortex of *rd1* mice.

Our follow-up studies in *rd1* mice have further shown that the functional expression of ChR2 in mouse retinal neurons by a single administration of viral vectors can last for the animals' entire life (Ivanova and Pan 2009). Functional expression of ChR2 can also be achieved by AAV-mediated delivery of vectors in nonhuman primates, although the transduction efficiency is much lower (Ivanova et al. 2010). Taken together, these early studies demonstrated the feasibility of ChR-based visual restoration in animal models. Optogenetic therapies for treating blindness through AAV-mediated ubiquitous expression of ChRs in RGCs are currently in clinical trials (NCT02556736 and NCT03326336).

## 38.3 The Development of Highly Light-Sensitive ChRs

Since the first demonstration of the feasibility of the optogenetic vision restoration using ChR2, the ability of such an approach to restore vision has been reported by using a variety of ChRs, including ChRs that have been modified by molecular engineering or variants that have been newly discovered in nature (Pan et al. 2014). Optogenetic vision restoration has also been reported by using G-protein couple optogenetic tools, such as melanopsin and vertebrate or human opsins (Gaub et al. 2015; Cehajic-Kapetanovic et al. 2015; Berry et al. 2019; Lin et al. 2008).

The use of ChRs as optogenetic tools for vision restoration has many advantages. In particular, since all ChRs use all-*trans* retinal as a chromophore, an exogenous supply of the chromophore is not required. Additionally, ChRs with different biophysical properties, such as those with ionic selectivity and spectral sensitivity, which are either found in nature or generated by molecular engineering, are becoming increasingly available. Thus, ChRs represent a versatile toolset with the potential to restore complex visual processing features in a degenerated retina. However, a major drawback of using ChR2 in

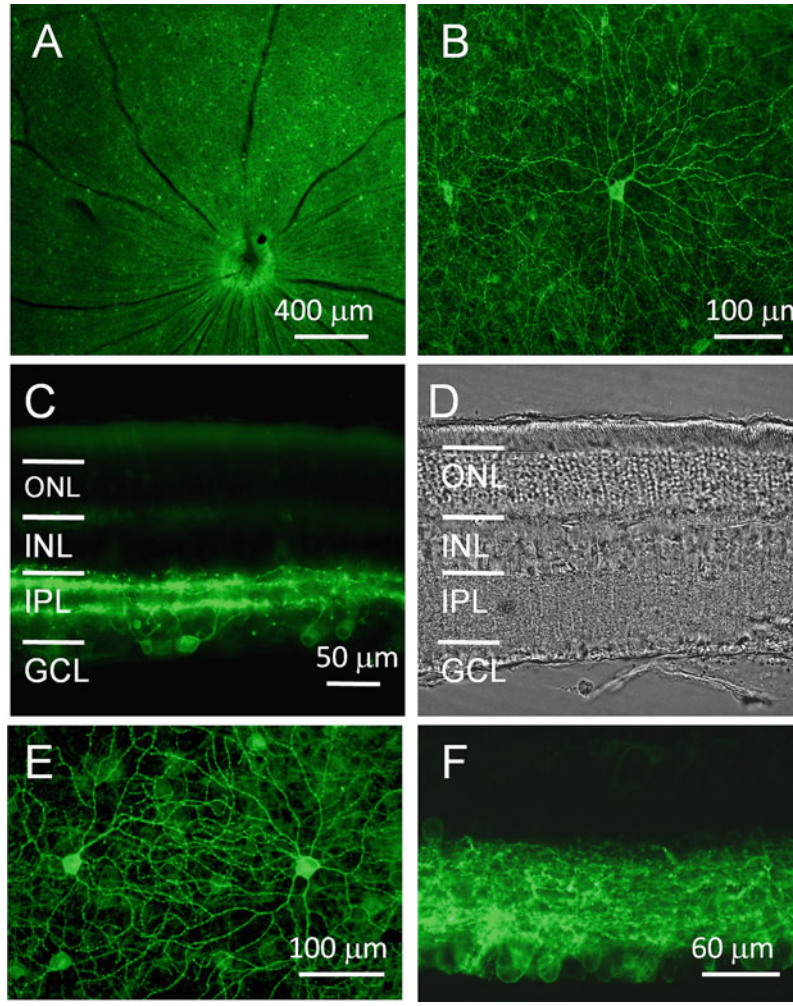


**Fig. 38.1** AAV-mediated in vivo expression of ChR2–GFP in retinal neurons. (**a, b**) ChR2–GFP expression in whole-mount retinas from wild-type rats at low (**a**) and high (**b**) magnifications. (**c**, **d**) Fluorescence image (**c**) and phase-contrast image (**d**) taken from vertically sliced sections of normal rat retinas that express ChR2–GFP. (**e**, **f**) Fluorescence images taken from whole-mount retinas (**e**) and vertical retinal sections (**f**) of *rd1* mice that express ChR2–GFP. *ONL* Outer nuclear layer, *INL* Inner nuclear layer, *IPL* Inner plexiform layer, *GCL* Ganglion cell layer. Modified from (Bi et al. 2006) with permission from Elsevier

particular and ChRs in general for vision restoration is their low light sensitivity (Pan et al. 2015). As shown in Fig. 38.3, the light sensitivity of ChR2-expressing RGCs is at least 4–5 log units lower than that of cone photoreceptors. Therefore, one of our efforts has been focused on the development of more light-sensitive ChRs.

Since ChRs are light-gated channels, their operational light sensitivity (hereafter referred to as light sensitivity) can be altered by molecular engineering. Specifically, for an individual ChR, the amplitude of its photocurrent, which is correlated with its light sensitivity, can be enhanced by slowing down its deactivation kinetics (or off-rate) through site-directed mutagenesis. While there is a trade-off between light sensitivity and temporal resolution, since vision restoration can tolerate relatively slower kinetics, an optimized balance between light sensitivity and temporal resolution for a ChR can be achieved. With this approach, we previously created an optimized ChR2 mutant, ChR2-L132C/T159S, which improved the light sensitivity by close to 2 log units over what was observed in wild-type ChR2 (Fig. 38.3) (Pan et al. 2014; Lu et al. 2018). Furthermore, we recently developed a more light-sensitive ChR variant, CoChR-H94E/L112C/K264T (CoChR-3M), by using a

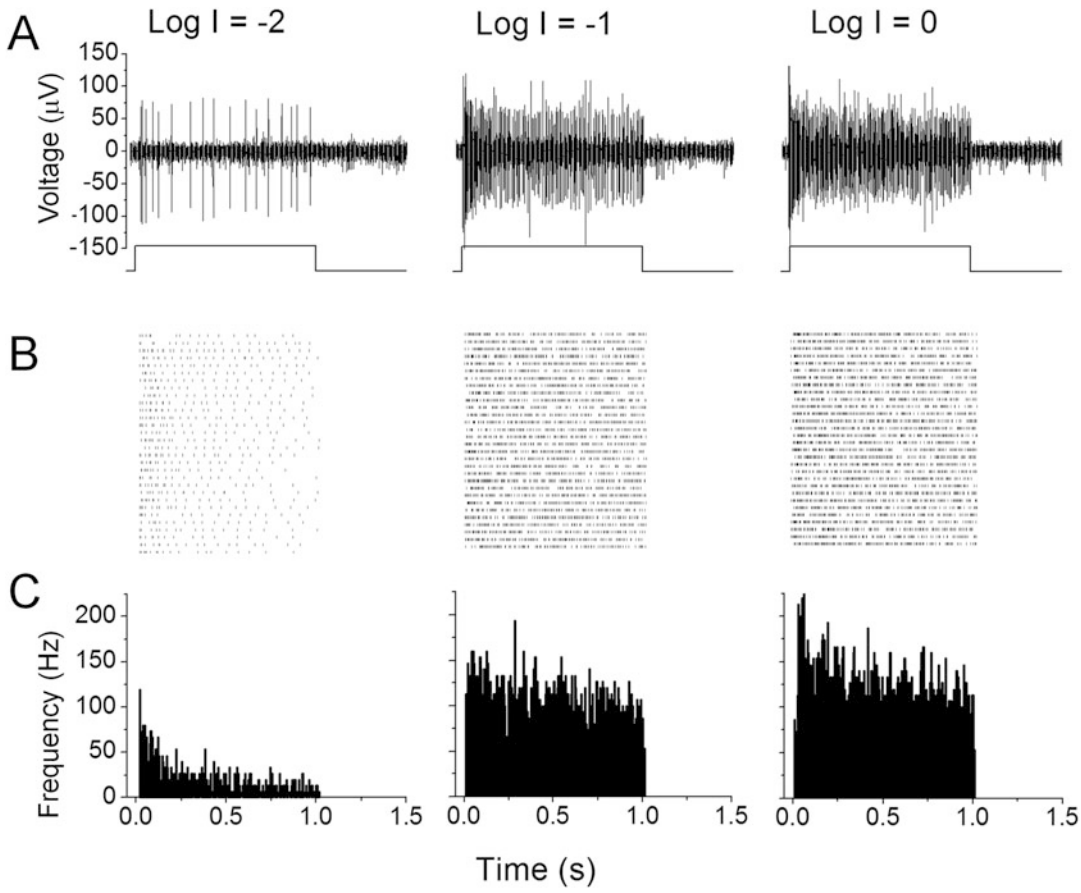


**Fig. 38.2** Multielectrode array recordings of ChR2-expressing retinas from *rd1* mice. A sample recording of light-evoked spike activity in response to three incremental light intensities. (**a**) Light-evoked spikes were recorded from a single electrode at three incremental light intensities. (**b**) Raster plots were constructed from 30 consecutive light-elicited spikes that originated from a single neuron. (**c**) Histograms demonstrate the average spike rates. Modified from (Bi et al. 2006) with permission from Elsevier

newly discovered *Chloromonas oogama* (CoChR) variant (Ganjawala et al. 2019). The light sensitivity for CoChR-3M is close to 3 log units higher than that of wild-type ChR2 (Fig. 38.3). By animal behavioral assessments using a blind mouse model, we showed that the expression of CoChR-3M in RGCs enables the restoration of remarkably good visual acuity and contrast sensitivity under ambient light conditions. Therefore, the low light sensitivity of ChR-based vision restoration is no longer an issue.

## 38.4 Possible Strategies for Restoring Intrinsic Visual Processing Features in the Degenerative Retina

One of the major advantages of the optogenetic approach for vision restoration is the possibility of restoring intrinsic visual processing features of the retina. This may be necessary because not only is the retina the site of initiating phototransduction but it also plays an essential

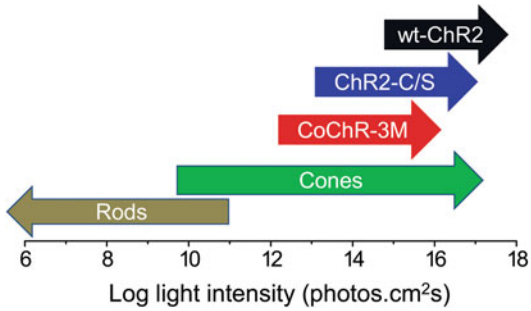


**Fig. 38.3** Comparison of the light sensitivities of rod and cone photoreceptors with wild-type channelrhodopsin 2 (ChR2), and ChR2-C/S and CoChR-3M. The estimated light sensitivities for photoreceptors are taken from (Dacey et al. 2005); those for ChR2 and its mutants are from Pan et al. (2014), and those for CoChR-3M are from Ganjawala et al. (2019). The light sensitivities are based on in vitro retinal whole-mount recordings from retinal ganglion cells

role in processing visual information before it is transmitted to higher visual centers in the brain. In particular, visual signals are processed in the retina through multiple parallel pathways, such as ON and OFF pathways, scotopic (rod) and photopic (cone) pathways, and pathways that are responsible for edge detection, motion and directional selectivity, and color coding. All photoreceptor cells become hyperpolarized in response to light. Bipolar cells and ganglion cells are divided into ON and OFF cells that depolarize and hyperpolarize, respectively, in response to increased light intensity (Fig. 38.4). The segregation of visual signals into ON and OFF pathways is believed to be important for enhancing contrast sensitivity. Light responses in inner retinal neurons, especially retinal ganglion cells, can also be divided into sustained and transient responses based on their temporal properties. The sustained and transient light responses are thought to code for distinct aspects of visual information, such as acuity and motion, respectively. Furthermore, horizontal cells and amacrine cells provide lateral inhibition that aids in the formation of center-surround antagonistic receptive fields in both bipolar and retinal ganglion cells (Fig. 38.4). This center-surround antagonistic receptive field is an essential feature of visual information processing that enables edge detection by enhancing spatial contrast. Thus, restoring these intrinsic visual processing features in the retina would be expected to improve the outcomes of restored visual functions, such as visual acuity and contrast sensitivity.

One possible strategy to restore intrinsic visual processing features with optogenetics in photoreceptor-degenerated retinas is to use optogenetic tools to target distal retinal neurons, such as bipolar cells or even surviving cone photoreceptors (Lagali et al. 2008; Busskamp et al. 2010). A major issue regarding such a strategy concerns the status of distal retinal neurons in the retina following photoreceptor degeneration. Substantial studies have shown that retinal degeneration results in progressive and time-dependent deterioration of inner retinal neurons and circuits, which is termed retinal remodeling (Strettoi et al. 2002; Marc et al. 2003; Strettoi and Pignatelli 2000). However, RGCs have been reported to be more resistant to retinal remodeling than other inner retinal neurons (Mazzoni et al. 2008; Damiani et al. 2012). Thus, in cases of advanced retinal degeneration, RGCs could be the only possible target for optogenetic vision restoration. In such cases, restoration of intrinsic retinal processing features would need to be implemented at the level of RGCs.

## 38.5 Restoration of OFF Light Responses in the Retina

The ectopic expression of cation-permeable ChRs, such as ChR2, can effectively convert inner retinal neurons, including RGCs, into sustained ON cells that respond to light with sustained membrane depolarization or spiking (Fig. 38.2). On the other hand, creation of OFF cells in inner retinal neurons would require expressing a light sensor capable of producing membrane hyperpolarization or suppressing spiking activity when stimulated with light. The following microbial opsins could be used for such a purpose: the light-driven outward proton pump bacteriorhodopsin (Oesterhelt and Stoeckenius 1973), the light-driven inward chloride ion pump halorhodopsin (NpHR) (Han and Boyden

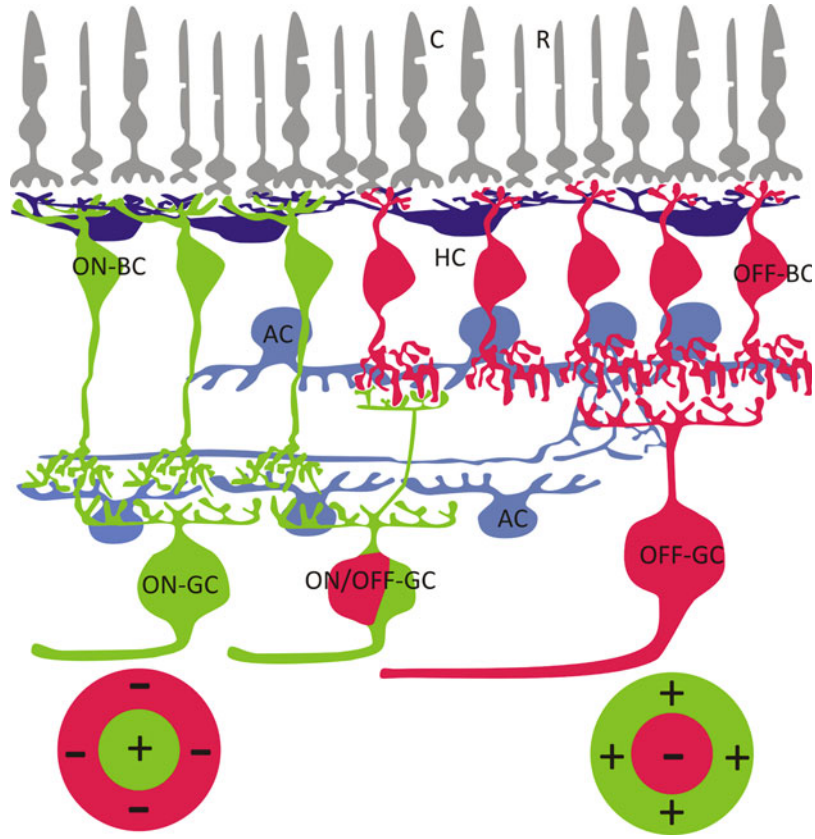


**Fig. 38.4** Visual information processing in the retina. This schematic diagram outlines the visual information processing features of the retina, specifically the ON and OFF pathways and center-surround antagonistic receptive fields. ON and OFF light responses originate at the level of bipolar cells and are carried downstream of retinal ganglion cells. The surround of the center-surround antagonistic receptive fields in retinal ganglion cells is formed by the lateral inhibition from horizontal and amacrine cells. The ON and OFF regions of the receptive fields are indicated by + and −, respectively. *R* Rod photoreceptors, *C* Cone photoreceptors, *HC* Horizontal cells, *AC* Amacrine cells, *GC* Ganglion cells

2007), or the more recently reported direct light-gated chloride channel, GtACR (Govorunova et al. 2015).

As a proof of concept, we investigated whether the expression of hyperpolarizing light sensors could restore OFF light responses in the retina by using NpHR (Zhang et al. 2009). In this study, an AAV2 vector with a ubiquitous CMV promoter was used to drive the expression of a fusion NpHR–mCherry transgene in RGCs in wild-type or *rd1* mice. Robust NpHR–mCherry expression was observed in inner retinal neurons; it was predominantly found in RGCs. More importantly, OFF light responses could be recorded in these NpHR-expressing retinal ganglion cells. As shown in Fig. 38.5, spiking activity was suppressed during light stimulation, while rebound spikes were observed after the light was turned off. Interestingly, both sustained and transient OFF responses were observed, although it remained to be investigated whether they corresponded with the intrinsic sustained and transient response properties of RGCs. Thus, the expression of NpHR can effectively convert RGCs into OFF cells in photoreceptor-deficient retinas.

## 38.6 Subcellular Targeting to Create Center-Surround Antagonistic Receptive Fields

Another key feature of the visual processing features of RGCs is their center-surround antagonistic receptive field. There are two types of center-surround receptive fields: ON center and OFF center. ON RGCs have a receptive field where the center is ON and the surround is OFF, while the receptive fields of OFF RGCs are reversed (i.e., OFF center and ON surround).

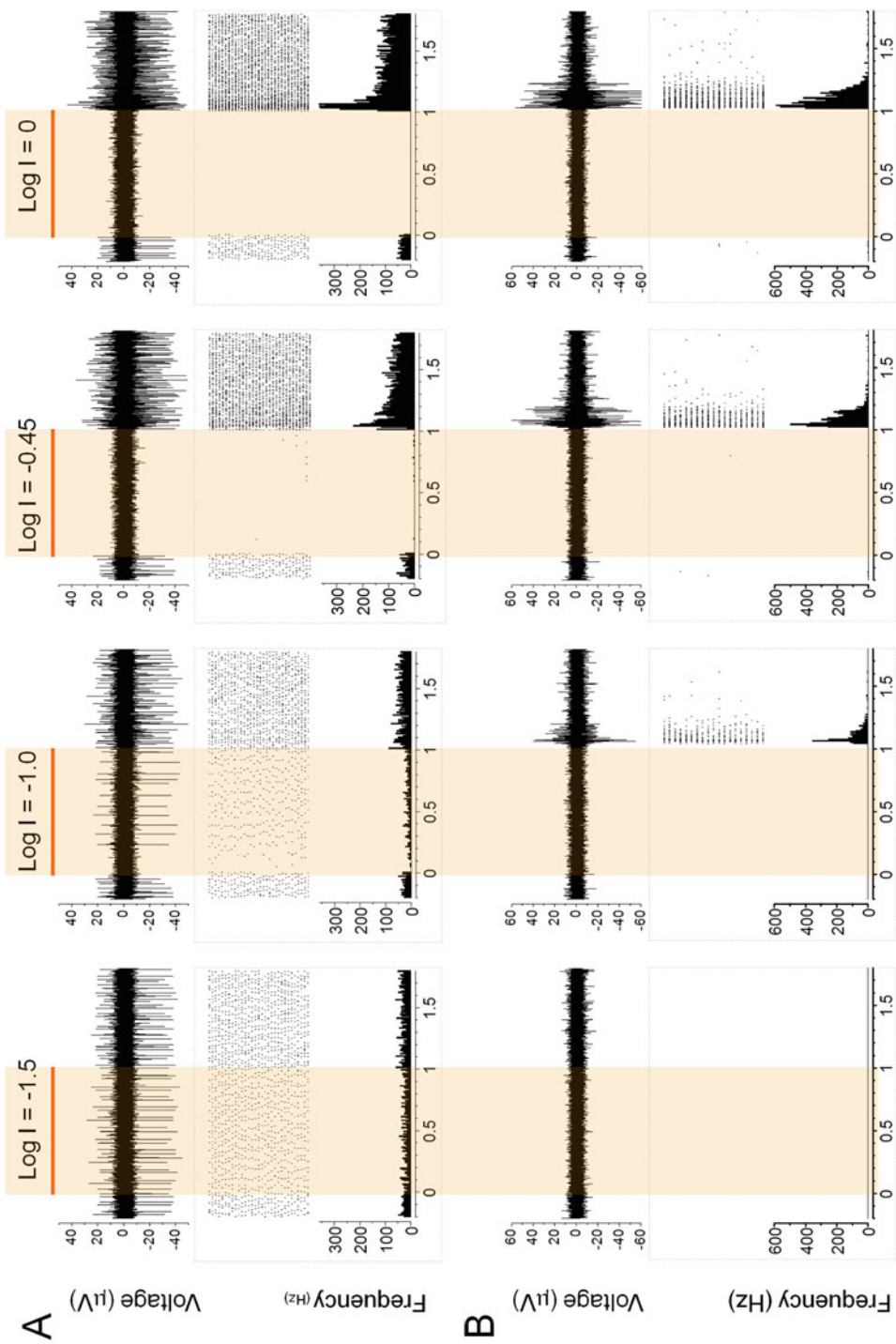


**Fig. 38.5** Multielectrode array recordings of NpHR-mediated spike responses from *rd1* retinas. (**a**) Sample recordings of NpHR-mediated spike activity from a sustained-OFF-type cell in response to four incremental light intensities. In each panel, a single trace of light-evoked spike activity, a raster plot of 30 consecutive recordings, and an averaged spike rate histogram are shown in the top, middle, and bottom panels, respectively. (**b**) Sample recordings of NpHR-mediated spike activity from a transient-OFF-type cell were recorded under the same conditions as those in (**a**). Modified from (Zhang et al. 2009)

Because the center-surround receptive field is generated by lateral inhibition from horizontal and amacrine cells, it is lost for the approach of directly rendering photosensitivity in RGCs.

However, it may be possible to recapitulate center-surround receptive fields in RGCs by differentially expressing the depolarizing and hyperpolarizing optogenetic sensors, such as ChR2 and NpHR, at the center and peripheral regions of the dendritic trees of retinal ganglion cells, respectively. This specificity in expression could be achieved by employing protein targeting motifs, which are known to be one of the mechanisms underlying the localization of membrane proteins to specific subcellular regions. In support of this idea, a previous study demonstrated that the differential expression of ChR2 and NpHR using ankyrin-G and postsynaptic density (PSD) motifs could be achieved using biolistic particle delivery, and it could consequently generate a center-surround receptive field in RGCs (Greenberg et al. 2011). However, potential therapeutic applications would require that motif targeting be achieved through a viral-mediated delivery system, such as AAV vectors. In addition, motifs that decrease axonal expression would be important because the responses generated by RGC axons could interfere with the retinotopic mapping in higher visual centers.

In an effort to identify motifs that could be used clinically, we identified two motifs that are suitable for AAV-mediated targeting in mice (Wu et al. 2013). One motif, from the voltage-gated $K^+$ channel 2.1 (Kv2.1), was shown to be capable of targeting ChR2 or NpHR to the cell soma and proximal dendrites of RGCs, making it possible to establish a center. A second motif, from neuroligin-1 (NLG1), targets the somatodendritic region of RGCs, which can be used to establish a surround. For both motifs, the expression in distal axons was significantly reduced. Figure 38.6 shows the center targeting ability of the Kv2.1-motif in an RGC that was cotransduced with two viral vectors carrying ChR2–mCherry without the motif and NpHR–YFP with the Kv2.1 motif. The dendritic field size expressing NpHR–YFP with the Kv2.1 motif is markedly smaller than the one expressing ChR2–mCherry without the motif. Additionally,

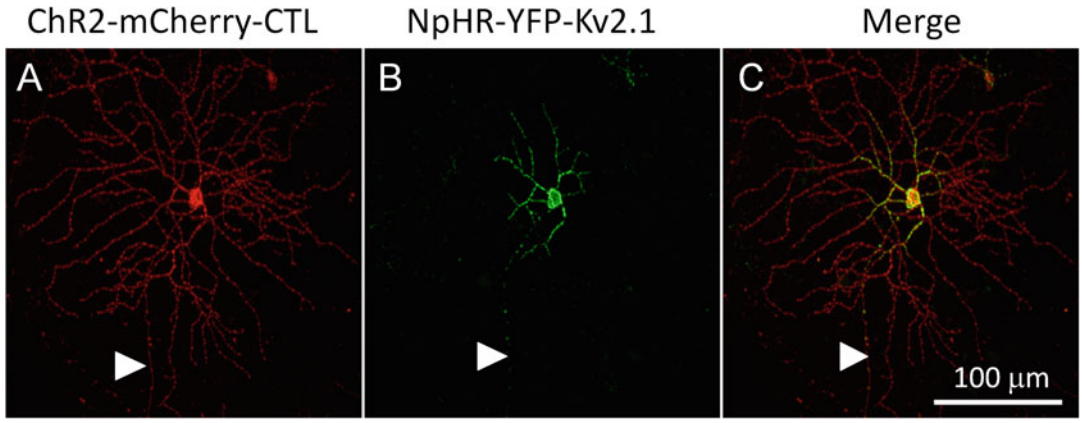


**Fig. 38.6** Coexpression of ChR2–mCherry and NpHR–YFP–Kv2.1 in retinal ganglion cells. (**a**–**c**) Eyes were coinjected with a viral vector carrying either ChR2–mCherry or NpHR–YFP–Kv2.1. The ChR2–mCherry (red; **a**) and NpHR–YFP–Kv2.1 (green; **b**) images were then merged to demonstrate a center-surround type organization in the dendritic field of a single RGC (**c**). The axon is indicated by arrowheads. Reprinted from (Wu et al. 2013)

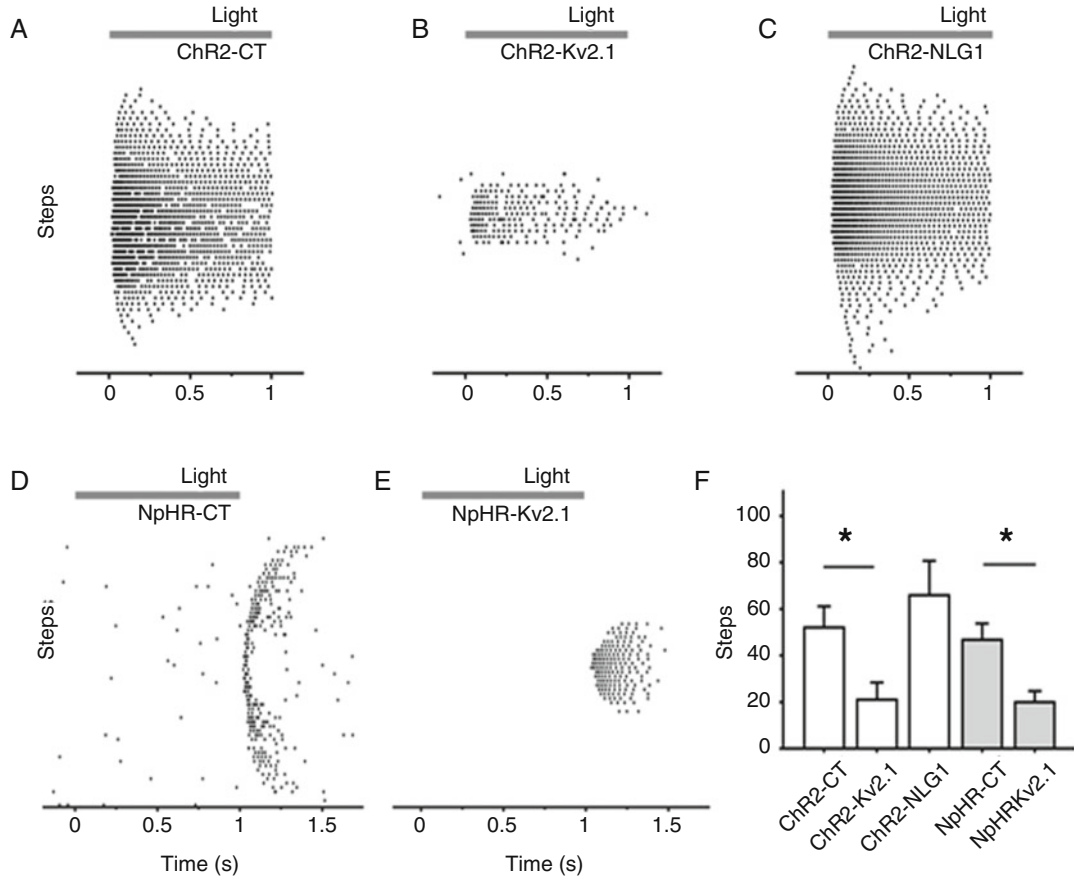


**Fig. 38.7** Motif-targeted physiological response field size assessed by multielectrode array recordings. (**a**–**c**) Sample MEA recording traces from ganglion cells that express ChR2–YFP (**a**), ChR2–YFP with a Kv2.1 motif (**b**), ChR2–YFP with an NLG1 motif (**c**), NpHR–YFP (**d**), and NpHR–YFP with a Kv2.1 motif (**e**); recordings are in response to a 200-μm light bar stimulus given at 20 μm increments. Each row of dots represents spiking activity elicited by a 1 s light pulse, and sequential rows represent sequential steps in the cell's receptive field. (**f**) Quantitative comparison of the response field sizes of ChR2–YFP- and NpHR–YFP-expressing retinal ganglion cells. For each cell, the physiologically receptive field size was estimated from the number of steps that elicited light-driven spiking activity. When compared to the ChR2–YFP control, the ChR2–YFP/Kv2.1 motif expression in cells resulted in a significantly smaller receptive field size. Similarly, the NpHR-mediated receptive field sizes between the cells with the NpHR–YFP control and the NpHR–YFP/Kv2.1 motif were significantly different. Reprinted from (Wu et al. 2013)

the reduced axonal expression of NpHR–YFP with the Kv2.1 motif can be noted (indicated by arrowheads in Fig. 38.6). Furthermore, we showed that when a light bar was used to map receptive fields, a reduction in the physiological receptive field size in the ChR2- or NpHR-mediated light responses can be observed when the Kv2.1 motif is used in comparison to that of either the NLG-1 motif or a control (Fig. 38.7).

## 38.7 Subcellular Targeting to Alter the Temporal Kinetics of ChR-Mediated Light Responses

RGCs are also classified as sustained and transient according to their temporal light response properties, which involve temporal aspects of visual processing, such as motion detection. The expression of depolarizing ChRs in RGCs usually only results in characteristically sustained light responses. However, our recent studies showed that the temporal light response property of RGCs could be altered by subcellular targeting (Zhang et al. 2015). Specifically, we found that AAV-mediated expression of ChR2 with a voltage-gated sodium channel motif, $Na_V$II-II, in mouse RGCs results in the expression of ChR in the axon initial segment (AIS). This targeted expression disrupted sodium channel clustering at the AIS and converted the spike firing patterns of RGCs from sustained to transient. Therefore, the targeting of optogenetic tools to the AIS through the use of a sodium channel motif may offer a potential way to create transient light responses in RGCs to enable vision restoration.

## 38.8 Conclusion

Proof-of-concept optogenetic vision restoration, especially using ChR-based optogenetic tools, has been well established in animal models. Optogenetic therapies with the first generation of ChR tools for treating blindness caused by RP are currently in clinical trials. Much improved ChRs have been recently developed and they show remarkably good functional efficacy in animal models. Although ubiquitous expression of ChR in RGCs may be sufficient for restoring useful vision, the restoration of intrinsic visual processing features in a photoreceptor degenerated retina may further improve outcomes of restored visual functions, such as visual acuity, contrast sensitivity, and motion detection. Optogenetic strategies, especially with versatile ChR-based tools, have the potential to restore intrinsic visual processing features in the retina, such as the ON and OFF, sustained and transient, and center-surround receptive field features.

**Acknowledgments** This work was supported by the Ligon Research Center of Vision at Kresge Eye Institute, Dryer Foundation, and an unrestricted grant by Research to Prevent Blindness to Department of Ophthalmology, Visual and Anatomical Sciences at Wayne State University School of Medicine.

## References

Berry MH, Holt A, Salari A, Veit J, Visel M, Levitz J, Aghi K, Gaub BM, Sivyer B, Flannery JG, Isacoff EY (2019) Restoration of high-sensitivity and adapting vision with a cone opsin. Nat Commun 10(1):1221. https://doi.org/10.1038/s41467-019-09124-x

Bi A, Cui J, Ma YP, Olshevskaya E, Pu M, Dizhoor AM, Pan ZH (2006) Ectopic expression of a microbial-type rhodopsin restores visual responses in mice with photoreceptor degeneration. Neuron 50(1):23–33. https://doi.org/10.1016/j.neuron.2006.02.026

Busskamp V, Duebel J, Balya D, Fradot M, Viney TJ, Siegert S, Groner AC, Cabuy E, Forster V, Seeliger M, Biel M, Humphries P, Paques M, Mohand-Said S, Trono D, Deisseroth K, Sahel JA, Picaud S, Roska B (2010) Genetic reactivation of cone photoreceptors restores visual responses in retinitis pigmentosa. Science 329(5990):413–417. https://doi.org/10.1126/science.1190897

Cehajic-Kapetanovic J, Eleftheriou C, Allen AE, Milosavljevic N, Pienaar A, Bedford R, Davis KE, Bishop PN, Lucas RJ (2015) Restoration of vision with ectopic expression of human rod opsin. Curr Biol 25(16):2111–2122. https://doi.org/10.1016/j.cub.2015.07.029

Dacey DM, Liao HW, Peterson BB, Robinson FR, Smith VC, Pokorny J, Yau KW, Gamlin PD (2005) Melanopsin-expressing ganglion cells in primate retina signal colour and irradiance and project to the LGN. Nature 433(7027):749–754. https://doi.org/10.1038/nature03387

Damiani D, Novelli E, Mazzoni F, Strettoi E (2012) Undersized dendritic arborizations in retinal ganglion cells of the rd1 mutant mouse: a paradigm of early onset photoreceptor degeneration. J Comp Neurol 520(7):1406–1423. https://doi.org/10.1002/cne.22802

Ganjawala TH, Lu Q, Fenner MD, Abrams GW, Pan ZH (2019) Improved CoChR variants restore visual acuity and contrast sensitivity in a mouse model of blindness under ambient light conditions. Mol Ther 27(6):1195–1205. https://doi.org/10.1016/j.ymthe.2019.04.002

Gaub BM, Berry MH, Holt AE, Isacoff EY, Flannery JG (2015) Optogenetic vision restoration using rhodopsin

for enhanced sensitivity. Mol Ther 23(10):1562–1571. https://doi.org/10.1038/mt.2015.121

Govorunova EG, Sineshchekov OA, Janz R, Liu X, Spudich JL (2015) NEUROSCIENCE. Natural light-gated anion channels: a family of microbial rhodopsins for advanced optogenetics. Science 349 (6248):647–650. https://doi.org/10.1126/science.aaa7484

Greenberg KP, Pham A, Werblin FS (2011) Differential targeting of optical neuromodulators to ganglion cell soma and dendrites allows dynamic control of center-surround antagonism. Neuron 69(4):713–720. https://doi.org/10.1016/j.neuron.2011.01.024

Han X, Boyden ES (2007) Multiple-color optical activation, silencing, and desynchronization of neural activity, with single-spike temporal resolution. PLoS One 2 (3):e299. https://doi.org/10.1371/journal.pone.0000299

Ivanova E, Pan ZH (2009) Evaluation of the adeno-associated virus mediated long-term expression of channelrhodopsin-2 in the mouse retina. Mol Vis 15:1680–1689

Ivanova E, Hwang GS, Pan ZH, Troilo D (2010) Evaluation of AAV-mediated expression of Chop2-GFP in the marmoset retina. Invest Ophthalmol Vis Sci 51 (10):5288–5296. https://doi.org/10.1167/iovs.10-5389

Lagali PS, Balya D, Awatramani GB, Munch TA, Kim DS, Busskamp V, Cepko CL, Roska B (2008) Light-activated channels targeted to ON bipolar cells restore visual function in retinal degeneration. Nat Neurosci 11(6):667–675. https://doi.org/10.1038/nn.2117

Lin B, Koizumi A, Tanaka N, Panda S, Masland RH (2008) Restoration of visual function in retinal degeneration mice by ectopic expression of melanopsin. Proc Natl Acad Sci U S A 105(41):16,009–16,014. https://doi.org/10.1073/pnas.0806114105

Lu Q, Ganjawala TH, Hattar S, Abrams GW, Pan ZH (2018) A robust optomotor assay for assessing the efficacy of optogenetic tools for vision restoration. Invest Ophthalmol Vis Sci 59(3):1288–1294. https://doi.org/10.1167/iovs.17-23278

Marc RE, Jones BW, Watt CB, Strettoi E (2003) Neural remodeling in retinal degeneration. Prog Retin Eye Res 22(5):607–655. https://doi.org/10.1016/s1350-9462(03)00039-9

Mazzoni F, Novelli E, Strettoi E (2008) Retinal ganglion cells survive and maintain normal dendritic morphology in a mouse model of inherited photoreceptor degeneration. J Neurosci 28(52):14282–14292. https://doi.org/10.1523/JNEUROSCI.4968-08.2008

Nagel G, Ollig D, Fuhrmann M, Kateriya S, Musti AM, Bamberg E, Hegemann P (2002) Channelrhodopsin-1: a light-gated proton channel in green algae. Science 296(5577):2395–2398. https://doi.org/10.1126/science.1072068

Nagel G, Szellas T, Huhn W, Kateriya S, Adeishvili N, Berthold P, Ollig D, Hegemann P, Bamberg E (2003) Channelrhodopsin-2, a directly light-gated cation-selective membrane channel. Proc Natl Acad Sci U S A 100(24):13,940–13,945. https://doi.org/10.1073/pnas.1936192100

Oesterhelt D, Stoeckenius W (1973) Functions of a new photoreceptor membrane. Proc Natl Acad Sci U S A 70 (10):2853–2857. https://doi.org/10.1073/pnas.70.10.2853

Pan ZH, Ganjawala TH, Lu Q, Ivanova E, Zhang Z (2014) ChR2 mutants at L132 and T159 with improved operational light sensitivity for vision restoration. PLoS One 9(6):e98924. https://doi.org/10.1371/journal.pone.0098924

Pan ZH, Lu Q, Bi A, Dizhoor AM, Abrams GW (2015) Optogenetic approaches to restoring vision. Annu Rev Vis Sci 1:185–210. https://doi.org/10.1146/annurev-vision-082114-035532

Strettoi E, Pignatelli V (2000) Modifications of retinal neurons in a mouse model of retinitis pigmentosa. Proc Natl Acad Sci U S A 97(20):11020–11025. https://doi.org/10.1073/pnas.190291097

Strettoi E, Porciatti V, Falsini B, Pignatelli V, Rossi C (2002) Morphological and functional abnormalities in the inner retina of the rd/rd mouse. J Neurosci 22 (13):5492–5504

Wu C, Ivanova E, Zhang Y, Pan ZH (2013) rAAV-mediated subcellular targeting of optogenetic tools in retinal ganglion cells in vivo. PLoS One 8(6):e66332. https://doi.org/10.1371/journal.pone.0066332

Zhang Y, Ivanova E, Bi A, Pan ZH (2009) Ectopic expression of multiple microbial rhodopsins restores ON and OFF light responses in retinas with photoreceptor degeneration. J Neurosci 29(29):9186–9196. https://doi.org/10.1523/JNEUROSCI.0184-09.2009

Zhang Z, Feng J, Wu C, Lu Q, Pan ZH (2015) Targeted expression of channelrhodopsin-2 to the axon initial segment alters the temporal firing properties of retinal ganglion cells. PLoS One 10(11):e0142052. https://doi.org/10.1371/journal.pone.0142052

# Application of Optogenetics in Epilepsy Research

39

Shin-Ichiro Osawa and Teiji Tominaga

**Abstract**

Epilepsy is a disease characterized by seizures arising from paroxysmal and self-limited hypersynchrony of neurons. However, the mechanism by which the normal brain develops epilepsy, which involves a chronic process of structural and morphological changes known as epileptogenesis, is not fully understood. Optogenetics involves the use of genetic engineering and optics to monitor or control nerve cell activity. Compared to classical electrophysiological experiments, the application of optogenetics in epilepsy research has many advantages because it allows selective photic stimulation of cell types and electrical observation without introducing artifacts.

**Keywords**

Epilepsy · Seizure · Animal model · Benign and chronic disease · Ethical issue

## Abbreviations

| | |
|---|---|
| AEDs | Antiepileptic drugs |
| DBS | Deep brain stimulation |
| GABA | Gamma-aminobutyric acid |
| VNS | Vagus nerve stimulation |

S.-I. Osawa (✉) · T. Tominaga
Department of Neurosurgery, Tohoku University Graduate School of Medicine, Sendai, Japan
e-mail: osawa@nsg.med.tohoku.ac.jp

## 39.1 Introduction

Epilepsy is a chronic neurological disorder characterized by recurrent epileptic seizures and associated with neurological, psychological, and cognitive consequences (Fisher et al. 2014). The prevalence of epilepsy in the global population has been estimated at 0.5–1.0% (Engel and Pedley 2008; Brodie et al. 2009).

Epileptic seizures are paroxysmal and self-limited phenomena characterized by the abnormal hypersynchrony of a large population of neurons (Traub and Wong 1982; Jefferys 1990; Fisher et al. 2005). Focal seizures, i.e., seizures that are generated in a certain region of the brain, are usually initiated with pathological causes and propagated to distant areas of the normal cerebral cortex. The hippocampus and surrounding limbic structures are the sites most prone to focal epileptic seizures, especially those that are resistant to medical treatment (Wiebe et al. 2001; Wieser 2004). Seizures are known to arise from various brain areas and they have varying symptoms associated with the areas of initiation and propagation (Brodie et al. 2009; Kwan et al. 2011). Epileptic seizures are habitual in individuals, but the frequency of seizures varies. The etiology of epilepsy can be divided into disorders that arise from genetic predispositions and those that are



H. Yawo et al. (eds.), *Optogenetics*, Advances in Experimental Medicine and Biology 1293,
https://doi.org/10.1007/978-981-15-8763-4_39

acquired. The genetic predisposition for developing seizures can arise from disturbed function of ion channel subunits or the proteins that regulate them (channelopathies) or abnormal metabolic cascades (Chang and Lowenstein 2003; Glasscock et al. 2007).

Current treatment options for epilepsy are AEDs or surgical treatment, which can involve focus resection, disconnection procedures, and neuromodulation therapy. AED treatment can suppress seizures; remission occurs in approximately 70% of patients, but AED treatment is ineffective in around 30% of cases. Surgical treatment is highly effective, but it is applied in only 3–6% of patients (Kwan et al. 2011). The lack of treatment specificity, along with the high percentage of AED nonresponders who as a consequence suffer a lower quality of life, necessitates a more advanced understanding of the fundamental mechanism of epileptogenesis, which is the chronic process of change in the brain that leads to epilepsy. Importantly, treating seizures with AEDs does not generally undo the process of epileptogenesis, and this is evidenced by seizure remittance and relapse rates (Shorvon and Goodridge 2013). This is unsurprising since the mechanism of epileptogenesis likely arises from a series of structural and morphological changes, including acute brain insults and a time course of developments that lead to spontaneous seizures, which are unlikely to be reversed by AEDs. Therefore, epileptogenesis is a central focus of animal studies that aim to elucidate its mechanism and thereby improve treatment outcomes (Chauvette et al. 2015). Specifically, the goal of epileptogenesis research is to elucidate how seizures initially arise in the healthy brain; establishing improved animal models of epileptic seizure is the key to achieving this goal.

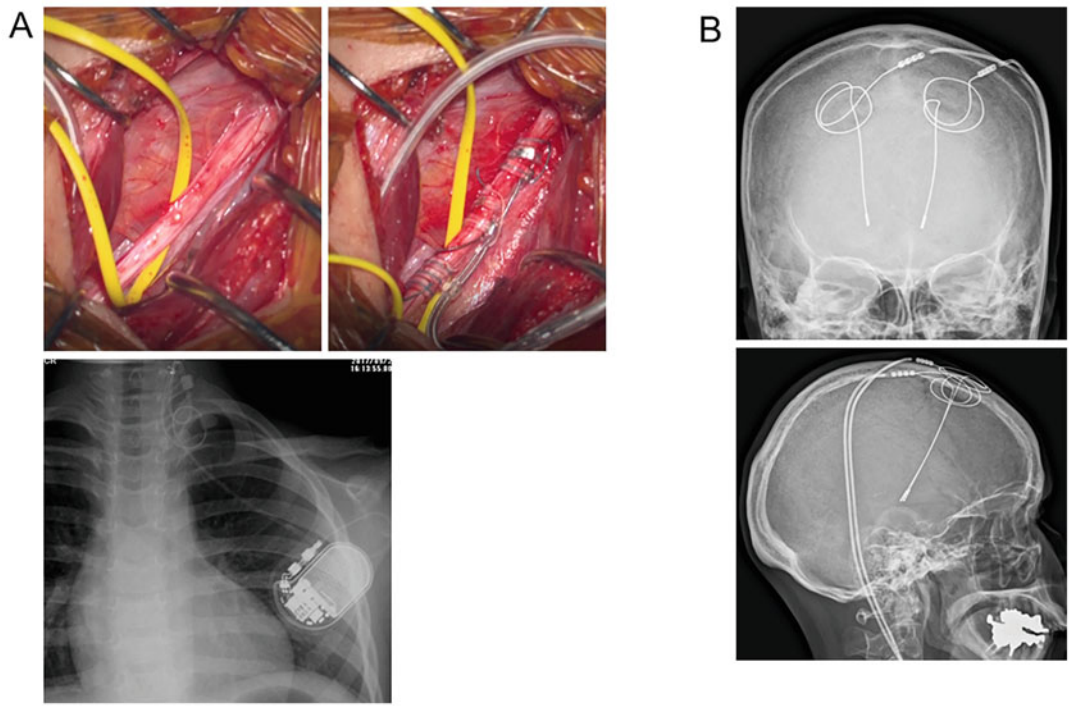


**Fig. 39.1** Neuromodulation therapy for epilepsy. Vagus nerve stimulation therapy. Exposed vagus nerve (top left) and attached electrodes to vagus nerve (top right). Placed vagus nerve stimulation system (bottom). (B) Deep brain stimulation therapy. Placed intracranial electrodes to bilateral anterior thalamic nucleus

## 39.2 Current Studies of Epilepsy Using Optogenetics

Despite numerous studies, the cellular basis of seizure formation remains unknown. Experiments that utilize brain imaging methods, such as functional magnetic resonance imaging, in both clinical patients and animal models can resolve the brain areas that participate in seizures but cannot resolve specific cell populations (Lenkov et al. 2013; Gottschalk et al. 2016). Therefore, to understand the cause of epileptogenesis, research into brain structures must also involve genetic identification and manipulation of activity in specific target cells.

Optogenetics is the use of genetic engineering and optics to monitor or control nerve cell activity. Current studies of epilepsy that employ optogenetics can be classified into two categories. One group of studies focuses on treatment options and the other aims to elucidate the mechanism of epilepsy.

### 39.2.1 Epilepsy Treatment Options

The majority of epilepsy studies that have used optogenetics have done so in an attempt to control seizure activity in epileptic seizure models (Wykes et al. 2012; Wang et al. 2017; Tonnesen et al. 2009). Some studies have shown that spontaneous seizures in the temporal lobe epilepsy model can be controlled by either stimulation of GABAergic cells or direct optogenetic inhibition of pyramidal cells in the hippocampus (Krook-Magnuson et al. 2013; Ladas et al. 2015; Lu et al.

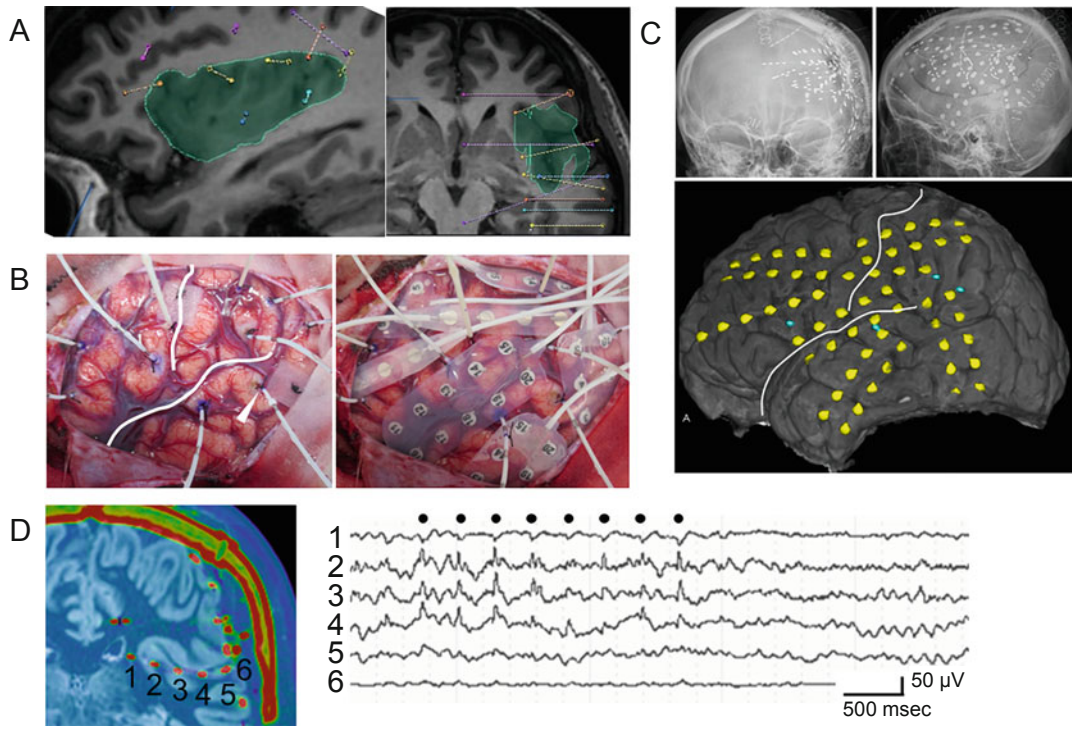


**Fig. 39.2** Intracranial electrode placement and recording electrocorticography. The intractable epilepsy patient suspected with the epileptic foci surrounds insular cortex (A) was placed intracranial depth (B, left) and subdural (B, right) electrodes with craniotomy. The location of the electrodes was confirmed by X-ray (C, top) and 3D-fusioned image of CT and MRI (C, bottom). The epileptic foci suspected from the waveform recorded by depth electrode (D). Note that the epileptiform activities (dotted) were concordant to the location of the electrode, not in white matter but the deep-seated cortex

2016). Inhibition of excitatory pyramidal cells has been shown to stop seizures in hippocampus (Tonnesen et al. 2009; Sukhotinsky et al. 2013; Berglind et al. 2014; Krook-Magnuson et al. 2015) as has inhibition of thalamocortical neurons using halorhodopsin (Paz et al. 2013).

In the clinical field of epilepsy, VNS (Fig. 39.1a), DBS (Fig. 39.1b), and closed-loop stimulation are already available and are being developed further as treatments (Englot et al. 2011; Lehtimäki et al. 2016; Geller et al. 2017; Jobst et al. 2017). Depth electrodes or grid subdural electrodes used in intracranial electroencephalography (Fig. 39.2) can both be exchanged for a light device. However, because electrical stimulation is nonspecific, the mechanisms that underlie or are involved in the effects of deep brain stimulation remain to be fully elucidated. Furthermore, the effects of optogenetic stimulation on epileptic focus in humans are difficult to predict. Epileptic seizure is rarely fatal and rarely causes a permanent deficit in patients (if a deficit does occur, it tends to progress over years or decades); therefore, genetic intervention is difficult to justify in epilepsy patients from the perspective of safety, risk, and ethics (Ramirez-Zamora et al. 2019).

### 39.2.2 Elucidating the Mechanism of Seizure Generation

How epileptic seizures arise and spread in the brain is not fully understood, largely because reproducing seizures that maintain all the features apparent in human epilepsy has proved difficult to achieve. Standard genetic perturbation techniques such as genetic knockdown, overexpression, and mutation are extremely effective for identifying the proteins involved in epilepsy phenotypes, but

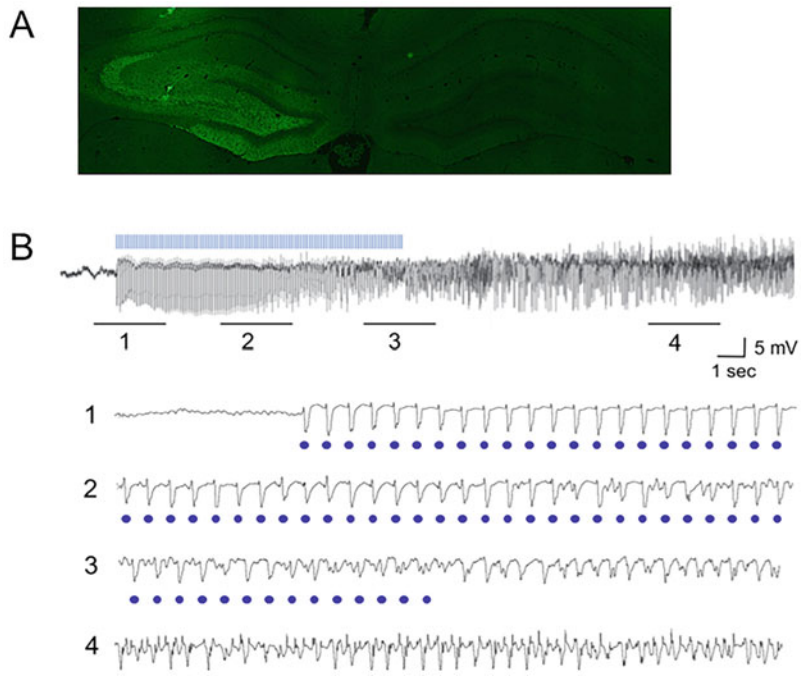


**Fig. 39.3** Electrical activities of seizure-like afterdischarges induced by light. Fluorescent images of ChR2V protein (green) expression in hippocampus of rat transfected by AAV5-ChR2V viral vector (top). Example traces of local field potentials recorded at the site of stimulation. The entire recording of photostimulation (10 Hz, 0.05 duty ratio) and induced afterdischarge is presented at the top. Magnified views below corresponded to the numbers. At the start of stimulation, only evoked potentials followed each photo pulse (1), but gradually spontaneous activities emerged (2) and persisted and changed after the stimulation ended (3,4)

they are less effective for explaining the mechanisms. It is possible that optogenetics can contribute to overcoming these issues given its advantage of artifact-free electrical observation. For example, in one study, the perturbation of hippocampal neurons in rats resulted in the expression of channelrhodopsin-2 in nonspecific neurons by viral vector and induced seizure-like activity with high reproducibility but low mortality (Fig. 39.3a) (Osawa et al. 2013). These optogenetically induced seizures could be studied with artifact-free observation of pathological activity even during the stimulation (Fig. 39.3b). Indeed, given that epilepsy is a disease of electrical abnormality, one of the main advantages of optogenetics in the study of epilepsy is artifact-free electrophysiological observation. In another study, selective intervention in specific types of neurons proved that interneurons play a central role in many types of epilepsy and that different populations of interneurons are linked to the initial seizure activity (Khoshkhoo et al. 2017). These optogenetic methodologies can therefore contribute to our understanding of epilepsy and help to determine new targets for drugs or surgery.

## 39.3 Conclusion

Epilepsy is an ideal candidate for study with optogenetics because of the many advantages associated with optogenetic methods. An optogenetic approach can circumvent many of the shortcomings of classical animal models of epileptic seizures. Indeed, optogenetics may improve the chances of developing new treatment options for epilepsy in years to come.

**Acknowledgments** This work was supported by JSPS KAKENHI Grant Number 18 K08960, JERF TENKAN 18003 and The Clinical Research Promotion Program for Young Investigators of Tohoku University Hospital 2018.

## References

Berglind F, Ledri M, Sorensen AT et al (2014) Optogenetic inhibition of chemically induced hypersynchronized bursting in mice. Neurobiol Dis 65:133–141

Brodie M, Elder AT, Kwan P (2009) Epilepsy in later life. Lancet Neurol 8:1019–1030

Chang BS, Lowenstein DH (2003) Epilepsy. New Engl J Med 349:1257–1266

Chauvette S, Soltani S, Seigneur J et al (2015) In vivo models of cortical acquired epilepsy. J Neurosci Methods 260:185–201

Engel J, Pedley T (2008) Epilepsy: a comprehensive text book. Wolters Kluwer Health, Philadelphia, PA

Englot DJ, Chang EF, Auguste KI (2011) Vagus nerve stimulation for epilepsy: a meta-analysis of efficacy and predictors of response. J Neurosurg 115:1248–1255

Fisher RS, Van Emde Boas W, Blume W et al (2005) Epileptic seizures and epilepsy: definitions proposed by the International League Against Epilepsy (ILAE) and the International Bureau for Epilepsy (IBE). Epilepsia 46:470–472

Fisher RS, Acevedo C, Arzimanoglou A et al (2014) ILAE official report: a practical clinical definition of epilepsy. Epilepsia 55:475–482

Geller EB, Skarpaas TL, Gross RE et al (2017) Brain-responsive neurostimulation in patients with medically intractable mesial temporal lobe epilepsy. Epilepsia 58:994–1004

Glasscock E, Qian J, Yoo JW et al (2007) Masking epilepsy by combining two epilepsy genes. Nat Neurosci 10:1554–1558

Gottschalk S, Fehm TF, Dean-Ben XL et al (2016) Correlation between volumetric oxygenation responses and electrophysiology identifies deep thalamocortical activity during epileptic seizures. Neurophotonics 4:011007

Jefferys JG (1990) Basic mechanisms of focal epilepsies. Exp Physiol 75:127–162

Jobst BC, Kapur R, Barkley GL et al (2017) Brain-responsive neurostimulation in patients with medically intractable seizures arising from eloquent and other neocortical areas. Epilepsia 58:1005–1014

Khoshkhoo S, Vogt D, Sohal VS (2017) Dynamic, cell-type-specific roles for GABAergic interneurons in a mouse model of optogenetically inducible seizures. Neuron 93:291–298

Krook-Magnuson E, Armstrong C, Oijala M et al (2013) On-demand optogenetic control of spontaneous seizures in temporal lobe epilepsy. Nat Commun 4:1376

Krook-Magnuson E, Armstrong C, Bui A et al (2015) In vivo evaluation of the dentate gate theory in epilepsy. J Physiol 593:2379–2388

Kwan P, Schachter SC, Brodie MJ (2011) Drug-resistant epilepsy. New Engl J Med 365:919–926

Ladas TP, Chiang CC, Gonzalez-Reyes LE et al (2015) Seizure reduction through interneuron-mediated entrainment using low frequency optical stimulation. Exp Neurol 269:120–132

Lehtimäki K, Möttönen T, Järventausta K (2016) Outcome based definition of the anterior thalamic deep brain stimulation target in refractory epilepsy. Brain Stimul 9:268–275

Lenkov DN, Volnova AB, Pope AR et al (2013) Advantages and limitations of brain imaging methods in the research of absence epilepsy in humans and animal models. J Neurosci Methods 212:195–202

Lu Y, Zhong C, Wang LL et al (2016) Optogenetic dissection of ictal propagation in the hippocampal-entorhinal cortex structures. Nat Commun 7:10,962

Osawa S, Iwasaki M, Hosaka R et al (2013) Optogenetically induced seizure and the longitudinal hippocampal network dynamics. PLoS One 8:e60928

Paz JT, Davidson TJ, Frechette ES et al (2013) Closed-loop optogenetic control of thalamus as a tool for interrupting seizures after cortical injury. Nat Neurosci 16:64–70

Ramirez-Zamora A, Giordano J, Boyden ES et al (2019) Proceedings of the sixth deep brain stimulation think tank modulation of brain networks and application of advanced neuroimaging, neurophysiology, and optogenetics. Front Neurosci 13:1–21

Shorvon SD, Goodridge DM (2013) Longitudinal cohort studies of the prognosis of epilepsy: contribution of the national general practice study of epilepsy and other studies. Brain 136:3497–3510

Sukhotinsky I, Chan AM, Ahmed OJ et al (2013) Optogenetic delay of status epilepticus onset in an in vivo rodent epilepsy model. PLoS One 8:e62013

Tonnesen J, Sorensen AT, Deisseroth K et al (2009) Optogenetic control of epileptiform activity. Proc Natl Acad Sci U S A 106:12,162–12,167

Traub RD, Wong RK (1982) Cellular mechanism of neuronal synchronization in epilepsy. Science 216:745–747

Wang Y, Xu C, Xu Z et al (2017) Depolarized GABAergic signaling in subicular microcircuits mediates generalized seizure in temporal lobe epilepsy. Neuron 95:92–105

Wiebe S, Blume WT, Girvin JP et al (2001) A randomized, controlled trial of surgery for temporal-lobe epilepsy. New Eng J Med 345:311–318

Wieser H-G (2004) ILAE commission report. Mesial temporal lobe epilepsy with hippocampal sclerosis. Epilepsia 45:695–714

Wykes RC, Heeroma JH, Mantoan L et al (2012) Optogenetic and potassium channel gene therapy in a rodent model of focal neocortical epilepsy. Sci Transl Med 4:161ra152

# Part VI

# Opto-Electro-Nano Technologies for Optogenetics

# Multimode Optical Fibers for Optical Neural Interfaces

40

Massimo De Vittorio and Ferruccio Pisanello

**Abstract**

Although multiphoton microscopy enables optical control and monitoring of neural activity with single cells resolution over a depth of several hundreds of micrometers, the scattering nature of the brain tissue requires implantable optical neural interfaces to access subcortical structures. If micro light-emitting devices (μLEDs) and solid-state waveguides represent important technological advancements for the field, multimodal optical fibers (MMFs) are still the most diffused tool in neuroscience labs to interface with deep regions of the brain. At a first glance, MMFs can be seen as very limited systems. However, new studies and discoveries in optics, photonics, and technological solutions for their application to neuroscience research have enabled applications of MMF where competing technologies fail. In this framework, the chapter starts with a description of optical neural interfaces based on MMF, with specific reference on recent works analyzing the performances of this approach to deliver and collect light from scattering tissue. The discussion then focuses on how peculiar features of MMFs can be exploited to obtain unconventional applications, including brain imaging through a single multimode fiber, multifunctional neural interfaces, and depth-resolved light delivery and functional fluorescence collection.

**Keywords**

Optical brain interfaces · Multimode optical fibers · Fiber photometry · Opto-fMRI · Tapered optical fibers · Neurotechnologies · Multifunctional neural interfaces

## Abbreviations

| | |
|---|---|
| AAV | Adeno-associated virus |
| BOLD | Blood-oxygenation-level-dependent signals |
| CMOS | Complementary metal–oxide semiconductor |
| COC | Cyclic olefin copolymer |
| CPE | Conductive polyethylene |
| DMD | Digital micromirror devices |
| eYFP | Enhanced yellow fluorescent protein |
| FLiP | Fluorescence lifetime photometry |

M. De Vittorio (✉)
Center for Biomolecular Nanotechnologies, Istituto Italiano di Tecnologia, Arnesano (LE), Italy

Dip. di Ingegneria dell'Innovazione, Università del Salento, Lecce, Italy
e-mail: massimo.devittorio@iit.it

F. Pisanello
Center for Biomolecular Nanotechnologies, Istituto Italiano di Tecnologia, Arnesano (LE), Italy
e-mail: ferruccio.pisanello@iit.it



H. Yawo et al. (eds.), *Optogenetics*, Advances in Experimental Medicine and Biology 1293,
https://doi.org/10.1007/978-981-15-8763-4_40

| | |
|---|---|
| fMRI | Functional magnetic resonance imaging |
| FRET | Forster resonance energy transfer |
| GRIN | Gradient refractive index |
| HOT | Holographic optical tweezers |
| LED | Light-emitting device |
| LS | Light sheet |
| MMF | Multimode fiber |
| mPFC | Medial prefrontal cortex |
| NA | Numerical aperture |
| PC | Polycarbonate |
| PKA | Protein kinase A phosphorylation |
| SEM | Scanning electron microscope |
| SLM | Spatial light modulators |
| TCSPC | Time-correlated single-photon counting |
| TDP | Thermal drawing of flexible multifunction probes |
| TF | Tapered fiber |
| TM | Transformation matrix |

## 40.1 Optical Manipulation: Light Delivery in Scattering Tissue with Flat-Cleaved Step-Index MMFs

Multimodal step-index optical fibers are the most common tools to deliver light into the brain for optogenetic control of neural activity in free-moving mice. They can be implanted both acutely or chronically and preparation protocols are available to increase the repeatability of experimental conditions and to improve the comparison between different experiments (Sparta et al. 2011). In their canonical configuration (Fig. 40.1a), fibers are implanted into the brain through a craniotomy and cemented over the skull. A ferrule-to-ferrule joint is then used to connect a patch cord that guides LED or laser light toward the implant. Total internal reflection in the core/cladding structure of the MMF allows light to reach the tissue, and photons are emitted within a specific angular aperture, which depends on the core, cladding, and brain refractive indexes ($n_{core}$, $n_{cladding}$, and $n_{brain}$, respectively) as $\alpha = \sqrt{n_{core}^2 - n_{cladding}^2}/n_{brain}$. However, since the first application of MMFs in behavioral experiments (Adamantidis et al. 2007; Aravanis et al. 2007), it was clearly observed that tissue absorption and scattering strongly influence the geometry and profile intensity of delivered light, which does not follow the emission cone expected in free-space propagation, as shown in the experimental data originally reported by Yizhar et al. (Yizhar et al. 2011) (Fig. 40.1b). Several models have been proposed to predict how light distributes into the brain just below the fiber facet, and some of them are reviewed in Fig. 40.1c–e. Aravanis et al. (2007) used fresh brain tissue slices to estimate how much light is transmitted through a specific tissue depth and found a clear dependence on wavelength (Yizhar et al. 2011). Although longer wavelengths are less attenuated in the wavelength range 473—635 nm, light transmitted deeper than 0.5 mm was found to be well below 40% (Fig. 40.1c). A similar approach was followed by Al-Juboori et al. (2013), who identified a different behavior for different regions of the brain, with the cerebral cortex measured to be the less-attenuating area (Fig. 40.1d). If compared with the ones reported in Yizhar et al. (2011), these data showed a higher attenuation, with transmission estimated to be below 40% already at a distance from the fiber facet of ~100 μm. To model the distribution of light outcoupled into the brain by an MMF, in 2016 Yona et al. (2016) proposed a Monte–Carlo method combined with an analytical approach based on the beam spread function, finding a good agreement with the experiments by Al-Juboori et al. (2013). Although there are some differences between the data found by different groups, all the models agree on the low penetration depth of light emerging from the fiber. This has, in turn, an important direct effect of the experimental design: the volume of the stimulated region is small, and the only ways to increase it are to (i) enlarge the fiber diameter or (ii) to increase the delivered light power.

The obvious consequence of option (i) is a bigger implant cross section, that unavoidably generates conspicuous tissue damage. The effects of the phenomenology related to option (ii) were instead clearly described by Schmid et al. (2016)

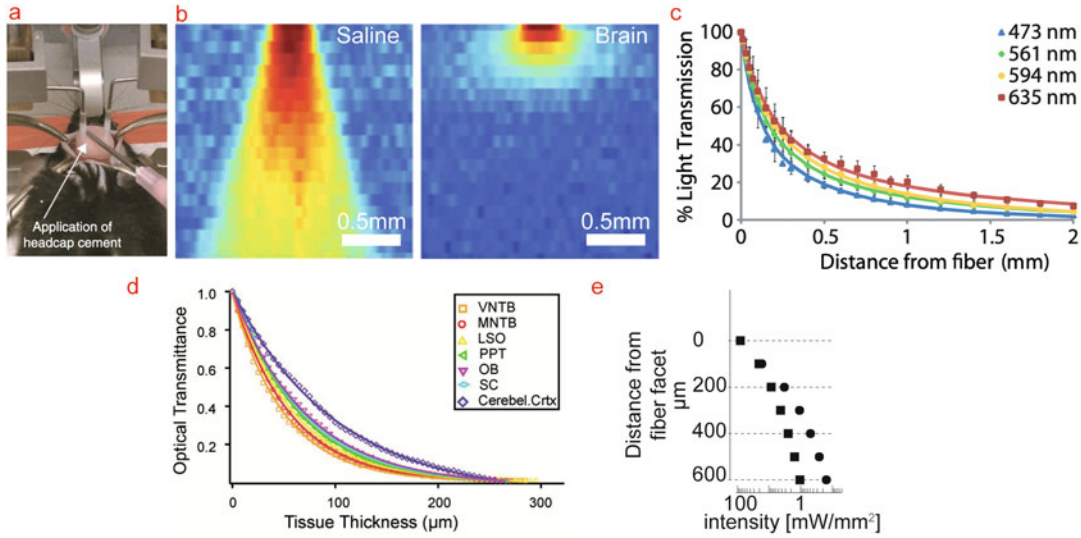


**Fig. 40.1** (**a**) Typical MMF implant in the mouse brain. Image reproduced with permission from Sparta et al. (2011). (**b**) Image of light spread in a saline solution and brain tissue. Reproduced with permission from Yizhar et al. (2011). (**c**) Light transmission through brain tissue as a function of the wavelength. Reproduced with permission from Yizhar et al. (2011). (**d**) Light transmission through brain tissue in different brain areas. Reproduced with permission from Al-Juboori et al. (2013). (**e**) Power density attenuation as a function of the distance from the fiber facet. Squares represent data from Aravanis et al. (2007), while circles are obtained with the spherical model proposed by Schmid et al. (2016)

(Fig. 40.1e), who estimated that to reach a power density in the range of 0.1–1 mW/mm$^2$ at 600 μm below the fiber surface, output power density should be ~100 mW/mm$^2$ at the fiber output. The range 0.1–1 mW/mm$^2$ was obtained by two different models: the highest value was estimated from the original experiments reported in Aravanis et al. (2007), while the value of 0.1 mW/mm$^2$ was found by taking into account a spherical propagation rather than a perfect conical light spread (Schmid et al. 2016). Compared with the average cortical depth of the mouse brain (~1 mm), this results in even higher power density requirement to enlarge the stimulation volume to the entire cortical depth.

The high-power density requirements and the resulting strong light gradient generate light-induced tissue heating, which has direct effects on brain physiology and can significantly influence experimental results (Owen et al. 2019). A detailed assessment of temperature increase was reported in 2015 by Stujneske and coworkers (Stujenske et al. 2015), who developed a Monte-Carlo method to estimate light distribution in scattering tissue and to link the obtained power density map to generated tissue heating. Representative data are reported in Fig. 40.2a, showing how both light and heat are distributed for two different fiber core diameters, and the temperature peak is a function of total delivered power.

Adverse effects of heating have been observed in several experimental designs, including functional magnetic resonance imaging (fMRI), opto/electrophysiology, and behavioral readout (Rungta et al. 2017; Owen et al. 2019). In the case of fMRI imaging, which measures blood-oxygenation-level-dependent signals (BOLD), several groups have measured significant effects of light in naive tissue, either in dead or alive animals (Christie et al. 2013; Rungta et al. 2017). An example of vasodilatation induced by blue light is displayed in Fig. 40.2b, measured by Rungta et al. at a wavelength of 473 nm (Rungta et al. 2017). They have assigned this effect to a decrease of $Ca^{2+}$ in smooth muscle cells and observed that the vasodilation can be measured

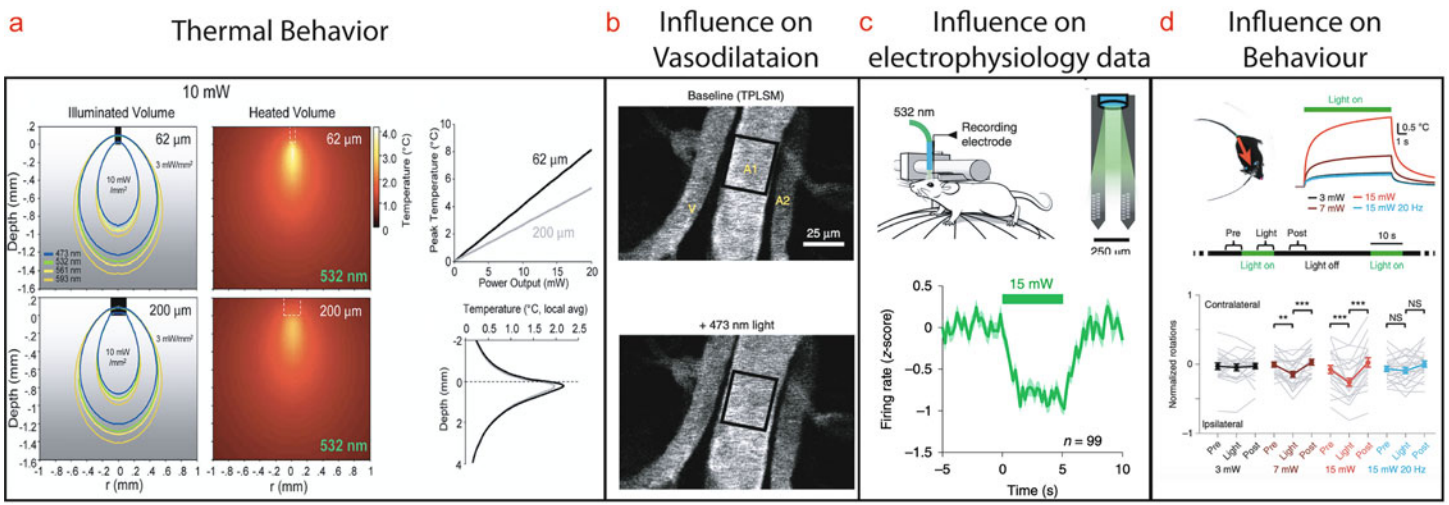


**Fig. 40.2** (**a**) Numerical data on light-induced heat for two fibers with different core diameters. Image reproduced with permission from Stujenske et al. (2015). (**b**) Vasodilatation induced by 473 light. Reproduced with permission from Rungta et al. (2017). (**c**) Reduction in spike rate recorded in the striatum upon illumination with 532 nm light. (**d**) Rotation behavior induced by light in mice at different light-delivery power. (**c**) and (**d**) are reproduced with permission from Owen et al. (2019)

also at very low delivered powers and small temperature gradients (~0.38° with a threshold of appearance of the effect at 0.07 °C). A persisting (but decreasing) vasodilation at longer wavelengths lets the authors suggest a combined mechanism, in which either the engagement of heat-dependent voltage-gated channels or absorption by a specific protein involved in vascular tone regulation can be envisioned. Temperature effects have been observed both in electrophysiology and behavioral experiments in Owen et al. (2019). Owen et al. have indeed observed light-induced suppression of neural activity in the striatum (Fig. 40.2c) as well as light-triggered rotational bias (Fig. 40.2d).

## 40.2 Neural Activity Recording: Functional Fluorescence Collection with Flat-Cleaved Step-Index MMFs

Together with the use of optogenetics to trigger or inhibit action potentials, collection of optical signals from genetically encoded indicators of neural activity is enabling cell-type-specific monitoring of microcircuits. This is mostly enabled by the wide span of molecular tools available in the scientific community, including indicators of $Ca^{2+}$ concentration (Yang et al. 2018) of neurotransmitters release (Patriarchi et al. 2018) and of membrane potential (Piatkevich et al. 2019). Also in this field, one-, two-, and three-photon microscopy can be applied (Ouzounov et al. 2017; Forli et al. 2018; Yildirim et al. 2019), enabling to get a time-resolved representation of optical signals in superficial brain regions with subcellular resolution. However, for reaching subcortical structures implanted devices are required (Warden et al. 2014; Pisanello et al. 2016; Pisanello 2019), and MMFs are again the first option for neuroscientists. The use of MMFs to monitor functional fluorescence, known as *fiber photometry* (Adelsberger et al. 2005), does not provide spatial resolution but presents the main advantages of easy implementation and compactness, allowing a straightforward combination with other readout techniques, including electrophysiology (Sych et al. 2019; Patel et al. 2020), behavioral tracking systems (Muir et al. 2018; Lee et al. 2019b), as well as fMRI monitoring (Desai et al. 2011; Schulz et al. 2012; Schmid et al. 2016).

In a typical fiber photometry experiment, the MMF is implanted into the brain and employed to deliver blue light to excite the optical indicators (Fig. 40.3a,b) (Adelsberger et al. 2005; Lütcke et al. 2010). Fluorescence is generated at higher wavelengths, it is collected by the same fiber and analyzed in terms of fluorescence variation over time ($\Delta F/F$). Therefore, both excitation and collected photons undergo to tissue scattering, requiring a careful combination of light emission and collection fields to estimate the tissue volume that can be probed with this approach. This type of quantitative evaluation can be done by a combined confocal/two-photon laser scanning microscope (Pisanello et al. 2019), which allow to measure both emission and collection fields in the same field of view ($\beta$ and $\eta$ in Fig. 40.3c and d), and to generate the so-called photometry efficiency field ($\rho$) displayed in Fig. 40.3e. $\rho$ is obtained by a pixel-by-pixel multiplication of $\beta$ and $\eta$, and it is a direct measure of collection efficiency of the MMF taking into account also the effectiveness of fluorescence excitation. The possibility to access the three-dimensional photometry efficiency fields enabled to highlight that fiber photometry with MMFs shares some limitations with optogenetic stimulation. The most relevant in this respect is the probed volume, which stays close to fiber facet and can be increased by increasing the fiber core diameter, rather than the numerical aperture of the implant (Pisanello et al. 2019).

On the other hand, one of the main advantages with respect to microscopy is the relatively small size of the optical elements sitting above the mouse head during the experiment. This has enabled the use of multiple fibers to probe neural activity in different brain regions simultaneously (Sych et al. 2019) as well as the combination of fiber photometry with brain-wide monitoring on neural activity with fMRI. The setup of this type of experiments is very similar to the combined MMF/fMRI approach described in the previous

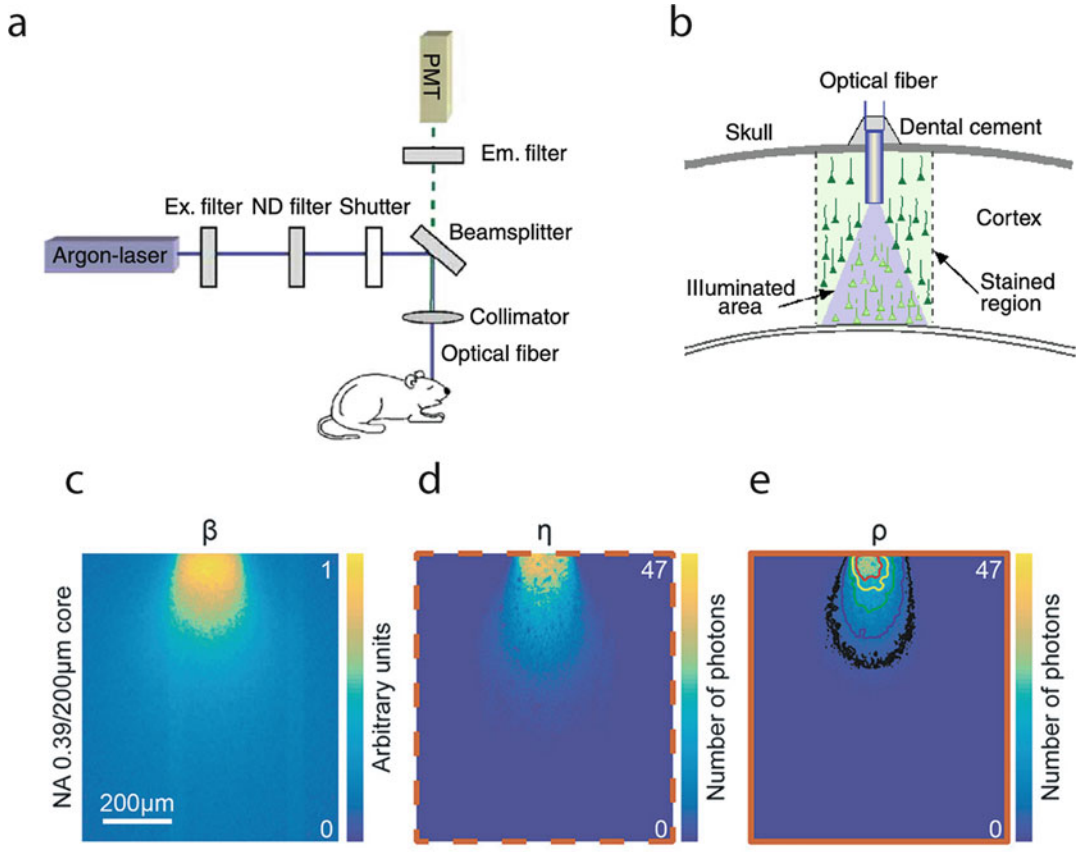


**Fig. 40.3** (**a**) Typical fiber photometry setup. (**b**) Schematic representation of fluorescence excitation and collection. Panels (**a**, **b**) are reproduced with permission from Adelsberger et al. (2005). (**c**–**e**) Representative measurement of light delivery (**c**), light collection (**d**), and photometry efficiency (**e**) fields. Panels (**c**–**e**) are reproduced with permission from Pisanello et al. (2019)

paragraph, and enabled simultaneous recording of BOLD and $Ca^{2+}$ signals, this latter generated by specific cell types (Schulz et al. 2012) (Fig. 40.4a). In 2016, Schmid et al. (2016) moved this approach to a further level by employing in the same experiment optogenetic excitation and Ca2+ fiber photometry in an fMRI magnet, enabling the investigation of the similarities between optogenetic and sensory activation in terms of evoked primary neuronal response and the related BOLD signal, and the number and density of activated cells. With a detailed experimental protocol published in 2018 by Schlegel and coworkers (Schlegel et al. 2018), the combination of fMRI and fiber photometry is now widely recognized as one of most powerful method to study the nature of the BOLD signal as well as for investigating the influence of specific cell types on brain-wide networks.

Fiber photometry with flat-cleaved MMFs also enabled the introduction of important novel concepts in the collection of functional fluorescence from behaving mice. Examples on this respect are the use of time-correlated single-photon counting (TCSPC) and fluorescence lifetime photometry (FLiP), extending the field of application of fiber photometry to the discrimination of different biophysical optical signals (Cui et al. 2013, 2014) and the track of peculiar intracellular biochemical states (Lee et al. 2019a, b). In 2013, Cui et al. (2013, 2014) proposed the TCSPC system displayed in Fig. 40.4b to distinguish

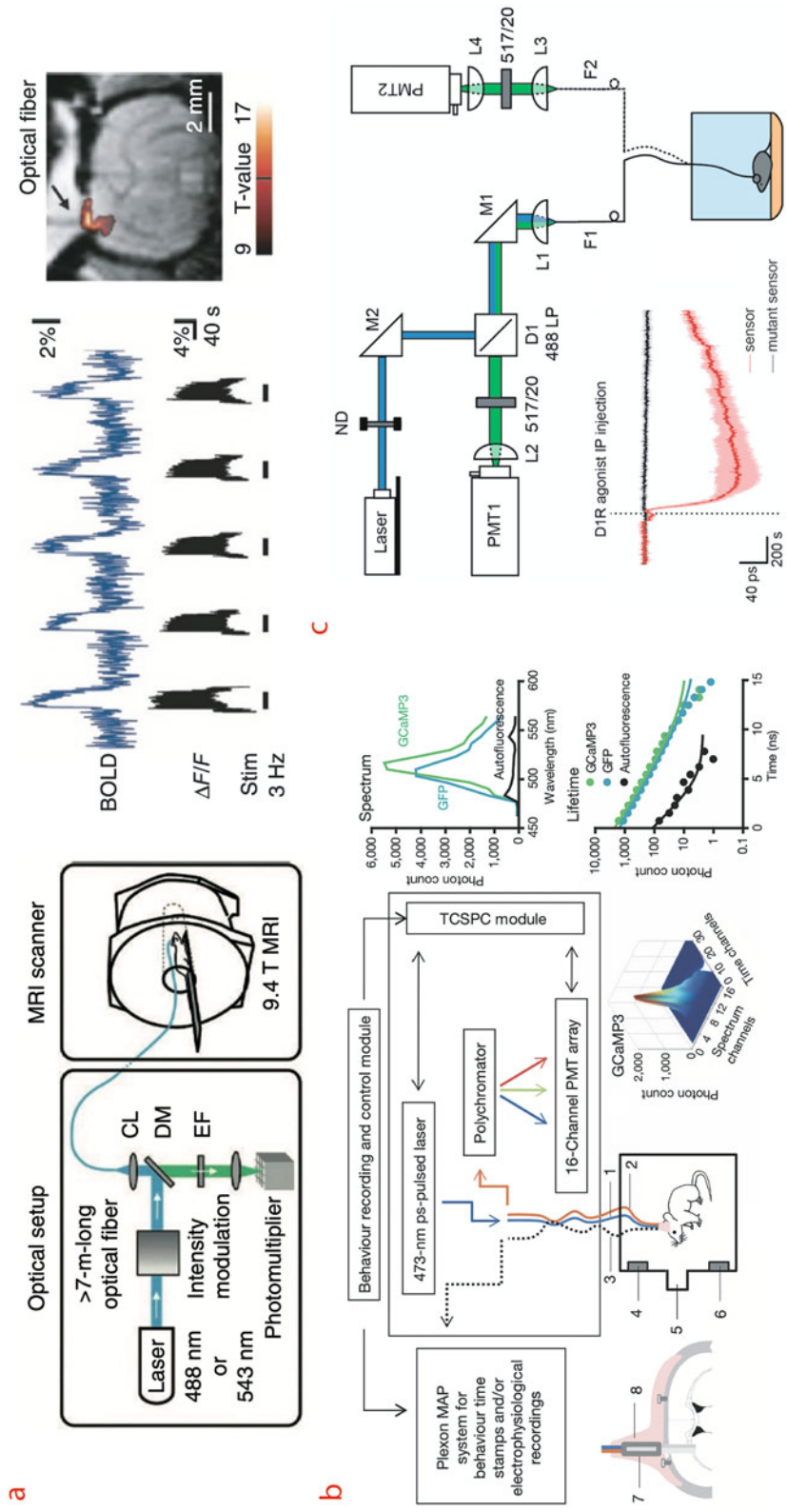


**Fig. 40.4** (**a**) Typical fiber photometry setup combined with fMRI. Panels on the right represent the correlation between BOLD signal and fluorescence variation over time. Reproduced with permission from Schulz et al. (2012). (**b**) Schematic of TCSPC setup with a PMT detector array, enabling measurement of time-resolved spectra of the collected functional fluorescence. Reproduced with permission from Cui et al. (2013). (**c**) Optical setup employed to perform FLiP. The bottom-left inset shows a representative variation of lifetime recorded over several hundreds of seconds. Reproduced with permission from Lee et al. (2019a)

between functional signal and autofluorescence in deep-brain nuclei. It is composed of a pair of optical fibers, one used to deliver a ps-pulsed laser beam for fluorescence excitation, and one employed to collect the emitted photons. Photons guided in this latter fiber were spectrally divided on a 16-channel photomultiplier tube array and analyzed in terms of spectral response, lifetime behavior, and overall intensity, enabling a better discrimination between photons emitted at similar wavelengths but from different physical processes (e.g., tissue autofluorescence or genetically encoded fluorescent indicators). In 2019, Lee et al. (2019a, b) applied a similar system for time-resolved monitoring of the biochemical state of a genetically encoded reporter. In particular, they used an activity reporter based on Forster resonance energy transfer (FRET) that moves the donor and acceptor close together as a consequence of protein kinase A phosphorylation (PKA), reducing the detected lifetime (Fig. 40.4c). This enabled the authors to monitor PKA phosphorylation during reward processing in the striatum, finding that it is enhanced and repressed during reward acquisition in direct and indirect pathway striatal projection neurons, respectively.

## 40.3 Thermally Drawn Multifunction Probes for Neuroscience

Neurotransmission and neurophysiology are multimodal by nature. Implanted probes for optogenetics should possess multiplexing capabilities and carefully engineered properties to enable bidirectional communication and delivering of electrical, optical, and chemical signals to and from neural tissues (Frank et al. 2019). Such neural interfaces will enable simultaneous recording and manipulation of physiological and biochemical signals, delivering of viral vectors, drugs, and optical activity indicators in the same local region of the nervous system. A multitude of factors must be considered when designing neural interfaces, including temporal and spatial resolution, sensitivity, cellular selectivity, low invasiveness, and tissue damage. Despite the recent development of multifunctional neural probes, integration of these multiple functions in a single biocompatible platform remains a challenge.

The pervasive use of commercial silica MMF fibers in optogenetics and fiber photometry studies has stimulated their discrete integration with multielectrode arrays, resulting often in cumbersome assemblies, in ineffective tissue illumination, and damaged brain tissue.

A different approach relies on processing of commercially available optical fibers, exploiting them as a technology platform to integrate multiple functionalities. Zhao et al. added a nanoelectronic coating to the surface of a silica optical fiber endowing it with electrical recording capabilities (Fig. 40.5a) (Zhao et al. 2017), while other approaches to pattern metal deposited on directly on the fiber optics (Pisanello et al. 2015a) rely on focused ion beam milling (Pisanello et al. 2014; Pisano et al. 2018) or direct laser writing (Rizzo et al. 2018).

Another powerful method exploits engineering of preforms before fiber drawing in order to add multimodal functions such as optical, electrical, and microfluidic features. The microfluidic integrated capability was first reported in a pioneering work by Lechasseur et al. (2011), who showed simultaneous electrophysiological recording and optical detection of individual neurons deep in brain tissue exploiting the new possibilities opened by fluorescence labeling techniques. They developed dual-core fiber optics-based microprobes with tips $<10$ μm, with an optical core to locally excite and collect fluorescence, and an electrolyte-filled hollow core for extracellular single-unit electrophysiology and demonstrated combined electrical and optical detection of single fluorescent neurons in rats and mice (LeChasseur et al. 2011).

Custom fiber thermal drawing of flexible multifunction probes (TDP) has emerged as a simple approach to integrate multiple functional features within microscale probes with materials with different mechanical properties (Fig. 40.5b). In addition to optical and electrical properties, probes with elastic moduli ranging from megapascals to a few gigapascals and integrated microfluidics for drug, markers, and viral delivery in a diameter

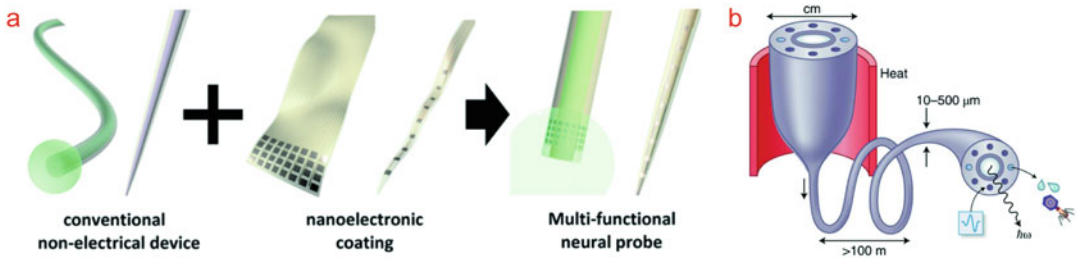


**Fig. 40.5** (**a**) Schematics of the nanoelectronics coated multifunctional probe. NEC devices were fabricated separately and attached onto the surface of conventional optical fibers and glass pipettes. Reproduced with permission from Zhao et al. (2017). (**b**) Thermal drawing of multimaterial macroscale models, preforms, into fibers comprising polymer waveguides, conductive composite or metallic electrodes, and microfluidic channels. Reproduced with permission from Frank et al. (2019)

smaller than 500 μm have been demonstrated (Canales et al. 2015, 2018). TDP starts with the assembly of a macroscopic preform that incorporates the materials and features of the desired final microscopic probe. By the application of heat and tension, the preform is drawn into a fiber, maintaining the macroscopic cross-sectional geometry but scaling down the cross section by 1−2 orders of magnitude. At the same time, the length of the final fiber increases by 2−4 orders of magnitude. Although traditionally applied to glasses to fabricate optical telecommunications fibers, the thermal drawing process (TDP) is compatible with a wide range of geometries and materials (Abouraddy et al. 2007). However, the choice of materials, their assembling in a preform, and the thermal drawing process must be carefully engineered. Materials must exhibit similar viscosities at the drawing temperature and similar glass transition ($T_g$) and melting ($T_m$) temperatures.

Canales et al. applied this TPD approach to produce polymeric fibers with electrophysiological recording, optical stimulation, and drug delivery capabilities (Canales et al. 2015). Park et al. (2017) developed a device composed of an optical waveguide, six electrodes, and two microfluidic channels produced via thermal fiber drawing all within the dimensions of silica fibers that are routinely used in optogenetic experiments (diameter <200 μm). They developed a custom conductive polymer composite to reduce electrode dimensions and impedance, allowing for integration of higher density electrophysiology (six electrodes). To improve electrode conductivity, conductive polyethylene (CPE) was mixed with 5% in weight of graphite, with 4.1-fold reduction of the sheet resistance of the composite. While a recent work indicates the potential of indium as a suitable electrode material (Davey et al. 2015), conductive carbon composites similarly offer a chemically inert and inexpensive platform for integration of recording capabilities into PC-based probes. High-resolution recordings and arrays of up to 36 electrodes have also been demonstrated in TDP technology (Canales et al. 2015).

For the waveguiding features, polycarbonate (PC, refractive index $n = 1.586$, glass transition temperature $T_g = 150\ ^\circ C$) and cyclic olefin copolymer (COC, refractive index $n = 1.53$, $T_g = 158\ ^\circ C$) were employed as core and cladding, respectively, with <1.5 dB/cm transmission loss in the visible spectral range and low autofluorescence.

A careful wrapping of COC cladding sheet around the preform allowed to produce hollow channels for fluids delivery. The preform was then heated and stretched into ~100-m-long fiber with preform feature dimensions reduced 50~200-fold (Fig. 40.5). By adjusting the drawing parameters, the diameter of the waveguide was tuned between 50 and 80 μm, whereas the sizes of electrodes and the microfluidic channels diameter were in the range of 20–30 μm. Microfluidic channels were used to deliver an adeno-associated

virus (AAV, serotype 5) carrying the gene for ChR2 fused to the enhanced yellow fluorescent protein (eYFP). Robust ChR2 expression in the mPFC was observed 2 weeks after the injection in the medial prefrontal cortex (mPFC) of wild-type (WT) mice with expression compatible with the injection volume (Park et al. 2017).

The integration of multiple functions allowed dynamic investigation of opsin expression across multiple brain regions and enabled combining the local optical stimulation with local pharmacological delivery in behaving animals.

Biocompatibility of the probes, enhanced by flexibility and miniature footprint, was demonstrated in stable long-term recordings of isolated single-neuron action potentials, with no significant decrease in signal to noise ratio at 3 months after implantation. When fabricated solely from polymers and polymer composites, the mechanical mismatch between stiff implanted devices (1–100 GPa) and the soft brain tissue (kilo- to megapascal) is minimized, as well as tissue damage associated with relative motion between brain and the probes, relevant when probes are fixed to the skull. Application of fiber drawing to elastomers made it possible to demonstrate stretchable probes suitable for chronic recording and optogenetic neuromodulation in the rodent spinal cord (Lu et al. 2017).

By integrating dense neural recordings with the delivery of transgenes and optical stimuli in a miniature footprint, TDP devices promise a great potential for studies of neural projections, electrophysiological dynamics, and opsin expressions in the same local deep brain region.

One of the current limits in TDP technology is that development of multiple functional interfaces along the fiber length is not possible. However, the small footprint of these devices allows their implantation into several brain regions, enabling optical control of behavior and electrophysiological readout of the projection dynamics.

## 40.4 Multimode Fibers (MMF) Endoscopes Imaging

Besides being able to collect photonic signals from endogenous or exogenous fluorescent indicators of neural activity and neurotransmitters concentration, real-time imaging in the deep brain allows to study the spatiotemporal organization of neural activity. Real-time neural dynamics in freely moving animals, fundamental to elucidating brain function, is only possible with miniaturized probes and endoscopic microscopes (Aharoni and Hoogland 2019). These headmountable microscopes exploit LEDs and Gradient Refractive Index (GRIN) microlenses to relay optical images from deep brain regions to compact CMOS imaging sensors, making it possible to visualize neural activity during behavioral tasks in animal models.

At their early stage, optical aberrations and low NA values of GRIN lenses prevented resolution comparable to conventional microscopy. Barretto et al. demonstrated for the first time near diffraction limited endoscopic imaging by coupling 1.0-mm-diameter plano-convex lens made of LaSFN9 glass with a 1.0-mm-diameter GRIN lens (0.45 NA), achieving by a micro-objective with NA~0.85 two-photon imaging of dendritic spines on hippocampal neurons and optical imaging of neuromuscular junctions in live mice (Barretto et al. 2009).

While a large field of view (~1 mm) can be useful, the implantable thickness and rigidity of grin lenses can be a strongly limiting factor in many behavioral experiments.

In recent years, it was demonstrated by Plöschner et al. (2015b) that commercial multimode fibers (MMFs) can operate as extremely precise optical components. As diffusers and scattering media, MMFs deliver signals in the form of apparently random speckled patterns, but, instead, they feature very faithful cylindrical symmetry and can deliver coherent light. This has been applied to collect high-quality images in vivo in behaving animals through both straight or even deformed segments of multimode fibers with length of tens of centimeters and resolution comparable to confocal microscopy (Vasquez-Lopez et al. 2018) (Fig. 40.6).

Deterministic light propagation within MMFs was previously applied to digital holography (Di Leonardo and Bianchi 2011) by empirical measurement of the transformation matrix (TM) developed in studies of light propagation

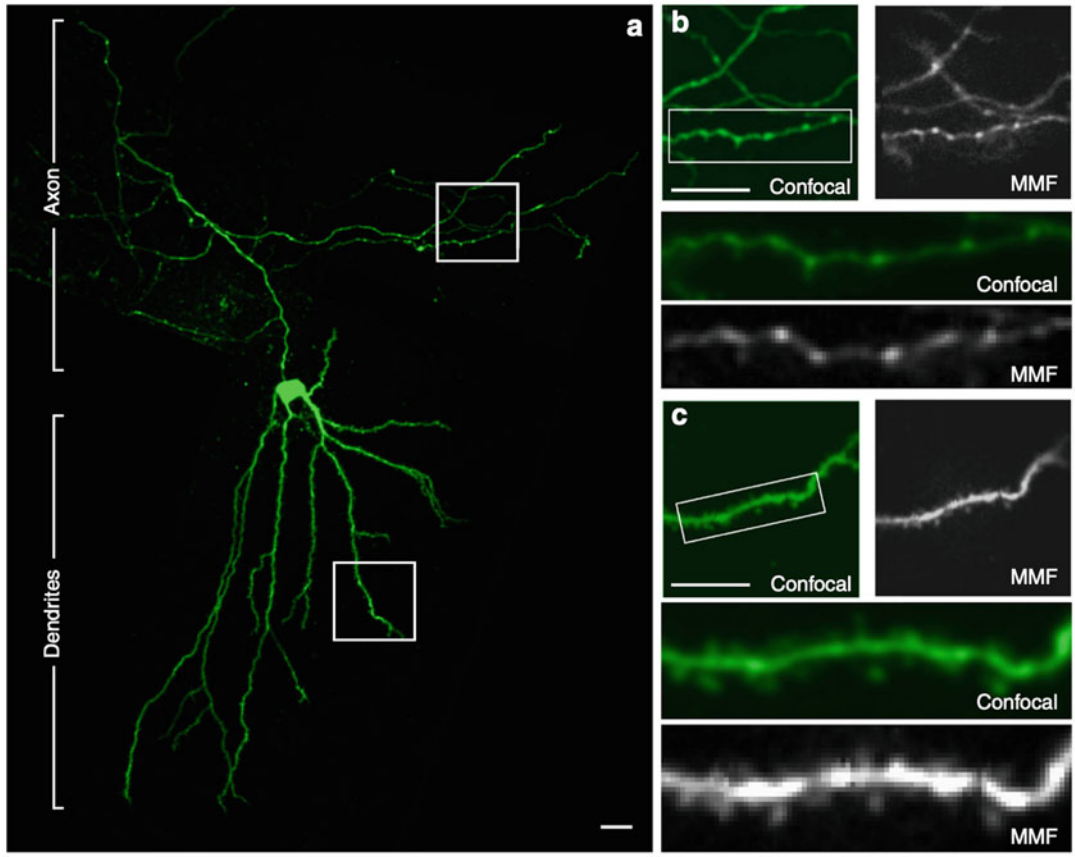


**Fig. 40.6** MMF imaging of ex vivo tissue reveals dendritic spines and axonal boutons. (**a**) Confocal image of a hippocampal neuron in a rat brain slice. (**b**, **c**) Structural images through the MMF (**b**, **c** gray images) and confocal microscopy (**b**, **c** green images) of the same regions of the neuron in (**a**). Axonal boutons (**b**) and dendritic spines (**c**) were clearly identified using each imaging modality. Scale bars: 20 μm. Reproduced with permission from Vasquez-Lopez et al. (2018)

through highly turbid media. The most critical limitation of this technology was that any bending or looping of the fiber results in changes of its TM, heavily affecting the image quality and requiring continuous and time-consuming measurement of the TM in all measurement conditions. It was therefore necessary the access to the distal end of the fiber, a major bottleneck of the technology. M. Plöschner et al. (2015b) showed that the TM can be obtained by numerical modeling, taking also into account polarization coupling and nonideal step-index fiber structure. They confirmed the existence of propagation-invariant modes within the fiber, but also predicted their output phases very accurately which resulted to be mandatory for imaging applications. By their study, Plöschner et al. could predict the behavior of even significantly bent fibers, allowing computation of their TM based purely on the observation of the fiber geometry, and shown that imaging can be achieved without experimental TM acquisition, in both straight and deformed fibers, at an arbitrary distance behind the distal fiber facet (Plöschner et al. 2015b).

The predictability in imaging of multimode fibers has enabled a variety of applications in fiber-based endoscopes, with great performance

both in terms of resolution and instrument footprint which is about an order of magnitude smaller.

MM fibers high-resolution observations of neuronal activity in vivo inside deep brain areas were shown by holographic control of light propagation in the deep brain (Turtaev et al. 2018). Turtaev et al. designed a compact and high-speed system for fluorescent imaging at the tip of a fiber, achieving a resolution of $1.18 \pm 0.04$ μm across a 50-μm field of view, yielding 7-kp images at a rate of 3.5 frames/s. Laser scanning microscopy utilized in this study relies on the formation of diffraction-limited foci behind the fiber, scanned by digital micromirror devices (DMDs), and combined with image reconstruction from fluorescence signals that are collected and guided backward.

The method was applied to in vivo observations of cell bodies and processes of inhibitory neurons within deep layers of the visual cortex and hippocampus of anesthetized mice.

Fluorescence microscopy based on digital holography and delivery of light-sheets through a multimode optical fiber was also demonstrated (Plöschner et al. 2015a). Light-sheet (LS) fluorescence microscopy has proven itself as a fast, high-contrast sectioning of the biological tissues with a minimum level of phototoxicity from sample irradiance, but, because of light scattering, the wavefront of light rapidly worsen when going deeper in tissues. Plöschner et al. used holographic wavefront engineering to pre-shape the coherent laser signals coupled to the proximal end of an MMF in order to obtain the LS at the distal end of the fiber. By taking advantage of the cylindrical symmetry of the fiber, they generated both Bessel and structured Bessel beam plane illumination, enabling an extended uniform illumination of the specimen, a significant extension of the field of view and higher resolution (~1 μm) then with standard Gaussian beam. The quality of imaging was assessed on fluorescent beads fixed in agarose gel and on the regenerating operculum prongs of *Spirobranchus lamarcki*.

Imaging and light manipulation properties of high-numerical-aperture MMF were also exploited for holographic optical tweezers (HOT), producing multiple three-dimensional (3D) traps, and enabling a new method of manipulation through probes comparable to the size of a single cell (Leite et al. 2018). Geometries used in HOT currently rely on bulk optics, and their exploitation in vivo is compromised by the optically turbid nature of tissues. Leite et al. demonstrated real-time manipulation of 3D arrangements of micro-objects as well as manipulation inside otherwise inaccessible cavities. This was achieved by a new class of all-solid step-index MMFs with NA $> 0.8$, necessary for stable optical confinement of particles, with a novel holographic algorithms that, by taking the mode-dependent power loss into account, enable the available NA to be harnessed almost completely. Particle trapping and holographic manipulation with nanometric resolution were achieved in fibers with lengths exceeding 100 mm (Fig. 40.7a,b).

Compared to GRIN microlenses and microobjectives, the volume of tissue lesion with MM fibers is reduced by about 100-fold, while preserving diffraction-limited imaging performance (Fig. 40.7c). Vasquez-Lopez et al. demonstrated high-resolution fluorescence imaging of subcellular neuronal structures, dendrites, and synaptic specializations, in deep-brain regions of living mice, as well as monitored stimulus-driven functional Ca2+ responses (Vasquez-Lopez et al. 2018) with the best trade-off between high-resolution imaging and tissue damage (Fig. 40.7d).

When multimode fibers are used for nonlinear microscopy, the bandwidth of the imaging system limits the ability to focus light from broadband pulsed lasers as well as the possibility of wavelength tuning during the imaging which would be useful with multiple fluorescent indicators or multi-opsin optogenetic stimulation. Pikálek et al. demonstrated that the bandwidth is limited by the dispersion of the off-axis hologram displayed on the spatial light modulators (SLM), which can be corrected by a careful selection of the fiber and by exploiting a prism pulse

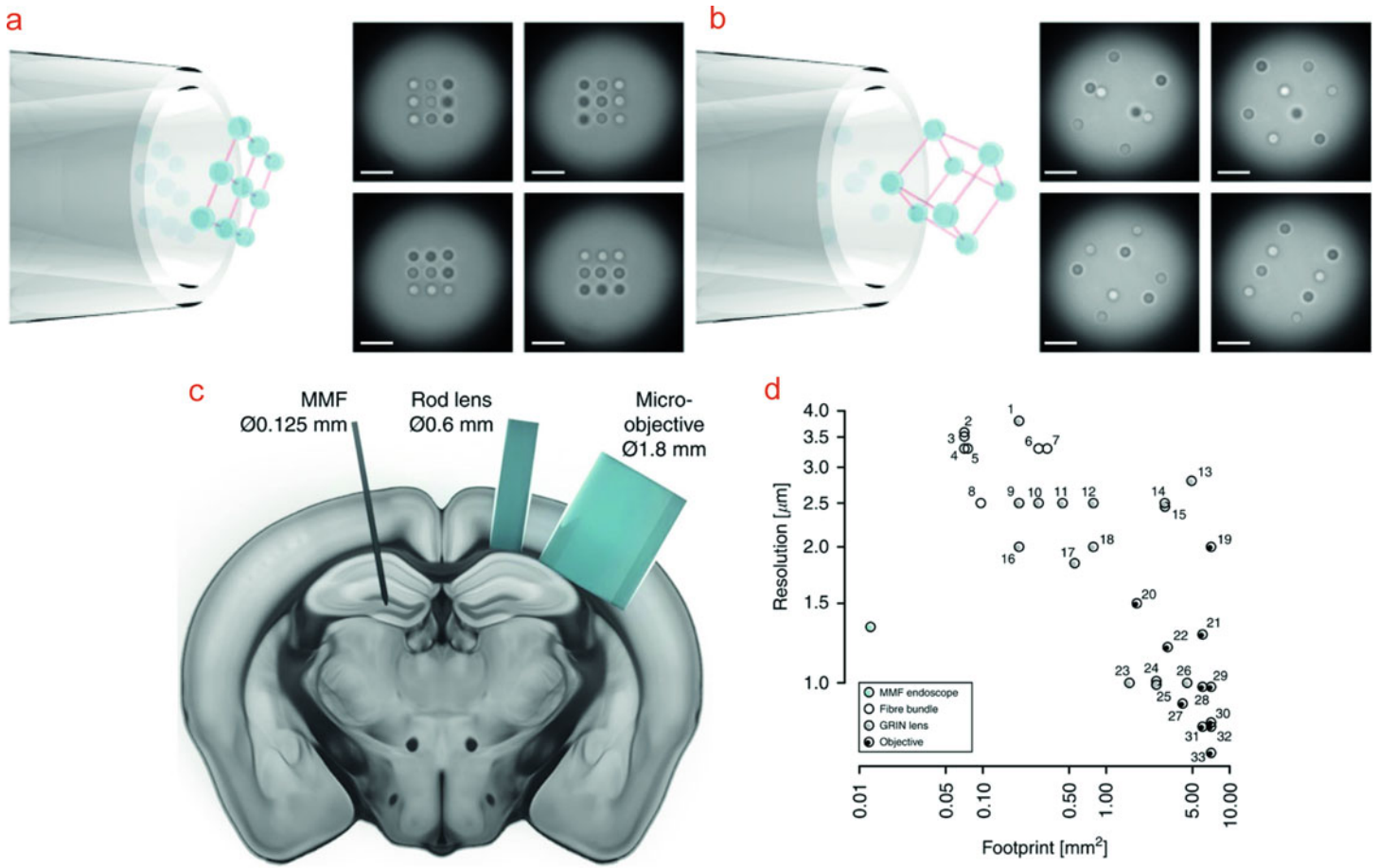


**Fig. 40.7** High-numerical aperture MMF exploited for holographic optical tweezers (HOT): trapping of nine particles in a square-grid arrangement (**a**) and eight particles forming a rotating 3D cube (**b**) Reproduced with permission from Ref. Leite et al. (2018). (**c**) Comparison of common endoscopic probes and an MMF. Reproduced with permission from Turtaev et al. (2018). (**d**) Relationship between image resolution and instrument footprint for in vivo imaging modalities. Reproduced with permission from Vasquez-Lopez et al. (2018)

compressor for material dispersion compensation achieving multiphoton imaging with a fiber endoscope (Pikálek et al. 2019).

## 40.5 Tapered Optical Fibers: Adding Depth Resolution

To overcome the limitations described in Paragraph 1, an alternative to flat-cleaved MMFs are tapered optical fibers (TF), recently shown to enable both wide-volume and depth-selective optical neural interfaces (Pisanello et al. 2014, 2017; Pisano et al. 2019). These devices will be the subject of this section, with particular reference to their optical properties and their exploitation in vivo.

### 40.5.1 Wide-Volume and Depth-Resolved Optical Control of Neural Activity

A schematic representation of a TF together with the behavior of guided modes along the tapered section is displayed in Fig. 40.8a: a step-index core-cladding MMF is tapered for a few millimeters and ends with a sub-micrometer tip.

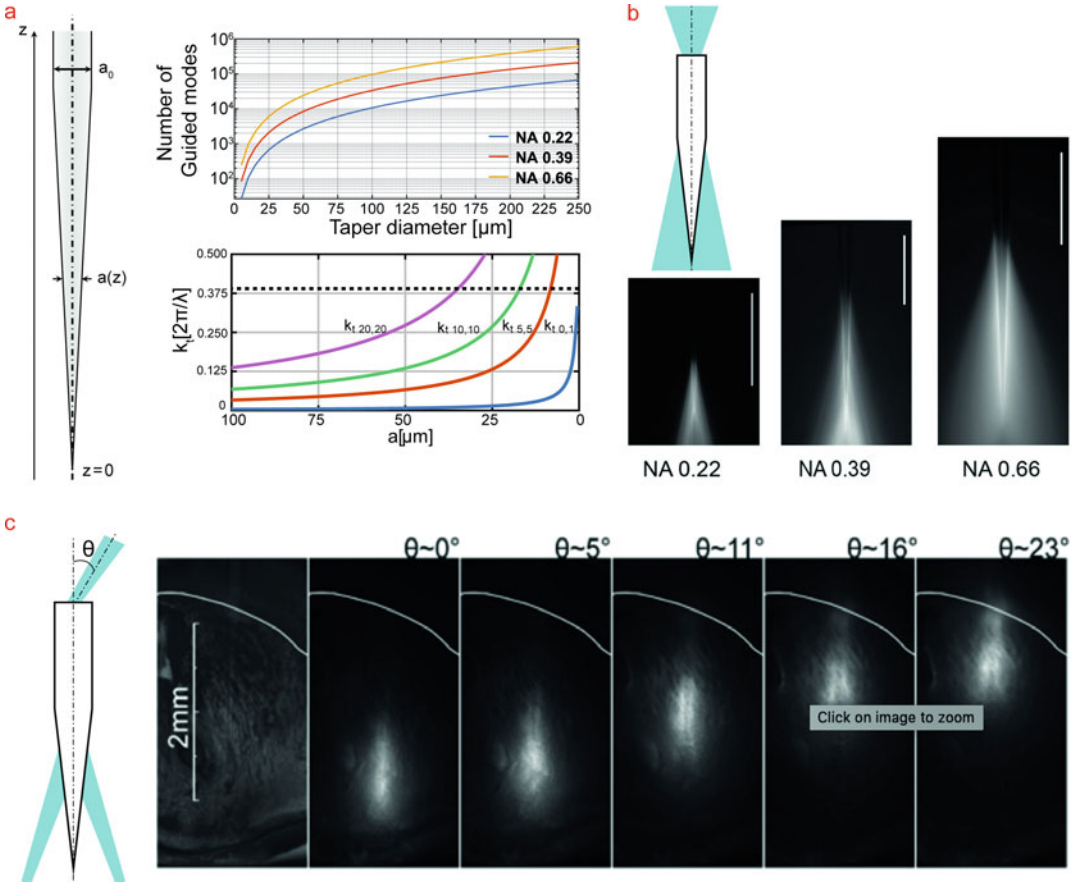


**Fig. 40.8** (**a**) Schematic representation of a tapered optical fiber and modes number (top) and $k_t$ (bottom) evolution along the narrowing waveguide. (**b**) Example of full-NA injection and resulting light-delivery geometry for TFs with different numerical apertures. Panels (**a**) and (**b**) are reproduced with permission from Pisanello et al. (2018). (**c**) Angle-selective light injection and related light delivery geometry in the striatum of a fluorescently stained coronal mouse brain slice. Reproduced with permission from Pisanello et al. (2017)

This linear and smooth variation of the waveguide's diameter is the optical elements generating the main optical feature of the device: while the waveguide narrows, the number of guided modes decreases, and guided modes not supported by the different tapered sections are irradiated. This happens because the transversal component of the wavevector of each mode propagating into the taper increases as the taper diameter decreases, until it reaches the value of the free-space wavevector $k_0$. When $k_t > k_0$, the mode is irradiated in the surrounding environment (Pisanello et al. 2018).

A direct consequence of this phenomenology is displayed in Fig. 40.8b: if light is injected into the fiber, filling the entire acceptance angle with a focusing Gaussian beam, almost all guided modes in the straight portion of the fiber are excited. While the taper narrows, guided modes are gradually emitted in the environment, generating an entire segment of the taper emitting light. Changing the taper angle and the fiber NA, the length of the emitting segment can be tailored from a few hundreds of micrometers to a few millimeters, matching the depth of functional structures of brain of different animal models (Pisanello et al. 2017, 2018). This approach was employed in 2017 in two different works (Acker et al. 2016; Pisanello et al. 2017) to extend light-triggered brain volumes in either the mouse and the nonhuman primate brain. In Pisanello et al. (2017), the authors targeted optical control of neural activity in the motor cortex in a mice expressing ChR2 in inhibitory interneurons, looking for optically silenced neural activity from pyramidal cells. As a direct consequence of the higher number cells engaged with respect to MMFs, TFs showed an inhibition light power threshold about five times lower. TFs were also successfully applied in nonhuman primates and combined to red-shifted opsins allowed Acker et al. (2016) to reach a stimulation volume of ~10 $mm^3$.

The mode selectivity of the fiber taper also enables site-selective optogenetic control of neural activity. This was achieved by injecting light into the fiber distal end facet with an angle $\theta$ (Fig. 40.8c). This enabled only a subset of guided modes to be injected in the straight portion waveguide, whose average $k_t$ value increases as the input angle $\theta$ increases. The result is that the emitting taper segment shortens to a few hundreds of micrometers, and it can be moved along the taper by acting on $\theta$ (Fig. 40.8c). One of the main features of this approach is that it can be employed for depth-selective control of neural activity in free-moving mice, by virtue of a limited influence of modal mixing induced by patch-fiber movements on the light-delivery geometry. The method was exploited to deliver light in either dorsal or ventral striatum while tracking mouse locomotion and posture, showing that excitation of indirect pathway striatal projection neurons differently modulate postural dynamic syllables during animal movements (Pisanello et al. 2017).

### 40.5.2 Wide-Volume or Depth-Resolved Fiber Photometry

The mode-selectivity properties of the fiber taper can be also exploited to obtain collection of functional fluorescence from either an extended volume or to subsample the region of interest. By virtue of the varying $k_t$ along the taper, guided modes can be gradually populated, therefore allowing to collect light from a length that extends up to ~2 mm along the narrowing waveguide. This effect was experimentally shown in Pisano et al. (2019), by using a two-photon laser scanning system to excite point source fluorescence around the TF while monitoring the collected light with photomultiplier tube (Fig. 40.9a). A direct measurement of TF's light collection field was therefore possible, whose extension is compared with the one of a flat-cleaved MMFs in Fig. 40.9b. The difference is even more evident when the same method is used to measure the light collection behavior in scattering tissue: TFs can collect light from the entire extent of cerebral cortex in the mouse brain, while standard fibers are limited to a few hundreds of micrometers below the fiber facet (Fig. 40.9b).

Importantly, by exploiting site-selective light delivery through the taper, fluorescence can be

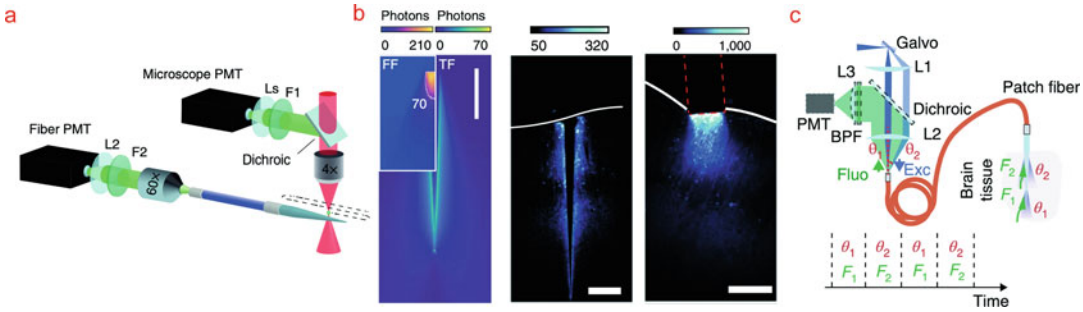


**Fig. 40.9** (**a**) The two-photon microscopy system employed to measure collection fields of tapered optical fibers. (**b**) Comparison between the light collection fields of a flat-cleaved and a tapered fiber in quasi-transparent solution (left, scale bar 500 μm) and in the cortex of coronal mouse brain slices (right, scale bars 250 μm). (**c**) Optical path employed for site-selective photometry. Reproduced with permission from Pisano et al. (2019)

generated and collected with depth resolution. This can be obtained with the optical setup displayed in Fig. 40.9c: a galvanometric mirror is used to inject laser light with an angle into the fiber, generating light delivery at specific sections of the taper. Delivered light generates fluorescence only in that specific site, that is then collected back from the taper in that specific region (Pisano et al. 2019). This approach was used in the striatum of a free-moving mice operating a reward-driven task to monitor dopamine release in the striatum, a region of the brain involved in motor control. It was observed, for the first time, that although both dorsal and ventral striatum dopamine transients track locomotion, only those in ventral striatum respond strongly to rewards (Pisano et al. 2019).

### 40.5.3 Microstructuring Tapered Optical Fibers: Few Cells Recordings in Implantable Optical Neural Interfaces

In both depth-resolved light delivery and fiber photometry, the optically active segment of the taper can be moved by changing the input angle of light in the fiber, but it cannot be smaller than a few hundreds of micrometers (Pisanello et al. 2018). This is due to unavoidable modal mixing during light propagation, making it difficult to target small cellular groups. A suitable approach to overcome this limitation relies on metallizing the tapered fiber and then removing the coating at specific sections of the waveguide by using either focused ion beam milling (Pisanello et al. 2014, 2015b; Pisano et al. 2018) or direct laser writing (Rizzo et al. 2018) (Fig. 40.10a). In both cases, the taper can be rotated while Ga2+ ions or ultraviolet photons mill the metal layer, generating customizable light-delivery patterns. Examples are displayed in the scanning electron microscope (SEM) images in Fig. 40.10a, showing: long slot line opened along the taper, ring-shaped windows for 360°-symmetric emission, and multiple optical excitation sites realized along 2 mm taper. The same microstructuring approach can be used to structure the light collection field from tapered fibers. This is shown in the two examples in Fig. 40.10b, displaying a device that collets light only from half of the waveguide and a TFs whose light collection field was restricted to a few cells by opening a 45 μm × 45 μm optical window.

## 40.6 Conclusions

Brain interfaces are more and more exploiting the optical domain for both manipulating and recording neural activity. Optical probes for accessing subcortical brain regions need careful design in order to achieve low invasiveness, controlled light delivery, and efficient light collection. The integration in optical probes of additional

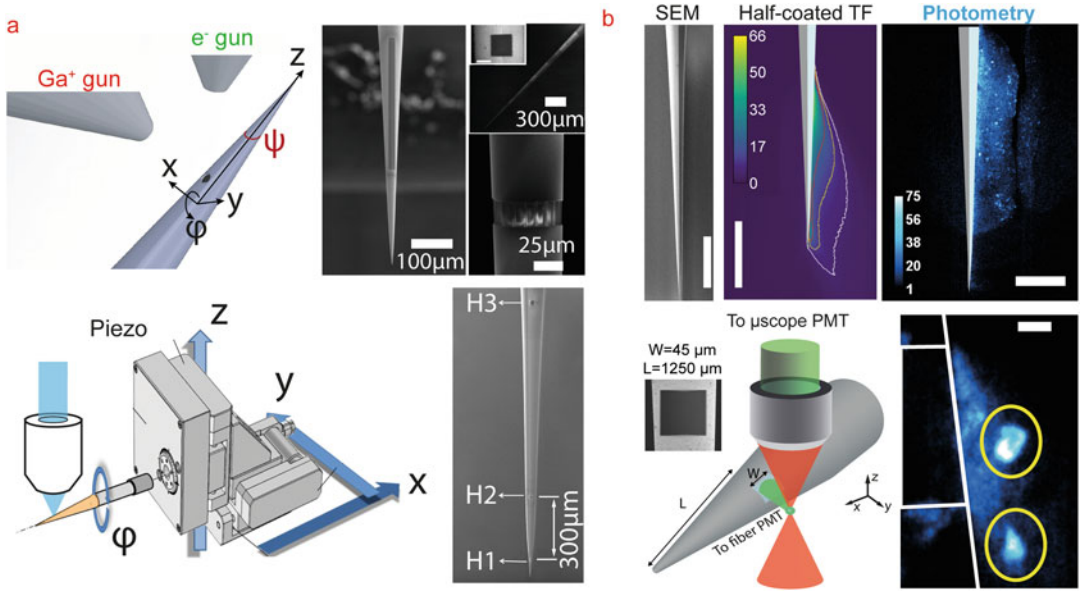


**Fig. 40.10** (**a**) Focused ion beam milling (top) and direct laser writing (bottom) approaches to structure the fiber taper. The inset shows representative results of the fabrication process. Top panels are reproduced with permission from Pisano et al. (2018), bottom panels are reproduced with permission from Rizzo et al. (2018). (**b**) Representative light collection fields from microstructures tapered optical fibers. Reproduced with permission from Pisano et al. (2019)

functions such as imaging, electrophysiology, drug delivery is being enabling recording and manipulation of physiological and biochemical signals with temporal and spatial resolution. This chapter has reported how multimodal optical fibers represent a powerful technological platform to produce multifunction brain probes with all the above-mentioned properties and high performances. The possibility to correlate signals of different nature across different brain regions is indeed a long-standing aim for the neuroscience community, as it would enable new studies on functional connectivity and a better link of neural activity to brain pathologies. Although the number of functionalities integrated in a single device is still limited, advances in micro and nanofabrication for optics and photonics are providing a set of methods to expand the capabilities of the single device and to extend the number of neurons that can be monitored or controlled simultaneously. On this respect, MMFs can exploit an intrinsically high-throughput nature by virtue of modal differentiation and can represent a key paradigm for the next generation of optical neural interfaces.

## References

Abouraddy AF, Bayindir M, Benoit G et al (2007) Towards multimaterial multifunctional fibres that see, hear, sense and communicate. Nat Mater 6:336–347. https://doi.org/10.1038/nmat1889

Acker L, Pino EN, Boyden ES, Desimone R (2016) FEF inactivation with improved optogenetic methods. Proc Natl Acad Sci U S A 113:E7297–E7306. https://doi.org/10.1073/pnas.1610784113

Adamantidis AR, Zhang F, Aravanis AM et al (2007) Neural substrates of awakening probed with optogenetic control of hypocretin neurons. Nature 450:420–424. https://doi.org/10.1038/nature06310

Adelsberger H, Garaschuk O, Konnerth A (2005) Cortical calcium waves in resting newborn mice. Nat Neurosci 8:988–990. https://doi.org/10.1038/nn1502

Aharoni D, Hoogland TM (2019) Circuit investigations with open-source miniaturized microscopes: past, present and future. Front Cell Neurosci 13:1–12. https://doi.org/10.3389/fncel.2019.00141

Al-Juboori SI, Dondzillo A, Stubblefield EA et al (2013) Light scattering properties vary across different regions of the adult mouse brain. PLoS One 8:1–9. https://doi.org/10.1371/journal.pone.0067626

Aravanis AM, Wang L-P, Zhang F et al (2007) An optical neural interface: in vivocontrol of rodent motor cortex with integrated fiberoptic and optogenetic technology. J Neural Eng 4:S143–S156. https://doi.org/10.1088/1741-2560/4/3/s02

Barretto RPJ, Messerschmidt B, Schnitzer MJ (2009) In vivo fluorescence imaging with high-resolution microlenses. Nat Methods 6:511–512. https://doi.org/10.1038/nmeth.1339

Canales A, Jia X, Froriep UP et al (2015) Multifunctional fibers for simultaneous optical, electrical and chemical interrogation of neural circuits in vivo. Nat Biotechnol 33:277–284. https://doi.org/10.1038/nbt.3093

Canales A, Park S, Kilias A, Anikeeva P (2018) Multifunctional fibers as tools for neuroscience and neuroengineering. Acc Chem Res 51:829–838. https://doi.org/10.1021/acs.accounts.7b00558

Christie IN, Wells JA, Southern P et al (2013) fMRI response to blue light delivery in the naïve brain: Implications for combined optogenetic fMRI studies. Neuroimage 66:634–641. https://doi.org/10.1016/J.NEUROIMAGE.2012.10.074

Cui G, Jun SB, Jin X et al (2013) Concurrent activation of striatal direct and indirect pathways during action initiation. Nature 494:238–242. https://doi.org/10.1038/nature11846

Cui G, Jun SB, Jin X et al (2014) Deep brain optical measurements of cell type-specific neural activity in behaving mice. Nat Protoc 9:1213–1228. https://doi.org/10.1038/nprot.2014.080

Davey CJ, Argyros A, Fleming SC, Solomon SG (2015) Multimodal optogenetic neural interfacing device fabricated by scalable optical fiber drawing technique. Appl Optics 54:10,068–10,072. https://doi.org/10.1364/AO.54.010068

Desai M, Kahn I, Knoblich U et al (2011) Mapping brain networks in awake mice using combined optical neural control and fMRI. J Neurophysiol 105:1393–1405. https://doi.org/10.1152/jn.00828.2010

Di Leonardo R, Bianchi S (2011) Hologram transmission through multi-mode optical fibers. Opt Express 19:247–254. https://doi.org/10.1364/OE.19.000247

Forli A, Vecchia D, Binini N et al (2018) Two-photon bidirectional control and imaging of neuronal excitability with high spatial resolution in vivo. Cell Rep 22:3087–3098. https://doi.org/10.1016/j.celrep.2018.02.063

Frank JA, Antonini M-J, Anikeeva P (2019) Next-generation interfaces for studying neural function. Nat Biotechnol 37:1013–1023. https://doi.org/10.1038/s41587-019-0198-8

LeChasseur Y, Dufour S, Lavertu G et al (2011) A microprobe for parallel optical and electrical recordings from single neurons in vivo. Nat Methods 8:319–325. https://doi.org/10.1038/nmeth.1572

Lee SJ, Chen Y, Lodder B, Sabatini BL (2019a) Monitoring behaviorally induced biochemical changes using fluorescence lifetime photometry. Front Neurosci 13:766

Lee SJ, Lodder B, Chen Y, et al (2019b) Cell-type specific asynchronous modulation of PKA by dopamine during reward based learning. bioRxiv 839035. doi: https://doi.org/10.1101/839035

Leite IT, Turtaev S, Jiang X et al (2018) Three-dimensional holographic optical manipulation through a high-numerical-aperture soft-glass multimode fibre. Nat Photonics 12:33–39. https://doi.org/10.1038/s41566-017-0053-8

Lu C, Park S, Richner TJ et al (2017) Flexible and stretchable nanowire-coated fibers for optoelectronic probing of spinal cord circuits. Sci Adv 3:e1600955. https://doi.org/10.1126/sciadv.1600955

Lütcke H, Murayama M, Hahn T et al (2010) Optical recording of neuronal activity with a genetically encoded calcium indicator in anesthetized and freely moving mice. Front Neural Circuits 4:1–12. https://doi.org/10.3389/fncir.2010.00009

Muir J, Lorsch ZS, Ramakrishnan C et al (2018) In vivo fiber photometry reveals signature of future stress susceptibility in nucleus accumbens. Neuropsychopharmacology 43:255–263. https://doi.org/10.1038/npp.2017.122

Ouzounov DG, Wang T, Wang M et al (2017) In vivo three-photon imaging of activity of GcamP6-labeled neurons deep in intact mouse brain. Nat Methods 14:388–390. https://doi.org/10.1038/nmeth.4183

Owen SF, Liu MH, Kreitzer AC (2019) Thermal constraints on in vivo optogenetic manipulations. Nat Neurosci 22:1061–1065. https://doi.org/10.1038/s41593-019-0422-3

Park S, Guo Y, Jia X et al (2017) One-step optogenetics with multifunctional flexible polymer fibers. Nat Neurosci 20:612–619. https://doi.org/10.1038/nn.4510

Patel AA, McAlinden N, Mathieson K, Sakata S (2020) Simultaneous electrophysiological recording and fiber photometry in freely behaving mice. Front Neurosci 14:807602. https://doi.org/10.1101/807602

Patriarchi T, Cho JR, Merten K et al (2018) Ultrafast neuronal imaging of dopamine dynamics with designed genetically encoded sensors. Science 360:1420. https://doi.org/10.1126/science.aat4422

Piatkevich KD, Bensussen S, Tseng H et al (2019) Population imaging of neural activity in awake behaving mice. Nature 574:413. https://doi.org/10.1038/s41586-019-1641-1

Pikálek T, Trägårdh J, Simpson S, Čižmár T (2019) Wavelength dependent characterization of a multimode fibre endoscope. Opt Express 27:28,239–28,253. https://doi.org/10.1364/OE.27.028239

Pisanello F (2019) Implantable micro and nanophotonic devices: toward a new generation of neural interfaces. Microelectron Eng 215:110979. https://doi.org/10.1016/j.mee.2019.110979

Pisanello F, Sileo L, Oldenburg IA et al (2014) Multipoint-emitting optical fibers for spatially addressable in vivo optogenetics. Neuron 82:1245. https://doi.org/10.1016/j.neuron.2014.04.041

Pisanello F, Sileo L, Pisanello M, et al (2015a) Nanomachined tapered optical fibers for in vivo optogenetics. In: IEEE-NANO 2015—15th international conference on nanotechnology

Pisanello M, Della Patria A, Sileo L et al (2015b) Modal demultiplexing properties of tapered and nanostructured optical fibers for in vivo optogenetic control of neural activity. Biomed Opt Express 6:4014. https://doi.org/10.1364/BOE.6.004014

Pisanello F, Sileo L, De Vittorio M (2016) Micro- and nanotechnologies for optical neural interfaces. Front Neurosci 10:70. https://doi.org/10.3389/fnins.2016.00070

Pisanello F, Mandelbaum G, Pisanello M et al (2017) Dynamic illumination of spatially restricted or large brain volumes via a single tapered optical fiber. Nat Neurosci 20:1180. https://doi.org/10.1038/nn.4591

Pisanello M, Pisano F, Sileo L et al (2018) Tailoring light delivery for optogenetics by modal demultiplexing in tapered optical fibers. Sci Rep 8:4467. https://doi.org/10.1038/s41598-018-22790-z

Pisanello M, Pisano F, Hyun M et al (2019) The three-dimensional signal collection field for fiber photometry in brain tissue. Front Neurosci 13:82

Pisano F, Pisanello M, Sileo L et al (2018) Focused ion beam nanomachining of tapered optical fibers for patterned light delivery. Microelectron Eng 195:41–49. https://doi.org/10.1016/j.mee.2018.03.023

Pisano F, Pisanello M, Lee SY et al (2019) Depth resolved fiber photometry with a single tapered optical fiber implant. Nat Methods 16:1185–1192

Plöschner M, Kollárová V, Dostál Z et al (2015a) Multimode fibre: light-sheet microscopy at the tip of a needle. Sci Rep 5:1–7. https://doi.org/10.1038/srep18050

Plöschner M, Tyc T, Čižmár T (2015b) Seeing through chaos in multimode fibres. Nat Photonics 9:529–535. https://doi.org/10.1038/nphoton.2015.112

Rizzo A, Lemma ED, Pisano F et al (2018) Laser micromachining of tapered optical fibers for spatially selective control of neural activity. Microelectron Eng 192:88–95. https://doi.org/10.1016/J.MEE.2018.02.010

Rungta RL, Osmanski B-F, Boido D et al (2017) Light controls cerebral blood flow in naive animals. Nat Commun 8:14,191. https://doi.org/10.1038/ncomms14191

Schlegel F, Sych Y, Schroeter A et al (2018) Fiber-optic implant for simultaneous fluorescence-based calcium recordings and BOLD fMRI in mice. Nat Protoc 13:840–855. https://doi.org/10.1038/nprot.2018.003

Schmid F, Wachsmuth L, Schwalm M et al (2016) Assessing sensory versus optogenetic network activation by combining (o)fMRI with optical $Ca^{2+}$ recordings. J Cereb Blood Flow Metab 36:1885–1900. https://doi.org/10.1177/0271678X15619428

Schulz K, Sydekum E, Krueppel R et al (2012) Simultaneous BOLD fMRI and fiber-optic calcium recording in rat neocortex. Nat Methods 9:597–602. https://doi.org/10.1038/nmeth.2013

Sparta DR, Stamatakis AM, Phillips JL et al (2011) Construction of implantable optical fibers for long-term optogenetic manipulation of neural circuits. Nat Protoc 7:12

Stujenske JM, Spellman T, Gordon JA (2015) Modeling the spatiotemporal dynamics of light and heat propagation for in vivo optogenetics. Cell Rep 12:525–534. https://doi.org/10.1016/j.celrep.2015.06.036

Sych Y, Chernysheva M, Sumanovski LT, Helmchen F (2019) High-density multi-fiber photometry for studying large-scale brain circuit dynamics. Nat Methods 16:553–560. https://doi.org/10.1038/s41592-019-0400-4

Turtaev S, Leite IT, Altwegg-Boussac T et al (2018) High-fidelity multimode fibre-based endoscopy for deep-brain in vivo imaging. Light Sci Appl 7:92

Vasquez-Lopez SA, Turcotte R, Koren V et al (2018) Subcellular spatial resolution achieved for deep-brain imaging in vivo using a minimally invasive multimode fiber. Light Sci Appl 7:110. https://doi.org/10.1038/s41377-018-0111-0

Warden MR, Cardin JA, Deisseroth K (2014) Optical neural interfaces. Annu Rev Biomed Eng 16:103–129. https://doi.org/10.1146/annurev-bioeng-071813-104733

Yang Y, Liu N, He Y et al (2018) Improved calcium sensor GCaMP-X overcomes the calcium channel perturbations induced by the calmodulin in GCaMP. Nat Commun 9:1504. https://doi.org/10.1038/s41467-018-03719-6

Yildirim M, Sugihara H, So PTC, Sur M (2019) Functional imaging of visual cortical layers and subplate in awake mice with optimized three-photon microscopy. Nat Commun 10:177. https://doi.org/10.1038/s41467-018-08179-6

Yizhar O, Fenno LE, Davidson TJ et al (2011) Optogenetics in neural systems. Neuron 71:9–34. https://doi.org/10.1016/J.NEURON.2011.06.004

Yona G, Meitav N, Kahn I, Shoham S (2016) Realistic numerical and analytical modeling of light scattering in brain tissue for optogenetic applications. eNeuro 3:420–424. https://doi.org/10.1523/ENEURO.0059-15.2015

Zhao Z, Luan L, Wei X et al (2017) Nanoelectronic coating enabled versatile multifunctional neural probes. Nano Lett 17:4588–4595. https://doi.org/10.1021/acs.nanolett.7b00956

# CMOS-Based Neural Interface Device for Optogenetics

41

Takashi Tokuda, Makito Haruta, Kiyotaka Sasagawa, and Jun Ohta

**Abstract**

Optical and electronic neural interface devices based on CMOS technology are presented. Concept, design strategy, and fabrication of the CMOS-based optoelectronic neural interface devices are described. The devices are based on a technology of implantable CMOS image sensor. To realize addressable local optical stimulation, blue light-emitting diode array chip was integrated on the implantable CMOS image sensors. Functional demonstrations of the devices are also presented. Optical stimulation capability was demonstrated in both in vitro and in vivo experiments. Further perspective including wireless device architecture is also presented.

**Keywords**

Optogenetics · Implantable device · CMOS image sensor · Integrated optical stimulator · On-chip imaging · Wireless implant

## Abbreviations

| | |
|---|---|
| ACP | Anisotropic conducting paste |
| ADC | Analog-to-digital converter |
| CMOS | Complementary metal–oxide semiconductor |
| GUI | Graphical user interface |
| I/O | Input/output |
| LED | Light-emitting diode |
| VSD | Voltage-sensitive die |

## 41.1 Introduction

The evolution of optogenetics has led to the realization of various methods to understand neural systems, and a great number of new approaches have continuously been demonstrated around the world.

As electronics technology such as electrodes and amplifiers has played important roles in the history of electrophysiology, for optogenetics, engineering is expected to provide devices and systems to stimulate and measure neural activity. The particular device function required in optogenetics is local and addressable light stimulation. Spatiotemporally limited stimulation realized with a combination of the genetic introduction of rhodopsin and optical stimulation device technology is one of the significant advantages of the optogenetic approach.

T. Tokuda (✉)
Institute of Innovative Research, Tokyo Institute of Technology, Tokyo, Japan
e-mail: tokuda@ee.e.titech.ac.jp

M. Haruta · K. Sasagawa · J. Ohta
Graduate School of Science and Technology, Nara Institute of Science and Technology, Nara, Japan



H. Yawo et al. (eds.), *Optogenetics*, Advances in Experimental Medicine and Biology 1293,
https://doi.org/10.1007/978-981-15-8763-4_41

Currently, a number of research groups are developing optical stimulation devices applicable for in vitro and in vivo optogenetics. We are developing a CMOS-based optoelectronic neural interface device based on implantable CMOS imaging device technology. In this article, we present the concept, design, and functional evaluations of a CMOS-based implantable neural interface device for optogenetics.

## 41.2 Concept of CMOS-Based Neural Interface Device for Optogenetics

### 41.2.1 Status of Optical Stimulation Devices for Optogenetics

Optical stimulation device technology, along with the modification of rhodopsin family of proteins and a genetic strategy to introduce the proteins into the target animal, plays an important role in optogenetics. Because most of the in vitro experiments are performed using a microscope-based platform, light projection onto a target using the optics of a microscope is widely employed. Using a laser or LED array, systems in which one can perform local illumination have been realized (Poher et al. 2008; Grossman et al. 2010). For in vivo applications, broad illumination was realized with optical fiber (Aravanis et al. 2007) or an LED fixed on a skull (Huber et al. 2008). To perform more specially localized light stimulation, an approach to fix an anesthetized animal under microscopy optics has been widely adopted. Currently, device technologies for local and addressable optical stimulation for freely moving animals are under development. We proposed and have been developing an optoelectronic neural stimulation device for both in vitro and in vivo optogenetics. We integrate a GaInN light-emitting diode (LED) array on an implantable CMOS image sensor to realize a device that can handle both light and electricity. Figure 41.1 shows the classifications of the optical stimulation device technologies and significance of our CMOS-based optoelectronic neural interface device.

### 41.2.2 Implantable CMOS Imaging Device Technology

We have developed a CMOS-based implantable neural imaging device (Ng et al. 2006; Tagawa et al. 2009; Kobayashi et al. 2012). Figure 41.2 shows the typical appearance of a CMOS-based implantable imaging device. We designed a small dedicated CMOS image sensor that can be operated with a minimum number of interconnections and mounted it on a polyimide flexible substrate. For fluorescence imaging, we integrated a color filter layer over the CMOS image sensor. LEDs are integrated surrounding the CMOS image sensor for illumination (regular imaging) or excitation (fluorescence imaging). In most cases, we use GaInN LEDs with peak emission wavelengths ranging from near UV to blue light.

Figure 41.3 shows an example result obtained with the implantable imaging device (Kobayashi et al. 2012). Fluorescence imaging using voltage-sensitive dye (VSD) was performed on the visual cortex of a mouse. Figure 41.3a shows a normal image obtained with external illumination and (b), (c) show VSD images. KCl injection ($K^+$ stimulation) was performed at an area indicated with a circle. We can clearly see blood vessels in Fig. 41.3a and the response of the brain tissue in Fig. 41.3c.

### 41.2.3 Contact-Type Implantable Optical Stimulator Using GaInN LED as Light Source

GaInN LEDs are small, power-efficient light sources that can emit at wavelengths near UV to green light. The typical stimulation intensity used in optogenetics experiments is within 10 mW/mm$^2$. On the other hand, a GaInN blue LED chip with a size smaller than 500 μm × 500 μm and typical emission flux larger than 10 mW is commercially available. This comparison suggests that if we place a GaInN blue LED near the target neural cells, we can perform optical stimulation of rhodopsin proteins.

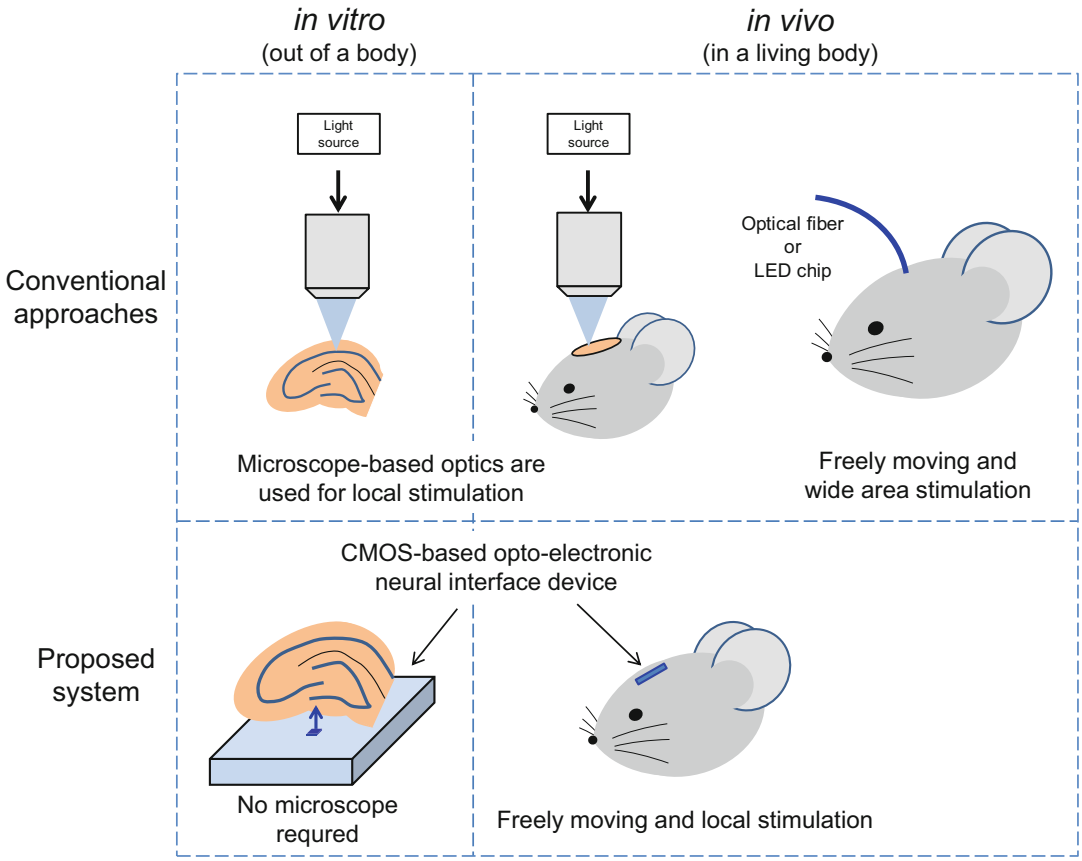


**Fig. 41.1** Classifications of optical stimulation devices for optogenetics

The implantable neural imaging device (see Fig. 41.2) includes GaInN LEDs, which we can use for optical stimulation in optogenetic experiments. However, all the LEDs are serially connected and simultaneously operated. To realize more specially localized and addressable optical stimulation, we proposed a novel CMOS-based implantable optoelectronic neural interface device (Tokuda et al. 2006).

Figure 41.4 shows the concept and schematic structure of the proposed optoelectronic neural stimulator. The core of the device is a multifunctional CMOS image sensor, which we developed in previous works (Tokuda et al. 2007a, b, 2012; Nakajima et al. 2012; Sawadsaringkarn et al. 2013). The multifunctional CMOS image sensor technology was originally proposed as a solution for various on-chip imaging applications. A pixel on the multifunctional CMOS image sensor has an on-chip electrode, and we can use the pixel as not only a light sensor but also as an electric potential sensor or current injection electrode. In the proposed neural stimulator, we integrate the multifunctional CMOS image sensor and GaInN LED array wafer with a flip-chip boding technique. Taking advantage of the addressable electric connection capability, we expect to operate arbitrary LEDs in the array and perform localized, patterned optical stimulation. Because GaInN is almost transparent to visible light, an on-chip imaging capability is also expected. In the following section, the design, packaging, and functionality of the proposed CMOS-based implantable neural stimulator are described.

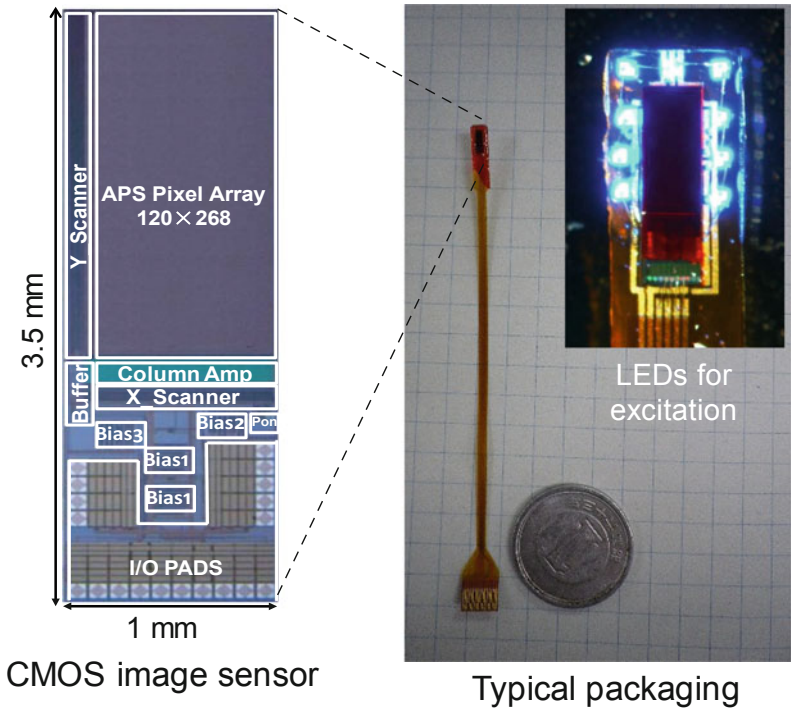


**Fig. 41.2** Appearance of CMOS-based implantable neural imaging device

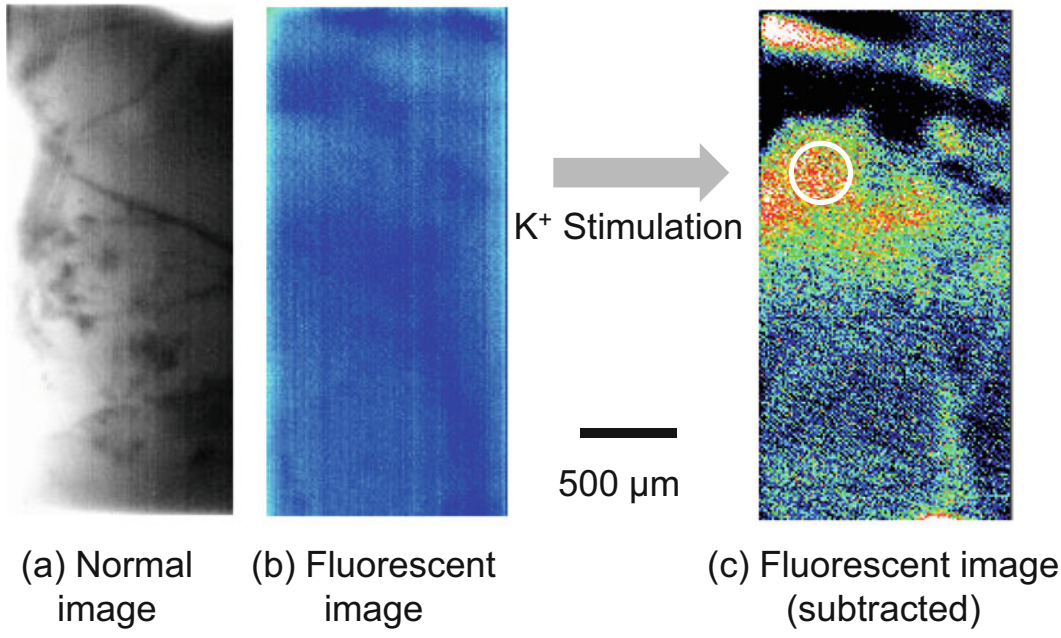


**Fig. 41.3** An example result of brain imaging using the implantable imaging device (Kobayashi et al. 2012)

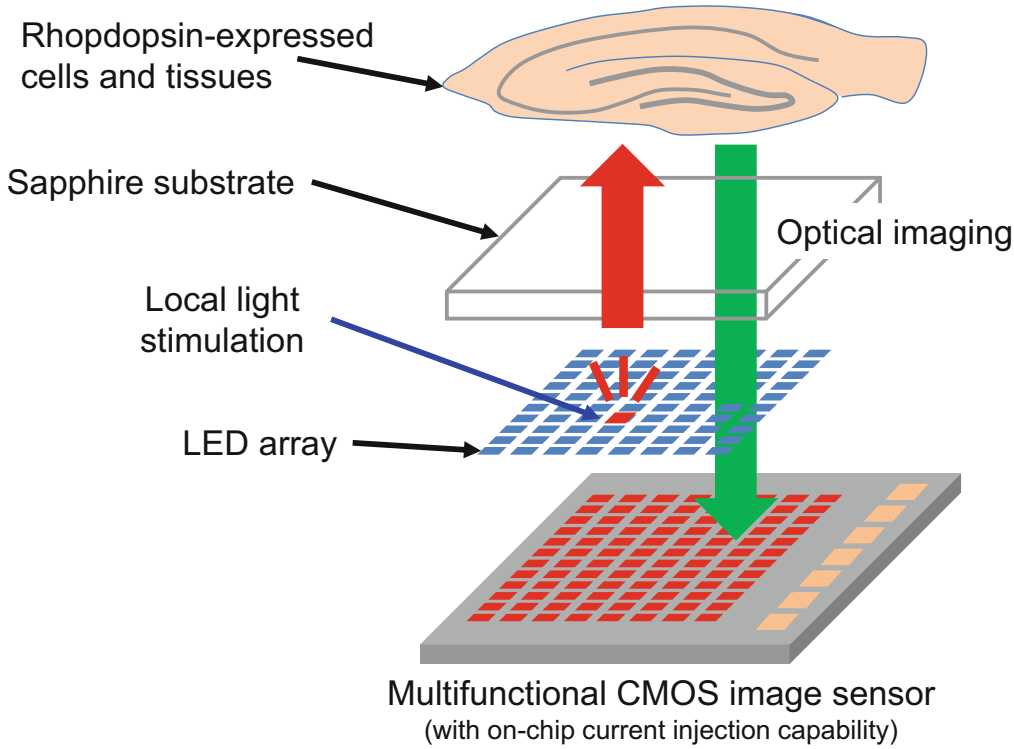


**Fig. 41.4** Concept of implantable CMOS-based optoelectronic neural stimulator for optogenetics

## 41.3 Design and Fabrication of Implantable CMOS-Based Optoelectronic Neural Interface Device

### 41.3.1 Design of Multifunctional CMOS Image Sensor

A multifunctional CMOS image sensor that acts as the core of the proposed neural interface device was designed and fabricated using a 0.35-μm, 2-poly, 4-metal standard CMOS process. Figures 41.5 and 41.6 show the layout and block diagram of the multifunctional CMOS image sensor, respectively. Table 41.1 shows the specifications of the sensor. The sensor has a 260 × 244 pixel array. The size of the pixels in the image sensor is 7.5 μm × 7.5 μm. The pixel circuitry includes a three-transistor active pixel sensor, which is a commonly used circuit for conventional CMOS image sensors. The operational voltage of the sensor is 3.3 V.

As a unique feature of the sensor, addressable electrodes for current injection and electronic sensing were implemented over the imaging pixel array. The electrodes were designed with a top metal layer and exposed to the air to establish an electrical connection to the on-chip measurement target or bonded devices such as an LED array. Openings beneath the electrode introduce light to pixel photodiodes. Thus, we introduced an electrical function without omitting the light-sensing function of the CMOS image sensor. However, it should be mentioned that the image quality was degraded when we bonded the LED array wafer on the CMOS sensor using flip-chip bonding with Au bumps. The main reason for this is the presence of electrode shadow on the captured image.

The sensor can drive the GaInN LED array bonded on the pixel array. We use the switch array (shown as a combination of CMOS switches and a scanner in Fig. 41.6) to establish an electrical connection between the cathode

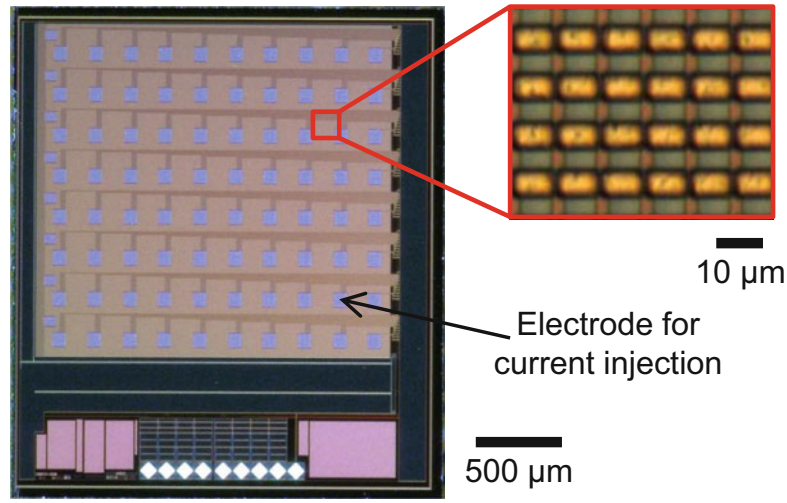


**Fig. 41.5** Layout of the multifunctional CMOS image sensor

electrode of the GaInN LED to an input line of the CMOS sensor prepared for LED operation. The current injection electrode was internally configured as a linear switchable electrode array. We can select one of the electrodes by applying reset and clock pulses to the electrode scanner unit. Transmission gate circuitry was used as the switch between the on-pixel electrodes to the common current injection line. In addition, we implemented a master switch that can enable/disable the electrode selection. Because the typical operational voltage of a GaInN LED is approximately 3.0 V, we used 5.0 V-compatible MOS transistors for the current injection circuitry. The I/O pads of the multifunctional CMOS image sensor were gathered on one side of its sides.

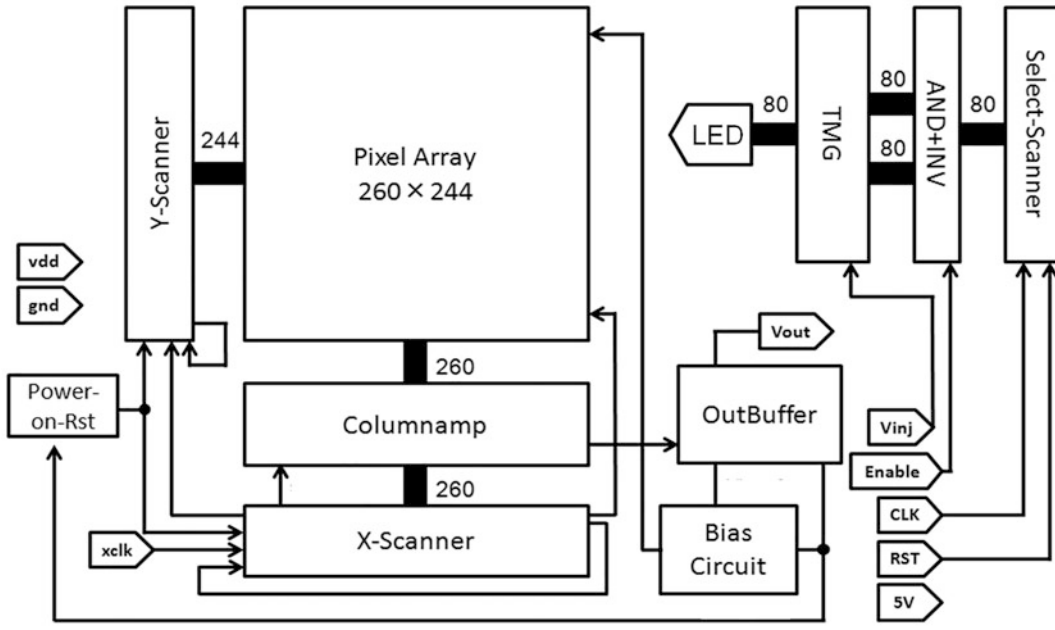


**Fig. 41.6** Block diagram of the multifunctional CMOS image sensor

**Table 41.1** Specifications of the multifunctional CMOS image sensor

| | |
|---|---|
| Process | 0.35-μm, 2-poly, 4-metal standard CMOS |
| Chip size | 2200 μm × 2500 μm |
| Array size | 260 × 244 |
| Pixel size | 7.5 μm × 7.5 μm |
| Pixel circuitry | 3-Tr active pixel sensor |
| LED channel | 1 |
| Electrode for LEDs | 8 × 10 |
| Operation voltage | 3.3 V (optical imaging)<br>5 V (LED operation) |

### 41.3.2 GaInN LED Array Chip

Because Si has an indirect bandgap semiconductor, no light-emitting device is available with current CMOS fabrication technologies. It is a realistic strategy to integrate LEDs fabricated from other materials to realize an on-chip light-emitting function for an optical neural stimulator. We adopted GaInN LEDs because they cover a wavelength region from near UV to green light, and the device is almost transparent to visible light. We prepared an 8 × 10 GaInN LED array with a peak emission wavelength of 470 nm. The size of each LED and LED array is approximately 200 μm × 230 μm and 1.8 mm × 1.9 mm, respectively. Each LED has its own anode (P-type) and cathode (N-type) electrodes. We can operate the LED by injecting current between these two electrodes.

### 41.3.3 Wafer Bonding and Device Packaging

All the electrodes of the GaInN LED array are on the surface LED array chip. The current injection electrodes of the multifunctional CMOS image sensor are also on the top surface of the CMOS chip. Therefore, to realize the addressable optical stimulator, we bonded the GaInN array and CMOS sensor chips using a flip-chip bonding technique. This structure is advantageous because the bottom side of the GaInN array wafer is used as the contact surface to target tissue or cells. The substrate of the GaInN array is sapphire, which is chemically stable and shows minuscule toxicity to biological targets. Prior to the flip-chip bonding process, we formed Au bumps on the electrodes of the GaInN LED array. Two chips are bonded with the help of anisotropic conducting paste (ACP), which is commonly used for the flip-chip bonding process. Figure 41.7a shows the appearance of the bonded chips. As shown on the rightmost image of Fig. 41.7a, the pixels of the CMOS sensor are visible through the GaInN array wafer. This figure suggests that optical imaging through the GaInN array chip is expected as a future functional extension. The device shown in Fig. 41.7a can be used for various optogenetic experiments in both in vitro and in vivo situations. Figure 41.7b–d shows typical device packages for in vitro and in vivo experiments.

### 41.3.4 Control and Data Acquisition System

Power and control signals to operate the proposed optoelectronic neural interface device were supplied on the multifunctional CMOS image sensor. The imaging function integrated on the CMOS sensor is compatible with our previous works (Ng et al. 2006; Tagawa et al. 2009; Kobayashi et al. 2012). We can operate the imaging function using only four I/O lines: vdd and gnd for power supply, a clock signal for image sensor operation (xclk), and a signal output line (Vout). For LED

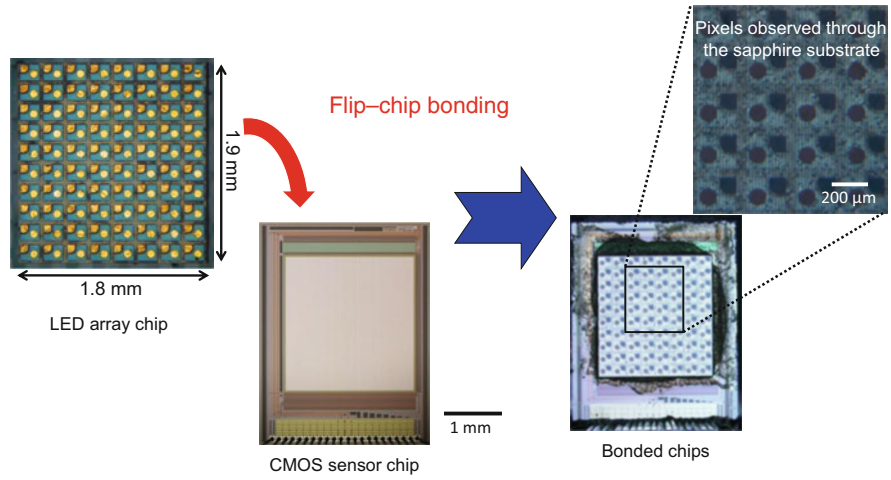


**Fig. 41.7** Device packaging
(**a**) Bonded LED array and CMOS sensor chips
(**b**) For in vitro applications
(**c**) For in vivo experiments (1)
(**d**) For in vivo experiments (2)

operation, we need to apply a 5 V power line (see Fig. 41.6) as well as a scanner reset (RST) and scanner clock (CLK) to reset and increment the electrode selection, respectively. We also need to apply a master signal (Enable) to enable/disable the current injection into an LED from the selected electrode and a current injection line (Vinj) to operate the selected LED.

We prepared an interconnection board equipped with conventional digital and analog buffers and analog-to-digital converter (ADC) chips between the neural stimulator and Windows PC. We also developed GUI-based control software on a Windows PC to control the device.

## 41.4 Functional Evaluation of the CMOS-Based Optoelectronic Neural Interface Device

### 41.4.1 Verification of LED Operation

The function of the local and addressable optical stimulation was characterized. Figure 41.8 shows both external images during LED operation and images captured with the imaging function of the multifunctional CMOS image sensor. Figure 41.8a, b was taken during single LED

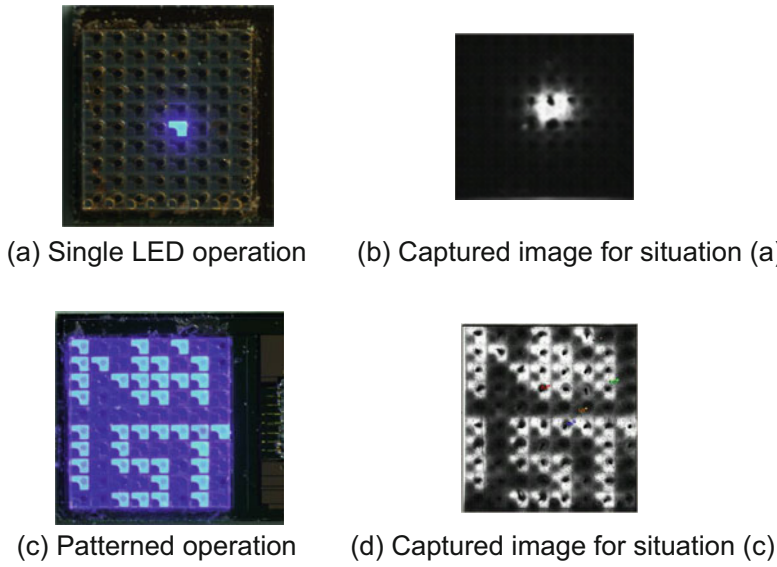


**Fig. 41.8** Images taken during (**a**), (**b**) single and (**c**), (**d**) patterned LED operation
- (**a**) Single LED operation
- (**b**) Captured image for (a)
- (**c**) Patterned LED operation
- (**d**) Captured image for (c)

operation. We successfully selected and operated an LED. It was also confirmed that we can monitor the LED condition during its operation from the image taken by the CMOS sensor (Fig. 41.8b). This result suggests that the imaging function can be used for both observing the on-chip biological target and monitoring LED operation. This capability will be quite advantageous to monitor the device functions, particularly in cases where the device is completely implanted into a freely moving animal.

Because the present multifunctional CMOS image sensor is equipped with a single current injection channel for LED operation, we can only operate one LED. However, by scanning the LED, we can perform quasi two-dimensional patterned stimulation. Figure 41.8c, d shows a case when we perform quasi two-dimensional LED operation (showing "NAIST" characters with rapid scan).

Figure 41.9 shows the emission flux as a function of the injected current in single LED operation. A corresponding intensity of 47 mW/mm$^2$, which is significantly larger than the typical stimulation intensity range to drive a typical rhodopsin protein (~10 mW/mm$^2$) was obtained. This result suggests that the proposed device is capable

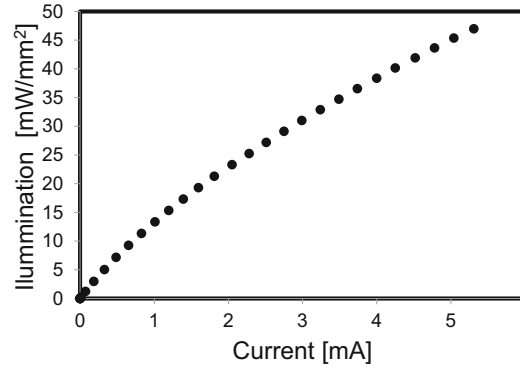


**Fig. 41.9** Emission flux in single LED operation

of performing the optical stimulation required in most optogenetic experiments.

### 41.4.2 Evaluation of Optical Imaging Function

As mentioned in the previous subsection, we can monitor the LED operation by taking advantage of the optical imaging function of the multifunctional CMOS image sensor. However, there is an issue regarding image quality as a consequence of the on-chip imaging system perspective of the

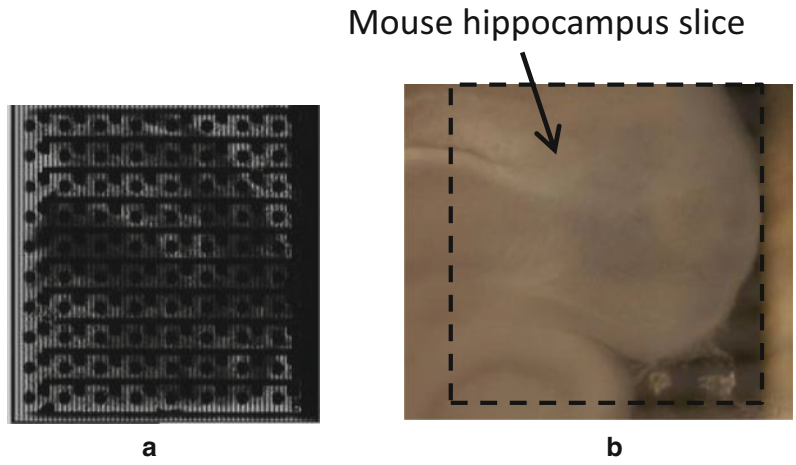


**Fig. 41.10** Example of result obtained in an on-chip imaging trial
(**a**) CMOS sensor image
(**b**) Externally observed slice (Dashed square indicates the position of pixel array)

biological target, i.e., observing tissues or cells contacting the device surface. Figure 41.10 shows an example of an imaging trial to observe a brain slice directly placed on the device surface. Compared with the image obtained with an external microscope, we can roughly observe the position and silhouette of the brain slice from the image captured with the CMOS sensor. Because of shadows caused by the anode and cathode electrodes and Au bumps, the image quality is significantly degraded. We will improve the image quality by adopting transparent electrodes and a bumpless bonding process as a future improvement in device functionality.

### 41.4.3 Cell Culturing on the Device Surface

To ensure suitability of the proposed device for various on-chip optogenetic experimental applications, the device surface must be biocompatible. Moreover, it should be confirmed that cell adhesion and culturing are possible on the device surface. Because the device has a polished sapphire surface, the toxicity to the biological targets is minuscule and thus negligible for acute and semichronic applications. To improve the adhesion of the cells on the sapphire surface, we confirmed that poly-L-lysine treatment is effective and succeeded in culturing Neuro2a cells on the device, as shown in the next section.

## 41.5 In Vitro Functional Verification of Optical Stimulation on ChR2-Expressed Cultured Cell

### 41.5.1 Experimental Setup and Procedure of Optical Stimulation Experiment

The functionality of the optical stimulation was verified in an in vitro experiment using ChR2-expressed Neuro2a cells. ChR2 is the most commonly used rhodopsin protein in optogenetics. Neuro2a is a neuron-like cell originating in mouse neuroblastoma. We initially introduced ChR2 into Neuro2a cells cultured on the device by means of lipofection and afterward, we performed a patch-clamp (voltage clamp) measurement to quantify the response of the Neuro2a cells caused by optical stimulation.

### 41.5.2 Observation of Neural Response Caused by Optical Stimulation

Figure 41.11 shows the (a) experimental setup and (b) a microscopic image obtained during the in vitro experiment. We performed optical stimulation of a cell on which the voltage clamp was established. Figure 41.11c shows an image obtained by the CMOS image sensor during the experiment. Although the cell position cannot be observed clearly in the image, the position of the glass electrode can be monitored using the imaging function.

Figure 41.12 shows the response observed in the membrane current caused by optical stimulation trials from the proposed CMOS-based optoelectronic neural interface device. An increase in membrane current was clearly observed. These results suggest that the proposed device can drive ChR2 and is applicable for optical stimulation in optogenetic experiments.

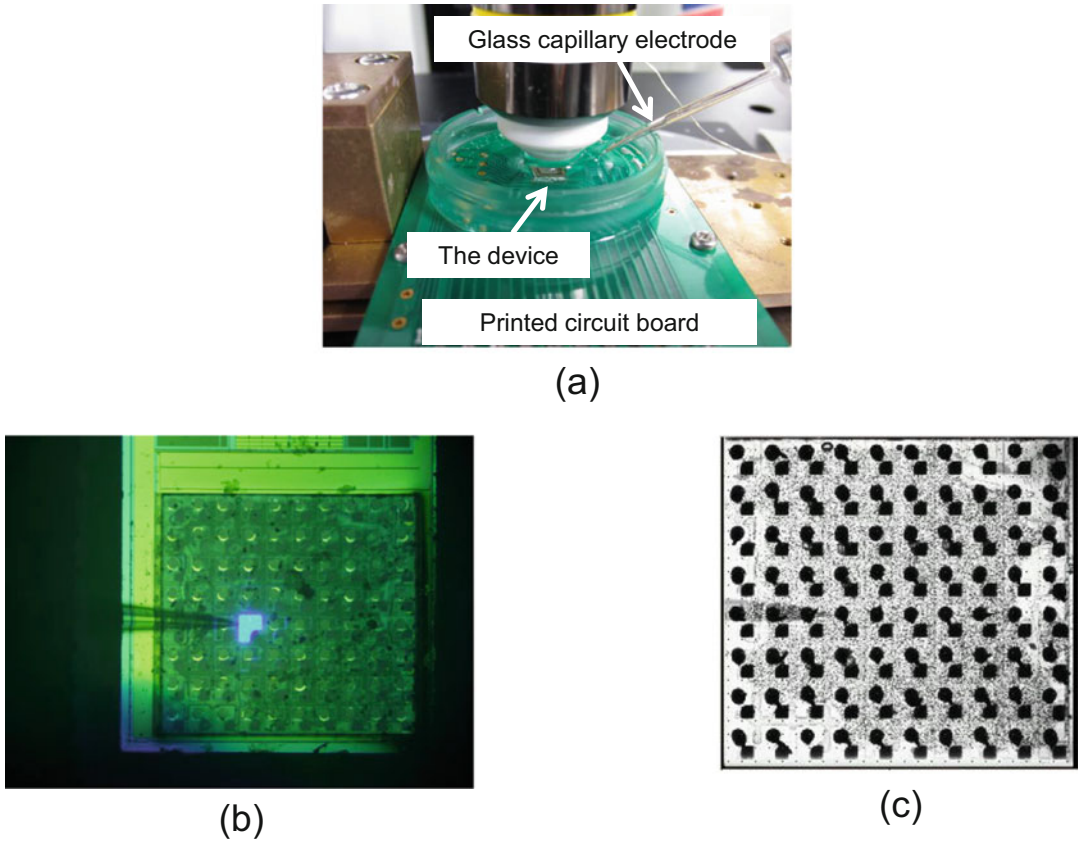


**Fig. 41.11** Experimental setup and images observed during in vitro experimental verification
(**a**) Experimental setup for in vitro functional evaluation
(**b**) Single LED operation
(**c**) Captured image

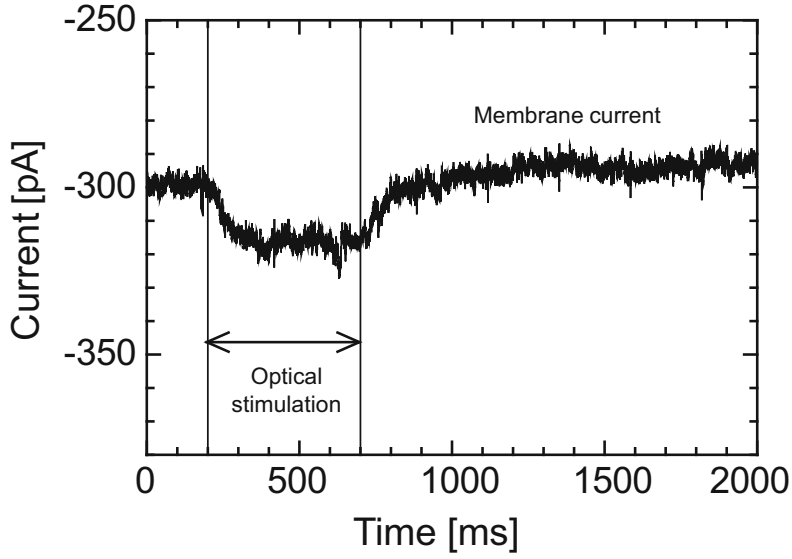


**Fig. 41.12** Response in membrane current caused by optical stimulation by the device

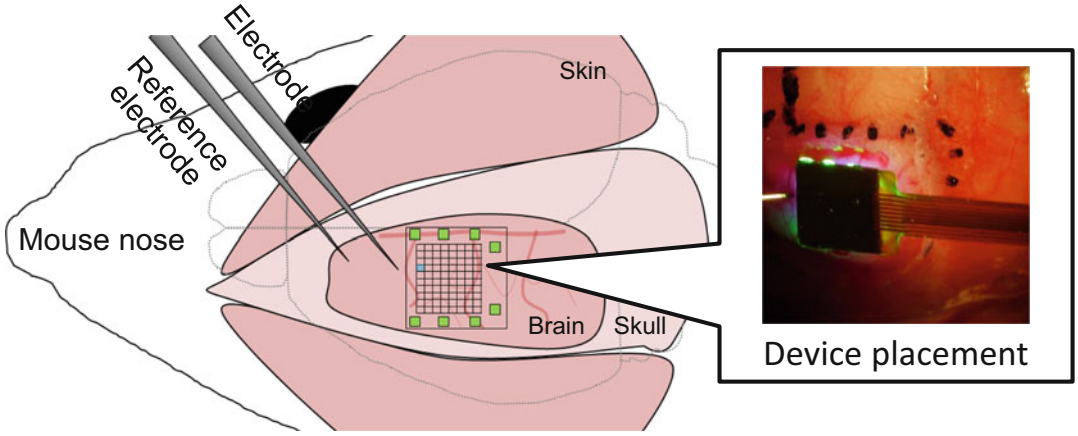


**Fig. 41.13** Experimental setup for the in vivo functional verification (Haruta et al. 2017)

## 41.6 In Vivo Functional Verification of Simultaneous Optical Stimulation and Imaging of ChR2-Expressed Mouse Brain

### 41.6.1 Experimental Setup and Procedure of Experiments

The device shown in Fig. 41.7d was used for the functional verification (Haruta et al. 2017). The device has eight additional green LEDs surrounding the CMOS image sensor integrated with the blue LED array wafer. The green LEDs can be used as illuminators for optical imaging. Figure 41.13 shows experimental setup for the functional evaluation (Haruta et al. 2017). ChR2-NestinCre transgenic mice were used for the experiments. All the animal experiments were conducted in accordance with the guidelines of the Nara Institute of Science and Technology. Optical stimulation was performed by the

presented device, and the brain response was observed electrophysiologically. Extracellular single-unit recordings using tungsten electrodes were performed. The imaging was performed using the intrinsic function of the CMOS image sensor using the green LEDs as the illuminators. The experiments were performed in anesthetized condition. Further details are presented in Haruta et al. (2017).

### 41.6.2 Results of Simultaneous Optical Imaging and Stimulation

Figure 41.14 shows the brain images taken by (a) an external microscope, and (b), (c) the present integrated device. In Fig. 41.14b, no LED was operated, and in Fig. 41.14c, LEDs with different positions were operated during the imaging. We

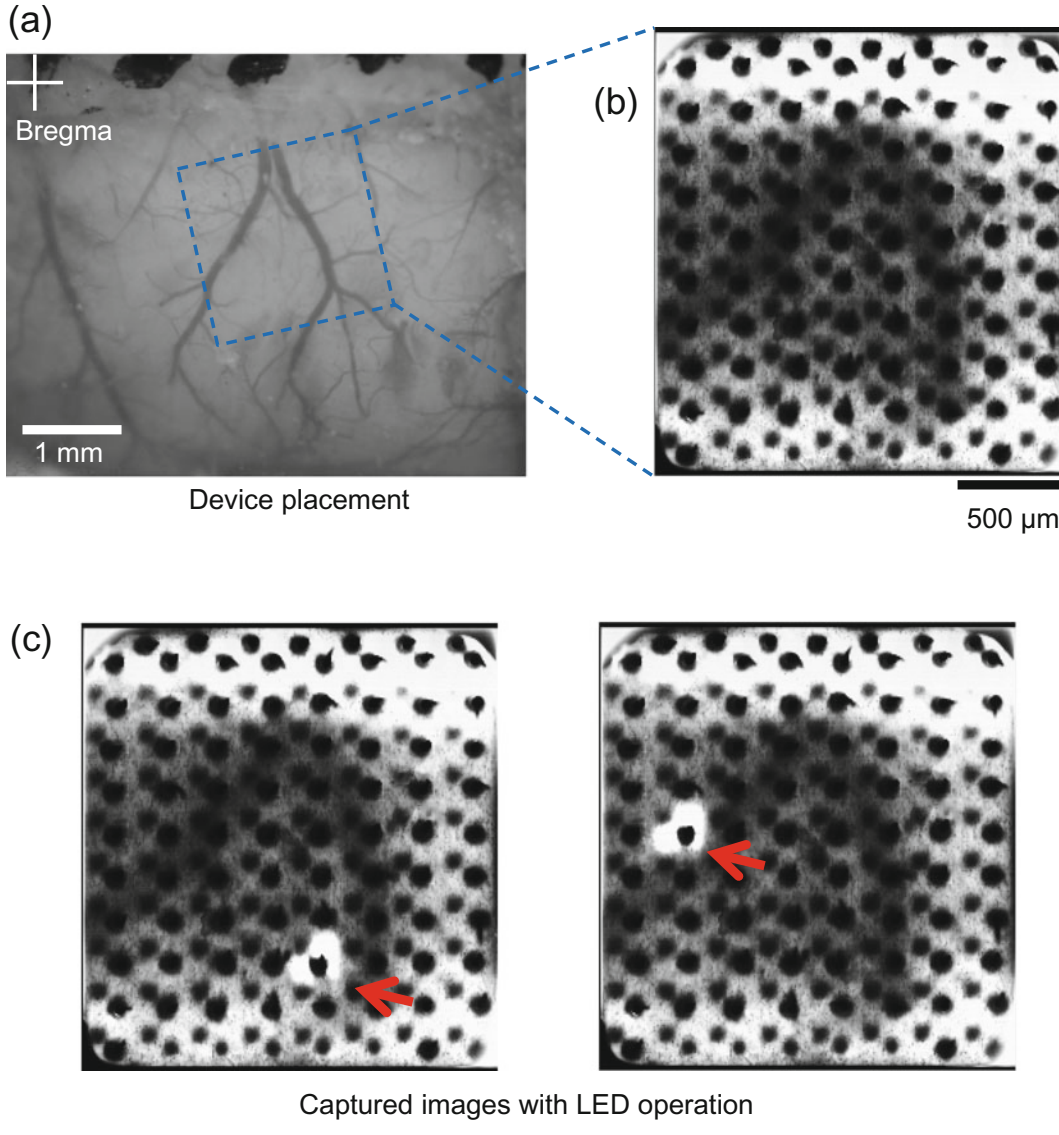


**Fig. 41.14** Brain surface image taken by (**a**) an external microscope, and the present device (**b**) without LED operation and (**c**) LED operation (Haruta et al. 2017)

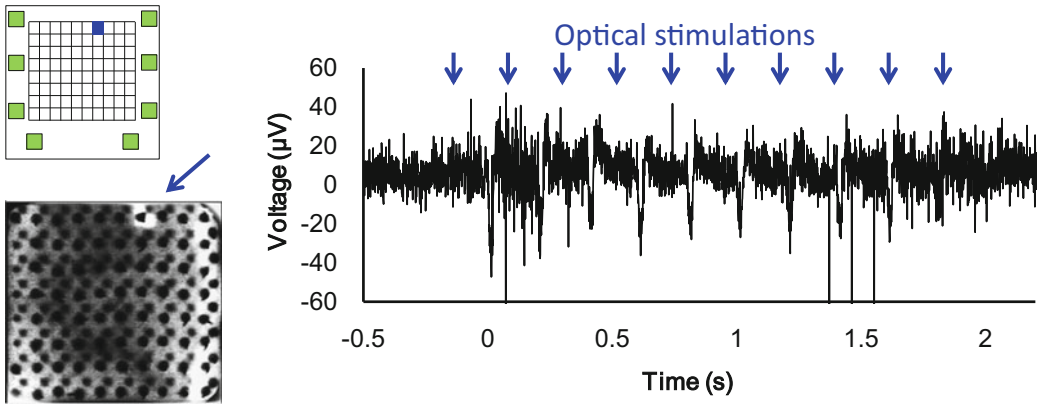


**Fig. 41.15** Results of simultaneous optical stimulation and imaging. The trace is an electrophysiologically measured extracellular signal (Haruta et al. 2017)

can see a clear image of major blood vessels. The LED operation is also observed, which is helpful to know the optical stimulation is appropriately performed. Figure 41.15 shows a result of simultaneous optical stimulation and imaging. Blue arrows indicate the timing of the optical stimulation. We successfully observed a series of responses from the stimulated neurons. It was also confirmed that the operation of the CMOS image sensor function does not cause significant artifact in the signal. Detailed data are presented in Haruta et al. (2017).

## 41.7 Conclusions and Future Work

A novel CMOS-based optoelectronic neural interface device was proposed and fabricated. The device was designed for optical stimulation and neural observation in optogenetic experiments. We integrated a multifunctional CMOS image sensor with on-chip addressable current injection capability and a GaInN LED array chip formed on a sapphire substrate. The device function to select and operate an LED in the array was evaluated and it was confirmed that the device has the capability to perform optical stimulation with sufficient intensity. The device functionality was demonstrated in both in vitro and in vivo experiments.

Future research will be focusing on various improvements of the device functions. An improvement in image quality by reducing the shadow caused by electrodes on an LED array chip and integration of an on-chip optical filter for fluorescence imaging is expected. We are also undertaking further development by applying the minimal-functionality approach. We are currently developing an integrated optical power transfer platform and producing an ultrasmall implantable optical stimulator as shown in Fig. 41.16 (Tokuda et al. 2018). The main objective is to extend the functionality of this device. We are also performing different kinds of circuit and device development to implement a variety of CMOS-based neural interface devices that covers both small and wide-area applications.

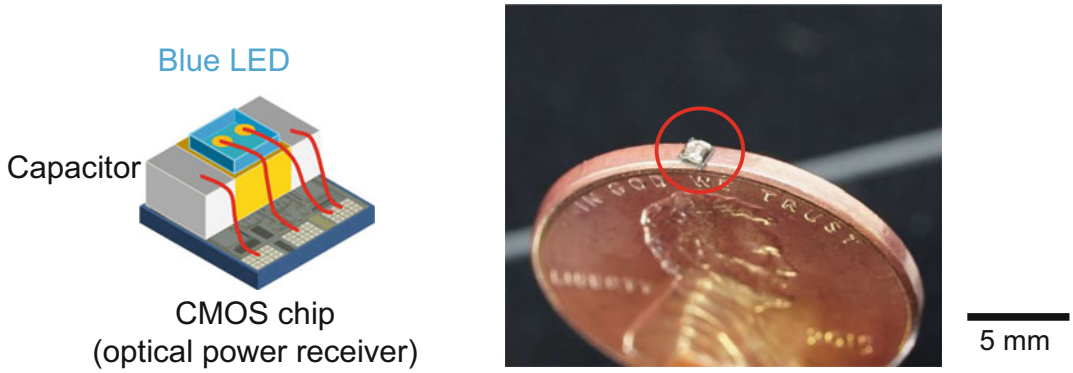


**Fig. 41.16** CMOS-based ultra-small implantable stimulator (Tokuda et al. 2018). *Device operation movie is available online (Tokuda et al. 2018)

**Acknowledgments** All the work presented in this article was achieved under collaboration with members of the Photonic Device Science Laboratory in the Graduate School of Materials Science, Nara Institute of Science and Technology. The optical stimulation experiment using ChR2-expressed cells was performed with great help from Professor Sadao Shiosaka and Assistant Professor Yasuyuki Ishikawa (currently Associate Professor, with Maebashi Institute of Technology) at the Graduate School of Bioscience, Nara Institute of Science and Technology.

*Financial Supports:* This work was partly supported by the Japan Science and Technology Agency, Precursory Research for Embryonic Science and Technology (JST-PRESTO), Grant-in-Aid for Challenging Exploratory Research #50314539 from Japan Society for the Promotion of Science, and VLSI Design and Education Center (VDEC) at the University of Tokyo, in collaboration with Cadence Design Systems, Inc.

## References

Aravanis AM, Wang L-P, Zhang F et al (2007) An optical neural interface: in vivo control of rodent motor cortex with integrated fiberoptic and optogenetic technology. J Neural Eng 4:S143–S156. https://doi.org/10.1088/1741-2560/4/3/S02

Grossman N, Poher V, Grubb MSMS et al (2010) Multi-site optical excitation using ChR2 and micro-LED array. J Neural Eng 7:16,004. https://doi.org/10.1088/1741-2560/7/1/016004

Haruta M, Kamiyama N, Nakajima S et al (2017) Implantable optogenetic device with CMOS IC technology for simultaneous optical measurement and stimulation. Jpn. J Appl Phys 56:057001. https://doi.org/10.7567/JJAP.56.057001

Huber D, Petreanu L, Ghitani N et al (2008) Sparse optical microstimulation in barrel cortex drives learned behaviour in freely moving mice. Nature 451:61–64. https://doi.org/10.1038/nature06445

Kobayashi T, Motoyama M, Masuda H et al (2012) Novel implantable imaging system for enabling simultaneous multiplanar and multipoint analysis for fluorescence potentiometry in the visual cortex. Biosens Bioelectron 38:321–330. https://doi.org/10.1016/j.bios.2012.06.035

Nakajima A, Kimura H, Sawadsaringkarn Y et al (2012) CMOS image sensor integrated with micro-LED and multielectrode arrays for the patterned photostimulation and multichannel recording of neuronal tissue. Opt Express 20:6097–6108. https://doi.org/10.1364/OE.20.006097

Ng DC, Tamura H, Tokuda T et al (2006) Real time in vivo imaging and measurement of serine protease activity in the mouse hippocampus using a dedicated complementary metal-oxide semiconductor imaging device. J Neurosci Methods 156:23–30. https://doi.org/10.1016/j.jneumeth.2006.02.005

Poher V, Grossman N, Kennedy GT et al (2008) Micro-LED arrays: a tool for two-dimensional neuron stimulation. J Phys D Appl Phys 41:094014. https://doi.org/10.1088/0022-3727/41/9/094014

Sawadsaringkarn Y, Miyatani T, Noda T et al (2013) A CMOS optoelectronic neural interface device based on an image sensor with on-chip light stimulation and extracellular neural signal recording for optogenetics. ITE Trans Media Technol Appl 1:184–189. https://doi.org/10.3169/mta.1.184

Tagawa A, Higuchi A, Sugiyama T et al (2009) Development of complementary metal oxide semiconductor imaging devices for detecting green fluorescent protein in the deep brain of a freely moving mouse. Jpn J Appl Phys 48:04C195. https://doi.org/10.1143/JJAP.48.04C195

Tokuda T, Yamamoto A, Kagawa K et al (2006) A CMOS image sensor with optical and potential dual imaging function for on-chip bioscientific applications. Sensors Actuators A Phys 125:273–280. https://doi.org/10.1016/j.sna.2005.08.023

Tokuda T, Tanaka K, Matsuo M et al (2007a) Optical and electrochemical dual-image CMOS sensor for on-chip biomolecular sensing applications. Sensors Actuators A Phys 135:315–322. https://doi.org/10.1016/j.sna.2006.08.027

Tokuda T, Kadowaki I, Kagawa K et al (2007b) A new scheme for imaging on-Chip dry DNA spots using optical/potential dual-image complementary metal oxide semiconductor sensor. Jpn J Appl Phys 46:2806–2810. https://doi.org/10.1143/JJAP.46.2806

Tokuda T, Kimura H, Miyatani T et al (2012) CMOS on-chip bio-imaging sensor with integrated micro light source array for optogenetics. Electron Lett 48:312. https://doi.org/10.1049/el.2011.4087

Tokuda T, Ishizu T, Nattakarn W et al (2018) 1 mm3-sized optical neural stimulator based on CMOS integrated photovoltaic power receiver. AIP Adv 8:045018. https://doi.org/10.1063/1.5024243

# Flexible Light Sources

# 42

Masaki Sekino

**Abstract**

Various light sources have been developed for the application of optical stimulation in the optogenetics field. Light transmission inside living tissue is limited to a distance of a few millimeters; hence, it is necessary to insert the light source near the nerve tissue to be stimulated. If a device is rigid, it causes mechanical stimulation to act on the nerve tissue. The application of mechanical stimulation may induce inflammation, obstructing neural activity. Fabricating such a device out of a soft material can prevent mechanical stimulation of cells and mitigate biological reactions such as inflammation or encapsulation. Minimizing the sizes of LED and other light sources as much as possible and mounting them on a flexible substrate can provide the entire device with flexibility. Micro-LEDs can be reduced to a size almost comparable to that of a cell and it has even been reported that some have been mounted on the tip of needle-shaped devices inserted into living tissue. A device using organic semiconductors is sufficiently soft to be bent, which is a characteristic not observed in inorganic semiconductors. Using organic LEDs can realize wide-area flexible light-emitting surfaces and they are widely anticipated to be the next generation of light sources. This chapter introduces technologies used to manufacture these soft light sources and examples of optical stimulation devices that incorporate them.

**Keywords**

Flexible electronics · Organic light-emitting diode · Thin-film device · Optogenetics · Light source

## Abbreviations

| | |
|---|---|
| ChR2 | Channelrhodopsin 2 |
| GaN | Gallium nitride |
| ITO | Indium tin oxide |
| LCD | Liquid crystal display |
| LED | Light-emitting diode |
| MRI | Magnetic resonance imaging |
| OECT | Organic electrochemical transistors |
| OLED | Organic light-emitting diode |
| PTC | Positive-temperature coefficient |

## 42.1 Introduction

In recent years, optogenetics has seen remarkable progress. It has been propelled by wide-ranging

M. Sekino (✉)
Department of Electrical Engineering and Information Systems, Graduate School of Engineering, The University of Tokyo, Tokyo, Japan
e-mail: sekino@bee.t.u-tokyo.ac.jp



H. Yawo et al. (eds.), *Optogenetics*, Advances in Experimental Medicine and Biology 1293,
https://doi.org/10.1007/978-981-15-8763-4_42

developments in basic neuroscientific research and the search for potential applications in the field of medicine (Yawo et al. 2013). Optogenetics allows researchers to control the activity of genetically engineered neurons in mammals and other organisms through optical stimulation, where an extrinsic light source is used to trigger the opening and closing of light-responsive ion channels expressed by the modified cells (Boyden et al. 2005; Fenno et al. 2011). Various light sources have been proposed and fabricated for this purpose (Grosenick et al. 2015). For instance, animals are often fitted with small, micro-light sources that can minimize physical constraints on their movements (Chow and Boyden 2013). Optical stimulation devices may also be directly fitted to the neurons; however, if the devices are made of a rigid material, mechanical stress would occur in response to tissue deformation, additionally stimulating cells and potentially causing inflammation or other unwanted reactions (Onuki et al. 2008). To address this issue, researchers have started developing technologies to manufacture light sources, electronic devices, and waveguides using softer materials. This chapter describes the principles, structures, and characteristics of "flexible" light sources.

As explained in the other chapters, optical stimulation can selectively target the neurons of interest; thus, it is superior to electrical stimulation, which involves passing a current across a cathode–anode pair to stimulate neurons located between them (Zhang et al. 2007). The current is conducted by the migration of ions, charge carriers, in living tissues whose behavior is governed by a conservation law. This indicates that an electric charge never disappears from the current as it passes between the electrodes. Therefore, even neurons physically at a distance from them shall be stimulated (as long as they lie along the current's path), if the current is stronger than their activation threshold. Optical stimulation, in contrast, involves light from a single source that is scattered and absorbed as it propagates through living tissues. Light is more susceptible to distance-related attenuation than electricity because photons are eliminated by absorption, indicating that the effects of optical stimulation are localized in the vicinity of the light source. In addition, only the cells expressing light-sensitive ion channels are stimulated by light, allowing the researchers to restrict the cell population of interest. Therefore, optical stimulation serves to be the more selective paradigm.

The scattering coefficient, absorption coefficient, and anisotropy are the factors that influence the propagation of light through biological tissues (Jacques 2013). These factors are dependent on wavelength (Ash et al. 2017). The propagation of light continues in the original (incident) direction and is deeper at low scattering/absorption coefficients and high anisotropy. Melanin and hemoglobin present in the skin and red blood cells, respectively, are the two most highly absorptive compounds that affect light propagation. Visible light, which is most often used in optical stimulation, can propagate through biological tissues in the order of a few millimeters. In comparison, the range of ultraviolet light reaches only up to a few tens of microns whereas that of near-infrared light can reach several centimeters. Based on these properties, the light source must be placed within a few millimeters of the target neurons for optical stimulation. Furthermore, it must be inserted in the vicinity of the target site as light from outside the body would be unable to reach the neurons inside.

## 42.2 Light Sources for Optogenetics

The performance of a light source depends on various factors such as wavelength, intensity, emission area, heat generation, size and shape, weight, biocompatibility, and softness of materials. The wavelength must be chosen in accordance with the target opsin. For example, channelrhodopsin 2 (ChR2) absorbs light optimally at 470 nm and halorhodopsin absorbs light optimally at approximately 600 nm (Fenno et al. 2011). The wavelength of the light source should have an emission peak wavelength that is as close as possible to the absorption peak wavelength of the opsin and the bandwidth of the peak should be narrow. If the peak is too wide,

considerable portions in the spectrum will not be absorbed by the opsin and will be converted into thermal energy, and the selectivity will decrease when multiple opsins are used. Light intensity requires that many light-responsive ion channels are activated simultaneously to cause depolarization of neurons. For ChR2, depolarization is possible if the intensity is about 1 $mW/mm^2$ or above (Senova et al. 2017). Lasers and light-emitting diodes (LEDs) are often used as light sources that satisfy the abovementioned wavelength characteristics and intensities. The luminescent area must be designed to match the size of the target nerve tissue. When a point light source such as a small LED or the end of an optical fiber is used, the light is attenuated according to the distance from the light source, which results in nonuniform intensities in the nerve tissue. To irradiate the nerve tissue uniformly, a light source that emits light in a planar manner is the most effective.

In optogenetic experiments, it is known that heat, in addition to light, also affects cell activity (Stujenske et al. 2015). In many experiments, the effect of heat is not negligible; hence, it is desirable to be able to control it. When light sources are classified according to the effects of heat, they can be divided into hot and cold sources. A hot source is a device that emits light directly from luminescent material placed near the nerve tissue. It is useful in that the structure can be simplified and the whole system can be made compact. However, less than approximately 25% of the energy supplied to the light source is used for generating light and the rest generates heat. Because the light source is implanted in the living body, often LEDs suitable for miniaturization are used. A cold source involves placing the luminescent material at a position away from the neurons, and an optical fiber guides light to the target tissue. The advantages are that the heat generated by the luminescent material does not directly affect the neurons and an inexpensive and high-power light source can be used. However, it is somewhat difficult to control the direction and irradiation range of emitted light compared to a hot source.

There are two main types of light emission: LEDs and lasers. An LED is a semiconductor device that has an anode and cathode and emits light based on the electroluminescence effect when current flows from the anode to the cathode. The wavelength of the emitted light is determined by the bandgap of the material, and if a blue LED using gallium nitride (GaN) is used, a wavelength suitable for ChR2 can be obtained. Furthermore, LEDs with various wavelengths from ultraviolet to infrared can be used. LEDs have a relatively simple structure. Therefore, they are suitable for miniaturization and are inexpensive. Lasers are also commonly used as light sources and are characterized by a higher output compared to LEDs and lower losses when they are introduced into an optical fiber. There are various types of lasers. For example, a semiconductor laser can be considered as an LED made to meet the conditions of laser oscillation. Laser oscillation is obtained by projecting light onto a population inversion, in which more electrons are distributed in the excited state than in the low-energy state in the semiconductor.

To continuously stimulate an animal in the awake state, light can be introduced by a fiber-optic cannula from a light source placed outside the body. However, the cannula is difficult to handle. If light sources and circuits are miniaturized, modularized, and attached to animals, unrestrained breeding will be possible. Some studies have used a small battery, a wireless power supply using electromagnetic fields, and infrared rays and solar cells to supply electricity to the light source.

Light stimulation is often generated in pulses, and its timing is generally controlled by an external controller. To make animals express multiple opsins, the wavelength of the light source should be switchable. To install a stimulus module onto an animal and stimulate it without restraint, researchers are using a device that allows them to apply the stimulus timing remotely through infrared signals.

## 42.3 Flexible Light Sources Based on Inorganic Semiconductors

### 42.3.1 Effects of Implanted Rigid Devices on Tissues

The propagation distance of light in biological tissue is limited to several millimeters. Therefore, inserting a light-emitting unit into the vicinity of the nerve tissue to be stimulated is necessary. If the device is rigid, then a mechanical stress will act on the neurons. If a rigid device is implanted in soft biological tissue, then the device hardly deforms even when the biological tissue deforms. Thus, stress concentrates in the tissue near the device. Peripheral nerves and the spinal cord deform when an animal moves, and small deformations occur repeatedly in the brain due to the pulsing of blood vessels. These mechanical stresses can lead to inflammation or interfere with nerve activity. In addition, in the process of encapsulation, tissue is formed between the device and the nerve tissue, which can cause the device function to deteriorate (Wisniewski and Reichert 2000). This is true not only in optogenetics but is a recognized problem for all internally implanted devices. Devices exist that use soft materials of excellent biocompatibility such as silicone, but most elements and parts that have electrical functions are composed of rigid materials.

### 42.3.2 Design and Fabrication of Flexible Devices

If creating these types of devices made of soft materials were possible, then much reduced mechanical stress would be applied to the cells. Therefore, reducing biological reactions such as inflammation and encapsulation would be feasible. Figure 42.1 shows micrographs of tissue sections a week after polyimide substrates of thicknesses of 128, 15, and 3 μm were subcutaneously implanted in rats. The 128-μm-thick substrate was rigid and therefore tissue hyperplasia occurred. By contrast, for the soft 3-μm-thick substrate, practically no hyperplasia occurred. In general, when a soft material is used, the device deforms along the surface of a tissue or organ, making it possible to cover the surface of the organ with a device or to wrap a device around a nerve fiber bundle. By arranging a light source to extend across the area to be optically stimulated, freely designing the area to be stimulated is possible.

LEDs are often made of inorganic semiconductors (e.g., GaN for a blue LED). The fact that the portion that uses the inorganic semiconductor is rigid is unavoidable. However, the light-emitting portion can be considerably miniaturized and then mounted on a flexible substrate to give flexibility to the whole device, as shown in Fig. 42.2 (Tomioka et al. 2017). Even when LEDs are to be arranged at many points, if the individual light sources can be sufficiently miniaturized, then the flexibility of the device will not suffer. Wiring can also be formed on a flexible substrate by depositing metals as thin films.

Representative materials for soft substrates are polyimides. They have excellent insulating capabilities, high mechanical strength, and high heat resistance, and they have been widely used in electronics industries. It is also known that polyimides have excellent biocompatibility. Transparent polyimides have also been developed. Internally implanted devices must also be waterproof, which means that after a device such as an LED is mounted on a substrate, it must be coated. As an example, coating material, parylene C can be used. Parylene C has excellent transparency, mechanical strength, and biocompatibility, and has been used as a coating material for medical devices. If a device is thin, then rigidity is required to insert it into the body. Therefore, a technique has been developed to bond a soft device onto a rigid needle-shaped substrate. The device is then inserted into the body, and the rigid substrate is detached and removed.

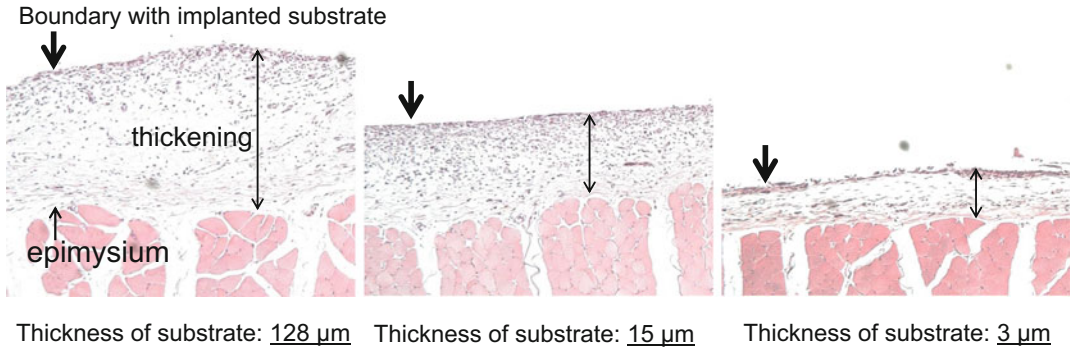


**Fig. 42.1** Hyperplasia of connective tissue as a foreign-body reaction to implanted film substrates. Thinner substrate exhibited less thickening because of reduced mechanical stimulation to tissues

### 42.3.3 Applications of Inorganic Devices

For the purpose of brain stimulation, various cases have been reported of devices in which inorganic micro LEDs are mounted on a soft substrate. For example, a device exists in which four GaN LEDs with sides of 50 μm in length are mounted on a thin flexible substrate, and the device can then be inserted like a needle (Kim et al. 2013). Platinum electrodes to record nerve activity and temperature sensors to monitor heat generation have been mounted together. Supplying power wirelessly to a device using radio waves is also possible. A monolithic device has been manufactured in which micro LEDs with sides of 22 μm in length are arranged in a two-dimensional array on a parylene C substrate, making it possible to turn on the arbitrary LEDs by selecting the row and column (Reddy et al. 2019). Recording electrodes have been mounted on both sides of a substrate to enable detailed recording of nerve activity. Finally, a case has been reported in which micro LEDs are arranged on a polyimide and implanted on the dura mater of the common marmoset to stimulate the brain (Komatsu et al. 2017). This implementation has proven successful for a period of several months.

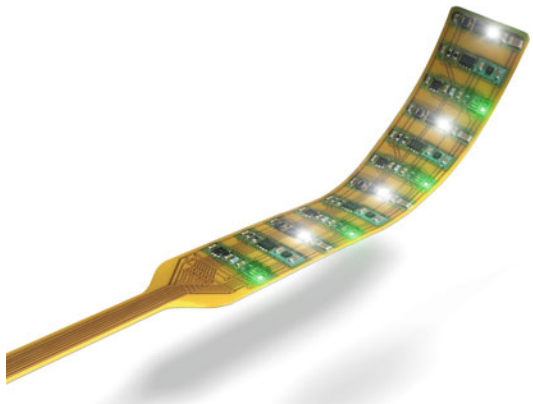

**Fig. 42.2** An array device of LED, temperature sensor, and phototransistor implemented on a flexible substrate. The device was developed for monitoring tissue circulation

Devices that are implanted in the spinal cord or on peripheral nerves require greater flexibility than for the brain. Thus, a case has been reported of mounting a micro LED on an elastomer substrate that can be stretched to stimulate the spinal cord of a mouse (Park et al. 2015). Antennas for wireless power supply have also been created on elastomer substrates, in which the conducting wire has a zigzag pattern to enable it to stretch. A cuff that uses micro LEDs has also been manufactured to stimulate the sciatic nerve of a mouse (Llewellyn et al. 2010). LEDs are placed around the sciatic nerve so that light can be irradiated from the circumference. Stimulation of the spinal cord and peripheral nerves is also important in future clinical applications.

As explained above, micro LEDs using inorganic semiconductors can be miniaturized to a size similar to that of a cell and are appropriate for light source patterning. Another advantage of inorganic semiconductors is their relatively high energy efficiency. However, when multiple LEDs are mounted on a single device, gaps must be provided between the LEDs to provide flexibility. Therefore, the area for light emission is limited to a given area of the device, and it must be kept in mind that the light intensity over the surface is not homogeneous.

## 42.4 Flexible Light Sources Based on Organic Semiconductors

### 42.4.1 Organic Semiconductors

Some organic materials exhibit properties characteristic of semiconductors. In materials that possess molecules with wide conjugated systems, such as polycyclic aromatic hydrocarbons, electrons can freely move through the electron cloud. Depending on the type of molecule, the material can be a p-type semiconductor, in which the movement of positive holes generates current, or an n-type semiconductor, in which the movement of electrons generates current. Devices that use organic semiconductors can achieve features that are impossible to achieve using inorganic semiconductors, such as the ability to flex and bend. Additionally, because organic semiconductors can be dissolved in solvents, they can be printed onto substrates. This process enables devices to be mounted on various substrates, such as paper and films, which adds the benefit of reducing construction costs in manufacturing processes. Furthermore, the device size is limited by wafer size when inorganic semiconductors are used, which is not the case in organic semiconductors, enabling significant increases in surface area. This characteristic can be utilized for a variety of applications, such as lighting, displays, photovoltaics, and bio-sensing devices (Someya et al. 2016).

### 42.4.2 Organic LEDs

Organic semiconductors can also be used in LED structures, and this technology is called organic LED (OLED). Electrons and positive holes are injected into the device by applying voltage to its cathodes and anodes. These electrons and holes pass through their respective electron transport layer and hole transport layer, joining at the light-emitting layer. The energy created by these couplings excites the luminescent material in the light-emitting layer. When these materials return to their ground state from the excited state, the released energy is emitted as light (Morton et al. 2016). A thin film of transparent indium tin oxide (ITO) is applied on the anode to enable transmission of light to the outside. Recently, OLED displays have been used for an increasing number of practical applications, and now hold a larger share of the market of small displays, such as those used in smartphones, than liquid crystal displays (LCDs). Various companies have been developing bendable displays as well. Additionally, OLED displays that are mere micrometers thick and can be rolled or stretched are in development and their applications in wearable devices are being explored as well (White et al. 2013).

Because OLEDs enable flexibility in the light-emitting components as well, the flexibility of a device is not compromised even when the light-emitting component is enlarged, unlike in the case of inorganic LEDs (Lochner et al. 2014; Bansal et al. 2015). Additionally, the ability to produce devices through printing makes OLEDs suitable for large-area devices. Inorganic LEDs and optical fibers are point light sources, whereas OLEDs are area light sources. The advantage of an area light source is that it can emit light with uniform intensity. With regard to stimulating specific areas of the brain or certain peripheral nerves, light with a uniform intensity is more stable, has high reproducibility, and achieves effective stimulation. When such devices are used to continuously stimulate animals, and the relative positions of the light device and the nerve tissue of animals fitted with these devices change as a result of

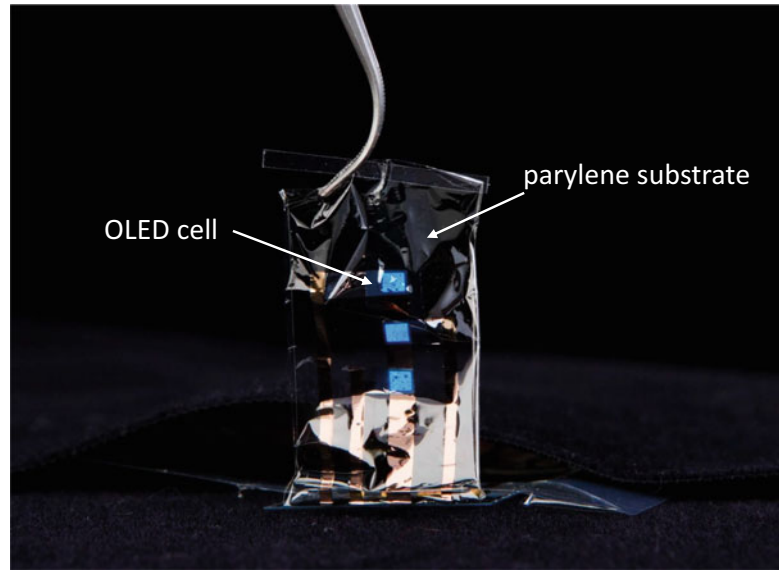


**Fig. 42.3** Ultrathin light source equipped with organic light-emitting diode (OLED) cells. The substrate is as thin as 2 μm

body motion, area light is less affected than point light.

When implanting devices inside a living organism, the devices must be disposable to reduce the risk of infection. OLEDs are suitable for disposable applications because the devices can be printed through low-cost processes. Additionally, the use of printing in the production of these devices also enables the light-emitting areas to be larger than a few millimeters per side.

Light-emitting materials used with OLEDs are easily degraded by moisture. For usage pertaining to displays, sealing the OLED components in glass largely impedes moisture penetration; however, when polymers and other flexible materials are used and the device is thin, moisture degradation can occur easily. Parylene C coating has a relatively high level of water resistance and can be used to seal OLED components (Yokota et al. 2016).

### 42.4.3 Applications of Organic Devices

Figure 42.3 depicts an example of a light source used for optical stimulation of nerves fabricated with OLEDs. The device has three light-emitting cells and is only 2 μm thick. It is made using exclusively nonmagnetic material for compatibility with MRI. The light emission spectrum has a peak of 455 nm and is suitable for ChR2 stimulation. With the photodiodes facing each other, the light output was measured to be 0.48 mW/mm$^2$, which is above the nerve excitation threshold. The electrodes were constructed using two layers of ITO and gold to achieve the aforementioned light intensity while suppressing losses using the high resistance of ITO. Consequently, the light-emitting efficiency at 10 V was increased to 2.4× that of ITO alone, reaching $4.3 \times 10^4$ Cd/m$^2$ and indicating the usefulness of two-layer electrode structures.

To verify the OLED optical stimulation, an experiment was conducted with rats. The gracilis muscle of their hind legs was exposed to stimulate the ends of the motor neurons expressing ChR2, and the OLED device was applied to the nerve fibers running over it. When the induced electromyogram was measured through the insertion of a needle electrode into the gracilis muscle, a muscle contraction response was recorded 4 ms after the stimulation, and movement of the lower limb corresponded with this stimulation. Even when muscle contraction occurred, the device could remain attached and supply stimulation due to the flexibility of the OLED surface.

As mentioned above, light sources that use organic semiconductors have unique properties, such as flexibility, and this technology is expected to be used in a broader range of applications in the future (Steude et al. 2016). Because the mobility of electrons and holes, which affects the performance of semiconductors, is generally lower for organic semiconductors than their inorganic counterparts, further research and development are needed on materials and device design to improve performance. Currently, device prototyping is being conducted almost exclusively in research laboratories; however, as the manufacturing processes become better developed, availability is expected to increase as well.

## 42.5 Optical Fibers and Waveguides

Optical fibers are composed of two layers: an inner core and an outer cladding material. The core has a higher refraction index than that of the cladding material. This results in the total reflection of light at the interface between the two materials, where light is transmitted through the core alone. The advantages of using optical fibers to transmit light from a light source to neurons include the following: optical fibers are minimally invasive in animals, the heat generated by the light source is not transferred to the cells, and optical fibers can be used to produce relatively low-cost systems. The light emitted from the tip is strongly directional along the axis of the fiber. As a result, the optical fiber must be kept in position to illuminate neurons. The pathway along which the light is transmitted can also be fabricated on a substrate. This is called a waveguide. Multichannel, integrated, and multifunctional devices can be produced by implementing light sources and waveguides on a substrate.

A device composed of micro-LEDs and needle waveguides arrayed on a flexible substrate has been reported (Kwon et al. 2015). SU-8 is used as the waveguide material, and the surface of the waveguide is coated in metal, which acts both to prevent light from leaking and as an electrode to record nerve activity. It is constructed to provide electric power wirelessly.

## 42.6 Multifunctional Light Sources

Outfitting a single device with an electrode and sensor along with a light source allows it to record the activity of nerves after optical stimulation and to monitor parameters such as temperature. However, when multiple light sources or sensors are placed on a device, the number of wires increases, which may result in a bigger or less-flexible device. Multiple light sources and sensors can share the same wiring, and the amount of wiring can be decreased by using electric circuits that incorporate transistors on the substrate. An overview of the multifunctional and flexible sensor and circuit technology of the device follows.

Gold or platinum are often used as flexible electrodes. Gold is a stable metal that is easy to pattern through deposition. It also has good adhesiveness on substrates made of materials such as parylene. However, when a large electric current such as that used for electrical stimulus is applied to gold, the gold may be damaged due to electrolysis. Using platinum is ideal for electrodes that are meant to conduct current. In addition, electrodes and wiring made of carbon materials such as carbon nanotubes have been developed. These nanostructured materials have excellent elastic properties (Cai et al. 2013).

The electric resistance of the wiring can be a source of noise when using an electrode to record nerve activity. Therefore, amplifying the signal from a position as close to the nerve as possible is ideal. Organic electrochemical transistors (OECTs) are transistors that incorporate ions from an electrolyte into a semiconductor channel to control the drain current. The injection of ions into the channel is controlled by a voltage applied to the gate. A method of using an OECT to amplify the electric potential of nerves directly has been reported, as shown in Fig. 42.4. This allows the electric potential evoked by optical

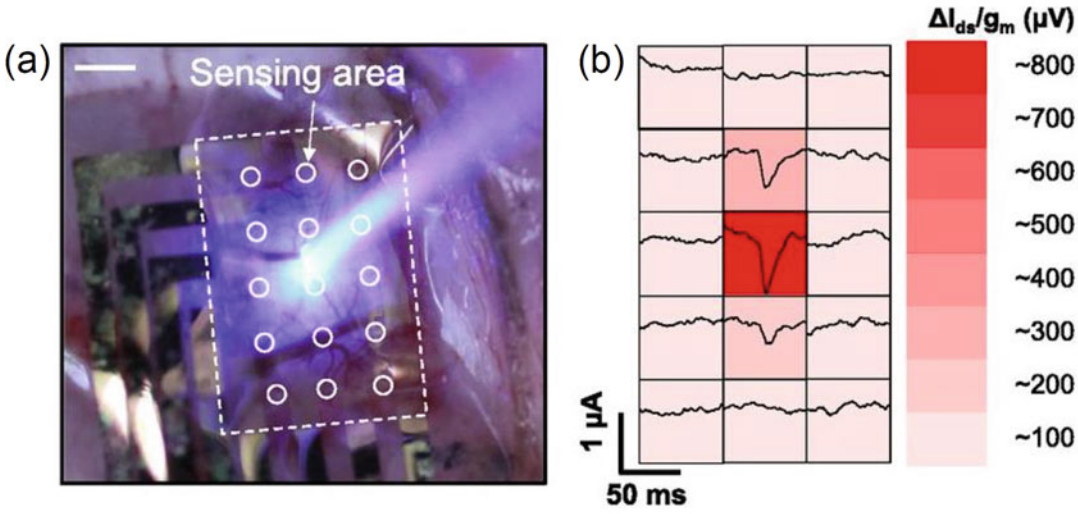


**Fig. 42.4** (**a**) Optical stimulation of the rat brain with neurons expressing ChR2. The light is applied through a transparent film device with organic electrochemical transistor (OECT) array. (**b**) The spatial distribution of the electrocorticogram measured by the 3 × 5 OECT array (Lee et al. 2017)

stimulation with high sensitivity to be recorded (Lee et al. 2017).

Heat generation accompanies strong optical stimuli. Therefore, monitoring the temperature of nerve tissue during optical stimulation is necessary. A flexible, high-sensitivity, positive-temperature coefficient (PTC) temperature sensor, which is used to measure body temperature, has been developed (Yokota et al. 2015). At temperatures approximating body temperature, the electric resistance of the polymer in the sensor changes rapidly and nonlinearly due to the phase change of the polymer. This gives this device its high sensitivity. The composition of the polymer can be adjusted to control the phase transition temperature.

Conducting optical stimulation and sensing at multiple points enables a spatial understanding of the propagation of nerve activity. However, having many channels on a substrate causes difficulties with the wiring. If the channels are arranged in a grid, an active matrix can be used in which each row and column has a wire running through it (Smith et al. 2014). Transistors are then placed where those wires intersect. This technology is generally used in displays. The general principle can be applied to measurements of physiological signals as well. Additional uses of the active elements of transistors and diodes include converting alternating current (which is used for wireless power supply) to direct current, which is used in circuits that generate the stimuli. Using organic semiconductors to produce these electronic circuits can vastly increase the flexibility of the device.

## 42.7 MRI Compatibility

Using electrodes to measure electric potential to record neural activity is suitable for recording local activity with high temporal resolution. In contrast, MRI is suitable for visualizing overall brain activity (Lee et al. 2010). MRI can also be used to grasp the transmission to a distant member from a cell that has been stimulated (Lee 2012; Abe et al. 2012). MRI detects changes in blood flow caused by the electrical activity of nerves.

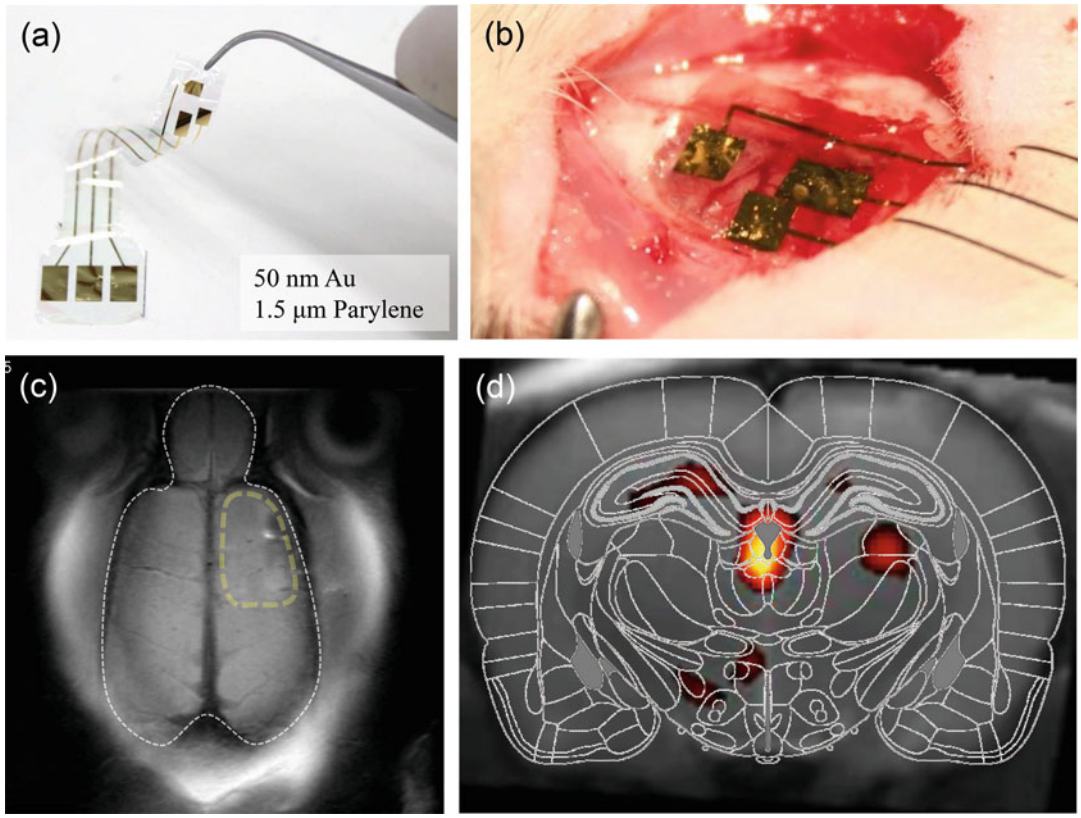


**Fig. 42.5** (**a**) An ultrathin flexible electrode for electrical stimulation of the rat brain. (**b**) The electrode conforms to the surface of the brain. (**c**) The electrode is compatible with MRI due to its thin metal layer. (**d**) Brain activities evoked by electric stimulations to the motor cortex (Kim et al. 2014)

MRI signals are based on magnetic resonance signals generated by hydrogen nuclei under a strong magnetic field. A magnetic resonance signal is generated as an electromagnetic wave ranging from tens to hundreds of megahertz in frequency. If a device enclosed in a living body contains ferromagnetic materials, the homogeneity of the magnetic field is distorted, and if the device contains a conductor, the transmission of the signals is affected. These effects cause defects in the images. Materials used in the optical fibers and waveguides are compatible with MRI. To ensure the MRI compatibility of an electronic device used for optical stimulation or measurement purposes, it is necessary not to use ferromagnetic materials and to minimize the use of conductors near the tissue to be imaged. As shown in Fig. 42.5, conductors such as conducting wires have no effect on obtaining MRI signals if they are drawn in thin films of sub-micrometers.

## 42.8 Future Prospects

We anticipate the flexible optical stimulation device introduced in this chapter to be broadly applied as an optogenetics research tool. Its performance, including light intensity, energy conversion efficiency, and mobility of holes and electrons, is also improving steadily. Organic semiconductor manufacturing technologies, including printing and sealing, are being established and can now be used for the mass

production of lighting and displays. Many manufacturing technologies are applicable in the fields of medical treatment and biotechnology, including optogenetics, and they are expected to accelerate the future development of optical stimulation devices. To search for clinical applications for optogenetics in the future, it is important that performance be improved while simultaneously guaranteeing safety. A method of guaranteeing the biological safety of semiconductor devices sealed with flexible materials is a technical challenge that must be overcome. Resolving these issues will permit the wide use of flexible devices. As stated above, adhesion with living tissue, mitigation of inflammation and other biological reactions, and the realization of area measurement and stimulation are characteristics that will be obtainable only using flexible devices.

**Acknowledgments** This chapter contains the outcome of the Exploratory Research for Advanced Technology (ERATO) of the Japan Science and Technology Agency (JST).

## References

Abe Y, Sekino M, Terazono Y et al (2012) Opto-fMRI analysis for exploring the neuronal connectivity of the hippocampal formation in rats. Neurosci Res 74:248–255

Ash C, Dubec M, Donne K et al (2017) Effect of wavelength and beam width on penetration in light-tissue interaction using computational methods. Lasers Med Sci 32:1909–1918

Bansal AK, Hou S, Kulyk O et al (2015) Wearable organic optoelectronic sensors for medicine. Adv Mater 27:7638–7644

Boyden ES, Zhang F, Bamberg E et al (2005) Millisecond-timescale, genetically targeted optical control of neural activity. Nat Neurosci 8:1263–1268

Cai L, Song L, Luan P et al (2013) Super-stretchable, transparent carbon nanotube-based capacitive strain sensors for human motion detection. Sci Rep 3:3048

Chow BY, Boyden ES (2013) Optogenetics and translational medicine. Sci Transl Med 5:177ps5

Fenno L, Yizhar O, Deisseroth K (2011) The development and application of optogenetics. Annu Rev Neurosci 34:389–412

Grosenick L, Marshel JH, Deisseroth K (2015) Closed-loop and activity-guided optogenetic control. Neuron 86:106–139

Jacques SL (2013) Optical properties of biological tissues: a review. Phys Med Biol 58:R37–R61

Kim T, McCall JG, Jung YH et al (2013) Injectable, cellular-scale optoelectronics with applications for wireless optogenetics. Science 340:211–216

Kim D, Chin Y, Reuveny A et al (2014) An MRI-compatible, ultra-thin, flexible stimulator array for functional neuroimaging by direct stimulation of the rat brain. Conf Proc IEEE Eng Med Biol Soc 2014:6702–6705

Komatsu M, Sugano E, Tomita H et al (2017) A chronically implantable bidirectional neural interface for non-human primates. Front Neurosci 11:514

Kwon KY, Lee HM, Ghovanloo M et al (2015) Design, fabrication, and packaging of an integrated, wirelessly-powered optrode array for optogenetics application. Front Syst Neurosci 9:69

Lee JH (2012) Informing brain connectivity with optogenetic functional magnetic resonance imaging. NeuroImage 62:2244–2249

Lee JH, Durand R, Gradinaru V et al (2010) Global and local fMRI signals driven by neurons defined optogenetically by type and wiring. Nature 465:788–792

Lee W, Kim D, Matsuhisa N et al (2017) Transparent, conformable, active multielectrode array using organic electrochemical transistors. Proc Natl Acad Sci U S A 114:10,554–10,559

Llewellyn ME, Thompson KR, Deisseroth K et al (2010) Orderly recruitment of motor units under optical control in vivo. Nat Med 16:1161–1165

Lochner CM, Khan Y, Pierre A et al (2014) All-organic optoelectronic sensor for pulse oximetry. Nat Commun 5:5745

Morton A, Murawski C, Pulver SR et al (2016) High-brightness organic light-emitting diodes for optogenetic control of Drosophila locomotor behaviour. Sci Rep 6:31117

Onuki Y, Bhardwaj U, Papadimitrakopoulos F et al (2008) A review of the biocompatibility of implantable devices: current challenges to overcome foreign body response. J Diabetes Sci Technol 2:1003–1015

Park SI, Brenner DS, Shin G et al (2015) Soft, stretchable, fully implantable miniaturized optoelectronic systems for wireless optogenetics. Nat Biotechnol 33:1280–1286

Reddy JW, Kimukin I, Stewart LT et al (2019) High density, double-sided, flexible optoelectronic neural probes with embedded μLEDs. Front Neurosci 13:745

Senova S, Scisniak I, Chiang CC et al (2017) Experimental assessment of the safety and potential efficacy of high irradiance photostimulation of brain tissues. Sci Rep 7:43,997

Smith JT, O'Brien B, Lee YK et al (2014) Application of flexible OLED display technology for electro-optical stimulation and/or silencing of neural activity. J Display Technol 10:514–520

Someya T, Bao Z, Malliaras GG (2016) The rise of plastic bioelectronics. Nature 540:379–385

Steude A, Witts EC, Miles GB et al (2016) Arrays of microscopic organic LEDs for high-resolution optogenetics. Sci Adv 2:e1600061

Stujenske JM, Spellman T, Gordon JA (2015) Modeling the spatiotemporal dynamics of light and heat propagation for in vivo optogenetics. Cell Rep 12:525–534

Tomioka Y, Enomoto S, Gu J et al (2017) Multipoint tissue circulation monitoring with a flexible optical probe. Sci Rep 7:9643

White MS, Kaltenbrunner M, Głowacki ED et al (2013) Ultrathin, highly flexible and stretchable PLEDs. Nat Photonics 7:811–816

Wisniewski N, Reichert M (2000) Methods for reducing biosensor membrane biofouling. Colloids Surf B Biointerfaces 18:197–219

Yawo H, Asano T, Sakai S et al (2013) Optogenetic manipulation of neural and non-neural functions. Develop Growth Differ 55:474–490

Yokota T, Inoue Y, Terakawa Y et al (2015) Ultraflexible, large-area, physiological temperature sensors for multipoint measurements. Proc Natl Acad Sci U S A 112:14,533–14,538

Yokota T, Zalar P, Kaltenbrunner M et al (2016) Ultraflexible organic photonic skin. Sci Adv 2: e1501856

Zhang F, Aravanis AM, Adamantidis A et al (2007) Circuit-breakers: optical technologies for probing neural signals and systems. Nat Rev Neurosci 8: 577–581

# Holographic Imaging and Stimulation of Neural Circuits

43

Weijian Yang and Rafael Yuste

**Abstract**

A critical neuroscience challenge is the need to optically image and manipulate neural activity with high spatiotemporal resolution over large brain volumes. The last three decades have seen the development of calcium imaging to record activity from neuronal populations, as well as optochemistry and optogenetics to optically manipulate neural activity. These methods are typically implemented with wide-field or laser-scanning microscopes. While the former approach has a good temporal resolution, it generally lacks spatial resolution or specificity, particularly in scattering tissues such as the nervous system; meanwhile, the latter approach, particularly when combined with two-photon excitation, has high spatial resolution and specificity but poor temporal resolution. As a new technique, holographic microscopy combines the advantages of both approaches. By projecting a holographic pattern on the brain through a spatial light modulator, the activity of specific groups of neurons in 3D brain volumes can be imaged or stimulated with high spatiotemporal resolution. In a combination of other techniques such as fast scanning or temporal focusing, this high spatiotemporal resolution can be further improved. Holographic microscopy enables all-optical interrogating of neural activity in 3D, a critical tool to dissect the function of neural circuits.

**Keywords**

Calcium imaging · Holography · Microscopy · Optochemistry · Optogenetics · Photostimulation · Two-photon · Wavefront shaping · Neural activity

## Abbreviations

| | |
|---|---|
| BFP | Back focal plane |
| CGH | Computer-generated holography |
| CNMF | Constrained nonnegative matrix factorization |
| DMD | Digital mirror device |
| FFP | Front focal plane |
| GPC | Generalized phase contrast |
| GS | Gerchberg–Saxton |
| PMT | Photomultiplier tube |

The original version of this chapter was revised by updating Table 43.1. The correction to this chapter can be found at https://doi.org/10.1007/978-981-15-8763-4_45

W. Yang (✉)
Department of Electrical and Computer Engineering, University of California, Davis, CA, USA
e-mail: wejyang@ucdavis.edu

R. Yuste
Neurotechnology Center, Department of Biological Sciences, Columbia University, New York, NY, USA

Donostia International Physics Center, DIPC, San Sebastian, Spain
e-mail: rmy5@columbia.edu



H. Yawo et al. (eds.), *Optogenetics*, Advances in Experimental Medicine and Biology 1293,
https://doi.org/10.1007/978-981-15-8763-4_43

| | |
|---|---|
| PSF | Point spread function |
| ROI | Region of interest |
| SLM | Spatial light modulator |
| SNR | Signal-to-noise ratio |
| TF | Temporal focusing |
| ZB | Zeroth-order beam block |

## 43.1 Introduction

One major challenge in science is to decipher how the brain works. The ability to image and manipulate neural activity in high spatiotemporal resolution is critical to dissect the function of neural circuits, a key step toward understanding how behaviors and mental states emerge from the activity of neurons and their interactions. Historically, the individual neuron was considered as the structural and functional unit in the nervous system by the so-called neuron doctrine (Shepherd 1991) by Cajal (Ramón y Cajal 1888) and Sherrington (Sherrington 1906). However, neuronal ensembles, which are groups of neurons functionally linked together and which show coherent neuronal activity, could be the basic functional units of the brain (Harris et al. 2003; Hebb 1949; Yuste 2015). Thus, it becomes critical to study the neuronal activity of a large population of neurons. Many approaches can be used to record and stimulate neuronal activity. Electrophysiology techniques such as patch clamp have subcellular spatial resolution and high temporal resolution. However, only a few cells can be probed at a time, and is challenging to perform it in vivo. Multielectrode arrays can record activity among hundreds of cells (Jun et al. 2017), but they lack spatial resolution and are highly invasive. Functional magnetic resonant imaging (fMRI) is noninvasive and can image the whole brain but in a tradeoff of low spatiotemporal resolution.

Optical microscopy fits in between electrophysiology and fMRI, offering subcellular resolution, high temporal resolution (>10 Hz) over a large field view (millimeter scale). When using efficient light-base sensors or actuators of neuronal activity, optical microscopy offers an ideal platform to read and write neuronal activity and to study and manipulate neuronal circuits. Using microscopes, light is delivered to brain tissue to image neuronal activity-dependent fluorescence from the sensors, or to stimulate (excite or suppress) neuronal activity through the actuators. Depending on the applications, the sample can either be illuminated over a wide field or through a scanning spot. In the former approach, a large area of the sample is illuminated simultaneously. This yields a good temporal resolution, but suffers from a poor spatial resolution or specificity, as the brain scatters light. Alternatively, in the scanning approach, the illumination is confined to be a spot that is temporally scanned across the sample. This generates a superior spatial resolution or specificity but with relatively poor temporal resolution. Holographic illumination, which has only recently been used in optical microscopes for neuroscience applications (Lutz et al. 2008; Nikolenko et al. 2008; Packer et al. 2012; Quirin et al. 2014; Watson et al. 2010; Yang et al. 2018, 2016), combines the advantages of wide-field illumination and point scanning. Instead of illuminating a large volume of samples at once or only in a small spot, a programmable holographic pattern can illuminate a region of interest designated by the users and can achieve both high spatial and temporal resolution or specificity in imaging or photostimulation. Because of these advantages, holographic microscopy has been playing an increasingly important role in neuroscience, particularly for high precision manipulation of neuronal activity.

In this chapter, we present the principle of holographic microscopy and discuss how it is applied in neuroscience. In Sect. 43.2, we provide the necessary background of optical microscopy, its application to image and manipulate neuronal activity, as well as computer-generated holography. In Sects. 43.3 and 43.4, we discuss techniques of holographic imaging and photostimulation of neural activity. In Sect. 43.5, we examine how all-optical holographic methods—combining imaging and photostimulation, can enable new investigation in neural circuits. Finally, in Sect. 43.6, we provide our outlook on the future of this field.

## 43.2 Background

### 43.2.1 Optically Imaging Neural Activity

Unlike electrical or biochemical signals, optical signals are not intrinsic signaling mechanisms in the central neural system. Thus, to detect neural activity optically, one needs to incorporate light-base neural activity sensors into the cells. A common neural activity sensor is a calcium indicator, which contains a calcium sensor and a chromophore. When calcium binds to the indicator, the intramolecular conformational changes lead to a change in the fluorescence emission. As a result, the calcium indicator can optically report the intracellular free calcium ion concentration ($[Ca2^{+}]_i$), which serves as an indirect reporter of neuronal activity (Smetters et al. 1999). The early generation of calcium indicators was chemical based, where the highly calcium-selective chelators like EGTA or BAPTA were hybridized with a fluorescent chromophore (Tsien 1980) (Fig. 43.1a). Using cell loading (such as through electrode into a single cell, or acetoxymethyl ester into a large population), indicators such as fura-2 became widely used in neuroscience (Yuste and Katz 1991), with Oregon Green BAPTA and fluo-4 dye families as more recent representatives (Paredes et al. 2008). The latter generation of calcium indicators were protein-based genetically encoded calcium indicators (GECIs) (Miyawaki et al. 1997) (Fig. 43.1b). They can be cell-type-specific and have a maintained and wide expression in the nervous system through viral transduction, in utero electroporation, or transgenic animal models. While the early GECIs suffers from poor sensitivity and slow kinetics, the most recent developed GECI, particularly GcaMP6 (Chen et al. 2013), and jGCaMP7 (Dana et al. 2019) have very high sensitivity toward single spike and fast kinetics. For a review of calcium indicators, the readers are referred to (Grienberger and Konnerth 2012).

A straightforward approach to perform calcium imaging is through epifluorescence microscopy (Yuste and Katz 1991), where excitation light illuminates the sample in a large volume, and the fluorescence is detected across a wide field with a camera (Fig. 43.2a). While the wide-field illumination and detection results in high frame rates, the out-of-focus emission not only yields phototoxicity but also blurs the signal at the focal plane. Furthermore, epifluorescence microscopy only works well in transparent samples, thin slices, or the superficial layers of scattering tissues, as optical scattering could induce significant crosstalk between pixels in the camera, and effectively degrade the spatial resolution. Another imaging modality is laser scanning microscopy, represented by confocal microscopy (Pawley 2006; Petran et al. 1968) and two-photon microscopy (Denk et al. 1990; Yuste and Denk 1995). In confocal microscopy, a single spot is scanned across the sample; the emitted fluorescence is spatially filtered by a pinhole and detected by a photomultiplier tube. While the out-of-focus light can be suppressed at detection, the excitation light still forms a double cone illumination pattern in the sample (Fig. 43.2d), resulting in fluorescence emission in the out-of-focus regions and thus phototoxicity. Through light scattering, the out-of-focus fluorescence could also pass the pinhole and thus contaminate the signal. Thus, confocal microscopy is also not immune to light scattering. Two-photon microscopy (Fig. 43.2b), on the other hand, resolves these issues. The excitation efficiency is proportional to the square of the light intensity, thus, effectively, only the focal point generates fluorescence excitation. A pinhole is no longer needed, yielding a higher collection efficiency at the photomultiplier tube. The longer wavelength of the excitation light enables its deeper penetration into the tissue as it experiences less scattering. While two photon has a superior spatial resolution and signal-to-background ratio, the imaging formation through scanning, like in all laser scanning applications, significantly reduces the imaging speed.

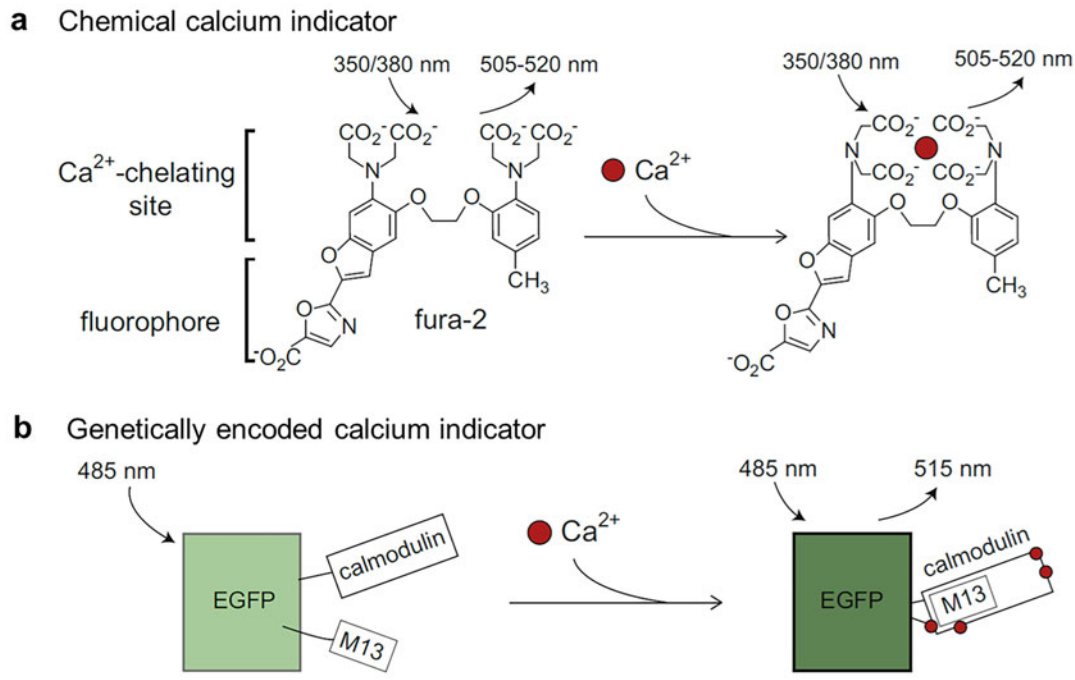


**Fig. 43.1** Calcium indicators. (**a**) Chemical calcium indicator. Fura-2 is excitable by 350/380 nm light and emits fluorescence peaks in between 505 and 520 nm. The binding of calcium ions into fura-2 results in changes in fluorescence emission. (**b**) An example of a genetically encoded calcium indicator. The binding of calcium ions into GCaMP leads to a conformational intramolecular change, resulting in an increase in the fluorescence emission at 515 nm. Reprinted with permission from (Grienberger and Konnerth 2012), Elsevier

### 43.2.2 Optically Manipulating Neural Activity

As the counterpart of reading neural activity through imaging calcium sensors, writing neural activity can be achieved through photostimulating neural activity actuators. There are two different methods to optically manipulate neural activity: optochemistry and optogenetics. In optochemistry, neurotransmitters are used to regulate neuronal activity and are attached to a light-activated molecule, a chemical "cage." Upon light excitation, the neurotransmitters detach from the cage, bind to receptors in the cell membrane, and thus regulate the neuronal activity (Adams and Tsien 1993; Ellis-Davies 2007). In optogenetics, light-sensitive ion channels can be incorporated in cell membranes through the expression of the genetically encoded opsins. Upon light excitation, these ion channels could open or close, regulating the neuronal activity (Boyden et al. 2005; Nagel et al. 2003).

Similar to imaging, there are two typical light illumination approaches for photostimulation: wide-field illumination and point scanning. Wide-field illumination stimulates a large volume of brain tissue, lacking cellular-level spatial resolution. This method is often used for in vivo optogenetics. While activating many neurons across a brain volume all together may produce a strong physiological effect, the lack of spatial specificity can generate off-target effects. Furthermore, without single-cell resolution, the specificity of optogenetics relies on molecular selectivity. This thus does not allow the study of causality within a molecularly defined population or between functionally rather than molecularly defined populations. Point scanning (one photon for cultured neurons or thin brain slices, and two photon for scattering samples), on the other hand,

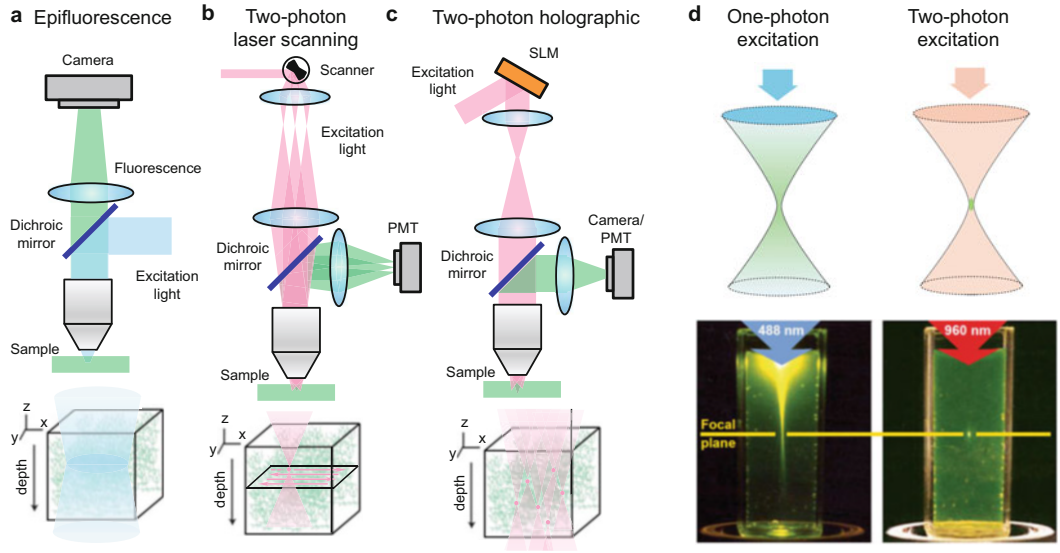


**Fig. 43.2** Basic types of microscopy. (**a**) Epifluorescence microscopy with wide-field illumination. The sample is illuminated by the excitation light over a large volume. (**b**) Two-photon laser scanning microscopy with point scanning illumination. The laser spot raster scans the sample. Only one single spot is excited at a time. (**c**) Two-photon holographic microscopy. User defined regions of interest (ROIs) can be illuminated simultaneously. (**d**) Comparison between one-photon and two-photon illumination. Top, in one-photon microscopy, visible light (indicated by blue color) is used for excitation, and an entire cone of fluorescence light (green) is generated; in two-photon microscopy, near infrared (indicated by red color) is used for excitation, and the fluorescence generation is localized to the vicinity of the focal spot. Reprinted with permission from (Helmchen and Denk 2005), Springer Nature. Bottom, an experimental illustration of the one-photon and two-photon excitation. The NA is 0.16 for both cases. Reprinted with permission from (Zipfel et al. 2003), Springer Nature

can stimulate neurons one by one. While it has a high spatial resolution, it suffers from a low temporal resolution.

### 43.2.3 Computer-Generated Holography

As discussed above, the two predominant light illumination approaches have a tradeoff between spatial and temporal resolution. Holographic illumination through computer-generated holography (Fig. 43.2c) can overcome this tradeoff. A hologram is a three-dimensional (3D) light field, which in principle can form any arbitrary light patterns by design. It is mostly used for 3D display (Georgiou et al. 2008). In biology, it has been used to generate discrete light patterns for particle trappings in optical tweeters (Reicherter et al. 1999). By designing the patterns to match the shape of desirable regions of interest (ROIs) over the 3D space in the tissue, these ROIs can be imaged or stimulated, either using one-photon (Lutz et al. 2008) or two-photon light (Nikolenko et al. 2008). As the light field at the front focal plane (in object space) and back focal/aperture plane of the objective lens forms a Fourier transform pair, to generate the desired holographic light pattern in the object space, one can simply modulate the light field at the back aperture plane of the objective lens. This can be implemented by a spatial light modulator (SLM) (Fig. 43.3a). While the SLM could modulate both the *phase* and *amplitude* of the light field, commonly used liquid-crystal-based SLMs only modulate the *phase* of the light field. By using fast iterative computation algorithms such as Gerchberg–Saxton (GS) algorithm (Gerchberg and Saxton

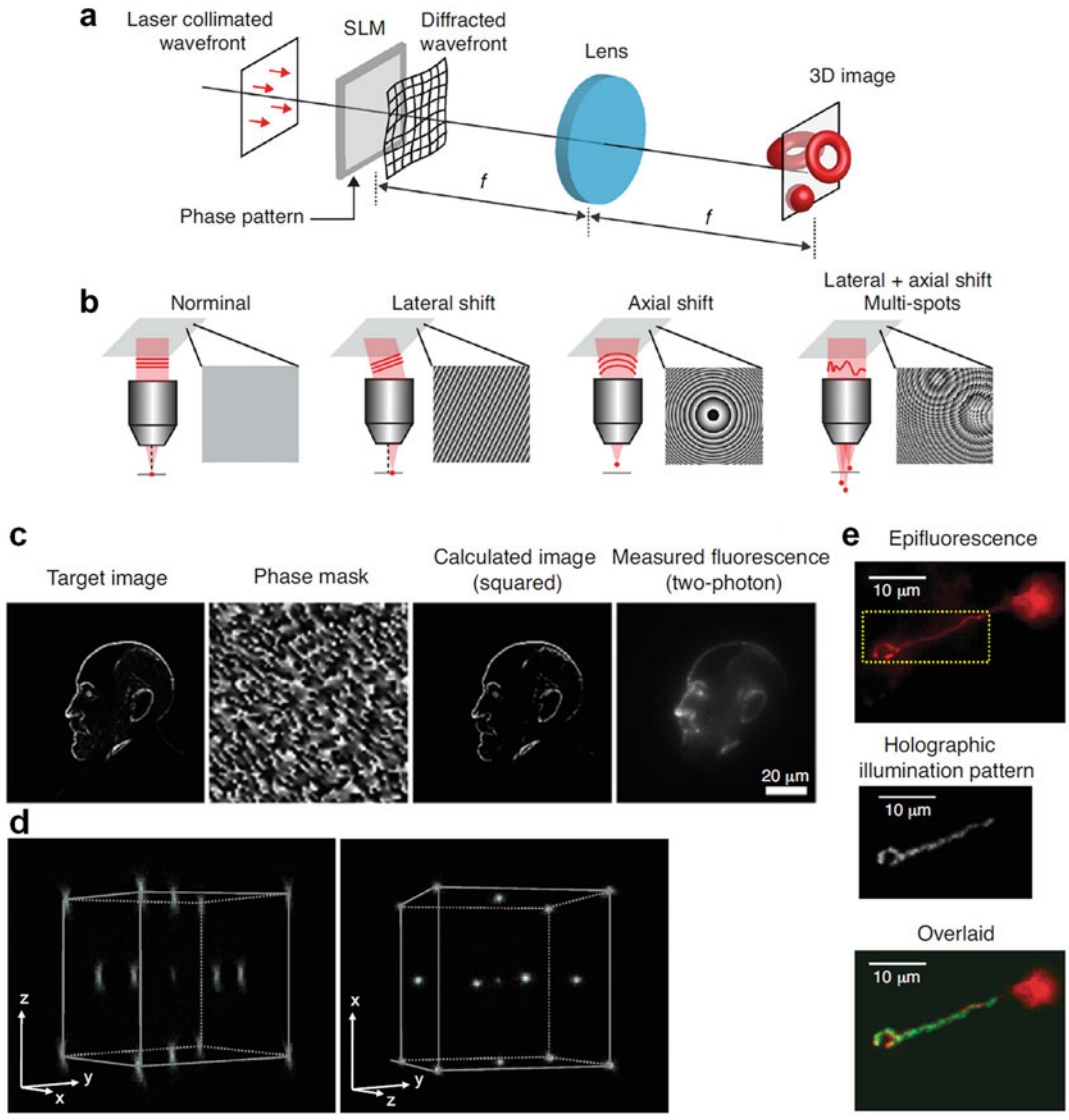


**Fig. 43.3** Computer-generated holography. (**a**) Schematic of the experimental setup to generate a 3D image pattern through computer-generated holography. The SLM modulates the wavefront of the input light through a spatial phase pattern. The lens performs a Fourier transform, and a 3D pattern can be formed in the imaging space. *f*, the focal length of the lens. Reprinted with permission from (Yang and Yuste 2018), Elsevier. (**b**) Phase holograms at the back aperture of the objective lens and the corresponding spot diagrams in the image space. Reprinted with permission from (Yang and Yuste 2018), Elsevier. (**c**) Example of a two-photon SLM hologram. The four panels illustrate the binary target image, the SLM phase hologram generated by the GS algorithm, the squared image (to mimic two-photon excitation) of the projected pattern back calculated from the phase hologram, and the experimentally measured two-photon fluorescence image generated by the SLM. A stylized picture of Cajal is used as a target image. Reprinted from (Nikolenko et al. 2008). (**d**) An example of a 3D spots pattern generated by computer-generated holography. The experimentally measured result is visualized in the side view (left) and axial view (right). The size of the guided cube is $20 \times 20 \times 20\ \mu m^3$. Reprinted with permission from (Yang et al. 2011), IOP publishing. (**e**) An example of excitation light shaping to match the fine cellular processes. Top, wide-field epifluorescence image of a cerebellar granule cell. Middle, illumination pattern generated to match the selected region of interest in the dashed box in the top panel. Bottom, overlaid image of the top and middle panel. Reprinted with permission from (Lutz et al. 2008), Springer Nature

1972), the phase pattern at the SLM (typically termed as a mask) can be calculated. This phase pattern is imposed onto the light incident onto the SLM. The output light passes through the objective lens and forms the desired pattern in the object space through interference. Essentially, the SLM performs the wavefront shaping, redistributes the power of incident light, and sculpts it into the targeted light intensity pattern. Various patterns can be formed, ranging from simple laterally or axially shifted spot from nominal focus, to multiple focal spots in 3D, and more complex patterns (Fig. 43.3b–e). An SLM can switch between different phase patterns in as short as 1 ms (Thalhammer et al. 2013), and could target different ROIs through time multiplexing. High pixel count with large array area (e.g., 1536 × 1536 pixel counts, 30.7 × 30.7 $mm^2$) SLMs are commercially available and they have high diffraction efficiency (>0.85) across a large steering angle (Marshel et al. 2019). Besides *phase*-only SLM, the *amplitude*-only SLM, such as a digital mirror device (DMD), can also be used to project patterns into the sample. This can be fulfilled using Lee hologram in a more complex optical setup, though it suffers from a very low light efficiency (Lee 1974). Alternatively, an imaging system can be used to directly map the amplitude pattern at the SLM to the sample with a scaling factor. This latter case is no longer a hologram and it cannot perform 3D patterning. It has a low light efficiency as the amplitude mask could block the majority of the incident light. Nevertheless, it finds application in one photon photostimulation in cultured neurons, brain slices or transparent samples (Wang et al. 2007; Zhu et al. 2012). For two-photon applications, where there is a limited laser power budget, the dominantly used SLMs are phase only, as they have a much higher power efficiency. In the following discussion, all SLMs are referred to as being phase only.

### 43.2.4 Summary of Three Different Light Illumination Approaches

We summarize this section in Table 43.1, which compares the advantages and limitations of the three different light illumination approaches for both imaging and photostimulation applications. In general, wide-field illumination is the simplest with the one-photon setting. It can achieve a very high temporal resolution, but it has a limitation in axial resolution, and low spatial specificity for photostimulation. Point scanning illumination has a good spatial resolution or specificity, particularly using two-photon light; however, as scanning is required, it has a low temporal resolution. Holographic illumination combines the advantage of the two and can achieve a good spatiotemporal resolution. It is the central topic in the following sessions.

## 43.3 Holographic Imaging of Neural Activity

The key feature of a hologram is to illuminate desirable ROIs simultaneously. Though it can be applied in one-photon imaging, its main application for imaging lies in two-photon microscopes. A one-photon hologram generally lacks axial confinement (see the double cone shape in Fig. 43.2d), so it is more applicable to image cultured neurons or thin brain slides, where epifluorescence microscopy is already well suited. A two-photon hologram, on the other hand, has tight axial confinement and can penetrate deep into the tissue. When applying in imaging, it can increase the temporal resolution compared with conventional two-photon laser scanning microscopy and shows many unique features. In the following, we discuss two different implementation approaches of a two-photon holographic microscope.

### 43.3.1 Extended Depth of Field Detection

One-photon epifluorescence microscopy uses wide-field illumination and a camera for wide-field detection, whereas two-photon microscopy typically uses point scanning for illumination and a single pixel detector for point detection. Two-photon holographic illumination creates a unique opportunity to hybridize these two

**Table 43.1** Comparison between different light illumination approaches used in optical microscopes

| | | | Wide-field illumination | Point scanning illumination | Holographic illumination |
|---|---|---|---|---|---|
| Imaging | Transparent sample | Technique | Epifluorescence (one photon) | Confocal (one photon) | Two-photon |
| | | Advantage | High temporal resolution | High spatial resolution | Low background; high spatial resolution; improved temporal resolution |
| | | Limitation | Low axial resolution; phototoxicity | Reduced temporal resolution; phototoxicity | |
| | Scattering sample | Technique | Epifluorescence (one photon), mainly for superficial layers | Two photon | Two photon |
| | | Advantage | High temporal resolution | Low background; high spatial resolution | Low background; high spatial resolution; improved temporal resolution |
| | | Limitation | High background; low spatial resolution; phototoxicity | Low temporal resolution | |
| Photo stimulation | Transparent sample | Technique | One photon | One photon/two photon | One photon/two photon |
| | | Advantage | High temporal specificity | Improved/high spatial specificity | Improved/high spatial specificity; high temporal specificity |
| | | Limitation | Low spatial specificity | Low temporal specificity | |
| | Scattering sample | Technique | One photon | Two photon | Two photon |
| | | Advantage | High temporal specificity | High spatial specificity | High spatial specificity; high temporal specificity |
| | | Limitation | Low spatial specificity | Low temporal specificity | |

conventional microscopy techniques and leverage their advantages. Here, the regions of interest, for example, a group of neurons, can be simultaneously illuminated with a two-photon hologram (Fig. 43.4a, path 1). Their fluorescence can then be recorded through a camera. There are multiple unique features in this imaging method. First of all, the two-photon excitation ensures tight axial confinement and thus eliminates any out-of-focus fluorescence that would occur in one-photon microscopy. Secondly, through the hologram, the sparsity of the excitation pattern can be controlled. Both features can greatly reduce the background fluorescence, and make the system more resistant to tissue scattering. Thirdly, compared to conventional laser scanning two-photon microscopy, the usage of a camera to record the fluorescence greatly increases the imaging speed. Furthermore, this scanless approach allows a greatly increased excitation dwell time on the ROIs, leading to an improved signal-to-noise ratio. Finally, 3D imaging can be achieved by applying the 3D holographic pattern and extended depth of field detection (Fig. 43.4a, path 1). Typically, only the objects in the objective focal plane get imaged sharply in the camera; objects outside the focal plane look blurred and lose spatial resolution and signal strength. The depth information essentially gets lost in the camera image. But in the extended depth of field scheme, a cubic phase plate is placed before the camera in the detection pathway (Quirin et al. 2014, 2013). The cubic phase generates a very special point spread function (PSF) (Fig. 43.4b), which can stay laterally confined over a large axial range. As a result, the objects can stay in

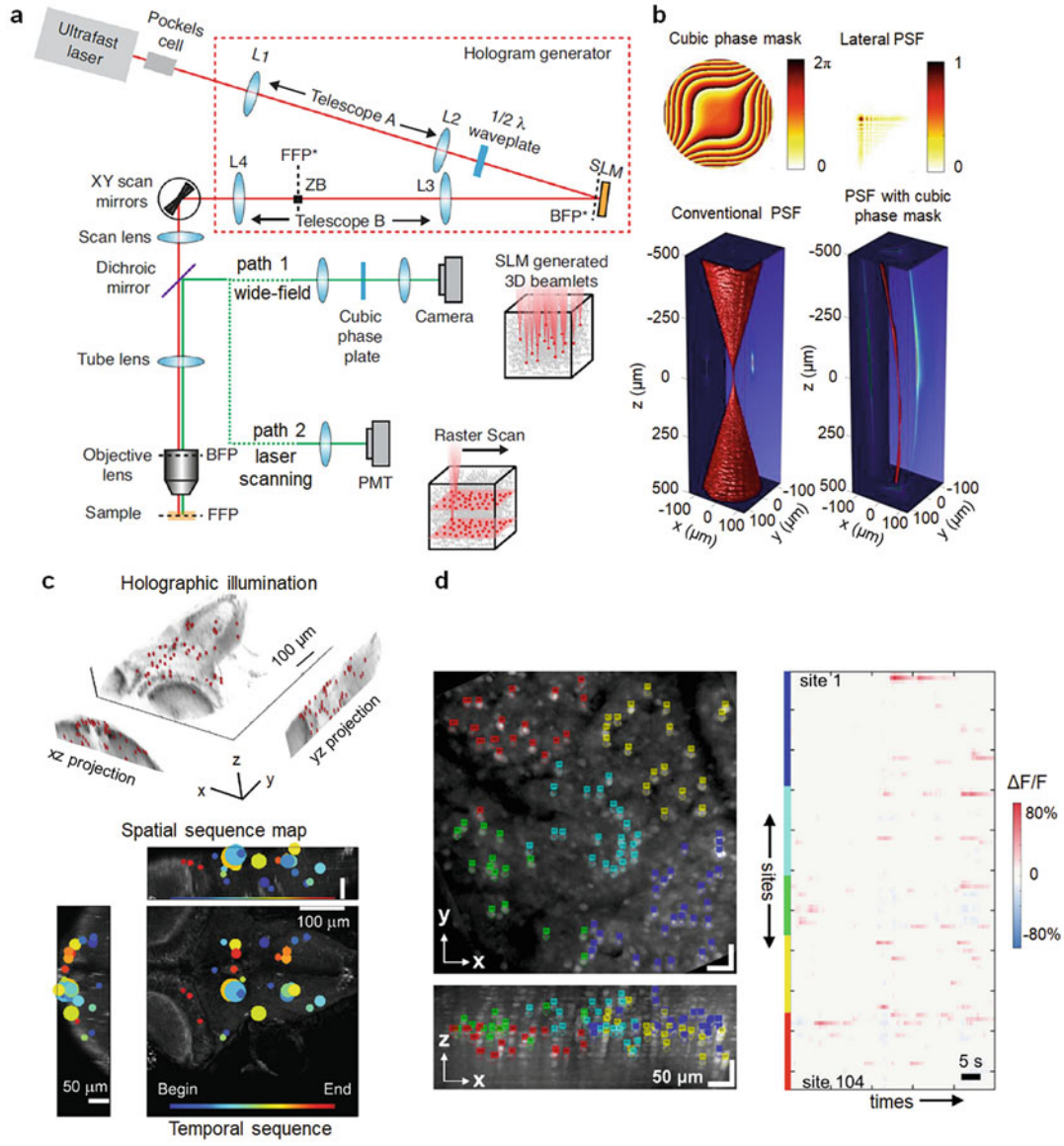


**Fig. 43.4** Two-photon scanless imaging with extended depth of field detection. (**a**) Schematics of a two-photon holographic illumination microscope. The hologram generator is composed of two telescopes for beam size conversion, an SLM, a half waveplate to align the laser polarization to the active axis of the SLM, and a zeroth-order beam block (ZB) to remove the residue light that is not modulated by the SLM. The SLM is at the conjugate plane (BFP*) of the back focal plane (BFP) of the objective lens. The ZB is at the conjugate plane (FFP*) of the front focal plane (FFP) of the objective lens. The microscope can be configured for wide-field detection with a camera (and extended depth of field technique) (path 1, XY scan mirror is optional), or laser scanning with a PMT as detector (path 2). Reprinted and adapted with permission from (Yang and Yuste 2018), Elsevier. (**b**) Top, cubic phase mask and the 2D PSF. Bottom, 3D PSF of the conventional microscope and the extended depth of field microscope using cubic phase mask. The 3D volume represents the 50% intensity cutoff of each axial plane. Reprinted with permission from (Quirin et al. 2013), Optical Society of America. (**c**) Simultaneous 3D imaging of 49 neurons in larval zebra fish at 30 Hz using two-photon scanless imaging with extended depth of field detection (cubic phase mask). Top, 3D distribution of the neurons to be imaged. Bottom, 3D projection of the recorded images of the larval zebra fish into *xy*, *xz*, *zy* views, revealing the spatial patterns of its temporal activity events. Reprinted from (Quirin et al. 2014). (**d**) 3D imaging of 104 neurons in mouse cortex at 10 Hz. Different groups of neurons (denoted by different color) were imaged by switching the hologram (and the offset angle of the XY galvanometer mirrors in the beam path). The extracted temporal fluorescence signal from all these neurons is shown on the right panel. Reprinted with permission from (Yang et al. 2015), Optical society of America

focus over a large depth range. Using this strategy, the neural activity of 49 neurons distributed within a 350 × 350 × 150 μm$^3$ volume in larval zebra fish was simultaneously imaged in 30 Hz (Quirin et al. 2014) (Fig. 43.4c). In addition to the cubic phase mask, a light field detection scheme can also be applied to achieve an extended depth of field detection (Yang et al. 2015). In this strategy, a microlens array is added into the detection path so that both the spatial and angular information of the light field from the imaged ROIs can be recorded at the camera. The image of individual ROIs at different depth can then be reconstructed. Using this approach and time multiplexing, where different groups of ROIs are imaged by switching the hologram (and the offset angle of the XY galvanometer mirrors in the beam path), 104 neurons across a 600 × 600 × 200 μm$^3$ volume in mouse cortex was imaged at 10 Hz (Yang et al. 2015) (Fig. 43.4d).

These strategies leverage sparse excitation through a two-photon laser so they can image deeper than the conventional epifluorescence microscopy with a camera. As the imaging depth increases, scattering eventually creates significant crosstalk between pixels in the camera, making it challenging to distinguish different imaged ROIs. The imaging approach discussed in the following section overcomes this limitation.

### 43.3.2 Multiplane Imaging

Compared with wide-field detection, two-photon laser scanning with the fluorescence detected by a single pixel detector (typically a photomultiplier tube [PMT]) can image much deeper into the tissue. However, its imaging speed is limited as only one single laser spot scans the sample. If multiple beams are used to scan the sample and the resulting fluorescence signals can be separated, the imaging speed can be increased. We recently developed such a two-photon holographic multiplane imaging technique (Yang et al. 2016) (Fig. 43.4a, path 2). We holographically create multiple diffraction-limited laser foci distributed across a 3D brain volume. These focal spots are then scanned simultaneously in the lateral direction, each imaging the neuronal activity at a specific plane. As the PMT integrates fluorescence signals generated at each focus, the resulting image is a superposition of the images generated by the individual laser focus (Fig. 43.5a). To separate the signals, we use a constrained nonnegative matrix factorization (CNMF) algorithm (Pnevmatikakis et al. 2016). This algorithm decomposes the recorded fluorescence signal (represented by a matrix with the two dimensions being spatial coordinates and time frames respectively) into a spatial matrix and a temporal matrix, which provide the spatial footprint and the fluorescence time course of each neuron, respectively. With the assumption that the neuronal activity is sparse in the time domain, which is the typical case under normal physiological states, the spatial and temporal matrix can be optimized to best explain the fluorescence recording. To acquire the plane identity of each neuron in the simultaneous multiplane recording, we first image the individual plane and use the CNMF algorithm to extract the spatial footprint and the calcium decay constant of each neuron. These parameters serve as priors and are used to initialize the spatial matrix in the analysis of the multiplane recording. CNMF can then demix the overlapped signals between different planes. Using this approach, neural activity in layers 2/3 and 5 of the mouse cortex could be simultaneously imaged in vivo at high speed (Yang et al. 2016) (Fig. 43.5b).

This multiplane imaging technique essentially projects the information of multiple pixels into one and uses a computational algorithm to demix the signal. In addition to generate multiple spots separated in an axial direction, a Bessel beam can also be generated holographically, either using a spatial light modulator or a fixed phase mask. In such cases, neural activity can be recorded along the continuous axial range illuminated by the Bessel beam (Lu et al. 2017; Song et al. 2017). This approach further increases the imaging throughput, although it typically requires a more sparse neuronal labeling to ensure high fidelity in data reconstruction.

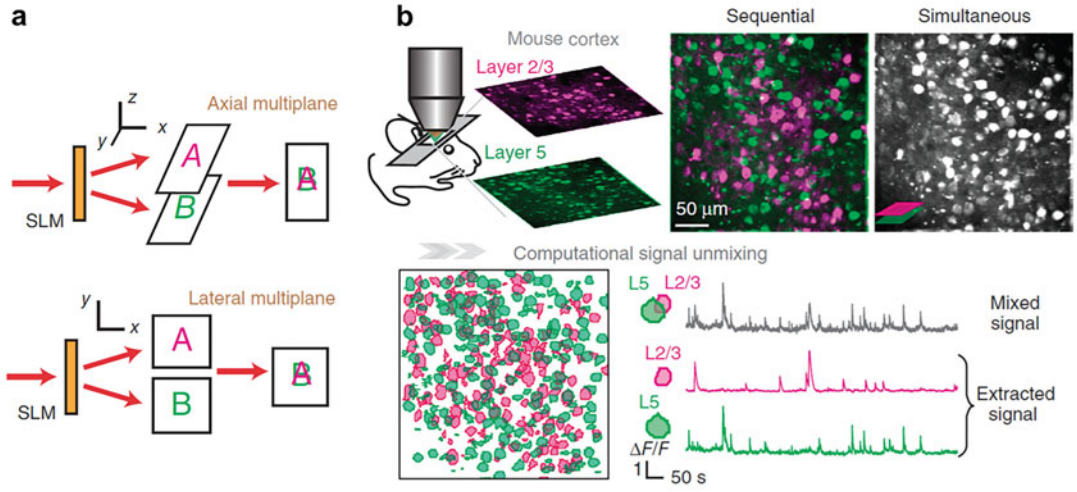


**Fig. 43.5** Holographic multiplane imaging. (**a**) Illustration of the principle for simultaneous axial/lateral multiplane imaging. An SLM splits the laser beam to illuminate different planes simultaneously. The images from different planes superimpose onto each other in the acquired images. (**b**) Simultaneous calcium imaging at layer 2/3 and 5 of mouse visual cortex in vivo. The images from the two individual planes are pseudo-color labeled. When they were imaged together, the neurons from these two planes superimposed to each other. Using the CNMF algorithm, the neuronal signals from the two different planes can be demixed. Reprinted and adapted with permission from (Yang et al. 2016), Elsevier, and (Yang and Yuste 2017) Springer Nature

## 43.4 Holographic Photostimulation of Neural Activity

In addition to imaging, holographic excitation is a very powerful tool for photostimulation of neural activity, as it can selectively photostimulate a designated group of ROIs. Holographic photostimulation in optochemistry was first reported in 2008, for both one-photon (Lutz et al. 2008) and two-photon (Nikolenko et al. 2008) excitation. In 2012, the first holographic photostimulation with optogenetics was reported, using two-photon excitation (Packer et al. 2012). Ever since then, the holographic photostimulation technique has flourished, particularly in two-photon optogenetics for in vivo applications. Depending on how the ROIs (typically neurons) are illuminated, there are two major implementations of holographic photostimulation: scanning holographic photostimulation, and sculpted holographic photostimulation. We discuss both approaches in this section.

### 43.4.1 Scanning Holographic Photostimulation

In this configuration, the hologram generates a group of diffraction-limited focal spots in 3D, each of which locates at the centroid of each targeted neuron. A pair of galvanometer mirrors then spirally or raster scan these spots all together within a small lateral range, so the entire body of each neuron can be illuminated (Fig. 43.6). Essentially, the focal spots sequentially activate the opsins located at different parts of the neurons during scanning. If the scanning time is short and the turnoff dynamics of the opsins is slow, the

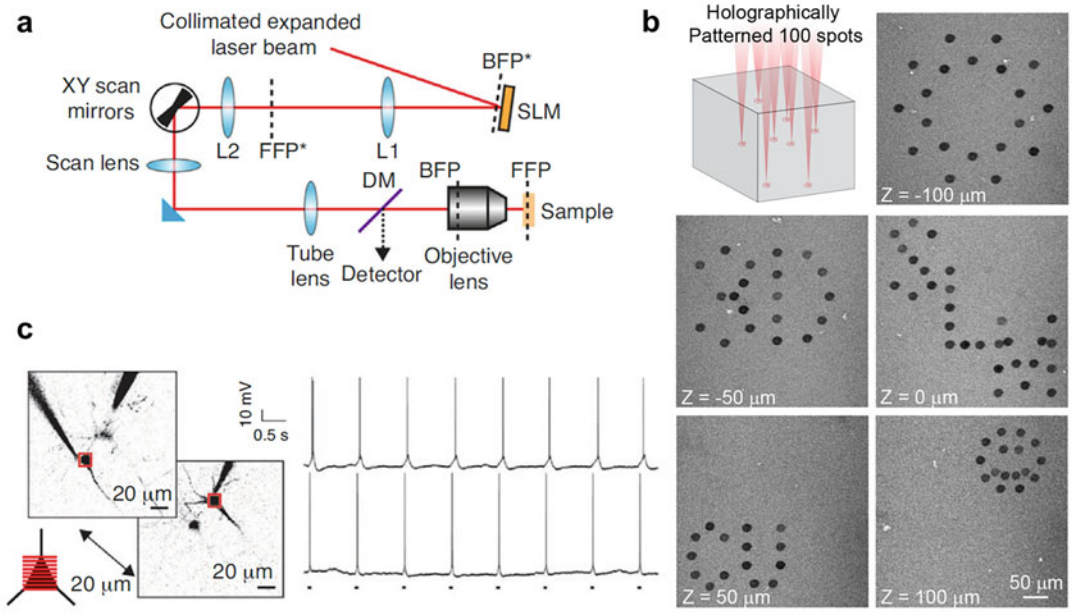


**Fig. 43.6** Two-photon scanning holographic photostimulation. (**a**) Schematics of the experiment setup of scanning holographic photostimulation. FFP (FFP*) and BFP (BFP*) represents the front focal plane (its conjugate plane) and the back focal plane (its conjugate plane) of the objective lens. Reprinted and adapted with permission from (Yang and Yuste 2018), Elsevier. (**b**) 100 spots holographic pattern spirally scanned by a post-SLM galvanometric mirror bleaching an autofluorescence plastic slide across five different planes. Reprinted from (Yang et al. 2018). (**c**) Two-photon 3D stimulation of two individual neurons (at two axial planes separated by 20 μm) expressing C1V1 in a mouse neocortical slice. The laser spot raster scans the cell body (32 lines, 2 ms per line). The right panel shows the simultaneous dual whole-cell recordings during photostimulation (black marks). Reprinted with permission from (Packer et al. 2012), Springer Nature

generated ionic current is integrated by each targeted neuron, leading to their firing. In the experiment setup, the SLM, the galvanometer mirrors, and the back focal plane of the objective are conjugate to each other. While this approach is compatible with one-photon excitation, particularly for cultured neurons or thin slices, it is more adaptable in two-photon systems that have already been equipped with the galvanometer mirrors. Furthermore, neurons distributed in a 3D volume can be readily stimulated within a single two-photon holographic pattern. Using this approach, we demonstrated two-photon photostimulation of neuronal ensembles in layer 2/3 of the visual cortex in awake mice. Using 300 mW of laser power on the brain (<100 ms), more than 80 neurons distributed in a volume of $480 \times 480 \times 150\ \mu m^3$ can be simultaneously photostimulated (Yang et al. 2018). By temporally interleaving different holographic patterns, different groups of neurons can be simulated in a fast temporal fashion.

In addition to spirally or raster scanning, the galvanometer mirrors can also provide a lateral offset to the centroid of the SLM's addressable field of view (determined by the pixel size of SLM and the spectrum width of the two-photon light pulses (Golan et al. 2009; Yang et al. 2016)). This effectively extends the lateral field of view of holographic photostimulation. While neurons across this enlarged field of view cannot be targeted simultaneously, groups of neurons located at different subfields can be targeted by switching the offset of the galvanometer mirror and the phase pattern on the SLM (Yang et al. 2015).

### 43.4.2 Sculpted Holographic Photostimulation

Differently from scanning holographic photostimulation, which leverages time multiplexing to illuminate the entire cell bodies, the sculpted holographic approach illuminates the entire cell bodies at once and it does not require laser scanning. In sculpted holographic photostimulation, ideally, the illumination pattern should be identical and overlapping with the 3D morphology of the targeted neurons. Unfortunately, as the holographic pattern grows from a spot to a disk (~10 μm, the diameter of mice cortical neurons) in the lateral dimension, it spreads very quickly in the axial direction, to a dimension much larger than a single neuron's diameter, even for two-photon excitation light (Papagiakoumou et al. 2008) (Fig. 43.7a). Due to this poor axial resolution, 3D volumetric patterns generated by pure hologram are typically not suitable to photostimulate neurons across a volume, though it is applicable in cultured neurons or thin slice samples, which do not require tight axial confinement. To improve the axial confinement and thus resolution, the holographic technique can be combined with temporal focusing. Temporal focusing was developed in 2005 (Oron et al. 2005; Zhu et al. 2005), aiming to improve the axial resolution and signal-to-background ratio in two-photon microscopy. A grating is inserted into the beam path, which spatially disperses the femtosecond laser pulse into many copies but each with a much longer pulse width, lower power, and thus much lower two-photon excitation efficiency. At the object space, these dispersed pulse copies combine at the focal plane to restore the original short pulse, and thus the high two-photon excitation efficiency. This extra nonlinearity in the temporal domain effectively enhances the axial confinement. When combined with a hologram, it improves the axial confinement in the volumetric patterns (Papagiakoumou et al. 2008) (Fig. 43.7a). In the experiment setup, the SLM is conjugate to the back focal plane of the objective lens, whereas the grating is in the intermediate plane of the spatial light modulator and it is conjugate with the front focal plane of the objective lens. The SLM projects the lateral shapes of the ROIs into the grating, which are then transferred to the focal plane in the sample.

As temporal focusing takes place at the 2D image projected to the grating, it typically only works for 2D patterns. In other words, only neurons at the same focal plane can be simultaneously stimulated. To achieve 3D photostimulation with temporal focusing, two SLMs can be used (Hernandez et al. 2016) (Fig. 43.7b). Both SLMs are separated into the same number of zones, which equals to the number of focal depths. The first SLM encodes hologram for the lateral patterns at each focal depth, one at each zone in the SLM. The grating locates at the intermediate plane of the first SLM, enabling temporal focusing. The second SLM locates at the intermediate plane of the grating, which encodes the actual axial depth for different lateral patterns, again one at each zone in the SLM. Thus, 3D sculpted holographic illumination can be achieved. Because the information for each focal plane only occupies one of the zones in both SLMs, which are conjugated to the back aperture/focal plane of the objective lens, the effective excitation NA reduces for each focal plane, which is one of the limitations of this approach.

Another approach for 3D temporal focusing requires only one SLM (Accanto et al. 2018; Pegard et al. 2017; Sun et al. 2018) (Fig. 43.7c). Here, a predefined 2D pattern, typically a disk, is projected to the grating. This pattern can be created by a fixed phase mask through a hologram. An SLM is placed at the intermediate imaging plane after the grating, which holographically replicates a group of the predefined 2D pattern, each being projected to a targeted cell in the sample. Here, the functionality of the SLM is essentially the same as in the scanning holographic photostimulation. In both cases, the SLM purely executes the function of replicating and assigning each copy to the desired location in 3D. In sculpted holographic case, it replicates the predefined pattern on the grating. In scanning holographic case, the replicas are a group of diffraction-limited focal spots, which are

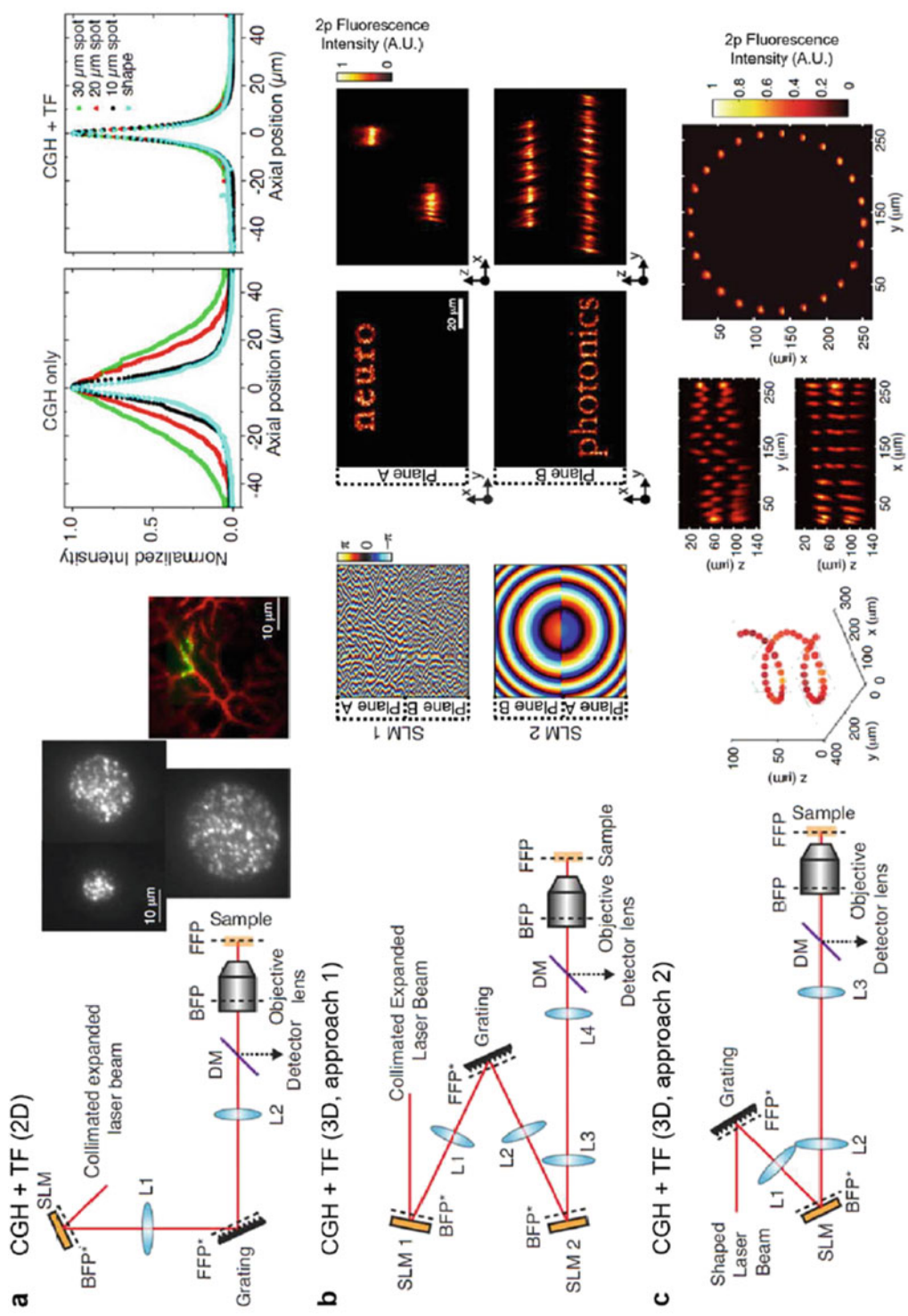
a CGH + TF (2D)
SLM
BFP*
Collimated expanded laser beam
L1
FFP*
Grating
BFP
DM
L2
FFP
Sample
Objective
Detector lens
10 μm
10 μm
CGH only
CGH + TF
30 μm spot
20 μm spot
10 μm spot
shape
Normalized Intensity
Axial position (μm)
b CGH + TF (3D, approach 1)
Collimated Expanded Laser Beam
SLM 1
SLM 2
BFP*
FFP*
L1
L2
L3
L4
Grating
BFP
DM
FFP
Objective
Sample
Detector lens
2p Fluorescence Intensity (A.U.)
neuro
photonics
20 μm
Plane A
Plane B
c CGH + TF (3D, approach 2)
Shaped Laser Beam
Grating
FFP*
L1
SLM
BFP*
L2
DM
BFP
FFP
Sample
L3
Objective
Detector lens
2p Fluorescence Intensity (A.U.)
x (μm)
y (μm)
z (μm)

**Fig. 43.7** Two-photon sculpted holographic photostimulation. (**a**) Combination of computer-generated holography (CGH) and temporal focusing (TF) techniques for 2D pattern photostimulation with tight axial confinement. Left, schematics of the experiment setup. Middle, images of holographic patterning of 10, 20, and 30 μm diameter spots on a thin fluorescent layer and a region of interest at a Purkinje cell. Right, comparison of the measured axial profile of the intensity distribution for the patterns in the middle panel, without and with TF. Reprinted with permission from (Papagiakoumou et al. 2008), Optical Society of America, and (Yang and Yuste 2018), Elsevier. (**b**) Combination of CGH and TF techniques for 3D pattern photostimulation with tight axial confinement (approach 1). Left, schematics of the experiment setup. Middle, phase profiles on SLM1 and SLM2 to generate the 3D light pattern in plane A (+20 μm) and plane B (−20 μm). Right, intensity images of the 3D pattern in *xy*, *xz*, and *yz* projection views. Reprinted with permission from (Hernandez et al. 2016), Springer Nature, and (Yang and Yuste 2018), Elsevier. (**c**) Combination of CGH and TF techniques for 3D pattern photostimulation with tight axial confinement (approach 2). Left, schematics of the experiment setup. The input beam to the grating can be pre-shaped by a static phase plate, an SLM, generalized phase contrast (GPC), a lens (a small spherical phase pattern), and so on (Accanto et al. 2018; Pegard et al. 2017; Sun et al. 2018). Each spectral component of the pulse should span across the SLM in the Fourier domain to ensure a high diffraction efficiency. Right, an example of a 3D light pattern, and the mean intensity images of the 3D pattern in *yz*, *xz*, and *xy* projection views. Reprinted with permission from (Pegard et al. 2017), Springer Nature, and (Yang and Yuste 2018), Elsevier. In (a)–(c), FFP (FFP*) and BFP (BFP*) represents the front focal plane (its conjugate plane) and the back focal plane (its conjugate plane) of the objective lens

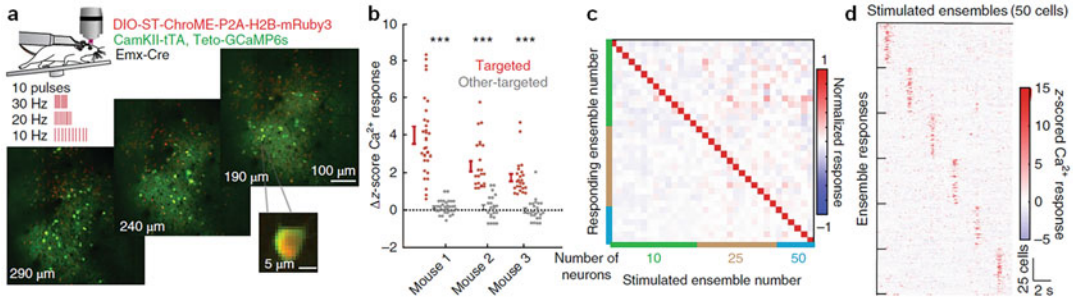


**Fig. 43.8** 3D photostimulation of different groups of neurons by switching the holographic patterns in a microscope combining CGH and TF techniques (approach shown in Fig. 43.7c). (**a**) Schematic illustrating simultaneous imaging (through GCaMP6s) and optogenetics (through ST-ChroME). 33 ensembles of 10, 25, or 50 neurons were photostimulated with 10 pulses (5 ms each) at 10–30 Hz, across three planes shown in the representative images (550 × 550 × 100 $\mu m^3$ field of view), with depth from pial surface noted. Inset: enlargement showing example calcium source expressing ST-ChroME. (**b**) Summary data from experiments in three mice. Each point represents the mean change in *z*-scored calcium response of all ensemble members in response to stimulation of the target ensemble (red) or mean response to stimulation of other ensembles (gray). Ensembles significantly increased their fluorescence only when they were stimulated (***$p < 0.001$; Mouse 1, $n = 33$ ensembles, $p = 3.5 \times 10^{-10}$; Mouse 2, $n = 22$ ensembles, $p = 2.8 \times 10^{-4}$; Mouse 3, $n = 24$ ensembles, $p = 5.5 \times 10^{-4}$, paired two-sided *t* test). (**c**) Normalized *z*-scored calcium response of the neurons that compose each stimulated ensemble upon stimulation of each ensemble. Color codes show the size of the ensembles (green, 10; brown, 25; blue, 50 neurons). (**d**) Responses of each neuron in each ensemble (50 neurons per ensemble) to each ensemble stimulation, grouped by ensemble identity. Reprinted with permission from (Mardinly et al. 2018), Springer Nature

subsequentially being scanned by the galvanometers mirrors to cover the cell bodies. Using 3D temporal focusing, neuronal ensembles containing a large number of neurons can be simultaneously photostimulated. By switching the holographic patterns, different groups of neurons can be sequentially photostimulated (Mardinly et al. 2018) (Fig. 43.8).

When using a phase-only spatial light modulation technique to generate the hologram, the light intensity but not the phase in the object space is optimized. This leads to random phases on the holographic pattern, which results in speckles (see examples shown in Fig. 43.7a, b), regardless of whether temporal focusing is used. The speckle patterns could cause a large variation in the actual light intensity from the desired ones. To make the intensity profile smooth, a technique called generalized phase contrast can be used in combination with temporal focusing and SLM. In generalized phase contrast technique (Banas and Gluckstad 2017; Gluckstad 1996; Rodrigo et al. 2008), a phase object can be transferred into an intensity image through a 4f system with a phase-contrast filter in its Fourier plane (Fig. 43.9a). The phase-contrast filter is essentially a phase mask. When passing through this filter, the light at the center of the filter picks up a different phase from the rest of the light. They then interfere at the imaging plane and create the intensity image corresponding to the phase of the object. This is essentially a common-path interferometer. By inserting this setup between the SLM and the grating, the phase pattern on the SLM can be directly transferred to the intensity pattern on the grating, which can then be further projected to the sample (Papagiakoumou et al. 2010) (Fig. 43.9b). The intensity pattern, in this case, can be smooth. This approach, however, could suffer from a low power efficiency and a limited excitation field (Papagiakoumou et al. 2010). One important note is that while SLM plays a role to generate the pattern here, the working mechanism is different from a computer-generated hologram. As this falls into the general topic of photostimulation using SLM, we include it here as an extended discussion.

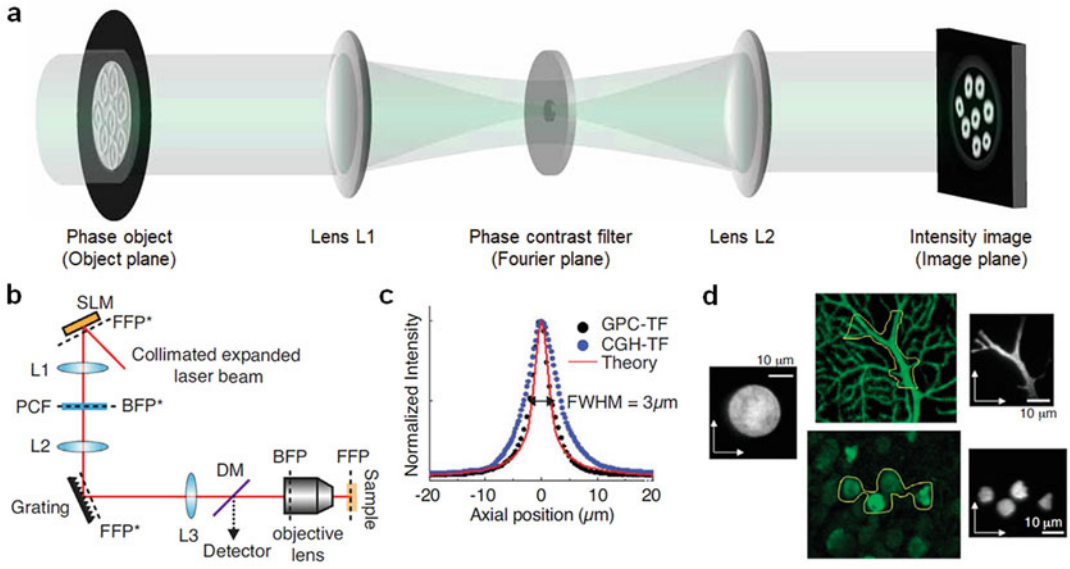


**Fig. 43.9** Generalized phase contrast technique coupled with SLM phase shaping for beam patterning. (**a**) Experimental realization of generalized phase contrast through a common-path interferometer—a 4f imaging system with a phase-contrast filter (PCF). Adapted and reprinted with permission from (Rodrigo et al. 2008), Optical Society of America. (**b**) Combination of SLM phase shaping, generalized phase contrast (GPC), and temporal focusing techniques to generate speckle-free patterns with tight axial confinement. FFP (FFP*) and BFP (BFP*) represents the front focal plane (its conjugate plane) and the back focal plane (its conjugate plane) of the objective lens. (**c**) Axial profile of fluorescence intensity of a 20 μm diameter spot generated by GPC-TF, CGH-TF, and theoretical curve for the axial integrated intensity profile in line-scanning two-photon microscopy. (**d**) Image of a 20 μm diameter spot (left) and shaped patterns (right) on a thin fluorescent layer, created by two-photon spatial light patterning with GPC and TF techniques. Shaped patterns were based on a confocal image of a Purkinje cell (center, top), and wide field fluorescence image of CA1 hippocampal neurons loaded with Oregon Green Bapta (center, bottom), in selected regions of interest (yellow outlines). Adapted and reprinted with permission from (Papagiakoumou et al. 2010), Springer Nature, and (Yang and Yuste 2018), Elsevier

### 43.4.3 Discussion

In this section, we discuss the strength and limitation of scanning holographic and sculpted holographic approaches with two-photon excitation light. The key difference between the two is whether the entire cell bodies are illuminated at once. Assuming the photostimulation duration $T$, pulse repetition rate $f_{\text{rep}}$, and the total two-photon excitation effect per unit area $E_{2p}$ are the same for both approaches, we compared the required laser power $P_{\text{scanning}}$ and $P_{\text{sculpted}}$. We denote the area of the cell and the laser focal spot size as $S$ and $S_0$ respectively. In general, if we do not take the turnoff dynamics of the opsin into consideration, we have $E_{2p} \propto (\text{laser intensity per pulse})^2 \times \text{number of pulses}$. In scanning holographic approach, $E_{2p\_\text{scanning}} \propto \left(\frac{P_{\text{scanning}}}{S_0}\right)^2 \frac{T f_{\text{req}}}{S/S_0}$. In sculpted holographic approach, $E_{2p\_\text{sculpted}} \propto \left(\frac{P_{\text{sculpted}}}{S}\right)^2 T f_{\text{req}}$. Equating $E_{2p\ \_\ \text{scanning}}$ and $E_{2p\ \_\ \text{sculpted}}$, we have $P_{\text{scanning}} \propto \sqrt{S_0/S} P_{\text{sculpted}} < P_{\text{sculpted}}$. When taking the temporal dynamics of opsin into account, a higher $P_{\text{scanning}}$ is expected or a higher pulse repetition rate and faster scanning are needed.

In many opsin channels, the turnoff time is long (Mattis et al. 2011) (10s ms, larger than the duration of each spiral scan (which can be <1 ms); but see also (Klapoetke et al. 2014) for opsins with short turnoff time), so scanning holographic photostimulation is suitable, with a lower required laser power than sculpted holographic approach (Yang et al. 2018) (Fig. 43.10). On the

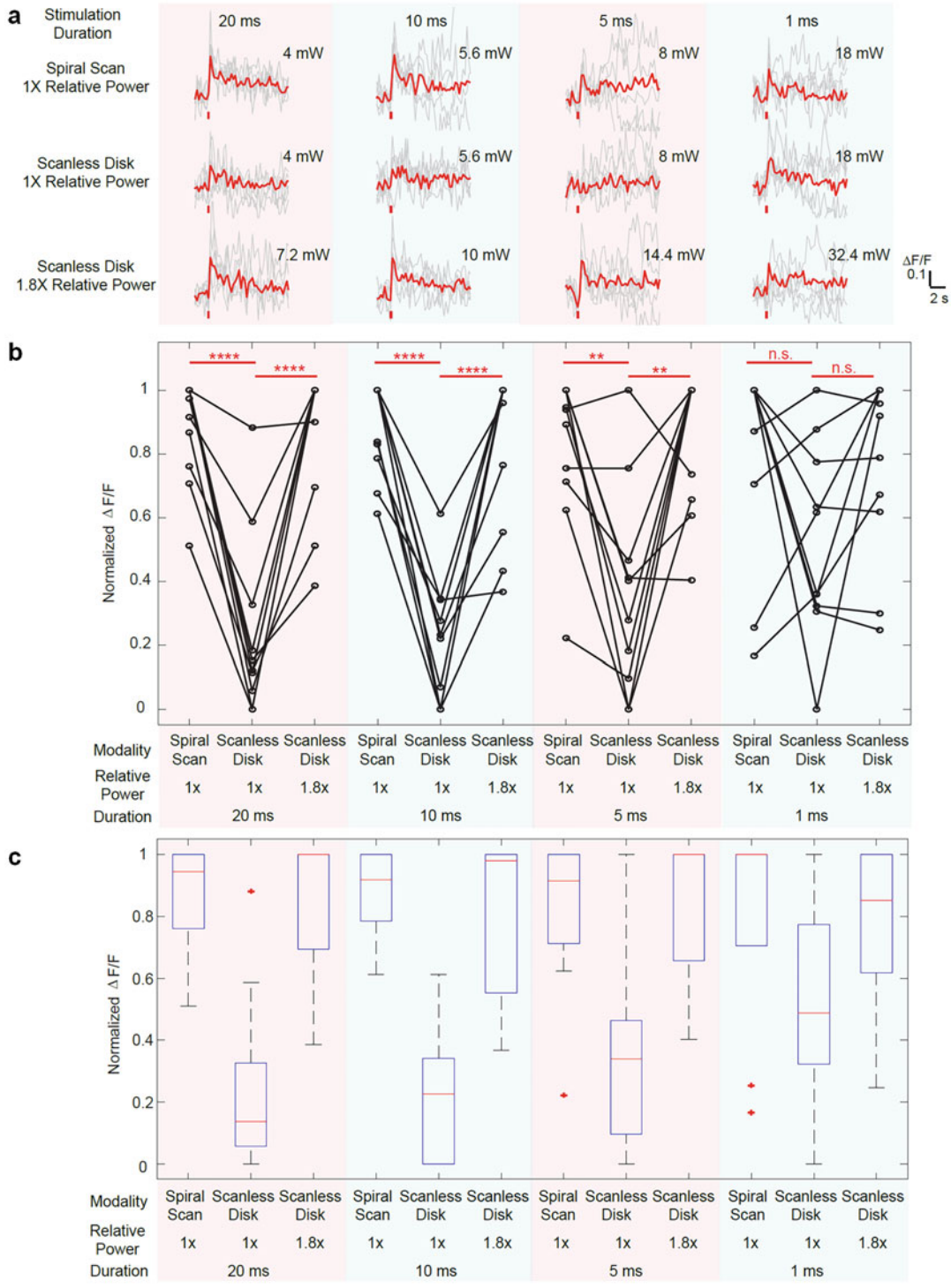


**Fig. 43.10** Comparison between spiral scan and scanless holographic approaches for photostimulation. In the scanning approach, the laser spot is spirally scanned over the cell body; in the scanless approach, a disk pattern (~12 μm in diameter) is generated by the SLM, covering the entire cell body at once. (**a**) Photostimulation triggered calcium response of a targeted neuron in vivo at mouse layer 2/3 of V1, for different stimulation modalities. For each

other hand, as the entire neuron is stimulated at the same time in the sculpted holographic approach, the jitter, defined as the standard deviation of the delay between the onset of photostimulation and neuronal firing, is typically lower. This translates into a more precise time control capability.

As holographic patterning delivers laser power simultaneously to multiple targets, the required laser power increases proportional to the number of simultaneously targeted neurons, regardless of whether active scanning is used. Since the laser power eventually turns into heat in the sample, it is critical to keep the average power $P_{\text{ave}}$ below the damage threshold (Podgorski and Ranganathan 2016). If we denote the laser peak power and temporal pulse width as $P_{\text{peak}}$ and $\tau_p$, we can elaborate more details on the $E_{2p}$ discussed earlier. Instead of average power or intensity, the peak power or intensity is more relevant to evaluate $E_{2p}$. We have $E_{2p} \propto$ (peak power per pulse)$^2$ $\times$ pulse width $\times$ number of pulses. Thus, $E_{2p} \propto P_{\text{peak}}^2 \tau_p T f_{\text{req}} = \left(\frac{P_{\text{ave}}}{f_{\text{req}}\tau_p}\right)^2 \tau_p T f_{\text{req}} = \frac{P_{\text{ave}}^2}{f_{\text{req}}\tau_p} T$. Keeping the same $P_{\text{ave}}$, the two-photon excitation effect increases by decreasing the laser repetition rate $f_{\text{req}}$ (and thus increasing $P_{\text{peak}}$). Thus, when photostimulating many neurons at the same time, a lower repetition rate laser is favorable.

When choosing the exact photostimulation scheme, and the laser specification, it is critical to take into account of the key requirement of the application, the number of cells to be stimulated, the desirable stimulation duration, and the opsin channel turnoff dynamics or the diffusion constant of the uncaged neurotransmitters in the case of optochemistry.

## 43.5 All-Optical Interrogation of Neural Circuits

Combining two-photon calcium imaging and two-photon photostimulation allows simultaneous reading and writing neuronal activity with cellular resolution in the brain. It enables a wide range of applications, from the functional mapping of neuronal circuits (Dal Maschio et al. 2017; Nikolenko et al. 2007; Yang et al. 2018) to biasing and controlling animal behaviors (Carrillo-Reid et al. 2019; Marshel et al. 2019), and to induce circuit plasticity (Marshel et al. 2019). Furthermore, it also enables closed-loop optogenetics (Grosenick et al. 2015; Zhang et al. 2018).

While it is possible to time multiplex a single two-photon laser so as to perform imaging and photostimulation on the same sample (Nikolenko et al. 2007), it is more flexible to use two lasers so imaging and photostimulation can be performed

modality, the multiplication of stimulation duration and the square of the laser power was kept constant over four different stimulation durations. The average response traces are plotted over those from the individual trials. (**b**) $\Delta F/F$ response of neurons on different photostimulation conditions (10 cells over two mice in vivo (photostimulated one at a time), layer 2/3 of V1, over a depth of 100–270 mm from the pial surface; one-way ANOVA test show significant different response between spiral scan and scanless approach at the same laser power for stimulation duration of 20, 10, and 5 ms. At 1 ms, the $p$ value is 0.17). For each neuron and each stimulation duration, the laser power used in the scanless disk modality is 1 and 1.8 times relative to that in the spiral scan. For each neuron and each modality, the multiplication of the stimulation duration and the square of the laser power were kept constant over four different stimulation durations. The power used in the spiral scan with 20 ms duration varies from 2.2 to 5 mW for different cells. (**c**) Boxplot summarizing the statistics in (**b**). The central mark indicates the median, and the bottom and top edges of the box indicate the 25th and 75th percentiles, respectively. The whiskers extend to the most extreme data points (99.3% coverage if the data are normal distributed) not considered outliers, and the outliers are plotted individually using the "+" symbol. In this experiment, the mice are transfected with GCaMP6f and C1V1-mCherry. Repetition rate of the photostimulation laser is 1 MHz. The spiral scan consists of 50 rotations with a progressively shrinking radius, and the scanning speed is adjusted to make different stimulation durations. Reprinted with permission from (Yang et al. 2018)

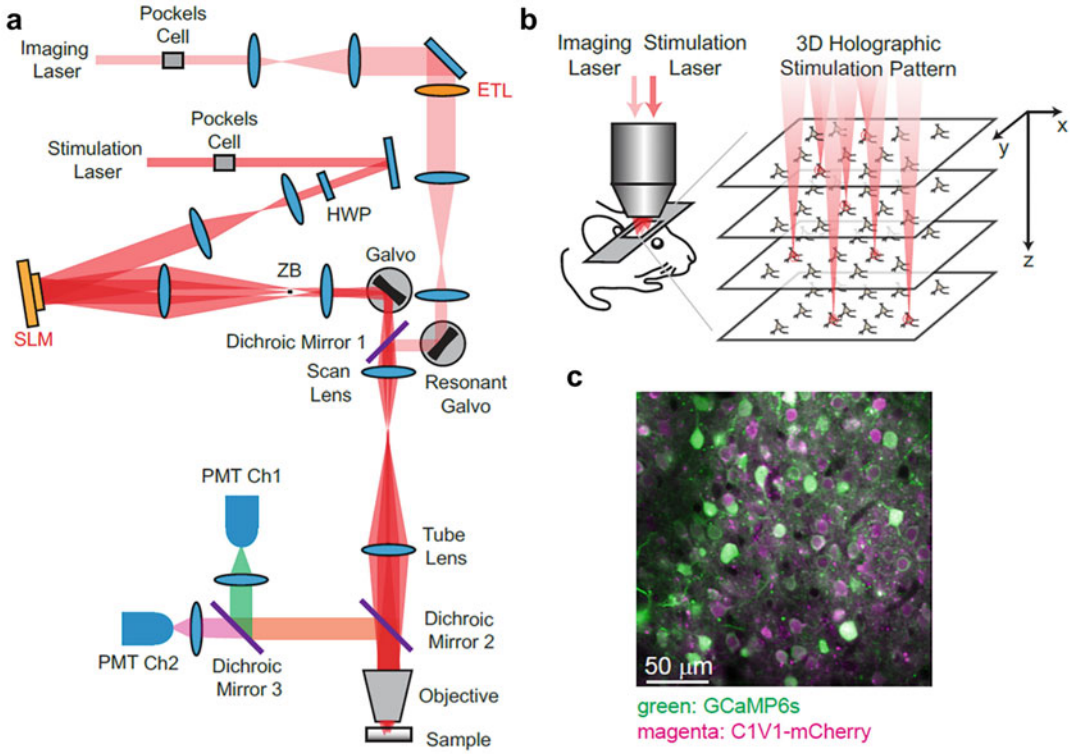


**Fig. 43.11** Two-photon imaging and photostimulation microscope. (**a**) Microscope setup. *HWP* Half-wave plate, *ZB* Zeroth-order beam block, *SLM* Spatial light modulator, *ETL* Electrically tunable lens, *PMT* Photomultiplier tube. In the imaging path, an ETL can remotely adjust the focal plane and enable fast volumetric imaging. In the photostimulation path, an SLM can project the holographic pattern to photostimulate groups of neurons distributed in 3D brain tissue. (**b**) Schematics for simultaneous volumetric calcium imaging and 3D holographic patterned photostimulation in the mouse cortex. (**c**) A typical field of view showing neurons coexpressing GCaMP6s for calcium imaging (green) and C1V1-mCherry for optogenetics (magenta). Reprinted from (Yang et al. 2018)

simultaneously and independently (Fig. 43.11). The calcium indicators and opsins (or caged compounds of the neural transmitter) should be carefully chosen to avoid overlap in their excitation spectrum. Typically, green calcium indicators such as GCaMP6 (Chen et al. 2013) or jGCaMP7 (Dana et al. 2019) are paired with red-shifted opsins such as C1V1 (Yizhar et al. 2011), ChrimsonR (Klapoetke et al. 2014), or ChRmine (Marshel et al. 2019). Alternatively, red calcium indicators such as jRCaMP1a/b (Dana et al. 2016) can be used together with blue activated opsin such as ChR2 (Boyden et al. 2005; Nagel et al. 2003). Based on the choice of calcium indicators and opsins, laser wavelengths can be selected. The focus of the two lasers could be controlled independently in their own beam paths, including their axial direction, before they are combined with a dichroic mirror and then directed to the objective lens and the samples. In recent reports of all-optical two-photon microscopes (Chen et al. 2019; Dal Maschio et al. 2017; Forli et al. 2018; Mardinly et al. 2018; Marshel et al. 2019; Packer et al. 2015; Yang et al. 2018; Zhang et al. 2018), the photostimulation path is equipped with the SLM module for holographic patterning, though the same can be implemented in the imaging path.

One important application of the all-optical holographic microscopy is to control behavior.

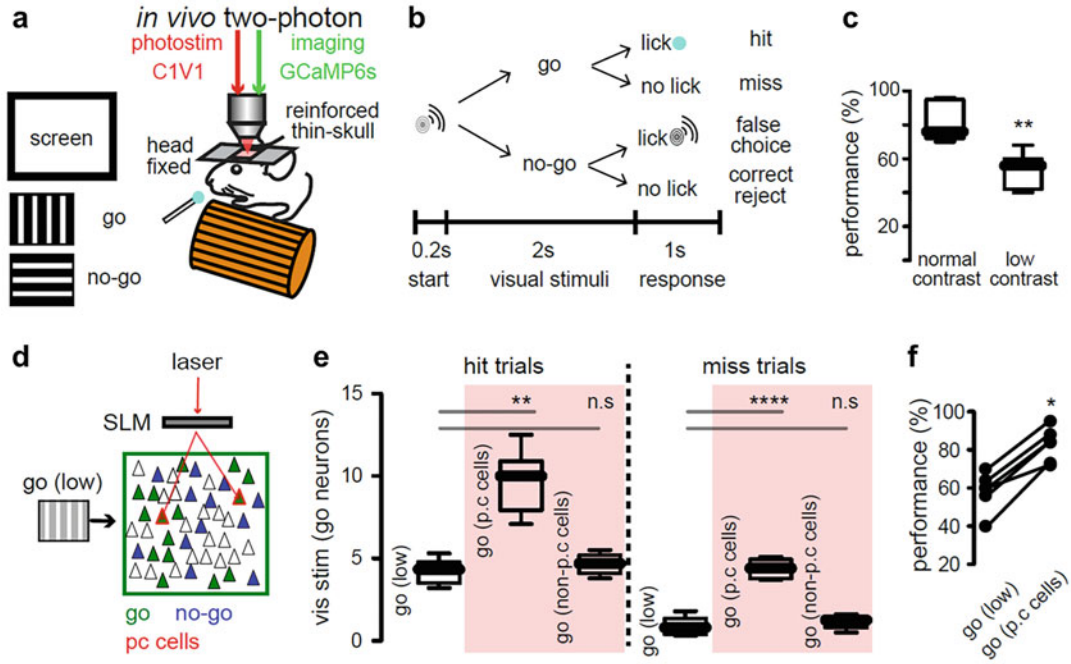


**Fig. 43.12** All-optical control of behavior by manipulating neuronal circuits. (**a**) Experimental design: simultaneous two-photon calcium imaging and two-photon holographic optogenetic manipulation of targeted neurons in a visually guided Go/No-Go task. (**b**) Protocol of the visually guided Go/No-Go task and assessment of the performance. (**c**) Tuning of behavioral performance by lowering the contrast of visual stimuli in expert animals (**$p < 0.005$; $n = 7$ mice; Mann–Whitney test). (**d**) Holographic photoactivation of the pattern completion (p.c.) neurons (red) that belonged to the Go ensemble, during the visually guided Go/No-Go task with low contrast visual stimuli. (**e**) Number of active neurons evoked by visual stimuli in low contrast and during concomitant photo-stimulation of pattern completion neurons (p.c. cells) and non-pattern completion neurons (non-p.c. cells) in hit and miss trials. Red shadow indicates photostimulation epochs (Hit trials: Go low versus Go p.c. cells: $p < 0.005$; Go low versus Go non-p.c. cells: $p > 0.05$; Miss trials: Go low versus Go p.c. cells: $p < 0.0001$; Go low versus Go non-p.c. cells: $p > 0.05$; $n = 6$ mice). (**f**) Behavioral response to low contrast Go-signal is significantly enhanced by the targeted activation of pattern completion neurons ($p < 0.05$; $n = 6$ mice). Reprinted with permission from (Carrillo-Reid et al. 2019), Elsevier

Typically, the neuronal activity of the circuit is first recorded during the relevant animal behavior. Holographic optogenetics can then activate a subset of neurons, while the circuit response and animal behavior are simultaneously recorded. The connectivity, organization, and function of the neuronal circuits can then be analyzed. In one example, in order to dissect how an ensemble of premotor neurons in larval zebra fish brain drives tail bending, holographic photostimulation was performed to identify minimal subsets of neurons that are sufficient to initiate tail movements; meanwhile, the induced network activity was recorded by multiplane calcium imaging, and the behavior-linked circuit dynamics could then be analyzed (Dal Maschio et al. 2017). In another example, the neuronal circuit in the mouse visual cortex was imaged when the animal performed a forced-choice visual discrimination task. By analyzing the calcium imaging data, the neuronal ensemble, and the core ensemble neurons related to the "Go-cue" of visual stimuli were extracted. Holographic photostimulation of two core ensemble neurons during the "Go-cue" evoked activity in other neurons within the ensemble and can increase the task performance, demonstrating pattern completion and a photostimulation of a subset of cells in a cortical ensemble could trigger animal behavior (Carrillo-Reid et al. 2019) (Fig. 43.12).

While holographic optogenetics can drive widespread recruitment of functionally related neurons, and elicit animal perception and behavior, it can also induce plasticity in neural networks. Hebbian plasticity states that connectivity between coactive neurons becomes strengthened (Hebb 1949). By photostimulating a group of neurons for an extended period, we have shown that the cross-correlation of the spontaneous activity in a subset of photostimulated neurons increased (Carrillo-Reid et al. 2017). In a similar forced-choice visual discrimination task as discussed above but studied independently in another group, holographic photostimulation of the "Go-cue" related ensemble was performed during the visual discrimination task training. After a few sessions of training, the animals had an improved task performance. Furthermore, holographic photostimulation on the ensemble alone (without visual stimuli) could elicit a high performance behavioral discrimination, as if the visual stimuli were presented. This interesting result suggests that the animal had "learnt" to associate the photoactivation of the ensemble with the discrimination task (Marshel et al. 2019). While further exploration of the spatiotemporal parameter space of the photostimulation as well as the behavioral paradigms are needed to extend the study on plasticity mechanisms underlying learning, the all-optical methods have demonstrated its great power to facilitate these studies.

Finally, real-time closed-loop optogenetics could dynamically control neuronal activity patterns in awake animals and is an important tool to probe the causal relationship between neural activity and behavior (Grosenick et al. 2015; Zhang et al. 2018). By rapidly reading the raw data in calcium recording and performing online analysis of the inferred neuronal activity, the photostimulation parameters can be reconfigured (Fig. 43.13a). In one exemplary demonstration, the neuronal activity of a neuron was clamped by active control of the photostimulation (Fig. 43.13b–g) (Zhang et al. 2018). In another demonstration, a group of "target" neurons was photostimulated when a "trigger" neuron fired action potential (Fig. 43.13h–k) (Zhang et al. 2018). A feedback time less than 25 ms was demonstrated, from the readout of a single frame of data to the actual holographic photostimulation (Zhang et al. 2018). Such closed-loop optogenetics allows on-the-fly manipulation of neuronal activity patterns. It is also promising as an intervention tool in disease states, such as to correct aberrant activity patterns in Alzheimer's disease or epilepsy. Finally, real-time closed-loop optogenetics could provide a foundation for the next generation of brain–machine interface.

## 43.6 Summary and Outlook

Optical microscopy has rapidly developed in the past decade for neuroscience applications. While there are different types of microscopes, their goals are generally the same: to deliver photons effectively to the sample while minimizing the dose, and to collect the emitted photons efficiently and perform measurements with high temporal and spatial resolution in as large as deep a territory as possible, all with a good signal-to-noise ratio (SNR). Holographic patterning, as a new illumination paradigm, compared to wide-field and laser scanning illumination, achieves many of these goals. In particular, two-photon holographic patterning enables high resolution light delivery to desired regions in the sample and increases the throughput of both imaging and photostimulation. When combining with other techniques such as rapid scanning or temporal focusing, it enables many advanced features. An all-optical holographic method, combining calcium imaging and holographic photostimulation, has become an important tool to study the connectivity, organization, and function of the neuronal circuits, and to investigate the link between neuronal activity and animal behavior. We foresee that it will play a critical role in many neuroscience studies.

While holographic patterning techniques have proven their powerful functionality in microscopes, and are being deployed in more and more neuroscience studies, there are still many areas where further improvements are needed. First of all, current liquid crystal-based

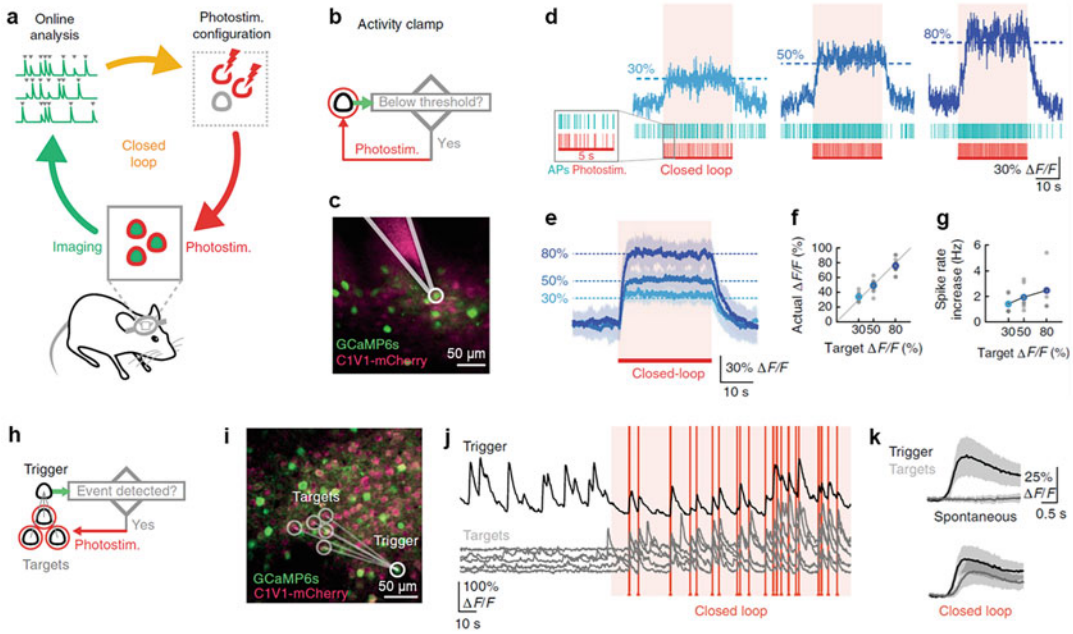


**Fig. 43.13** Closed-loop all-optical control. (**a**) Schematic of the closed-loop all-optical control system with simultaneous two-photon imaging and two-photon photostimulation (photostim.). (**b–g**) Activity clamp. (**b**) Paradigm for the activity clamp. (**c**) Simultaneous cell-attached recording from a neuron (white circle) that was under activity clamp in layer 2/3 of mouse somatosensory cortex coexpressing GCaMP6s and C1V1. Alexa 594 was filled in the pipette for visualization. (**d**) Top, calcium transient from a single neuron clamped at three different activity levels (30%, 50%, and 80% $\Delta F/F$; 30 s clamping period). Middle, raster plot of electrophysiologically recorded action potentials (APs) from the neuron in (**c**) during single trials. Bottom, photostimulation times. (**e**) Mean activity clamp (30 s clamp period) of 18 cells in the somatosensory and visual cortex of awake animals. The shaded area is a standard derivation. Same photostimulation parameters as in (**d**). $n = 18$ cells in six animals. (**f**) Calcium signal levels achieved during activity clamp in (**e**) versus target calcium signal levels. Gray points are individual cells, colored points are average. (**g**) Spike rate increases during activity clamp at three different target calcium signal levels, measured by simultaneous electrophysiological recording ($n = 7$ cells in five mice under anesthesia). (**h–k**) Triggered photostimulation. (**h**) Paradigm for dynamic interrogation of ensembles with a single trigger neuron and multiple targets. (**i**) Field of view in layer 2/3 of mouse somatosensory cortex showing neurons coexpressing GCaMP6s for calcium imaging and C1V1 for optogenetics in an awake mouse. A trigger neuron (thick white circle) was selected to drive photostimulation of five target neurons (thin white circles). (**j**) Calcium signals are recorded from trigger neurons (top) and target neurons (bottom). Target neurons were photostimulated (red vertical lines) upon detection of an event in trigger neurons during a closed-loop control period (140 s, shaded area). (**k**) Calcium transients (mean ± standard derivation) averaged across detected events during spontaneous activity period (top) and closed-loop control period (bottom) ($n = 6$ trigger neurons, black trace; each trigger neuron was associated with a different group of five target neurons, gray trace). Reprinted with permission from (Zhang et al. 2018), Springer Nature

SLMs have a relatively slow speed. This limits how fast the SLM can switch patterns between different ROIs in imaging or photostimulation. A current state of the art SLM has a 1 ms switching speed (Thalhammer et al. 2013). Further advancement, particularly through a microelectromechanical system (MEMS) (Yang et al. 2014), could enable new applications for both imaging and photostimulation. Secondly, while the newly developed calcium indicator jGCaMP7 (Dana et al. 2019) and opsin ChRmine (Marshel et al. 2019) have greatly improved the sensitivity over previous constructs, more sensitive calcium indicators and opsins could further reduce the required laser power for imaging or photostimulation. Furthermore, a larger spectrum

separation between the calcium indicators and opsins could reduce their cross talk. While calcium indicators and opsins are typically transfected in separate viruses, a single virus integrating the two together (Akerboom et al. 2013; Marshel et al. 2019) is expected to increase the coexpression rate of the sensor and actuator in neurons. Thirdly, conventional opsins express in both the soma and neurites of the neurons. But, since the dendritic and axonal arbors of some nontarget neurons could course around the soma of targeted neurons, photostimulating the soma of the targeted neurons may also stimulate nontarget neurons. This issue becomes more severe as the photostimulated ensemble contains more and more neurons. This undesirable effect could be suppressed by using somatic restricted opsins (Baker et al. 2016; Mardinly et al. 2018; Marshel et al. 2019; Shemesh et al. 2017), with reduced expression in dendritic and axonal arbors. Thus, somatic restricted opsins are recommended. Finally, three-photon excitation (Ouzounov et al. 2017; Rowlands et al. 2017) could be used in combination with holographic illumination to increase light penetration depth, optical sectioning, and signal-to-background ratio. One of the biggest challenges is the large amount of laser power required in three-photon holographic patterning. In this regard, opsins with a high three-photon absorption cross section would be greatly desirable.

The future of microscopy is likely to become hybrid and integrate different technologies, combining their advantages (Yang and Yuste 2017). Indeed, as seen in this chapter, different techniques can be integrated with holographic illumination to improve the overall performance of the microscopes. SLMs are very useful for microscopy, as they can in principle mimic arbitrary optical transfer functions. They can also be used to correct optical aberration from both the microscope system and sample through adaptive optics (Ji 2017), allowing a larger penetration depth, higher SNR, and higher signal-to-background ratio. Because of this, SLMs and similar holographic devices could continue to revolute optical microscopy and enable new investigations and applications in neuroscience and biology.

**Acknowledgments** We thank past and current members of the Yuste lab for the development of holographic microscopy and fruitful discussions. This work is supported by the National Eye Institute (R01EY011787 [RY], R21EY029472 [WY]), National Institute of Neurological Disease and Stroke (R01NS110422, R34NS116740 [RY], R01NS118289 [WY]), National Institute of Mental Health (R01MH115900 [RY]), National Science Foundation (CRCNS 1822550 [RY], CAREER 1847141 [WY]), and Burroughs Wellcome Fund (Career Award at the Scientific Interface 1015761 [WY]).

*Conflict of Interest:* RY is listed as the inventor of the following patents: "Devices, apparatus and method for providing photostimulation and imaging of structures" (United States Patent US9846313B2), and "System, method and computer-accessible medium for depth of field imaging for instantaneous and targeted three dimensional sensing utilizing a spatial light modulator microscope" (2013, USPA provisional 61/756803). RY and WY are listed as inventors of the following patent: "System, method and computer-accessible medium for multiplane imaging of neural circuits" (United States Patent US10520712B2).

## References

Accanto N, Molinier C, Tanese D, Ronzitti E, Newman ZL, Wyart C, Isacoff E, Papagiakoumou E, Emiliani V (2018) Multiplexed temporally focused light shaping for high-resolution multi-cell targeting. Optica 5:1478–1491

Adams SR, Tsien RY (1993) Controlling cell chemistry with caged compounds. Annu Rev Physiol 55:755–784

Akerboom J, Carreras Calderon N, Tian L, Wabnig S, Prigge M, Tolo J, Gordus A, Orger MB, Severi KE, Macklin JJ et al (2013) Genetically encoded calcium indicators for multi-color neural activity imaging and combination with optogenetics. Front Mol Neurosci 6:2

Baker CA, Elyada YM, Parra A, Bolton MM (2016) Cellular resolution circuit mapping with temporal-focused excitation of soma-targeted channelrhodopsin. elife 5: e14193

Banas A, Gluckstad J (2017) Holo-GPC: holographic generalized phase contrast. Opt Commun 392:190–195

Boyden ES, Zhang F, Bamberg E, Nagel G, Deisseroth K (2005) Millisecond-timescale, genetically targeted optical control of neural activity. Nat Neurosci 8:1263–1268

Carrillo-Reid L, Han S, Taralova E, Jebara T, Yuste R (2017) Identification and targeting of cortical ensembles. bioRxiv. doi: https://doi.org/10.1101/226514

Carrillo-Reid L, Han S, Yang W, Akrouh A, Yuste R (2019) Controlling visually guided behavior by

holographic recalling of cortical ensembles. Cell 178:447–457

Chen TW, Wardill TJ, Sun Y, Pulver SR, Renninger SL, Baohan A, Schreiter ER, Kerr RA, Orger MB, Jayaraman V et al (2013) Ultrasensitive fluorescent proteins for imaging neuronal activity. Nature 499:295–300

Chen IW, Ronzitti E, Lee BR, Daigle TL, Dalkara D, Zeng H, Emiliani V, Papagiakoumou E (2019) In vivo submillisecond two-photon optogenetics with temporally focused patterned light. J Neurosci 39:3484–3497

Dal Maschio M, Donovan JC, Helmbrecht TO, Baier H (2017) Linking neurons to network function and behavior by two-photon holographic optogenetics and volumetric imaging. Neuron 94:774–789.e5

Dana H, Mohar B, Sun Y, Narayan S, Gordus A, Hasseman JP, Tsegaye G, Holt GT, Hu A, Walpita D et al (2016) Sensitive red protein calcium indicators for imaging neural activity. elife 5:e12727

Dana H, Sun Y, Mohar B, Hulse BK, Kerlin AM, Hasseman JP, Tsegaye G, Tsang A, Wong A, Patel R et al (2019) High-performance calcium sensors for imaging activity in neuronal populations and microcompartments. Nat Methods 16:649–657

Denk W, Strickler JH, Webb WW (1990) Two-photon laser scanning fluorescence microscopy. Science 248:73–76

Ellis-Davies GC (2007) Caged compounds: photorelease technology for control of cellular chemistry and physiology. Nat Methods 4:619–628

Forli A, Vecchia D, Binini N, Succol F, Bovetti S, Moretti C, Nespoli F, Mahn M, Baker CA, Bolton MM et al (2018) Two-photon bidirectional control and imaging of neuronal excitability with high spatial resolution in vivo. Cell Rep 22:3087–3098

Georgiou A, Christmas J, Moore J, Jeziorska-Chapman A, Davey A, Collings N, Crossland WA (2008) Liquid crystal over silicon device characteristics for holographic projection of high-definition television images. Appl Opt 47:4793–4803

Gerchberg RW, Saxton WO (1972) A practical algorithm for the determination of the phase from image and diffraction pictures. Optik 35:237–246

Gluckstad J (1996) Phase contrast image synthesis. Opt Commun 130:225–230

Golan L, Reutsky I, Farah N, Shoham S (2009) Design and characteristics of holographic neural photo-stimulation systems. J Neural Eng 6:066004

Grienberger C, Konnerth A (2012) Imaging calcium in neurons. Neuron 73:862–885

Grosenick L, Marshel JH, Deisseroth K (2015) Closed-loop and activity-guided optogenetic control. Neuron 86:106–139

Harris KD, Csicsvari J, Hirase H, Dragoi G, Buzsaki G (2003) Organization of cell assemblies in the hippocampus. Nature 424:552–556

Hebb DO (1949) The organization of behavior: a neuropsychological theory. John Wiley & Sons Inc., New York

Helmchen F, Denk W (2005) Deep tissue two-photon microscopy. Nat Methods 2:932–940

Hernandez O, Papagiakoumou E, Tanese D, Fidelin K, Wyart C, Emiliani V (2016) Three-dimensional spatiotemporal focusing of holographic patterns. Nat Commun 7:11,928

Ji N (2017) Adaptive optical fluorescence microscopy. Nat Methods 14:374–380

Jun JJ, Steinmetz NA, Siegle JH, Denman DJ, Bauza M, Barbarits B, Lee AK, Anastassiou CA, Andrei A, Aydin C et al (2017) Fully integrated silicon probes for high-density recording of neural activity. Nature 551:232–236

Klapoetke NC, Murata Y, Kim SS, Pulver SR, Birdsey-Benson A, Cho YK, Morimoto TK, Chuong AS, Carpenter EJ, Tian Z et al (2014) Independent optical excitation of distinct neural populations. Nat Methods 11:338–346

Lee WH (1974) Binary synthetic holograms. Appl Opt 13:1677–1682

Lu RW, Sun WZ, Liang YJ, Kerlin A, Bierfeld J, Seelig JD, Wilson DE, Scholl B, Mohar B, Tanimoto M et al (2017) Video-rate volumetric functional imaging of the brain at synaptic resolution. Nature Neurosci 20:620–628

Lutz C, Otis TS, DeSars V, Charpak S, DiGregorio DA, Emiliani V (2008) Holographic photolysis of caged neurotransmitters. Nat Methods 5:821–827

Mardinly AR, Oldenburg IA, Pegard NC, Sridharan S, Lyall EH, Chesnov K, Brohawn SG, Waller L, Adesnik H (2018) Precise multimodal optical control of neural ensemble activity. Nat Neurosci 21:881–893

Marshel JH, Kim YS, Machado TA, Quirin S, Benson B, Kadmon J, Raja C, Chibukhchyan A, Ramakrishnan C, Inoue M et al (2019) Cortical layer-specific critical dynamics triggering perception. Science 365: eaaw5202

Mattis J, Tye KM, Ferenczi EA, Ramakrishnan C, O'Shea DJ, Prakash R, Gunaydin LA, Hyun M, Fenno LE, Gradinaru V et al (2011) Principles for applying optogenetic tools derived from direct comparative analysis of microbial opsins. Nat Methods 9:159–172

Miyawaki A, Llopis J, Heim R, McCaffery JM, Adams JA, Ikura M, Tsien RY (1997) Fluorescent indicators for Ca2+ based on green fluorescent proteins and calmodulin. Nature 388:882–887

Nagel G, Szellas T, Huhn W, Kateriya S, Adeishvili N, Berthold P, Ollig D, Hegemann P, Bamberg E (2003) Channelrhodopsin-2, a directly light-gated cation-selective membrane channel. Proc Natl Acad Sci U S A 100:13,940–13,945

Nikolenko V, Poskanzer KE, Yuste R (2007) Two-photon photostimulation and imaging of neural circuits. Nat Methods 4:943–950

Nikolenko V, Watson BO, Araya R, Woodruff A, Peterka DS, Yuste R (2008) SLM microscopy: scanless two-photon imaging and photostimulation with spatial light modulators. Front Neural Circuits 2:5

Oron D, Tal E, Silberberg Y (2005) Scanningless depth-resolved microscopy. Opt Express 13:1468–1476

Ouzounov DG, Wang T, Wang M, Feng DD, Horton NG, Cruz-Hernandez JC, Cheng YT, Reimer J, Tolias AS, Nishimura N et al (2017) In vivo three-photon imaging of activity of GCaMP6-labeled neurons deep in intact mouse brain. Nat Methods 14:388–390

Packer AM, Peterka DS, Hirtz JJ, Prakash R, Deisseroth K, Yuste R (2012) Two-photon optogenetics of dendritic spines and neural circuits. Nat Methods 9:1202–1205

Packer AM, Russell LE, Dalgleish HW, Hausser M (2015) Simultaneous all-optical manipulation and recording of neural circuit activity with cellular resolution in vivo. Nat Methods 12:140–146

Papagiakoumou E, de Sars V, Oron D, Emiliani V (2008) Patterned two-photon illumination by spatiotemporal shaping of ultrashort pulses. Opt Express 16:22,039–22,047

Papagiakoumou E, Anselmi F, Begue A, de Sars V, Gluckstad J, Isacoff EY, Emiliani V (2010) Scanless two-photon excitation of channelrhodopsisssn-2. Nat Methods 7:848–854

Paredes RM, Etzler JC, Watts LT, Zheng W, Lechleiter JD (2008) Chemical calcium indicators. Methods 46:143–151

Pawley JB (2006) Handbook of biological confocal microscopy, 3rd edn. Springer, New York

Pegard NC, Mardinly AR, Oldenburg IA, Sridharan S, Waller L, Adesnik H (2017) Three-dimensional scanless holographic optogenetics with temporal focusing (3D-SHOT). Nat Commun 8:1228

Petran M, Hadravsk M, Egger MD, Galambos R (1968) Tandem-scanning reflected-light microscope. J Opt Soc Am 58:661

Pnevmatikakis EA, Soudry D, Gao Y, Machado TA, Merel J, Pfau D, Reardon T, Mu Y, Lacefield C, Yang W et al (2016) Simultaneous denoising, deconvolution, and demixing of calcium imaging data. Neuron 89:285–299

Podgorski K, Ranganathan GN (2016) Brain heating induced by near infrared lasers during multi-photon microscopy. J Neurophysiol 116:1012–1023

Quirin S, Peterka DS, Yuste R (2013) Instantaneous three-dimensional sensing using spatial light modulator illumination with extended depth of field imaging. Opt Express 21:16007–16021

Quirin S, Jackson J, Peterka DS, Yuste R (2014) Simultaneous imaging of neural activity in three dimensions. Front Neural Circuits 8:29

Ramón y Cajal S (1888) Estructura de los centros nerviosos de las aves. Rev Trim Histol Norm Pat (in Spanish) 1:1–10

Reicherter M, Haist T, Wagemann EU, Tiziani HJ (1999) Optical particle trapping with computer-generated holograms written on a liquid-crystal display. Opt Lett 24:608–610

Rodrigo PJ, Palima D, Gluckstad J (2008) Accurate quantitative phase imaging using generalized phase contrast. Opt Express 16:2740–2751

Rowlands CJ, Park D, Bruns OT, Piatkevich KD, Fukumura D, Jain RK, Bawendi MG, Boyden ES, So PTC (2017) Wide-field three-photon excitation in biological samples. Light Sci Appl 6:e16255

Shemesh OA, Tanese D, Zampini V, Linghu C, Piatkevich K, Ronzitti E, Papagiakoumou E, Boyden ES, Emiliani V (2017) Temporally precise single-cell-resolution optogenetics. Nat Neurosci 20:1796–1806

Shepherd GM (1991) Foundations of the neuron doctrine. Oxford University Press, New York

Sherrington CS (1906) Observations on the scratch-reflex in the spinal dog. J Physiol London 34:1–50

Smetters D, Majewska A, Yuste R (1999) Detecting action potentials in neuronal populations with calcium imaging. Methods 18:215–221

Song A, Charles AS, Koay SA, Gauthier JL, Thiberge SY, Pillow JW, Tank DW (2017) Volumetric two-photon imaging of neurons using stereoscopy (vTwINS). Nat Methods 14:420

Sun B, Salter PS, Roider C, Jesacher A, Strauss J, Heberle J, Schmidt M, Booth MJ (2018) Four-dimensional light shaping: manipulating ultrafast spatiotemporal foci in space and time. Light Sci Appl 7:17,117

Thalhammer G, Bowman RW, Love GD, Padgett MJ, Ritsch-Marte M (2013) Speeding up liquid crystal SLMs using overdrive with phase change reduction. Opt Express 21:1779–1797

Tsien RY (1980) New calcium indicators and buffers with high selectivity against magnesium and protons: design, synthesis, and properties of prototype structures. Biochemistry 19:2396–2404

Wang S, Szobota S, Wang Y, Volgraf M, Liu Z, Sun C, Trauner D, Isacoff EY, Zhang X (2007) All optical interface for parallel, remote, and spatiotemporal control of neuronal activity. Nano Lett 7:3859–3863

Watson BO, Nikolenko V, Araya R, Peterka DS, Woodruff A, Yuste R (2010) Two-photon microscopy with diffractive optical elements and spatial light modulators. Front Neurosci 4:29

Yang W, Yuste R (2017) In vivo imaging of neural activity. Nat Methods 14:349–359

Yang W, Yuste R (2018) Holographic imaging and photostimulation of neural activity. Curr Opin Neurobiol 50:211–221

Yang S, Papagiakoumou E, Guillon M, de Sars V, Tang CM, Emiliani V (2011) Three-dimensional holographic photostimulation of the dendritic arbor. J Neural Eng 8:046002

Yang WJ, Sun TB, Rao Y, Megens M, Chan T, Yoo BW, Horsley DA, Wu MC, Chang-Hasnain CJ (2014) High speed optical phased array using high contrast grating all-pass filters. Opt Express 22:20,038–20,044

Yang SJ, Allen WE, Kauvar I, Andalman AS, Young NP, Kim CK, Marshel JH, Wetzstein G, Deisseroth K (2015) Extended field-of-view and increased-signal 3D holographic illumination with time-division multiplexing. Opt Express 23:32,573–32,581

Yang W, Miller JE, Carrillo-Reid L, Pnevmatikakis E, Paninski L, Yuste R, Peterka DS (2016) Simultaneous multi-plane imaging of neural circuits. Neuron 89:269–284

Yang W, Carrillo-Reid L, Bando Y, Peterka DS, Yuste R (2018) Simultaneous two-photon imaging and two-photon optogenetics of cortical circuits in three dimensions. elife 7:e32671

Yizhar O, Fenno LE, Prigge M, Schneider F, Davidson TJ, O'Shea DJ, Sohal VS, Goshen I, Finkelstein J, Paz JT et al (2011) Neocortical excitation/inhibition balance in information processing and social dysfunction. Nature 477:171–178

Yuste R (2015) From the neuron doctrine to neural networks. Nat Rev Neurosci 16:487–497

Yuste R, Denk W (1995) Dendritic spines as basic functional units of neuronal integration. Nature 375:682–684

Yuste R, Katz LC (1991) Control of postsynaptic Ca2+ influx in developing neocortex by excitatory and inhibitory neurotransmitters. Neuron 6:333–344

Zhang Z, Russell LE, Packer AM, Gauld OM, Hausser M (2018) Closed-loop all-optical interrogation of neural circuits in vivo. Nat Methods 15:1037–1040

Zhu G, van Howe J, Durst M, Zipfel W, Xu C (2005) Simultaneous spatial and temporal focusing of femtosecond pulses. Opt Express 13:2153–2159

Zhu P, Fajardo O, Shum J, Zhang Scharer YP, Friedrich RW (2012) High-resolution optical control of spatiotemporal neuronal activity patterns in zebrafish using a digital micromirror device. Nat Protoc 7:1410–1425

Zipfel WR, Williams RM, Webb WW (2003) Nonlinear magic: multiphoton microscopy in the biosciences. Nat Biotechnol 21:1369–1377

# Upconversion Nanoparticle-Mediated Optogenetics

44

Zhigao Yi, Angelo H. All, and Xiaogang Liu

**Abstract**

Upconversion nanoparticle-mediated optogenetics enables remote delivery of upconverted visible light from a near-infrared light source to targeted neurons or areas, with the precision of a pulse of laser light in vivo for effective deep-tissue neuromodulation. Compared to conventional optogenetic tools, upconversion nanoparticle-based optogenetic techniques are less invasive and cause reduced inflammation with minimal levels of tissue damage. In addition to the optical stimulation, this design offers simultaneously temperature recording in proximity to the stimulated area. This chapter strives to provide life science researchers with an introduction to upconversion optogenetics, starting from the fundamental concept of photon upconversion and nanoparticle fabrication to the current state-of-the-art of surface engineering and device integration for minimally invasive neuromodulation.

**Keywords**

Upconversion nanoparticle · Near-infrared · Remote control · Opsin · Optogenetics · Neuromodulation

## Abbreviations

| | |
|---|---|
| $Ca^{2+}$ | Calcium |
| $Dy^{3+}$ | Dysprosium |
| $Er^{3+}$ | Erbium |
| $Eu^{3+}$ | Europium |
| $Gd^{3+}$ | Gadolinium |
| $Ho^{3+}$ | Holmium |
| $Lu^{3+}$ | Lutetium |
| $Mn^{2+}$ | Manganese |
| NIR | Near-infrared |
| $Sm^{3+}$ | Samarium |
| $Tb^{3+}$ | Terbium |
| $Tm^{3+}$ | Thulium |
| $Y^{3+}$ | Yttrium |
| $Yb^{3+}$ | Ytterbium |

Z. Yi
Department of Chemistry, National University of Singapore, Singapore, Singapore

A. H. All
Department of Chemistry, Faculty of Science, Hong Kong Baptist University, Kowloon, Hong Kong
e-mail: angelo@hkbu.edu.hk

X. Liu (✉)
Department of Chemistry, National University of Singapore, Singapore, Singapore

The N1 Institute for Health, National University of Singapore, Singapore, Singapore
e-mail: chmlx@nus.edu.sg


H. Yawo et al. (eds.), *Optogenetics*, Advances in Experimental Medicine and Biology 1293,
https://doi.org/10.1007/978-981-15-8763-4_44

## 44.1 Introduction

Optogenetics is an advanced optical approach for targeted, spatiotemporal modulation of specific neural functions through dynamic manipulation of light-sensitive opsin proteins in the plasma membrane of neurons. In contrast to conventionally pharmacological, genetic, electrical, and magnetic strategies (Kramer et al. 2013; Miller 1989; Zamponi 2016; Kringelbach et al. 2007), optogenetic tools take advantages of light modulation with fast "on–off" kinetics, tunable excitation and emission wavelengths, and precise delivery of stimulatory light to targeted regions. This approach has made it possible to enable spontaneous modulation of depolarization and hyperpolarization of neurons at an even single-cell level. In this context, light-sensitive opsin proteins play a core role in mediating cellular response through external light excitation. When triggered by light at a specific wavelength, such proteins undergo conformational changes that affect an influx or efflux of cations or anions through the ion channels of the cell membrane. The current generated by the cation flux depolarizes the membrane of the neuron, resulting in the activation of cellular signaling pathways. The neuron fires an action potential that propagates to adjacent neurons. Optogenetics provides a powerful toolbox to investigate cellular biology, neuroscience, and behavior correlation at a wide range of spatiotemporal scales (Fenno et al. 2011; Deisseroth 2011).

The evolving field of optogenetics is mainly attributed to the discovery of various opsin variants (e.g., channelrhodopsins and halorhodopsins) combined with the implementation of different light sources (e.g., lasers and light-emitting diodes). Action potential stimulation was first demonstrated in Aplysia ganglia neurons using a blue laser (Fork 1971). A milestone in optogenetics was the manipulation of mammalian neurons, which was achieved with the use of Channelrhodopsin-2 (ChR2) (Boyden et al. 2005; Ishizuka et al. 2006). Despite numerous successful efforts in vitro, effective stimulation of targeted neurons in vivo remains a formidable challenge because current opsins only respond to visible light usually at 430–630 nm, a spectral range where living tissues show strong absorption and scattering. It is difficult to directly deliver visible light through layers of tissues to achieve efficient, targeted neuromodulation. To address this issue, current optogenetic approaches generally adopt optical fiber insertion or implantation of microchips with light-emitting diodes to deliver visible light into targeted areas in deep tissues and organs (Cardin et al. 2010; McAlinden et al. 2015). However, these invasive procedures inevitably induce side effects and damages such as inflammation and limit free movement of the animal under study, thereby hindering their practical use in long-term and behavioral studies.

Two possible strategies could be carried out to overcome the limitations imposed by conventional techniques. One is to develop new types of opsin proteins that can respond to near-infrared (NIR) light capable of deep-tissue penetration. Although channelrhodopsins with red-shifted wavelength responses have been exploited, their stimulating wavelengths are still confined within the visible range (Zhang et al. 2008; Urmann et al. 2017). The other possible strategy is to deliver NIR light to the targeted area and simultaneously convert to visible light in situ utilizing certain converters. In 2010, Deisseroth et al. put forth an innovative concept that realizes NIR-to-visible conversion in vivo with the mediation of upconverting nanoparticles (Deisseroth and Anikeeva 2016). From then onward, luminescent nanomaterials, especially upconversion nanoparticle-mediated optogenetics has witnessed tremendous research efforts and progress (All et al. 2019; Wang et al. 2019; Yu et al. 2019).

Upconversion nanoparticles can serve as powerful nano-antenna absorbing NIR light and emitting visible light ranging from ultraviolet to NIR regions, bridging the spectral gap between established opsin proteins and NIR light source excitation. Importantly, upconversion nanoparticle-mediated optogenetics holds the unique advantages of wireless control, minimal invasion, and negligible cytotoxicity in vivo

(Wang et al. 2017a, b; Chen et al. 2018; Chen 2019). Therefore, this could become a general trend in the customization of upconversion nanoparticles for specific research purposes in neuromodulation and optogenetics. Mastering basic knowledge of optical mechanisms, chemical engineering, and properties optimization is necessary to accommodate the expansion of the upconversion nanoparticle-based optogenetic tool. In this regard, we will focus on introducing basic mechanisms, synthesis methods, surface modifications, and excitation/emission optimization strategies of upconversion nanoprobes, as well as presenting recent progress in upconversion nanoparticle-mediated optogenetics.

## 44.2 Background Information on Upconversion Nanomaterials

### 44.2.1 Upconversion Mechanism

The concept of upconversion was established in the 1950s by Nicolas Bloembergen (Bloembergen 1959). In recent decades, upconversion nanomaterials have been theoretically and experimentally investigated because of their potential applications in optics, display, security, storage, nanomedicine, and neuroscience. In brief, upconversion nanomaterials consist of a host crystal and lanthanide dopants capable of absorbing two or more low-energy photons and converting them into one photon with higher energy. As shown in Fig. 44.1, upconverting processes can be classically categorized into five types: (a) excited-state absorption, (b) energy transfer upconversion, (c) photon avalanche, (d) cooperative sensitization, and (e) energy migration-mediated upconversion (Auzel 2004; Wang et al. 2011a, b).

Energy transfer upconversion, as the most efficient and adopted upconversion process, requires a sensitizer for photon absorption and an activator for photon emission. This requirement can be met with specific lanthanide pairs such as ytterbium/erbium, ytterbium/thulium, and ytterbium/holmium ($Yb^{3+}/Er^{3+}$, $Yb^{3+}/Tm^{3+}$, and $Yb^{3+}/Ho^{3+}$, Wang and Liu 2009). Various emission colors can be easily achieved by tuning the types of lanthanide dopants and their concentrations in the host lattice. Energy transfer efficiency is sensitive to doping concentration. The tradeoff between energy loss through cross-relaxation effects and the probability of energy transfer determines the critical doping concentration for maximum energy transfer efficiency. Energy migration-mediated upconversion is an attractive approach to realize photon upconversion through other types of lanthanide activators (dysprosium $Dy^{3+}$, terbium $Tb^{3+}$, europium $Eu^{3+}$, samarium $Sm^{3+}$, etc.) and even transition metal activators (manganese $Mn^{2+}$). Through the use of a multiple core-shell nanostructure design, the energy migrators (typically gadolinium $Gd^{3+}$ ions) can be controlled to absorb photons from $Yb^{3+}/Tm^{3+}$ couples and then migrate the excitation energy to activators over a large distance (Wang et al. 2011a, b; Han et al. 2016; Liu et al. 2017). The energy migration strategy dramatically improves the upconversion efficiency of these activators with ladder-like intermediate energy states through spatial confinement of lanthanide ions.

The characteristics of photon upconversion nanoparticles include large anti-Stokes shift, narrow emission peaks, full-spectral tunable emission, stable physicochemical and optical properties, good biocompatibility, and programmable surface functionality. Upconversion nanoparticles are considered as alternative probes to organic dyes and quantum dots and hold promise for applications in biosensing, deep-tissue imaging, disease diagnosis, and therapy as well as in neuroscience.

### 44.2.2 Synthesis Methods

Size, morphology, and surface functional group of nanoparticles affect their physicochemical properties such as dispersity and stability in physiological conditions and their in vivo behaviors such as interactions with cells, circulation time, biodistribution, and biocompatibility (Wang et al. 2012; Gnach et al. 2015). Therefore, precise

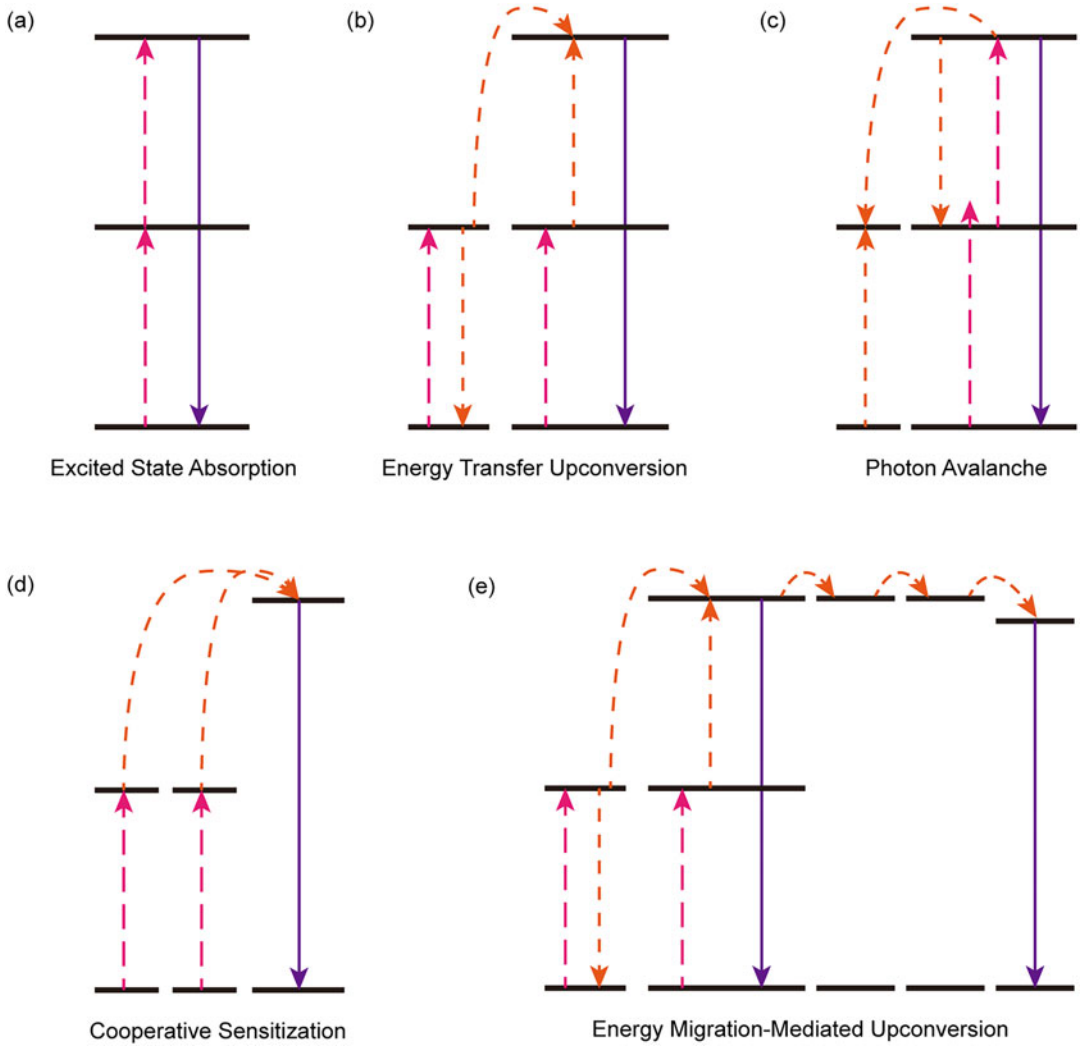


**Fig. 44.1** Schematic illustration of typical upconversion processes, where dashed arrows in the red stand for direct excitation processes, dashed arrows in orange represent energy transfer processes and full arrows in purple show radiative emission processes

control of these factors in fabrication and post-treatment of upconversion nanoparticles is crucial to their further bio-applications, particularly in optogenetics. It is worth mentioning that current chemical synthesis methods mainly contain thermal decomposition, coprecipitation, and hydrothermal reactions (Fig. 44.2).

Thermal decomposition is the most effective method to fabricate ultrasmall upconversion nanocrystals, even sub-10 nm in diameter. This method takes advantage of an oxygen-free reaction where organic precursors are decomposed in boiling organic solvents at high temperatures with the assistance of surfactants. The first demonstration of this method was the synthesis of high-quality $LaF_3$ nanocrystals (Zhang et al. 2005). In the work, one-step, mass production of single-crystalline and monodisperse $LaF_3$ triangular nanoplates (2.0 nm in thickness) was realized via thermolysis of lanthanum trifluoroacetate in a hot oleic acid/octadecene solution. In 2007, Yi and Chow applied hot

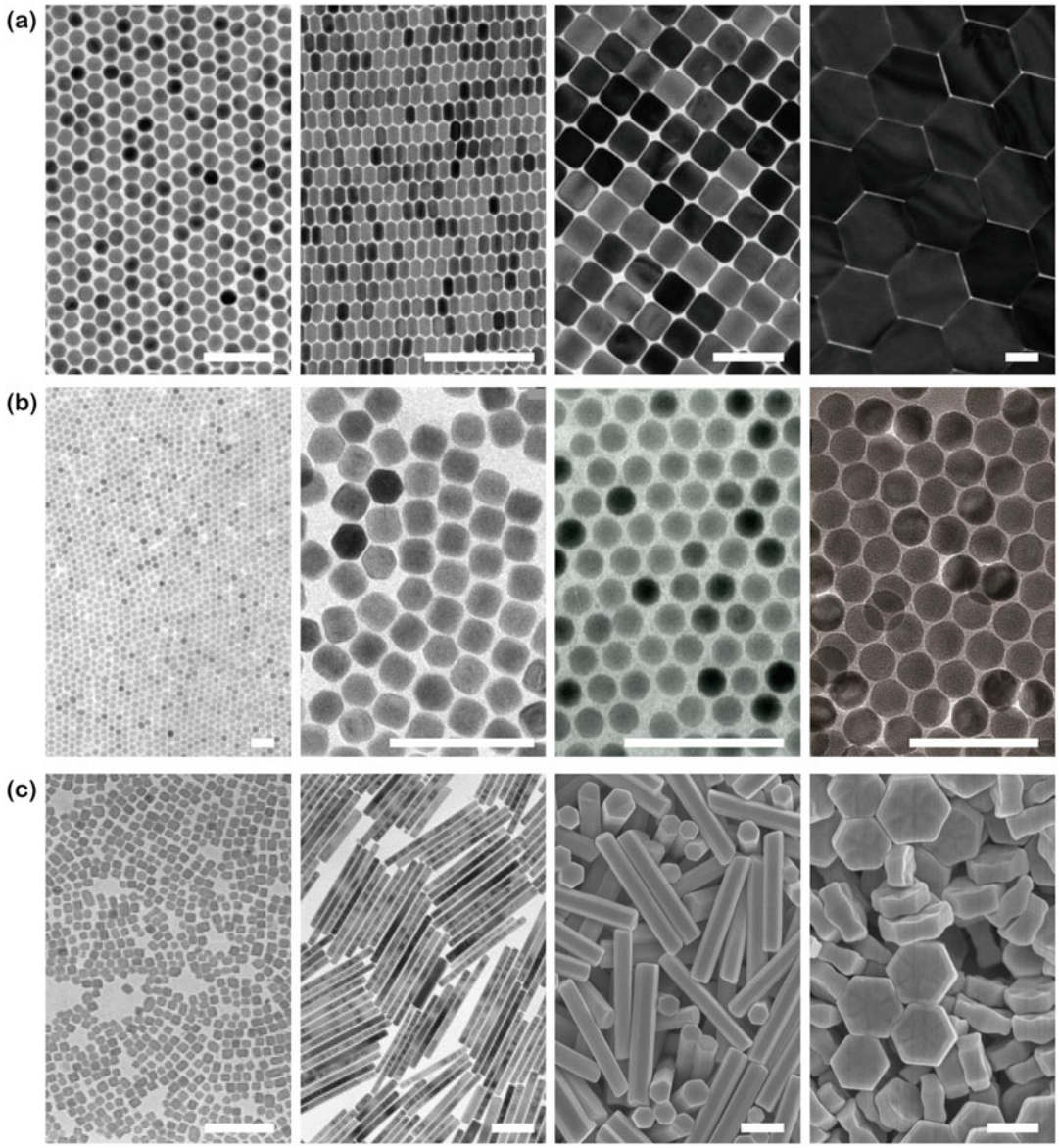


**Fig. 44.2** Electron micrographs of typical sodium lanthanide fluoride-based upconversion materials. (**a**) $NaYF_4$ nanoparticles, nanorods, nanocubes, and nanodisks synthesized by thermal decomposition method (Ye et al. 2010). (**b**) $NaYF_4$, $NaGdF_4$, $NaYbF_4$, $NaLuF_4$ nanoparticles synthesized by coprecipitation method (Li and Zhang 2008; Wang et al. 2014, 2015; Chen et al. 2019). (**c**) $NaYF_4$ nanoparticles and nanorods, $NaYF_4$ micro-rods, and $NaLuF_4$ micro-disks synthesized by hydrothermal method (Wang and Li 2007; Zhang et al. 2016). Scale bar: 500 nm for the last two graphs and 100 nm for the rest. Note that only host materials other than dopants are denoted here

injection techniques with the thermal decomposition method and successfully obtained core-shell structured nanoparticles with an average diameter of ~12 nm (Yi and Chow 2007). Ye et al. fabricated monodispersed, homogeneous upconversion nanoparticles with a controllable size ranging from several to hundreds of nanometers using sodium and lanthanide

trifluoroacetate as precursors and a molten salt bath as a heat source (Ye et al. 2010).

Coprecipitation is one of the most popular methods to fabricate upconversion nanoparticles, which involves nucleation at room temperature and subsequent epitaxial growth at high temperatures. Li and Zhang first developed a coprecipitation method to synthesize hydrophobic hexagonal $NaYF_4$:Yb/Er/Tm nanoparticles by adding a methanol solution of sodium hydroxide and ammonium fluoride into a uniform solution containing lanthanide chlorides, oleic acid, and 1-octadecene to realize room-temperature nucleation and then elevating the temperature to 300 °C to perform Ostwald ripening growth of nanoparticles (Li and Zhang 2008). With this method, homogeneous nanoparticles with different shapes and sizes from several to a hundred nanometers can be fabricated through changing reaction parameters such as reaction time, temperature, and dosage of reagents. Liu's group and van Veggel's group further improved the coprecipitation method by replacing lanthanide chlorides with lanthanide acetates as starting materials to synthesize core-shell nanostructures (Wang et al. 2011a, b; Abel et al. 2009).

Another versatile approach to synthesize highly crystallized upconversion nanoparticles is the hydrothermal method, where a homogenous aqueous solution containing lanthanide ions and anions (typically fluoride) is subjected to thermal treatment under high pressure and temperature provided by a sealed, Teflon-lined autoclave. Li group first proposed a general hydrothermal approach to synthesize nanocrystals through a liquid–solid-solution phase transfer and separation process, where they fabricated $NaYF_4$ nanocrystals of 10 nm in diameter (Wang et al. 2005; Wang and Li 2007). Liu group reported a modified hydrothermal method to simultaneously tune the phase, size, and shape of $NaYF_4$ nanoparticles through lanthanide doping (Wang et al. 2010). In their work, lanthanide dopants with large ionic radii such as $Gd^{3+}$ played a significant role in stabilizing the hexagonal-phase structure and decreasing crystal size. Liu group further developed an epitaxial growth strategy based on a hydrothermal method for controllable fabrication of upconversion micro-disks and micro-rods that can emit multiple colors at single-particle levels under NIR excitation (Zhang et al. 2016). The advantages of hydrothermal methods are that the crystallographic phase, size, shape, and luminescent properties can be easily tuned by controlling experimental parameters, such as hydrothermal temperature, reaction time, solvents, surfactants, pH value, concentration, the ratio of dopants, and so on. Distinctive from thermal decomposition and coprecipitation, the hydrothermal method starts with inexpensive reagents and can produce nano−/micro-sized crystals with hydrophobic or hydrophilic surfaces through a one-pot or multistep synthesis. Nevertheless, the homogeneity and monodispersity of hydrothermally synthesized nanoparticles are inferior to those obtained from decomposition and coprecipitation. Although several other methodologies have been established, the three strategies mentioned earlier are the most widely used to realize efficient upconversion emission, especially in fluoride host materials and core-shell nanostructure design.

### 44.2.3 Surface Functional Modification

Reliable biocompatibility and efficient optical output of upconversion nanoparticles are the prerequisites to their practical use in in vivo optogenetics and deep brain modulation. Although hydrophilic nanoparticles can be directly prepared by a hydrothermal reaction in aqueous solutions, they often have a broad size distribution, unsatisfied water solubility, and insufficient optical output. In contrast, commonly adopted approaches in organic solvents can produce nanoparticles with uniform morphology and high-efficiency photon conversion. But these nanoparticles are indispersible in aqueous solutions because of hydrophobic ligand coating. To address this problem, the surface functional modification should be implemented (Fig. 44.3).

A straightforward approach to improve the aqueous dissolution of upconversion nanoparticles is to eliminate hydrophobic ligands

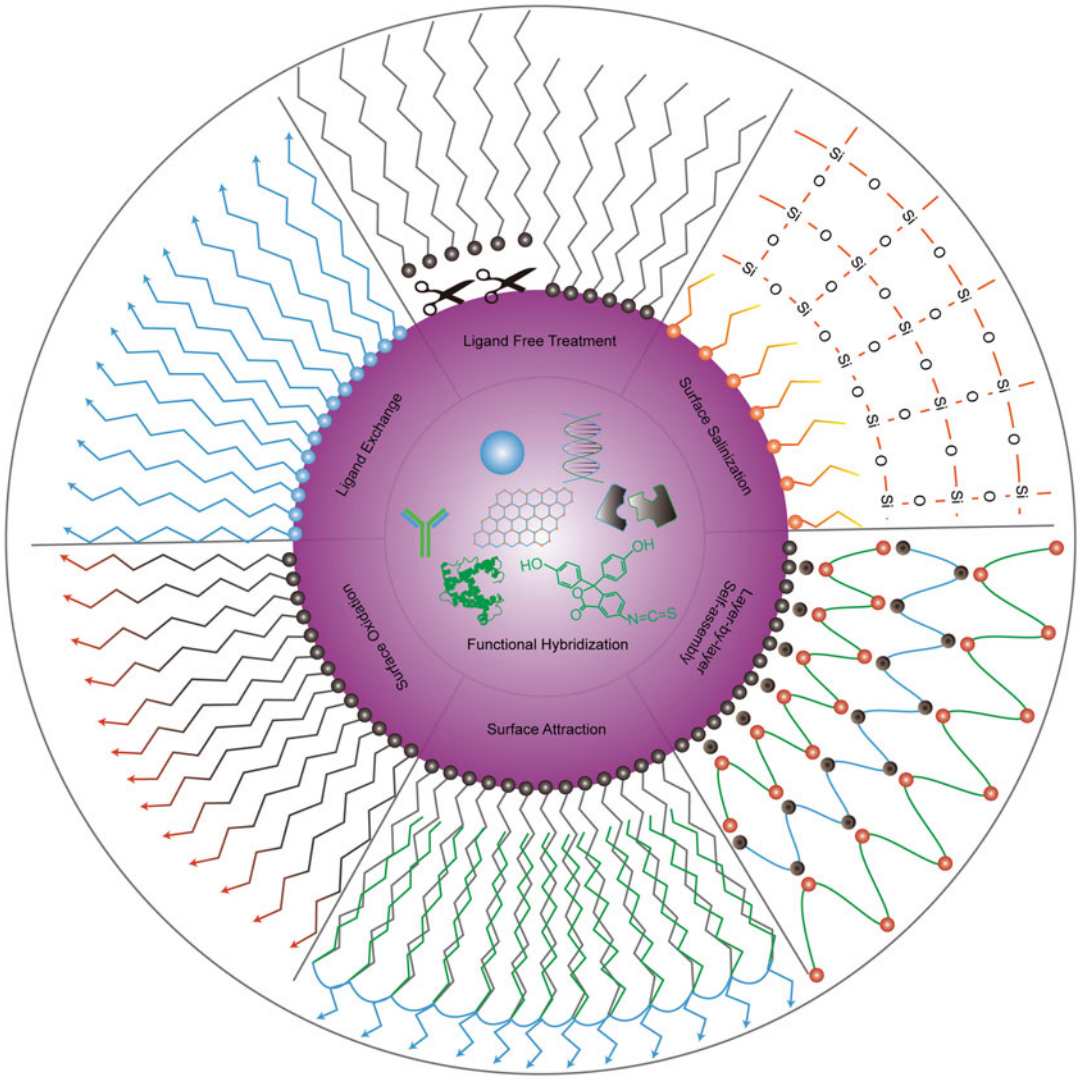


**Fig. 44.3** Common strategies for surface modification of upconversion nanoparticles, including ligand-free treatment, ligand exchange, surface oxidation, surface attraction, layer-by-layer self-assembly, surface salinization, and functional hybridization

on the surface through an acid treatment (Bogdan et al. 2011; Deng et al. 2011). However, the exposure of "naked" nanoparticles to physiological conditions may lead to unexpected aggregation and cytotoxicity. Attractive strategies include posttreatment with hydrophilic segments through ligand exchange, ligand oxidation, polymer attraction, and surface salinization, as well as layer-by-layer self-assembly using polyelectrolytes (Wang and Liu 2009; Sedlmeier and Gorris 2014). Ligand exchange method utilizes hydrophilic organic ligands with a highly coordinative capability to replace those hydrophobic and poorly coordinative ligands. For instance, long carbon chains from oleic acid can be easily exchanged by polyacrylic acid or polyethylene glycol (Xiong et al. 2010; Zeng et al. 2012). The carbon–carbon double bond of surface ligands can be oxidized by Lemieux-von Rudloff reagent, thus improving the nanoparticles' water

solubility. But this method only works for a limited number of ligands. Surface salinization is the most widely used method to make nanoparticles biocompatible. A solid or mesoporous silica layer can be directly coated onto hydrophobic particles (Li and Zhang 2006; Liu et al. 2012).

Wrapping upconversion nanoparticles with other functional nanomaterials or biomolecules as a hybrid nanoplatform opens the opportunity to advanced optogenetics with specific purposes and multiplex neuromodulation. For example, Liu group reported the integration of manganese dioxide nanosheet on the surface of upconversion nanoparticles, which was demonstrated for the detection of intracellular glutathione through optical sensing (Deng et al. 2011). Surface attachment of ultrasmall gold nanoparticles can suppress upconversion emission at short wavelengths and enhance the photothermal conversion of upconversion nanoparticles (Han et al. 2017). Antibody-conjugated upconversion nanoparticles have been applied to in situ molecular mappings of different cancer biomarkers (Zhou et al. 2015a, b). Recently, cell membranes have been cloaked onto nanoparticle's surface to achieve immune escaping and homologous targeting of cancer (Rao et al. 2016; Yi et al. 2019). Upconversion nanoparticles have been combined with a variety of functional materials or molecules, including quantum dot, graphene, perovskite, organic dye, enzyme, protein, and DNA.

## 44.3 Optical Optimization of Upconversion Nanoparticles

### 44.3.1 Spectral Overlapping

To perform upconversion nanoparticle-mediated optogenetics, the emission wavelength of nanoparticles must be tuned to match the absorption bands of targeted opsins for efficient neural modulation (Yi and Chow 2006; Suyver et al. 2006). Visible emission modulation can be readily achieved through co-doping of $Yb^{3+}$ with $Tm^{3+}$, $Ho^{3+}$, $Er^{3+}$ in nanocrystals (Fig. 44.4). Although blue band (ChR2) and green band (VChR1 and C1V1) absorption can be well addressed by $Tm^{3+}$ and $Er^{3+}$ doping, the yellow band from 550 to 650 nm for controlling $Cl^-$-pumping halorhodopsins remains a challenge. This deficiency can be overcome by utilizing $Eu^{3+}$ emission at 590 and 616 nm with energy-migration or cooperative-sensitization processes (Wang et al. 2011a, b; Zhou et al. 2015a, b).

Lanthanide activators usually emit at multiple wavelengths under NIR excitation. For optogenetics, the impurity of stimulating light may cause unwanted effects in some cases, meaning that these redundant emission peaks need to be removed. For example, $Er^{3+}$ ions exhibit four characteristic upconversion emission peaks at 409, 525, 546, and 659 nm, of which 409 and 659 nm emissions are not used for stimulating VChR1 and C1V1. There are several smart approaches to address this issue. For instance, inhibition of red emission at 659 nm can be achieved by decreasing the dopant concentration of $Yb^{3+}$ in the matrix while enhancing green emission at 546 nm (Wang and Liu 2008). Additionally, pure red color with single-band emission can be achieved through an energy back-transfer process involving codoping of $Mn^{2+}$ ions in host lattices (Tian et al. 2012; Wang et al. 2011a, b). Apart from compositional modulation, nano-sized color filters are also effective for realizing monochromatic upconversion emission. In 2015, a general method was developed to achieve single band upconversion by using organic dyes as a filter to absorb unwanted emissions (Zhou et al. 2015a, b).

### 44.3.2 Irradiation Wavelength Broadening

Examples of upconversion-mediated optogenetics are currently focused on $Yb^{3+}$-sensitized nanoparticles, in which a 980 nm laser was usually applied as the excitation source. Considerable absorption by water in this spectral region may result in tissue overheating, a major concern especially for in vivo deep brain stimulation. The currently adopted solution is to minimize the overheating effect through modulation

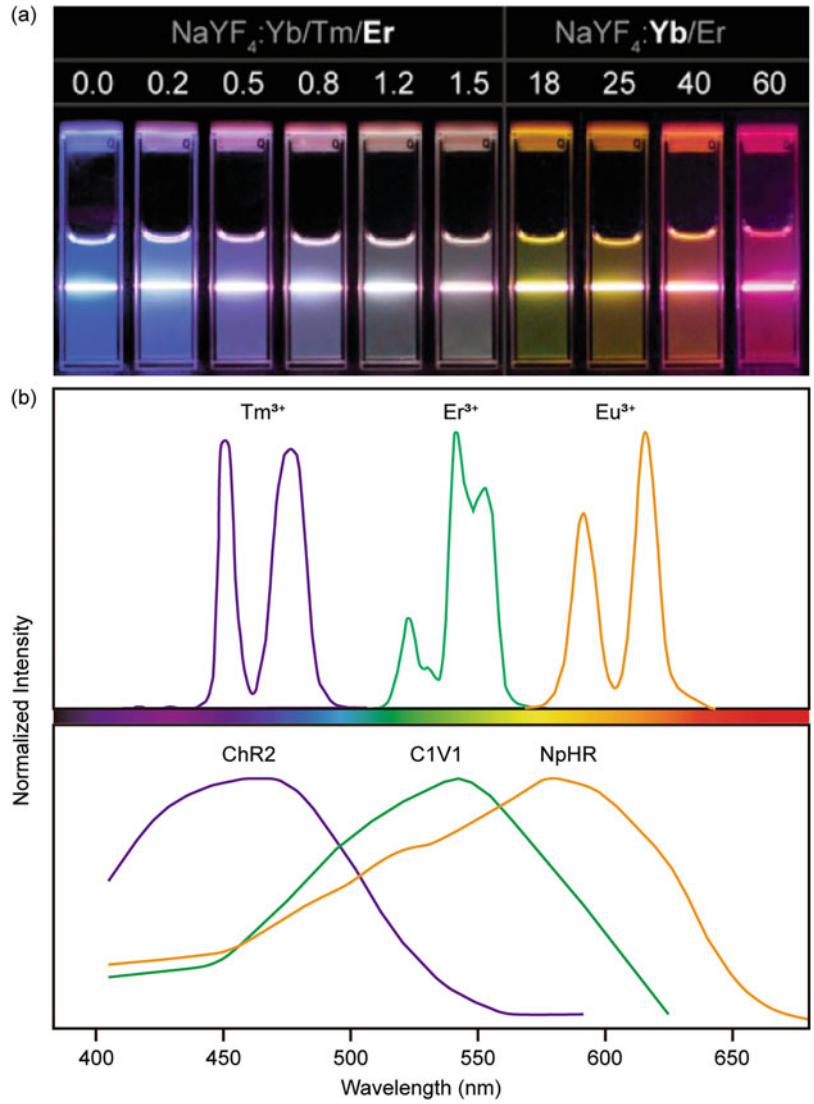


**Fig. 44.4** (**a**) Photographs of upconversion nanoparticles under NIR excitation showing multicolor emission tuning in $NaYF_4$ host with varying concentrations of $Er^{3+}$ and $Yb^{3+}$ (Wang and Liu 2008). The upper labels represent the corresponding concentration of highlighted dopant ions. (**b**) Representative emission peaks from typical lanthanide activators and absorption bands from commonly used opsins

of peak intensity, pulse frequency, and duration time of the laser input, as well as reserving sufficient time for heat dissipation (Wang et al. 2017a, b; Chen et al. 2018; Miyazaki et al. 2019). Another interesting strategy is to vary the irradiation wavelength at a spectral region where absorption from water and bio-tissue is relatively low. Recently, co-doping of $Nd^{3+}/Yb^{3+}$ as sensitizers has allowed effective excitation at 808 nm, where the coefficient of water absorption is almost one-tenth of that at 980 nm (Shen et al. 2013; Xie et al. 2013; Liang et al. 2016). Liu group also reported an $Nd^{3+}$-free approach by which intense visible emissions can be obtained through self-sensitizing $Er^{3+}$ at multiple wavelengths such as 808, 980, and 1532 nm (Chen et al. 2017). Additionally, the excitation wavelength for photon upconversion can be broadened by utilizing organic dyes as sensitizers (Wu et al. 2016; Liang et al. 2019a, b). The variation in excitation responses of different sensitizers renders upconversion nanoparticles with orthogonal emissions under irradiation at different wavelengths (Zheng et al. 2018), which

can be utilized for the design of multiplex neuromodulation.

### 44.3.3 Output Brightness Enhancement

As with spectral overlapping, the intensity of upconversion emission is also essential for in vivo optogenetics. A strong upconverted emission guarantees sufficient stimulation of opsins so that light-induced depolarization can surpass the threshold potential and generate an action potential in targeted neurons. Enhancing upconversion emission intensity can be achieved through external or internal factors. In principle, a higher excitation power density (below the saturation intensity) produces a higher emission intensity according to the classical theory of nonlinear optics (Pollnau et al. 2000). However, increasing the input may not be the best choice since it may aggravate living neurons considering the risk of overheating. Instead, pulsed excitation input with high peak intensity but relatively low average power density is commonly adopted for effective delivery of light with minimal tissue heating and dynamic modulation of neurons in vivo (Wang et al. 2017a, b; Chen et al. 2018; Miyazaki et al. 2019).

Luminescence enhancement could boost energy conversion efficiency (Fig. 44.5). Lanthanide ions intrinsically exhibit low light-absorption coefficients because of parity-forbidden f–f transitions. For example, $Nd^{3+}$ ion possesses a relatively higher photon-absorption coefficient at 808 nm compared to the conventional sensitizer $Yb^{3+}$ at 980 nm. Co-doping of $Nd^{3+}$ with $Yb^{3+}$ in the host lattice would be an effective way to enhance upconversion emission (Shen et al. 2013). Organic dyes have also proven effective in boosting photon absorption in upconversion nanocrystals as their light-absorption coefficients are orders of magnitude higher than those of lanthanide ions (Zou et al. 2012; Chen et al. 2015a, b; Wang et al. 2017a, b).

To promote conversion efficacy in upconversion nanoparticles, the main challenge is to reduce nonradiative energy loss. Over the past few decades, several strategies have been developed, including the host–lattice modulation, crystal composition variation, nanostructure design, and nanoplatform engineering. Heer et al. first identified $NaYF_4$ as a matrix material with relatively low phonon energy (~350 $cm^{-1}$) to achieve multicolor emission (Heer et al. 2004). An effective method to boost upconversion emission involves the modulation of host lattice symmetry by host–dopant ion substitution (Chen et al. 2008). Other practices have dedicated to regulating dopant types and concentrations for alleviated quenching effects (Zhao et al. 2013; Gargas et al. 2014). One commonly adopted approach is surface passivation of nanoparticles through a core-shell design. Suitable shell coating can restrain defect-induced radiative quenching (Wen et al. 2018). In view of composition and functionality, a shell layer can be categorized as an optically inert shell (e.g., $CaF_2$, $SiO_2$, and dopant-free host crystal) and an optically active shell (e.g., sensitizer or activator ions doping) (Chen et al. 2012; Li and Zhang 2006; Ren et al. 2012). In a recent study, tetherless deep brain stimulation was reported by Lin et al., who carried out a core–shell–shell design and demonstrated a considerable emission enhancement by optimizing the $Yb^{3+}$ concentration of the middle shell (Lin et al. 2018). Nanoplatform engineering mainly involves surface plasmon coupling, photonic crystal engineering, and microlens amplification. Recently, Liu group reported a new method to amplify upconversion emission through dielectric superlensing modulation (Liang et al. 2019a, b). The utilization of dielectric microbeads can modulate the wavefront of both excitation and emission fields, resulting in emission enhancement up to five orders of magnitude. Another extraordinary work by the same group has realized ultrafast radiative decay of activators with remarkable emission enhancement by taking advantage of surface plasmon coupling effects (Wu et al. 2019).

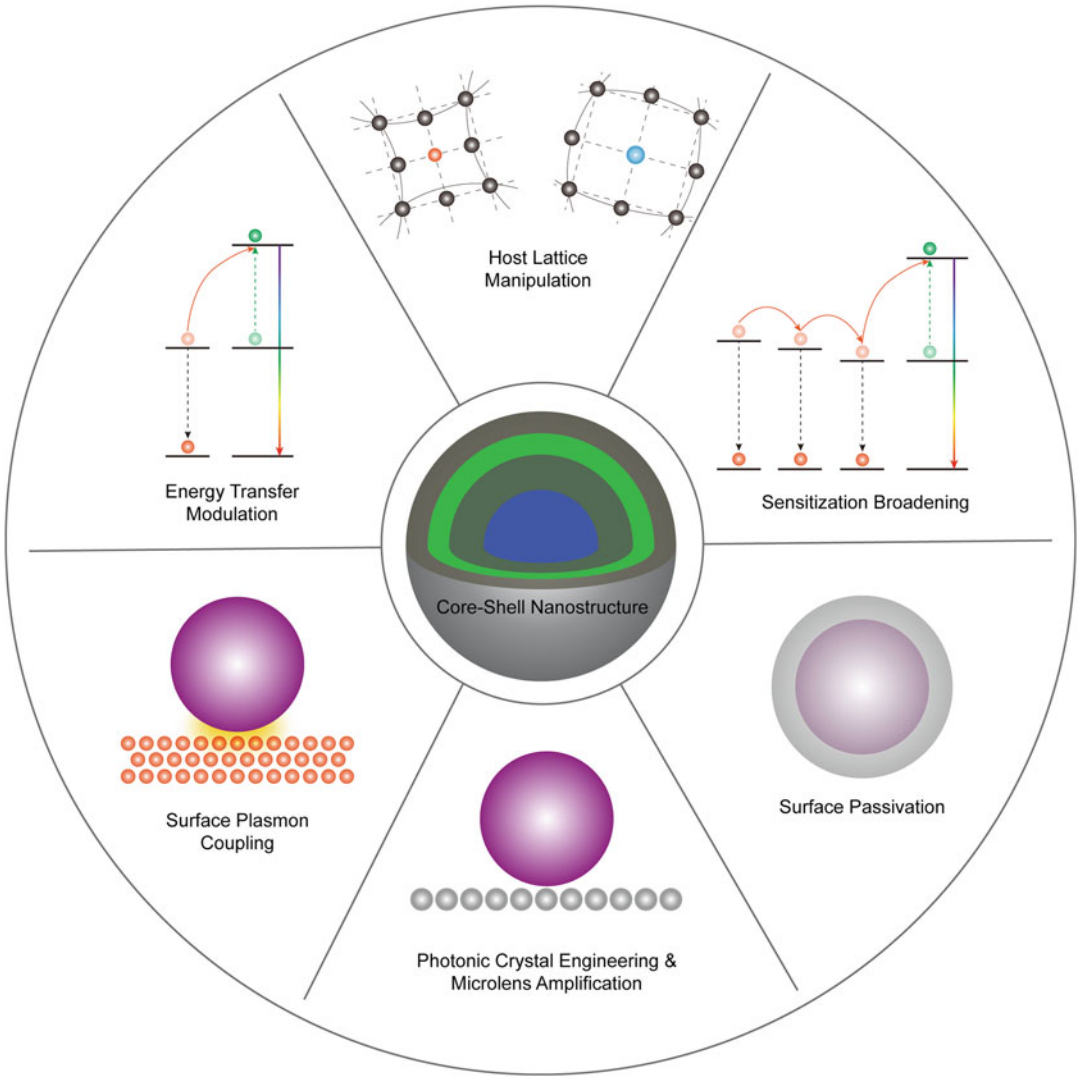


**Fig. 44.5** Generic strategies for emission enhancement of upconversion nanoparticles, including host lattice manipulation, energy transfer modulation, surface plasmon coupling, photonic crystal engineering, microlens amplification, surface passivation, sensitization broadening, and core-shell nanostructure design

## 44.4 Recent Progress in Upconversion Nanoparticle-Mediated Optogenetics

NIR optogenetic systems overcome the limitation of traditional optogenetics, such as insufficient delivery of visible light to the targeted area and inevitable tissue damage induced by invasive insertion of optical fiber and light source implantation. Over the past few years, upconversion nanoparticle-mediated optogenetics has been applied in in vitro cultured neurons and in vivo animal models such as *Caenorhabditis elegans*, zebra fish, and rodents (Fig. 44.6).

In 2015, in vitro neuron activity induced by NIR light was performed using a well-designed neuron culture system in which core-shell structured upconversion nanoparticles were

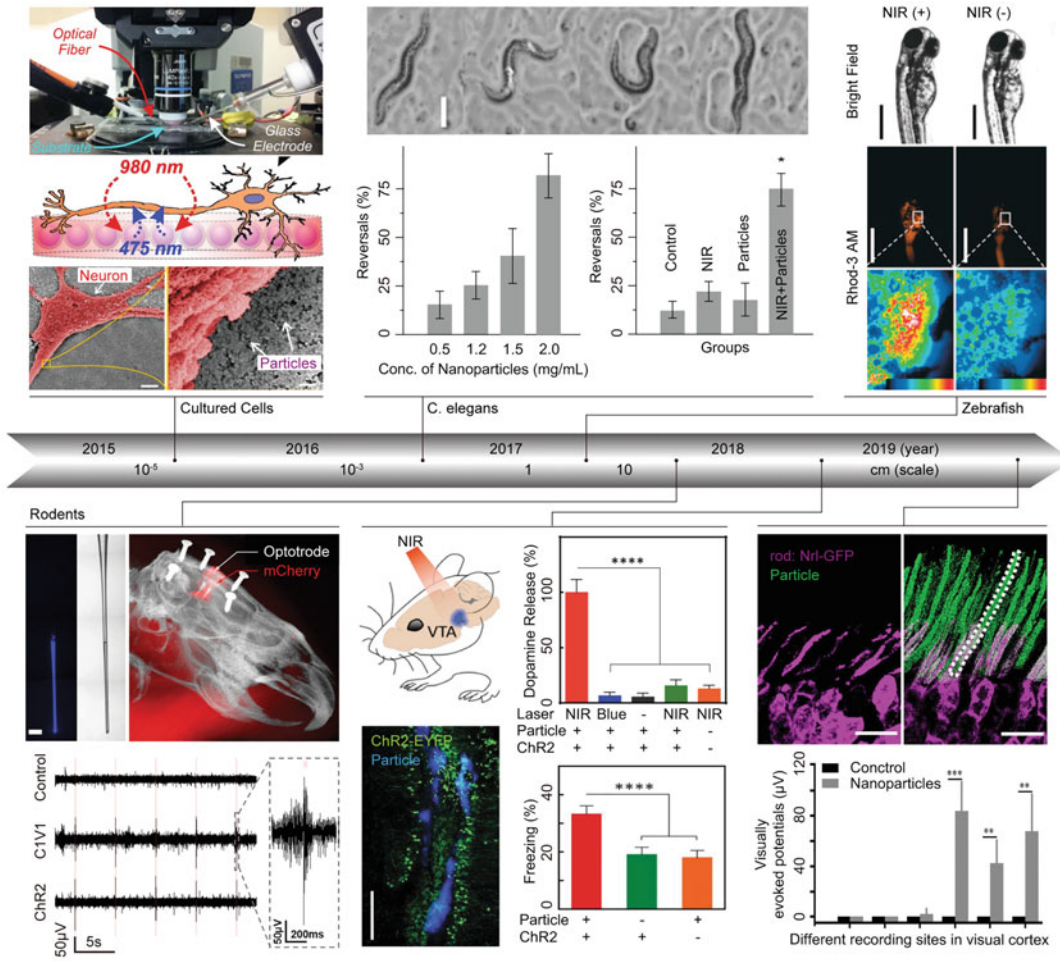


**Fig. 44.6** Representative breakthroughs in upconversion nanoparticle-mediated optogenetics. Panel for cultured cells: a photograph of the whole-cell patch-clamp system for in vitro NIR-enabled electrophysiological measurements (top), a schematic illustration of neurons cultured on the nanoparticle-containing substrate (middle), and the corresponding electron microscopy images (bottom) (Shah et al. 2015). Scale bar: 5 μm for the bottom left and 200 nm for the bottom right. Panel for *C. elegans*: microscopic images showing reversal behaviors of a ChR2-expressing worm under 980-nm laser irradiation, the effect of nanoparticle concentrations on the percentage of worms showing a reversal response (bottom left), and the reversal response percentage of different experimental groups (bottom right) (Bansal et al. 2016). Panel for zebra fish: bright-field and luminescence images of zebra fish incubated without/with upconversion nanoparticles (Ai et al. 2017). Scale bar:10 μm. Panels for rodents. Left panel: bright-field and fluorescent photographs of the nanoparticle-embedded micro-optrodes (top left), X-ray and luminescent merged image showing the co-localization of implanted micro-optrodes in ChR2-expressing region (top right), and electrophysiological records of NIR-driven spiking traces in rat expressing ChR2 or C1V1 (bottom) (Wang et al. 2017a, b). Scale bar: 500 μm. Middle panel: schematic illustration showing transcranial NIR stimulation of VTA dopamine neurons in vivo (top left) and dopamine release percentage in different experimental groups (top right), a confocal image showing the overlap between nanoparticles and ChR2 expression (bottom left), and freezing level of different groups (bottom right) (Chen et al. 2018). Scale bar: 200 μm. Right Panel: merged fluorescent images of the retina without/with nanoparticle injection (top) and visually evoked potentials triggered by 980-nm light at different sites in the visual cortex (bottom) (Ma et al. 2019). Scale bar: 10 μm

embedded into the cell culture substrate to in situ convert remotely delivered NIR light to the visible light (Shah et al. 2015). Under pulsed NIR excitation, high-temporal resolution neuron responses were recorded, and repetitive action potentials were observed at frequencies up to 10 Hz. In the same year, Yawo group also demonstrated the feasibility of NIR-induced neurostimulation using a whole-cell patch-clamp technique at the cellular level (Hososhima et al. 2015). In this study, C1V1 and *Platymonas subcordifonnis* (PsChR) expressing ND7/23 cells were cultured on collagen films containing upconversion nanocrystals, and whole-cell patch-clamp studies were adopted to record electrical signals on the cell membrane. Upon excitation of upconversion nanocrystals with a NIR laser, the researchers observed activated expressions of C1V1 or PsChR and neuronal responses induced by the upconverted visible light.

Early demonstrations of NIR-enabled in vivo optogenetics were carried out in *C. elegans* and zebra fish. *C. elegans* is a micron-sized, optically transparent worm with a nervous system of 302 neurons. *C. elegans* can be regarded as a simple in vivo model for genetic tractability and known connectome (Shipley et al. 2014). Bansal et al. successfully operated upconversion-mediated in vivo optogenetics in *C. elegans* (Bansal et al. 2016). In their study, nanoparticle-containing *C. elegans* with ChR2-expressing mechanosensory neurons exhibited altered movements in the presence or absence of NIR irradiation. Overheating and particle-induced toxicity were suppressed by utilizing a quasi-continuous wave laser with a low average power density and by optimizing the dosage of nanoparticles. Additionally, zebra fish is also a popular model in neurobehavioral studies because of its physiological and genetic homology with mammals (Best and Alderton 2008). In 2017, Ai et al. performed in vivo optogenetic manipulation on $Ca^{2+}$-mediated biological functions of zebra fish through activation of ChR2 ion channels by 808 nm-excitable and blue-emitting nanoparticles (Ai et al. 2017). The substitution of 980 nm with 808 nm excitation can effectively eliminate tissue overheating due to water absorption at 980 nm.

Despite the implementation of successful practices in cultured cells and transparent in vivo models, it is still challenging to apply NIR light-enabled optogenetics in mammals for transcranial deep brain modulation. The most effective way is to design better nanoparticle systems with the adequate capability of photon conversion under "remote" delivery of NIR light. Additionally, direct injection of nanoparticles to targeted areas is likely to maintain a desirable density of nanoparticles in situ in living animals. Suitable modifications on the surface of nanoparticles may address the concerns of possible particle-induced cytotoxicity, diffusion, and metabolism.

Mice is a commonly used animal model in genetic and medical research for the physiological resemblance of humans. Shi and Wang's groups managed to manipulate the motor behaviors of mice through activation and inhibition of neurons with implantable micro-scaled fibers embedded with upconversion nanoparticles (Wang et al. 2017a, b; Lin et al. 2017, 2018). Recently, Yamanaka's group also remotely controlled the free movement of mice by activating and inhibiting neurons where upconversion microparticles were directly injected at 2 mm below the brain surface (Miyazaki et al. 2019).

In 2018, Chen et al. demonstrated that precise control of multiplex deep brain modulation in rodents is viable through transcranial NIR excitations (Chen et al. 2018). In their work, ChR2-expressed neurons activated fear memory recollection through dopamine regulation, where core-shell structured nanoparticles with a silica coating at the outer layer were directly injected into the hippocampus of transgenic mice. Under NIR irradiation, the freely movable mice exhibited fear-induced freezing behavior even at 2 weeks after the injection. This approach was further expanded for inhibition of neural circuitry and provoking hippocampal theta oscillations. Nanoparticles were observed in the targeted area even 1 month after injection with low diffusion and long-term stability. Meanwhile, no obvious tissue damage, inflammation, or apoptosis was

found, implying low particle- or photo-induced cytotoxicity. This investigation elucidated the potential of luminescent nanomaterial-mediated optogenetics in mammals, especially on deep brain stimulation and neurological disorder therapies.

Upconversion-mediated optogenetics can also be a tool for breaking physiological visual limits. In 2019, Ma et al. first realized NIR image vision in rodent models through subretinal injection of photoreceptor-binding upconversion nanoparticles (Ma et al. 2019). After ocular injection, the mice could not only perceive NIR light but also see NIR light patterns with native daylight vision unaffected. This technique may present a new opportunity for security, ophthalmic therapy, and other medical use.

In addition to lanthanides-doped nanomaterials, triplet–triplet annihilation (TTA) molecules also present photon upconverting capability which may be used for NIR-mediated optogenetics. A recent study demonstrated the application of a TTA molecule-embedded hydrogel in NIR optogenetic genome editing where the morphology of hippocampal neurons can be regulated (Sasaki et al. 2019). However, TTA based optogenetics technology is still in its infancy since most of these molecules suffer common drawbacks from insolubility, structural and optical stability in physiological conditions, massive optical quenching effects, and their resultant upconversion efficiency limitation.

Other types of nanomaterials with photothermal or magnetothermal conversion capability can be used for neuromodulation. Commonly used photothermal nanotransducers include small molecules such as indocyanine green dye, organic polymers, carbon-based materials, noble metals, and semiconductors. For example, semiconducting polymer nanobioconjugates bound to TRPV1 (transient receptor potential cation channel subfamily V member 1) channels can act as energy transducers to convert NIR light to heat for the activation of intracellular $Ca^{2+}$ influx (Lyu et al. 2016). Similarly, magnetothermal conversion regulated by ferroferric oxide nanoparticles under alternating magnetic field was also identified for triggering widespread and reversible firing of $TRPV1^{+}$ neurons (Chen et al. 2015a, b). With further advances in nanoscience and nanotechnology, nanomaterials with energy-conversion capability can be instrumental to uncover the complex neural activities that would not be otherwise discoverable using conventional probes.

## 44.5 Outlook and Perspectives

Recent decades have witnessed significant progress in NIR light-enabled optogenetics. In this chapter, we have illustrated how upconversion nanomaterials can be used to manipulate cation flux in membrane vesicles with minimal invasiveness, deep-tissue penetration capability, and precise spatiotemporal perturbation. As with any other technique, upconversion nanoparticle-based optogenetics is not free of limitations. In particular, upconversion efficiency and biocompatibility of the nanoparticles need to be improved. Surface quenching effects may dominate in small-sized upconversion nanoparticles and cause complications for optogenetic manipulation. This could be overcome by rational design of dopant composition and core-shell structure. Additional surface modification of nanoparticles can boost biocompatibility and impart added functions such as bio-labeling, targeting, and multiplex control of neurons. The advances in NIR-mediated optogenetics will also rely on new populations of opsin variants as well as innovative instrumentation. Exploiting new classes of opsins will enable us to maximize the potential of upconversion emission and optimize the effect of the optical response. Next-generation NIR-mediated light sources and opsin-mediated neural modulation in combination with novel recording instruments will certainly improve outcomes of in vivo optogenetic techniques.

**Acknowledgments** This work was supported by the Singapore Ministry of Education (MOE2017-T2-2-110), Agency for Science, Technology and Research (A*STAR) (A1883c0011 and A1983c0038), National Research Foundation, Prime Minister's Office, Singapore under the NRF Investigatorship programme (Award No. NRF-NRFI05-

2019-0003), and National Natural Science Foundation of China (21771135).

## References


Abel KA, Boyer JC, Veggel FCJM (2009) Hard proof of the $NaYF_4/NaGdF_4$ nanocrystal core/shell structure. J Am Chem Soc 131:14,644–14,645

Ai X, Lyu L, Zhang Y et al (2017) Remote regulation of membrane channel activity by site-specific localization of lanthanide-doped upconversion nanocrystals. Angew Chem Int Ed 56:3031–3035

All AH, Zeng X, Teh DBL et al (2019) Expanding the toolbox of upconversion nanoparticles for in vivo optogenetics and neuromodulation. Adv Mater 31:1803474

Auzel F (2004) Upconversion and anti-stokes processes with f and d ions in solids. Chem Rev 104:139–174

Bansal A, Liu H, Jayakumar MKG et al (2016) Quasi-continuous wave near-infrared excitation of upconversion nanoparticles for optogenetic manipulation of C. elegans. Small 12:1732–1743

Best JD, Alderton WK (2008) Zebrafish: an in vivo model for the study of neurological diseases. Neuropsychiatr Dis Treat 4(3):567–576

Bloembergen N (1959) Solid state infrared quantum counters. Phys Rev Lett 2:84–85

Bogdan N, Vetrone F, Ozin GA et al (2011) Synthesis of ligand-free colloidally stable water dispersible brightly luminescent lanthanide-doped upconverting nanoparticles. Nano Lett 11:835–840

Boyden ES, Zhang F, Bamberg E et al (2005) Millisecond-timescale, genetically targeted optical control of neural activity. Nat Neurosci 8:1263–1268

Cardin JA, Carlén M, Meletis K et al (2010) Targeted optogenetic stimulation and recording of neurons in vivo using cell-type-specific expression of Channelrhodopsin-2. Nat Protoc 5:247–254

Chen S (2019) Optical modulation goes deep in the brain. Science 365:456–457

Chen G, Liu H, Liang H et al (2008) Upconversion emission enhancement in $Yb^{3+}/Er^{3+}$-codoped $Y_2O_3$ nanocrystals by tridoping with $Li^+$ ions. J Phys Chem C 112:12,030–12,036

Chen G, Shen J, Ohulchanskyy TY et al (2012) ($\alpha$-$NaYbF_4$:$Tm^{3+}$)/$CaF_2$ core/shell nanoparticles with efficient near-infrared to near-infrared upconversion for high-contrast deep tissue bioimaging. ACS Nano 6:8280–8287

Chen G, Damasco JA, Qiu H et al (2015a) Energy cascaded upconversion in an organic dye-sensitized core/shell fluoride nanocrystal. Nano Lett 15:7400–7407

Chen R, Romero G, Christiansen MG et al (2015b) Wireless magnetothermal deep brain stimulation. Science 347:1477–1480

Chen Q, Xie X, Huang B et al (2017) Confining excitation energy in $Er^{3+}$-sensitized upconversion nanocrystals through $Tm^{3+}$-mediated transient energy trapping. Angew Chem Int Ed 56:7605–7609

Chen S, Weitemier AZ, Zeng X et al (2018) Near-infrared deep brain stimulation via upconversion nanoparticle-mediated optogenetics. Science 359:679–684

Chen B, Kong W, Wang N et al (2019) Oleylamine-mediated synthesis of small $NaYbF_4$ nanoparticles with tunable size. Chem Mater 31:4779–4786

Deisseroth K (2011) Optogenetics. Nat Methods 8:26–29

Deisseroth K, Anikeeva P (2016) Upconversion of light for use in optogenetic methods: U.S. patent 9,522,288

Deng R, Xie X, Vendrell M et al (2011) Intracellular glutathione detection using $MnO_2$-nanosheet-modified upconversion nanoparticles. J Am Chem Soc 133:20,168–20,171

Fenno L, Yizhar O, Deisseroth K (2011) The Development and Application of Optogenetics. Annu Rev Neurosci 34:389–412

Fork RL (1971) Laser stimulation of nerve cells in Aplysia. Science 171:907–908

Gargas DJ, Chan EM, Ostrowski AD et al (2014) Engineering bright sub-10-nm upconverting nanocrystals for single-molecule imaging. Nat Nanotechnol 9:300–305

Gnach A, Lipinski T, Bednarkiewicz A et al (2015) Upconverting nanoparticles: assessing the toxicity. Chem Soc Rev 44:1561–1584

Han S, Qin X, An Z et al (2016) Multicolour synthesis in lanthanide-doped nanocrystals through cation exchange in water. Nat Commun 7:13,059

Han S, Samanta A, Xie X et al (2017) Gold and Hairpin DNA functionalization of upconversion nanocrystals for imaging and in vivo drug delivery. Adv Mater 29:1700244

Heer S, Kömpe K, Güdel HU et al (2004) Highly efficient multicolour upconversion emission in transparent colloids of lanthanide-doped $NaYF_4$ nanocrystals. Adv Mater 16:2102–2105

Hososhima S, Yuasa H, Ishizuka T et al (2015) Near-infrared (NIR) up-conversion optogenetics. Sci Rep 5:16,533

Ishizuka T, Kakuda M, Araki R et al (2006) Kinetic evaluation of photosensitivity in genetically engineered neurons expressing green algae light-gated channels. Neurosci Res 54:85–94

Kramer RH, Mourot A, Adesnik H (2013) Optogenetic pharmacology for control of native neuronal signaling proteins. Nat Neurosci 16:816–823

Kringelbach ML, Jenkinson N, Owen SLF et al (2007) Translational principles of deep brain stimulation. Nat Rev Neurosci 8:623–635

Li Z, Zhang Y (2006) Monodisperse silica-coated polyvinylpyrrolidone/$NaYF_4$ nanocrystals with multicolor upconversion fluorescence emission. Angew Chem Int Ed 45:7732–7735

Li Z, Zhang Y (2008) An efficient and user-friendly method for the synthesis of hexagonal-phase $NaYF_4$: Yb,Er/Tm nanocrystals with controllable shape and

upconversion fluorescence. Nanotechnology 19:345606
Liang L, Xie X, Loong DTB et al (2016) Designing upconversion nanocrystals capable of 745 nm sensitization and 803 nm emission for deep-tissue imaging. Chem Eur J 22:10,801–10,807
Liang L, Qin X, Zheng K et al (2019a) Energy flux manipulation in upconversion nanosystems. Acc Chem Res 52:228–236
Liang L, Teh DBL, Dinh ND et al (2019b) Upconversion amplification through dielectric superlensing modulation. Nat Commun 10:1391
Lin X, Wang Y, Chen X et al (2017) Multiplexed optogenetic stimulation of neurons with spectrum-selective upconversion nanoparticles. Adv Healthc Mater 6:1700446
Lin X, Chen X, Zhang W et al (2018) Core-shell-shell upconversion nanoparticles with enhanced emission for wireless optogenetic inhibition. Nano Lett 18:948–956
Liu J, Bu W, Zhang S et al (2012) Controlled synthesis of uniform and monodisperse upconversion core/mesoporous silica shell nanocomposites for bimodal imaging. Chem Eur J 18:2335–2341
Liu X, Wang Y, Li X et al (2017) Binary temporal upconversion codes of $Mn^{2+}$-activated nanoparticles for multilevel anti-counterfeiting. Nat Commun 8:899
Lyu Y, Xie C, Chechetka SA et al (2016) Semiconducting polymer nanobioconjugates for targeted photothermal activation of neurons. J Am Chem Soc 138:9049–9052
Ma Y, Bao J, Zhang Y et al (2019) Mammalian near-infrared image vision through injectable and self-powered retinal nanoantennae. Cell 177:243–255
McAlinden N, Gu E, Dawson MD et al (2015) Optogenetic activation of neocortical neurons in vivo with a sapphire-based micro-scale LED probe. Front Neural Circuits 9:25
Miller C (1989) Genetic manipulation of ion channels: a new approach to structure and mechanism. Neuron 2:1195–1205
Miyazaki T, Chowdhury S, Yamashita T et al (2019) Large timescale interrogation of neuronal function by fiberless optogenetics using lanthanide micro-particles. Cell Rep 26:1033–1043
Pollnau M, Gamelin DR, Lüthi SR et al (2000) Power dependence of upconversion luminescence in lanthanide and transition-metal-ion systems. Phys Rev B 61:3337–3346
Rao L, Bu LL, Cai B et al (2016) Cancer cell membrane-coated upconversion nanoprobes for highly specific tumor imaging. Adv Mater 28:3460–3466
Ren W, Tian G, Jian S et al (2012) Tween coated $NaYF_4$: Yb,Er/$NaYF_4$ core/shell upconversion nanoparticles for bioimaging and drug delivery. RSC Adv 2:7037–7041
Sasaki Y, Oshikawa M, Bharmoria P et al (2019) Near-infrared optogenetic genome engineering based on photon upconversion hydrogels. Angew Chem Int Ed 58:2–9
Sedlmeier A, Gorris HH (2014) Surface modification and characterization of photon-upconverting nanoparticles for bioanalytical applications. Chem Soc Rev 44:1526–1560
Shah S, Liu JJ, Pasquale N et al (2015) Hybrid upconversion nanomaterials for optogenetic neuronal control. Nanoscale 7:16,571–16,577
Shen J, Chen G, Vu AM et al (2013) Engineering the upconversion nanoparticle excitation wavelength: cascade sensitization of tri-doped upconversion colloidal nanoparticles at 800 nm. Adv Opt Mater 1:644–650
Shipley FB, Clark CM, Alkema MJ et al (2014) Simultaneous optogenetic manipulation and calcium imaging in freely moving C. elegans. Front Neural Circuits 8:28
Suyver JF, Grimm J, Van Veen MK et al (2006) Upconversion spectroscopy and properties of $NaYF_4$ doped with $Er^{3+}$, $Tm^{3+}$ and/or $Yb^{3+}$. J Lumines 117:1–12
Tian G, Gu Z, Zhou L et al (2012) $Mn^{2+}$ dopant-controlled synthesis of NaYF4: Yb/Er upconversion nanoparticles for in vivo imaging and drug delivery. Adv Mater 24(9):1226–1231
Urmann D, Lorenz C, Linker SM et al (2017) Photochemical properties of the red-shifted channelrhodopsin Chrimson. Photochem Photobiol 93:782–795
Wang L, Li Y (2007) Controlled synthesis and luminescence of lanthanide-doped $NaYF_4$ nanocrystals. Chem Mater 19:727–734
Wang F, Liu X (2008) Upconversion multicolor fine-tuning: visible to near-infrared emission from lanthanide-doped $NaYF_4$ nanoparticles. J Am Chem Soc 130:5642–5643
Wang F, Liu X (2009) Recent advances in the chemistry of lanthanide-doped upconversion nanocrystals. Chem Soc Rev 38:976–989
Wang X, Zhuang J, Peng Q et al (2005) A general strategy for nanocrystal synthesis. Nature 437:121–124
Wang F, Han Y, Lim CS et al (2010) Simultaneous phase and size control of upconversion nanocrystals through lanthanide doping. Nature 463:1061–1065
Wang F, Deng R, Wang J et al (2011a) Tuning upconversion through energy migration in core-shell nanoparticles. Nat Mater 10:968
Wang J, Wang F, Wang C et al (2011b) Single-band upconversion emission in lanthanide-doped $KMnF_3$ nanocrystals. Angew Chem Int Ed 50:10,369–10,372
Wang B, He X, Zhang Z et al (2012) Metabolism of nanomaterials in vivo: blood circulation and organ clearance. Acc Chem Res 46:761–769
Wang F, Deng R, Liu X (2014) Preparation of core-shell $NaGdF_4$ nanoparticles doped with luminescent lanthanide ions to be used as upconversion-based probes. Nat Protoc 9:1634–1644
Wang Z, Zhang P, Yuan Q et al (2015) $Nd^{3+}$-sensitized $NaLuF_4$ luminescent nanoparticles for multimodal imaging and temperature sensing under 808 nm excitation. Nanoscale 7:17,861–17,870
Wang Y, Lin X, Chen X et al (2017a) Tetherless near-infrared control of brain activity in behaving animals

using fully implantable upconversion microdevices. Biomaterials 142:136–148
Wang X, Valiev RR, Ohulchanskyy TY et al (2017b) Dye-sensitized lanthanide-doped upconversion nanoparticles. Chem Soc Rev 46:4150–4167
Wang Z, Hu M, Ai X et al (2019) Near-infrared manipulation of membrane ion channels via upconversion optogenetics. Adv Biosyst 3:1800233
Wen S, Zhou J, Zheng K et al (2018) Advances in highly doped upconversion nanoparticles. Nat Commun 9:2415
Wu X, Zhang Y, Takle K et al (2016) Dye-sensitized core/active shell upconversion nanoparticles for optogenetics and bioimaging applications. ACS Nano 10:1060–1066
Wu Y, Xu J, Poh ET et al (2019) Upconversion superburst with sub-2 μs lifetime. Nat Nanotechnol 14:1110. https://doi.org/10.1038/s41565-019-0560-5
Xie X, Gao N, Deng R et al (2013) Mechanistic investigation of photon upconversion in $Nd^{3+}$-sensitized core-shell nanoparticles. J Am Chem Soc 135:12,608–12,611
Xiong L, Yang T, Yang Y et al (2010) Long-term in vivo biodistribution imaging and toxicity of polyacrylic acid-coated upconversion nanophosphors. Biomaterials 31:7078–7085
Ye X, Collins JE, Kang Y et al (2010) Morphologically controlled synthesis of colloidal upconversion nanophosphors and their shape-directed self-assembly. Proc Natl Acad Sci U S A 107:22,430–22,435
Yi GS, Chow GM (2006) Synthesis of hexagonal-phase $NaYF_4$:Yb,Er and $NaYF_4$:Yb,Tm nanocrystals with efficient up-conversion fluorescence. Adv Funct Mater 16:2324–2329
Yi GS, Chow GM (2007) Water-soluble $NaYF_4$:Yb,Er (Tm)/$NaYF_4$/polymer core/shell/shell nanoparticles with significant enhancement of upconversion fluorescence. Chem Mater 19:341–343
Yi Z, Luo Z, Barth ND et al (2019) In vivo tumor visualization through MRI off-on switching of $NaGdF_4$–$CaCO_3$ nanoconjugates. Adv Mater 31:1901851
Yu N, Huang L, Zhou Y et al (2019) Near-infrared-light activatable nanoparticles for deep-tissue-penetrating wireless optogenetics. Adv Healthc Mater 8:1801132
Zamponi GW (2016) Targeting voltage-gated calcium channels in neurological and psychiatric diseases. Nat Rev Drug Discov 15:19–34
Zeng S, Tsang MK, Chan CF et al (2012) PEG modified $BaGdF_5$:Yb/Er nanoprobes for multi-modal upconversion fluorescent, in vivo X-ray computed tomography and biomagnetic imaging. Biomaterials 33:9232–9238
Zhang YW, Sun X, Si R et al (2005) Single-crystalline and monodisperse $LaF_3$ triangular nanoplates from a single-source precursor. J Am Chem Soc 127:3260–3261
Zhang F, Prigge M, Beyrière F et al (2008) Red-shifted optogenetic excitation: a tool for fast neural control derived from Volvox carteri. Nat Neurosci 11:631–633
Zhang Y, Huang L, Liu X (2016) Unraveling epitaxial habits in the $NaLnF_4$ system for color multiplexing at the single-particle level. Angew Chem Int Ed 55:5718–5722
Zhao J, Jin D, Schartner EP et al (2013) Single-nanocrystal sensitivity achieved by enhanced upconversion luminescence. Nat Nanotechnol 8:729–734
Zheng K, Han S, Zeng X et al (2018) Rewritable optical memory through high-registry orthogonal upconversion. Adv Mater 30:1801726
Zhou B, Shi B, Jin D et al (2015a) Controlling upconversion nanocrystals for emerging applications. Nat Nanotechnol 10:924–936
Zhou L, Wang R, Yao C et al (2015b) Single-band upconversion nanoprobes for multiplexed simultaneous in situ molecular mapping of cancer biomarkers. Nat Commun 6:6938
Zou W, Visser C, Maduro JA et al (2012) Broadband dye-sensitized upconversion of near-infrared light. Nat Photonics 6:560–564

# Correction to: Holographic Imaging and Stimulation of Neural Circuits

Weijian Yang and Rafael Yuste

**Correction to:**
**Chapter 43 in: H. Yawo et al. (eds.), *Optogenetics*, Advances in Experimental Medicine and Biology 1293, https://doi.org/10.1007/978-981-15-8763-4_43**

This chapter was inadvertently published with incorrect information in Table 43.1, which has been corrected as below:

The updated online version of this chapter can be found at
https://doi.org/10.1007/978-981-15-8763-4_43



H. Yawo et al. (eds.), *Optogenetics*, Advances in Experimental Medicine and Biology 1293,
https://doi.org/10.1007/978-981-15-8763-4_45

**Table 43.1** Comparison between different light illumination approaches used in optical microscopes

| | | | Wide-field illumination | Point scanning illumination | Holographic illumination |
|---|---|---|---|---|---|
| Imaging | Transparent sample | Technique | Epifluorescence (one photon) | Confocal (one photon) | Two-photon |
| | | Advantage | High temporal resolution | High spatial resolution | Low background; high spatial resolution; improved temporal resolution |
| | | Limitation | Low axial resolution; phototoxicity | Reduced temporal resolution; phototoxicity | |
| | Scattering sample | Technique | Epifluorescence (one photon), mainly for superficial layers | Two photon | Two photon |
| | | Advantage | High temporal resolution | Low background; high spatial resolution | Low background; high spatial resolution; improved temporal resolution |
| | | Limitation | High background; low spatial resolution; phototoxicity | Low temporal resolution | |
| Photo stimulation | Transparent sample | Technique | One photon | One photon/two photon | One photon/two photon |
| | | Advantage | High temporal specificity | Improved/high spatial specificity | Improved/high spatial specificity; high temporal specificity |
| | | Limitation | Low spatial specificity | Low temporal specificity | |
| | Scattering sample | Technique | One photon | Two photon | Two photon |
| | | Advantage | High temporal specificity | High spatial specificity | High spatial specificity; high temporal specificity |
| | | Limitation | Low spatial specificity | Low temporal specificity | |

# Index





H. Yawo et al. (eds.), *Optogenetics*, Advances in Experimental Medicine and Biology 1293,
https://doi.org/10.1007/978-981-15-8763-4